



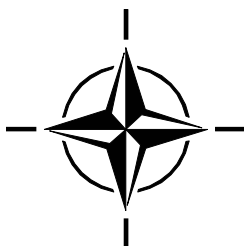
RTO TECHNICAL REPORT

TR-AVT-080

Vortex Breakdown over Slender Delta Wings

(Eclatement tourbillonnaire sur les ailes delta effilées)

This Report documents the goals and achievements
of NATO/RTO/AVT Task Group AVT-080.



Published October 2009





RTO TECHNICAL REPORT

TR-AVT-080

Vortex Breakdown over Slender Delta Wings

(Eclatement tourbillonnaire sur les ailes delta effilées)

This Report documents the goals and achievements
of NATO/RTO/AVT Task Group AVT-080.

The Research and Technology Organisation (RTO) of NATO

RTO is the single focus in NATO for Defence Research and Technology activities. Its mission is to conduct and promote co-operative research and information exchange. The objective is to support the development and effective use of national defence research and technology and to meet the military needs of the Alliance, to maintain a technological lead, and to provide advice to NATO and national decision makers. The RTO performs its mission with the support of an extensive network of national experts. It also ensures effective co-ordination with other NATO bodies involved in R&T activities.

RTO reports both to the Military Committee of NATO and to the Conference of National Armament Directors. It comprises a Research and Technology Board (RTB) as the highest level of national representation and the Research and Technology Agency (RTA), a dedicated staff with its headquarters in Neuilly, near Paris, France. In order to facilitate contacts with the military users and other NATO activities, a small part of the RTA staff is located in NATO Headquarters in Brussels. The Brussels staff also co-ordinates RTO's co-operation with nations in Middle and Eastern Europe, to which RTO attaches particular importance especially as working together in the field of research is one of the more promising areas of co-operation.

The total spectrum of R&T activities is covered by the following 7 bodies:

- AVT Applied Vehicle Technology Panel
- HFM Human Factors and Medicine Panel
- IST Information Systems Technology Panel
- NMSG NATO Modelling and Simulation Group
- SAS System Analysis and Studies Panel
- SCI Systems Concepts and Integration Panel
- SET Sensors and Electronics Technology Panel

These bodies are made up of national representatives as well as generally recognised 'world class' scientists. They also provide a communication link to military users and other NATO bodies. RTO's scientific and technological work is carried out by Technical Teams, created for specific activities and with a specific duration. Such Technical Teams can organise workshops, symposia, field trials, lecture series and training courses. An important function of these Technical Teams is to ensure the continuity of the expert networks.

RTO builds upon earlier co-operation in defence research and technology as set-up under the Advisory Group for Aerospace Research and Development (AGARD) and the Defence Research Group (DRG). AGARD and the DRG share common roots in that they were both established at the initiative of Dr Theodore von Kármán, a leading aerospace scientist, who early on recognised the importance of scientific support for the Allied Armed Forces. RTO is capitalising on these common roots in order to provide the Alliance and the NATO nations with a strong scientific and technological basis that will guarantee a solid base for the future.

The content of this publication has been reproduced
directly from material supplied by RTO or the authors.

Published October 2009

Copyright © RTO/NATO 2009
All Rights Reserved

ISBN 978-92-837-0078-4

Single copies of this publication or of a part of it may be made for individual use only. The approval of the RTA Information Management Systems Branch is required for more than one copy to be made or an extract included in another publication. Requests to do so should be sent to the address on the back cover.

Table of Contents

	Page
List of Figures	xiv
List of Tables	xxxiv
Working Group Members	xxxv
 Executive Summary and Synthèse	 ES-1
 Chapter 1 – Introduction and Highlights	 1-1
Abstract	1-1
1.1 Introduction and Background	1-1
1.2 Objectives and Criteria of AVT-080	1-3
1.2.1 Objectives	1-3
1.2.2 Requirements for Candidate of Experimental Cases	1-3
1.3 Progress of Experimental Sub-Group	1-4
1.3.1 Test Case Categories	1-4
1.3.2 Overview of Published Experimental Data Sets	1-5
1.3.3 Benchmark for the CFD Exercise	1-8
1.4 Overview of CFD Solutions	1-8
1.5 Overview of Analytical Solutions	1-12
1.6 Conclusions and Recommendations	1-13
1.7 Acknowledgments	1-13
1.8 References	1-13
 Chapter 2 – Critical Assessment of Test Cases on Vortex Breakdown over Slender Delta Wings under Static Model Conditions	 2-1
Abstract	2-1
List of Symbols	2-1
2.1 Introduction	2-2
2.2 Results on Measured Vortex Breakdown Locations	2-3
2.3 Criteria of the Assessment	2-4
2.4 Effects of Leading-Edge Shape, Centerbody and Different Test Conditions	2-5
2.4.1 Leading-Edge Shape Effect	2-5
2.4.2 Centerbody Effects	2-7
2.4.3 Reynolds Number and Mach Number Effects	2-8
2.5 Assessment for the Results with 65° Delta Wing	2-9
2.6 Assessment of the Results with 70° Delta Wing	2-11
2.7 Conclusions	2-12
2.8 References	2-12

Chapter 3 – Experimental Data Base Selected for Numerical and Analytical Validation and Verification: ONERA 70-Deg Delta Wing **3-1**

Abstract	3-1
3.1 Nomenclature	3-1
3.2 Introduction	3-1
3.3 Wind Tunnel	3-2
3.4 Models	3-3
3.5 Experimental Methods	3-5
3.5.1 Laser Sheet Visualization	3-6
3.5.2 Surface Oil Flow	3-8
3.5.3 Surface Pressure	3-8
3.5.4 Laser Doppler Velocimetry (LDV)	3-8
3.6 Experimental Error and Accuracy	3-9
3.7 Results	3-9
3.7.1 Laser Sheet Visualization	3-9
3.7.2 Surface Oil Flow	3-11
3.7.3 Surface Pressure	3-12
3.7.4 Laser Doppler Velocimetry	3-13
3.8 Conclusions	3-17
3.9 References	3-17

Chapter 4 – Experimental Investigation of the Flow about a 65° Delta Wing in the NASA Langley National Transonic Facility **4-1**

Abstract	4-1
4.1 Nomenclature	4-1
4.2 Introduction	4-2
4.3 Experimental Program	4-3
4.3.1 Facility	4-3
4.3.2 Model	4-4
4.3.3 Test Program	4-5
4.4 Sample Results	4-5
4.4.1 Contrast of Sharp-Leading-Edge and Blunt-Leading-Edge Flows	4-5
4.4.2 Reynolds Number Effect	4-6
4.4.3 Compressibility Effect	4-6
4.4.4 Separation Onset and Progression Analysis	4-6
4.5 Concluding Remarks	4-7
4.6 References	4-7

Appendix – AVT-080 Data Set **4-9**

1.0 General Description of Model	4-9
2.0 Model Geometry	4-9
3.0 Wind/Water Tunnel	4-10
4.0 Model Motion	4-10
5.0 Test Conditions	4-10
6.0 Measurements and Observations	4-11

7.0	Instrumentation	4-11
8.0	Data Presentation	4-12
9.0	Comments on Data	4-13

Chapter 5 – Comprehensive Experimental Studies on Vortex Dynamics over Military Wing Configurations in IAR **5-1**

Abstract	5-1
5.1 Introduction	5-1
5.2 Experimental Set-Up	5-2
5.2.1 Exploited Areas	5-2
5.2.2 Wind Tunnels	5-3
5.2.3 Models	5-3
5.2.4 Rigs	5-4
5.2.4.1 Roll Rig	5-4
5.2.4.2 Pitch Rig	5-4
5.2.4.3 Coning Rig	5-4
5.2.4.4 Rigs in Static Tests	5-5
5.2.5 Experimental Techniques	5-5
5.2.5.1 Flow Visualization	5-5
5.2.5.2 Unsteady Measurements	5-5
5.2.5.3 PSP and PIV Techniques	5-5
5.2.5.4 Free-to-Roll and “Forced” Free-to-Roll Operation	5-6
5.3 Samples of Experimental Results	5-6
5.3.1 Surface Flow Visualization	5-6
5.3.2 Off Surface (Laser Smoke Sheet and PIV) Flow Visualization	5-7
5.3.3 Off Surface (Dye Injection) Flow Visualization	5-7
5.3.4 Force and Moment Measurements	5-8
5.3.5 Surface Pressure Measurements	5-9
5.3.6 Free-to-Roll Experiments	5-11
5.3.7 Forebody/Wing/Tail Results	5-11
5.4 Conclusions	5-11
5.5 References	5-11
Appendix – Briefing of IAR Program	5-12
General Description of the Models	5-12
Model Geometry	5-12
Wind Tunnels/Water Tunnel	5-12
Model Motion	5-12
Test Conditions	5-13
Measurements	5-13
Instrumentation	5-14

Chapter 6 – Unsteady Aspects of Leading-Edge Vortices **6-1**

Abstract	6-1
Nomenclature	6-1
6.1 Introduction	6-2

6.2	Shear Layer Instabilities	6-2
6.3	Vortex Wandering	6-4
6.4	Vortex Breakdown	6-6
6.4.1	Helical Mode Instability	6-7
6.4.2	Oscillations of Breakdown Location	6-10
6.5	Leading Edge Vortices in Unsteady Flows	6-16
6.6	Vortex Breakdown in Unsteady Flows	6-17
6.6.1	Response of Vortex Breakdown	6-19
6.6.2	Mechanism of Time Lag	6-21
6.7	Vortex Shedding	6-22
6.8	Wing and Fin Buffeting	6-24
6.9	Wing Rock Phenomenon	6-27
6.10	Unsteady Vortex Control	6-28
6.11	Issues and Challenges	6-30
6.12	Acknowledgements	6-31
6.13	References	6-31

Chapter 7 – Leading Edge Vortex Flow Studies at the University of Notre Dame Steady and Unsteady Investigations 1983-2000 **7-1**

Abstract		7-1
7.1	Background	7-1
7.2	Introduction	7-1
7.3	Leading Edge Vortex Structure	7-3
7.3.1	Flow Visualization Results	7-3
7.3.2	Seven Hole Probe Measurements	7-4
7.3.3	LDV Measurements	7-5
7.3.4	Vorticity and Circulation Distribution	7-9
7.3.5	Vorticity	7-10
7.3.6	Circulation	7-12
7.3.7	Vortex Strength Correlation	7-13
7.4	Unsteady Slender Wing Aerodynamics and Flow Structure	7-16
7.5	Free and Forced to Roll Motion Studies	7-19
7.6	Summary	7-23
7.7	Acknowledgements	7-24
7.8	References	7-24

Chapter 8 – Topology of the Flow on 65° Delta Wings **8-1**

Abstract	8-1
Keywords	8-1
8.1 Introduction	8-1
8.2 Brief of Topology	8-2
8.2.1 Surface Flow Topology	8-2
8.2.2 Bifurcation in Flow Topology	8-4
8.2.3 Correlation Studies of Two Topological Spaces	8-5

8.3	TUD Experiments	8-7
8.3.1	Experimental Set-Up	8-7
8.3.2	Flow Visualisation and Topological Analysis	8-7
8.3.2.1	Observed Unsteady Behaviour	8-7
8.3.2.2	Flow Pattern on Lower Surface and its Topology	8-7
8.3.2.3	Flow Pattern on Upper Surface and its Topology	8-9
8.3.2.4	Flow Pattern on Apex Models	8-11
8.4	IAR/USAF Experiments	8-14
8.4.1	Experimental Set-Up	8-14
8.4.2	Flow Visualisation and Topological Analysis	8-15
8.4.2.1	Flow Visualisation	8-15
8.4.2.2	Flow Topology Analysis	8-18
8.4.2.3	Evolution of Flow Topologies	8-21
8.4.2.4	Correlation Study between Topology Change and Critical States	8-21
8.4.2.5	Possible Three-Dimensional Flow Structure	8-23
8.5	Conclusions	8-24
8.6	References	8-24

Chapter 9 – TsAGI 70° and 65° Delta Wings Test Cases 9-1

Abstract	9-1
9.1	Introduction 9-1
9.2	Aerodynamic Models Geometry 9-1
9.3	Wind Tunnel 9-2
9.4	Dynamic Rigs 9-2
9.5	Data Processing Technique 9-3
9.6	Some Comparisons with Published Data in Steady Cases 9-4
9.7	Some Comparisons in Dynamic Cases 9-5
9.8	Steady Experimental Results 9-5
9.9	Large Amplitude Pitch Oscillations Experimental Results 9-6
9.10	Small Amplitude Pitch Oscillations Experimental Results 9-6
9.11	Concluding Remarks 9-7
9.12	Acknowledgement 9-7
9.13	References 9-7

Chapter 10 – Experimental Investigation of Vortex Dynamics on a 65° Delta Wing 10-1

Abstract	10-1
Nomenclature	10-2
10.1	Introduction 10-3
10.2	Experimental Facilities 10-4
10.2.1	Static Tests 10-6
10.2.2	Dynamic Tests 10-9
10.2.3	IR Thermography 10-10
10.3	Concluding Remarks 10-12
10.4	References 10-12

Chapter 11 – Vortical Flow Prediction Using an Adaptive Unstructured Grid Method **11-1**

Abstract	11-1
11.1 Introduction	11-1
11.2 Computational Method	11-3
11.2.1 Grid Generation	11-4
11.2.2 Flow Solution	11-4
11.2.3 Grid Adaptation	11-5
11.3 Results	11-6
11.3.1 65-Degree Delta Wing	11-7
11.3.1.1 Sharp Leading-Edge (Radius = 0.0 % <i>MAC</i>)	11-9
11.3.1.2 Medium Leading-Edge (Radius = 0.15 % <i>MAC</i>)	11-18
11.3.1.3 Large Leading-Edge (Radius = 0.30 % <i>MAC</i>)	11-22
11.3.2 Modular Transonic Vortex Interaction Configuration	11-27
11.4 Concluding Remarks	11-34
11.5 Acknowledgements	11-35
11.6 References	11-35

Chapter 12 – Origin of Stationary Shear-Layer Sub-Structures above Delta Wings **12-1**

Abstract	12-1
12.1 Introduction	12-1
12.2 Computational Approach	12-3
12.2.1 Governing Equations	12-3
12.2.2 Spatial Discretization	12-4
12.2.3 Low-Pass Spatial Filtering Scheme	12-4
12.2.4 Evaluation of Coordinate Transformation Metrics	12-5
12.2.5 Time Integration	12-5
12.3 Results	12-6
12.3.1 Flow Configuration and Boundary Conditions	12-6
12.3.2 Preliminary Considerations	12-7
12.3.3 Reynolds Number Effects	12-7
12.3.4 Instantaneous Shear-Layer Structure	12-9
12.3.5 Time-Averaged Shear-Layer Structure	12-11
12.3.6 Relation of Unsteady and Time-Averaged Vortical Substructures	12-11
12.4 Concluding Remarks	12-12
12.5 Acknowledgments	12-12
12.6 References	12-13

Chapter 13 – Unsteady Euler and Detached-Eddy Simulations of Full-Span ONERA 70° Delta Wing **13-1**

Abstract	13-1
Symbols	13-1
13.1 Introduction	13-2
13.2 Present Work	13-2

13.3	Aspects of Unsteady Vortex Breakdown	13-3
13.4	Computational Method	13-3
13.4.1	Dual Time Stepping	13-4
13.4.2	Detached-Eddy Simulation	13-4
13.5	Wing Geometry and Computational Grids	13-5
13.5.1	Navier-Stokes Grid	13-5
13.5.2	Euler Grid	13-6
13.6	Discussion and Analysis of Results	13-6
13.6.1	Time-Accurate Euler Simulations	13-6
13.6.1.1	CFL Number and Time-Step Size	13-6
13.6.1.2	Flow Field Visualization	13-7
13.6.1.3	Time History of Aerodynamic Coefficients	13-8
13.6.1.4	Power Spectral Density of C_N	13-9
13.6.1.5	Fluctuations of Breakdown Locations	13-11
13.6.2	Detached-Eddy Simulations	13-12
13.6.2.1	Time-Step Study	13-12
13.6.2.2	Results Full-Span Model	13-14
13.6.2.3	Grid-Sensitivity Study	13-17
13.6.2.4	Computational Efficiency	13-18
13.7	Visualization using Fully-Immersive Virtual Reality	13-18
13.8	Conclusions and Outlook	13-19
13.9	References	13-20
	Appendix – Video Files	13-36

Chapter 14 – Grid Study for Euler Simulations of a 70° Delta Wing with the Unstructured Flow Solver Edge **14-1**

	Abstract	14-1
	Nomenclature	14-1
14.1	Introduction	14-2
14.2	Computational Method	14-2
14.3	General Grid Description	14-3
14.4	Mesh Refinement Study	14-3
14.4.1	Grid Description	14-3
14.4.2	Results and Discussion	14-4
14.5	Wake Refinement Study	14-4
14.5.1	Grid Description	14-5
14.5.2	Results and Discussion	14-5
14.6	Wind Tunnel Wall Effect	14-6
14.6.1	Simulation of Wing in Wind Tunnel	14-6
14.6.1.1	Grid Description	14-6
14.6.1.2	Results	14-6
14.6.2	Wind Tunnel Correction Methods for Delta Wing Flow	14-7
14.6.3	Simulation of Wing in Corrected “Free Air” Conditions	14-8
14.7	Conclusion	14-9

14.8	Acknowledgements	14-10
14.9	References	14-10

Chapter 15 – High Reynolds Number Detached-Eddy Simulations of Vortex Breakdown over a 70 Degree Delta Wing **15-1**

Abstract	15-1
15.1 Introduction	15-1
15.2 Experimental Method and Facilities	15-2
15.3 Numerical Method	15-3
15.3.1 Turbulence Models	15-4
15.3.1.1 Spalart-Allmaras Turbulence Model	15-4
15.3.1.2 Detached-Eddy Simulation	15-4
15.3.2 Grid Generation	15-4
15.4 Computational Results	15-5
15.4.1 Laminar-Turbulent Transition	15-11
15.5 Concluding Remarks	15-14
15.6 Acknowledgements	15-14
15.7 References	15-15

Chapter 16 – RANS Solutions of 70° Delta Wing in Steady Flow **16-1**

Abstract	16-1
Key Words	16-1
Nomenclature	16-1
16.1 Introduction	16-2
16.2 Numerical Method	16-2
16.2.1 Computation Grid	16-2
16.2.2 Computation Method	16-3
16.2.2.1 Hardware	16-4
16.2.2.2 Initial and Boundary Conditions	16-4
16.3 Results	16-5
16.4 Conclusion	16-12
16.5 References	16-12

Chapter 17 – Steady RANS Simulations of a 70° Delta Wing – with Tunnel Effects **17-1**

Abstract	17-1
Nomenclature	17-1
17.1 Introduction	17-1
17.2 Computational Method	17-3
17.3 Test Case: ONERA 70° Wing	17-3
17.4 Computational Grids	17-4
17.5 Verification and Validation	17-5
17.6 Tunnel Effects – No Support	17-8
17.7 Tunnel Effects – With Support	17-11

17.8	Conclusions	17-13
17.9	Acknowledgements	17-14
17.10	References	17-14

Chapter 18 – Simulation of Vortical Flow over ONERA 70-Degree Delta Wing Experiencing Vortex Breakdown **18-1**

Abstract	18-1
18.1 Background	18-1
18.2 Flow Modelling	18-2
18.3 Results and Discussion	18-3
18.4 Conclusions	18-11
18.5 References	18-12

Chapter 19 – Unsymmetric Vortex Breakdown for Symmetric Free Stream Conditions **19-1**

Abstract		19-1
19.1	Introduction	19-1
19.2	Numerical Method	19-3
19.3	Results	19-4
19.3.1	Artificially Symmetric Solutions	19-4
19.3.1.1	Time History	19-4
19.3.1.2	Flow Analysis	19-6
19.3.1.3	Discussion	19-8
19.3.2	Unsymmetric Solutions	19-8
19.3.2.1	Time History	19-8
19.3.2.2	Flow Analysis	19-10
19.3.2.3	Discussion	19-16
19.4	Performance	19-16
19.5	Conclusions	19-16
19.6	References	19-17

Chapter 20 – Computational Investigation of the Centerbody Effects on the Aerodynamics of Delta Wings **20-1**

Abstract		20-1
20.1	Introduction	20-1
20.2	IAR Delta and Diamond Wing Models	20-2
20.3	Flow Solutions	20-4
20.3.1	Computational Grids	20-4
20.3.2	Flow Solvers	20-5
20.3.2.1	FJ3SOLV	20-5
20.3.2.2	CFD-FASTRAN	20-5
20.4	Results and Discussions	20-5
20.4.1	65° Delta Wing (Model G2)	20-6
20.4.1.1	Convergence History	20-6
20.4.1.2	Surface Pressure Distributions	20-6

20.4.2	55° Diamond Wing (Model G1)	20-7
20.5	Concluding Remarks	20-11
20.6	References	20-11

Chapter 21 – ‘Engineering’ Models of Delta Wing Vortex Breakdown and its Effect on Aerodynamic Characteristics **21-1**

Abstract		21-1
21.1	Nomenclature	21-1
21.2	Introduction	21-2
21.2.1	Vortex Breakdown Modelling	21-3
21.2.2	Vortex Lift-Loss Modelling	21-3
21.3	Vortex Breakdown Modelling	21-4
21.3.1	Modelling Approach	21-4
21.3.1.1	Assumptions	21-4
21.3.1.2	Helical Vortices	21-5
21.3.1.3	Continuity Constraint	21-5
21.3.1.4	Rotational Velocity Constraint	21-6
21.3.1.5	Helix Orientation	21-6
21.3.1.6	Centreline Stagnation	21-7
21.3.1.7	Swirl Ratio	21-7
21.3.1.8	Helix Pitch and Frequency Content	21-7
21.3.1.9	Helix Inclination and the Swirl Ratio	21-8
21.3.2	Burst Onset	21-9
21.3.3	Comparisons with Experimental Data	21-9
21.3.3.1	‘Inner’ and ‘Outer’ Core Dynamics	21-9
21.3.3.2	Helix Convection Velocity	21-10
21.3.3.3	Helix Inclination	21-10
21.3.3.4	Helix Pitch	21-10
21.3.3.5	Vortex Passing Frequency	21-11
21.4	Vortex-Induced Lift-Loss	21-12
21.4.1	Current ‘Lift-Loss’ Modelling Techniques	21-12
21.4.1.1	The Modelling Process	21-12
21.4.1.2	Empirical ‘Lift-Loss Factor’ Models	21-12
21.4.1.3	Semi-Empirical ‘Lift Reduction’ Models	21-14
21.4.2	A New Approach	21-15
21.4.2.1	Current ‘Explanations’	21-15
21.4.2.2	Burst Interaction with the Leading-Edge Flow	21-15
21.4.3	Effect of Helical Burst on Shedding Process	21-16
21.4.3.1	Estimation of Velocities at the Leading-Edge	21-16
21.4.3.2	Magnitude of Lift Loss	21-18
21.4.4	Other Implications	21-19
21.4.4.1	Surface Pressure Distribution	21-19
21.4.4.2	Time Lag in Lift-Loss Response to Wing Motion	21-19
21.4.4.3	Alleviation of Vortex Lift Loss	21-20
21.5	Conclusions	21-20
21.6	References	21-22

21.7 Acknowledgements	21-27
Appendix A – Velocities Induced by a Helical Vortex	21-33
A.1 Helix Geometry	21-33
A.2 Self-Induced Velocities	21-33
A.3 Binormal Velocity Component V_B	21-33
A.4 Tangential Velocity Component W_B	21-34
A.5 Axial Velocity Induced on the Centreline	21-34
A.6 Numerical Solution	21-35
Appendix B – Delta Wing Vortex Correlations	21-37
B.1 Vortex Core Location	21-37
B.2 Vortex Strength	21-37
B.3 Vortex Core Radius	21-37
Appendix C – Estimation of Induced Cross-Flow Velocity	21-40
C.1 Approximation to Upper Surface Velocity	21-40
C.2 Correlation for Lower Surface Velocity	21-40
C.3 Physical Interpretation of Correlation Function	21-41
 Chapter 22 – Non-Linear Indicial Response and Internal State-Space (NIRISS) Representation and its Applications on Delta Wing Configurations	 22-1
Abstract	22-1
22.1 Introduction	22-1
22.2 Dominant Effect of Vortex Breakdown on Airloads	22-3
22.3 Mathematical Modeling	22-3
22.4 Validation and Verifications with Experimental Results	22-7
22.5 Conclusions	22-9
22.6 References	22-9
 Chapter 23 – Applying Vortex Breakdown Empiricisms to Predict Aerodynamic Characteristics in Symmetric & Asymmetric Situations	 23-1
Abstract	23-1
Nomenclature	23-1
23.1 Introduction & Background	23-1
23.2 Methods, Techniques, Model	23-2
23.2.1 Boundary Layer, TE Separation	23-2
23.2.2 Experimental Model for Evaluation of Approach	23-2
23.3 Symmetric Flows & Vortex Breakdown Results	23-2
23.4 Asymmetric Flows & Vortex Breakdown	23-3
23.5 Comparisons with Experiment	23-3
23.6 Inferences, Concluding Remarks & Further Work	23-4
23.6.1 Possible Future Work	23-4
23.7 Acknowledgements	23-4
23.8 References	23-4
 Chapter 24 – Conclusions and Recommendations	 24-1

List of Figures

Figure		Page
CHAPTER 1		
Fig. 1	Vortical crossflow structure	1-17
Fig. 2	Illumination of shear layer instability	1-17
Fig. 3	Evolution of transition process in shear layer	1-17
Fig. 4	Leading-edge vortex breakdown	1-17
Fig. 5	Evolution of transition process in shear layer	1-18
Fig. 6	Vortex breakdown/tail-fin interaction of F-18 HARV at $\alpha=25^\circ$	1-18
Fig. 7	Measured vortex breakdown on 65° delta wings at different facilities	1-18
Fig. 8	ONERA 70° delta wing	1-18
Fig. 9	Model sting/support assembly in ONERA F2 tunnel	1-18
Fig. 10	NASA LaRC 65° delta wing	1-19
Fig. 11	IAR interchangeable 65° delta wing	1-19
Fig. 12	Test rigs installed in TsAGI wind tunnel	1-19
Fig. 13	Computed spiral and bubble breakdown	1-19
Fig. 14	AMR-grid instantaneous solution	1-19
Fig. 15	AMR-grid instantaneous solution	1-19
CHAPTER 2		
Fig. 1	Vortex breakdown location on 50° delta wing	2-27
Fig. 2	Vortex breakdown location on 55° delta wing	2-27
Fig. 3	Vortex breakdown location on 60° delta wing	2-27
Fig. 4	Vortex breakdown location on 65° delta wing	2-27
Fig. 5	Vortex breakdown location on 70° delta wing	2-27
Fig. 6	Vortex breakdown location on 75° delta wing	2-27
Fig. 7	Vortex breakdown location on 80° delta wing	2-28
Fig. 8	Standard and maximum deviations of measured vortex breakdown location	2-28
Fig. 9a	Deviation in measured breakdown location	2-28
Fig. 9b	Time histories of the port and starboard breakdown locations	2-28
Fig. 10a	Measured normal force (flat upper)	2-28
Fig. 10b	Measured normal force (bevel upper)	2-28
Fig. 11	Comparisons of surface pressure between sharp and round leading edges, $M=0.4$, $Re=6 \times 10^6$, $\alpha=10^\circ$	2-29
Fig. 12	PSP measurements at different model conditions	2-30
Fig. 13	Digitized PSP results on leading-edge sharp effect ($U=60$ m/s, $\alpha=21^\circ$)	2-30
Fig. 14	Digitized pressure distributions on wings with sharp and round leading-edges	2-31

Fig. 15	Delta wing velocity vectors on cross-sectional planes at the mid-root chord stations showing primary, secondary, and “tertiary” vortices: (a) sharp leading edge, (b) medium leading edge, and (c) large leading edge	2-31
Fig. 16	PSP images between with/without centerbody	2-32
Fig. 17	Centerbody effect on pressure distributions at different locations, $U=60\text{m/s}$ (3E with centerbody; 3A without centerbody)	2-32
Fig. 18	Comparison of surface pressure between with and without centerbody (Model G1, $M=0.18$, $\alpha=15^\circ$)	2-33
Fig. 19	Comparisons of pressure distributions between with/without centerbody at different chordwise locations ($M=0.18$, $\alpha=15$, NF no centerbody, 3E with centerbody)	2-33
Fig. 20	Comparison of surface pressure between with and without centerbody (Model G2, $M=0.17$, $\alpha=21^\circ$)	2-33
Fig. 21	Comparisons of pressure distributions between with/without centerbody at different chordwise locations ($M=0.17$, $\alpha=21^\circ$, 3A no centerbody, 3E with centerbody)	2-33
Fig. 22	Re number effect on surface pressure with sharp leading-edge	2-34
Fig. 23	Unsteady pressure spectral on 65° delta wing at different static angles of attack	2-34
Fig. 24	Flow visualization of shear layer over delta wing	2-35
Fig. 25	Evolution of vortex structure with increasing Reynolds number	2-35
Fig. 26	Evolution of shear layer structure with increasing Reynolds number depicted using an isosurface of axial vorticity	2-35
Fig. 27	Instantaneous azimuthal vorticity distribution in a plane that passes through the axis	2-35
Fig. 28	Time histories of breakdown locations for left and right breakdowns for $\alpha_0=29^\circ$ and $\alpha_0=42^\circ$	2-35
Fig. 29	Sequence of frames of laser-light sheet images	2-36
Fig. 30	Effect of angle of attack on surface pressure of round leading edge, $M=0.4$, $Re=6 \times 10^6$	2-36
Fig. 31	Effect of Re number increase on surface pressure of round leading edge, $M=0.4$, $Re=60 \times 10^6$	2-36
Fig. 32	Mach number effect on surface pressure with sharp leading-edge, $Re=6 \times 10^6$, $\alpha=10^\circ$	2-37
Fig. 33	Mach number effect on surface pressure with sharp leading-edge, $Re=6 \times 10^6$, $\alpha=20^\circ$	2-37
Fig. 34	Mach number effect on surface pressure with round leading-edge, $Re=6 \times 10^6$, $\alpha=10^\circ$	2-38
Fig. 35	Comparisons of Mach number effects between sharp and round leading-edge, $M=0.8$, $Re=6 \times 10^6$, $\alpha=20^\circ$	2-38
Fig. 36	Assessed results for 65° delta wings	2-39
Fig. 37	Normalized results for 65° delta wings	2-39
Fig. 38	Deformations estimated at $\alpha=30^\circ$ and $x_{VB}=0$	2-39
Fig. 39	Deformations estimated at $\alpha=29^\circ$ and $x_{VB}=1$	2-39
Fig. 40	Assessed results for 70° delta wings	2-40
Fig. 41	Normalized results for 70° delta wings	2-40

CHAPTER 3

Fig. 1	ONERA's F2 Wind Tunnel	3-2
Fig. 2	Experimental configuration in F2 (a) Sketch (b) Actual test section configuration	3-3
Fig. 3	Experimental delta wing model configuration (a) Sketch (b) Actual model in wind tunnel test section (c) Delta wing model configured for surface pressure measurements with 232 pressure taps	3-4
Fig. 4	Experimental configuration demonstrating the adjustable reference plane (a) View looking forward (b) Side view	3-5
Fig. 5	Coordinate system	3-6
Fig. 6	Instantaneous photographs of laser light sheet taken at $U_\infty = 24$ m/s and $\alpha = 27^\circ$ (a) side view (b) zoomed in on vortex breakdown region	3-6
Fig. 7	Instantaneous photographs of laser light sheet taken at $U_\infty = 24$ m/s and $\alpha = 26^\circ$ (a) upstream of vortex breakdown at $X/c = 0.63$ (b) in the vortex breakdown region at $X/c = 0.74$	3-7
Fig. 8	Instantaneous photographs of laser light sheet taken at $U_\infty = 24$ m/s (a) $\alpha = 27^\circ$ (b) $\alpha = 30^\circ$	3-7
Fig. 9	Evolution of X_b/c as a function of α ($U_\infty = 24$ m/s)	3-10
Fig. 10	Time history of the port and starboard vortex breakdown locations at $U_\infty = 24$ m/s (a) $\alpha = 27^\circ$ (b) $\alpha = 30^\circ$	3-11
Fig. 11	Surface oil flow visualization at $\alpha = 27^\circ$ and $U_\infty = 24$ m/s	3-12
Fig. 12	Constant C_p lines on the leeward surface of the delta wing at $\alpha = 27^\circ$, $U_\infty = 24$ m/s	3-13
Fig. 13	3-D LDV results showing the non-dimensional axial velocity component (U/U_∞) and the corresponding streamlines at $\alpha = 27^\circ$ and $U_\infty = 24$ m/s (a) $X = 500$ mm (b) $X = 600$ mm (c) $X = 700$ mm (d) $X = 800$ mm	3-14
Fig. 14	3-D LDV results showing the axial vorticity (Ω_x) at $\alpha = 27^\circ$ and $U_\infty = 24$ m/s (a) $X = 500$ mm (b) $X = 600$ mm (c) $X = 700$ mm (d) $X = 800$ mm	3-15
Fig. 15	3-D LDV results showing the turbulent kinetic energy (k) at $\alpha = 27^\circ$ and $U_\infty = 24$ m/s (a) $X = 500$ mm (b) $X = 600$ mm (c) $X = 700$ mm (d) $X = 800$ mm	3-16
Fig. 16	3-D LDV results showing U/U_∞ in the plane which longitudinally intersects the vortex core at $\alpha = 27^\circ$ and $U_\infty = 24$ m/s	3-17
Fig. 17	3-D LDV results showing the turbulent kinetic energy (k) in the plane which longitudinally intersects the vortex core at $\alpha = 27^\circ$ and $U_\infty = 24$ m/s	3-17

CHAPTER 4

Figure 1	Some leading-edge vortex properties, sharp-edged delta wings	4-14
Figure 2	Bluntness effects on leading-edge vortex structure	4-14
Figure 3	National Transonic Facility (NTF)	4-15
Figure 4	National Transonic Facility circuit	4-15
Figure 5	Schematic of NTF delta wing	4-16
Figure 6	Streamwise leading-edge contours for NTF delta wing	4-16
Figure 7	Delta wing mounted in the NTF	4-17
Figure 8	Test conditions	4-17

Figure 9	Comparison of sharp and blunt leading-edge vortex flow	4-18
Figure 10	Reynolds number effect on blunt leading-edge separation	4-18
Figure 11	Mach number effect on blunt leading-edge separation	4-19
Figure 12	Correlation of separation onset with blunt leading-edge pressure	4-19
Figure 13	Reynolds number effect on leading-edge separation onset and progression	4-20
Figure 14	Mach and Reynolds number effects for the progression of leading-edge separation	4-20

CHAPTER 5

Fig 1	IAR 55° diamond wing and delta wing model with interchangeable leading-edges	5-20
Fig. 2a	IAR 65° delta wing model with interchangeable parts	5-20
Fig. 2b	Combinations of IAR 65° delta wing models with interchangeable centerbody and leading-edge	5-20
Fig. 3	IAR/AFRL 65° delta wing model	5-21
Fig. 4	IAR/AFRL 80°/65° double delta wing model	5-21
Fig. 5	IAR/AFRL 65° wing/body/tail model	5-21
Fig. 6	IAR water tunnel 65° and 55° delta wing models	5-22
Fig. 7	Roll rig in IAR and SARL wind tunnels	5-22
Fig. 8	General view and installation of pitch rig in SARL wind tunnel	5-22
Fig. 9	OPLEC Coning rig in IAR water tunnel	5-23
Fig. 10	Skin friction topologies on 65° delta wing in roll	5-23
Fig. 11	Evolutions of topological changes at different roll and sting angles ($\Lambda=65^\circ$)	5-24
Fig. 12	Gray level profiles through vortex core under rolling oscillatory conditions ($\sigma=30^\circ$, $\Delta\phi=40^\circ$, $k=0.04$, $\phi_0=0^\circ$)	5-24
Fig. 13	Rotational vortex core diameter development in static and dynamic conditions	5-25
Fig. 14	Vortex core positions at different roll angles ($\sigma=30^\circ$, $\Lambda=65^\circ$)	5-25
Fig. 15	Rolling frequency effect on vortex breakdown location	5-26
Fig. 16	Rolling amplitude effect on vortex breakdown location	5-26
Fig. 17	Different vortex breakdown appearances ($s=30^\circ$, $L=65^\circ$)	5-27
Fig. 18	Different response speeds of the critical points within vortex breakdown region ($\sigma=30^\circ$, $\Lambda=65^\circ$)	5-27
Fig. 19	Vortex breakdown location movement during static and dynamic situations ($\sigma=30^\circ$, $\Lambda=65^\circ$)	5-27
Fig. 20	Deformed wing and its effect on vortex breakdown	5-28
Fig. 21	Velocity vector field of PIV measurement over 65° delta wing ($\sigma=24^\circ$, $\Lambda=65^\circ$, $U=20\text{m/sec}$)	5-28
Fig. 22	Vortex breakdown locations over delta wings with different sweepback angles	5-29
Fig. 23	Effect of coning motion on leading-edge vortex breakdown	5-29
Fig. 24	Rolling moment vs. roll angle at different sting angles	5-29
Fig. 24	(Cont.) Rolling moment vs. roll angle at different sting angles ($\Lambda=65^\circ$)	5-30
Fig. 25	Rolling moment vs. coning rate at different sting angles ($\phi=0^\circ$)	5-30

Fig. 26	Normal force and pitch moment vs. coning rate at different sting angles ($\Lambda=65^\circ$, $\phi=0^\circ$)	5-30
Fig. 27	Measured airloads at different rolling frequencies, amplitudes and roll offsets	5-31
Fig. 28	Rolling moment response to ramp motions ($\sigma=30^\circ$, $\Lambda=65^\circ$)	5-31
Fig. 29	Normal force response to ramp motions ($\alpha=0^\circ\sim60^\circ$, $L=65^\circ$)	5-32
Fig. 30	Effect of vortex breakdown on rolling moment in different cases	5-32
Fig. 31	Surface pressure at different chordwise locations and angles of attack ($\Lambda=65^\circ$)	5-33
Fig. 32	PSP measurements on 65° delta wing with different combinations	5-33
Fig. 33	PSP measurements on IAR 55° diamond/delta wings with different leading-edge shapes	5-34
Fig. 34	Leading-edge shape effect on PSP results at different chordwise location ($U=60$ m/s, $\Lambda=55^\circ$, $\alpha=21^\circ$)	5-34
Fig. 35	Unsteady pressure spectra measurements at static model conditions and different angles of attack	5-35
Fig. 36a	Pitch motion and pressures in time domain, $\alpha=50^\circ\rightarrow70^\circ$	5-37
Fig. 36b	Measured pressure in frequency domain, $\alpha=50^\circ\rightarrow70^\circ$	5-37
Fig. 37	Pitch motion and pressures in time domain, $\alpha=70^\circ\rightarrow50^\circ$	5-37
Fig. 38a	Pitch motion and pressures in time domain, $\alpha=10^\circ\rightarrow70^\circ$	5-38
Fig. 38b	Measured pressure in frequency domain, $\alpha=10^\circ\rightarrow70^\circ$	5-38
Fig. 39a	Pitch motion and pressures in time domain, $\alpha=70^\circ\rightarrow10^\circ$	5-38
Fig. 39b	Measured pressure in frequency domain, $\alpha=70^\circ\rightarrow10^\circ$	5-39
Fig. 40a	Pitch motion and pressures in time domain, $\alpha=20^\circ\rightarrow40^\circ$	5-39
Fig. 40b	Measured pressure in frequency domain, $\alpha=20^\circ\rightarrow40^\circ$	5-39
Fig. 41a	Pitch motion and pressures in time domain, $\alpha=40^\circ\rightarrow20^\circ$	5-40
Fig. 41b	Measured pressure in frequency domain, $\alpha=40^\circ\rightarrow20^\circ$	5-40
Fig. 42	Surface pressure at static and rolling oscillation conditions	5-41
Fig. 43	Surface pressure at static and ramp-and-hold conditions	5-41
Fig. 44	Surface pressure during free-to-roll motion ($\Lambda=65^\circ$, $\phi_0=64^\circ$)	5-42
Fig. 45	Free-to-roll motion histories at different released roll angles ($\Lambda=65^\circ$)	5-43
Fig. 46	Static loads on IAR/AFRL forebody/wing/tail model (Elliptical, major axes horizontal)	5-43

CHAPTER 6

Figure 1	Schematic of Shear Layer and Leading-Edge Vortices over a Delta Wing	6-2
Figure 2	Vortical Substructures around the Primary Vortex over a Delta Wing	6-3
Figure 3	Instantaneous Flow Showing the Transition Process with Increasing Reynolds Number; and Time-Averaged Flow Showing Mean Vortical Substructures	6-4
Figure 4	Variation of rms Swirl Velocity across the Vortex Core; Together with Time-Averaged Axial and Swirl Velocity Profiles	6-4

Figure 5	(a) Probability Density Functions of Swirl Velocity for Different Radial Distances, $x/c=0.6$, $\alpha=20^\circ$; (b) Probability Density Functions of Swirl Velocity for the Wandering Q-Vortex	6-5
Figure 6	Flow Visualization of Shear Layer	6-6
Figure 7	Variation of Maximum rms Swirl Velocity as a Function of Reynolds Number	6-6
Figure 8	Flow Visualization of Vortex Breakdown over a Delta Wing	6-7
Figure 9	Pressure Fluctuations Near Trailing-Edge ($x/c=0.93$) for Different Angle of Attack, $y/s=0.5$	6-7
Figure 10	Instantaneous Azimuthal Vorticity Distribution in a Plane that Passes through the Axis	6-8
Figure 11	Variation of Dimensionless Frequency as a Function of Angle of Attack for Different Sweep Angles	6-9
Figure 12	Variation of Dimensionless Frequency as a Function of Dimensionless Circulation	6-9
Figure 13	Time Histories of Breakdown Locations for Left and Right Vortices for $\alpha=37^\circ$ and $\Lambda=70^\circ$	6-10
Figure 14	Spectra of Difference and Average of Breakdown Locations for $\Lambda=75^\circ$ and $\alpha=42^\circ$	6-10
Figure 15	Spectra of the Difference and Average Pressure Fluctuations, $\alpha=50^\circ$, $\Lambda=80^\circ$	6-11
Figure 16	Spectrum of Unsteady Flow Phenomena over Delta Wings as a Function of Dimensionless Frequency	6-12
Figure 17	Possible Interaction Mechanisms: (a) Cross-Flow Instability, (b) Streamwise Instability	6-13
Figure 18	(a) PVC Algorithm; (b) PVC Histogram for $\alpha=42^\circ$ and $\Lambda=75^\circ$	6-14
Figure 19	Time Histories of Breakdown Locations for Left and Right Breakdowns for $\alpha_0=29^\circ$ and $\alpha_0=42^\circ$ for $\alpha_1=3^\circ$, $f_c/U_\infty=0.1$	6-15
Figure 20	Variation of the Ratio R with Reduced Frequency, $\alpha_0=42^\circ$, $\alpha_1=3^\circ$	6-15
Figure 21	Height of Vortex Center above the Wing Following a Sudden Change of Incidence	6-16
Figure 22	Variation of Height of Dyed Region in a Cross-Flow Plane as a Function of Angle of Attack for a Periodically Pitching Delta Wing	6-17
Figure 23	Flow Visualization of Vortex Breakdown for Unsteady Free Stream $U/U_\infty=1+R\cos(\omega t)$, $\alpha=25^\circ$, $\omega c/2U_\infty=1.395$, $R=0.70$	6-18
Figure 24	Contours of Constant Azimuthal Vorticity for Transient Vortex Breakdown over a Pitching Delta Wing	6-18
Figure 25	Chordwise Location of Vortex Breakdown for a Pitching Delta Wing	6-19
Figure 26	Amplitude Ratio and Phase Lag of Vortex Breakdown Location as a Function of Reduced Frequency	6-20
Figure 27	Phase Lag of Vortex Breakdown Location for Different Types of Unsteady Motion	6-20
Figure 28	Time Constants Estimated from Surface Pressure Changes in Response to Blowing	6-21
Figure 29	Symmetric and Antisymmetric Modes of Vortex Shedding from Delta Wings	6-23
Figure 30	(a) Dominant Frequencies in the Wake for $\Lambda=76^\circ$; (b) Breakdown Location over Delta Wings for $\Lambda=75^\circ$	6-23
Figure 31	Variation of Dimensionless Frequency for Unsteady Phenomena as a Function of Angle of Attack	6-24

Figure 32	(a) Buffeting on a Slender Delta Wing Model; (b) Wing-Tip Acceleration on a Slightly Flexible Delta Wing, $\Lambda=60^\circ$	6-25
Figure 33	Time Histories of Breakdown Location for Different Fin Oscillation Frequencies for a Fin Location of $y_f/s=0.8$	6-26
Figure 34	Variation of the Amplitude Ratio as a Function of Forcing Frequency	6-27
Figure 35	(a) RMS Pressure on a Fin; (b) Breakdown Location for $\Lambda=60^\circ$	6-27
Figure 36	Wing Rock Time History for $\alpha=30^\circ$ Showing Build-Up	6-28
Figure 37	Wing Rock Amplitude as a Function of Angle of Attack for Wings with Different Sweeps	6-28
Figure 38	Flow Visualization of Leading-Edge Vortex for (a) Jet Off, (b) Jet On, (c) Just After the Jet is Turned Off	6-30
Figure 39	Dual Vortex Structure (of the Same Sign of Vorticity) over a Nonslender Delta Wing with a Sweep Angle of $\Lambda=50^\circ$	6-31
Figure 40	Interaction of Leading-Edge Vortex with a Flexible Delta Wing	6-31

CHAPTER 7*

Fig. 1	Leading edge vortex above a delta wing	7-2
Fig. 2	Flow visualization of leading edge vortices on 70° and 85° delta wings	7-6
Fig. 3	Seven hole probe flow field surveys over 70° and 85° delta wings	7-8
Fig. 4	Comparison of seven hole probe and laser Doppler anemometer measurements at mid chord on a 70° delta wing at increasing angle of attack	7-10
Fig. 6	Axial Vorticity at $\Lambda=75^\circ$, $\alpha=20^\circ$, $x/c=0.5$	7-11
Fig. 7	Chordwise Axial Vorticity Profiles, $\Lambda=75^\circ$, $\alpha=20^\circ$	7-12
Fig. 8	Radial Circulation Profiles, $\Lambda=75^\circ$, $\alpha=20^\circ$	7-13
Fig. 11	Correlation of circulation predictions using the Hemsch and Luckring relationship for g vs. K	7-14
Fig. 12	Correlation of circulation predictions using the Hemsch and Luckring relationship for $g(x/c)$ vs. K	7-14
Fig. 13	Unsteady Breakdown location for $0-60^\circ$ oscillation	7-17
Fig. 14	Unsteady surface pressure data and chordwise progress of vortex breakdown	7-18
Fig. 15	Unsteady pressure data for $2-60^\circ$ motion range as a function of reduced frequency	7-18
Fig. 16	A typical roll time history illustrating the buildup to the limit cycle motion called wing rock	7-20
Fig. 17	Roll moment coefficient during a build up cycle	7-21
Fig. 18	Vortex position hysteresis	7-22
Fig. 19	Static and dynamic position of the vortices during a wing rock motion	7-22
Fig. 20	Unsteady pressure profiles during a wing rock motion, $\alpha = 30^\circ$	7-23

CHAPTER 8

Fig. 1	Classification of phase portraits in (p,q) plane	8-4
--------	--	-----

* Figures 5, 9 and 10 were not provided for Chapter 7.

Fig. 2	Singular points on and off the wing surface	8-4
Fig. 3	Different bifurcation diagram	8-5
Fig. 4	TUD Delta wing geometry	8-7
Fig. 5	Upper-surface flow pattern visualized using different fluids	8-7
Fig. 6	Topology of skin-friction line pattern on lower surface	8-8
Fig. 7	Flow pattern observed on nose	8-8
Fig. 8	Conjectured topology of flow on nose	8-8
Fig. 9	Topology of flow at apex	8-9
Fig. 10	Bubble-type of boundary-layer separation	8-9
Fig. 11	Topology of skin-friction line pattern on upper surface	8-9
Fig. 12	Topology of two-vortex flow at apex of delta wing, as conjectured by Délery	8-9
Fig. 13	Topology of four-vortex flow at apex delta wing, as conjectured by Délery	8-10
Fig. 14	Topology of flow at apex, as conjectured by Peake and Tobak	8-10
Fig. 15	Crossflow topology (a) upstream and (b) downstream of transition region	8-11
Fig. 16	Topology of boundary-layer transition region	8-11
Fig. 17	Topology of flow at left-hand wing tip	8-11
Fig. 18	Apex models	8-12
Fig. 19	Flow visualization of Model 1	8-12
Fig. 20	Flow patterns on Model 1 for $\alpha = 35^\circ$	8-13
Fig. 21	Flow patterns on Model 2 for $\alpha = 30^\circ$	8-14
Fig. 22	IAR 65° delta wing model	8-15
Fig. 23	Concentrated vortex patterns and related section views	8-16
Fig. 24	Vortex “whorl” patterns	8-16
Fig. 25	Vortex bursting patterns observed on different wing areas	8-17
Fig. 26	Flow visualization of spiral flow patterns	8-18
Fig. 27	Evolution of surface flow topology on a 65° delta wing at different attitudes	8-20
Fig. 28	Conjectured three-dimensional flow structures interpreted from surface flow topologies	8-23

CHAPTER 9

Figure 1	Large 70° delta wing model	9-9
Figure 2	Small 70° delta wing model	9-9
Figure 3	65° delta wing model	9-9
Figure 4	65° delta wing model with additional body	9-9
Figure 5	TsAGI low subsonic wind tunnel T-103	9-10
Figure 6	TsAGI large amplitude forced oscillations rig at wind tunnel T-103	9-10
Figure 7	Small amplitude pitch forced oscillations rig	9-11
Figure 8	Example of α and vertical force signals during large amplitude forced oscillations	9-11

Figure 9	Example of alpha and pitching moment signals during small amplitude forced oscillations	9-12
Figure 10	Example of one period averaging for large amplitude forced oscillations	9-12
Figure 11	Example of aerodynamic damping derivatives obtained during small amplitude forced oscillations with various frequencies	9-12
Figure 12	Comparison of 65° delta wing longitudinal aerodynamic characteristics	9-13
Figure 13	Comparison of 65° delta wing rolling moment dependencies upon bank angle for various incidences	9-13
Figure 14	Comparison of 70° delta wing unsteady aerodynamic derivatives for small amplitude pitch oscillations obtained at TsAGI and DERA, Bedford	9-14
Figure 15	DERA, Bedford dynamic rig	9-15
Figure 16	Comparison of rounded leading edges 70° delta wing large and small models experimental data	9-15
Figure 17	70° delta wing influence of leading edges shape	9-15
Figure 18	65° delta wing influence of additional center body	9-15
Figure 19	70° delta wing large amplitude oscillations $\alpha_0 = 15^\circ$, $\Delta\alpha = 15^\circ$	9-16
Figure 20	70° delta wing large amplitude oscillations $\alpha_0 = 30^\circ$, $\Delta\alpha = 25^\circ$	9-16
Figure 21	70° delta wing unsteady aerodynamic loads during small amplitude pitch oscillations with various frequencies	9-16
Figure 22	70° delta wing vertical force unsteady aerodynamic derivatives	9-17
Figure 23	70° delta wing pitching moment unsteady aerodynamic derivatives	9-17

CHAPTER 10

Fig. 1	The model	10-15
Fig. 2.a	The experimental setup	10-15
Fig. 2.b	The IRT experimental setup	10-15
Fig. 3	The vortex breakdown position vs α in symmetric flow conditions	10-15
Fig. 4	The vortex breakdown position vs α in asymmetric flow conditions	10-15
Fig. 5	The vortex core incidence vs α	10-16
Fig. 6	The normal force coefficient C_Z at different Reynolds numbers	10-16
Fig. 7	The pitching moment coefficient C_m at different Reynolds numbers	10-16
Fig. 8	The static derivatives $C_{Z\alpha}$ and $C_{L\alpha}$ in symmetric flow conditions	10-16
Fig. 9	The normal force coefficient C_Z at different sideslip angles	10-16
Fig. 10	The pitching moment coefficient C_m at different sideslip angles	10-16
Fig. 11	The rolling moment coefficient C_l at different sideslip angles	10-17
Fig. 12	The yawing moment coefficient C_n at different sideslip angles	10-17
Fig. 13	Vortex burst asymmetry and lateral stability characteristics at $\beta = 5^\circ$	10-17
Fig. 14	The effect of Reynolds number on static pressure measurements	10-17
Fig. 15	The effect of angle of attack on static pressure measurements (low α)	10-17
Fig. 16	The effect of angle of attack on static pressure measurements (high α)	10-17

Fig. 17	The pressure coefficient at different wing locations	10-18
Fig. 18	The effect of sideslip angle on pressure measurements	10-18
Fig. 19	The effect of reduced frequency on vortex breakdown position	10-18
Fig. 20	The phase lag between the dynamic vortex breakdown position and the model primary motion	10-18
Fig. 21	The effect of reduced frequency on vortex breakdown propagation speed	10-18
Fig. 22	Comparison of the vortex breakdown propagation speed for $K = 0.1$	10-18
Fig. 23	The dynamic pitching moment coefficient C_m (stable)	10-19
Fig. 24	The dynamic pitching moment coefficient C_m (stable to unstable)	10-19
Fig. 25	The dynamic pitching moment coefficient C_m (stable to unstable)	10-19
Fig. 26	The dynamic pitching moment coefficient C_m (unstable)	10-19
Fig. 27	The pitching damping coefficient	10-19
Fig. 28	The temperature on the model surface ($\alpha = 10^\circ$ - $Re = 1100000$)	10-19
Fig. 29	The chordwise St distribution as a function of Re ($\alpha = 15^\circ$ - $y/s = 0.0$)	10-20
Fig. 30	The spanwise St distribution as a function of Re ($\alpha = 15^\circ$ - $x/c = 0.65$)	10-20
Fig. 31	Effect of transition on chordwise St distribution ($\alpha = 20^\circ$ - $y/s = 0.0$)	10-20

CHAPTER 11

Figure 1	Anatomy of vortex flow on a delta wing at high angle of attack	11-2
Figure 2	Demonstration of adaptive refinement steps by local remeshing for a vortical flow example: (a) initial grid, (b) flow solution indicating a forebody vortex, (c) removal of affected cells, and (d) locally refined grid	11-6
Figure 3	65-degree Delta wing model assembly and support system	11-7
Figure 4	Unstructured Euler grid on the 65° Delta wing showing triangular surface mesh and cross-section of tetrahedral volume grid (352,011 cells)	11-8
Figure 5	Initial (unadapted) grid (352,011 tetrahedral cells) and Euler inviscid flow solution on the sharp leading-edge Delta wing	11-9
Figure 6	Tetrahedral cells featuring high entropy regions in the initial grid for the sharp leading-edge Delta wing	11-10
Figure 7	Final adapted grid (1,612,307 cells) and Euler inviscid flow solution on the sharp leading-edge Delta wing	11-11
Figure 8	Final adaptive grid refinement of high entropy region for the sharp leading-edge Delta wing	11-12
Figure 9	Adapted inviscid flow solution on the sharp leading-edge Delta wing	11-13
Figure 10	Unadapted refined grid (2,720,797 cells) and Navier-Stokes flow solution on the sharp leading-edge Delta wing	11-14
Figure 11	Cross-sections of the sharp leading-edge Delta wing, unadapted refined grid, and entropy contours showing the leading-edge vortices at the mid-root-chord station	11-15
Figure 12	Viscous flow solution on the sharp leading-edge Delta wing	11-16
Figure 13	Comparison of spanwise surface pressure coefficients for the 65-degree Delta wing with a sharp leading edge, $M_\infty = 0.4$, $\alpha = 20.0^\circ$, and $Re_{MAC} = 6.0 \times 10^6$	11-17

Figure 14	Comparison of Navier-Stokes flow solutions on medium leading-edge Delta wing: (a) unadapted grid (1,689,852 cells) and (b) inviscid portion of grid refined adaptively (4,000,156 cells)	11-19
Figure 15	Comparison of viscous flow solutions on medium leading-edge Delta wing at the mid-root-chord stations: (a) unadapted grid and (b) inviscid portion of grid refined adaptively	11-20
Figure 16	Comparison of spanwise surface pressure coefficients for the 65-degree delta wing with a medium radius leading edge at $M_\infty = 0.4$, $\alpha = 20.0$ degrees, and $Re_{MAC} = 6.0 \times 10^6$	11-21
Figure 17	Comparison of Navier-Stokes flow solutions on large leading-edge Delta wing: (a) unadapted grid (1,839,186 cells) and (b) inviscid portion of grid refined adaptively (4,718,896 cells)	11-23
Figure 18	Comparison of Navier-Stokes flow solutions on large leading-edge Delta wing at the mid-root-chord station, (a) unadapted grid and (b) inviscid portion of grid refined adaptively	11-24
Figure 19	Comparison of spanwise surface pressure coefficients for the 65-degree Delta wing with a large radius leading edge at $M_\infty = 0.4$, $\alpha = 20.0$ degrees, and $Re_{MAC} = 6.0 \times 10^6$	11-25
Figure 20	Delta wing velocity vectors on cross-sectional planes at the mid-root chord stations showing primary, secondary, and “tertiary” vortices: (a) sharp leading edge, (b) medium leading edge, and (c) large leading edge. Navier-Stokes solutions at $M_\infty = 0.4$, $\alpha = 20.0^\circ$, and $Re_{MAC} = 6.0 \times 10^6$	11-26
Figure 21	Modular Transonic Vortex Interaction (MTVI) configuration: (a) wind tunnel model and (b) two types of fuselage forebody cross-sections	11-28
Figure 22	Initial (163,619 cells) and adapted (564,727 cells) unstructured grids on the MTVI configuration: (a) surface mesh and (b) surface/volume grid	11-29
Figure 23	Initial and adapted static pressure distributions on the MTVI configuration: (a) surface and (b) surface/volume	11-30
Figure 24	Local grid refinement at high entropy regions on the MTVI volume grid: (a) initial grid and (b) final adapted grid indicating the chine vortex burst	11-32
Figure 25	Wind tunnel visualization of flow around the MTVI configuration showing chine vortex burst at $M_\infty = 0.4$	11-32
Figure 26	Adapted grid (1,049,716 cells) showing computed chine and wing vortices and their breakdowns on the MTVI configuration, $M_\infty = 0.40$, $\alpha = 30^\circ$	11-33
Figure 27	Experimental visualization of vortical flow around the MTVI configuration, $M_\infty = 0.40$, $\alpha = 30^\circ$	11-33

CHAPTER 12

Figure 1	Flow configuration and grid structure for swept leading edge	12-16
Figure 2	Effect of grid resolution on mean axial vorticity distribution in the vortex core, $Re_L = 2.5 \times 10^4$, $x/L = 0.2$	12-16
Figure 3	Effect of spatial discretization scheme on instantaneous vorticity magnitude on vertical plane through the vortex core for $Re_L = 5.0 \times 10^4$: (a) Second-order scheme (E2), (b) Sixth-order scheme (C6)	12-16
Figure 4	Effect of spatial discretization scheme on mean streamwise velocity and axial vorticity distributions in the vortex core, $Re_L = 5.0 \times 10^4$, $x/L = 1.0$	12-16
Figure 5	Evolution of vortex structure with increasing Reynolds number	12-16

Figure 6	Evolution of shear layer structure with increasing Reynolds number depicted using an isosurface of axial vorticity	12-17
Figure 7	Contours of instantaneous axial vorticity at several crossflow planes along the wing, $Re_L = 2.5 \times 10^4$	12-17
Figure 8	Instantaneous (upper half) and time-averaged (lower half) limiting streamline pattern on wing upper surface, $Re_L = 2.5 \times 10^4$, (Note: spanwise scale enlarged for the purpose of clarity)	12-17
Figure 9	Contours of instantaneous vorticity magnitude on longitudinal plane through the vortex core, $Re_L = 2.5 \times 10^4$	12-17
Figure 10	Instantaneous shear-layer structure depicted using an isosurface of axial vorticity, $Re_L = 2.5 \times 10^4$	12-17
Figure 11	Instantaneous (upper half) and time-averaged (lower half) limiting streamline pattern on wing upper surface, $Re_L = 5.0 \times 10^4$, (Note: spanwise scale enlarged for the purpose of clarity)	12-17
Figure 12	Contours of instantaneous axial vorticity at several crossflow planes along the wing, $Re_L = 5.0 \times 10^4$	12-18
Figure 13	Contours of instantaneous vorticity magnitude on longitudinal plane through the vortex core, $Re_L = 5.0 \times 10^4$	12-18
Figure 14	Instantaneous shear-layer structure depicted using an isosurface of axial vorticity, $Re_L = 5.0 \times 10^4$	12-18
Figure 15	Isosurface of instantaneous axial vorticity showing break-up of vortical substructures along their axes, $Re_L = 5.0 \times 10^4$	12-18
Figure 16	Time histories of spanwise velocity within the unsteady shear layer at several streamwise locations, $Re_L = 5.0 \times 10^4$	12-18
Figure 17	Spectra of spanwise velocity fluctuations within the shear layer at two streamwise locations, $Re_L = 5.0 \times 10^4$	12-18
Figure 18	Streamwise variation of dominant non-dimensional frequency of shear layer fluctuations	12-19
Figure 19	Time-averaged shear layer structure depicted using an isosurface of mean axial vorticity, $Re_L = 2.5 \times 10^4$	12-19
Figure 20	Time-averaged shear layer structure depicted using an isosurface of mean axial vorticity, $Re_L = 5.0 \times 10^4$	12-19
Figure 21	Contours of mean axial vorticity on horizontal plane cutting the shear layer and vortex core, $Re_L = 5.0 \times 10^4$	12-19
Figure 22	Contours of time-averaged axial vorticity on several crossflow planes along the wing, $Re_L = 5.0 \times 10^4$	12-19
Figure 23	Contours of RMS streamwise velocity fluctuations on several crossflow planes along the wing, $Re_L = 5.0 \times 10^4$.	12-19
Figure 24	Contours of RMS pressure fluctuations on several crossflow planes along the wing, $Re_L = 5.0 \times 10^4$	12-20

CHAPTER 13

Figure 1	Water-tunnel visualization of spiral and bubble-type vortex breakdown	13-26
Figure 2	Spiral breakdown: stages in behavior of axial filament and sense of the spiral	13-26
Figure 3	Geometry of full-span delta wing model with cut-off trailing edge	13-26

Figure 4	Geometry of full-span delta wing model with sharp trailing edge	13-26
Figure 5	Full-span HCH grid: planform view	13-26
Figure 6	Full-span HCH grid: sectional 3D-view	13-26
Figure 7	Time-dependent particles at different instances in time ($M_\infty=0.2$, $\alpha=30^\circ$, Euler)	13-27
Figure 8	Contours of surface pressure coefficient and entropy iso-surface showing spiral-type vortex breakdown/surface interaction ($M_\infty=0.2$, $\alpha=27^\circ$, Euler)	13-28
Figure 9	Time sequence of images showing the evolution from spiral to intermittent bubble-type breakdown: instantaneous particles and iso-surface of entropy ($M_\infty=0.2$, $\alpha=30^\circ$, Euler)	13-29
Figure 10	Normal-force coefficient time history ($M_\infty=0.2$, Euler)	13-30
Figure 11	Detailed view of normal-force coefficient time history ($M_\infty=0.2$, Euler)	13-30
Figure 12	Rolling-moment coefficient time history ($M_\infty=0.2$, Euler)	13-30
Figure 13	Power Spectral Density of C_N as a function of frequency ($M_\infty=0.2$, Euler)	13-30
Figure 14	Power Spectral Density of C_N as a function of the Strouhal number ($M_\infty=0.2$, Euler)	13-30
Figure 15	Strouhal numbers of current data (Euler) superimposed on experimental data	13-31
Figure 16	Comparison between computed and experimental Strouhal number as function of α	13-31
Figure 17	Time history of computed vortex breakdown locations ($M_\infty=0.2$, Euler)	13-31
Figure 18	Time history of computed vortex breakdown locations ($M_\infty=0.2$, Euler)	13-31
Figure 19	Conv. history of residual and lift coeff. ($M_\infty=0.2$, $Re=1.56 \times 10^6$, $\alpha=27^\circ$, S-A turbulence model, steady-state calculation, semi-span model)	13-31
Figure 20	C_N time history, diff. time steps ($M_\infty=0.2$, $Re=1.56 \times 10^6$, $\alpha=27^\circ$, DES, semi-span model)	13-31
Figure 21	Normal-force coefficient time history ($M_\infty=0.2$, $Re=1.56 \times 10^6$, $\alpha=27^\circ$, DES)	13-32
Figure 22	Power Spectral Density of C_N as function of f ($M_\infty=0.2$, $Re=1.56 \times 10^6$, $\alpha=27^\circ$, DES)	13-32
Figure 23	Computed vortex breakdown locations compared to experimental data ($M_{\infty,exp}=0.7$, $M_{\infty,CFD}=0.2$, $Re=1.56 \times 10^6$)	13-32
Figure 24	Computed C_p compared to exp. data ($M_\infty=0.2$, $Re=1.56 \times 10^6$, $\alpha=27^\circ$, DES)	13-32
Figure 25	Computed and measured upper-surface pressure distribution compared ($M_{\infty,CFD}=0.2$, $M_{\infty,exp}=0.07$, $Re=1.56 \times 10^6$, $\alpha=27^\circ$)	13-33
Figure 26	Computed skin-friction lines and surface oil flow photograph ($M_{\infty,CFD}=0.2$, $M_{\infty,exp}=0.07$, $Re=1.56 \times 10^6$, $\alpha=27^\circ$)	13-33
Figure 27	Computed and measured longitudinal component of velocity in various crossplanes ($M_{\infty,CFD}=0.2$, $M_{\infty,exp}=0.07$, $Re=1.56 \times 10^6$, $\alpha=27^\circ$)	13-34
Figure 28	Computed and measured transverse component of velocity in various crossplanes ($M_{\infty,CFD}=0.2$, $M_{\infty,exp}=0.07$, $Re=1.56 \times 10^6$, $\alpha=27^\circ$)	13-34
Figure 29	Computed and measured normal component of velocity in various crossplanes ($M_{\infty,CFD}=0.2$, $M_{\infty,exp}=0.07$, $Re=1.56 \times 10^6$, $\alpha=27^\circ$)	13-34
Figure 30	Influence of grid refinement on surface pressure distr. ($M_\infty=0.2$, $Re=1.56 \times 10^6$, $\alpha=27^\circ$, DES)	13-35
Figure 31	Influence of grid refinement on longitudinal velocity component ($M_\infty=0.2$, $Re=1.56 \times 10^6$, $\alpha=27^\circ$, DES)	13-35

Figure 32	Time-dependant flow over delta wing visualized in virtual-reality environment (animation, head tracking and stereo viewing switched off)	13-35
Figure 33	Time-dependant flow visualized in virtual-reality environment (animation, head tracking and stereo viewing switched off)	13-35

CHAPTER 14

Figure 1	Wing geometry	14-11
Figure 2	View of the symmetry plane of the medium mesh	14-11
Figure 3	Close-up on the wing and the symmetry plane of the medium grid	14-11
Figure 4	Comparison of wing surface mesh for the medium and fine meshes	14-12
Figure 5	Comparison of surface pressure distribution: experiment, medium and fine grids	14-12
Figure 6	Comparison of C_p distribution: experiment, medium and fine grid	14-13
Figure 7	Comparison of the mesh in the symmetry plane: no wake refinement, short wake refinement and full wake refinement	14-14
Figure 8	Comparison of surface pressure distribution: no wake refinement and short wake refinement	14-14
Figure 9	Comparison of C_p distribution: experimental, no wake refinement, short wake and full wake	14-15
Figure 10	Global view of the mesh with the wing in the wind tunnel	14-16
Figure 11	View of the wing surrounded by the wind tunnel walls	14-16
Figure 12	Surface pressure distribution on the wing in the wind tunnel	14-16
Figure 13	Comparison of C_p distribution: experiment, free air wing, wing in wind-tunnel and wing in corrected free air conditions	14-17
Figure 14	Corrected angle of attack obtained with Traub's method applied to the 70° delta wing in ONERA wind tunnel	14-18
Figure 15	Surface pressure distribution on the wing in corrected free air conditions	14-18

CHAPTER 15

Fig. 1	Sketch of the delta wing model with nozzles for along-the-core blowing near the apex	15-2
Fig. 2	Instantaneous iso-surfaces of vorticity magnitude colored by the span-wise component of vorticity for four grids: a) G1 (1.2M cells), b) G2 (2.7M cells), c) G3 (6.7M cells), and G4 (10.7M cells)	15-6
Fig. 3	Average surface pressure coefficients at four chord-wise stations (500mm, 600mm, 700mm, and 800mm) for grids G1, G2, G3, and G4	15-6
Fig. 4	Resolved turbulent kinetic energy nondimensionalized by the square of the freestream velocity along the core for four grids	15-7
Fig. 5	Instantaneous iso-surfaces of vorticity magnitude colored by the span-wise component of vorticity for three views of the 70° delta wing G9A4 grid in a freestream (i.e., no wind tunnel walls and no sting)	15-8
Fig. 6	Instantaneous iso-surfaces of vorticity magnitude colored by the span-wise component of vorticity for three views of the 70° delta wing G7A1 grid with wind tunnel walls and a truncated sting modeled	15-8

Fig. 7	Power spectral density (PSD) analysis of the delta wing normal force for three grids	15-9
Fig. 8	Average surface pressure coefficients along the span for the G7A1 and G9A4 grid SADES solutions and the experiment at four chord-wise stations: a) 500mm, b) 600mm, c) 700mm, and d) 800mm	15-10
Fig. 9	Average surface pressure coefficients along the span scaled by the square root of 2 for the G9A4 grid SADES solutions and the experiment at four chord-wise stations	15-10
Fig. 10	Experimentally and numerically obtained resolved turbulent kinetic energy nondimensionalized by the freestream velocity squared in a horizontal plane passing through the vortex core	15-11
Fig. 11	Experimentally and numerically obtained streamwise velocity component nondimensionalized by the freestream velocity in a horizontal plane passing through the vortex core	15-11
Fig. 12	Surface oil flow patterns for a) experiments of Mitchell et. al., b) grid G9A4 fully turbulent, c) grid G9A4 laminar to turbulent transition at 30% root chord, and d) grid G9A4 laminar to turbulent transition at 40% root chord	15-12
Fig. 13	Experimentally and numerically obtained resolved turbulent kinetic energy nondimensionalized by the freestream velocity squared in a horizontal plane passing through the vortex core	15-13
Fig. 14	Resolved turbulent kinetic energy (TKE) nondimensionalized by the freestream velocity squared along the core of the vortex for the G9A4 grid with a fully turbulent assumption, and an assumed laminar to turbulent transition at 30% root chord, and laminar to turbulent transition at 40% root chord	15-13
Fig. 15	Iso-surfaces of turbulent kinetic energy for the 70° delta wing	15-14

CHAPTER 16

Fig. 1	H-H mesh – upper block	16-4
Fig. 2	Residuals of conservative variables – SST	16-4
Fig. 3	Wing upper-surface pressure distribution	16-5
Fig. 4	Wing upper-surface streamline pattern	16-5
Fig. 5	Distribution of the mean u/U velocity component	16-6
Fig. 6	Distribution of the mean v/U velocity component	16-7
Fig. 7	Distribution of the mean w/U velocity component	16-8
Fig. 8	Distribution of the axial-vorticity component	16-9
Fig. 9	Distribution of the nondimensionalized turbulent kinetic energy	16-10
Fig. 10	Distribution of the mean u/U velocity component in the vortex plan	16-10
Fig. 11	Distribution of the mean w/U velocity component in the vortex plan	16-10
Fig. 12	Distribution of the turbulent kinetic energy in the vortex plan	16-11
Fig. 13	Comparison of pressure distribution along four stations	16-11

CHAPTER 17

Figure 1	Support geometry and dimensions	17-5
Figure 2	ONERA 70° wing, View of ONERA F2 tunnel mesh	17-5

Figure 3	Dependency of upper surface pressure distribution with grid refinement	17-6
Figure 4	Comparison of upper surface pressure distribution with experiment	17-6
Figure 5	Distribution of turbulent kinetic energy through the vortex core	17-6
Figure 6	Comparison of axial velocity distribution through vortex core ($x/c_r = 0.53$)	17-7
Figure 7	Comparison of helix angle distribution through vortex core ($x/c_r = 0.53$)	17-7
Figure 8	Distribution of axial vorticity through the vortex core	17-7
Figure 9	Comparison of upper surface pressure distributions, $x/c_r = 0.32$	17-8
Figure 10	Comparison of upper surface pressure distributions, $x/c_r = 0.52$	17-8
Figure 11	Comparison of upper surface pressure distributions, $x/c_r = 0.63$	17-9
Figure 12	ONERA 70° wing, Pressure distributions along vortex cores	17-9
Figure 13	Steady flow tunnel wall pressure distributions	17-10
Figure 14	ONERA 70° wing, Flow angles at 1.5 wing span lengths from wing	17-10
Figure 15	ONERA 70° wing, Comparison of helix angles through vortex cores at $x/c_r = 0.52$	17-10
Figure 16	ONERA 70° wing, Tunnel centreline pressure distributions	17-10
Figure 17	ONERA 70° wing, Comparison of circulation distributions	17-10
Figure 18	Pressure distribution along a horizontal plane, support $0.5c_r$ from wing trailing edge	17-12
Figure 19	Pressure distribution along a horizontal plane, support $1.0c_r$ from wing trailing edge	17-12
Figure 20	Axial pressure gradient at tunnel side wall with supports	17-13

CHAPTER 18

Figure 1	Impression of the Flow Domain Topology and Computational Grids	18-2
Figure 2	Computational Time History of C_p Contours Leading to a Steady-State Obtained with a Large Time Step ($\Delta t^* = 0.1$)	18-4
Figure 3	Computational Power Density Spectra of the Normal Force Coefficient	18-5
Figure 4	Computational and Experimental Time-Averaged C_p Contours	18-6
Figure 5	Computational and Experimental Spanwise C_p Distributions	18-6
Figure 6	Computational Surface C_f Contours and Limiting Streamlines Compared with the Experimental Oilflow Pattern	18-7
Figure 7	Computational Crossflow Distribution of the Axial Velocity	18-8
Figure 8	Computational and Experimental Longitudinal Distribution of the Axial Velocity	18-8
Figure 9	Computational Crossflow Distributions of the Transversal (v / U_0) and Normal (w / U_0) Velocity	18-9
Figure 10	Computational and Experimental Crossflow Distributions of the Axial Vorticity Component	18-9
Figure 11	Computational and Experimental Longitudinal Distribution of the Azimuthal Vorticity Component	18-10
Figure 12	Computational Crossflow Distributions of the Turbulence Kinetic Energy	18-10
Figure 13	Computational Iso-Surfaces of the Total Pressure Loss	18-11

CHAPTER 19

Fig. 1	Geometry and surface grid for the cropped delta wing ($A = 1.38$, $\lambda = 0.15$, $\varphi = 65^\circ$)	19-2
Fig. 2	Section of the mesh for Euler calculations using O-O-topology and 1 879 605 gridpoints	19-4
Fig. 3	Lift coefficient for left and right half-wing as function of dimensionless time	19-5
Fig. 4	Frequency spectrum for the lift coefficient	19-5
Fig. 5	Lift coefficient for left and right half-wing as function of dimensionless time with intervals for detailed analysis	19-6
Fig. 6	Flow analysis for the time interval $t^* \approx 35.1$ according to Fig. 5	19-6
Fig. 7	Flow analysis for the time interval $t^* \approx 38.4$ according to Fig. 5	19-7
Fig. 8	Flow field in the cross section at $x / c_i = 0.72$ for the time interval $t^* \approx 35.1$	19-7
Fig. 9	Flow field in the cross section at $x / c_i = 0.72$ for the time interval $t^* \approx 38.4$	19-8
Fig. 10	Lift coefficient for left and right half-wing as function of dimensionless time	19-9
Fig. 11	Frequency spectrum for the lift coefficient of left and right half-wing	19-9
Fig. 12	Lift coefficient for left and right half-wing as function of dimensionless time with intervals for detailed analysis	19-10
Fig. 13	Flow analysis for the time interval $t^* \approx 79.3$ according to Fig. 12: a) Left vortex, axes, side view; b) Left and right vortex axes, top view; c) Right vortex axes, side view	19-10
Fig. 14	Flow analysis for the time interval $t^* \approx 79.3$ according to Fig. 12: a) Left vortex, axes, side view; b) Mean upper surface pressure distribution, lines $\bar{c}_p = \text{const.}$; c) Right vortex axes, side view	19-11
Fig. 15	Flow analysis for the time interval $t^* \approx 85.7$ according to Fig. 12: a) Left vortex, axes, side view; b) Left and right vortex axes, top view; c) Right vortex axes, side view	19-12
Fig. 16	Flow analysis for the time interval $t^* \approx 85.7$ according to Fig. 12: a) Left vortex, axes, side view; b) Mean upper surface pressure distribution, lines $\bar{c}_p = \text{const.}$; c) Right vortex axes, side view	19-12
Fig. 17	Flow field in the cross section at $x / c_i = 0.72$ for the time interval $t^* \approx 79.3$. Lines of constant mean values of total pressure loss, $1 - \bar{p}_t / p_{t\infty} = \text{const.}$	19-13
Fig. 18	Flow field in the cross section at $x / c_i = 0.72$ for the time interval $t^* \approx 79.3$. Lines of constant standard deviation of total pressure, $p'_t / p_{t\infty} = \text{const.}$	19-13
Fig. 19	Flow field in the cross section at $x / c_i = 0.72$ for the time interval $t^* \approx 85.7$. Lines of constant mean values of total pressure loss, $1 - \bar{p}_t / p_{t\infty} = \text{const.}$	19-14
Fig. 20	Flow field in the cross section at $x / c_i = 0.72$ for the time interval $t^* \approx 85.7$. Lines of constant standard deviation of total pressure, $p'_t / p_{t\infty} = \text{const.}$	19-14
Fig. 21	Instantaneous flow field for $t^* = 85.7$: Lines of constant total pressure loss, $1 - \bar{p}_t / p_{t\infty} = \text{const.}$ in the cross section at $x / c_i = 0.72$	19-15
Fig. 22	Instantaneous flow field for $t^* = 85.7$: Vortex axes and upper surface pressure distribution with lines $c_p = \text{const.}$	19-15

CHAPTER 20

Figure 1	Vortex flow structures on a sharp-edged delta wing at high angle of attack	20-2
Figure 2	Wind tunnel and CFD model configurations	20-3

Figure 3	Computational surface grids of the with-centerbody wing models	20-4
Figure 4	65° delta wing, convergence histories of lift and pitching moment coefficients	20-6
Figure 5	65° delta wing, comparison of overall surface pressure distributions and correlation with PSP data, $M_\infty=0.17$ and $\alpha=21^\circ$	20-8
Figure 6	65° delta wing, comparison of surface C_p distributions at different chordwise locations, $M_\infty=0.17$ and $\alpha=21^\circ$	20-9
Figure 7	55° delta wing, comparison of overall surface pressure distributions and correlation with PSP data, $M_\infty=0.18$ and $\alpha=15^\circ$	20-10
Figure 8	55° delta wing, comparison of surface C_p distributions at different chordwise Locations, $M_\infty=0.18$ and $\alpha=15^\circ$	20-10

CHAPTER 21

Figure 1	Spiral and bubble vortex breakdown	21-28
Figure 2	Particle paths in a spiral burst: (a) experimental, and (b) computational	21-28
Figure 3	Schematic of basic helical vortex breakdown model	21-28
Figure 4	Velocities induced on a vortex element	21-28
Figure 5	Helix inclination and radius as a function of swirl ratio ($\delta=0.78$)	21-29
Figure 6	Effective disturbance convection velocity (replotted from Reference 10)	21-29
Figure 7	Effective disturbance wavelength: (a) replotted from Reference 10, (b) variation with estimated vortex strength	21-29
Figure 8	Disturbance frequency: (a) from Reference 10, (b) non-dimensionalised using estimated vortex strength	21-30
Figure 9	Mabey's vortex shedding frequency correlation (key as Figure 8)	21-30
Figure 10	Effect of burst onset and sweep angle on lift curve slope	21-30
Figure 11	Example of scatter in vortex burst position correlations	21-30
Figure 12	Model for vortex breakdown in roll from Reference 38	21-31
Figure 13	Lan & Hsu's lift-loss factor, replotted from [34]	21-31
Figure 14	Suction peak reduction ahead of vortex breakdown	21-31
Figure 15	A 'bubble' model for the effects of vortex breakdown	21-31
Figure 16	Cross-flow velocities induced by a leading-edge vortex	21-31
Figure 17	Helical vortex in the cross-flow plane	21-31
Figure 18	Effect of burst spiral radius on upper surface cross-flow velocity at the leading-edge	21-32
Figure 19	Effect of incidence and sweep on vorticity shedding parameter	21-32
Figure 20	Predicted vortex lift factor k	21-32
Figure 21	Vortex lift factor k derived from experimental force data in Reference 9	21-32
Figure A-1	Helical vortex geometry, showing positive sense for all parameters	21-36
Figure A-2	Effect of helix pitch on binormal and tangential induced velocity coefficients	21-36
Figure B-1	Low incidence variation in core position with angle of attack	21-39
Figure B-2	Variation in core height with angle of attack	21-39
Figure B-3	Correlation of spiral burst radius with incidence	21-39
Figure C-1	Effect of sweep angle on estimated lower and upper leading-edge velocities V_L and V_U	21-42

Figure C-2	Effect of Reynolds Number on estimated lower surface leading-edge velocity	21-42
Figure C-3	Contribution from component of freestream velocity parallel to the wing surface	21-42

CHAPTER 22

Fig. 1	65° delta wing model	22-10
Fig. 2	Effect of vortex breakdown on rolling moment in static case	22-10
Fig. 3	Effect of vortex breakdown on rolling moment in dynamic case	22-10
Fig. 4	Effect of vortex breakdown on normal force in static case	22-10
Fig. 5	Vortex breakdown locations over delta wings with different sweepback angles	22-10
Fig. 6	Predicted and measured vortex breakdown location for rolled 65° delta wing ($\sigma=30^\circ$)	22-11
Fig. 7	Static lift coefficient for delta wings with different sweep angles	22-11
Fig. 8	Comparisons of normal force at static and rolling oscillation conditions	22-12
Fig. 9	Comparisons of pressure coefficient for different static conditions ($\sigma = 30^\circ$, $x/c=0.75$)	22-12
Fig. 10	Free-to-roll motion histories	22-13
Fig. 11	Phase portrait of 65° delta wing free-to-roll motion trajectories ($\sigma=30^\circ$)	22-13
Fig. 12	Experimental case of free-to-roll motion for validation and verification	22-13
Fig. 13	Diagram of direct method for free-to-roll motion	22-13
Fig. 14	Contributions of different motion components on vortex breakdown	22-13
Fig. 15	Comparisons between measured and direct method during free-to-roll motion histories	22-14
Fig. 16	Instantaneous surface pressure at point A ($\phi_t=0^\circ$)	22-14
Fig. 17	Instantaneous surface pressure at point B ($\phi_t=-17.143^\circ$)	22-14
Fig. 18	Instantaneous surface pressure at point C ($\phi_t=0.303^\circ$)	22-14
Fig. 19	Instantaneous surface pressure at point D ($\phi_t=12.308^\circ$)	22-15
Fig. 20	Instantaneous surface pressure at point E ($\phi_t=2.183^\circ$)	22-15
Fig. 21	Instantaneous surface pressure at point F ($\phi_t=19.818^\circ$)	22-15
Fig. 22	Diagram of Iterative method	22-15
Fig. 23	Comparisons between measured free-to-roll motion histories and predicted (iterative) results	22-15

CHAPTER 23

Fig. 1	Vortex flow prediction & applications with LE & TE devices & challenges	23-6
Fig. 2	Evaluation method incorporating attained thrust, LE suction analogy & vortex breakdown empiricisms, symmetric & asymmetric situations	23-6
Fig. 3	Previous experimental knowledge on vortex breakdown onset on delta wings & swept wings	23-7
Fig. 4	Extended qualification of vortex flows, starting from Lamar's work	23-8
Fig. 5	Lan & Hsu method for incorporating vortex breakdown, symmetric flows on delta wings	23-8
Fig. 6	Analysis & extension of vortex breakdown progression, using Lan & Hsu parameters	23-9

Fig. 7	Introducing Mach number compressibility effects on vortex breakdown	23-9
Fig. 8	Results for planar, sharp-edged delta wings of varying LE sweep	23-10
Fig. 9	Experimental model with pivoted twisted & cambered wings	23-10
Fig. 10	Typical modelling of symmetric wing 58°	23-10
Fig. 11 (a-b)	Typical results on a symmetric 58° planar wing with vortex breakdown, spanwise loads & total forces, Mach 0.35	23-10
Fig. 12	Typical results on a symmetric 58° cambered wing with vortex breakdown, total forces depicted, $M=0.35$	23-11
Fig. 13	Side-slipping wing flow, visualisation & LE suction distribution	23-11
Fig. 14	Modelling of side-slipping wing	23-11
Fig. 15	Typical results on a planar 58° wing, $\beta = 10^\circ$, with vortex breakdown, total forces	23-11
Fig. 16	Typical results on a cambered 58° wing, $\beta = 10^\circ$, with vortex breakdown, total forces	23-11
Fig. 17	Typical results on a planar 53° wing, sideslip 10° , with vortex breakdown, total forces, $M=0.2$	23-12
Fig. 18	Typical results on a cambered 53° wing, $\beta = 10^\circ$, with vortex breakdown, total forces spanwise loads, $M = 0.2$	23-12
Fig. 19	CL – α graphs on cambered 53° wing, $\beta = 10^\circ$, theory & experiment, $M = 0.2$	23-12
Fig. 20	53° cambered wing, sideslip effect on C_l & C_n relationships, theory with stall model, $M = 0.2$, Re: R1 & R3	23-12
Fig. 21	53° cambered wing, ΔC_l & ΔC_n (Discount intercepts at $\alpha = 0^\circ$) relationships, theory & experiment, $\beta = 10^\circ$, $M = 0.2$, Re: R1 & R3	23-12
Fig. 22	Challenges, winglets, cranks	23-12

List of Tables

Table		Page
CHAPTER 2		
Table 1	Summary of experimental investigations considered in this Chapter	2-23
CHAPTER 5		
Table 1	Wind tunnel and water tunnel entries	5-16
Table 2	Wind/water tunnel models tested	5-17
CHAPTER 9		
Table 1	Steady Experiments Test Matrix	9-5
Table 2	Large Amplitude Pitch Oscillations Test Matrix	9-6
Table 3	Small Amplitude Pitch Oscillations Test Matrix	9-7
CHAPTER 12		
Table 1	Grid designation for delta wing computations	12-7
Table 2	Onset of instability as a function of local Reynolds number	12-8
CHAPTER 13		
Table 1	Dimensional and non-dimensional time-step size, number of computed time steps, CPU time and total file size (Euler)	13-7
Table 2	DES time-step study: dimensional and non-dimensional time-step size, number of time steps per period of oscillation, Strouhal number	13-14
CHAPTER 14		
Table 1	Comparison of longitudinal vortex breakdown locations for the different meshes studied	14-10
CHAPTER 15		
Table 1	Unstructured grids developed for the ONERA 70° delta wing during the NATO Research and Technology Organization task group AVT-080	15-3
Table 2	Vortex breakdown positions for the experiments and various grids	15-7
CHAPTER 17		
Table 1	ONERA 70° wing test cases	17-4
Table 2	Viscous grid dimensions	17-5
Table 3	Summary of steady breakdown locations for ONERA 70° wing at 27° angle of attack	17-8
Table 4	Vortex breakdown locations with and without supports	17-11
CHAPTER 20		
Table 1	Mesh sizes of the computed configurations	20-4

Working Group Members

CANADA

Dr. Xing Zhong HUANG
Principal Research Office
Aerodynamics Laboratory
National Research Council Canada
U-66, Uplands Campus
Ottawa, Ontario K1A 0R6
Email: xingzhong.huang@nrc-cnrc.gc.ca
Tel: 1-613-990-6796
Fax: 1-613-998-1281

FRANCE

Dr. J.-F. LE ROY
ONERA/DAAP/MMH
Institut de Mécanique des Fluides
5 Boulevard Painlevé
59045 Lille Cedex
Email: leroy@imf-lille.fr
Tel: 33 320 496 946
Fax: 33 320 529 593

Dr. Ovide RODRIGUEZ
ONERA/DAAP/MMH
Institut de Mécanique des Fluides
5 Boulevard Painlevé
59045 Lille Cedex
Email: rodriguez@imf-lille.fr
Tel: 33 320 496 946
Fax: 33 320 529 593

Dr. Jean-Pierre ROSENBLUM
DGT/DTA/IAP/MCFD
Dassault Aviation
78, quai Marcel Dassault
92214 Saint-Cloud
Email: Jean-pierre.rosenblum@dassault-aviation.fr
Tel: 33 1 47 11 5275
Fax: 33 1 47 11 4535

GERMANY

Prof. Dietrich HUMMEL
Institut fuer Stroemungsmechanik Techn.
Univers. Braunschweig
Bienroder Weg 3
D-38106 Braunschweig
Email: d.hummel@tu-bs.de
Tel: 49 531 391 2972
Fax: 49 531 391 5952

ITALY

Prof. Fulvia B. QUAGLIOTTI
Aerospace Engineering Department
Politécnico di Torino
Corso Duca Degli Abruzzi 24
10129 Torino
Email: quagliotti@polito.it
Tel: 39 011 5646819
Fax: 39 011 5646899

NETHERLANDS

Dr. Bambang SOEMARWOTO
NLR
Dept. of Computational Fluid Dynamics
& Aeroelasticity
Anthony Fokkerweg 2
1059 CM Amsterdam
Email: soemarwt@nlr.nl
Tel: 31 20 5113 698
Fax: 31 20 5113 210

Mr. Niek VERHAAGEN
Delft University of Technology
Aerodynamics Group
Department of Aerospace Engineering
P.O. Box 5058
2600 GB, Delft
Email: n.g.verhaagen@tudelft.nl
Tel: 31 15 278 6385
Fax: 31 15 278 3533

RUSSIA

Dr. A. KHRABROV
TSAGI
Zhukovsky 140180
Email: akhrab@tsagi.rssi.ru
Tel: 7 095 954 9816

SWEDEN

Dr. Stefan GÖRTZ
Dept. of Aeronautics, KTH
Teknikringen 8
10044 Stockholm
Email: Goertz@kth.se
Tel: 46 8 790 7602
Fax: 46 8 20 7865

SWEDEN (cont'd)

Mr. Yann LE MOIGNE
Dept. of Aeronautics, KTH
Teknikringen 8
10044 Stockholm
Email: Lemoigne@kth.se
Tel: 46 8 790 6465
Fax: 46 8 20 7865

Prof. Art RIZZI
Dept. of Aeronautics, KTH
Teknikringen 8
10044 Stockholm
Email: rizzi@aero.kth.se
Tel: 46 8 790 7620
Fax: 46 8 20 7865

UNITED KINGDOM

Dr. Mark ALLAN
Computational Fluid Dyn. Group
Dept. of Aerospace Engineering
University of Glasgow
Glasgow G12 8QQ
Email: Mallan@aero.gla.ac.uk
Tel: 0141 330 6481
Fax: 0141 330 5560

Dr. Ken BADCOCK
Computational Fluid Dyn. Group
Dept. of Aerospace Engineering
University of Glasgow
Glasgow G12 8QQ
Email: Gnaa36@aero.gla.ac.uk
Tel: 0141 330 4106
Fax: 0141 330 5560

Prof. Doug I. GREENWELL
Dept. of Aerospace Engineering
University of Bristol
Queens Building
University Walk
Clifton, Bristol BS8 1TR
Email: Doug.Greenwell@bristol.ac.uk
Tel: 44 1179 546868

Dr. Ismet GURSUL
Dept. of Mechanical Engineering
University of Bath
Bath BA2 7AY
Email: Ensiag@bath.ac.uk
Tel: 44 1225 826394
Fax: 44 1225 826928

Dr. R.K NANGIA
WestPoint
78 Queens Road
Bristol B58-1QX
Email: nangia@blueyonder.co.uk
Tel: 44 117 987 3995

UNITED STATES

Dr. Charles E. JOBE
AFRL/VAAA
2130 Eighth Street, Bldg. 45, Room 261
Wright-Patterson AFB
Ohio 45433-7542
Email: Charles.job@va.afrl.af.mil
Tel: 1-937-255-8484
Fax: 1-937-656-7868

Dr. Jim LUCKRING
NASA Langley Research Center
Subsonic Aerodynamics Branch
Bldg 1212, Room 133, M.S. 286
17 West Taylor Street
Hampton, VA 23681-2199
Email: j.m.luckring@larc.nasa.gov
Tel: 1-757-864-2869
Fax: 1-757-864-8195

Dr. Tony MITCHELL
HQ USAFA/DFAN
2354 Fairchild Drive, Suite 6H27
USAFA
CO 80840-6222
Email: Tony.mitchell@usafa.af.mil
Tel: 1-719-333-3435
Fax: 1-719-333-4013

Dr. Scott MORTON
HQ USAFA/DFAN
2354 Fairchild Drive, Suite 6H27
USAFA
CO 80840-6222
Email: Scott.Morton@usafa.af.mil
Tel: 1-719-333-9387
Fax: 1-719-333-4813

Dr. Robert C. NELSON
106 Hessert Center
Dept. of Aerospace and Mechaneeing
University of Notre Dame
Notre Dame, IN 46556-5684
Email: rmelson@nd.edu
Tel: 1-574-631-4733
Fax: 1-574-631-8355

UNITED STATES (cont'd)

Dr. Shahyar Z. PIRZADEH
NASA Langley Research Center
Configuration Aerodynamics Branch
Bldg 1251, Room 102A
M.S. 499
16 Victory Street
Hampton, VA 23681-2199
Email: s.pirzadeh@larc.nasa.gov
Tel: 1-757-864-2245
Fax: 1-757-864-8469

Dr. Miguel R. VISBAL
Computational Sciences Branch
Air Vehicles Directorate
Air Force Research Laboratory
Wright-Patterson AFB
OH 45433
Email: Miguel.visbal@wpafb.af.mil



Vortex Breakdown over Slender Delta Wings

(RTO-TR-AVT-080)

Executive Summary

Highly manoeuvrable military aircraft and tactical missiles are expected to perform at extreme flight conditions, which often result in the development of complicated three-dimensional separated flow fields. For such air vehicles slender or delta-type wings are often applied in order to gain extra aerodynamic force and control power while maintaining a compact structure over weight advantage. At such flight conditions, several vortical structures materialize from the rolling up of the viscous free shear layer previously confined within the attached wing boundary layer. As the angle of attack or the manoeuvring rate increases to certain value, the vortical structures, and in particular the leading-edge vortices, experience a sudden disorganization known as vortex breakdown. This flow phenomenon can severely limit, if not eliminate, the control power gained. Due to the lack of sufficient understanding of the flow physics, numerical and predictive capabilities have largely lagged behind operational requirements. The rapid progress in hardware and computational fluid dynamics (CFD) software, however, has made it possible to simulate numerically the behaviour of vortical flow up to including vortex breakdown. However, before a specific code can be used with confidence for the prediction of vortical flow behaviour, it is crucial to validate its correctness in describing the flow physics and to verify its accuracy against valid experimental data. As far as the latter data is concerned, a problem is that, due to the complexity of the vortical flow over slender wings at high incidence, experimental results obtained with identical wind tunnel models at similar test conditions seldom satisfactorily reproduced when tested in different facilities.

A primary task thus is to collect and assess reliable experimental data sets and to validate CFD and analytical solutions against a selected reliable experimental database. In view of this, a Technical Activity Proposal (TAP) for “Vortex Breakdown over Slender Wings” was approved by RTO/AVT. A special Task Group AVT-WG 080 was founded to perform the task. The objectives of this group were in general to compile experimental data sets on leading-edge vortex behaviour over a simplified military wing configuration, to select a reliable experimental database and to validate different CFD codes and analytical solutions versus the reliable experimental database.

A total of eight experimental cases, ten state-of-the-art CFD solutions and three analytical solutions have been included. The collected experimental databases include time-average results at static model conditions, ensemble-average results at dynamic model conditions and unsteady results at static/dynamic model conditions. The numerical solutions have been generated using different numerical methods, codes and grids on a benchmark test case, an ONERA 70° delta wing, but also other cases are considered. In addition, the effects of tunnel wall interference and interactions between vortices are included in the numerical solutions.

Eclatement tourbillonnaire sur les ailes delta effilées

(RTO-TR-AVT-080)

Synthèse

Les avions militaires hautement manœuvrables et les missiles tactiques sont censés opérer dans des conditions de vol extrêmes, ce qui se traduit souvent par le développement de champs d'écoulement tridimensionnels compliqués et séparés. Pour de tels engins aériens, les ailes effilées ou les ailes deltas sont souvent utilisées pour bénéficier d'une force aérodynamique supplémentaire et pour contrôler la puissance tout en maintenant une structure compacte en plus du gain de poids. Dans de telles conditions de vol, plusieurs structures tourbillonnaires se matérialisent à partir de l'enroulement de la couche de cisaillement de surface libre auparavant confinée dans la couche limite solidaire de l'aile. Quand l'incidence ou le taux d'évolution atteignent une certaine valeur, les structures tourbillonnaires et en particulier les tourbillons de bord d'attaque subissent une désorganisation soudaine connue sous le nom de rupture du vortex. Ce phénomène d'écoulement peut sévèrement limiter, voire éliminer la marge de puissance acquise. En raison d'un manque de connaissances suffisantes sur la physique des flux, les capacités numériques et d'anticipation ont pris énormément de retard au regard des exigences opérationnelles. Cependant, les progrès rapides en matériels et en logiciels de calculs de dynamique des fluides (CFD) ont rendu possible la simulation numérique du comportement tourbillonnaire jusque et y compris le décrochement du vortex. Cependant, avant que l'on puisse utiliser avec confiance un code spécifique pour la prévision du comportement du flux tourbillonnaire, il est crucial de valider sa justesse pour la description de la physique des flux et de vérifier sa précision pour avoir des données expérimentales valables. Pour ce qui concerne ces dernières données, le problème est que, à cause de la complexité du flux tourbillonnaire à incidence élevée sur les ailes effilées, les résultats expérimentaux obtenus avec des modèles de souffleries identiques dans des conditions d'essais identiques se reproduisent rarement avec satisfaction quand les tests ont lieu dans différents centres.

De ce fait, le premier travail a été de récupérer et d'évaluer des ensembles de données expérimentales fiables et de valider les solutions CFD et analytiques pour une base de données sélectionnée expérimentale fiable. Dans ce but, un Projet d'Activité Technique (TAP) sur « la Rupture du vortex sur les ailes effilées » a été approuvé par le RTO/AVT. Un Groupe Opérationnel spécial AVT-WG 080 a été créé pour remplir cette mission. D'une manière générale, les objectifs de ce groupe étaient de compiler des ensembles de données sur le comportement du vortex de bords d'attaque pour une configuration d'aile militaire simplifiée, de sélectionner la base de données expérimentale fiable et de valider les différents codes CFD et les solutions analytiques confrontés à la base de données expérimentale fiable.

Un total de huit cas expérimentaux, 10 solutions CFD de pointe et trois solutions analytiques ont été inclus dans l'étude. Les bases de données expérimentales récupérées comprennent des mesures moyennes temporelles en conditions statiques, des mesures moyennes d'ensemble en conditions dynamiques et des mesures d'écoulement non stationnaire en conditions statiques et dynamiques. Les solutions numériques ont été générées en utilisant différentes méthodes numériques, codes et grilles sur un test d'évaluation, une aile delta ONERA 70° mais d'autres cas ont également été examinés. De plus, les effets de l'interférence avec les parois de la soufflerie et des interactions entre les tourbillons ont été inclus dans les solutions numériques.

Chapter 1 – INTRODUCTION AND HIGHLIGHTS

X.Z. Huang

Institute for Aerospace Research
National Research Council
M10, 1200 Montreal Rd.
Ottawa, Ont. Canada K1A 0R6
xingzhong.huang@nrc.ca

N.G. Verhaagen

Delft University of Technology
Department of Aerospace Engineering
P.O. Box 5058, 2600 GB, Delft, the Netherlands
n.g.verhaagen@tudelft.nl

ABSTRACT

This chapter highlights the goals and achievements of NATO/RTO/AVT Task Group AVT-080: Leading-edge Vortex Breakdown over Slender Wings. After a survey and assessment of current experimental data sets in NATO and PfP countries, eight reliable experimental data sets have been collected and compiled. These data sets include time-average results at static model conditions, ensemble-average results at dynamic model conditions and unsteady results at static/dynamic model conditions. Ten state-of-the-art numerical solutions have been obtained on an ONERA 70° delta wing test case using different numerical methods, codes and grids. For other wing configurations and test cases, the effects of tunnel wall interference and of interactions between vortices are calculated. In addition to the experimental data and computational solutions, three advanced analytical solutions are included.

1.1 INTRODUCTION AND BACKGROUND

The tactical advantage of high manoeuvrability and agility of military air vehicles has been an incentive to continually expand their flight envelope. For such vehicles, delta-type wings are often used since the formation of leading-edge vortices generates more lift than straight wings and their compact structure has a weight advantage. A disadvantage, however, is that the leading-edge vortices may break down under certain conditions. This results in severe discontinuities and a loss of lift, which deteriorates the aircraft performance, stability and control. The traditional linear or local-linear aerodynamic models are not valid under these conditions. This makes the development of adequate prediction methods more complex and difficult. As a consequence, hitherto predictive capabilities have largely lagged behind operational requirements. A fundamental obstacle is the lack of sufficient understanding of the flow physics associated with vortex breakdown.

The flow over a delta wing at high angle of attack is characterized by the formation of strong leading-edge vortices. For simplicity, the basic cross flow structure of such a three-dimensional vortex is given in Fig. 1. The free shear layer rolls up in a spiral fashion to the rotational or outer core. The smaller viscous sub-core or inner core region in the center of the vortex is dominated by viscous forces and characterized by large gradients of velocity and pressure (Verhaagen and Ransbeeck [1]). A key feature of three-dimensional vortex cores is the strong interaction between the swirl and the axial velocities, and the low pressures in the sub-core region. The core induces strong swirl velocities and associated with this a strong negative pressure (suction) on the leeward surface of the wing. Due to the interaction between the core and

INTRODUCTION AND HIGHLIGHTS

the boundary layer on this surface, a secondary vortex and at certain conditions even a tertiary vortex is formed near the leading edge.

Non-intrusive velocity measurements and numerical simulations have revealed the existence of vortical sub-structures in the free shear layer. Gursul [3], [4] gives an in-depth discussion of these sub-structures. Observations by Lawson [5], and Gad-el-Hak and Blackwelder [6] learn that the free shear layer rolls up periodically into discrete vortical substructures. This is thought to be a consequence of a Kelvin-Helmholtz (K-H) type of instability of the shear layer. The frequencies of the sub-structures correspond to those predicted from linear stability analysis of the cross-flow shear layer. Gursul also discusses the correlation between the presence of the K-H instability and random displacements of the vortex core (“vortex wandering”). Apart from the unsteady K-H instability, steady sub-structures formed by the stationary small-scale vortices are observed in the free shear layer. These spatially fixed sub-structures are evident in time-average measurements. The sub-structures follow a helical trajectory around the core and the spacing (frequency) between the sub-structures remain relatively constant. Measurements by Mitchell [9] show these structures, which can even persist after vortex breakdown (Fig. 5). The sub-structures tend to diffuse with increasing turbulence [1]. Numerical simulations of the time-average flow solution by Visbal and Gordnier [6] confirm the existence of these sub-structures. They also give the instantaneous flow solutions and show the transition process with increasing Reynolds number (Fig. 3). At certain conditions, e.g. at high incidence, the primary vortex core will break down. Lambourn & Bryer [6] visualized two types of breakdown in a water tunnel (Fig. 4a); a bubble- and spiral-type of breakdown. The latter type is most frequently observed in delta wing experiments. In that case, downstream from the breakdown point the core filament abruptly kinks and starts to spiral around at a certain frequency and eventually disintegrates into a “wake-like” turbulent flow (Fig. 4b). Nevertheless, this breakdown process gives the flow in the vicinity of the spiral a spatial and temporal periodicity that has an effect on the wing pressure distribution. The unsteady flow downstream of the vortex breakdown point induces an oscillating pressure distribution on the wing causes a loss of lift, wing buffeting and an unstable pitching and rolling behavior.. Interaction of burst vortices with tail surfaces is the cause of structural vibrations and fatigue problems occurring in tail fins of modern fighter aircraft (Fig. 6). All these unwanted phenomena limit the performance and manoeuvrability of military aircraft. Since the breakdown of leading-edge vortices has a large impact on the aerodynamic behavior and flight mechanics of current and future military aircraft, understanding of the flow physics and the parameters that affect the onset of vortex breakdown is essential.

Different theories were developed to explain the onset of vortex breakdown: from a quasi-cylindrical approach [8], positive feedback of negative azimuthal vorticity [9], critical state or wave theory [10], to weakly non-linear wave theory [11]. A number of review articles have been published on vortex breakdown aspects [12-18]. Nevertheless, it is still difficult to predict the onset of vortex breakdown and its response to motion variables in real applications. Thus, it is important to collect and to clarify existing experimental results in order to develop a sound theory and to validate numerical solutions.

The behavior of vortex breakdown has been the subject of a large number of experimental studies since Werlé [19] first observed this phenomenon over a delta wing in 1954. A problem is that the correlation between the data is often poor. For example, Fig. 7 [20] shows that there is a significant scatter in the vortex breakdown location over simple delta wings measured in different wind tunnels. This complicates the understanding of the vortex flow physics. The rapid progress in computer hardware and Computational Fluid Dynamics (CFD) codes has made it possible to numerically simulate the complex flow associated with vortex breakdown. However, before a specific code can be used with confidence, it is crucial to validate its correctness in predicting the flow physics and to verify its accuracy against valid experimental data. Thus, to first assess and clarify existing experimental data is a prerequisite.

In view of these requirements, a proposal titled “Vortex Breakdown over Slender Wings” was approved by the Applied Vehicle Technology (AVT, Research and Technology Organization (RTO) as the Task

Group, AVT-080. This Task Group was formed in the autumn of 2000 and has since met twice a year till summer 2003 when the activities of the various participants was presented at an AIAA summer conference. The participants represent ten NATO and PfP countries and are active in the corresponding experimental, CFD and theoretical fields. The objective and working strategy of the AVT-080 are described below.

1.2 OBJECTIVES AND CRITERIA OF AVT-080

1.2.1 OBJECTIVES

In general, an AVT Task Group's activity aims at allowing researchers from different nations to work together in order to solve a particular research and technology problem of relevance to NATO's interests. The objectives of AVT-080 are briefly as follows:

- (1) To collect reliable experimental data sets on the leading-edge vortex behavior over delta wing configurations.
- (2) To generate different CFD solutions for the flow over a delta wing at high angle of attack and to validate these solutions against a reliable experimental data base.
- (3) To develop analytical solutions at flow conditions where vortex breakdown occurs.

In order to fulfil these objectives, the AVT-080 has been subdivided into three sub-groups: The Experimental, CFD and Analytical sub-group. The following working steps were decided upon for these sub-groups:

- (1) To conduct a survey and collect reliable candidate experimental databases on vortex breakdown over delta wings with well described test conditions. These include time-average results in static model conditions, ensemble-average results in dynamic model conditions and unsteady results in static/dynamic model conditions
- (2) To compile, compare and clarify the results of the candidate data sets with the aim of fulfilling current and future requirements of CFD validation and verification on military applications.
- (3) To generate CFD solutions with different grid configurations, turbulence models, etc. for the test conditions of the selected experimental data set and to compare these solutions with the selected data set.
- (4) To obtain solutions with a validated CFD code for the case of the wing in free flight conditions. Corrections should be derived for the presence of wind tunnel walls and supports.
- (5) To develop and validate analytical solutions that help to understand and predict the aerodynamics when vortices and their breakdown are involved.

1.2.2 REQUIREMENTS FOR CANDIDATE OF EXPERIMENTAL CASES

The following criteria were guidelines for choosing candidate experimental cases:

- (1) The geometry of the model configuration should be closely related to high-performance military aerial vehicle and yet be as simple as possible.
- (2) The experimental test conditions should be clearly defined and the measured data should be sufficiently accurate and detailed.
- (3) Those cases should be either fulfill the current requirement of CFD validation and verification or be ahead of current status of CFD capability so that the CFD researcher can use these as a staircase for

INTRODUCTION AND HIGHLIGHTS

future applications.

Specifically, the experimental test case should provide the following information:

- (1) Accurately measured model shape and surface finish.
- (2) The actual position and motion of the model, including both static and dynamic deformations if it occurs.
- (3) The behavior of the boundary layer on the model.
- (4) The tunnel wall geometry and boundary layer behavior.
- (5) Specification of model support and tunnel wall interference
- (6) Specification of the measurement methods and the accuracy of the measured data.

Since the delta wing configuration is widely used for military air vehicles and is simple in geometry, this configuration was chosen for the considered benchmark.

Even for a simple delta wing due to the complexity of vortical flow at high incidence, traditionally conducted experiments tend to produce qualitative rather than the accurate quantitative results that are needed for validating CFD solutions. Moreover, experimental results obtained on one and the same delta wing geometry seldom reproduce when tested in different facilities. Significant discrepancies, especially in the vortex breakdown location, are present in the data obtained at different institutes. Small geometric variations, model deformations due to aerodynamic loads as well as differences in the test conditions, and measuring techniques significantly affect the measured vortex breakdown position and thus degrade the accuracy of the results. A reliable assessment of the accuracy of the data generated in ground tests is a first requirement [Chapter-2]. Thus, an evaluation of the data sets is imperative, so that accurate data can be selected that can be properly used for the development of state-of-the-art theoretical or computational flow models. These models will aid in the improvement of the performance of existing highly manoeuvrable military aircraft and help design the configuration of future combat aircraft. The objective hence is to extract as much useful and quantitative information as possible after a critical examination and comparison of existing data sets of the flow over delta wings with special attention to vortex behavior and vortex breakdown.

After a thorough screening of the available candidate experimental test cases, the cases of delta wings with a 65° and 70° leading-edge sweep back angle were found to be best suited to fulfil our requirements.

1.3 PROGRESS OF EXPERIMENTAL SUB-GROUP

1.3.1 TEST CASE CATEGORIES

Leading-edge vortex flow and, especially, breakdown are characterized by the occurrence of unsteady flow phenomena. In order to avoid neglecting important information about these flow phenomena, the Experimental Sub-group has considered the following three test case categories:

- (1) Time-averaged results obtained at static model conditions,
- (2) Ensemble-averaged results obtained at dynamic model conditions
- (3) Unsteady results obtained at static/dynamic model conditions.

The first category includes the measured time-averaged vortex breakdown location, air loads, surface pressure distributions measured by pressure taps and Pressure Sensitive Paint (PSP), three-dimensional velocity vector field measured by Laser Doppler Velocimetry (LDV) or Particle Image Velocimetry (PIV) and surface flow topology at static model conditions.

The second category consists of ensemble-average air loads, surface pressure distribution (measured with unsteady pressure transducers), smoke/laser-light-sheet flow visualization, as well as free and forced

motion history at dynamic model conditions.

The third one includes the results of instantaneous azimuthal vorticity, RMS swirl velocity, spectra and fluctuation of breakdown locations, pressure fluctuations on wing and tail fin, etc. at static or dynamic model conditions.

The three categories cover relatively simple to more complicated test cases. In the following overview examples are given of test cases belonging to these three categories. It should be noted that this overview is not complete; many good test cases could not be included due to limited time and resources.

1.3.2 OVERVIEW OF PUBLISHED EXPERIMENTAL DATA SETS

1) ONERA 70° delta wing data set

Mitchell [9] reports on ONERA data sets in Chapter 3. Provided are profound time-average and quantitative data for the surface pressures and the on- and off-the-surface flow over a delta wing at static conditions. The model was a simple 70° delta wing with a flat upper surface and sharp leading-edges (Fig. 8). The lower surface edges were bevelled at 15°. In contrast to most delta wings tested in other experiments, the trailing edge was not sharp but blunt. The root chord was 0.95 m. The model was supported by a sting/support assembly on the lower surface that kept the wing at about the center axis of the test section with changing α . (Fig. 9). The tests were conducted in the ONERA F2 wind tunnel with a test section 1.4-m wide, 1.8-m high and 5.0-m long. Most data were acquired at $\alpha = 27^\circ$ and an air speed of 24 m/s ($M = 0.069$), yielding a $Re_c = 1.56 \times 10^6$. The characteristics of the vortices and their breakdown locations were determined from qualitative and quantitative surface and flow field visualization and measurement techniques. Laser sheet visualization and 3-D LDV results were analyzed in order to provide details on the flow field and on the vortex breakdown phenomena. Surface oil flow visualization and steady surface pressure measurements were examined to identify the influence of vortex breakdown on the leeward surface of the delta wing. At abovementioned conditions the breakdown location was identified at $x/c = 0.65$. Transition of the upper-surface boundary layer from laminar to turbulent was evident from a kink in the secondary-separation line at $x/c = 0.40$. It is worthwhile to mention that the support interference and blockage caused by the sting/support assembly was estimated to cause an upwash of by $2\sim 3^\circ$. This upwash may have promoted the vortex breakdown location upstream and have an effect on the level of the surface pressures and flow field data.

2) NASA Langley Research Center 65° delta wing data sets

Chu and Luckring [23] report on a NASA LaRC test case in [Chapter-4]. The test case is characterized by profound pressure data at high Reynolds and Mach numbers (Re up to $120(?) \times 10^6$ and M up to 0.9). The model was a 65° delta wing and is depicted in Fig. 10. It had a length of 0.654 m (25.734 in). The central part of the model was flat with a sting fairing at the rear. A bent sting assembly supported the model. Four interchangeable leading-edge sets were available with sharp, small, medium and large radii. Normalized by the mean aerodynamic chord, the radii had values of 0, 0.05, 0.15 and 0.30 percent, respectively. The wing and sting surfaces are represented by fully analytical functions. The model had a total of 183 pressure taps distributed over the upper and lower surface of the wing. In addition, normal force and pitching-moment coefficients were also presented for the above Reynolds and Mach number ranges. The tests were conducted in the National Transonic Facility at NASA Langley which has test section 8.2 ft high by 8.2 ft wide by 25 ft long with a slotted ceiling and floor. This data set gathered for a wide range of Reynolds and Mach numbers and different leading-edge shapes could help to investigate the effect of boundary conditions, compressibility and viscosity on the characteristics of the vortex flow.

3) IAR/USAF-AFRL static and dynamic test cases

The IAR/AFRL database collected and reported by Huang [24] in Chapter 5 has information for all three

INTRODUCTION AND HIGHLIGHTS

categories of test cases, from time-averaged results at static model conditions to unsteady results at static/dynamic model conditions. Many different kinds of model have been tested; from diamond to delta wing with leading-edge sweep angles from 55° to 75° . Moreover, individual parts of the models, such as the leading edge, center body and fairing, etc., were designed to be interchangeable, with one example shown in Fig. 11. The contributions of individual parts on aerodynamics can thus be investigated. The data were acquired at both static and dynamic test conditions. The dynamic tests were conducted at high angular rate in roll, pitch and non-planar coning motions. The waveforms of the motion include sinusoid, ramp-and-hold and free-to-roll motion. The database consists of surface oil-flow visualization results, off-surface laser-smoke sheet and PIV measurements, surface pressures (acquired through 57 pressure taps, unsteady pressure transducers and PSP), aerodynamic loads and motion histories. Most of the tests were conducted either in the IAR 6ft by 9ft low-speed wind tunnel or in the AFRL 7ft by 10ft wind tunnel. The coning test was conducted in the IAR 15in by 20in water tunnel. The angle of attack, roll angle and coning angle ranges from 0° to 90° , -90° to $+90^\circ$ and -360° to $+360^\circ$, respectively with maximum non-dimensional angular rate of 0.2 in pitch and roll (in wind tunnel) and 0.6 in coning (in water tunnel). Most of the tests were carried out at a Mach number $M = 0.3$ and a Reynolds number Re between 2 and 3×10^6 based on mean aerodynamic chord.

4) Bath's University unsteady flow behavior test cases

Gursul's experimental data [5], [6] reported in Chapter 6 are helpful for the validation of solutions of the unsteady characteristics of burst and unburst vortices. His data has been obtained on delta wings with sweep angles of 60° , 65° , 70° , 75° , 76° and 80° . The models had a flat upper surface and were beveled at 45° on the windward side. The experiments were carried out in an open-circuit wind tunnel with a 0.30 m wide and 0.30 m high cross section. The models were sting mounted and the measurements conducted at Reynolds numbers ranging from 2.5 to 10×10^4 . The data set includes information about the fluctuations in the velocity, pressure and vortex breakdown locations. Large amplitude velocity fluctuations including the variation of RMS swirl velocity, time-averaged swirl velocity and their characteristic value of probability density function were measured. Moreover the effect of Re on the maximum RMS swirl velocity and the effect of vortex breakdown on pressure fluctuation of the helical mode instability were investigated. A dimensional circulation was introduced to study the helical mode instability and the dominant dimensionless frequency. In addition, the time history of axial breakdown location and its spectra as well as the dominant frequencies in the wake of breakdown were reported in its data set. These data will be very valuable if for the validation and verification of CFD solutions of the unsteady behavior of the vortex and its breakdown.

5) Notre Dame University pitch and roll test case

Nelson [2][20] discusses the Notre-Dame University test case in Chapter 7. This case is one of the earliest experiments presented in this RTO report. It has information for static and dynamic test conditions. Both pitching and rolling oscillations with large amplitudes were carried out. Moreover, wing rock experiments were conducted and investigated. Delta wings and double-delta wings with different sweep back angles were tested. The experiments were performed in the 2 ft by 2 ft test section low-speed wind tunnel at the University of Notre Dame Aerospace Engineering Laboratory. The maximum velocity is approximately 52.5 ft/s with a corresponding Re of 3×10^5 per ft root chord. Results include smoke and laser-sheet flow visualization, surface pressure, velocity, vorticity vector field measured by hot wire probe and balance data. A typical laser light sheet illumination of the vortical flow over an 85° swept delta wing at $\alpha = 10^\circ$ is shown in Fig. 3. The Kelvin-Helmholtz instability of the free shear layer and its sub-structures can be clearly observed from that figure.

6) Delft University and IAR 65° Delta Wing Surface flow topology studies

The topology of the wing surface skin-friction lines determined with surface oil-streak techniques

provides important information about the time-averaged effect of the vortex flow on the surface boundary layer. Several investigators of the Experimental Sub-group have performed detailed studies of the topology on delta wings. Verhaagen and Jobe [22] studied the flow over a 65° delta wing at sideslip in a low-speed wind tunnel at the Delft University of Technology. The model had a chord length of 0.665 m, a flat upper surface and bevelling on the bottom surface. The model was tested at a constant $\alpha = 30^\circ$ and at angles of sideslip ranging from -20 to $+20^\circ$. Special attention was paid to the flow on the apex, the boundary-layer transition and tip regions. The topologies for the flow on the apex give insight in the origin of the vortices over the delta wing and may help the numerical modelling of the flow in this region. Huang [23] studied the topology evolution, or bifurcation, and different flow topology patterns as a function of various flow parameters e.g. roll angle, angle of attack, flow speed, etc. Tests were conducted in the IAR and USAF/AFRL low speed wind tunnels mainly on a 65° delta wing at different sting angles and wide range of roll angles. Special attention was paid to the critical states in the airloads. High resolution results clearly show the evolution in time-averaged flow patterns, the vortex whorl at the end of secondary and tertiary vortices and possible correlation between flow topology changes and the airload critical states under certain conditions.

Owing to large time scale existing in the response of vortex breakdown to motion variables, the behavior of the vortex and its breakdown in dynamic model conditions is quite different from static conditions for the same attitude. The dynamic case will also be of high interest for military applications. To meet this demand the Subgroup selected the following test cases.

7) TsAGI static and dynamic test case

In Chapter 9 Khrabrov and Greenwell summarizes the results of 70° and 65° delta wings tested in the TsAGI low-subsonic wind tunnel T-103 [1]. The 70° delta wing has two different sizes and leading-edge shapes. To verify TsAGI's dynamic data an identical 70° delta was manufactured and tested at DERA, Bedford, UK. For the 65° delta wing, there were also two models, one of which has the same shape as the IAR/USAF 65° delta wing. Static and pitch oscillation dynamic tests were conducted in the T-103 wind tunnel, which has an open working section with elliptical cross section 2.33 m x 4.0 m. As shown in Fig. 12, two different dynamic rigs (large and small amplitude pitch oscillation) were constructed and used in the tests. A five-component internal balance was used to measure the airloads during tests. Leading-edge shape and center body effects in static and dynamic tests with large and small amplitude were also studied using a mean angle of attack in the range of -10° to 36° , an amplitude of 5° to 26° and an oscillation frequency of 0.2 to 1.5 Hz.

8) TPI Test Case

De Luca et al. tested a 65° delta wing in the low-speed wind tunnel of Politecnico di Torino (T.P.I.) both in static and dynamic conditions [25] and [Chapter-10]. The model had a flat upper surface and a sting connected to the lower surface covered by a center body. The internal balance measured the static coefficients. The static tests included flow visualizations, force and pressure measurements. Steady pressure coefficients were measured on the model's upper surface to estimate the effect of vortex breakdown on the surface steady pressure distribution. The dynamic test consisted of flow visualizations and force measurements under small amplitude forced oscillations in roll and pitch. Damping derivatives in pitch and roll were measured by the direct forced oscillation technique. Boundary-layer transition was analyzed by means of infra-red thermography (the upper model surface was artificially heated). The tests were conducted at free stream velocities from 10 to 40 m/s and α ranging from 5 to 45° with amplitude $\Delta\alpha = 5^\circ$. This data set provides information on the transition of the boundary layer on a delta wing.

INTRODUCTION AND HIGHLIGHTS

1.3.3 BENCHMARK FOR THE CFD EXERCISE

Although three categories of test cases have been collected by the Experimental Sub-group, considering the limited time, manpower and CFD capability available, the AVT-080 has decided to limit the benchmark for this current CFD exercise to the first category, i.e. a study of the time-averaged vortex behavior at static model conditions. In addition, the following conditions were taken into consideration for the CFD exercise:

A straight leading-edge delta-wing configuration was selected as being a simple but sufficient representation of wings applied to high-performance military air vehicles.

Sharp leading edges were chosen in order to fix boundary-layer separation.

The test data should contain accurate global information, such as surface pressure and/or vortex flow field vorticity or velocity distributions.

To reduce the number of CFD solutions, the test conditions were limited to a certain angle of attack and a speed range of interest to military aircraft in high- α flight conditions.

After having compared and evaluated the data sets mentioned in the former section and, considering the limited capabilities available for the CFD exercise, the ONERA 70° swept delta wing data set reported by Mitchell [7] and [Chapter-3] has been taken as a benchmark for the validation and verification of the CFD solutions.

1.4 OVERVIEW OF CFD SOLUTIONS

A part of the overview of the computations conducted by members of the CFD-Subgroup is given below. If not stated otherwise, the solutions were obtained for the steady conditions of the ONERA delta wing experiment ($\alpha=27^\circ$, $U_\infty=24$ m/s and $Re=1.5 \times 10^6$).

1) NASA LaRC solutions

Pirzadeh in his publications [26] and [Chapter-11] emphasis the effectiveness of an adaptive grid procedure in “capturing” concentrated vortices generated at sharp edges or flow separation lines of lifting surfaces flying at high angles of attack. His method is based on a tetrahedral unstructured grid technology developed at the NASA Langley Research Center. Two steady-state, subsonic, inviscid and Navier-Stokes flow test cases are presented to demonstrate the applicability of the method for solving vortical flow problems. The first test case concerns vortex flow over a simple 65° delta wing with different values of leading-edge radius. Although the geometry is quite simple, it poses a challenging problem for computing vortices originating from blunt leading edges. The second case is that of a more complex fighter configuration. The superiority of the adapted solutions in capturing the vortex flow structure over the conventional unadapted results is demonstrated by comparisons with the wind-tunnel experimental data. The study shows that numerical prediction of vortical flows is highly sensitive to the local grid resolution and that the implementation of grid adaptation is essential when applying CFD methods to such complicated flow problems.

2) USAF WPAFB solutions

Visbal and Gordnier conducted study of the substructures of the leading-edge vortices [28] and [Chapter-12]. They applied a very high-order (6th-order) spatial discretization capable of capturing finer scales of the flow field on a given mesh resolution. Computations are performed for a 75° semi-infinite swept leading-edge at an angle of attack of 25° and Reynolds number $Re_c=1.8 \times 10^4$, 2.5×10^4 and 5×10^4

respectively. This configuration is selected in order to isolate the shear layer dynamics from disturbance associated with vortex breakdown or trailing-edge separation, which can be present in a finite wing. It has found that in contrast to previous numerical efforts, beyond a critical value of Re number, unsteady substructures appear in the shear layer above the wing, and their origin moves closer to the apex. The onset of this unsteady phenomenon is associated with unsteady separation of the wing upper surface boundary layer. The unsteady substructures, which are initially very coherent, exhibit secondary instabilities along their axes further downstream. This process results in the formation of concentrations of vorticity which are stretched and convected in helical paths around the leading-edge vortex. A time-averaged representation of the highly unsteady computed flow field is characterized by the existence of helical substructures which co-rotate with the primary vortex similar to those observed in high Reynolds number mean experimental data. This finding suggests that the so-called stationary helical pattern, seen in the time-averaged experimental measurements, is created by the secondary instability of the unsteady substructure as they breakup and convect into the helical velocity field of the primary vortex. It is therefore postulated that, in unsteady delta wing flows, the so-called unsteady and stationary substructures are not two different physical phenomena but rather different representations of the same complex shear transition process.

3) KTH solutions

Görtz, Le Moigne and Rizzi of KTH performed time-accurate Euler and Detached-Eddy Simulations (DES) of the vortex breakdown over the full-span ONERA delta wing at $\alpha = 27, 30$ and 35° [29]-[31], [Chapter-13] and [Chapter-14]. The blunt trailing edge of the ONERA wing was modeled as a sharp one. The unsteady, three-dimensional Euler equations were solved using second-order accurate Runge-Kutta and dual time-stepping, respectively. The simulations capture the mutual interaction between the port and starboard vortices. This interaction is more intense at higher incidences. Spiral-type vortex breakdown was observed to be predominant. The spiral breakdown structure showed good qualitative agreement with the spiral-type breakdown observed in experiments. Spectral analysis of the temporal variation of the aerodynamic coefficients showed that high-frequency oscillations were due to the interaction of the spiral windings with the upper surface of the wing. Periodically, a transformation from spiral- to bubble-type of breakdown occurred (Fig. 13). It alternated between the port and starboard side. Its appearance was associated with a significant upstream movement of the breakdown location, resulting in asymmetry between the port and starboard breakdown locations. The breakdown location fluctuations and the asymmetry were responsible for low frequency oscillations of the aerodynamic load coefficients.

In addition, a time-step study was performed for the implicit DES calculations. It demonstrated the demanding nature of vortex breakdown with a time-step size of the order of 10^{-4} s required for time accuracy. Furthermore, a grid sensitivity study was carried out. Patched grid refinement over the wing by a factor of two in all directions had little influence on the surface pressure distribution. However, the vortex core was better resolved on the refined grid, leading to a significantly better agreement between the computed and experimental breakdown location. These first results showed that DES is capable of predicating the fluctuating vortex breakdown location quite accurately (with reservation for grid influences, which may be greater than the effect of viscosity). The surface pressure distribution, however, was underestimated (with reservation for the wall interference effects in the experiment). This work on DES is only beginning, and more needs to be done to draw firm conclusions.

4) USAF Academy solutions

Morton from the USAF Academy computed the flow around the ONERA delta wing in free flight using a commercial CFD code, COBALT [30] and [Chapter-15]. This package solved the unsteady, three-dimensional, compressible N-S equations on a hybrid unstructured grid. DES simulation was applied to simulate three-dimensional eddies which occur in the unsteady, massive separated (locally reversed) flow of the burst vortex core. Unsteady simulations were run for 10,000 time steps with an iteration plus three

sub-iterations per time step. Average quantities were based on the latter 8,000 iterations. A study was made of the time accuracy and grid insensitivity effects on the solutions. These are important parameters when computing unsteady flow phenomenon such as vortex breakdown. An appropriate time step, non-dimensionalized by freestream velocity and root chord, of 0.0025 with three sub-iterations per time step was determined. The grid sensitivity was investigated by comparing a baseline grid with 2.7 million cells with a 3.2 million grid. For the latter grid an Adaptive Mesh Refinement (AMR) technique was used to increase the number of points in vorticity containing regions such as the free shear layer and the core. The baseline-grid solution shows a vortex breakdown structure that corresponds to that of the experiment, a secondary vortex and also alternating pairs of spanwise coherent vortices flowing off the (blunt) trailing edge. The AMR-grid solution (Fig. 14) displays some additional features such as the stationary sub-structures in the free shear layer that were observed in the experiment. The computed breakdown point is found to lie within the scatter of the experimental data. The trailing edge vortices are evident in the flow behind the trailing edge. These vortices as predicted give rise to a strong peak at a Strouhal number of 8 in a power spectral density analysis of the unsteady normal force.

5) ONERA solutions

LeRoy and Rodriguez from the ONERA Lille Center computed the flow using ELSA, a software package that solves the compressible, three-dimensional, Reynolds-Averaged Navier-Stokes (RANS) equations in a cell-centered finite-volume formulation [31] and [Chapter-16]. The computations on a semi-span representation of the ONERA delta wing were performed on a H-H topology structured mesh. Two turbulence models were used; the Spalart-Allmaras-Rotation-Correction (SARC) and Shear-Stress-Transport (SST). Calculations were stopped after 4000 and 5000 iterations for SARC and SST, respectively, because the residues stopped decreasing and the vortex breakdown point stopped moving. The latter point was predicted to be located at $x/c=0.76$ with the SST model, and at $x/c=0.93$ with the SARC model (in the experiment, burst is at $x/c=0.65$). The computed spiral structure of the burst is in agreement with the experiment, however, the surface pressure distributions and turbulent kinetic energy were less well predicted.

6) University of Glasgow solutions

Allan, Badcock, Barakos and Richards studied the wind tunnel wall effects on the vortex breakdown over a steady and pitching semi-span WEAG-TA15 delta wing that had a leading-edge sweep of 65° and cropped wing tips [32] and a 70° delta wing [Chapter-17]. A cell-centered finite volume technique was used to solve the Euler and RANS equations. The diffusive terms were discretized using a central differencing scheme and the convective terms used a Roe's scheme. Flow simulations were initially run on an explicit scheme to smooth out the flow and then switched to an implicit algorithm to accelerate convergence. Computations were performed on the delta wing in free flight and in a wind tunnel with three different cross sections. The flow in the wind tunnel was modeled using an H-H topology structured mesh. The steady computations were performed at $\alpha = 21^\circ$ and $M=0.4$, and were compared with experimental data generated by Löser [33]. The solutions show that the presence of sidewalls moves the breakdown point upstream towards the apex of the delta wing. The roof and floor have a small influence on the burst location. Tunnel blockage does not have a large effect on vortex breakdown. Results for the flow over a pitching delta wing were also presented.

7) NLR solutions

Soemarwoto of NLR Netherlands employed the time-dependent RANS equations as provided in NLR's CFD system ENFLOW [34] and [Chapter-18]. A variant of the Wilcox $k - \omega$ turbulence model was used, with free-stream dependency and the singular behaviour of ω near solid walls resolved. Excessive production of the eddy viscosity inside vortex cores, (typical with RANS-based vortical flow simulation), was avoided by limiting the production of the turbulence kinetic energy through a promoted production of

the dissipation rate. The ratio of the vorticity and strain-rate magnitudes was used to detect vortex cores. The spatial discretization employed a cell-centered finite volume scheme, using Jameson-type artificial dissipation fluxes with matrix coefficients to increase the accuracy. For the time-accurate calculation, a second-order dual-time stepping scheme was applied, using a five-stage explicit Runge-Kutta scheme for each physical time step. Low Mach number pre-conditioning was applied. A semi-span delta-wing/sting representation of the ONERA wing was considered with the flow assumed to be symmetric. The flow domain was divided into 3,694,080 structured grid cells in 50 blocks. A non-dimensional time step of 0.0025 was used. After the transient had decayed, a self-sustained unsteady flow solution was evident. A Fourier analysis gave a dominant frequency corresponding to a Strouhal number $St \approx 9$. The instantaneous flow solutions indicated a variation of non-dimensional vortex breakdown location in the range of 67-75%, noting that the calculation had not yet covered the period of the lowest frequency.

8) University of Braunschweig solution

Hummel and Estorf [35] and [Chapter-19] applied unsteady Euler equations to a cropped delta wing at a large angle of attack. Compared with most of the other computational solutions, which have been carried out on half wings using a symmetry condition in the centre section of the wing, Hummel and Estorf did the calculations both for with or without a symmetry condition in the centre section of the wing. The computations have been obtained using the CFD code FLOWer, which was compiled for the NEC-SX5 architecture in sequential mode. The software has been developed by the Institute of Design Aerodynamics at the DLR Braunschweig, Germany. The conservation laws of mass, momentum and energy in integral form have been solved on a structured mesh. A second order cell-vertex scheme and central differences are used for discretization. For the damping of numerical oscillations, artificial second and fourth order dissipative terms are added to the governing equations. The fourth order term, which is dominant in the absence of shocks, is controlled by the user-defined damping coefficient $k^{(4)}$. Integration with respect to time utilizes a five stage Runge-Kutta scheme to converge the solution. For the unsteady calculations, a global time stepping procedure without implicit residual smoothing is used. Spiral-type vortex breakdown has been calculated for both sides of the wing. Using a symmetry condition the flow field turns out artificially symmetrical. Without such a symmetry condition, even for symmetrical free stream conditions the flow field turned out to be unsymmetrical: Different vortex breakdown positions, frequencies and phase differences in the rotation of the spiral vortex axes and modifications of the vortex axes have been found for both sides of the wing. After a long running time of the calculations a rather irregular behaviour of the flow quantities turned out.

9) IAR solutions

Benmeddours deployed numerical method to study the geometry effect [36] and [Chapter-20]. The vortex behaviour over a 55° diamond wing and a 65° wing model with or without centerbody were investigated. The inviscid vortex flows over the wings were simulated using a 3D unstructured tetrahedral grids generated via the Octree based Tetra module of ICEM CFD and an in-house Euler flow solver, FJ3SOLV developed at IAR. FJ3SOLV is a cell-centered code based on the finite volume formulation. The convective fluxes were discretized using Jameson's central difference scheme where second and fourth order dissipation terms were added explicitly for stability. Time integration to steady state was achieved by means of an explicit 4-stage multi-step scheme and convergence was accelerated using a combination of local time stepping, implicit residual smoothing, and enthalpy damping techniques. Boundary conditions were imposed using fictitious cells outside the boundaries. Appropriate flow properties were set in these cells to satisfy the slip conditions on the solid boundaries, where the normal velocity was set to zero. At the far-field boundaries a characteristic approach based on Riemann invariants subject to one-dimensional analysis was used. Only sharp-edged models of the wings were considered. The respective mesh sizes (grid cells) used for the different configurations of the two wings were 0.37 million and 0.5 million for 55° diamond wing and 65° delta wing respectively. The effects of the centerbody were

INTRODUCTION AND HIGHLIGHTS

investigated for one flow condition for each wing.

In general, there are no global differences in these comparisons for both wing models. The vortex core location at $x/c=0.4$ is a little outboard with the centerbody than that without the centerbody. Moreover, it appears that the wing without the centerbody has slightly more suction in the forward portion and less suction in the aft portion. There is little bump in the pressure distribution at where the centerbody edge locates. The local flow acceleration on the centerbody shoulder may cause this local suction bump. Nevertheless, the comparisons show that centerbody may not cause global effects on the pressure distribution at the present conditions.

1.5 OVERVIEW OF ANALYTICAL SOLUTIONS

1) Greenwell's method

Greenwell [37] and [Chapter-21] presented an engineering model for the structure and behavior of the vortex in its burst state. He used a model for the burst process that consists of four regions, viz. a straight vortex core, followed by an inner core deceleration region, a transition region downstream of the bursting point and finally a semi-infinite helical vortex. The breakdown process was modelled as a symmetry-breaking sub critical bifurcation from an axisymmetrical unburst vortex to a helically symmetric translating spiral burst form. Applying continuity and rotational velocity constraints to the motion of a semi-infinite helix resulted in a critical swirl ratio similar to that given by conventional stability analyses. In order to apply his model to experimental data obtained on delta wings, Greenwell treated the dynamics of the inner and outer core regions separately. This was based on the fact that most of the vorticity is contained in the outer core and critical swirl values are reached there first. It is the inner core, however, that conventional flow visualization techniques tend to mark. Model predictions agreed reasonable well with measured helix pitch, inclination, radius, induced and convection velocity, and frequency content. To predict the impact of vortex breakdown on the delta wing characteristics, a simple lift-loss model is developed. Predictions for the magnitude and the rate of onset of burst-induced lift loss agree with experimental data.

2) Huang's method

Huang [38] and [Chapter-22] proposed a modified Non-linear Indicial Response theory based upon Tobak [39] in conjunction with Internal State-Space representation method (NIRISS). It was determined that the leading-edge vortex behavior has a dominant effect on the aerodynamics of delta wing and therefore the time-averaged vortex breakdown location was chosen as an internal variable to approximately describe the state of separated and vortex flow over the delta wing. The response of this internal variable to arbitrary motion was estimated by a modified non-linear indicial response functional. By means of a vortex filament method, this vortex breakdown location offers the additional information required at a given instantaneous attitude for calculating the outputs - surface pressure and air loads. The flight equations and trajectories of a 65° wing under a free-to-roll condition were then solved. The method was applied to estimate time-averaged vortex breakdown locations, normal force over delta wings with different sweep back angles, surface pressures and free-to-roll motion histories on a 65° delta wing. The comparisons between measured and estimated data showed that within the framework of the proposed mathematical model, it is possible to apply this NIRISS method to predict quantities in the non-linear flight regime.

3) Nangia's method

Nangia [40] and [Chapter-23] discussed an empirical method which can be used to predict the forces and moments on delta-wing/body (and other) configurations in symmetric and asymmetric flights, including Mach and Reynolds number effects. His method used subsonic lifting surface theory, semi-empirical

“attained” thrust and vortex effects This method was coupled with a model to predict vortex breakdown. Empirical criteria were developed for wings with low sweep. A trailing-edge separation model was included. The vortex breakdown model was based on a model by Lan & Hsu [41] that determined the onset of vortex breakdown from the local maximum in the unattained leading-edge suction distribution. The upstream movement of the burst point was also estimated. Predictions for the forces and moments of 53° and 58° swept trapezium wings, with and without sideslip, for various Mach and Reynolds numbers were presented. The predictions showed a promising correlation with available experimental data.

1.6 CONCLUSIONS AND RECOMMENDATIONS [Chapter 24]

Plentiful and substantial results for experimental, computational and analytical cases have been obtained. After careful assessment, eight experimental cases, ten computational results and three analytical methods have been published indicating the great success obtained by this Task Group.

However, there is still an imminent demand for comprehensive experimental data set with both force-moment and flowfield measurements. Unsteady surface and flowfield data are needed along with the steady data to establish a complete dataset. It is imperative that the experimental configuration be closed to advanced military vehicles, clearly define and include model, sting and wind tunnel test section geometries. Computational results demonstrate the importance of the turbulence and treatment in modelling the leading-edge, especially the rounded leading-edge, vortices. The location of transition from laminar flow to turbulent flow and the location of the primary vortex separation have remarkable impact on the vortex breakdown and the character of the phenomena. Additionally, the geometries of the wind tunnel walls and sting have a measurable influence on the results.

1.7 ACKNOWLEDGMENTS

Funding for this work was provided by the Research and Technology Organization (RTO), the different nations and organizations. Their contributions make members of this group be able to work together and make these achievements and thus gratefully acknowledged.

The authors would like to thank all Task Group members and all contributors for their collaboration, dedication and tremendous effort, which achieve this excellent work.

The Chapters related to experimental cases and computational cases were reviewed by Dr. J. Luckring and by Dr. M. Visbal respectively. Their experience and knowledge in the field contributed very much to the publications.

1.8 REFERENCES

- [1] Verhaagen, N.G. and VanRansbeeck, P., “Experimental and Numerical Investigation of the Flow in the Core of a Leading-Edge Vortex”, AIAA 90-0384, January 1990.
- [2] Nelson, R., “Unsteady Aerodynamics of Slender Wings,” *Aircraft Dynamics at High Angles of Attack: Experiments and Modeling*, AGARD R776. March 1990.
- [3] Gursul, I., “Review of Unsteady Vortex Flows over Delta Wings,” AIAA 2003-3942, June 2003.
- [4] Menke, M. and Gursul, I., “Unsteady Nature of Leading-Edge Vortices,” *Physics of Fluids*, Vol. 9, No. 10, 1997, pp. 2960-2966.

INTRODUCTION AND HIGHLIGHTS

- [5] Lowson, M.V., "Visualization Measurements of Vortex Flows," AIAA-89-0191, January 1989
- [6] Gad-el-Hak, M. and Blackwelder, R.F., "The Discrete Vortices from a Delta Wing," AIAA Journal, Vol. 23, No. 6, 1985.
- [7] Visbal, M. and Gordnier, R., "On the Structure of the Shear Layer emanating from a Swept Leading Edge at Angle of Attack," AIAA 2003-4016, June 2003.
- [8] Lambourne, N.C. and Bryer, D.W., "The bursting of Leading-Edge Vortices – Some Observations and Discussion of the Phenomenon. Aeronautical Research Council R. & M. 3282, April 1961.
- [9] Mitchell, A., "Experimental Data Base selected for RTO/AVT Numerical and Analytical Validation and Verification: ONERA 70-deg Delta Wing," AIAA 2003-3941, June 2003.
- [10] Délerly, J.M., "Aspects of Vortex Breakdown," *Progress in Aerospace Sciences*, Vol. 3, 1994, pp. 1-59.
- [11] Brown, G. L. and Lopez, J. M., "Axisymmetric Vortex Breakdown," J. Fluid Mech. (1990) Vol. 221, pp. 553-576.
- [12] Squire, H. B., "Analysis of the Vortex Breakdown Phenomenon," Part 1. Imperial College of Science and Technology, Aeronautics Dept. Report No. 102, 1960.
- [13] Hall, M.G., "Vortex Breakdown," Annual Review of Fluid Mechanics, Vol. 4, 1972.
- [14] Leibnovich, S., "The Structure of Vortex Breakdown," Annual Review of Fluid Mechanics, Vol. 10, 1978.
- [15] Leibnovich, S. and Ma, H. Y., "Soliton Propagation on Vortex Cores and the Hasimoto Solution," *Phys. Fluids* 26(11), 3173-3179., 1983.
- [16] Escudier, M., "Vortex Breakdown: Observations and Explanations," *Prog. In Aerospace Sci.* Vol. 25 189-229, 1988.
- [17] Leibovich, S., "Vortex Stability and Breakdown: Survey and Extension," AIAA Journal, Vol. 22, No. 9, 1983.
- [18] Delery, J., "Physics of Vortical Flows," *Journal of Aircraft*, Vol. 29, No. 5, 1992, pp. 856-876.
- [19] Delery, J., "Aspect of Vortex Breakdown," *Prog. Aerospace Sci.* Vol. 30, pp. 1-59, 1994.
- [20] Nelson, R.C. and Pelletier, A., "The Unsteady Aerodynamics of Slender Wings and Aircraft undergoing Large Amplitude Maneuvers," *Progress in Aerospace Sciences*, Vol. 39, 2003, pp. 185-248.
- [21] Werlé, H., "Quelques Resultats Expérimentaux sur les Ailes en Flèche, aux faibles Vitesses, obtenues en Tunnel Hydrodynamique", *La Recherche Aéronautique*, no. 41, Sept.-Oct. 1954, pp. 15–21.
- [22] Huang, X.Z. , Jobe C. and Hanff, E., "A Critical Assessment and Requirement for Ground testing on Vortex Breakdown Locations over Delta Wings," Symposium on Advanced Flow Management Part A - Vortex Flows and High Angle of Attack for Military Vehicles, RTO-MP-069.

- [23] Chu, J. and Luckring, J., "Experimental Surface Pressure Data obtained on 65° Delta Wing across Reynolds Number and Mach number Ranges," NASA Technical Memorandum 4645, February 1996.
- [24] Verhaagen, N.G. and Jobe, C.E., "Effects of Sideslip on the Characteristics of a 65-deg Delta Wing", AIAA 2003-0736, January 2003.
- [25] Huang, X. and Hanff, E., "Surface Flow Topology on a Delta Wing Rolling at High Incidence," AIAA/NPU AFM Conf., June, 1996
- [26] Huang, X.Z., "Comprehensive Experimental Research on Vortex Behavior over Military Wing Configurations," AIAA 2003-3940, June 2003.
- [27] DeLuca, L., Guglieri, G., Cardone, G. and Carlomagno, G.M., "Experimental Analysis of Surface Flow on a Delta Wing by Infrared Thermography, *AIAA Journal*, Vol. 33, No. 8, 1995.
- [28] Pirzadeh, S.Z., "A Solution-Adaptive Unstructured Grid Method by Grid Subdivision and Local Remeshing," *Journal of Aircraft*, Vol. 37, No. 5, pp. 818-824, 2000.
- [29] Visbal, M. and Gordnier, R., "On the Structure of the Sgear Layer Emanating from a Swept Leading Edge at High Angle of Attack," AIAA 2003-4016, 2003.
- [30] Görtz, S., "Time-Accurate Euler Simulations of a Full-Span Delta Wing at High Incidence," AIAA 2003-4304, June 2003
- [31] Görtz, S., "Detached-Eddy Simulations of a Full-Span Delta Wing at High Incidence," AIAA 2003-4215, June 2003.
- [32] Morton, S., "High Reynolds Number DES Simulations of Vortex Breakdown over a 70 Degree Delta Wing," AIAA 2003-4216, June 2003
- [33] LeRoy, J. and Rodriguez, O., "RANS for ONERA 70-deg Delta Wing Steady Flows," AIAA 2003-4219, June 2003
- [34] Allan, M., Badcock, K., Barakos, G. and Richards, B., "A RANS Investigation of Wind Tunnel Interference Effects on Delta Wing Aerodynamics," AIAA 2003-4214, June 2003
- [35] Löser, T., "Dynamic Force and Pressure Measurements on an Oscillating Delta Wing at Low Speeds", Report IB 129-96/9 DLR Braunschweig, 1997.
- [36] Soewarmoto, B., "Numerical Investigation of Vortical Flows Using RANS Equations," AIAA 2003-4215, June 2003
- [37] Müller, J. and Hummel, D., "Numerical Analysis of the Unsteady Flow above a Slender Delta Wing at Large Angles of Attack," ICAS Proceedings 2000, Paper ICA 0252, 2000.
- [38] Benmeddour, A., Mebarki, Y., and Huang, X.Z., " Euler/RANS Simulations of Steady Flow over the IAR 65 degree Delta Wing," IAR CPR-AL-2004-0007, 2004.
- [39] Greenwell, D., "A simple Engineering Model for Vortex Breakdown," AIAA 2003-3943, June 2003.
- [40] Huang, X.Z., "Non Linear Indicial Response and Internal State-Space Representation," AIAA 2003-

INTRODUCTION AND HIGHLIGHTS

3944, June 2003.

- [41] Tobak, M., Chapman, G.T. and Unal, A., "Modeling Aerodynamic Discontinuities and the Onset of Chaos in Flight Dynamical Systems," NASA TM 89420, Dec. 1986..
- [42] Nangia, R., "Applying Vortex Breakdown Empiricisms to Predict Wing Aerodynamic Characteristics in Symmetric and Asymmetric Situations," AIAA 2003-3945, June 2003.
- [43] Lan, C.E. and Hsu, C.H., "Effects of Vortex breakdown on Longitudinal and lateral Aerodynamics of Slender Wings by the Suction Analogy", AIAA 82-1385, 1982.

FIGURES

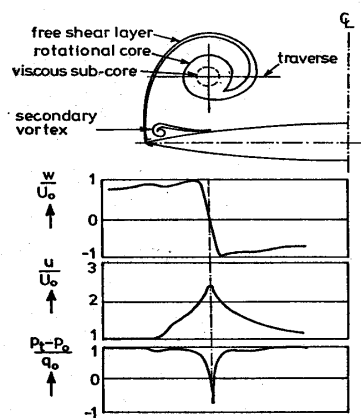


Fig. 1 Vortical crossflow structure [1]

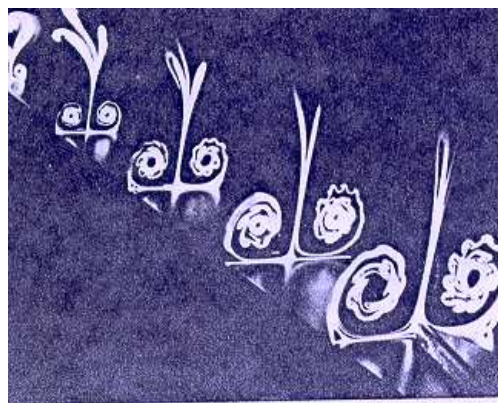


Fig. 2 Illumination of shear layer instability [2]

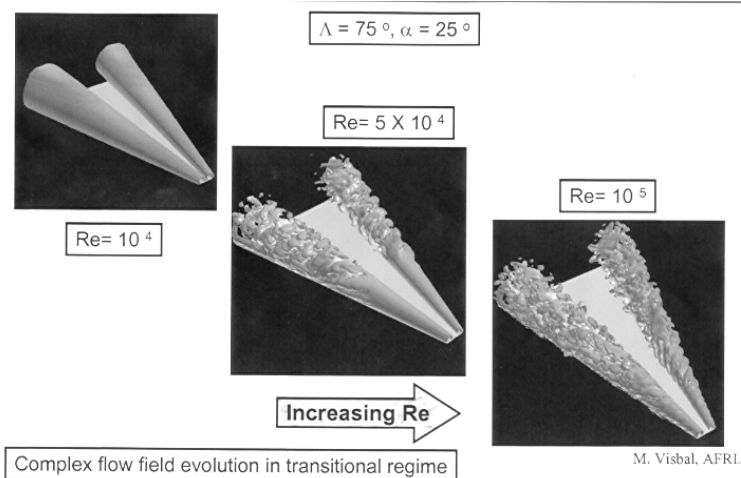


Fig. 3 Evolution of transition process in shear layer [5]

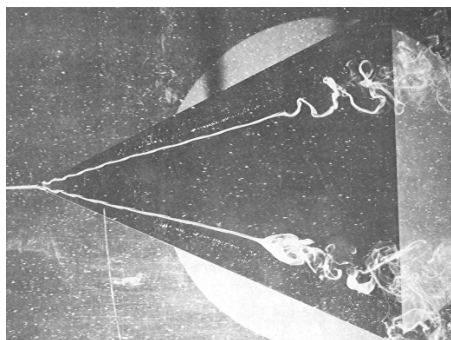


Fig. 4a Image of leading-edge vortex breakdown

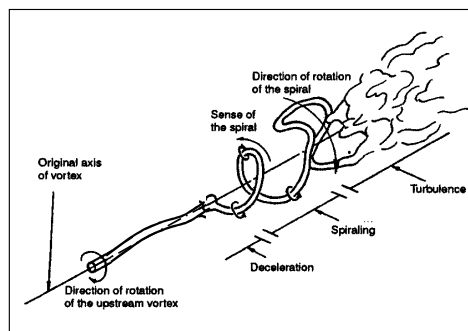


Fig. 4b Spiral of breakdown structure

Fig. 4 Leading-edge vortex breakdown [6]

INTRODUCTION AND HIGHLIGHTS

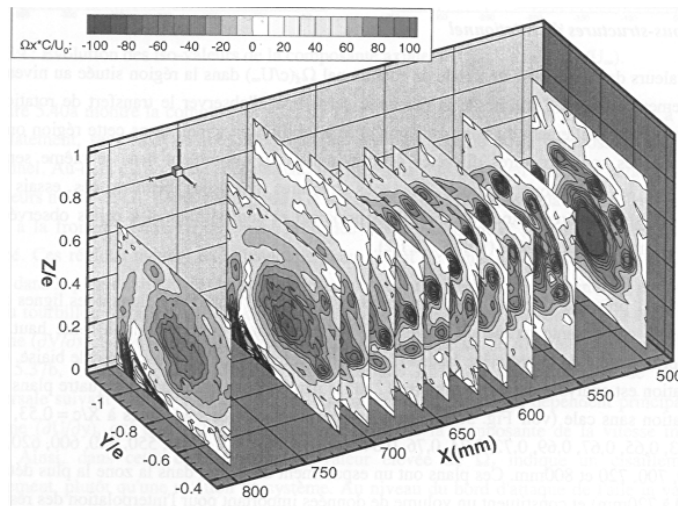


Fig. 5 Evolution of transition process in shear layer [5]



Fig. 6 Vortex breakdown/tail-fin interaction of F-18 HARV at $\alpha=25^\circ$ (NASA Photo)

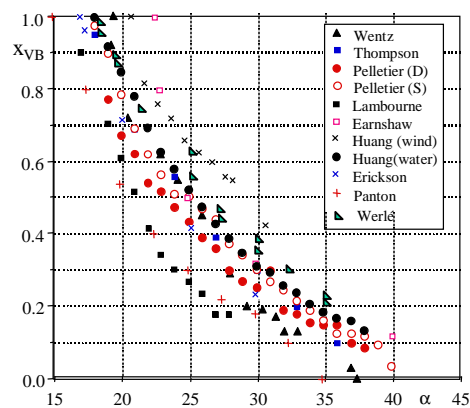


Fig. 7 Measured vortex breakdown on 65° delta wings at different facilities [20]

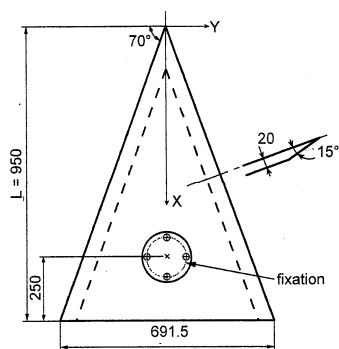


Fig. 8 ONERA 70° delta wing

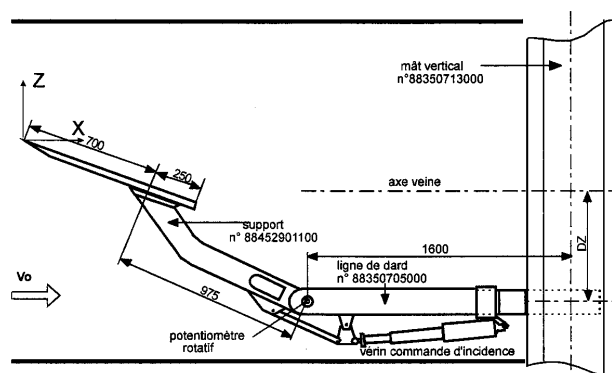


Fig. 9 Model sting/support assembly in ONERA F2 tunnel

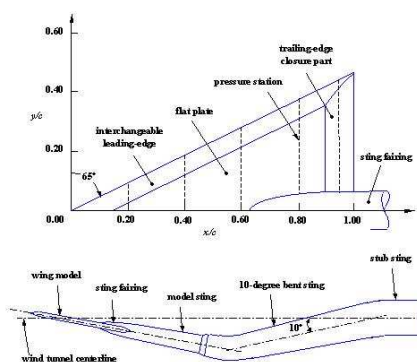


Fig. 10 NASA LaRC 65° delta wing

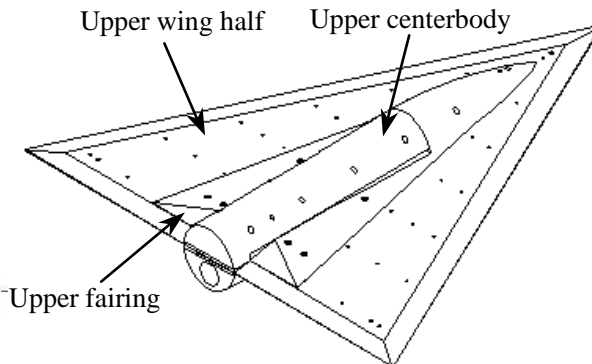


Fig. 11 IAR interchangeable 65° delta wing

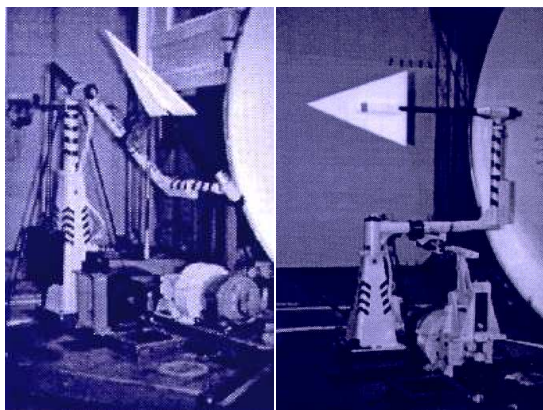


Fig. 12 Test rigs installed in TsAGI wind tunnel

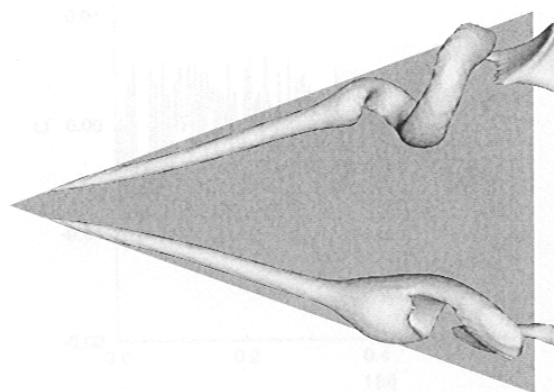


Fig. 13 Computed spiral and bubble breakdown [29]

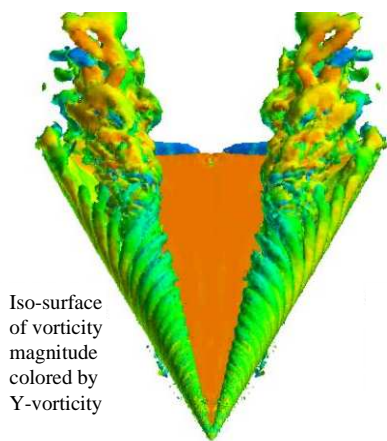


Fig. 14 AMR-grid instantaneous solution [31]

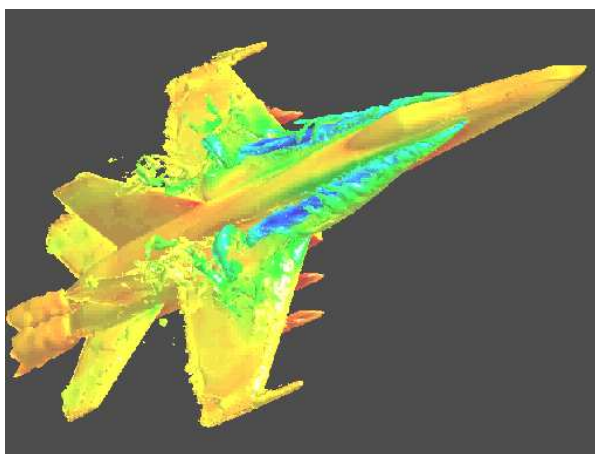


Fig. 15 AMR-grid instantaneous solution [31]

INTRODUCTION AND HIGHLIGHTS



Chapter 2 – CRITICAL ASSESSMENT OF TEST CASES ON VORTEX BREAKDOWN OVER SLENDER DELTA WINGS UNDER STATIC MODEL CONDITIONS

Xing Zhong Huang
Institute for Aerospace Research
National Research Council
1200 Montreal Rd.
Ottawa, Ont. Canada K1A 0R6

xingzhong.huang@nrc.ca

ABSTRACT

A critical assessment of more than thirty test cases on leading-edge vortex breakdown has been conducted. The test cases contain test data obtained on more than eighty wing configurations at high angles of attack and static model conditions. Special attention has been paid to related test conditions, such as model geometry, model blockage, model deformation under aerodynamic loads, wind tunnel wall and model support interference, the methodologies used in the experiments and the definition of vortex breakdown location. A screening process has been performed to help identify the relative merits of the various data sets and to extract reasonable confidence and quantitative information from the scattered database. This synthesized information is helpful to assess and validate numerical results.

List of Symbols

a	speed of sound in air
b	bevel width
c	wing chord
c_0	wing chord along the centre-line of the wing
h	height of a forward-facing step
M	Mach number, $M = \frac{V}{a}$
r	blockage, $r = \frac{S_{wing, \alpha=30}}{S_{test\ section}}$
Re_c	Reynolds number based on chord, $Re_c = \frac{V \cdot c}{\nu}$
Re_x	Reynolds number based on length, $Re_x = \frac{V \cdot x}{\nu}$
$S_{wing, \alpha=30}$	wing projection area from front at $\alpha=30^\circ$
V	velocity or flight speed
x	flat plate length in stream-wise direction

x_{VB}	vortex breakdown location in ratio with wing centre-line chord, $x_{VB} = X_{VB}/c_0$
X_{VB}	distance to vortex breakdown location measured along wing centre-line chord
α	angle of attack
δ	half bevel section angle
δ^*	boundary layer displacement thickness
Δ_{max}	difference between measured most downstream vortex breakdown location and mean vortex breakdown location
Δ_{min}	difference between measured most upstream vortex breakdown location and mean vortex breakdown location
Λ	angle of leading edge sweep
λ	ratio of bevel dimension to boundary layer displacement thickness, $\lambda = \frac{b}{\delta^*}$
σ	standard deviation
μ_0	viscosity of air
ν	kinematic viscosity of air
ρ	air density

2.1 INTRODUCTION

The tactical advantage of high maneuverability and agility has been the incentive for designers of fighter aircraft to continually expand the flight envelope of their designs. For such aircraft, slender or delta-type wings are often selected in order to gain extra aerodynamic force and control power while maintaining a compact structure over weight advantage. Modern combat aircraft routinely operate at high incidence and/or high angular rates, under which the flow field is usually dominated by strong leading-edge vortices, and where loss of controllability may be encountered.

In general, the flow over the delta wing surface may experience four different statuses of separation as the angle of attack increases. At low angle of attack there is no flow separation from the leading edge. The attached flow induces a leading-edge suction, which can be predicted from slender wing theory. As the angle of attack increases, depending on the leading-edge shape, flow separation starts to occur on the leading edge and progresses downstream as the second status of separation. A further increase of the angle of attack results in the third status: the formation of curved free shear layers and the vortex. The free shear layers roll up periodically into discrete vortical substructures. The substructures wind up spatially into a core over the leeward side of the wing forming a so-called leading-edge vortex. Further increasing the angle of attack leads to the last status: breakdown of the leading-edge vortex core. When breakdown occurs over a wing surface, it causes a sudden lift loss and a severe non-linearity in the aerodynamic loads.

Apart from non-linearity, vortex breakdown also causes a time dependence of aerodynamic loads. As a consequence, linear or local-linear aerodynamic models are no longer valid at flight conditions where vortex

breakdown occurs. Due to the lack of sufficient understanding of the flow physics and of reliable data sets, predictive capabilities have largely lagged behind operational requirements. A better insight into the vortex behavior, in particular vortex breakdown, is an essential requirement for developing CFD solutions and analytical models capable of adequately capturing the flow behavior in the advanced maneuvering regime.

For these reasons, for the past five decades, the behavior of leading-edge vortices, with special attention to vortex breakdown, has been the subject of a considerable number of experimental investigations as well as analytical and computational studies. On this subject, at least twenty theoretical and review articles were devoted.¹⁻²⁰ However, due to difficulties inherent to vortical-flow experiments, measurements traditionally tended to produce qualitative rather than quantitative results. Furthermore, experimental results obtained on identical wings were seldom satisfactorily duplicated when tested in different facilities, with even relatively simple measurements of the vortex breakdown locations showing little correlation. Significant discrepancies are found in the data obtained by different investigators. Geometric variations, different test conditions, model deformations under aerodynamic loads, as well as differences in measuring techniques, significantly affected some measured results and contributed to the lack of correlation to the observations reported by others. A reliable assessment of the data generated in ground tests remains one of the most vexing problems to be solved in order to satisfactorily design military aerial vehicles and validate CFD codes. Thus, an evaluation of the existing experimental data sets was imperative so that the extensive work already performed at a very high cost could be properly used in the design of new military aerial vehicles and the development of analytical and computational models.

As vortex breakdown phenomena have important influences on aircraft performance, this paper attempts to extract as much useful and quantitative information as possible from critical examinations and correlations of existing data sets on vortex breakdown locations.

2.2 RESULTS ON MEASURED VORTEX BREAKDOWN LOCATIONS

A brief, but by no means complete, survey of published results for the time-averaged primary vortex breakdown locations over delta wings at static model conditions with leading edge sweep angles (Λ) ranging from 50° to 80° is depicted in Figs. 1 to 7. It is worthwhile to mention that most experimental results have not been corrected for wind/water tunnel wall and support interference effects and other test related effects. In order to facilitate further investigations, the model(s), test facilities and conditions of the referred test cases are listed separately in Table 1. As the 65° and 70° sweep delta wings are typical and closely related to high-performance military aerial vehicles, most attention has been paid to results reported for these two angles of sweep.

For $\Lambda = 65^\circ$ and 70° , the preliminary comparisons shown in Figs. 4 and 5 reveal significant differences in the measured non-dimensional breakdown location, $x_{VB} = X_{VB}/c_0$, where X_{VB} is the distance from the apex to the measured vortex breakdown location and c_0 is the centerline chord. For $\Lambda = 65^\circ$ and $\alpha = 22.5^\circ$, for example, x_{VB} can be anywhere, from the trailing edge $x_{VB} = 1.0$ (Earnshaw^{26, 27}) to $x_{VB} = 0.4$ (Lambourne & Bryer²⁴). Similar scatter is found in the measurements on 70° delta wings. At $\alpha \approx 31^\circ \sim 32^\circ$, the measured breakdown location varies from $x_{VB} \approx 0.8$ (Earnshaw & Lawford, et.al.^{26, 27}) to $x_{VB} \approx 0.35$ (Wentz & Kohlmann³³⁻³⁵). Finally, for $\Lambda = 70^\circ$, and $\alpha \approx 31^\circ \sim 32^\circ$, one data set (Wentz & Kohlmann³³⁻³⁵) exhibits a “knee”, reflecting a rapid, possibly discontinuous movement of the breakdown location from mid-chord to aft of the trailing edge over a small change in the angle of attack. The large scatter in the measured vortex breakdown locations and

the possible presence of the discontinuity leads to different understanding and explanations^{101,109,112}. This uncertainty will also jeopardize any attempt to model the vortex breakdown behavior.

Given that the vortex breakdown is basically an unsteady, non-linear and time dependent process, some uncertainty in the measurements of the breakdown location is to be expected. Furthermore, the effects of the proximity of wind tunnel walls and support geometry, model blockage and model deformations under the aerodynamic loads increase the scatter in the measurements. These effects unavoidably degrade the consistency of results. In addition, the experimental data given in the reports also depend on the criteria and the methodology used to define the breakdown location, e.g. whether a laser sheet is orientated normal to or along the vortex axis, seeding injection method, Schlieren system set-up and experimental accuracy. All of these considerations complicate the assessment.

On the other hand, it has been found that in a given investigation, the breakdown location can be very stable with high repeatability if the test conditions are well maintained^{92, 112, 126}. As examples, Fig. 8 depicts the standard deviations, σ , as well as maximum and minimum deviations, Δ_{\max} , Δ_{\min} , of the breakdown location for a 75° delta wing¹¹² at $Re_c = 1.5 \times 10^4$, while Fig. 9 shows Mitchell's¹²⁶ results conducted at $Re_c = 1.56 \times 10^6$ for a 70° delta wing. Those figures clearly show that the deviation of breakdown location is small, although a slightly increased scatter in the data can be observed when the breakdown location occurs over the aft part of the model. Lowson & Riley⁹⁰ repeated the experiments of Wentz & Kohlman³³ and Lambourne & Buyer²⁴ and found Wentz & Kohlman's data to be repeatable if the models and test conditions were accurately reproduced.

2.3 CRITERIA OF THE ASSESSMENT

In the author's opinion, the fundamental issue for assessing the data sets is not which data sets are "good" or "bad" but what kind of data sets are necessary, suitable or representative to certain flow conditions. The assessment in this paper is mainly a filtering process for screening the available data. In principle, the sources of discrepancies for the same normalized model geometry in different experiments could result from facility-related or simulation-related sources. The former include free-stream conditions (such as flow non-uniformity, angularity, unsteadiness and noise), wall and support interference and test condition repeatability. The later include Reynolds number based on c_o , Mach number and differences in detail model dimensions, i.e., the shapes of leading edges, trailing edges, fairings and centre-bodies. Those sources will be investigated as much as possible so that the process will lead to a better reconciliation of the different results. The assessment consists of the following main steps:

- a) Collect as many data as possible relating to vortex breakdown. Pay more attention to the described test conditions.
- b) Weigh the accuracy of those data in terms of the quantitative or qualitative information about the test conditions.
- c) Normalize the various data sets into "equivalent" delta wings having sharp leading edges and a flat upper surface by relying on the well accepted assumption that for a delta wing with a flat upper surface and sharp leading-edges, x_{VB} is independent of Reynolds number. Correct for Reynolds number effects on other leading-edge shapes such as leeward bevels and rounded edges.
- d) For the data sets with many parameters, preference is given to the data sets where a minimum number of other parameters is varied.

- e) As different experiments employed different leading-edge shapes and centerbody settings, clarification of these effects is the prerequisite for the assessment.

2.4 EFFECTS OF LEADING-EDGE SHAPE, CENTERBODY AND DIFFERENT TEST CONDITIONS

2.4.1 Leading-Edge Shape Effect

Since boundary layer separation initiates from the leading-edge (where the vorticity flux inside the boundary layer is transported to the free shear layer and eventually rolls up into a vortex) then leading-edge shape may affect the vorticity flux and the effects of leading-edge geometry have to be considered.

Basically there are two kinds of leading-edge: sharp and round. A leading edge is defined as “sharp” if the boundary layer separation line coincides with the junction line of the upper and the lower wing surfaces and if the separation onset is fixed and at the apex of the wing. A leading edge is defined as “round” if, the separation line is not fixed and the onset of the separation is also not from the apex. Furthermore, with a round leading edge, both the separation line and the separation onset will move depending on the flow conditions.

Kegelman & Roos⁶⁰, Pelletier^{91,93}, Huang^{112,136,140}, Luckring^{100-103,132,135,139}, Wentz and Kohlmann³⁴ conducted experiments while Pirzadeh¹⁴¹ applied CFD methods to investigate the effect of leading-edge shape on vortex behavior or vortex breakdown.

For a sharp leading-edge, the effect of leading-edge bevel may lead to changes in effective angle of attack. If the bevel size is large enough, as a first approximation, the following equation for modifying the effective angle, $\Delta\alpha$, at static model conditions and at high Reynolds number, may apply^{76, 82, 87}.

$$\Delta\alpha = \tan\Lambda \cdot \cos\delta \quad (1)$$

However this equation can only be used conditionally. For example, the results of Kegelman and Roos⁶⁰ show that the change in effective angle of attack is only 1/3 of the value predicted by the above equation. In contrast, the water tunnel experiments of Pelletier^{91,93} and Huang¹¹⁴ exhibit negligible difference in x_{VB} between different leading-edge shapes. Likewise, Wentz & Kohlmann's³⁴ results of breakdown location for a 60° delta wing with either beveled or square leading edges are very similar. On the other hand, the studies of Hanff and Huang¹⁰⁴ and Huang, Mebarki and Benmeddour¹⁴⁰ at high Reynolds numbers with large leading-edge bevels show that the breakdown locations are almost 20% farther downstream than others' on models with small size leading-edge bevels. This change is equivalent to a decrease of 4° in effective angle of attack. Similar information can be found from airloads and pressure measurements. Huang¹³⁶ and Huang et al.¹⁴⁰ reported that the measured normal force exhibits two discontinuities: one corresponding to vortex breakdown near the trailing edge and one corresponding to breakdown at the apex. These references show that for a delta wing with a bevelled leading-edge, the latter discontinuity appears on the angle of attack 4° higher than that with a flat upper surface (Fig. 10a and Fig. 10b) indicating the effective angle of attack on the bevelled wing model may be 4° less than that with the flat upper surface wing model.

From the above discussion it follows that equation (1) cannot be applied in isolation without considering other additional factors. One important fact appears to be the ratio, λ , of the size of the bevel (e.g. bevel width, b) to the thickness of the boundary layer in the vicinity of separation, δ^* . Thus,

$$\lambda = \frac{b}{\delta^*}$$

The breakdown location, x_{VB} , varies directly with λ . It can be imagined that if $\lambda \ll 1$, the bevel acts as local or minor disturbance while the large flat upper surface, which is downstream of the bevel, will be the geometric feature that has a global effect on the flow. Actually, in the experiments of Wentz & Kohlmann¹¹¹ and Pelletier^{91,93}, λ was 1/15 and 1/7 of that in the experiments of Hanff & Huang¹⁰⁴, explaining the negligible bevel effect in the former as compared to that in the latter. The water tunnel experimental results reported by Huang¹¹⁴ with $\lambda > 1$ also confirm that if the bevel on the leeward side is large enough it will delay the vortex breakdown. The reduction in angle of attack is close to the value estimated from equation (1).

In order to quantitatively analyse the effect of relative size of the leading-edge bevel, λ , on the flow, it is worthwhile to look at typical permissible surface discontinuities that may have negligible effect on boundary layer flow. Braslow et al.⁶¹ found the allowable forward-facing step height, h , for a flat-plate in a laminar boundary-layer and a zero pressure gradient is roughly:

$$h(\text{ft}) \approx \frac{1800}{\text{Re}_x/\text{ft}}, \text{ where } \text{Re}_x/\text{ft} \text{ is the Reynolds number per foot.}$$

For a Reynolds number of $\text{Re}_x = 1 \times 10^6/\text{ft}$, the typical permissible surface discontinuity is roughly $h = 0.025\text{in}$, while the boundary layer displacement thickness, δ^* , on a 2-D flat plate can be determined from Blasius profile¹⁴¹:

$$\delta^* = 1.72 \sqrt{\frac{\nu x}{u_0}}$$

where u_0 is the velocity in the free stream, x is the length of the plate and ν is the kinematic viscosity.

At this Reynolds number (i.e. $\text{Re}_x = 1 \times 10^6/\text{ft}$) and the chordwise location (x), δ^* , is estimated to be 0.06in . From the two numbers, h and δ^* , in the example, it can be concluded that if λ is approximately less than 0.4, the disturbance caused by the surface discontinuity may be neglected.

For a round leading-edge, if the relative bevel size, λ , is relatively small, the above analysis may still be valid and the effect of the rounded leading-edge shape could be ignored. However for relatively large size of rounded leading-edge, the experiments of Huang¹³⁶, which examined the normal force, show similar results between wings with bevelled and rounded leading-edges, indicating the difference of time-averaged vortex breakdown locations between those wings might be small. However, it does not mean that the vortex behavior is similar. Luckring^{132,135,139} and Huang et al.¹⁴⁰ conducted experiments respectively to investigate the leading-edge shape effect on the flow behavior at high Reynolds numbers. Luckring applied very dense pressure orifices while Huang et al. applied PSP technology as well as pressure orifices to study the pressure distribution and related airloads. Huang et al.¹⁴⁰ also digitized the PSP images to obtain the pressure distribution along different lines, either at different chordwise locations or at different conical lines starting from the apex. As examples Luckring's results for the comparisons between a sharp and round leading-edge delta wing at $M=0.4$, $\text{Re}=6 \times 10^6$ and $\alpha=10^\circ$ are shown in Fig. 11, while Huang et al.'s PSP images, digitized pressure distributions along different lines on the PSP images are illustrated in Fig. 12 to Fig. 14. Luckring's and Huang et al.'s results at different chordwise locations clearly show that for a rounded leading-edge the attached flow pressures are apparent in the forward portion, while leading-edge vortex-like pressures appear

in the rear portion. The separation onset or the origin of the leading-edge vortex on a rounded leading-edge is not at the apex but somewhere downstream of the apex. The PSP images in Fig. 12a exhibit that for sharp leading-edge the high suction area (blue area) is conical and originates from the apex, while for a rounded leading-edge the suction area is not conical (Fig. 12b). The enlarged PSP images in the forward part (Fig. 12c) show that the blue line in the forward part is very close to the edge, indicating the attached flow induced leading-edge suction in that area. The digitized spanwise pressure distributions clearly show the attached flow induced suction along the round leading-edge (Fig. 13). The digitized pressures along a conical line on a sharp leading-edge or along a line (shown in the figure) are shown in Fig. 14. It appears that the suction peak is further upstream and stronger on a round leading-edge than that on sharp and beveled leading-edge.

Pirzadeh¹⁴² applied Navier-Stokes solutions on three leading-edge cases. His results show quite different flow behavior between sharp and rounded leading-edges. As examples, Fig. 15a to Fig. 15c show the velocity vectors on cross-sectional planes at the mid-root-chord station. These Figures clearly show that the size as well as the height of the primary vortex decreases as the radius of the leading-edge increases. Although as he pointed out that the accuracy of vortex flow computations, especially those featuring vortex breakdowns, is highly susceptible to the local grid resolution, and vortex flows induced by blunt leading-edge present an even greater challenge to CFD, such as turbulence models, flow transition, and other numerical elements that influence the accuracy of predicted flow separation, nevertheless the comparison is physically acceptable.

From the above analysis, the following conclusion may be drawn:

- a) The leading-edge shape may not cause a significant effect on vortex breakdown location if the size of the different shapes is relatively small.
- b) If the size of leading-edge shape is relative large compared to the thinness of the boundary layer, the effect of leading-edge shape on the vortex can not be ignored and the amount of the effect depends on the shape of the leading-edge.
- c) For large size, sharp and beveled leading-edges equation (1) may be used to approximately modify the effective angle of attack and corresponding vortex breakdown location.
- d) For large size but rounded leading-edge, there appears attached flow in the forward part and the attached flow induced suction is very close to the edge area. The separation line and its onset are not fixed and are dependent on the test conditions. The corresponding vortex breakdown location, in general, will be downstream of that obtained with a flat upper surface but close to that with a beveled and sharp leading-edge.

2.4.2 Centerbody Effects

In many experiments, a centerbody was inevitably required to house the balance and/or the model's support. Also a centerbody is commonly used in unmanned combat aerial vehicle (UCAV). Since a centerbody is different from a forebody, investigation of centerbody effects is not only of interest in assessing the experimental data but it can also be useful in the design of the new UCAV and similar aerial vehicles. A centerbody is usually located aft of the leading-edge and in the separation zone. As a result, its effect is even more difficult to analyse than that of forebody.

Pelletier^{91, 93}, Huang¹¹⁴, and Huang et al.¹⁴⁰ investigated centerbody effects in wind tunnel or in water tunnel experiments by comparing the results with and without centerbody in the experiments. Huang's results

conducted in a water tunnel at a Reynolds number $Re_c \approx 1.5 \times 10^4$ shows that the centerbody effect on vortex breakdown location is negligible except when the vortex breakdown location is near the trailing edge. This may be caused by the sudden expansion of the flow at the end of the centerbody. Similar trends can be found in the experiments of Pelletier^{91,93} and Huang¹⁴⁰ where the Reynolds numbers are 1.5×10^5 and 2.4×10^6 respectively. The PSP and pressure orifice experiments of Huang¹⁴⁰ conducted at higher Reynolds numbers ($Re_c \approx 2.4 \times 10^6$) are shown from Fig. 16 to Fig. 17. Huang's pressure orifice measurements at different chordwise locations with and without a centerbody show that the centerbody only causes a local effect and no global effect is observed. Other than those experimental results, Benmeddour, Mebarki and Huang¹⁴⁸ conducted numerical studies with and without centerbody¹⁴⁸. They applied the in-house solver, FJ3SOLV, and the commercial software, CFD-FASTRAN, to calculate the effect of the centerbody on the surface pressure over a 65° delta wing and a 55° diamond wing. Their CFD results are shown in Fig. 18 to Fig. 21. In general, their CFD results agree with experimental results. It may be concluded that a centerbody, with the size and shape as in these studies, has negligible global effects on the aerodynamic characteristics.

2.4.3 Reynolds Number and Mach Number Effects

It is well accepted that with a sharp leading-edge the vortex breakdown location is approximately independent of Reynolds number. The time averaged pressure distribution is also less affected by the Reynolds number as shown by Luckring¹³⁹ (Fig. 22). However, the amount of unsteadiness in the vortex depends on the Reynolds number. This unsteadiness may cause oscillations in vortex core location, vortex breakdown location and interactions between the left and right vortices. Thus, the measured time-averaged locations of vortex core and vortex breakdown may be nearly the same, but the time-dependent value and the asymmetry of the two vortices will depend on the Reynolds number, thereby resulting in increased scatter in the measurements and even bifurcation when tested at higher Reynolds number.

The Reynolds number related unsteadiness in the vortex comes from many sources. First, depending on the Reynolds number, the vorticity within the boundary layer may transport discontinuously into the free shear layer. Second, the Reynolds number will affect the type of Kelvin-Helmholtz (K-H) instability. At high Reynolds number, discrete and small-scale vortices appear and follow a helical trajectory around the core resulting in another source of unsteadiness. Thirdly, when a vortex breaks down at high angle of attack, at high Reynolds number there is ample unsteadiness within the breakdown region. This gives the flow in the vicinity of the spiral a spatial and temporal periodicity. Finally, at high Reynolds number, there exists a strong axial and related spiral fluctuation in the vortex breakdown location. The time history of breakdown location consists of low-frequency, large-amplitude fluctuations and high-frequency, low-amplitude fluctuations. As examples Huang¹⁴⁴ presents pressure spectral measurements conducted at high Reynolds number which show that there is a peak at low frequency when vortex breakdown moves over the wing area (Fig. 23).

The above facts show that the Reynolds number effect may not cause too much effect on time-averaged vortex breakdown location over a delta wing with a sharp leading-edge, but the time-dependent behavior will be much affected by the Reynolds number.

In order to understand Reynolds number effects on the unsteadiness of the vortex, the unsteadiness at different Reynolds numbers has been the focus of extensive research. Some examples are shown below. Results from experimental and computational studies regarding the effect of Reynolds number on the free shear layer are shown in Fig. 24 and Fig. 25 to Fig. 26 by Lowson^{58, 117} and Visbal^{92, 97} respectively. They found that at low Reynolds number the free shear layer is laminar. As Reynolds number increases, the free shear layer transitions from laminar to turbulent at somewhere along the leading-edge. Visbal further found

that the transition progresses toward the apex as Reynolds number increases further (Fig. 25 and Fig. 26). The instantaneous azimuthal vorticity distribution in a plane passing through the vortex axis obtained by Rockwell⁸⁸ is shown in Fig. 27. Gursul⁹⁵ measured time histories of breakdown locations which are illustrated in Fig. 28. Huang used high speed visualization method to study the unsteadiness inside the vortex breakdown at high Reynolds number ($Re_{c0}=3.6 \times 10^6$). Following Lambourne's²⁹ description of vortex breakdown, in Fig. 29 Huang^{112,142} denoted the vortex filament kink point as "point A" while the vortex breaks down into large scale turbulence as "point B". Huang found that the unsteady behaviors of points A and B are quite different. As examples sequence of frames of the images are shown in Fig. 29. In the sequence, point A moves in excess of $0.1c_0$ while point B remains more or less stationary. The speed of response of point A corresponds to half convection speed, i.e. $0.5V_\infty \cos \alpha$, whereas point B barely moves at all. Thus if the kink point is defined as the vortex breakdown location as in most of researchers' measurement, the fluctuation of point A will deteriorate the measurements. On the other hand, if the point B is taken as the vortex breakdown location as Huang and Hanff⁸² did in a section view of laser-smoke sheet normal to the vortex axes, the breakdown location will be $0.1 c_0$ downstream of the point A which is defined as breakdown location by others' experiments.

For a round leading-edge, the Reynolds number effect is more complex. As mentioned above there is attached flow in the forward part of the leading-edge followed by leading-edge vortex like flow in the aft. Luckring's results^{132, 135, 139} show that the attached flow area increases as the angle of the attack decreases (Fig. 30). Also, increasing Reynolds number will expand the attached flow area (Fig. 31). However it is worthwhile to mention that this only happens at a certain range of angle of attack. At a small angle of attack where the attached flow is weak or at high angle of attack where the vortex flow dominates, the Reynolds number effect is small. This can be drawn from comparing Fig. 30 with Fig. 31 at different angles of attack.

Similar to the Reynolds number effect, the free stream turbulence intensity will also affect the experimental results. As the turbulence intensity increases, the unsteadiness in the vortex and vortex breakdown also increase, which will affect the measured results in experiments.

As for the effect of Mach number, Luckring^{100-103, 132, 135, 139} has conducted comprehensive experiments on surface pressure. For a sharp leading-edge at small angle of attack, where the vortex flow is weak, the effect of Mach number is minor (Fig. 32). However at high angle of attack, where the vortex flow is stronger, profound Mach number effects can be found in the forward part of the wing (Fig. 33). For a round leading edge, an increase in Mach number will reduce the attached flow area and increase the vortex flow area (Fig. 34). Thus at transonic speed the difference between a round and a sharp leading-edge will become smaller as Mach number increases. The flow will, most likely become leading-edge vortex like flow (compare Fig. 35 with Fig. 11).

2.5 ASSESSMENT FOR THE RESULTS WITH 65° DELTA WING

With those pre-analysis in hand and applying the above mentioned criteria to the results of 65° sweep delta wings, especially for those with large scatter, it was found that:

- a). Lambourne & Buyer's²⁴ experiments were conducted in water tunnel and wind tunnel with a flat upper and bevelled 16° on the lower surface. The ratios of the wingspan to the relevant tunnel span were 61% and 41% resulting in the blockages of 13% and 7.2% for water tunnel and wind tunnel respectively. Moreover the thickness reached $t/c_0=6.3\%$ in the wind tunnel, the highest value among other tests. Although it is not known exactly how much they should be corrected, Weinberg's³⁵ results

show that the increases of model thickness and blockage could promote vortex breakdown by as much as 20% of centerline chord (i.e., move closer to the wing apex).

- b). Earnshaw's^{26, 27} results were obtained with a model with $t/c=4\%$ and symmetrical cubic curve section. According to the equation of the model surface, the section half angle (normal to the leading-edge) at the leading-edge is 14.2° . As the bevel width is comparable with the thickness of the boundary layer before separation, the bevel effect corresponds to a decrease in the effective angle of attack. If the average slope is taken in Earnshaw's experiment, the effective angle of attack could be reduced by as much as 3° .
- c). Hanff & Huang's^{70-72, 77, 82, 87} early experiments were conducted at the $Re_{c0} \approx 3.6 \times 10^6$ in two different wind tunnels using different model supports. The blockage of the wing model at $\alpha=30^\circ$ is 1.8% and 1.4% for two wind tunnels respectively. The data were repeatable and the differences of the results obtained from two facilities were minor. In the experiments, breakdown location was found by means of a laser sheet normal to the vortex axis and determined by a blurring of the vortex ring. This criterion is consistent with Lambourne's²⁹ definition for spiral vortex breakdown. Subsequent tests by Huang and Hanff¹⁰⁵ with a laser sheet containing the vortex axis showed the location measured by the criteria to be approximately 10% of centerline chord downstream of the kink point. Moreover, as the experiments were conducted at high Re number resulting in the bevel size relatively larger than the thickness of the boundary layer in the vicinity of the separation area. Thus a 4° angle of attack correction due to leading-edge bevel was proposed by Hanff and Huang¹⁰⁴. Taking the correction into account, the modified data are close to their later experiments¹¹⁴ conducted in the water tunnel.
- d). Pelletier's^{91, 93} experiments were conducted in 2ft by 2ft wind tunnel with the models similar to Hanff & Huang's¹⁰⁴ and Huang's¹³⁶ models but half size, $c_0=14\text{in}$, $t/c=1.8\%$ and at $Re_{c0} \approx 1 \times 10^5$. The blockage is 7.9% at $\alpha=30^\circ$. Smoke was injected into the free stream near the apex of the model through two small smoke ports. The vortex breakdown was determined by the kink point in the top view. The single-bevel wing has a flat upper surface and bevelled 45° on the lower surface. The double-bevel wing has a symmetric 20° bevel inclusive which is identical to the wing tested by Hanff and Huang^{70, 82, 104}. The difference in vortex breakdown locations between the two wing models is less than 5%. The bevel effect on the vortex breakdown location is negligible which agrees with above analysis as the ratio of bevel size to the size of the boundary layer thickness is much smaller than that in the case of Huang and Hanff's experiments.
- e). The experiments conducted by Addington and Cipolla's^{119, 107} were similar to the model in Huang and Hanff's experiments. In the former, the experiments were conducted in 2ft by 2ft wind tunnel at $Re=2.9 \times 10^5$ while in the later the experiments were conducted in water tunnel at $Re=32400$. Vortex breakdown was visualized by dye injection from ports on the upper surface near the apex. Their results at $\alpha=30^\circ$ and $\phi=0^\circ$ falls closer to Huang's¹¹⁴ water tunnel results.

The original data sets have been assessed and correlated into a delta wing with flat upper surface by the above approach as shown in Fig. 34 which exhibits less scatter and more confidence than in Fig. 4. Further, if we assume a normal probability distribution, the normalized mean value representing time-averaged vortex breakdown location over 65° delta wing with flat upper surface can be obtained as shown in Fig. 35. The R-squared value is 0.96 for the measured results. With 95% interval of confidence based upon the standard deviation (σ) of the results, the true mean for the time-averaged breakdown location is given by

$$x_{vb} = \bar{x}_{vb} \pm t_{v,95} \bar{\sigma}$$

where \bar{x}_{vb} is mean value shown in Fig. 35, $t_{v,95}$ is Student's t value and $\bar{\sigma} = \frac{\sigma}{\sqrt{N}}$.

The largest precision interval is of the order of 4% at $\alpha \approx 30^\circ$.

2.6 ASSESSMENT OF THE RESULTS WITH 70° DELTA WING

In the case of the 70° delta wing, in addition to a scatter similar to that of the 65° wing, a discontinuity movement of the breakdown location in the aft of the wing was observed in Wentz & Kohlman's³³⁻³⁵ results. Both of them have to be further investigated.

- a). Wentz & Kohlmann's³³⁻³⁵ experiment employed a wing model with non-dimensional thickness (thickness/root chord) $t/c_0 = 0.007$, nearly an order of magnitude less than that in others' experiments. Owing to a 7.5° bevel on the lower surface, the model was further exacerbated on the forward part. Thus the effect of the aeroelastic deformation on vortex behavior has to be considered. The deformation under the reported test conditions in Wentz & Kohlmann's³⁵ test ($q=30$ psf) was estimated by the finite element method where the loading was based on the reported breakdown locations, x_{vb} , at the trailing edge, $x_{vb}=1$, and at $x_{vb}=0.4$ for $\alpha \approx 29^\circ$ and 30° respectively. The calculated deflections are large and their effects can not be ignored (see Fig. 36 and Fig. 37). Specifically, at $\alpha \approx 30^\circ$ the wing has a negative camber with 1.3° deflection angle at the apex while at $\alpha \approx 29^\circ$ it exhibits a positive camber over most of wing area. In light of the above, it follows that when α decreases from 30° , initially the negative camber will result in a premature vortex breakdown. As α decreases, the vortex breakdown location begins to move downstream. That movement redistributes the load such that it tends to reduce the negative camber which, in turn, makes the breakdown location move further downstream. A positive feedback is clearly present in the coupling between the deformation changes and the loading changes, leading to the reported discontinuous behavior. In fact Wentz & Kohlmann's³⁵ reported angular deflections, as high as 3~4 degrees at the apex section for these slender delta wings and their possible effect on breakdown location. Considering the above, it is reasonable to assume that discontinuous vortex breakdown location in Wentz & Kohlmann's report for $\Lambda \geq 70^\circ$ delta wing is anomalous due to aeroelastic effects and cannot, therefore, be deemed to be representative of the breakdown behavior over a rigid model. Similar conclusion had been obtained by Lowson⁹⁰.
- b). Lemay's⁵⁶ model has 23° bevel on the upper surface along the leading-edge while Earnshaw's²⁷ model has a 14° slope on the upper surface. Since the bevel widths are relatively larger than those of Erickson⁴², Miau⁸⁴ and Huang¹¹⁴ in their water tunnel experiments, in the Lemay's⁵⁶ and Earnshaw's²⁷ cases the bevel may result in a reduction of the effective angle of attack with corresponding delays in the vortex breakdown location.
- c). Mitchell's¹²⁸ and Molton's⁸⁰ experiments were carefully conducted. However the asymmetric support in the experimental set-up may cause the up wash resulting in the increase of the effective angle of attack, $\Delta\alpha$, and the upstream movement of the vortex breakdown. Actually this up-wash and effective angle of attack increase was observed by earlier experiment conducted by Molton⁸⁰ where it was estimated $\Delta\alpha$ could reach 2~3° at high angles of attack range. In addition, the blockage and the flow angularity induced by asymmetric support may cause some problem as the blockage of vertical and horizontal supports was roughly 7% while the model blockage at $\alpha=30^\circ$ was 6.5%. As Lambourne & Bryer's²⁴ experiments show large blockage which may promote the vortex breakdown.

In viewing of the above considerations, similar to the 65 sweep delta wing the assessed data set and the normalized data set of time-averaged vortex breakdown locations for the 70° delta wing with sharp leading-edges and flat upper surface are depicted in Fig. 38 and Fig. 39 respectively. The largest precision interval is of the order of 5% at $\alpha \approx 40^\circ$.

2.7 CONCLUSIONS

- A screening process has been performed on more than eighty experimental cases about vortex breakdown over delta wings with different sweptback angles at high angles of attack and static model conditions. Vortex breakdown locations over 65° and 70° delta wings with flat upper surface have been normalized.
- The effects of leading-edge shape, centerbody and other test conditions have been critically investigated.
- The leading-edge shape may affect the vortex behavior which depends on relative size of the leading-edge shape to the thickness of the boundary layer. Its effect may be neglected if the relative size is small.
- If the relative size is large, different leading edge shapes, e.g. sharp and round leading-edges, may have different effects on the vortex, either at the separation lines or the onset of the separation location. The difference in time-averaged vortex breakdown locations between sharp and round leading-edges needs further clarification.
- For the discussed centerbody setting, no global but only local effect on the pressure has been observed. Centerbody may have minor effect on the vortex breakdown.
- Increase Reynolds number may promote transition in the free shear layer and delay the onset of separation line on round leading-edge. However Reynolds number may have less effect on time-averaged vortex breakdown location, even on wings with round leading edges.
- Increase Mach number results in the reduction of the effect of the leading-edge shape. It also promotes vortex breakdown upstream. Reynolds number Effect

2.8 REFERENCES

- [1] Squire, H. B., "Analysis of the Vortex Breakdown Phenomenon," Part I, Imperial College of Science and Technology, Aeronautics Dept. Report No. 102, 1960.
- [2] Hall, M.G., "A Theory for the Core of a Leading-Edge Vortex," J. Fluid Mech. 11, 209-228, 1961.
- [3] Hall, M.G., "The Structure of Concentrated Vortex Cores," Prog. Aerospace Sci. 7, 53-110, 1966.
- [4] Benjamin, T.B., "Theory of the Vortex Breakdown Phenomenon," J. Fluid Mech. 14(4), 593-629, 1962.
- [5] Sarpkaya, T., "On Stationary and Traveling Vortex Breakdowns," J. Fluid Mech., Vol. 45, Part 3, 1971.

- [6] Sarpkaya, T., "Vortex Breakdown in Swirling Conical Flows," AIAA Journal, Vol. 9, Sept. 1971.
- [7] Hall, M.G., "Vortex Breakdown," Ann. Rev. Fluid Mech., Vol. 4, 1972..
- [8] Leibovich, S., "The Structure of Vortex Breakdown," Ann. Rev. Fluid Mech. 10, 221-246, 1978.
- [9] "High Angle of Attack" AGARD CP-247, January 1979.
- [10] Wedemeyer, E., "Vortex Breakdown," No. 9, AGARD-LS-121, Dec. 1982.
- [11] "Aerodynamics of Vortical Type Flows in Three Dimensions" AGARD-CP 342, July 1983.
- [12] Leibovich, S., "Vortex Stability and Breakdown," AGARD-CP-342, No. 23, April 1983.
- [13] Leibovich, S., "Vortex Stability and Breakdown: Survey and Extension," AIAA Journal, Vol. 22, No. 9, Sept. 1984.
- [14] Leibovich, S., "On a Theoretical Scenario for Vortex Breakdown," Vortex Control and Breakdown Behavior, Second International Colloquium on Vortical Flows, Baden, Switzerland, April 1987.
- [15] Delery, J., Pagan, D. and Solignac, J.L., "On the Breakdown of the Vortex Induced by a Delta-Wind," ONERA T.P. n° 1987-105, 1987.
- [16] Mario Lee and Ho, C.M., "Lift Force of Delta Wings," Appl Mech Rev, Vol. 43, No. 9, Sept. 1990.
- [17] Nelson, R.C. and Visser, K.D., "Breaking Down the Delta Wing Vortex – The Role of Vorticity in the Breakdown Process," AGARD Symposium on Vortex Flow Aerodynamics, October 1-4, 1990.
- [18] "Vortex Flow Aerodynamics" AGARD CP-494, July 1991.
- [19] Delery, J.M., "Aspect of Vortex Breakdown," Prog. Aerospace Sci. Vol. 30, pp. 1-59, 1994.
- [20] "Advanced Flow Management, Part A: Vortex Flow and High Angle of Attack" RTO AVT Symposium May 2001.
- [21] Lee, G.H., "Note on the Flow Around Delta Wings with Sharp Leading Edges," ARC R&M 3070, Sept. 1953.
- [22] Elle, B.J., "An Investigation at Low Speed of the Flow Near the Apex of Thin Delta Wings with Sharp Leading-Edges," ARC R&M 3176, January 1958.
- [23] Elle, B.J., "On the Breakdown at High Incidence of the Leading Edge Vortices on Delta Wings," J. of the Royal Aero. Soc., Vol. 64, August 1960.
- [24] Lambourne, N.C. and Bryer, D.W., "The Bursting of Leading-Edge Vortices – Some Observations and Discussion of the Phenomenon," ARC R&M 3282, April 1961.

- [25] Harvey, P.M., "Some Observations of the Vortex Breakdown Phenomena," J. Fluid Mech., Vol. 14, 1962.
- [26] Earnshaw, P.B. and Lawford, J.A., "Low-Speed Wind-Tunnel Experiments on Series of Sharp-Edged Delta Wings," ARC R&M 3424, March 1964.
- [27] Earnshaw, P.B., "Measurements of Vortex-Breakdown Position at Low Speed on a Series of Sharp-Edged Symmetrical Models," ARC CP 828, Nov. 1964.
- [28] Lowson, M.V., "Some Experiments with Vortex Breakdown," J. of the Royal Aero. Soc., Vol. 68, May 1964.
- [29] Lambourne, N.C., "The Breakdown of Certain Types of Vortex," NPL AERO REPORT 1166, 1965.
- [30] Hummel, D., "Research on Vortex Breakdown on Slender Delta Wings," Zeitschrift fur Flugwissenschaften, 13, 5, Aircraft Research Association Ltd., Bedford Library Translation, No. 12, May 1965.
- [31] Hummel, D., "Experimental Investigation of the Flow on the Suction Side of a Thin Delta Wing," Z. Flugwiss., Jahrg. 13, Heft 7, pp. 247-252, July 1965
- [32] Hummel, D. and Srinivasan, P.S., "Vortex Breakdown on Slender Sharp-Edged Wings," Journal of the Royal Aeronautical Society, Vol. 71, pp.319-322, April 1967.
- [33] Earnshaw, P.B., "Measurements of the Effects of Thickness on Vortex Breakdown Position on a Series of Sharp-Edged Delta Wings," ARC CP No. 1018, 1968.
- [34] Wentz, W.H. Jr. and Kohlmann, D.L., "Vortex Breakdown on Slender Sharp-Edged Wings" J. Aircraft Vol. 8, No.3, March 1971 or NASA CR 98737, Nov. 1968.
- [35] Wentz, W.H. Jr. and Kohlman, D.L., "Wind Tunnel Investigations of Vortex Breakdown on Slender Sharp-Edged Wings," NASA N69-14762, 1968.
- [36] Wentz, W.H. Jr., "Wind Tunnel Investigation of Vortex Breakdown on Slender Sharp-Edged Wings," Ph.D. Thesis, University of Kansas, 1969.
- [37] Wentz, W.H. Jr., "Effects of Leading-Edge Camber on Low-Speed Characteristics of Slender Delta Wings," NASA-CR-2002, Oct. 1972.
- [38] Werle, H., "Sur L'éclatement Des Tourbillons," ONERA Note Technique, N° 175, 1971.
- [39] Chigier, N.A., "Measurement of Vortex Breakdown over a Delta Wing Using Laser Anemometer," NEAR-TR-62, 1974.
- [40] Thompson, D.H., "A Water Tunnel Study of Vortex Breakdown over Wings with Highly Swept Leading Edges," Aerodynamics Note, ARL/A. 356, Australian Defense Scientific Service, May 1975.

- [41] Hummel, D., "On the Vortex Formation over a Slender Wing at Large Angles of Incidence," AGARD-CP-247, Oct. 1978.
- [42] Erickson, G.E., "Water Tunnel Flow Visualization: Insight Into Complex Three-Dimensional Flow Fields," AIAA Paper 79-1530, also AIAA 80-1423, 1979.
- [43] Erickson, G.E., "Vortex Flow Correlation," Tech. Rept. AFWAL-TR-80-3143, 1980.
- [44] Erickson, G.E., "Flow Studies of Slender Wing Vortices," AIAA Paper 80-1423, 1980.
- [45] Erickson, G.E., "Water-Tunnel Studies of Leading-Edge Vortices," Journal of Aircraft, Vol. 19, No. 6, June 1982.
- [46] Skow, A.M. and Erickson, G.E., "Modern Fighter Aircraft Design for High-Angle-of-Attack Maneuvering," AGARD LS121, 4-1 to 4-59, Dec. 1982.
- [47] Wedemeyer, E., "Vortex Breakdown," AGARD LS121, 9-1 to 9-17, Dec. 1982.
- [48] Escudier, M.P., and Keller, J.J., "Vortex Breakdown: A Two Stage Transition," AGARD-CP-342, No. 25, April 1983.
- [49] McKernan, E.C., "An Investigation of the Breakdown of the Leading Edge Vortices on a Delta Wing at High Angles of Attack," Master Thesis, University of Notre Dame, Jan. 1983.
- [50] Gad-el Hak, M. and Blackwelder, R.F., "The Discrete Vortices from a Delta Wing," AIAA Journal, Vol. 23, No. 6, pp. 961-962, June 1985.
- [51] Payne, M., Ng, T.T., Nelson, R.C. and Schiff, L., "Visualization and Flow Surveys of the Leading Edge Vortex Structure on Delta Wing Planforms," AIAA Paper 86-0330, 1986.
- [52] Boersen, S.J., "US/European Vortex Flow Experiment Test Report of Wind Tunnel Measurements on 65° Delta Wing in the NLR Supersonic Facility SST," NLR TR 86117 U, 1986.
- [53] Reynolds, G.A. and Abtahi, A.A., "Instabilities in Leading-Edge Vortex Development," AIAA Paper 87-2424, 1987.
- [54] Payne, F. M., "The Structure of Leading Edge Vortex Flows Including Vortex Breakdown," Ph.D. Dissertation, University of Notre Dame, 1987.
- [55] Payne, F.M., Ng, T.T., and Nelson, R.C., "Experimental Study of the Velocity Field on a delta Wing," AIAA Paper 87-1231, 1987.
- [56] Lemay, S.P., Batill, S.M. and Nelson, R.C., "Leading Edge Vortex Dynamics on a Pitching Delta Wing," AIAA Paper 88-2559, 1988, also J. Aircraft, Vol. 27, No.2 Feb. 1990, pp. 131-138.

- [57] McKeenan, J.F. and Nelson, R.C., "An Investigation of the Breakdown of the Leading Edge Vortices on a Delta-Wing at High Angles of Attack," AIAA Paper 83-2114. Also J. Aircraft, Vol. 25, No. 11, Nov. 1988.
- [58] Lowson, M.V. and Riley, A.J., "The Three Dimensional Vortex Sheet Structure on Delta Wings," AGARD-CP-438, October 1988.
- [59] Brandon, J.M. and Shah, G.H., "Effect of Large Amplitude Pitching Motions on the Unsteady Aerodynamic Characteristics of Flat-Plate Wings," AIAA Paper 88-4331, 1988.
- [60] Kegelman, J and Roos, F. "Effect of Leading-Edge Shape and Vortex Burst on the Flowfields of a 70 Degree Sweep Delta-Wing," AIAA Paper 89-0086, 1989.
- [61] Braslow, A.L. and Collier, F.S., "Applied Aspect of Laminar-Flow Technology," Viscous Drag Reduction in Boundary Layers, Progress in Astronautics and Aeronautics, Vol. 123, 1989.
- [62] Panton, R.L., "The Effect of a Contoured Apex on Vortex Breakdown, AIAA Paper 89-0193, 1989.
- [63] Magness, C., Robinson, O. and Rockwell, D., "Control of Leading-Edge Vortices on a Delta Wing," AIAA Paper 89-0999, 1989.
- [64] Hawk, J.D., Barnett, R.M. and O'Neil, P.J., "Investigation of High Angle of Attack Vortical Flows over Delta Wings," AIAA Paper 90-0101, 1990.
- [65] O'Neil, Roos, F.W., Kegelman, R.M., Barnett, R.M. and Hawk, J.D., "Investigation of Flow Characteristics of a Developed Vortex," NADC-89114-60, May 1989, Also AIAA Paper 90-0383, 90-0599.
- [66] Roos, F.W. and Kegelman, J.T., "Recent Exploration of Leading-Edge-Vortex Flowfields," McDonnell Douglas Research Laboratories, 1990.
- [67] Torlund, P.A., "Force Measurements and Visualization on a 60° Delta Wing in Oscillatory and Stepwise Pitching Motion," ICAS 90-3.3.2, 1990.
- [68] Wolffelt, K.W., "Investigation on the Movement of Vortex Burst Position with Dynamically Changing Angle of Attack for a Schematic Delta Wing in a Water Tunnel Correlation to Similar Studies in Wind Tunnel," AGARD CP 413-27.
- [69] Roos, F.W. and Kegelman, J.T., "An Experimental Investigation of Sweep Angle Influence on Delta-Wing Flows," AIAA Paper 90-0383, 1990.
- [70] Hanff, E.S. and Jenkins, S.B., "Large-Amplitude High Rate Rolling Experiments on a Delta and Double Delta Wing," AIAA Paper 90-0224, 1990.
- [71] Hanff, E.S. Kapoor, K., Anstey, C.R. and Prini, A., "Large-Amplitude High-Rate Roll Oscillation System for the Measurement of Non-Linear Loads," AIAA Paper 90-1426, 1990.

- [72] Hanff, E.S. and Ericsson, L.E., "Multiple Roll Attractors of a Delta Wing at High Incidence," AGARD CP-494, Oct. 1990.
- [73] Gordnier, R.E. and Visbal, M.R., "Numerical Simulation of the Unsteady Vortex Structure over a Delta Wing," AIAA Paper 91-1811, 1991.
- [74] Nelson, R.C., "Unsteady Aerodynamics of Slender Wings," AGARD-R-776, pp. 1-1 to 1-26, 1991.
- [75] Lowson, M.V., "Visualization Measurements of Vortex Flows," Journal of Aircraft, Vol. 28, No. 5, pp.320-327, May 1991.
- [76] Ericsson, L.E., "Analysis of Wind-Tunnel Data Obtained in High-Rate Rolling Experiments with Slender Delta Wings," NRC IAR-CR-14, August 1991.
- [77] Hanff, E.S. and Huang, X.Z., "Roll-Induced Cross-Loads on a Delta Wing at High Incidence," AIAA Paper 91-3223, 1991.
- [78] Weinberg, X. "Effect of Tunnel Walls on Vortex Breakdown Location over Delta Wings," AIAA Journal Vol. 30, No. 6, June, 1992.
- [79] Stahl, W.H., Mahmood, M. and Asghar, A., "Experimental Investigations of the Vortex Flow on Delta Wings at High Incidence," AIAA Journal, Vol. 30, No. 4, pp. 1027-1032, April 1992.
- [80] Molton, P., "Etude Experimentale de leclatement tourbillonnaire sur aile delta en coulement incompressible. Caracterisation du champ externe," ONERA Rapport Tech. N° 5/1147 AN, 1992.
- [81] Miller, L.S. and Gile, B.E., "Effects of Blowing on Delta Wing Vortices During Dynamic Pitching," AIAA Paper 92-0407, Also J. Aircraft Vol. 30, No.3, 1993, pp.334-339.
- [82] Huang, X.Z. and Hanff, E.S., "Prediction of Leading-Edge Vortex Breakdown on a Delta Wing Oscillating in Roll," AIAA Paper 92-2677, June 1992.
- [83] Guglieri, G. and Quagliotti, F.B., "Experimental Investigation of Vortex Dynamics on Delta Wings," AIAA Paper 92-2731, 1992.
- [84] Miao, J.J., Chang, R.C. and Chou, J.H., "Nonuniform Motion of Leading-Edge Breakdown on Ramp Pitching Delta Wing," AIAA Journal Vol. 30, No. 7, July 1992.
- [85] Visser, K.D. and Nelson, R.C., "Measurements of Circulation and Vorticity in the Leading-Edge Vortex of a Delta Wing," AIAA Journal Vol. 31, No. 1 pp. 104-111, 1993.
- [86] Towfighi, J. and Rockwell, D., "Instantaneous Structure of Vortex Breakdown on a Delta Wing via Particle Image Velocimetry," AIAA Journal, Vol. 31, No. 6, pp. 1160-1162, June 1993.
- [87] Huang, X.Z. and Hanff, E.S., "Prediction of Normal Force on a Delta Wing Rolling at High Incidence," AIAA Paper 93-3686, 1993.

- [88] Rockwell, D., "Three-Dimensional Flow Structure on Delta Wings at High Angle-of-Attack: Experimental Concepts and Issues," AIAA Paper 93-0550, January, 1993.
- [89] Straka, W.A. and Hemsch, M.J., "Effect of a Fuselage on the Leading-Edge Vortex Breakdown of a Delta Wing," J. Aircraft, Vol. 31, No. 4, 1994, pp.1002-1005.
- [90] Lowson, M.V. and Riley, A.J., "Vortex Breakdown Control by Delta Wing Geometry," AIAA Paper 94-3487, 1994.
- [91] Pelletier, A. and Nelson, R.C., "An Experimental Study of Static and Dynamic Vortex Breakdown on Slender Delta Planforms," AIAA Paper 94-1879, 1994.
- [92] Gordnier, R.E. and Visbal, M.R., "Unsteady Vortex Structure over a Delta Wing," Journal of Aircraft, Vol. 31 No. 1, pp. 243-248, 1994.
- [93] Pelletier, A., "An Experimental Investigation of Vortex Breakdown on Slender Delta Planforms," Final Contract Report, Hessert Center for Aerospace Research, Notre Dame University, August 1994.
- [94] Ericsson, L.E., "Comments on Effect of Fuselage on Delta Wing Vortex Breakdown," Journal of Aircraft Vol. 31, No. 4, pp. 1002-1005, 1994.
- [95] Gursul, I., Unsteady Flow Phenomena over delta Wings at High Angle of Attack," AIAA Journal, Vol. 32, No. 2, pp. 225-231, Feb. 1994.
- [96] Gursul, I. and Yang, H., "On Fluctuations of Vortex Breakdown Location," Physics of Fluids, Vol. 7, No. 1, pp. 229-231, 1995.
- [97] Gordnier, R.E. and Visbal, M.R., "Instabilities in the Shear Layer of Delta Wing," AIAA Paper 95-2281, 1995.
- [98] Lowson, M.V., Riley, A.J. and Swales, C., "Flow Structure over Delta Wings," AIAA Paper 95-0586, 1995.
- [99] Traub, L.W. and Redinioties, O.K., "Instabilities of Vortex Breakdown; Their Structure and Growth," AIAA Paper 95-2308, 1995.
- [100] Chu, J. and Luckring, J.M., "Experimental Surface Pressure Data Obtained on Delta Wing Across Reynolds Number and Mach Number Ranges," Vol. 1 – Sharp Leading Edge," NASA TM-4645, February 1996.
- [101] Chu, J. and Luckring, J.M., "Experimental Surface Pressure Data Obtained on Delta Wing Across Reynolds Number and Mach Number Ranges," Vol. 2 – Small Leading Edge," NASA TM-4645, February 1996.

- [102] Chu, J. and Luckring, J.M., "Experimental Surface Pressure Data Obtained on Delta Wing Across Reynolds Number and Mach Number Ranges," Vol. 3 – Medium Leading Edge," NASA TM-4645, February 1996.
- [103] Chu, J. and Luckring, J.M., "Experimental Surface Pressure Data Obtained on Delta Wing Across Reynolds Number and Mach Number Ranges," Vol. 4 – Large Leading Edge," NASA TM-4645, February 1996.
- [104] Hanff, E.S. and Huang, X.Z., "Highlights of the IAR/WL High-Alpha Joint Program," NPU/AIAA AFM 96-016, 1996.
- [105] Huang, X.Z. and Hanff, E.S., "Unsteady Behavior of Spiral Leading-Edge Vortex Breakdown," NPU/AIAA AFM 96-038, 1996.
- [106] Huang, X.Z. and Hanff, E.S., "Surface Flow Topology on a Delta Wing Rolling at High Incidence," NPU/AIAA AFM 96-041, 1996.
- [107] Cipolla, K.M., "Structure of the Flow Past a Delta Wing with Variations in Roll Angle," Ph.D. Dissertation, Leigh University, May 1996.
- [108] Huang, X.Z., Hanff, E.S. and Jobe, C.E., "Surface Flow Topology on a Delta Wing at High Incidence for a Range of Roll Angles," AIAA Paper 96-2398, 1996.
- [109] Ericsson, L.E., "Flow Physics of Critical States for Rolling Delta Wings," Journal of Aircraft Vol. 33, No. 2, pp. 347-352, 1996.
- [110] Ericsson, L.E., "Pitch Rate Effects on Delta Wing Vortex Breakdown," Journal of Aircraft Vol. 33, No. 2, pp. 639-642, 1996.
- [111] Ericsson, L.E., "Difficulties in Predicting Vortex Breakdown Effects on a Rolling Delta Wing," Journal of Aircraft Vol. 33, No. 3, pp. 477-484, 1996.
- [112] Huang, X.Z. and Hanff, E.S., "Unsteady Behavior of Spiral Leading-Edge Vortex Breakdown," AIAA Paper 96-3408, 1996.
- [113] Guglieri, G. and Quagliotti, F.B., "Experimental Investigation of Vortex Dynamics on a 65° Delta Wing in Sideslip," The Aeronautical Journal, March 1997..
- [114] Huang, X.Z. Sun, Y.Z., and Hanff, E.S., "Further Investigation of Leading-Edge Vortex Breakdown Over Delta Wings," AIAA Paper 97-2263, 1997.
- [115] Huang, X.Z. Sun, Y.Z., and Hanff, E.S., "Circulation Criterion for Leading-Edge Vortex Breakdown over Delta Wings," AIAA Paper 97-2265, 1997.
- [116] Ericsson, L.E., "Effect of Angle of Attack on Roll Characteristics of 65 Degree-Delta Wing," Journal of Aircraft Vol. 34, No. 4, pp. 573-575, 1997.

- [117] Lowson, M.V. and Riley, A.J., "Development of a Three-Dimensional Free Shear Layer," J. Fluid Mech. 369, pp. 49-89, 1998.
- [118] Jobe, C.E., "Vortex Breakdown Location over 65° Delta Wings – Empiricism and Experiment" AIAA Paper 98-2526, 1998.
- [119] Addington, G.A., "The Role of Flow Field Structure in Determining the Aerodynamic Response of a Delta Wing," Ph.D. Dissertation, University of Notre Dame, Notre Dame, Indiana, April, 1998.
- [120] Ericsson, L.E., "Effect of Fuselage Geometry on Delta Wing Vortex Breakdown," Journal of Aircraft Vol. 35, No. 6, pp. 898-904, 1998.
- [121] Huang, X.Z., Lui, T.C. and Hanff, E.S., "Selected Data Set from Static and Rolling Experiments on a 65° Delta Wing at High Incidence," AGARD WG-22, Chapter 16, 1998.
- [122] Hummel, D. and Lossner, T., "Low Speed Wind Tunnel Experiments on a Delta Wing Oscillating in Pitch," ICAS 98-3.9.3, Sept. 1998.
- [123] Ericsson, L.E., "Effect of Fuselage Geometry on Delta Wing Vortex Breakdown," Journal of Aircraft, Vol. 35, No.6, 1998, pp898-904.
- [124] Ericsson, L.E., "Vortex Characteristics of Pitching Double-Delta Wings," Journal of Aircraft Vol. 36, No. 2, March-April 1999.
- [125] Huang, X.Z. and Hanff, E.S., "Free-to-Roll Trajectory and Related Attractors of a 65 Delta Wing Rolling at High Incidence," AIAA Paper 99-4103, 1999.
- [126] Huang, X.Z. and Hanff, E.S., "Visualization of Bifurcating Vortex Breakdown Location Over Slender Delta Wings," 9th International Symposium on Flow Visualization, August 2000.
- [127] Ericsson, L.E., "Further Analysis of Fuselage Effects on Delta Wing Aerodynamics, AIAA Paper 2000-0981, 2000.
- [128] Mitchell, a. M., Molton, P. Barberis, D. and Délery, J., "Characterization of Vortex Breakdown by Flow Field and Surface Measurements," AIAA Paper 2000-0788, 2000.
- [129] Hanff, E.S., Jenkins, J.E., Huang, X.Z., Myatt, J.H., and Addington, G.A., "Highlights of the NRC/USAF/DND Joint Program on Maneuvering Aerodynamics," Canadian Aeronautics and Space Journal, Vol. 47, No. 3, Sept. 2001.
- [130] Mitchell, A.M. and Molton, P., "Vortical Substructures in the Shear Layers Forming Leading-Edge Vortices," AIAA Journal, Vol. 40, No. 8, pp. 1689-1692. August 2002.
- [131] Ericsson, L.E., "Further Analysis of Fuselage Effects on Delta Wing Aerodynamics," AIAA Paper 2000-0981, 2000.

- [132] Luckring, J.M., "Reynolds Number and Leading-Edge Bluntness Effects on 65° Delta Wing Aerodynamics," AIAA Paper 2002-0419, 2002.
- [133] Taylor, G.S., Gursul, I., and Greenwell, D.I., "Investigation of Support Interference in High-Angle-of-Attack Testing," *Journal of Aircraft* Vol. 40, No. 1, pp. 143-152, January-February 2003.
- [134] Ericsson, L.E., "Multifaced Influence of Fuselage Geometry on Delta-Wing Aerodynamics," *Journal of Aircraft*, Vol. 40, No.1, pp. 204-206, January-February 2003.
- [135] Luckring, J.M., "Transonic Reynolds Number and Leading-Edge Bluntness Effects on a 65° Delta Wing," AIAA Paper 2003-0753, January 2003.
- [136] Huang, X.Z., "Comprehensive Experimental Studies on Maneuvering Aerodynamics over Military Wing Configurations in IAR," CASI Paper 357, 2003.
- [137] Gordnier, R.E. and Visbal, M.R., "High-Order Compact Difference Schemes Applied to the Simulation of a Low Speed Delta Wing Flow," AIAA Paper 2003-0620, 2003.
- [138] Visbal, M.R. and Gordnier, R.E., "On the Structure of the Shear Layer Emanating from a Swept Leading Edge at Angle of Attack," AIAA Paper 2003-4016, 2003.
- [139] Luckring, J.M., "Reynolds Number, Compressibility and Leading-Edge Bluntness Effects on 65° Delta Wing Aerodynamics," ICAS 2004-4.1.4, September 2004.
- [140] Huang, X.Z., Mebarki, Y. and Benmeddour, A., "Experimental and Numerical Configuration Study on UCAV's Aerodynamics," ICAS 2004-P.7, 2004.
- [141] Panton, Ronald L., "Incompressible Flow," A Wiley-Interscience Publication, 1984.
- [142] Pirzadeh, S.Z., "Vortical Flow Prediction Using an Adaptive Unstructured Grid Method," RTO AVT Report-084, 2006.
- [143] Huang, X.Z., "IAR Program on Maneuvering Aerodynamics over Military Wing Configurations, Vol. II: Surface and Off-Surface Flow Visualization, IAR Report to be published in 2006.
- [144] Huang, X.Z., "IAR Program on Maneuvering Aerodynamics over Military Wing Configurations, Vol. III: Aerodynamic Loads at Static and Different Dynamic Motions," IAR Report to be published in 2006.
- [145] Huang, X.Z., "IAR Program on Maneuvering Aerodynamics over Military Wing Configurations, Vol. IV: Surface Pressure Measurements at Static and Different Dynamic Motions," IAR Report to be published in 2006.
- [146] Klein, C., etc., "Development of PSP Technique for Application on the VFE-2 65° Delta Wing Configuration," AIAA Paper 2006-59, 2006.

- [147] Konrath, R., etc., “Analysis of PSP Results Obtained for the VFE-2 65° Delta Wing Configuration at Sub- and Transonic Speeds,” AIAA Paper 2006-60, 2006.
- [148] Al-Garni, A.Z., etc., “Experimental and Numerical Investigation of 65-deg Delta and 65/40-deg Double-Delta Wings,” AIAA Paper 2006-63, 2006.
- [149] Benmeddour, A., Mebarki, Y. and Huang, X.Z., “Computational Investigation of the Centerbody Effects on the Aerodynamics of Delta Wings,” RTO-AVT Rep. 084, Chapter 20, 2006.
- [150] Straka, William A. and Hemsch, Michael J., “Leading-Edge Vortex Breakdown for Wing Planforms with the Same Slenderness Ratio,” Journal of Aircraft, Vol. 31, No. 3, 1994.

Table 1 Summary of experimental investigations considered in this Chapter.

Case No.	1	2	3	4
Λ	70	65, (55-70)	45-76	65, 70
Model Type	Half	Full ,Half	Full	Full
L.E.(Upper)	flat	flat	Convex	Convex
L.E.(Lower)	7° bevel	16°	Convex	Convex
T.E.	blunt	blunt		
c	7.75in	8.5in ,47.5in	0.59-1.18ft	18in, 21in
t	.0625in	0.1875, 3in		
t/c (%)	0.8	2.2, 6.32	6	4
Type	water	Water, wind	wind	wind
Test Section Size	5ftx5ft	13inx10in, 9ftx7ft	4ftx3ft	4ft'x3ft
Re_c	0.7x10E6 (12ft/s)	0.01~4.6x10 ⁶	0.2~0.4x10 ⁶ (80ft/s)	1x10 ⁶
Turbulence				
Support	Semi & false floor	Strut	Sting	Sting
Blockage, r	0.25%	13.0% (Half model)	1.70%	5%
Vis. method	Air bubble	Dye, vapor	Fine tufts	Schlieren
Publication	Ref. 22	Ref. 24	Ref. 26	Ref. 27

Case No.	5	6	7	8
Λ	60, 68.2, 76	45-85	60, 65, 70, 75, 80	60-80, 60/70, 70/80
Model Type	Full	Full	Full	Full
L.E.(Upper)	flat	7.5° bevel		15°
L.E.(Lower)	3°	7.5° bevel		15°
T.E.		7.5° bevel		15°
c	0.625m	10-18"	100-300cm	150mm
t	1.52cm	0.1in		1.8mm
t/c (%)	0.022			
Type	wind	wind	water	water
Test Section Size	1.3 m		0.22mx0.22m	0.25mx0.25m
Re_c	1.7x10 ⁶	0.3~1x10 ⁶	20cm/s	9.8x10 ³
Turbulence				
Support	Suspended on wires	2-point strut	Sting	Strut
Blockage, r	4.60%	1.80%		8.39%
Vis. method	Stethoscope/smoke	Schlieren	Dye	Dye & Bubble
Publication	Ref. 28	Ref. 32-35	Ref. 39	Ref. 40

CRITICAL ASSESSMENT OF TEST CASES ON VORTEX BREAKDOWN OVER SLENDER DELTA WINGS UNDER STATIC MODEL CONDITIONS



Case No.	9	10	11	12
Λ	60-80	65	70	70, 75, 80, 85
Model Type	Full	Full	Full	Full
L.E.(Upper)	flat	flat	flat	flat
L.E.(Lower)			26°	25°
T.E.			blunt	
c			16"	16"
t	0.05in		0.75in	0.25"
t/c (%)			4.7	1.56
Type	water	water	wind	wind
Test Section Size	16inx24inx6ft	0.46mx0.6m	2ftx2ft	2ftx2ft
Re_c	4.1×10^4	3×10^4	0.225×10^6	0.085×10^6
Turbulence			0.1-0.2%	0.1-0.2%
Support	Sting	Sting	Strut	Strut
Blockage			8%	8%
Vis. method	Dye	Dye	Smoke (section)	Smoke (section)
Publication	Ref. 42-45	Ref. 46	Ref. 49	Ref. 51, 54, 55

Case No.	13	14	15	16
Λ	60	75	70	45, 70, rectangular
Model Type	Full	Full	Full	Full
L.E.(Upper)	flat	flat	23°	flat
L.E.(Lower)	12°	20°	23°	
T.E.	blunt		23°	
c	100mm	0.31m	16.375in	
t	3 mm	4.6mm	0.5in	
t/c (%)	3		3	
Type	water	water	wind	wind
Test Section Size	0.45 x 0.55 m	0.8 x 0.4 m	2inx2in'	12 ft Diameter?
Re_c		0.08m/s~0.2 m/s	0.26×10^6	1×10^5
Turbulence			0.10%	
Support	Strut	Strut	Strut	Strut
Blockage			8%	
Vis. method	Air bubble		Smoke (Axes)	Smoke
Publication	Ref. 68	Ref. 83	Ref. 56	Ref. 59

CRITICAL ASSESSMENT OF TEST CASES ON VORTEX BREAKDOWN OVER SLENDER DELTA WINGS UNDER STATIC MODEL CONDITIONS

Case No.	17	18	19	20
Λ	75	65	60, 70	60
Model Type	Full	Full	Half	Full
L.E.(Upper)	flat	flat	flat	flat
L.E.(Lower)	40°	20°	25°	12°
T.E.			25°	blunt
c	241, 508mm	150mm	76, 54cm	500mm
t	12mm	3.175mm	1.27 cm	4 mm
t/c (%)		2.12	1.7	0.8
Type	water	water	wind	wind
Test Section Size	610x914mm	400x180mm	91cm x74cm	2x2m
Re_c	$1.2\sim3.6\times10^4$	25cm/s, 3.5×10^4	$0.3\sim2\times10^6$	$0.7\sim1.43\times10^6$
Turbulence			0.20%	0.1~0.2%
Support	Sting	Strut	Semi & splitter	Strut
blockage			7.80%	
Vis. method	Dye, Hydrogen bubble	Fluorescent dye	Smoke (section)	Smoke/Schlieren
Publication	Ref. 63	Ref. 62	Ref. 65	Ref. 67

Case No.	21	22	23	24
Λ	65	59, 63.4, 67, 70	60, 76	75
Model Type	Full	Full	Full	Full
L.E.(Upper)	flat	blunt	5.7, 11.3	flat
L.E.(Lower)	30		5.7, 11.3	25
T.E.	30	blunt	blunt	
c	850mm	15, 19, 20 cm	0.27, 0.31m	16in
t	20mm	1mm	1.27mm	0.25in
t/c (%)	2.35			1.56
Type	wind	water	water	wind
Test Section Size	3 m (Diameter)	60x60 cm	0.61 x 0.91 m	2inx2in
Re_c	$5.8\sim2.1\times10^6$	9×10^3	3.3×10^4 (0.12m/s)	0.25×10^6
Turbulence	0.30%	0.80%		
Support	Sting	Sting	Sting	Strut
blockage		2.10%		6.00%
Vis. method	Helium-soap bubble	Dye	Dye	Anemometer
Publication	Ref. 83	Ref. 84	Ref. 81	Ref. 81

CRITICAL ASSESSMENT OF TEST CASES ON VORTEX BREAKDOWN OVER SLENDER DELTA WINGS UNDER STATIC MODEL CONDITIONS



Case No.	25	26	27	28
Λ	65	66.33, 69.33 (W+B)	50 to 80, in steps of 5	65, 70, 75, 80, 85
Model Type	Full	Full	Full	Full
L.E.(Upper)	12	blunt	flat/10	
L.E.(Lower)	12	blunt	45/10	
T.E.	12	blunt	blunt/10	
c	2.04ft	9.483in	8in, 14in	
t	0.375in	0.05in	0.25in	
t/c (%)	1.53	0.5		
Type	wind	water	wind	wind
Test Section Size	7ftx10ft	16inx24in	2ftx2ft	0.8mx0.6m
Re_c	3.6×10^6	$0.25 \text{ft/s } 1.85 \times 10^4$	$0.05-0.1 \times 10^6$	
Turbulence			0.1-0.2%	0.05%
Support	Sting	Sting	Sting	
Blockage			7.93%	
Vis. method	Smoker/Laser	Dye	Smoke (top)	
Publication	Ref. 70, 71, 72, 87	Ref. 150	Ref. 91, 93	Ref. 90

Case No.	29	30	31	32
Λ	65 (W+B)	65	55, 60, 65, 69, 70, 71, 75	55, 65
Model Type	Full	Full	Full	Full
L.E.(Upper)	10	sharp/round	flat/bevel	flat/bevel
L.E.(Lower)	10	sharp/round	bevel/flat	flat/bevel
T.E.	10			
c	202 mm	25.734in	5in	18-24in
t		0.875in	0.08in	0.375in
t/c (%)				
Type	wind	wind	water	wind
Test Section Size	1m	8.2x8.2ft	15"x20"	6ftx9ft
Re_c		$6 \times 10^6 - 120 \times 10^6$	36000/ft	$2 \times 10^6 - 3.6 \times 10^6$
Turbulence				
Support		Sting	Sting	Sting
Blockage	3.62%			
Vis. method		pressure taps	Dye	PSP, pressure taps
Publication	Ref. 107	Ref. 100-103, 132,	Ref. 114	Ref. 140

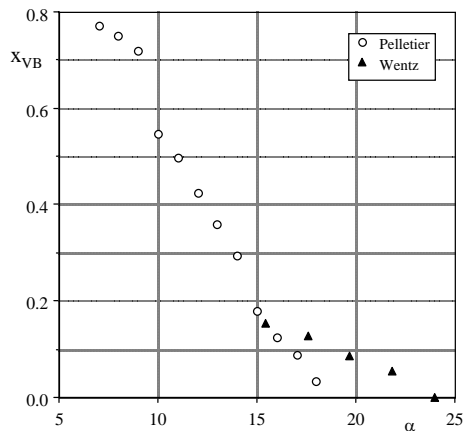


Fig. 1 Vortex breakdown location on 50° delta wing

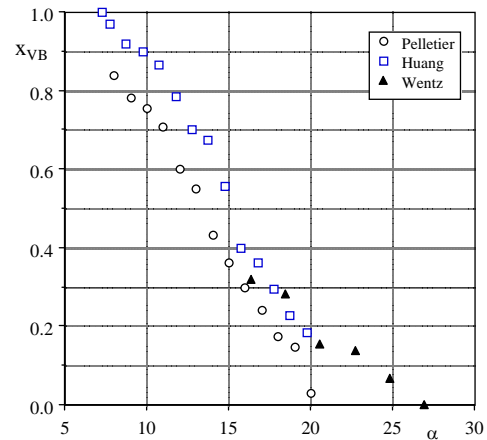


Fig. 2 Vortex breakdown location on 55° delta wing

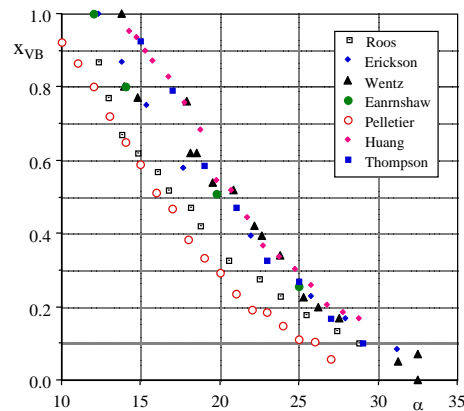


Fig. 3 Vortex breakdown location on 60° delta wing

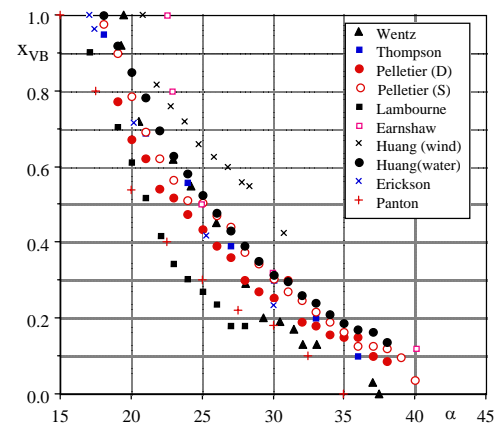


Fig. 4 Vortex breakdown location on 65° delta wing

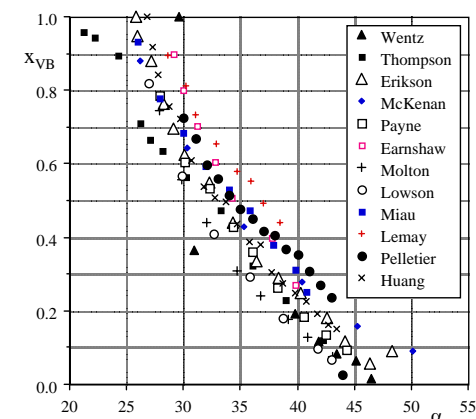


Fig. 5 Vortex breakdown location on 70° delta wing

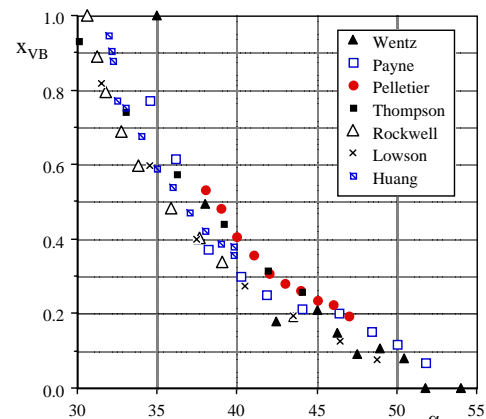


Fig. 6 Vortex breakdown location on 75° delta wing

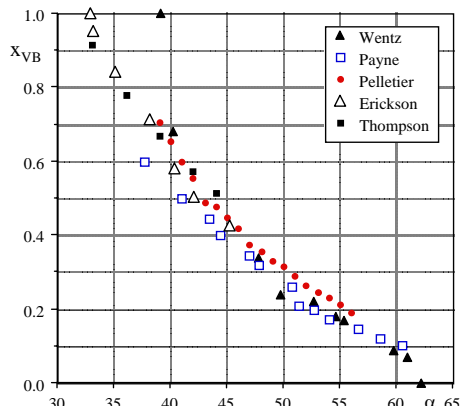


Fig. 7 Vortex breakdown location on 80° delta wing

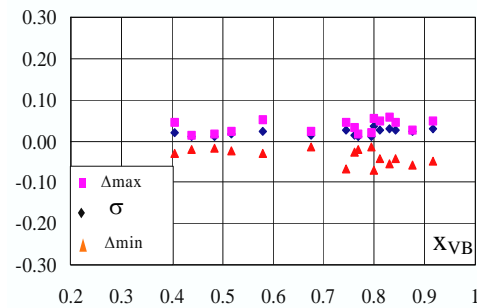


Fig. 8 Standard and maximum deviations of measured vortex breakdown location

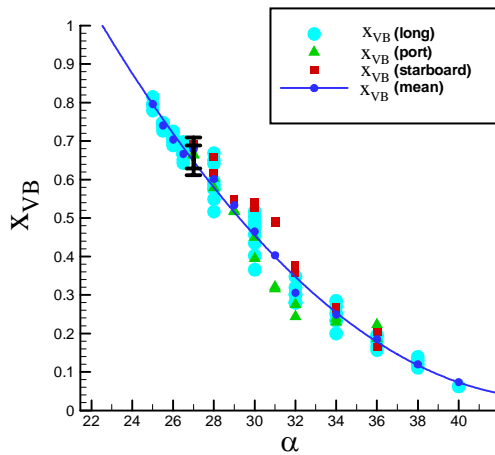


Fig. 9a Deviation in measured breakdown location

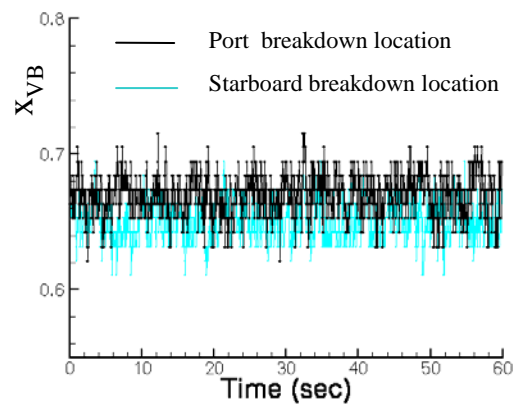


Fig. 9b Time histories of the port and starboard breakdown locations

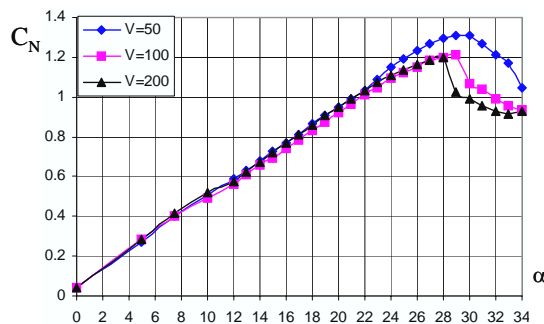


Fig. 10a Measured normal force (flat upper)

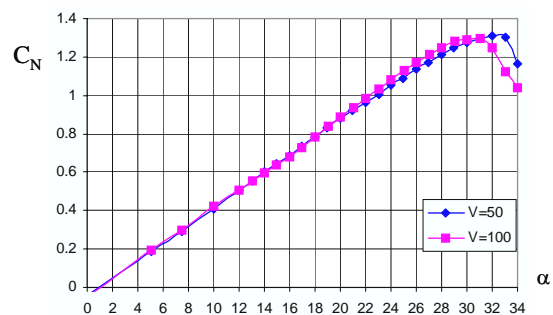


Fig. 10b Measured normal force (bevel upper)

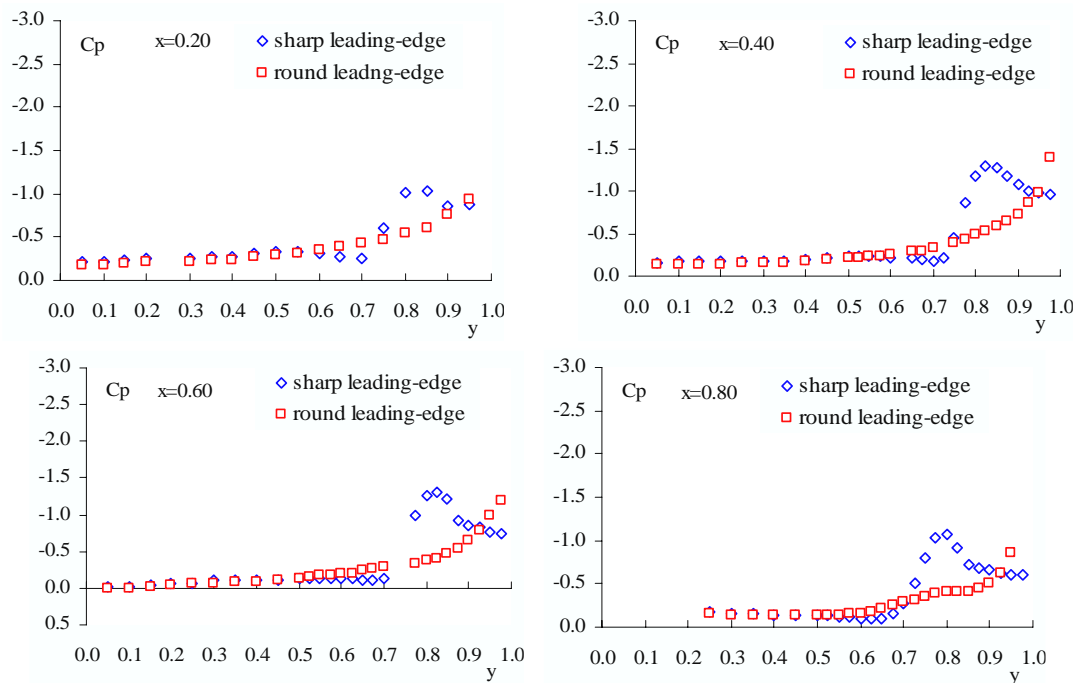


Fig. 11 Comparisons of surface pressure between sharp and round leading edges, $M=0.4$, $Re=6 \times 10^6$, $\alpha=10^\circ$

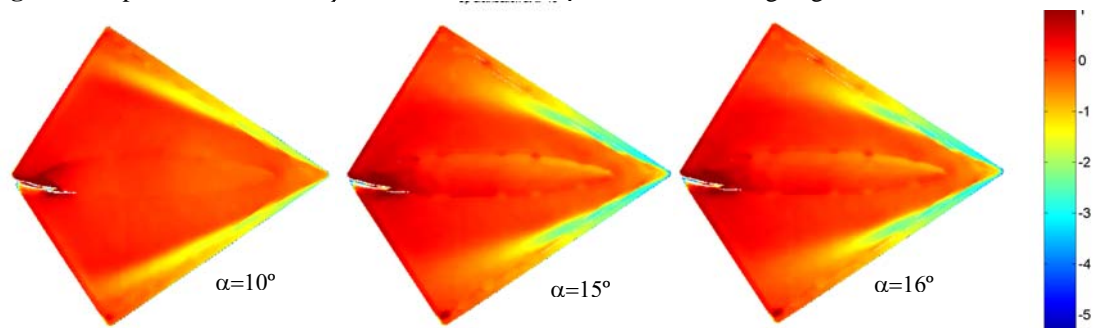


Fig. 12a PSP images on sharp leading-edge at different angles of attack

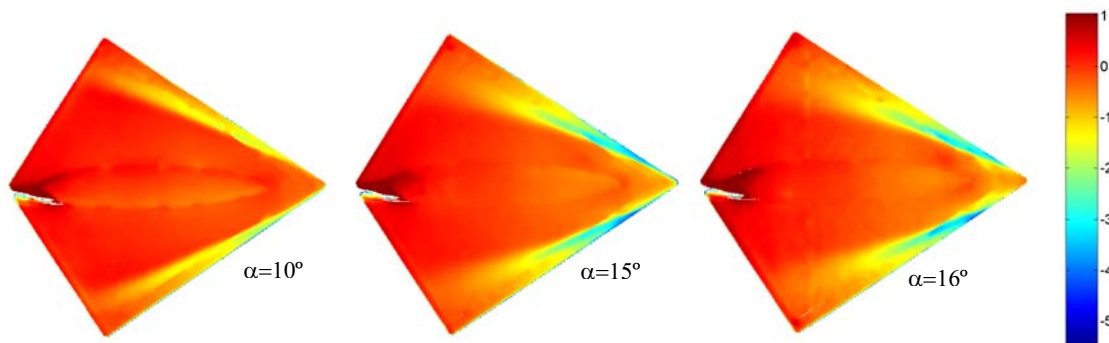


Fig. 12b PSP images on round leading-edge at different angles of attack

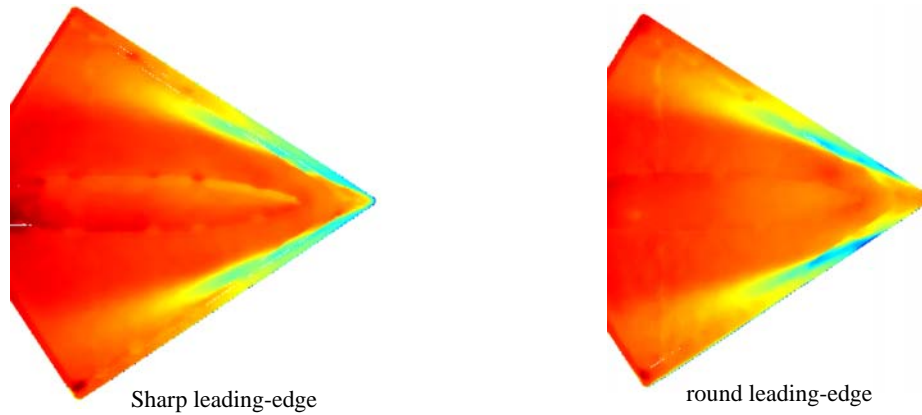


Fig. 12c enlarged PSP images on sharp and round leading-edge wing models ($\alpha=16^\circ$)

Fig. 12 PSP measurements at different model conditions

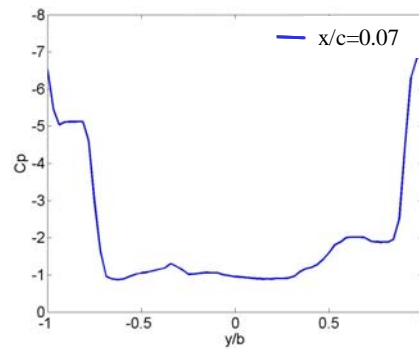


Fig. 13a round leading-edge

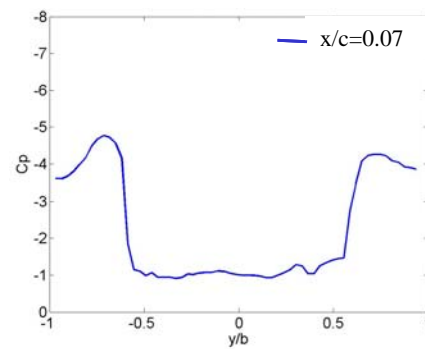


Fig. 13b Sharp leading-edge

Fig. 13 Digitized PSP results on leading-edge shape effect ($U=60$ m/s, $\alpha=21^\circ$)

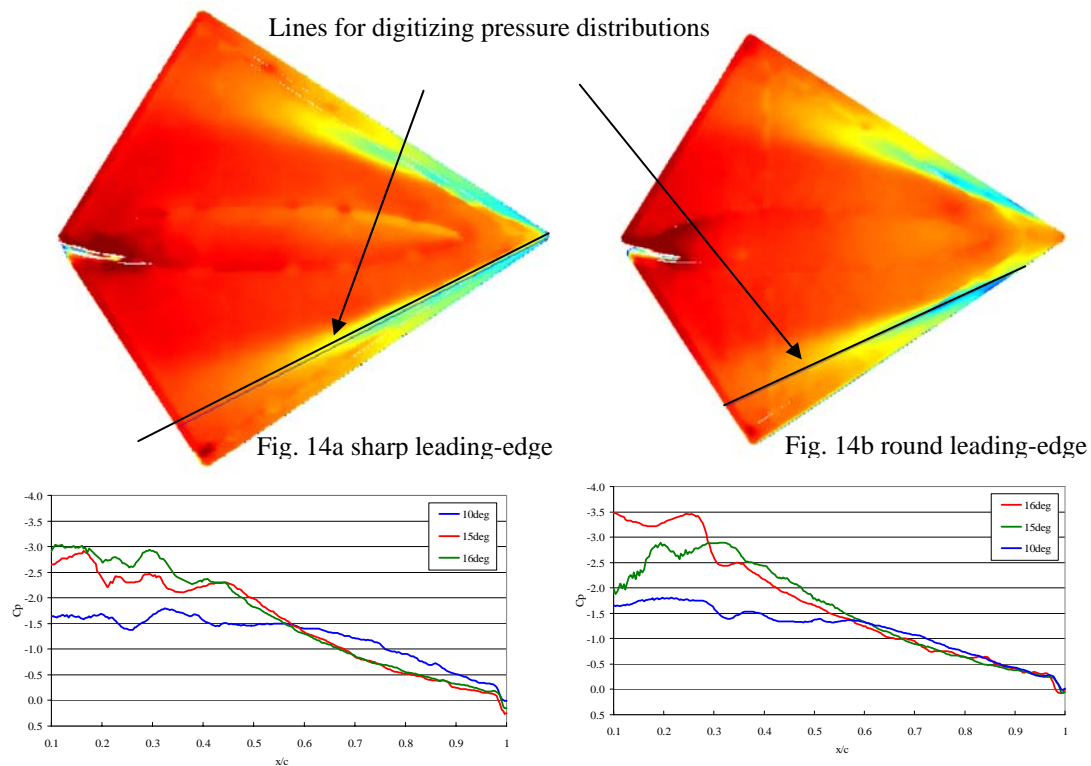


Fig. 14 Digitized pressure distributions on wings with sharp and round leading-edges

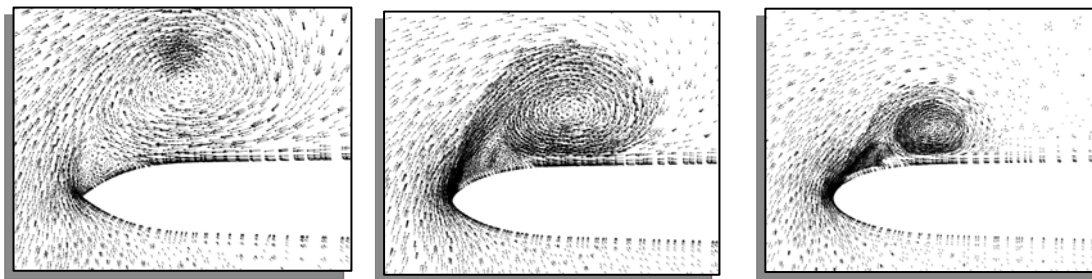


Fig.15a

Fig.15b

Fig. 15c

Fig. 15: Delta wing velocity vectors on cross-sectional planes at the mid-root chord stations showing primary, secondary, and "tertiary" vortices: (a) sharp leading edge, (b) medium leading edge, and (c) large leading edge. Navier-Stokes solutions at $M_\infty=0.4$, $\alpha=20^\circ$, and $Re_{MAC}=6.0 \times 10^6$.

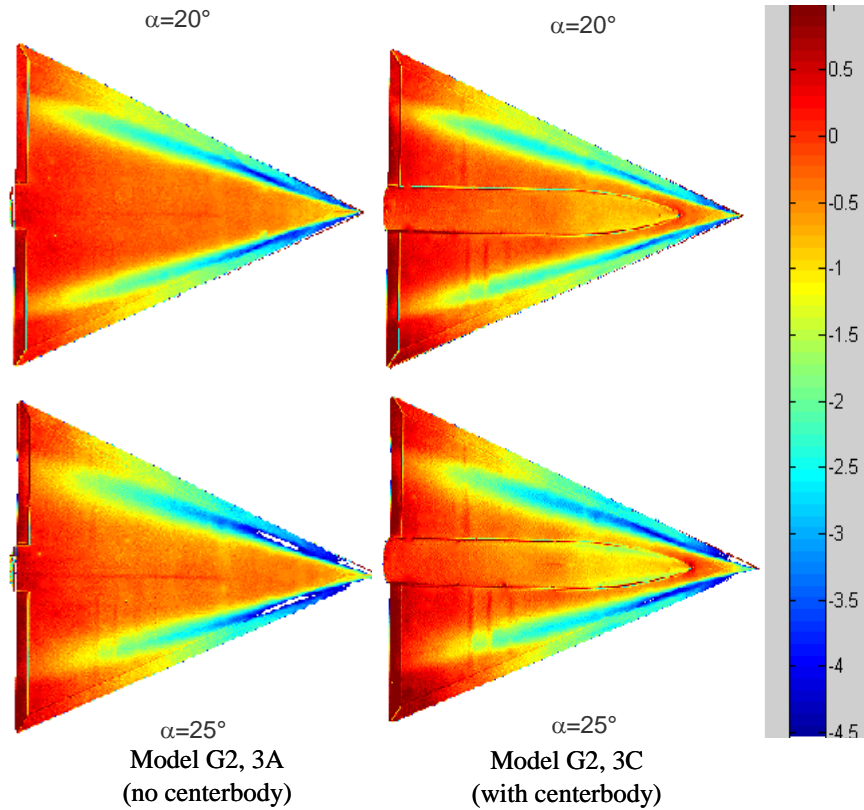


Fig. 16 PSP images between with/without centerbody

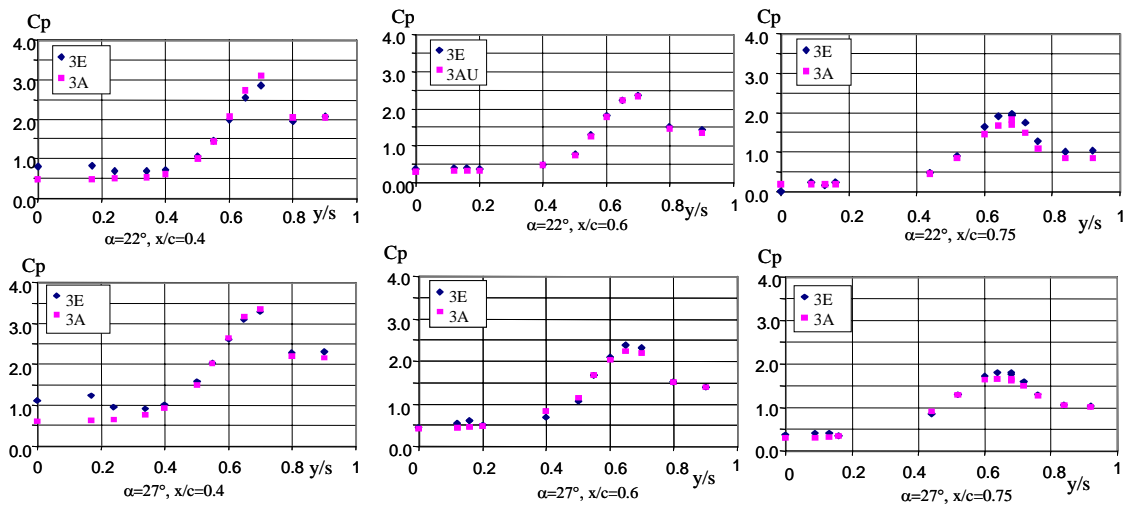


Fig. 17 Centerbody effect on pressure distributions at different locations, $U=60\text{m/s}$
(3E with centerbody; 3A without centerbody)

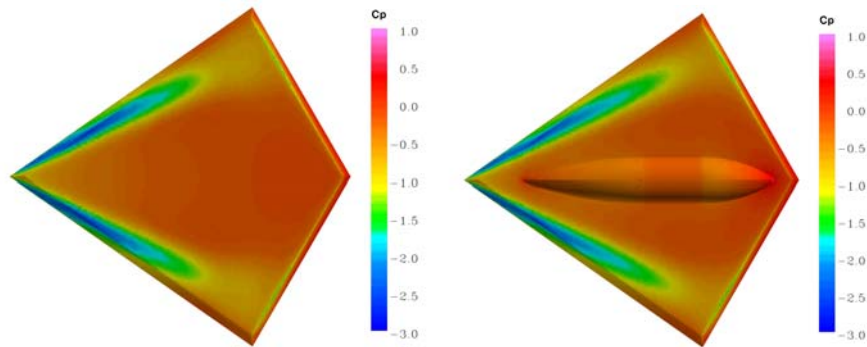


Fig. 18 Comparison of surface pressure between with and without centerbody (Model G1, $M=0.18$, $\alpha=15^\circ$)

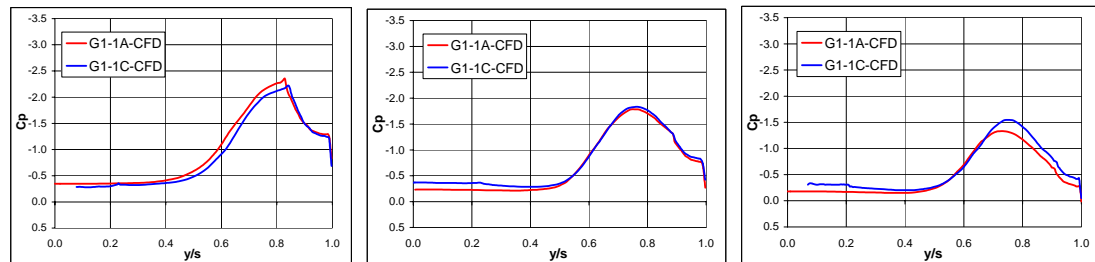


Fig. 19 Comparisons of pressure distributions between with/without centerbody at different chordwise locations ($M=0.18$, $\alpha=15$, NF no centerbody, 3E with centerbody)

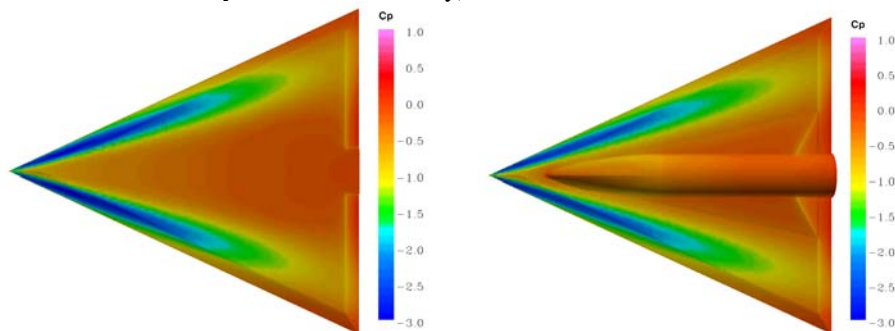


Fig. 20 Comparison of surface pressure between with and without centerbody (Model G2, $M=0.17$, $\alpha=21^\circ$)

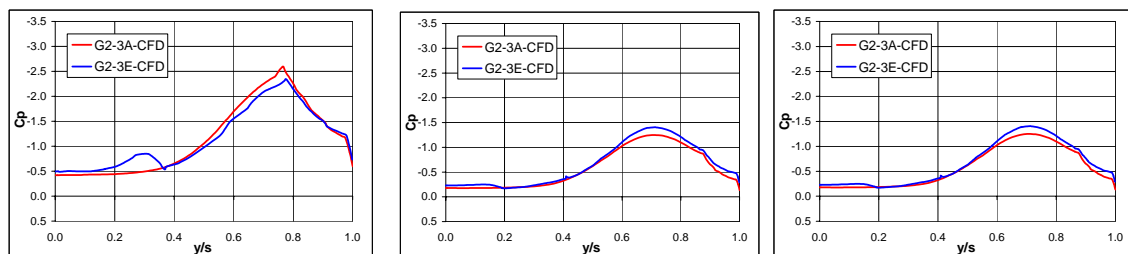
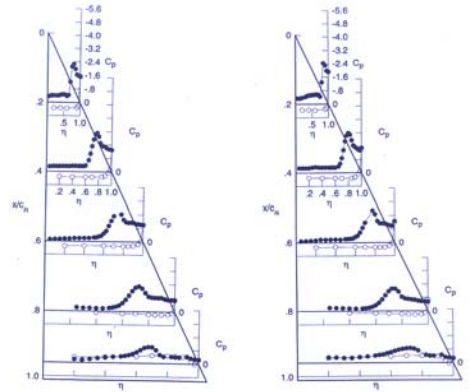


Fig. 21 Comparisons of pressure distributions between with/without centerbody at different chordwise locations ($M=0.17$, $\alpha=21^\circ$, 3A no centerbody, 3E with centerbody)



$Re=5.8 \times 10^6$, $M=0.4$

$Re=60 \times 10^6$, $M=0.4$

Fig. 22 Re number effect on surface pressure with sharp leading-edge

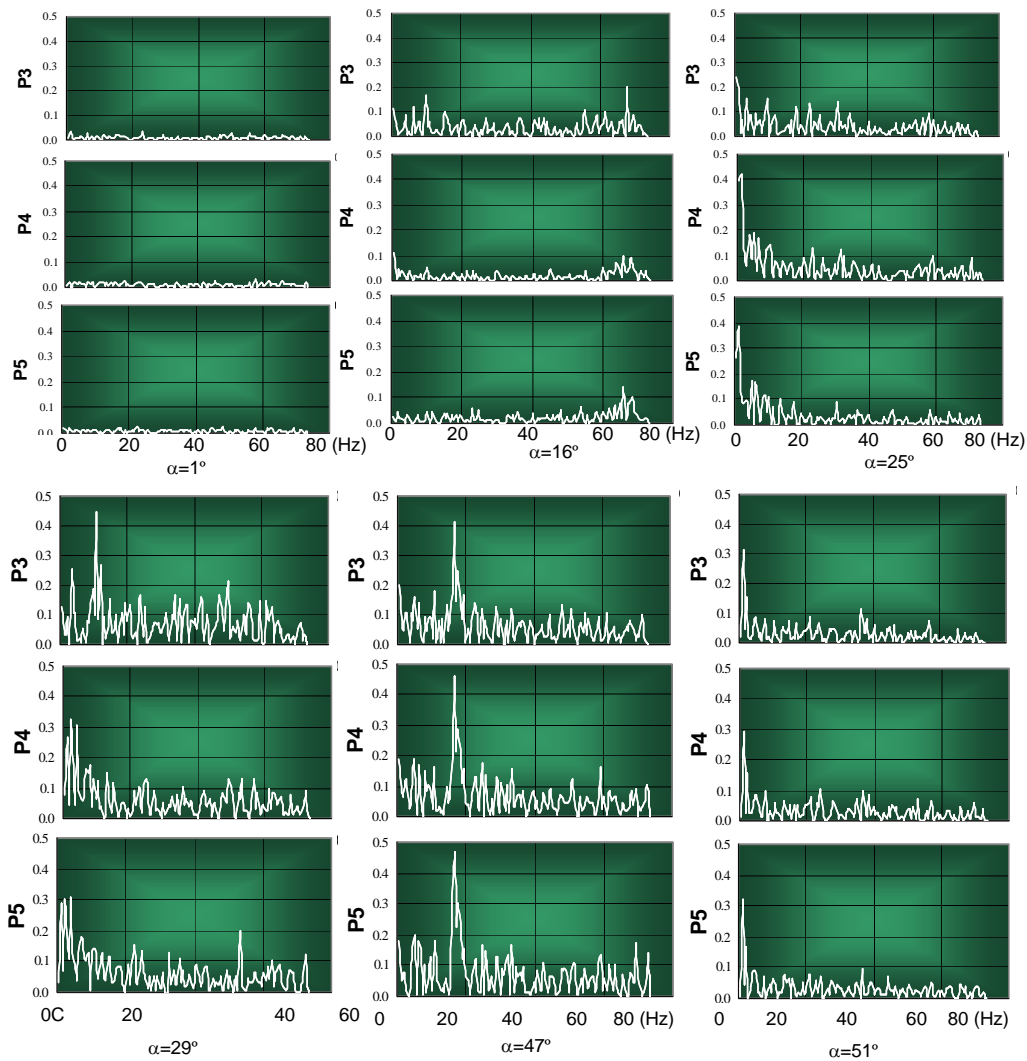


Fig. 23 Unsteady pressure spectral on 65° delta wing at different static angles of attack

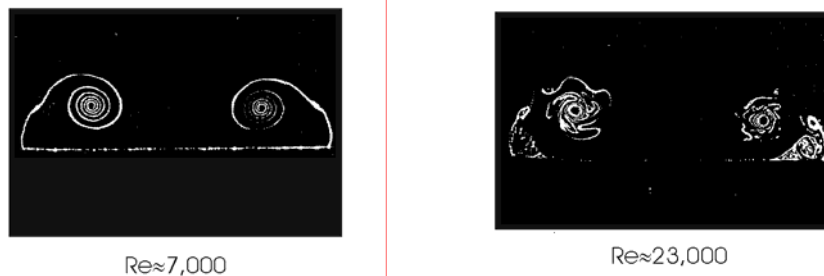


Fig. 24: Flow visualization of shear layer over delta wing

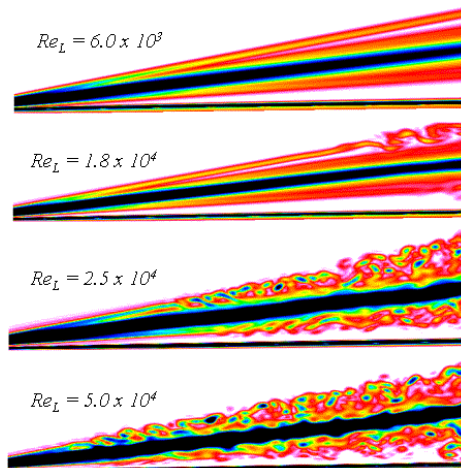


Fig. 25: Evolution of vortex structure with increasing Reynolds number. Contours of instantaneous vorticity magnitude on vertical plane through vortex core

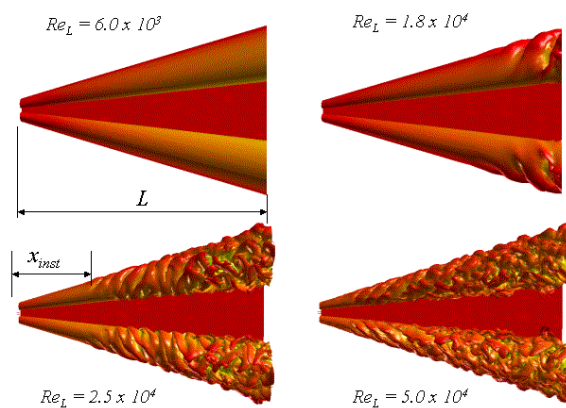


Fig. 26: Evolution of shear layer structure with increasing Reynolds number depicted using an isosurface of axial vorticity

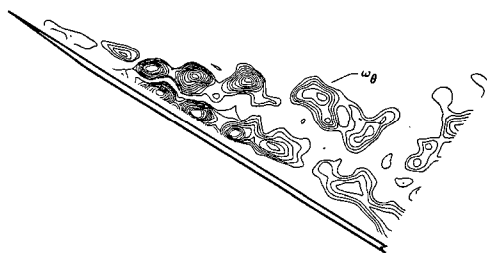


Fig. 27: Instantaneous azimuthal vorticity distribution in a plane that passes through the axis

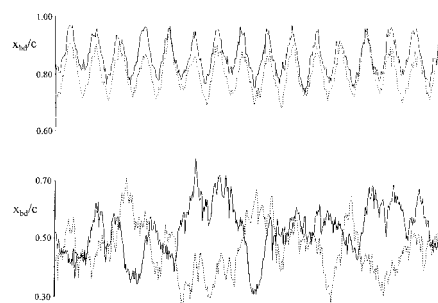


Fig. 28: Time histories of breakdown locations for left and right breakdowns for $\alpha_0 = 29^\circ$ (top) and $\alpha_0 = 42^\circ$ (bottom)

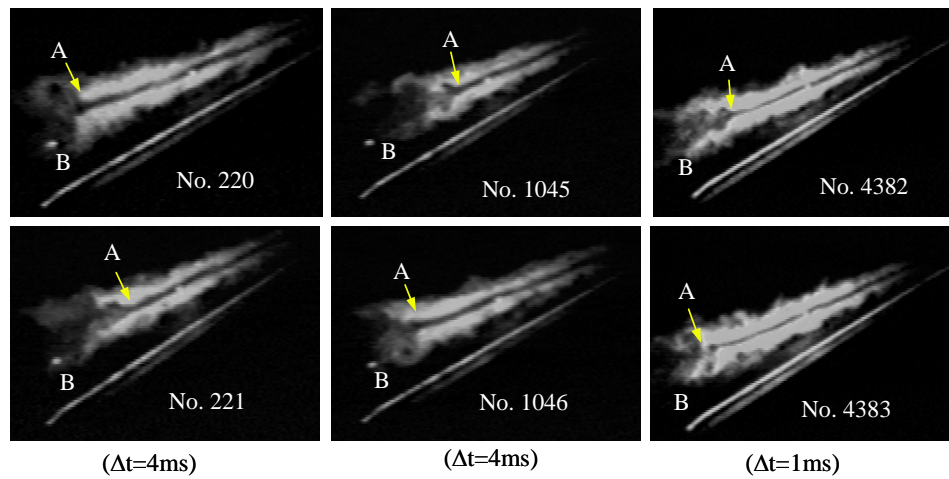


Fig. 29 Sequence of frames of laser-light sheet images

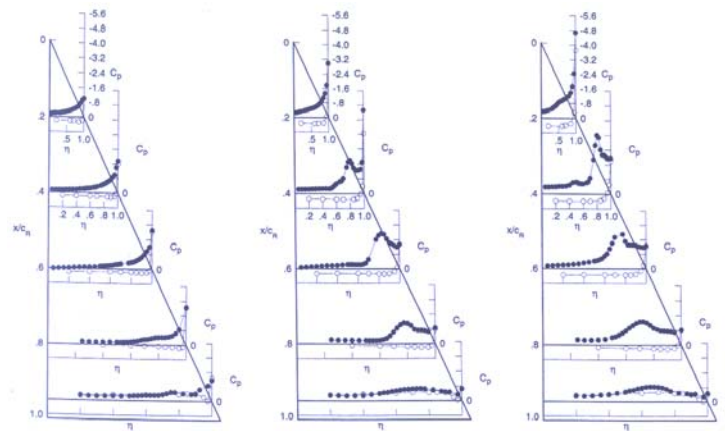


Fig. 30a $\alpha=10.3^\circ$ Fig. 30b $\alpha=16.4^\circ$ Fig. 30c $\alpha=20.2^\circ$
Fig. 30 Effect of angle of attack on surface pressure of round leading edge, $M=0.4$, $Re=6 \times 10^6$

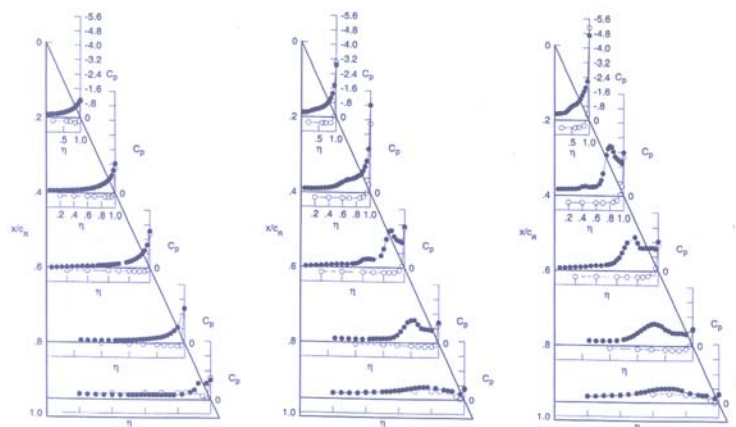


Fig. 31a $\alpha=9.9^\circ$ Fig. 31b $\alpha=16.1^\circ$ Fig. 31c $\alpha=20.2^\circ$
Fig. 31 Effect of Re number increase on surface pressure of round leading edge, $M=0.4$, $Re=60 \times 10^6$

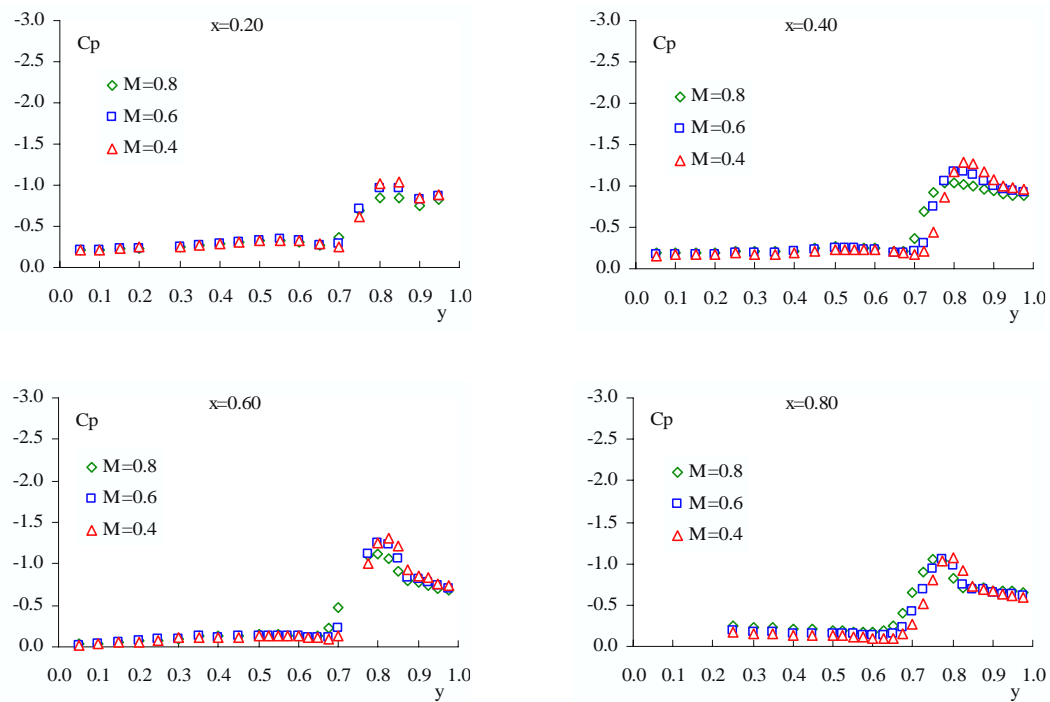


Fig. 32 Mach number effect on surface pressure with sharp leading-edge, $Re=6 \times 10^6$, $\alpha=10^\circ$

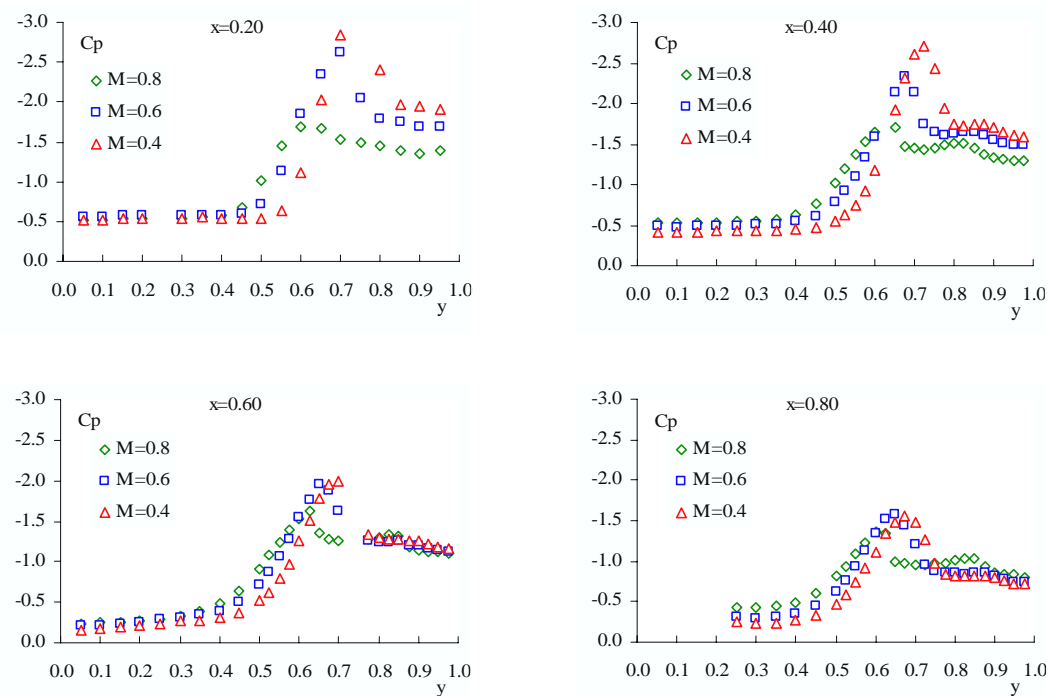


Fig. 33 Mach number effect on surface pressure with sharp leading-edge, $Re=6 \times 10^6$, $\alpha=20^\circ$

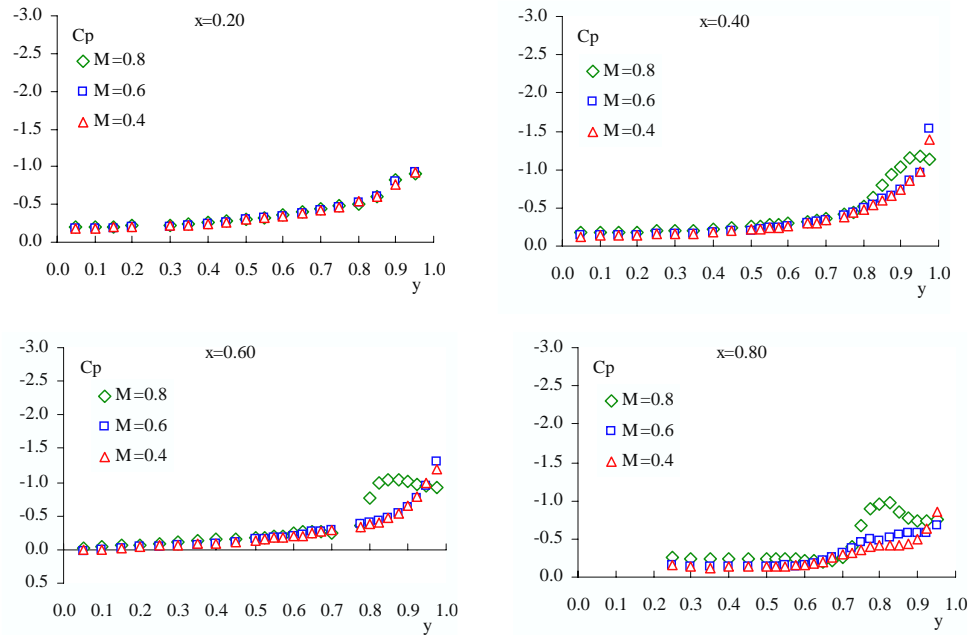


Fig. 34 Mach number effect on surface pressure with round leading-edge, $Re=6 \times 10^6$, $\alpha=10^\circ$

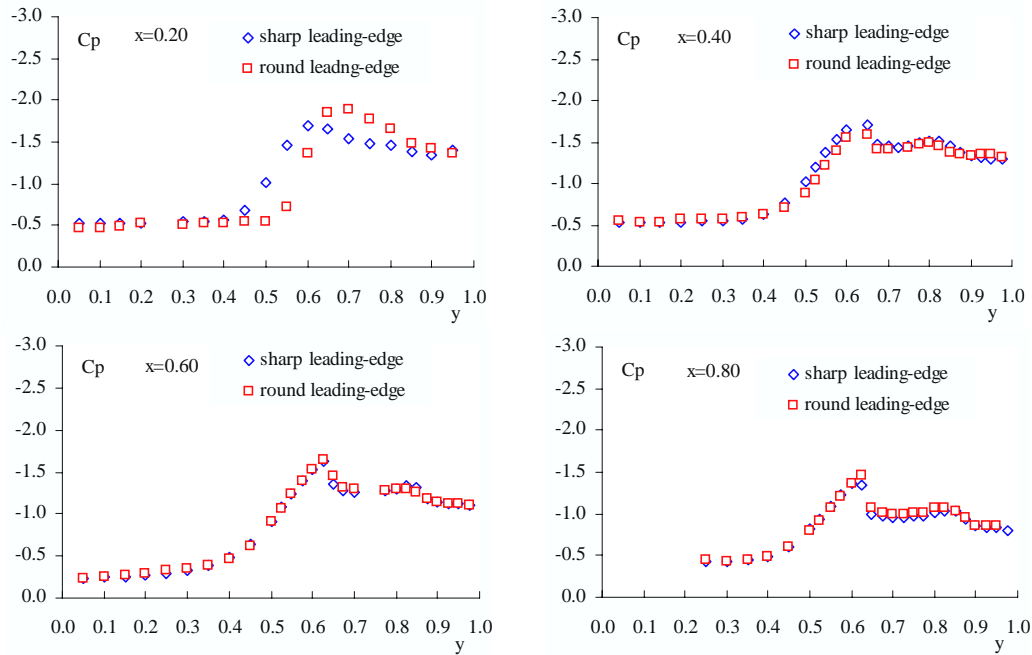


Fig. 35 Comparisons of Mach number effects between sharp and round leading-edge, $M=0.8$, $Re=6 \times 10^6$, $\alpha=20^\circ$

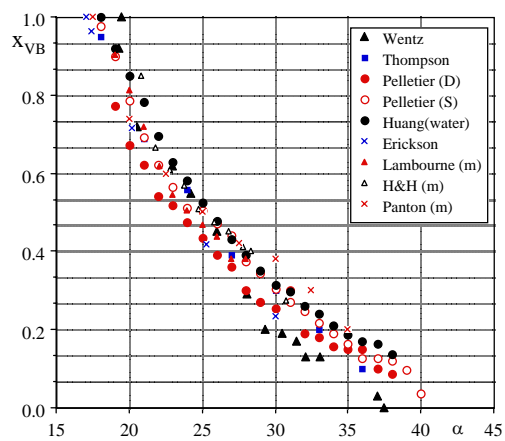


Fig. 36 Assessed results for 65° delta wings

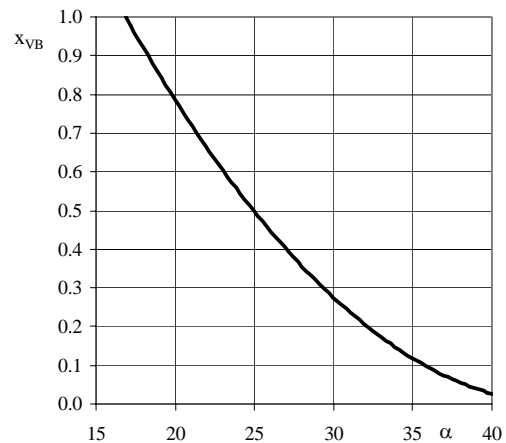


Fig. 37 Normalized results for 65° delta wings

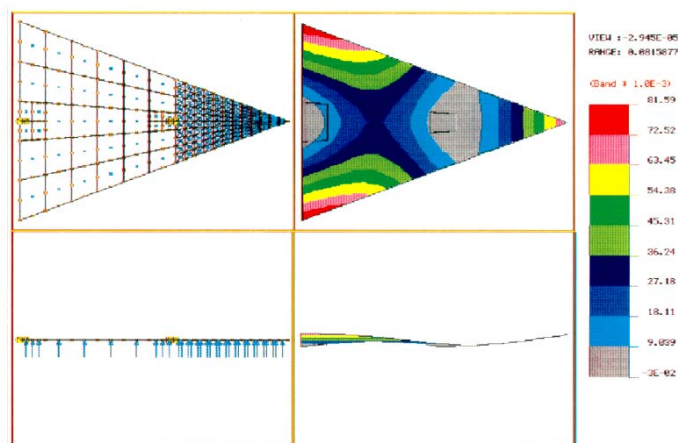


Fig. 38 Deformations estimated at $\alpha=30^\circ$ and $x_{VB}=0$

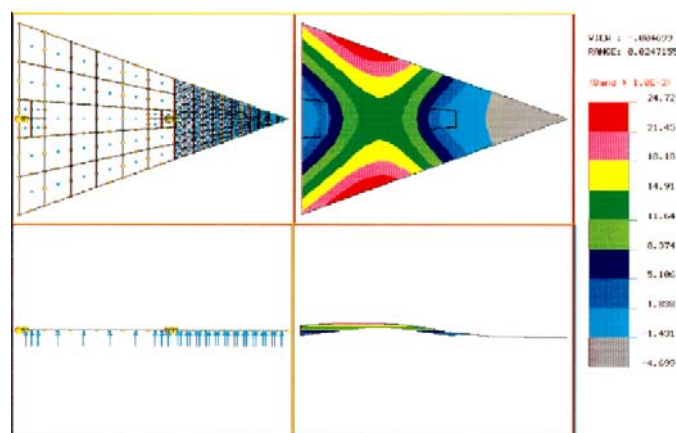


Fig. 39 Deformations estimated at $\alpha=29^\circ$ and $x_{VB}=1$

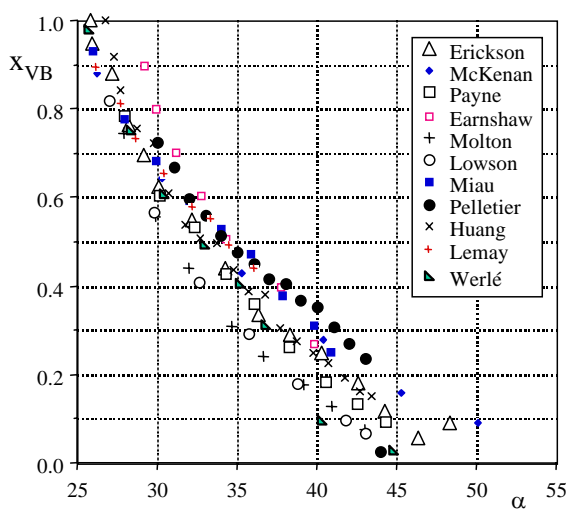


Fig. 40 Assessed results for 70° delta wings

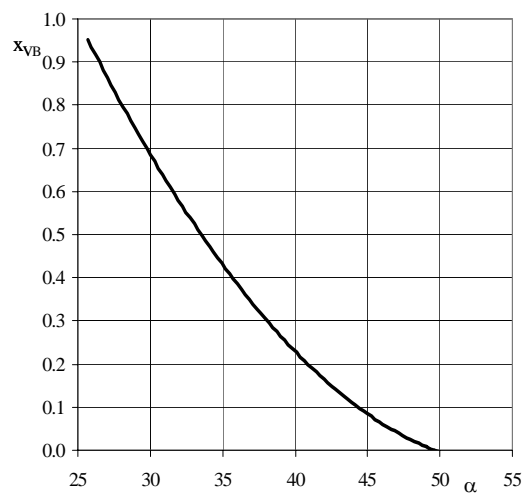


Fig. 41 Normalized results for 70° delta wings

Chapter 3 – EXPERIMENTAL DATA BASE SELECTED FOR NUMERICAL AND ANALYTICAL VALIDATION AND VERIFICATION: ONERA 70-DEG DELTA WING

Anthony M. Mitchell

Department of Aeronautics

United States Air Force Academy, CO 80840

Tony.Mitchell@aoard.af.mil

ABSTRACT

The objective of this chapter is to discuss detailed experimental results of the vortical flow field around a slender delta wing model with a 70° sweep angle and a root chord of 950 mm. These experimental results from wind tunnel tests at Onera were selected as the benchmark for validation and verification of computational fluid dynamic codes by the NATO Research and Technology Organization (RTO) Applied Vehicle Technology (AVT) Task Group-080 “Vortex Breakdown Over Slender Wings.” The rigorous definition of the experimental configuration and test conditions provides sufficient information for establishing computational grids and for matching test conditions. Both qualitative and quantitative surface and flow field visualization and measurement techniques were implemented to identify the characteristics of the vortical flow field and the associated vortex breakdown phenomena. Results from laser light sheet visualization reveal details of the flow instabilities and oscillating breakdown location. Surface measurements are analyzed to determine the influence of the leading-edge vortices on the leeward surface of the wing as well as their ability to detect the vortex breakdown location. Three-dimensional Laser Doppler Velocimetry (LDV) measurements within the vortical flow field and around the vortex breakdown are discussed. The combination of experimental techniques provides more details of the characteristics of the vortical flow structure and of the vortex breakdown phenomena.

3.1 NOMENCLATURE

c	Root chord length	X_b	Vortex breakdown location from wing apex
C_p	Pressure coefficient	X_b/c	Non-dimensional vortex breakdown location
C_{pmin}	Minimum value of the pressure coefficient	Y/b	Non-dimensional wing span location
Re_c	Reynolds number with respect to root chord	α	Incidence angle, angle of attack
U_∞	Freestream velocity	Λ	Sweep angle
X	Chordwise distance downstream of wing apex	Ω	Vorticity ($\nabla \times \mathbf{V}$)

3.2 INTRODUCTION

Modern military aircraft and missile systems are expected to perform at extreme flight conditions which often result in the development of complicated three-dimensional separated flow fields. The delta wing configuration is a good design choice for systems required to perform at high angles of attack because of the non-linear lift gains generated by the vortical structures around the body.

The flow field around delta wings at moderate to high angles of attack has been examined for the past 50 years. The experimental delta wing research results were published in the mid to late 1950s. [1-3] This

early research spawned numerous related research activities as well as several theories governing vortex breakdown; however, none of these theories has been universally accepted. Periodic reviews of vortex breakdown have been published.[4-10] The global characteristics of vortex breakdown are relatively well understood, but exact details of the phenomena are still only vaguely described by experimental and computational data.

This chapter will discuss detailed experimental results of the vortical flow field around a slender delta wing model with a 70° sweep angle and a root chord of 950 mm. These experimental results from wind tunnel tests at Onera were selected as the benchmark for validation and verification of computational fluid dynamic codes by the NATO Research and Technology Organization (RTO) Applied Vehicle Technology (AVT) Task Group-080 “Vortex Breakdown Over Slender Wings.” The rigorous definition of the experimental configuration and test conditions provides sufficient information for establishing computational grids and for matching test conditions and to validate and verify computational and analytical methods. These computational and analytical techniques will hopefully provide more insight into the cause and effect of the vortical flow field and vortex breakdown on the aerodynamics of the vehicle.

3.3 WIND TUNNEL

F2 is a closed-return atmospheric wind tunnel incorporating a rectangular test section with a width of 1.4m, a height of 1.8m, and a length of 5m (Fig. 1).

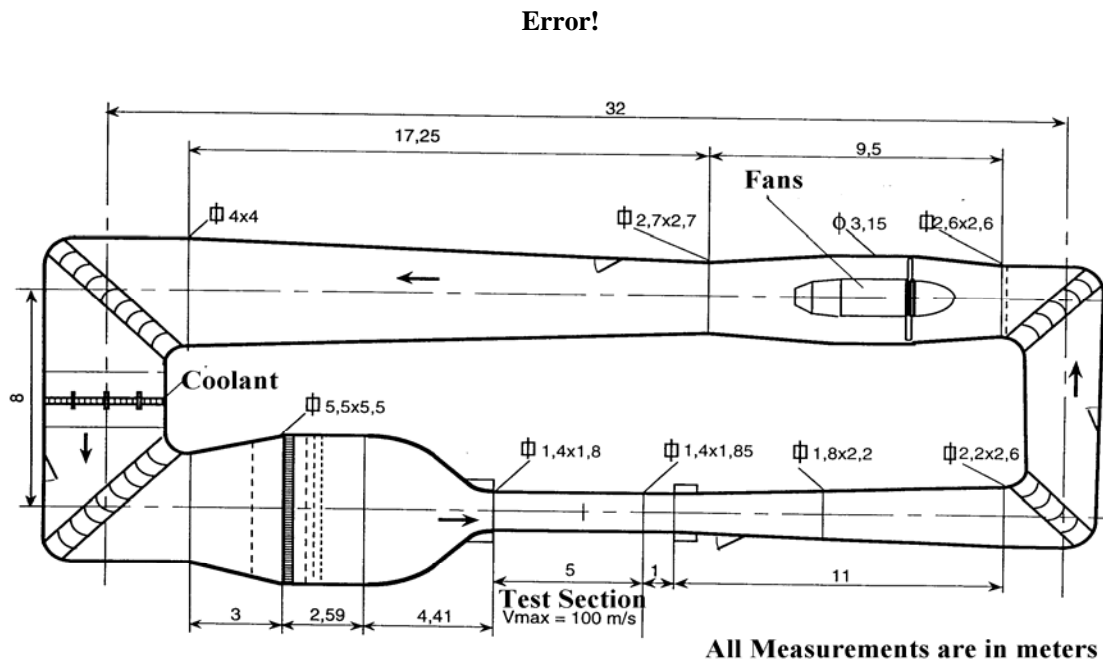


Fig. 1: ONERA's F2 Wind Tunnel.

The wind tunnel is powered by a 680kW DC motor that drives a fan with blades spanning 3.15m and provides a maximum freestream velocity in the test section of 105m/s. A cooling system in the closed-return portion of the wind tunnel facility maintains a constant freestream temperature in the test section.

There is a combination of screens and a honeycomb mesh upstream of the settling chamber to reduce transverse turbulence levels. The contraction ratio of the tunnel from the settling chamber to the test section is 12. The test section is composed of a number of large windows that enable a variety of flow and surface visualization techniques, especially 3-D Laser Doppler Velocimetry. The mean intensity of turbulence in F2 is 0.1%. [11]

In F2, the delta wing model was mounted on a sting with a horizontal support and an elbow for adjusting the angle of attack (Fig. 2). CAD drawings of the support system are available and were used to generate computational grids of the model-support system. During the tests, the horizontal support was manipulated in height along a vertical column so as to maintain the model close to the center axis of the test section. The model was mounted in the test section with no yaw angle with respect to the freestream flow.

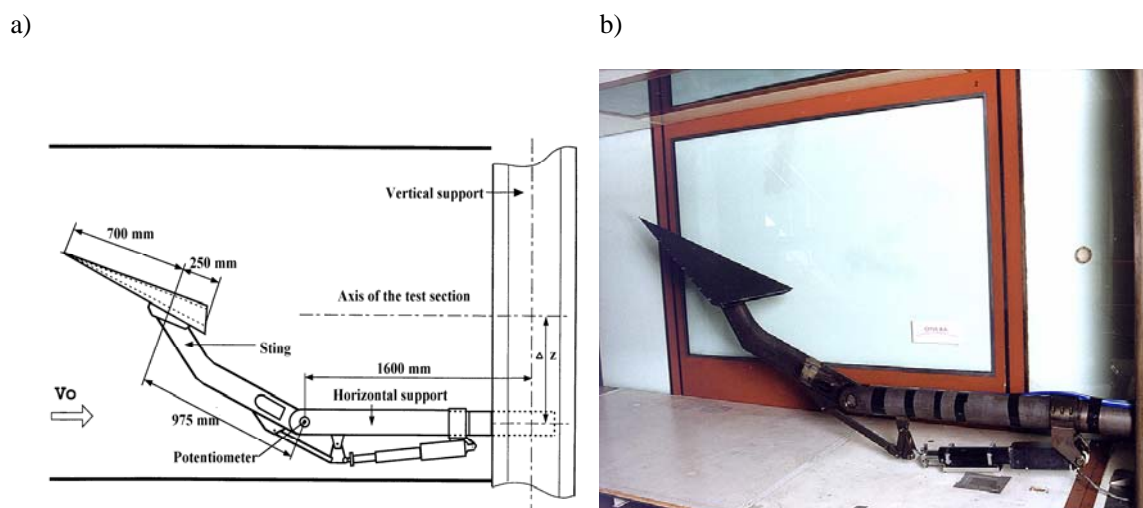


Fig. 2: Experimental configuration in F2 (a) Sketch (b) Actual test section configuration.

3.4 MODELS

Two, geometrically identical, delta wing models with 70° sweep angles (Λ) and root chords (c) of 950 mm have been configured to collect qualitative and quantitative surface and flow field measurements and data. Each model has a wingspan of 691.5 mm at its trailing edge, is 20 mm thick, and is bevelled on the windward side at an angle of 15° to form sharp leading edges (Fig. 3). The trailing edge of the model is blunt without any bevel. Each model is attached to the sting by screws that “cover” the thickness of the wing. The holes are inscribed around a 150 mm diameter circle situated along the root chord of the wing, 250 mm upstream of the trailing edge.

The first model, without surface instrumentation, is used to obtain flow field and surface oil flow results. It was painted with a flat black epoxy paint to avoid reflections of the laser sheet in both the laser light sheet and Laser Doppler Velocimetry tests. White reference lines were painted on the leeward surface to facilitate the interpretation of the flow visualization results. Additionally, an external reference grid was fabricated to align with the laser light sheet in the space above the leeward surface of the wing. This reference plane enabled more precise evaluation of the vortex breakdown location over the leeward surface of the delta wing. The reference plane was adjusted before each test to ensure that it bisected the axis of the leading-edge vortex between the apex of the wing and the trailing edge. Video footage was taken of the reference plane prior to each laser light sheet test. Analysis of the vortex breakdown location

was accomplished based on this reference plane that eliminated some of the potential uncertainty caused by the difference between the camera angle (tangent to the laser light sheet plane) and the leeward surface of the wing.

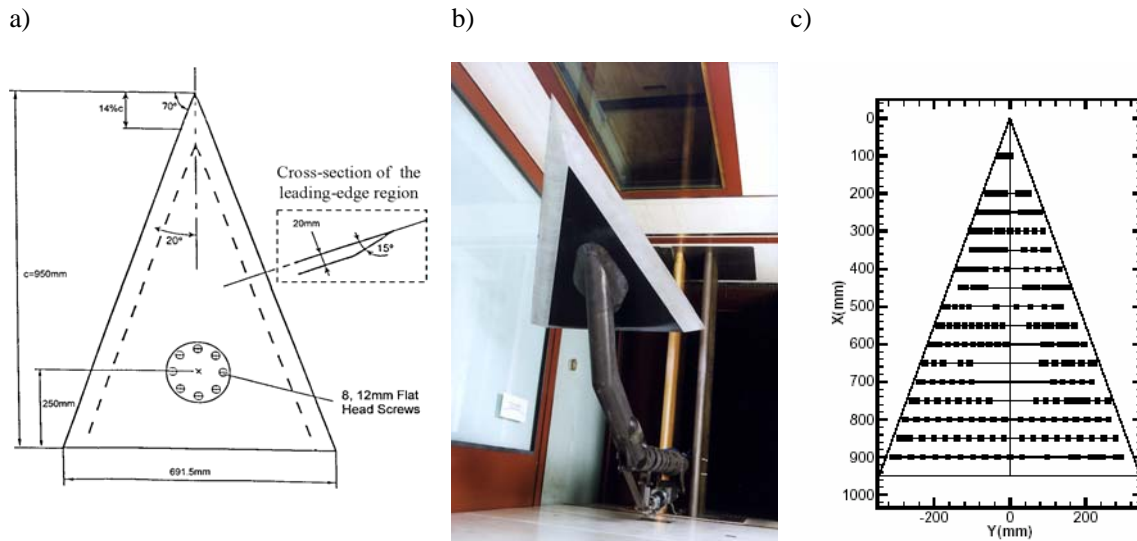


Fig. 3: Experimental delta wing model configuration (a) Sketch (b) Actual model in wind tunnel test section (c) Delta wing model configured for surface pressure measurements with 232 pressure taps.

The second model with 232 pressure taps is used to collect steady surface pressure data (Fig. 3c). These pressure taps are 2 mm in diameter and are situated in 16 transverse sections normal to the root chord between $-0.95 < Y/e < 0.95$ (e is the half-span of the model for a given chord-wise location). The first row of pressure taps is 100 mm behind the apex ($X/c = 0.11$). Beginning with the second row of pressure taps, 200 mm aft of the apex ($X/c = 0.21$), all other rows are spaced at 50 mm ($X/c = 0.05$) intervals along the chord. The last row of pressure taps was located at a position of $X/c = 0.95$. The location of the pressure taps correspond to X locations of: $X = 100, 200, 300, 350, 400, 450, 500, 550, 600, 650, 700, 750, 800, 850$ and 900 mm from the apex.

The model was also configured with an adjustable reference plane above the leeward surface of the delta wing (Fig. 4). This reference plane was fabricated after the initial laser light sheet experiments were accomplished to enable a more accurate identification of the vortex breakdown location in the space above the leeward surface of the delta wing. The reference plane was adjusted during a wind-on test so that it intersected both vortex cores between the wing apex and the trailing edge. Video images perpendicular to the adjustable reference plane were taken before the laser light sheet data was recorded. During the data analysis, the laser light sheet results were superimposed over the reference plane and the surface grid was used to identify the vortex breakdown location of both the port and starboard vortices. The adjustable reference plane reduced some error in determining the vortex breakdown locations by eliminating the effect of the small angle between the leeward surface of the delta wing and the angle of the reference plane that intersected the vortex cores.

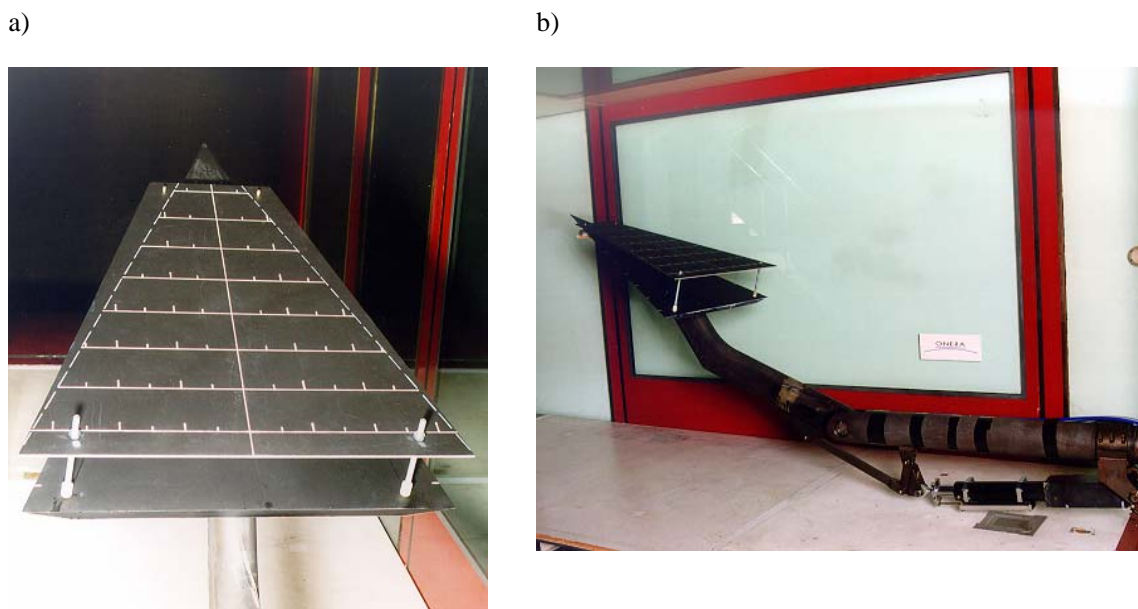


Fig. 4: Experimental configuration demonstrating the adjustable reference plane (a) View looking forward (b) Side view.

3.5 EXPERIMENTAL METHODS

Both qualitative and quantitative surface and flow field visualization and measurement techniques were implemented to identify the characteristics of the vortical flow field and the associated vortex breakdown phenomena. Results from laser light sheet visualization reveal details of the flow instabilities and oscillating breakdown location. Surface measurements are analyzed to determine the influence of the leading-edge vortices on the leeward surface of the wing as well as their ability to detect the vortex breakdown location. Three-dimensional Laser Doppler Velocimetry (LDV) measurements within the vortical flow field and around the vortex breakdown are discussed.

Results relating to the position of the vortices or the vortex breakdown location are presented using a Cartesian axis system attached to the leeward surface of the delta wing, the origin being defined at the apex: the x-coordinate is defined parallel with the leeward surface and runs along the root chord; the y-coordinate is also defined parallel to the leeward surface and is perpendicular to the x-axis in the spanwise direction; the z-coordinate is defined perpendicular to the leeward surface and is positive with respect to the right-hand-rule (Fig. 5).

The flow field velocity measurements are all based on the wind tunnel test section with the axial velocity component, U , following the centerline of the test section. The tangential velocity component, V , is directed along the Y-axis with the positive direction defined toward the right hand side of the test section. The normal velocity component, W , is directed along the vertical axis in the test section.

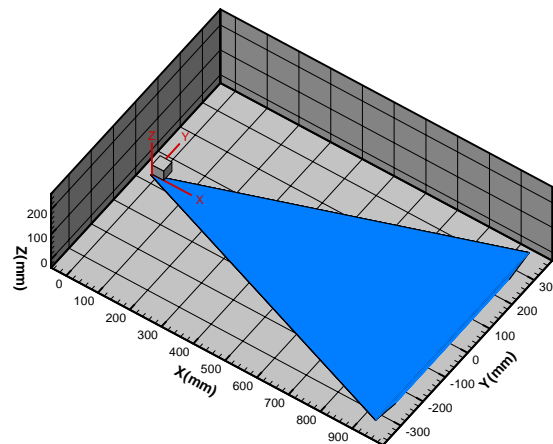


Fig. 5: Coordinate system.

3.5.1 Laser Sheet Visualization

The laser sheet flow visualizations were accomplished with a 15 W argon laser. The beam was diffracted around a cylinder to create a thin sheet of light oriented in the test section by a series of mirrors. The mirrors permitted adjustment of the elevation as well as rotation of the laser sheet. Theater smoke (P/Smog FS25) was generated in a commercial smoke machine and then entrained into the freestream flow downstream of the model and subsequently filled the closed-return circuit.

During the first series of tests, the laser sheet was oriented perpendicular to the leeward surface of the delta wing and along the portside vortex core (Fig. 6). Additional tests were accomplished with the laser sheet perpendicular to the leeward surface in a spanwise direction (Fig. 7). In later tests, the laser sheet was directed to intersect the two leading-edge vortex cores above the leeward surface of the delta wing model (Fig. 8). The original series of laser sheet visualization results were recorded by a limited number of still photographs of the phenomena at random time intervals during each run.

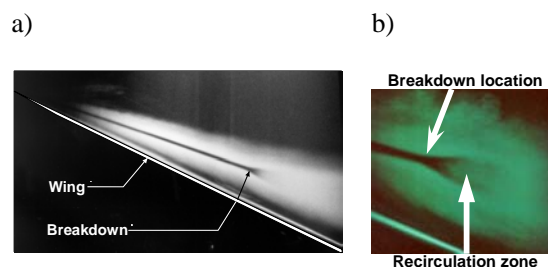


Fig. 6: Instantaneous photographs of laser light sheet taken at $U_\infty = 24$ m/s and $\alpha = 27^\circ$ (a) side view (b) zoomed in on vortex breakdown region.

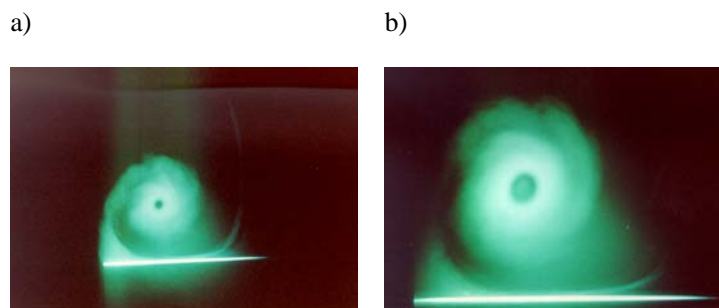


Fig. 7: Instantaneous photographs of laser light sheet taken at $U_\infty = 24$ m/s and $\alpha = 26^\circ$ (a) upstream of vortex breakdown at $X/c = 0.63$ (b) in the vortex breakdown region at $X/c = 0.74$.

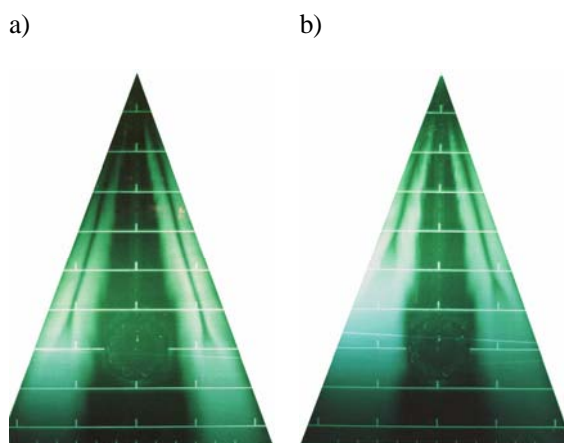


Fig. 8: Instantaneous photographs of laser light sheet taken at $U_\infty = 24$ m/s (a) $\alpha = 27^\circ$ (b) $\alpha = 30^\circ$.

As the tests conditions were focused on angles of attack of 27° and 30° , the laser sheet visualization data was captured by digital video cameras, which recorded images at a rate of 50 frames/second. In both cases, the cameras were positioned perpendicular to the laser sheet being used.

There are two distinct regions in each image: a highly luminous region where the laser light is reflected off of the tracer particles and dark regions, void of particles, representing the core of the vortices (Figs. 6, 7 and 8). In the luminous region, the laser illuminates and reflects off of seeding particles that are entrained into the flow as they traverse the thin sheet of light. The leading-edge vortex cores upstream of the breakdown location appear as dark, void, regions surrounded by a well-seeded and highly reflective flow. In effect, the tracer particles are ejected from the core of the vortex by centrifugal forces and by the elevated axial velocity in the core upstream of vortex breakdown so few particles remain to reflect the laser light. The dark region is therefore characteristic of the presence of a vortical flow with high axial and rotational velocities. The vortex breakdown phenomenon is signified by a rapid expansion of the diameter of the vortex core and an increase in the number of tracer particles reflecting the laser light sheet. This is due to the deceleration of the axial velocity, a diminishing of the rotational velocity and a region of recirculating flow.

In these laser light sheet results, vortex breakdown was identified as the position where the vortex core began to expand. The streamwise distance of the breakdown locations from the apex of the delta wing (X_b) were measured directly from the recorded laser sheet images. These values were divided by the root chord

length of the delta wing measured from the same images, thus providing non-dimensional lengths (X_b/c). A value of $X_b/c = 1$ indicates the vortex breakdown location is at the trailing edge of the delta wing. Measurement uncertainty of the distances obtained is estimated to be of the order of $0.01c$.

3.5.2 Surface Oil Flow

Two-tone surface oil flow visualization was accomplished with a viscous coating composed of paraffin oil, zinc titanium and oleic acid. The majority of the leeward surface of the delta wing was covered with a thin layer of the green mixture. The leading-edge region was subsequently covered with a layer of the same mixture which included a red pigment. Skin friction caused the viscous coatings to build up in certain areas and to diffuse in others. These results revealed the interaction of the surface effects on the leeward surface of the model and along the leading edges. The evolution of the surface oil flow tests was recorded on video. Photographs were taken at the end of each test run for each α and U_∞ .

3.5.3 Surface Pressure

Steady surface pressure data was obtained using a scanivalve data acquisition system consisting of thirteen analog data channels and the surface pressure model describe in Fig. 3. Six of the channels returned surface pressure data while the other seven recorded position, α and freestream conditions. Five hundred measurements were acquired, at 7 kHz, for each channel before the scanivalve system was advanced, stabilized, and recycled to capture data from the next six pressure taps. The average surface pressure values were computed from these data and are plotted with respect to the spanwise location on the wing divided by the wingspan at the respective distance from the wing apex (Y/b). No blockage, wall, or wake corrections were made to the data.

3.5.4 Laser Doppler Velocimetry (LDV)

LDV is a non-intrusive technique for measuring the average local velocity in a flow field as well as the associated Reynolds tensor. The system at Onera, installed around the test section in F2, utilizes two 15 Watt argon lasers as the sources of light in a forward scattering mode. The first laser, functioning at 8 W, provides two beams, green and blue, with respective wavelengths of $0.488 \mu\text{m}$ and $0.514 \mu\text{m}$. The separation of the two wavelengths is assured by the use of a semitransparent filter. The second laser functioning at 2.5 W provides the third, purple, beam with a wavelength of $0.4765 \mu\text{m}$. These three beams are divided into pairs by a network of beam-splitters and mirrors. The three pairs of beams are then focused in a volume of approximately 0.35 mm^3 and form three fringe patterns. To facilitate detection of each of the three velocity components, the pairs of beams pass through Bragg cells (acoustic-optic modulators) which induce specific frequencies on the respective fringes. The pairs of beams are also oriented at different angles with respect to the wind tunnel test section.

The reception end of the LDV system involves two telescopes that are mounted on the same mechanical structure as the emitting end. This ensures uniformity as the measurement volume is systematically moved throughout the flow field of interest. The first receiving telescope uses filters that separate the pairs of green and blue beams while the second telescope filters the pair of purple beams. The signals from the telescopes pass through a photomultiplier and the resulting data is then analyzed by an automated data acquisition system, which ensures that the three measured velocity components are computed relative to the same particle. More details of the physical set-up of the LDV system around the wind tunnel F2 can be found in reference 12.

Smoke particles from incense are emitted into the wind tunnel downstream of the test section so as to avoid disturbing the flow field in the test section. The particles permeate the test section and limited numbers pass through the volume being analyzed around the delta wing. For each volume of exploration, the three instantaneous velocity components related to a specific particle are acquired and then averaged

for 2000 particles. Using statistics[12], the mean velocity component in each of the three directions as well as the Reynolds tensors are then calculated.

3.6 EXPERIMENTAL ERROR AND ACCURACY

In Onera's F2 wind tunnel, the relative freestream velocity, $\Delta U_\infty/U_\infty$, is estimated to have an accuracy of $\pm 1\%$, while the mean intensity of turbulence is approximately 0.1%. The model was mounted on a sting with a horizontal support and flexible joint for adjusting the angle of attack, with an accuracy of $\pm 0.05^\circ$. The horizontal support was manipulated in height along a vertical column so as to maintain the model close to the center axis of the test section. The model was mounted in the test section with no yaw angle with respect to the freestream flow (estimated accuracy of $\pm 0.1^\circ$).

The LDV system installed in F2 utilizes two 15W argon lasers as the sources of light in a forward scattering mode. The global accuracy of the LDV system is estimated to have a relative error, $\Delta U/U$, of less than 1.5% assuming an absolute error of the angle between the velocity vector and a horizontal reference of 0.5° . Therefore the estimated accuracy of the magnitude of the velocity is $\pm 1\text{m/s}$ and the direction of the velocity vector is $\pm 1^\circ$. [13]

3.7 RESULTS

The laser sheet and surface oil flow visualization results examined during these tests were acquired at angles of attack ranging from 20° to 40° at freestream velocities from 10 m/s to 75 m/s. The steady surface pressure measurements were obtained at varying incidence angles from $20^\circ < \alpha < 35^\circ$ for a range of freestream velocities from 10 m/s to 75 m/s ($Re_c = 6.5 \times 10^5$ to 4.9×10^6). Laser Doppler Velocimetry measurements were taken at freestream conditions of $\alpha = 26^\circ, 27^\circ$ and 30° and $U_\infty = 24\text{ m/s}$ and 40 m/s ($Re_c = 1.56 \times 10^6$ and 2.6×10^6 respectfully). All of the tests were accomplished at atmospheric pressure and temperature.

A complete set of all of these results is presented in reference 12. The results presented in this paper and the respective interpretation will focus on the test conditions at $\alpha = 27^\circ$ and $U_\infty = 24\text{ m/s}$. However, when additional data from other tests conditions reveals important characteristics of the phenomena, these data will be presented.

3.7.1 Laser Sheet Visualization

The ensemble of the laser sheet visualization results characterizes the physical location of the leading-edge vortices, upstream of the vortex breakdown location, in the flow field above the leeward surface of the delta wing. At $\alpha = 27^\circ$, both of the leading-edge vortex cores are situated in a plane which intersects the wing apex at an angle of 7° . Guy *et al.*[14] stated that the angle between the leeward surface and the vortex core is a function of the angle of attack – a value of approximately 0.26α . The current results demonstrated that at $\alpha = 27^\circ$ the angle is 7° (Fig. 6) and at $\alpha = 30^\circ$ the angle is 7.8° , which confirms this statement. The vertical distance of each vortex core above the leeward surface of the wing was measured using a laser sheet perpendicular to the leeward surface of the delta wing at various chordwise distances (Fig. 7). These measurements confirm the angle of the laser sheet plane discussed above. Additionally, each vortex core follows a path which begins at the wing apex and continues along a sweep angle of 77° until it reaches the trailing edge where it turns in the direction of the freestream velocity.

The vortex breakdown locations, at various angles of attack, determined from photographs of the laser sheet oriented perpendicular to the leeward surface of the delta wing and along the portside vortex core are presented in Fig. 9. Blue circles represent these data points. The vortex breakdown locations determined from photographs of the laser sheet intersecting the two vortex cores above the leeward surface are also

shown in Fig. 9. These portside and starboard vortex breakdown locations are represented by green triangles and red squares, respectively. The average values of the port and starboard breakdown locations at each angle of attack were computed and are represented by points subsequently fit with a second order polynomial curve from a least-squares algorithm. Thus, the blue, green and red symbols represent various instantaneous vortex breakdown locations from several photographs of the phenomena. The dispersion of these data points around the mean values is representative of the various amplitudes of the fluctuations of the vortex breakdown location.

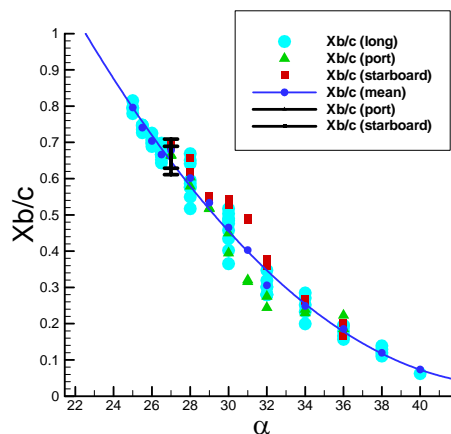


Fig. 9: Evolution of X_b/c as a function of α ($U_\infty = 24$ m/s).

The video data obtained at $\alpha = 27^\circ$ provides a time history of the vortex breakdown locations from laser sheet tests. Frame by frame analysis of approximately 1500 data points was accomplished and these data have been averaged to determine each of the mean vortex breakdown locations. These mean port and starboard vortex breakdown locations are located at the center of each of the error bars depicted in Fig. 9. The maximum and minimum values of the error bars represent the corresponding extremes of the measured values of X_b/c in each of the data sets.

The general characteristics in Fig. 9 confirm that the vortex breakdown location moves upstream over the delta wing, from the trailing edge toward the apex, as α is increased. The breakdown location is shown to transition from downstream of the trailing edge of the delta wing to a mean location of 80% of the chord for an angle of attack of 25° . Between $\alpha = 25^\circ$ and 36° , the forward movement of the breakdown location is relatively linear. For angles of attack greater than 36° , the vortex breakdown is close to the wing apex and its forward progression appears to be slowed.

The unsteady flow characteristics as well as the asymmetry in the port and starboard vortex breakdown locations (seen in Fig. 8) are lost by presenting the mean vortex breakdown location data in this format. Therefore, Figure 10 is a representation of the evolution of the vortex breakdown location as a function of time for two separate angles of attack ($\alpha = 27^\circ$ and $\alpha = 30^\circ$). It is evident in the results of Fig. 10 that the port and starboard vortex breakdown locations oscillate around an average location. The oscillations appear to have two components: a low frequency but large amplitude oscillation and a higher frequency oscillation with lower amplitude.

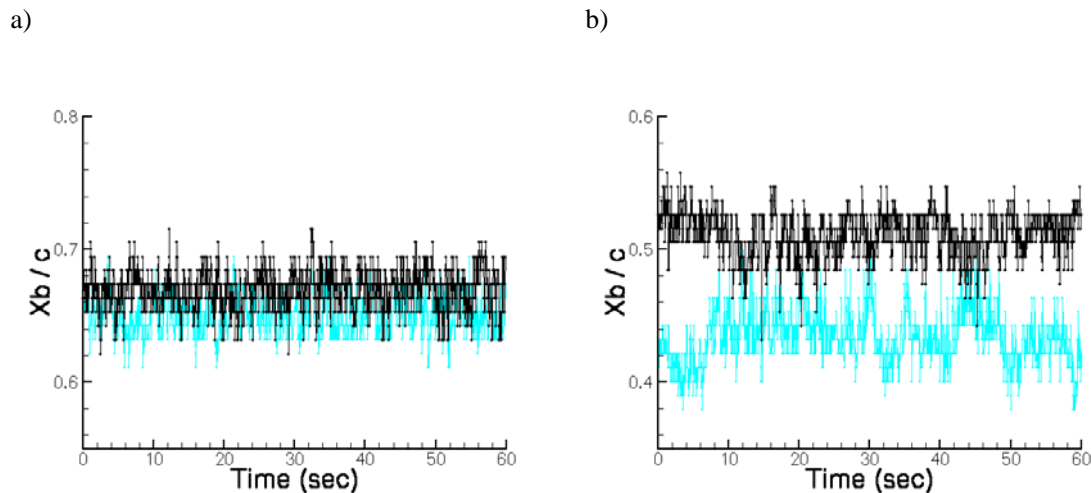


Fig. 10: Time history of the port and starboard vortex breakdown locations at $U_\infty = 24$ m/s (a) $\alpha = 27^\circ$ (b) $\alpha = 30^\circ$. Black symbols and lines represent the port breakdown locations. Blue symbols and lines represent the starboard breakdown locations.

The instantaneous vortex breakdown location data was used to calculate the Root Mean Square (RMS) of the data. The RMS values are an indicator of the level of the fluctuations of the vortex breakdown location around each mean position. Additionally, by performing spectral analysis on this data, the frequency of the oscillations can be determined. The principle frequencies of the oscillations are found to occur between 1.07 Hz and 1.22 Hz. These frequencies correspond to Strouhal numbers from 0.0424 to 0.0483.[12] A number of authors have addressed the oscillating nature of the vortex breakdown location and this author would refer you to these references for additional information.[15-19]

3.7.2 Surface Oil Flow

The traces of the skin friction lines in the viscous coating on the leeward surface of the delta wing represent a number of different phenomena. By interpreting the topology of the oil streaks with the use of the critical point theory and some details of the flow field above the surface, a correlation between the vortical flow field and the surface skin friction pattern can be established.[10,20] Figure 11 is a photograph of the surface oil flow results at freestream conditions of $\alpha = 27^\circ$ and $U_\infty = 24$ m/s. The reference grid on the model's leeward surface indicates the chordwise locations downstream of the delta wing apex. The first line is situated at $X = 200$ mm. Each consecutive line is 100 mm further downstream, with the final chordwise reference line at $X = 900$ mm.

Due to the sharp leading edges of the model, the primary separation lines of the vortices are fixed at the leading-edges of the delta wing and are thus difficult to distinguish in the oil flow streaks. However, the primary attachment lines clearly co-exist along the root chord of the model. The symmetry of the skin friction lines on both sides of the root chord indicates the existence of two leading-edge vortices whose traces converge on the secondary separation lines that follow the border of the green and red colors along each leading edge.

The skin friction lines, near each secondary separation line, indicate the existence of a laminar-turbulent transition zone between $X = 360$ mm and $X = 380$ mm. This transition is evident from the rapid changes in the directions of the secondary separation lines. Each secondary separation line, initially well inboard of the leading edges, dramatically turns outward to approach its corresponding leading edge. This transition is a result of the turbulent boundary layer being more resistant to separation than the laminar boundary

layer and thus leading to an enlargement of the distance between the primary attachment lines (along the root chord) and the secondary separation lines.

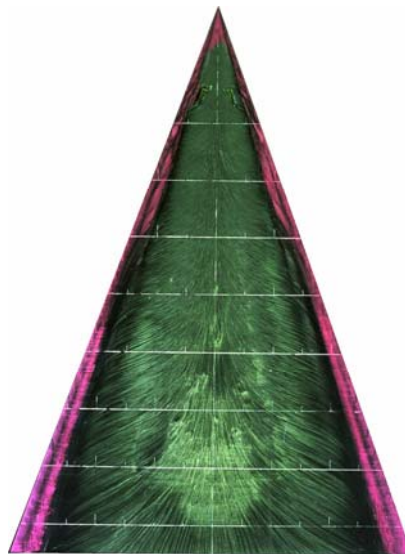


Fig. 11: Surface oil flow visualization at $\alpha = 27^\circ$ and $U_\infty = 24$ m/s.

The time-averaged vortex breakdown locations at the test conditions of $\alpha = 27^\circ$ and $U_\infty = 24$ m/s are shown to be approximately $X_b/c = 0.65$ (Fig. 9). There are no major changes in the skin friction lines in this region of the wing indicating vortex breakdown. Similar analysis has been accomplished at other test conditions resulting in the same results. Therefore, the vortex breakdown location for 70° swept delta wings at these Reynolds numbers cannot be determined solely from skin friction lines on the leeward surface of the wing. These results confirm observations by Dallmann, *et al.*[21] that surface flow topology, defined by wall shear stress, is unaltered over a wide range of α even though separated vortices and breakdown exist above the surface.

3.7.3 Surface Pressure

A detailed analysis of the influence of freestream velocity and angle of attack on the pressure coefficient (C_p) has been accomplished with data from steady surface pressure measurements on the leeward surface of the delta wing. During these tests, the freestream velocity was varied from 15m/s to 75m/s and the angle of attack was varied from 20° to 35° . The surface pressure distributions for each test configuration are typical for vortical flows over a highly swept delta wing with the existence of a suction peak, situated at approximately 66% of the non-dimensional wingspan location (Y/b), which corresponds to the location of the leading-edge vortices over the wing. Secondary peaks, which disrupt the relatively constant plateau in the C_p values between the suction peak and the leading edges, are indicative of the existence of secondary vortices. The minimum value of the pressure coefficient (C_{pmin}) is situated near the apex of the delta wing. Figure 12 is one example of the C_p data obtained at $\alpha = 27^\circ$ and $U_\infty = 24$ m/s.

Additional surface pressure plots at various freestream velocities and angles of attack are available in reference 12. These additional plots show a detailed examination of the symmetry of the flow over the delta wing at various chordwise locations for a number of angles of attack. The plots will not be presented here, but the global results will be discussed briefly. The surface pressure data did capture the asymmetry in the port and starboard vortex breakdown locations observed in the laser light sheet images, although not nearly as dramatically. The second part of the study examined the effect of angle of attack on the steady

surface pressures. These results revealed that the suction peaks are greater at higher angles of attack. One also observes a gradual movement of the suction peak towards the apex of the wing as the angle of attack is increased. This happens in conjunction with a dissipation of the suction peak downstream in the region of the vortex breakdown and in the post-breakdown region. The third aspect of the study analyzed the influence of Reynolds Number on the pressure distribution. Increasing the Reynolds Number had a minimal effect on the suction peak of the leading-edge vortex; however, the changing Reynolds Number of the flow significantly alters the secondary vortices. These differences in the secondary vortices indicate the importance of transition from laminar to turbulent flow on the secondary separation. This confirms the results observed in the surface oil flow images indicating a “kink” in the secondary separation line where the flow over the delta wing transitions from laminar to turbulent state.

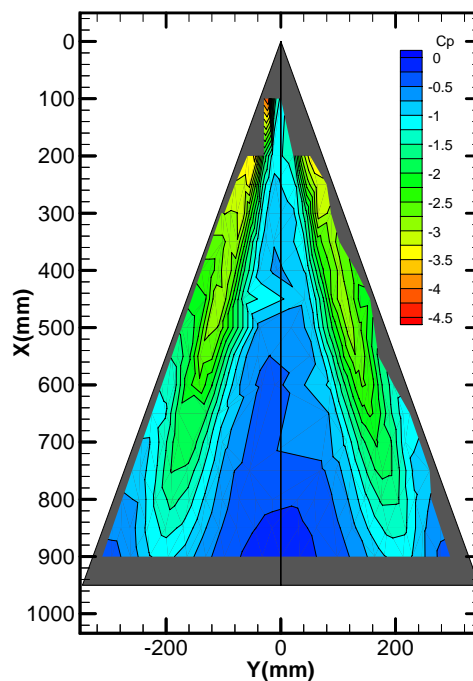


Fig. 12: Constant C_p lines on the leeward surface of the delta wing at $\alpha = 27^\circ$, $U_\infty = 24$ m/s.

The steady surface pressure results demonstrate the difficulty of identifying the vortex breakdown location from individual configurations. At the test conditions shown in Figure 12, the mean breakdown location was at approximately 65% of the chord (see Fig. 9). The steady pressure results show the influence of the leading-edge vortices on the leeward surface of the delta wing as well as the significant adverse effects attributed to the vortex breakdown phenomena. The steady pressure results, however, do not indicate any remarkable changes in the vicinity of the mean vortex breakdown location.

3.7.4 Laser Doppler Velocimetry

Due to the symmetry of the flow field over the leeward surface of the delta wing, only the portside flow field was examined. Four planes perpendicular to the leeward surface of the wing and one longitudinal plane following the axis of the vortex core were explored. The four perpendicular planes are located at $X = 500, 600, 700$ and 800 mm: corresponding to a region where the leading-edge vortex is well developed, a zone just upstream of vortex breakdown location, a zone downstream of the vortex breakdown location, and finally a region further downstream where the flow is disorganized. Each

perpendicular measurement mesh consisted of approximately 1400 points located between $0.4 < Y/b < 1.1$, evenly spaced at 5 mm intervals.

Figure 13 presents the non-dimensional axial velocity component (U/U_∞) measured in each of the four perpendicular planes. A strong, jet-like, acceleration of the flow along the vortex core is observed upstream of vortex breakdown phenomena ($X = 500$ and 600 mm) with values of $U/U_\infty \geq 3.5$ in the vortex core. The projected streamlines (not shown) in these two planes, indicate the existence of at least one limit cycle which separates the vortical flow field into at least two cells, confirming previous experimental work [22] and the theoretical solution of Sullivan [23]. At these locations upstream of the vortex breakdown, the gradients of the vertical and horizontal components of the tangential velocity (V and W) are very intense, indicating a strong rotation of the vortical structure.

In the perpendicular planes at $X = 700$ mm and $X = 800$ mm, vortex breakdown has occurred. The non-dimensional velocity ratio in the vortex core is negative, indicating recirculating flow and the diameter of the vortex core is remarkably expanded. The axial velocity component of the core has evolved from a jet-like profile upstream of vortex breakdown to wake-like behavior downstream.

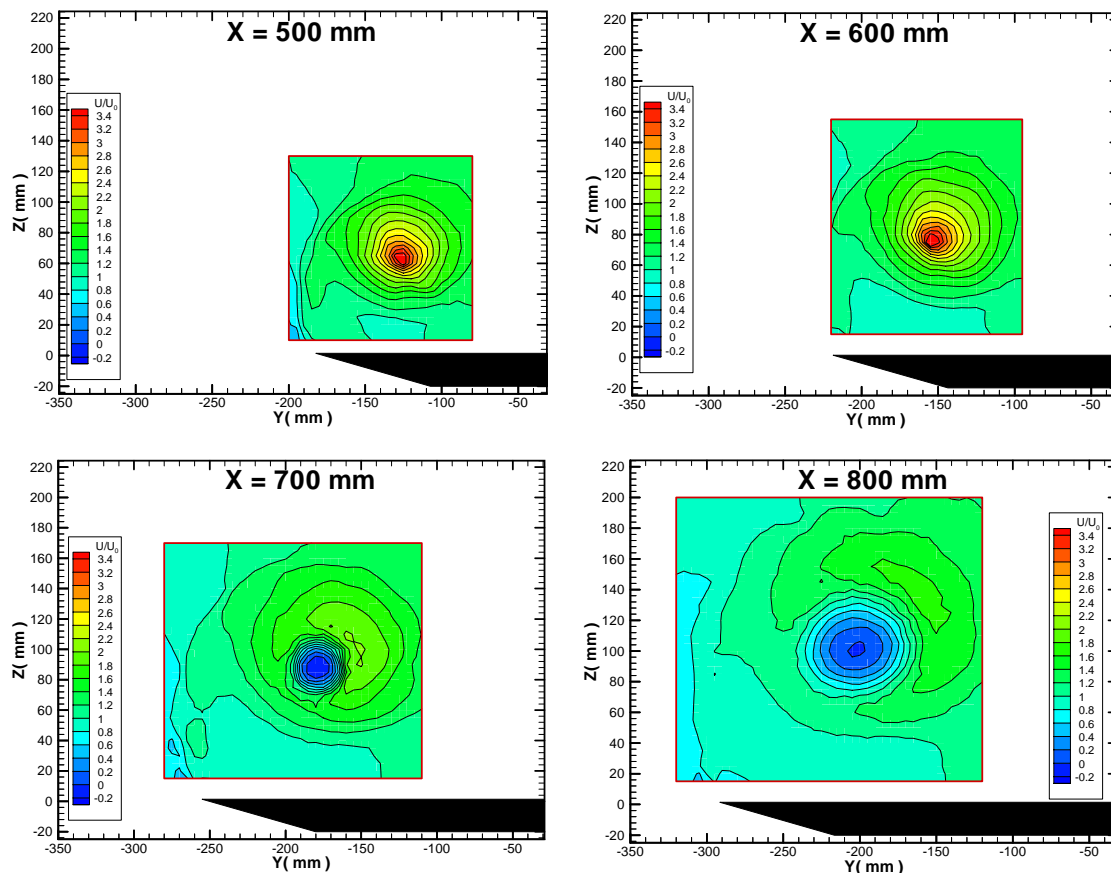


Fig. 13: 3-D LDV results showing the non-dimensional axial velocity component (U/U_∞) and the corresponding streamlines at $\alpha = 27^\circ$ and $U_\infty = 24$ m/s (a) $X = 500$ mm (b) $X = 600$ mm (c) $X = 700$ mm (d) $X = 800$ mm.

Fig. 14 represents the axial vorticity ($\Omega_x = \frac{\partial W}{\partial y} - \frac{\partial V}{\partial z}$) in each perpendicular plane that is calculated from

the measured mean velocity components in the flow field and central differential scheme to evaluate the derivatives. These traces reveal the highly rotational zones in the flow field. In each part of Fig. 14, there are two significant regions. One region consists of the vortex core with a highly negative vorticity while the second region clearly includes pockets of vorticity in the shear layer as it separates from the leading edge. These isolated mean-flow sub-structures of vorticity are clearly identified. Similar vortical structures have been observed in laser sheet visualization studies at lower Reynolds numbers. The substructures of vorticity observed in the mean flowfield are addressed thoroughly in references 24, 25 and 26.

It is clear from the dissipation of the vorticity in the vortex core, in Figs. 14c and 14d, that vortex breakdown has occurred. However, the vortical sub-structures are still present in the flow field. Additionally, in all four of the traces, there are regions of positive vorticity near the leading edge, along the leeward surface of the wing, which are indicative of the existence of the secondary vortex.

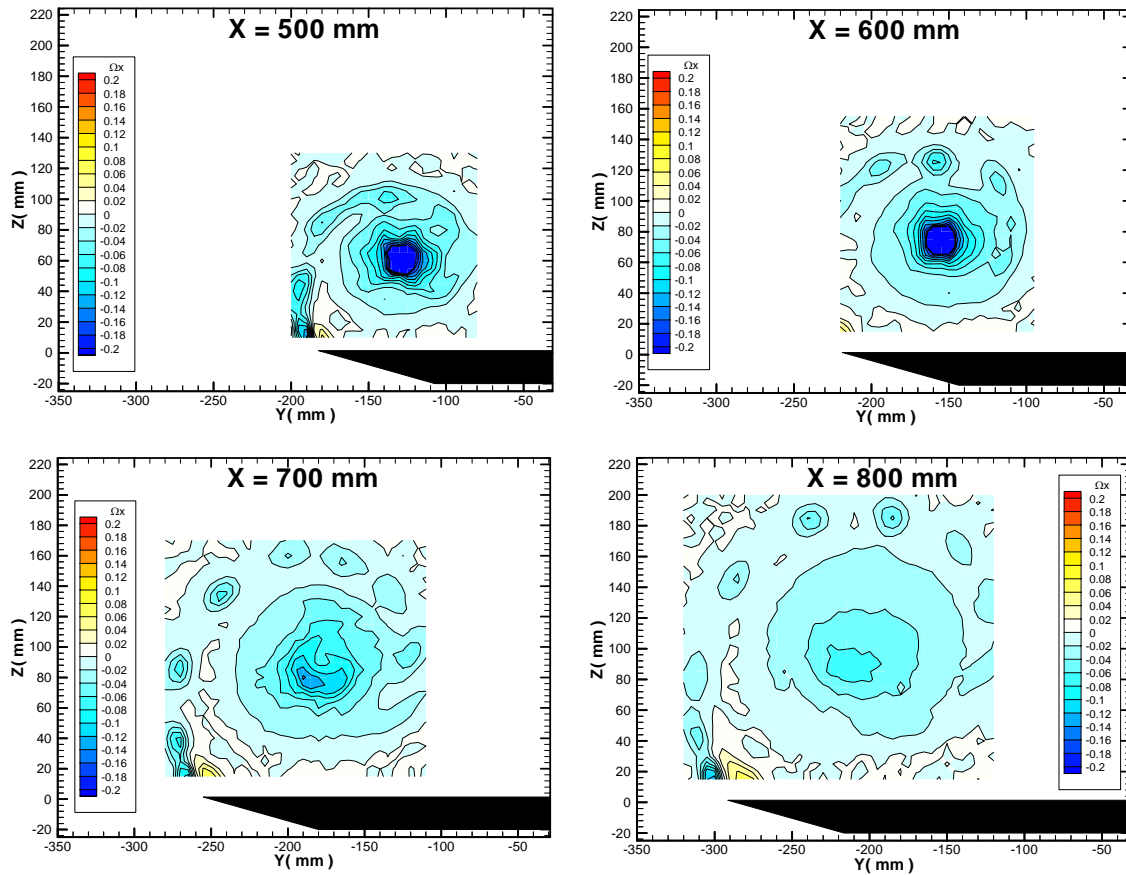


Fig. 14: 3-D LDV results showing the axial vorticity (Ω_x) at $\alpha = 27^\circ$ and $U_\infty = 24$ m/s (a) $X = 500$ mm (b) $X = 600$ mm (c) $X = 700$ mm (d) $X = 800$ mm.

In Fig. 15, the turbulent kinetic energy, $k = \frac{1}{2}(\overline{u'^2} + \overline{v'^2} + \overline{w'^2})$, is obtained from the mean velocity components and the Reynolds tensor data. For the two plots upstream of the vortex breakdown phenomena, values of k are relatively low and reveal the general trends within the leading-edge vortex. In Fig. 15c ($X=700$ mm), there is a high level of turbulent kinetic energy due to the longitudinal oscillations

of the vortex breakdown location, which by their very nature increase the fluctuations in the flow field. In Fig. 15d, the oscillating breakdown location no longer influences the measurements, but there is an increased level of turbulent kinetic energy in the highly disorganized flow field.

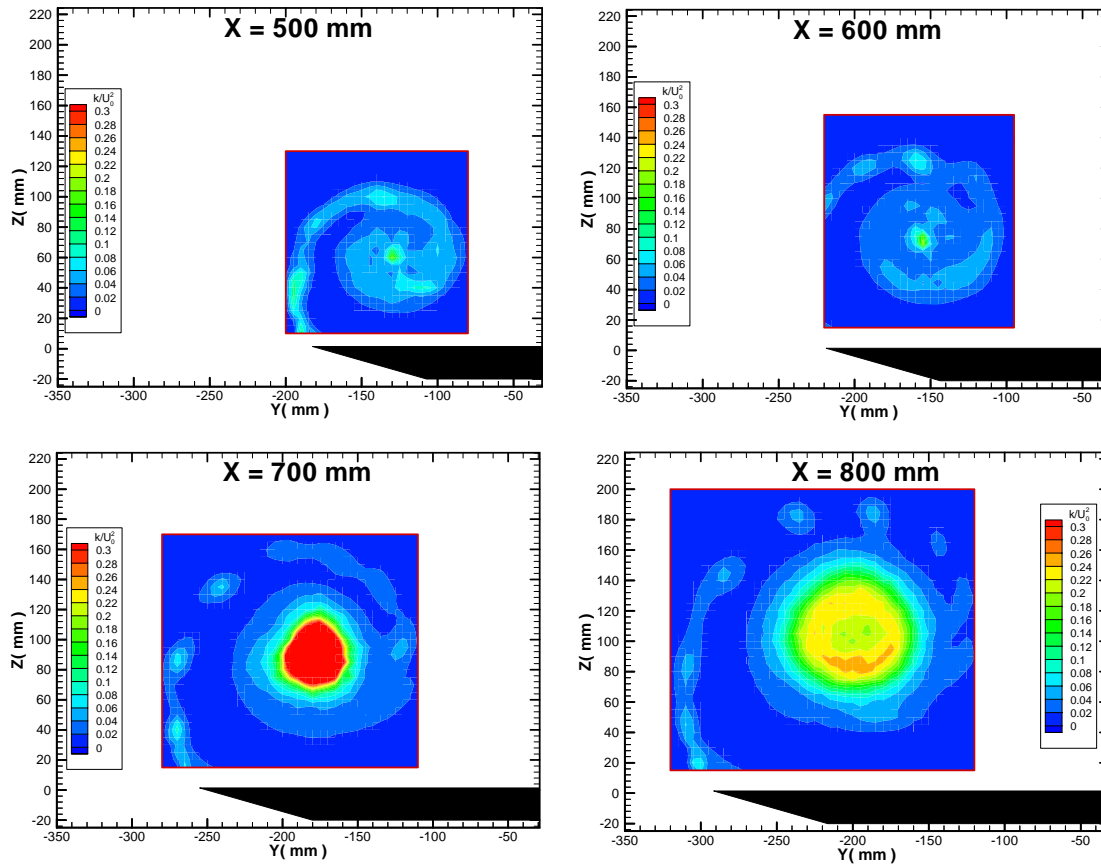


Fig. 15: 3-D LDV results showing the turbulent kinetic energy (k) at $\alpha = 27^\circ$ and $U_\infty = 24$ m/s. (a) $X = 500$ mm (b) $X = 600$ mm (c) $X = 700$ mm (d) $X = 800$ mm.

The longitudinal LDV plane, along the leading-edge vortex core, was explored from $X = 500$ mm to $X = 800$ mm, with chordwise zones every 20 mm with meshes of 525 points. The location of the vortex core was identified previously by the position of the maximum value of the axial velocity component (U) and at the same time, the reduction of the tangential velocity components (V , W) toward zero. Figs. 15 and 16 show the characteristics of U/U_∞ and k in the longitudinal plane that intersects the portside vortex core. These results confirm the previous data and describe the global development of the leading-edge vortex and the vortex breakdown phenomena.

In Fig. 16, the non-dimensional axial velocity increases along the vortex core until a rapid deceleration occurs and is followed by a zone of recirculation and remarkable increase in the diameter of the vortex core. These data provide a concise description of the development of the axial velocity component with respect to the vortex breakdown phenomena previously discussed in Fig. 13.

The turbulent kinetic energy, shown in Fig. 17, shows the large increase in the magnitude of k at the vortex breakdown location and just downstream of the stagnation point. The location and dimensions of this region of turbulent kinetic energy closely correspond to the X_b/c values measured during the laser

sheet study and the distance observed between the extremum of these data for the given test condition (Fig. 9).

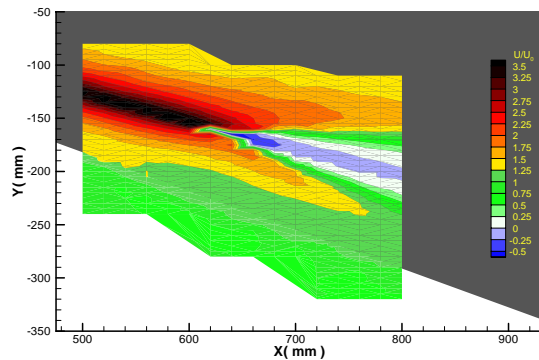


Fig. 16: 3-D LDV results showing U/U_∞ in the plane which longitudinally intersects the vortex core at $\alpha = 27^\circ$ and $U_\infty = 24$ m/s.

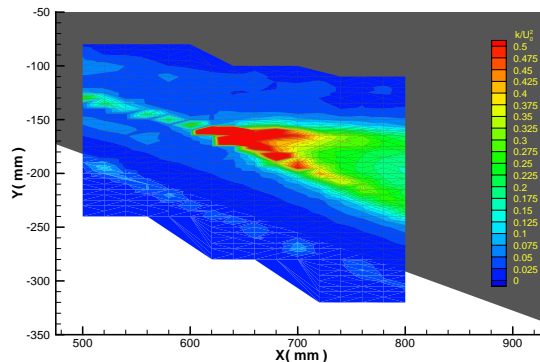


Fig. 17: 3-D LDV results showing the turbulent kinetic energy (k) in the plane which longitudinally intersects the vortex core at $\alpha = 27^\circ$ and $U_\infty = 24$ m/s.

3.8 CONCLUSIONS

A detailed description of the vortex breakdown was accomplished with surface and flow field visualization and measurement techniques around the Onera 70° delta wing. The compilation of this data enabled the identification of the vortex breakdown location and provided characteristic details of the flow field and the vortex breakdown phenomena. Surface oil flow visualization provided a link between the surface and flow field measurements in demonstrating the influence of the secondary vortices and the transition between laminar and turbulent flow over the leeward surface of the wing. However, there was no indication of the vortex breakdown location in the surface oil flow results. Steady surface pressure measurements captured the pressure sink generated by the leading-edge vortices but cannot be used to accurately identify the vortex breakdown location. The Laser Doppler Velocimetry data confirm previous studies of the trends in the leading-edge vortices including the shift from a jet-like axial velocity profile upstream of the breakdown location to a wave-like profile. These data, at higher Reynolds numbers than previous experiments, also demonstrate the existence of vortical sub-structures within the separating shear layer that roll up to form the leading-edge vortices.

This data set was judged by the NATO Research and Technology Organization (RTO) Applied Vehicle Technology (AVT) Task Group-080 members to be one of the most comprehensive experimental studies on the flow field around a delta wing. Unfortunately, the data set does not include force measurements nor does it include quantitative unsteady flow field measurements (such as Particle Image Velocimetry or unsteady pressure measurements). Despite these shortcomings, these experimental results around the Onera 70° delta wing will be used to validate and verify computational techniques within the RTO AVT Task Group-080. The combined insight from the experimental and computational results will enable the development of new models of the vortex breakdown phenomena for future studies.

3.9 REFERENCES

- [1] Werlé, H., "Quelques résultats expérimentaux sur les ailes en flèche, aux faibles vitesses, obtenus en tunnel hydrodynamique", *La Recherche Aéronautique*, No 41, 1954.

- [2] Peckham, D.H., Atkinson, S.A., "Preliminary Results of Low Speed Wind Tunnel Tests on a Gothic Wing of Aspect Ratio 1.0", A.R.C. Technical Report, C.P. No 508, T.N. Aero 2504, 1960.
- [3] Lambourne, N.C., Bryer, D.W., "The Bursting of Leading-Edge Vortices-Some Observations and Discussion of the Phenomenon", ARC, R&M No. 3282 (22775), 1962.
- [4] Werlé, H., "Sur l'éclatement des tourbillons", Onera Note Technique No. 175, 1971.
- [5] Hall, M.G., "Vortex Breakdown," *Annual Review of Fluid Mechanics*, Vol. 4, 1972.
- [6] Leibovich, S., "The Structure of Vortex Breakdown," *Annual Review of Fluid Mechanics*, Vol. 10, 1978, pp. 221-46.
- [7] Leibovich, S., "Vortex Stability and Breakdown: Survey and Extension", *AIAA Journal*, Vol. 22, No. 9, pp. 1192-1206, 1984.
- [8] Escudier, M., "Vortex Breakdown: Observations and Explanations", *Progress in Aerospace Sciences*, Vol. 25, pp. 189-229, 1988.
- [9] Nelson, R.C., "Unsteady Aerodynamics of Slender Wings," Aircraft Dynamics at High Angles of Attack: Experiments and Modeling, AGARD-R-776, pp.1-1 to 1-26, 1991.
- [10] Délery, J., "Aspects of Vortex Breakdown," *Progress in Aerospace Sciences*, Vol. 30, p. 1-59, 1994.
- [11] Afchain, D., Broussaud, P., Frugier, M., Rancarani, G., "La soufflerie F2 du centre du Fauga-Mauzac" Onera TP 1983-139, No. 193880.
- [12] Mitchell, A.M., "Caractérisation et contrôle de l'éclatement tourbillonnaire sur une aile delta aux hautes incidences," Ph.D. Thèse, Université de Paris 6, Département de Mécanique, Juillet 2000.
- [13] Barberis, D., "Test Cases for CFD Validation," ONERA TP No. 1993-161, 1993.
- [14] Guy, Y., Morrow, J.A., McLaughlin, T.E., Wygnanski, I., "Velocity Measurements on a Delta Wing with Periodic Blowing and Suction," AIAA-2000-0550, 38th AIAA Aerospace Sciences Meeting and Exhibit, Reno, NV, Jan. 2000.
- [15] Seginer, A., Salomon, M., "Augmentation of Fighter Aircraft Performance by Spanwise Blowing Over the Wing Leading Edge," NASA-TM-84330, March 1983.
- [16] Mitchell, A.M., Barberis, D., Délery, J., "Oscillation of Vortex Breakdown Location and Its Control by Tangential Blowing," AIAA-98-2914, AIAA 29th Fluid Dynamics Conference, Jun. 1998, Albuquerque, NM.
- [17] Gursul, I., Yang, H., "On Fluctuations of Vortex Breakdown Location," *Physics of Fluids*, Vol. 7, No. 1, 1995, pp. 229-231.
- [18] Menke, M., Yang, H., Gursul, I., "Further Experiments on Fluctuations of Vortex Breakdown Location," AIAA-96-0205, 34th Aerospace Sciences Meeting and Exhibit, Jan. 1996, Reno, NV.
- [19] Menke, M., Yang, H., Gursul, I., "Self-Excited Oscillations of Vortex Breakdown Location Over Delta Wings," AIAA-96-0744, 35th Aerospace Sciences Meeting and Exhibit, Jan. 1997, Reno NV.
- [20] Chanetz, B., "Contribution à l'étude expérimentale et théorique de l'éclatement tourbillonnaire en air incompressible," Ph.D. Thèse, Université de Lyon, septembre 1986.
- [21] Dallmann, U., Hilgenstock, A., Riedelbauch, S., Schulte-Werning, B., Vollmers, H., "On the Footprints of 3-D Separated Vortex Flows Around Bluff Bodies", Vortex Flow Aerodynamics, AGARD Conference Proceedings 494, pp. 9-1-9-13, 1990.

- [22] Détery, J., Molton, P., "Topology of the Flow Resulting from Vortex Breakdown Over a Delta Wing at Subsonic Speed", Acta Mechanica, Suppl. 4, pp. 297-304, Springer-Verlag 1994.
- [23] Sullivan, R.D., "A Two-Cell Vortex Solution of the Navier-Stokes Equations", Journal of the Aerospace Sciences, November 1959, pp. 767-768.
- [24] Mitchell, A.M., Molton, P., Barberis, D. and Détery, J., "Vortical Substructures in the Shear Layers Forming Leading-Edge Vortices", AIAA Paper 2001-2424, June 2001.
- [25] Mitchell, A.M., Morton, S., Forsythe, J., "Analysis of Delta Wing Vortical Substructures Using Detached-Eddy Simulation", AIAA Paper 2002-2968, June 2002.
- [26] Mitchell, A.M. and Molton, P., "Vortical Substructures in the Shear Layers Forming Leading-Edge Vortices", AIAA Journal, Vol. 40, No. 8, August 2002, pp. 1689-1692.



Chapter 4 – EXPERIMENTAL INVESTIGATION OF THE FLOW ABOUT A 65° DELTA WING IN THE NASA LANGLEY NATIONAL TRANSONIC FACILITY

James M. Luckring
NASA Langley Research Center
Hampton, Virginia 23681
USA

james.m.luckring@nasa.gov

ABSTRACT

An experimental investigation for the flow about a 65° delta wing has been conducted in the NASA Langley National Transonic Facility (NTF). The tests were conducted at Reynolds numbers, based on the mean aerodynamic chord, ranging from 6 million to 120 million and at Mach numbers ranging from 0.4 to 0.9. The model incorporated four different leading-edge bluntness values. The data include detailed static surface-pressure distributions as well as normal-force and pitching-moment coefficients. The test program was designed to quantify the effects of Mach number, Reynolds number, and leading-edge bluntness on the onset and progression of leading-edge vortex separation.

4.1 NOMENCLATURE

AR	wing aspect ratio, 1.8652
b_{le}	leading-edge bluntness, r_{le}/c_{bar}
$b/2$	wing semispan, 1.0 ft.
C_m	pitching moment coefficient about $0.25c_{bar}$
C_N	normal force coefficient
C_p	pressure coefficient
c	wing chord
c_{bar}	wing mean aerodynamic chord, 1.4297 ft.
c_r	wing root chord, 2.1445 ft.
c_t	wing tip chord, 0 ft.
d	sting diameter, 0.275 ft.
d/b	nondimensional sting diameter, 0.1375

E	Young's modulus of elasticity
M	Mach number
q	free-stream dynamic pressure
Rn	Reynolds number, based on c_{bar}
r_{le}	streamwise leading-edge radius
S	wing reference-area, 2.1445 ft ²
t	wing thickness, 0.875 in.
t/c_{bar}	nondimensional wing thickness, 0.051
w_{ts}	NTF test section width, 8.2 ft.
x,y,z	Body-axis Cartesian coordinates
x_v	Longitudinal distance to vortex origin
α	angle of attack
η	percent semispan location, $2y/b$
Λ_{le}	wing leading-edge sweep, 65°.
λ	wing taper ratio, c_t/c_r , 0.

4.2 INTRODUCTION

Separation-induced vortex flows have been a topic of sustained aerodynamic research and application for many decades. Slender and highly swept wings are conducive to the formation of these vortex flows, and as such much of the vortex flow research has been directed at highly maneuverable military aircraft applications. The manifestation of the vortex flow effects on full aircraft configurations is, however, quite complex.

The delta wing has proven to be very useful for the study and understanding of the basic features of separation-induced vortex flows since many aspects of these vortex flows relevant to aircraft applications can be generated with this simple shape. Much of this work was initially performed on delta wings with sharp leading edges in order to fix the location of primary vortex separation and thus be able to study the basic structure of the leading-edge vortex itself as well as its interaction with the wing. Two notable examples of this work are presented in Figure 1. In Figure 1a, taken from Hummel¹, the basic structure of the primary and secondary vortices is illustrated along with their relation to static surface pressure distributions. In Figure 1b, taken from Polhamus², the ability to predict vortex lift is demonstrated from his leading-edge suction analogy. The fundamental experimental and theoretical research, such as Hummel's and Polhamus', has contributed greatly to the practical realization of this flow on complex aircraft configurations. AGARD, and now the RTO, have played a key role in this practical realization through sponsoring periodic symposia⁵⁻⁸ to assess the

state of the art of vortex flows as they pertain to military aircraft.

The characteristics of these vortex flows are greatly complicated by a blunt leading edge, as illustrated in Figure 2 (taken from Luckring⁹). With a blunt leading edge the origin of the leading-edge vortex is no longer affixed at the apex of the wing. In addition, primary separation itself is no longer affixed circumferentially at the leading edge, and the onset of leading-edge vortex separation will now be a function of flow conditions and wing geometry. For example, at low to moderate angles of attack the wing could develop fully attached flow. Due to the upwash distribution at the delta wing leading edge the leading edge separation will first occur near the wing tip and then progress up the leading edge with further increase in angle of attack. For an angle-of-attack range the wing will exhibit partial span leading-edge vortex separation with attached flow on the upstream portion of the wing and leading edge vortex separation on the downstream portion. Because the leading-edge separation is now occurring from a smooth surface, the physics of this flow could be quite different from the sharp-edged case. Strength, position, and the very existence of the vortex will be affected by leading-edge radius and will change with Mach number, Reynolds number, and angle of attack. This added complexity could have considerable impact on the performance and maneuver aerodynamics of slender wings.

The experimental program discussed in this paper was designed to create a fundamental database addressing blunt leading edge effects for separation-induced leading-edge vortex flows. A brief description of this program is presented, followed by selected examples from the experimental database. All materials in this report have been previously published, and much of the information in this document is drawn from the author's recent publications⁹⁻¹².

4.3 EXPERIMENTAL PROGRAM

This experimental program was designed to quantify the effects of Reynolds number and Mach number on separation-induced leading-edge vortex flows for a 65-degree swept delta wing with blunt leading edges. A brief description of the facility, the model, and the experimental test program is provided in the following sections. Additional details can be found in the Appendix.

4.3.1 Facility

The National Transonic Facility (NTF) was developed as a unique wind tunnel to obtain high Reynolds number flows as well as Reynolds number effects at transonic conditions for a broad class of configurations. Pilot work was performed during the 1970's, facility construction began in 1979, and preliminary operations began in 1982.

An aerial view of the NTF is shown in Figure 3, and the basic circuit is shown in Figure 4. The NTF is a closed-circuit, fan-driven, continuous-flow pressure tunnel that can test in either dry air or nitrogen. The facility can be operated at Mach numbers from 0.1 to 1.2, at total pressures from 1.1 to 8.8 atmospheres, and at total temperatures from approximately 120 degrees Fahrenheit down to -250 degrees Fahrenheit. The cryogenic test conditions are achieved through the evaporation of injected liquid nitrogen. Through combination of pressure and cryogenic temperature the NTF can achieve a maximum unit Reynolds number of 146 million per foot at Mach 1. The test section is 8.2 feet by 8.2 feet and approximately 25 feet long. The floor and ceiling of the test section are slotted (approximately six percent open) and the sidewalls are solid. Additional facility characteristics can be found in References 13-15.

Because facility operations have three degrees of freedom (speed, pressure, and temperature), experimental campaigns can be constructed to isolate the effects of an aerodynamic parameter while holding two other such parameters constant. Thus, for example, Reynolds number can be varied while holding both the Mach number and the ratio of dynamic pressure to Young's modulus (q/E) constant. Such testing allows Reynolds number effects to be isolated for those due to compressibility or aeroelasticity. Other variations (such as isolating compressibility effects) can be achieved within tunnel envelope and model load constraints. Because Reynolds number effects can be highly coupled with those due to aeroelasticity and compressibility, this capability to experimentally isolate each of these effects can be of comparable importance to the capability of simulating high Reynolds flows. Overviews of facility usage have been given by Wahls¹⁶ and Luckring¹⁷.

4.3.2 Model

The model is a full-span sting-mounted delta wing with interchangeable leading-edge components. The model and the near-field sting geometries are fully analytical with continuity through second derivative and, hence, curvature. It was anticipated that such analytical definitions could help facilitate Computational Fluid Dynamics (CFD) analysis.

A schematic of the model is shown in Figure 5. The wing is an uncambered flat plate with special consideration given to the leading and trailing edges. The wing was designed for a series of interchangeable leading-edge components and the leading edge contours are shown in Figure 6. They were defined with a NACA-like airfoil polynomial¹⁹ for four values of leading-edge bluntness, r_{le}/c_{bar} , that were 0 (sharp), 0.0005, 0.0015, and 0.0030 in the streamwise direction. These bluntness values were chosen to be relevant to several aircraft that incorporate thin highly swept wings.⁹

The leading-edge contours matched the flat-plate wing over a distance of 15 percent root chord and were constant spanwise to match the flat-plate central portion of the wing. This leading-edge contour region is also indicated in Figure 5. The central flat plate portion of the wing was 5.1 percent thick (referenced to the mean aerodynamic chord) and this thickness was closed out over the last 10-percent of the root chord to a sharp trailing edge. The model was polished to an 8-microinch surface finish.

The support mechanism was a ten degree offset sting designed to position the model at the center of the test section over the angle of attack range investigated. The offset allowed for testing at angles of attack of nominally -2 to 28 degrees. The near-field sting was an uncambered body of revolution that emerged symmetrically from the wing slightly aft of the 60% root chord station. It was also a fully analytical surface based upon the same functions used to represent the leading-edge shapes. The sting diameter was designed to be the minimum allowable to accommodate the design load of 6500 pounds normal force and to also house necessary instrumentation leads.

The model was instrumented with 183 static surface orifices that had an internal diameter of 0.010 inches. (See Figure 5.) The orifice arrangement allowed for fairly good spanwise resolution at five chordwise stations. Pressure orifices were also located directly on the blunt leading edges to help track the onset and progression of leading-edge vortex separation. In order to avoid fuselage effects and to minimize sting interference effects, most instrumentation was situated remotely to the model. Pressure tubing was routed through the sting to electronically scanned pressure (ESP) modules. Because of the number of pressure tubes, there was no room for a conventional force balance. However, normal force and pitching moment quantities were measured through a novel gauging arrangement with the near-field sting. Balance accuracy gauging on the sting itself allowed for the measurement of these quantities. Unfortunately, there was no similar means to obtain axial-force measurements. Angle of attack was determined from the combination of arc-sector setting

and calibrated sting-bending effects using the sting gauges just mentioned. On-board inclinometers were too large to include in this thin-wing model. A photograph of the model installed in the NTF test section is shown in Figure 7.

4.3.3 Test Program

The NTF operating envelope, scaled to the delta wing of the present investigation, is shown in Figure 8a. Here the facility Reynolds numbers are based upon the delta wing mean aerodynamic chord and represent maximum operating capability. The Mach and Reynolds number extent for the delta wing experimental program is also shown and is well within the maximum facility capability. In addition, a variety of slender vehicle operating conditions are shown along with those for a typical High-Wing Military Transport (C-17). Although the delta wing is a very fundamental shape, the test program was designed to include conditions relevant to aircraft operations.

The tests were conducted in 1991, and a representative matrix of test conditions is shown in Figure 8b. Not all of these conditions were achieved for every configuration due to resource limitations. The data were obtained at Mach numbers ranging from 0.4 to 0.9. Reynolds number was varied from 6 million to 120 million in such a way to facilitate analysis at Reynolds numbers based upon either the wing mean aerodynamic chord or the wing leading-edge radius. Data were obtained at only two total temperatures, nominally 120° F and -250° F. Total pressure was varied nominally between 1.1 and 5.3 atmospheres to obtain the desired free-stream test conditions.

It was anticipated that the flow would naturally be turbulent over the Reynolds numbers tested, so artificial transition strips were not used. Moreover, there were no clear transition-strip test techniques for these vortex flows.

A number of potential pseudo-Reynolds-number effects were considered and minimized in the design of the experiment. Calculations indicated that aeroelastic deformation would be small due to the low aspect ratio of the wing, the thickness of the wing, and the stiffness of the material. The 8-microinch surface finish was sufficient for the model to be hydraulically smooth over the range of conditions tested. Wind tunnel wall interference was believed to be negligible due to the slotted test section and the relative size of the delta wing to the test section ($b/w_{ts} = 0.244$). In addition, test section walls, model support walls, and reentry flaps were all set to minimize wall effects based upon facility guidelines. The model support mechanism was designed to keep the model centered in the test section. This essentially eliminated pseudo-angle-of-attack effects associated with the model traversing the test section flow and/or getting too close to the ceiling at high angles of attack.

4.4 SAMPLE RESULTS

In this section representative examples of the data are presented. The full data set has been published¹⁸⁻²¹, and these papers include both tabulated and plotted results for all measurements taken. In addition, several papers have been recently been published⁹⁻¹² with focused analysis of subsets of the data from this experimental program.

4.4.1 Contrast of Sharp-Leading-Edge and Blunt-Leading-Edge Flows

A comparison of static surface pressure coefficients is presented in Figure 9 for the sharp-edged and one of

the blunt-edged wing geometries. The data density of this figure is representative of the entire data set.

The surface pressures for the sharp-edged delta wing show typical separation-induced leading-edge vortex properties. The primary vortex suction peak is situated conically on the wing and diminishes in magnitude as the trailing edge is approached. Outboard of this suction peak turbulent secondary separation is indicated. The surface pressures for the blunt-edged delta wing clearly demonstrate part span leading-edge vortex separation. Attached flow pressures are evident at 20% root chord while leading-edge vortex-like pressures are evident from 60% root chord aft. The origin of the blunt leading-edge vortex for this case is in the vicinity of 30% root chord. The direct comparison of the pressures in Figure 9 at 60% root chord demonstrates the outboard shift of the vortex footprint due to leading-edge bluntness.

4.4.2 Reynolds Number Effect

A representative effect of Reynolds number on the blunt leading edge vortex flow is summarized in Figure 10. Results on the left portion of this figure are the same ones used in Figure 9 to compare with sharp-edged flow. Comparison of these results at $R_n = 6$ million (typical of wind-tunnel conditions) to those at 60 million (representative of flight conditions) show significant recovery of attached flow at the higher Reynolds number. The origin of the leading-edge vortex separation has shifted downstream in association with the higher Reynolds number.

4.4.3 Compressibility Effect

A representative effect of compressibility on leading-edge vortex separation is presented in Figure 11. Results on the left portion exhibit extensive attached flow at Mach number of 0.4. However, the increase of Mach number to 0.6 has a profound effect on this separation. The 60% root chord station shows well-developed vortex separation and the 40% root chord station also appears to have separated. The origin of leading-edge vortex separation has moved significantly upstream in association with the increase in free stream Mach number from 0.4 to 0.6.

4.4.4 Separation Onset and Progression Analysis

Leading-edge pressures provide a useful means to identify the passage of separation onset, and these data were taken in sufficient density to facilitate this analysis. An example is presented in Figure 12. At low angles of attack the leading-edge pressure will follow a trend that can be deduced from attached-flow slender wing theory, $C_{p,le} = C_0 - C_2 \sin^2 \alpha$, and departure from this trend can correlate with separation onset. An application of this analysis is presented in Figure 13 to quantify the effect of Reynolds number on the onset and progression of leading-edge separation. Here Reynolds number is shown to delay separation at three root chord stations, and the Reynolds number effects occur over a significant angle of attack range at values typical of maneuver conditions.

The leading-edge pressure analysis can be to estimate the onset and progression of the leading-edge separation. An example of such analysis is shown in Figure 14 and includes both Reynolds number and Mach number effects. The data show, for the onset and progression of leading-edge vortex separation, how Reynolds number delays this phenomena and Mach number promotes it. These effects are comparable in magnitude but opposite in sign. Such results demonstrate the importance of isolating these effects for the purposes of prediction to other conditions of interest.

4.5 CONCLUDING REMARKS

A brief summary has been presented for an experimental investigation of the flow about a 65° delta wing with blunt leading edges. The tests were conducted in the NASA Langley National Transonic Facility (NTF) and the data have been published in the public domain. The data demonstrate significant effects of Reynolds number, Mach number, and leading-edge bluntness on the onset and progression of leading-edge vortex separation. The data indicate there is much to be learned regarding blunt leading-edge vortex flows, and the fully analytical nature of this particular delta wing could be useful for future experimental and computational studies.

4.6 REFERENCES

- [1] Hummel, D., "On the Vortex Formation Over a Slender Wing at Large Incidence," AGARD CP-247, Paper No. 15, January 1979.
- [2] Polhamus, E. C., "A Concept of the Vortex Lift of Sharp-Edged Delta Wings Based on a Leading-Edge Suction Analogy," NASA TN D-3767, 1966.
- [3] Peckham, D. H., "Low-Speed Wind-Tunnel Tests on a Series of Uncambered Slender Pointed Wings with Sharp Edges," ARC R&M 3186, 1961.
- [4] Tosti, L. P., "Low-Speed Static Stability and Damping in Roll Characteristics of Some Swept and Unswept Low-Aspect-Ratio Wings," NACA TN 1468, 1947.
- [5] "High Angle of Attack Aerodynamics," AGARD CP-247, January 1979.
- [6] "Aerodynamics of Vortical Type Flows in Three Dimensions," AGARD CP-342, July 1983.
- [7] "Vortex Flow Aerodynamics," AGARD CP-494, July 1991.
- [8] "Advanced Flow Management: Part A - Vortex Flow and High Angle of Attack," RTO MP-069, May 2001.
- [9] Luckring, J. M., "Reynolds Number, Compressibility, and Leading-Edge Bluntness Effects on Delta Wing Aerodynamics," ICAS paper 2004-4.1.4, September 2004
- [10] Luckring, J. M., "Reynolds Number and Leading-Edge Bluntness Effects on a 65° Delta Wing," AIAA Paper 2002-0419, January 2002.
- [11] Luckring, J. M., "Transonic Reynolds Number and Leading-Edge Bluntness Effects on a 65° Delta Wing," AIAA Paper 2003-0753, January 2003.
- [12] Luckring, J. M., "Compressibility and Leading-Edge Bluntness Effects for a 65° Delta Wing," AIAA Paper 2004-0765, January 2004.
- [13] Fuller, D. E., "Guide for Users of the National Transonic Facility," NASA TM-83124, 1981.
- [14] Igoe, W. B., "Analysis of Fluctuating Static Pressure Measurements in the National Transonic Facility,"

NASA TP-3475, March 1996.

- [15] Bobbitt, C. W., and Everhart, J. L., "NTF Characterization Status," AIAA Paper 01-755, January 2001.
- [16] Wahls, R. A., "The National Transonic Facility – A Research Retrospective," AIAA Paper 01-0754, January 2001.
- [17] Luckring, J. M., "An Overview of National Transonic Facility Investigations for High Performance Military Aerodynamics" AIAA Paper 01-0906, January 2001.
- [18] Chu, J., and Luckring, J. M., "Experimental Surface Pressure Data Obtained on 65° Delta Wing Across Reynolds Number and Mach Number Ranges. Volume 1 – Sharp Leading Edge," NASA TM-4645, February 1996.
- [19] Chu, J., and Luckring, J. M., "Experimental Surface Pressure Data Obtained on 65° Delta Wing Across Reynolds Number and Mach Number Ranges. Volume 2 – Small Leading Edge," NASA TM-4645, February 1996.
- [20] Chu, J., and Luckring, J. M., "Experimental Surface Pressure Data Obtained on 65° Delta Wing Across Reynolds Number and Mach Number Ranges. Volume 3 – Medium Leading Edge," NASA TM-4645, February 1996.
- [21] Chu, J., and Luckring, J. M., "Experimental Surface Pressure Data Obtained on 65° Delta Wing Across Reynolds Number and Mach Number Ranges. Volume 4 – Large Leading Edge," NASA TM-4645, February 1996.

APPENDIX – AVT-080 DATA SET

1.0 General Description of Model

1.1	Designation	NTF 65° Delta Wing
1.2	Type	Full-span, sting mount
1.3	Additional remarks	Mach number, Reynolds number, leading-edge bluntness effects
1.4	References	References 18, 19, 20, 21

2.0 Model Geometry

2.1	Planform	Delta wing
2.2	Aspect ratio	1.865
2.3	Leading edge sweep	65 degrees (reference dimension)
2.4	Trailing edge sweep	0 degrees
2.5	Twist	0 degrees
2.6	Leading edge bevel (leeward)	0 degrees
2.7	Leading-edge bevel (windward)	0 degrees
2.8	Trailing edge bevel (leeward)	0 degrees
2.9	Trailing edge bevel (windward)	0 degrees
2.10	Leading-edge radius (streamwise)	$r/cbar = 0$ (sharp), 0.0005, 0.0015, 0.0030
2.11	Tolerance of leading-edge radius	$\Delta r/cbar = +/- 0.000025$
2.12	Trailing edge radius	0 (sharp)
2.13	Tolerance of trailing edge radius	n/a
2.14	Model thickness (flat area)	0.072917 feet
2.15	Root chord	2.144507 feet
2.16	Model span	2 feet (reference dimension)
2.17	Area of planform	2.144507 feet ²
2.18	Mean aerodynamic chord	1.429671 feet
2.19	Balance reference center	none
2.20	Shape/radius of balance housing or center-body	References 18, 19, 20, 21
2.21	Form of wing-body junction	sharp
2.22	Form of wing tip	none
2.23	Model weight	Not available
2.24	Model material	Vascomax C-200 steel
2.25	Additional remarks	8 micro-inch surface finish
2.26	Drawings and references	References 18, 19, 20, 21

3.0 Wind/Water Tunnel

3.1	Designation	National Transonic Facility (NTF)
3.2	Type of tunnel	Closed circuit, pressure, cryogenic
3.3	Test section dimensions	8.202 feet square with filleted corners, 25 feet long
3.4	Test section cross sectional area	66.8 feet ²
3.5	Contraction ratio	14.95:1
3.6	Maximum speed	M = 1.2
3.7	Sources and levels of noise or turbulence in empty tunnel	References 14, 15
3.8	Flow angularity	Reference 15
3.9	Uniformity of velocity over test section	Uncertain
3.10	Tunnel resonance	References 14, 15
3.11	Type of roof and floor	slotted
3.12	Type of side walls	solid
3.13	Thickness of side wall boundary layer	Approximately 1 inch
3.14	Thickness of boundary layers at roof and floor	Approximately 1 inch
3.15	Additional remarks	none
3.16	References on tunnel	References 13, 14, 15

4.0 Model Motion

4.1	General description	Arc-sector support
4.2	Method of applying motion	Arc-sector rotation
4.3	Accuracy of the model orientation	Uncertain, but equal to or less than $\Delta\alpha = \pm 0.1^\circ$
4.4	Waveform of the model motion	none
4.5	Maximum angular rate	n/a
4.6	Maximum amplitude	n/a
4.7	Maximum of angular acceleration	n/a
4.8	Tare friction	n/a

5.0 Test Conditions

5.1	Model planform area/tunnel cross sectional area	0.0321
5.2	Model span/tunnel height	0.244
5.3	Blockage	From 0.0027 at $\alpha = 0^\circ$ to 0.0161 at $\alpha = 30^\circ$
5.4	Flow angularity	$\Delta\alpha = 0.13^\circ$
5.5	Model sting/support	Sting and arc-sector

5.6	Detail of sting/ support	Figures 5, 7
5.7	Support deformation under aerodynamic loads	Included in angle-of-attack calibration
5.8	Support/model resonance under aerodynamic loads	Not recorded
5.9	Position of model in tunnel	Test section centerline
5.10	Range of tunnel velocities	$0.4 < M < 0.9$
5.11	Range of tunnel total pressure	$1.05 < P_t, \text{ atm} < 5.34$
5.12	Range of tunnel total temperature	$-251 < T_t, ^\circ\text{F} < 127$
5.13	Range of model steady or mean incidence	$-1^\circ < \alpha < 27^\circ$
5.14	Position of transition, if free	Not measured.
5.15	Position and type of trip, if transition fixed	none
5.16	Flow instabilities during tests	n/a
5.17	Additional remarks	Free transition is anticipated to be close to wing apex at the Reynolds numbers of this investigation.
5.18	Drawings for set-up in tunnel and related references	References 18, 19, 20, 21

6.0 Measurements and Observations

6.1	Visualisation method of surface flow	none
6.2	Visualisation method of off-surface flow	none
6.3	Visualisation of vortex behavior	none
6.4	Criteria of vortex breakdown	none
6.5	Measurement of velocity vector	none
6.6	Measurement of flow turbulence	none
6.7	Steady pressure for static conditions	Pressure transducers
6.8	Unsteady pressures for static conditions	none
6.9	Unsteady pressure for dynamic conditions	n/a
6.10	Steady forces by integration of pressures	Not performed
6.11	Unsteady forces by integration of pressure	n/a
6.12	Steady forces measured directly from balance	Normal force and pitching moment
6.13	Unsteady forces measured directly from balance	n/a
6.14	Motion history in dynamic conditions	n/a
6.15	Observation or measurement of boundary layer properties	none
6.16	Additional remarks	none

7.0 Instrumentation

7.1	Oil flow method	none
-----	-----------------	------

7.2	Laser light set-up in static situation	none
7.3	Laser light set-up in dynamic situation	none
7.4	PIV set-up	none
7.5	Steady pressure	
7.8.1	Position of orifices spanwise and chordwise	Figure 5, References 18, 19, 20, 21
7.8.2	Diameter of orifices	0.010 inches
7.8.3	Type of transducers	Piezio Electric
7.8.4	Type of measuring system	Electronically Scanning Pressure (ESP) system
7.8.5	Signal acquisition	Digital
7.8.6	Principle and accuracy of calibration	In-situ periodic within-system calibration, 0.5 percent of full scale
7.6	Unsteady pressure	none
7.8.1	Position of orifices spanwise and chordwise	n/a
7.8.2	Diameter of orifices	n/a
7.8.3	Type of transducers	n/a
7.8.4	Type of measuring system	n/a
7.8.5	Signal acquisition	n/a
7.8.6	Principle and accuracy of calibration	n/a
7.7	Steady loads	
7.8.1	Type of transducers	Strain Gauge
7.8.2	Signal acquisition	Digital
7.8.3	Accuracy of calibration	Nominally 0.5% of full scale
7.8	Unsteady loads	none
7.8.1	Type of transducers	n/a
7.8.2	Signal acquisition	n/a
7.8.3	Principle and accuracy of calibration	n/a
7.9	Motion measurement	none
7.9.1	Type of transducers	n/a
7.9.2	Signal acquisition	n/a
7.9.3	Accuracy	n/a
7.9.4	Sting acceleration	none

8.0 Data Presentation

8.1	Test cases for which data could be made available	Full data set
8.2	Test cases for which data are included in this document	Only sample highlights
8.3	Surface flow topology	none
8.4	Vortex behavior and breakdown location	none
8.5	Velocity vector	none
8.6	Turbulence	none

8.7	Steady pressures	Spanwise distributions every 20% root chord
8.8	Unsteady pressures	none
8.9	Steady forces or moments	Normal-force and pitching-moment coefficients
8.10	Unsteady forces and moments	none
8.11	Other forms in which data could be made available	Reports, data files
8.12	Reference giving other representations of data	References 18, 19, 20, 21

9.0 Comments on Data

9.1	Accuracy	
9.1.1	Mach number	+/- 0.0005
9.1.2	Model orientation	Uncertain, but equal to or less than $\Delta\alpha = +/- 0.1$ degrees
9.1.3	Reduced frequency	n/a
9.1.4	Vortex breakdown location	n/a
9.1.5	Velocity vector	n/a
9.1.6	Steady pressure coefficients	References 18, 19, 20, 21
9.1.7	Unsteady pressure coefficients	n/a
9.1.8	Static loads	References 18, 19, 20, 21
9.1.9	Dynamic loads	n/a
9.2	Influence of tunnel total pressure	Static aeroelastic effects are felt to be negligible
9.3	Wall interference corrections	none
9.4	Other relevant tests on same model	none
9.5	Relevant tests on other models of nominally the same shapes	None published
9.6	Any remarks relevant to comparison between experiment and theory	none
9.7	Available CFD solutions for test case	none
9.8	Additional remarks	none
9.9	References on discussion of data	References 9, 10, 11, 12

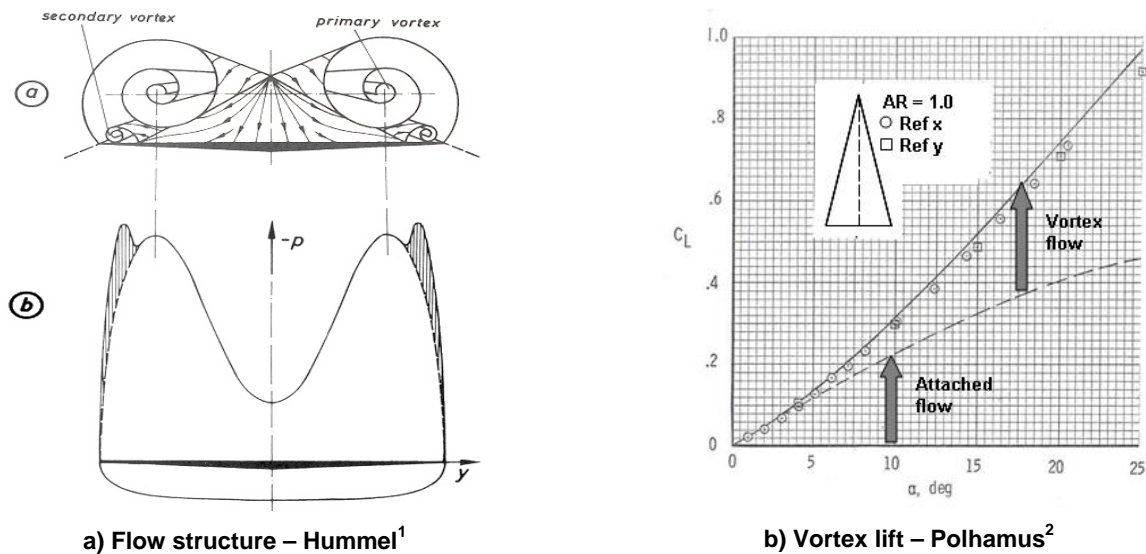
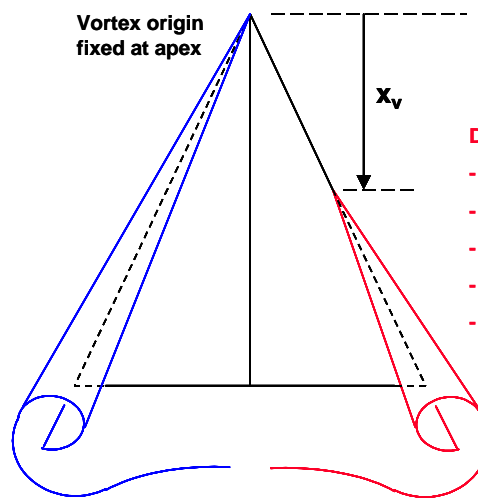


Figure 1: Some leading-edge vortex properties, sharp-edged delta wings.

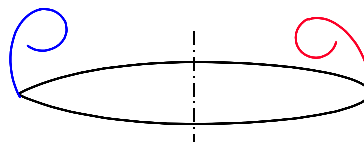
Sharp leading edge

Vortex properties vary with:

- Angle of attack
- Mach number
- Reynolds number
- etc.



Primary vortex separation
at leading edge



Blunt leading edge

Displaced vortex origin varies with:

- Angle of attack
- Mach number
- Reynolds number
- Leading-edge radius
- etc.

Vortex properties still vary with:

- Angle of attack
- Mach number
- Reynolds number
- Leading-edge radius
- etc.

Primary vortex separation
near leading edge

Figure 2: Bluntness effects on leading-edge vortex structure – Luckring⁹.



Figure 3: National Transonic Facility (NTF).

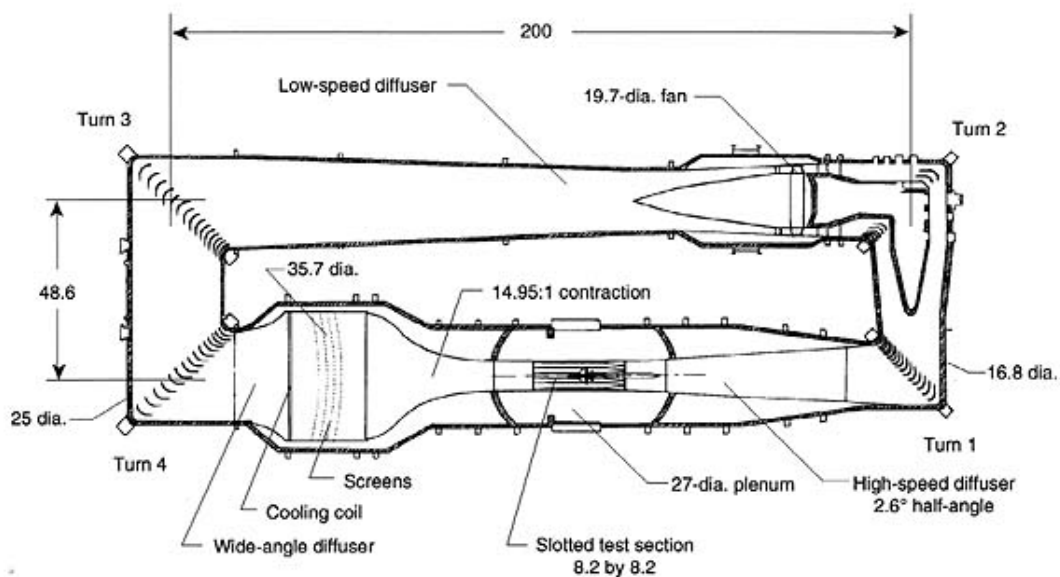


Figure 6. Plan view of NTF tunnel circuit. All linear dimensions are in feet.

Figure 4: National Transonic Facility circuit. Dimensions in feet.

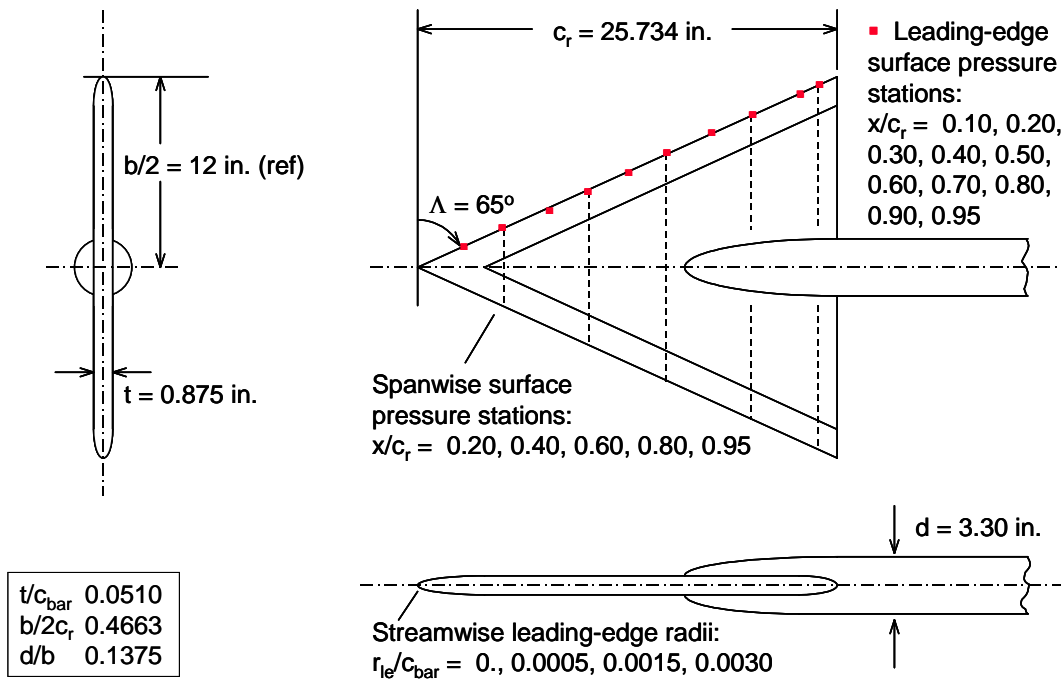


Figure 5: Schematic of NTF delta wing.

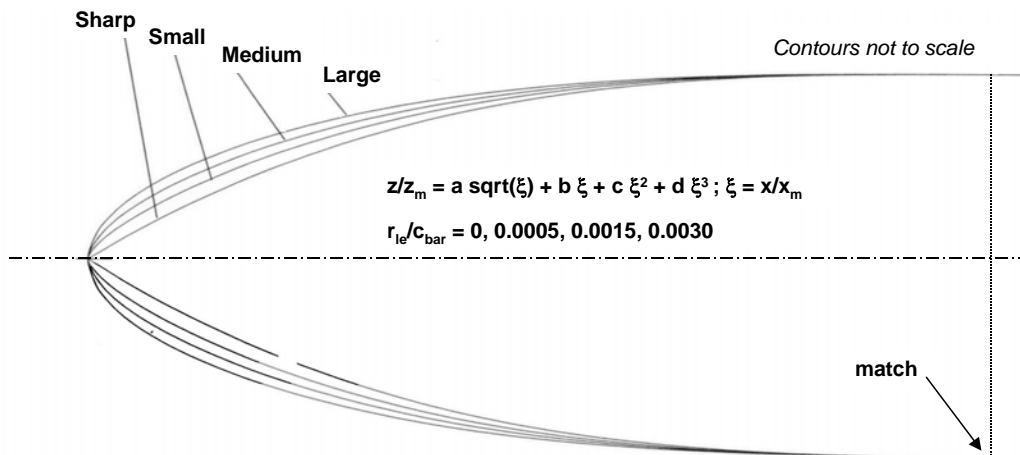
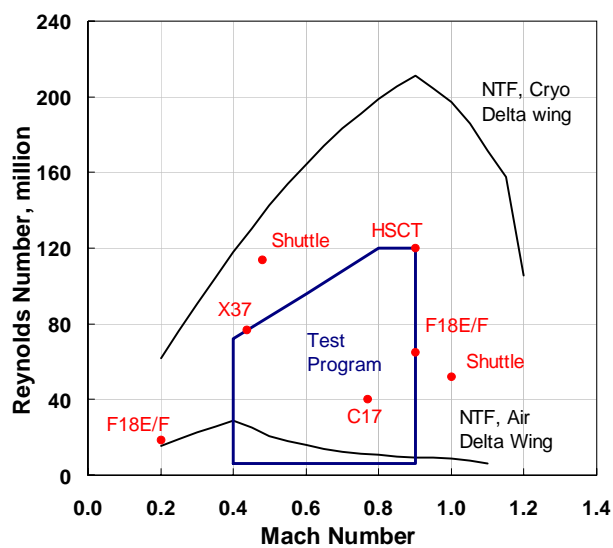


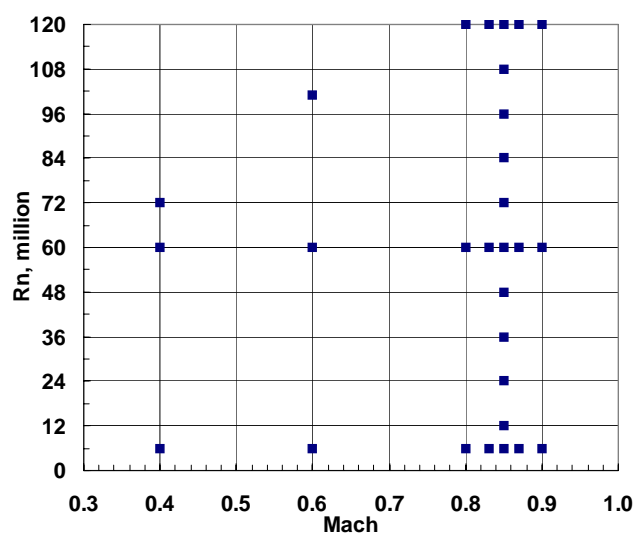
Figure 6: Streamwise leading-edge contours for NTF delta wing.



Figure 7: Delta wing mounted in the NTF.



a) NTF envelopes and aircraft operating conditions.



b) Representative delta-wing test matrix

Figure 8: Test conditions

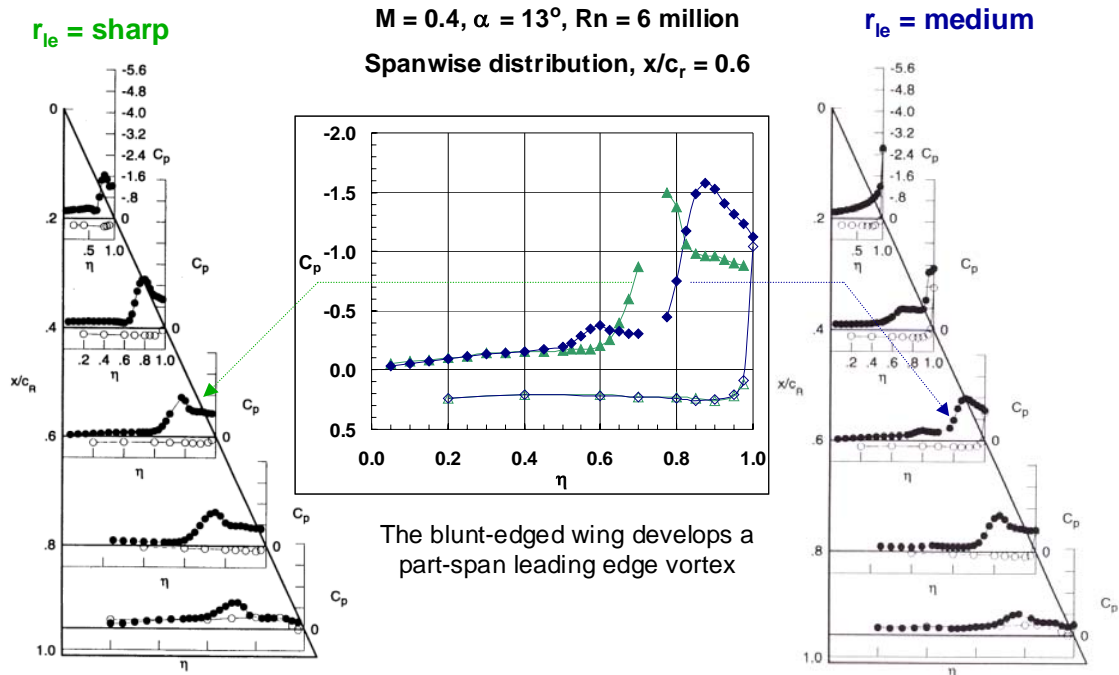


Figure 9: Comparison of sharp and blunt leading-edge vortex flow.

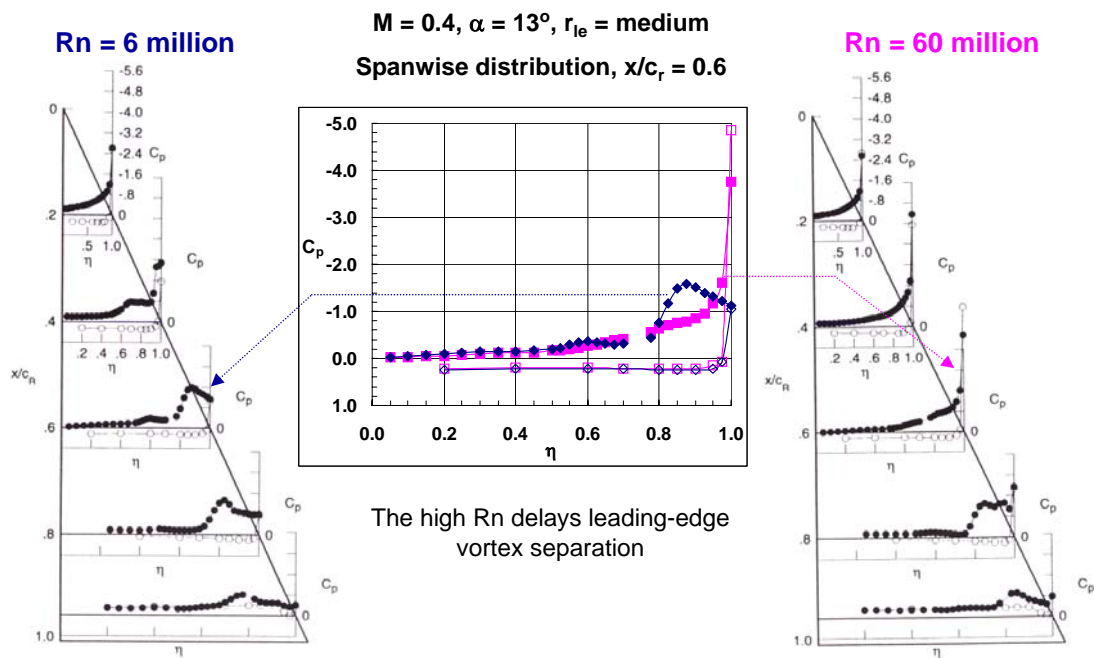


Figure 10: Reynolds number effect on blunt leading-edge separation.

EXPERIMENTAL INVESTIGATION OF THE FLOW ABOUT A 65° DELTA WING IN THE NASA LANGLEY NATIONAL TRANSONIC FACILITY

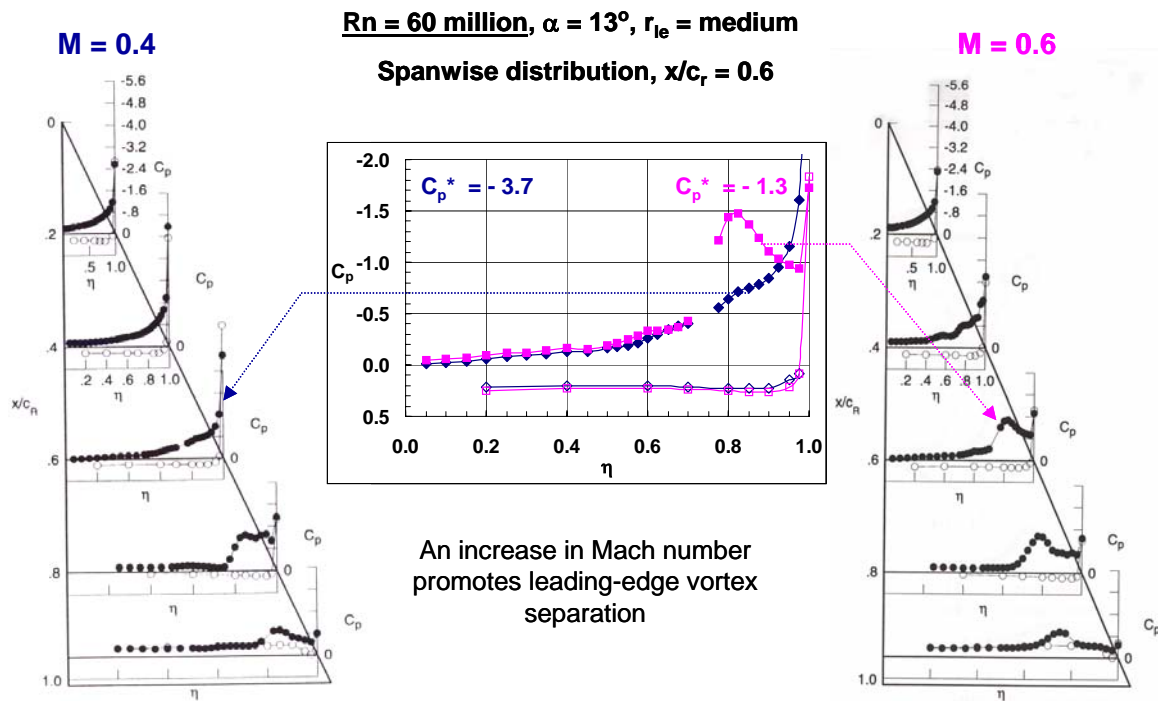


Figure 11: Mach number effect on blunt leading-edge separation

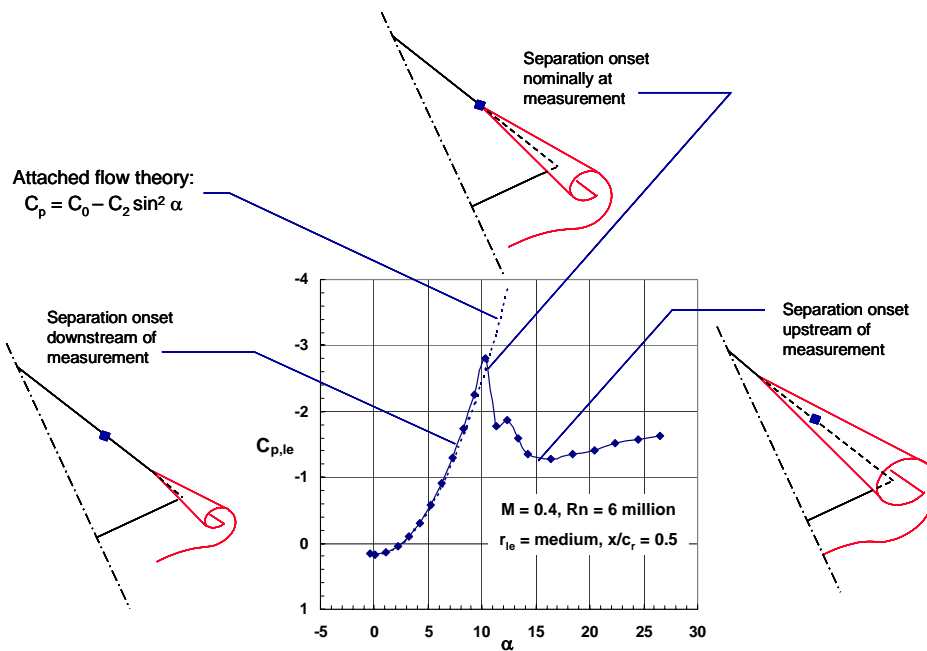


Figure 12: Correlation of separation onset with blunt leading-edge pressure.

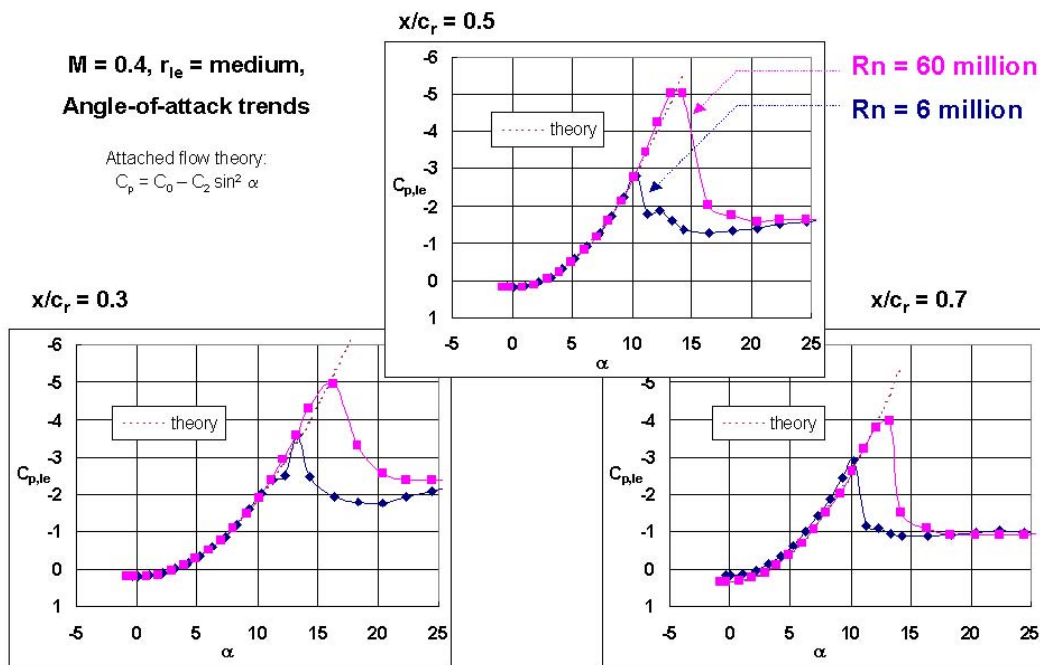


Figure 13: Reynolds number effect on leading-edge separation onset and progression.

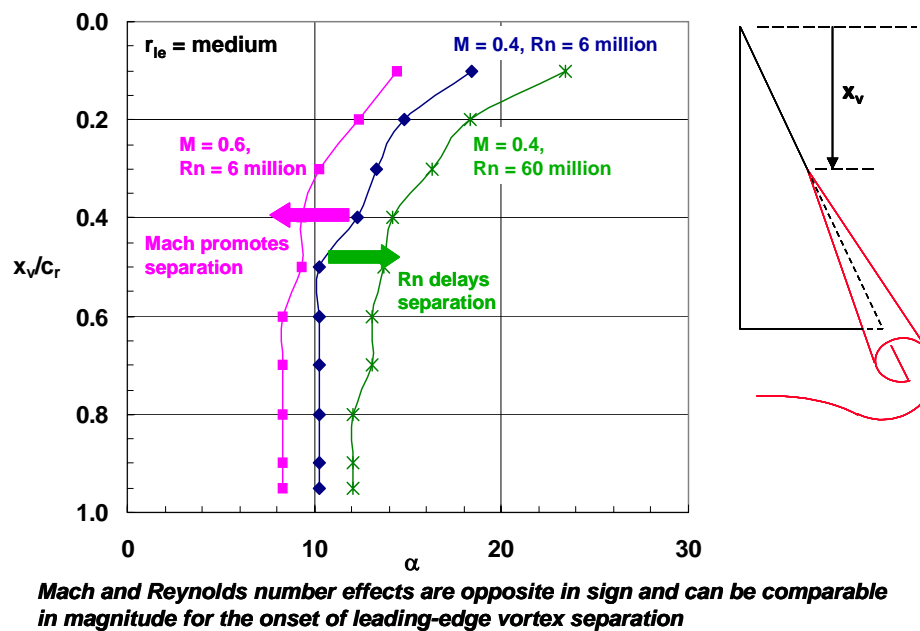


Figure 14: Mach and Reynolds number effects for the progression of leading-edge separation.

Chapter 5 – COMPREHENSIVE EXPERIMENTAL STUDIES ON VORTEX DYNAMICS OVER MILITARY WING CONFIGURATIONS IN IAR

Xing Huang

Aerodynamics Laboratory
Institute for Aerospace Research
National Research Council of Canada
1200 Montreal Rd., Ottawa Ont. Canada K1A 0R6

xingzhong.huang@nrc.ca

ABSTRACT

Vortex dynamics over more than 50 types of military wing configurations have been experimentally investigated. Diamond and delta wings with sweep back angles from 55° to 75° have been tested. The experiments were conducted in two wind tunnels and a water tunnel with more than 10,000 runs at different test conditions. Investigations include flow visualisations (surface and off-surface flow field and vortex behavior), surface pressures (steady and unsteady pressure), air loads (steady and unsteady loads) and motion histories (harmonic, ramp-and-hold, free-to-roll and “forced” free-to-roll), geometry and Re number effects in pitch, roll and coning motion plans. The ranges of angle of attack, roll angle and coning angle are $0^\circ \sim 90^\circ$, $\pm 180^\circ$ and $\pm 360^\circ$ respectively with maximum non-dimensional frequency 0.2 in pitch and roll and 0.6 in coning respectively. The maximum Re number is 3×10^6 and maximum Mach number is 0.4 in wind tunnel experiments. The comprehensive data sets have been edited into eight volumes of IAR reports while only a brief of the program is presented here.

5.1 INTRODUCTION

The tactical advantage of high maneuverability and agility of military air vehicles has been an incentive to continually expand their flight envelope. Many high manoeuvre aerial vehicles including UCAVs, take delta wing, double delta wing or diamond wing as basic configurations and operate at near- and post-stall regimes. The flow over the wing area is characterised by the strong leading-edge vortices used for extra aerodynamic forces and control power required to expand the flight envelope and to improve the tactical advantage in air combat. A disadvantage, however, is that the vortices may breakdown resulting in non-linear and time dependent airloads. Conventional aerodynamic models cannot model these features. Due to lack of sufficient understanding of the flow physics, current CFD capabilities and mathematical models are unable to accurately predict the flight mechanics at those flight conditions. Thus, it is crucial to study the flow physics and to establish a completed, comprehensive and quantitatively reliable data set for the development of CFD and analytic solutions applicable to those regimes.

In order to meet the challenges, the Aerodynamics Laboratory in the Institute for Aerospace Research (AL/IAR) has launched a research program. It was initiated from a joint program between IAR and SARL in USAF conducted by E. Hanff (IAR) and J. Jenkins (AFRL/USAF) and their colleagues from 1989 to 1994^{1,2}. It produced results on air loads under static and dynamic situation based on a 65° delta wing configuration but it has less information on flow behavior such as surface pressure, off-surface velocity field, geometry effect (e.g. leading-edge shape, sweep back angle or centerbody effect), and Reynolds number effects, etc. Also since the experiments were conducted in different facilities at different times with different data formats, it was imperative to edit and to evaluate the data sets, so that the extensive work already performed at a high cost could be properly used. Thus more experimental studies were performed thereafter in IAR until 2003 to broaden the base of the original program. All data sets were

edited and presented in Ref. 3 in a user-friendly format.

Up to now more than 50 types of different military wing configurations were tested in three facilities (two wind tunnels and one water tunnel) with different support systems. The main wind-tunnel entries are listed in Table 1 where some supplementary tests may not be included. A total of over 10,000 runs were conducted between 1989 and 2003. All three motion plans (pitch, roll and coning) and different waveforms were investigated. Comprehensive measurements include surface and off surface flow field, surface pressure, air loads, geometry effect and Reynolds number's effect etc. The experiments were performed at angle of attack up to 90° , roll angle up to 180° , Reynolds number up to 3.6×10^6 and non-dimensional frequency up to ± 0.2 and ± 0.6 in pitch or roll and coning respectively.

The comprehensive program and results have been edited into eight volumes of IAR reports [2], namely:

- Vol. 1 Test matrix and conditions
- Vol. 2 Highlights of the results
- Vol. 3 Surface and off-surface flow visualisations in static and dynamic model conditions
- Vol. 4 Surface pressure in static model conditions
- Vol. 5 Surface pressure in dynamic model conditions
- Vol. 6 Aerodynamic loads and moments in static and dynamic model conditions
- Vol. 7 Free-to-roll and "forced" free-to-roll results
- Vol. 8 Non-planar experimental results

From author's knowledge it is one of the most completed, comprehensive and state-of-the-art data set on vortex dynamics over military wing configurations. Given the large amount of information acquired between 1989 and 2003, only briefing of the program and highlights of the results are given here.

5.2 EXPERIMENTAL SET-UP

5.2.1 EXPLOITED AREAS

The test program covers the following exploited areas:

- Measurements obtained:
 - (1) Surface and off-surface flow field, including oil flow, Laser-smoke sheet and Particle-Image-Velocimetry (PIV) measurements.
 - (2) Surface pressure, including steady surface pressure obtained by pressure sensitive paint (PSP), pressure taps and unsteady pressure by and unsteady pressure transducers.
 - (3) Air loads, including time-averaged loads in steady model conditions and instantaneous or ensemble average unsteady loads in dynamic model conditions.
 - (4) Geometrical effects, such as leading-edge shape, wing planform (delta wing or diamond wing), centre-body, forebody or aft body etc.
 - (5) Re number effect.
- Motion plan and motion variable:
 - (1) Experiments were conducted either in roll, pitch or coning motion at either static or dynamic model

conditions.

- (2) In rolling motion, roll angle ranged from -180° to $+180^\circ$ with maximum amplitude of 40° around maximum offset of $\pm 50^\circ$ and with a maximum non-dimensional frequency 0.2. In addition, free-to-roll motion and “forced” free-to-roll motion were also performed.
- (3) In pitch motion, the angle of attack ranged from -4° to 93° with maximum angular rate, maximum angular acceleration and non-dimensional frequency 1900 $^\circ/\text{s}$, 79,000 $^\circ/\text{s}^2$ and 0.2 respectively.
- (4) In coning motion, the coning angle ranged from -360° to $+360^\circ$ with a maximum non-dimensional coning rate of 0.6.
- (5) The motion waveforms included harmonic oscillation, ramp-and-hold motion, quasi-steady coning motion, free-to-roll and “forced” free-to-roll motions.

5.2.2 WIND TUNNELS

The tests were conducted in the IAR low speed wind tunnel (LSWT), USAF/AFRL subsonic tunnel (SARL) and the IAR 1520 water tunnel. Both IAR LSWT and USAF/AFRL SARL wind tunnels are atmospheric facilities with a maximum wind speed of 120 and 200 m/s respectively. The IAR wind tunnel test section is 2.7m wide, 1.83 m high and 4.57m long. Its turbulence intensity levels in wind tunnel are 0.12% at 30m/s and 0.15% at 75m/s. The SARL facility is an open return wind tunnel with test section 2.1m wide, 3m high and 4.57m long. The contraction ratio is 36:1 resulting in a turbulence intensity level of 0.1%. The water tunnel section is 0.38x0.5 m. Both wind tunnels and water tunnel have excellent visual access to the test section, thus facilitating flow visualization experiments.

5.2.3 MODELS

More than 50 types of models were tested including diamond wing, delta wing, double delta wing, wing/body/tail configurations with different leading-edge shapes and centerbody combinations. The tested models can be classified into five major groups:

- (1) 55° diamond or delta wing models with different leading-edge shapes and wing-body combinations.
- (2) 65° delta wing models with different leading-edge shapes and wing-body combinations.
- (3) $80^\circ/65^\circ$ double delta wing model.
- (4) 65° delta-wing/body/tail models.
- (5) Models tested in water tunnel with sweep back angles from 55° to 75° .

The first group models (Fig. 1) were made of aluminium alloy tested in static condition. They have interchangeable leading-edge, aft portion of the wing, centerbody and aft body. Thus the model could be easily changed from diamond to delta wing with different leading-edge shapes and with or without centerbody or aftbody.

The second group (65° wing model) has two different sub-groups (Fig. 2 and Fig. 3). The first sub-group was designed for using in static test condition. The wing consists of upper and bottom halves made of PVC and stainless steel respectively. The upper half (PVC wing half) has 57 pressure taps while the bottom half, which was made of stainless steel, supports the air loads. The leading-edge and centerbody are interchangeable (Fig. 2a). Therefore they have many kinds of combinations (Fig. 2b) such as sharp or rounded leading-edge, with or without centerbody, etc. The second sub-group of 65° delta wing (Fig. 3) took the same geometry as the first sub-group but was designed for using in dynamic test conditions. It can withstand a normal force of 900 kg while having a high stiffness to prevent aeroelastic effects and very low mass and moments of inertia to minimize the inertial loads prevailing under the severe dynamic

test conditions.

The third group (double delta wing) was obtained by extending an 85° leading-edge extension (LEX) on a 65° wing model (Fig. 4).

The fourth group has a tail and a tangent ogive forebody with interchangeable cylindrical and elliptical cross-sections mounted on a 65° wing model. The major axis of the elliptical cross-section can be changed from parallel to perpendicular to the wing (Fig. 5a and Fig. 5b). The tail was built with a multi-layer graphite skin and foam core and the centerbody was entirely made of graphite composite. Noses and forebodies were made of aluminium alloys.

The fifth group tested in water tunnel consists of a 55° model and a 65° model in coning tests (Fig. 6a and 6b) and a series of delta wing model with leading-edge sweep angles ranging from 50° to 75°.

5.2.4 RIGS

Different rigs were used in the tests, namely roll rig, pitch rig and coning rig, which are briefly described below:

5.2.4.1 ROLL RIG

The roll rig is capable of operating in static, forced motion (oscillatory and ramp-and-hold motions), free-to-roll and “forced” free-to-roll motion modes. The installation of the roll rig in the LSWT is depicted in Fig. 7a where the angle of attack was adjusted on a horizontal arc. In the case of installation in SARL the angle of attack was adjusted by means of a sector (Fig. 7b). The model was mounted on a one-piece internal five-component strain gauge balance (no axial force). In order to conduct unsteady surface pressure tests, the balance was replaced by a dummy of similar geometry which provided a connector for the pressure transducers leads. The desired model motion was imparted by a hydraulic rotary actuator. The roll angle was sensed by an incremental optical encoder attached to the aft end of the actuator shaft. Free-to-roll tests were performed by modifying the aft end of the rig to include a clutch. By disengaging the clutch, the model was free to roll except for the small friction of the bearings. Under these conditions the roll angle could be monitored by the rotary encoder which was attached to the aft end of the driveshaft.

5.2.4.2 PITCH RIG

A general view of the pitch rig is shown in Fig.8. The model was mounted on a balance that was an integral part of the sting, which was supported by bearings at the end of the support strut. A linear hydraulic actuator caused the model to pitch via a bell crank and linkage that connected it to an extension of the sting aft of the supporting bearings. The pitch axis was 431.8 mm aft of the balance reference center. The pitch angle was obtained from the output of a linear encoder incorporated in the actuator.

5.2.4.3 CONING RIG

The coning rig is a unique orbital platform apparatus. Fig. 9 shows its installation in IAR water tunnel. An annular platform rode on the thinner outer surface of a stationary cylinder. This configuration resulted in minimal aerodynamic interference as the strong interference of support was eliminated by virtue of the absence of the rotating support arm which is inevitable in conventional rotary rigs. A 5-component internal balance supported the model and was connected to the annual platform. The model could be tested in static, quasi-steady coning or ramp-and-hold coning motions. The maximum coning rate was ± 0.6 . The Re number was in the order of 10^4 in the water tunnel.

5.2.4.4 RIGS IN STATIC TESTS

The rigs employed in static wind tunnel or water tunnel experiments were conventional sting type support with a five- or six-component internal balance.

5.2.5 EXPERIMENTAL TECHNIQUES

5.2.5.1 FLOW VISUALIZATION

Emphasis in flow visualisation was placed on the observation of the three-dimensional separated flow and, particularly, the vortical flow present on the leeward side of the model. Furthermore, surface oil flow visualisation was performed under static conditions which was extensively used to determine skin friction topology and its evolution as the attitudes (angle of attack, roll and sideslip angle, etc.) were changing.

In the roll experiments with laser-smoke sheet techniques, the flow was seeded with kerosene or Rosco fluid by a single vapor dispensing probe located approximately 1.5m and 2.3m upstream of the model apex at LSWT and SARL respectively. Under these conditions the plume diameter was approximately 6 - 8 cm at the impingement location, which was selected to maximise the visibility of the leading-edge vortices. A light sheet produced with a 15 W argon-ion laser oriented normal to the model axis was traversed to observe the flow at different model stations. Images were recorded with two cameras: a high speed video camera capable of recording at 1000 frames/sec and a Super VHS studio quality camera to produce better definition.

In the pitch experiments natural condensation was used to seed the flow in view of the large vertical displacement of the model apex. Likewise, the laser sheet orientation was selected to longitudinally intersect one leading-edge vortex core while being approximately normal to the wing surface.

Surface flow visualization was accomplished by means of mineral and/or silicone oils mixed with titanium dioxide. The viscosity of the mixture was tailored to optimize the observation of the desired features. Photographs were taken to capture the surface flow patterns during and after the wind tunnel runs. Videos were taken during the run to resolve some ambiguities regarding the direction of the flow.

The coning test and part of the geometry effect on vortex breakdown were conducted in water tunnel. Dye was injected from orifices with diameter of 0.39 mm located on both wing halves at 6.2% centerline chord. Flow visualization images were taken by two CCD cameras that provide a side and a rear view of the flow field.

5.2.5.2 UNSTEADY MEASUREMENTS

The dynamic data consist of forces, moments and surface pressures coherent with the model motion.

The signals of forces and moments are typically more or less contaminated by noise due to unsteadiness of dynamic test, which must be minimised in order to obtain representative results. This was done by taking ensemble averages of the signals over a number of motion periods which in turn required data sampling synchronous with the model motion. Hydraulic servo-valves of different capacities were used to generate the desired and more accurate motions over the large range of amplitudes and angular rates used. Tare measurements were done in air due to the impossibility of evacuating the wind tunnel.

Unsteady surface pressures were measured by means of 14 unsteady pressure transducers mounted on the leeward surface of the 65° delta wing at 0.75 root chord as shown in Fig. 3.

5.2.5.3 PSP AND PIV TECHNIQUES

The working principle of Pressure Sensitive Paint (PSP) is based on the photoluminescence of some molecules, which are dissolved in a polymer, being quenched by oxygen. The air pressure at the polymer surface determines the amount of oxygen in the film. As a result, the intensity emitted by the paint depends on the pressure at the paint surface. The advantage of PSP is that it provides the pressure data at any point where the surface is optically accessible. It is particularly useful for CFD validation where the results need to be assessed everywhere on the model. The usual graphical presentation of CFD results can thus be easily and globally compared to PSP measurements. However, at low speed flow conditions, special care in data acquisition and reduction has to be considered since the relative changes of intensity could be below the noise level of the intensity measurements or smaller than the effect of a temperature gradient on the model.

In Particle Image Velocimetry (PIV) measurements, a double frame/double exposure and cross-correlation method was used to record the traces and their local displacement. Different sizes of interrogation window and time period between the laser pulses were used to yield the best correlation results. Both global and local seeding methods were applied. For local seeding method, the local seeds were made of kerosene or Rosco fluid by means of a single vapor dispensing probe located approximately 1.5m upstream of the model apex in LSWT. While for global seeding method, an MDG water-base fog fluid was released downstream test section from a fog machine while the fan idled to help circulate the fog. When the tunnel was judged to have sufficient seeding particles, the wind speed was increased to achieve the desired wind speed.

5.2.5.4 FREE-TO-ROLL AND “FORCED” FREE-TO-ROLL OPERATION

In free-to-roll operation mode the model motion history was recorded with the sampling process being started by the clutch release command, thereby ensuring that the recorded signal covered the required time interval.

Given the impossibility of directly obtaining unsteady surface pressure data during free-to-roll motions, these pressure data were obtained in the forced motion mode by duplicating the model motion equal to that obtained under free-to-roll conditions. Unsteady pressure transducers mounted on the upper surface of the port wing half were used to obtain the instantaneous value of the pressures. The corresponding pressures on the starboard wing were inferred by conducting experiments with the same motion histories with roll angles of opposite sign.

5.3 SAMPLES OF EXPERIMENTAL RESULTS

The extensive database has been collected and edited into eight volumes and the data set will be accessible to authorised organisations through the web in the future. Here only few of some of the sample results are briefly described.

5.3.1 SURFACE FLOW VISUALIZATION

Varieties of mean surface flow topologies and evolutions have been observed as the governing parameter changes. As an example the evolution of the flow topology on 65° delta wing as a function of roll angle is shown from Fig. 10a to Fig. 10d. At very high model roll angles, the topology exhibits a concentrated leading edge vortex on the leeward wing half, characterised by the presence of one, two or three separation lines corresponding to the primary, secondary and tertiary vortices (Fig. 10a). At lower roll angles at least one whorl corresponding to a focus where the secondary or tertiary vortex lifts off the surface (Fig. 10b). Further reductions in roll angle results in the primary vortex breakdown moving on to the model creating the characteristic kink in the secondary separation line at the breakdown location (Fig. 10c). When the wing half under consideration is sufficiently to windward, and the primary vortex breakdown is near or at the apex, a variety of spiral or reverse patterns may develop (Fig. 10d). At extreme roll angles a

separation bubble develops destroying any discernible pattern. The evolution of correlating topology is shown in Fig. 11.

5.3.2 OFF SURFACE (LASER SMOKE SHEET AND PIV) FLOW VISUALIZATION

A bulk of the off-surface flow visualisation was performed to investigate vortex characteristics, including core diameter and location, its image brightness profile, vortex breakdown movement and unsteady behavior.

For 65° delta wing model, Fig. 12 shows the grey level profiles instantaneously taken from individual images through vortex core under oscillatory conditions at different model stations. For a given attitude the non-dimensional core diameter (diameter/local semi-span) in the intact part of the vortex has been found to be relatively constant, and the smaller this diameter the further aft breakdown occurs. Under rolling oscillations, the core diameter shrinks when the corresponding wing half moves to leeward (Fig. 13). Fig. 14 depicts the position of the vortex core as a function of roll angle, showing that the normal position of the core is essentially independent of roll angle and frequency suggesting that its response time is in the order of a convection time for 65° delta wing configuration. To compare with, the response of breakdown location is at least an order of magnitude longer. As examples Fig. 15 and Fig. 16 show the effect of oscillation frequency or amplitude on breakdown location respectively.

The unsteady behavior of the breakdown region, defined as the region between the first kink in the vortex filament (Point A) and breakdown to large scale turbulence (Point B) is also quite remarkable with different appearances (Fig. 17). Fig. 18 shows a sequence of frames separated by 4 ms or 1 ms. Point A is seen to move in excess of 20% centerline chord, whereas Point B remains virtually stationary. The speed of response of point A is found to be approximately $0.5U_{\infty} \cos\alpha$ on the basis of the consecutive pairs of images as seen in Fig. 18.

Under dynamic test conditions a deterministic motion of points A and B are superimposed to the above unsteady behavior. Significant time lags are present in the instantaneous positions of points A and B with respect to their corresponding average static locations. This lag is a function of the motion history leading up to the instant in question. Furthermore, the distance between points A and B increases and decreases relative to the steady value during pitch-up and pitch down motions respectively (Fig. 19).

The motion induced camber effect on vortex breakdown has been investigated. As an example Fig. 20a shows rolling motion induced quasi-steady camber effect on vortex breakdown by a deformed wing surface (Fig. 20b) which satisfies the simulation of quasi-steady condition at rolling motion. The motion induced camber effect delays vortex breakdown on rolling-down side while promote vortex breakdown on rolling-up side. Investigations on other motion plans were also conducted and can be found in Ref. 3.

The PIV measurements clearly show the field of velocity vector and vorticity vector over upper surface. As an example, Fig. 21 shows a preliminary result over a 65° delta wing. More post-processed figures can be found in the fellow-up reports (Ref. 3).

5.3.3 OFF SURFACE (DYE INJECTION) FLOW VISUALIZATION

Off surface flow visualisation in water tunnel was conducted by dye injection. To investigate the effects of leading-edge sweep back angle, leading-edge shape, centerbody and coning rate on the vortex behavior were the major tasks in the water tunnel experiments.

Fig. 22 shows the observed time-averaged vortex breakdown locations over various delta wings vs. angle of attack covering a sweep angle range of 55°~75°. These figures clearly show that the relationship between the time-averaged breakdown locations and angle of attack is smooth with increasing slope

toward the trailing edge. The increment of angles of attack for 75° delta wing is much smaller when vortex breaks down in the aft reflecting its faster movement at lower angles of attack. Nevertheless, the relationship between the vortex breakdown location and the angle of attack exhibits a continuous and parabolic behavior, which is, in principle, similar to those wings with smaller sweepback angles.

The effects of leading-edge shape, trailing edge shape and centerbody on vortex breakdown were also investigated and can be found in Ref. 3. The results about different leading-edge bevels suggest that the effectiveness of the leading-edge bevel is related to the ratio of its width to the thickness of the pre-separation boundary layer, which stands to reason that the bevel modifies the pressure gradient in the vicinity of the leading edge, thus influencing the vorticity generation. No significant effect of centerbody on vortex breakdown appears during the experiments.

The effect of motion induced quasi-steady camber effect on vortex breakdown during coning motion is shown in Fig. 23. Generally speaking, coning motion promotes the breakdown on advancing side of the wing while delays the breakdown on the receding side. Other than vortex breakdown location, the trajectory of vortex core is also affected as seen in Fig. 23.

5.3.4 FORCE AND MOMENT MEASUREMENTS

Static force and moment tests revealed the extremely non-linear nature of the aerodynamic airloads at high incidence. As an example, Fig. 24 shows the static rolling moment coefficient as a function of roll angle for different sting angles. At $\sigma=15^\circ$ there is only one roll stable point at $\phi=0^\circ$, whereas at $\sigma=30^\circ$ there are three trim points. Interestingly the attractor basin for the trim point at 0° is very small. For $\sigma=35^\circ$, the point at $\phi=0^\circ$ becomes unstable. Similar phenomena can be observed in coning motion as shown in Fig. 25. The rolling moment coefficient is mostly affected by the coning rate. When the angle of attack exceeds certain value, the rolling moment becomes nonlinear with unstable point at $\phi=0^\circ$. The results in pitch cases also exhibit similar behavior. As an example, Fig. 26 shows the normal force and pitching moment on a 55° diamond. The angles when the vortex breakdown is across the trailing edge or at the apex are also marked in these figures. It is clear that there are severe discontinuities appear at these two angles. It is found that the free stream speed and the leading-edge shape have noticeable effect on the angle where the discontinuity appears, especially for 55 wing as shown in Fig. 26.

Dynamic tests also revealed severe nonlinearities in airloads but they are quite different from static ones. As examples, Fig. 27 shows the rolling moment and normal force at different rolling frequencies and roll angle offset respectively. It should be noted that the unsteady effects are not only observed at moderate to high reduced angular rate ($\dot{\phi}$) but even at extremely low ones as shown in Fig. 28 where transient ramp-and-hold motion results between $\phi = \pm 16^\circ$ are depicted together with static ones for $\sigma = 30^\circ$. The dynamic loads agree closely with the static ones for $16^\circ > |\phi| > 12^\circ$. Elsewhere the dynamic loads overshoot the static values by increasing amounts depending on the reduced angular rate. As can be observed, even for non-dimensional rolling frequency $\dot{\phi} < 0.001$ a very distinct overshoot is present, which persists for most of the motion. However, the dynamic loads retain the "wiggle" present in the static case. These nonlinearities and differences from static ones are also observed in pitching cases as one example depicted in Fig. 29 during transient pitching maneuvers between $\alpha = 0^\circ$ and 60° .

The importance of vortex breakdown on the loads can also be observed in rolling cases as shown in Fig. 30. The rolling moment coefficient observed at different reduced frequencies is compared with a hypothetical steady value that assumes no breakdown on the leeward wing and breakdown at the apex on the windward one. The solid symbols indicate points on the oscillation cycle where the aforementioned hypothetical condition is met, whereas the clear symbols indicate that breakdown occurs over at least one of the two wing halves. It is immediately apparent that significant discrepancies between the two curves are present only in the latter case. From the above it follows that for the cases under consideration, the

steady value of the rolling moment is approximately applicable even under dynamic conditions provided that no breakdown is present on the wings.

5.3.5 SURFACE PRESSURE MEASUREMENTS

Surface pressure measurements include results from pressure taps, PSP measurements and unsteady pressure transducers obtained in either pitch or roll plan.

Pressure taps were applied to measure the surface pressure on models with different combinations (leading-edge shape, centerbody or faring, etc.). As examples measurements between with and without centerbody are shown in Fig. 31 for different angles of attack. It is noticed that only at higher angle of attack the centerbody causes more suction on the vicinity of nose area. There is no global effect is observed when the centerbody exists.

PSP provided profound pressure informations on 55° diamond wing, 55° delta wing and 65° delta wing with different leading-edge and centerbody conditions. The information provided by PSP is particularly useful for CFD validation where the results need to be assessed everywhere on the model. It is also very useful for investigating the geometry effect. As examples the surface pressure on different combinations of 65° delta wing, 55° diamond wing and 55° delta wing with different combinations (rounded or sharp leading-edge, with or without centerbody) are shown in Fig. 32 and Fig. 33. Compare with 65° delta wing the vortex core over 55° diamond or delta wing locates more close to the leading-edge. The results between 55° diamond wing and 55° delta wing exhibit that the location of vortex breakdown over diamond wing is aft of corresponding delta wing. The leading-edge shape has larger effect than that of 65° delta wing. For the sharp leading edge the leading edge vortex starts right at the apex. As examples Fig. 34 show the comparisons of section results from PSP plots between sharp leading-edge and round leading-edge as shown in Fig. 34. For the sharp leading-edge, the leading-edge vortex starts right at the apex (see left two graphics). While for the round leading-edge, the leading-edge vortex forms at almost 8% downstream of the apex. Moreover, the primary vortex orthemain suction over the wing with round leading-edge is more outboard compared with the wing with sharp leading edge. Furthermore, the secondary vortex is much weaker over the wing with round leading edge than that with sharp leading edge.

The unsteady surface pressures measured at static and dynamic model conditions provide important information about the spectra of the pressure, which indicates the footprint of the vortex and its breakdown. These data further confirm the fluctuations observed in the flow visualizations. As examples the results obtained on the 65° delta wing in pitch plan (either in static or dynamic) are presented from Fig. 35 to Fig. 44. More information about unsteady pressure measured of the two models in pitch, roll and free-to-roll conditions are included in Ref. 2.

The pressure measurements on the 65° delta wing under static model conditions at several typical angles of attack are shown in Fig. 35a to Fig. 35f for different angles of attack, e.g. 1) $\alpha=1^\circ$; 2) $\alpha=16^\circ$; 3) $\alpha=25^\circ$ and 29° ; 4) $\alpha=47^\circ$ and 5) $\alpha=51^\circ$, corresponding to different flow states: 1) no separation, 2) weakly vortex forming, 3) strong vortex and breakdown across the transducer, 4) strong reverse flow and 5) wake flow.

At $\alpha=1^\circ$ the signals from the pressure transducers shown in Fig. 35a can be taken as the back ground noise from the wind tunnel since there is no flow separation. When angle of attack increases to the second period ($\alpha=16^\circ$), there are clear peaks that appear at high frequencies and at the pressure transducers P3 to P5 as seen in Fig. 35b, indicating the existence of spiral vortex. Further increasing the angle of attack, results in the vortex breakdown location moving close to the transducers, and a fluctuation in the lower frequency band becomes obvious as illustrated in Fig. 35c to 35d for $\alpha=25^\circ$ and 29° respectively. These figures confirm the existence of a serious axial fluctuation in the vortex breakdown location as observed in

flow visualization experiments. When vortex breakdown is near the apex, the spiral and reverse flow remain alive until the flow becomes separated wake flow at even higher angles of attack. The corresponding pressure footprint can be found in Fig. 35e and 35f for $\alpha=47^\circ$ and 51° respectively. At $\alpha=47^\circ$ there are some remarkable pressure fluctuations at $f=18\text{Hz}$, corresponding to $St=0.84$. While at $\alpha=51^\circ$ this peak moves to a lower frequency, indicating a large-scale low frequency wake-like flow pattern.

Under dynamic conditions much more profound information about the unsteady pressure has been found. As examples, Fig. 36 to Fig. 41 show the unsteady pressure measurements, either in the time domain or in the frequency domain, at pitch-up or pitch-down conditions (α : $50^\circ \leftrightarrow 70^\circ$, $10^\circ \leftrightarrow 70^\circ$, $20^\circ \leftrightarrow 40^\circ$ and $30^\circ \leftrightarrow 40^\circ$).

Fig. 36 and Fig. 37 show the unsteady pressures during pitch-up (α : $50^\circ \rightarrow 70^\circ$) or pitch-down (α : $70^\circ \rightarrow 50^\circ$) respectively. The time period is 0.675sec. These pressure measurements are the simplest among the other test cases as there is no vortex breakdown and spiral flow involved. The pressures in the time domain show that there is neither a noticeable phase shift between the motion and the measured pressure nor phase shift between pressures obtained in different pressure transducers. The spectra show that there very little power other than that at the primary motion frequency.

Comparing the pressure footprints for the cases when there is a simple vortex, vortex breakdown, or spiral flow appears, is much more complex. Fig. 38 and Fig. 39 show the unsteady pressures at pitch-up (α : $10^\circ \rightarrow 70^\circ$) or pitch-down (α : $70^\circ \rightarrow 10^\circ$) respectively at $\Delta t=0.675$ sec. The results in time domain show that the pressure response functions at each pressure transducer are quite different. Also there are quite significant phase shifts between the different pressure transducers, indicating there exists a spanwise wave in pressure. The spectra shown in Fig. 39b exhibit that, in addition to the primary motion, the axial and spanwise fluctuation of the vortex and its breakdown location may result in a noticeable power density at higher frequencies.

The above complex spectral and spanwise phase shift become even vigorous when the vortex and its breakdown occupy the major period of the motion. As examples Fig. 40 and Fig. 41 show the unsteady pressure spectra and time histories measured at each pressure transducer for pitch-up (α : $20^\circ \rightarrow 40^\circ$) or pitch-down (α : $40^\circ \rightarrow 20^\circ$) respectively at $\Delta t=0.675$ sec. In the time domain there are almost opposite pressure response functions between pressures at transducers P1 to P3 and P4 to P6, while the pressure response function in P7 takes another shape. These figures clearly demonstrate that the vortex and its breakdown will result in a much stronger spanwise wave compare with the case that no vortex or vortex breakdown is involved.

In addition to spectral information, the moving average of the results in time dominie during dynamic model condition, either in roll or in pitch motion, shows the dynamic correlation between the pressure and the motion. As an example, Fig. 41 shows plots and contours of the pressure coefficient as a function of roll angle for non-dimensional rolling frequency $k=0$ and 0.14 respectively. The spanwise stations of those pressure transducers are indicated in Fig. 3. The first plot in Fig. 42 depicts static data plotted according to a fictitious sinusoidal roll motion. The maximum suction, corresponding to the condition when the leading edge vortex is strongest over the instrumented model station, occurs at $\phi \approx 5^\circ$ where $C_p = -1.8$. The second plot shows the case that the model was oscillated with an amplitude of 40° at $k=0.14$. Here the maximum suction has increased considerably ($C_p = -2.5$) and has shifted to $\phi \approx 30^\circ$ where the wing is on the windward side during the downstroke. The features in the two plots are quite different, demonstrating the dramatic impact of dynamic effects. In pitch case, the surface pressures at the seven transducers on the port wing half with the corresponding motion in Fig. 19 are shown in Fig. 43. The static ones are superimposed. These characteristics consistent with that of vortex breakdown movement and normal force (Fig. 19 and Fig. 30) and provide good correlation between vortex breakdown, normal

force and surface pressure in dynamic situation. The unsteady pressure during free-to-roll motion was measured by a duplicated free-to-roll operation mode or “forced” free-to-roll mode. As an example, Fig 44 shows the changes of surface pressure during free-to-roll motion when the model was released from $\phi = 64^\circ$. The corresponding free-to-roll motion history is described in the following section.

5.3.6 FREE-TO-ROLL EXPERIMENTS

In free-to-roll experiments, the 65° and $65^\circ/80^\circ$ models were release from different roll angles at different angles of attack. One of the early findings of the program was the presence of multiple roll trim points (attractors), a phenomenon not previously observed. Fig. 45 depicts four free-to-roll motion histories in the phase plane. It is interesting that the 65° delta wing at $\sigma = 30^\circ$ consistently trims at $\phi = 0$ for $2^\circ > \phi_i > 60^\circ$. For other values of the initial roll angle, the model trims at $\pm 21^\circ$ depending on the sign of the initial angle. The presence of intersections between the trajectories clearly indicates that the rolling moment does not only depend on the instantaneous roll angle and angular rate but is dramatically affected by the motion history.

5.3.7 FOREBODY/WING/TAIL RESULTS

As expected, the addition of a forebody has an important impact on the flow, specifically, the presence of forebody vortices and their interaction with the leading-edge ones result in very substantial changes of the airloads at moderate to high angles of attack. As no attempt was made to fix transition on the forebody, an erratic behavior of the static loads was observed which is contrary to the case of the delta wing that separation is well defined at the sharp leading edge. Fig. 46 depicts the loads observed at several runs for $\sigma = 30^\circ$. Most of the scatter occurs at small roll angles although it is present everywhere to a lesser extent. The loads are not symmetrical (or anti-symmetrical) about the origin due to the asymmetric forebody vortex shedding, which as suggested by the load discontinuities switch position at $\phi \sim -8^\circ$. Tests could not be performed near the above roll angle as potentially damaging, rapidly diverging lateral oscillations of the sting were induced. The large oscillation amplitude suggests that a positive feedback results from the coupling between the forebody vortex switching and model motion.

5.4 CONCLUSIONS

The data sets cover wide areas. It is one of the most completed and comprehensive data set about vortex dynamics over military wing configurations.

There are numerous findings in these data sets, which are important and valuable.

It is not only valuable for validation and verification of current CFD solutions but especially valuable for validation and verification of future CFD solutions as so many unsteady and detail information provided.

As the data sets have been edited in a consistent and user-friendly format, it will be very convenient for the users in their applications.

5.5 REFERENCES

- [1] Hanff, E.S., and Jenkins, S., "Large-Amplitude High-Rate Rolling Experiments on a Delta and Double Delta Wing," AIAA Paper 90-0224, Jan. 1990.
- [2] Hanff, E.S., Jenkins, J.E., Huang, X.Z., Myatt, J.H. and Addington, G.A., "Highlights of the NRC/USAF/DND Joint Program on Manoeuvring Aerodynamics", *Canadian Aeronautics and Space Journal*, September 2001, Volume 47, No. 3.
- [3] Huang, X., "IAR program on maneuvering aerodynamics over military wing configurations", To be published in 2005.

APPENDIX – BRIEFING OF IAR PROGRAM

GENERAL DESCRIPTION OF THE MODELS

Designation	IAR Military Wing Program
Wind tunnel/water tunnel entries	See Table 1
Type	Full model
Reference	Ref. 1, 2, 3

MODEL GEOMETRY (more than 50 types of models tested see Fig. 1 in [1])

IAR and IAR/AFRL 65° delta wings (wind tunnel models)	see table 2 for detail
IAR 55° diamond wings and 55° delta wings (wind tunnel models)	see table 2 for detail
IAR/AFRL80/65 double delta wings (wind tunnel models)	see table 2 for detail
IAR/AFRL 65° wing/body/tail configurations (wind tunnel models)	see table 2 for detail
IAR 55° and 65° delta wings (water tunnel models in coning tests)	see table 2 for detail
IAR 50°~75° delta wings (water tunnel models)	see table 2 for detail

WIND TUNNELS/WATER TUNNEL

LSWT wind tunnel (IAR)	
Type of tunnel	Close-circuit atmospheric type
Test section dimensions	Height: 6 ft, width: 9ft, length: 15 ft
Maximum speed	390 ft/sec
Contraction ratio	9
Turbulence in empty tunnel	$\leq 0.12\%$ at free stream speed of 100 ft/sec
Type of side walls	Solid with large optical quality plexiglass windows
Type of roof	Solid with large optical quality plexiglass windows
Support	Sting attached to wind tunnel strut (Fig. 2)
Tunnel resonance	No evidence of resonance in present test
Reference	Ref. 2
SARL wind tunnel (AFRL)	
Type of tunnel	Open-circuit atmospheric type
Test section dimensions	Height 10 ft, width 7ft, length: 15 ft
Maximum speed	660 ft/sec
Contraction ratio	36
Turbulence in empty tunnel	$\leq 0.1\%$
Type of side walls	Solid with large optical quality plexiglass windows
Type of roof	Solid with large optical quality plexiglass windows
Support	Sting installed on quadrant (Fig. 2)
Tunnel resonance	No evidence of resonance in present test
Reference	Ref. 3
IAR water tunnel (Eidetics)	
Type of tunnel	Close-circuit with open-test section and vertical return
Test section dimensions	Height 20 in., width 15in and length 6 ft
Maximum speed	1 ft/sec
Contraction ratio	6:1
Turbulence intensity level	$\leq 1\%$
Velocity uniformity	$\leq \pm 2\%$
Mean flow angularity	$\leq \pm 1^\circ$ in both pitch and yaw angle
Type of side walls	Large optical quality plexiglass windows
Support	OPLEC or sting installed on quadrant (Fig. 2)
Reference	Ref. 4

MODEL MOTION

Motion plan	Pitch, roll and coning plans
General description of the motions	Rolling about body axis

	Pitching about an axis downstream of the reference centre
	Coning about balance reference centre
Motion waveforms	Static
	Sinusoid oscillation in roll and in pitch
	Ramp-and-hold:
	Constant velocity
	Constant acceleration at both ends
	Only constant acceleration at both ends (double parabola)
	Quasi-steady in coning
	Free-to-roll
Motion parameters	
Maximum oscillation amplitude	$\Delta\sigma=90^\circ$ in pitch, $\Delta\phi=40^\circ$ in roll and $\Delta\Omega=360^\circ$ in coning
Maximum mean angle	$\phi_0 = \pm 50^\circ$ in roll, $\sigma_0=0^\circ\sim 90^\circ$ in pitch and $\Omega_0=360^\circ$ in coning
Maximum non-dimensional frequency	$\varpi=0.2$ in pitching and rolling oscillation and $\ddot{\Omega}=0.6$ in coning
Maximum of angular rate in pitch and roll	4500 °/sec
Maximum of angular acceleration	500,000 °/sec ²
Maximum initial roll angle in free-to-roll	90°
Tare friction in free-to-roll	Approximately constant (independent of rate)
Mechanical Inertial in free-to roll	0.15 lbs-in-sec ²
Method of applying motion	Inexorable hydraulic system in pitching and rolling motions
	OPLEC system in coning motion
Motion precision	0.175° in roll and pitch, 0.1° in coning
Sting angle precision	0.1°

TEST CONDITIONS

Maximum model planform area/tunnel area	0.0296 (SARL)
	0.0357 (LSWT)
	0.1286 (water tunnel)
Maximum model span/tunnel width	0.272 (SARL) and 0.4 (water tunnel)
Maximum model span/tunnel height	0.300 (LSWT)
Maximum model root-chord/ tunnel-height	0.204 (SARL)
Maximum model root- chord/ tunnel-width	0.227 (LSWT)
Maximum blockage at $\alpha=30^\circ$	0.0148 (SARL)
	0.0179 (LSWT)
	0.074 (water tunnel)
Position of model in tunnel	Standard side position (LSWT)
	Standard upright position (SARL)
	Standard downright position in static test (Water tunnel)
Range of wind tunnel total pressure	Atmospheric (SARL)
	Atmospheric static pressure (LSWT)
Definition of model sting angle	Angle between body axis and tunnel axis

MEASUREMENTS

Surface skin friction and topology	Oil flow	✓
Off-surface flow visualization and topology	Laser-smoke sheet	✓
Vortex core location and diameter		✓
Vortex breakdown locations		✓
Off-surface flow field	PIV measurements	✓
Steady pressure in static conditions	pressure taps	✓
Steady pressure in static conditions	PSP measurements	✓
Steady pressures in static conditions	pressure transducers	✓
Unsteady pressures in static conditions	pressure transducers	✓
Unsteady pressures in dynamic conditions	pressure transducers	✓
Steady forces in static conditions	Measured directly	✓
	Integrated pressure	✓
Unsteady forces in dynamic conditions	Measured directly	✓

Measurement of actual motion of model	✓
Measurement of free-to-roll motion history	✓
Wind tunnel interference assessment	✓
Support interference assessment	✓

INSTRUMENTATION

Pressure transducers	
Type of transducers	Kulite pressure transducers (LQ-47-25A) with “B” screen
	Operation mode Absolute
	Sensitivity range: 3.21~4.46 mv/psi.
	Zero pressure output: $<\pm 5\%$ full scale
Position of transducers	See Fig. 1
Installation of transducers	Using RTV adhesive flush ($\begin{smallmatrix} 0.000 \\ -0.005 \end{smallmatrix}$) to upper surface. Fill trough with clear epoxy filler fair to upper surface.
Principle and accuracy of calibration	Kulite: static calibration at beginning of tunnel entry, offset measurement every 30 minutes.
Position of orifices	See Fig. 1
Pressure sensitive paint (PSP)	
Calibration method	Both <i>in situ calibration</i> and <i>a priori</i> calibration methods were used for 65° delta wing while only <i>a priori</i> calibration method with a constant temperature assumption was used for 55° diamond and delta wing.
Position of thermocouples	only on 65° delta wing, See Fig. 1
Position of pressure taps	See Fig. 1.
Pressure taps	
Number of pressure taps and thermocouple	57 taps on 65° delta wing, 3 taps on canter body of 55° diamond and delta wings, 2 thermocouples on 65° delta wing
Position of taps and thermocouple	See Fig. 1
Diameter of pressure taps and thermocouple	0.032 in.
Steady loads (Internal balance 1)	Used in SARL and LSWT wind tunnel
Type of transducers	Strain gauge
Type of measuring system	Five components balance with maximum range:
	Normal force N=2,000 lbs
	Side force Y=1,000 lbs
	Rolling moment $\ell=3,000$ lbs-in
Method and accuracy of calibration	Maximum and relative deviations:
	Normal force $\Delta N_{\max}=\pm 2$ lbs, $\delta N_{\max}=0.1\%$
	Pitch moment $\Delta \mu_{\max}=\pm 5$ lbs-in ($\Delta x_{\max}=0.005$ in)
	Side force $\Delta Y_{\max}=\pm 2$ lbs, $\delta Y_{\max}=0.1\%$
	Yawing moment $\Delta v_{\max}=\pm 5$ lbs-in ($\Delta y_{\max}=0.005$ in)
	Rolling moment $\Delta \ell_{\max}=\pm 6$ lbs-in $\delta C_{\ell_{\max}}=0.2\%$
Steady loads (Internal balance 2)	Able Corporation 1” MKXXII B six-component balance
Type of transducers	Strain gauge
Type of measuring system	Six components balance with maximum range:
	Normal force N=950 lbs
	Side force Y=600 lbs
	Axial force X=120 lbs
	Rolling moment $\ell=350$ lbs-in
	Pitching moment m=1,900 lbs-in
	Yawing moment n=990 lbs-in
	Accuracy 0.25% of maximum load in any series of loading of a single element or 0.5% compared with the best straight line fit.

Interactions	Seventy percent of the possible first order interactions are $\leq 0.5\%$. An additional 20% of the first order interactions are $\leq 1\%$. The remaining 10% of the first order interactions are $\leq 3\%$. All interactions in excess of 1% are linear within $\pm 10\%$ of the interaction output.
Steady loads (Internal balance 3)	Used in IAR 1520 water tunnel
Type of transducers	Strain gauge with diameter 7/16 in and length of 2.7 in.
Type of measuring system	Five components balance with maximum range: Normal force: N=14 lbs Side force Y=1.75 lbs Pitching moment m=7 lbs-in. Yawing moment n=1.75 lbs-in. Rolling moment ℓ =3 lbs-in.
Calibration loading	Normal force 0.44 lbs Side force 0.22 lbs Torque 0.3 lbs-in.
Resolution	1% of maximum calibration load
Sensitivities	N=3.07 mv/lbs S=24.53 mv/lbs m=6.16 mv/lbs-in. n=24.4 mv/lbs-in ℓ =11.5mv/lbs-in
Unsteady loads	
Type of transducers	Internal balance 1
Measurement method	Ensemble average of coherent samples over several cycles
Method and accuracy of calibration	
Model motion	
Method of measurement	Angular encoder on drive shaft aft end
Accuracy	$\pm 0.1^\circ$
Sting acceleration (horiz. and vert.)	Accelerometer EGA-125*-10D Non-linearity: $\pm 1\%$ Range: ± 10 g Limit: ± 50 g Them.Z $\pm 1\%FS/100^\circ F$ TSS $\pm 2.5\% / 100^\circ F$
Processing of unsteady loads	
Pressure signal conditioning system	See Fig. 11 (up to 1991) and Fig. 12
Loads signal conditioning system	See Fig. 11 (up to 1991) and Fig. 12
Processing data	Ensemble average over more than 30 (harmonic motion), or 9 cycles (ramp-and-hold motion)
PIV measurement	
Seeding	Local seeding and global seeding method
Data acquisition	Cross-correlation method

Table 1 Wind tunnel and water tunnel entries

Year	Tunnel	Configuration	Motion	Measurements
1989	IAR 6x9 LSWT	IAR/AFRL 65° delta wing IAR/UFRL 85°/65° double delta wing	Roll Free-to-roll	Surface flow Laser sheet smoke Motion history Unsteady loads Unsteady pressure
1990	IAR 6x9 LSWT	IAR/AFRL 65° delta wing	Roll Free-to-roll	Surface flow Laser sheet smoke Motion history Unsteady loads Unsteady pressure
1991	USAF/AFRL/SARL 7x10 wind tunnel	IAR/AFRL 65° delta wing	Roll Free-to-roll	Surface flow Laser sheet smoke Motion history Unsteady loads Unsteady pressure
1993 summer	USAF/AFRL/SARL 7x10 wind tunnel	IAR/AFRL 65° delta wing	Static in roll and pitch	Surface flow Laser sheet smoke Static loads
1993 Fall	USAF/AFRL/SARL 7x10 wind tunnel	IAR/AFRL 65° delta wing IAR/AFRL 65° delta wing/Forebody/Tail	Pitch	Surface flow Laser sheet smoke Motion history Unsteady loads Unsteady pressure
1994	USAF/AFRL/SARL 7x10 wind tunnel	IAR/AFRL 65° delta wing IAR/AFRL 65° delta wing/Forebody/Tail	Roll	Surface flow Laser sheet smoke Motion history Unsteady loads Unsteady pressure
1995	IAR 6x9 LSWT	IAR 65° deformed delta wing	Roll induced camber	Laser sheet smoke
1996~1997	IAR 15x20 Water tunnel	IAR 50°~79° delta wings	Static in roll and pitch	Off-surface flow vis. Geometry effect Reynolds number's effect
1998~1999	IAR 15x20 Water tunnel	IAR 65°, 70° delta wings	Static in pitch	Off-surface flow vis. Active vortex control
2000	IAR 15x20 Water tunnel	IAR 55°, 65° delta wings	Coning	Off-surface flow vis. Static/quasi static loads
2001	IAR 15x20 Water tunnel	IAR 65°, 70° delta wings	Static in pitch	Off-surface flow vis. Active vortex control
2002	IAR 6x9 LSWT	IAR 65° delta wings	Static in roll and pitch	Surface flow Laser sheet smoke PSP PIV Static loads Static pressure Reynolds number's effect Geometry effect

Table 1 Wind tunnel and water tunnel entries (Cont.)

Year	Tunnel	Configuration	Motion	Measurements
2003	IAR 6x9 LSWT	IAR 55° diamond wing IAR 55° delta wings IAR 65° delta wings		Surface flow Laser sheet smoke PSP PIV Static loads Static pressure Reynolds number's effect Geometry effect

Table 2 Wind/water tunnel models tested

Table 2a IAR/USAF wind tunnel models

Name	IAR/USAF 65° delta wing	IAR/USAF 80°/65° delta wing	IAR/USAF 65° delta wing/body/tail
Planform	65° delta wing	80°/65° delta wing	65° delta wing
Leading-edge sweep	65°	80°/65°	65°
Trailing edge sweep	0°	0°	0°
Span	22.835 in.	22.835 in.	22.835 in.
Root chord	24.485 in.	30.310 in.	24.485 in.
Area of planform	279.49 in ²	289.11 in ²	279.49 in ²
Twist	0	0	0
Leading-edge shape	10° bevel on both sides	10° bevel on both sides	10° bevel on both sides
Leading-edge radius	0.02 in.	0.02 in.	0.02 in
Tolerance of leading-edge radius	±10%	±10%	±10%
Trailing edge shape	10° bevel on both sides	10° bevel on both sides	10° bevel on both sides
Mean aerodynamic chord	16.323 in.	17.466 in.	16.323 in.
Thickness of wing	0.375 in.	0.375 in.	0.375 in.
Tail leading-edge			40°
Tail height			5 in
Reference center	10.610 in. upstream of the trailing edge	10.610 in. upstream of the trailing edge	10.610 in. upstream of the trailing edge
Center-body	yes	yes	yes
Center-body diameter	3.150 in.	3.150 in.	3.150 in.
Forebody shape	$r = \sqrt{24.103^2 - (12.243 - x)^2} - 22.528$	$r = \sqrt{24.103^2 - (12.243 - x)^2} - 22.528$	$r = \sqrt{63.0097^2 - (26.485 - x)^2} - 61.434$
Model material	Composite	Composite	Composite
Instrumentation	14 unsteady pressure transducers	14 unsteady pressure transducers	14 unsteady pressure transducers

Table 2b IAR wind tunnel models

Name	IAR 65° delta wing	IAR 55° diamond wing	IAR 55° delta wing
Planform	65° delta wing	55° diamond wing	55° delta wing
Leading-edge sweep	65°	55°	55°
Trailing edge sweep	0°	30°	0°
Span	22.835 in.	22.835 in.	22.835 in.
Root chord	24.485 in.	22.90 in.	16.300 in.
Area of planform	279.49 in ²	249.30	186.14 in ²
Configurations	10° bevel (B), body, fairing (3E)	large radius, r ₀ =0.046 in. (1A)	large radius, r ₀ =0.046 in. (2A)
	10° bevel (B), body, no windward fairing (3D)	small radius, r ₀ =0.023 in. (1B)	small radius, r ₀ =0.023 in. (2B)
	10° bevel (B), body, no leeward fairing (3C)	bevel on both sides (1C)	30° bevel (B) (2C)
	10° bevel (B), body, no fairing (3B)	30° bevel (W), flat leeward (1D)	30° bevel (W), flat leeward (2D)
	10° bevel (B), no leeward body and fairing (3AU)	30° bevel (W), flat leeward, no leeward body (1F)	30° bevel (W), flat leeward, no leeward body (2F)
	10° bevel (B), no leeward body, no fairing (3U)	30° bevel (L), flat windward (1E)	30° bevel (L), flat windward (2E)
	10° bevel (W), body, fairing (2E)	30° bevel (B), no leeward body (1G)	30° bevel (B), no leeward body (2G)
	10° bevel (W), body, no windward fairing (2D)		large radius, r ₀ =0.046 in., no aft body (3A)
	10° bevel (W), body, no leeward fairing (2C)		small radius, r ₀ =0.033 in., no aft body (3B)
	10° bevel (W), body, no fairing (2B)		bevel on both sides, no aft body (3C)
	10° bevel (W), no leeward body and fairing (2AU)		flat leeward, 30° bevel (W), no aft body (3D)
	10° bevel (W), no leeward body, no fairing (2U)		flat leeward, 30° bevel (W) no leeward body, no aft body (3F)
	10° bevel (L), body, fairing (1E)		flat windward, 30° bevel (L), no aft body (3E)
	10° bevel (L), body, no leeward fairing (1D)		30° bevel (B), no leeward body and aft body (3G)
	10° bevel (L), body, no leeward fairing (1C)		
	10° bevel (L), body, no fairing (1B)		
	10° bevel (L), no leeward body and fairing (1AU)		
	10° bevel (L), no leeward body, no fairing (1U)		
MAC	16.323 in.	15.261 in.	16.323 in.
Wing thickness	0.375 in.	0.375 in.	0.375 in.
Reference center	10.610 in. upstream of the trailing edge	10.610 in. upstream of the trailing edge	10.610 in. upstream of the trailing edge
Center-body diameter	3.150 in.	3.150 in.	3.150 in.
Forebody shape	$r = \sqrt{24.103^2 - (12.243 - x)^2} - 22.528$	$r = \sqrt{24.103^2 - (12.243 - x)^2} - 22.528$	$r = \sqrt{24.103^2 - (12.243 - x)^2} - 22.528$
Aft body shape		$r = \sqrt{9^2 - x^2} - 7.612$	$r = \sqrt{9^2 - x^2} - 7.612$
Model material	PVC(Upper) Stainless steel (lower)	Aluminum alloy	Aluminum alloy
Instrumentation	PSP, 57 pressure taps six-component balance	PSP, pressure taps, six-component balance	PSP, pressure taps, six-component balance

Table 2c IAR water tunnel models

Name	water tunnel 55° delta wing	water tunnel 65° delta wing used in coning motion	water tunnel delta wing models
Planform	55° delta wing	65° delta wing	Delta wings
Leading-edge sweep	55°	65°	55°, 60°, 65°, 67°, 69°, 70°, 71°, 75°
Trailing edge sweep	0°	0°	0°
Span	6 in.	6 in.	4.66 in., 4.24 in., 3.83 in., 3.64 in., 3.44 in., 2.68
Root chord	4.28 in.	6.433 in.	3.33 in, 4.04 in., 5 in.
Area of planform	12.85 in ²	19.30 in ²	from 6.698 in ² to 11.657 in ²
Twist	0	0°	0°
Leeward leading-edge shape	flat(L) 15° bevel (W)	10° bevel (B)	flat, 10° bevel, 30° bevel, 45° bevel
trailing edge shape	flat(L) 15° bevel (W)	10° bevel (B)	flat, 10° bevel, 30° bevel, 45° bevel
Mean aerodynamic chord	2.856 in	4.2887 in	from 2.22 in to 3.333 in
Thickness of flat area	0.375 in.	0.099 in.	0.04 in., 0.08 in., 0.37 in. in.
Reference center	10.610 in. upstream of the trailing edge	2.787 in. upstream of the trailing edge	
Center-body diameter	0.821 in.	0.821 in.	0.821 in. (65° delta wing only)
Forebody shape	$r = \sqrt{6.380^2 - (1.275 - x)^2} - 5.970$	$r = \sqrt{6.380^2 - (3.224 - x)^2} - 5.970$	$r = \sqrt{6.380^2 - (3.224 - x)^2} - 5.970$ 65° delta wing only
Tolerance of leading-edge radius	±10%	±10%	±10%
Model material	Aluminum alloy	Aluminum alloy	Aluminum alloy
Instrumentation	5-component balance and 2 dye orifices	5-component balance and 2 dye orifices	2 dye orifices

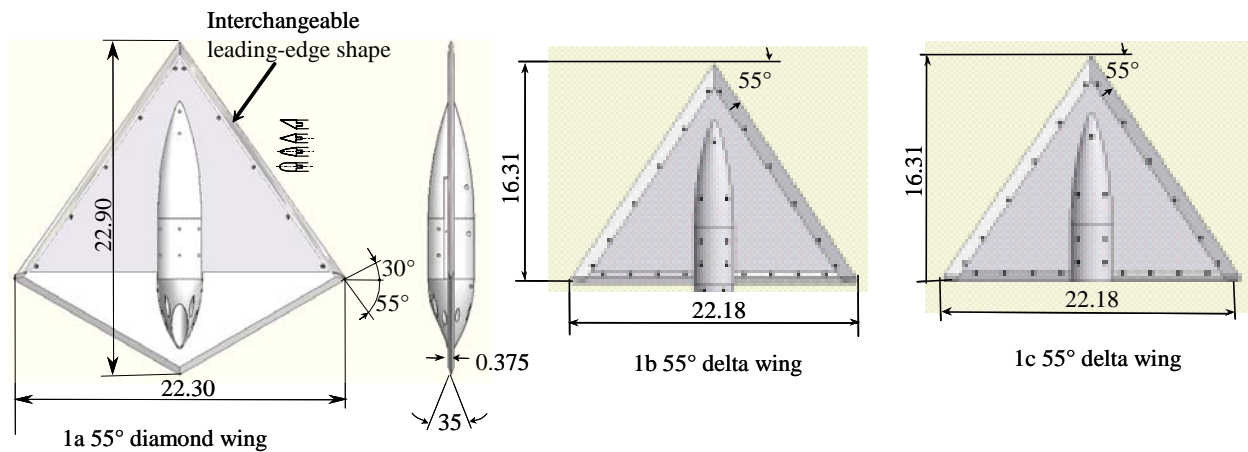


Fig 1 IAR 55° diamond wing and delta wing model with interchangeable leading-edges

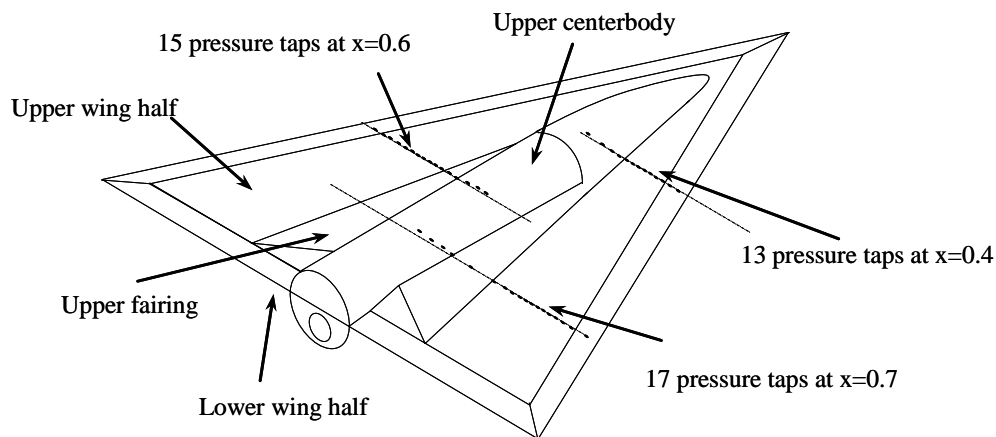


Fig. 2a IAR 65° delta wing model with interchangeable parts

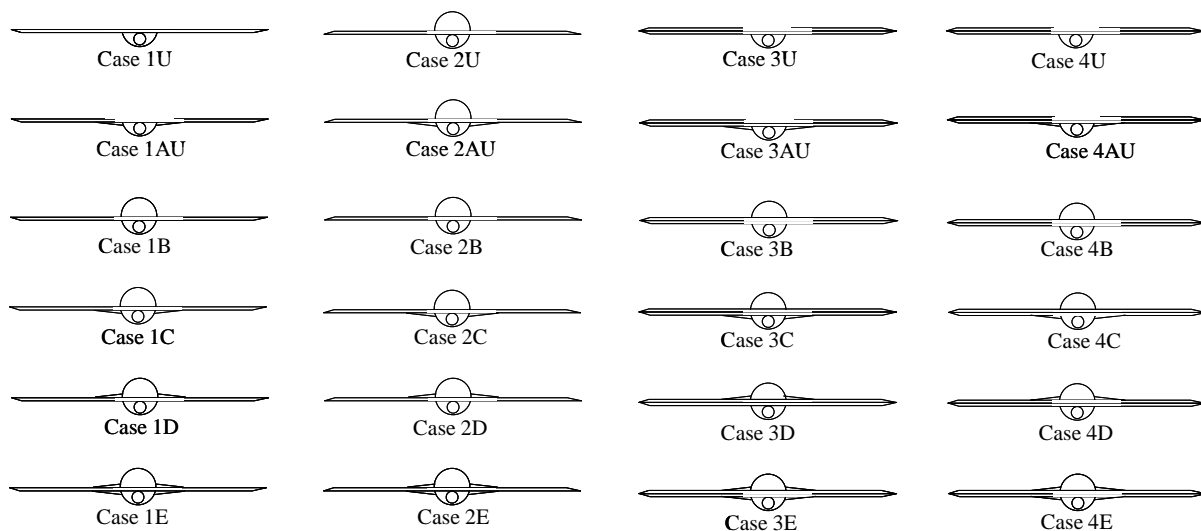


Fig. 2b Combinations of IAR 65° delta wing models with interchangeable centerbody and leading-edge

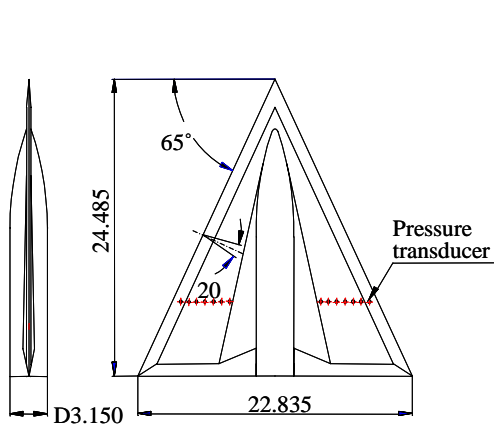


Fig. 3 IAR/AFRL 65° delta wing model

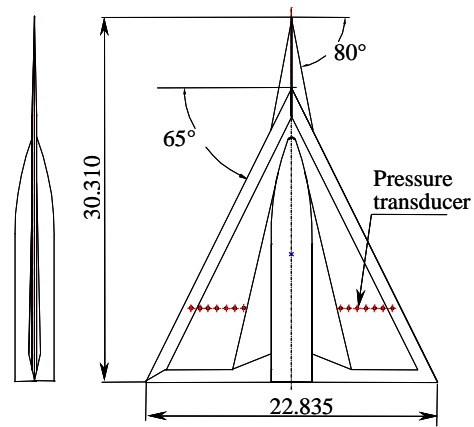


Fig. 4 IAR/AFRL 80°/65° double delta wing model

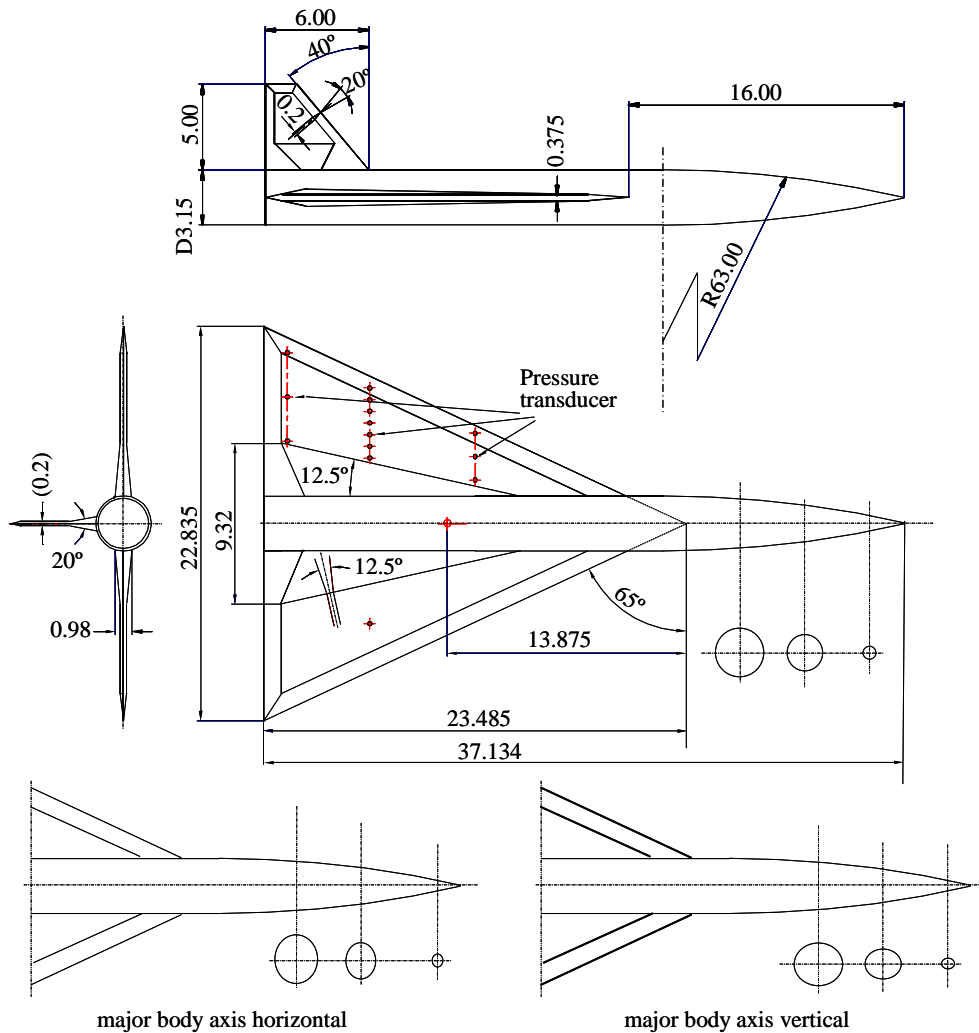


Fig. 5 IAR/AFRL 65° wing/body/tail model

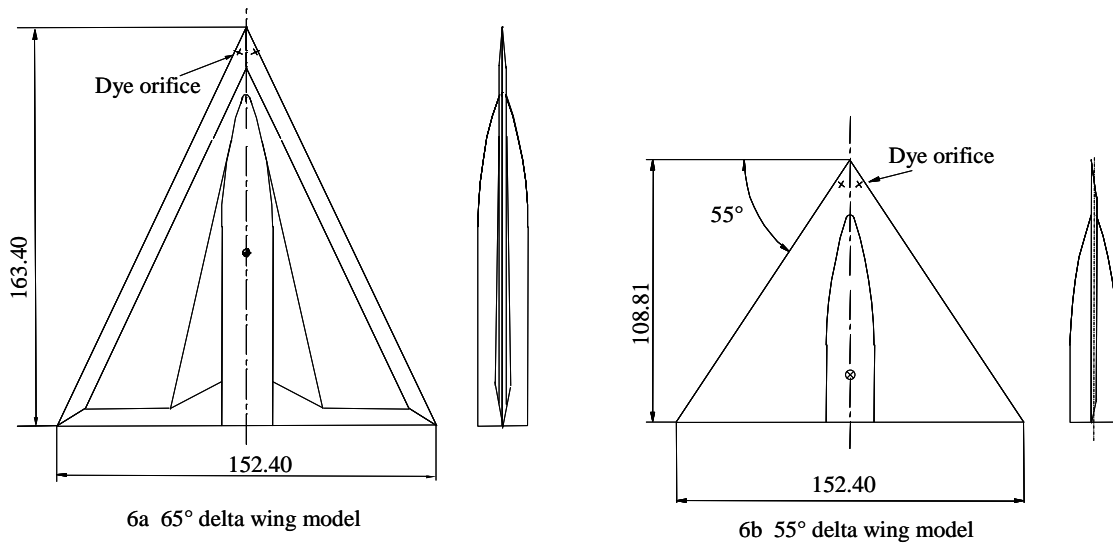


Fig. 6 IAR water tunnel 65° and 55° delta wing models

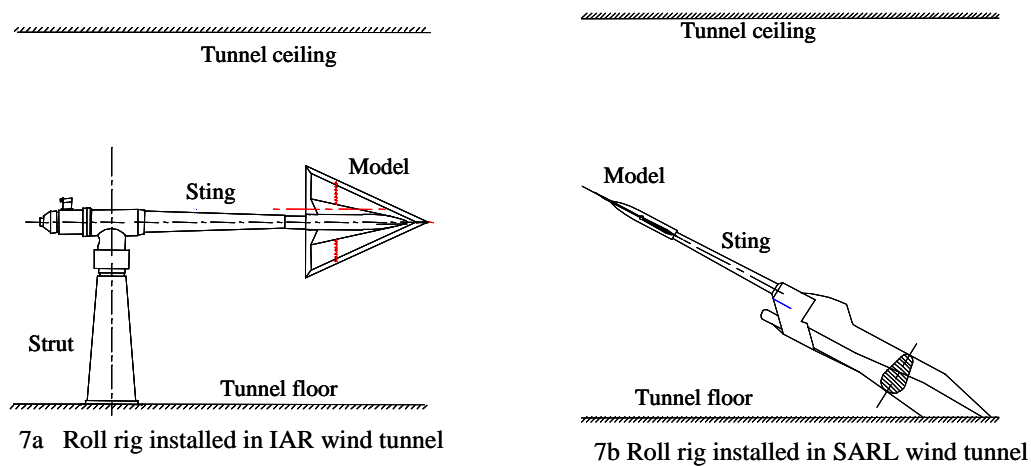
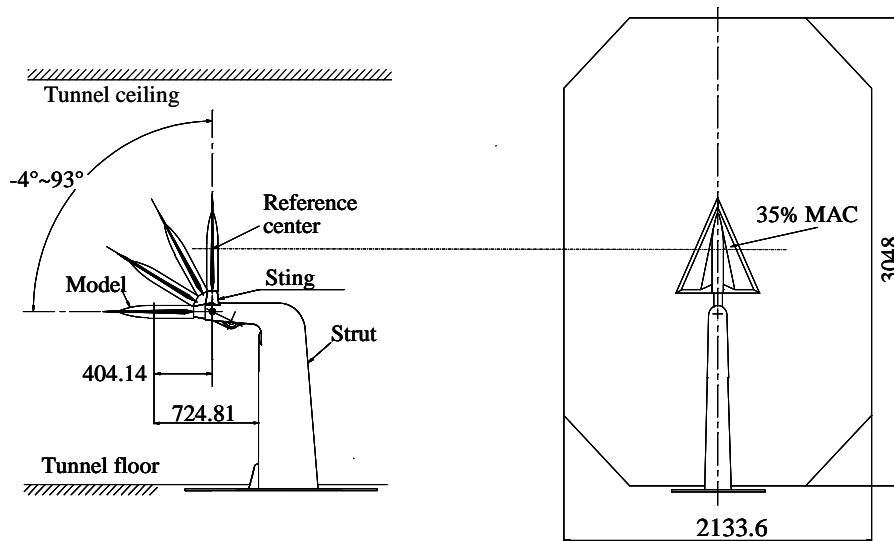


Fig. 7 Roll rig in IAR and SARL wind tunnels



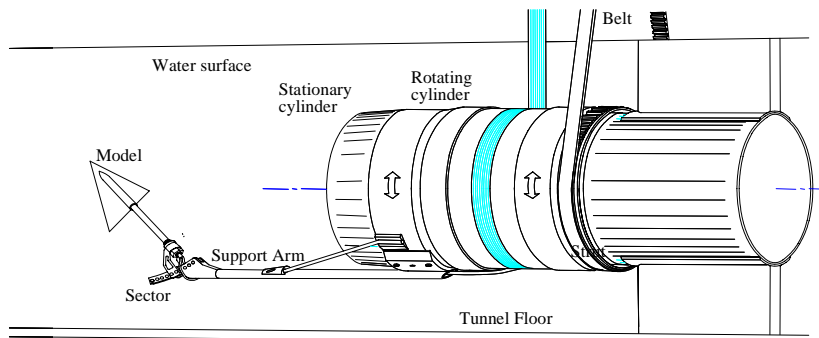
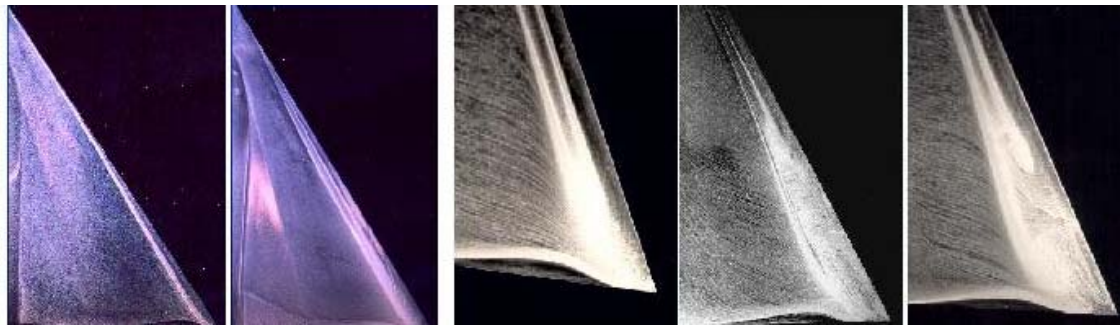


Fig. 9 OPLEC Coning rig in IAR water tunnel



$\sigma=30^\circ, \phi=-28^\circ$

$\sigma=30^\circ, \phi=-16^\circ$

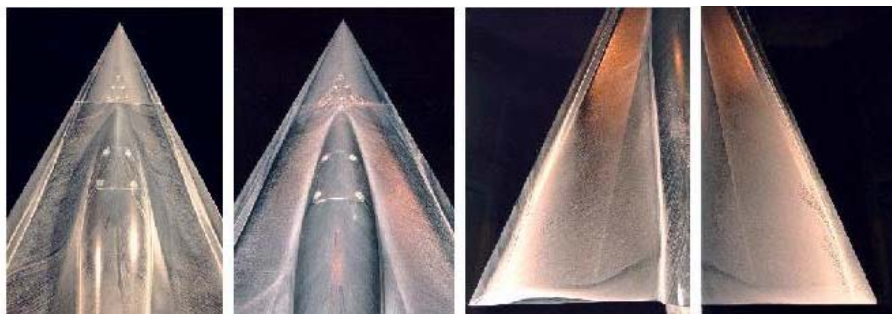
$\sigma=30^\circ, \phi=-14^\circ$

$\sigma=30^\circ, \phi=-7^\circ$

$\sigma=30^\circ, \phi=-4.6^\circ$

10a concentrated vortex pattern

10b vortex "whorl" pattern



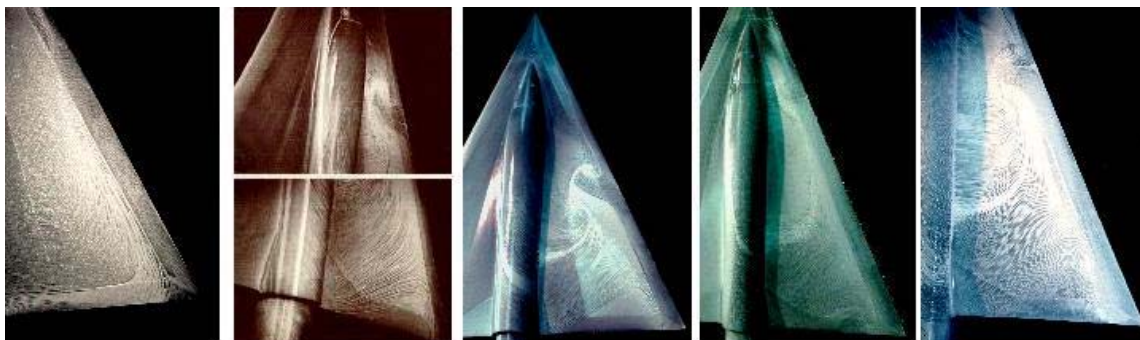
$\sigma=30^\circ, \phi=0^\circ$

$\sigma=35^\circ, \phi=2.5^\circ$

$\sigma=35^\circ, \phi=2.5^\circ$

$\sigma=35^\circ, \phi=2.5^\circ$

10c vortex bursting patterns observed on different wing areas



$\sigma=30^\circ, \phi=14^\circ$

$\sigma=30^\circ, \phi=47^\circ$

$\sigma=30^\circ, \phi=51^\circ$

$\sigma=35^\circ, \phi=59^\circ$

$\sigma=35^\circ, \phi=62^\circ$

10d reversed flow patterns observed on windward wing half

Fig. 10 Skin friction topologies on 65° delta wing in roll

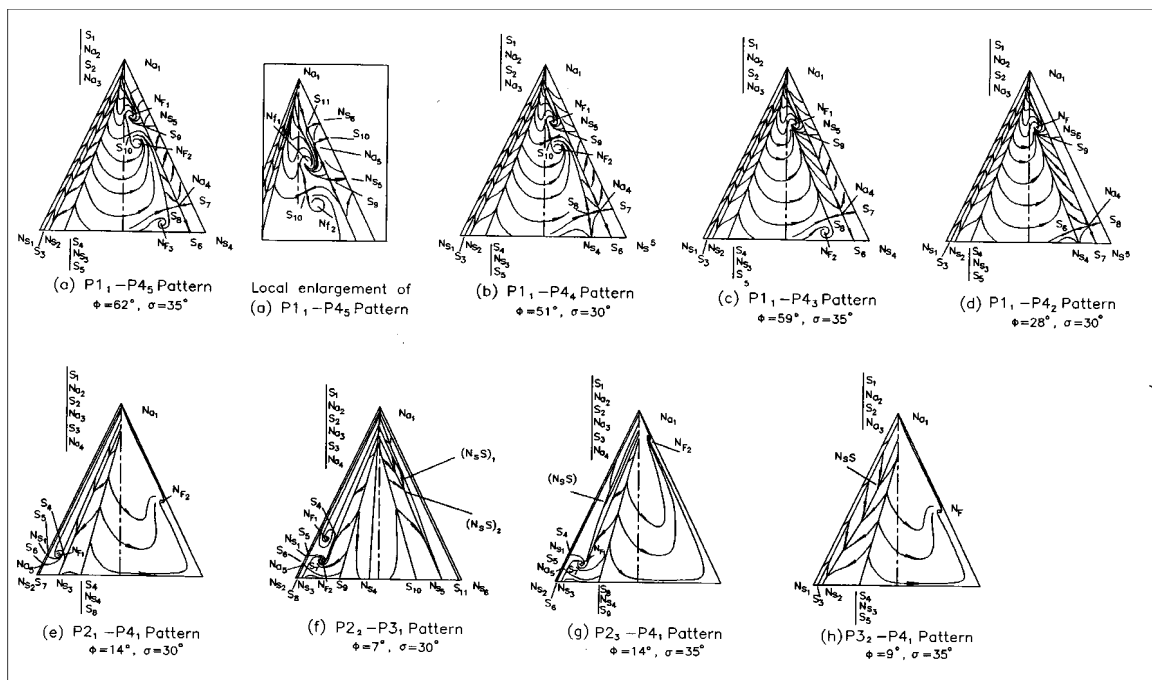


Fig. 11 Evolutions of topological changes at different roll and sting angles ($\Lambda=65^\circ$)

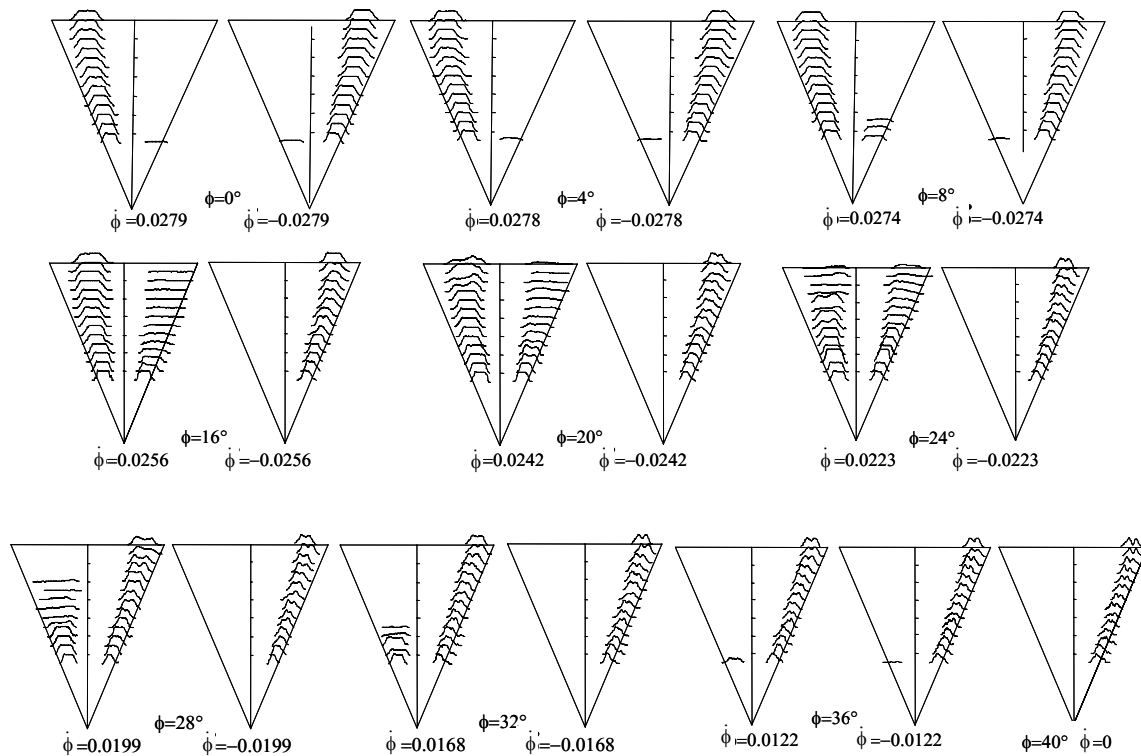


Fig. 12 Gray level profiles through vortex core under rolling oscillatory conditions ($\sigma=30^\circ$, $\Delta\phi=40^\circ$, $k=0.04$, $\phi_0=0^\circ$)

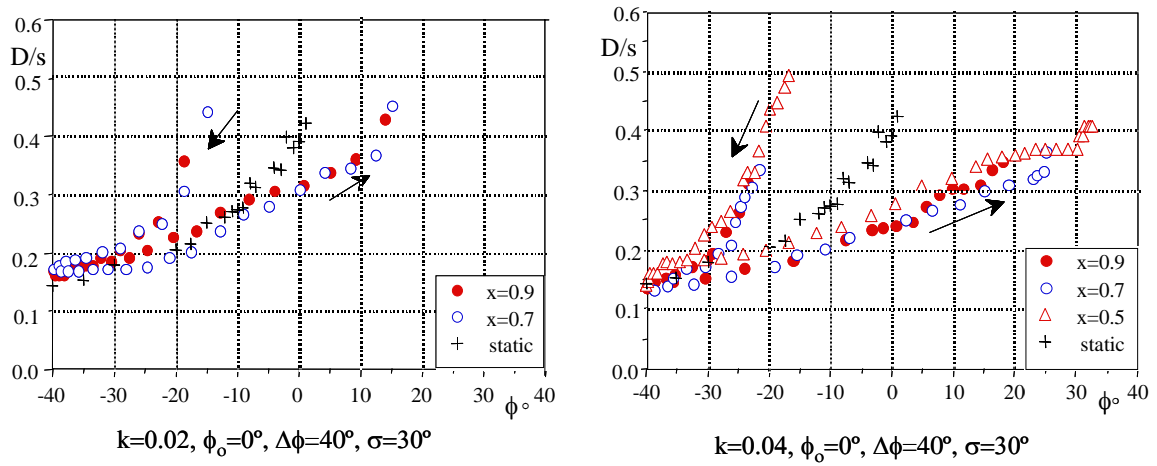


Fig. 13 Rotational vortex core diameter development in static and dynamic conditions

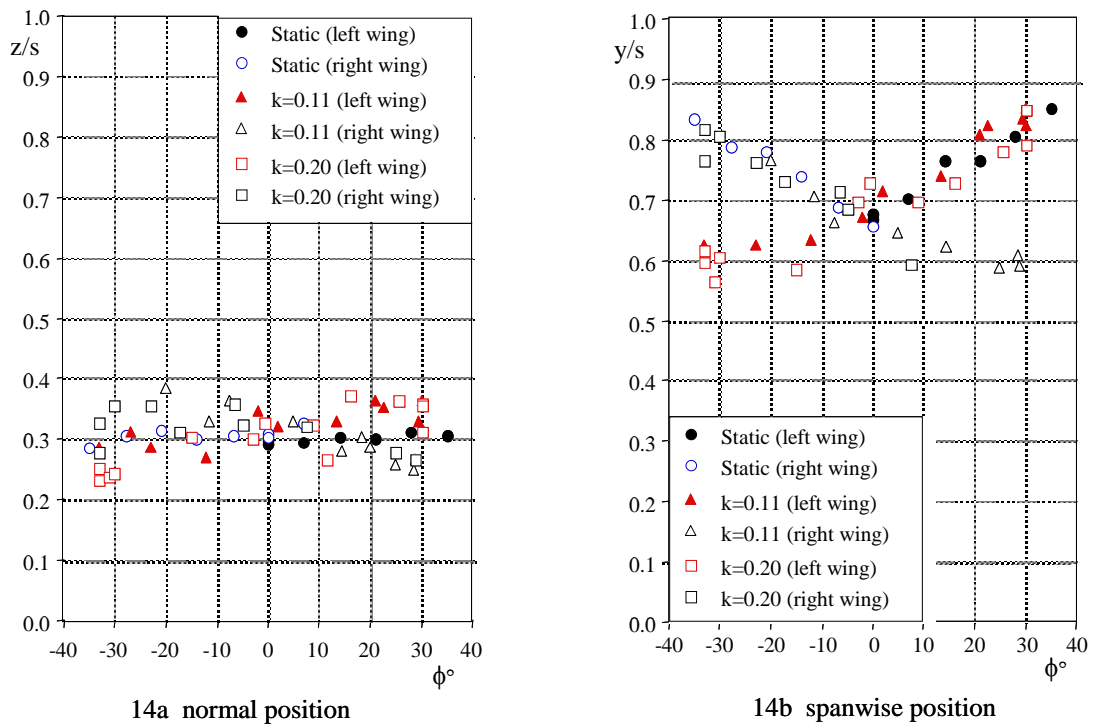


Fig. 14 Vortex core positions at different roll angles ($\sigma=30^\circ$, $\Lambda=65^\circ$)

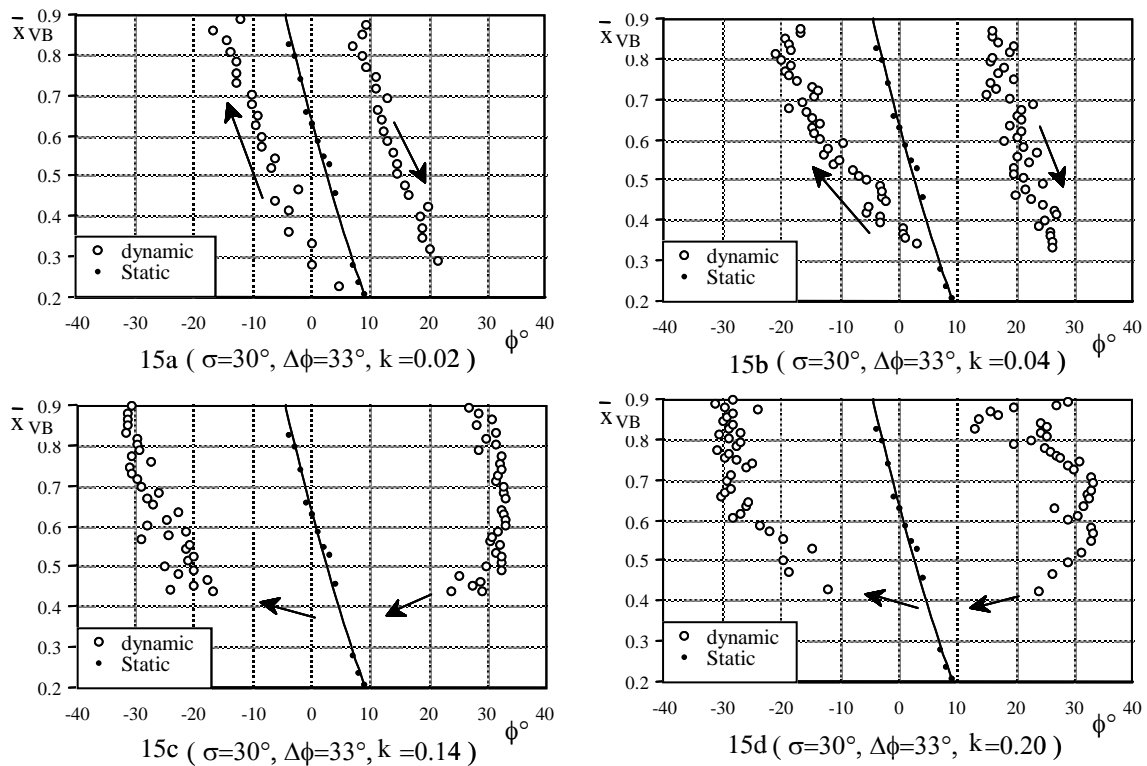


Fig. 15 Rolling frequency effect on vortex breakdown location

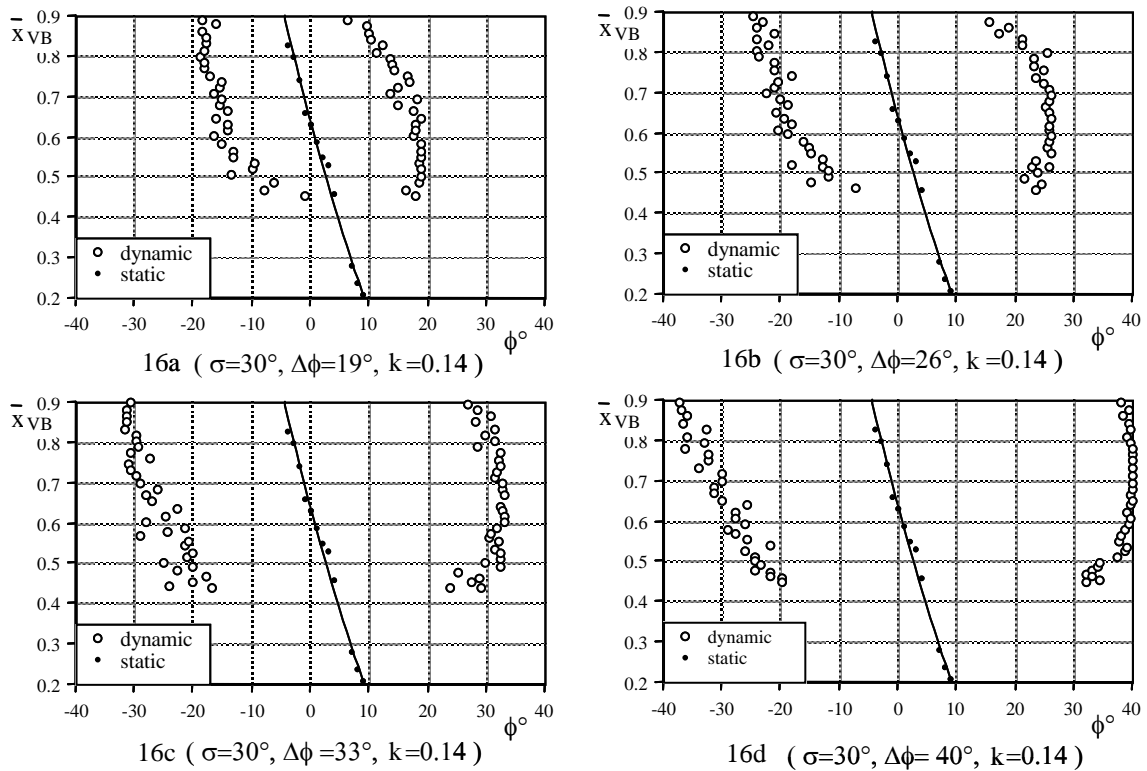


Fig. 16 Rolling amplitude effect on vortex breakdown location

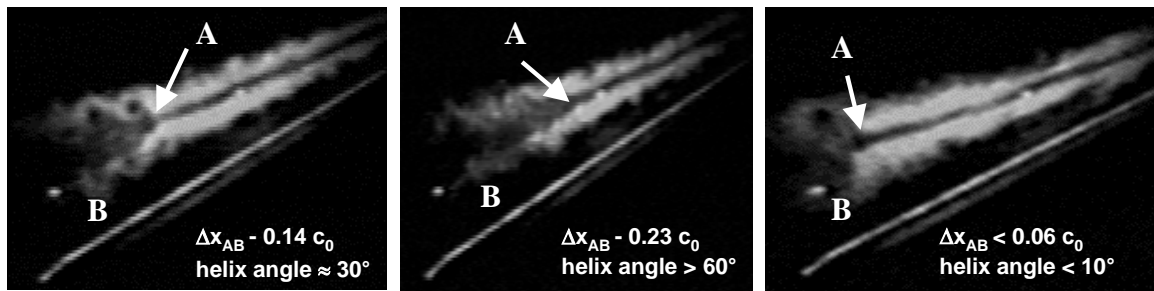


Fig. 17 Different vortex breakdown appearances ($s=30^\circ$, $L=65^\circ$)

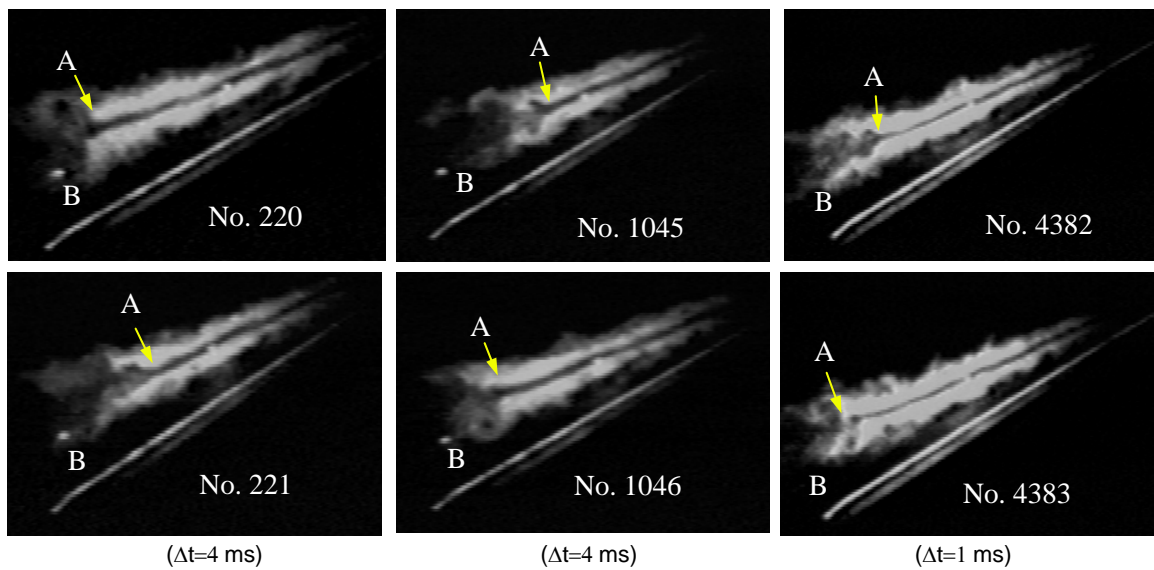
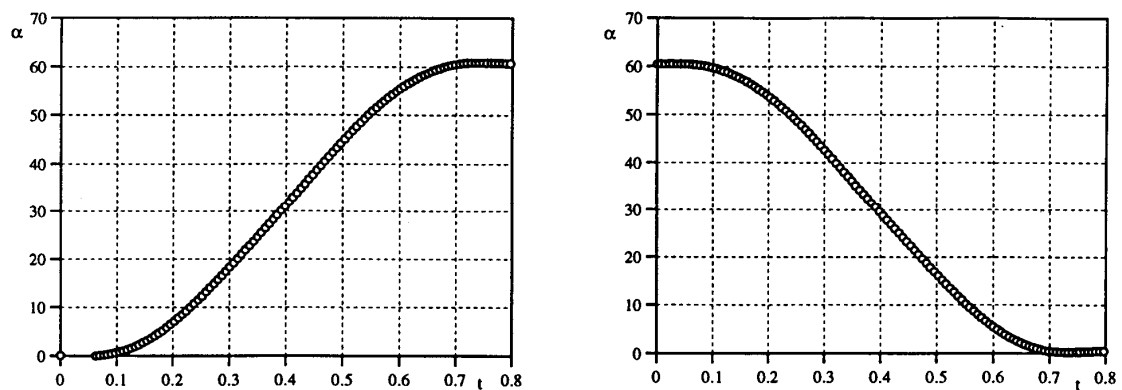


Fig. 18 Different response speeds of the critical points within vortex breakdown region ($\sigma=30^\circ$, $\Lambda=65^\circ$)



19a Motion histories

Fig. 19 Vortex breakdown location movement during static and dynamic situations ($\sigma=30^\circ$, $\Lambda=65^\circ$)

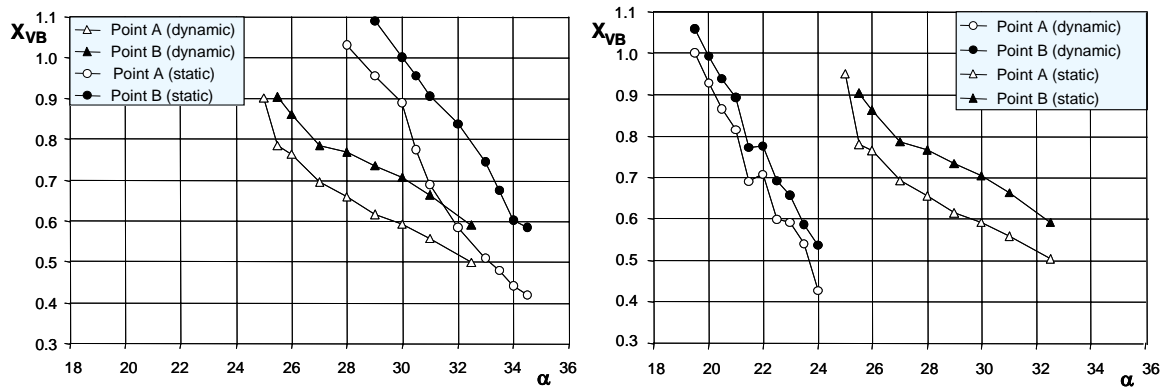


Fig. 19 (cont'd) Vortex breakdown location movement during static and dynamic situations ($\sigma=30^\circ$, $\Lambda=65^\circ$)

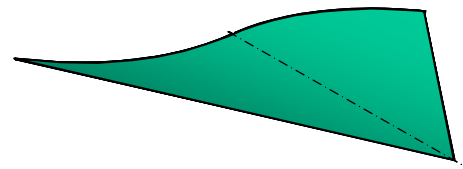
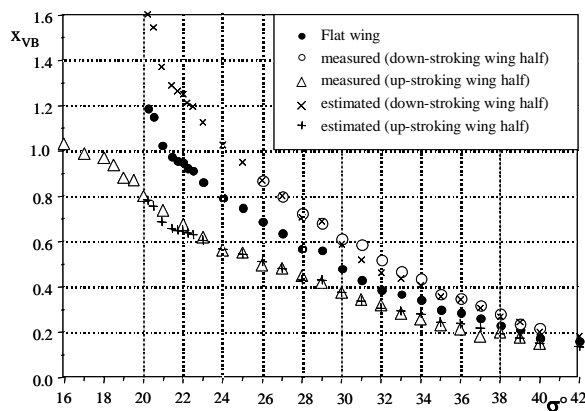
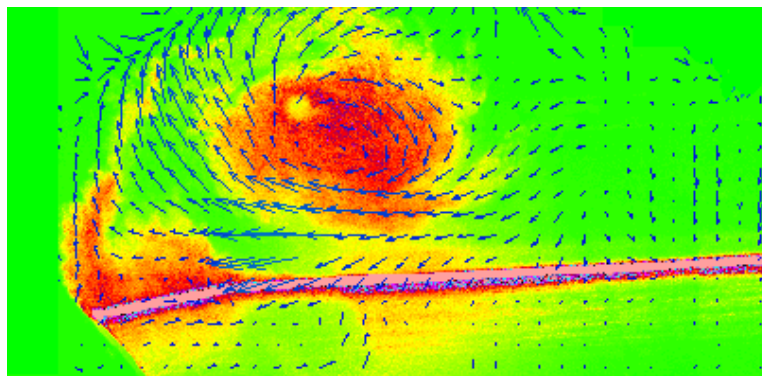


Fig. 20 Deformed wing and its effect on vortex breakdown



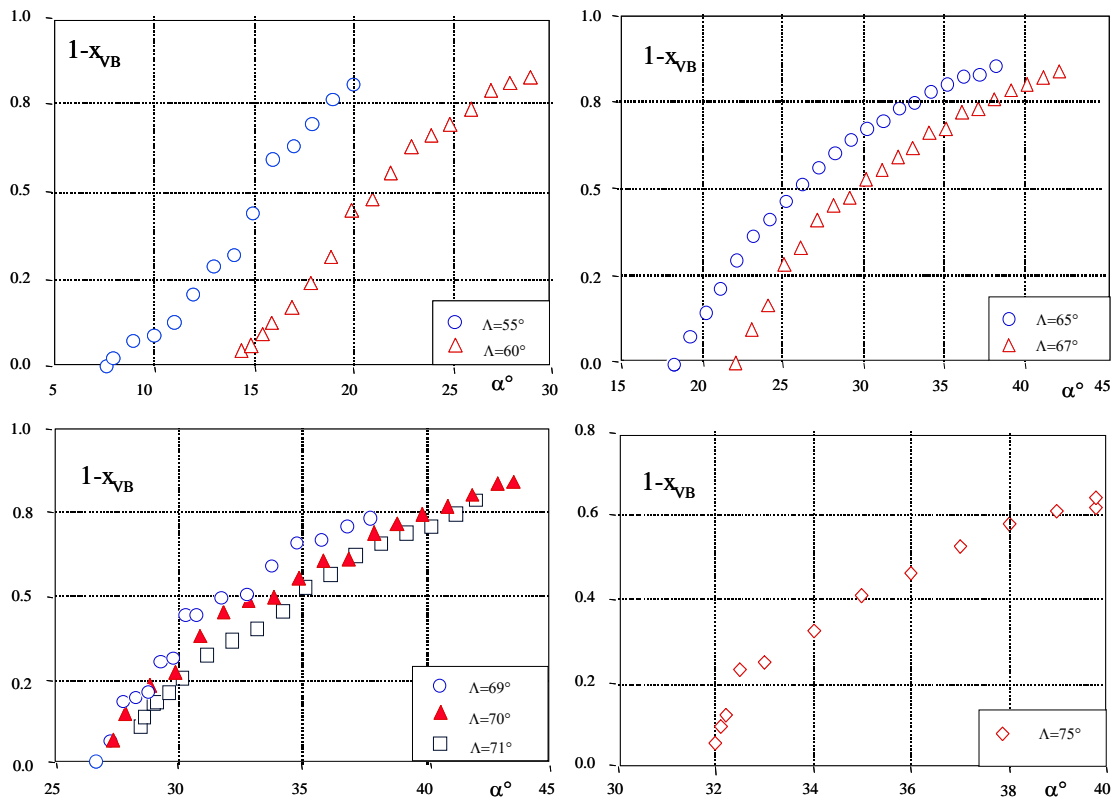
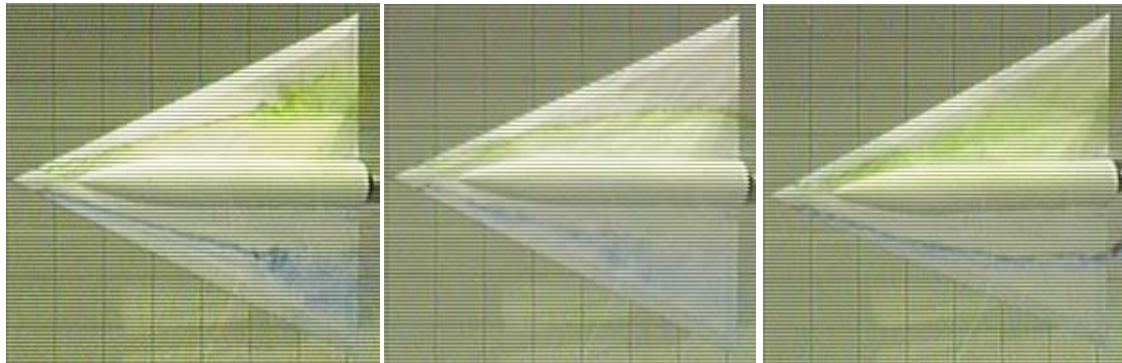


Fig. 22 Vortex breakdown locations over delta wings with different sweepback angles



$\sigma=25^\circ$, $\Lambda=65^\circ$, $\Omega=0$ $\sigma=25^\circ$, $\Lambda=65^\circ$, $\Omega=0.25$ $\sigma=25^\circ$, $\Lambda=65^\circ$, $\Omega=-0.25$

Fig. 23 Effect of coning motion on leading-edge vortex breakdown

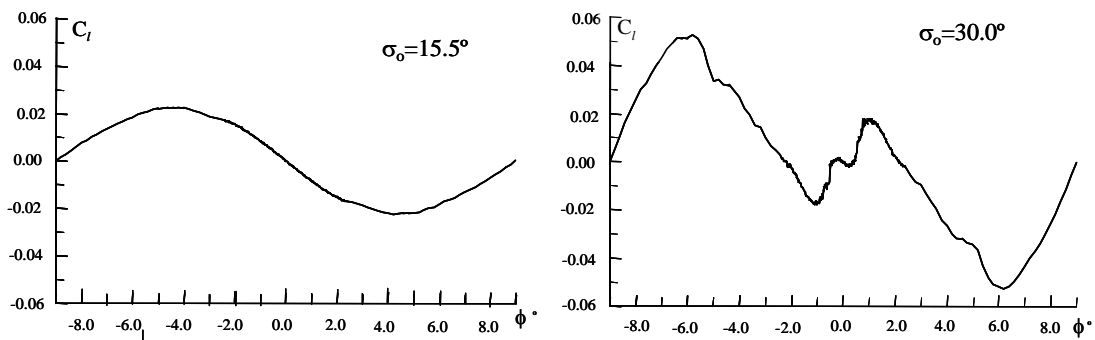


Fig. 24 Rolling moment vs. roll angle at different sting angles

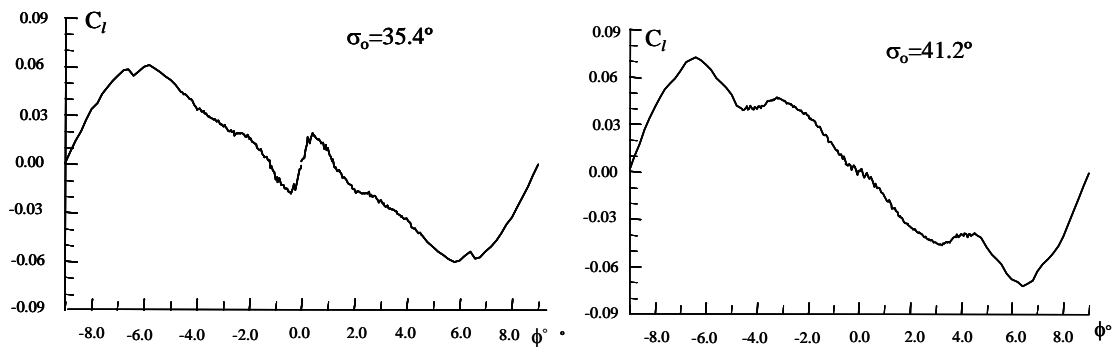


Fig. 24 (Cont.) Rolling moment vs. roll angle at different sting angles ($\Lambda=65^\circ$)

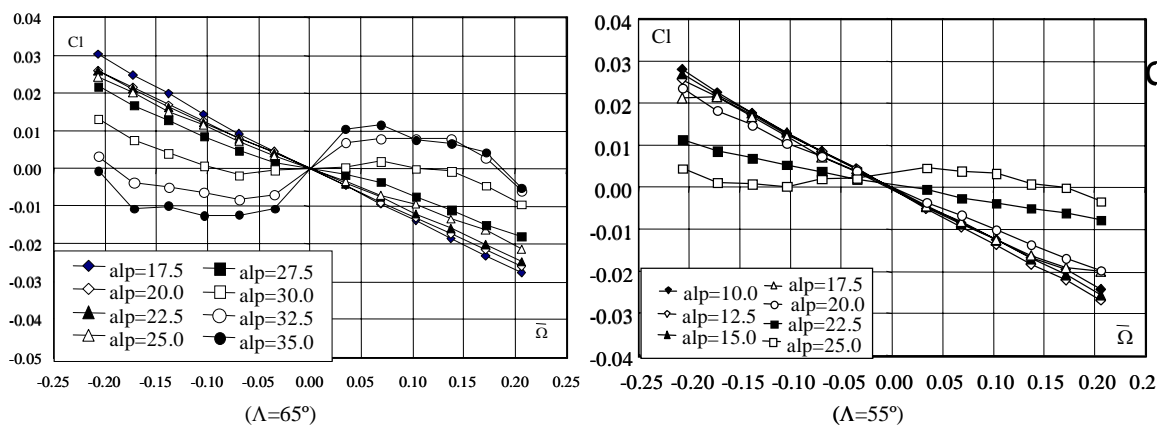


Fig. 25 Rolling moment vs. coning rate at different sting angles ($\phi=0^\circ$)

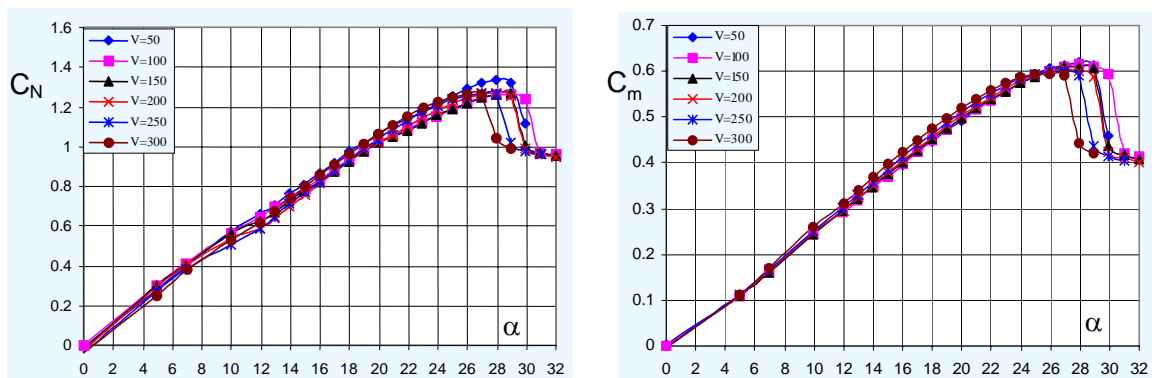
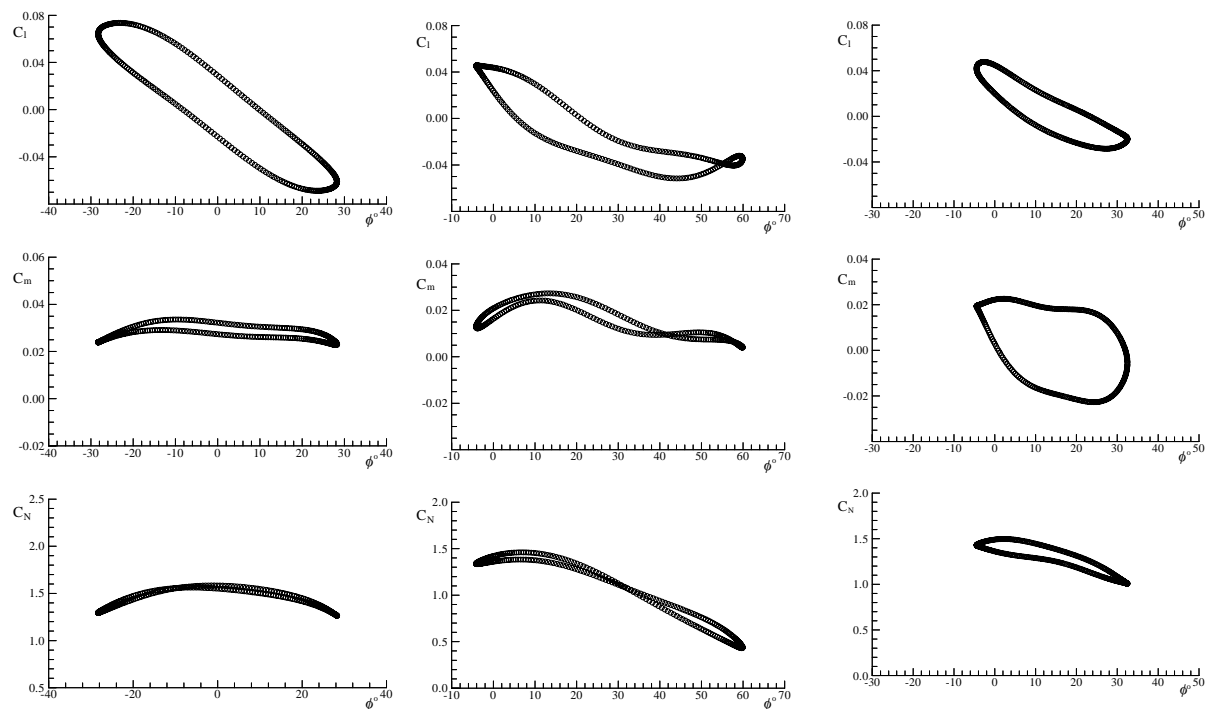


Fig. 26 Normal force and pitch moment vs. coning rate at different sting angles ($\Lambda=65^\circ$, $\phi=0^\circ$)



27a $\sigma=30^\circ, \phi_0=0^\circ, \Delta\phi=28.3^\circ, k=0.2$

27b $\sigma=30^\circ, \phi_0=27.4^\circ, \Delta\phi=31.5^\circ, k=0.2$

27c $\sigma=30^\circ, \phi_0=10^\circ, \Delta\phi=14.47^\circ, k=0.14$

Fig. 27 Measured airloads at different rolling frequencies, amplitudes and roll offsets

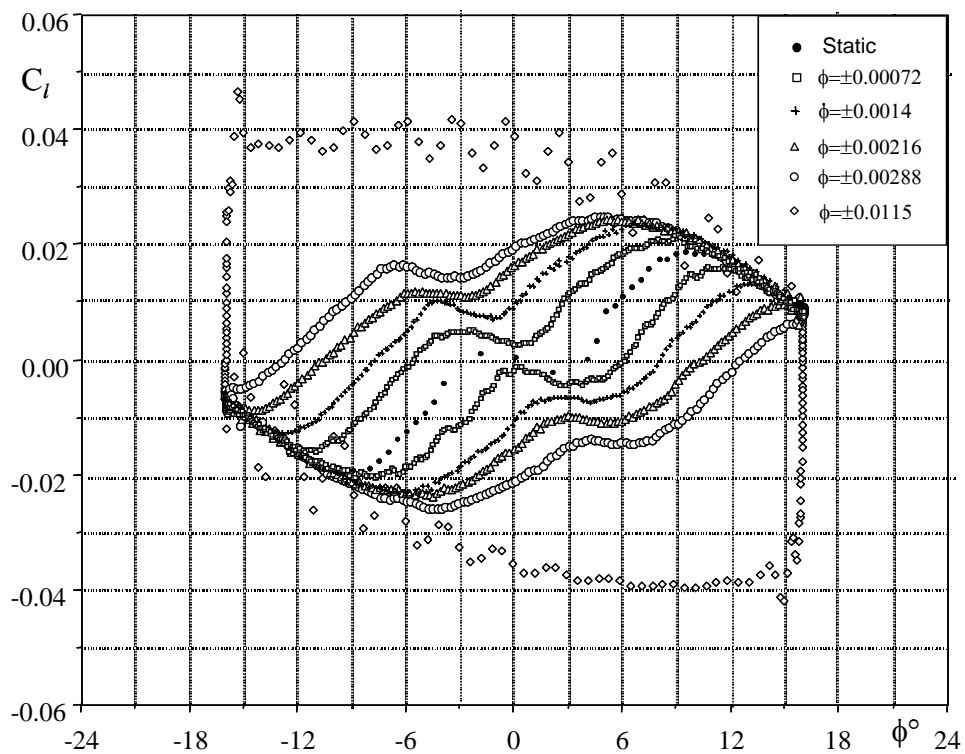


Fig. 28 Rolling moment response to ramp motions

($\sigma=30^\circ, \Lambda=65^\circ$)

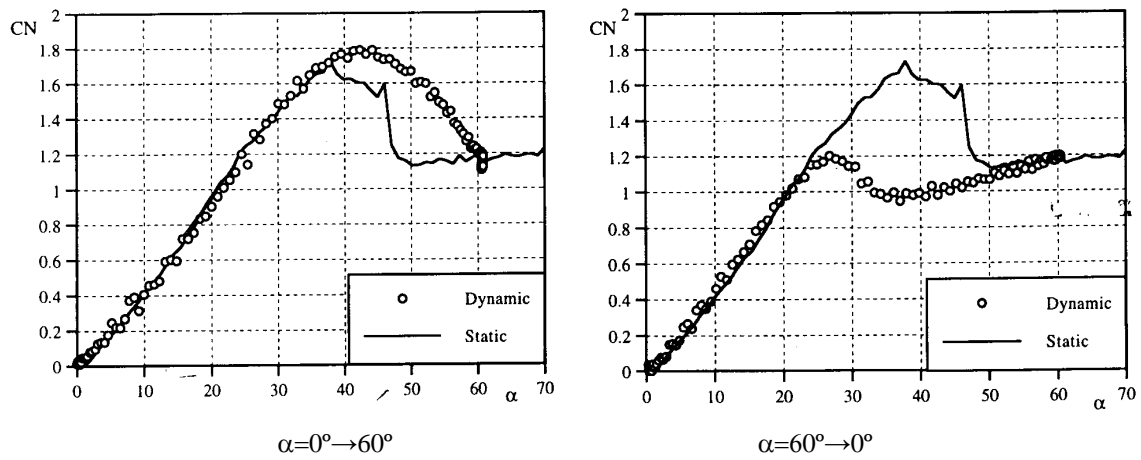


Fig. 29 Normal force response to ramp motions ($\alpha=0^\circ \sim 60^\circ$, $L=65^\circ$)

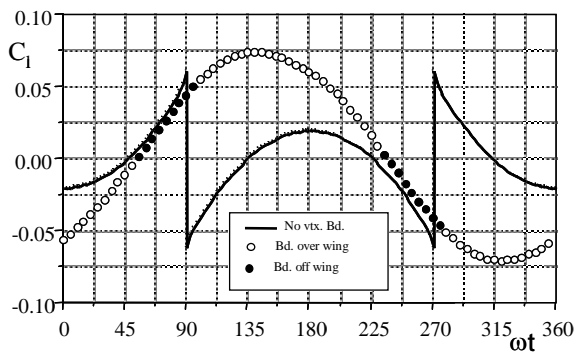
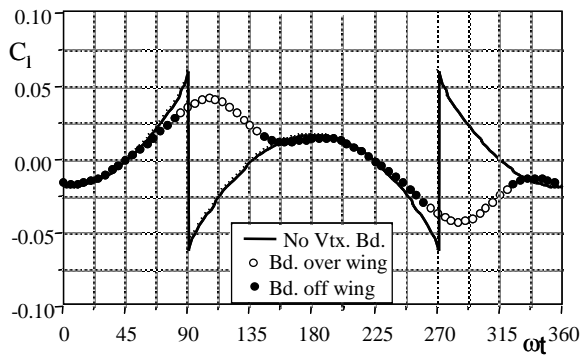
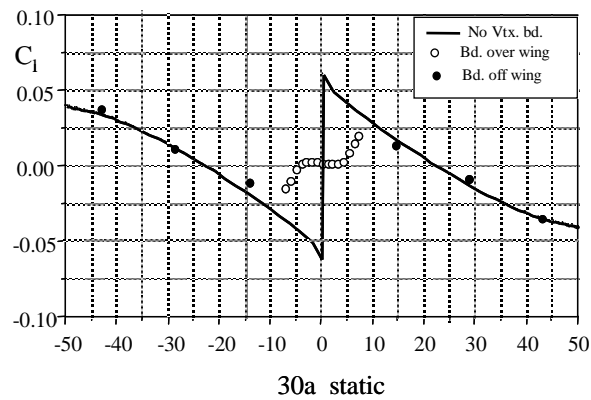


Fig. 30 Effect of vortex breakdown on rolling moment in different cases

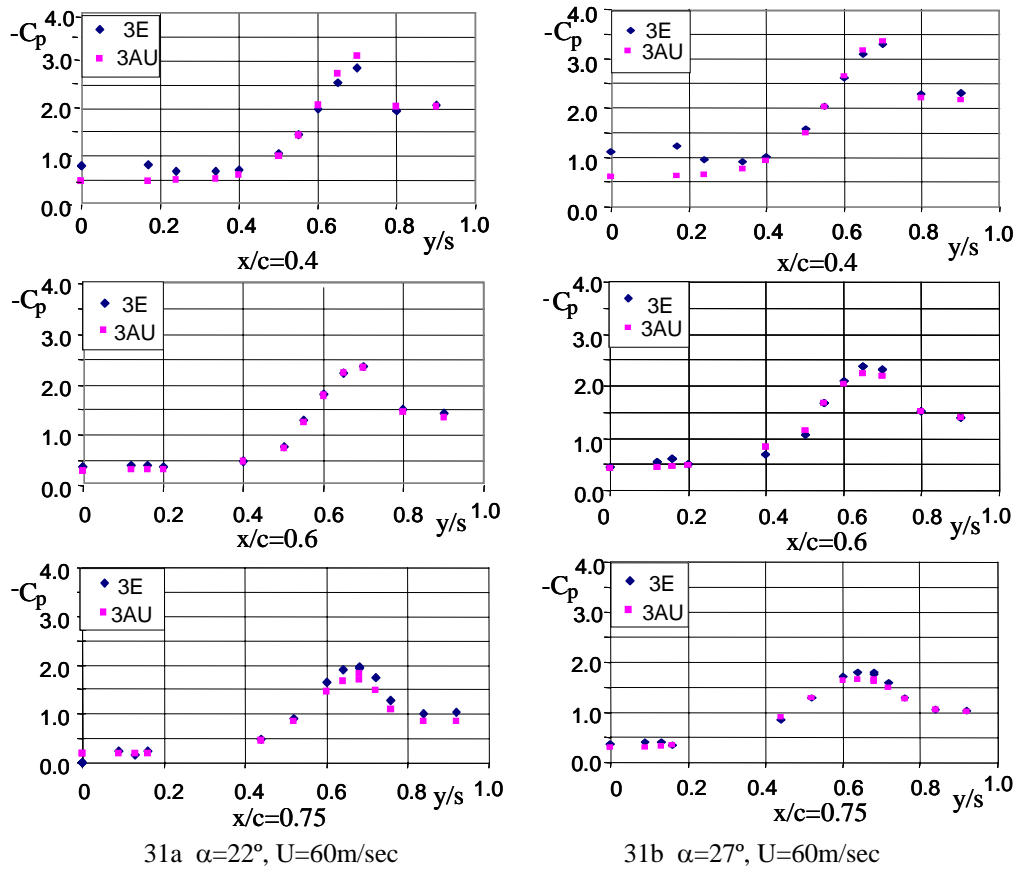


Fig. 31 Surface pressure at different chordwise locations and angles of attack ($\Lambda=65^\circ$)

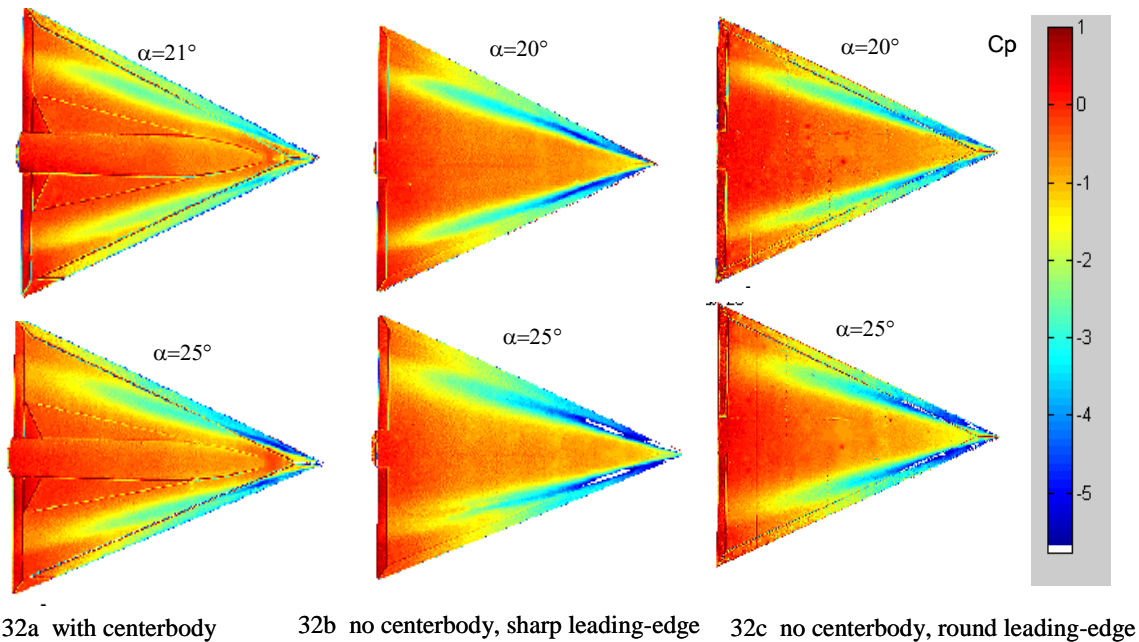
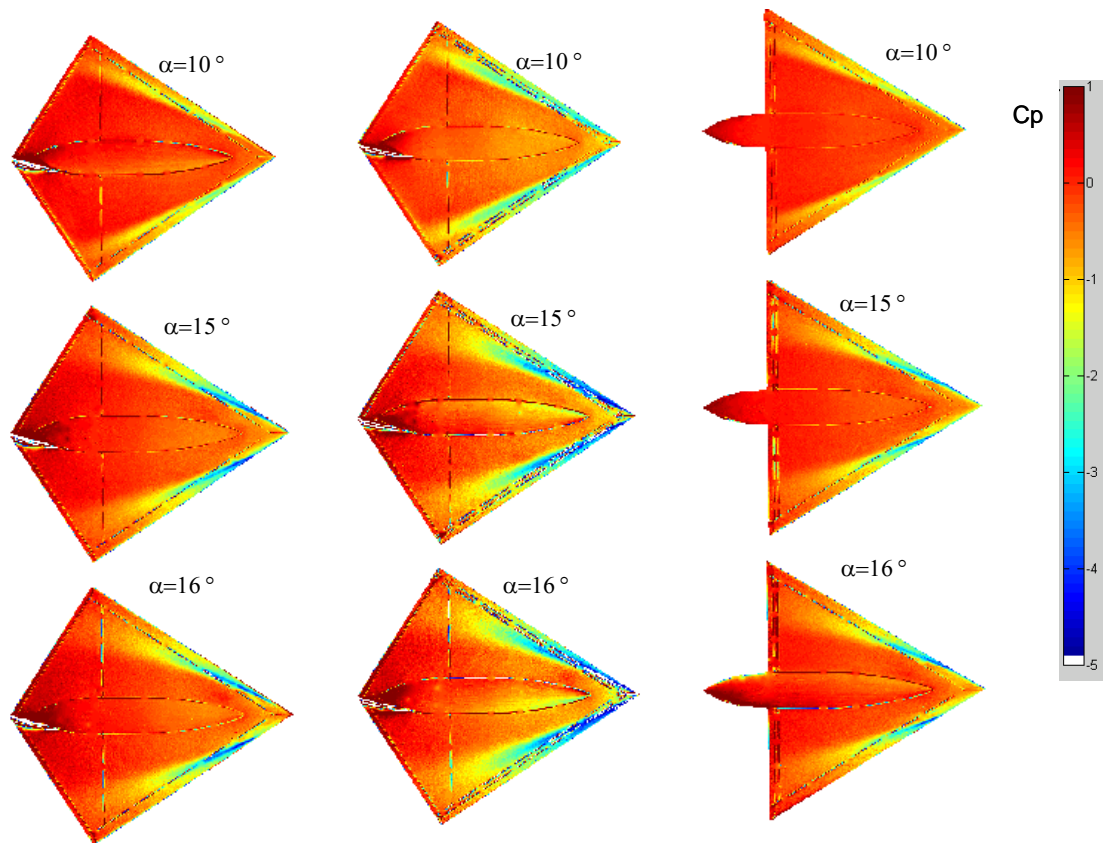


Fig. 32 PSP measurements on 65° delta wing with different combinations



33a sharp leading-edge

33b round leading-edge

33c sharp leading-edge

Fig. 33 PSP measurements on IAR 55° diamond/delta wings with different leading-edge shapes

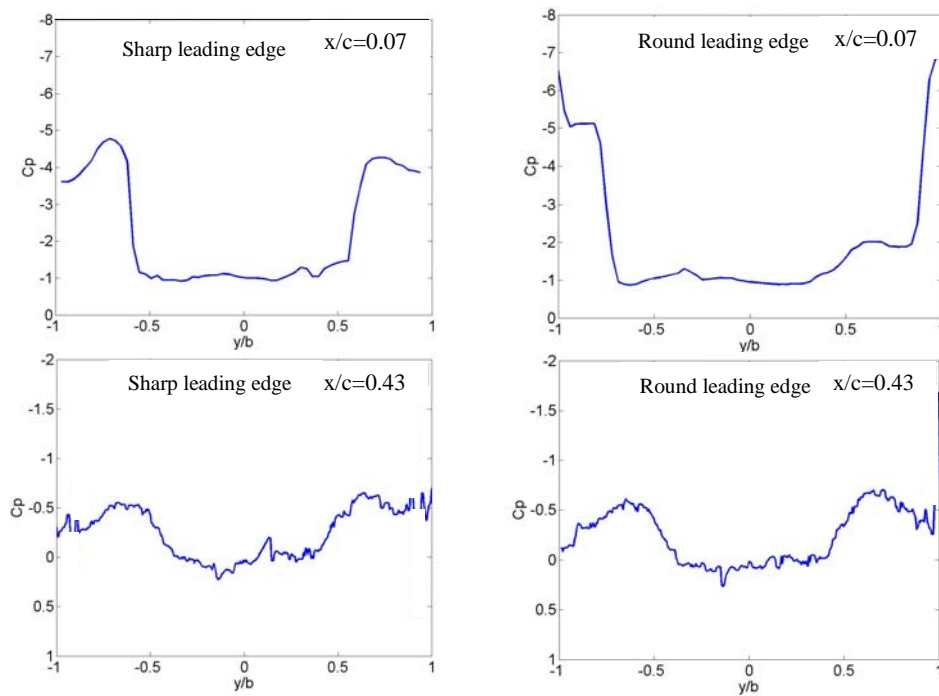


Fig. 34 Leading-edge shape effect on PSP results at different chordwise location ($U=60$ m/s, $\Lambda=55^\circ$, $\alpha=21^\circ$)

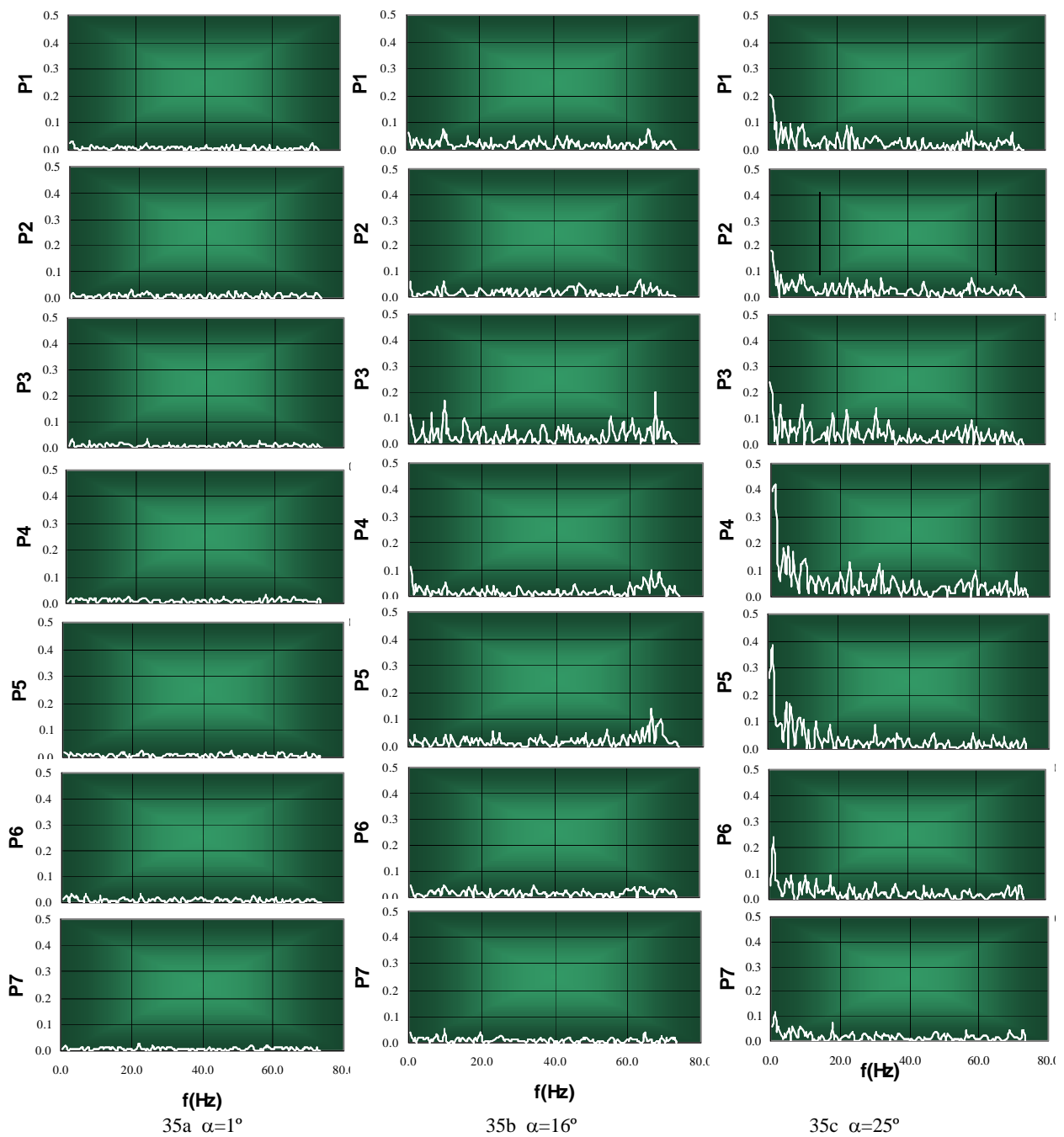


Fig. 35 Unsteady pressure spectra measurements at static model conditions and different angles of attack

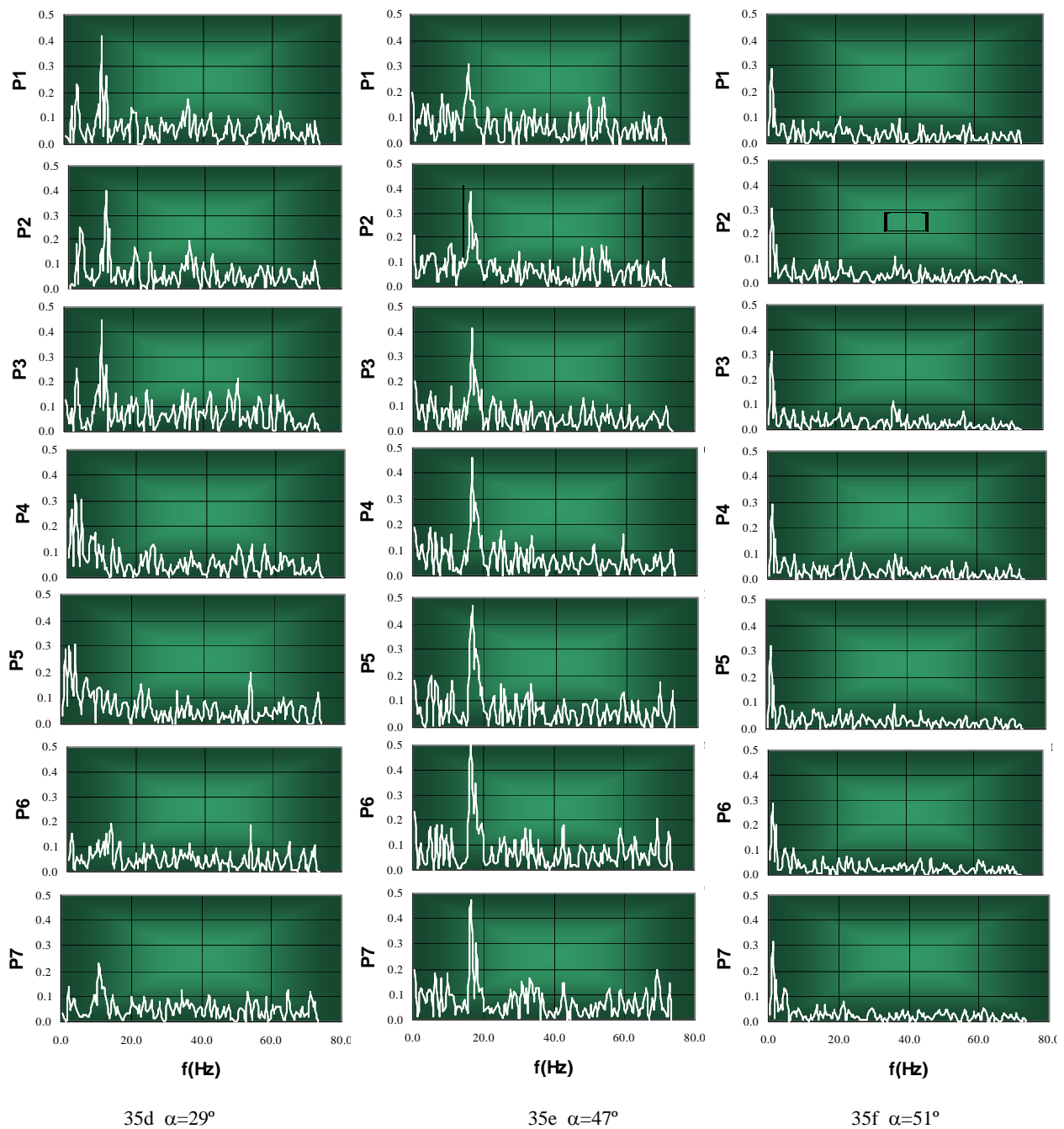


Fig. 35 (Cont.) Unsteady pressure spectra measurements at static model conditions and different angles of attack

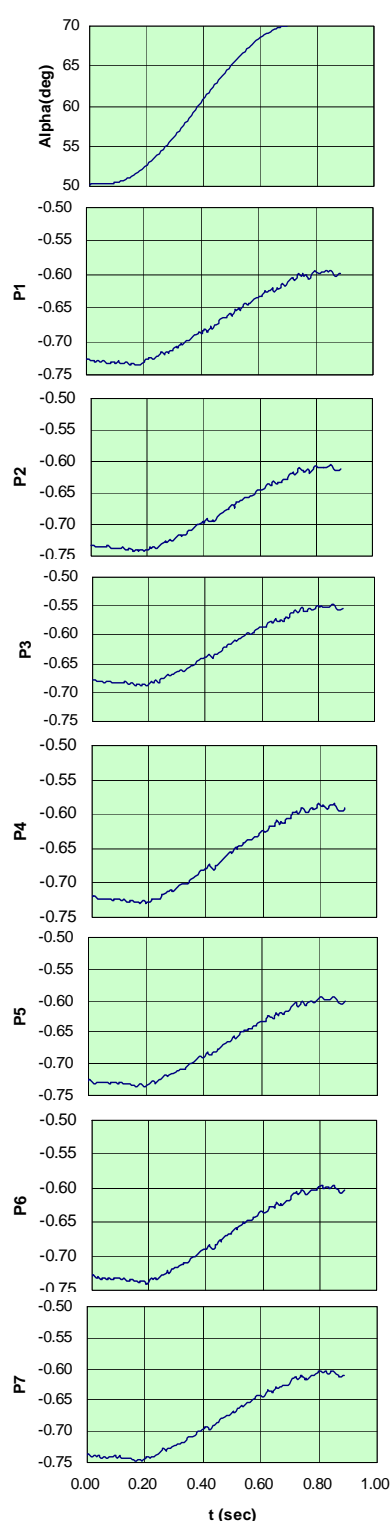


Fig. 36a pitch motion and pressures in time domain, $\alpha = 50^\circ \rightarrow 70^\circ$

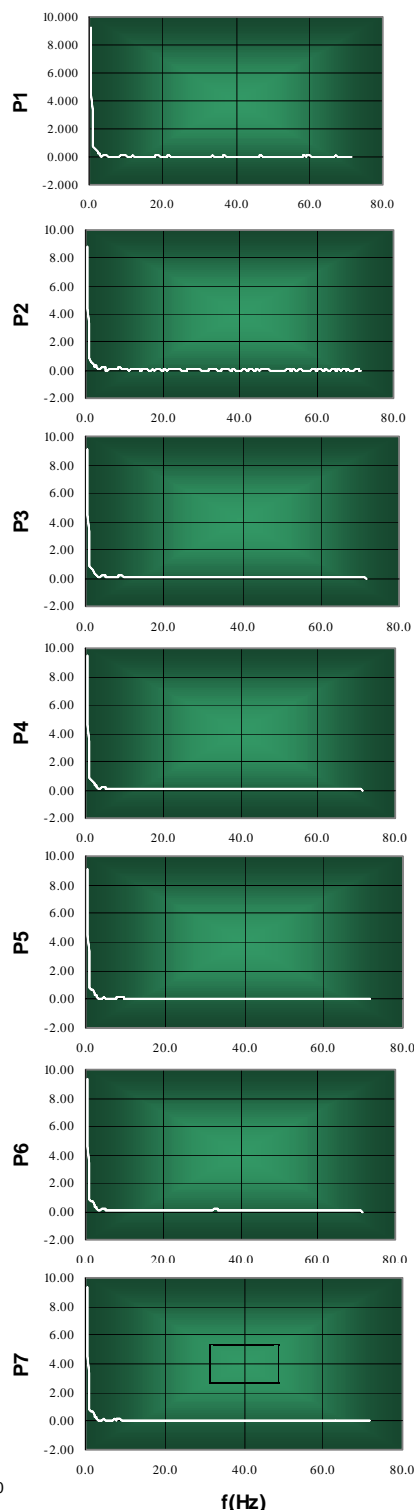


Fig. 36b measured pressure in frequency domain, $\alpha = 50^\circ \rightarrow 70^\circ$

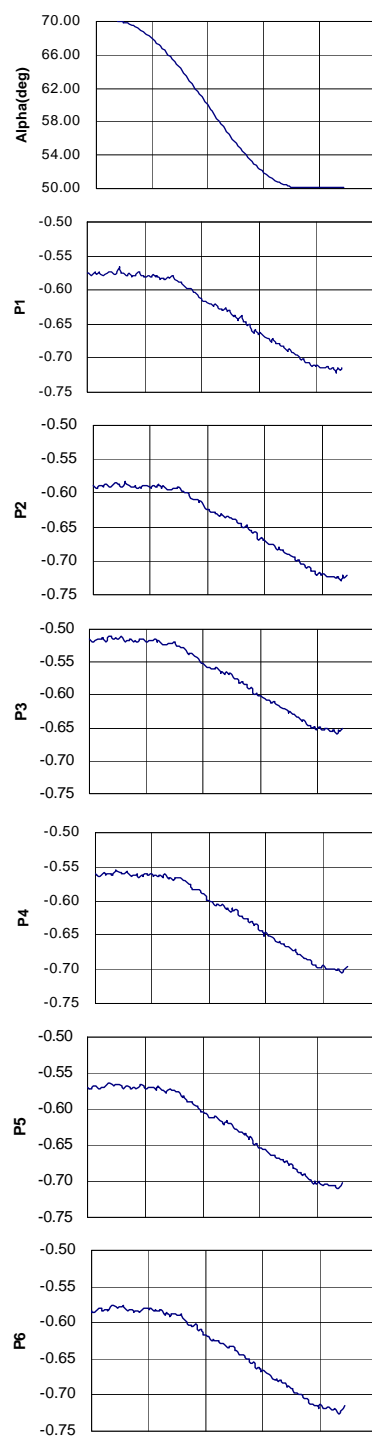


Fig. 37 pitch motion and pressures in time domain, $\alpha = 70^\circ \rightarrow 50^\circ$

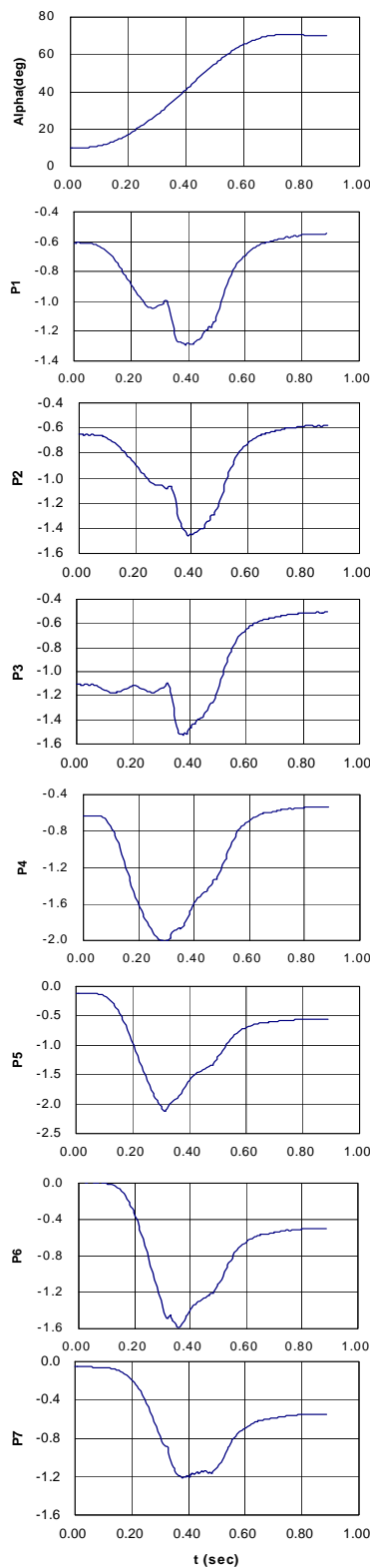


Fig. 38a pitch motion and pressures in time domain, $\alpha=10^\circ \rightarrow 70^\circ$

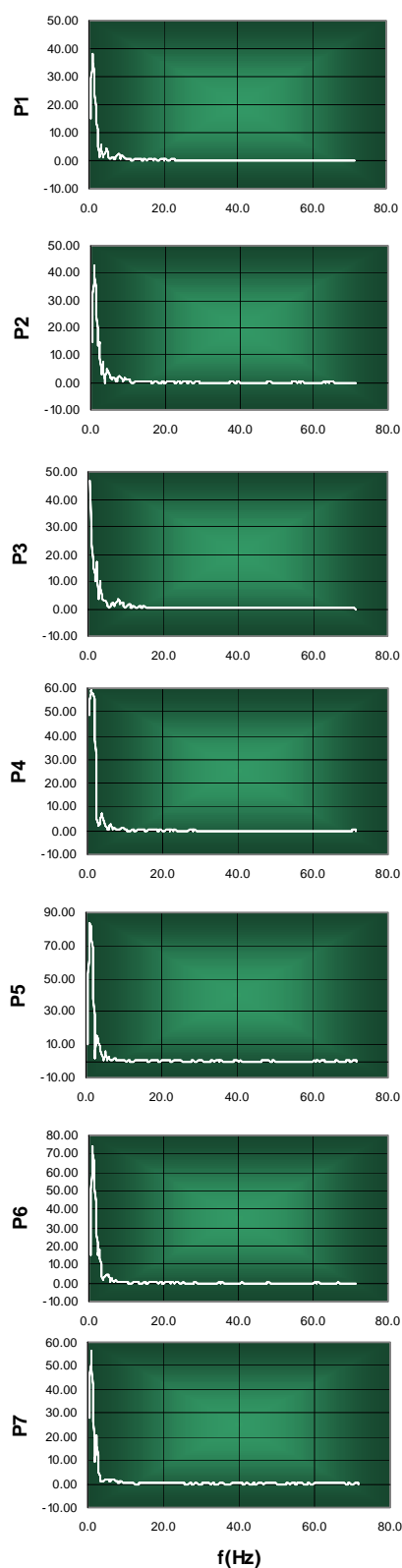


Fig. 38b measured pressure in frequency domain, $\alpha=10^\circ \rightarrow 70^\circ$

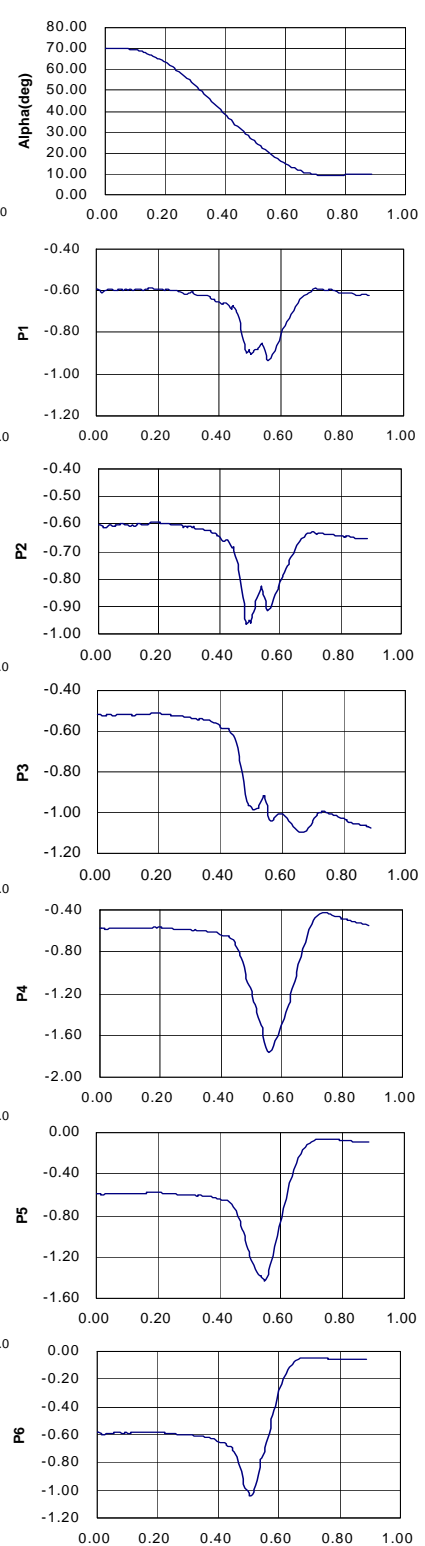


Fig. 39a pitch motion and pressures in time domain, $\alpha=70^\circ \rightarrow 10^\circ$

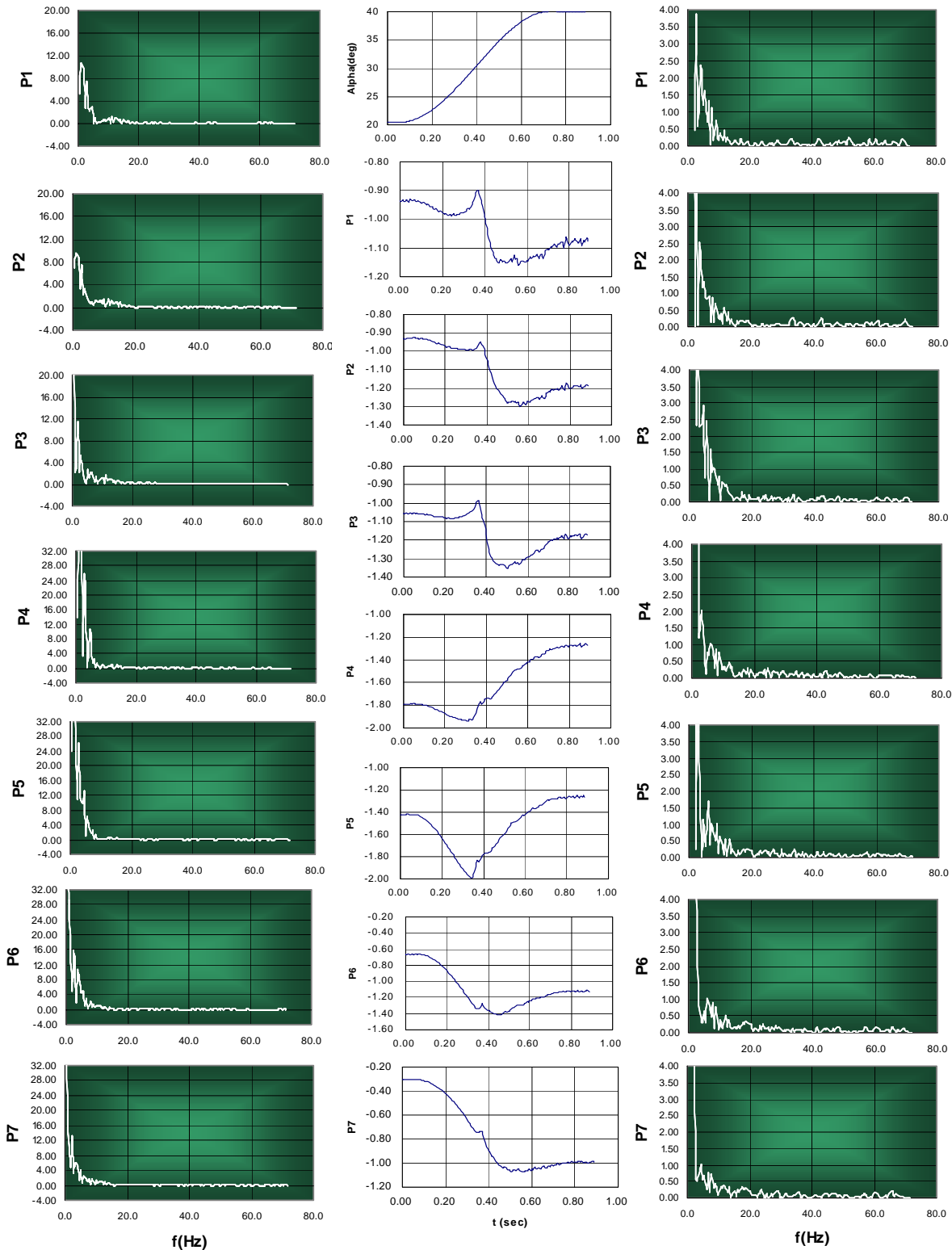


Fig. 39b measured pressure in frequency domain, $\alpha=70^\circ \rightarrow 10^\circ$

Fig. 40a pitch motion and pressures in time domain, $\alpha=20^\circ \rightarrow 40^\circ$

Fig. 40b measured pressure in frequency domain, $\alpha=20^\circ \rightarrow 40^\circ$

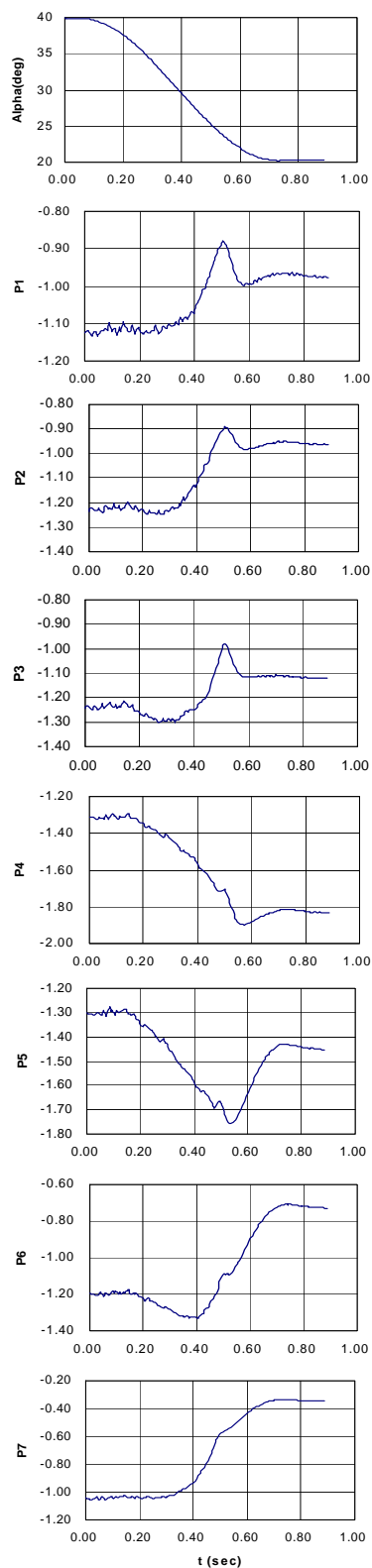


Fig. 41a pitch motion and pressures in time domain, $\alpha=40^\circ \rightarrow 20^\circ$

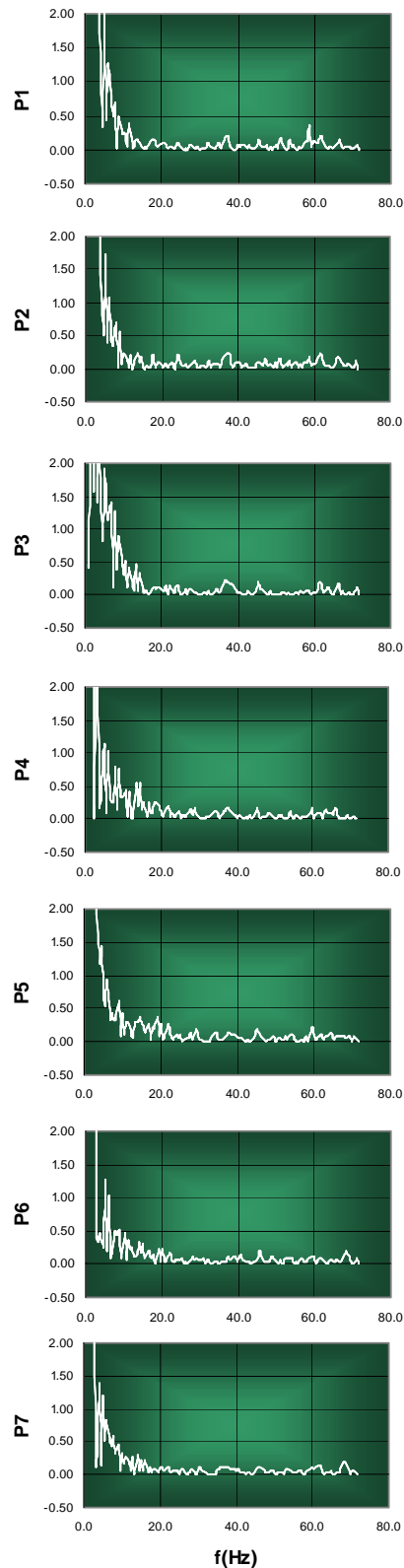


Fig. 41b measured pressure in frequency domain, $\alpha=40^\circ \rightarrow 20^\circ$

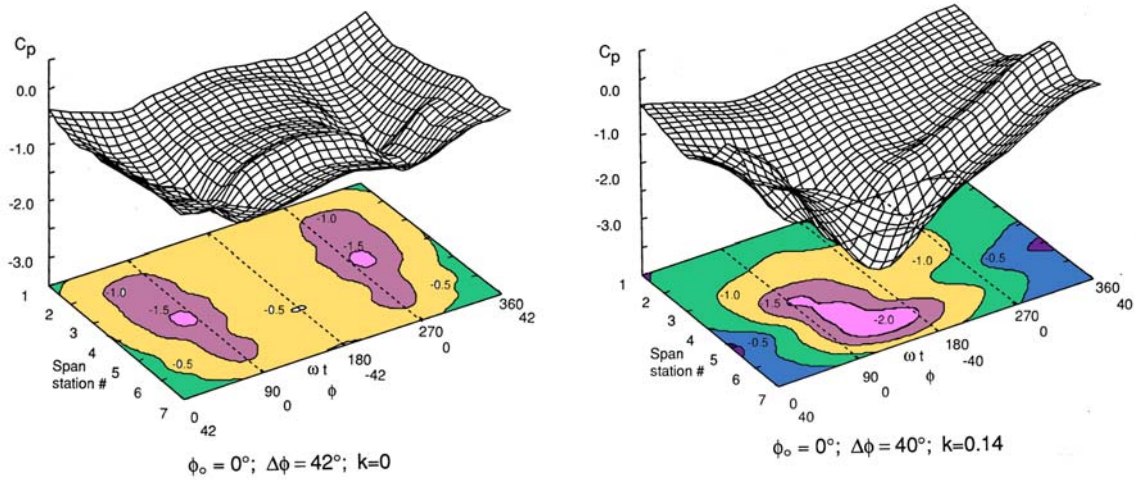


Fig. 42 Surface pressure at static and rolling oscillation conditions

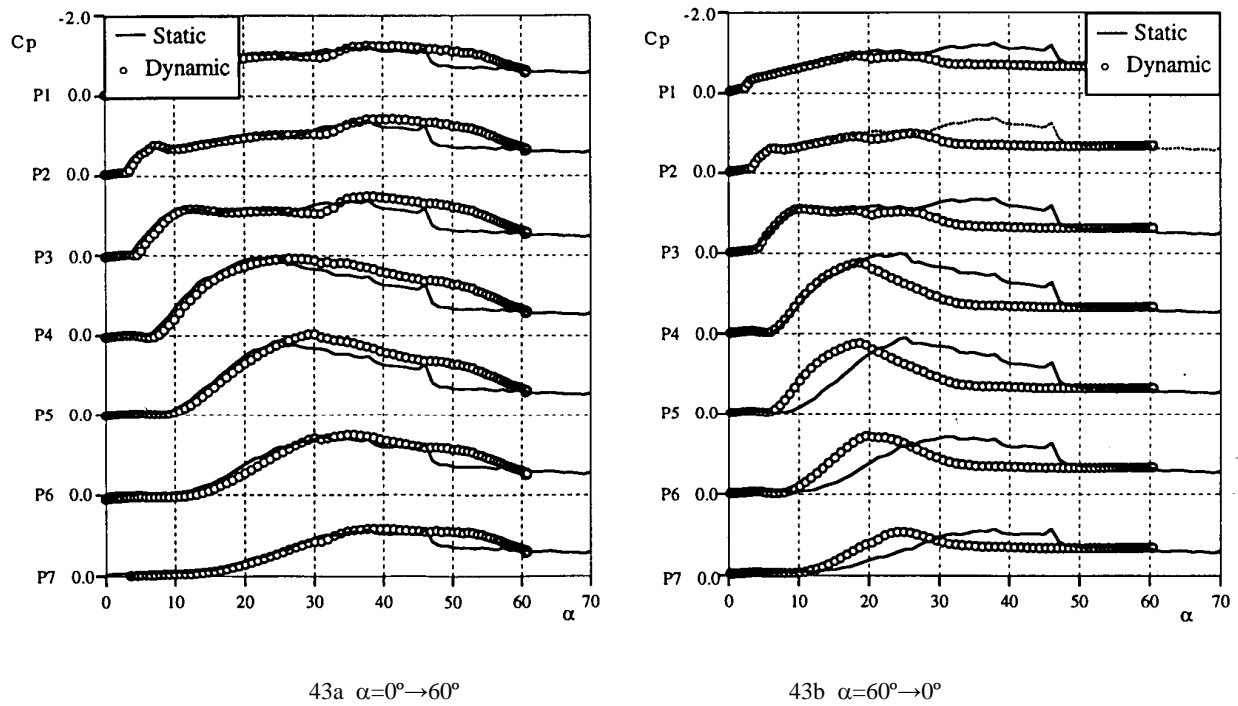


Fig. 43 Surface pressure at static and ramp-and-hold conditions

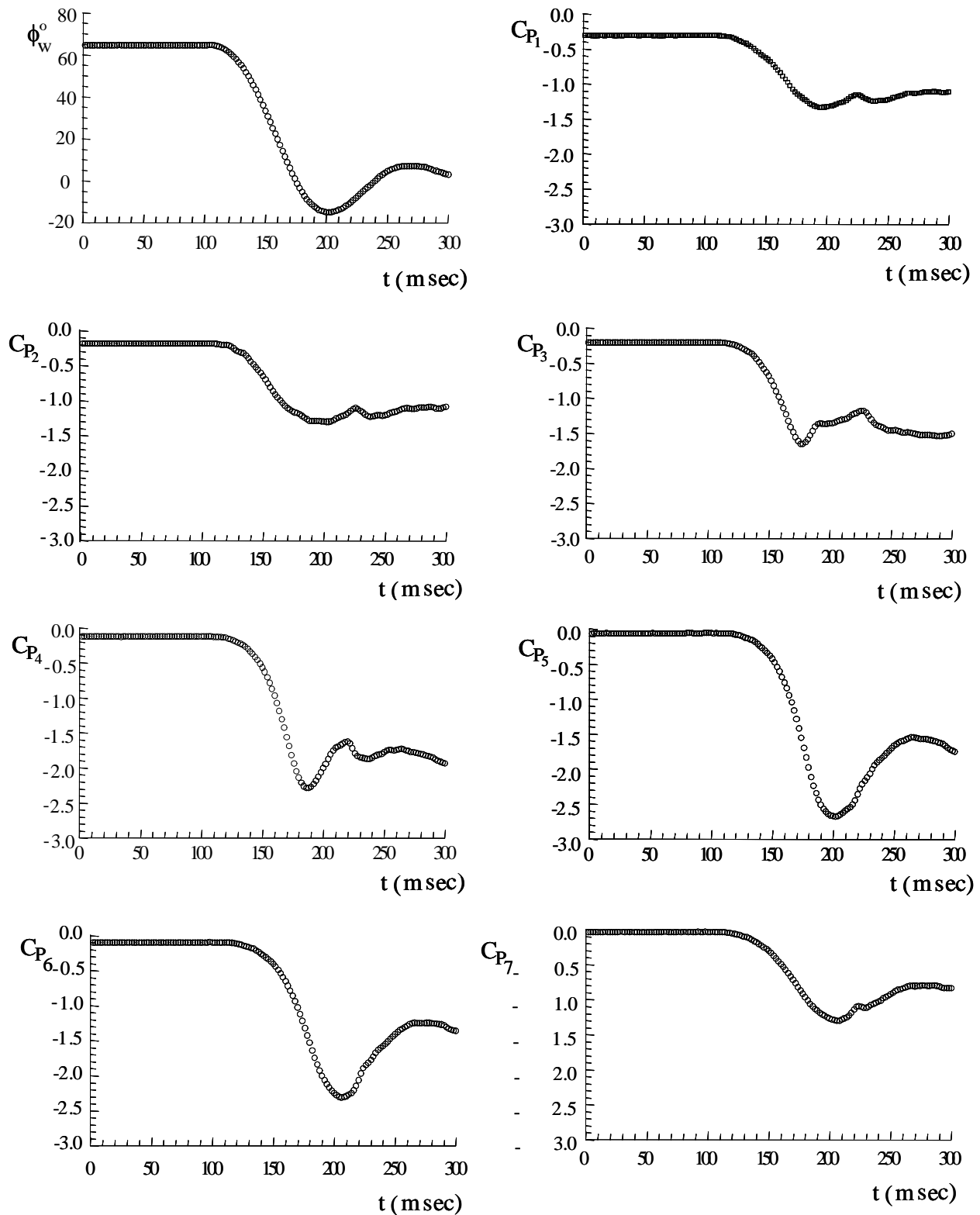


Fig. 44 Surface pressure during free-to-roll motion

($\Lambda=65^\circ$, $\phi_0=64^\circ$)

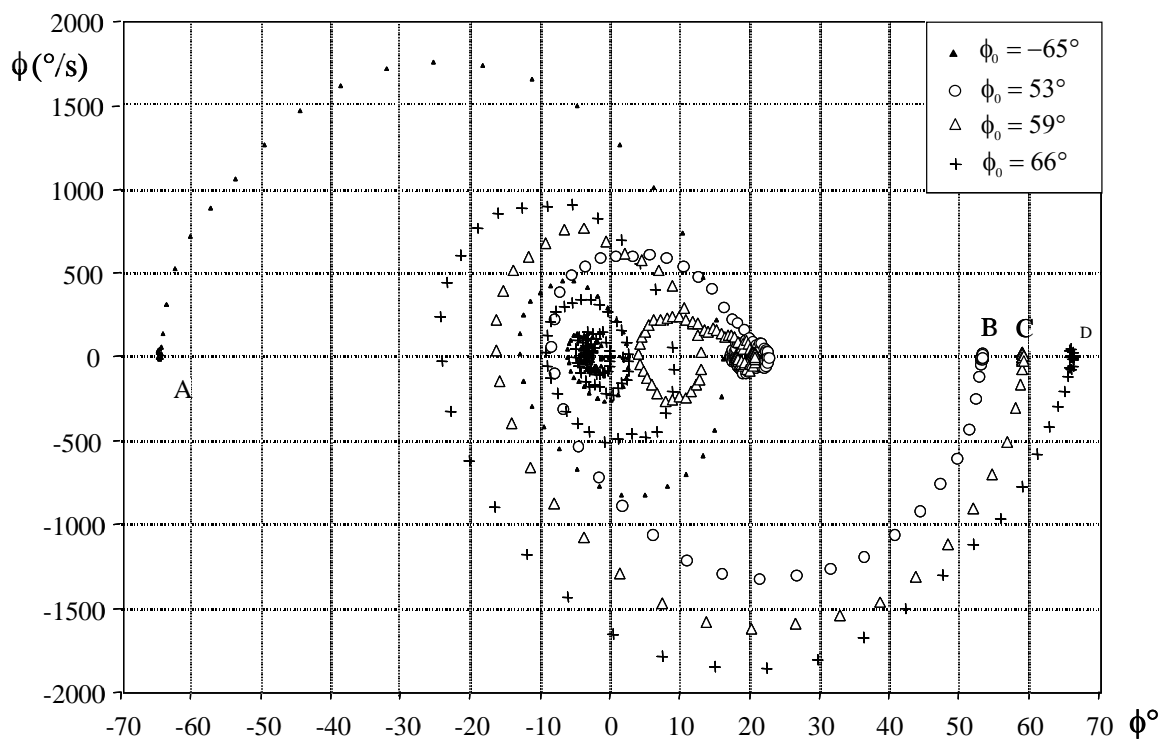
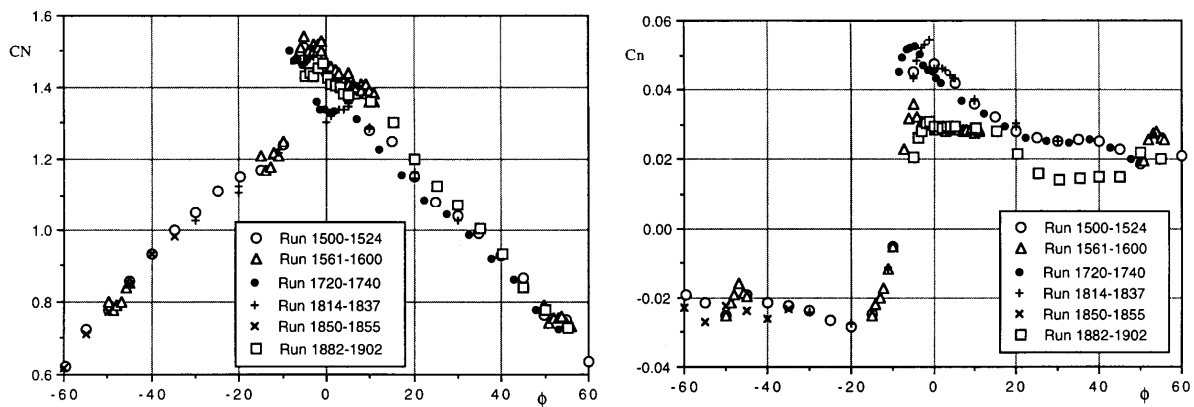


Fig. 45 Free-to-roll motion histories at different released roll angles ($\Lambda=65^\circ$)



46a normal force

46b yawing moment

Fig. 46 Static loads on IAR/AFRL forebody/wing/tail model (Elliptical, major axes horizontal)



Chapter 6 – UNSTEADY ASPECTS OF LEADING-EDGE VORTICES

Ismet Gursul

Department of Mechanical Engineering
University of Bath
Bath BA2 7AY
UNITED KINGDOM

i.a.gursul@bath.ac.uk

ABSTRACT

A wide range of unsteady phenomena relevant to vortex flows over stationary and maneuvering delta wings is reviewed. The origin, characteristics, and physical mechanisms of these unsteady phenomena are discussed. Dynamic response of leading-edge vortices for maneuvering wings and mechanisms of hysteresis and time-lag effects are reviewed. Issues and challenges for unsteady vortex flows over delta wings are outlined.

NOMENCLATURE

AR	amplitude ratio; aspect ratio
B	probability density function of velocity
c	root chord length
f	frequency
k	reduced frequency; axial wave number
n	wave number in angular direction
p	pressure fluctuation
P	probability
Re	Reynolds number based on chord length
s	local semispan
S	spectral density
t	time
T	period
u	axial velocity
U_{∞}	free stream velocity
v	swirl velocity
x	streamwise distance
x_{bd}	breakdown location
y	spanwise distance
z	vertical distance above wing surface
Φ	fin angle
Γ	circulation
Λ	sweep angle
α	angle of attack
δ	flap angle
ν	kinematic viscosity
τ	time constant
ω	vorticity; radial frequency

6.1 INTRODUCTION

Highly swept wings, often referred to as delta wings due to their triangular planform, are used in a variety of aerospace vehicles. At high angles of attack, delta wings can generate higher lift than rectangular wings, with better aircraft stability and control characteristics. The development of highly maneuverable fighter aircraft and missiles has raised interest in the study of delta wings.

The flow over a delta wing at high angles of attack is dominated by two large, counter-rotating leading-edge vortices that are formed by the roll-up of vortex sheets as sketched in Figure 1. The flow separates from the leading edge of the wing to form a curved free shear layer above the suction side of the wing, which rolls up into a core. The time-averaged axial velocity is roughly axisymmetric and its maximum can be as large as four or five times the free stream velocity. These large axial velocities are due to very low pressures in the vortex core, which generate additional suction and lift force on the delta wings.

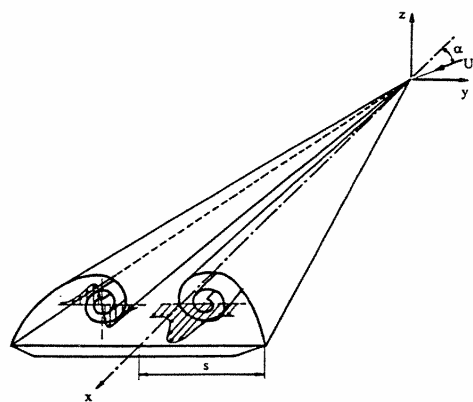


Figure 1: Schematic of Shear Layer and Leading-Edge Vortices over a Delta Wing.

At a sufficiently high angle of attack, the vortices undergo a sudden expansion known as vortex breakdown, which was first observed by Werle [127] in 1954 in a water tunnel facility. Vortex breakdown has adverse effects on the time-averaged performance. For example, the magnitude of the lift and pitching moment decreases after vortex breakdown. A great deal of effort has been focused on the study of these vortices, vortex breakdown phenomenon, and aerodynamics of delta wings, as summarized in several review articles [14, 69, 126].

There has been less emphasis on the unsteady aspects of these flows, which have an impact on aircraft stability and control, and wing/fin buffeting. For example, vortex breakdown may cause large structural vibrations and severe fatigue damage of fins. The dynamic response of leading edge vortices and breakdown is important for flight of modern fighter aircraft. It is crucial to understand these unsteady vortex flows in order to ensure successful, highly maneuverable aircraft. Unsteady flow structure and aspects of vortex breakdown phenomenon were reviewed by Rockwell [108] and Visbal [122]. Unsteady aerodynamic loading of delta wings was reviewed by Ashley et al [2]. The objective of this paper is to review a wide range of unsteady phenomena of leading-edge vortices over stationary and dynamic delta wings.

6.2 SHEAR LAYER INSTABILITIES

The separated shear layers sketched in Figure 1 roll up periodically into discrete vortical substructures, as visualized by Gad-el-Hak and Blackwelder [25], at low Reynolds number flow over a delta wing. This phenomenon was attributed to a Kelvin-Helmholtz type instability of the shear layer. The unsteady

Kelvin-Helmholtz (K-H) instability was observed by flow visualization [25], hot-wire velocity measurements [26], particle image velocimetry measurements [10, 113] and numerical simulations [29]. Riley and Lowson [107] suggested that the appearance of the unsteady K-H instability is due to extraneous inputs peculiar to the particular wind/water tunnel and that this unsteady instability is not a generic part of the flow. They reported that the appearance of the unsteady instability was dependent on a certain range of tunnel velocities. Also, Lowson [76] found that the shear layer was “forced” by vibrational inputs of the tunnel motor cooling fan running at a constant speed of 50 Hz. It should be noted that both Gad-el-Hak and Blackwelder [25] and Lowson [75] in another publication reported that the frequency of the unsteady instability varies with the free stream velocity. It is well known that disturbances in individual facilities may cause wide scatter of dominant frequencies for two-dimensional shear layers [48, 52] since the shear layer is unstable to a wide range of frequencies. However, in the absence of any discrete disturbances, the instability will develop at the most unstable frequency. This is the case in the numerical simulations [29] in which no deliberate forcing of the shear layer is applied. In both experiments [10] and computations [29], the observed frequencies were found to agree with the predictions from the linear stability analysis of the cross-flow shear layer. Therefore, the unsteady K-H instability over delta wings is a generic part of the flow as much as it is for two-dimensional shear layers. Another important feature of the unsteady K-H instability is that it exists in both laminar and turbulent mixing layers [52]. Likewise, these vortical structures were detected over delta wings by hot-wire measurements [26] at Reynolds numbers much higher than those corresponding to flow visualization experiments.

Several researchers [94, 107, 125] revealed the existence of stationary, small-scale vortices around the primary vortex. Such steady structures can persist even after vortex breakdown as shown in Figure 2 (from Mitchell and Molton [94]). The origin of these steady structures is not well understood and has been subject to a variety of hypotheses. The spatially fixed substructures were measured by velocity probes at fixed locations, and were identified as a result of time-averaging the flow. Their relation to the temporal substructures was recently demonstrated by direct numerical simulations [123]. Instantaneous flow shows the temporal substructures and the transition process with increasing Reynolds number (see Figure 3). More interestingly, the time-averaged flow shows isosurfaces of the time-averaged axial vorticity and mean vortical substructures. These results indicate that “steady” and “unsteady” substructures are not necessarily two separate phenomena.

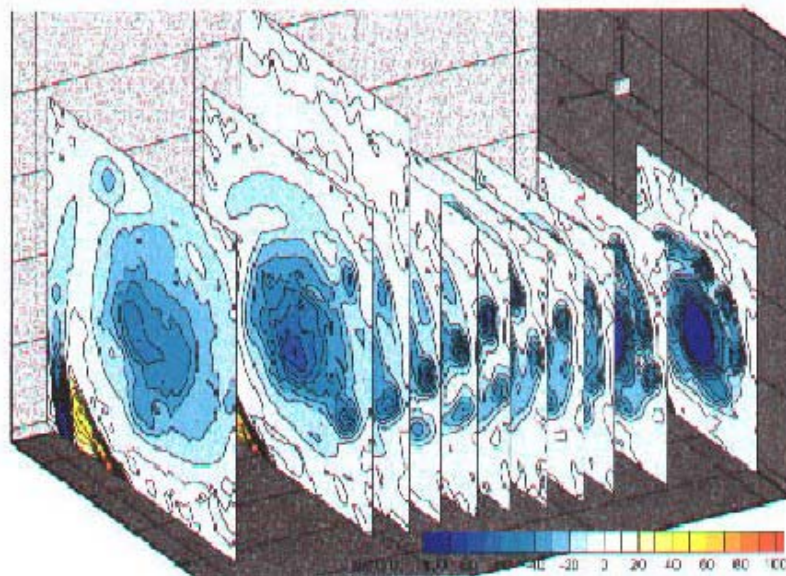


Figure 2: Vortical Substructures around the Primary Vortex over a Delta Wing (Mitchell and Molton, 2002).

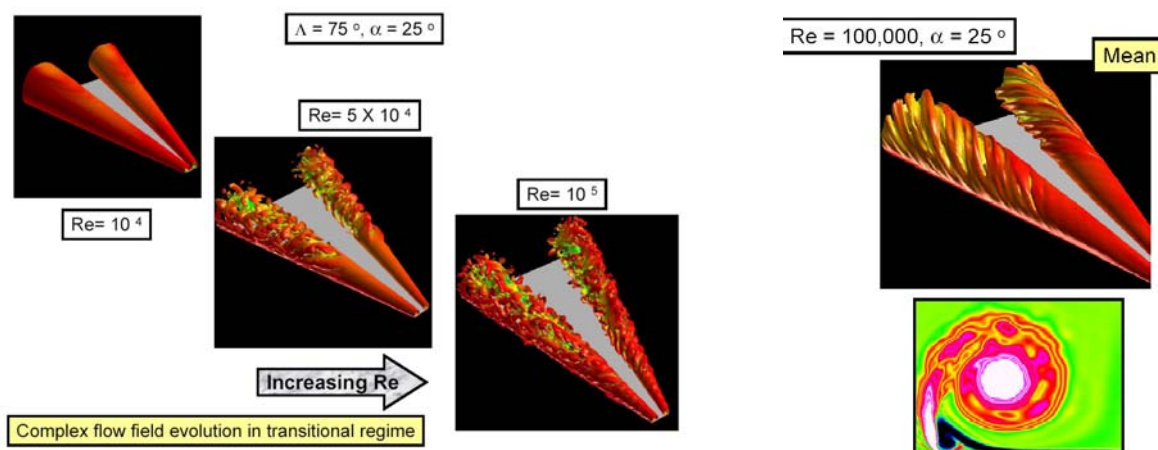


Figure 3: Instantaneous Flow Showing the Transition Process with Increasing Reynolds Number (left); and Time-Averaged Flow Showing Mean Vortical Substructures (right) (Visbal, 2002).

6.3 VORTEX WANDERING

It was shown by Menke and Gursul [85] that large amplitude velocity fluctuations occur upstream of breakdown and also in the absence of breakdown over delta wings. The variation of rms swirl velocity is sketched in Figure 4. The rms swirl velocity is large within the subcore and has a maximum at the axis of the time-averaged vortex. The maximum rms swirl velocity can exceed the free stream velocity depending on the angle of attack. Other investigators also observed large velocity fluctuations in vortex cores over delta wings [61, 111], an aircraft model [11] and an ogive-cylinder [13] over a wide range of Reynolds numbers. Large velocity fluctuations in the vortex cores are common regardless of geometry and Reynolds number. Note that the amplitude of the velocity fluctuations depends on the time-averaged velocity, which is a function of particular geometry and angle of attack. It was shown that maximum rms swirl velocity is roughly half of maximum time-averaged swirl velocity.

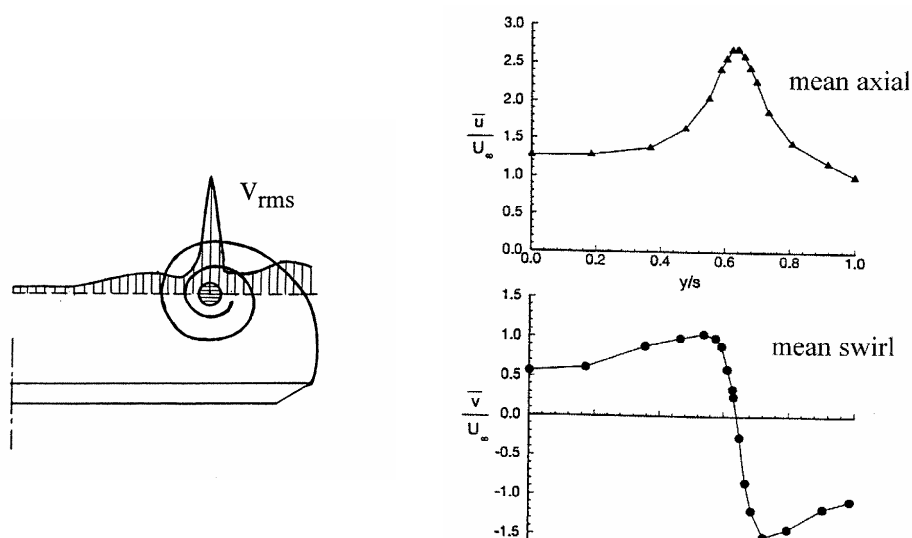


Figure 4: Variation of rms Swirl Velocity across the Vortex Core (left); Together with Time-Averaged Axial and Swirl Velocity Profiles (right) (adapted from Menke and Gursul, 1997).

It was suggested that these large amplitude, broad band random velocity fluctuations are due to random displacements of the vortex core. This “wandering” of vortex core was also observed in tip vortices trailing from rectangular wings [6, 16, 33]. A useful statistical quantity that was employed by Menke and Gursul [85] to study these velocity fluctuations is the probability density function (pdf), which is a measure of the relative amount of time that the velocity spends at various levels. It was shown that the probability density function of swirl velocity is very close to the Gaussian near the vortex axis, but becomes similar to a lognormal distribution away from the axis (see Figure 5). Menke and Gursul [85] proposed a simple model of the flow in which the axis of the Q-vortex has random displacements around a mean location. This simple model produced all the essential features of the measured probability density functions as seen from the comparison of laboratory and model flows (see Figure 5).

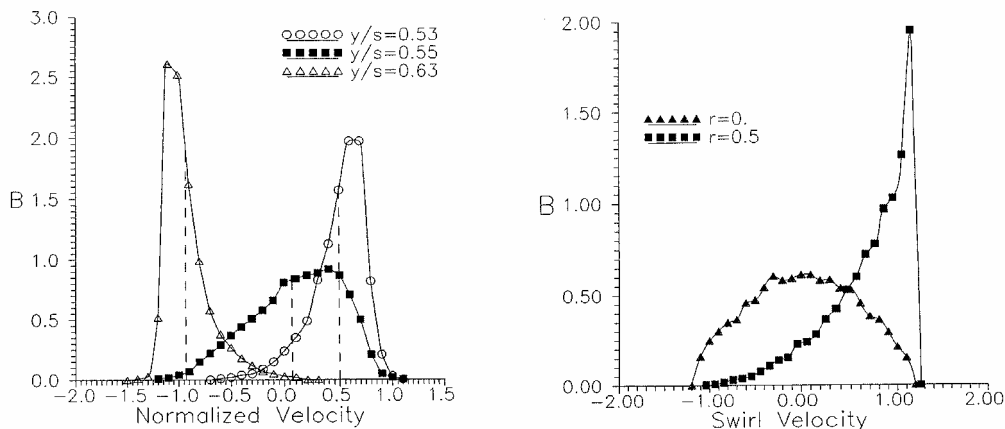


Figure 5: (a) Probability Density Functions of Swirl Velocity for Different Radial Distances, $x/c=0.6$, $\alpha=20^\circ$ (left); (b) Probability Density Functions of Swirl Velocity for the Wandering Q-Vortex (right) (Menke and Gursul 1997).

Several possibilities for the origin of vortex wandering were suggested. For example, it is suggested in the investigations by Baker et al [6] and Devenport et al [16] that vortex wandering in tip vortices is due to free stream turbulence. However, for leading edge vortices, Menke and Gursul [85] showed that vortex core displacements are much larger than those caused by free stream turbulence. Several possibilities, including the Kelvin-Helmholtz instability in the shear layer and unsteady turbulent flow in the wake of the wing, were discussed as potential sources of vortex wandering over delta wings. It is known that shear layer vortices due to the Kelvin-Helmholtz instability exist in the separated shear layer. However, as can be seen from Figure 4, the swirl velocity fluctuations rapidly decrease with the radial distance from the centerline of the time-averaged vortex, and the fluctuations in the shear layer are not as energetic. Whether these weak fluctuations in the shear layer can induce very large fluctuations in the vortex core has not been clear. This issue was later clarified by comparing velocity fluctuations in the absence and presence of the Kelvin-Helmholtz instability.

As shown by Lowson [76], at low Reynolds numbers the flow is laminar and the separated shear layer is steady (upper picture in Figure 6). As the Reynolds number is increased, the flow becomes unsteady and vortical structures appear within the separated free shear layer (lower picture in Figure 6). The variation of the maximum value of v_{rms}/U_∞ is shown in Figure 7 as a function of Reynolds number $Re=U_\infty c/\nu$ (Gursul and Xie [46]). The two arrows in Figure 7 indicate the corresponding Reynolds numbers of the flow visualization pictures in Figure 6. A definite correlation between the vortex wandering and the presence of the Kelvin-Helmholtz instability was demonstrated. This is explained by the Biot-Savart induction of small-scale vortices, which displace the primary vortex. Nonlinear interactions of small vortices and the

primary vortex lead to random displacements of the primary vortex core. In a theoretical model of the oscillations of a side-edge vortex, Sen [112] showed that the trajectory of the primary vortex became chaotic due to the interaction with a small vortex.

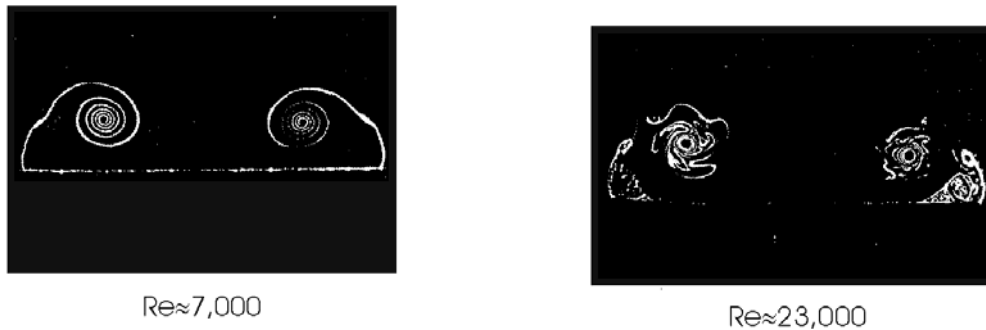


Figure 6: Flow Visualization of Shear Layer (Lowson, 1991).

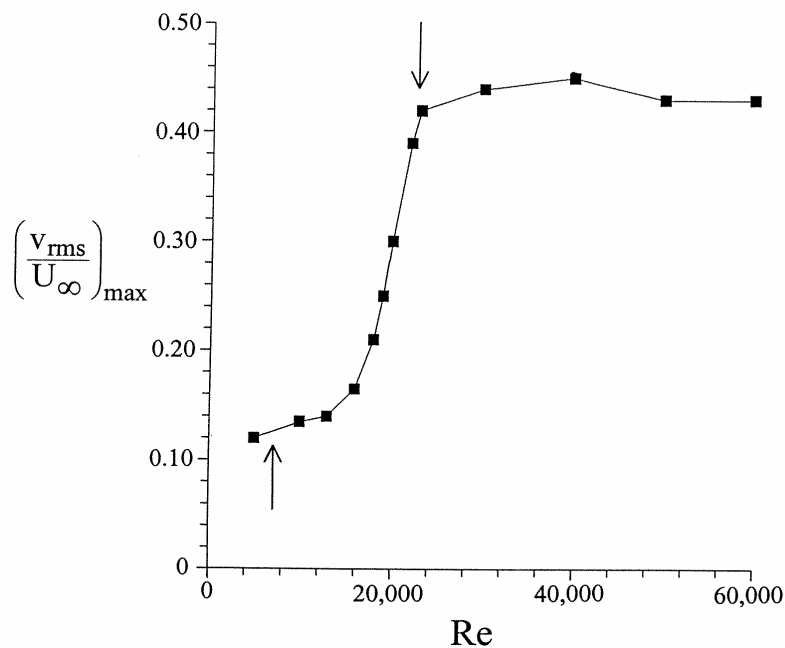


Figure 7: Variation of Maximum rms Swirl Velocity as a Function of Reynolds Number (Gursul and Xie, 2000).

6.4 VORTEX BREAKDOWN

Vortex breakdown is an intriguing phenomenon that has been observed on delta wings. Flow visualization of Lambourne and Bryer [65] revealing the so-called “bubble” type and “spiral” type vortex breakdowns is shown in Figure 8. Subsequent research suggested that the spiral type is more common over delta wings. In fact, even the bubble type of vortex breakdown switches to the spiral type from time to time in experiments.

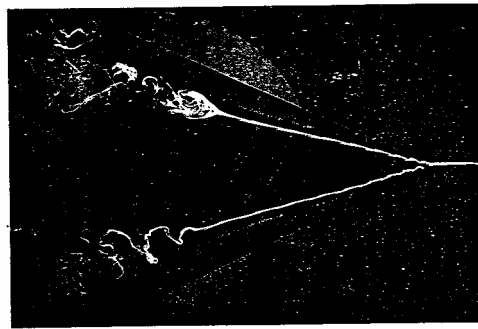


Figure 8: Flow Visualization of Vortex Breakdown over a Delta Wing (Lambourne and Bryer, 1962).

Different explanations of the vortex breakdown phenomenon based on hydrodynamic instability, wave propagation, and flow stagnation are summarized in several review articles [21, 49, 71]. It is now generally agreed that this phenomenon is a wave propagation phenomenon, and there is a strong analogy to shocks in gas dynamics. Concepts of supercritical and subcritical flows based on wave propagation characteristics play an important role in the understanding of vortex breakdown.

Both experiments and theoretical explanations show that there are two important parameters affecting the occurrence and movement of vortex breakdown: swirl level and external pressure gradient outside the vortex core. An increase in either parameter promotes the earlier occurrence of breakdown. For leading-edge vortices, both parameters depend on the wing geometry, such as incidence and sweep angle.

6.4.1 Helical Mode Instability

It is well known that the flow downstream of vortex breakdown exhibits a well-documented hydrodynamic instability. Periodic oscillations were observed in a variety of swirling flows after breakdown occurred. With regard to leading edge vortices, examples of time histories of wing surface pressure at $x/c=0.93$ are shown in Figure 9 (taken from Gursul and Yang [42]). For the smallest angle of attack $\alpha=15^\circ$, the breakdown location is not over the wing. With increasing angle of attack, the amplitude of the pressure fluctuations increases as vortex breakdown moves over the wing. The quasi-periodic pressure fluctuations are clearly seen while the frequency content also varies with the angle of attack.

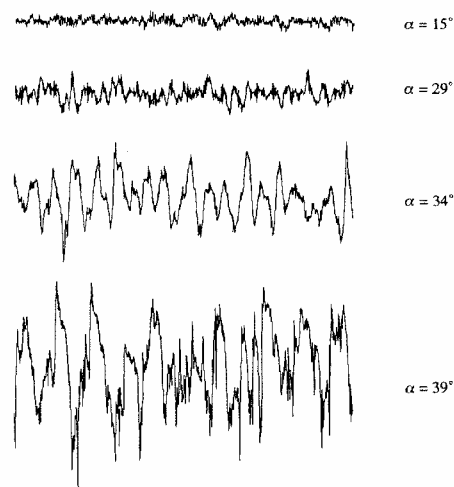


Figure 9: Pressure Fluctuations Near Trailing-Edge ($x/c=0.93$) for Different Angle of Attack, $y/s=0.5$. Length of time record is approximately $10c/U_\infty$ (Gursul and Yang, 1995).

Unsteady pressure measurements on delta wings and fins revealed downstream convection of a wave pattern associated with vortex breakdown [36, 68, 77]. Experimentally observed periodic velocity/pressure oscillations [27, 36] correspond to the most unstable normal modes of the time-averaged velocity profiles of the vortex (downstream of breakdown) based on the linearized, inviscid stability analysis. The disturbances are represented as $\exp\{i(kx+n\phi-\omega t)\}$, where ω is the frequency, k the wave number in the axial direction, and n the wave number in the angular direction. By using two-point pressure measurements in the axial and spanwise directions [36], it was demonstrated that these fluctuations are due to the first helical mode ($n=1$). If one considers constant phase surfaces at a certain instant, the description for a helix is obtained, i.e., $kx+\phi=\text{constant}$, which shows that the sense of the helix is **opposite** to the direction of rotation in the vortex [115]. However, the whole structure rotates with a frequency ω in the **same** direction as the vortex. Experiments also indicate that the frequency decreases in the streamwise direction, which implies that the pitch of the helix increases in the streamwise direction. This was confirmed by the instantaneous azimuthal vorticity distribution [118] in a plane that passes through the axis (see Figure 10). The vorticity concentrations are staggered like Karman vortex street and the spacing increases in the streamwise direction.

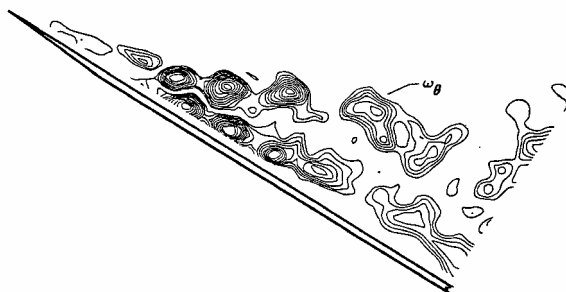


Figure 10: Instantaneous Azimuthal Vorticity Distribution in a Plane that Passes through the Axis (Towfighi and Rockwell 1993).

The proposed model of the helical mode instability as a helical vortex filament is consistent with observations of unsteady velocity and pressure measured by probes immersed into breakdown wake. For example, Jaworski et al [55] and Lee and Brown [67] showed that the rms values of velocity and pressure are minimum at the axis, and become maximum at a certain radial distance. On the other hand, the location of the maximum rms pressure on the wing surface is directly beneath the vortex axis [36, 55]. This can be confirmed by considering a simple flow model [44] in which an infinite helical vortex is located at a certain distance over an infinite plane.

Also, this description of the helical mode instability is consistent with well-known observations of the spiral breakdown over delta wings [65]. It is well known that this is the dominant mode observed over delta wings [65, 74, 126]. It was also observed in flight [23] of an F-18, which indicated that it was not limited to low Reynolds numbers. Analyzing flow visualization studies in wind tunnels, Jumper et al [58] indicated that even in the cases where breakdown looked like a bubble type, a spiral form was identified in instantaneous pictures with a short exposure time. This supports the view that the spiral form is a consequence of the instability of the bubble form [21]. For spiral breakdown, the sense of the helix is opposite to the direction of rotation in the main vortex as observed over delta wings [58]. However, in some vortex-tube experiments [22, 110], it was reported that the sense of helix is the same as the direction of swirl, while in some others (with tangential inlets) the opposite was found [21]. Leibovich [71] attributed this inconsistency to the differences in the way swirl is generated. However, in recent experiments in which swirl is also generated by guide-vanes [8], the sense of helix was found to be opposite to the direction of swirl. The sense of helix was found opposite to the direction of swirl in all swirling flows but with two exceptions [22, 110], and the reason behind this difference remains unknown. The opposite sense is consistent with unsteady flow in the breakdown wake. Also, Jumper et al [58] pointed out in a simple model of breakdown that the sense of helix

should be opposite to the direction of swirl in order to have axial velocities (due to the Biot-Savart induction) opposite to the free stream flow to generate stagnant flow behind the vortex breakdown.

Flow visualization at low Reynolds numbers indicates that the helical vortex filament persists for several turns before breaking up into large scale turbulence. However, coherent pressure fluctuations were detected at downstream locations that are very far away from the breakdown location. In addition, these coherent fluctuations were detected at high Reynolds numbers [109] of the order of 10^6 as well as on full-scale aircraft [89]. The dominant frequencies for aircraft models also agree with the frequency of the helical mode instability [59].

As discussed earlier, the pitch (wavelength) of the helical mode instability increases in the streamwise direction, while the frequency decreases. Measurements of pressure fluctuations at different streamwise locations on delta wings suggest that the dimensionless frequency fx/U_∞ is nearly constant for a given geometry [36, 109]. Knowledge of the dominant frequency of the helical mode instability as a function of wing geometry (angle of attack and sweep angle) is important for buffeting problems, particularly fin buffeting. Figure 11 shows the dimensionless frequency fx/U_∞ as a function of angle of attack for different sweep angles [36]. The range of the data is nearly the same for different wings, which suggests that a single relationship can be obtained if a unique parameter is found. Gursul [36] suggested that $\Gamma/U_\infty x$, where Γ is the circulation of the leading edge vortex, is a proper dimensionless number. Figure 12 shows that all of the data collapse except for $\Lambda=60^\circ$. Since the method used to estimate circulation is a good approximation for slender delta wings, the discrepancy for $\Lambda=60^\circ$ is believed to be due to the incapability of the method to estimate circulation. Note that the dimensionless number $\Gamma/U_\infty x$ is related to the rate of increase of the circulation along the streamwise direction (or the rate at which vorticity is fed into the leading edge vortex) for a conical flow. It is also interesting to note that this dimensionless number provides a good correlation for the location of vortex breakdown over delta wings [37].

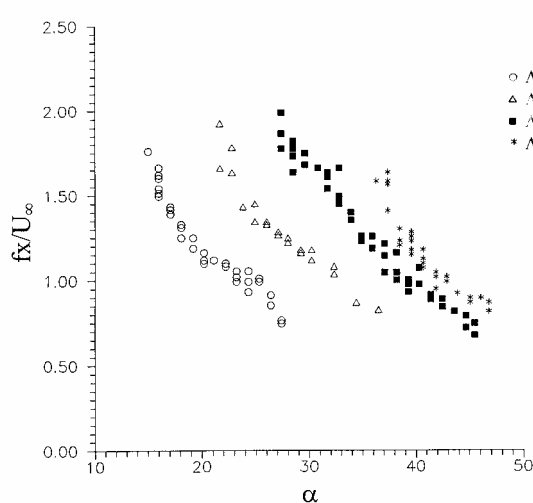


Figure 11: Variation of Dimensionless Frequency as a Function of Angle of Attack for Different Sweep Angles (Gursul, 1994).

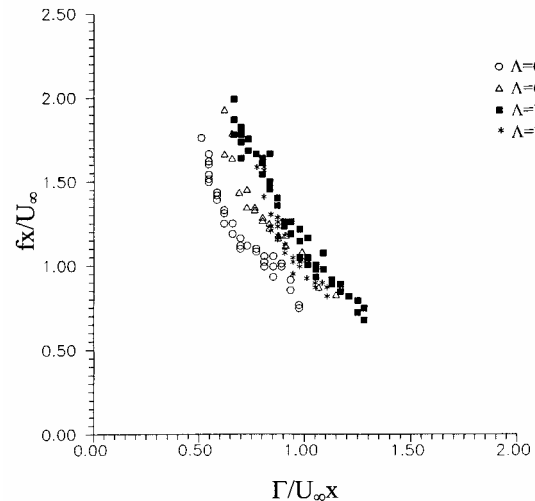


Figure 12: Variation of Dimensionless Frequency as a Function of Dimensionless Circulation (Gursul, 1994).

Using the data shown in Figure 11, Mabey [79] proposed a relationship in the form of $fc \cot \Lambda \sin \alpha/U_\infty = 0.27$ for the frequency at the trailing edge (i.e., $x=c$), which gives a useful design rule for delta wings. As summarized here, there is sufficient information on the dominant frequency of the helical mode instability, which can be used for rapid calculations. It should be noted that these data are valid for vortex

breakdown naturally occurring over slender delta wings. However, at smaller angles of attack, breakdown can be induced, for example, by the presence of a fin. There is no available data on the dominant frequencies for this type of premature vortex breakdown, which would be useful for fin-buffeting predictions.

6.4.2 Oscillations of Breakdown Location

It was observed in several experiments that vortex breakdown location over stationary delta wings is not steady and exhibits fluctuations along the axis of the vortices [74, 100]. Subsequently it was discovered that these oscillations are in the form of an antisymmetric motion of breakdown locations for left and right vortices [5]. An example of time histories of breakdown locations for left (solid lines) and right (dashed lines) vortices are shown in Figure 13 for $\alpha=37^\circ$ and $\Lambda=70^\circ$ (from Menke and Gursul [86]). The two breakdowns, which are almost mirror images, oscillate in an antisymmetric motion. The correlation coefficient in this case is -0.61 . The amplitude of these fluctuations can be a significant fraction of the chord length. These oscillations may be very important for the stability and control of highly maneuverable aircraft, and also have important consequences for wing and tail buffeting.

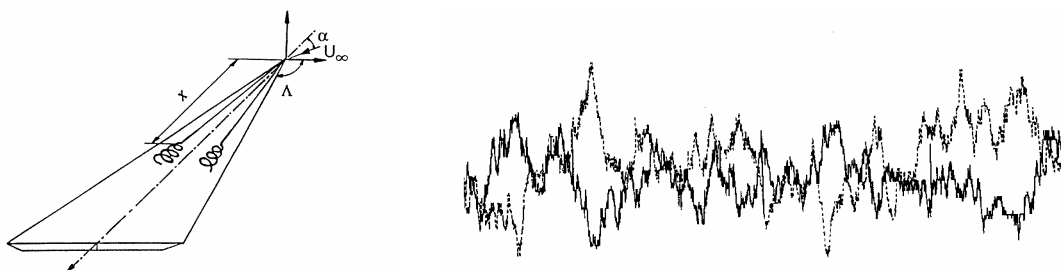


Figure 13: Time Histories of Breakdown Locations for Left (solid lines) and Right (dashed lines) Vortices for $\alpha=37^\circ$ and $\Lambda=70^\circ$ (Menke and Gursul 1997).

It was also reported that oscillations of breakdown locations are quasi-periodic [5, 43, 88, 102]. This coherent antisymmetric motion was clearly demonstrated by studying the difference between the breakdown locations $(x_{\text{left}} - x_{\text{right}})/c$ and the average breakdown location $(x_{\text{left}} + x_{\text{right}})/2c$. The spectra of these are shown in Figure 14 for $\Lambda=75^\circ$ and $\alpha=42^\circ$ (taken from Menke and Gursul [87]). It is seen that most of the energy is concentrated in the difference, and there is a dominant peak corresponding to the quasi-periodic antisymmetric oscillations.

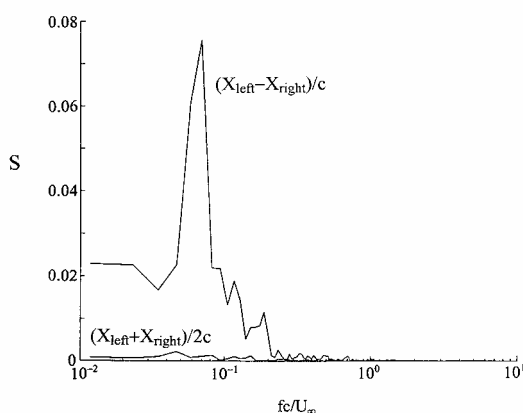


Figure 14: Spectra of Difference and Average of Breakdown Locations for $\Lambda=75^\circ$ and $\alpha=42^\circ$ (Menke and Gursul 1999).

Similar observations of quasi-periodic oscillations of breakdown location were also made by other investigators by using flow visualization in water tunnels. It is interesting that these oscillations were observed at Reynolds numbers as low as $Re=2,250$. A similar range of dominant frequencies has been observed in all water tunnel experiments. Recently, Mitchell et al [92] carried out smoke flow visualization in a wind tunnel at $Re=9.75 \times 10^5$ to 2.6×10^6 , and reported a similar range of dominant frequencies of oscillations of breakdown location. Lambert and Gursul [63] presented further quantitative evidence of oscillations of breakdown location at $Re=1.6 \times 10^6$ by using two-point surface pressure measurements. The spectra of the difference $(p_{\text{left}} - p_{\text{right}})$ and the average $(p_{\text{left}} + p_{\text{right}})/2$ are shown in Figure 15. Again, it is seen that most of the energy is concentrated in the difference, which confirms that pressure fluctuations are mostly out-of-phase. Of course, the same conclusion could be reached by examining the amplitude and phase of the cross-spectrum of left and right pressure signals as shown by Lambert [64]. In summary, recent investigations indicate that the phenomenon of quasi-periodic oscillations of breakdown location also exists at high Reynolds numbers.

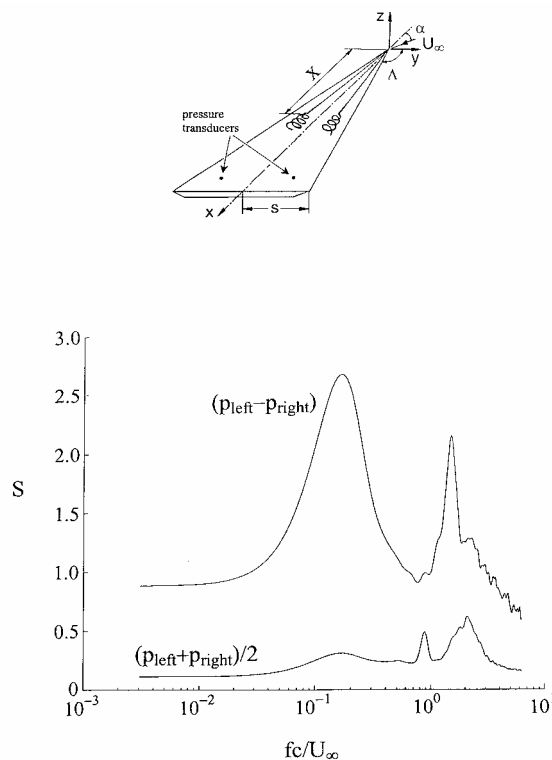


Figure 15: Spectra of the Difference and Average Pressure Fluctuations, $\alpha=50^\circ$, $\Lambda=80^\circ$ (Lambert and Gursul, 1999).

A possible relationship between these quasi-periodic oscillations and the hydrodynamic instability of breakdown wake (i.e., the helical mode instability) was investigated by Gursul and Yang [43]. However, it was shown that the dominant frequency of the oscillations of breakdown location occurred at much lower frequencies than the frequency of the helical mode instability. Therefore, the helical mode instability has no effect on the oscillations of breakdown location. In fact, it was shown by Menke et al [88] that the frequency of this organized motion is much smaller than the frequency of any other known instabilities. The spectrum of unsteady flow phenomena over delta wings as a function of dimensionless frequency is shown in Figure 16. The frequency range of vortex shedding is also shown, although this phenomenon is distinctly different from other phenomena presented in the figure and is not observed until the vortex breakdown location reaches the apex. When compared with the frequency of other phenomena,

the frequency range of oscillations of breakdown location for a stationary delta wing is much closer to the frequency range of typical aerodynamic maneuvers (up to $fc/U_\infty \approx 0.03$). The response of breakdown location and possible coupling between the wing motion and breakdown location in this frequency range is very important.

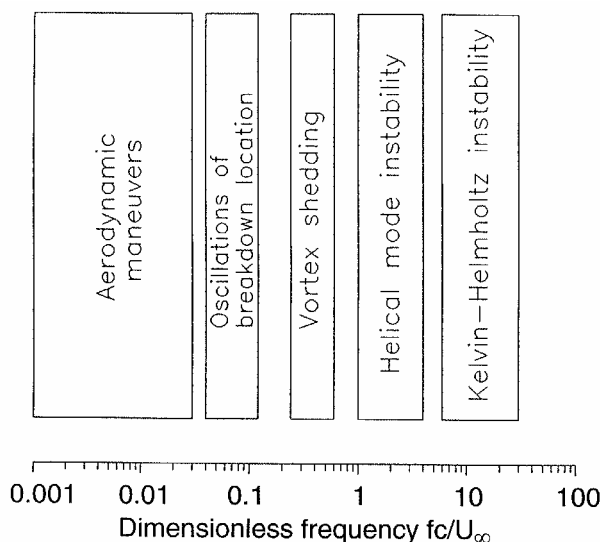


Figure 16: Spectrum of Unsteady Flow Phenomena over Delta Wings as a Function of Dimensionless Frequency (Menke et al 1999).

In order to understand the mechanism leading to oscillations of breakdown location, extensive experiments were conducted, and spectral analysis and other statistical concepts were used to quantify the unsteady behaviour of vortex breakdown location obtained from flow visualization [88]. It was found that oscillations become larger and more coherent as time-averaged breakdown locations get closer to each other when the angle of attack or sweep angle is increased. Although these kinds of vortex interactions are more of a concern for slender wings, evidence of such interactions at a relatively low sweep angle of $\Lambda=60^\circ$ was recently reported [32]. Wing tip accelerations occurred in an antisymmetric structural mode for a slightly flexible delta wing when vortex breakdown occurred on the wing.

The detailed mechanism that is responsible for this interaction is not clear. One possible mechanism is that the interaction is the result of a cross-flow instability (see Figure 17). This is very similar to the well-known vortex asymmetry problem in forebody flows, except that the asymmetry for delta wing vortices is time-dependent while the time-averaged locations of vortex cores are symmetric. The oscillations of vortex cores could be imagined to arise from a loss of stability by the symmetric mean flow. It is possible that this interaction causes the location of breakdown to vary periodically in an antisymmetric motion. Although no signs of cross-flow instability were observed in flow visualization experiments, this may be due to the small amplitude of core displacements. A second possible mechanism is that the interaction is the result of a streamwise instability of breakdown regions, and vortex breakdown is a necessary part of the onset of the instability. Further studies are needed to clarify the physical mechanism of the interaction in the light of recent evidence [70], which indicates that cross-flow instability may exist. Also, periodic oscillations of vortex cores about mean symmetric positions have been observed in flow visualization experiments for a circular cone [116]. This quasi-periodic phenomenon was observed visually near the onset angle of attack of asymmetry and over a certain range of Reynolds numbers. A recent theoretical work [54] revealed that vortices over a thin slender delta wing are stable to all disturbances of small amplitude based on the slender-body theory for an inviscid incompressible flow, but the vortices may become unstable with increasing wing thickness.

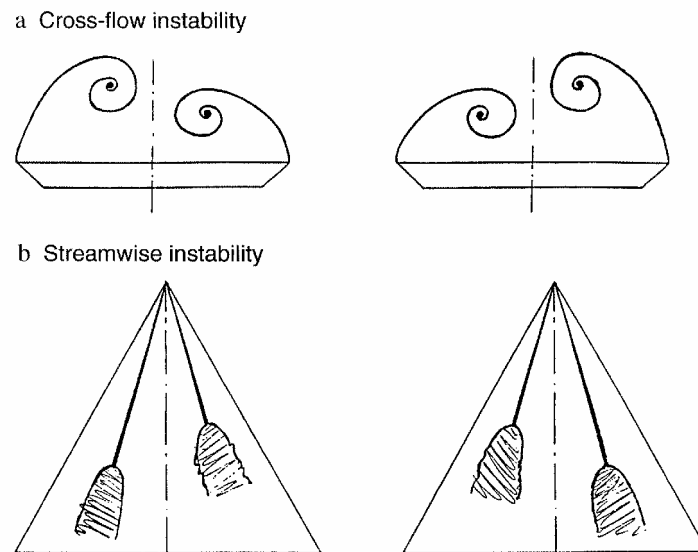


Figure 17: Possible Interaction Mechanisms:
(a) Cross-Flow Instability, (b) Streamwise Instability.

Another interesting aspect of vortex interactions was revealed by velocity measurements performed upstream of breakdown location [88]. The quasi-periodic velocity oscillations, which are induced by the oscillations of breakdown location through upstream influence, were confined to the primary vortex core as well as to the secondary vortex. Hence a secondary interaction between the primary and secondary vortices is evident. It is not known what effect this has on the unsteady aerodynamics of delta wings.

It is obvious from the time series of breakdown location that there exists much small scale motion. The time history of breakdown location consists of low-frequency, large-amplitude fluctuations and high-frequency, low-amplitude fluctuations. As discussed earlier, the low-frequency, large-amplitude motion dominates the spectrum and is responsible for the large scale displacements. On the other hand, the source of the small scale motion is not clear. More information about the high-frequency fluctuations was obtained by the Peak-Valley-Counting (PVC) technique developed for studying the small-scale motion from velocity traces in shear layers [53, 136]. The principle of this technique is to identify every local maximum and every local minimum due to the high-frequency fluctuations and to assign a pulse of (+1) or (-1), as shown in Figure 18a. The interval between successive positive (or negative) pulses represents the period of that particular event. The probability density function of the interval between successive positive pulses is shown as a histogram in Figure 18b for $\Lambda=75^\circ$ and $\alpha=42^\circ$. The PVC histogram shows a maximum around $f_c/U_\infty \approx 6.1$. Similar histograms for the other test cases reveal that there exists a maximum of the pdf for a frequency between $f_c/U_\infty=6$ and $f_c/U_\infty=10$. This range of dimensionless frequency falls in the same range of frequency of the Kelvin-Helmholtz instability (see Figure 16).

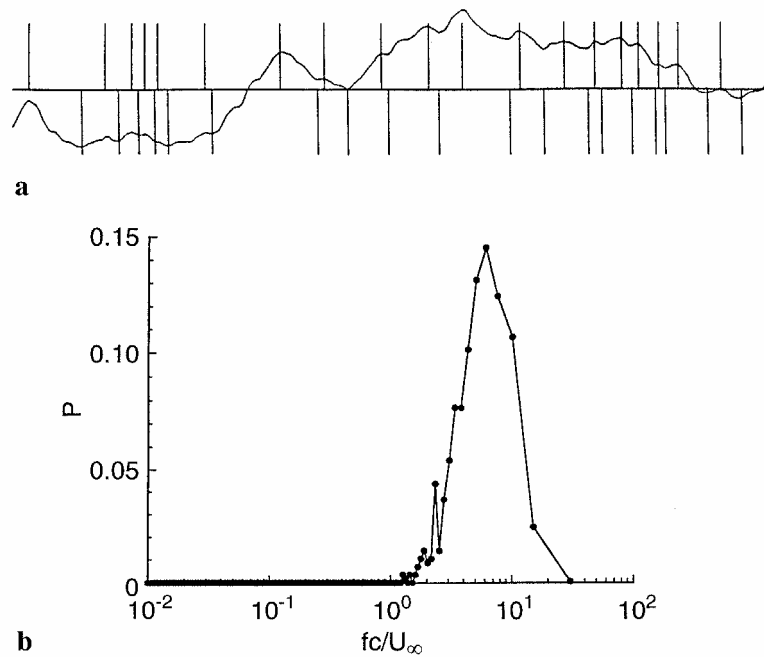


Figure 18: (a) PVC Algorithm; (b) PVC Histogram for $\alpha=42^\circ$ and $\Lambda=75^\circ$ (Menke et al 1999).

Vortex interactions over delta wings may become even more complex for maneuvering aircraft. Recent research has shown that the dynamic response of breakdown location to small amplitude pitching oscillations of a delta wing may be very complex [87]. At moderate angles of attack, left and right breakdown locations are in-phase and locked to the pitching frequency (see Figure 19). At large angles of attack, the natural antisymmetric oscillations and the symmetric oscillations caused by the pitching motion are observed simultaneously. The resulting motion is no longer periodic and a phase-averaging (ensemble-averaging) technique is not appropriate to study the variation of breakdown. There is also a remarkable antisymmetry between the left and right breakdowns. It was shown that the mode competition between the symmetric and antisymmetric modes is strongly affected by the excitation frequency. The relative amplitude of the symmetric mode increases with increasing frequency. This was demonstrated by considering the rms values of the difference and the average. The ratio of these rms values is defined as

$$R = \frac{\left(x_{\text{left}} + x_{\text{right}} \right)_{\text{rms}}}{2 \left(x_{\text{left}} - x_{\text{right}} \right)_{\text{rms}}} \quad (1)$$

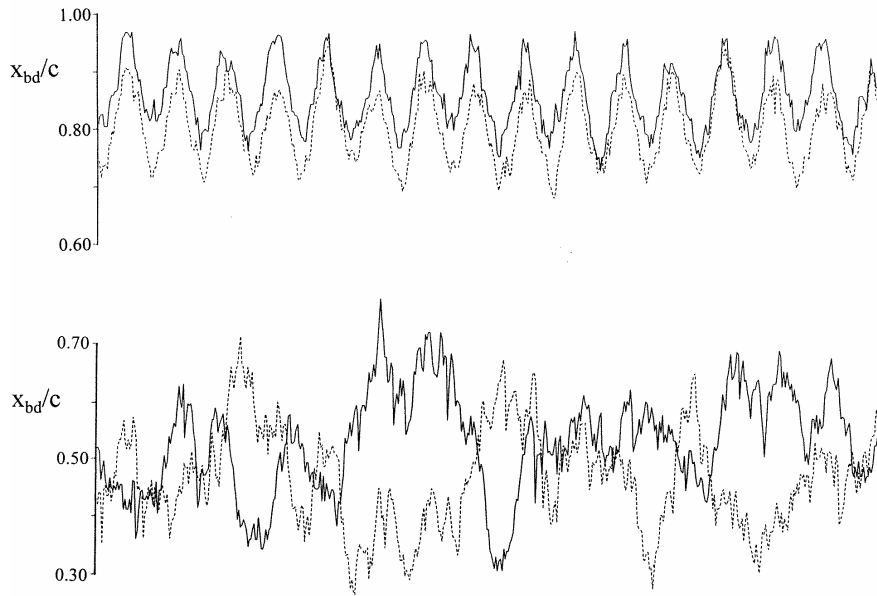


Figure 19: Time Histories of Breakdown Locations for Left and Right Breakdowns for $\alpha_0=29^\circ$ (top) and $\alpha_0=42^\circ$ (bottom) for $\alpha_1=3^\circ$, $fc/U_\infty=0.1$. Length of time record is $170c/U_\infty$ (Menke and Gursul, 1999).

The variation of this ratio with reduced frequency is shown in Figure 20. It is seen that this ratio increases with increasing reduced frequency, confirming that the symmetric mode becomes more important with increasing reduced frequency. The effect of the reduced frequency on the mode competition can be also seen by studying the correlation coefficient, which increases with reduced frequency. The physical mechanism of this observation remains to be explored.

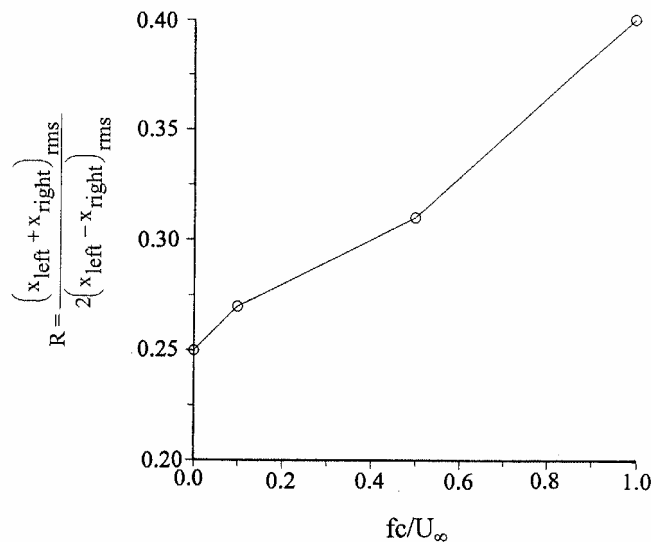


Figure 20: Variation of the Ratio R with Reduced Frequency, $\alpha_0=42^\circ$, $\alpha_1=3^\circ$.

The response of breakdown location to small amplitude pitching oscillations of the delta wing showed that it has some features of a nonlinear system, such as the existence of multiple frequencies in the spectrum. Also, there are other indications that it has some similarities to a “self-excited” oscillator [91]. For example, even very small amplitude pitching motion is sufficient to cause a large increase in the amplitude of the antisymmetric oscillations of breakdown location compared to that of the stationary wing.

6.5 LEADING EDGE VORTICES IN UNSTEADY FLOWS

Up to this point only stationary delta wings have been considered. In this section unsteady flow phenomena will be considered over dynamic delta wings. The earliest investigation in this direction was a flow visualization study over a delta wing oscillating in heave [81]. When the variation of the height of vortex core (relative to the wing surface) was studied, it was found that there existed a phase lag of the motion of the vortex core with respect to its variation in the quasi-steady case.

Lambourne et al [66] investigated the transient behavior of leading-edge vortices over a plunging delta wing. This study was conducted in a water tunnel and was concerned with how vortices and separated shear layers developed after the model was driven at a constant plunge velocity, which corresponded to a sudden increase in angle of attack from zero. An example of the variation of the height of vortex center above the wing as a function of dimensionless time is shown in Figure 21. These results indicate that after the start of the plunge, the movement of the vortex core with respect to the wing is almost completed within one local convective time unit (the time required for the free stream to travel from the apex to the cross-flow plane). Note also that the response of vortex core is similar to that of a first order dynamic system to a step function input. Therefore, with this model, one also expects to find a phase lag in the variation of position of vortex core, which is consistent with the findings of Maltby et al [81] in oscillatory experiments.

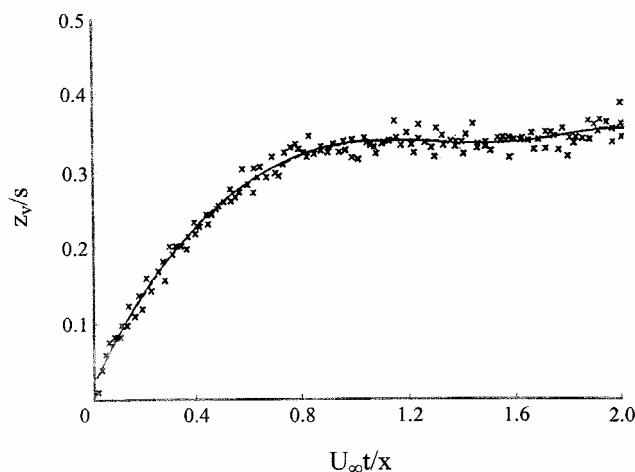


Figure 21: Height of Vortex Center above the Wing Following a Sudden Change of Incidence (Lambourne et al, 1969).

Gad-el-Hak and Ho [24] conducted a flow visualization study on pitching delta wings. It was noted that leading-edge vortices executed a growth-decay cycle and the flow patterns revealed the existence of a hysteresis loop. The variation in the height of the dyed region in the cross-plane as a function of angle of attack is shown in Figure 22. During the upstroke motion, the dyed region was thinner than that of the quasi-steady case (at a given angle of attack) due to the time delay in the development of the vortex. During the downstroke motion, the height of the dyed region again lagged behind the quasi-steady value,

which resulted in a thicker dyed region. In summary, reported phase lags and hysteresis loops indicate that a time lag in the development of the cross-sectional flow pattern exists in unsteady flows.

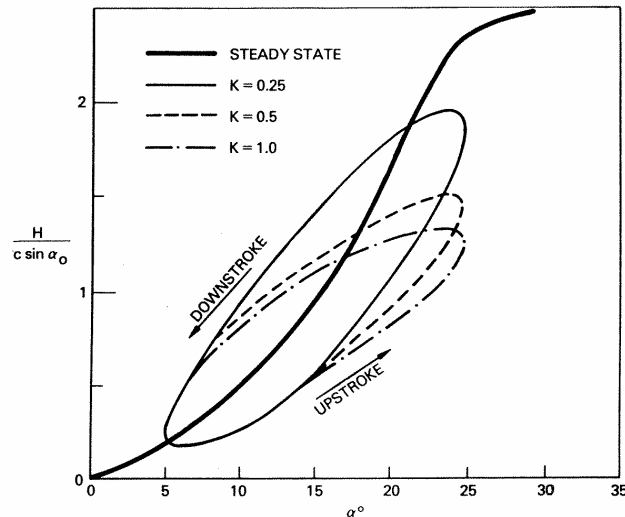


Figure 22: Variation of Height of Dyed Region in a Cross-Flow Plane as a Function of Angle of Attack for a Periodically Pitching Delta Wing (Gad-el-Hak and Ho, 1985).

6.6 VORTEX BREAKDOWN IN UNSTEADY FLOWS

Extensive experimental studies of the dynamic response of vortex breakdown due to wing motion have been conducted. The most important observation from these experiments was that the vortex breakdown had a time delay with respect to the quasi-steady case. Computational results [121] for transient vortex breakdown above a delta wing subject to a pitch-and-hold maneuver to high angle of attack showed that the onset and delay of vortex breakdown are strongly linked to the adverse pressure gradient along the vortex axis, which depends on the wing angle of attack and pitching motion.

The effect of adverse pressure gradient is also important for vortex breakdown over a stationary delta wing in unsteady free stream [41]. If the vortex breakdown location is away from the trailing-edge and closer to the apex in steady free stream, the unsteadiness does not affect the burst position. Otherwise, the breakdown may appear suddenly at an upstream location, depending on the frequency and amplitude as shown in Figure 23 (Gursul and Ho [40]). It was suggested that the time-dependent nature of burst position is due to the relative variations in pressure gradient on the wing surface, which is expected to be more important near the trailing-edge. It is also noted that the shape and size of vortex breakdown region/wake may be very different in unsteady flows. For example, a highly elongated shape of breakdown at $t/T=0$ is very unusual compared to the bubble type of breakdown at $t/T=0.25$.

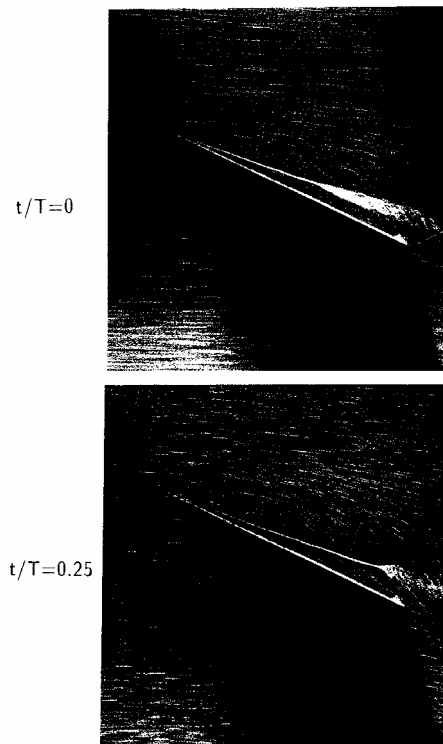


Figure 23: Flow Visualization of Vortex Breakdown for Unsteady Free Stream
 $U/U_\infty = 1 + R \cos(\omega t)$, $\alpha = 25^\circ$, $\omega c/2U_\infty = 1.395$, $R = 0.70$ (Gursul and Ho, 1993).

Abrupt transformations of the leading-edge vortex have been observed when a delta wing was pitched to high angle of attack [73]. These abrupt transformations are characterized by different propagation speeds of breakdown (by one order of magnitude) and different shapes of wake region. An example of contours of constant azimuthal vorticity showing abrupt transformation of structure of leading edge vortex is given in Figure 24. During the initial stage of pitch-up maneuver ($t^* = 0.28$), the shape of the vortex breakdown region is more like the bubble type, whereas at a later stage ($t^* = 0.42$) it has a highly elongated shape. The changes in propagation speed have obvious consequences for the time lags during a maneuver. Also, changes in wake region are likely to affect the instabilities associated with vortex breakdown, such as the helical mode instability, as evidenced by a recent experimental investigation [12].

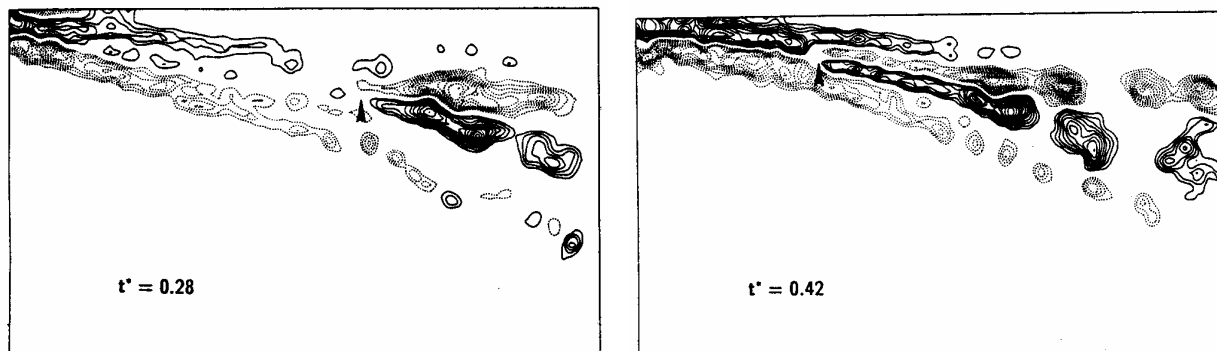


Figure 24: Contours of Constant Azimuthal Vorticity for Transient Vortex Breakdown over a Pitching Delta Wing (Lin and Rockwell, 1995).

6.6.1 Response of Vortex Breakdown

As discussed above, when a delta wing undergoes pitching motion at high angle of attack, there is a time lag of vortex breakdown location with respect to its variation in the quasi-steady case. The earliest reference to the time lag of breakdown location was made by Lowson [74]. Subsequently, Krishnamoorthy [62] and Woodgate [133] observed the time lag in water tunnel and wind tunnel experiments, respectively. Recently, more detailed observations of the phase lag were made by Wolffelt [131], Atta and Rockwell [3, 4], and LeMay et al [72]. These studies revealed that, for a periodic pitching motion, vortex breakdown location forms hysteresis loops when plotted as a function of angle of attack. An example is shown in Figure 25. The loops become wider with increasing frequency. It was also shown that the time lag (or phase lag) increases with increasing reduced frequency, without significant influence of the Reynolds number.

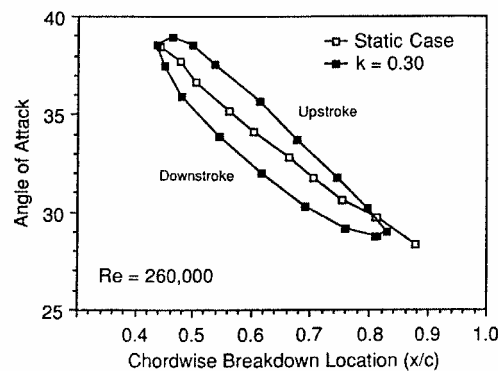


Figure 25: Chordwise Location of Vortex Breakdown for a Pitching Delta Wing (LeMay et al, 1990).

This time lag, which is important for the stability and control of aircraft, has also been observed for other types of wing motion, such as plunging and rolling (see Greenwell and Wood [34] for a summary). The response of breakdown location was also studied for transient motions such as a finite ramp pitching motion or plunging motion by Thompson et al [117], Miao et al [90], Reynolds and Abtahi [106], and Magness [80]. Similar observations of time lag and hysteresis effects were made for pitch-up and pitch-down motions. Also, similar time lags were observed for a variety of wing shapes including diamond, cropped, delta, and double delta wings [95]. It was commonly observed that, upon completion of the wing motion, vortex breakdown required a very long time (of the order of 10 convective time units) to reach the steady-state position. Although this has been interpreted by several investigators as a separate phenomenon with a large time scale, there is no firm evidence of that, as pointed out by Greenwell and Wood [34]. An alternative interpretation is that the response of breakdown location is similar to that of a first order system to a step function input, and the time constant is much smaller than 10 convective time units. For a first order system, the output reaches the steady-state level very gradually in the form of an exponential rise, which is very similar to the response of breakdown location. With this idealization, the time constant τ can be estimated from the time history of breakdown location in response to a given unsteady wing/surface motion. The estimated values of the time constant for different types of motion are given by Srinivas et al [115]. The normalized time constant $\tau U_\infty/c$, which is of the order of unity, depends on the type and amplitude of the motion, the breakdown location in the static case, and the sweep angle of the wing. For $\Lambda \geq 70^\circ$, the normalized time constant is around $\tau U_\infty/c = 1$ to 2. For lower sweep angles, the time constant is larger. Greenwell and Wood [34] modelled the dynamic response of the breakdown location by a first order as well as a second order system. By curve fitting to the experimental values of the phase lag for pitching wings, they obtained $\tau U_\infty/c = 1.67$ for a first order system (see Figure 26). Reisenhel et al [105] studied the dynamic response of breakdown location to an oscillating fin over a delta wing. They indicated that the time constant associated with the upstream motion of the vortex breakdown location is larger than that associated with its

UNSTEADY ASPECTS OF LEADING-EDGE VORTICES

downstream motion. It was suggested that dynamic hysteresis of vortex breakdown location can be explained by the discrepancy in the time constants.

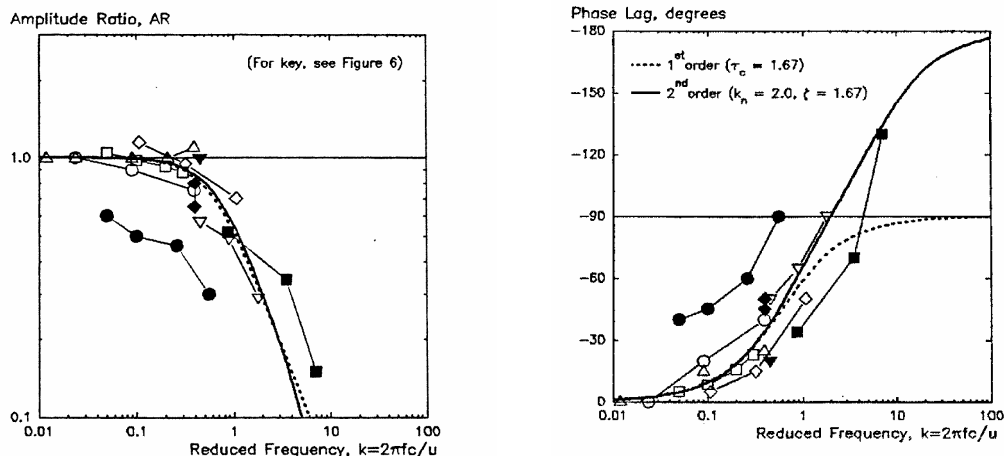


Figure 26: Amplitude Ratio and Phase Lag of Vortex Breakdown Location as a Function of Reduced Frequency (Greenwell and Wood, 1994).

Recent investigations of vortex breakdown control techniques revealed similar time lags. The measured phase lag of breakdown location with respect to the quasi-steady case is shown in Figure 27 as a function of the reduced frequency $K=\omega c/2U_\infty$ for oscillating leading-edge flaps [15] and leading-edge extensions [135] together with pitching wings [42, 72]. Although there is a larger scatter of data at high frequencies, there is a consistent trend of increasing phase lag with increasing reduced frequency. Several factors are important for phase lag and contribute to the data scatter: the breakdown location in the static case, amplitude of motion, fluctuations of breakdown location which are also observed for stationary wings, the number of cycles used for phase-averaging, and the method used to calculate phase lag. In particular, at large frequencies, the amplitude of the phase-averaged variations of breakdown location becomes smaller. Calculated phase lag is sensitive to the number of cycles used for phase-averaging. Keeping these factors in mind, collapse of data is not expected for different motions. The purpose of Figure 27 is simply to show that the phase lags are similar for α , Λ , and δ variations.

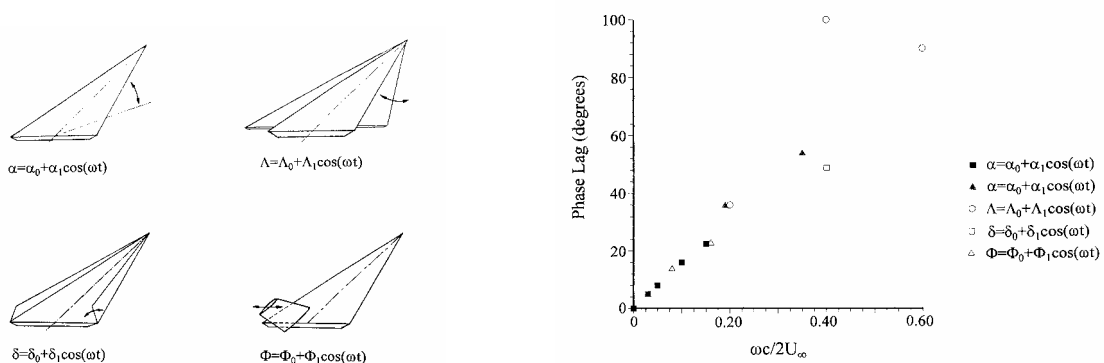


Figure 27: Phase Lag of Vortex Breakdown Location for Different Types of Unsteady Motion (Gursul, 2000).

Also shown in Figure 27 is the phase lag of breakdown location for an oscillating fin placed near the trailing-edge of a delta wing [39, 105]. It is interesting that the phase lag agrees very well with that of

pitching wings. The effect of fin oscillations $\Phi(t)$ is expected to be different than that of the other types of motion (shown in Figure 27) for which the development of the leading edge vortex is time-dependent. The flow upstream is steady (in the sense of being free of periodic perturbations due to the oscillating fin) in this case. Yet, the measured phase lag due to the oscillating fin is very similar. This is not the only example where the wing is stationary, and yet a time lag of breakdown is observed. Parmenter and Rockwell [98] investigated the transient response of breakdown location to suction applied through a probe located well downstream of the breakdown location. Time delays and hysteresis of breakdown location were found. Another example is a stationary delta wing placed in an unsteady free stream [41]. Large time-dependent variations in breakdown location were observed depending on the angle of attack. In summary, whether the unsteadiness is due to pitching, plunging, rolling, oscillating flaps/surfaces/fins, or time-dependent suction, similar phase lags have been found as a function of frequency. This suggests that the mechanism of time lag with respect to the quasi-steady case is universal regardless of the type of unsteady motion.

6.6.2 Mechanism of Time Lag

There have been different suggestions as to the origin of the time lag of breakdown location in unsteady flows. In this section, these different explanations will be critically reviewed. The first possibility was that the observed phase lag of breakdown location was due to a time lag in the development of vortex flow. Indeed, the investigations by Maltby et al [81], Lambourne et al [66], and Gad-el-Hak and Ho [24] established that there exists a phase shift in the development of the cross-sectional flow pattern in the absence of vortex breakdown. However, this time lag of vortex development is very small compared to the large time lag of breakdown location, as indicated by Rockwell [108] and Ericsson [19]. For example, the data shown in Figure 21 suggests that the normalized time constant associated with the movement of vortex core is around $\tau U_\infty/c \approx 0.35$. On the other hand, Greenwell and Wood [34] obtained $\tau U_\infty/c = 1.67$ associated with the movement of vortex breakdown location over pitching wings. Also, Greenwell and Wood [34] presented a comparison of the time constants (estimated from the surface pressure changes in response to blowing) in the absence and presence of vortex breakdown, which are different by one order of magnitude as shown in Figure 28. Also, if the case of the oscillating fin (shown in Figure 27) is considered, the upstream flow is free of unsteady effects and there is no time lag in the development of vortical flow, yet there is considerable time lag of the vortex breakdown location.

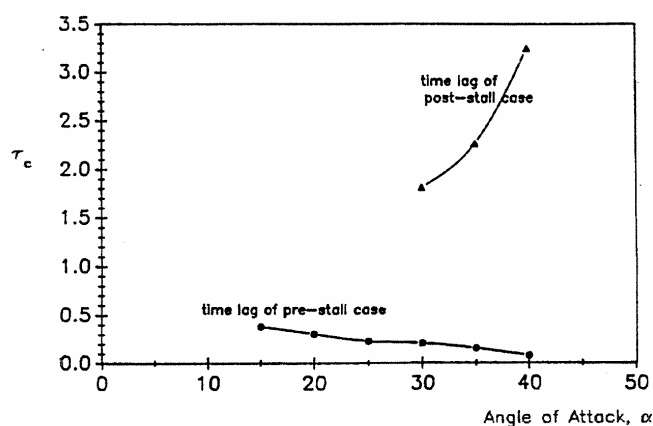


Figure 28: Time Constants Estimated from Surface Pressure Changes in Response to Blowing (Greenwell and Wood, 1994).

For a pitching delta wing, the observed time lag of breakdown location was explained by the variations of the effective angle of attack and motion-induced longitudinal camber [19, 20]. Both effects are due to

UNSTEADY ASPECTS OF LEADING-EDGE VORTICES

wing motion and fail to explain the phenomenon of the time lag of breakdown location when the wing is stationary. Explanations of the time lag of breakdown location with concepts that are based on wing motion (such as effective angle of attack and longitudinal camber) are not possible for many other cases where the wing is stationary.

Vortex breakdown location is determined by two important parameters: swirl angle (or vortex strength) and external pressure gradient outside the vortex core. Hence the variation of these parameters upstream of breakdown [42, 135] was considered in an attempt to explain the time lag of breakdown location for a pitching delta wing. These investigations indicate that the variation of swirl angle has a very small phase lag, while the variation of the external pressure gradient has a comparable phase lag to that of breakdown location. Hall [49] showed that small external pressure gradients can be amplified along the core of the vortices, leading to a stagnation point. Thus, the large sensitivity of the breakdown location to a streamwise pressure gradient along the exterior of the vortex is very much expected. For other types of motion (other than pitching), the variation of external pressure gradient has not been investigated in relation to vortex breakdown. However, velocity measurements [41, 135] show that the variation of swirl angle has a small phase lag, suggesting that the external pressure gradient plays a major role in the dynamic response of breakdown location.

Unlike the other cases shown in Figure 27, in which both the external pressure gradient and the strength of the vortex are simultaneously changed as a result of moving surfaces/geometry, the case of the oscillating fin is fundamentally different. The swirl angle upstream of breakdown is constant, and therefore is not a variable. Yet, the vortex breakdown location is time-dependent because of the time-dependent external pressure gradient set by the oscillating fin. The observed time lags and hysteresis of the vortex breakdown location are presumably due to the unsteady behavior of the external pressure gradient as it is the only dynamic parameter. Although this and other examples point towards a suspected relationship between the external pressure gradient and breakdown location, it is not clear whether this is a universal explanation of phase lag of breakdown location. Also, it is not clear how different types of motion or unsteadiness can generate similar phase lags of external pressure gradient.

Gursul [39] has proposed an explanation of the time lag, which is based on the theory of vortex breakdown as a wave propagation phenomenon, and is universally applicable to slender vortex flows. A stationary breakdown can be considered as the superposition of an upstream moving wave and a uniform free stream velocity (in the downstream direction), which makes the wave stationary. In the dynamic case, wave speed depends on the axial wave number. For example, for a cylindrical vortex with Rankine velocity distribution and no axial velocity, the exact dispersion relation is given by Kelvin, and the speed of the waves travelling upstream can be found numerically [134]. The speed of the waves travelling upstream decreases with increasing wave number (or frequency). As a result, the equilibrium location (vortex breakdown location) is different in the dynamic case compared to the quasi-steady case. This model predicts phase lags that increase with increasing frequency, which is well known from experimental observations for a variety of unsteady flows.

6.7 VORTEX SHEDDING

Based on two-point velocity measurements in the wake of a delta wing, Rediniotis et al [103, 104] showed that vortex shedding occurs at large angles of attack. It was suggested that both symmetric and antisymmetric modes of shedding existed (see sketches in Figure 29). They conducted experiments on several delta wings with a sweep angle of $\Lambda=76^\circ$. It was shown that this quasi-periodic phenomenon occurs over a wide range of angles of attack, without significant influence of Reynolds number. In the range of $Re=39,000$ to $902,000$, there was no noticeable effect on the dominant frequency of the vortex shedding. They suggest that up to $\alpha=70^\circ$, only the symmetric mode of vortex shedding occurs. At angles of attack larger than 70° , both shedding modes exist simultaneously, although the symmetric mode is more

dominant. Since the vortex shedding involves an interaction between the shear layers, wing span was used as a characteristic length in the definition of the dimensionless frequency.

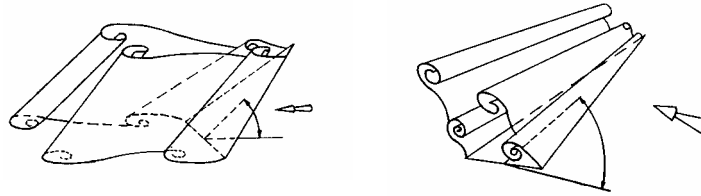


Figure 29: Symmetric and Antisymmetric Modes of Vortex Shedding from Delta Wings (Rediniotis et al, 1990).

The dominant frequencies of velocity fluctuations measured in the wake (at $x/c=1.5$) by Rediniotis et al [103] were used to calculate the conventional definition of dimensionless frequency (fc/U_∞) in order to compare with frequencies of other unsteady phenomena (see Figure 30a). Also, shown in Figure 30b is the variation of breakdown location over delta wings with $\Lambda=75^\circ$, using reported values from the literature [37]. The angle of attack at which breakdown location reaches the apex was estimated as between $\alpha=58^\circ$ and 60° by extrapolation of data. It is clear that the data shown in Figure 30a include vortex breakdown over the wing (at angle of attack up to 60°) as well as vortex shedding (at larger angles of attack). It was discussed in Section 4.1 that vortex breakdown over the wing corresponds with the helical mode instability. Figure 30a also suggests that the dominant frequencies of the helical mode instability and those of vortex shedding form a continuous curve. This rather interesting result, which can be interpreted as a smooth transition from one phenomenon to the other, is misleading because the helical mode instability has locally varying properties.

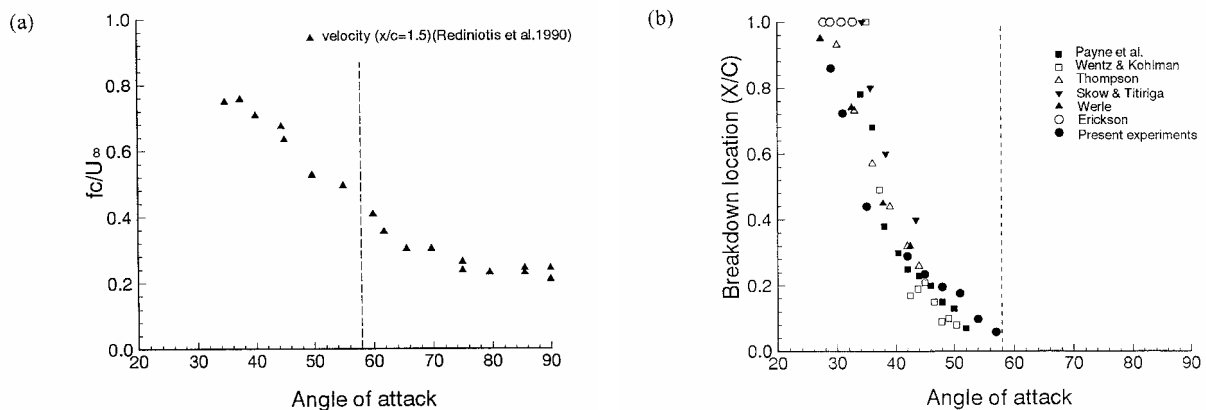


Figure 30: (a) Dominant Frequencies in the Wake for $\Lambda=76^\circ$; (b) Breakdown Location over Delta Wings for $\Lambda=75^\circ$ (from Gursul and Xie, 1999).

Detailed investigation of this transition was carried out by Gursul and Xie [45]. Measurements of the streamwise velocity at the trailing-edge ($x/c=1.0$) and pressure on the wing surface ($x/c=0.89$) indicate that the helical mode instability of swirling flow disappears after vortex breakdown reaches the apex, and the dominant frequency of the vortex shedding appears in the spectra. The transition from the helical mode instability to the vortex shedding was found to be abrupt as indicated by a jump in the frequency parameter, and occurred at the angle of attack at which breakdown reached the apex (see Figure 31). When the source of the quasi-periodic oscillations is the helical mode instability (for $\alpha < 60^\circ$), the measured frequencies at

$x/c=1.0$ are much larger than those in the wake at $x/c=1.5$ (compare with Figure 30a). This was explained by the significant changes in the wavelength of the helical mode instability in the streamwise direction in the near wake. On the other hand, when the source of the quasi-periodic oscillations is the vortex shedding (for $\alpha > 60^\circ$), the measured frequencies at $x/c=1.0$ and in the wake $x/c=1.5$ agree very well. This implies that the frequency of the vortex shedding is nearly constant in the near wake.

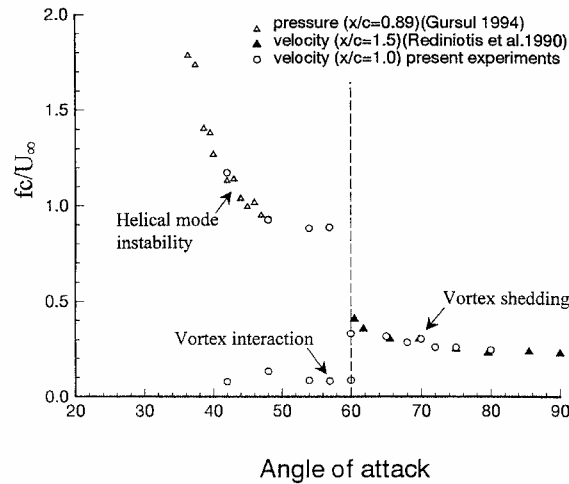


Figure 31: Variation of Dimensionless Frequency for Unsteady Phenomena as a Function of Angle of Attack (Gursul and Xie, 1999).

6.8 WING AND FIN BUFFETING

Buffeting is defined as the structural response of aircraft structures (such as wing, fin, tail, flap, and rudder) due to unsteady flow [78]. Several unsteady flow phenomena may excite different structural modes depending on angle of attack and free stream velocity, and cause severe structural fatigue damage.

The measurements of buffeting on a slender delta wing model were reported by Mabey [77] (see Figure 32a). When the vortex breakdown location moved across the trailing edge (for $\alpha \leq 20^\circ$), buffeting increased very rapidly as seen in Figure 32a. Also, sharply increased fluctuations in the normal force coefficient for delta wings were observed when vortex breakdown moved over the wing [17]. Hence the most important source of wing buffeting is the vortex breakdown phenomenon. However, light buffeting is observed in the absence of breakdown, and has been attributed to vortex wandering [44]. Figure 32b shows the variation of wing-tip acceleration for a slightly flexible delta wing (with a sweep angle of $\Lambda=60^\circ$) with angle of attack [32]. It was found that maximum rms buffeting occurs when vortex breakdown is close to the apex of the wing (breakdown reaches the apex at around $\alpha \approx 32^\circ$). The rms acceleration drops very rapidly in the vortex shedding regime at higher angles of attack.

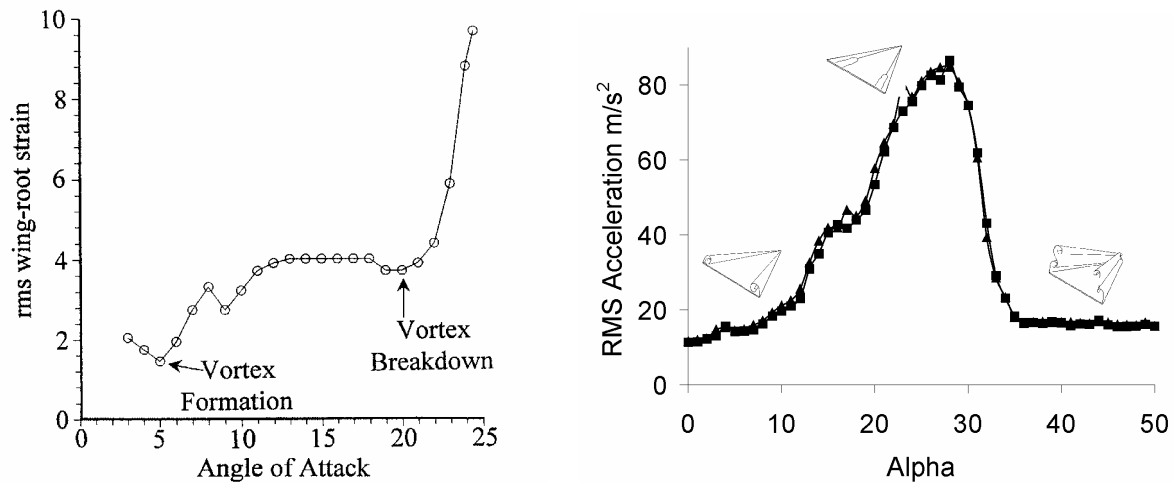


Figure 32: (a) Buffeting on a Slender Delta Wing Model (Mabey, 1973) (left); (b) Wing-Tip Acceleration on a Slightly Flexible Delta Wing, $\Delta=60^\circ$ (Gray et al, 2003) (right).

Vortex breakdown is also the major source of fin buffeting in many cases. Distortion of incident vortex and interaction of vortex breakdown with fins have been investigated in detail [9, 83]. Measurements of unsteady surface pressure, surface acceleration, and strain on fins generally showed that spectra had a dominant peak at high angle of attack due to the helical mode instability. Wolfe et al [129] reviewed a wide variety of investigations of both simplified fin-delta wing configurations and fins on actual model aircraft. They demonstrated that the shapes of the surface pressure spectra are similar, and the dominant frequencies obey a simple scaling law over a wide range of Reynolds numbers (10^4 to 10^6). It was shown that the dimensionless frequency fx_{bd}/U_∞ , where x_{bd} is the distance of breakdown location from the origin of the vortex, is roughly constant (with a value around unity). Wolfe et al [129] also show that dominant frequencies of surface pressure fluctuations on fins agree very well with those on the surface of delta wings [36] without a fin. The dominant frequencies for aircraft models also agree with the frequency of the helical mode instability [59].

An important feature of the spectra of buffeting is the existence of a low frequency peak. For several vortex-fin interactions, a low frequency peak was observed in the spectra of fin surface pressure, tip acceleration, strain, and velocity fluctuations around the fin [50, 67, 130]. Also, a low frequency component in the pressure/velocity spectra was observed in the wake of breakdown in several investigations [43, 55, 59, 109] in the absence of a fin. It was suggested by Wolfe et al [130] that this low frequency peak is due to the fluctuations of breakdown location in the streamwise direction. Recent investigations [88] show that vortex breakdown location may exhibit large fluctuations along the axis of vortices. Moreover, the quasi-periodic oscillations due to vortex interactions may be an important source of buffeting at high angles of attack [44]. Another possible source of buffeting is the coupling between the unsteady flow separation over the fin surface and vortex breakdown [45], which was originally suggested by Patel and Hancock [99] and Gordnier and Visbal [30]. Studies of pressure fluctuations on the fin surface [30, 130] revealed low-frequency components, which agreed well with the dominant frequencies in the spectra of the fluctuations of breakdown location. These quasi-periodic oscillations of breakdown location, which are not observed for nonimpinging flows at low angle of attack, are an indication of a feedback effect on vortex breakdown, and may play an important role in the buffeting of fins. Note that the disturbances generated at the leading-edge of the fin may propagate upstream in the subcritical flow downstream of vortex breakdown [71].

Also, disturbances due to aeroelastic effects (surface deflections) may propagate upstream, resulting in large oscillations of breakdown location. This aspect was investigated in detail by Gursul and Xie [47].

UNSTEADY ASPECTS OF LEADING-EDGE VORTICES

For excitation frequencies lower than a cutoff frequency (which is around $f_c/U_\infty \approx 0.40$), the response of vortex breakdown location is quasi-periodic, and the amplitude of the variations of breakdown location decreases with increasing frequency (see Figure 33). For excitation frequencies higher than the cutoff frequency, vortex breakdown does not respond to fin oscillations. The amplitude ratio, which was defined as the ratio of the rms value of the fluctuations of breakdown location to its quasi-steady counterpart, is shown in Figure 34 as a function of dimensionless frequency for different fin locations on the wing. It is seen that the amplitude ratio decreases with increasing frequency, and the amplitude attenuation is similar to that of a lowpass filter. It is also seen that the amplitude response is very similar for pitching delta wings and oscillating fins. In a recent investigation [119], it was found that vortex breakdown had a similar response to an oscillating body in the wake. A proposed mechanism based on the wave propagation characteristics of vortex flows was presented by Gursul and Xie [47]. It is based on the concept of subcritical flow which exists downstream of breakdown location. Disturbances due to fin deflections may propagate upstream and the group velocity of the disturbances depends on the axial wavenumber. The ability of disturbances to propagate upstream decreases with increasing wavenumber (or frequency). A simple model predicts that disturbances with frequencies higher than a cutoff frequency will not propagate upstream, which agrees very well with the experimental observations.

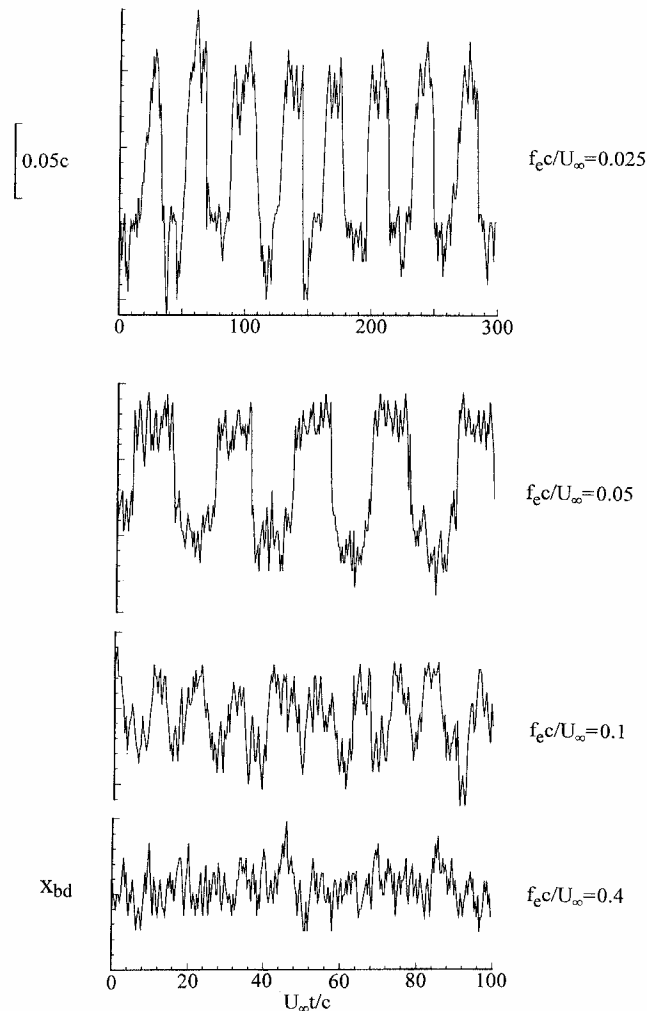


Figure 33: Time Histories of Breakdown Location for Different Fin Oscillation Frequencies for a Fin Location of $y_f/s=0.8$ (Gursul and Xie, 2001).

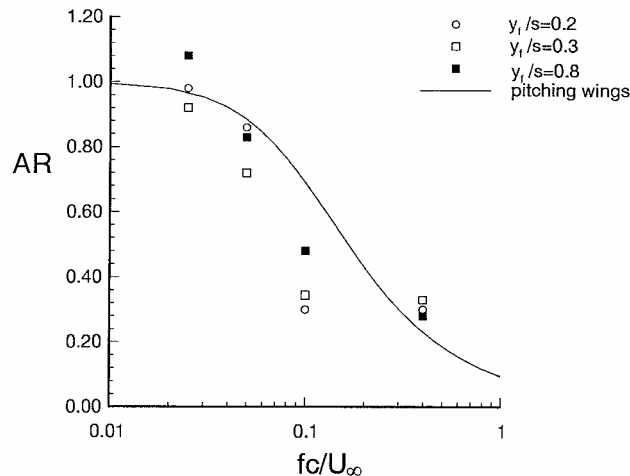


Figure 34: Variation of the Amplitude Ratio as a Function of Forcing Frequency (Gursul and Xie, 2001).

Bean et al [7] demonstrated that buffeting of centerline fins is possible at very large angles of attack where leading edge vortex no longer exists. Figure 35a shows the rms pressure fluctuations on the fin as well as the buffeting response as a function of angle of attack. Their delta wing had a sweep angle of $\Lambda=60^\circ$. By using reported breakdown locations from the literature [38] as shown in Figure 35b, one expects the breakdown location to reach the apex of the wing around $\alpha \approx 32^\circ$. Bean et al showed that, for both rigid and flexible fins, the unsteady loading starts to increase around $\alpha=34^\circ$ and reaches a sharp peak at $\alpha=43^\circ$. It was shown that unsteady pressure on the fin surface exhibited quasi-periodic behavior. It is interesting that the buffeting was small for $\alpha < 34^\circ$, i.e., vortex breakdown did not excite the fin, because the fin was located at the wing centerline near the trailing edge and therefore was away from the vortex axis. Instead, buffeting occurred in the poststall region where the vortex shedding from the wing takes place.

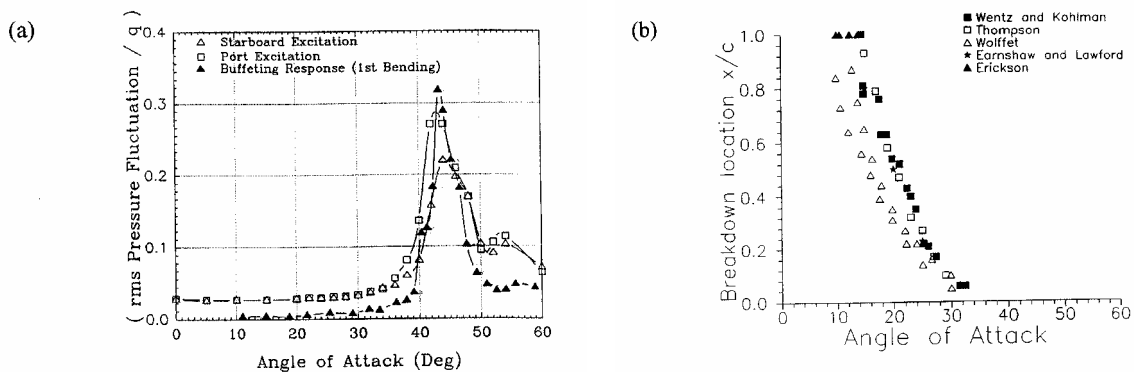


Figure 35: (a) RMS Pressure on a Fin (Bean et al, 1993);
(b) Breakdown Location for $\Lambda=60^\circ$ (Gursul, 1997).

6.9 WING ROCK PHENOMENON

Wing rock is a self-induced limit cycle roll oscillation, which has been observed for slender delta wings as well as aircraft configurations. In particular, it has been observed in the subsonic, high angle-of-attack regime, where the leading-edge vortices are one of the most important features of the flow. An example of

the time history of the roll angle is shown for $\alpha=30^\circ$ for a $\Lambda=80^\circ$ delta wing [1] in Figure 36. As the angle of attack is increased, the wing rock motion first appears at a specific incidence, known as the onset angle of attack. The amplitude of the roll oscillations strongly depends on the angle of attack. An example of the measured wing-rock amplitude [96] is shown in Figure 37 as a function of angle of attack. A particularly important observation is that the onset angle of attack at which wing rock starts, decreases as the wing platform becomes more slender. This indicates a possible relation between the onset of wing-rock and the proximity of leading-edge vortices. In fact, there may be a link to the hypothesized cross-flow instability sketched in Figure 17. This instability was suggested as a possible mechanism for the quasi-periodic, antisymmetric motion of breakdown locations, which becomes larger and more coherent as angle of attack or sweep angle is increased.

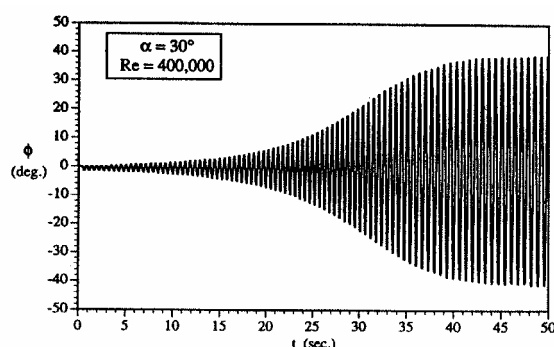


Figure 36: Wing Rock Time History for $\alpha=30^\circ$ Showing Build-Up (Arena & Nelson, 1994).

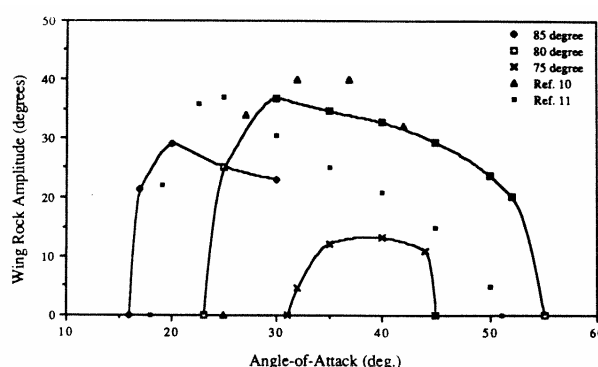


Figure 37: Wing Rock Amplitude as a Function of Angle of Attack for Wings with Different Sweeps (Ng et al, 1989).

Several aerodynamic phenomena have been suggested as the mechanism(s) leading to the self induced oscillations, including vortex lift-off and vortex breakdown. Ng et al [96] suggested that wing rock is initiated by vortex interaction, which results in asymmetries in vortex strength. Also, the importance of the proximity of the leading-edge vortices was noted. Interactions of forebody and wing vortices can also cause wing rock of slender configurations [97]. It has been generally agreed that vortex breakdown is not a necessary condition for wing rock. For slender delta wings, no breakdown was seen on the wing during the oscillations at the onset of the motion. Ericsson [18] suggested that the wing rock starts at the angle of attack at which the roll damping of the wing is lost. The mechanism(s) that start wing rock are likely to be different than those that sustain it. Arena and Nelson [1] suggested that a possible mechanism to sustain the wing rock motion is the time lag in the position of the vortices normal to the wing surface.

6.10 UNSTEADY VORTEX CONTROL

Here a brief review of vortex control methods is presented with emphasis on unsteady aspects. Use of unsteady effects for vortex control over stationary and maneuvering wings is considered. Efforts in this direction have two main goals:

- i) Control of leading-edge vortices to generate forces/moments for flight control; and
- ii) Control (delay) of vortex breakdown with stability and buffeting considerations.

A review of research into vortex breakdown control is given by Mitchell and Delery [93]. It should be noted that some flow control techniques may cause premature vortex breakdown at moderate incidences while increasing the vortex lift at low angles of attack due to increased strength of vortex.

Since the vorticity of the leading-edge vortices originates from the separation line along the leading-edge, control of separation characteristics or shear layer can be used to influence the strength and location of the vortices as well as the location of vortex breakdown. Steady blowing and suction at the leading-edge [35, 84, 132] are known to be effective tools. In addition, Gu et al [35] applied periodic suction-blowing in the tangential direction along the leading-edge of the wing and reported a delay of vortex breakdown. The most effective period of the alternate suction-blowing corresponded to $f_c/U_\infty=1.3$. It was shown that oscillatory blowing at the leading edge can enhance the lift at high angles of attack [82], and optimum reduced frequency varied in the range of $f_c/U_\infty=1$ to 2. The relationship between these reported values of optimum frequency and characteristic frequencies of unsteady flow phenomena needs to be investigated.

Leading-edge flaps are particularly attractive tools that can be used to influence the strength and location of these vortices. By using particle streak photography, Spedding et al [114] reported that leading edge vortices doubled in strength for a delta wing with flap. Deng and Gursul [15] showed that the circulation of the vortices became maximum at an optimum flap angle. Spedding et al [114] considered large amplitude harmonic oscillations of flaps, and revealed a 35% increase in vortex circulation over the equivalent stationary flap configuration. For small amplitude flap oscillations, the strength of the vortices was larger than that of the quasi-steady case [15]. The effect of oscillating leading edge flaps on breakdown was investigated for a delta wing with upward-deflected flaps [15]. The time-averaged breakdown location over one cycle may move upstream or downstream compared to the quasi-steady case, depending on the amplitude of flap oscillations and angle of attack. Combined use of leading-edge flaps and intermittent trailing-edge blowing simultaneously to achieve optimum conditions for vortex control has been demonstrated by Vorobieff and Rockwell [124]. Variable leading edge extension that effectively varies the sweep angle during a maneuver has been used to control leading edge vortices and breakdown over a pitching delta wing [135]. Oscillations of sweep angle with the same frequency as pitching were employed, but with a phase angle. In a related study, by using the same delta wing model, Srinivas et al [115] demonstrated that active control of vortex breakdown can be achieved. The pressure fluctuations induced by the helical mode instability of vortex breakdown can be measured and used as a feedback signal for active control.

Flow control techniques applied near the wing apex received considerable attention. Since most of the vorticity within the leading-edge vortex originates from a small region near the apex of the wing, control of flow separation or shear layer can be successfully used without the need to apply flow control along the entire leading edge. Klute et al [60] showed that a drooping apex flap can delay vortex breakdown, and is equally effective in dynamic maneuvers.

Remaining vortex control techniques to be discussed are applied in locations/regions other than the leading edge. The earliest example is given by Werle [128], who demonstrated a delay of vortex breakdown by applying suction along the vortex axis at a location downstream of the onset of vortex breakdown. Parmenter and Rockwell [98] conducted similar experiments and described the transient response of vortices to suction. Blowing from surface ports located beneath the vortex core at different angles [56] proved useful in delaying vortex breakdown. This technique was also effective for pulsed blowing during pitch-up maneuver [57]. Helin and Watry [51], and Shih and Ding [113] demonstrated that a trailing edge jet can significantly delay vortex breakdown on a delta wing. Phillips et al [101] showed that vortex breakdown can be delayed even in the presence of a fin, resulting in elimination or significant delay of fin buffeting. Figure 38 shows flow visualisation images for (a) jet off (b) jet on (in a “steady-state case”) and, (c) just after the jet is turned off. It is seen that the leading-edge vortex is drawn towards and parallel to the jet in the steady-state case. When the jet is turned off, the wing vortex realigns itself to become nearly parallel to the free stream. Vortex breakdown then slowly propagates upstream, and eventually reaches a steady-state location similar to that shown in Figure 38(a). These results also illustrate the hysteresis and large phase lags associated with the wing vortical flow. The presence of large time-constants associated with this complex jet-vortex interaction is important for the dynamic aspects of thrust vectoring, flight dynamics and control.

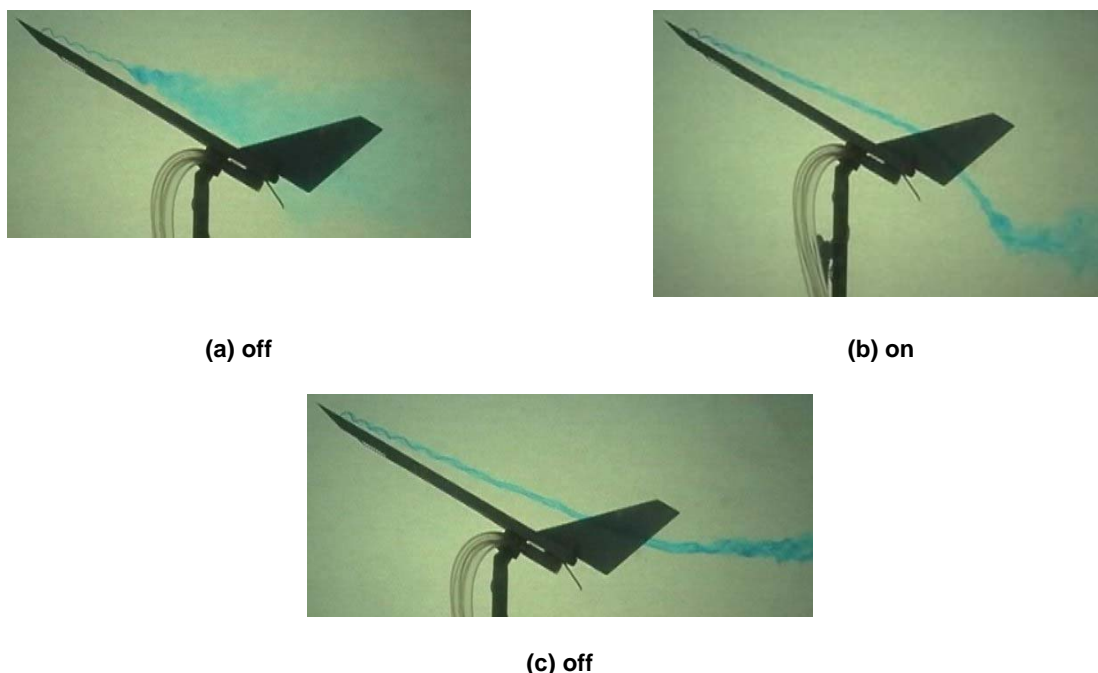


Figure 38: Flow Visualization of Leading-Edge Vortex for (a) Jet Off, (b) Jet On, (c) Just After the Jet is Turned Off (Phillips et al, 2003).

6.11 ISSUES AND CHALLENGES

Much of our knowledge on vortex flows is related to slender vortices. Very little is known about the structure of vortices over nonslender delta wings ($\Lambda \leq 55^\circ$) and unsteady flow phenomena. Figure 39 shows an example of flow visualization for a $\Lambda = 50^\circ$ delta wing, where a dual vortex structure is identified. PIV measurements [120] and direct numerical simulations [31] confirmed that both vortices have the same sign of vorticity. Another area that received little attention is the unsteady interactions for multiple vortices, such as found on double delta wings. Future unmanned aircraft will be highly maneuverable and highly flexible, with the capability of performing extreme maneuvers at high g. At such high reduced frequencies, there is a possibility of coupling of aerodynamic maneuvers with the vortex instabilities reviewed in this paper. For flexible delta wings, vortex/wing interaction (see Figure 40) may lead to limit-cycle-oscillations, where the vortex acts like an aerodynamic spring [28]. Figure 40 shows the growth and decay of the leading-edge vortex over a flexible wing that exhibits limit-cycle-oscillations. Unsteady flow phenomena may interact and couple with structural vibrations. Finally, vortices at low Reynolds numbers are very relevant to micro air vehicles. Certain vortex flows show great sensitivity to Reynolds number, and unsteady aspects of these flows as well as unsteady aerodynamics due to gust loads are important.

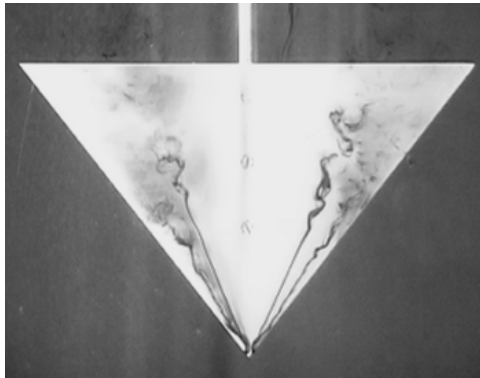


Figure 39: Dual Vortex Structure (of the Same Sign of Vorticity) over a Nonslender Delta Wing with a Sweep Angle of $\Lambda=50^\circ$ (Taylor et al, 2003).

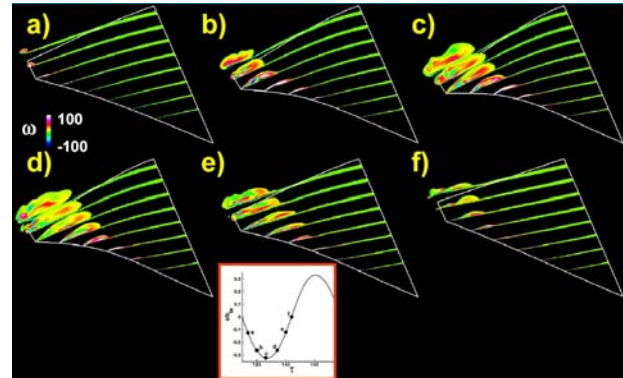


Figure 40: Interaction of Leading-Edge Vortex with a Flexible Delta Wing (Gordnier, 2002).

6.12 ACKNOWLEDGEMENTS

Research programs funded by the Air Force Office of Scientific Research, the European Office of Aerospace Research and Development, and the Engineering and Physical Sciences Research Council in the UK contributed to this review paper.

6.13 REFERENCES

- [1] Arena, A.S. and Nelson, R.C., "Experimental Investigation on Limit Cycle Wing Rock of Slender Wings", *Journal of Aircraft*, Vol. 31, No. 5, September-October, 1994, pp. 1148-1155.
- [2] Ashley, H., Katz, J., Jarrah, M.A., and Vaneck, T., "Survey of Research on Unsteady Aerodynamic Loading of Delta Wings", *Journal of Fluids and Structures*, Vol. 5, 1991, pp. 363-390.
- [3] Atta, R. and Rockwell, D., "Hysteresis of Vortex Development and Breakdown on an Oscillating Delta Wing", *AIAA Journal*, Vol. 25, No. 11, 1987, pp. 1512-1513.
- [4] Atta, R. and Rockwell, D., "Leading-edge Vortices Due To Low Reynolds Number Flow Past A Pitching Delta Wing", *AIAA Journal*, 28, 6, June 1990, pp. 995-1004.
- [5] Ayoub, A. and McLachlan, B.G., "Slender Delta Wing at High Angles of Attack- A Flow Visualization Study", AIAA Paper 87-1230.
- [6] Baker, G.R., Barker, S.J., Bofah, K.K. and Saffman, P.G., "Laser Anemometer Measurements of Trailing Vortices in Water", *Journal of Fluid Mechanics*, Vol. 65, Part 2, 1974, pp. 325-336.
- [7] Bean, D.E., Greenwell, D.I. and Wood, N.J., "Vortex Control technique for the Attenuation of Fin Buffet", *Journal of Aircraft*, Vol. 30, No. 6, 1993, pp. 847-853.
- [8] Brucker, C. "Study of vortex breakdown by particle tracking velocimetry (PTV). Part 2: spiral-type vortex breakdown", *Experiments in Fluids*, Vol. 14, 1993, pp. 133-139.
- [9] Canbazoglu, S., Lin, J.C., Wolfe, S. and Rockwell, D., "Buffeting of Fins: Distortion of Incident Vortex", *AIAA Journal*, Vol. 33, No. 11, November 1995, pp. 2144-2150.

UNSTEADY ASPECTS OF LEADING-EDGE VORTICES

- [10] Cipolla, K.M. and Rockwell, D., "Small-Scale Vortical Structures in Crossflow Plane of a Rolling Delta Wing", *AIAA Journal*, Vol. 36, No. 12, 1998, pp. 2276-2278.
- [11] Cornelius, K.C., "Analysis of Vortex Bursting Utilizing Three-Dimensional Laser Measurements", *Journal of Aircraft*, Vol. 32, No. 2, 1995, pp. 297-306.
- [12] Coton, F.N., Jupp, M.L., and Green, R.B., "Analysis of Unsteady Pressure Signals on a Pitching Delta Wing", *AIAA Journal*, Vol. 39, No. 9, September 2001, pp. 1750-1757.
- [13] Degani, D. and Zilliac, G.G., "Experimental Study of Nonsteady Asymmetric Flow Around an Ogive-Cylinder at Incidence", *AIAA Journal*, Vol. 28, No. 4, 1990, pp. 642-649.
- [14] Delery, J.M. "Aspects of vortex breakdown", *Progress in Aerospace Sciences*, Vol. 30, 1994, pp. 1-59.
- [15] Deng, Q. and Gursul, I., "Vortex Breakdown over a Delta Wing with Oscillating Leading Edge Flaps", *Experiments in Fluids*, Vol. 23, 1997, pp. 347-352.
- [16] Devenport, W.J., Rife, M.C., Liapis, S.I., and Follin, G.J., "The Structure and Development of a Wing-Tip Vortex", *Journal of Fluid Mechanics*, Vol. 312, 1996, pp. 67-106.
- [17] Earnshaw, P.B. and Lawford, J.A., "Low speed wind tunnel experiments on a series of sharp-edged delta wings", R&M 3424, August 1964.
- [18] Ericsson, L.E., "Slender Wing Rock Revisited", *Journal of Aircraft*, Vol. 30, No. 3, May-June, 1993, pp. 352-356.
- [19] Ericsson, L.E., "Pitch Rate Effects on Delta Wing Vortex Breakdown", *Journal of Aircraft*, Vol. 33, No. 3, 1996, pp. 639-642.
- [20] Ericsson, L.E., "Impact of Initial Conditions on Vortex Breakdown on Pitching Delta Wings", *Journal of Aircraft*, Vol. 34, No. 3, 1997, pp. 452-454.
- [21] Escudier, M. 1988, Vortex breakdown: observations and explanations, *Progress in Aerospace Sciences*, **25**, 189-229.
- [22] Faler, J.H. and Leibovich, S., "Disrupted states of vortex flow and vortex breakdown, *Physics of Fluids*, Vol. 20, 1977, pp. 1385-1400.
- [23] Fisher, D.F., Del Frate, J.H. and Richwine, D.M., "In Flight Flow Visualization Characteristics of the NASA F-18 High Alpha Research Vehicle at High Angles of Attack", NASA Technical Memorandum 4193, May 1990.
- [24] Gad-el-Hak, M. and Ho, C.M., "The Pitching Delta Wing", *AIAA Journal*, Vol. 23, No. 11, 1985, pp. 1660-1665.
- [25] Gad-el-Hak, M. and Blackwelder, R.F. "The discrete vortices from a delta wing", *AIAA Journal*, Vol. 23, 1985, pp. 961-962.
- [26] Gad-el-Hak, M. and Blackwelder, R.F., "Control of the Discrete Vortices from a Delta Wing", *AIAA Journal*, Vol. 25, No. 8, 1987, pp. 1042-1049.
- [27] Garg, A.K. and Leibovich, S., "Spectral Characteristics of Vortex Breakdown Flowfields", *Physics of Fluids*, Vol. 22, No. 11, 1979, pp. 2053-2064.

- [28] Gordnier, R., "High-Fidelity Computational Simulation of Nonlinear Fluid-Structure Interaction Problems", *Workshop on Aerodynamic Issues of Unmanned Air Vehicles*, 4-5 November 2002, University of Bath, UK.
- [29] Gordnier, R. and Visbal, M.R. "Unsteady vortex structure over a delta wing", *Journal of Aircraft*, Vol. 31, No. 1, 1994, pp. 243-248.
- [30] Gordnier, R.E. and Visbal, M.R., "Numerical Simulation of the Impingement of a Streamwise Vortex on a Plate", AIAA-97-1781, 28th AIAA Fluid Dynamics Conference, June 29-July 2, 1997, Snowmass Village, CO.
- [31] Gordnier, R.E. and Visbal, M.R., "Higher-Order Compact Difference Scheme Applied to the Simulation of a Low Sweep Delta Wing Flow", AIAA-2003-0620, 41st Aerospace Sciences Meeting and Exhibit, 6-9 January, 2003, Reno, Nevada.
- [32] Gray, J.M., Gursul, I., and Butler, R., "Aeroelastic Response of a Flexible Delta Wing due to Unsteady Vortex Flows", AIAA-2003-1106, 41st Aerospace Sciences Meeting and Exhibit, 6-9 January, 2003, Reno, Nevada.
- [33] Green, S.I. and Acosta, A.J., "Unsteady Flow in Trailing Vortices", *Journal of Fluid Mechanics*, Vol. 227, 1991, pp. 107-134.
- [34] Greenwell, D.I. and Wood, N.J., "Some Observations on the Dynamic Response to Wing Motion of the Vortex Burst Phenomenon", *Aeronautical Journal*, February 1994, pp. 49-59.
- [35] Gu, W., Robinson, O. and Rockwell, D., "Control of Vortices on a Delta Wing by Leading-Edge Injection", *AIAA Journal*, Vol. 31, No. 7, July 1993, pp. 1177-1186.
- [36] Gursul, I. "Unsteady Flow Phenomena over Delta Wings at High Angle of Attack", *AIAA Journal*, Vol. 32, No. 2, February 1994, pp. 225-231.
- [37] Gursul, I., "Criteria for Vortex Breakdown Location over Delta Wings", *The Aeronautical Journal*, May 1995, pp. 194-196.
- [38] Gursul, I., "Comment on "Counter-Rotating Structures over a Delta Wing", *AIAA Journal*, Vol. 35, No. 4, 1997, pp. 758-759.
- [39] Gursul, I., "Proposed Mechanism for Time Lag of Vortex Breakdown Location in Unsteady Flows", *Journal of Aircraft*, Vol. 37, No. 4, 2000, pp. 733-736.
- [40] Gursul, I. and Ho, C-M. "Vortex Breakdown over Delta Wings in Unsteady Freestream", AIAA-93-0555, 31st Aerospace Sciences Meeting and Exhibit, January 11-14, 1993, Reno, NV.
- [41] Gursul, I. and Ho, C-M. "Vortex Breakdown over Delta Wings in Unsteady Freestream", *AIAA Journal*, Vol. 32, No. 2, February 1994, pp. 433-436.
- [42] Gursul, I. and Yang, H. "Vortex breakdown over a pitching delta wing", *Journal of Fluids and Structures*, Vol. 9, 1995, pp. 571-583.
- [43] Gursul, I. and Yang, H., "On Fluctuations of Vortex Breakdown Location", *Physics of Fluids*, Vol. 7, No. 1, 1995, pp. 229-231.
- [44] Gursul, I., and Xie, W., "Physics of Buffeting Flows over Delta Wings", AIAA 98-0688, 36th Aerospace Sciences Meeting and Exhibit, January 12-15, 1998, Reno, NV.

UNSTEADY ASPECTS OF LEADING-EDGE VORTICES

- [45] Gursul, I. and Xie, W., "Buffeting Flows over Delta Wings", *AIAA Journal*, Vol. 37, No. 1, 1999, pp. 58-65.
- [46] Gursul, I. and Xie, W., 2000, "Origin of Vortex Wandering over Delta Wings", *Journal of Aircraft*, Vol. 37, No.2, 2000, pp. 348-350.
- [47] Gursul, I. and Xie, W., 2001, "Interaction of Vortex Breakdown with an Oscillating Fin", *AIAA Journal*, Vol. 39, No. 3, pp. 438-446.
- [48] Gutmark, E. and Ho, C-M., "Preferred Modes and the Spreading Rates of Jets", *Physics of Fluids*, Vol. 26, No. 10, 1983, pp. 2932-2936.
- [49] Hall, M.G., "Vortex Breakdown", *Annual Review of Fluid Mechanics*, Vol. 4, 1972, pp. 195-218.
- [50] Hauch, R.M., Jacobs, J.H., Dima, C. and Ravindra, K., "Reduction of Vertical Tail Buffet Response Using Active Control", *Journal of Aircraft*, Vol. 33, No. 3, May-June 1996, pp. 617-622.
- [51] Helin, H.E. and Watry, C.W., "Effects of Trailing-Edge Jet Entrainment on Delta Wing Vortices", *AIAA Journal*, Vol. 32, No. 4, 1994, pp. 802-804.
- [52] Ho, C-M. and Huerre, P., "Perturbed Free Shear Layers", *Annual review of Fluid Mechanics*, Vol. 16, 1984, pp. 365-424.
- [53] Huang, L-S. and Ho, C-M., "Small-scale transition in a plane mixing layer", *Journal of Fluid Mechanics*, Vol. 210, 1990, pp. 475-500.
- [54] Huang, M.K. and Chow, C.Y., "Stability of Leading-Edge Vortex Pair on a Slender Delta Wing", *AIAA Journal*, Vol. 34, No. 6, 1996, pp. 1182-1187.
- [55] Jaworski, A.J., Harvey, J.K. and Mabey, D.G., "Experimental Studies of the Unsteady Characteristics of Vortex Breakdown", Royal Aeronautical Society Conference, July 17-18, 1996.
- [56] Johari, H., Olinger, D.J. and Fitzpatrick, K.C., "Delta Wing Vortex Control via Recessed Angled Spanwise Blowing", *Journal of Aircraft*, Vol. 32, No. 4, 1995, pp. 804-810.
- [57] Johari, H. and Moreira, J., "Delta Wing Vortex Manipulation Using Pulsed and Steady Blowing During Ramp-Pitching", *Journal of Aircraft*, Vol. 33, No. 2, March-April 1996, pp. 304-310.
- [58] Jumper, E.J., Nelson, R.C. and Cheung, K., "A Simple Criterion for Vortex Breakdown", AIAA-93-0866, 31st Aerospace Sciences Meeting and Exhibit, January 11-14, 1993, Reno, NV.
- [59] Klute, S.M. and Telionis, D.P., "The Unsteady Characteristics of the Flow Over an F/A 18 at High Alpha", AIAA Paper 96-0824, 1996.
- [60] Klute, S.M., Rediniotis, O.K., and Telionis, D.P., "Flow Control over a Maneuvering Delta Wing at High Angles of Attack", *AIAA Journal*, Vol. 34, No. 4, April 1996, pp. 662-668.
- [61] Kommallein, S. and Hummel, D., "LDA Investigations of the Separated Flow Over Slender Wings", *Physics of Separated Flows--Numerical, Experimental, and Theoretical Aspects*, edited by Klaus Gersten, Vieweg, Braunschweig, 1993, pp. 275-282.
- [62] Krishnamoorthy, V., "Vortex Breakdown and Measurements of Pressure Fluctuations over Slender Wings", PhD Thesis, 1966, The University of Southampton.

- [63] Lambert, C. and Gursul, I., "Insensitivity of Unsteady Vortex Interactions To Reynolds Number", *AIAA Journal*, Vol. 38, No. 5, 2000, pp. 937-939.
- [64] Lambert, C., "Vortex Interactions over a Highly Swept Delta Wing", Department of Mechanical Engineering Report, University of Bath, Bath, United Kingdom, May 1999.
- [65] Lambourne, N.C. and Bryer, D.W., "The Bursting of Leading Edge Vortices: Some Observation and Discussion of the Phenomenon", Aeronautical Research Council, R&M 3282, 1962.
- [66] Lambourne, N.C., Bryer, D.W. and Maybrey, J.F.M., "The Behaviour of the Leading-Edge Vortices over a Delta Wing Following a Sudden Change of Incidence", Aeronautical Research Council, R.&M. 3645, March 1969.
- [67] Lee, B.H.K. and Brown, D., "Wind-Tunnel Studies of F/A-18 Tail Buffet", *Journal of Aircraft*, Vol. 24, No. 1, January-February 1992, pp. 146-152.
- [68] Lee, B.H.K. and Tang, F.C., "Characteristics of the Surface Pressures on a F/A-18 Vertical Fin Due to Buffet", *Journal of Aircraft*, Vol. 31, No. 1, January-February 1994, pp. 228-235.
- [69] Lee, M. and Ho, C-M., "Lift Force of Delta Wings", *Applied Mechanics Reviews*, Vol. 43, No. 9, 1990, pp. 209-221.
- [70] Lee, Y.L. and Gursul, I., "An Investigation of Unsteady Interactions of a Vortex Pair over Delta Wings", AIAA-2003-423, 41st Aerospace Sciences Meeting and Exhibit, 6-9 January 2003, Reno, Nevada.
- [71] Leibovich, S., "Vortex Stability and Breakdown: Survey and Extension", *AIAA Journal*, Vol. 22, No. 9, 1984, pp. 1192-1206.
- [72] LeMay, S.P., Batill, S.M. and Nelson, R.C., "Vortex Dynamics on a Pitching Delta Wing", *Journal of Aircraft*, Vol. 27, No. 2, February 1990, pp. 131-138.
- [73] Lin, J.C. and Rockwell, D., "Transient Structure of Vortex Breakdown on a Delta Wing", *AIAA Journal*, Vol. 33, No. 1, January 1995, pp. 6-12.
- [74] Lowson, M.V., "Some experiments with vortex breakdown", *Journal of the Royal Aeronautical Society*, Vol. 68, 1964, pp. 343.
- [75] Lowson, M.V., "The Three Dimensional Vortex Sheet Structure on Delta Wings", *Fluid Dynamics of Three-Dimensional Turbulent Shear Flows and Transition*, AGARD-CP-438, Çesme, Turkey, October 1988, pp. 11.1-11.16.
- [76] Lowson, M.V., "Visualization Measurements of Vortex Flows", *Journal of Aircraft*, Vol. 28, No. 5, 1991, pp. 320-327.
- [77] Mabey, D.G., "Beyond the Buffet Boundary", *Aeronautical Journal*, Vol. 77, April 1973, pp. 201-215.
- [78] Mabey, D.G., "Some Aspects of Aircraft Dynamic Loads Due to Flow Separation", *Prog. Aerospace Sci.*, Vol. 26, 1989, pp. 115-151.
- [79] Mabey, D.G., "Similitude Relations for Buffet and Wing Rock on Delta Wings", *Prog. Aerospace Sci.*, Vol. 33, 1997, pp. 481-511.

UNSTEADY ASPECTS OF LEADING-EDGE VORTICES

- [80] Magness, C.L., "Unsteady Response of the Leading-Edge Vortices on a Pitching Delta Wing", PhD Thesis, Lehigh University, May 1991.
- [81] Maltby, R.L., Engler, P.B. and Keating, R.F.A., "Some Exploratory Measurements of Leading-Edge Vortex Positions on a Delta Wing Oscillating in Heave", Aeronautical Research Council, R.&M. 3410, July 1963.
- [82] Margalit, S., Greenblatt, D., Seifert, A. and Wygnanski, I., "Active Flow Control of a Delta Wing at High Incidence Using Segmented Piezoelectric Actuators", AIAA-2002-3270, 1st Flow Control Conference, 24-26 June, 2002, St. Louis, MO.
- [83] Mayori, A. and Rockwell, D., "Interaction of a Streamwise Vortex with a Thin Plate: A Source of Turbulent Buffeting", *AIAA Journal*, Vol. 32, No. 10, October 1994, pp. 2022-2029.
- [84] McCormick, S. and Gursul, I., "Effect of Shear Layer Control on Leading Edge Vortices", *Journal of Aircraft*, Vol. 33, No. 6, November-December 1996, pp. 1087-1093.
- [85] Menke, M. and Gursul, I., "Unsteady nature of leading edge vortices", *Physics of Fluids*, Vol. 9, No. 10, 1997, pp. 1-7.
- [86] Menke, M. and Gursul, I., "Self-Excited Oscillations of Vortex Breakdown Location over Delta Wings", AIAA 97-0744, 35th Aerospace Sciences Meeting and Exhibit, January 6-10, 1997, Reno, NV.
- [87] Menke, M. and Gursul, I., "Nonlinear Response of Vortex Breakdown over a Pitching Delta Wing", *Journal of Aircraft*, Vol. 36, No. 3, 1999, pp. 496-500.
- [88] Menke, M., Yang, H., and Gursul, I., "Experiments on the Unsteady Nature of Vortex Breakdown over Delta Wings", *Experiments in Fluids*, Vol. 27, No. 3, 1999, pp. 262-272.
- [89] Meyn, L.A. and James, K.D., "Full Scale Wind Tunnel Studies of F/A-18 Tail Buffet", AIAA-93-3519, AIAA Applied Aerodynamics Conference, 1993.
- [90] Miao, J.J., Chang, R.C., Chou, J.H., and Lin, C.K., "Nonuniform Motion of Leading-Edge Vortex Breakdown on Ramp Pitching Delta Wings", *AIAA Journal*, Vol. 30, No. 7, 1992, pp. 1691-1702.
- [91] Minorsky, N., **Nonlinear Oscillations**, Van Nostrand Co., 1962.
- [92] Mitchell, A.M., Barberis, D. and Delery, J., "Oscillation of Vortex Breakdown Location and its Control by Tangential Blowing", AIAA Paper 98-2914, 1998.
- [93] Mitchell, A.M. and Delery, J., "Research into Vortex Breakdown Control", *Progress in Aerospace Sciences*, Vol. 37, 2001, pp. 385-418.
- [94] Mitchell, A.M. and Molton, P., "Vortical Substructures in the Shear Layers Forming Leading-Edge Vortices", *AIAA Journal*, Vol. 40, No. 8, 2002, pp. 1689-1692.
- [95] Myose, R.Y., Lee, B.K., Hayashibara, S., and Miller, L.S., "Diamond, Cropped, Delta, and Double-Delta Wing Vortex Breakdown During Dynamic Pitching", *AIAA Journal*, Vol. 35, No. 3, 1997, pp. 567-569.
- [96] Ng, T.T., Malcolm, G.N. and Lewis, L.C., "Experimental Study of Vortex Flows over Delta Wings in Wing-Rock Motion", *Journal of Aircraft*, 1991, pp. 598-603.

- [97] Ng, T.T., Suarez, C.J., Kramer, B.R., Ong, L.Y., Ayers, B., and Malcolm, G.N., "Forebody Vortex Control for Wing Rock Suppression", *Journal of Aircraft*, Vol. 31, No. 2, March-April 1994, pp. 298-305.
- [98] Parmenter, K. and Rockwell, D., "Transient Response of Leading-Edge Vortices to Localized Suction", *AIAA Journal*, Vol. 28, No. 6, June 1990, pp. 1131-1133.
- [99] Patel, M.H. and Hancock, G.J., "Some Experimental Results of the Effect of a Streamwise Vortex on a Two-Dimensional Wing", *Aeronautical Journal*, April 1974, pp. 151-155.
- [100] Payne, F.M., Ng, T.T., Nelson, R.C., and Schiff, L.B., "Visualization and wake surveys of vortical flow over a delta wing", *AIAA Journal*, Vol. 26, 1988, pp. 137.
- [101] Phillips, S., Lambert, C., and Gursul, I., "Effect of a Trailing-Edge Jet on Fin Buffeting", *Journal of Aircraft*, 2003, in print.
- [102] Portnoy, H., "Unsteady Motion of Vortex Breakdown Positions on Delta Wings", ICAS Congress, August 28-September 2, 1988, Jerusalem, Israel.
- [103] Rediniotis, O.K., Stapountzis, H. and Telionis, D.P., "Vortex Shedding over Delta Wings", *AIAA Journal*, Vol. 28, No. 5, 1990, pp. 944-946.
- [104] Rediniotis, O.K., Stapountzis, H. and Telionis, D.P., "Periodic Vortex Shedding over Delta Wings", *AIAA Journal*, Vol. 31, 1993, pp. 1555-1562.
- [105] Reisenhel, P.H., Xie, W. and Gursul, I., "An Analysis of Fin Motion Induced Vortex Breakdown", AIAA-99-0136, 37th Aerospace Sciences Meeting and Exhibit, Reno, NV.
- [106] Reynolds, G.A. and Abtahi, A.A., "Instabilities in Leading-Edge Vortex Development", AIAA 87-2424, August 1987.
- [107] Riley, A.J. and Lowson, M.V., "Development of a Three-Dimensional Free Shear Layer", *Journal of Fluid Mechanics*, Vol. 369, 1998, pp. 49-89.
- [108] Rockwell, D., "Three-Dimensional Flow Structure on Delta Wings at High Angle-of-Attack: Experimental Concepts and Issues", AIAA Paper 93-0550, January, 1993.
- [109] Roos, F.W. and Kegelmann, J.T., "Recent Explorations of Leading-edge Vortex Flowfields", NASA High-Angle-of-Attack Technology Conference, NASA Langley Research Center, Hampton, VA, October 30-November 1, 1990.
- [110] Sarpkaya, T., "On stationary and travelling vortex breakdown", *Journal of Fluid Mechanics*, Vol. 45, 1971, pp. 549-559.
- [111] Schmucker, A. and Gersten, K., "Vortex Breakdown and its Control on Delta Wings", *Fluid Dynamics Research*, Vol. 3, 1988, pp. 268-272.
- [112] Sen, R., "Vortex-Oscillation Model of Airfoil Side-Edge Noise", *AIAA Journal*, Vol. 35, No. 3, 1997, pp. 441-449.
- [113] Shih, C. and Ding, Z., "Trailing-Edge Jet Control of Leading-Edge Vortices of a Delta Wing", *AIAA Journal*, Vol. 34, No. 7, 1996, pp. 1447-1457.

- [114] Spedding, G.R., Maxworthy, T., and Rignot, E., "Unsteady Vortex Flows over Delta Wings", Proceedings of the 2nd AFOSR Workshop on Unsteady and Separated Flows, Colorado Springs, CO, U.S. Air Force Academy, 1987, pp. 283-287.
- [115] Srinivas, S., Gursul, I., and Batta, G., "Active Control of Vortex Breakdown Over Delta Wings", AIAA 94-2215, 25th AIAA Fluid Dynamics Conference, June 20-23, 1994, Colorado Springs, CO.
- [116] Stahl, W.H. and Asghar, A., "Change of Asymmetric Vortex-Flow Pattern as Function of Reynolds Number and Incidence Behind Circular Cone", AIAA Paper 96-3389, 1996.
- [117] Thompson, S.A., Batill, S.M. and Nelson, R.C. "Separated flowfield on a slender wing undergoing transient pitching motions", *Journal of Aircraft*, Vol. 28, 1991, pp. 489.
- [118] Towfighi, J. and Rockwell, D., "Instantaneous Structure of Vortex Breakdown on a Pitching Delta Wing", *AIAA Journal*, Vol. 31, No. 7, 1993, pp. 1160-1162.
- [119] Taylor, G., Gursul, I., and Greenwell, D.I., "An Investigation of Support Interference in High Angle of Attack Testing", *Journal of Aircraft*, 2003, in print.
- [120] Taylor, G., Schnorbus, T. and Gursul, I., "An Investigation of Vortex Flows over Low Sweep Delta Wings", AIAA-2003-4021, AIAA Fluid Dynamics Conference, 23-26 June, 2003, Orlando, FL.
- [121] Visbal, M.R., "Onset of Vortex Breakdown Above a Pitching Delta Wing", *AIAA Journal*, Vol. 32, No. 8, August 1994, pp. 1568-1575.
- [122] Visbal, M.R., "Computational and Physical Aspects of Vortex Breakdown on Delta Wings", AIAA Paper 95-0585, January, 1995.
- [123] Visbal, M.R., "Computational and Physical Aspects of UAV Vortical Flows", *Workshop on Aerodynamic Issues of Unmanned Air Vehicles*, 4-5 November 2002, University of Bath, UK.
- [124] Vorobieff, P.V. and Rockwell, D., "Vortex Breakdown on Pitching Delta Wing: Control by Intermittent Trailing-Edge Blowing", *AIAA Journal*, Vol. 36, No. 4, April 1998, pp. 585-589.
- [125] Washburn, A.E. and Visser, K.D., "Evolution of the Vortical Structures in the Shear Layer of Delta Wings", AIAA Paper 94-2317, 1994.
- [126] Wedemeyer, E., "Vortex breakdown", *High Angle-of-Attack Aerodynamics*, AGARD 121, March 1982.
- [127] Werle, H., "Quelques resultants experimentaux sur les ailes en fleche, aux faibles vitesses, obtenus en tunnel hydrodynamique", *La Recherche Aeronautique*, No. 41, September-October 1954.
- [128] Werle, H., "Sur l'eclatement des tourbillons d'apex d'une aile delta aux faibles vitesses", *La Recherche Aeronautique*, No. 74, January-February 1960.
- [129] Wolfe, S., Canbazoglu, S., Lin, J.C. and Rockwell, D., "Buffeting of Fins: An Assessment of Surface Pressure Loading", *AIAA Journal*, Vol. 33, No. 11, 1995, pp. 2232-2234.
- [130] Wolfe, S., Lin, J.C. and Rockwell, D., "Buffeting at the Leading-Edge of a Flat Plate Due to a Streamwise Vortex: Flow Structure and Surface Pressure Loading", *Journal of Fluids and Structures*, Vol. 9, 1995, pp. 359-370.

- [131] Wolffelt, K.W., "Investigation on the Movement of Vortex Burst Position with Dynamically Changing Angle of Attack for a Schematic Delta Wing in a Water Tunnel with Correlation to Similar Studies in Wind Tunnel", *Aerodynamic and Related Hydrodynamic Studies Using Water Facilities*, AGARD-CP-413, 1987.
- [132] Wood, N.J., Roberts, L. and Celik, Z., "Control of Asymmetric Vortical Flows over Delta Wings at High Angles of Attack", *Journal of Aircraft*, Vol. 27, No. 5, May 1990, pp. 429-435.
- [133] Woodgate, L., "Measurements of the Oscillatory Pitching-Moment Derivatives on a Sharp-Edged Delta Wing at Angles of Incidence for Which Vortex Breakdown Occurs", Aeronautical Research Council, R.&M. 3628, Part III, 1971.
- [134] Xie, W., "An Experimental Investigation of Buffeting Flows over Delta Wings", MS Thesis, 1998, University of Cincinnati.
- [135] Yang, H. and Gursul, I., "Vortex Breakdown over Unsteady Delta Wings and Its Control", *AIAA Journal*, Vol. 35, No. 3, 1997, pp. 571-574.
- [136] Zohar, Y. "Fine scale mixing in a plane mixing layer", Ph.D. Thesis, 1990, University of Southern California, Los Angeles, CA.



Chapter 7 – LEADING EDGE VORTEX FLOW STUDIES AT THE UNIVERSITY OF NOTRE DAME STEADY AND UNSTEADY INVESTIGATIONS 1983-2000

by

F.M. Payne*, K.D. Visser and R.C. Nelson*****

Abstract

A review of leading edge vortex studies conducted at the University of Notre Dame is presented. The research studies include fundamental investigations of the leading edge vortex structure including vortex breakdown and investigations into the influence of model motion on vortex breakdown, surface pressure distributions, and aerodynamic loads. Flow visualization and detailed flow surveys provide important information of the vortex breakdown location, velocity, vorticity, circulation and pressure variations through the leading edge vortex structure. The final part of this paper reviews some of the important findings from a series of dynamic experiments where the delta wing model was undergoing either a large amplitude pitching or rolling motion. The unsteady motion of the model results in both significant changes in vortex breakdown location and the aerodynamic loads. The unsteady effects were found to be a function of the amplitude range of the motion and the reduced frequency. The combination of aerodynamic loads, surface pressures and detailed flow information for static and dynamic models should be quite useful to researchers developing and validating computational codes for high angle of attack flow predictions.

7.1 Background

For nearly two decades researchers at the University of Notre Dame have been engaged in various studies of the leading edge vortices over slender delta wings¹⁻²¹. The goal of the experiments was to provide a better understanding of the leading edge vortex structure over delta wings. The studies included both stationary wings and wings undergoing either large amplitude motions in pitch or roll. The initial investigations focused on the leading edge vortex structure before and after vortex breakdown on stationary delta wings of various leading edge sweep angles. This was accomplished by conducting detailed flow surveys through leading edge vortices using a either a seven hole pressure probe, Laser Doppler Velocimeter (LDV) or hot wire sensors. These studies provided a comprehensive set of measurements on the leading edge vortex flow structure including velocity, vorticity and pressure distributions surveys as well as circulation and information on vortex breakdown. Later, the influence of transient and sinusoidal motions pitching motions on the leading edge vortex structure was examined. These studies provided information on vortex breakdown movement, unsteady surface pressures and aerodynamic loads as a function of reduced frequency and motion amplitude. In addition, to the pitching motion experiments both free and forced to roll motion experiments were examined. Because of the large number of research investigations during this period, only selected studies will be highlighted in the chapter. The review will present a brief summary of experiments dealing with the leading edge vortex structure for stationary wings and wings undergoing large amplitude pitching or rolling motions.

7.2 Introduction

The flow over a delta wing at high angles of attack is highly complex. If the combination of sweep and angle of attack is high enough, a pair of leading edge vortices will form above the

* Boeing Commercial Airplane Group, ** Assistant Professor Clarkson University, *** Professor University of Notre Dame.

wing as illustrated in Figure 1. The flow approaching a delta wing initially attaches on the lower surface, and then separates as it attempts to negotiate the sharp turn at the leading edge. Driven by the pressure gradient on the upper surface, the separated shear layer immediately begins to roll up into a concentrated vortex. This results in a strong outflow of the attached flow beneath the vortex leading to a secondary separation and a counter rotating secondary vortex on the surface of the wing underneath and outboard of the primary vortex. The main effect of the secondary vortex is the displacement of the primary vortex upwards and inwards. This effect is greater if the upper surface boundary layer is laminar because the flow separation occurs earlier and the secondary vortex is larger. Outboard of the secondary vortex, the flow reattaches and approaches the leading edge. At the leading edge, the flow again separates and joins the flow from the lower surface in the shear layer as it is swept downstream.

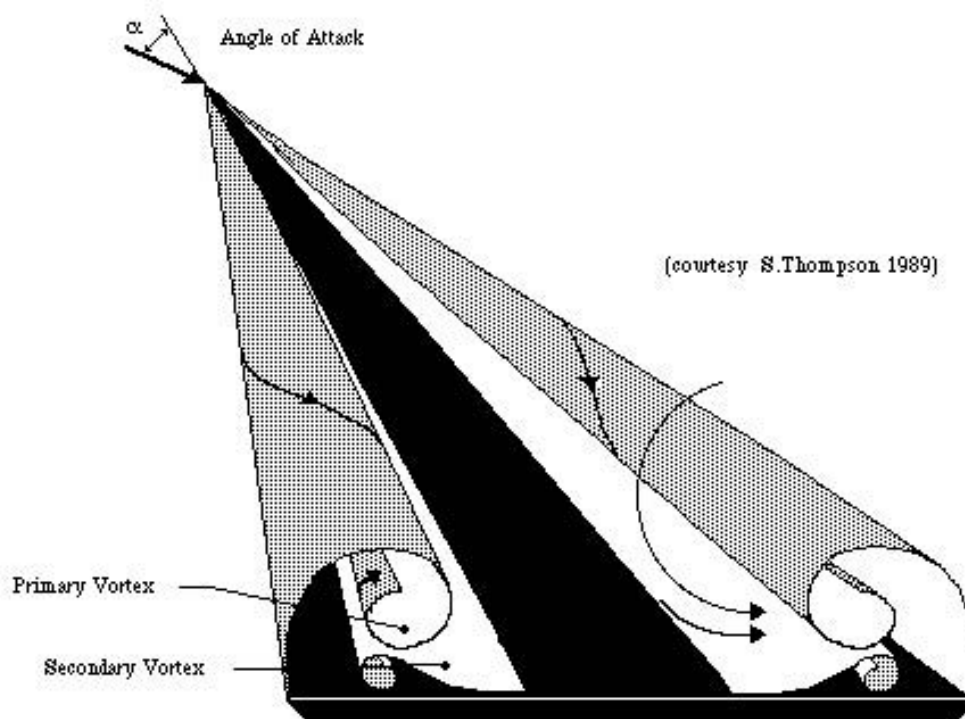


Fig. 1. Leading edge vortex above a delta wing.

As the angle of attack of a delta wing is increased, the leading edge vortex grows in strength, with the axial velocity in the core reaching more than three times the free stream value. This acceleration cannot be maintained for very long, however, in the adverse pressure gradient downstream of the leading edge, and the core flow eventually stagnates causing a sudden transformation into large scale turbulence known as vortex breakdown. The position along the vortex where breakdown takes place is a function of sweep and angle of attack as shown by Peckam²² and Elle²³. For highly swept wings at low angles of attack, the breakdown occurs in the vortex downstream of the trailing edge. With an increase of angle of attack or a decrease of sweep, the breakdown moves upstream to a position above the wing. Vortex breakdown results in loss of lift on the wing and a change in pitching moment.

Lambourne and Bryer²⁴ described vortex breakdown as a structural change at some position along the vortex from a strong regular spiral motion to a weaker turbulent motion. There is a sudden deceleration of fluid along the vortex axis and an expansion of the vortex around a stagnant core downstream of which the flow is turbulent. Lambourne and Bryer observed two

distinctive types of breakdown, a bubble and a spiral, both of which were also observed in the Notre Dame experiments.

Much of what is known about vortex breakdown was observed in experiments on isolated vortices in tubes. The work of Harvey²⁵, Sarpkaya²⁶, Faler and Leibovich²⁷, Escudier²⁸, and others, have provided information on the various forms of breakdown beyond the basic bubble and spiral, as well as measurements of the flow structure. From these studies it has been learned that the type and position of vortex breakdown is a function of tube Reynolds number, circulation number (swirl), and pressure gradient. Increasing the tube Reynolds number, swirl, or pressure gradient, all promote vortex breakdown. Which type of breakdown occurs depends on the particular combination of these parameters.

7.3 Leading Edge Vortex Structure

Payne³ studied the leading edge vortices above a family of delta wings having sweep angles of 70, 75, 80, and 85 degrees. The wing models were all flat plate delta wings with an underside leading edge bevel. The experimental study included flow visualization measurements of vortex breakdown location, seven hole pressure probe and LDV surveys at selected chordwise locations above the delta wing models.

Qualitative and quantitative experiments were undertaken to examine the structure of the leading edge vortices on the four delta wings. The location of the vortex cores and the location of breakdown was tracked for a range of conditions from 10 to 40 degrees angle of attack, and tunnel speeds of 3 to 23 m/s. Both still and high speed cinema photography were used to record the flow visualization results. A combination of lateral and longitudinal cross sectional views using a Lexel Model-95, 8-Watt argon laser or a 4-Watt argon ion laser were obtained to provide information on the three-dimensional nature of the vortex structure before, during, and after breakdown. Close-up high speed motion picture photography provided details of the dynamic characteristics of the breakdown process.

Wake survey measurements were obtained using a seven-hole probe (SHP) attached to a computer controlled stepper motor driven traversing system. The probe was calibrated in pitch and yaw at angles up to $\pm 60^\circ$ following the method of Gerner²⁹ et al. The flow angle measurements had an average standard deviation of less than 0.6° at over the calibration range. The SHP results were validated using a Laser Doppler Velocimeter (LDV), with and without the probe in place.

Full details of the experimental setup are described in References 3, 30-33 and a data sheet describing the test facility, model, test conditions and data uncertainty is included in an appendix at the end of this report.

7.3.1 Flow Visualization Results

Figure 2 shows examples of smoke flow visualization on 70° and 85° sweep models at 40 degrees angle of attack. Three types of illumination are shown for each sweep angle: flood lighting (top), lateral laser sheet (middle) and longitudinal laser sheet (bottom). The free stream velocity is 10 ft/s (3 m/s). In all cases, a column of smoke was introduced upstream of the test section and positioned to impinge on the apex of the model where the smoke was entrained into the vortices. On the 70° wing, both vortices tended to break down at about the same location. As expected, the breakdown occurred farther aft on the lower aspect ratio (higher sweep) wings. The breakdown position was relatively steady and symmetric on the 70° wing except for a high frequency, low magnitude oscillation. However, with increasing sweep, the breakdown became increasing asymmetric and unsteady. On the 85° wing only one vortex would usually be breaking down above the wing at a time, and the breakdown location varied over approximately fifty percent of the chord length. The breakdown would switch sides at random intervals, usually moving downstream along one vortex and then appear at some downstream location on the other vortex before moving back upstream. This large scale migration occurred only at very low speeds and would stabilize at tunnel speeds above about 25 ft/s (8 m/s), although the asymmetry in

location between the port and starboard sides would remain. The unsteadiness in chordwise location at low speeds was probably in response to fluctuations in the free stream flow conditions due to outside influences (such as wind gusts). In the photo at upper right, a bubble type breakdown can be clearly seen on the starboard side of the 85° wing, about halfway down the model.

The middle photographs in Figure 2 are multiple exposure images using a lateral laser sheet to illuminate cross sections of the flow. The laser sheet was moved in between exposures. Vortex breakdown is identifiable by the disappearance of the clear core and the onset of a diffuse region of turbulence. Details of secondary structure in the shear layers is clearly visible on the 85° wing (middle right), where the fourth laser cross section from the apex is cutting directly across a bubble type breakdown on the port side of the wing. The secondary structure visible in the shear layer appears to consist of small streamwise vortices which develop in a manner similar to a Kelvin-Helmholtz type instability. The observed structures are static, they do not rotate with the vortex, but appear to emanate from near the leading edge and follow a spiral path fixed with respect to the shear layer. The shear layer vortices are visible on the 85° wing at 10 ft/s (3 m/s) because the flow was laminar at these conditions. When the free stream velocity was increased, the flow became turbulent, and the smoke in the vortex became too diffuse to make out details. On the lower sweep wings, the angle between the leading edge and the free stream flow was higher, resulting in a stronger vortex with higher axial and circumferential velocities and the flow became turbulent at lower angles of attack. Only the 85° delta still had laminar flow at the angle of attack at which vortex breakdown was occurring above the model.

The bottom photographs in Figure 2 were obtained by rotating the laser sheet by 90°. The high speed axial flow in the core of both vortices appear as regions void of smoke. The core is only visible for a short distance because the vortices are curving out of plane as they move downstream.

The laser light sheet technique was used in conjunction with high speed cinema photography to capture the dynamic processes involved in vortex breakdown. Still photographs from individual frames are documented and discussed in References 30 and 31. As has been observed in many experimental studies the breakdown location oscillates about some mean position on the wing. The high speed motion picture photography captures these oscillations as well as changes in the breakdown structure. In the high speed movie the smoke images of the breakdown region appear to change from a bubble to a spiral type of breakdown. The breakdown tends to look like the bubble form when it is moving upstream and a spiral form when moving downstream. However, close examination of the bubble images show a tightly wound spiral that emanates from just behind the recirculation region of the bubble. The appearance of what looks like a bubble may be a manifestation of the compression of the spiral core as it moves upstream.

7.3.2 Seven Hole Probe Measurements

Due to the susceptibility of the vortex breakdown process to probe interference, non-intrusive techniques such as Laser Doppler Velocimetry (LDV) are generally preferred over physical probes for studies of this nature. However, away from breakdown, a physical probe is a convenient tool for quickly obtaining accurate mean flow conditions.

The question of probe interference on vortex measurements is discussed in detail in Reference 33. In general, the influence of the probe on a vortex at critical (near breakdown) conditions was found to be dependent on the size of the probe and the position of the breakdown on the wing. Seven Hole Probe (SHP) measurements were made in the Notre Dame delta wing experiments at a wide range of conditions. The measurements were compared with LDV measurements at the mid-span location of the four delta wings described above, at angles of attack of 10, 20, 30 and 40 degrees. The two sets of measurements were found to be in close agreement except in regions of reversed flow. Details of the calibration process for the SHP used in these experiments can be found in Reference 3 and 33.

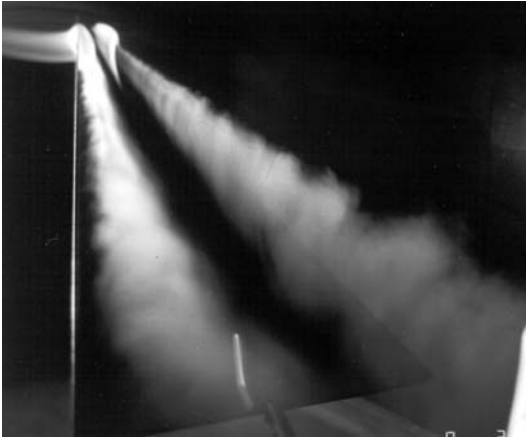
With the limitations of the SHP in mind, a series of tests were run to map the flow on the 70, 75, 80, and 85 degree delta wings at angles of attack from 10 to 40 degrees. The probe was aligned with the surface of the model, with the streamwise, spanwise, and normal components, designated as u , v , and w , respectively. The flow surveys were made at $x/c = 0.500$ for all four models, except for the 85° wing, where surveys were also made at $x/c = 0.550, 0.600, 0.650, 0.675, 0.700, \text{ and } 0.750$. Each survey covered half the span of the model from $y/s = 0.0$ to 1.5 and $z/s = 0.0$ to 1.5. This resulted in a square grid, 36 points wide and 30 points high, for a total of 1080 points. There was a seven second delay before each point was acquired to allow for the response of the probe. The use of long runs of very thin tubing minimized the size of the probe, but increased the lag time. Data was sampled for five seconds at 20 Hz and then averaged. Movement of the probe to the next data point took about one second. The total elapsed time per point was thirteen seconds. With 1080 points, each survey took almost four hours to run. The flowfield data was plotted in the form of total pressure contour plots, streamwise (parallel to model) speed contours, and crossflow vector diagrams. For clarity in the vector diagrams, only every other point was plotted. The free stream velocity was 30 ft/s (9.1 m/s) for all surveys, corresponding to a Reynolds number of 255,000 based on root chord.

Flowfield surveys over the 70° and 85° sweep wings at $x/c = 0.50$ and 30° angle of attack are compared in Figure 3. At these conditions the minimum total pressure coefficient on the 70° wing was -7.95 , and the maximum core flow velocity ratio, u/U_∞ was 3.28. It was apparent from the parallel velocity contour plot (middle, left in Figure 3) that something unusual was happening. Underneath and outboard of the vortex core region, where the velocity ratio has peaked at $u/U_\infty = 3.28$, there is a small stagnation region where the velocity is near zero. It is somewhat surprising to find both a strong intact core and stagnation region in the same cross section. Apparently the vortex is beginning to break down, most likely due to the presence of the probe. The intact core and the stagnation region probably did not exist simultaneously, but appear together in the plot due to the fact that the surveys were acquired over an extended amount of time and therefore represent an average result. A similar finding was reported by Hummel³³ in a five hole probe survey of the flow past a 79° delta wing at 31° angle of attack. In Hummel's flow visualization experiments it was found that a breakdown was caused by the probe which otherwise did not occur at this angle of attack.

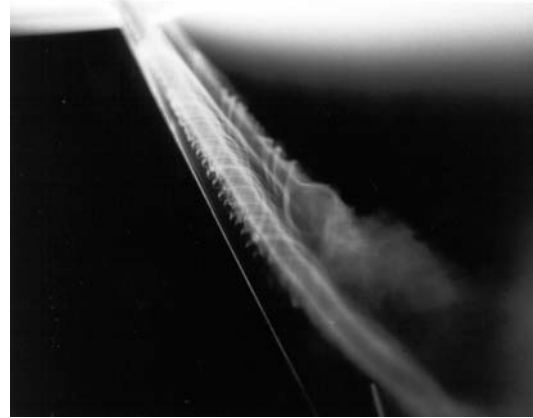
With increasing sweep at constant angle of attack, the leading edge vortices were seen to grow in size relative to the wing and move upward and away from the surface. The minimum total pressure was not as low, and the maximum velocity not as high; in other words, the vortices were not as strong. Flow surveys over the 85° wing are shown on the right side of Figure 3. Like the flow visualization, details of the secondary structure are much better defined on the 85° delta, and show a multi-lobed pattern similar in structure to the flow visualization results; but probably for a different reason. The flow visualization was clearer on the 85° wing, because the flow was laminar at 10 ft/s (3 m/s). The wake surveys, however, were acquired at 30 ft/s (where the flow was steadier), but turbulent, even on the 85° delta. The improved definition in the wake surveys may therefore be due to improved resolution on the 85° wing, where the data points are closer together. The same non-dimensional space was covered with the same number of points, but since the span on the 85° delta is only about a quarter of the 70° wing, the density of points was that much greater. The result does suggest that the observed secondary structure is present, even when the flow is turbulent and is not a by-product of the flow visualization method.

7.3.3 LDV Measurements

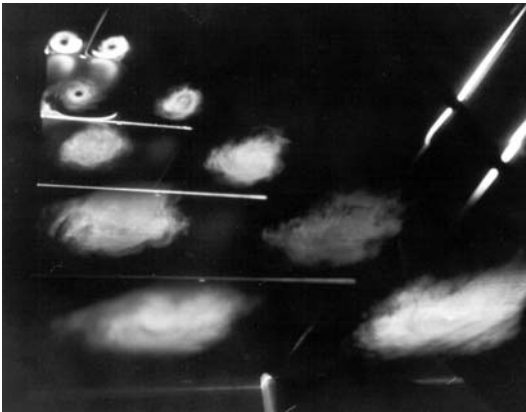
To address the question of probe intrusiveness on a vortical flowfield, seven hole probe (SHP) measurements were compared with Laser Doppler Velocimeter (LDV) measurements, with and without the SHP in the flow. The measurements were taken at a fixed station ($x/c=0.500$) and four angles of attack (10°, 20°, 30°, 40°) for two sweep angles (70° and 85°). Results from the 70° delta are presented in Figure 4. Components of velocity parallel with the



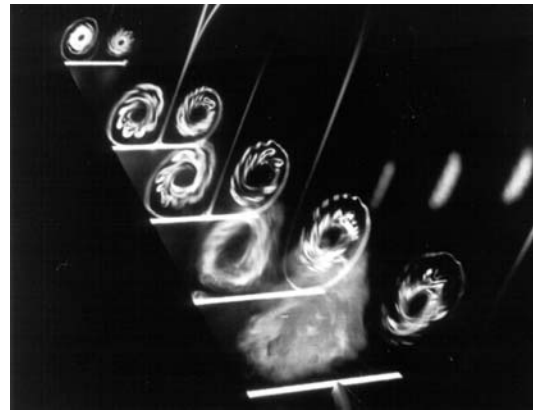
Smoke flow visualization on 70° delta wing at $\alpha = 40^\circ$.



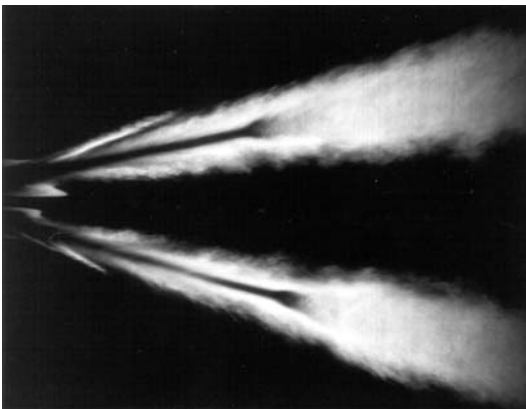
Smoke flow visualization on 85° delta wing at $\alpha = 40^\circ$.



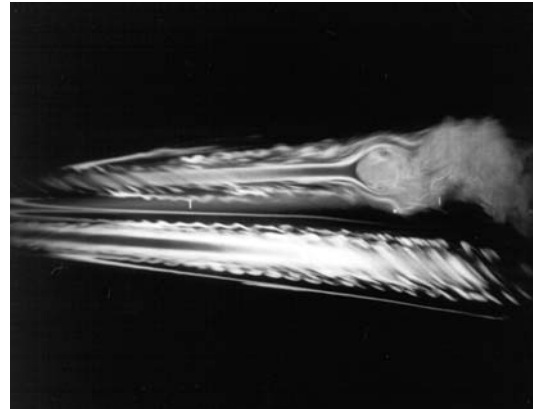
Lateral laser sheet cross sections over 70° delta wing at $\alpha = 40^\circ$.



Lateral laser sheet cross sections over 85° delta wing at $\alpha = 40^\circ$.



Longitudinal laser sheet cross section over 70° delta wing at $\alpha = 40^\circ$.



Longitudinal laser sheet cross section over 85° delta wing at $\alpha = 40^\circ$.

Fig. 2. Flow visualization of leading edge vortices on 70° and 85° delta wings.

wing (u/U) and normal to the wing (w/U) are shown. The data plots labeled “SHP” are seven hole probe measurements; the data labeled “LDA+SHP” are laser measurements slightly upstream of the probe nose; and data labeled “LDA” are laser measurements with the probe retracted from the flow field.

At 10° angle of attack, the two LDA mean velocity measurements (with and without probe) are in reasonable agreement, especially the w/U component; except in the core region, where the lack of seeding particles made it difficult to obtain measurements. At this angle of attack, the vortex was relatively weak and the parallel velocity component inside the core reached only about 1.5 times the free stream velocity. Breakdown does not occur naturally over the wing at this condition, and the probe interference was found to be small.

As the model angle of attack was increased to 20° , the vortex grew dramatically in strength and the core velocity approached 2.8 times the free stream value. However, as indicated by the close agreement between the LDA and LDA+SHP measurements, there is still no strong interference attributable to the probe. The affect of the probe is a slight inboard displacement of the maximum u location. An inspection of the w velocity component, reveals that there is virtually no effect on the angular velocity in the core region. Again, at this angle of attack, no natural breakdown occurs over the wing and the affect of the probe is relatively minor.

At 30° angle of attack, it is evident that the presence of the probe is causing the vortex to breakdown. At this angle of attack the vortex naturally breaks down at $x/c=0.600$. The insertion of the probe upstream of the natural breakdown location moved the breakdown upstream to the tip of the probe.

At 40° angle of attack, vortex breakdown occurs naturally at approximately $x/c=0.250$. In this case, the presence of the probe at $x/c=0.50$ did not significantly affect the location of breakdown since the breakdown was already occurring well upstream of the measurements. The u profiles indicate a somewhat wider wake/reversal flow region when the SHP is in place, and the w profiles are in good agreement.

In summary, measurements over the 70° wing indicate that the effect of a probe on breakdown location depends on the probe position relative to the breakdown and also on the location of the natural (undisturbed) breakdown location. At low angles of attack where the vortex is relatively weak and breakdown does not normally occur over the wing, the affect of the probe was limited to a small displacement of the vortex and a slight reduction in the u component in the core. For conditions where breakdown does occur naturally above the wing, or in the wake close to the trailing edge, placing the probe upstream of the natural breakdown location can precipitate a breakdown at the probe location. Placing the probe downstream of the natural breakdown point had relatively minor affect on the breakdown process.

It is well known that the stability of the natural (undisturbed) breakdown location is dominated by pressure gradient and is a function of sweep and angle of attack. The effect of a probe on the breakdown location was found to depend on these same factors. At low angles of attack, when the breakdown is near the trailing edge, the natural breakdown location is the most unstable and the effect of a probe is the greatest. At high angles of attack, when the breakdown is near the apex, the effect of a probe is minimal. If the breakdown was at a given location on both the 70° and 80° wings, the breakdown on the 70° wing was observed to be more unstable and more sensitive to interference. Naturally, the size of the probe relative to the model is also a factor. This was observed by Sforza³⁵ et al, in measurements on an 80° delta wing (with 118 cm chord) for an angle of attack of 29° . Sforza found that a 0.953 cm probe caused a breakdown (.008 probe/chord ratio), whereas a 0.318 cm probe (.003 probe/chord ratio) did not. The probe used in the Notre Dame experiments was 0.280 cm, used with 40.6 cm root chord models (.007 probe/chord ratio).

In general, it has been shown that reasonably accurate measurements can be taken with a SHP in highly swirling flows at low Reynolds numbers, except in conditions very close to breakdown, in regions where the local flow features are too small for the probe to resolve, or where the local flow is reversed. Full details are discussed in Reference 33.

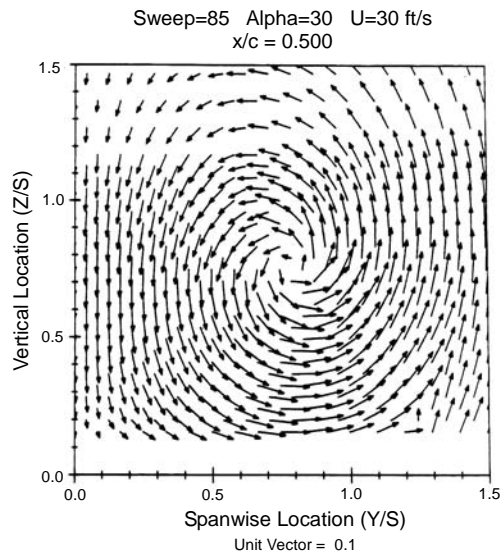
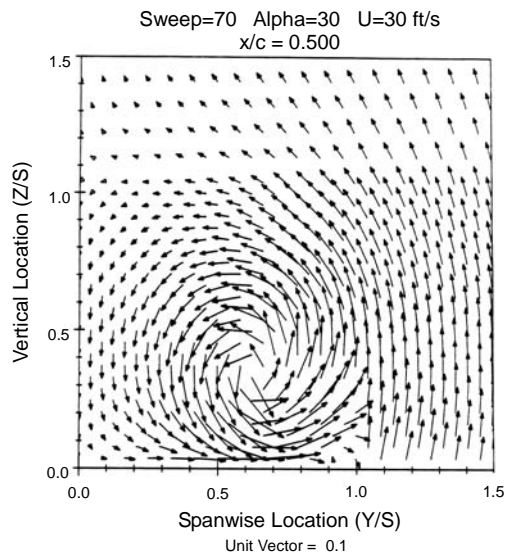
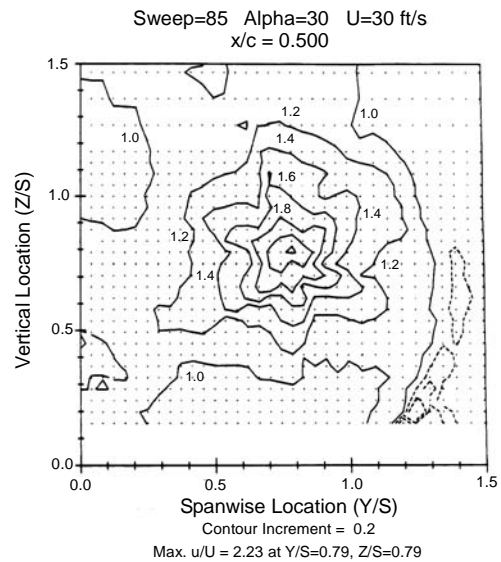
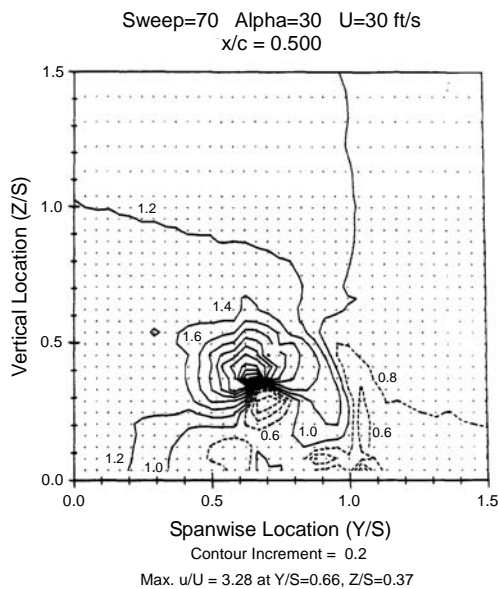
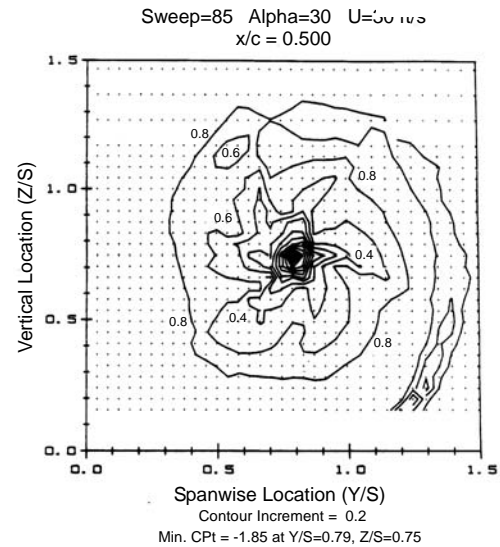
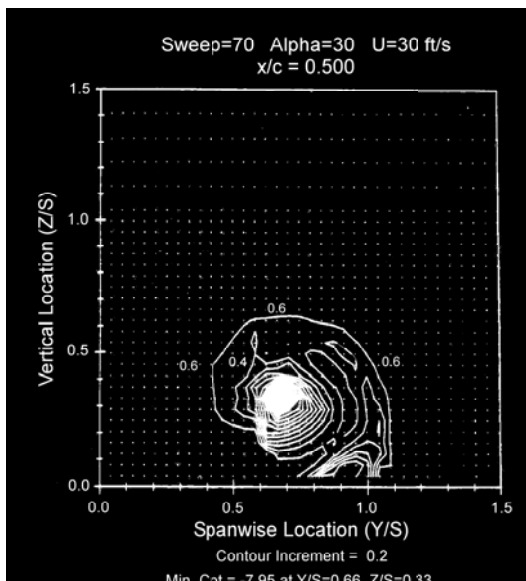


Fig. 3. Seven hole probe flow field surveys over 70° and 85° delta wings.

Based upon a detailed analysis of his experimental measurements Payne³ reached the following conclusions.

1. Photographs obtained using a laser light sheet technique revealed secondary vortical structures in the leading edge shear layers which developed in a manner analogous to Kelvin-Helmholtz type instabilities. The recirculation zone associated with bubble type breakdowns appeared to consist of a single celled structure in contrast to the two celled bubbles observed in vortex tube experiments. High speed motion picture photography clearly shows the unsteady nature of the breakdown region. Vortex breakdown appears to oscillate about some mean position on the wing. The movies show the breakdown changing from a bubble to a spiral form when breakdown is moving downstream and the reverse when it moves upstream. The movies also show the bubble form of breakdown with a spiraling core just downstream of the recirculation region. The appearance of what looks like a bubble may actually be due to the compression of the spiral as it moves upstream.
2. The influence of an intrusive probe on a vortex flowfield at critical (near breakdown) conditions was found to depend on the size of the probe, the wing sweep angle, and the position of the breakdown on the wing. Seven hole probe (SHP) measurements compared favorably with Laser Doppler Anemometer (LDA) measurements, except in conditions very close to breakdown, in regions where the local flow features were too small for the probe to resolve, or where the local flow was reversed.
3. Total pressure contours from wake surveys over the 85° wing had a multi-lobed pattern with a structure similar to that observed using the laser sheet technique, suggesting that the observed secondary structure was not a by-product of the visualization method. The multi-lobed pattern was present in the total pressure contours even when the flow was turbulent.

7.3.4 Vorticity and Circulation Distribution

In a subsequent investigation Visser¹³ conducted an experimental study of the leading edge vortex flow field using multiple sensor hot wire techniques. From these measurements he determined the circulation and vorticity distribution through the leading edge vortices above both a 70 and 75 degree swept delta wing. The models used in this experiment were flat plate delta wings having a windward 25° beveled edge, identical to that of Payne³.

Additional velocity measurements were made using a half span model of the same sweep and edge bevel as the full span models, but a root chord of 685.5mm (26.95 inches). This enabled the effect of a finer grid resolution to be examined in conjunction with a smaller relative probe size. A splitter plate was employed during these tests. Details of the experimental facility, model geometry, test conditions and data uncertainty are included in a data sheet in the appendix.

The majority of data was accumulated over a 75° sweep delta wing at 20° angle of attack. Measurements were made at various chordwise stations in grid planes normal to the upper surface. Surveys were taken through the starboard vortex only, encompassing a z/s^* of 0.06 to approximately 1.0 and y/s^* from the chord centerline out to a spanwise location beyond the right edge of the wing, where s^* is the local semi-span. Data was also acquired at $\alpha = 30^\circ$, however aft of the $x/c = 0.5$ location the probe induced breakdown and thus only stations unaffected by the probe, upstream of this location, were measured. Finally, a 70° sweep configuration was utilized at 20° angle of attack in an effort to observe the effect of sweep. The performance of this cross wire technique was evaluated by comparison with previous data obtained above the planform using a seven hole probe Payne³ as the inherent complexity of the equations made an assessment of the error for each component difficult to isolate. Further comparisons of this measurement procedure, for configurations other than presented here, can be found in Visser¹³. All tests were conducted at a centerline chord Reynolds number of 250,000.

7.3.5 Vorticity

The spatial progression of the vorticity was examined in light of both its positive and negative components by central differencing the velocity field to obtain the axial vorticity component:

$$\Omega_x = \frac{\partial w}{\partial y} - \frac{\partial v}{\partial z} \quad (1)$$

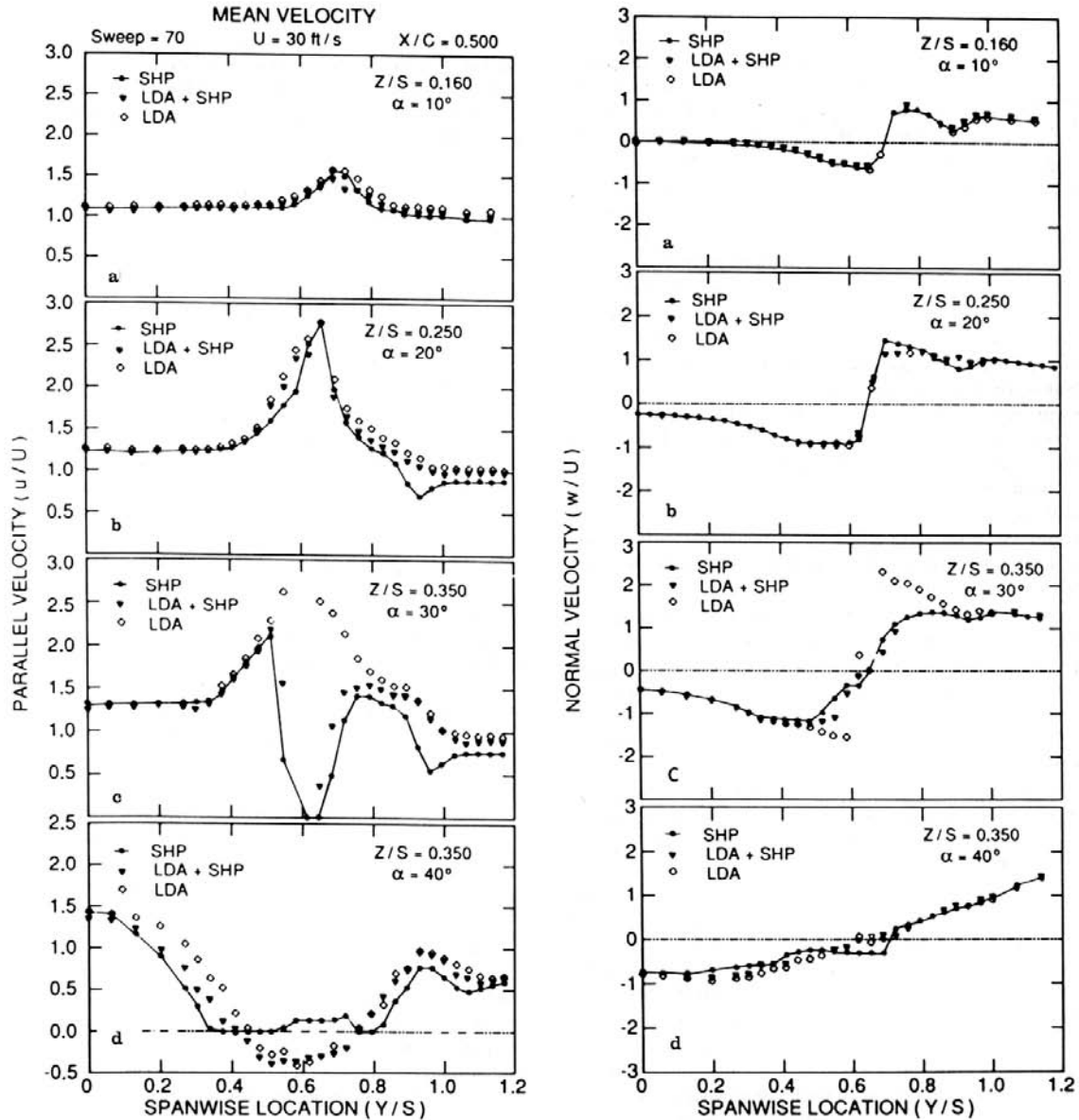


Fig. 4. Comparison of seven hole probe and laser Doppler anemometer measurements at mid chord on a 70 delta wing at increasing angle of attack. Vortex breakdown occurs at 30° when the SHP is present and at 40° with or without the SHP.

The local semi-span, s^* , was used to scale the results, along with the freestream velocity, to examine the effect of the local geometry.

An example of the resulting vorticity field estimated from the velocity data $\alpha = 20^\circ$ is presented in Figure 6. The majority of the axial vorticity is concentrated in the region immediately around the core of the primary vortex. The extent of this region is approximately $y/s^* = 0.55$ to 0.75 and $z/s^* = 0.3$ to 0.5 , or approximately 20% of the span. Note that this area is about twice the diameter of the subcore region, typically defined as the distance between the maximum tangential velocity components. Outside of this regime, the flow presents itself as essentially free of the positive axial vorticity component. A smaller region of flow with vorticity of the opposite sign and a much lower magnitude is located in the vicinity of the secondary vortex.

The chordwise behavior of the vorticity was further examined using the velocity profiles taken through the vortex core. Under the assumption that the radial velocity and its gradient were negligible compared to the other terms, the axial vorticity based on a single traverse through the core is defined as:

$$\Omega_x = \frac{V_\phi}{r} + \frac{\partial V_\phi}{\partial r} = \frac{w}{r} + \frac{\partial w}{\partial r} \quad (2)$$

utilizing polar coordinates. The axial core vorticity profiles for the $\alpha = 20^\circ$ configuration are overlaid for each of the measured x/c locations in Figure 7. Similar profiles are seen to exist at each station. The majority of the axial vorticity component was contained within 20% of the semispan, dropping to less than 10% of the peak value for $r/s^* > \pm 0.10$ about the core center location. The vorticity data at the angle of attack of 20° scales in the same manner as the axial velocity profiles, that is linearly with distance from the apex which indicates a conical behavior of the flow field. Similar distributions for the $\alpha = 30^\circ$ gave no indication, such as a noticeably changing peak value or distribution, of the imminent breakdown present at $x/c > 0.5$.

The observed behavior of the axial vorticity strongly supports the conical nature of the delta wing vortex in the region preceding breakdown. Scaling both the maximum vorticity values and the profiles based on a traverse through the core by the local spanwise geometry indicates that the distribution of the axial vorticity to be similar at each chordwise station. The majority of the

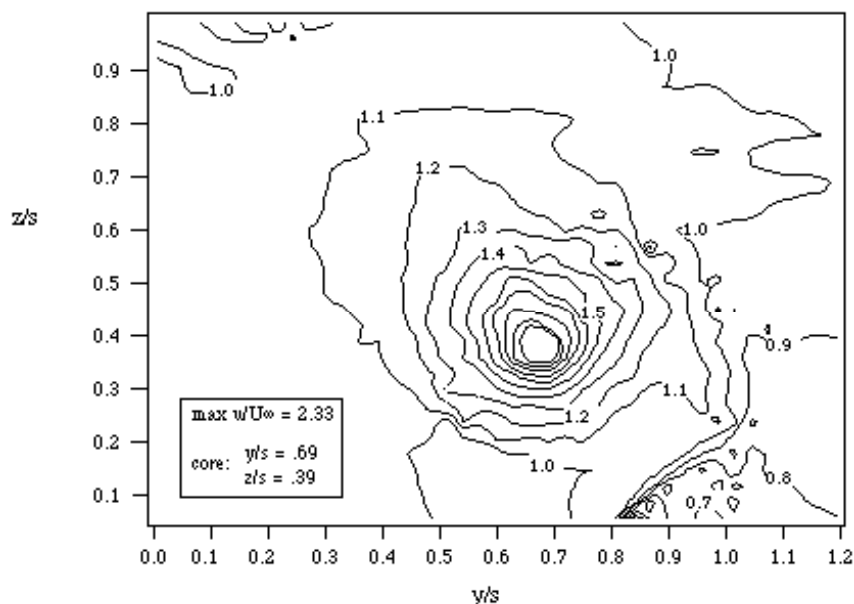


Fig. 6. Axial Vorticity at $\Lambda=75^\circ$, $\alpha=20^\circ$, $x/c=0.5$

axial vorticity appears to be confined to the subcore region of the vortex, at least with respect to the pre-breakdown vortex state. The use of the maximum value of axial vorticity can be deceptive, however, in determining the local strength of the vortex structure. Factors such as grid resolution should be accounted for when comparisons of data are made. The maximum azimuthal vorticity also maintains a more or less constant value in the vortex upstream of breakdown, but is observed to become negative upon entering the breakdown zone.

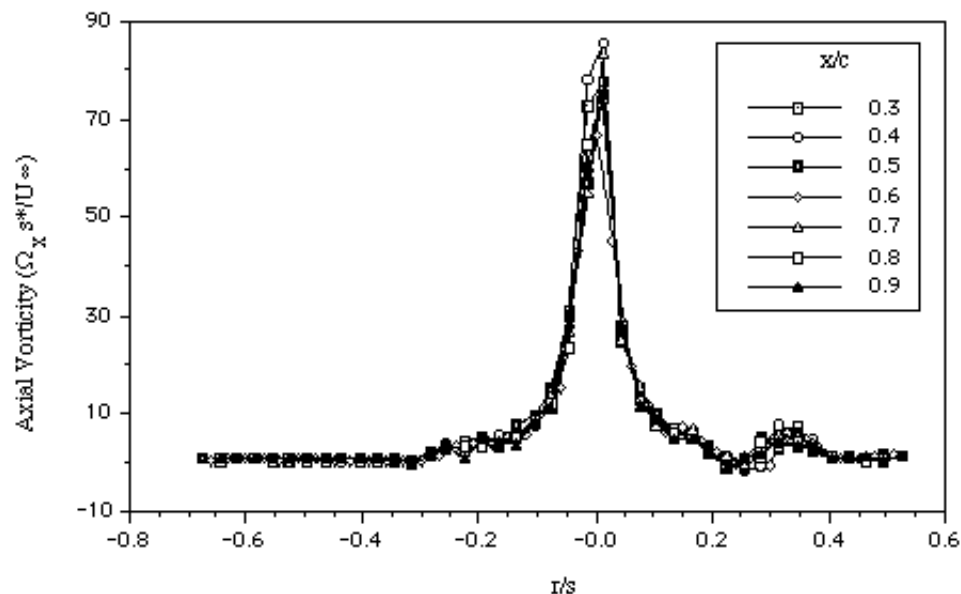


Fig. 7. Chordwise Axial Vorticity Profiles, $\Lambda=75^\circ$, $\alpha=20^\circ$

7.3.6 Circulation

The circulation, Γ was calculated from the crossflow velocity components, in the plane of the survey grids, and is compared with the spatially integrated vorticity field distribution for the 20° incidence case in Figure 8. The values have been nondimensionalized by the freestream velocity and the root chord. Distributions are plotted outward from the core center ($r = 0$), where the radial distance has been scaled by the local semispan. Each curve represents a chordwise location and the circulation can be seen to grow in a chordwise manner. The circulation is also observed to increase at a decreasing rate from the center of the vortex and reaches a maximum inside of the planforms leading edge. The profiles gain an additional rise in circulation as the integration path encloses the shear layer outboard of the leading edge.

The observed behavior of the circulation agrees with the axial vorticity and velocity distributions in indicating that a near conical flow field exists for the majority of the pre-breakdown leading edge vortex. The strength of the vortex, as defined by the circulation in the yz plane, increased in a near linear manner with angle of attack for a fixed chord location and with distance from the apex over the forward region of the planform. This increase in strength is inevitably followed by breakdown which reduces the concentration of axial vorticity about the vortex axis. The onset of breakdown cannot be solely attributable to the total vortex strength in absolute terms, for the total circulation of the vortex is still increasing with x/c , even after breakdown. Instead it is believed that the local circulation taken about the core region plays a most significant role in the onset of breakdown. There is a sharp decrease in this value after breakdown, presumably in a non-reversible manner for the flow never transitions to the pre-breakdown state. It should be emphasized that there are other flow parameters which have an influence on the breakdown and are not been accounted for here. The circulation was determined solely from the velocity flow field plane normal to the wing surface.

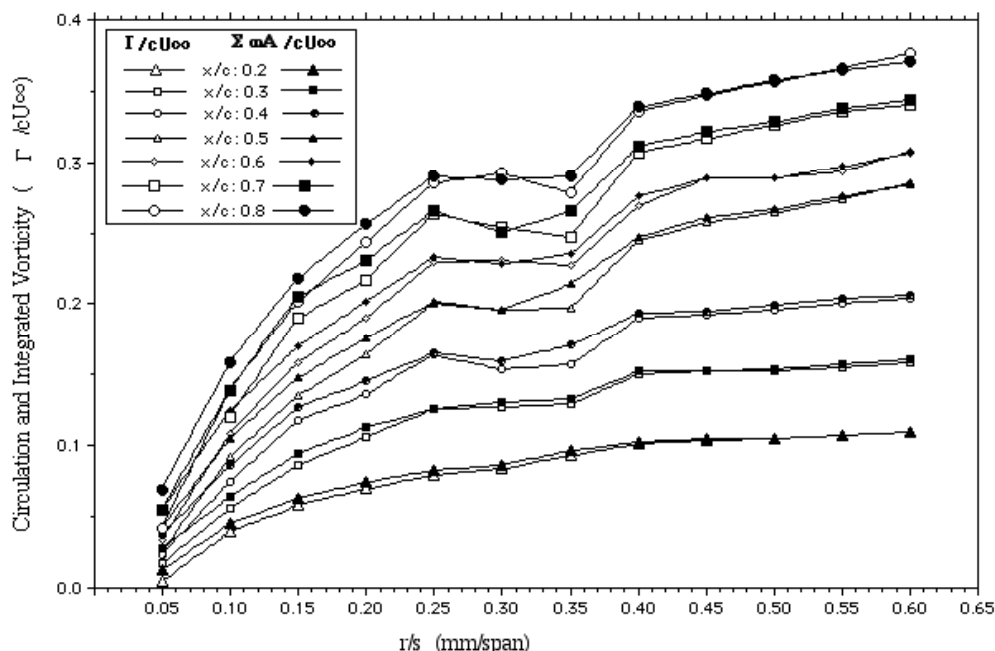


Fig. 8. Radial Circulation Profiles, $\Lambda=75^\circ$, $\alpha=20^\circ$

7.3.7 Vortex Strength Correlation

A similarity relationship was proposed by Hemsch and Luckring³⁶ based upon slender body assumptions by Sychev³⁷ for the vortex circulation as a function of the apex half angle, ϵ , angle of attack, α , chord, c , and freestream velocity, U_∞ . It has the form:

$$g = \frac{\Gamma}{U_\infty c \tan^2 \epsilon \cos \alpha} = AK^n \quad \text{where } K = \frac{\tan \alpha}{\tan \epsilon} \quad (3)$$

for some value n . Hemsch and Luckring³⁶ found that if g and K are plotted in a log-log format, a fit of the form $g = AK^{1.2}$ was seen for data obtained from Wentz and MacMahon³⁸, $\Lambda = 62^\circ$, and Delery, Pagan, and Solignac³⁹ ranging from g of 0.5 to 10.0 and K of 0.2 to 2.0. Theory by Smith⁴⁰ resulted in the form $g = 4.63K^n$. For comparison, seven hole probe data from Payne is plotted in Figure 11 with that of Wentz and MacMahon³⁸ and the curve of Smith for $n = 1.2$. Payne's data represents sweep angles of 70° , 75° , 80° , and 85° at various chord locations. It is seen to follow the line of Smith to a value of g up to 100 and a value of K up to 10.

The present tests were conducted at locations above the wing surface, and a further scaling of g by the local chord ratio, x/c , was found to bring the data into line with that of Smith as shown in Figure 12. Manipulation of the above expression of Hemsch and Luckring³⁶ to include the ratio x/c and expressing it in terms of s^* leads to the following:

$$g = \frac{\Gamma}{U_\infty s^* \tan \epsilon \cos \alpha} \quad (4)$$

Further data and analysis can be found in Visser^{13,41}.

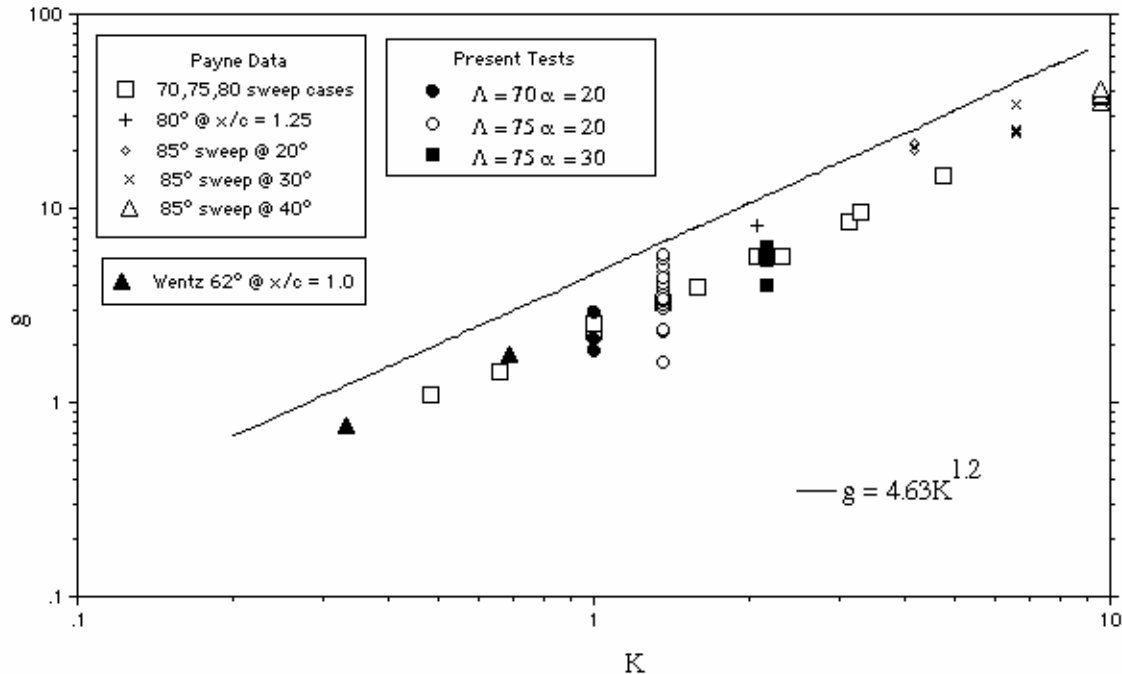


Fig. 11. Correlation of circulation predictions using the Hemsch and Luckring³⁶ relationship for g vs. K

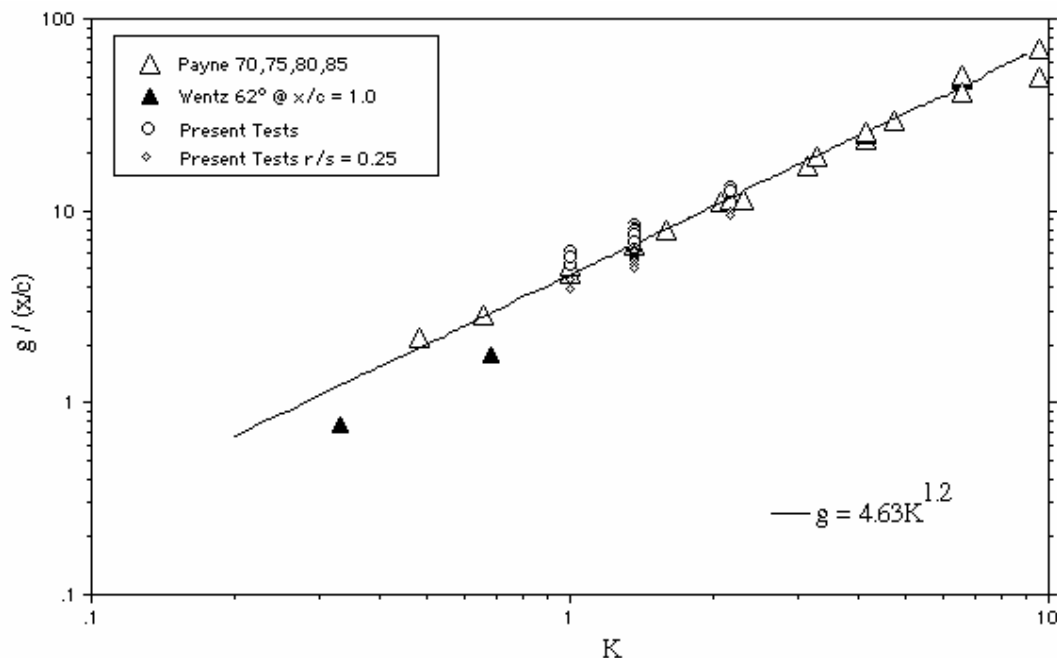


Fig. 12. Correlation of circulation predictions using the Hemsch and Luckring³⁶ relationship for $g(x/c)$ vs. K

Experimental crosswire measurements of the flowfield above a 70° and 75° flat plate delta wing were performed at a Reynolds number of 250,000. Survey grids were taken normal to the planform at a series of chordwise locations for angles of attack of 20° and 30°. Axial and

azimuthal vorticity field distributions were derived from the velocity fields. The circulation was observed to scale with the local semispan and grow approximately linearly in the chordwise direction. For regions of the flow outside of the vortex subcore, the circulation at any chordwise station varied logarithmically with distance from the vortex axis. The circulation was also found to increase linearly with angle of incidence at a given chordwise station.

The preceding discussion strongly supports the argument that the flow over a delta wing, upstream of the breakdown regions and away from the apex and trailing edge regions, behaves in a conical manner in that properties remain constant along rays emanating from the apex. Spanwise vorticity and velocity distributions based on a single traverse through the core of the vortex scale with the local geometry in the pre-breakdown state. Dimensional scaling of the radial circulation distribution by the local semispan also indicates this flow property to be similar at each chordwise locations upstream of breakdown. Thus the local semispan represents a viable length scale for flat plate delta planforms and is a variable which should be incorporated into any nondimensionalization scheme used to examine flows generated by swept leading edge geometries. This is further substantiated by the results obtained using the correlation of Hemsch and Luckring. Incorporating the factor x/c correlates the circulation distributions in regions where the vortex size and strength are increasing, such as over a delta wing. The dominating factors leading to the onset of breakdown are felt to be the local circulation of the vortex and the accompanying pressure field.

The conical nature of the properties noted above occurs most strongly over the central portion of the planform, that is away from the apex and trailing edge regions. Near the apex, the geometry of the flat plate delta wing is such that the span of the wing is on the order of the thickness and the fluid senses a blunt body rather than a slender, thin planform. In the same manner, the field is altered as it approaches the trailing edge by the pressure recovery of the flow. The jet core and subcore growth rates both appear to be functions of the local semispan, although they are growing at different rates. Relative to the local geometry, the subcore appears to be constant and the jet core shrinking in size in the axial direction. Finer grid data and flow visualization indicate that the subcore decreases in size relative to the local geometry; that is, it maintains a constant diameter.

A reduction in the local circulation about the vortex axis occurred at breakdown. The spanwise distribution of axial vorticity was severely altered through the breakdown region and the spanwise distribution of axial vorticity present appeared to reach a maximum immediately preceding breakdown. The local concentration of axial vorticity about the vortex axis was reduced while the magnitude of the azimuthal vorticity decreased throughout the breakdown zone. The axial vorticity components with a negative sense, found in the secondary vortex, remained unaffected by changes in wing sweep or angle of attack, in direct contrast to the positive components.

Several other conclusions were reached and are summarized below:

1. The use of the present cross wire technique, employing four spatial passes and two different probe configurations for a single survey, was satisfactory in measuring the flow velocities.
2. Employing the maximum value of axial vorticity in determining the local strength or state of the vortex structure is deceptive. Grid resolution dependence and the locally steep gradients deter this type of quantification.
3. The majority of the pre-breakdown positive axial vorticity is concentrated about the vortex axis in a region approximately twice the diameter of subcore.
4. Adjustment of the flow field to changing test conditions occurred for the most part in the positive axial vorticity regions. The negative axial vorticity distributions, concentrated in the secondary vortex region, did not change significantly with distance from the apex for both angles of attack investigated.

5. The circulation profiles exhibited a logarithmic dependence over a given radial distance from the vortex axis pointing to a possibly substantial influence of Reynolds stress terms in the flow field.

Additional information regarding Visser's investigation can be found in References 13, 41-43.

7.4 Unsteady Slender Wing Aerodynamics and Flow Structure

For large amplitude pitching motions, the aerodynamic characteristics of delta wings are quite different from what would be predicted from static measurements. The unsteady lift or normal force curves are similar to the dynamic stall curves observed on pitching airfoils. Starting in the mid 1980s a number of experimental studies were conducted to determine the unsteady aerodynamics of delta wings undergoing large amplitude pitching motions⁴⁴⁻⁵⁰. These studies have documented the hysteretic nature of the forces and moments and how the magnitude of the aerodynamic loading is a function of the type of motion and the motion history.

Thompson¹⁴ designed an experiment to investigate the relationship between the aerodynamic loads and vortical flow characteristics of a highly sweep delta wing undergoing large amplitude oscillating pitching motions. A 70 degree delta wing was selected for this study. The experiments included measurement of the location of the vortex core, position of vortex breakdown, and surface pressure distributions as a function of reduced frequency, angle of attack range, and mean angle of attack. Additional information on Thompson's experiments can be found in References⁵¹⁻⁵⁴ and the data summary sheet included with this report.

An unsteady motion of a delta wing results in a modification of the flow field in response to the maneuver. This can cause delays in flow separation and vortex formation at low angles of attack, and changes in vortex location and onset of breakdown at higher angles of attack. During oscillatory or transient motions, a hysteresis develops in the position of the vortex core and the vortex breakdown relative to the static locations. Due to the hysteresis in the flow field, there is a corresponding modification of the aerodynamic loads on the delta wing. The results presented in the following section show the importance of flow field hysteresis in vortex breakdown on the unsteady loads and surface pressure distributions of a simple delta wing model.

Thompson¹⁴ determined the location of vortex breakdown from flow visualization experiments. Figure 13 shows the unsteady breakdown location for a 70 degree delta wing undergoing large amplitude pitching motions. The wing was oscillated in pitch over an angle of attack range from 0 to 60 for various reduced frequencies. The arrow in Figure 13 indicates the direction of the motion (angle of attack increasing or decreasing). The steady breakdown location data is not shown in the figure in order to maintain clarity. The unsteady data bracketed the steady state breakdown location. The hysteresis, which is characteristic of unsteady high angle of attack aerodynamic loads, is also seen in the breakdown data. At a given instantaneous angle of attack, the difference in breakdown location is as much as 0.45c, depending on the direction of motion. The size of the hysteresis loop increases with increasing reduced frequency. At very high angles of attack, over 50, the flow is fully separated, similar to a bluff body flow. As the wing pitches down, the leading edge vortex system reforms with breakdown near the apex. Breakdown then moves aft as the angle of attack continues to decrease.

The vortex breakdown data clearly illustrates how the flow lags the model motion.. For the upward motion, there is a lag in the development of the vortex core and the upstream progression of vortex breakdown. For the downward motion, there is a lag in the reformation of the vortex system (from fully separated flow) and in the downstream progression of vortex breakdown. These lags give rise to the large unsteady effects observed in the aerodynamic loads on the wing.

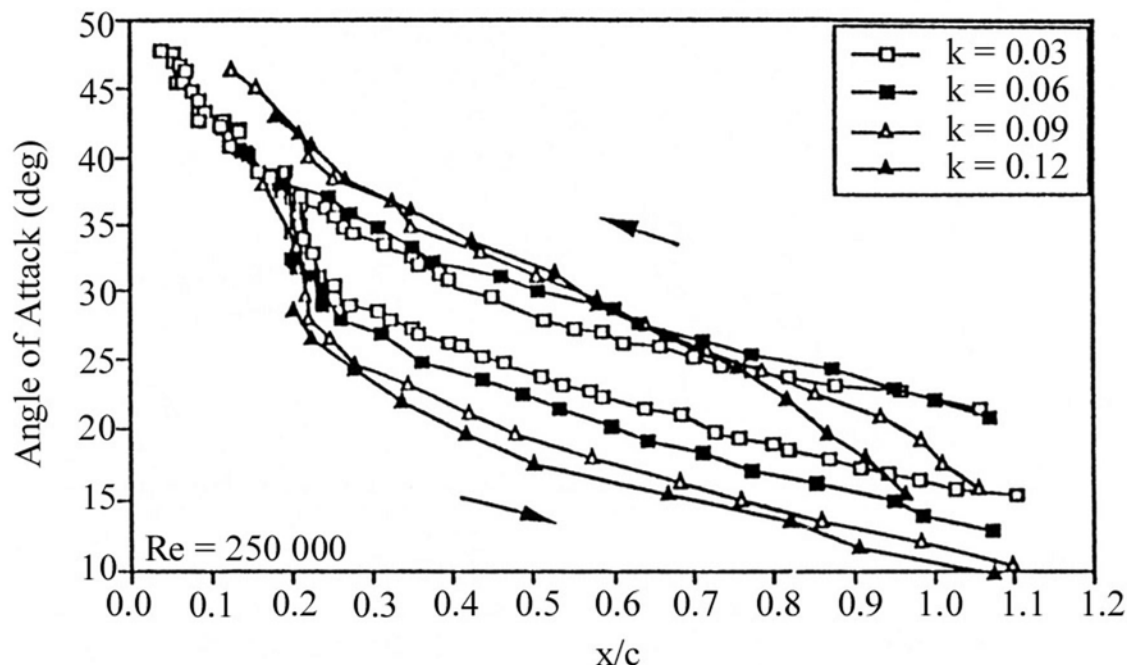


Fig. 13. Unsteady Breakdown location for 0-60° oscillation

Thompson also measured the unsteady surface pressures and correlated the changes in pressure with the state of the leading edge vortex, i.e. the position of the vortex relative to the surface and the location of vortex breakdown. Figure 14 shows an example of the unsteady pressure data in the form of a non-dimensional pressure coefficient $C_p = (P_{\text{tap}} - P_{\infty})/Q_{\infty}$ where P_{tap} is the local static pressure, P_{∞} is the freestream static pressure and Q_{∞} is the freestream dynamic pressure. The pressure coefficient is shown as a function of instantaneous angle of attack, along with the steady data. The data is for a single surface pressure tap located at $x/c = 0.25$ and located beneath the primary vortex. The location of vortex breakdown has been noted at specific points along the curve. As the angle of attack increases, the pressures uniformly decrease. With the occurrence of breakdown on the wing the pressure gradient begins to decrease. Further increases in angle of attack moves the breakdown to the apex. This precedes the total separation of the leeward side, and as a result, the pressures begin increasing due to the lack of an organized flow structure over the wing. However, before the pressure field can become relatively uniform (as for the steady high angles of attack case), the wing pitches down again, until the point is reached at which the leading edge vortex structure reforms (with breakdown near the apex). Thus a pressure recovery begins and the pressures begin decreasing. Breakdown then moves down the length of the wing and into the wake. Concurrent with this behavior of the vortex is a partial recovery of the suction pressures. Further decreases in angle of attack result in a collapse of the vortex system and the vortex-induced pressure field.

Figure 15 shows the unsteady pressure at two different chordwise positions of $x/c = 0.25$ and 0.75 underneath the leading edge vortex for two pitching frequencies. The reduced frequency is defined as $k = 2\pi fc/U_{\infty}$, where f is the pitching frequency in Hz, c is the chord and U_{∞} is the freestream velocity. During the upstroke the pressure data is the same up until between 30-35 degrees. The influence of the pitching frequency is seen to cause an increase in both the overshoot and the undershoot relative to the static data.

In summary Thompson examined the surface pressures for sinusoidal pitching motions for several ranges of angle of attack. He found the pressure data could be divided into two categories depending on angle of attack range. For an angle of attack range where breakdown always occurred over the wing or where breakdown did not occur over the wing the unsteady effects were relatively small. On the other hand, for angle of attack ranges where vortex

breakdown moved on and off the wing the unsteady effects were quite large. The unsteady surface pressure and breakdown position were both found to increase with increasing reduced frequency.

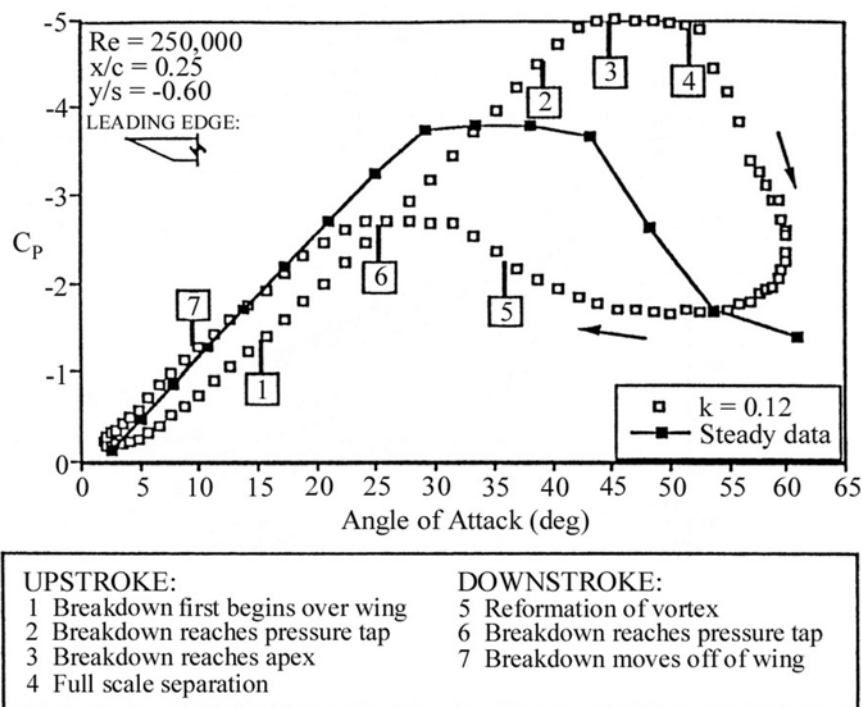


Fig. 14. Unsteady surface pressure data and chordwise progress of vortex breakdown

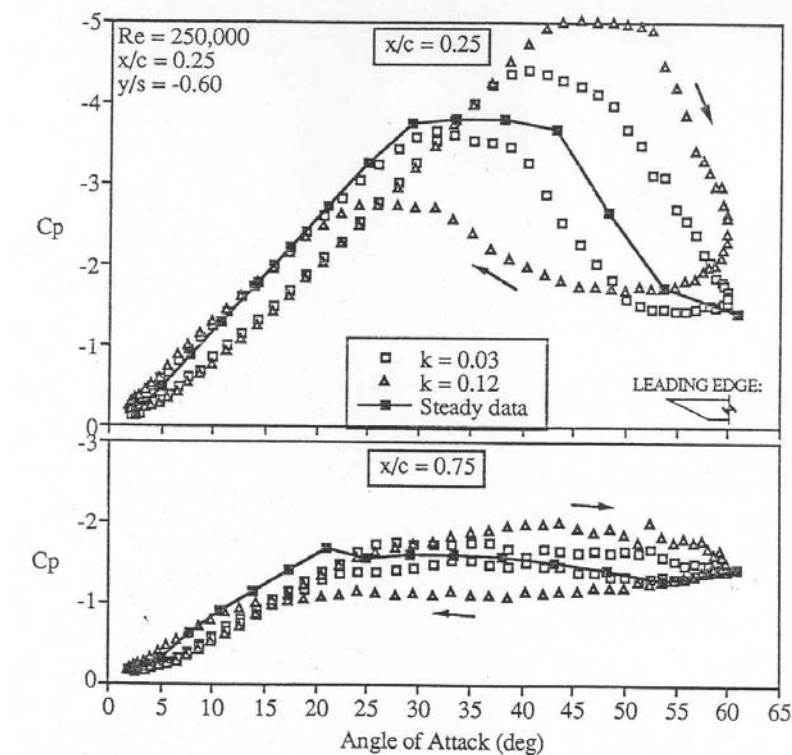


Fig. 15. Unsteady pressure data for 2-60° motion range as a function of reduced frequency.

7.5 Free and Forced to Roll Motion Studies

Wing rock is a roll instability experienced by many fighter aircraft. The motion is characterized by an oscillatory roll angle buildup to a constant amplitude rocking motion. An excellent review of the wing rock phenomena is presented by Katz⁵⁵. Wing rock motions can occur at both subsonic and transonic speeds. In the transonic speed regime the wing rock motion is typically associated with unsteady shock movement or shock induced flow separation over the wing. However, for subsonic flow the wing rock motion is primarily due to interactions between the wing and forebody vortices. Much of what is known about subsonic wing rock motion is due to fundamental experiments on simple delta wings. References 56-62 are some of the experimental papers dealing with the wing rock of slender delta wings. There are far fewer wing rock studies of aircraft configurations^{12, 63-66}.

Arena^{10, 15} conducted a series of experiments to understand the flow physics associated with the limit cycle rolling motion of slender flat plate delta wings. His experimental investigation concentrated on three main areas: motion characteristics obtained from time history plots, static and dynamic flow visualization of the vortex position, static and dynamic flow visualization of vortex breakdown, instantaneous roll moment and surface pressures on a delta wing during a wing rock motion. The flow visualization studies were correlated with model motion to determine the characteristics of vortex position and breakdown during the wing rock motion. Visualization of the leading edge vortices in the cross flow plane clearly showed the difference between the static and dynamic behavior of the vortices.

Arena^{10, 15} developed two unique experimental systems. The systems permitted the measurement of the aerodynamic torque, leading edge vortex trajectories in the cross flow plane and unsteady surface pressures on a slender delta wing undergoing a wing rock motion. The first experimental apparatus included an air bearing and an optical encoder to examine the free to roll motion on an 80° flat plate delta wing. The air bearing reduced the mechanical damping in the system by an order of magnitude over that of conventional low friction bearings. This was important due to the very low aerodynamic damping associated with low aspect ratio delta wings. Arena was able to measure the spanwise and normal position of the leading edge vortices above the wing, vortex breakdown location if it occurred and the roll moment coefficient on the model during a wing rock motion. The instantaneous roll moment coefficient was estimated using the predicted the angular acceleration determined from the optical encoder data, system mass moment of inertia, model geometry and tunnel test conditions.

To provide additional insight into how the rolling moment was created a second experimental setup was designed for the measurement of the unsteady surface pressures on a wing undergoing a wing rock motion. This was accomplished by using a computer controlled DC servo motor to drive the model through the same roll angle trajectory that was measured in the free to roll experiments. Arena used this system to measure the spanwise distribution of the unsteady pressures at three chordwise locations. The unsteady pressures were measured for both the build up portion of the wing rock motion as well as when the motion reached the limit cycle oscillation.

Figure 16 is an example of a typical wing rock motion. The model is initially held in place and then being released, the motion builds up slowly to a limit cycle oscillation. Two cycles are noted on the figure one during the build up and the other during wing rock. The curves in Figures 17 and 18 are the instantaneous roll moment during a cycle of motion during the roll build up and the wing rock motion. The arrows on the curves indicate direction in time. The area enclosed by the curves is a measure of the energy being added or dissipated during a cycle. It can be easily shown that when a loop encloses an area in the clockwise sense, energy is being added to the system, whereas a counter-clockwise loop indicates that energy is being dissipated from the system. During the build up portion of the motion the roll moment curve indicates that energy is being added to the system. Therefore one would expect the motion to continue to grow as it does. Once the motion reaches the limit cycle the inner portion of the roll moment curve indicates

energy extraction while the outer lobes imply energy dissipation. The net energy change is zero during a limit cycle oscillation. The model is unstable at the lower roll angles but develops damping at large roll angles that causes a limit in the roll oscillation.

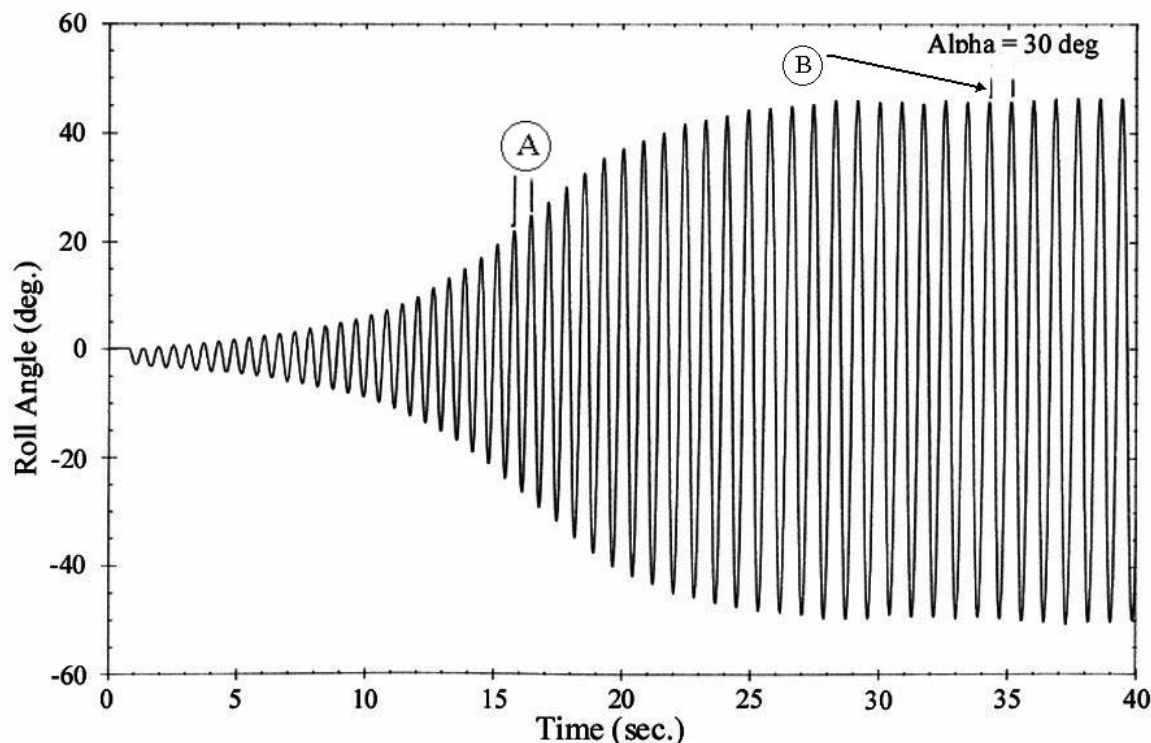


Fig. 16. A typical roll time history illustrating the buildup to the limit cycle motion called wing rock.

From the flow visualization experiments Arena was able to measure the vertical and spanwise position of the leading edge vortices as well as the chordwise location of vortex breakdown if it occurred during the motion. Figure 19 compares the static and dynamic position of the leading edge vortices during a wing rock motion. Through analysis of this data Arena showed that the lag in the normal position of the vortices provided the instability mechanism for the wing rock motion. On the other hand, his analysis of the hysteresis in vortex breakdown showed that breakdown provided damping to the system. Since wing rock could occur without vortex breakdown occurring over the wing there had to be another mechanism in addition to the lag in vortex breakdown that could provide damping at the large roll angles.

Arena^{15, 71} conducted a computational study that showed the unsteady behaviour of the vortex strength at large roll angles provided the necessary damping to create a limit cycle motion. A critical angle of attack had to be reached before the wing would experience wing rock. Increasing the angle increased the limit cycle amplitude until vortex breakdown started occurring over the wing. The additional damping contributed by vortex breakdown caused the peak amplitude of the motion to decrease. Further increases in angle attack resulted in an ever increasing reduction of the wing rock amplitude until it vanished.

Arena also determined the unsteady spanwise surface pressure distributions at various chordwise locations along the wing. Figure 20 is a plot of the unsteady pressure profiles at an $x/c = 0.6$ for three different roll angles for both directions of motion. The roll angle of $\phi = \pm 45^\circ$ was chosen because it corresponded to the approximate center of damping lobes in the roll moment data. For the large roll angles $\pm 45^\circ$ the pressure distribution on the top surface of the wing is seen

to contribute to a roll damping moment. At $\phi = 0^\circ$, the top surface pressure distribution contributes a destabilizing rolling moment..

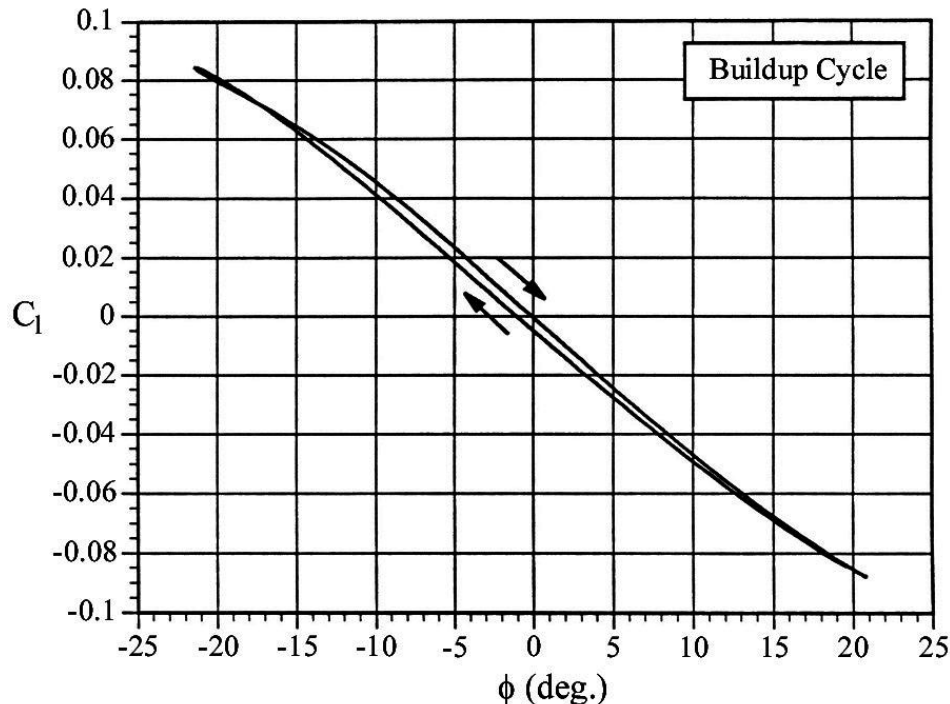


Fig. 17. Roll moment coefficient during a build up cycle.

In summary Arena was able to determine the fluid mechanisms controlling the wing rock motion of slender wings at low subsonic speeds. His experimental results and analytical predictions allowed him to conclude that the destabilizing moment necessary for sustaining the wing rock motion was due to the time lag in vortex position normal to the model's surface. While the lag in the normal position of the vortices provides a mechanism for growth in the roll amplitude, it is the time lag in the vortex strength that provides the damping at large roll angles to limit the roll amplitude. He also showed that when vortex breakdown started occurring over the model the amplitude of the rocking motion began to decrease. More information on Arena's experiments and computational study can be found in the accompanying data sheet and References 10, 15 and 67-73.

Finally two other studies that should be of interest to the CFD community are the research efforts by Grismer¹⁸ and Pelletier²⁰. Grismer examined the aerodynamic loads and vortex structure on a strake-wing model. In her research she measured the unsteady aerodynamic loads, leading edge vortex trajectory, vortex interaction and breakdown location for sinusoidal pitching motions. Her experimental research is summarized in a data sheet and References 18, 74-78.

Pelletier²⁰ examined the dynamic motions of a double delta wing. In his study he conducted an experimental investigation of the dynamic behavior of an 80°/65° double-delta wing at high angles of attack. Dynamic motions were obtained on a double-delta wing using the free to roll apparatus developed by Arena^{10, 15}. Different dynamic rolling motions were observed depending on the angle of incidence of the model sting. These dynamic regimes included damped oscillations, quasi-limit-cycle wing-rock motion, and chaotic oscillations. The presence of vortex breakdown on the model was shown to influence the type of dynamic regime obtained and the location of the roll attractors. Additional information on this experiment can be found in the data sheet summary and References 20, 79-81.

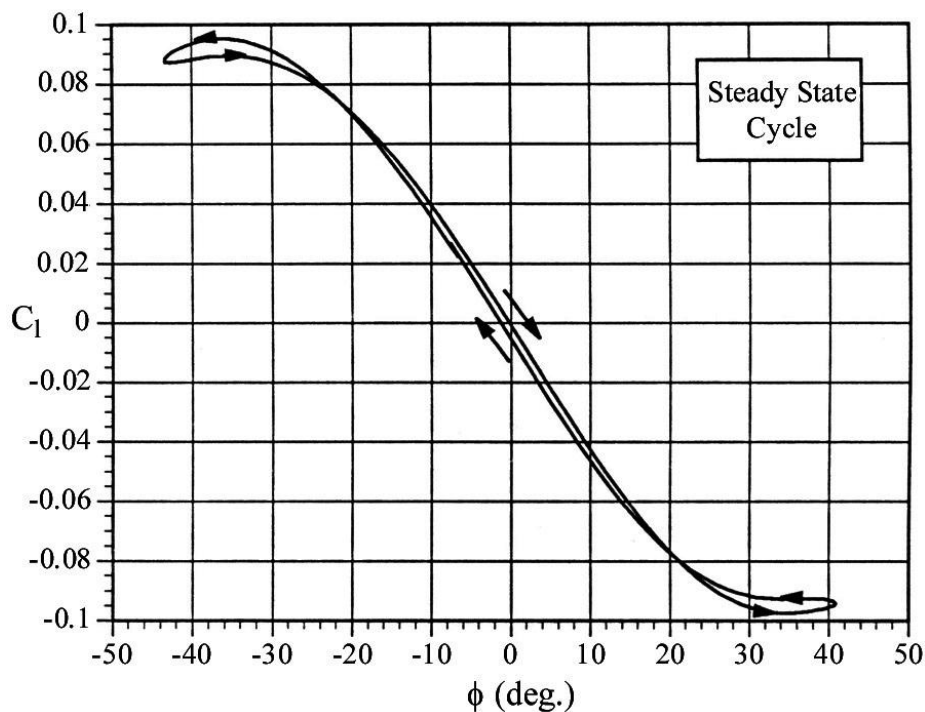


Fig. 18. Vortex position hysteresis

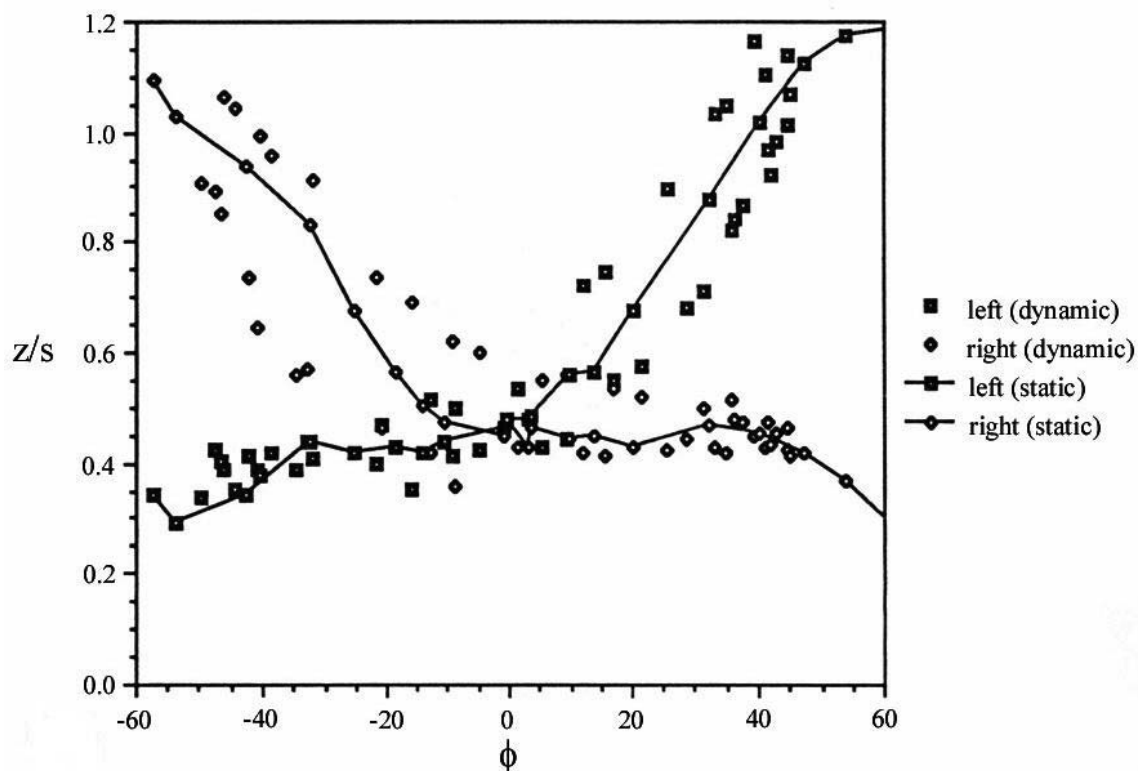


Fig. 19 Static and dynamic position of the vortices during a wing rock motion.

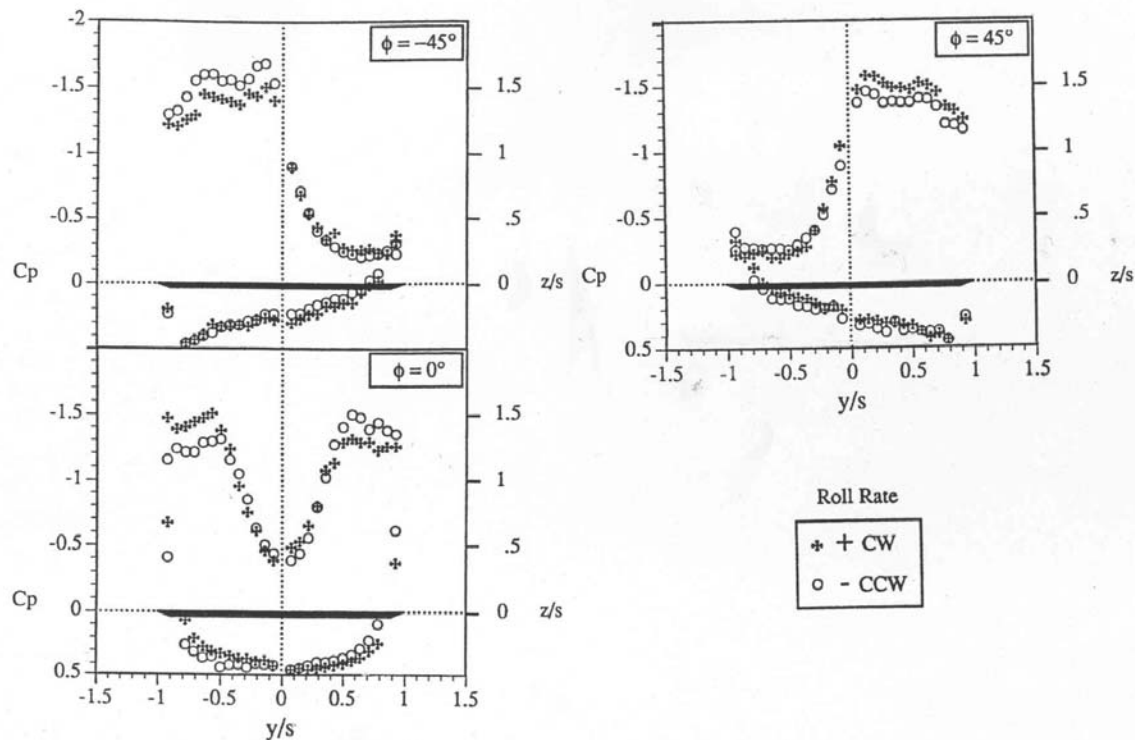


Fig. 20. Unsteady pressure profiles during a wing rock motion, $\alpha = 30^\circ$.

7.6 Summary

In summary this report outlines a set of experimental investigations of the leading edge vortex flow field above slender delta wings conducted at the University of Notre Dame. The experimental studies reviewed include investigations of the flow structure within the leading edge vortices for stationary models before and after vortex breakdown and measurement of vortex breakdown and unsteady loads on non-stationary models undergoing pitching or rolling motions. The experimental data and analysis included in the Notre Dame studies is a valuable resource for the CFD and analytical community.

The major findings regarding the leading edge vortex structure above a stationary delta wing are summarized below. Flow visualization of the leading edge vortices using a laser light sheet technique revealed secondary vortical structures in the leading edge shear layers which developed in a manner analogous to Kelvin-Helmholtz type instabilities. Also high speed motion pictures of the breakdown process seem to suggest that the spiral mode is still visible in what appears as a bubble breakdown.

The influence of probe interference on the vortex flowfield was assessed. Intrusive probes such as pressure and hot wire probes compared favorably with the nonintrusive Laser Doppler Anemometer (LDA) measurements, except for conditions close to breakdown.

The experimental velocity and vorticity surveys through the leading edge vortices upstream of vortex breakdown exhibit a conical behavior. The axial vorticity before breakdown is concentrated in the region approximately twice the diameter of the viscous subcore, defined as the distance between the peak tangential velocities. Further evidence of the conical nature of the vortex field is demonstrated by the successful correlation of the vortex circulation using the parameters developed by Hemsch and Luckring.

When a delta wing is undergoing either a pitching or rolling motion the aerodynamic loads are modified due to lags in the development of the leading edge vortex structure. For

pitching delta wings the unsteady loads are a function of the angle of attack range, motion history and reduced frequency. The largest unsteady aerodynamic were correlated with the lag in vortex breakdown.

For a free to roll delta wing at low subsonic speeds, the phenomenon known as wing rock begins when a critical angle of attack is reached where the lag in the adjustment of the vortices above the delta wing can cause a driving moment that can overcome the aerodynamic damping of the wing. Wing rock motion can occur without vortex breakdown occurring over the wing. When breakdown does begin occurring on the wing during the rocking motion the maximum rocking amplitude begins to decrease. This is so because the lag in vortex breakdown over the rocking wing provides damping to the system. Since wing rock can occur without breakdown there must be another damping mechanism. Arena's computational study showed that the lag in vortex strength at the large roll angles provided the necessary damping to cause the limit cycle motion.

7.7 Acknowledgements

The authors wish to thank the faculty of the Hessert Laboratory for their contributions to some of the research reported in this article. In particular, we would like to acknowledge the contributions of Drs. Stephen M. Batill, Eric J. Jumper and Terry Ng (University of Toledo) for their help in directing some of the research projects. Finally, Dr. Nelson would like to express his appreciation to all the individuals who participated in the leading edge vortex flow research from 1983-2003. These individuals include John McKernan, Daniel Hunter, Frank Payne, Kenneth Iwanski, Scott LeMay, Kenneth Visser, Sedra Walton, Scott Thompson, Paul Olsen, Andrew Arena, Todd Graves, Thomas Quast, Kenneth Cheung, Deborah Grismer, David Williams, Alain Pelletier, and Gregory Addington.

7.8 References

1. McKernan, J.F., "An investigation of the breakdown of the leading edge vortices on a delta wing at high angles of attack", Master's thesis, University of Notre Dame, January 1983.
2. Hunter, D., "An experimental study of leading edge flaps on delta wing performance", Master's thesis, University of Notre Dame, May 1986.
3. Payne, F. M., "An experimental study of the leading edge vortex structure of a delta wing", Ph. D. dissertation, University of Notre Dame, May 1987.
4. Iwanski, K., "An investigation of the vortex flow over a delta wing with and without external jet blowing", Master's thesis, University of Notre Dame, May 1988.
5. LeMay, S., "Leading edge vortex dynamics on a pitching delta wing", Master's thesis, University of Notre Dame, May 1988.
6. Visser, K. D.; "An investigation of the effects of an external jet on the performance of a highly swept delta wing", Master's thesis, University of Notre Dame, May 1988.
7. Walton, W., "A comparison of the aerodynamic characteristics of half-span and full span delta wings", Master's thesis, University of Notre Dame, April 1989.
8. Thompson, S.A., "Surface pressure distributions on a delta wing undergoing large amplitude pitching oscillations", Master's thesis, University of Notre Dame, July, 1989.
9. Olsen, P., "Vortex interaction over a double delta wing at high angles of attack", Master's thesis, University of Notre Dame, April 1989.
10. Arena, A. S., Jr., "An experimental study of the nonlinear wing rock phenomenon", Master's thesis, University of Notre Dame, April, 1990.
11. Graves, T., "Vortical interaction over strake/wing configurations," Master's thesis, University of Notre Dame, April, 1990.
12. Quast, T., "Static and dynamic measurements of the vortex structure on a scale model of the HARV", Master's thesis, University of Notre Dame, May, 1991.

13. Visser, K. D., "An experimental analysis of critical factors involved in the breakdown process of leading edge vortex flows", Ph. D. dissertation, University of Notre Dame, May, 1991.
14. Thompson, S. A., "The unsteady aerodynamics of a delta wing undergoing large amplitude motions", Ph. D. dissertation, University of Notre Dame, May, 1992.
15. Arena, A. S., Jr., "An experimental and computational investigation of slender wings undergoing wing rock", Ph. D. dissertation, University of Notre Dame, May, 1992.
16. Cheung, K., "A simple criterion for vortex breakdown", Master's thesis, University of Notre Dame, May, 1993.
17. Pelletier, A., "An experimental investigation of vortex breakdown on slender delta-wing planforms", Master's thesis, University of Notre Dame, May 1994.
18. Grismer, D., "Unsteady aerodynamics of strake wing aircraft at high angles of attack", Ph. D. dissertation, University of Notre Dame, May, 1995.
19. Williams, D., "Dynamic, lateral behavior of low-aspect-ratio, rectangular wings at high angle of attack", Ph. D. dissertation, University of Notre Dame, May, 1996.
20. Pelletier, A., "A study of the non-linear aerodynamic characteristics of a slender double-delta wing in roll", Ph. D. dissertation, University of Notre Dame, May, 1998.
21. Addington, G. A., "The role of flow field structure in determining the aerodynamic response of a delta wing", Ph. D. dissertation, University of Notre Dame, May, 1998.
22. Peckham, D.H. and Atkinson, S.A., "Preliminary results of low speed wind tunnel tests on a gothic wing of aspect Ratio 1.0", A.R.C. CP-508, April 1957.
23. Elle, B.J., "An investigation at low speed of the flow near the apex of thin delta wings with sharp edges," A.R.C., R. &M. No. 3176, 1958.
24. Lambourne, N.C. and Bryer, D.W., "The bursting of leading-edge vortices – some observations and discussion of the phenomenon," A.R.C., R. & M. No. 3282, April 1961.
25. Harvey, J. K., "Some observations of the vortex breakdown phenomena," J. Fluid Mech., Vol. 14, 1962.
26. Sarpkaya, T., "Vortex breakdown in swirling conical flows," AIAA Journal, Vol. 9, Sept. 1971.
27. Faler, J. H., and Leibovich, S., "Disrupted states of vortex flow and vortex breakdown," Phys. Fluids, Vol. 20, No. 9, Sept. 1977.
28. Escudier, M. P., and Zehnder, N., "An experimental map of the internal structure of a vortex breakdown," J. Fluid Mech., Vol. 115, 1982.
29. Gerner, A. A., Maurer, C. L., and Gallington, R. W., "Non-nulling seven-hole probes for high angle flow measurement," Exp. Fluids 2, 95-103, 1984.
30. Payne, F. M., Ng, T. T., and Nelson, R. C., "Visualization and flow surveys of the leading edge vortex structure on delta wing planforms, AIAA Paper 86-0330, 1986.
31. Payne, F.M., Ng, T.T., Nelson, R.C., and Schiff, L.B., "Visualization and Wake Surveys of the Vortical Flow Over a Delta Wing," *AIAA Journal*, Vol. 26, No. 2, February 1988, pp. 137-143
32. Payne, F. M., Ng, T. T., and Nelson, R. C., "Experimental study of the velocity field on a Delta wing," AIAA Paper 87-1231, 1987.
33. Payne, F. M., Ng, T. T., and Nelson, R. C., "Seven hole probe measurement of leading edge vortex flows," *Experiments in Fluids*, 7, 1-8, 1989.
34. Hummel, D., "Research on vortex breakdown on slender delta wings," *Zeitschrift fur Flugwissenschaften*, 13, 5, Aircraft Research Association Ltd., Bedford Library Translation No. 12, May, 1965.
35. Sforza, P. M., Stasi, W., Pazienza, J., and Smorto, M., "Flow measurements in leading edge vortices," AIAA Paper 77-11, 1977.

36. Hemsch, M., and Luchring, J., "Connection between leading-edge sweep, vortex lift, and vortex strength for delta wings", *Journal of Aircraft* No. 7, Vol. 5, 1990, pp 473-475.
37. Sychev, V. V., "Three dimensional hypersonic gas flow past slender bodies at high angles of attack", *Journal of Applied Mathematics and Mechanics*, Vol. 24, 1960, pp296-306.
38. Wentz, W. H., and MacMahon, M. C., "Further experimental investigations of delta and double delta flowfields at low speeds", NASA CR-714, February 1967.
39. Delery, J., Pagan, D., and Solignac, J. L., "On the breakdown of the vortex induced by a delta wing", *Colloquium on Vortex Control and breakdown behavior*, Baden, Switerland, ONERA TP 1987-105, April 6-7, 1987.
40. Smith, J. H. B., "Calculations of the flow over Thick, Conical, Slender Wings with Leading Edge Separation", A. R. C., R. M., No.3694, March 1971.
41. Visser, K. D., and Nelson, R. C., "Measurement of Circulation and Vorticity in the Leading Edge vortex of a Delta Wing", *AIAA Journal* No. 31 Vol. 1, 1993, pp 104-111.
42. Nelson, R. C. and Visser, K. D., "Breaking Down the Delta Wing Vortex - The Role of Vorticity in the Breakdown Process," AGARD Symposium on Vortex Flow Aerodynamics, October 1-4, 1990, Schevenigen, Netherlands.
43. Visser, K. D., Nelson, R. C., and Ng, T. T., "A Method of Cold Smoke Generation for Vortex Core Tagging", *AIAA Journal of Aircraft*, Vol. 25, No. 11, November 1988, pp. 1069-1071.
44. Ashley, H., Katz, J., Jarrah, M-A. M., and Vaneck, T., "Unsteady aerodynamic loading of a delta wings for low and high angles of attack", *International Symposium on NonsteadyFluid Dynamics*, June 1990.
45. Bragg, M. B., and Soltani, M. R., "An experimental study of theeffect of asymmetrical vortex bursting on a pitching delta wing", *AIAA Paper* No. 88-4334, August 1988.
46. Brandon, J. M. and Shah, G. H., "Effect of large amplitude pitching motions on the unsteady aerodynamics of flat-plate wings", *AIAA Paper* No. 88-4331, August 1988.
47. Jarrah, M-A. M., "Unsteady aerodynamics of delta wings performing maneuvers to high angle of attack", Ph.D. dissertation, Stanford University, December 1988.
48. Jarrah, M-A. M., "Low-speed wind tunnel investigation of the flow about delta wings, oscillating inpitch to very high angles of attack", *AIAA Paper* No. 89-0295, January 1989.
49. Den Boer, R. G., and Cunningham, A. M. Jr., "Low-speed unsteady aerodynamics of a pitching straked wing at high incidence -Part I: Harmonic Analysis", *AIAA Journal of Aircraft*, Vol. 27, Jan, 1990, pp. 31-41.
50. Cunningham, A. M. Jr., and Den Boer, R. G., "Low-speed unsteady aerodynamics of a pitching straked wing at high incidence -Part II: Test Program", *AIAA Journal of Aircraft*, Vol. 27, Jan, 1990, pp. 23-30.
51. Thompson, S. A., Batill, S. M., and Nelson, R. C., "The Separated Flow on a Slender Wing Undergoing Transient Pitching Motions", *AIAA Paper* 89-0194, January 1989
52. Thompson, S. A., Batill, S. M., and Nelson, R. C., "Unsteady Surface Pressure Distributions on a Delta Wing Undergoing Large Amplitude Oscillations," *AIAA Paper* 90-0311, January 1990.
53. Thompson, S. A., Nelson, R. C. and Batill, S.M., "Delta Wing Surface Pressures for High Angle of Attack Maneuvers," *AIAA Paper* No. 90-2813, August 1990.
54. Thompson, S. A., Batill, S. M., and Nelson, R. C., "The Separated Flow Field on a Slender Wing Undergoing Transient Pitching Motions," *AIAA Journal of Aircraft*, Vol. 28, No. 8, pp. 489-495, August 1991.
55. Katz, J., "Wing/vortex interactions and wing rock", *Progress in Aerospace Sciences*, Vol. 35, pp. 727-750, 1999.

56. Nguyen, L. T., Yip, L., and Chambers, J. R., "Self-induced wing rock of slender delta wings", AIAA paper 81-1883, August 1981.
57. Levin, D. and Katz, J., "Dynamic load measurements with delta wings undergoing self-induced roll-oscillations", AIAA paper 82-1320, August 1982.
58. Ng, T. T., Malcolm, G. N., and Lewis, L.C., "Experimental study of vortex flows over delta wings in wing rock-motion", AIAA paper 89-2187.
59. Morris, S. L., and Ward, D. T., "A video-based experimental investigation of wing rock", AIAA paper 89-3349, August 1989.
60. Ng, T. T., and Malcolm, G. N., "Effect of leading edge roundness on delta wing-rock motion", AIAA Paper No. 90-3080, June 1990.
61. Jun, Y.W. and Nelson, R.C., "Leading Edge Vortex Dynamics on a Delta Wing Undergoing a Wing Rock Motion," AIAA Paper No. 87-0332, January 1987.
62. Jun, Y-W. and Nelson, R. C., "Leading Edge Vortex Dynamics on a Slender Oscillating Wing", *AIAA Journal of Aircraft*, Vol. 25, No. 9, September 1988, pp. 815-819.
63. Ross, A. J., "Investigation of nonlinear motion experienced on slender-wing research aircraft", *AIAA Journal of Aircraft*, Vol. 8, No.9, pp. 625-631, 1972.
64. Hwang, C, and Pi, W. S., "Investigation of steady and fluctuating pressures associated with the transonic buffeting and wing rock of a one-seventh scale model of the F-5A aircraft", NASA Contractor Report 3061, 1978.
65. Quast, T., Nelson, R. C., and Fisher, D. F., "A study of high alpha dynamics and flow visualization for a 2.5% model of the F-18 HARV undergoing wing rock", AIAA Paper No. 91-3267, August 1991.
66. Guglieri, G., Quagliotti, F., Static and Oscillatory Tests on a Generic Combat Aircraft Model in a Low Speed Wind Tunnel, 19th ICAS Congress, Anaheim, USA, 1994
67. Arena, A. S. and Nelson, R. C., "The Effect of Asymmetric Vortex Wake Characteristics on a Slender Delta Wing Undergoing Wing Rock Motion," AIAA Paper 89-3348, August 14-16, 1989.
68. Arena, Jr., A. S., Nelson, R. C. and Schiff, L. B., "An Experimental Study of the Nonlinear Dynamic Phenomenon Known as Wing Rock," AIAA Paper No. 90-2813, August 1990.
69. Arena, Jr., A. S. and Nelson, R. C., "Unsteady Surface Pressure Measurements on a Slender Delta Wing Undergoing Limit Cycle Wing Rock," AIAA Paper No. 91-0434, January 1991.
70. Nelson, R. C., Arena, A. S., Jr., Thompson, S. A., "Aerodynamic and Flow Field Hysteresis of Slender Wing Aircraft Undergoing Large-Amplitude Motions," AGARD Fluid Dynamics Panel Specialists Meeting on Maneuvering Aerodynamics, Toulouse, France, April, 1991.
71. Arena, Jr., A. S. and Nelson, R. C., "A Discrete Vortex Model for Predicting Wing Rock of Slender Wings," AIAA Paper 92-4497, August 1992.
72. Arena, A. S. Jr. and Nelson, R. C., "Experimental Investigations on Limit Cycle Wing Rock of Slender Wings", *AIAA Journal of Aircraft* , Vol. 31, No. 5, pp. 1148-1155, Sept.-Oct. 1994.
73. Arena, Jr., A. S., and Nelson, R. C., " Measurement of Unsteady Surface Pressure on a Slender Wing Undergoing a Self-Induced Oscillation," *Experiments in Fluids*, Vol. 16, No. 6, pp. 414-416 1994.
74. Grismer, D., Nelson, R. and Ely, W., "An Experimental Study of Double Delta Wings in Sideslip," AIAA Paper 91-3308, September 1991.
75. Grismer, D., Nelson, R. C., and Ely, W., "The Aerodynamic Effects of Sideslip on Double Delta Wings," AIAA Paper 93-0053, January 1993.
76. Grismer, D. and Nelson, R., "Aerodynamics of a Double Delta Wing Undergoing Pitching Motions With and Without Sideslip," AIAA Paper 94-1855, June 1994.

77. Grismer, Deborah S., Nelson, Robert C., and Ely, Wayne L., "The Influence of Sideslip on Double Delta Wing Aerodynamics," *AIAA Journal of Aircraft*, Vol. 32, No. 2, pp. 451-453, March-April 1995.
78. Grismer, Deborah S. and Nelson, Robert C., "Double-Delta-Wing Aerodynamics for Pitching Motions with and without Sideslip," *AIAA Journal of Aircraft* Vol. 32, No. 6, pp. 1303-1311, November-December 1995.
79. Pelletier, A. and Nelson, R.C., "Dynamic Behavior of an 80°/65° Double-Delta Wing in Roll," AIAA Paper 98-4353, August 1998.
80. Pelletier, A. and Nelson, R. C., "Problems Associated with Nonlinear Aerodynamic Phenomena", AIAA Paper 2000-3906, August 2000.
81. Nelson, R.C. and Pelletier, A., "Unsteady Aerodynamics of Slender Wings on Aircraft Undergoing Large Amplitude Maneuvers," *Journal of Progress in Aerospace Sciences*, Elsevier Science Limited, Vol. 39/2-3, pp 185-248.

Chapter 8 – TOPOLOGY OF THE FLOW ON 65° DELTA WINGS

N.G. Verhaagen, MSc

Delft University of Technology, Department of Aerospace Engineering
P.O. Box 5058, 2600 GB Delft, The Netherlands
n.g.verhaagen@tudelft.nl

X. Z. Huang

The Institute for Aerospace Research, National Research Council Canada
1200 Montreal Rd. Ottawa, Ont. Canada K1A 0R6
xingzhong.huang@nrc.ca

ABSTRACT

The flow topological structures over two 65° swept delta wings (a flat plate TUD wing and an IAR delta wing) have been investigated at various angles of attack, sideslip and roll angles. The observed skin-friction line pattern has been used to infer the topology of the flow on the wing surface. Special attention was paid to the flow on the nose, the boundary-layer transition and the topological evolution as the attitude (control parameter) changes. Two large-scale wind tunnel models of the apex were constructed to obtain more data on the flow in this region. A correlative studies between kinematical flow space and critical states in dynamic space was conducted which shows useful information for further studies.

KEYWORDS

Flow visualisation, Topology, Delta wing, Vortices, Vortex breakdown

8.1 INTRODUCTION

Modern fighter aircraft are designed to rely on the lift generated by vortex flow to enhance maneuverability. Strong vortices generated at the leading edge of highly swept lifting surfaces are part of the overall flow field of such aircraft and may have a dominant effect on the whole flow field and the air loads. At high angles of attack a sudden change in the vortex flow occurs when the core of the vortex breaks down which introduces additional discontinuities and transients in the aerodynamics. Experimental studies of these flows are needed to develop mathematical models to represent the interaction between the vehicle motion and the air loads. As a prerequisite, understand the flow physics and the complex structure are the important stages towards solving the problem.

The widely used topology and singular (fixed) point analyses is a powerful tool towards understanding the flow physics and its complex structures, such as the location, structure and the origin of the boundary-layer separation lines, the status and the transition of boundary-layer, the structure of vortices - their left off, interference or breakdown, etc. It also can picture the evolution and the development of the flow structures when the attitude (control parameter) is changing. Moreover, the bifurcation in topologic evolution can be taken as useful information to diagnose the critical states in air loads, which is crucial to construct the mathematical model.

On the other hand, there are many limitations which should be kept in mind. The predictive ability of topology and singular point analyses is limited by their inherent qualitative nature and the fact that the Taylor expansion around a singular point is highly localised. The flow visualisation from surface oil flow streak only represents the time invariant equilibrium flow or time-averaged flow pattern on the surface

where all unsteady informations are missing. The projection of the surface oil flow streak, or the skin-friction lines, into three-dimensional flow field off the wing is non-unique. The topological changes far away from the wing surface have a diminished effect on the skin-friction line topology as their pressure perturbations are damped over distance or overwhelmed by local flow field structure. Most important limit is that this analysis is in a kinematical space of surface flow streaks and not in the dynamic space of air loads.

Thus a complete and careful study both experimental and theoretical is necessary in order to understand the flow behaviour and to recognize the complex flow pattern. An reliable experimental correlation between the bifurcation in kinematical space and the critical states in dynamic space may help to explore the relations and to remedy the deficiency theoretically.

In viewing of this, extensive series of flow visualisation experiments on delta wing models were carried out both at the Delft University of Technology (TUD) in the Netherlands and in a joint program between the Institute for Aerospace Research (IAR) in Canada and US Air Force (SARL). A 65° swept leading-edge angle model was chosen as a benchmark in those studies. Profound results have been obtained and partly reported by Verhaagen and Jobe, Huang and Hanff, and Addington et al. [1]-[7] which are summarized in this chapter.

8.2 BRIEF OF TOPOLOGY

8.2.1 SURFACE FLOW TOPOLOGY

As this paper emphasis on the topology analysis about surface flow streaks, a brief introduction on surface flow topology theory is helpful for analysis the experimental results and theoretical considerations. Skin-friction lines describe the flow immediately on the surface of a body. Lighthill [8] postulates that these lines form the trajectories of a continuous vector field. When the visualization fluid is applied to the surface, it follows the path of least resistance along the surface. Streak lines on the surface indicate this path left behind by the fluid which is dragged along by the skin friction forces. The pattern formed by the streak lines can be used to determine a time-averaged phase portrait of the surface flow, which consists of a continuous vector field, $V(\chi)$, with a limited number of singular points. The characterization of the flow of a vector field in the neighborhood of a singular point is a classical topic of differential equations. The

“linear part” or **Hessian** matrix of the vector field at that point, $\frac{\partial V^2}{\partial \chi_i \partial \chi_j}$, is the main content of the topology

theory and it dominates the local flow behavior. The importance of knowing those singular points and related topological analysis is at that all those singular points have an importance that the non singular points do not have. Basically they organize the entire qualitative nature of the velocity vector fields. The all qualitative properties of $V(\chi)$ on the surface are known if we know the locations and the types of all isolated singular points. Thus, the rules in topology are powerful tools for performing surface topological analysis and constructing corresponding flow patterns.

A fundamental background for the above concept published in literature can be given as follows. Consider a surface of a body with the general orthogonal coordinates $\chi(\xi, \eta)$ on the surface \mathcal{R}^2 and a coordinate ζ normal to it. The components of the skin friction vector parallel to ζ and χ can be denoted $t_1(\zeta, \xi, \eta, 0)$ and $t_2(\zeta, \xi, \eta, 0)$. For a steady or time-invariant equilibrium flow, the skin friction lines are defined by the following autonomous (time invariant) differential system:

$$\frac{d\xi}{t_1(\xi, \eta, 0)} = \frac{d\eta}{t_2(\xi, \eta, 0)}$$

This equation defines the trajectories of the surface shear stress vector. Singular points in the pattern of the skin-friction lines occur at isolated points where the skin friction vector (t_1, t_2) becomes identically

zero:

$$\tau_1(\xi, \eta, 0) = \tau_2(\xi, \eta, 0) = 0$$

If the discussion is limited to the local behaviour of the singular point $\chi(?, ?)$, based on Taylor expansion around a highly localized singular point in the boundary layer on the surface, the nature of the phase portrait near this individual singular point may be determined by considering the two-dimensional linear system and by solving the eigenvalues of the matrix A .

$$\begin{bmatrix} d\xi \\ d\eta \end{bmatrix} = A \begin{bmatrix} \xi \\ \eta \end{bmatrix}$$

Bakker [9] classifies the phase portraits in terms of the trace ($p = \lambda_{11} + \lambda_{22}$) and Jacobian ($q = \lambda_{11}\lambda_{22} - \lambda_{12}\lambda_{21}$) where $\lambda_{ij} = \frac{d\tau_i}{d\chi_j}$. A classification of the phase portraits in the plane (p, q) is shown in Fig. 1.

Depending on the value of (p, q), phase portraits can be classified into different forms. At the conditions of $p \neq 0, q \neq 0$ and $\Delta = p^2 - 4q \neq 0$, the phase portraits take the forms of saddles, nodes and foci as marked S, N_a and N_s , and N_f , respectively, shown in Fig. 1. They are isolated, non-degenerate, or Morse critical points. For the conditions of either $p=0, q=0$ or $\Delta=0$ the corresponding points take the forms of centers, star shaped sinks and sources. They are non-isolated, non-degenerate, or non-Morse critical points and they are eventually conveying to the isolated points under perturbation.

A singularity is defined to be stable when all skin-friction lines pass through its origin. Through a saddle S pass only two skin-friction lines, while all the other lines miss the origin and take directions consistent with those of the adjacent lines. Following this definition, a saddle is unstable, because most of the skin-friction lines miss the origin. Nodes can be subdivided into nodal points and foci. At a nodal point there is one tangent line. All skin-friction lines are either directed outward away from the node (a nodal point of attachment N_a) or inward toward the node (a nodal point of separation N_s). The other type of node, the focus N_f , has no common tangent line. All skin-friction lines spiral around the origin, either out of it (a focus of attachment) or into it (a focus of separation). Node and foci of attachment are stable singularities, because all skin-friction lines pass through their origin. Unstable nodes and foci are rare occurrences in skin-friction line phase portraits. If $q = 0$, the phase portrait consists of a line of singular points. These may be combinations of nodes and saddles, or foci and saddles. As will be noted later, these combinations occur frequently in the topology of the flow on a delta wing.

The singular points obey the following rules governing the topology of the skin-friction line patterns as derived in Refs [8], [10] and [11]:

- All skin-friction lines originate at a node of attachment (or source) and must end at a node of separation (or sink).
- Flow separation lines may originate from a saddle point (close separation) and end at a node of separation or it may originate from an ordinal point (open separation)
- Since the vector field is continuous, kinks in the separation lines are possible only with a node-saddle point combination
- The focus invariably appears in company with a saddle point
- On a closed body the number of nodes exceeds the number of saddles by two

The skin-friction lines give a direct indication of the flow close to the wing surface. As suggested by Hunt et al. [11], in the flow field off the wing, nodes and saddles can be defined just as they were for the flow on the surface (Fig. 2). The symbols A and S are used to designate the attachment and separation lines on

the surface, respectively. Subscript numbers indicate the order, e.g., S'_2 marks the secondary-separation line. Just as the singular points on the surface, those off the surface satisfy certain topological rules. It should be noted that the projection of the two-dimensional skin-friction lines into the three-dimensional flow field off the wing is non-unique. The topological changes far away from the wing surface have a diminished effect on the skin-friction line topology as their pressure perturbations are damped over distance or overwhelmed by local flow field structure.

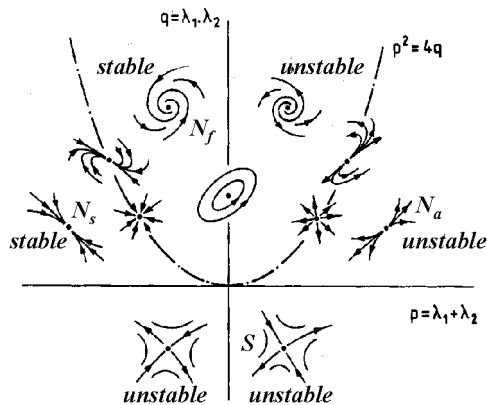


Fig. 1 Classification of phase portraits in (p,q) plane (Bakker)

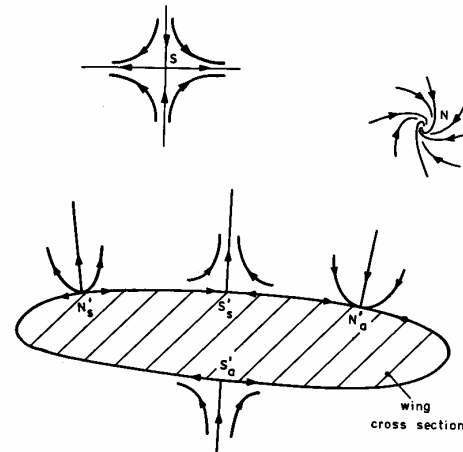


Fig. 2 Singular points on and off the wing surface

The above fundamental concept of topology theory will be applied on analyzing the flow pattern obtained in experiments and on understanding and constructing the surface flow structure at a fixed attitude such as an angle of attack, sideslip angle or roll angle, etc. However when the attitude, or the control parameter, changes the bifurcation in topology is another important aspect which should be investigated.

8.2.2 BIFURCATION IN FLOW TOPOLOGY

As modern fighter aircraft is expected to flight over wide range of angle of attack, sideslip and roll angle, the topological analysis is not only limited to the flow structure at certain attitude but, more importantly, to understand how the flow structure changes when the attitude varies. Even for the time-invariant equilibrium flows, the flow topology may change or evaluate as the parameter changes. For this time-invariant equilibrium flow the evolution equation can be described as:

$$\dot{\mathbf{x}} = \mathbf{F}(\mathbf{x}; \mathbf{l})$$

where \mathbf{F} refers to a vector field which does not explicitly depend on the independent variables t , vector \mathbf{x} is a state vector, $\mathbf{x} \in \mathcal{R}^n$, \mathcal{R}^n is an n -dimensional state space and \mathbf{l} is the vector of control parameters. The singular points are obtained by the vanishing of the vector field i.e.

$$\mathbf{F}(\mathbf{x}; \mathbf{l}) = 0.$$

When changes of the parameters cause an alteration of the number and type of singularities, the set of control parameters at which transition occurs is called the bifurcation set. From its effective area, bifurcation can be divided into two types of bifurcation: local and global bifurcation. The former one means a qualitative change occurring only in the neighbourhood of a singular point or a periodic solution of the system. While any other qualitative change is global bifurcation. The bifurcation has quite different stability feature, such as Inaccessibility, Modality (two or more distinct physical states), Divergence,

Hysteresis, Anomalous (defined by a probability over the space of state variables rather than by an isolated point), Variance, Sudden Jumps, etc. These bifurcations can be classified into continues and discontinues or catastrophic bifurcations, depending on whether the states of the flow patterns vary continuously or discontinuously as the control parameter varies gradually through its critical value. Discontinue bifurcations can be further subdivided into dangerous and explosive bifurcations, depending on whether the system response jumps to a remote disconnected attractor or explodes into a large attractor, with the new attractor including the old attractor as a proper subset. The sudden jump can be understood as a large change (“sudden jump”) in the value of the state variable and the system jumps from one local minimum to another caused by a small change in the value of the control parameter. The flow may experience a loss of analytic dependence on the parameter. The simple diagram shown in Fig. 3 can be taken as examples of different bifurcations. Fig. 3a is an example of supercritical bifurcation. In this bifurcation there is at least one branch of stable bifurcating solutions that is continuous with the original solution at the bifurcation point. While in a subcritical bifurcation shown in Fig. 3b there is no branch of stable bifurcating solutions that is continuous with the original branch and normally the solution will jump from one stable branch to another. The diagram of Fig. 3c is a hybrid of super- and sub- bifurcation.

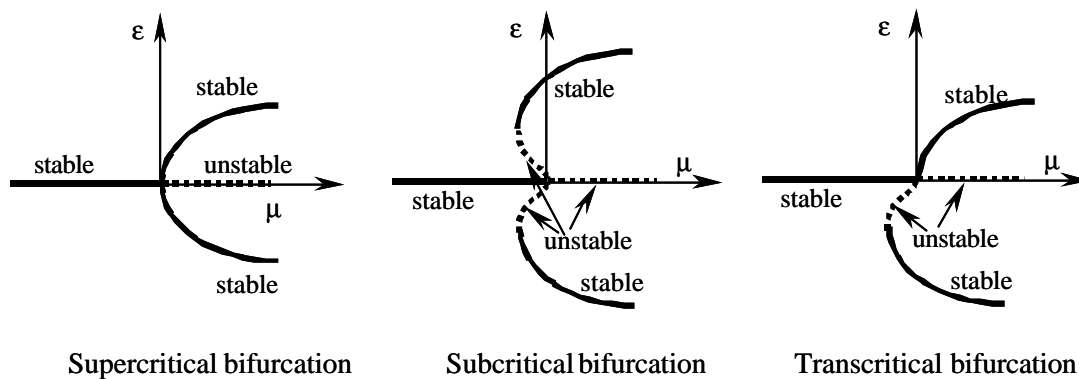


Fig. 3 Different bifurcation diagram

In conducted flow visualization experiments it has been observed that several singular points merge into less number singular points or split into more singular points shown below:

$N_s - S \Leftrightarrow N_s S \Leftrightarrow \text{regular point}$

$N_a - S - N_a \Leftrightarrow N_a S S N_a \Leftrightarrow N_a$

$N_s - S - N_s \Leftrightarrow N_s S N_s \Leftrightarrow N_s$

$N_f - S - N_f \Leftrightarrow N_s$

Detail discussions of these bifurcations are beyond the scope of this chapter. However recognising the presence and the type of bifurcation is often an important input for the proper description of a physical system. This input can be used either to save work or to provide qualitative and even quantitative information when even a mathematical description (i.e., equations) doesn't exist.

8.2.3 CORRELATION STUDIES OF TWO TOPOLOGICAL SPACES

As emphasized earlier that all those previous discussions on surface flow topology are based on Taylor expansion around a highly localized singular point in the boundary layer on the surface. Moreover, the eigenvalues of the matrix A is based on the behaviour of streamlines which are in kinematic space and not in dynamic space related to flight dynamics. Therefore one cannot use the information obtained in the kinematic space to simply derive any information in dynamic space. In addition, the surface oil flow results only reflect time-average surface streaks. No unsteady behavior, which is important in high angle of attack, could be obtained. Thus, following a pilot study in an attempt to remedy the deficiency by

Tobak [12], additional studies, both theoretical and experimental, have been conducted. Some of the theoretical consideration is presented here while the experimental correlation studies between the topological evolution and the critical states measured in dynamic space will be presented in the corresponding experimental part.

In the following discussion some assumption of a physical or intuitive nature, such as quasi-static evolution or adiabaticity (i.e., all time derivatives are very small) is imposed. Under this assumption the possible relations between two topological spaces are investigated.

From a familiar relation between skin friction, \mathbf{t} , and vorticity, \mathbf{w} , on an arbitrarily curved wall surface δs , the surface friction shear stress is one of a pair orthogonal vectors between skin friction, \mathbf{t} , and vorticity, \mathbf{w} :

$$\mathbf{t} = \mathbf{v}\mathbf{w} \times \mathbf{n}$$

While the vorticity (\mathbf{w}) has some relations with the surface pressure gradient. Applying the tangent components of Navier-Stokes equation on δs , the boundary vorticity flux from δs defined by $\mathbf{s} \equiv -\mathbf{v}\partial\mathbf{w}/\partial n$ has the following relation:

$$\mathbf{s} \equiv -\mathbf{v}\partial\mathbf{w}/\partial n = -\mathbf{n} \times \nabla p + \mathbf{v}(\mathbf{n}\nabla_t \cdot \mathbf{w} - \mathbf{w} \cdot \mathbf{K})$$

where \mathbf{K} is the curvature tensor of δs and the suffix t denotes tangent components of any vector. If the viscosity term is omitted, the pressure gradient can be approximately expressed as:

$$\nabla p = \mathbf{n} \times \mathbf{s}$$

The above first and the third equations show that \mathbf{t} , \mathbf{w} and ∇p , \mathbf{s} are two pairs of orthogonal vectors on the surface element, δs . It is interesting to see that the two pairs belong to kinematical and dynamic spaces respectively. The second pair looks less directly related to the identification of the surface flow topology. However, since the vorticity flux is the root of all vorticity in the flow, the surface topology must be the consequence of the development of the second pair, $(\nabla p, \sigma)$. By combining the first and the third equations we have:

$$\tilde{\nabla} p = \mathbf{n} \cdot (-\mathbf{v}\partial\mathbf{w}/\partial n)$$

The above equations show that ω , σ and $\tilde{\nabla} p$ are vectors and should be subject to topological rules. These three fields can be understood as mapping from one to another in Banach space. From the definition of differentiable at a point of control parameter, in the case of subcritical bifurcation in boundary vorticity vector, the loss of analytic dependence on the parameter will result in the loss of analytic dependence of the pressure gradient and related aerodynamic loads on the parameter.

The above consideration can be further evaluated from boundary-layer equation if the discussion is limited at the surface excluding boundary-layer separation. In that region there are two layers of flow: a boundary-layer flow and an oil film flow underneath. By combining two familiar equations corresponding to the boundary-layer and the oil film and noticing that at the singular point: $u=\tau_t=0$ it is obtained that at each singular point:

$$\frac{\partial p}{\partial x} = \frac{\partial p}{\partial y} = 0$$

which means as mentioned by Tobak [12], the existence of singular point in skin friction pattern is a sufficient but not necessary condition for the existence of a surface pressure extremum. Thus it could be imaged that in the case of subcritical bifurcation in flow topology, where a singular point (or points) discretely jumps from one location to another, the pressure extrema follow suit may result in a discontinuity in the pressure distribution and thus on the air loads.

In accompanying with the theoretical effort, flow visualisation experiments were conducted particularly

around the parameters where airloads exhibited discontinuities and will be presented in the corresponding experimental section.

8.3 TUD EXPERIMENTS

8.3.1 EXPERIMENTAL SET-UP

Tests were conducted on a model of a flat-plate 65° swept delta wing. As shown in Fig. 4, the wing has a chord length c of 0.665 m and a span b of 0.620 m. The thickness equals 20 mm, yielding a thickness-to-chord ratio t/c of 0.03. The leading and trailing edges are sharp and beveled on only the lower surface at 31 and 23°, respectively. An x, y, z wing-axes system is used with the origin at the apex. The wing was tested in the Low-Turbulence-Tunnel of the TUD Department of Aerospace Engineering in the Netherlands. This is a closed-circuit tunnel with an octagonal test section 1.80-m wide, 1.25-m high and 2.60-m long. The tests were conducted a constant angle of attack α of 30° and at an airspeed of 50 m/sec, yielding a chord Reynolds number of 2.3 million. Although α was exactly 30° at zero airspeed, the elastic deformation of the strut and balance system under aerodynamic load and the tunnel-wall-interference effects are estimated to yield an effective α as large as 36° [1].

The flow on the wing was visualized using two different fluids. One fluid, briefly called oil-flow fluid, consisted of a mixture of titanium dioxide, pipe clay, a surface tension relaxant and kerosene. The other fluid was a mixture of fluorescent-dye and oil. To visualize the latter mixture, it had to be illuminated using ultraviolet light. Fig. 5 shows the upper-surface pattern visualized with the oil-flow and fluorescent-dye fluid. These pictures were taken during the study of the effect the angle of sideslip (β) on the flow over the delta wing [1].

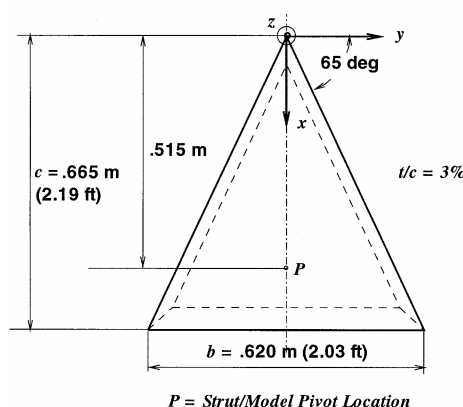


Fig. 4 TUD Delta wing geometry

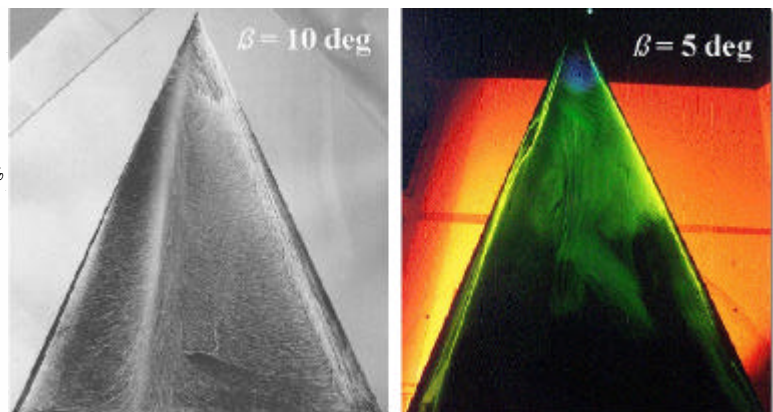


Fig. 5 Upper-surface flow pattern visualized using different fluids

8.3.2 FLOW VISUALISATION AND TOPOLOGICAL ANALYSIS

8.3.2.1 Observed Unsteady Behaviour

Flow visualisation tests indicated that the core of both the left and right leading-edge vortex breaks down at $x/c = 0.20$. The flow at the vortex breakdown point is unstable and oscillating. The breakdown points were observed to oscillate at a frequency of 4 - 5 Hz. The amplitude of the oscillations was about 3 % chord.

8.3.2.2 Flow Pattern on Lower Surface and its Topology

Fig. 6 shows the skin-friction line pattern on the lower surface. Short-dashed lines mark the inboard boundary of the beveled edges on this surface. The transition from the beveled edges to the flat lower surface is sharp, not rounded. For reference, the inside corners of the transition lines are marked A, B and

TOPOLOGY OF THE FLOW ON 65° DELTA WINGS

C. A long-dash-dot line is used to mark the centerline of the wing. Solid lines (or curves) are used to mark surface skin-friction lines, as well as separation and attachment lines.

In Fig. 6, on the nose an attachment line is visible at the centerline. Downstream of the nose, this line splits into two separate lines. Outboard of these lines, the shear flow bends towards the leading edge and will leave the wing to mix with the shear layer from the upper surface to a free shear layer that rolls up into a primary vortex. Inboard of the two attachment lines, the skin-friction lines are parallel to the wing centerline and directed towards the trailing edge.

On the nose the skin-friction line pattern has been observed depicted in Fig. 7. The pattern suggests an attachment line at the centerline. From the attachment line the boundary layer flows outwards into the direction of the leading edges. Since at the present angle of attack the free flow impinges on the nose just downstream of the apex, a stagnation point can be expected to be located there. As shown in Fig. 8, this can be simulated by a node of attachment N_a .

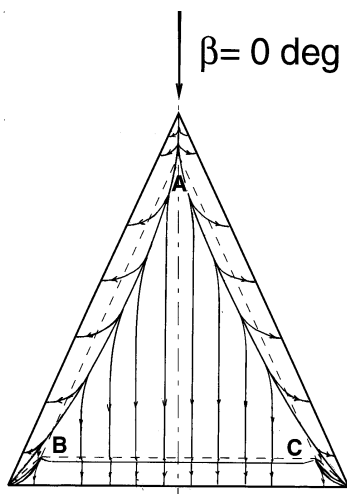


Fig. 6 Topology of skin-friction line pattern on lower surface

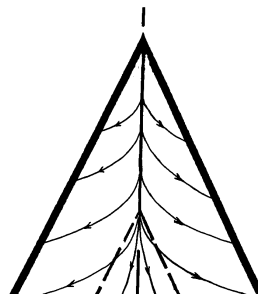


Fig. 7 Flow pattern observed on nose

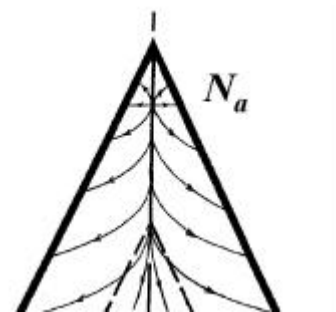


Fig. 8 Conjectured topology of flow on nose

In the experiment, the resolution of the streak line pattern is too low to resolve this stagnation point. To understand the origin of the vortices over the wing, it is important to know the development of the flow downstream from this point. Theoretically, an idea of this can be obtained by considering the apex on a microscopic scale. Lighthill [8] suggests a topology for the flow on a thus blunt apex, as reproduced here in Fig. 9. It consists of a node of attachment N_a on the upper and lower surface, and a saddle S at the apex. At the saddle, two separation lines are formed which separate the skin-friction lines from the upper and the lower surface.

On the rear part of the wing, a bubble-type of boundary-layer separation occurs at the sharp transition between the flat central surface and the beveled trailing edge. The crossflow topology of this bubble is shown in Fig. 10. In Fig. 10, the attachment line A' is marked by a solid line at a short distance downstream from transition line BC.

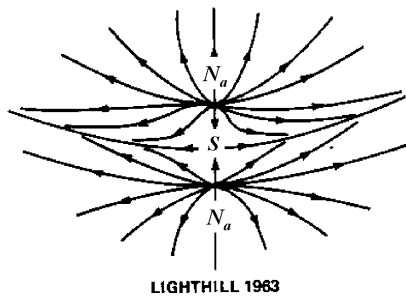


Fig. 9 Topology of flow at apex (Lighthill [8])

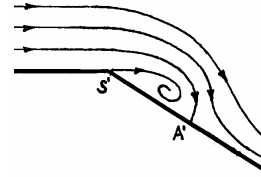


Fig. 10 Bubble-type of boundary-layer separation

8.3.2.3 Flow Pattern on Upper Surface and its Topology

Fig. 11 shows the skin-friction line pattern on the upper surface. The pattern, well known from earlier experiments, is characterized by an attachment line at the wing centerline and a secondary separation line. At $x/c \sim 0.16$, a kink is visible in the latter line. This is due to a transition of the boundary layer on the central part of the wing from laminar to turbulent. With N_a at the nose of the lower surface, a total of 10 nodes and 8 saddles is conjectured on the wing. This satisfies the topological rule which states that the number of nodes should exceed the number of saddle points by two. In the following, the topology of the flow at the apex, transition and tip region will be discussed in more detail.

The flow pattern on the nose is not well resolved in the experiment. Several theoreticians have made conjectures for the topology of the flow in this region. The nose in these theories is magnified to such a degree that the leading edge becomes rounded and the apex blunt. Lighthill [8] suggests the $N_a S N_a$ topology shown in Fig. 11. Associated with this, Déclery [12] suggests a topology for the 3-d flow as shown in Fig. 12. From the saddle S , a primary-separation line S_1 starts from which a streamline surface originates that rolls up into a spiraling vortex. If secondary separation occurs, the topology is conjectured to extend to that depicted in Fig. 13 with two saddle-nodes on the centerline. In the present experiment, a tertiary-separation line was observed upstream of the boundary-layer transition region. Based on this observation, the origin of the vortex system over the delta wing is believed to be a triple $N_a S$ combination.

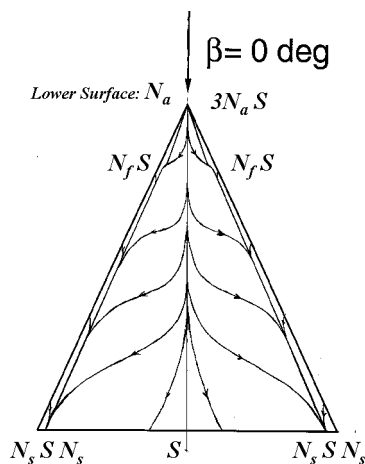


Fig. 11 Topology of skin-friction line pattern on upper surface

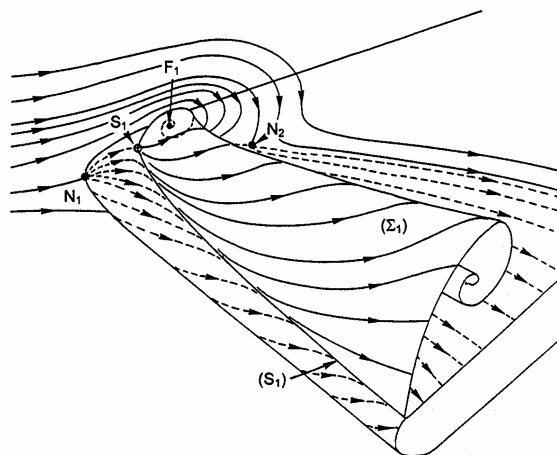


Fig. 12 Topology of two-vortex flow at apex of delta wing, as conjectured by Déclery [13]

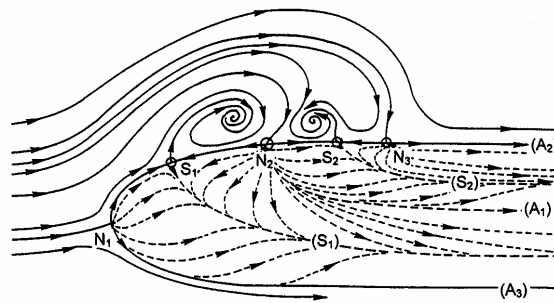


Fig. 13 Topology of four-vortex flow at apex delta wing, as conjectured by Déclery [12]

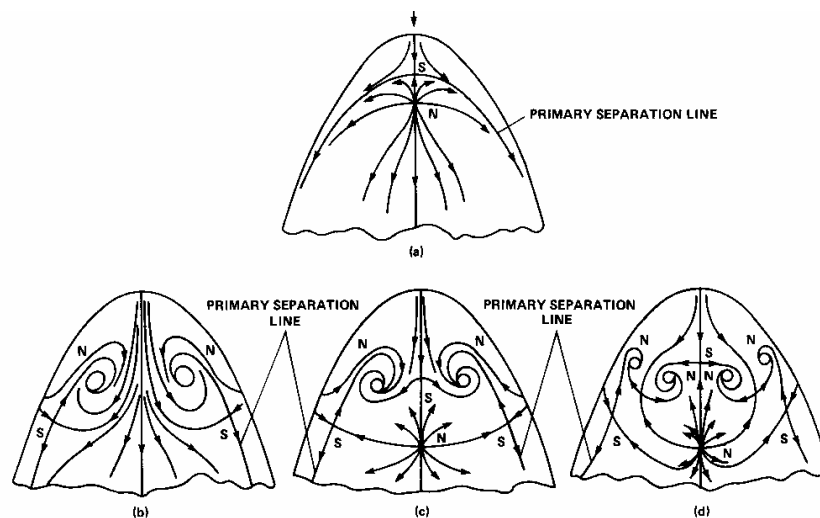


Fig. 14 Topology of flow at apex, as conjectured by Peake and Tobak [14]

Peake and Tobak [14] suggest a development of the flow as shown in Fig. 14. The topology of diagram (a) is similar to that suggested by Lighthill, with the exception that the skin-friction lines at the node are conjectured to be tangent to the centerline. Diagram (b) is based on conjectures by Legendre [15] that the skin-friction line pattern consists of a $N_f S$ combination associated with a “horn-type” of separation. Diagram (c) and (d) show an increasing number of singularities. The latter diagram is based on an interpretation of the oil-flow pattern observed on a slender, rectangular wing by Wickens [16].

Since the skin-friction pattern on the nose is poorly resolved, the above theoretical topologies could not be verified in the present experiment. To better resolve the pattern, at TUD large-scale wind tunnel models of the apex have been constructed. Currently, wind tunnel tests are carried out to investigate the flow over these models. The models and some preliminary test results will be discussed in the next Sections.

The conjectured topology of the crossflow upstream and downstream of the boundary-layer transition region is sketched in Fig. 15. The primary, secondary and tertiary separation lines are marked S_1 , S_2 and S_3 , respectively, while the attachment line on the lower surface is denoted A_0 , and A_1 , A_2 and A_3 on the upper surface.

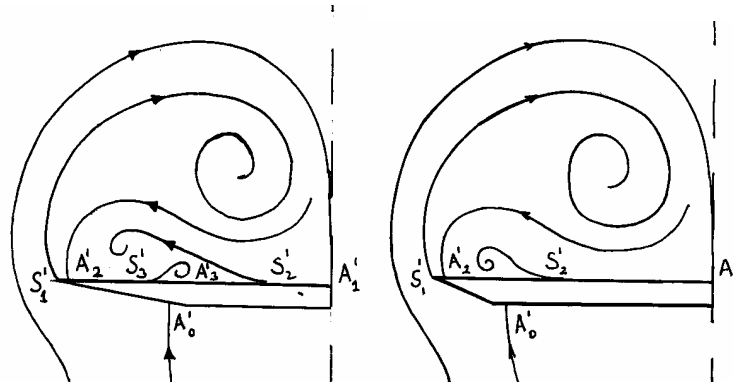


Fig. 15 Crossflow topology (a) upstream and (b) downstream of transition region

Fig. 16 shows a schematic for the topology of the skin-friction line pattern in this region. This is characterized by a N_f S combination at the kink in the secondary-separation line

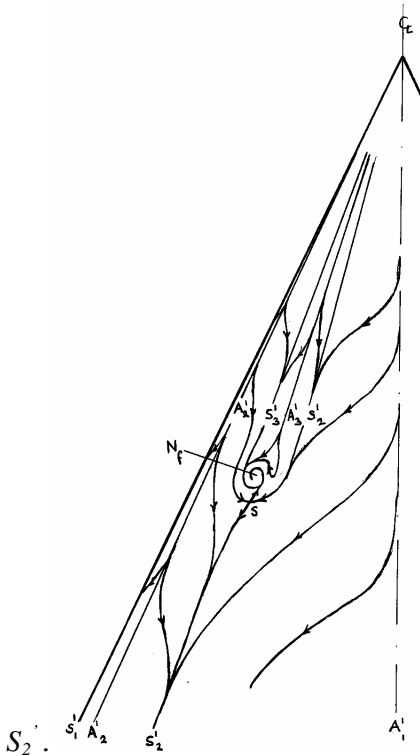


Fig. 16. Topology of boundary-layer transition region

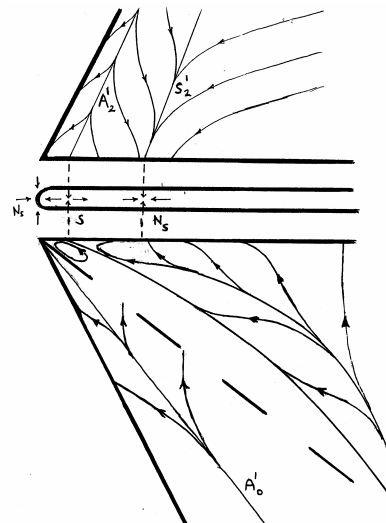


Fig. 17. Topology of flow at left-hand wing tip

At the wing trailing edge, a saddle is conjectured at the center and a $N_s S N_s$ combination at both tips. The topology of the flow at the left-hand tip on a microscopic scale is shown in Fig. 17. The upper plot shows the pattern of the skin-friction lines on the upper surface, the central plot shows the singularities on the trailing edge enlarged to such a scale that it can be considered smooth and rounded, while the lower plot depicts the pattern on the bottom surface.

8.3.2.4 Flow Pattern on Apex Models

The two apex models are shown in Fig. 18. If one magnifies the apex region of the delta wing, the edges will no longer be sharp but of finite radius. Model 2 represents the smallest magnification of this region.

It has a triangular cross section and rounded 65-deg swept leading edges. Leading edge and nose radii are 20 mm, the model length and span are 187 and 200 mm, respectively. Further magnification of the apex region may result in a hemisphere-cone configuration. This is represented by Model 1, which has a nose radius of 40 mm, a length of 160 mm and a span of 200 mm.

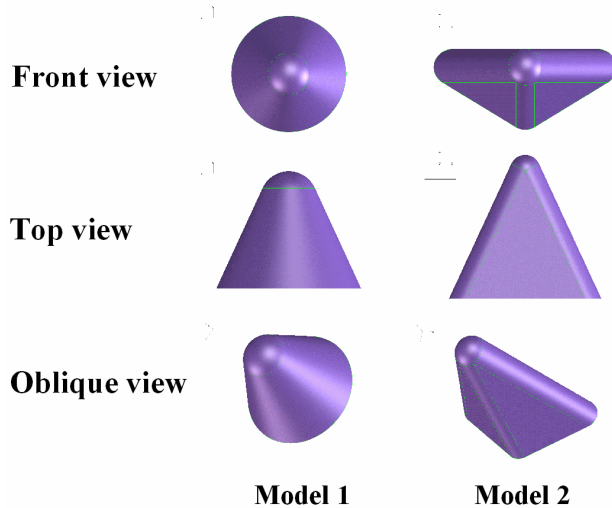


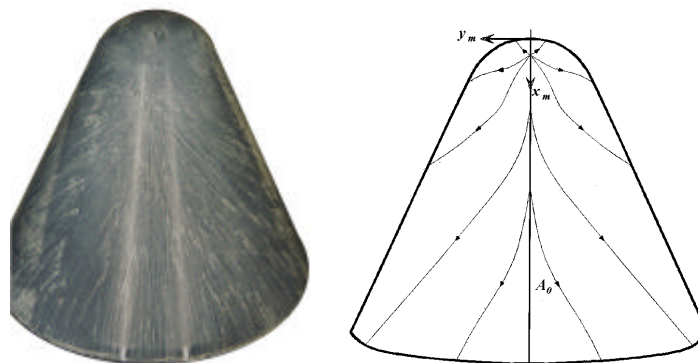
Fig. 18. Apex models



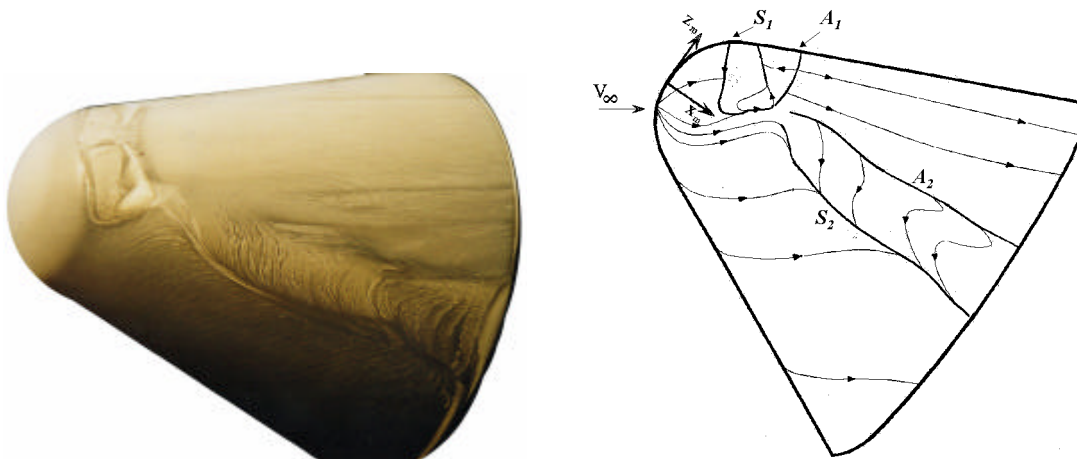
Fig. 19. Flow visualization of Model 1

The models were constructed of PVC material and painted black for a higher contrast with the visualization fluids. Currently, an extended test program is being carried out to visualize in detail the flow on both models at various angles of attack and sideslip. For visualization the same two fluids are used as for the visualization of the flow on the delta wing. The tests are performed in an open low-speed wind tunnel with a nozzle of 0.40 m wide and 0.40 m high. An advantage of an open test section is that the visualization fluid can be applied to the model after the air has reached the desired speed. A closed test section has to be opened and the visualization fluid applied at zero air speed. It then takes some time to close the test section and bring the air to full speed. During this transition time part of the visualization fluid may dry resulting in a streak-line pattern that does not correspond to the flow pattern generated when the fluid is applied at full speed. The latter is a problem with models whose surface flow is sensitive to Reynolds number effects. Fig. 19 shows the test setup behind the nozzle of the open tunnel, oil flow is applied to Model 1. The model is mounted on a sting that is fixed to a (*a, b*) traversing mechanism.

Preliminary tests have been conducted at an air speed of 20 m/s, being the largest speed attainable with the present set-up. In the following, the results of these tests are discussed.



a. Bottom surface flow

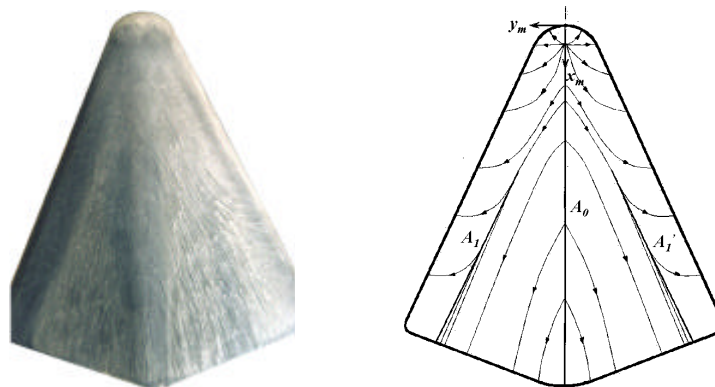


b. Side surface flow

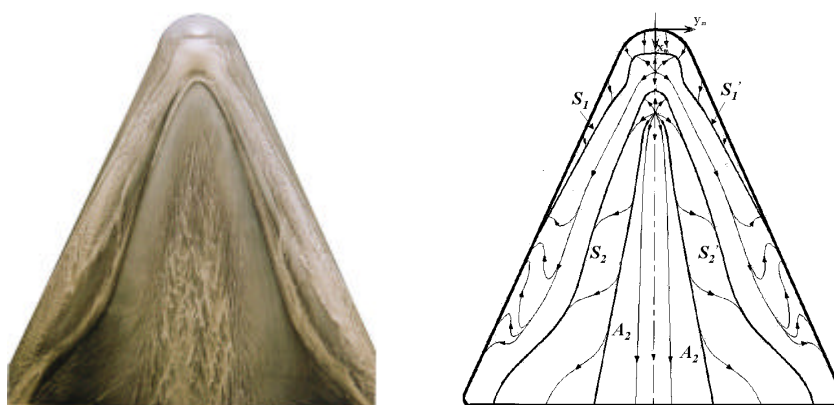
Fig. 20 Flow patterns on Model 1 for $\alpha = 35^\circ$

Fig. 20 shows photographs of the streak-line pattern and schematics of the skin-friction line pattern on the bottom surface and the side of Model 1 at $\alpha = 35^\circ$. On the bottom surface, a stagnation point is evident and an attachment line A_0 on the centerline. On the upper surface, a bubble-type of separation occurs at the hemisphere/cone transition. The bubble separates at line S_1 and reattaches at line A_1 . The boundary layer from the lower surface separates at line S_2 and reattaches at line A_2 . Note that these lines are not connected to the first separation and attachment lines. In between S_2 and A_2 integral-shaped streak lines are visible. The curvature of these lines increases on the aft surface of the model due to trailing edge effects. The streak line pattern shows the footprint of a single vortex on each half of the model.

Fig. 21 shows the patterns on the lower and upper surface of Model 2 at $\alpha = 30^\circ$. The flow attaches on the bottom surface at a stagnation point a short distance downstream of the apex. An attachment line A_0 emanates from this point. Closer to the leading edge another attachment line A_1 is visible. The streak lines outboard of this line sweep around the round leading edge to separate at the primary-separation line S_1 . The separated flow reattaches at line A_2 on the upper surface and separates again at secondary-separation line S_2 . Between these lines, integral-shaped lines mark the footprint of the secondary separation. The attachment and separation lines start at the centerline of the model and proceed along rays towards the trailing edge. This correlates with the flow topology suggested by Délery [12]. Upstream of the trailing edge, a kink can be noted in the secondary-separation lines. This is believed to be due to trailing-edge effects. The pattern on the upper surface hence shows the onset of a primary- and secondary separation. There are no markings of a tertiary separation.



a. Lower surface flow



b. Upper surface flow

Fig. 21 Flow patterns on Model 2 for $\alpha = 30^\circ$

The preliminary tests have been conducted at an air speed of 20 m/s. Based on chord length the Reynolds number of the models is of the order of 10^5 . A question is how to actually define the Reynolds number of these models. If this number would be based on e.g. the leading edge radius, which is 200 times larger than that of the delta wing model, or on the chord of a delta wing 200 times larger than the one tested here, the Reynolds number would be of the order of 10^7 . An important effect of increased leading edge radius is the occurrence of Reynolds number sensitivities, especially as regards to separation onset. Using sharp leading edges as in the case of the 65° delta wing eliminates this Reynolds number sensitivity. The capability for studying the sensitivity of the streak-line patterns of the apex models to Reynolds number is limited. The viscosity of the visualisation fluid requires a minimum air speed of 10 m/s, while the maximum speed for the present test set up is about 20 m/s. In this speed range effects have been observed on the streak-line pattern of Model 1. At air speeds below 15 m/s the separation lines S_1 and S_2 become connected. In addition, an extension of the vortex footprint area between the lines A_2 and S_2 has been observed. No effects of the air speed have been observed on the streak-line pattern of Model 2.

8.4 IAR/USAF EXPERIMENTS

8.4.1 EXPERIMENTAL SET-UP

Wind-tunnel tests were conducted at the Wright Laboratory 7 ft x 10 ft open-return atmospheric tunnel (SARL) and at the IAR 6 ft x 9 ft close-return wind tunnel (LSWT). A 65° delta wing model (Fig. 22) was statically tested over a range of angles of attack at 0° sideslip angle or over a range of sting angles (σ) and roll angles (ϕ). The positive roll angle is defined as the port wing half rolls down. Most of the tests were conducted at a Reynolds number 2.4 million based on the mean aerodynamic chord and a Mach number of 0.3. In order to obtain clear picture, the viscosity of the silicon oil and titanium dioxide mixture was tailored to optimise the observation of prescribed features. Photographs were taken to capture the surface flow patterns during/after wind on. High-resolution videos recorded the development of these patterns and were used to resolve some ambiguities in the flow direction near the surface. In addition, different oil and tailored dioxide mixture was used at each interested attitude so that the oil and dioxide particles separated from surface or attached to surface can be visualized, which was found very helpful to understand the possible three-dimensional flow structure near the surface. An important aspect of the experiment was to investigate the evolution of the topological change as the attitude varies. Detailed oil flow patterns were recorded at various attitude angles such that all possible topologies would be identified. Very intensive experiments were conducted at the vicinity of each recognized topological change in order to understand how possible topological change appears. Particular attention was placed around those angles where airloads exhibited various types of discontinuities founded in previous static experiments.

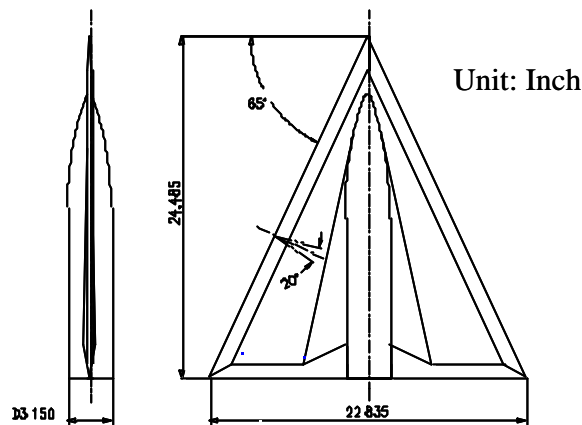


Fig. 22 IAR 65° delta wing model

8.4.2 FLOW VISUALISATION AND TOPOLOGICAL ANALYSIS

8.4.2.1 FLOW VISUALISATION

Profound flow visualisation results have been obtained either in pitch or in roll plane. Varieties of mean surface flow patterns, their evolutions have been observed as the governing parameter (roll angle or angle of attack) changes. As examples the results in roll plane for two sting angles $\sigma \neq 30^\circ$ and 35° and roll angles $-21^\circ < \phi < 62^\circ$, are presented from Fig. 23 to Fig. 26 and discussed here.

At very high roll angle (Fig. 23a left), the flow pattern exhibits a concentrated leading edge vortex on the leeward wing half, characterised by the presence primary and secondary separation. The tertiary vortex is hard to see at this attitude. This is probably due to at very high roll angle the equivalent leading-edge sweep-back angle for the corresponding leeward wing half becomes very large as the following equation shows:

$$\Lambda = \Lambda_0 \pm \tan \sigma * \sin \phi$$

From the equation, the corresponding leading-edge sweep-back angle at the flow condition of Fig. 23a ($\sigma=30^\circ$, $\phi=28^\circ$) is around 80.5° . At such large swept back angle the circulation and axial vorticity is insufficient to introduce the tertiary vortex. Also the corresponding leeward wing becomes very narrow as shown in Fig. 23a. Both of them are unfavourable to the tertiary vortex to appear. Moreover, it looks there is no any visible kink point in the secondary separation line indicating the boundary layer in the reattached area may still be laminar due to shorter length of streamline and lower local Re number. At a little lower roll angle the tertiary separation line appears (Fig. 23b). The kink point in the secondary line appears roughly at middle chord. Those two feathers are clearly seen from corresponding section views shown in Fig. 23c and Fig. 23d)



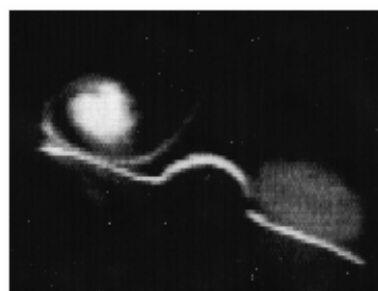
23a Pattern $P1_2$ ($s=30^\circ$, $f=28^\circ$)



23b Pattern $P1_1$ ($s=30^\circ$, $f=16^\circ$)



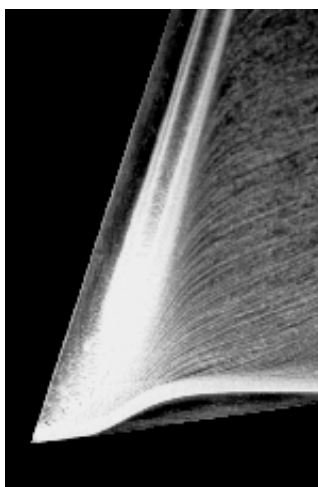
23c laser smoke section view
($s=30^\circ$, $f=28^\circ$)



23d laser smoke section view
($s=30^\circ$, $f=16^\circ$)

Fig. 23 Concentrated vortex patterns and related section views

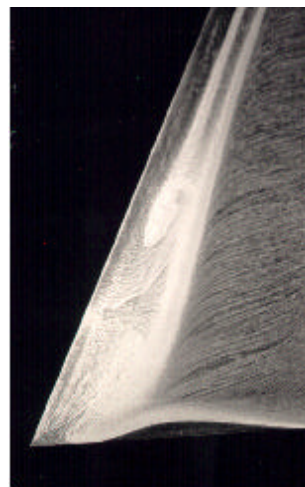
When roll angle decreases more, at least one whorl corresponding to a focus at where the secondary or tertiary vortex lifts off the surface (Fig. 24) indicating breakdown of those vortices. Fig. 24a shows the secondary vortex is well organised but the tertiary one is close to breakdown near the trailing edge with a “whorl” lift-off from the surface. When the roll angle further decreases the secondary one is also close to breakdown so that two “whorls” appear on both of them as depicted in Fig. 24b. Further decrease of roll angle leads the tertiary one merges into secondary vortex and the “whole” on the end of secondary vortex move forward (Fig. 24c).



24a Pattern $P2_1$ ($s=30^\circ$, $f=14^\circ$)



24b Pattern $P2_2$ ($s=30^\circ$, $f=7^\circ$)



24c Pattern $P2_3$ ($s=30^\circ$, $f=4.6^\circ$)

Fig. 24 Vortex “whorl” patterns

Further reductions in roll angle results in the primary vortex breakdown location moving on to the wing (Fig. 25a to Fig. 25d). The kink point in the secondary separation line can be clearly observed in the forward portion of the wing at ~10% of the root chord (Fig. 25a). This pattern could appear either at windward half or leeward half when the roll angle is relatively smaller. As seen from Fig. 25b on windward side (right wing half), the vortex breakdown location is around 10% of the root chord. There is no any sign of tertiary vortex and related separation line on windward side, indicating the strength of the vortex on this half is much weaker than leeward half as seen in Fig. 25b, 25c and 25d.

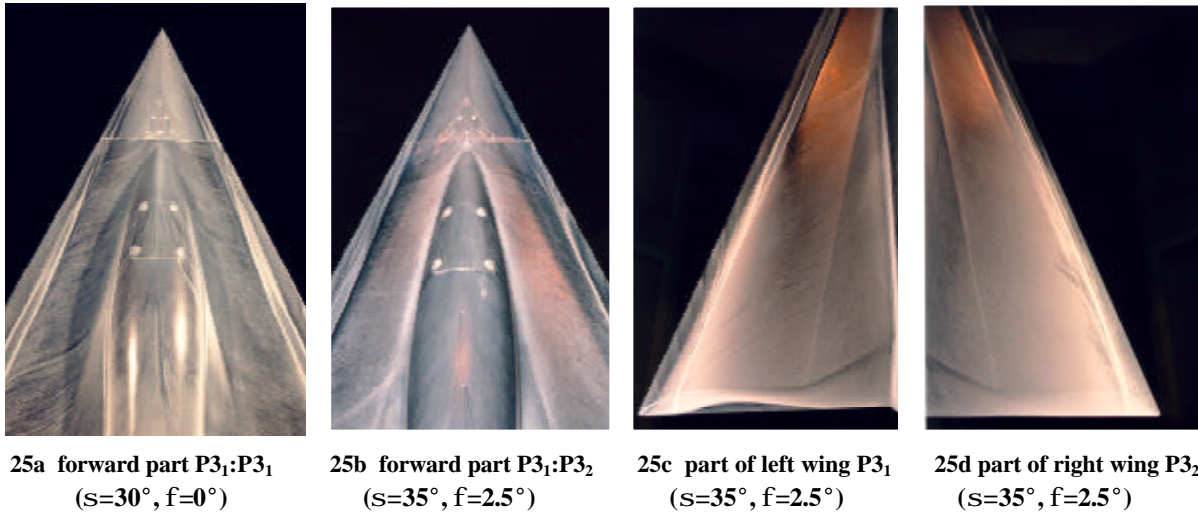
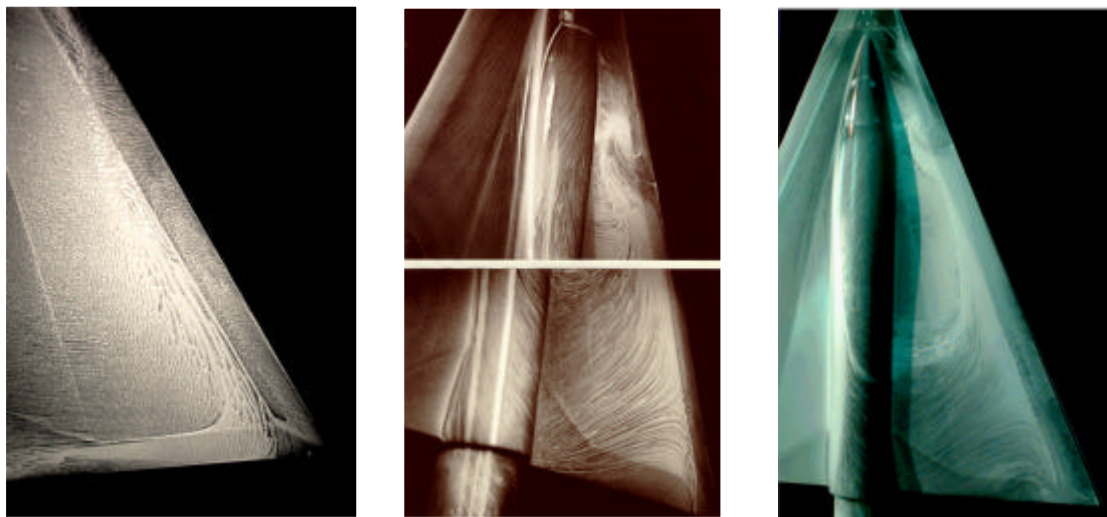
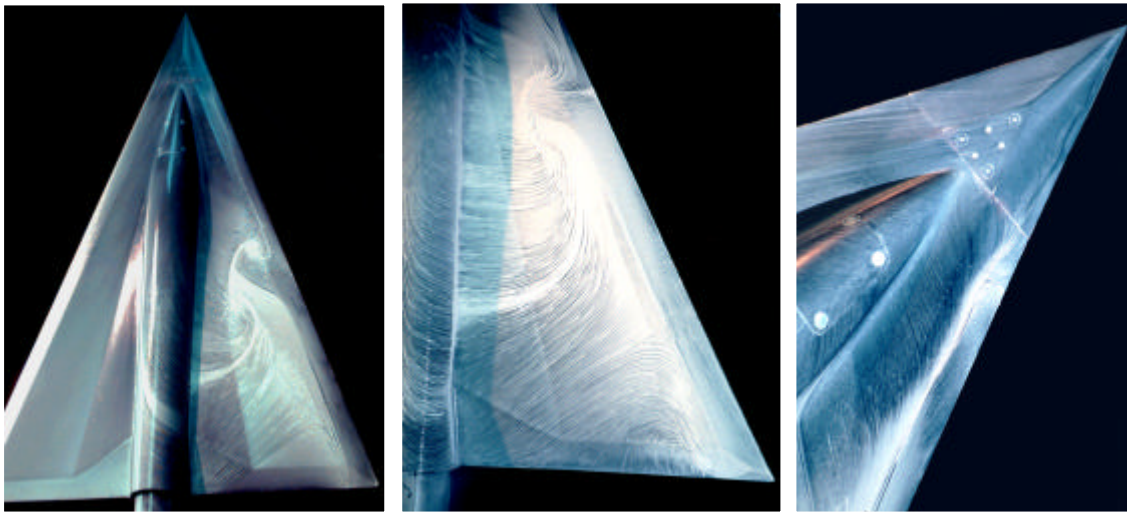


Fig. 25 Vortex bursting patterns observed on different wing areas

When the wing half under consideration is sufficiently to windward, and the primary vortex breakdown location is near or at the apex, a variety of spiral or reverse patterns may develop (Fig. 26). All those patterns are mainly due to the interaction and balance between the spiral flow starting from leading-edge and reverse flow from trailing edge.





26d pattern P₄₄ (s=30°, f=51°) **26e** P₄₅ (aft part, s=35°, f=62°) **26f** P₄₅ (apex, s=35°, f=62°)

Fig. 26 Flow visualization of spiral flow patterns

It is important to note that a strong spiral flow is still alive during this period. In addition, the reverse flow on the windward half is getting fiercely due to the equivalent sweep-back angle decreases and the trailing edge resembles partly as wing side edge as the roll angle decreases further. Moreover the axes of spiral flow at first is still along the axes of vortex as in the previous stage but as the roll angle increases further, its axes lift off the surface eventually due to the stronger reverse flow. This lift-off process is gradually getting stronger as the roll angle increases. At first, the strength of spiral flow is still stronger or equivalent to that of the reverse flow leading to a tiny focus appears along middle chord near the leading-edge as shown in Fig. 26a. When the roll angle further increases the reverse flow becomes stronger than the spiral flow which pushes the influence area of spiral flow upstream as shown in Fig. 26b. Also the strong reverse flow mixes with spiral flow resulting in a remarkable focus on the wing surface as seen in Fig. 26b. Part of spiral flow is involved in the reversed flow from trailing edge results an additional focus develops near the trailing edge as shown in Fig. 26b, 26c and 26e. Also it was found that if one focus is not enough to handle all the vorticities in the reverse flow two foci could appear as observed in Fig. 26d and 26e. It is remarkable that the range of roll angles when the spiral flow exists is quite large in roll case comparing with the range of angles of attack in pure pitch case. This is probably due to the fact that in roll case, roll angle induced effective angle of attack and sideslip angle can be obtained from the following equations:

$$\tan \alpha = \tan \sigma * \cos \phi$$

$$\sin \beta = \sin \sigma * \sin \phi$$

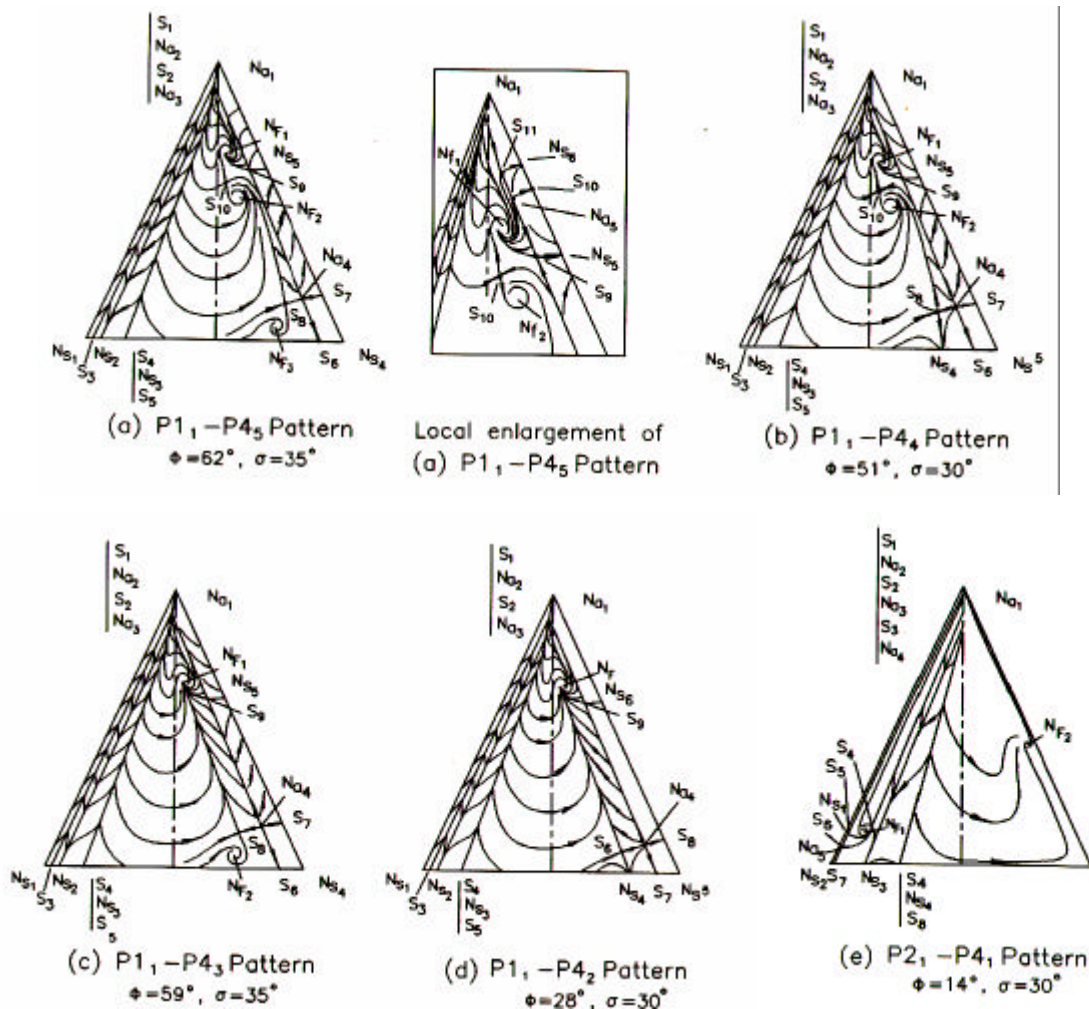
The effective angle of actually, decreases as the roll angle increases, which partly cancels out the roll effect resulting in the spiral pattern existed in large range of roll angle. For example at 50° roll angle and 30° sting angle, the effective angle of attack, sideslip and leading-edge sweepback angle is only 20°, 26° and 2° respectively. At such attitude, the flow will not be like dead water but separated and reattached on the surface downstream of leading edge. Actually from section view of laser sheet visualisation a reformed leading-edge vortex has been observed at such high roll angle.

At extreme roll angles a separation bubble develops destroying any discernible pattern.

8.4.2.2 FLOW TOPOLOGY ANALYSIS

By synthesizing our results with those of other flow visualization experiments the flow visualization results have been interpreted into various topology patterns. As examples the topological changes in roll

plane at eight attitudes are sketched in Fig. 27. The singular points and corresponding topologies associated with the centerbody have been omitted in Fig. 24 for the sake of simplicity. The variety of mean surface flow topologies can be classified into five major categories: concentrated vortex pattern (P1), vortex “whorl” patterns (P2), bursting vortex patterns (P3), reverse flow patterns (P4) and totally separated flow pattern (P5). The above list reflects the patterns in the order in which they appear on a wing half as it moves from leeward to windward. Each category may include more than one pattern depending on attitude. Patterns are topologically different due to the addition or deletion of nodes or saddles. The nodes are denoted N_a for a node of attachment, N_s for a node of separation, and N_f for a focus or spiral node. The saddle is denoted by S . The numerical subscript identifies the specific singularity. Combined or higher-order singularities are enclosed in parentheses e.g. $(N_s S)_1$. Bear in mind that the figures describing the topology are not drawn to scale. Furthermore, to avoid excessive cluttering of lines converging toward the apex, the closely spaced singular points there have been separated longitudinally and labelled on a line next to the apex. Those points are, in fact, merged singular points and thus appear to be of a higher order. A similar approach is used at the trailing edge where the primary reattachment saddle is virtually coincident with a node of separation and the reattachment saddle associated with the left wing half spiral flow. The single attachment node on the windward, lower surfaces is common to all patterns and is denoted by N_{a1} at the right of the apex.



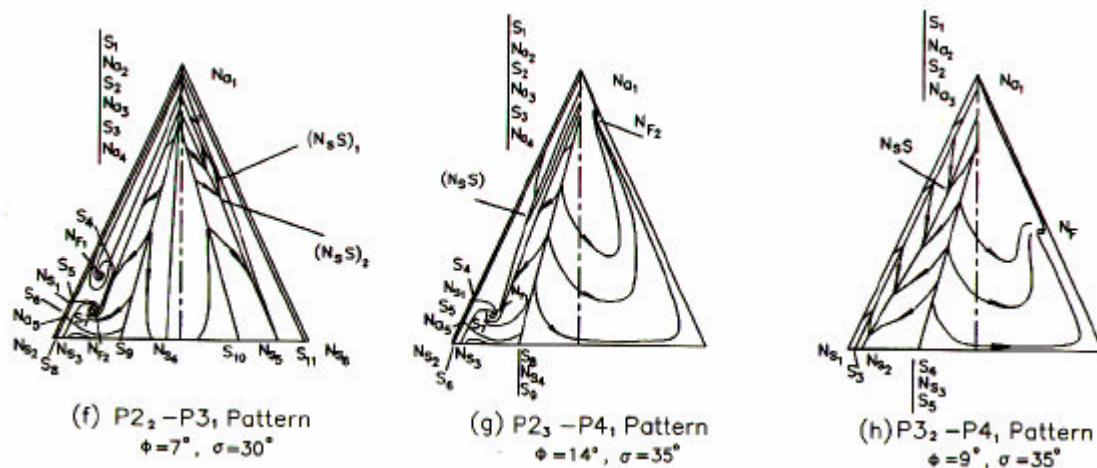


Fig. 27 Evolution of surface flow topology on a 65° delta wing at different attitudes

The concentrated vortex pattern, P1 in Fig. 27a to Fig. 27d, appears on the leeward wing half (port) at very large roll angles. When roll angle is reduced, a “whorl” pattern (P21 in Fig. 24e) suddenly appears on the leeward wing half, characterized by the presence of a ‘whorl’. This is a focus, N_F , where the flow sharply lifts off from the surface due to the tertiary vortex lifting off. The topology abruptly evolves from the original node of separation, N_S , and the reattachment saddle, S , associated with the tertiary vortex into combinations of singular points:

$$N_S? N_{S1}-S_2-N_{F1}$$

$$S? S_3-N_{a2}-S_1$$

As the roll angle is decreased further, this whorl moves forward and a second one reflecting the lifting-off of the secondary vortex suddenly appears (P2₂ in Fig. 27f) with the following topological evolution:

$$N_S \rightarrow N_{S1}-S_2-N_{F2}$$

$$S \rightarrow S_3-N_{a2}-S_6$$

Additional reduction in the roll angle results in the rapid disappearance of the first whorl (and corresponding topological change (from Fig. 27f to Fig. 27g) i.e. $S_4 - N_{F1} \rightarrow N_S S$, followed by the disappearance of the secondary whorl leading to a bursting vortex patterns (P3). The corresponding surface flow topologies are shown by sub-patterns (P3₁ and P3₂) in Fig. 27f and Fig. 27h respectively.

Once the wing half under consideration is sufficiently to windward and breakdown is near to or at the apex, the shear stress of the flow near the surface is considerably reduced leading to the disappearance of the separation and reattachment lines on the surface. However, there is a weak spiral flow appears as indicated by a focus near mid-chord (Fig. 27e and Fig. 27h) which gradually moves forward as the wing half rotates to windward.

Further reduction in the roll angle results in this focus moving aft accompanied by a strengthening of the shear stress, possibly due to the reduced angle of attack. The original focus splits into $N_F \rightarrow N_{F1}-S_7-N_{S6}$ as seen in Fig. 27d. It was experimentally difficult to determine exactly when these changes occurred as they take place near the model tip where the resolution of the images is not sufficient. Concurrently, some new singular points also appear near the trailing edge. At even lower roll angles, the spiral flow area becomes even stronger resulting in the appearance of a second focus as seen in Fig. 27a, 27b and 27c.

Finally, at very low roll angles, the spiral flow over the windward wing half disappears and a separation bubble is formed. Under these conditions no discernible oil flow pattern is produced (P5) leading to its exclusion from Fig. 27.

8.4.2.3 EVOLUTION OF FLOW TOPOLOGIES

From the above observed topology changes the evolution of flow patterns on the model corresponding to a variety of attitudes in roll plane are listed in a Table below. In some cases there is an uncertainty regarding a particular pattern due to limitations in the image quality or due to excessive flow unsteadiness that does not seem to result in discernible mean pattern. The sting angles in the table have been corrected for the sting deformation under airloads. Careful study by intensive experiments along bifurcation point of roll angle shows that there are at least three different types of topology evolution exist when the roll angle is changing near a bifurcation point. One is local and gradual topology change. The second is local but sudden topology change. And the third one is global and sudden change in flow topology. For the first one, the singular points in surface flow topology either move continuously on the surface or gradually merge or split into other types of singular points. As an example the flow topology pattern changes from $P4_1$ to $P4_2$ is this type of bifurcation. For the second one the singular points change suddenly but limited in some local area. The tertiary vortex lefts off with corresponding topology change from $P2_1$ to $P2_2$ is an example of this evolution. For the third one the topology pattern changes suddenly and globally. It looks as the flow topology jumps between two distinctive flow patterns no matter how small the roll angle changes. The topology changes from $P1_1$ to $P4_1$ or from $P3_1$ to $P4_1$ belong to this type of bifurcation. In addition, an oscillatory bifurcation between two flow patterns was also recognized in the experiments. The information of topology evolution is helpful in the correlation studies between surface flow topology and critical states in airloads.

Flow topologies ($\sigma=30^\circ$)			Flow topologies ($\sigma=35^\circ$)		
ϕ°	Port	Starboard	ϕ°	Port	Starboard
0	$P3_1$	$P3_1$	0	$P3_1$	$P3_1$
4	$P3_1$	$P3_1$	1.2	$P3_1$	$P3_1$
4.6	$P2_2$	$P3_1$	2.5	$P3_1$	$P3_2$
4.8	$P2_2$	$P3_1$	6	$P3_1$	$P4_1$
5.2	$P2_2$	$P3_1$	7	$P3_1/P2_3$	$P4_1$
6	$P2_2$	$P3_1$	9	$P3_1/P2_3$	$P4_1$
6.5	$P2_2$	$P3_1$	12	$P1_1/P2_3$	$P4_1?$
7	$P2_2$	$P3_1$	14	$P1_1/P2_3$	$P4_1?$
7.5	$P2_2$	$P4_1$ (weak)	21	$P1_1$	$P4_1/P4_2$
8.4	$P2_2$	$P4_1$	28	$P1_1$	$P4_2$
10	$P2_2$	$P4_1$	37	$P1_1$	$P4_2$
11.2	$P2_2$	$P4_1$	42	$P1_1$	$P4_2$
12	$P2_2 \ll P2_1$	$P4_1$	59	$P1_1$	$P4_3$
14	$P2_1$	$P4_1$	62	$P1_1$	$P4_5$
16	$P2_1$	$P4_1$	67	$P1_1$	$P5$
21	$P1_1$	$P4_2$	69	$P1_1$	$P5$
28	$P1_1$	$P4_2$			
32	$P1_1$	$P4_2$			
40	$P1_1$	$P4_2$			
42	$P1_1$	$P4_2$			
47	$P1_1$	$P4_2$			
51	$P1_1$	$P4_4$			
57	$P1_1$	$P1_1$			

8.4.2.4 CORRELATION STUDY BETWEEN TOPOLOGY CHANGE AND CRITICAL STATES

An important step for understanding and applying the nonlinear indicial response method and other nonlinear flight mechanics is the recognition of “critical states” defined as points within the motion history

where Fréchet differentiability of the aerodynamic response functional is lost. How to locate or how to detect the critical states is a prerequisite for solving the non-linear flight mechanics. As previously mentioned that the sub-bifurcation in surface flow topology might be a sufficient but not necessary condition for the critical states. It is worthwhile to study the related experimental results. Thus the critical states found by measured airloads in stationary model condition are compared with topological bifurcation as shown in the table below. It is interesting to see that for each governing parameter (roll angle) where a statically measured critical state exists, there is a corresponding topological change nearby as shown briefly in the table. Detail looking the evolution of topologies when governing parameter (roll angle) is across that value, it is found that the topological change behaves as it jumps between two quite different topologies as a kind of subcritical bifurcation involved.

Critical states	Topological changes	Observations in flow visualization experiment
$\sigma=29^\circ, \phi=5^\circ$	$P3_1:P3_1 \leftrightarrow P2_2:P3_1$	two whorls appear suddenly on secondary and tertiary vortices
$\sigma=29^\circ, \phi=8.2^\circ$	$P2_2:P3_1 \leftrightarrow P2_2:P4_1(\text{weak})$	separation and attach line of secondary vortex disappeared while a very weak focus appear at the middle area of the wing
$\sigma=29^\circ, \phi=11.6^\circ$	$P2_2:P4_1 \leftrightarrow P2_1:P4_1$	a whorl at the end of secondary vortex suddenly disappeared
$\sigma=29^\circ, \phi=50.1^\circ$	$P1_1:P4_2 \leftrightarrow P1_1:P4_4$	one focus suddenly splitted into two bigger foci
$\sigma=29^\circ, \phi=51.5^\circ$	$P1_1:P4_4 \leftrightarrow P1_1:P5$	skin-friction line disappeared suddenly
$\sigma=35^\circ, \phi=1.2^\circ$	$P3_1:P3_1 \leftrightarrow P3_1:P3_2$	secondary vortex disappeared suddenly
$\sigma=35^\circ, \phi=3.5^\circ$	$P3_1:P3_2 \leftrightarrow P3_1:P4_1$	separation and attach line of secondary vortex disappeared while a very weak focus appeared at the middle area of the wing
$\sigma=35^\circ, \phi=62.1^\circ$	$P1_1:P4_3 \leftrightarrow P1_1:P4_5$	large focus appeared suddenly near the trailing edge

On the other hand there are some topology changes (for example $P2_1:P4_1$? $P1_1:P4_1$ and $P1_1:P4_1$? $P1_1:P4_2$ corresponding to the attitudes of $\sigma=30^\circ, \phi=14^\circ\sim 16^\circ$ and $\sigma=35^\circ, \phi=21^\circ$) which are not associated with a measurable critical state. One thing is noticed that the effects of those topological changes on the airloads are probably too small to be detected. For instance, when topology changes from $P2_1$ to $P1_1$, the only change is the tertiary vortex. Its effect on the loads might be very small. As for the topology change from $P4_1$ to $P4_2$ with increasing roll angle, the continuous video images show that the N moves forward smoothly till the vicinity of the apex and then moves back resulting in the smooth flow pattern changes from $P4_1$ to $P4_2$. At its onset, the topology changes may be associated with small-scale structures that have minimal effects on the aerodynamic forces, or they may be related to gradual process, e.g., a critical point of high order. In either case, the changes in flow topology may not have measurable effects on the aerodynamic forces, moments, or their derivatives.

From comparisons shown above it looks as if the subcritical bifurcation, jumps or discontinuities in airloads can be expected. In other words a subcritical bifurcation in flow topology could be referred to as the sufficient condition for a loss in analytic dependency of the aerodynamic response. However it is worthwhile to reiterate that the above measured critical states come from static measurement, which ignores any spectral analysis or unsteady behavior and assumes the equilibrium states being time-invariant. Also the measured amount of discontinuity is limited by the uncertainty of experiments. That means much of the work needed for the reliability and the completeness. For example when vortex breakdown is across the trailing edge the principle change is the large time scale and fluctuation which could not be found by static test. Also when wing surface has geometrical discontinuity such as trailing edge bevel, it will result in vortex breakdown jumping between two relatively stable locations: one is downstream of trailing edge and another is upstream of trailing edge so as the related discontinuity in airloads. Identifying singular points in the skin-friction-line pattern does not go very far in clarifying the critical states and it can never be conclusive by means of experiment, no matter how carefully it is carried

out.

8.4.2.5 POSSIBLE THREE-DIMENSIONAL FLOW STRUCTURE

One of the intentions in flow visualization experiment was to visualize the particles either separated from the surface or attached on the surface as these results are helpful to understand where and how the flow separates from or attaches to the surface and to construct possible three-dimensional flow structures near the surface. However, it should be emphasised that in order to unambiguously define the three-dimensional flow it is necessary to have other independent information, such as local pressure, etc. in addition to the surface flow visualization. Thus the possible three-dimensional flow structure presented here only corresponds to the best conjecture based on the observed topology and information from smoke flow visualization.

From observed flow patterns and topological analysis, possible three-dimensional flow structures corresponding to typical topological cases (P1 to P4) are hypothesised in Fig. 28. These flow structures can be imaged as contributions and interactions of three different types of flow: vortical flow from leading-edge, spiral flow over the wing surface and reversed flow from trailing edge. The first one is the flow separated from the leading-edge through free shear layer and rolls up into a concentrated vortex (P1) or partially breakdown (P2). The three-dimensional structures are shown on starboard wing half in Fig. 28a to Fig. 28d. The second type flow corresponds to that the leading-edge vortex is totally breakdown but it reattaches on the surface. It happens at high roll angle where the trailing edge acts partly as side edge resulting in stronger reverse flow along the trailing edge as the third type of flow. The interaction of these two flows lead to verity of P4 pattern as sown on port side wing half in Fig. 28.

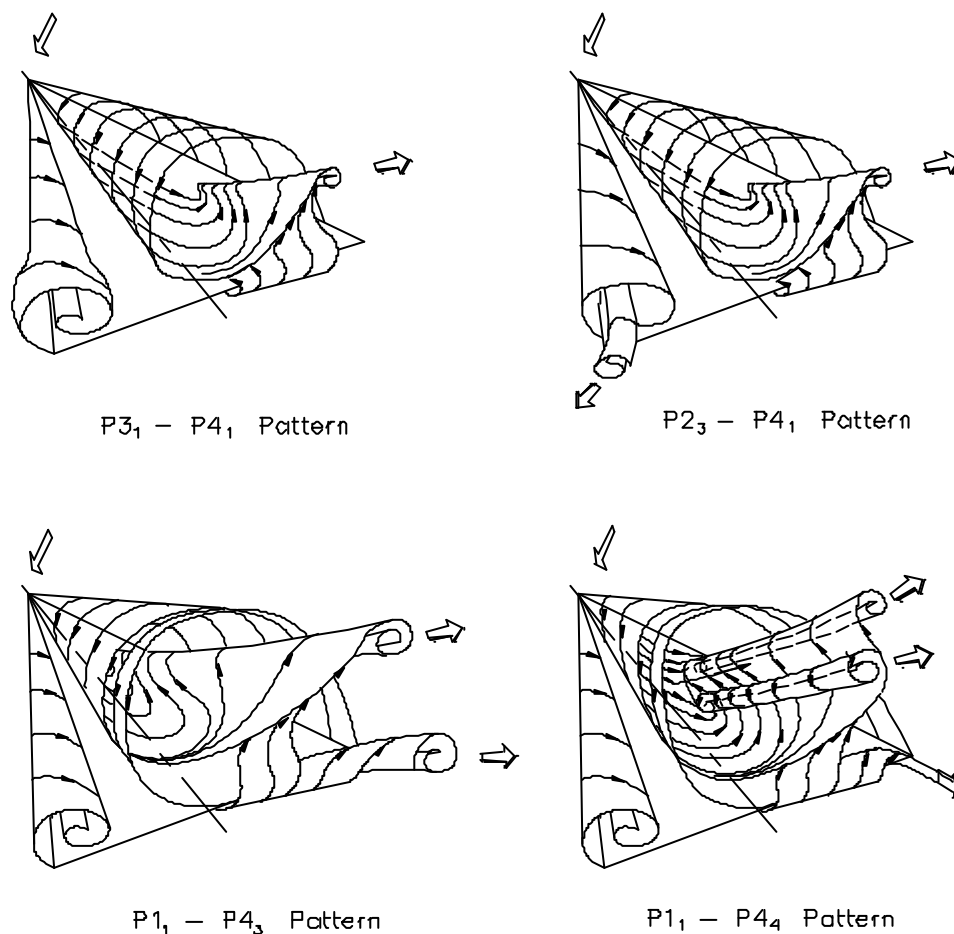


Fig. 28 Conjectured three-dimensional flow structures interpreted from surface flow topologies

8.5 CONCLUSIONS

The flow visualization on 65° delta wings observed at various of angle of attack, sweep back angles and roll angles were described. Topology theory is used to qualitatively describe the flow on the wing. Special attention is paid to the complex flow at the apex, boundary-layer transition and the evolution of topologies, especially in the vicinity of the critical state in dynamic space. Two large-scale wind tunnel models of the apex have been constructed in order to obtain more data on the flow in this region. Flow visualisation on these models shows the onset of primary and secondary vortices and results indicate that the conjecture of the flow topology near the apex of a delta wing by Delery [12] may be accurate. Correlation studies between flow topology and critical states strongly suggest that the subcritical bifurcation in flow topology may be a sufficient but not necessary condition for the critical states in airloads.

8.6 REFERENCES

- [1] Verhaagen, N.G. and Jobe, C.E., "Topology of the Flow on a 65-deg Delta Wing at Sideslip," AIAA 2002-0095, Reno, Jan. 2002
- [2] Huang, X.Z., Hanff, E.S., Jenkins, J.E. and G. Addington, "Leading-Edge Vortex Behavior on a 65° Delta Wing Oscillating in Roll," AIAA Paper 94-3507.
- [3] Huang, X. Z. and Hanff, E.S., "Leading-Edge Vortex Behavior and Surface Flow Topology," AIAA Workshop III: Delta Wings-Unsteady Aerodynamics and Modeling, AIAA Atmospheric Flight Mechanics Conference, 1995.
- [4] Jobe, C.E., Huang, X.Z. and Jenkins, J.E., "Impact of Static Topological Changes on Dynamic Airloads," AIAA Workshop III: Delta Wings-Unsteady Aerodynamics and Modeling, AIAA Atmospheric Flight Mechanics Conference, 1995.
- [5] Huang, X. Z. and Hanff, E.S., "Surface Flow Topology on a Delta Wing Rolling at High Incidence," NPU/AIAA Atmospheric Flight Mechanics, Xian, China, 1996.
- [6] Jobe, C.E., Hsia, A.H., Jenkins, J.E., and Addington, G.A., "Critical States and Flow Structure on a 65° Delta Wing," J. of Aircraft, Vol. 33, No. 2, March-April, 1996.
- [7] Addington, G.A., "The Role of Flow Field Structure in Determining the Aerodynamic Response of a Delta wing," Ph.D. Dissertation, University of Notre Dame, April 1998
- [8] Lighthill, M.J., "Boundary Layer Theory," *Laminar Boundary Layers*, L. Rosenhead, ed., Oxford, Cambridge, 1963, pp. 46-113.
- [9] Bakker, P.G., "Bifurcations in Flow Patterns: Some applications of the qualitative theory of differential equations in fluid dynamics," *Kluwer Academic Publishers*, the Netherlands, 1991.
- [10] Tobak, M. and Peake, D.J., "Topology of Three-Dimensional Separated Flows," *Annual Review of Fluid Mechanics*, Vol. 14, 1982, pp. 61 - 85
- [11] Hunt, J.C.R., Abell, C.J., Peterka, J.A. and Woo, H., "Kinematic Studies of the Flows around Free or Surface-mounted Obstacles; Applying Topology to Flow Visualization," *J. Fluid Mech.* (1978), Vol. 86, Part I, pp. 179-200.
- [12] Tobak, M and Coon, M.D., "Topology of Pressure Surfaces in Three-Dimensional Separated Flows," AIAA Paper 96-0319, 1996.
- [13] Délerly, J.M., "Robert Legendre and Henri Werlé: Towards the Elucidation of Three-Dimensional Separation" *Annual Review of Fluid Mechanics*. 2001. Vol. 33, pp. 129-154.
- [14] Peake, D.J. and Tobak, M., "Three-Dimensional Interactions and Vortical Flows with Emphasis on

High Speeds”, *AGARDograph* No. 252, July 1980.

- [15] Legendre, R., “Lignes de Courant d’un Écoulement Continu,” *La Recherche Aéronautique*, No. 105, 1965, pp. 3-9.
- [16] Wickens, R.H., “The Vortex Wake and Aerodynamic Load Distribution of Slender Rectangular Plates,” National Research Council of Canada Aero Report LR-458, July 1966.



Chapter 9 – TsAGI 70° AND 65° DELTA WINGS TEST CASES

A. Khrabrov

Central Aerohydrodynamics Institute (TsAGI)
RUSSIA

khrabrov@postman.ru

D. Greenwell

Bristol University
UK

Doug.Greenwell@bristol.ac.uk

ABSTRACT

Some experimental results for 70° and 65° delta wings obtained at TsAGI in steady and dynamic tests are presented. The comparison with published data for similar configurations is given. The considerable influence of dynamic vortex breakdown effects on unsteady aerodynamics is demonstrated.

9.1 INTRODUCTION

It is well known that vortex breakdown process at high incidence has dramatic effect on aerodynamic characteristics of slender wing aircraft. At high angles of attack we deal usually with the dynamic motion of aircraft. So at TsAGI during the investigation of delta wing aerodynamics the main focus was at experimental investigations of unsteady effects. In current chapter the results for 70° and 65° delta wings aerodynamic characteristics obtained at TsAGI low subsonic wind tunnel in steady and unsteady cases are presented. Some of the experimental results were published earlier [1,2,3].

9.2 AERODYNAMIC MODELS GEOMETRY

A number of various delta and double delta wings were investigated. In the current report only some experimental results for 70° and 65° delta wings are considered. Three 70° delta wing models were tested. The large model has planform area $S=0,4224 \text{ m}^2$. The root chord of the wing is 1,090m (MAC=0,727m) and the wing span is 0,775m. The scheme of the wing is shown in Fig. 1. The model was made from the duralumin plate of 12.5 mm thickness. The leading edges of the wing was rounded. The trailing edge was symmetrically bevelled, with bevel angle 20°. The strain gauge balance was attached to the model with the use of special docking adapter under the wing. The balance reference center is 0.5 of the mean aerodynamic chord. The weight of the model is about 12,5kg. The second 70° delta wing model was made from the plywood of 12 mm thickness. The root chord of the wing is 0,741m (MAC=0,494m) and the wing span is 0,540m. The reference area of the model is $S=0,200 \text{ m}^2$. The shape of the model is similar to the previous one. The leading edges of the wing was rounded. The trailing edge was bevelled with the same bevel angle 20°. The weight of this model is about 2.5 kg. The difference of the third 70° delta wing model from the second one is only the shape of leading edges. It has bevelled leading edges with a symmetric bevel angle of 20°. The scheme of this model is shown in Fig. 2. The second and third models have balance housing. The details are presented on the scheme. The balance reference center is also 0.5 of the mean aerodynamic chord.

During the investigations of delta wing unsteady aerodynamics a 65° aerodynamic model was manufactured also. The scheme of this delta wing model is similar to the above small 70° delta wing model with bevelled

leading edges and is presented in Fig. 3. The reference area of the model is also $S = 0.2 \text{ m}^2$, the wing span is $b = 0,611 \text{ m}$ and the root chord is $c = 0.655 \text{ m}$ (MAC = 0,437 m). The balance reference center is also 0.5 of the MAC.

The widely studied 65° delta wing model [4]–[12] has rather wide center body. To investigate the influence of such center body and to compare TsAGI's data the additional center body of the published shape was manufactured. The body was divided into two pieces (one could be placed on the top of the model, second – on the bottom). So there was the possibility to investigate 65° delta wing model with and without additional center body. The scheme of the model with the additional center body is presented in Fig. 4.

9.3 WIND TUNNEL

The experimental investigations were executed in the TsAGI low subsonic wind tunnel T–103. This wind tunnel has an open working section and continuous type of action. The dimensions of elliptical cross section of the wind tunnel are 2.33x4.0 m. Level of the turbulence in the empty wind tunnel is about $\varepsilon = \sqrt{\Delta V^2}/V_\infty = 0,3\%$. A scheme of the T–103 wind tunnel is shown in Fig. 5.

The range of the flow velocity is from $V_\infty = 5 \text{ m/s}$ up to $V_\infty = 70 \text{ m/s}$. Dynamic tests are performed usually at $30 \div 50 \text{ m/s}$, so the Reynolds number is about $Re = \frac{V_\infty c}{\nu} \approx 10^6$ for the model with the chord around 1 m.

The dynamic experimental setup is mounted on a special platform which is installed on the rotating floor of the wind tunnel working section (turntable). With the rotation of the turntable the mean angle of attack or sideslip can be changed in dependency of the aerodynamic model orientation.

9.4 DYNAMIC RIGS

To investigate the dynamic effects of vortex breakdown processes on delta wing unsteady aerodynamic a large amplitude forced oscillation rig was used. The general view of the large amplitude pitch oscillation rig is shown in Fig. 6. The photo of the 70° delta wing model on the rig is shown also. The angle of attack variation is approximately sinusoidal. The mean angle of attack can be varied in the range $\alpha_0 = -10^\circ \div 36^\circ$. The range of oscillations amplitude variations is $\Delta \alpha = 5^\circ \div 26^\circ$. The frequency of oscillations can be varied from $f = 0.2 \text{ Hz}$ up to 1.5 Hz . The rotation of the wind tunnel working section turntable permits investigations for sideslip angles from -90° up to $+20^\circ$. With the use of this setup conventional steady experiments can be executed also. In addition slow sweep motion experiments with continuous variation of angle of attack at constant rate of order 2–4 degrees per second are possible with the use of this rig.

The unsteady aerodynamics of delta wings under consideration was also investigated with the use of a small amplitude pitch forced oscillation rig. The scheme of the rig and corresponding photo is shown in Fig. 7. The variation of mean angle of attack in this case is reached by the rotation of wind tunnel turntable in the range from -90° up to $+90^\circ$. The possible oscillations amplitudes are $\Delta \alpha = 3^\circ$ and $\Delta \alpha = 5^\circ$. The frequency of oscillations can be varied from 0.5 Hz up to 3.0 Hz . During the experiments with this rig the unsteady aerodynamic characteristic variation can be studied and aerodynamic damping derivatives can be measured. After the data processing the in-phase aerodynamic derivatives C_{N_α} , C_{m_α} and out-of-phase derivatives $C_{N_{q+\dot{\alpha}}}$, $C_{m_{q+\dot{\alpha}}}$ can be obtained.

The same five component (no axial force component) internal strain gauge balance is used for the measurements of forces and moments acting on the model during unsteady motion.

9.5 DATA PROCESSING TECHNIQUE

During dynamic data processing to obtain the pure aerodynamic loads the inertia, centrifugal and gravitational components have to be excluded. Using mathematical model of forces and moments acting on the strain gauge balance during oscillations in the absence of wind tunnel flow ("wind off" conditions) one can obtain with the use of linear regression technique the unknown values of model weight, the real position of model center of gravity, and the damping coefficient in still air. During "wind on" data processing these values are used to obtain the pure aerodynamic dependencies of forces and moments acting on the model.

The examples of measured data for angle of attack and vertical force variations during large amplitude pitch oscillations are shown in the upper plots of Fig. 8. In the lower plots the corresponding 16 periods of oscillation frequency spectrum are shown for an experiment with large amplitude forced oscillations in pitch with amplitude 25° and frequency $f = 0.25$ Hz. The mean angle of attack was $\alpha_0 = 31^\circ$. The similar data for angle of attack increment and pitching moment during small amplitude oscillations are shown in Fig. 9. It was the small amplitude forced oscillations with amplitude 3° and frequency $f = 1$ Hz. From spectrum data it is seen that first eigen frequency of elastic oscillations of the model on the sting is about 8 Hz. To remove the noise the digital low pass Butterworth filter [13] with cut-off frequency $f_0 = 4$ Hz was used. The results of digital filter data processing are shown in Fig. 8 and Fig. 9 by dashed lines.

It is seen that after digital filtering dependencies of aerodynamic signals are rather regular but some fluctuations are still observed. To remove these fluctuations the mean dependencies for one period of oscillations should be obtained from a number of measured periods. In Fig. 10 the instantaneous dependency of vertical force coefficient upon angle of attack for a number of periods of large oscillations is shown by thin solid line. The corresponding mean dependency for one period is shown by thick dashed line. By the line with the markers the respective steady state dependency is shown. It is seen that the maximum deviation of instantaneous dependency from the mean one is rather small.

In the case of small amplitude forced oscillations experiments during data processing not only mean unsteady aerodynamic coefficients but the aerodynamic damping derivatives should be obtained also. The mathematical model of linear variation of pitching moment coefficient during small amplitude pitch oscillations at a given mean angle of attack can be expressed in a usual manner

$$C_m(t) = C_{m_0} + C_{m_\alpha} \Delta\alpha(t) + C_{m_{q+\dot{\alpha}}} \frac{c}{2V_\infty} \dot{\alpha}(t). \quad (1)$$

This is a typical equation for a linear regression model [14] with the dependent variable the time-varying pitching moment $C_m(t)$. Independent arguments are the instantaneous values of angle of attack increment $\Delta\alpha(t)$ and its rate of change $\dot{\alpha}(t)$. The unknown parameters of the regression are mean value C_{m_0} and in-phase C_{m_α} and out-of-phase $C_{m_{q+\dot{\alpha}}}$ derivatives. For other aerodynamic loads the mathematical models can be expressed in the same way.

So the problem of finding unknown parameters of the regression is the problem of mathematical statistics. To use the available technique it is necessary only to calculate $\dot{\alpha}(t)$. But after the application of digital filtering technique the process $\Delta\alpha(t)$ is rather smooth and calculation of the derivative with the use, for example, of local polynomials of best approximation is straight forward. The example of out-of-phase derivatives dependencies upon angle of attack obtained for various frequencies of small amplitude oscillations are shown in Fig. 11. It is seen that at low incidence there is no dependency upon the oscillations frequency. At high incidence this dependency is rather considerable.

9.6 SOME COMPARISONS WITH PUBLISHED DATA IN STEADY CASES

It is necessary to present some comparisons of TsAGI results with results for similar delta wings available in published articles. The most suitable wing for comparison is the 65° delta wing. The configuration of this model with additional center body was very close to the widely studied American/Canadian 65° delta wing model. In paper [10] static normal force and pitching moment data were presented besides with ramp and hold data for this wing. The experiments were conducted in the U.S. Air Force Subsonic Aerodynamic Research Laboratory (SARL) wind tunnel. This wind tunnel is an open circuit facility with very high (36 to 1) contraction ratio. The working section is closed with octagonal cross section (7 ft width and 10 ft height).

In Fig. 12 the digitized data for normal force and pitching moment coefficients from paper [10] are compared with the steady and slow sweep motion data from TsAGI wind tunnel. The American data are shown by circles. The conventional steady TsAGI data are shown by crosses. The data from slow sweep motion experiments are shown by solid lines (increasing incidence and decreasing incidence). For angles of attack lower than 30° the coincidence of all data for normal force coefficient are rather good. At higher angles of attack where vortex breakdown exerts influence on the aerodynamic characteristics some quantitative discrepancy is evident. Qualitatively the data are rather similar. The positions of all critical states did not changed. One evident reason for such discrepancy is the various types of wind tunnel working sections (closed and open). Another possible reason is turbulence level of wind tunnel. The SARL wind tunnel is known as a facility with an extremely low level of turbulence. TsAGI's low subsonic wind tunnel turbulence properties are higher since it is a closed circuit facility.

Similar data for the pitching moment coefficient are shown in Fig. 12 also. Unfortunately in the paper [10] the position of the internal strain gauge balance reference point along the wing chord was not indicated. In another paper [12] which also deals with experimental investigations of the same model in SARL wind tunnel, the lateral results were obtained for C.G. position (balance reference point) at 35% of MAC. So it was accepted that the results of paper [10] were obtained for the same position of C.G. The TsAGI results for pitching moment coefficient obtained for C.G. position at 50% of MAC were converted to the C.G. position at 35% of MAC. The results of conversion are presented in comparison with the results of [10]. Also, static data and slow sweep motion results for increasing and decreasing of incidence are shown. As in the case of normal force coefficient at low angles of attack there is a good qualitative agreement of various data. At angles of attack higher than $\alpha = 45^\circ$ there is a discrepancy which could be attributed to the influence of various wind tunnels.

Comparison of 65° delta wing rolling moment dependencies upon bank angle for various incidences are shown in Fig. 13, with the digitized data from paper [10] shown by markers. They are presented in the plane σ (sting inclination angle) and ϕ (roll angle). Variation of ϕ at constant σ results in variation of angle of attack α and angle of sideslip β . In symmetrical case ($\phi = \beta = 0$) $\sigma = \alpha$. TsAGI results were obtained in the plane α and β . So to compare the results 2-dimensional spline interpolation from one plane to another is needed. The results of TsAGI slow sweep data interpolation to (σ, ϕ) plane are shown by solid lines in Fig. 13.

The results for sting inclination angle $\sigma = 15.5^\circ$ upon the roll angle ϕ are very close to TsAGI data. For sting inclination angle $\sigma = 25^\circ$ it is seen that outside the region of strong nonlinearities ($\phi > 10^\circ$) the current data are similar to the results of [12]. Inside the region of strong nonlinearity ($\phi < 10^\circ$) there is some discrepancy in various experimental data. There is the obvious hysteresis obtained during increasing and decreasing sideslip TsAGI experiments. Boundaries of the hysteresis precisely coincide with the bank angles of crossing critical states due to windward and leeward vortices breakdown. Flutter dependencies between the critical states for TsAGI data could be attributed also to the influence of various wind tunnels. One additional possible reason for discrepancy is the errors of interpolation. The results of comparisons for $\sigma = 30^\circ$ and $\sigma = 35.4^\circ$ are mainly the same.

9.7 SOME COMPARISONS IN DYNAMIC CASES

To verify TsAGI dynamic data a special 70° delta wing aerodynamic model was manufactured at DERA. The shape and sizes of the model were the same as the TsAGI large 70° delta wing model with rounded leading edges. Investigations of the model unsteady aerodynamics using forced oscillation rig in the 13 ft by 9 ft low speed DERA wind tunnel at Bedford give results rather close to that of TsAGI. For example the comparisons of unsteady aerodynamic derivatives due to pitch oscillations obtained with the use of various rig and wind tunnels are shown in Fig. 14. The scheme of the DERA forced oscillation rig is shown in Fig. 15. The maximum angle of attack for DERA oscillation rig is about 40°.

9.8 STEADY EXPERIMENTAL RESULTS

The investigation of unsteady aerodynamics as a rule starts from the measurement of steady aerodynamic characteristics. In this section the steady aerodynamic longitudinal characteristics of all 70° and 65° delta wing models will be presented. The test matrix of the performed steady tests for symmetrical flow case is shown in Table 1.

Table 1: Steady Experiments Test Matrix

Delta wing	S (m ²)	V _∞ (m/s)	Range of α	β
70° rounded l.e.	0,4224	25	-20°–50°	0°
70° rounded l.e.	0,200	40	0°–60°	0°
70° sharp l.e.	0,200	40	0°–60°	0°
65° without body	0,200	40	0°–60°	0°
65° with body	0,200	40	0°–60°	0°

In Fig. 16 the experimental data for large and small 70° delta wing models with rounded leading edges are presented. The data for model with reference area $S=0,4224 \text{ m}^2$ were obtained for wind tunnel speed $V_\infty = 25 \text{ m/s}$. The corresponding data for the similar model with reference area $S=0,2 \text{ m}^2$ were obtained for wind tunnel speed $V_\infty = 40 \text{ m/s}$, so the Reynolds numbers in both experiments were rather close. These velocities were chosen so that maximum vertical force acting on the model could not exceed 50 kg due to internal strain gauge balance limits. This results in good coincidence of experimental data for various models. For the small 70° delta wing model the experiment was repeated three times. One experiment was executed before the dynamic tests. The second experiment was performed with smaller steps in angle of attack in the region of vortex breakdown occur above the wing. The last experiment was executed after the dynamic tests. It is seen that repeatability of the results is rather good.

In Fig. 17 the steady experimental data for small 70° delta wing models with rounded and sharp leading edges are shown. As was expected for the model with sharp leading edges the vortices are stronger which results in increased normal force. The second consequence is vortex breakdown on lower angles of attack.

In Fig. 18 the steady dependencies of normal force and pitching moment coefficients are presented for 65° delta wing model with and without additional center body. It is seen that at low angles of attack the presence of center body has no effect on aerodynamic characteristics of the model, but in the region of vortex breakdown the presence of the additional body results in a reduction of normal force.

9.9 LARGE AMPLITUDE PITCH OSCILLATIONS EXPERIMENTAL RESULTS

Numerous studies have documented the dynamic hysteresis and overshoot characteristics exhibited by delta wings undergoing large amplitude pitch oscillations at vortex breakdown regimes. The reason of the phenomenon is the dynamic time lag in vortex breakdown development in comparison with steady conditions. During incidence increase this dynamic time lag in vortex breakdown starts at higher angles of attack. During incidence decrease vortex flow without breakdown is developed at lower angles of attack. Systematic investigations of this effect were undertaken using various delta wing models. The test matrix of the large amplitude pitch oscillation experiments for symmetrical case $\beta = 0$ is shown in Table 2.

Table 2: Large Amplitude Pitch Oscillations Test Matrix

Delta wing	S (m ²)	V _∞ (m/s)	α_0	$\Delta\alpha$	f (Hz)
70° rounded l.e.	0,4224	25	15°	15°	0.4, 0.8, 1.2, 1.6
		25	30°	25°	0.2, 0.4, 0.8
70° rounded l.e.	0,200	40	21°, 30°, 40°	10°	0.5, 1.0, 1.5
		40	21°, 30°, 40°	20°	0.5, 1.0, 1.2
70° sharp l.e.	0,200	40	21°, 30°, 40°	10°	0.5, 1.0, 1.5
		40	21°, 30°, 40°	20°	0.5, 1.0, 1.2
65° with and without body	0,200	40	21°, 30°, 40°	10°	0.5, 1.0, 1.5
		40	21°, 30°, 40°	20°	0.5, 1.0, 1.2

The obtained experimental results for the various delta wings model are qualitatively the same. In Fig. 19 the example of experimental data obtained for large 70° delta wing model during oscillations with various frequencies are shown. These results relate to the dynamic motion at angles of attack where vortex breakdown above the wing does not appear. Here the deviation of dynamic data from the steady one is linear and not large. The aerodynamic responses could be simulated with the use of an unsteady aerodynamics mathematical model using the unsteady derivative concept.

In Fig. 20 the corresponding dynamic results are shown for the motion in the incidence region where the vortex breakdown is developed. It is seen that here the vortex breakdown time lag effects are very considerable and nonlinear. It is not possible to describe the aerodynamic responses with the use of the traditional mathematical model of unsteady aerodynamics based on the derivative concept.

9.10 SMALL AMPLITUDE PITCH OSCILLATIONS EXPERIMENTAL RESULTS

Conventional small amplitude pitch oscillation experiments to obtain the unsteady aerodynamic derivatives for all delta wing models were also executed. The corresponding test matrix is presented in Table 3.

Table 3: Small Amplitude Pitch Oscillations Test Matrix

Delta wing	S (m ²)	V _∞ (m/s)	α_0	$\Delta\alpha$	f (Hz)
70° rounded l.e.	0,4224	25	0–60°	3°	0.5, 1.0, 1.4
70° rounded l.e.	0,200	40	0–60°	3°	0.5, 1.0, 1.5
70° sharp l.e.	0,200	40	0–60°	3°	0.5, 1.0, 1.5
65° with and without body	0,200	40	0–60°	3°	0.5, 1.0, 1.5

The unsteady aerodynamic characteristics obtained during these tests for large 70° delta wing model for two frequencies of oscillations are shown in Fig. 21. The corresponding steady results are shown by thick solid lines. The unsteady dependencies for various mean angles of attack are shown by thin solid lines. It is seen also that for angles of attack with unburst vortex flow the dynamic data are very close to the steady ones. At high incidence with vortex breakdown the dynamic properties of the flow becomes considerable.

In Fig. 22 the in-phase and out-of-phase derivatives of vertical force coefficient obtained during small amplitude pitch oscillations with various frequencies are shown. The results for the small 70° delta wing model with rounded and sharp leading edges are presented. Corresponding data for pitching moment coefficient are shown in Fig. 23. The influence of leading edge shape on unsteady aerodynamic derivatives is correlated with its influence on steady aerodynamic characteristics. It is seen also that at low angles of attack the aerodynamic derivatives do not depend upon the oscillation frequency. At high incidence where vortex breakdown above the wing upper surface is developed the strong nonlinear dependency of both in-phase and out-of-phase derivatives upon the oscillations frequency is evident. This fact prevents the use of the mathematical model of type (1) to describe the unsteady aerodynamic response for wing arbitrary motion at high angles of attack.

9.11 CONCLUDING REMARKS

The presented experimental data for large and small amplitude forced oscillations of delta wings in the case of zero sideslip demonstrate the importance of dynamic interaction between wing motion and vortex burst development. Similar nonlinear and time lag effects are seen in other types of executed wind tunnel dynamic experiments: plunge oscillations, oscillatory coning motion, free-to-roll experiments etc. These effects should be taken into account in flight dynamics simulation at high incidence.

9.12 ACKNOWLEDGEMENT

The performed delta wings unsteady aerodynamics experimental investigations was partially supported by QinetiQ (previously DERA, UK).

9.13 REFERENCES

- [1] N. Abramov, M. Goman, A. Khrabrov, K. Kolinko, Simple Wings Unsteady Aerodynamics at High Angles of Attack: Experimental and Modeling Results. AIAA Atmospheric Flight Mechanics Conference, Portland OR, USA, 9–11 August 1999, AIAA Paper 99–4013.
- [2] M. Goman, D. Greenwell, A. Khrabrov, The Characteristic Time Constants Approach for Mathematical Modeling of High Angle of Attack Aerodynamics. Proceedings of 22 nd International

Congress of Aeronautical Sciences (ICAS 2000), Harrogate, UK, 27 August — 1 September, 2000, pp. 223.1–223.12.

- [3] N. Abramov, M. Goman, D. Greenwell, A. Khrabrov, Two-Step Linear regression Method for Identification of High Incidence Unsteady Aerodynamic Model. AIAA Atmospheric Flight Mechanics Conference, Montreal, Canada, 6–9 August 2001, AIAA Paper 2001–4080.
- [4] A.H. Hsia, J.H. Myatt, J. Jenkins, Nonlinear and Unsteady Aerodynamic Responses of a Rolling 65° Delta Wing. AIAA Paper 93–3682, 1993.
- [5] X.Z. Huang, E.S. Hanff, Prediction of Normal Force on a Delta Wing Rolling at High Incidence. AIAA Paper 93–3686, 1994.
- [6] X.Z. Huang, E.S. Hanff, J. Jenkins, G. Addington, Leading-Edge Vortex Behaviour on a 65° Delta Wing Oscillating in Roll. AIAA Paper 94–3507, 1994.
- [7] L.E. Ericsson, E.S. Hanff, Unique High-Alpha Roll Dynamics of a Sharp-Edged 65° Delta Wing. J. Aircraft, Vol. 31, No. 3, pp. 520–525, 1994.
- [8] D.S. Grismer, J.H. Myatt, P.D. McKeehen, J.M. Buffington, Application of a Nonlinear Indicial Responce Model to a Tailless Aircraft Simulation. AIAA Paper 97–3644, 1997.
- [9] C.E. Jobe, Vortex Breakdown location over 65° Delta Wings, Empiricism and experiment. AIAA Paper 98–2526, 1998.
- [10] J.H. Myatt, Multiple Time Scale Effects for Pitching 65° Delta Wing. AIAA Paper 98–4354, 1998.
- [11] G.A. Addington, R.C. Nelson, The Correspondence between Flow Field Structure and Critical States on a 65-degree Delta Wing. AIAA Paper 98–4520, 1998.
- [12] X.Z. Huang, E.S. Hanff, Non-Linear Rolling Stability of a 65° Delta Wing Model at High Incidence. AIAA Paper 99–4102, 1999.
- [13] R.K. Otnes, L. Enochson, Applied time series analysis, John Wiley and Sons, 1978.
- [14] A.A. Afifi, S.P. Azen, Statistical Analysis. A computer oriented Approach, Academic press, 1979.

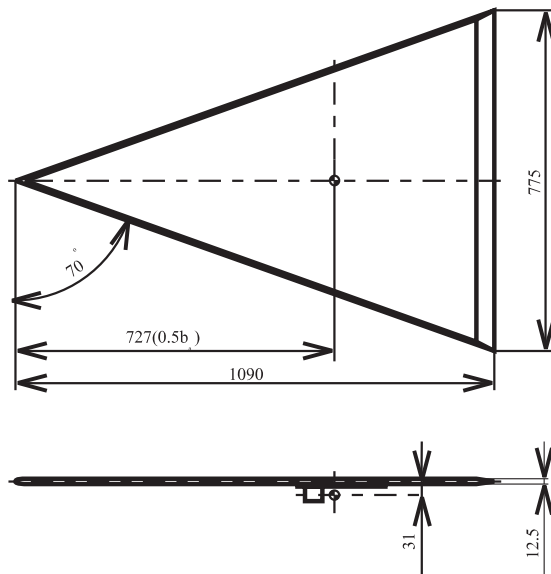


Figure 1. Large 70° delta wing model

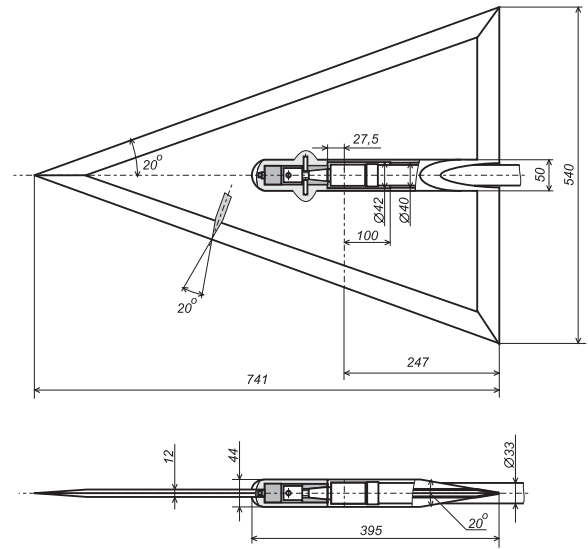


Figure 2. Small 70° delta wing model

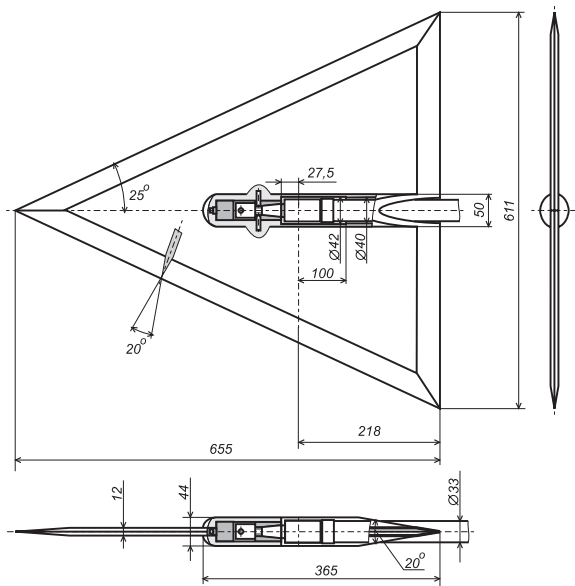


Figure 3. 65° delta wing model

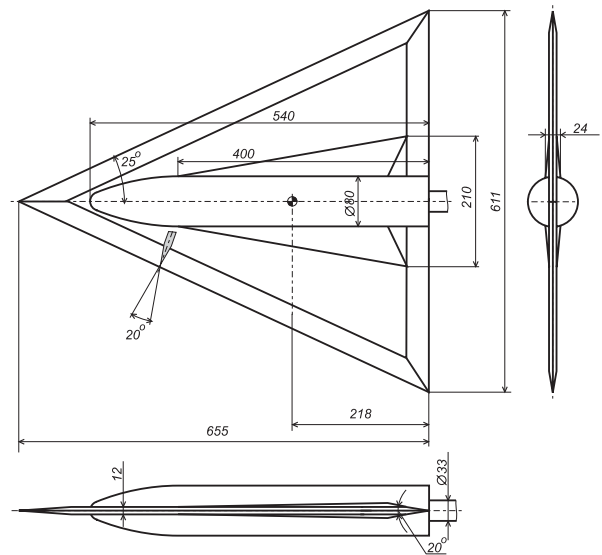


Figure 4. 65° delta wing with additional body

TsAGI 70° AND 65° DELTA WINGS TEST CASES

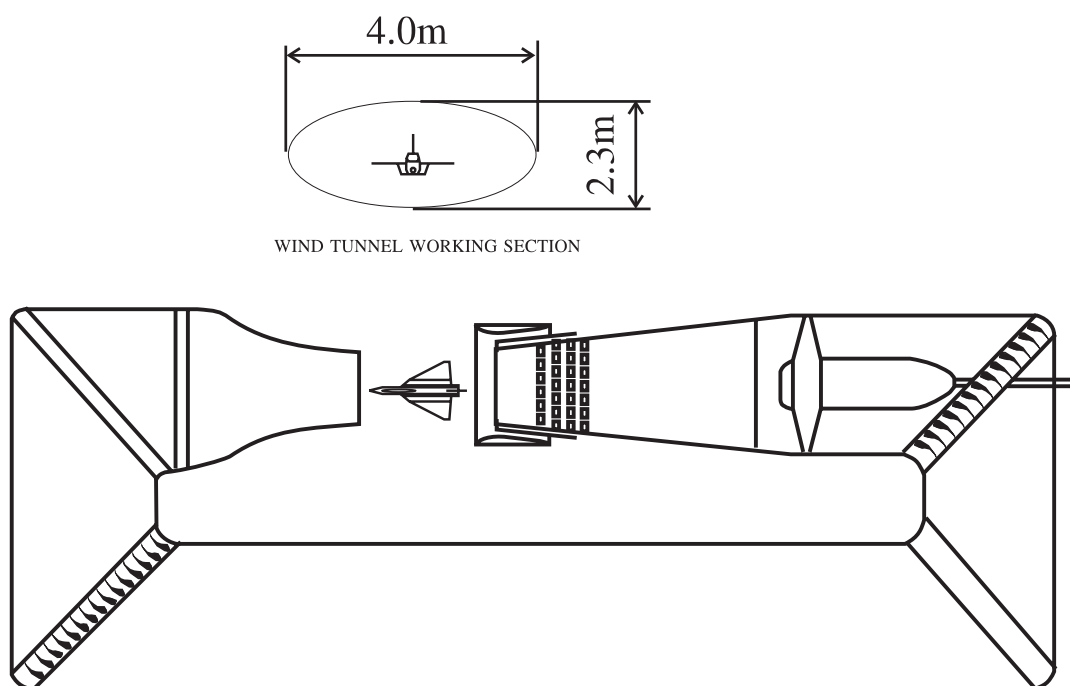


Figure 5. TsAGI low subsonic wind tunnel T-103

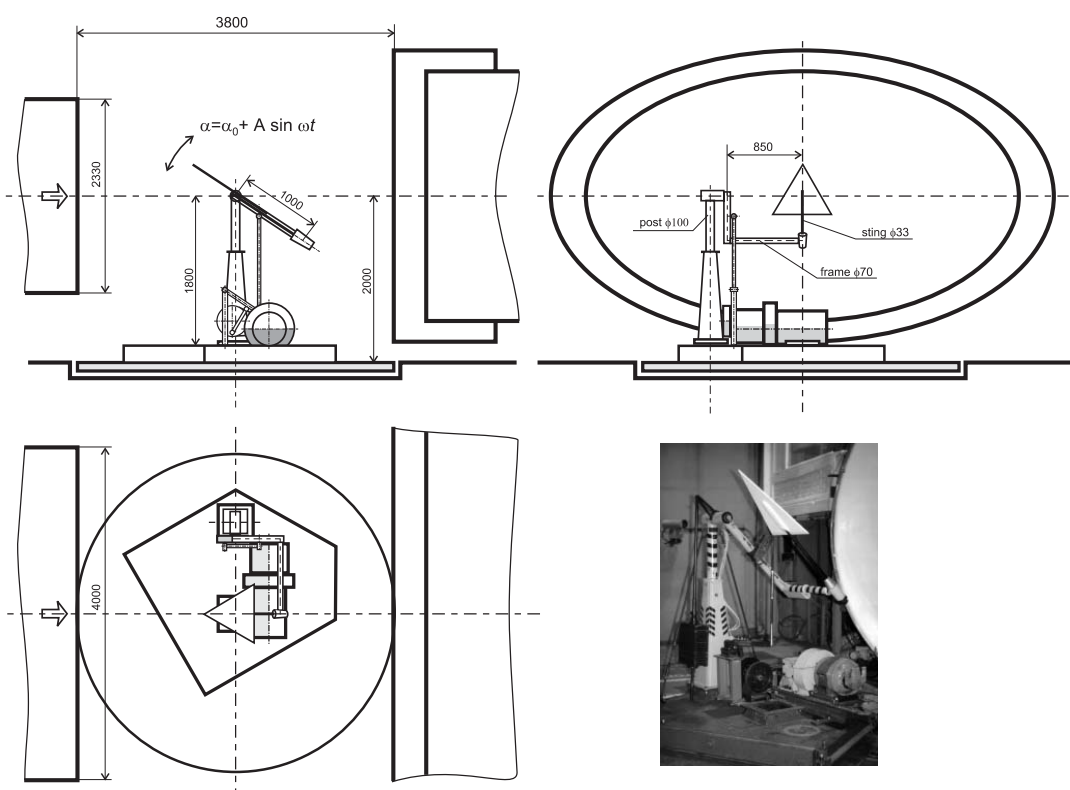


Figure 6. TsAGI large amplitude forced oscillations rig at wind tunnel T-103

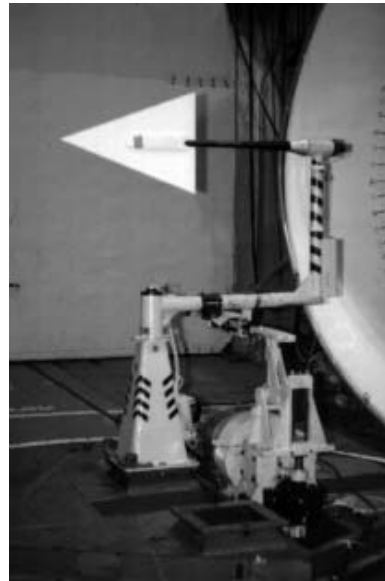
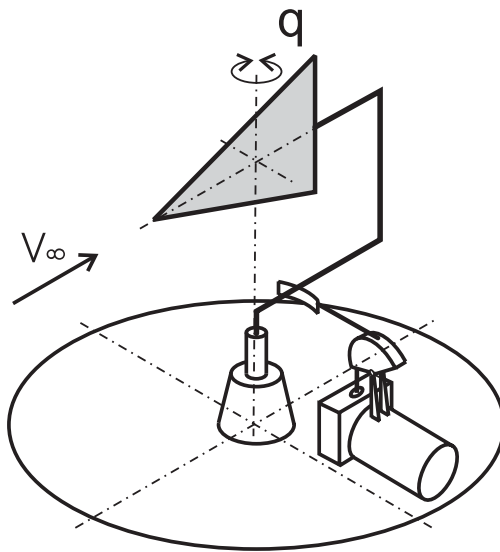


Figure 7. Small amplitude pitch forced oscillations rig

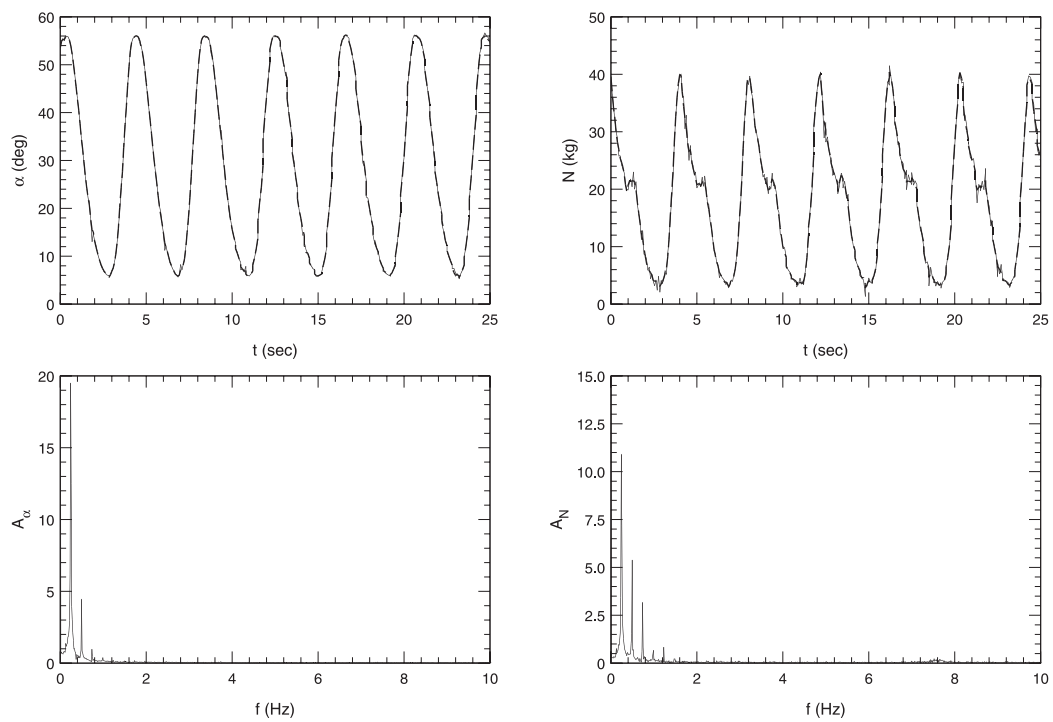


Figure 8. Example of alpha and vertical force signals during large amplitude forced oscillations

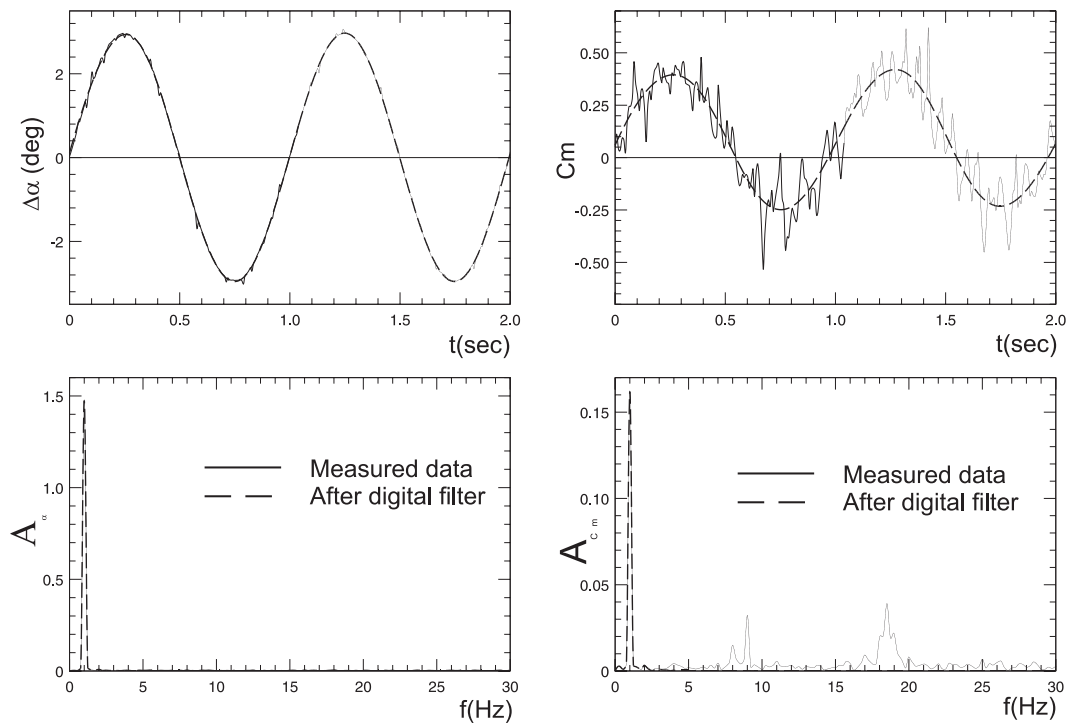


Figure 9. Example of alpha and pitching moment signals during small amplitude forced oscillations

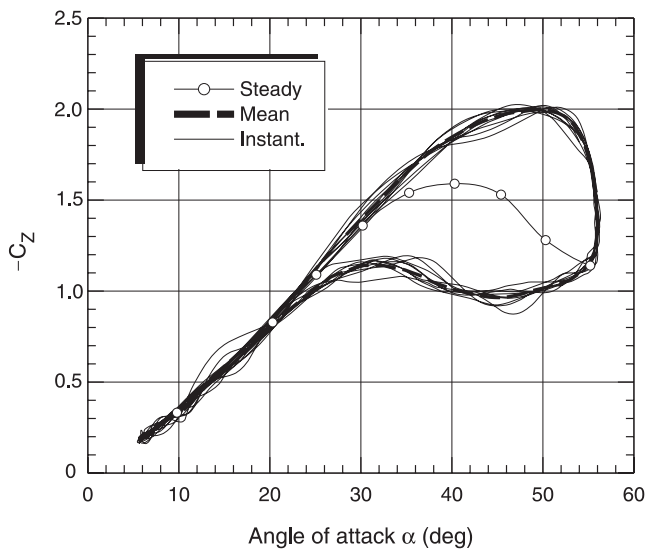


Figure 10. Example of one period averaging for large amplitude forced oscillations

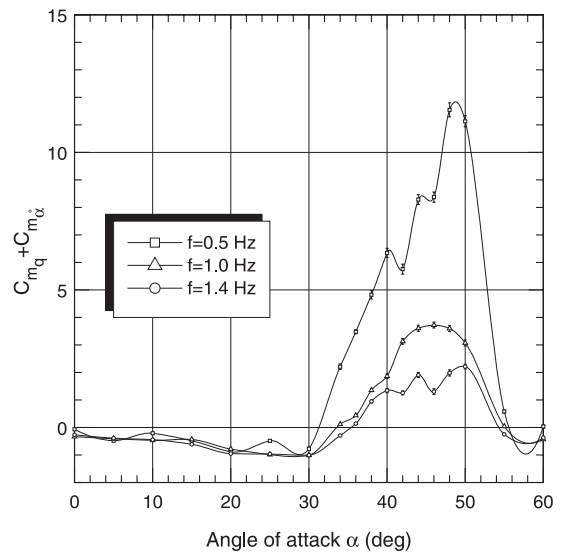


Figure 11. Example of aerodynamic damping derivatives obtained during small amplitude forced oscillations with various frequencies

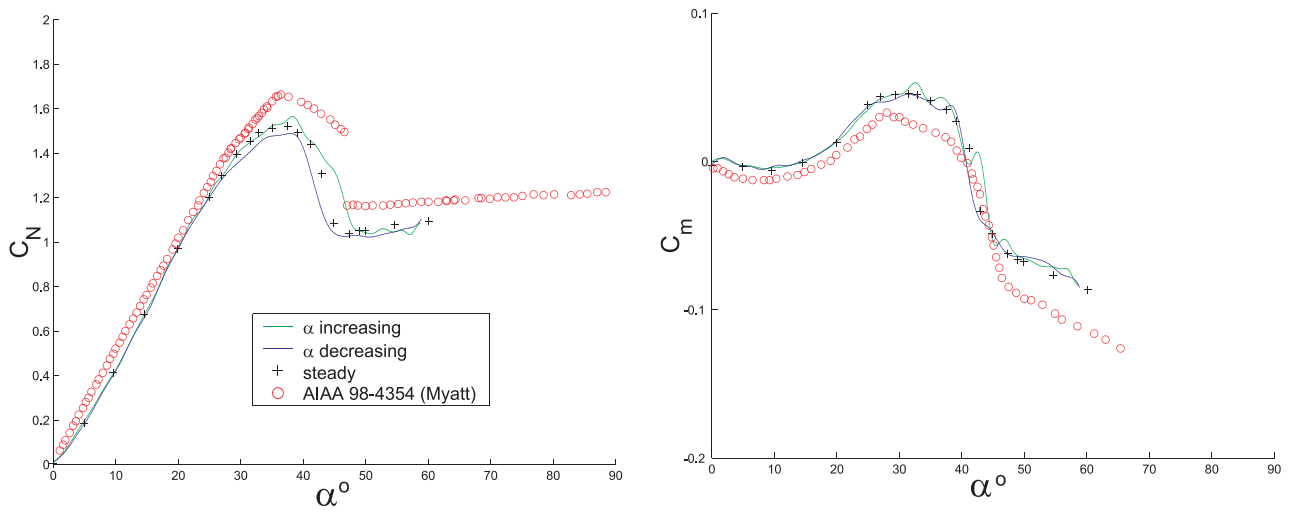


Figure 12. Comparison of 65° delta wing longitudinal aerodynamic characteristics

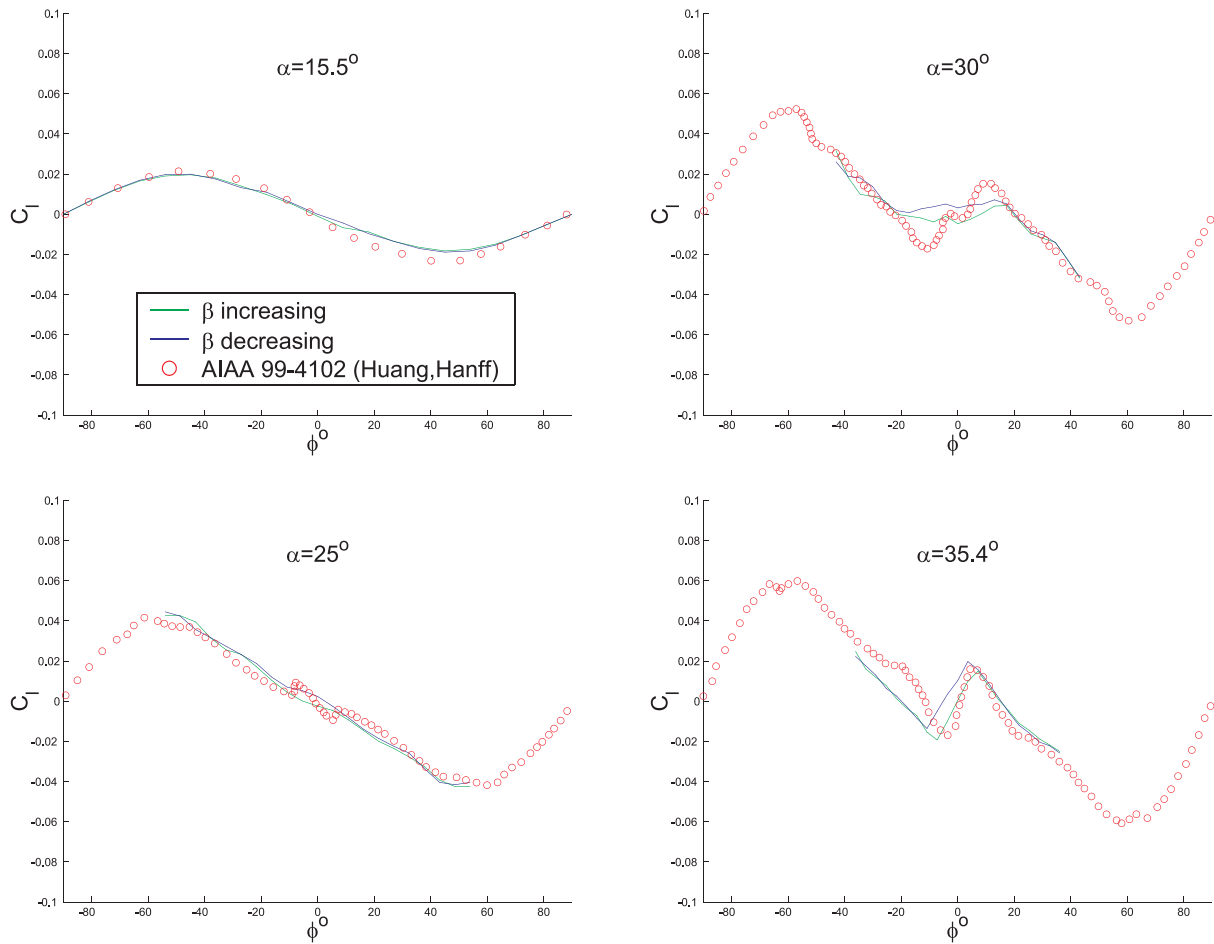


Figure 13. Comparison of 65° delta wing rolling moment dependencies upon bank angle for various incidences

TsAGI 70° AND 65° DELTA WINGS TEST CASES

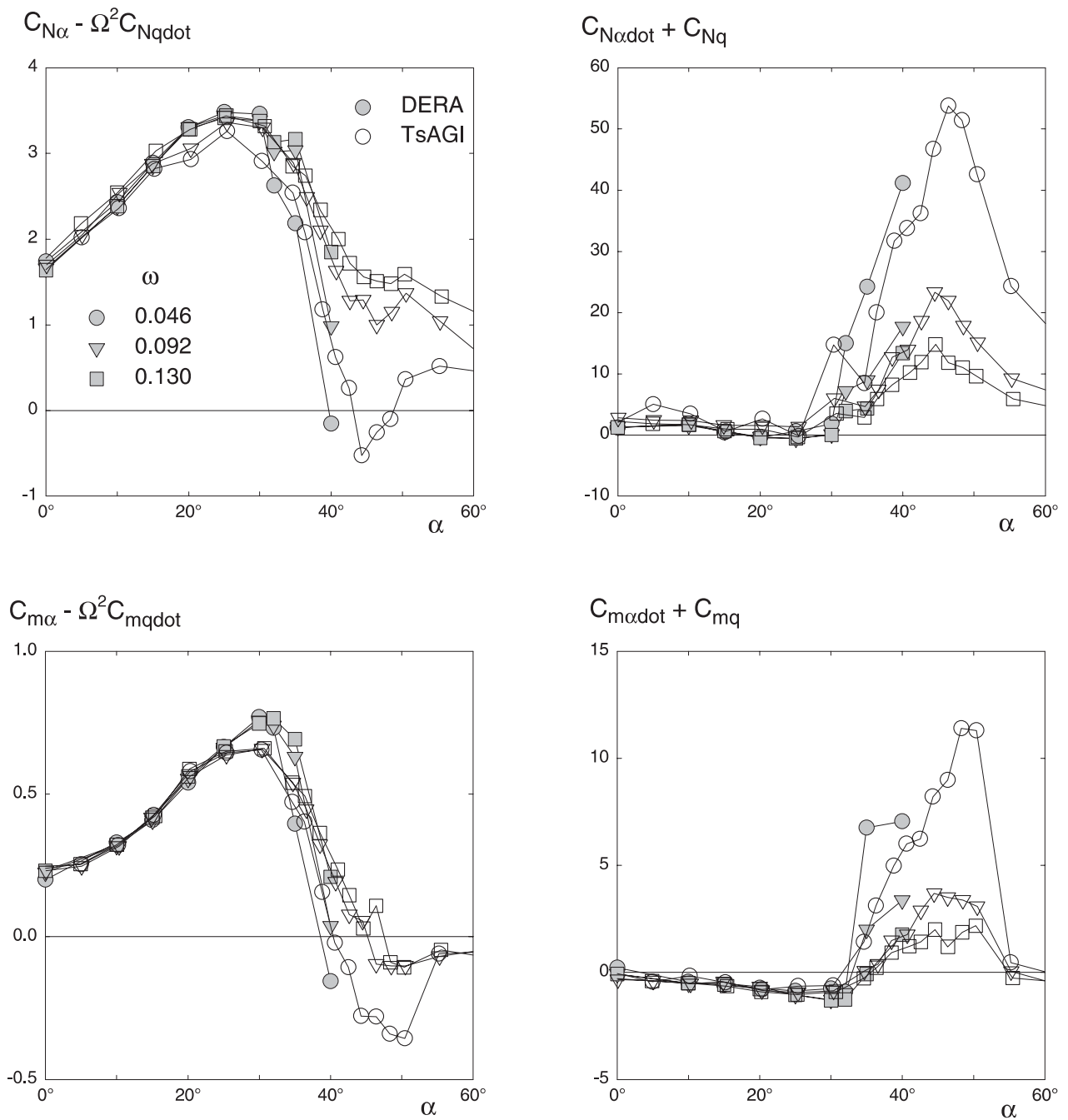


Figure 14. Comparison of 70° delta wing unsteady aerodynamic derivatives for small amplitude pitch oscillations obtained at TsAGI and DERA, Bedford

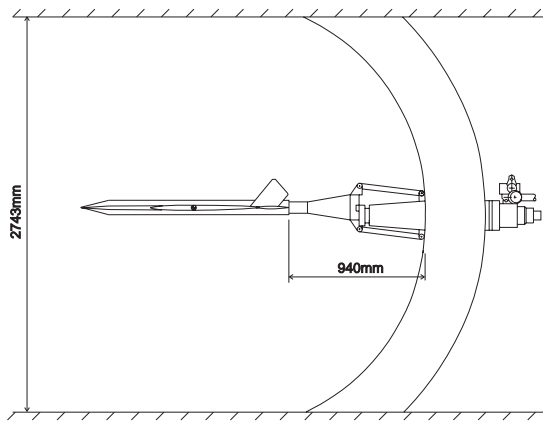


Figure 15. DERA, Bedford dynamic rig

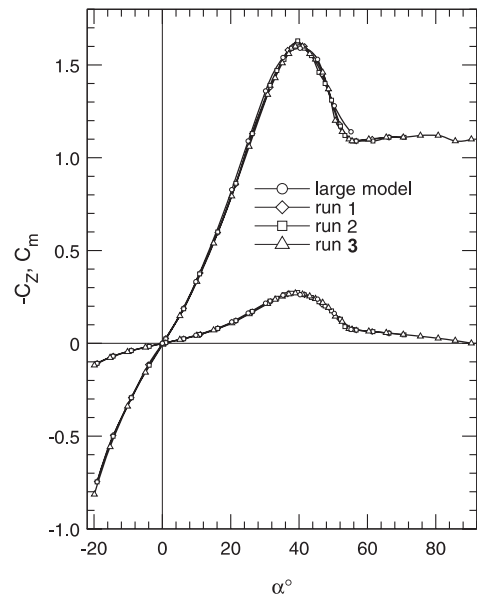


Figure 16. Comparison of rounded leading edges 70° delta wing large and small models experimental data

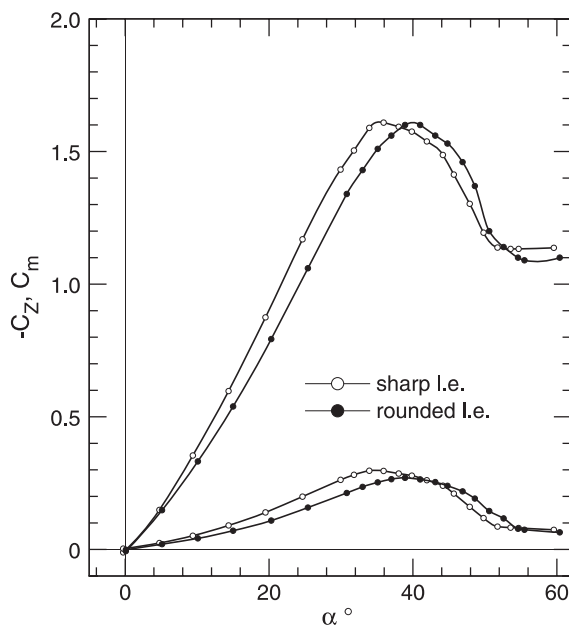


Figure 17. 70° delta wing influence of leading edges shape

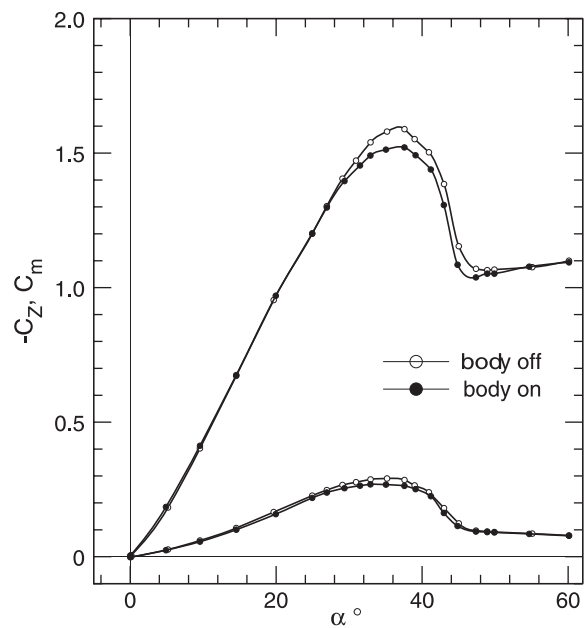


Figure 18. 65° delta wing influence of additional center body

TsAGI 70° AND 65° DELTA WINGS TEST CASES

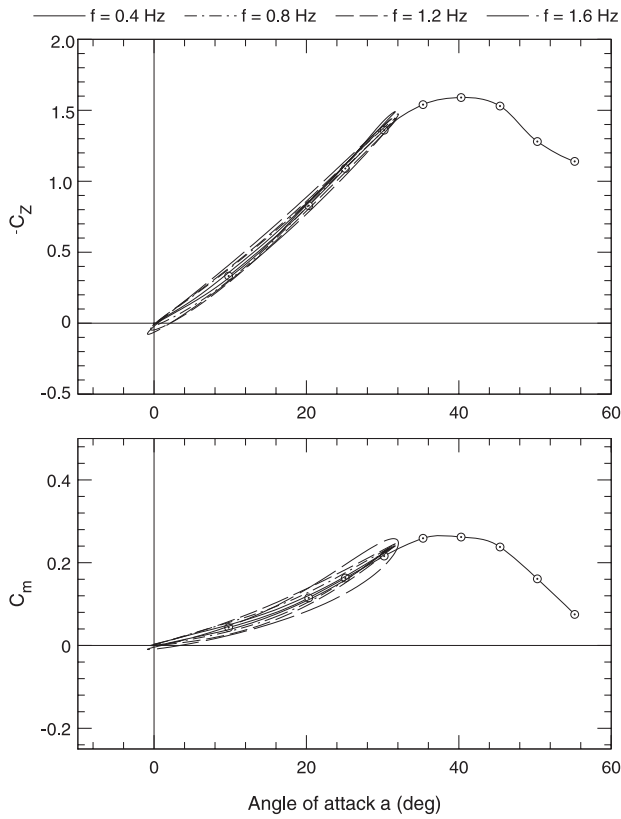


Figure 19. 70° delta wing large amplitude oscillations $\alpha_0 = 15^\circ$, $\Delta\alpha = 15^\circ$

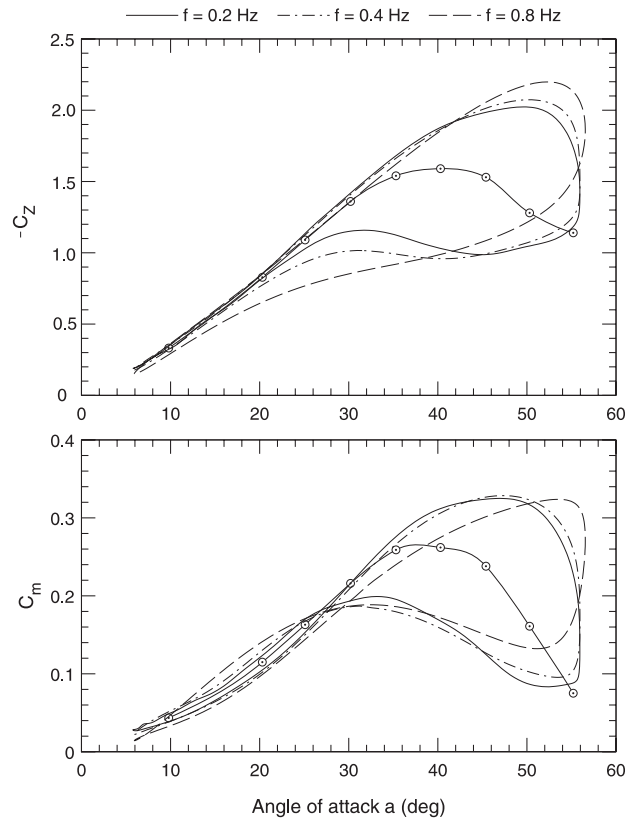


Figure 20. 70° delta wing large amplitude oscillations $\alpha_0 = 30^\circ$, $\Delta\alpha = 25^\circ$

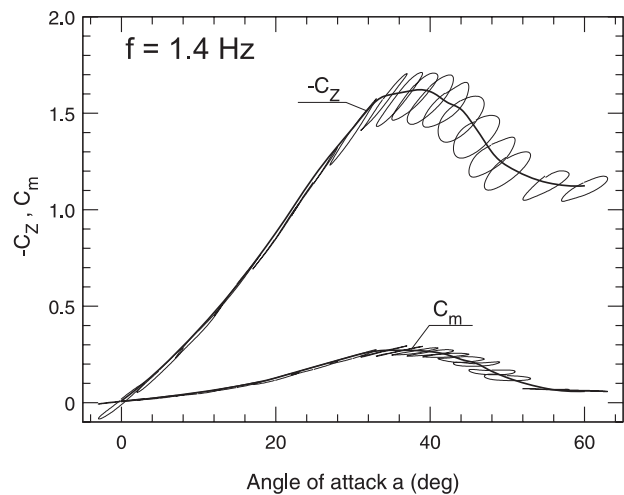
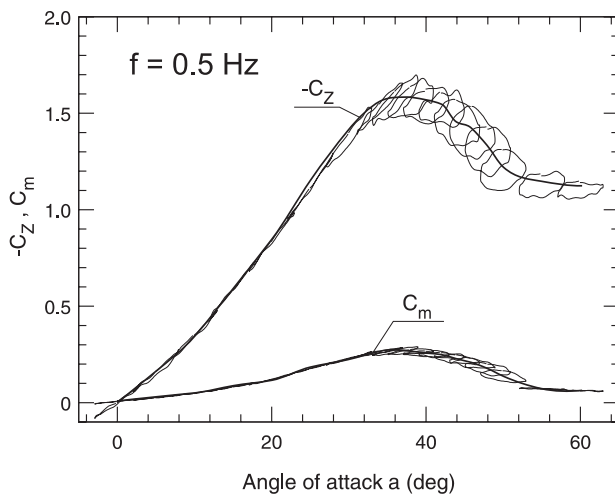


Figure 21. 70° delta wing unsteady aerodynamic loads during small amplitude pitch oscillations with various frequencies

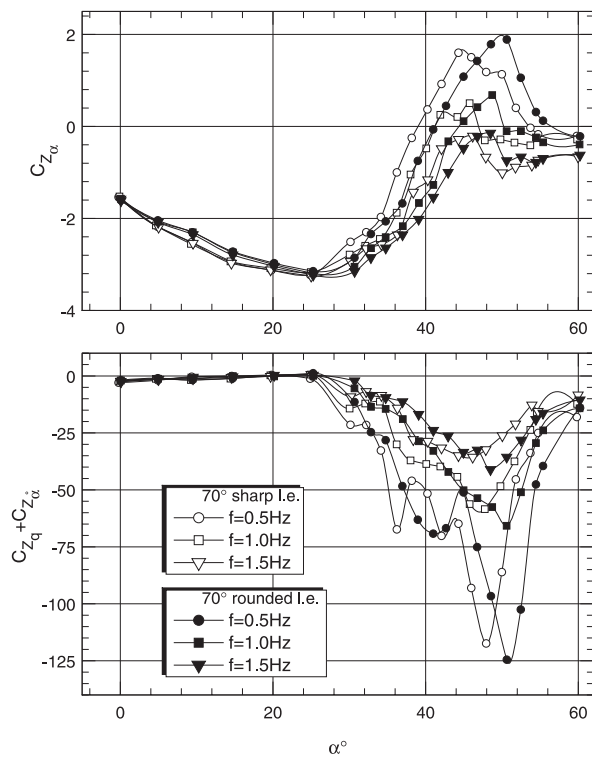


Figure 22. 70° delta wing vertical force unsteady aerodynamic derivatives

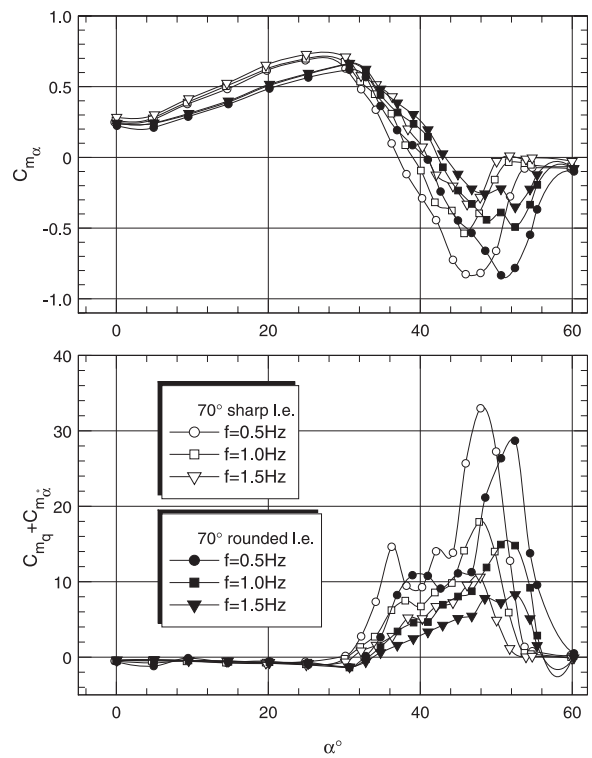


Figure 23. 70° delta wing pitching moment unsteady aerodynamic derivatives



Chapter 10 –

Experimental Investigation of Vortex Dynamics on a 65° Delta Wing

G. Guglieri - F.B. Quagliotti

Politecnico di Torino

Dipartimento di Ingegneria Aeronautica e Spaziale

Torino - Italy

giorgio.guglieri@polito.it - fulvia.quagliotti@polito.it

Abstract

The flow structure on the upper side of a delta wing is extremely complex. At moderate angle of attack the flow field is dominated by organized vortical flow structures emanating from the leading edge. The pressure distribution created on the wing surface by these leading edge vortices causes an increment of lift, that may be a relevant percentage of the total wing lift, depending on sweep angle. Delta wing performance is conditioned, however, by a phenomenon known as vortex breakdown or vortex bursting, that appears at high angle of attack. This leads to a drastic change in the flow field which influences the trend of the aerodynamic coefficients. With the aim of giving a contribution to the understanding of the phenomenon of vortex breakdown, a 65° delta wing has been extensively tested in the low speed wind tunnel of Politecnico di Torino both in static and dynamic conditions. Many experiments have been carried out in an effort to understand the factors which can affect the breakdown by varying angle of attack, sideslip angle and Reynolds number. Flow visualizations have been performed using helium bubble tracers. This technique showed a very good capability for visualizing vortical flows and breakdown, both in static and dynamic conditions. For the static case, pressure distributions are presented, correlated to force measurements and flow visualizations, at different angles of attack and sideslip, for different flow conditions. For the dynamic case, force measurements are shown, compared with flow visualizations, for different angles of attack and for different oscillation frequencies. Finally, surface flow was also investigated in steady flow conditions by means of IR thermography in order to gain some new insights into the correlation between separation and boundary layer transition.

Nomenclature

c	root chord
C_P	pressure coefficient
c_p	specific heat capacity at constant pressure
C_l	rolling moment coefficient
$C_{l\beta}$	rolling moment derivative $\partial C_l / \partial \beta$
C_L	lift coefficient $C_L = C_Z \cos \alpha$
$C_{L\alpha}$	lift derivative $\partial C_L / \partial \alpha$
C_m	pitching moment coefficient
C_n	yawing moment coefficient
C_Y	side force coefficient
C_Z	normal force coefficient
$C_{Z\alpha}$	normal force derivative $\partial C_Z / \partial \alpha$
h	convective heat transfer coefficient
K	reduced frequency ($\omega c / U_o$)
Re	Reynolds number (reference length: c)
s	wing semispan
S	wing area
St	Stanton number
t	time
TPI	Politecnico di Torino
U_o	free stream velocity
U_x	vortex breakdown propagation speed
x	longitudinal coordinate (chordwise with origin at wing apex)
y	lateral coordinate (spanwise)
α	angle of attack ($\alpha = \theta$)
α_m	mean angle of attack
β	sideslip angle ($\beta = -\psi$)
Δ	increment
λ	wing aspect ratio ($\lambda = b^2/S$)
ω	oscillation frequency
θ	pitch angle (body axes)
ψ	yaw angle (body axes)
ρ	air density
l	leeward (subscript)
max	maximum (subscript)
min	minimum (subscript)
w	windward (subscript)

10.1 Introduction

Combat aircraft have been historically, as well as currently, expected to be controllable within their manoeuvre envelopes. At the extremes of the envelope an alteration of flow characteristics may occur with its attendant dual impact of lift loss and the possibility of aircraft controllability being compromised [1]. This is the reason of the development of experimental and CFD studies concerning vortical flows on delta wings.

As regards these particular slender wings, at moderate angle of attack the leeward flow field is dominated by highly organized vortical flow structures created by the separation of the boundary layer at the leading edge. The free shear layer then rolls up into a pair of primary vortices, one either side of the apex, the shear layer becoming bigger the further it gets from the leading edge. The primary vortex induces a spanwise flow velocity which can then separate again to form a secondary vortex, below and outboard of the primary.

It has been suggested that the primary vortex can be divided into three separate regions [2]: free shear layer, rotational core and viscous subcore. The free shear layer is the medium by which vorticity is diffused from the leading edge into the rotational core (approx. 30% of the wing semispan). The viscous subcore (5% of the wing semispan) is the centre of the vortex and rotates as a solid body. Note that the gradients of the local flow parameters within this core are very high.

From pressure distributions over a delta wing surface, correlated with flow visualizations, it can be seen that large suction peaks occur underneath the leading edge vortices, contributing the so-called 'vortex lift increment' to the overall lift. Each suction peak decreases with distance along the root chord. But, downstream, vorticity is added by the shear layer from the leading edge. Hence, the vortex grows and acts over a larger percentage of the wingspan. Therefore, the shape of the suction peak can be related with vortex strength and vortex core height above wing surface [3].

The vortex occurring on the suction side of a delta wing is stable for moderate angle of attack. The stability can be attributed to the balance [4] of vorticity diffused from the leading edge and vorticity convected downstream by the component of velocity tangential to the leading edge. When the balance of these two factors is disrupted, the flowfield is severely affected, resulting in a breakdown of the organized vortical structure.

Therefore, when the angle of attack increases, the vortex breakdown phenomenon appears, consisting of an abrupt expansion of the vortex itself. It is characterized by a decrease of axial and circumferential velocity, an increase in vortex diameter and a dissipation of turbulence energy. Both the pressure distributions over the wing surface and the shape of the suction peaks are altered [3].

As the angle of attack increases, the breakdown moves up the wing surface until it reaches the apex of the wing. At this point complete separation occurs.

This behaviour is evident when the primary delta wing vortices are marked by means of tracers during wind tunnel experiments: the vortex appears to break and the marked core increases in diameter, suddenly breaking into turbulent swirling flow. Note that the core bursting on delta wings is not always exactly the same, as spiral and bubble vortex breakdown modes are observed.

When the spiral mode occurs, the core flow appears to decelerate and an abrupt kink occurs, where the axial filament is deflected into a spiral configuration. The flow then begins to spiral downstream,

about an expanding zone of stagnant fluid. Eventually the filaments break up.

In the case of a bubble breakdown, the axial filaments also appear to decelerate and reach a stagnation point. However, at this point, the flow expands around a recirculating body of fluid in an axisymmetric manner. A wake then forms downstream prior to the break up of the filaments.

Note that the bubble mode appears infrequently and for short durations on delta wings. Only the spiral mode breakdown was observed during the research reported here. Many theories [5] and explanations have been suggested for the prediction of vortex breakdown location [6], but none of them has been generally agreed, even if a widely accepted criterion for breakdown is the stagnation of core flow.

In dynamic regimes, analysis of the delta wing characteristics becomes even more difficult, due to the time dependence of motion variables and aerodynamic reactions. During oscillatory motions the wing vortices change their strength and position as a function of aerodynamic angles. Furthermore, the location of vortex breakdown is time-dependent and the aerodynamic reactions will not occur in phase with the wing oscillation, as a consequence of convective time lag and hysteresis [7] during the dynamic flow field evolution.

These arguments suggest that research into vortex breakdown phenomena is difficult and the formulation of a comprehensive theory will probably require the combined consideration of vortex unsteadiness, asymmetry, nonlinearity and the effect of ambient turbulence in the fluid medium [8]. Moreover, the extension of the results of theoretical predictions for vortex burst location on slender delta wings to the behaviour of aircraft vortex breakdown is still limited by the complexity of the problem. Hence, experimental data are still required for the complete understanding of delta wing vortex dynamics.

10.2 Experimental Facilities

The D3M low speed wind tunnel is a closed circuit tunnel with a circular closed test section (the diameter is 3 m). The turbulence level is 0.3 % at 50 m/s. The maximum speed is 70 m/s. See the Appendix and Refs. [11, 23, 24] for additional details concerning the experimental facilities.

The model is a 65° delta wing, with sharp leading edges (see Fig. 1). Experimental requirements constrained the design of the wing. The model has a fuselage with a semicircular section and an ogival nose, which contains the force transducers and the devices for the pressure measurements. Two different upper surfaces can be used, one of them being provided with pressure taps located on one side of the wing at constant span and root chord percentages. The second surface can be heated for the analysis of surface flow by infrared thermography [9].

The dimensions of the model are: wing semi-span $s = 396.5$ mm, root chord $c = 850$ mm, wing area $S = 0.337$ m², aspect ratio $\lambda = 1.866$, bevel angle (normal to leading edge) 30° , wing thickness 20 mm.

A specific servo-mechanical unit [10, 11] was designed in order to perform static tests and to generate the oscillatory motion of the model with respect to its centre of gravity, measured including fuselage and internal balance (Fig. 2a). A vertical strut supports the delta wing through a five-

component strain gauge balance. Model setting in sideslip is obtained by yawing the model support assuming $\alpha = \theta$ and $\beta = -\psi$.

The harmonic motion of the model is excited by a driving unit, that is placed under the floor of the test section; it is powered by a DC motor and it is linked to the pivoting balance by means of two rods located aft of the vertical strut. Setting the flywheel radius of the driving unit, it is possible to modify the pitch oscillation amplitude of the model, within a limit of 3.5° . The oscillation frequency of the model (maximum value 5 Hz) is set by the rotation speed of the DC motor.

The mean angle of attack of the model ranges from -7° to $+60^\circ$ and the angle of sideslip from -15° to $+15^\circ$.

The aerodynamic loads acting on the model were measured by a 5 component internal strain gauge balance (excluding axial force). The overall static measurement uncertainty is 0.5 % as a percentage of full-scale loads evaluated at $U_o = 40$ m/s.

Different data acquisition units were used for static and dynamic load measurements.

The static balance outputs were multiplexed and measured by a high precision integrating voltmeter, interfaced with the computer by a programmable software language simulation card.

The dynamic signals were measured with a high speed 12 bit analog-to-digital converter. Parallel sampling was obtained with a specific sample-and-hold unit. The analysis of these signals required more care because of the various electronic and structural interferences on the final results. This software is based on the Fourier analysis of the signals, which identifies the spectra of the two vectorial components of the driving torque acting on the oscillating model, both in wind-on and wind-off conditions. Only the harmonic components that were influenced by the aerodynamic behaviour of the pitching delta wing were taken into account. A time correlation between the primary oscillation and the signal acquisition was introduced using a trigger reference signal generated by the motion unit.

Static pressure measurements were carried out on the upper surface of the starboard wing. The position of the pressure taps (see Fig. 1) was defined by constant values of the parameters x/c (0.40, 0.55, 0.65, 0.78, 0.94) and y/s (0.00, 0.35, 0.50, 0.60, 0.69, 0.78). An integrated self-calibrating pressure measurement system (accuracy 0.06 % with 68.9 mbar range) was used for data acquisition and reduction.

Low speed flow visualizations were performed with the helium bubble technique. This methodology permits visualization of the flow with small soap bubbles, filled by helium, which are injected in the flow near to the model apex, with an injection pipe. As the helium specific weight is lower than air, a correct helium-soap proportion generates a bubble having a neutral buoyancy. The bubbles were made visible using a light sheet, located aft of the model support. Both in static and dynamic conditions, the flow visualizations were filmed by a Super VHS video-camera. Oscillatory vortex breakdown positions were obtained by freezing video-frames with an accuracy $\Delta x/c = 0.01$. The burst positions were estimated tracking the chordwise location where the vortex core begins to expand.

The IR thermography measurements [9] were performed in steady conditions (U_o ranges from 20 to 40 m/s and Re ranges from 1.10×10^6 to 2.2×10^6) at different angles of attack ($\alpha =$

5°, 10°, ..., 45°). Only symmetric flow conditions were considered (sideslip angle $\beta = 0^\circ$).

The effect of induced transition was investigated in a limited number of tests: a strip was placed along wing span at $x/c = 0.18$.

The model was suspended (see Fig. 2b) almost at the center of the test section in a 90° rotated position. The C-shaped sting support was able to rotate about the vertical axis (in order to vary the angle of attack α) and the motion was driven by a servo-mechanical unit placed under the floor of the test chamber. A step motor was interfaced by a digital unit with the control computer.

The upper wing surface is manufactured in polyurethane foam fixed on a layer of plywood and an iron plate used for fuselage and support connections. The top surface is made of a printed circuit board which is glued over the polyurethane foam (20 mm thickness); the circuit is used to generate, by Joule effect, a uniform heat flux on the delta wing surface, while the polyurethane layer thermally insulates the model face not exposed to the wind.

The printed circuit board is designed so as to achieve a constant heat flux boundary condition over the model surface. Therefore, the thickness and width of its conducting tracks are realized with very close tolerances. Tracks are 35 μm thick and 6 mm wide. The overall thickness of the board is 0.3 mm. The viewed surface of the board is coated with a thin layer of black paint which has an emissivity coefficient equal to 0.95 in the wavelength of interest.

The IR thermographic system is based on an AGEMA Thermovision 880 scanner. The field of view (which depends on the optical focal length and on the viewing distance) is scanned by a Hg-Cd-Te detector in the 8 – 12 μm window. Nominal sensitivity, expressed in terms of noise equivalent temperature difference, is 0.1 °C when the scanned object is at ambient temperature. The scanning spatial resolution is 175 instantaneous fields of view per line at 50 % SRF (Slit Response Function). A 20°x20° lens is used during the test at a distance of about 1.8 m.

The thermal image is digitized in a frame of 8 bits 140x140 pixels. An application software has been developed to correlate the measured temperatures to heat transfer coefficients. The IR camera takes temperature maps of the wing surface and these maps are correlated to the local heat transfer coefficient by means of the so called heated-thin-foil technique. In particular, for each pixel, the convective heat transfer coefficient is calculated as:

$$h = \frac{q_j - q_l}{T_w - T_a} \quad (1)$$

where q_j is the Joule heating, q_l is the heat loss (including radiation and internal conduction), T_w and T_a are the wall (measured by IRSR) and the ambient temperatures respectively. The radiative thermal losses are computed from the measured T_w while the conductive ones through the back side of the circuit - i.e. towards the polyurethane foam - are neglected. Typical heat fluxes are of the order of 10^3 W/m^2 .

Several technical details and reference data about the experimental program can be found in the Appendix.

10.2.1 Static Tests

The vortex breakdown position x/c - as a function of model angle of attack - has been identified.

These measurements are typically influenced by support interference, tunnel effects [12], Reynolds number and geometry of the wing. The last factor is the most important, particularly the detail geometry of the apex and the leading edge bevel angle may influence vortex breakdown [13, 14].

Flow visualizations were performed at $U_o = 5$ m/s. The burst is located at the trailing edge for $\alpha = 15^\circ$ and it reaches the leading edge at approximately $\alpha = 30^\circ$ (Fig. 3). The influence of the fuselage is identified in the plot: in this case the breakdown occurs at 30 % lower x/c (i.e. burst location is shifted forward) with respect to the case of fuselage off for the same angle of attack. Only static vortex breakdown positions for the fuselage off configuration were previously measured for on a flat 65° delta wing (root chord $c = 0.620$ m). These data are compared with other experimental results [1, 15] and with analytical predictions [16] of vortex burst locations.

In Fig. 4 the vortex breakdown position of both vortices in asymmetric flow conditions is shown. The results show that the leeward vortex has a greater stability, due to an increase of the effective leading edge sweep angle.

The trend of the geometrical angle between the vortex core axis (the imaginary line that passes through the model apex and the burst location) and the wind direction defined by U_o was obtained and related to α . Similar linear functions versus α were obtained in [1, 17] for 70° delta wings (see Fig. 5).

Static force measurements were performed for different flow conditions. The coefficients were measured adopting a body axes reference system with origin at model centre of gravity. The Reynolds number ranged from 5.8×10^5 to 2.146×10^6 (i.e. $U_o = 10 - 35$ m/s); its effect on normal force and pitching moment coefficients (see Fig. 6,7) is weak, due to the sharp leading edge profile.

The trend of the aerodynamic loads can be related to the static flow visualizations. When the vortex burst occurs at trailing edge ($\alpha = 15^\circ$), the slope of the normal force coefficient versus α begins to reduce its value and, when the breakdown is located at the wing apex, the maximum load is found (see Fig. 8).

The effect of sideslip on normal force and pitching moment (see Fig. 9,10) is to decrease the magnitude of $C_{Z_{\max}}$ and $C_{m_{\max}}$. Moreover, the condition $C_{Z_\alpha} = 0$ (i.e. maximum C_Z) occurs at higher angle of attack. This latter effect is due to the added stability of the leeward vortex.

Another effect can be seen at $\alpha \approx 25^\circ$ and $\beta = 10^\circ$ where a change of slope C_{Z_α} is shown. This corresponds to the windward vortex burst reaching the apex and affecting the flow field. The continued increase in lift and pitch up is due to the leeward vortex burst still not having reached the apex. The post stall behaviour of the various sideslip angles is very similar.

Flow asymmetry has a remarkable effect on the rolling moment coefficient (see Fig. 11), which is confirmed as being roughly zero for symmetric flow.

An explanation of sideslip effects on C_l is presented.

At low α , for a sideslip angle of 5° , the suction surface of the windward semi-span has a lower effective sweep angle and hence a greater increase in lift with angle of attack than the leeward side. This produces an increase in negative rolling moment. As the vortex burst approaches the trailing edge on the windward side, its increase in lift with α slowly decreases and the rolling moment coefficient steadily becomes less negative. The lift capability of the leeward side becomes greater than the

windward and a positive rolling moment is produced. This trend continues until $\alpha \approx 26^\circ$, where a positive peak is reached corresponding to the windward vortex burst reaching the apex. The rolling moment then decreases, becoming negative again and stabilizes its value at $\alpha \approx 37^\circ$; this can be attributed to the leeward vortex reaching the apex.

For larger sideslip angles (e.g. $\beta = 10^\circ$) the nonlinear effect of differential lift between windward and leeward side is enhanced. This severe nonlinearity of static roll stability is related with wing stall [18]. Linear and locally linearized aerodynamic models, traditionally adopted for flight mechanics predictions, are invalidated [19].

The yawing moment coefficient C_n is particularly sensitive to an increase of the sideslip angle as a consequence of the presence of the fuselage, and, when differentiated with respect to β , a destabilizing behaviour is found (see Fig. 12). The directional coefficient C_n (differently from other lateral-directional loads, i.e. side force and rolling moment) gives evidence of directional asymmetry even for low angle of attack and $\beta = 0$ due to the presence of a ventral slot in the lower part of the fuselage.

A further correlation between the vortex breakdown location and the delta wing lateral stability is attempted. The difference of vortex burst location x/c between the two sides of the wing was obtained by analyzing the flow visualization patterns for $\beta = 5^\circ$. This parameter was related to the static derivative $C_{l\beta}$ (lateral stability parameter) obtained from static data at several angles of attack (see Fig. 13). The difference $((x/c)_l - (x/c)_w)$ of the vortex breakdown positions changes substantially in the considered α - range. Initial destabilizing reduction of the lateral stability parameter $C_{l\beta}$ corresponds with the angle of attack at which vortex breakdown asymmetry is maximum [1]. Nevertheless, in the vicinity of complete separation, where $((x/c)_l - (x/c)_w)$ is substantially reduced, the static lateral derivative exhibits a further local stabilizing change of sign.

Surface pressure distributions correlated well with the movement of the vortex breakdown obtained from flow visualizations.

The effect of Reynolds number on surface pressure measurements was investigated in the range $1.16 - 2.33 \times 10^6$ (i.e. $U_o = 20 - 40$ m/s). The effects of Reynolds number on the pressure coefficients are weak (see Fig. 14) in the considered test conditions. A moderate sensitivity of the peak values $C_{p_{max}}$ was detected for higher angles of attack.

The onset of breakdown can be viewed graphically by comparing the spanwise pressure distributions, at a certain chordwise position, with increasing angle of attack. Fig. 15 shows an example at $x/c = 0.40$ and $Re = 1.75 \times 10^6$. At low angle of attack the vortex core appears to be slightly outboard of the pressure tapings. As the angle of attack increases, the vortex core moves inboard. More importantly, as the angle of attack increases, the suction beneath the vortex becomes stronger, corresponding to the increase in vortex lift prior to breakdown.

In the range $20^\circ \leq \alpha \leq 25^\circ$ this increase in suction stops. This indicates that vortex breakdown has reached that chordwise position on the wing surface. This result confirms the static flow visualizations of vortex breakdown positions presented in Fig. 3. At higher angles of attack (see Fig. 16) there can be seen a gradual pressure redistribution [20] and a further increase in vortex diameter.

The movement of the breakdown was also tracked by plotting pressure coefficients C_p beneath

the vortex core against angle of attack, for various chordwise positions (see Fig. 17). In particular, when the burst reaches the x/c locations of the pressure measurements, the suction effect approaches a maximum.

The leeward and windward spanwise pressure distributions for $\alpha = 10^\circ$ and $\beta = 5^\circ$, at $x/c = 0.40$ are presented in Fig. 18. The symmetric pressure distribution has been included for reference. The increase in strength of the windward vortex, and hence an increase in suction, is clearly seen, along with the decrease in suction of the leeward vortex. Furthermore, there is no sign of breakdown for the windward vortex of this low angle of attack and the chordwise position (see Fig. 4).

Pressure measurements performed on the yawed model verify that the effect of increasing the sideslip angle for a delta wing is to reduce/increase the effective sweep angle on the windward/leeward side of the wing, respectively. This has several consequences for the leading edge vortices:

- an increase in vortex strength for the windward vortex and a decrease for the leeward vortex
- an inboard movement of the vortex core on the windward side and an outboard movement on the leeward side
- an early onset of breakdown for the windward vortex and a delay for the leeward vortex
- the vortex core of the windward side moves nearer the surface, while the leeward moves further away from the surface.

10.2.2 Dynamic Tests

Dynamic flow visualizations were obtained at $U_o = 5$ m/s, corresponding to $Re = 2.95 \times 10^5$. The dynamic measurements were performed with symmetric flow ($\beta = 0^\circ$), oscillating in pitch with an amplitude of 3.5° , with different mean angles of attack, chosen within the vortex breakdown α – range. The plots presented (Fig. 19) refer to one of these sets of data. Some important effects of the oscillation frequency on the shape of the cyclic loops of the burst position can be noted. Increasing the K parameter, the ratio between the length $\Delta(x/c)$ and the width $\Delta\alpha$ of the loop is reduced and the axes of the loop rotate counter-clockwise, using the static curve ($K=0$) as reference. The phase lag (see Fig. 20) between the vortex breakdown position and the primary oscillation was evaluated, and it was related to K. This mathematical relationship is almost linear [21] and its slope is insensitive to the mean angle of attack for $\alpha < 20^\circ$.

Differentiating burst locations with a first order numerical scheme, the non dimensional vortex breakdown propagation speed U_x/U_o (parallel to wing chord and positive when directed towards the wing apex) can be plotted (Fig. 21) as a function of α and K. These loops are approximately symmetric for lower values of K; only for $K=1.068$ is a severe non-linearity present, and U_x changes consistently during the oscillation. For this last condition, the magnitude of the delay of the sign inversion of U_x is evident. When the minimum angle of attack is reached and during the first part of the upstroke, the breakdown position continues to move backwards. The opposite phenomenon is detected at the maximum value of α .

In order to verify the order of magnitude of propagation speed, a comparison for $K = 0.1$ with results of other researchers is given in Fig. 22. Note that the reduced frequency K is exactly the same, but the test conditions are different. These flow visualizations [21] were performed at $U_o \approx 10$ m/s with $\alpha = 34^\circ \pm 5^\circ$ on a 70° delta wing. Furthermore, a higher order scheme with a smoothing effect was adopted in [21] for computations of propagation speed.

The pitching moment coefficient was measured in dynamic conditions, at the same reduced frequencies, amplitude (i.e. 3.5°) and mean angles of attack adopted for the flow visualizations on the oscillating model. Reynolds number was different. The angles of attack where the stable damping-in-pitch becomes unstable, and the region in which the reduced frequency has a large effect on pitch damping were identified.

At low angle of attack the trend of C_m is cyclic (counter-clockwise) and the delay with respect to the primary motion is evident: this condition is stable (see Fig. 23).

At a certain α the damping of the delta wing will change from stable to unstable. This means that a crossover point will occur between energy dissipated by the system and energy taken in. It appears on the load diagrams as the point between two counter rotating loops (see the effect of increasing α in Figs. 24 and 25).

The effect of increasing reduced frequency K was to delay to higher angle of attack the appearance of the crossover point.

For the model tested, by $\alpha = 40^\circ$, a large increase in energy (clockwise cycle) taken into the system for the lowest reduced frequency was found (see Fig. 26). In these particular conditions, the aerodynamic loads acting on the model depend on reduced frequency [22]. At higher angle of attack this frequency-sensitive negative damping is remarkably reduced.

These considerations are confirmed by the measurements of damping derivative $C_{m_q} + C_{m_{\dot{\alpha}}}$ reported in [23]. After breakdown reaches the trailing edge, the damping parameter (Fig. 27) can be seen to decrease steadily, becoming unstable for $20^\circ \leq \alpha \leq 25^\circ$. The lower the reduced frequency, the greater this decrease in dynamic stability appears to be, and a positive unstable peak of the derivative is observed when the burst reaches the apex.

Additional details concerning static and dynamic tests (flow visualizations, force and pressure measurements) performed at Politecnico di Torino are reported in [24].

10.2.3 IR Thermography

In discussing the results hereafter presented, it should be considered that when the model top surface is electrically heated in wind on conditions, regions where higher temperatures are detected are characterized by lower heat transfer coefficients (see eq. 1) - i.e. lower wall friction coefficients c_f , and vice versa.

The thermogram shown in Fig. 28 ($\alpha = 10^\circ$ and $Re = 1.10 \times 10^6$) recovers all the features of the separated flow typical of delta wings. Freestream temperature is equal to 27.5°C .

The central region of the wing surface is characterized by an almost two-dimensional flow. Moving from the model apex in streamwise direction along the root chord, a gradual increase in temperature is first observed, followed by a sharp drop. This kind of distribution is attributed to the laminar

boundary layer development (clear arrow shaped area), so that the initial temperature increase is due to the growth of boundary layer thickness. After laminar-to-turbulent transition, the heat transfer is intensified and the temperature decreases. Finally, the thickening of turbulent boundary layer produces another slighter positive temperature gradient. In the vicinity of the leading edge a second region characterized by a relatively high heat transfer is clearly evident. Moving along the wing span (from the root chord) a well defined decrease in temperature is found, even if a local maximum can be clearly identified close to the leading edge. Indeed, the locus of such local temperature maxima is a straight line originating from the wing apex and should be correlated with the secondary separation line.

By increasing Reynolds number it was found that transition is promoted and the laminar region reduces its extension. The region where secondary separation occurs is split in two parts, the second one being shifted outboard. This behavior can be explained considering that boundary layer development in the crossflow plane influences separation and keeping in mind that transition delays separation.

At higher angle of attack, the laminar core becomes larger and transition is delayed, as a consequence of the reduction of the axial velocity component.

Furthermore, if transition is artificially induced, the laminar region disappears and, downstream of the line marked by the strip, the temperature drops abruptly. The secondary separation presents turbulent characteristics too.

Quantitative heat transfer distributions (in terms of Stanton number) are going to be described hereafter. Local Stanton number is defined as $h/(\rho c_p U_o)$, where thermophysical quantities are evaluated at film temperature.

The chordwise distribution of St as a function of Re is presented in Fig. 29. When the condition $Re = 1.65 \times 10^6$ is considered, a minimum of heat transfer coefficient is found at $x/c \approx 0.4$. The decrease of St moving away from the wing apex recovers the analogous trend of the heat transfer coefficient (and so the skin friction c_f) for laminar boundary layer on a flat plate. For $x/c \geq 0.4$ the sharp increase of St demonstrates that transition occurred, so that a maximum is detected when surface flow becomes completely turbulent ($x/c \approx 0.55$). Finally, moving towards the trailing edge, St slowly decreases. It may be observed that the increment of Re has an evident promoting effect on transition (Fig. 29), as the minimum of St moves forward.

The strong effect of Re on the secondary separation (Fig. 30) can be evaluated by comparing the position of spanwise St minima (i.e. the y/s locations where secondary separation occurs) for $Re = 1.1 \times 10^6$ and $Re = 2.2 \times 10^6$, which are located at $y/s = 0.66$ and $y/s = 0.82$, respectively.

The comparison of measurements made with and without transition trip (Fig. 31) demonstrates that transition, when the strip is present on the model top surface at $x/c = 0.18$, is immediate. The magnitude of the Stanton number peak, associated with the high skin friction coefficient, is higher when transition is induced, even if at the model apex and nearby the trailing edge the two St trends overlap.

10.3 Concluding Remarks

The agreement of the results presented with those of other experimental programmes, performed in similar test conditions, is encouraging. The current experimental programme confirmed some conclusions about vortex breakdown development on a 65° delta wing:

- a) the position of vortex burst on a delta wing is a non linear function of α ;
- b) the vortex core incidence varies linearly with the angle of attack;
- c) the trend of the static aerodynamic loads is influenced by the vortex breakdown position on the wing and by the burst asymmetries, when the effect of sideslip angle β is considered;
- d) the phase lag between dynamic vortex breakdown position and primary motion is a linear function of reduced frequency;
- e) at high angle of attack, a frequency-sensitive unstable condition was found for the model oscillating in pitch;
- f) experimental results generally confirm the capability of the IR technique to analyze the complex surface flow field by means of convective heat transfer coefficient measurements;
- g) in the central part of the wing, where nearly parallel flow conditions are established, a laminar core is present, followed by a transitional region after which the boundary layer becomes turbulent (the data obtained by increasing angle of attack and Reynolds number have proved that the behavior of this portion of surface flow can be correctly explained with current boundary layer theories);
- h) in the region influenced by crossflow a significant effect of Reynolds number is confirmed: the secondary separation line is deflected outboard in the x/c location where transition occurs.

10.4 References

- [1] Erickson, G.E., Skow, A.M., Modern Fighter Aircraft Design for High Angle of Attack Maneuvering, AGARD-LS-121, 1982
- [2] Earnshaw, P.B., An Experimental Investigation of the Structure of the Leading Edge Vortex, RAE Tech. Note Aero 2740, 1961
- [3] Greenwell, D.I., Wood, N.J., Determination of Vortex Burst Location on Delta Wings from Surface Pressure Measurements, AIAA Journal, vol. 30, n. 11, 1992
- [4] Lee, M., Ho, C.M., Lift Force of Delta Wings, Appl. Mech. Rev., vol.43, n.9, 1990
- [5] Wedemeyer, E., Vortex Breakdown, AGARD-LS-121, 1982
- [6] Gursul, I., Criteria for Location of Vortex Breakdown over Delta Wings, Aeronautical Journal, vol. 99, n. 985, 1995
- [7] Brandon, J.M., Shah, G.H., Effect of Large Amplitude Pitching Motions on the Unsteady Aerodynamic Characteristics of Flat-Plate Wings, AIAA Paper 88-4331, 1988

- [8] Hall, J.L., An Introduction to Vortex Breakdown and Vortex Core Bursting, NAE-AN-28, Ottawa, 1985
- [9] DeLuca L., Guglieri, G., Cardone, G., Carlomagno, G.M., Experimental Analysis of Surface Flow on a Delta Wing by Infrared Thermography, AIAA Journal, vol. 33, n. 8, 1995
- [10] Fusco, F., Guglieri, G., Experimental Investigation on Aircraft Dynamic Stability Parameters, Meccanica, vol. 28, n. 1, 1992
- [11] Guglieri, G., Quagliotti, F., Dynamic Stability Derivatives Evaluation in a Low Speed Wind Tunnel, Journal of Aircraft, vol. 30, n. 3, 1993
- [12] Weinberg, Z., Effect of Tunnel Walls on Vortex Breakdown Location over Delta Wings, AIAA Journal, vol. 30, n. 6, 1992
- [13] Lowson, M.V., Riley, A.J., Vortex Breakdown Control by Delta Wing Geometry, Journal of Aircraft, vol. 32, n. 4, 1995
- [14] Miao, J.J., Kuo, K.T., Liu, W.H., Hsieh, S.J., Chou, J.H., Lin, C.K., Flow Developments Above 50-deg Sweep Delta Wings with Different Leading Edge Profiles, Journal of Aircraft, vol. 32, n. 4, 1995
- [15] Wentz, W.H., Kohlman, D.L., Vortex Breakdown on Slender Sharp Edged Delta Wings, AIAA Paper 69-778, 1969
- [16] Traub, L.W., Simple Prediction Method for Location of Vortex Breakdown on Delta Wings, Journal of Aircraft, vol. 33, n. 2, 1996
- [17] Chigier, N.A., Measurement of Vortex Breakdown over Delta Wing using a Laser Anemometer, NEAR-TR-62, 1974
- [18] Grismer, D.S., Nelson, R.C., Ely, W.L., Influence of Sideslip on Double Delta Wing Aerodynamics, Journal of Aircraft, vol. 32, n. 2, 1995
- [19] Jobe, C.H., Hsia, A.H., Jenkins, J.E., Addington, G.A., Critical States and Flow Structure on a 65-deg Delta Wing, Journal of Aircraft, vol. 33, n. 2, 1996
- [20] Nelson, R.C., Arena, A.S., Thompson, S.A., Aerodynamic and Flow Field Hysteresis of Slender Wing Aircraft Undergoing Large-Amplitude Motions, AGARD-CP-497, 1991
- [21] LeMay, S.P., Batill, S.M., Nelson, R.C., Vortex Dynamics on a Pitching Delta Wing, Journal of Aircraft, vol. 27, n. 2, 1990
- [22] Gursul, I., Lin, H., Ho, C.M., Effects of Time Scales on Lift of Airfoils in an Unsteady Stream, AIAA Journal, vol. 32, n. 4, 1994

- [23] Guglieri, G., Quagliotti, F., Vortex Breakdown Study on a 65° Delta Wing Tested in Static and Dynamic Conditions, ICAS paper 92-4.10.2, 1992
- [24] Guglieri, G., Quagliotti, F., Experimental Investigation of Vortex Dynamics on a 65° Delta Wing in Sideslip, The Aeronautical Journal, vol. 101, n. 1003, 1997

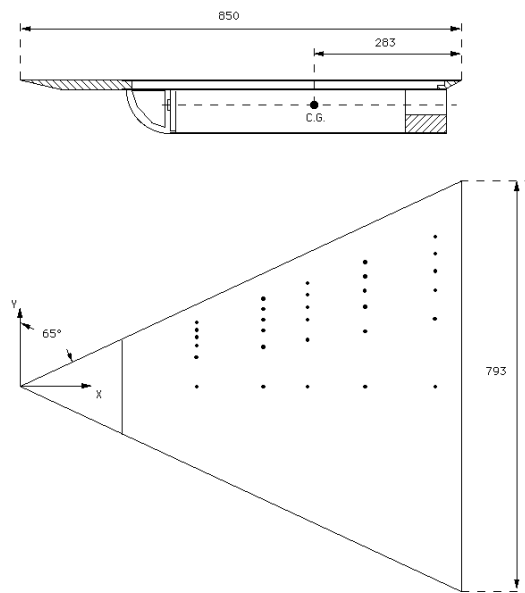


Fig. 1 - The model.

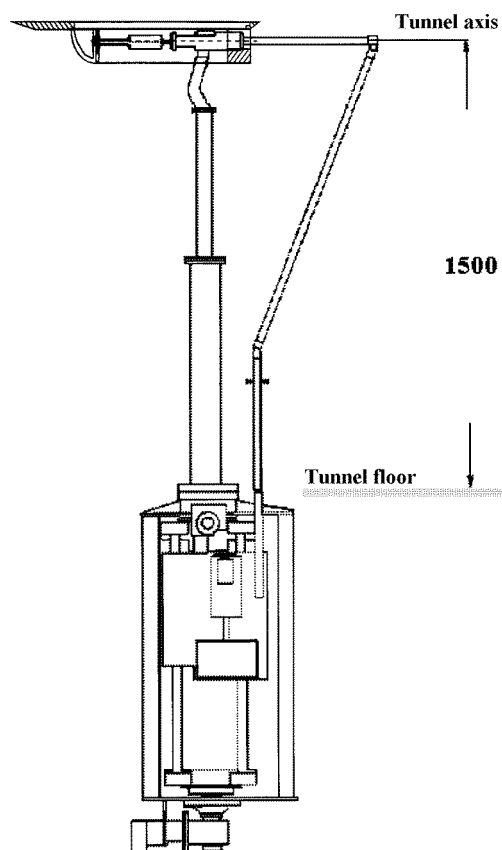


Fig. 2.a - The experimental setup.

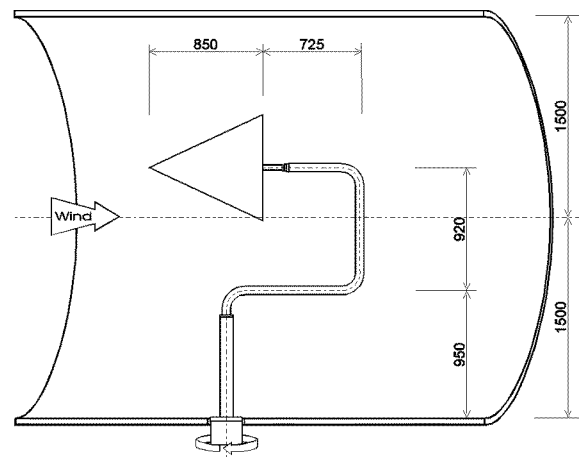


Fig. 2.b - The IRT experimental setup

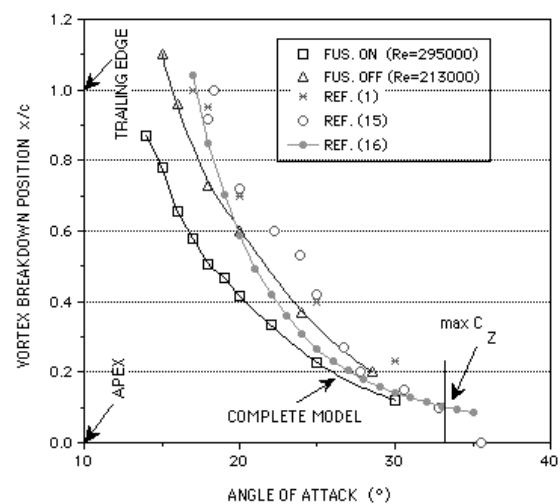


Fig. 3 - The vortex breakdown position vs α in symmetric flow conditions.

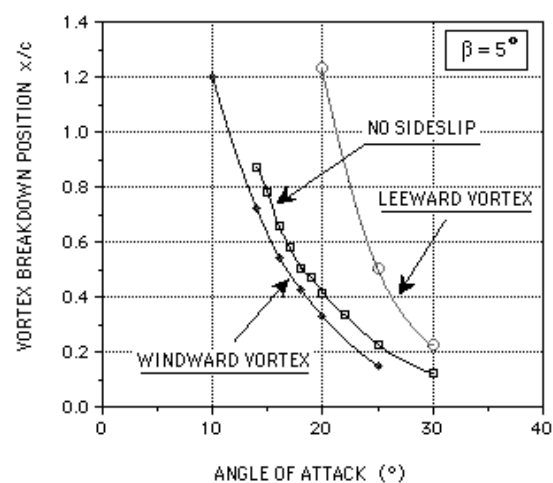


Fig. 4 - The vortex breakdown position vs α in asymmetric flow conditions.

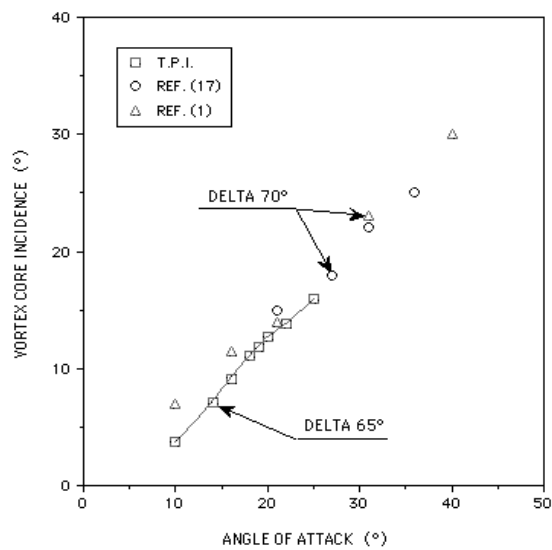


Fig. 5 - The vortex core incidence vs α .

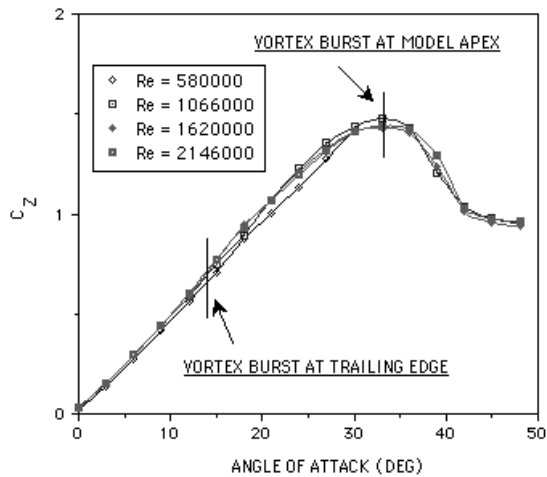


Fig. 6 - The normal force coefficient C_z at different Reynolds numbers.

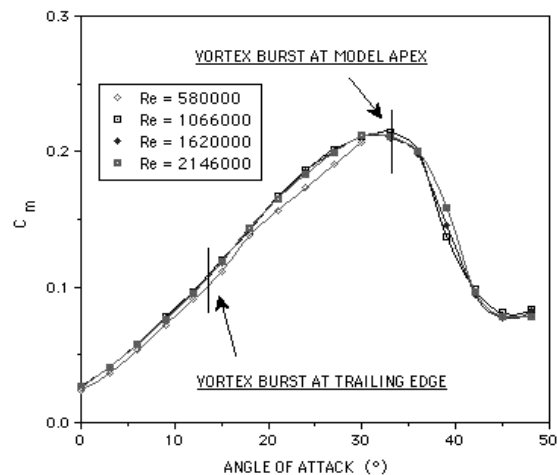


Fig. 7 - The pitching moment coefficient C_m at different Reynolds numbers.

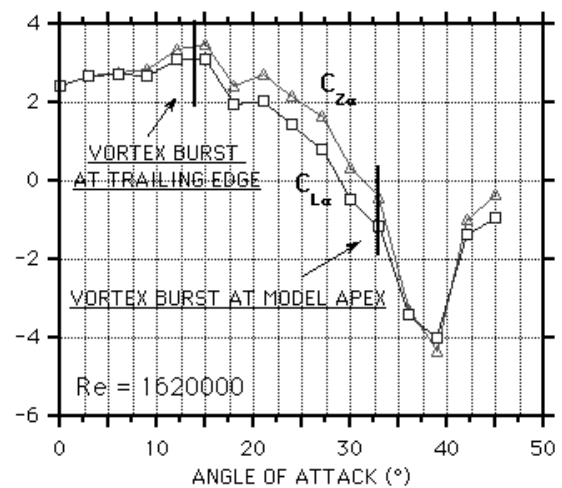


Fig. 8 - The static derivatives $C_{z\alpha}$ and $C_{L\alpha}$ in symmetric flow conditions.

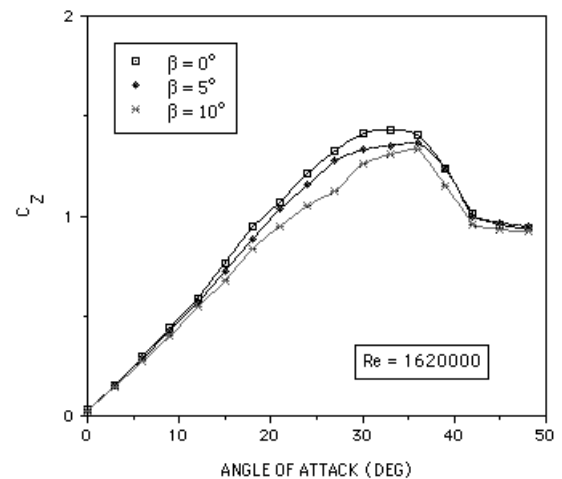


Fig. 9 - The normal force coefficient C_z at different sideslip angles.

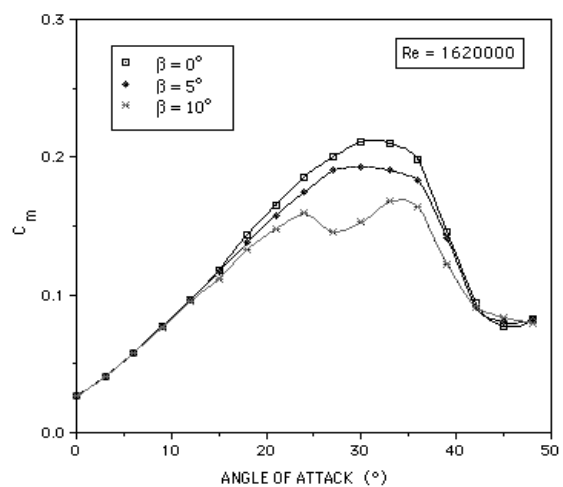


Fig. 10 - The pitching moment coefficient C_m at different sideslip angles.

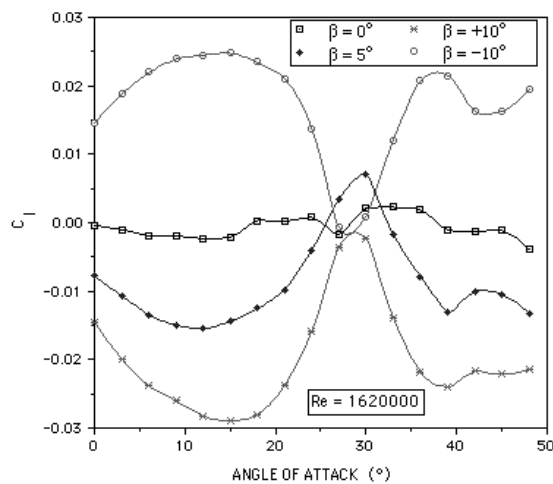


Fig. 11 - The rolling moment coefficient C_l at different sideslip angles.

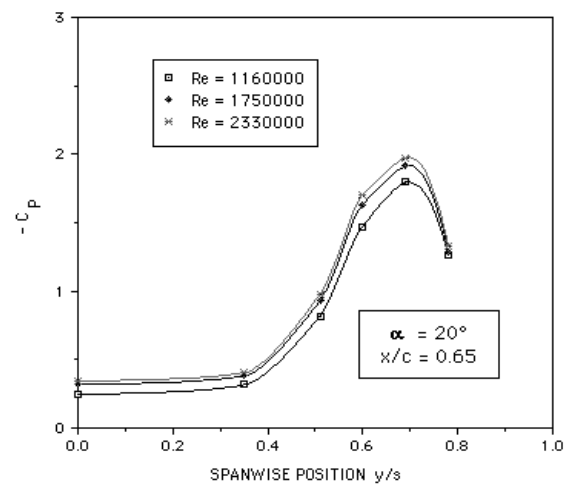


Fig. 14 - The effect of Reynolds number on static pressure measurements.

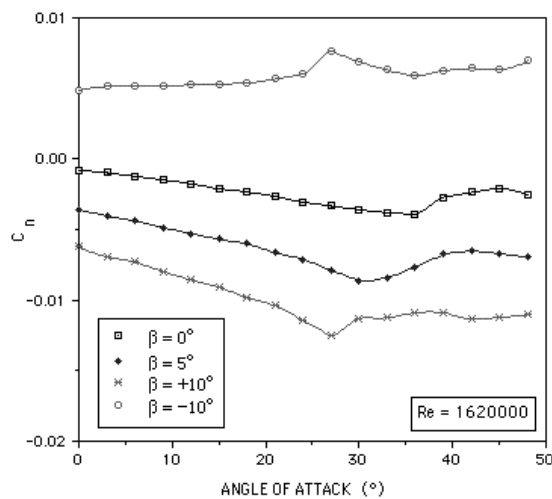


Fig. 12 - The yawing moment coefficient C_n at different sideslip angles.

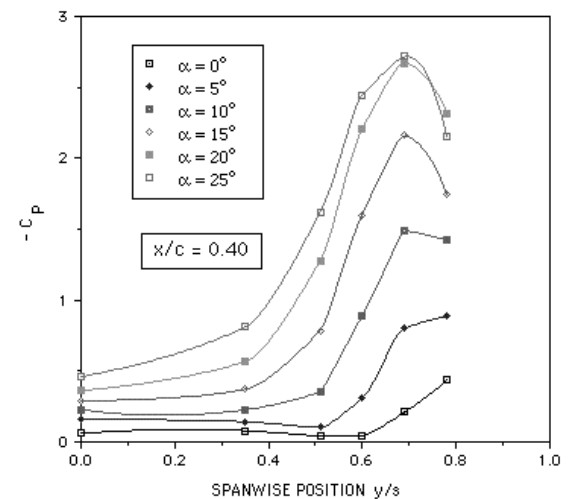


Fig. 15 - The effect of angle of attack on static pressure measurements (low α).

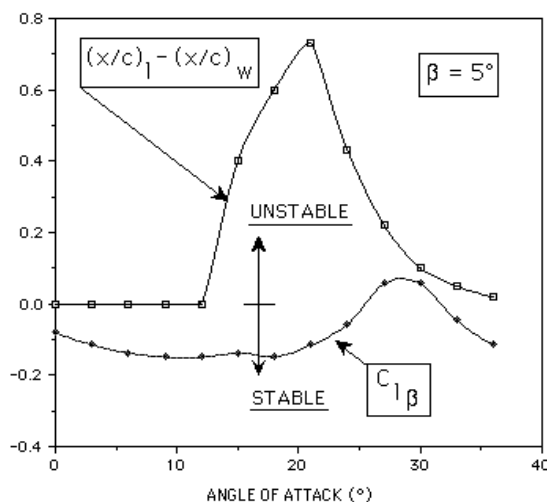


Fig. 13 - Vortex burst asymmetry and lateral stability characteristics at $\beta = 5^\circ$.

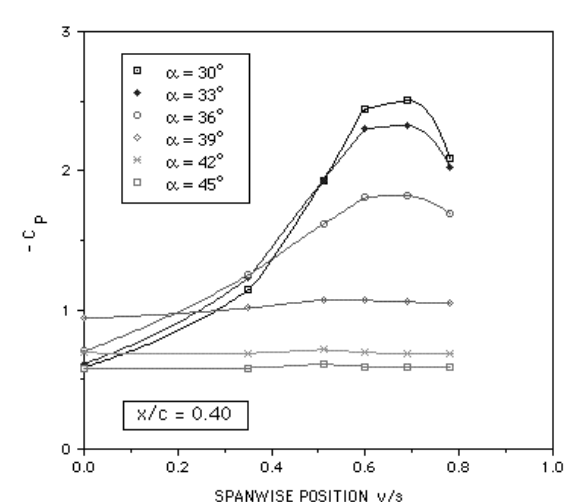


Fig. 16 - The effect of angle of attack on static pressure measurements (high α).

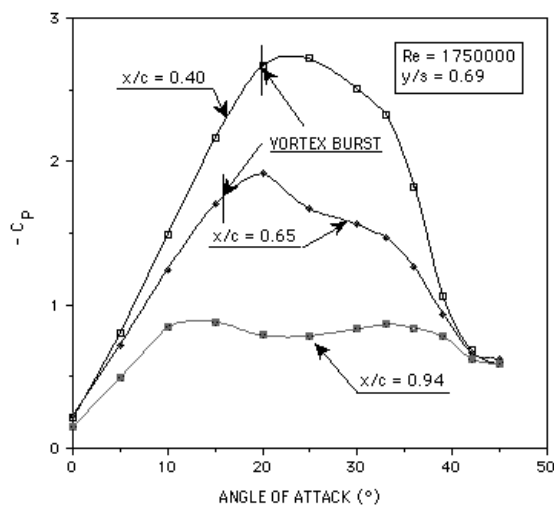


Fig. 17 - The pressure coefficient at different wing locations.

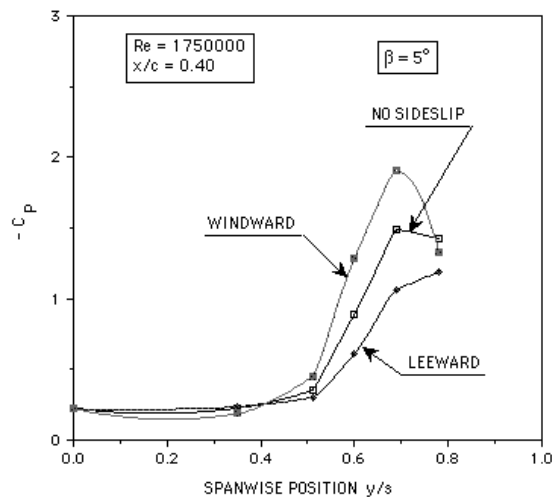


Fig. 18 - The effect of sideslip angle on pressure measurements.

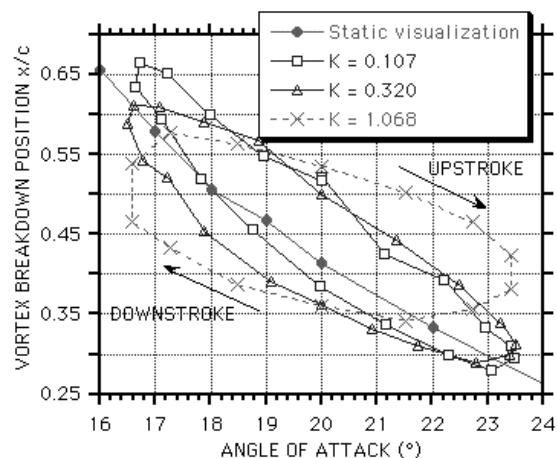


Fig. 19 - The effect of reduced frequency on vortex breakdown position.

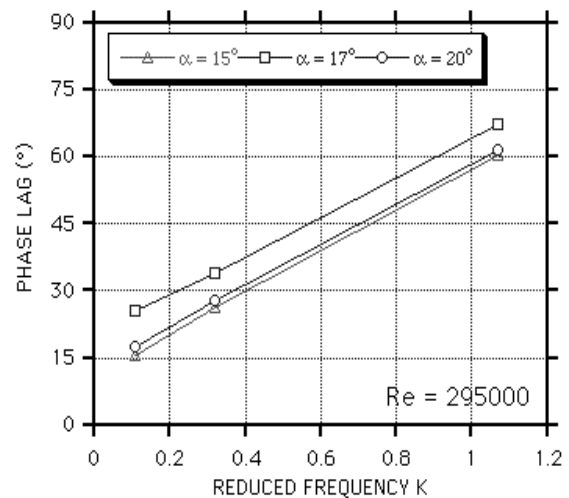


Fig. 20 - The phase lag between the dynamic vortex breakdown position and the model primary motion.

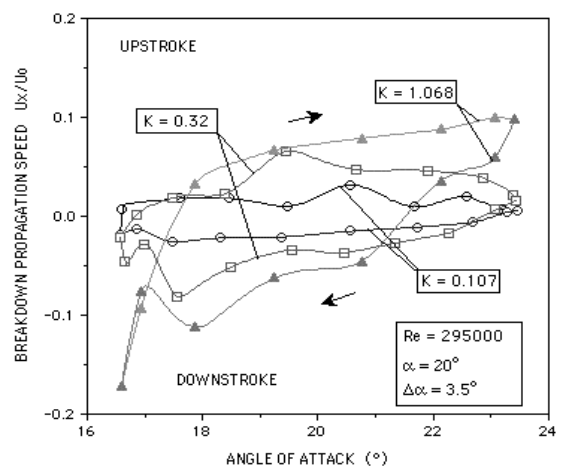


Fig. 21 - The effect of reduced frequency on vortex breakdown propagation speed.

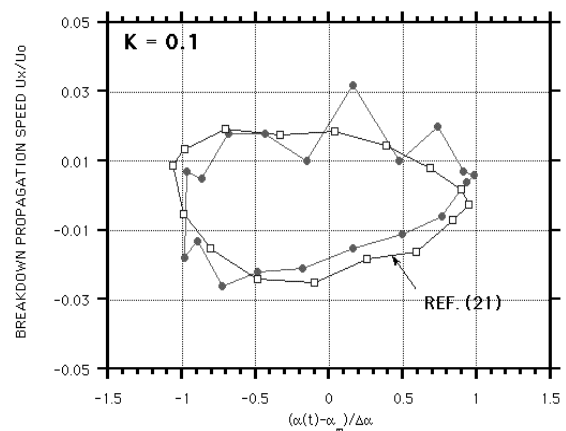


Fig. 22 - Comparison of the vortex breakdown propagation speed for $K=0.1$.

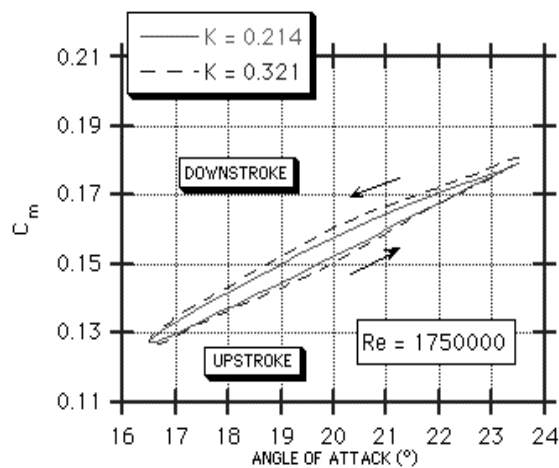


Fig. 23 - The dynamic pitching moment coefficient C_m (stable).

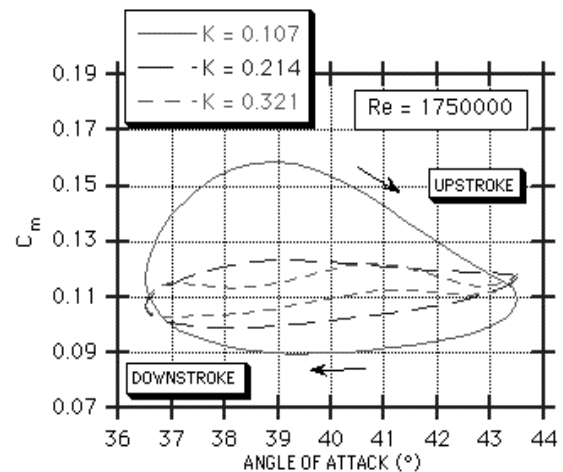


Fig. 26 - The dynamic pitching moment coefficient C_m (unstable).

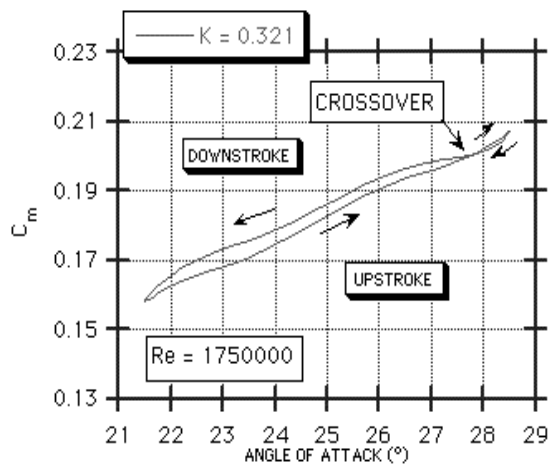


Fig. 24 - The dynamic pitching moment coefficient C_m (stable to unstable).

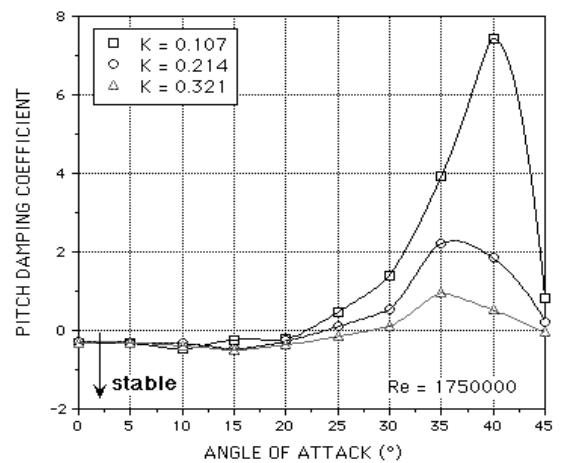


Fig. 27 - The pitch damping coefficient.

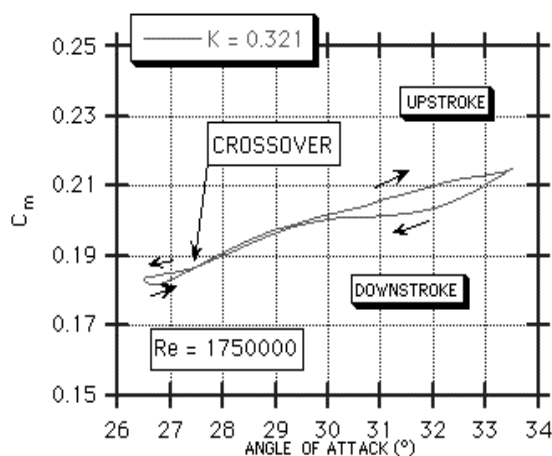


Fig. 25 - The dynamic pitching moment coefficient C_m (stable to unstable).

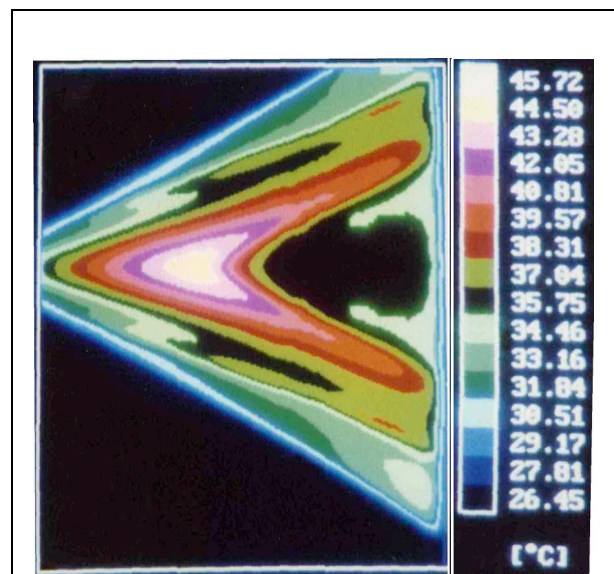


Fig. 28 - The temperature on the model surface ($\alpha = 10^\circ$ - $Re = 1100000$)

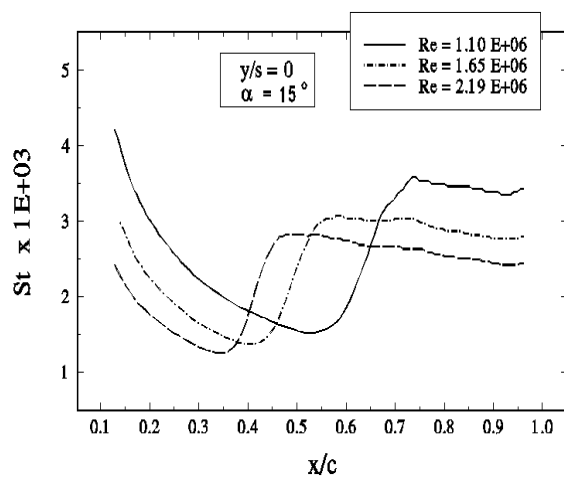


Fig. 29 – The chordwise St distribution as a function of Re ($\alpha = 15^\circ$ - $y/s = 0.0$)

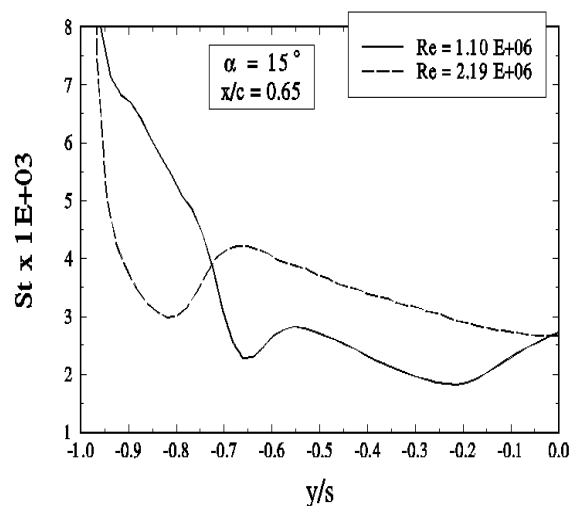


Fig. 30 – The spanwise St distribution as a function of Re ($\alpha = 15^\circ$ - $x/c = 0.65$)

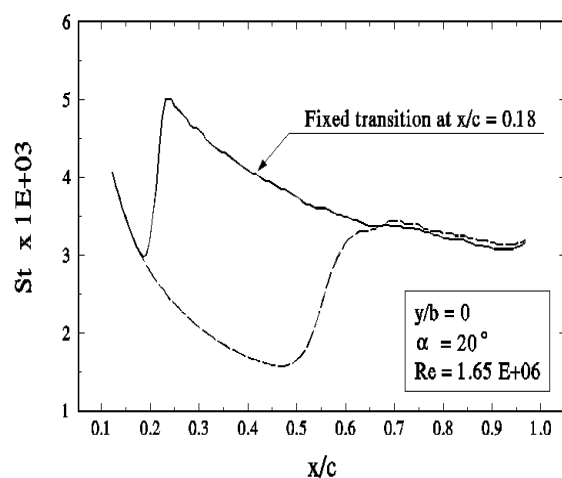


Fig. 31 – Effect of transition on chordwise St distribution ($\alpha = 20^\circ$ - $y/s = 0.0$)

Chapter 11 – VORTICAL FLOW PREDICTION USING AN ADAPTIVE UNSTRUCTURED GRID METHOD

Shahyar Z. Pirzadeh
NASA Langley Research Center
Hampton, Virginia 23681-2199, U.S.A.

Shahyar.Z.Pirzadeh@nasa.gov

ABSTRACT

A computational fluid dynamics (CFD) method has been employed to compute vortical flows around slender wing/body configurations. The emphasis of the paper is on the effectiveness of an adaptive grid procedure in "capturing" concentrated vortices generated at sharp edges or flow separation lines of lifting surfaces flying at high angles of attack. The method is based on a tetrahedral unstructured grid technology developed at the NASA Langley Research Center. Two steady-state, subsonic, inviscid and Navier-Stokes flow test cases are presented to demonstrate the applicability of the method for solving vortical flow problems. The first test case concerns vortex flow over a simple 65° delta wing with different values of leading-edge radius. Although the geometry is quite simple, it poses a challenging problem for computing vortices originating from blunt leading edges. The second case is that of a more complex fighter configuration. The superiority of the adapted solutions in capturing the vortex flow structure over the conventional unadapted results is demonstrated by comparisons with the wind-tunnel experimental data. The study shows that numerical prediction of vortical flows is highly sensitive to the local grid resolution and that the implementation of grid adaptation is essential when applying CFD methods to such complicated flow problems.

11.1 INTRODUCTION

Study of slender wings and bodies flying at high angles of attack has long been of interest for the design of advanced flight vehicles such as highly agile fighters, supersonic commercial airplanes, aerospace vehicles, and guided missiles. A common characteristic of flows over such vehicles is the induced aerodynamic forces and moments due to formation of vortices usually emitted from the leading edges of lifting surfaces or the smooth surface of slender bodies. These vortices induce strong swirling velocity fields that create regions of low pressure near the surface. An important effect of such flows on flight vehicles is the generation of additional aerodynamic load known as the "vortex lift".

The beneficial effects of vortices have been exploited by the airplane designers for achieving high lift during takeoff/landing and enhancing the maneuverability of the advanced fighters over the past three decades. More recently, the advent of the chined and faceted airplanes has revived the interest in vortical flows for improving the design of low-observable aircraft and maximizing their performance. Despite the significant research (mainly experimental) during the past several years, many aspects of the vortical flows and the complex interactions of vortices are still unknown to the aerodynamic scientists. Vortical flows, if not properly understood and controlled, may manifest themselves as undesirable aerodynamic effects which can severely influence the flight stability as well as the fatigue life of the aircraft structure [1]. Consequently, there is a continued need for better understanding of vortex flow characteristics such as induced unsteady and asymmetric flows, unexpected vortex breakdown, and complex interactions of vortices with each other, shock waves, and airframe components. A thorough understanding of the vortex flow behavior would help the designers to develop more effective means for controlling these flow

phenomena and better exploit their benefits to enhance the aircraft performance and maneuverability.

The experimental study of aircraft aerodynamics provides the most reliable information about the vortex flow behavior. However, accurate experimentation in the wind- or water-tunnels requires extensive amount of time, effort, and expense. On the other hand, the capabilities of computational techniques have steadily improved over the years, but their applications are often limited to relatively uncomplicated vortical flows. Despite considerable CFD advances accomplished on the subject in the past, there is still a need for more research, development, and extensive validation of computational methods to further substantiate their viability for solving complex vortex flows. During the past several years, there has been an outbreak of new CFD developments, providing the researchers with a variety of solution techniques. Different computational methods involve various degrees of approximation (and thus uncertainty) depending on their level of complexity. To effectively apply a solution technique to a particular vortex flow problem, one should have a basic understanding of the problem at hand and the capability of the computational tool at his/her disposal.

The formation of vortices on slender configurations (see Figure 1) is essentially triggered by the separation of flow and subsequent shedding of vorticity from the lifting surfaces [2]. For example, the separation of flow from the leading edge of a swept-back wing sheds vorticity that forms into a free shear layer. This layer coils into a helical structure surrounding a concentrated core that ejects flow downstream. Although vortex flows are inherently viscous, the bulk of the swirling flow outside the boundary layer can be assumed non-dissipative and irrotational except at the vortex core [3]. Therefore, once a vortex flow is established, it may be simulated by the potential flow approximation and simplified mathematical models. The Euler equations, on the contrary, are capable of computing rotational flows and can actually "capture" the formation of vortices from the "sharp" leading edges of lifting surfaces. The separation and rolling

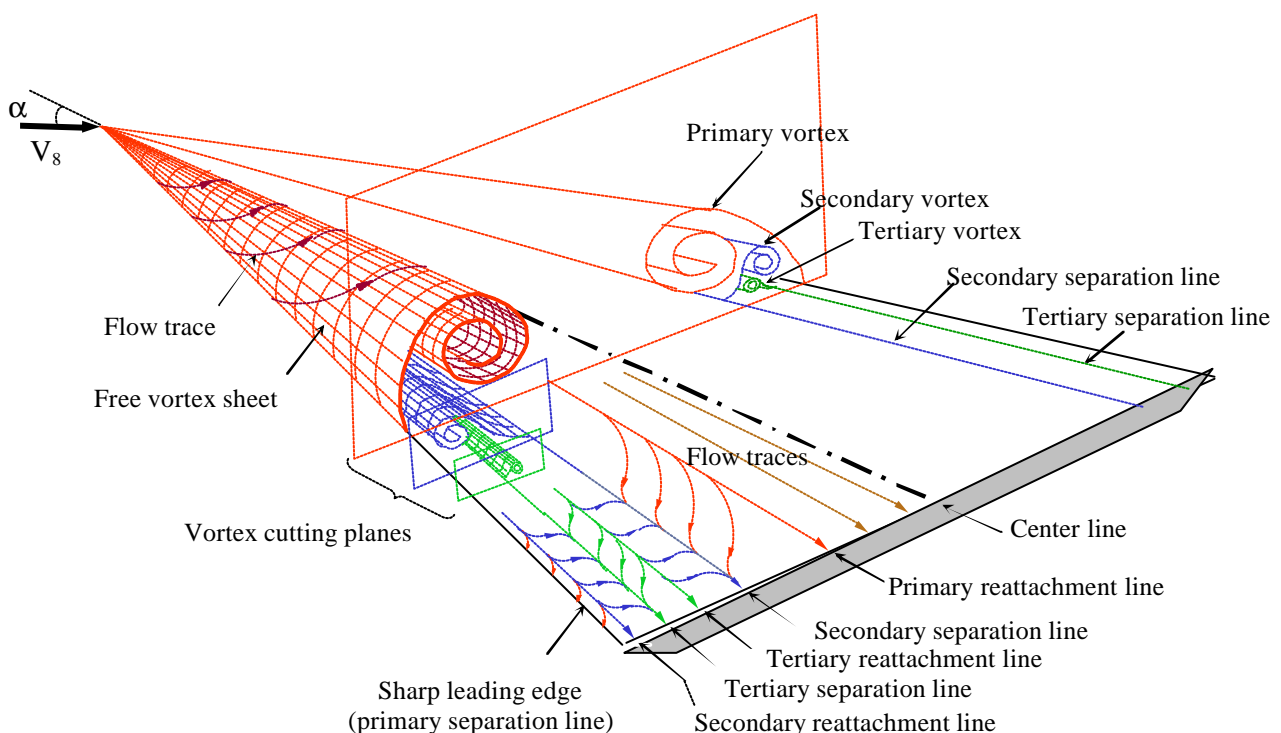


Figure 1: Anatomy of vortex flow on a delta wing at high angle of attack.
(primary separation line)

effect of the free shear layer in such cases are primarily induced by the geometry (regardless of the flow properties) which enable the Euler equations to predict the generation of vortices. The Euler equations can also predict the complex phenomenon of vortex breakdown. The stability of the vortex core is highly sensitive to the axial pressure gradient along the core [3], which is predictable by the Euler equations. The inviscid flow approximation is, however, limited to relatively simple cases of vortex flow. For example, the development of a vortex from a smooth surface (e.g., blunt leading edge) depends on the Reynolds number effects and, thus, requires modelling of the full viscous flow. In addition, a strong primary vortex often creates a lateral adverse pressure gradient on the surface, which may induce a secondary separation of the boundary layer and an additional vortex. This secondary vortex, rotating in the opposite direction sense of the primary vortex, may lead to yet another adverse pressure gradient and a tertiary vortex. The underlying cause of these additional vortices is viscous-dominated and, obviously, cannot be predicted with the potential flow approximation or the Euler equations even on sharp edges. Furthermore, vortical flows at very high angles of attack usually involve large regions of flow separation on the upper surface that influence the axial pressure gradient and, thus, the burst of the vortex core. Inadequate to account for the flow separation and its effects, the Euler equations may predict the onset of the vortex burst incorrectly and, therefore, produce a misleading result. Accurate prediction of such complex flows requires advanced CFD tools based on the full Navier-Stokes equations.

The primary objective of this paper is to evaluate the suitability of a CFD method for solving vortex flows around slender configurations. The method is based on an unstructured-grid technology developed at the NASA Langley Research Center. The emphasis is particularly focused on the application of an adaptive grid refinement technique for resolving concentrated vortices. Several adapted as well as conventional unadapted solutions are presented for two vortex-flow problems: flow over a simple delta wing and a generic fighter configuration simulated at a high angle of attack. The grid adaptation has been fully implemented for generating inviscid solutions but applied only to the grid segments outside the boundary layer for obtaining viscous solutions. The full extension of the adaptive grid technology for computing viscous flows is currently under way.

11.2 COMPUTATIONAL METHOD

The unstructured grid methodology has gained increasing popularity in the CFD community in recent years. Two salient features of unstructured grids have contributed to this overwhelming recognition: 1) the inherent flexibility of the grid structure for discretizing complex domains and 2) the convenience with which the generated grids can be post-processed and modified. While the former reduces the computational cycle time by nearly an order of magnitude for a typical complex configuration, the latter facilitates the implementation of automatic grid adaptation to the flow and/or geometric features. Adaptive meshing is a powerful tool in CFD that substantially enhances the accuracy, efficiency, and automation of the numerical methods.

For the past several years, a coordinated activity has been underway at the NASA Langley Research to develop an integrated system of unstructured grid codes. The primary objective of this team effort was to bring the state-of-the-art in CFD to a higher level of usability in the design environment. The outcome has been a system of user-friendly software referred to as TetrUSS [4]. The system consists of a tetrahedral grid generation package (GridTool and VGRIDns), an Euler and Navier-Stokes solver (USM3D), a post-processing analysis code (ViGPLOT), and several other tools and extensions of the codes for solving specific problems. Although these codes are often used in combination, the TetrUSS system is modular allowing external unstructured grid codes to be used within the system synergistically.

The results presented in this paper have been produced using TetrUSS along with an adaptive grid refinement technique developed recently as an extension to the system. A brief description of the TetrUSS components is presented below for completeness. Further information about the underlying methodology

can be found in the cited references.

11.2.1 Grid Generation

The unstructured grid code VGRIDns generates single-block, tetrahedral grids for both the Euler and Navier-Stokes computations. The grid generation method is based on the Advancing-front [5] and the Advancing-layers [6] techniques. Both techniques resemble marching procedures by which tetrahedral cells grow in the computational field from a triangular surface mesh (initial front). The advancing process continues until the entire domain is filled with contiguous tetrahedral cells. The advancing-front technique inserts individual cells in the inviscid portion of the flow field in an irregular fashion. The lack of an apparent order in which the grid is generated contributes to the flexibility of the method. On the contrary, the advancing layers method generates thin layers of tetrahedral cells packed in the boundary-layer region in a more orderly manner. The systematic way of generating grids by the advancing layers method is favored for the ease of generation and better quality of tetrahedral cells in the boundary layer. The distribution of grid points on the surface and in the field is accomplished by means of some user-prescribed source elements and the solution to a Poisson equation on a "transparent" background grid [7].

The geometry of interest, to be girded, is first defined in terms of a set of bi-linear parametric and/or non-uniform rational B-spline (NURBS) surface patches using the graphical grid-utility code GridTool [8]. The source elements for clustering grid points are also defined and placed in the domain with GridTool. The individual surface patches are then triangulated with VGRIDns using the two-dimensional (2D) versions of the advancing-front and advancing-layers methods in the parametric frames. The collection of all triangulated patches forms the surface mesh (or the initial front) for generating the three-dimensional (3D) volume grid. Some salient features of the VGRIDns system include a grid restart capability, local remeshing [9], grid movement [10], and generating anisotropic stretched grids [11]. The grid stretching capability is an important feature of VGRIDns by which grid points can be clustered differently in various directions producing stretched grid elements. The result is a reduction in the cell count by a factor of three without losing the grid resolution in essential directions.

11.2.2 Flow Solution

USM3Dns is a tetrahedral cell-centered, finite volume Euler and Navier-Stokes solver. The inviscid flux quantities are computed across the cell faces using the Roe's flux-difference splitting scheme, and the spatial discretisation is accomplished by a novel analytical reconstruction process [12]. The solution is advanced in time to steady state using an implicit backward-Euler time-stepping scheme. Flow turbulence is modelled by the Spalart-Allmaras one-equation model, optionally coupled with a wall function, which substantially reduces the need for large number of grid points in the sublayer of the boundary layer. All computations presented in this paper were performed using the wall-function feature of USM3Dns run in a fully turbulent mode.

USM3Dns runs on massively parallel computers and on vector processors, such as the Cray supercomputers, with multi-tasking. The parallel version of the code has also been ported to personal computer (PC) clusters. The code requires 175 eight-bit words of memory per tetrahedron. It runs with a speed of 34 μ sec/cell/cycle/processor on a Cray C90 and 230 μ sec/cell/cycle/processor on the SGI Origin 2000 parallel computer.

USM3Dns supports standard boundary conditions such as the flow tangency, no-slip solid surface, characteristic inflow/outflow (for subsonic flows), and freestream-inflow/extrapolation-outflow (for supersonic flows). In addition, some special boundary conditions including wall functions, wake flow, jet engine, and propeller are available in the code. The flow analysis capability of USM3D has been extended in a separate version for the low-speed flow regimes by implementing a local preconditioning approach [13]. Applications with this version of the code have demonstrated convergence behavior and solution

quality that is nearly independent of the Mach number.

11.2.3 Grid Adaptation

Generation of appropriate grids for CFD applications usually requires some prior knowledge of the problem under consideration for adjusting the grid to the flow characteristics. Tailoring the grid is especially essential for the flow problems that exhibit prominent features, such as shock waves and vortices, whose accurate prediction is susceptible to the local grid density. In the absence of adequate flow information in advance, a conscientious CFD analyst often undergoes several iterative steps between grid generation and flow solution before obtaining the final result. Alternatively, a globally fine grid is usually generated to ensure the accuracy of the solution. In both cases, the amount of time, effort, and computational resources become excessive for solving complex problems. Even with a prior knowledge of flow features, such as the presence of vortices in the flow field, it is generally difficult to manually adjust the concentration of grid points in 3D, for example, along the vortex path. As will be seen in the examples presented in this paper, changing the grid resolution can drastically alter the nature of the predicted vortex flow.

Automatic grid adaptation is an effective technique by which the grid adjusts itself to the flow through several iterations as the solution evolves. Since the distribution of grid points is automatically determined based on a feedback from the ongoing solution, the process ideally produces an improved mesh that, in turn, would provide a more accurate solution. In addition to automation and accuracy, adapted grids offer computational efficiency since they contain considerably fewer elements than unadapted grids with comparable local resolution at the crucial locations.

Although the adaptation of grid may appear a simple procedure in theory, its implementation has proven to be nontrivial for solving general 3D problems. The success of an adaptive method depends on how accurately the scheme 'picks' the flow features, which require grid refinement, and how effectively the grid adjusts itself to the flow without user's intervention. Although the subject has been of much interest in the CFD community for many years, it remains an emerging technology even to date.

The present adaptive grid work was initiated at Langley as part of a project concerning the Euler technology assessment for rapid simulation of nonlinear vortical flows experienced by high-performance military aircraft flying at high angles of attack. It has also been implemented for automatic capturing of flow discontinuities at transonic and supersonic flow regimes [14]. The method exploits the flexibility of unstructured grids and their convenience for post-processing modification. The grid refinement, in this method, is based on subdivision of the surface mesh triangles and local remeshing of the volume grid. Starting with a reasonably coarse mesh and the corresponding initial solution, the adaptation proceeds with an assessment of the current flow solution to determine where in the field the solution requires further improvement. Once the regions of interest are identified, the respective grid nodes and cells are removed creating voids in the mesh. If any portion of the surface mesh is exposed in the empty pockets, the corresponding triangles are refined by subdivision. The pockets are then locally remeshed with a modified (usually finer) grid resolution. Next, a new solution is obtained on the modified grid followed by yet another grid refinement. The iterative process continues until some prescribed criteria based on the solution accuracy are satisfied or, simply, certain numbers of adaptation cycles are performed.

The process of adaptive grid refinement is demonstrated on a hypothetical problem in Figure 2. In this example, a vortex-dominated flow is assumed around a fighter configuration flying at a high angle of attack. For clarity, the process of grid refinement is shown on the plane of symmetry displaying the triangular sides of the tetrahedrons. The initial grid (Figure 2a), along with a corresponding flow solution, is supplied to the adaptive refinement scheme. Suppose the adaptation procedure detects a vortex originated from the aircraft fore-body through an appropriate flow or error analysis scheme (Figure 2b). Typical of most CFD grids, the resolution of the initial mesh in this example is adequate around the

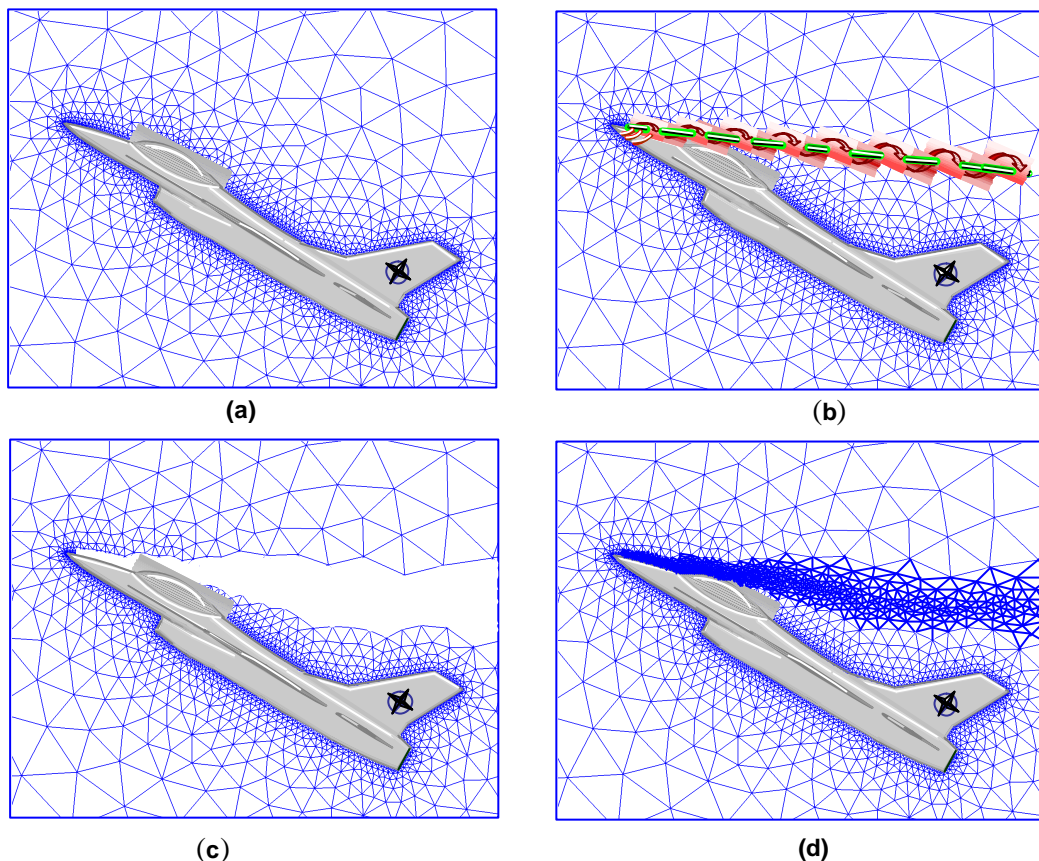


Figure 2: Demonstration of adaptive refinement steps by local remeshing for a vortical flow example: (a) initial grid, (b) flow solution indicating a forebody vortex, (c) removal of affected cells, and (d) locally refined grid.

geometry but is too coarse in the field to resolve the vortex accurately. Following a flow assessment, the grid elements experiencing abrupt variations in the flow (due to the vortex presence) are identified and automatically removed leaving a void in the mesh as shown in Figure 2c. The remaining grid points and cells are then renumbered, and the void is remeshed using the restart capability of VGRIDns (Figure 2d). The process of adaptive remeshing is repeated several times before the final solution with the desired accuracy is obtained.

11.3 RESULTS

To demonstrate the capability of the present unstructured-grid CFD methodology for solving vortical flow problems, two test cases have been considered for presentation in this paper. The first test was performed on a simple 65-degree delta wing model with interchangeable leading edges. The emphasis of this test was placed on the vortex-capturing capability of the present method in the absence of any additional complex features such as shock waves and/or geometry interactions with the vortices. Of particular interest was to assess the ability of the method in predicting the onset of flow separation and vortex formation on blunt leading edges as well as the vortex breakdown phenomenon. The second case concerns vortical flow over a more complex configuration, an experimental high-performance fighter model. The purpose of this test was to study the interaction of vortices with the airframe components.

Both models have been tested in wind tunnels at the NASA Langley Research Center.

11.3.1 65-degree Delta Wing

A delta wing model with a leading-edge sweep of 65 degrees has been tested in the Langley National Transonic Facility (NTF) [15]. The objective of the experiment was to investigate the effects of Reynolds and Mach numbers on vortex flows on a slender wing with different values of leading edge bluntness. The untwisted, uncambered wing consists of a flat plate section, an interchangeable leading edge, a trailing-edge closure segment, and a sting fairing as shown in Figure 3a. All the wing components are defined

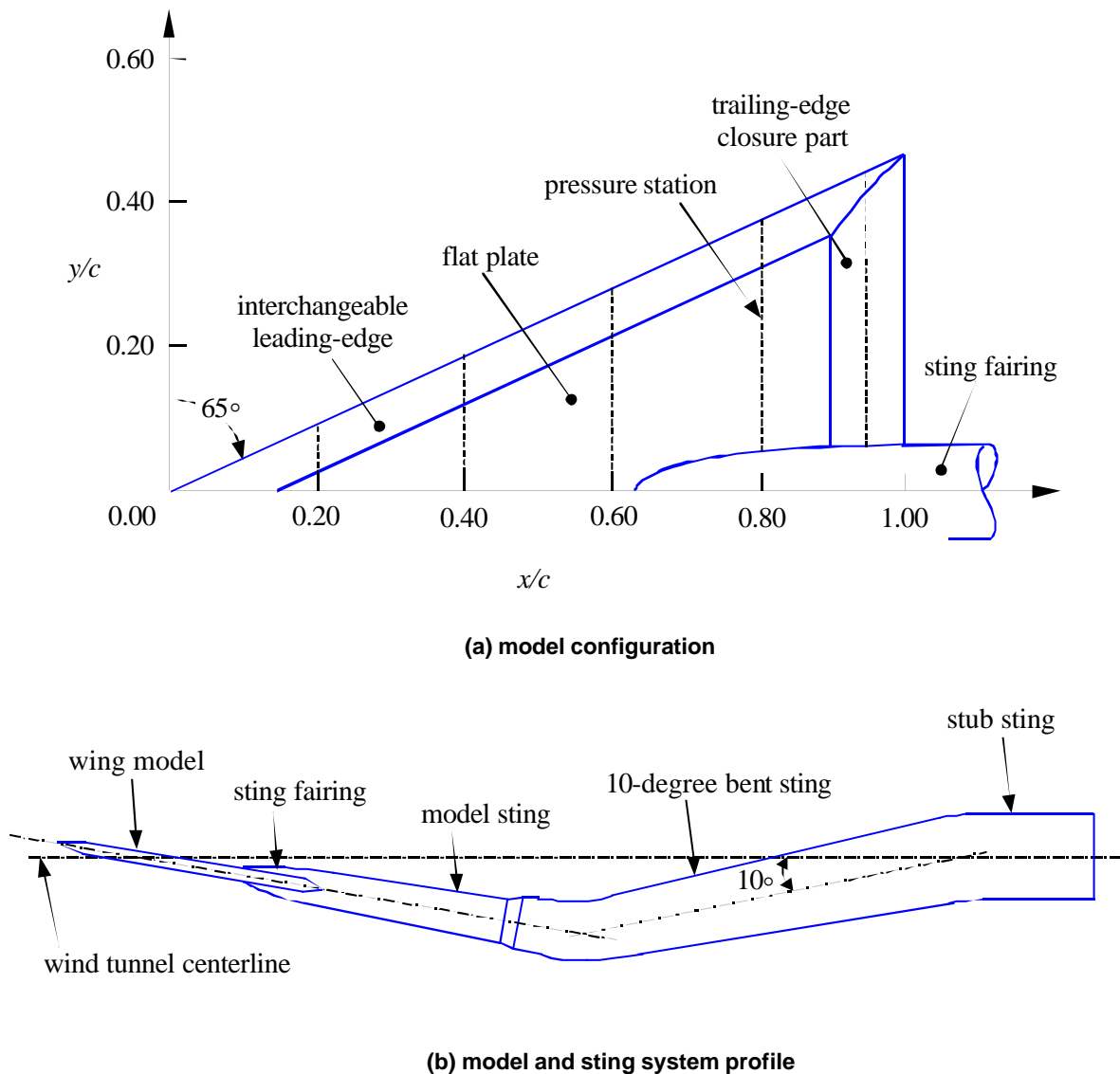


Figure 3: 65-degree Delta wing model assembly and support system.

analytically and presented in Ref. [15]. The model dimensions are specified by a root chord (c) of 25.734 inches, a wingspan (s) of 24 inches, a wing maximum thickness of 0.875 inches, and a mean aerodynamic chord (MAC) of 17.156 inches. The model has been tested with four different leading edges attached to the flat section of the wing. The leading-edge radii are 0.0, 0.05, 0.15, and 0.30 percent of the MAC and are designated as sharp, small, medium, and large, respectively. The wing was supported in the tunnel with a model sting attached to the sting fairing at the aft end of the geometry as well as a 10-degree bent sting connected to a stub sting (see Figure 3b). The experiments have produced extensive amount of surface pressure data, which are compiled and presented in tabular and graphical formats. The normal force and pitching moment coefficients have also been measured in these tests by a force/moment balance. However, the primary purpose of the force and moment measurements was to monitor the safety of the model support, and their accuracy might be considered inadequate for aerodynamic analyses. Unfortunately, no off-body measurements or flow visualization data are available for these experiments to compare the predicted vortex locations and their breakdowns. The surface-pressure data set is open to the public and is accessible electronically from the Langley Technical Report Server (LTRS).

To make the CFD configuration resemble the model in the tunnel as closely as possible, the computational grids were generated on the complete geometry including the support system. However, the shape and dimensions of the sting components were approximated based on the photographs of the model as no actual definition of these components were readily available at the time of this study. Such an

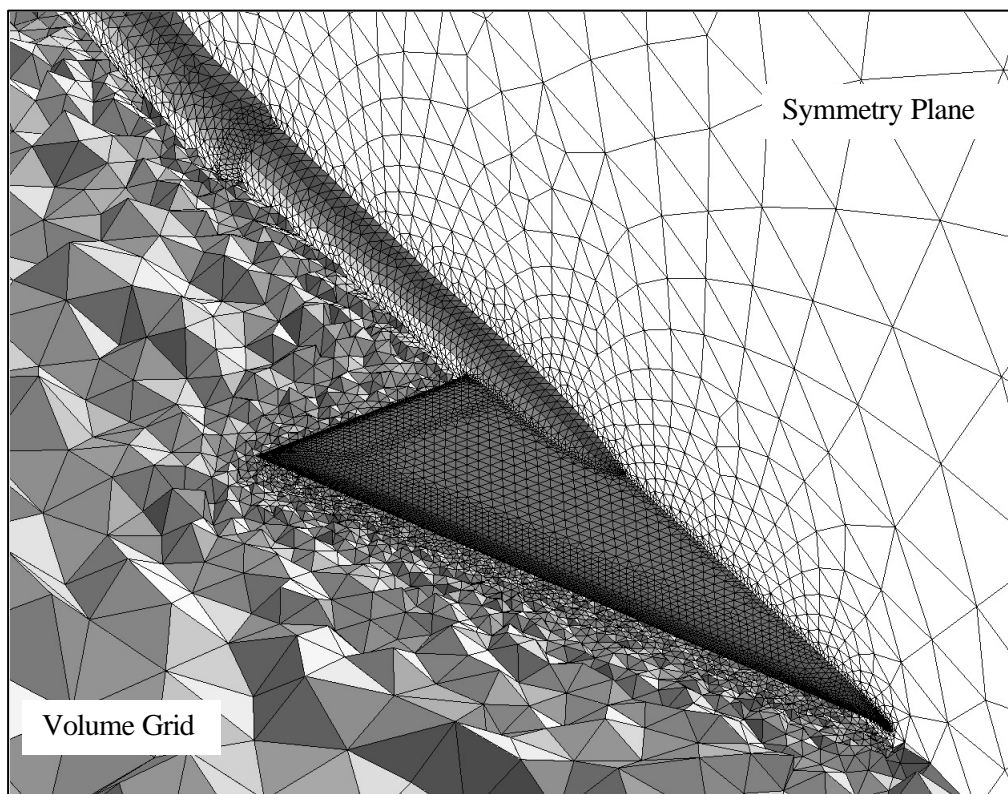


Figure 4: Unstructured Euler grid on the 65° Delta wing showing triangular surface mesh and cross-section of tetrahedral volume grid (352,011 cells).

approximation is assumed to have minimal influence on the accuracy of the solutions, as only the secondary effect of the support system on aerodynamics of the model and the vortex formation is important for this investigation. Figure 4 shows a sample initial (unadapted) grid including triangulation on the wing model, sting, and part of the symmetry plane as well as a cross-section of the tetrahedral volume grid. To minimize the effect of the far-field boundary on accuracy of the solutions near the geometry, the outer boundaries were placed at 15 *MAC*'s in the upstream, downstream, upper, and lower directions and 7.5 *MAC*'s in the semi-span direction. In addition, the stub sting was extended downstream all the way to the outflow boundary.

Several inviscid and viscous flow computations were performed for this case. The results include unadapted, adapted, and "semi-adapted" solutions to study the grid sensitivity of the solution scheme with regard to the vortical flow problems. The present adaptive grid capability is limited to the "inviscid" grids generated with the advancing-front method. Therefore, only the grid segments along the vortex core outside the boundary layer were refined for the viscous flow computations. Obviously, this type of partial grid adaptation is not sufficient, especially, for capturing the onset of flow separation and vortex formation on blunt leading edges that require adequate grid resolution on and near the surface. Work is currently under way to develop a full adaptive grid refinement capability for the Navier-Stokes calculations.

11.3.1.1 Sharp Leading-Edge (Radius = 0.0 % *MAC*)

The first computation on the delta wing concerns an inviscid flow analysis of the wing with a sharp leading edge. The flow condition is at a freestream Mach number of 0.4 and an angle of attack of 20 degrees. The computation was performed on a semi-span, unadapted grid with 12,944 boundary nodes, 66,166 total nodes, and 352,011 tetrahedrons. No attempt was made to cluster extra grid points in the field at the vortex location. The surface mesh on the upper surface of the wing is shown in the upper portion of Figure 5. As evident, a finer grid resolution has been prescribed at the edges of the wing, whereas the grid

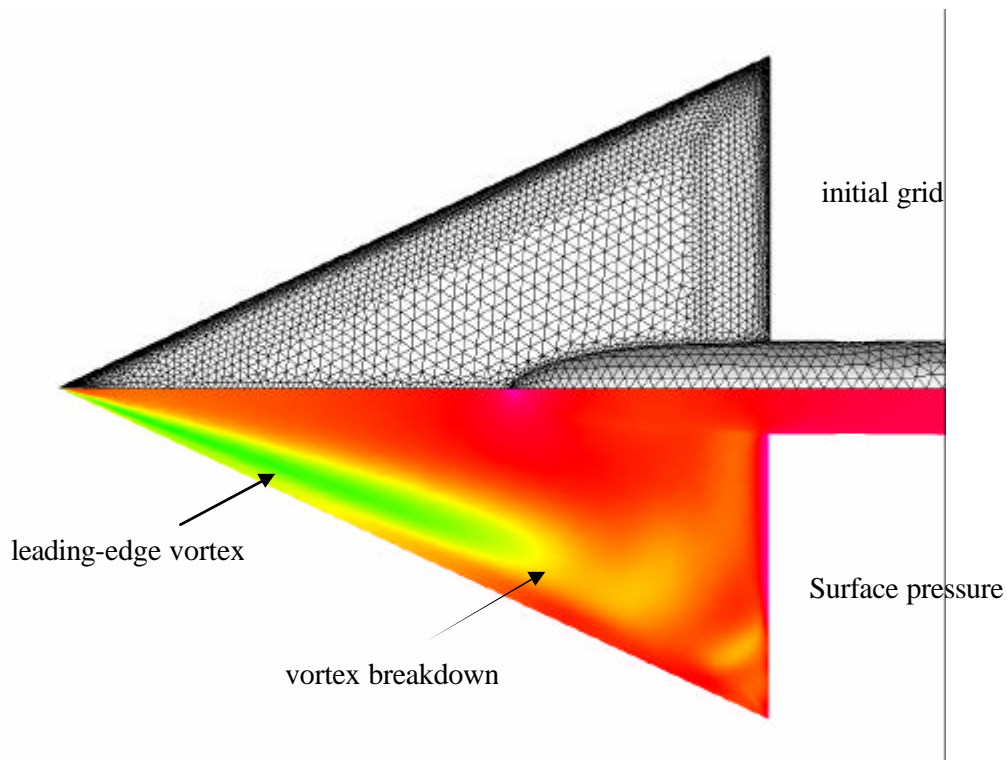


Figure 5: Initial (unadapted) grid (352,011 tetrahedral cells) and Euler inviscid flow solution on the sharp leading-edge Delta wing. $M_\infty=0.4$, $\alpha=20^\circ$.

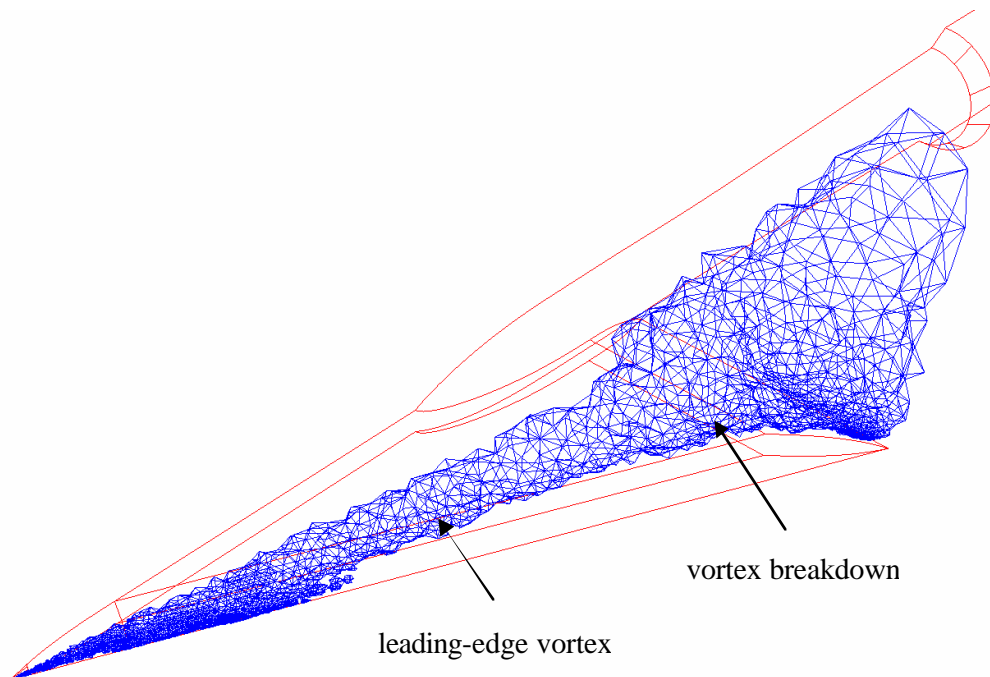


Figure 6: Tetrahedral cells featuring high entropy regions in the initial grid for the sharp leading-edge Delta wing.

on the flat portion of the wing is coarser and nearly uniform, typical of conventional (unadapted) grids. A corresponding flow solution on this grid is displayed in the lower portion of Figure 5. In this figure, the surface pressure distribution is represented by variation of colors from red (indicating a higher pressure) to blue. The footprint of a leading-edge vortex on the surface is evident from the low-pressure (mainly green and blue) region. The affected area extends from the wing apex to about 70 percent of the wing root chord at which the surface pressure increases abruptly. Such a sudden change in the pressure distribution is indicative of the vortex burst. The predicted vortex breakdown at this location is also observed by examination of the flow properties in the field. Figure 6 illustrates a group of tetrahedral cells featuring solution entropy levels that are higher than a prescribed threshold. The "high" entropy region remains confined to a relatively narrow segment of the grid concentrated around the vortex core and then suddenly expands further downstream, which is an indication of the vortex breakdown.

Experience with earlier test cases had shown that the vortex behavior is highly dependent on the local grid resolution. To verify the earlier findings, the initial grid was refined based on the entropy as indicated by the initial solution. In other words, the grid cells experiencing higher levels of entropy than a prescribed value (about 0.008 in this case) were flagged (Figure 6) and remeshed with finer grid elements as explained before. Figure 7 shows the grid and solution after the third iteration of adaptation. The surface grid, on the upper portion of the figure, indicates the automatic grid refinement at locations that are affected by the vortex. The adapted grid contains 24,328 nodes on the surface, 287,279 total nodes, and 1,612,307 tetrahedrons. Comparing these numbers with those of the initial (unadapted) grid reveals that a large proportion of the new nodes are placed in the field along the vortex core. The corresponding surface pressure distribution in Figure 7 shows a stronger footprint of the vortex on the surface as compared to that of the unadapted solution in Figure 5. More significantly, the character of the vortex breakdown appears to be changed drastically after adaptation as indicated by the surface pressure distribution. Figure 8 displays the volume cells featuring high levels of entropy production due to the vortex presence (similar to Figure 6). As evident, the vortex definition has considerably improved (has become sharper) after

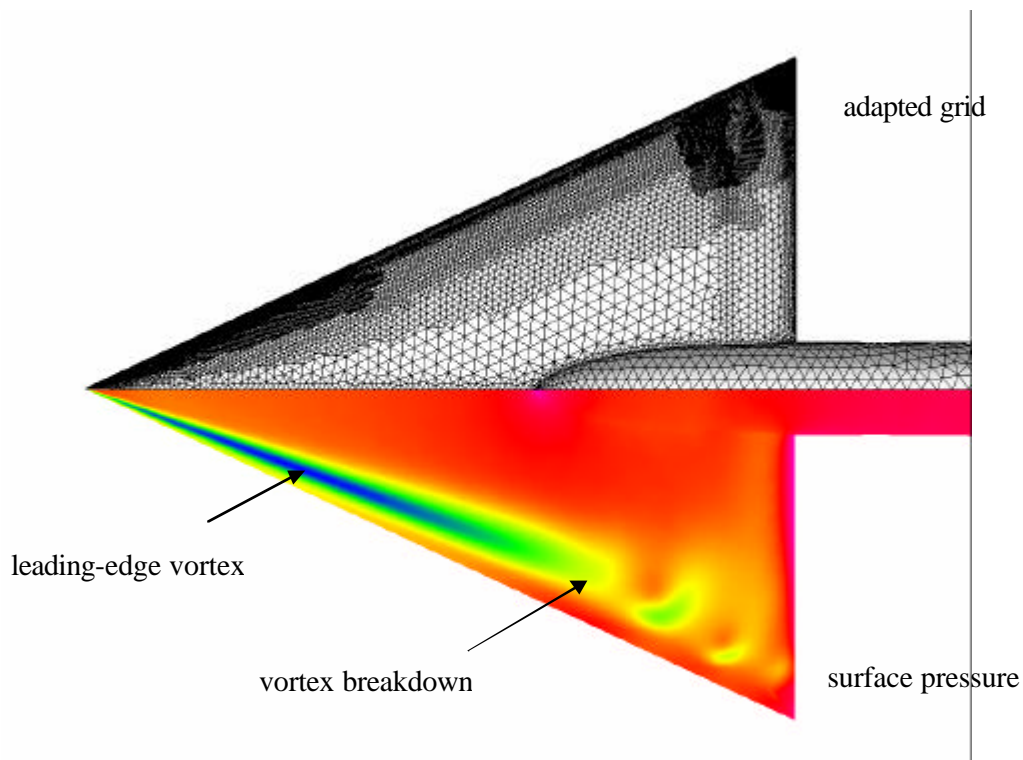


Figure 7: Final adapted grid (1,612,307 cells) and Euler inviscid flow solution on the sharp leading-edge Delta wing. $M_\infty=0.4$, $\alpha=20^\circ$.

adaptation, and the breakdown pattern has distinctively changed from that resembling a "bubble" burst before grid refinement (Figure 6) to a "spiral" type breakdown after adaptation. It is interesting that the computation has not only predicted the vortex burst but also captured the details of the vortex structure after breakdown. In addition, the adapted solution has even predicted the sense of the spiral breakdown winding, which is opposite to the direction of rotation of the vortex itself. Such a counter-rotating phenomenon has also been observed experimentally for leading edge vortices [16]. The composite images in Figure 9 illustrate the vortex structure and its breakdown in more details. The vortices are represented in Figure 9a by several cross-sections of pressure contours and several particle traces (selectively seeded at the leading edge) swirling through the vortex cores. The orderly structure of the vortices persists up to the onset of their bursts at about two-third of the wing root chord. At this location, the pressure contours exhibit an asymmetric pattern, and the particle traces start dispersing downstream. Figure 9b portrays a shaded iso-entropy surface that clearly shows the leading edge vortices and their "counter-winding" spiral breakdowns. Included in Figure 9b is also the surface pressure gradient showing the footprint of the vortex.

Unfortunately, no wind tunnel visualization data is currently available to confirm the existence of the vortex breakdown as predicted by the present inviscid flow computation. In fact, the surface pressure measurements appear to contradict the computation and show no sign of vortex burst for this case. To further investigate the flow, a Navier-Stokes computation was performed on the same case at a Reynolds number (based on MAC) of 6.05×10^6 . The "viscous" grid for this run was generated with a prior knowledge of the vortex location as revealed by the inviscid solution. Accordingly, more grid nodes were manually clustered both on the surface and in the field by inserting grid sources in appropriate locations in the field. This strategy was intentionally exercised to examine the effectiveness of manual tailoring of a grid as opposed to automatic grid adaptation. The grid contains 31,529 boundary nodes, 475,385 total nodes, and

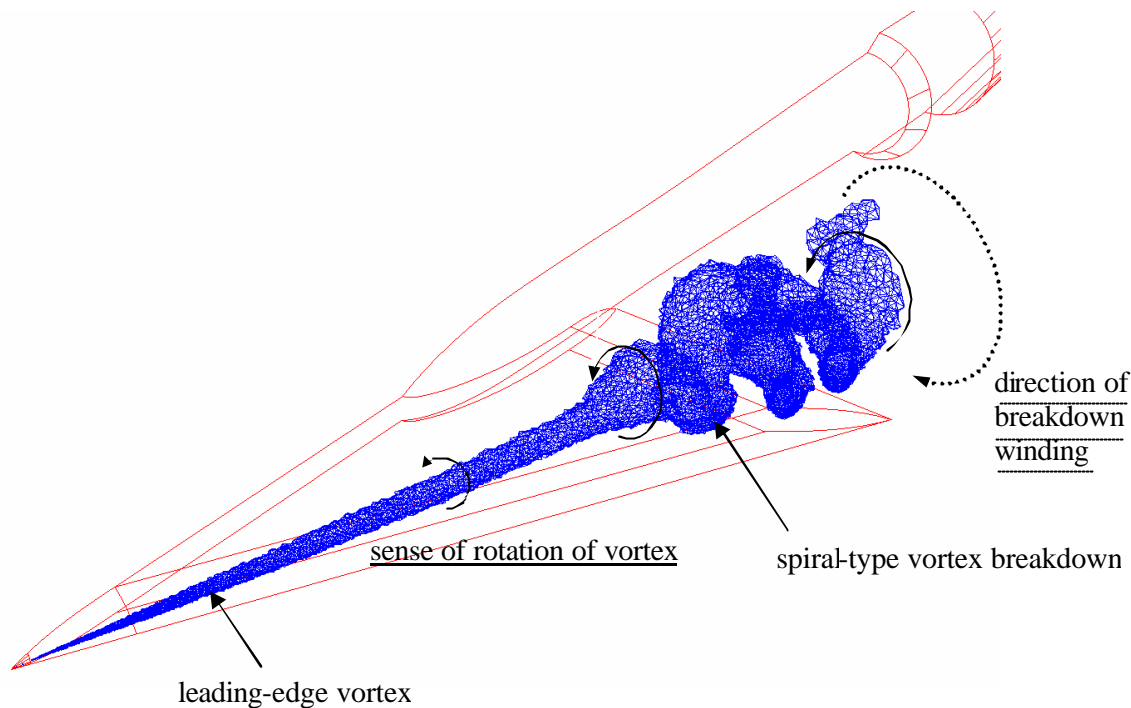


Figure 8. Final adaptive grid refinement of high entropy region for the sharp leading-edge Delta wing.

2,720,797 tetrahedrons. The upper portion of Figure 10 shows the surface grid with a fine distribution of nodes at the wing leading edge and along the vortex trace projected on the surface. The pressure distribution on the surface is shown in the lower portion of Figure 10. As evident, the viscous solution has produced a quite different flow pattern from that shown in Figure 7. Noticeably, no sign of vortex burst is evident over the wing as the low-pressure signature extends to the trailing edge of the wing. The abrupt change of color shade at the trailing edge is not an indication of the vortex burst but is rather due to a rapid closure of the trailing edge to a sharp edge, which suddenly deflects the surface from the vortex core.

As mentioned earlier, the breakdown of a vortex is extremely sensitive to the flow properties such as the swirl ratio (circumferential/axial velocity component) [2] and the external pressure gradient in axial direction of the vortex. Apparently, the Euler solution has created the critical condition that triggers the breakdown of the vortex in this case, whereas the viscous effects have dampened the adverse condition at the vortex core allowing it to stay intact further downstream. While a definite explanation of this discrepancy is not clear to the author presently, it may be argued that the Euler solution produces a stronger swirl ratio, causing the vortex to burst earlier at the presence of an adverse pressure gradient. Another difference between the two solutions is the ability of the Navier-Stokes computation in predicting the secondary vortex as indicated in Figure 10 by a dim trail of low pressure between the leading edge and the primary vortex. Furthermore, the primary vortex appears to be shifted slightly towards the wing root as compared with that of the inviscid solution shown in Figure 7. A profile of the field grid/solution normal to the wing axial direction is shown in Figure 11. The figure illustrates the cross-sections of the wing, the tetrahedral grid, and the entropy contours, all at the mid-root-chord station. The high-aspect-ratio "viscous" cells are visible in the boundary layer around the geometry. Indicated in the figure is also

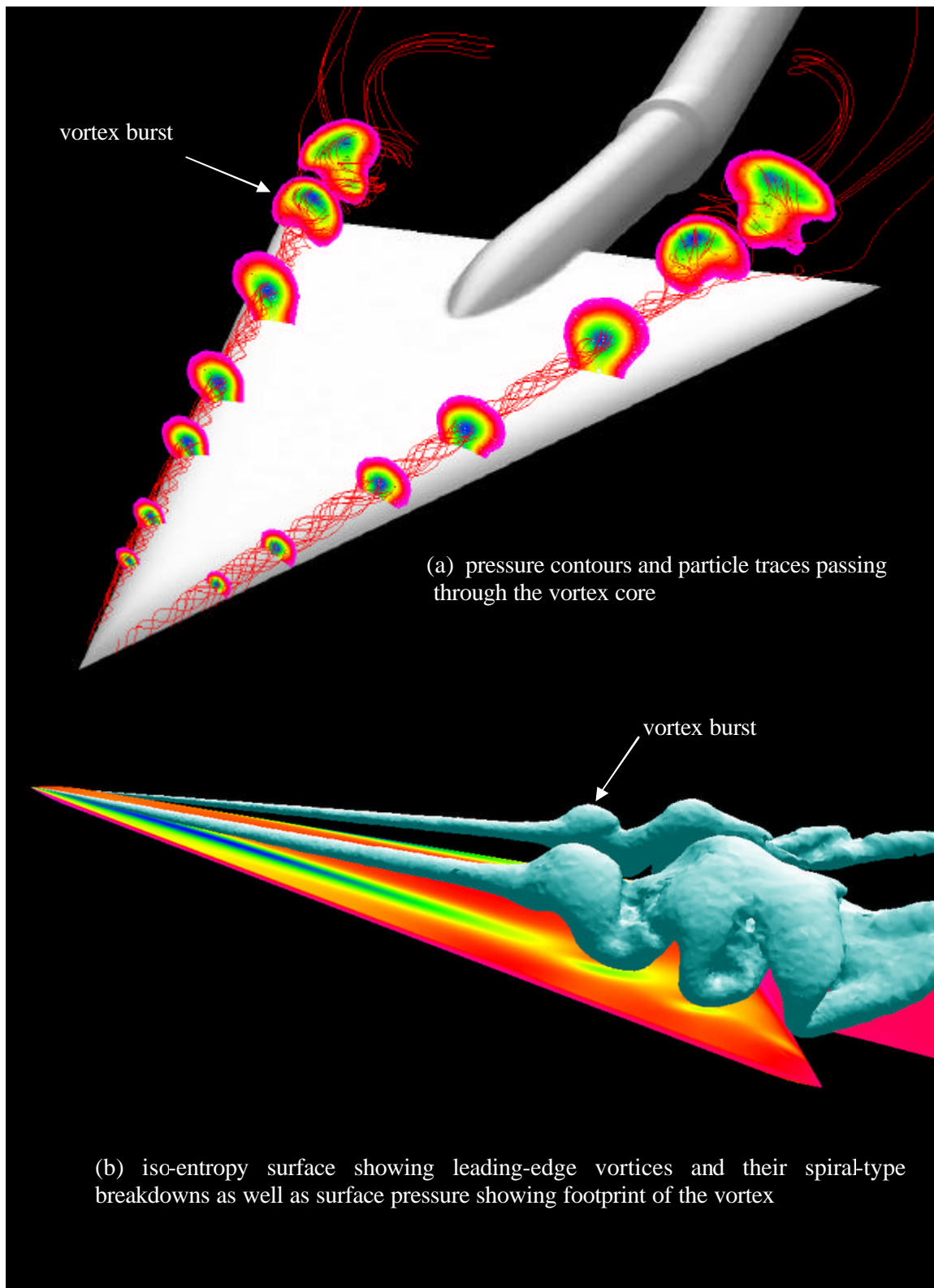


Figure 9: Adapted inviscid flow solution on the sharp leading-edge Delta wing. $M_\infty=0.4$, $\alpha=20^\circ$.

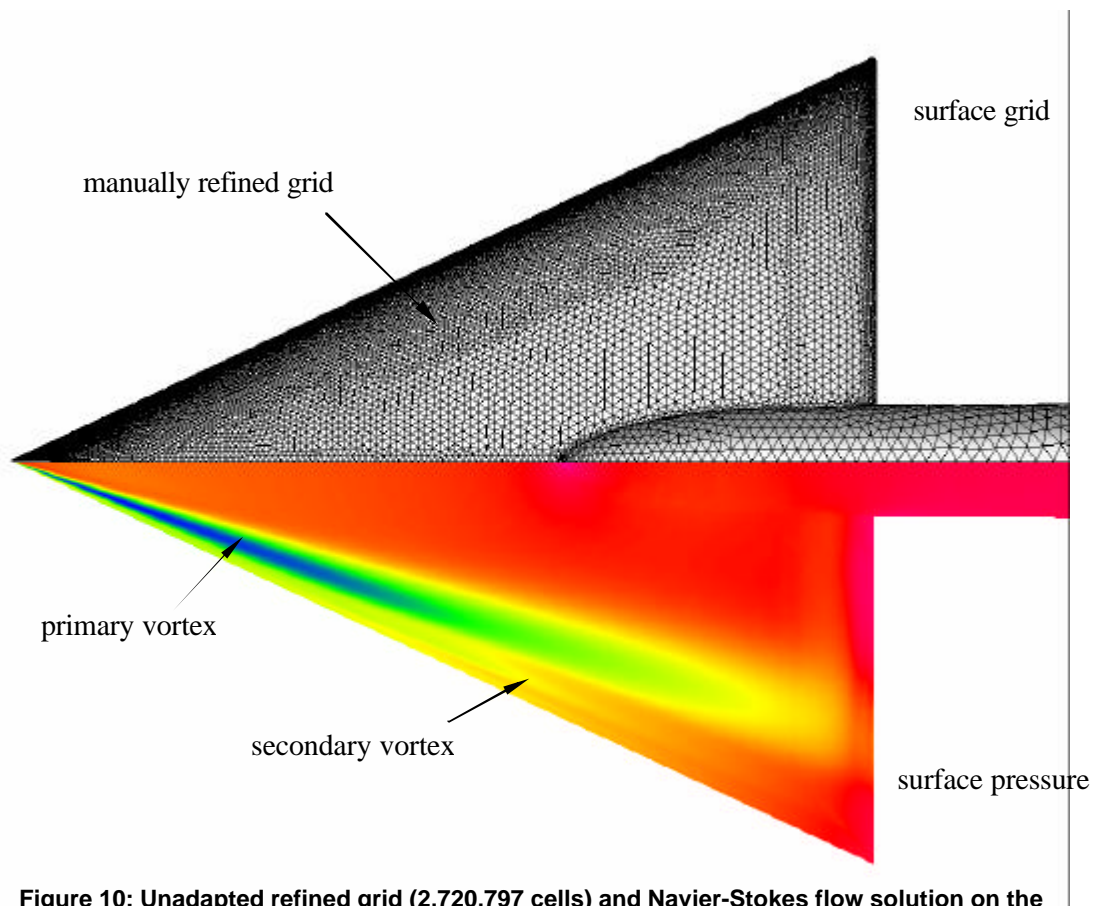


Figure 10: Unadapted refined grid (2,720,797 cells) and Navier-Stokes flow solution on the sharp leading-edge Delta wing. $M_\infty=0.4$, $\alpha=20^\circ$, $Re_{MAC}=6.0 \times 10^6$.

the manual refinement of the grid points around the leading edge and at the vortex location. Although the grid was generated with some prior knowledge of the vortex location, the concentration of points (by insertion of source elements) has clearly missed the vortex core due to its displacement from that predicted by the inviscid solution. This experience highlights the importance of an automatic grid adaptation for vortex flows, which eliminates the need for any "guess-work" in capturing the vortices. Figure 11 also depicts contours of entropy at the free vortex sheet, around the vortex core, and in the boundary layer. A secondary vortex is clearly indicated rotating in the opposite direction of the primary vortex. Note that the distinct annular cluster of contours (concentric rings) around the vortex core in Figure 11 is due to superposition of two sets of contours (with slightly different levels) for better visualization and has no physical significance.

Figure 12 displays 3D views of the wing and vortices similar to those in Figure 9. The drastic change of flow behavior from inviscid to viscous computation is clearly illustrated in these figures. The absence of vortex burst in the viscous result is indicated by axisymmetric distributions of pressure around the vortex core extended further downstream in Figure 12a and the undisturbed iso-entropy tubes in Figure 12b. The strong entropy generation at the free vortex sheet is also shown by the iso-entropy surface in Figure 12b.

The distributions of surface pressure coefficient (C_p) in the spanwise direction (y/b , where b is the local semi-span) are depicted in Figure 13 for five chordwise (x/c) stations. In these plots, the wind tunnel experimental data are compared with those of the inviscid unadapted, inviscid adapted, and viscous (fine grid) solutions for both upper and lower surfaces of the wing. All computational results show good

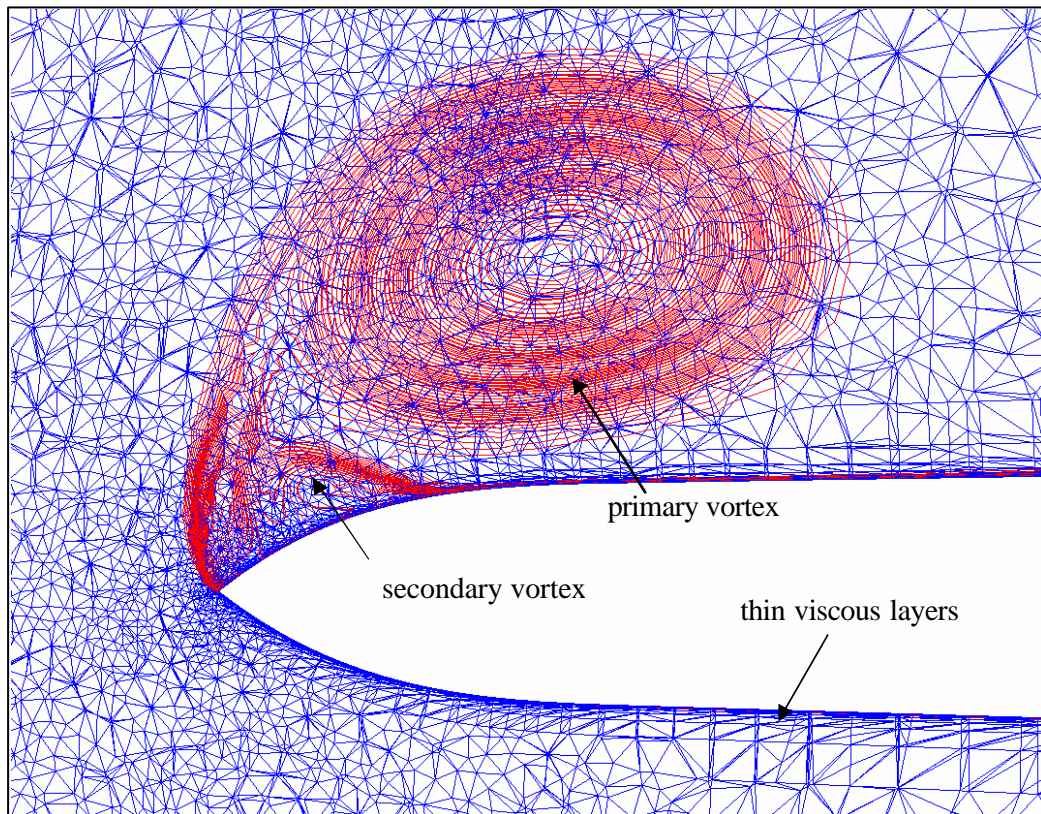


Figure 11. Cross-sections of the sharp leading-edge Delta wing, unadapted refined grid, and entropy contours showing the leading-edge vortices at the mid-root-chord station.

agreement with the experimental measurements on the lower surface in all stations. Similarly, the computational pressure data agree well with the wind tunnel measurements at the inboard section (close to the wing root) on the upper surface everywhere except for the inviscid solutions at the last ($x/c=0.95$) station. The unadapted Euler computation has produced a poor solution in which the vortex-induced pressure is under-predicted in the upstream stations due to the grid coarseness. In the last station, the predicted vortex burst has caused a shift in the C_p distribution to the low-pressure side across the semi-span with a peak region that is completely out of place compared to the experiment data. The adaptive refinement has improved the Euler solution considerably, however the result still mismatches the wind tunnel data as expected from inviscid solutions. As illustrated in Figure 13, the solution increasingly deviates from the experimental data in the chordwise direction, from apex to trailing edge of the wing. The last two stations demonstrate the largest discrepancies due to the computed vortex breakdown. Another obvious weakness of the inviscid solutions is their failure of predicting the secondary vortex as indicated by the monotonic decline of C_p curves near the leading edge (see, for example, the Euler C_p curves at Station $x/c=0.60$.) The Navier-Stokes computation has further enhanced the accuracy of the predicted surface pressure distributions as shown by the solid curves in Figure 13. As evident, both the magnitude and location of the vortex peaks are substantially improved in all stations by the viscous effects, and the secondary vortex is indicated by a smaller peak near the wing leading edge.

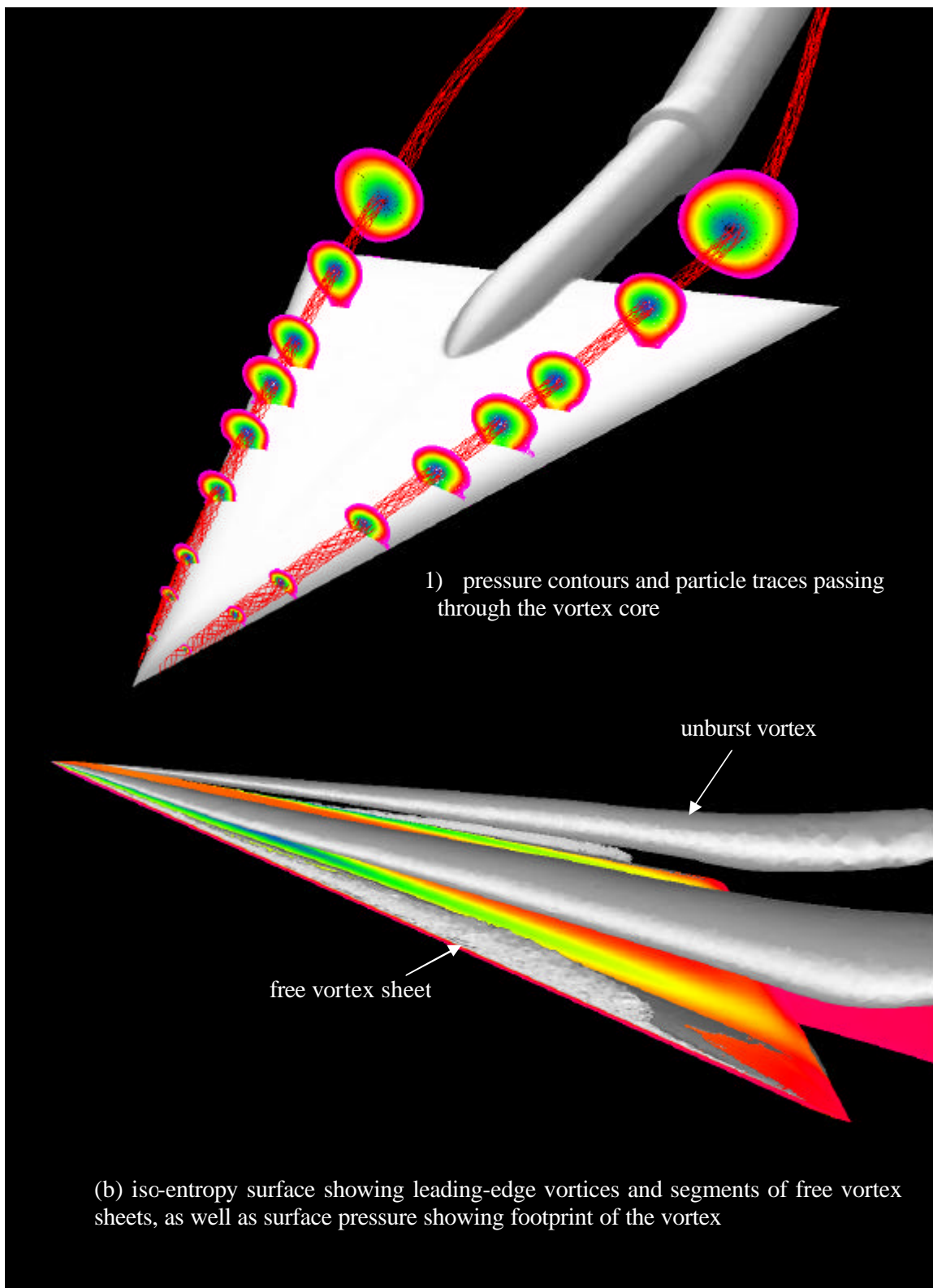


Figure 12: Viscous flow solution on the sharp leading-edge Delta wing. $M_{\infty}=0.4$, $\alpha=20^\circ$, $Re_{MAC}=6.0 \times 10^6$.

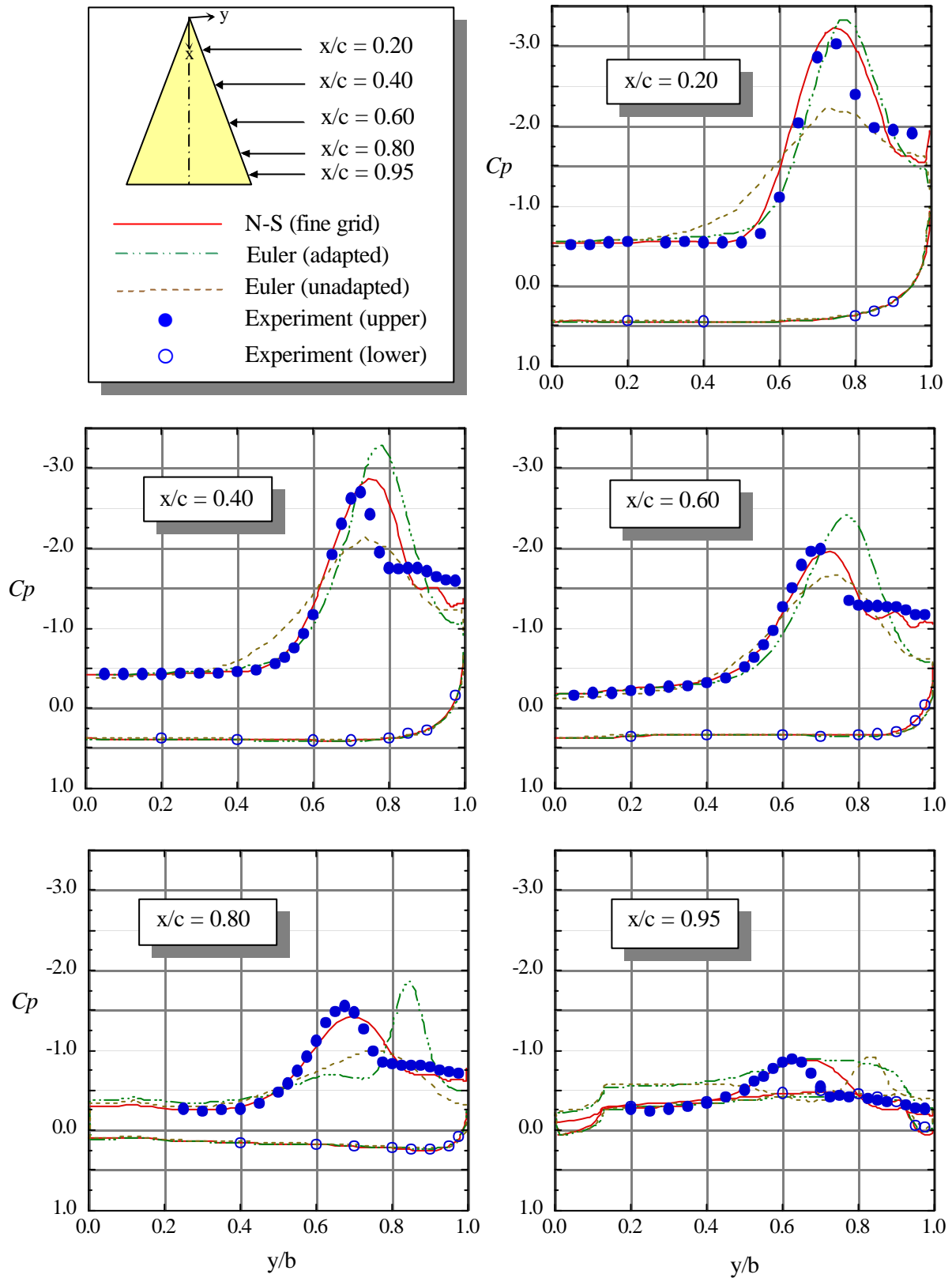


Figure 13: Comparison of spanwise surface pressure coefficients for the 65-degree Delta wing with a sharp leading edge, $M_\infty = 0.4$, $\alpha = 20.0^\circ$, and $Re_{MAC} = 6.0 \times 10^6$.

11.3.1.2 Medium Leading-Edge (Radius = 0.15 % MAC)

To further study the capability of the present CFD method in predicting vortex flows, the Delta wing with blunt leading edge was also computed at the same flow condition. While the primary separation line is fixed at a sharp leading edge, its location on a blunt edge is governed mainly by the flow condition and, thus, becomes part of the problem to be solved. Prediction of vortex flows on such configurations presents a greater challenge for CFD since the problem is more involved with the flow physics (Reynolds number effects) rather than geometric features. The main objective of this test was to investigate the effectiveness of the present Navier-Stokes computation in "capturing" the leading-edge flow separation and vortex formation. Therefore, no attempt has been made to perform Euler computations for the following blunt leading-edge cases.

A surface mesh similar in resolution to that of the preceding viscous grid was generated for the case that features a leading edge of medium radius. Although the surface mesh was refined to resolve the leading edge, no manual refinement of the volume grid at the vortex core was implemented for this initial grid. The grid contains 31,938 boundary nodes, 300,227 total nodes, and 1,689,852 tetrahedrons. Figure 14a portrays the surface grid with a fine resolution around the leading edge and footprint of the vortex on the upper surface of the wing. The figure also shows the corresponding pressure distribution on the upper surface. The influence of the leading-edge bluntness on the vortex flow can easily be observed from a delayed formation of the vortex on the wing by about 26 percent of the root chord. While the sharp leading edge induces flow separation (and vortex formation) up front at the wing apex, the blunt edge restrains the boundary layer for some distance downstream of the apex before it eventually separates and forms a vortex. Another noticeable effect of the blunt leading edge is on the strength of the generated vortices. The primary vortex appears to be smaller than that in the sharp leading-edge case, but the secondary vortex is as strong. As in the case of sharp leading edge, no sign of vortex breakdown is evident from the surface pressure distribution.

As mentioned earlier, the present adaptive method lacks the capability of refining the thin "viscous" cells in the boundary layer at this time. However, the primary features of the vortex flow usually develop outside the boundary layer at high angles of attack. Therefore, it is possible to adapt the inviscid portion of the grid around the vortex core without disturbing the viscous portion. A drawback of such procedure is that, similar to the viscous portion of the grid, the surface mesh also remains intact. Obviously, the lack of surface mesh refinement would adversely affect the computed surface pressure. As before, an entropy production measure was employed to partially adapt the initial grid. The final adapted grid has 31,938 boundary nodes (unchanged), 696,412 total nodes, and 4,000,156 tetrahedrons. Figure 14b shows the surface grid and the solution after adaptation. Although the surface mesh remains unchanged, the pressure distribution shows some improvement (increased strength) of the primary vortex. Figure 15 illustrates cross-sections of the grids and solutions at the mid-root-chord station before and after adaptation. The initial solution is shown in Figure 15a, indicating a fairly diffused vortex system. The partial adaptation has added many grid nodes at the primary and secondary vortex locations and, consequently, strengthened the vortex structure as seen in Figure 15b. A comparison of this solution to that shown in Figure 11 suggests that the edge bluntness has created a smaller primary vortex and has moved the vortex cores closer to the surface and further inboard away from the leading edge.

The surface C_p distributions for the medium leading edge are presented in Figure 16. The plots display the results of the initial and adapted solutions compared with the experimental data at the same chordwise stations as before. Both the initial and adapted solutions have failed to capture the leading edge vortex at the first station ($x/c=0.20$). The onset of the vortex is predicted slightly downstream of this station at about $x/c=0.23$ as evident from the surface pressure plots in Figure 14. The reason for the delay in the

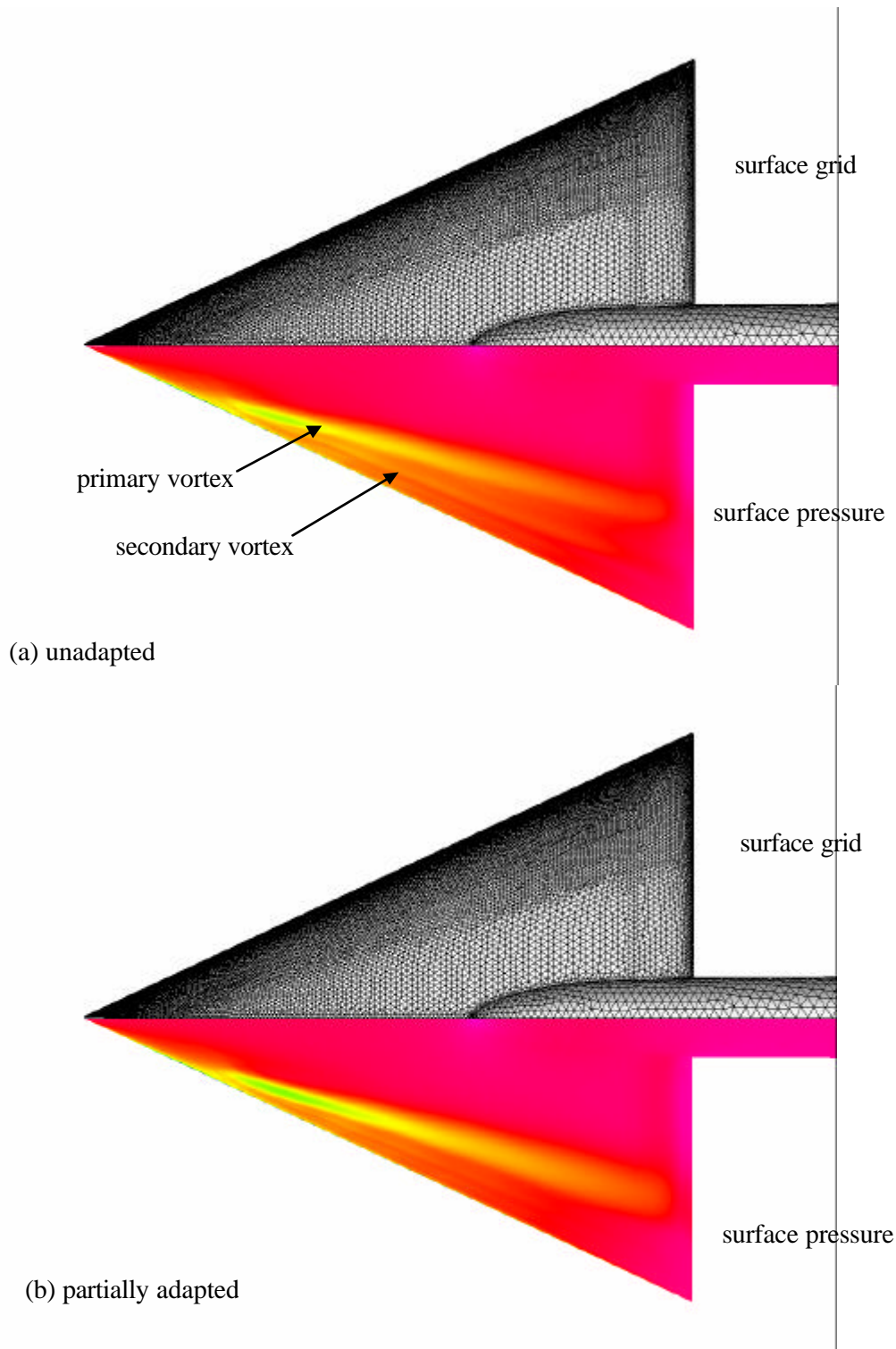


Figure 14: Comparison of Navier-Stokes flow solutions on medium leading-edge Delta wing: (a) unadapted grid (1,689,852 cells) and (b) inviscid portion of grid refined adaptively (4,000,156 cells). $M_\infty=0.4$, $\alpha=20^\circ$, $Re_{MAC}=6.0 \times 10^6$.

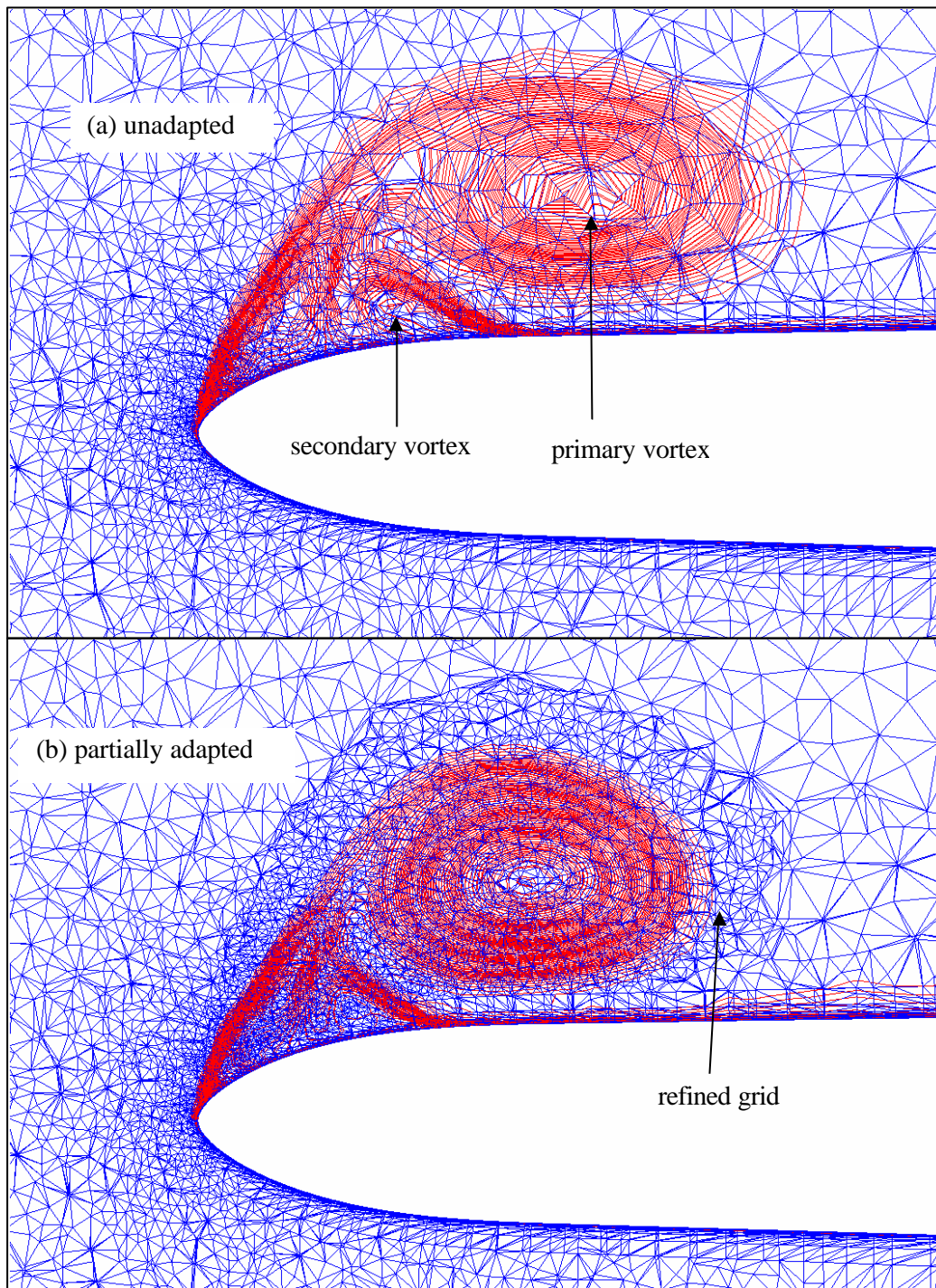


Figure 15: Comparison of viscous flow solutions on medium leading-edge Delta wing at the mid-root-chord stations: (a) unadapted grid and (b) inviscid portion of grid refined adaptively. $M_\infty=0.4$, $\alpha=20^\circ$, $Re_{MAC}=6.0 \times 10^6$.

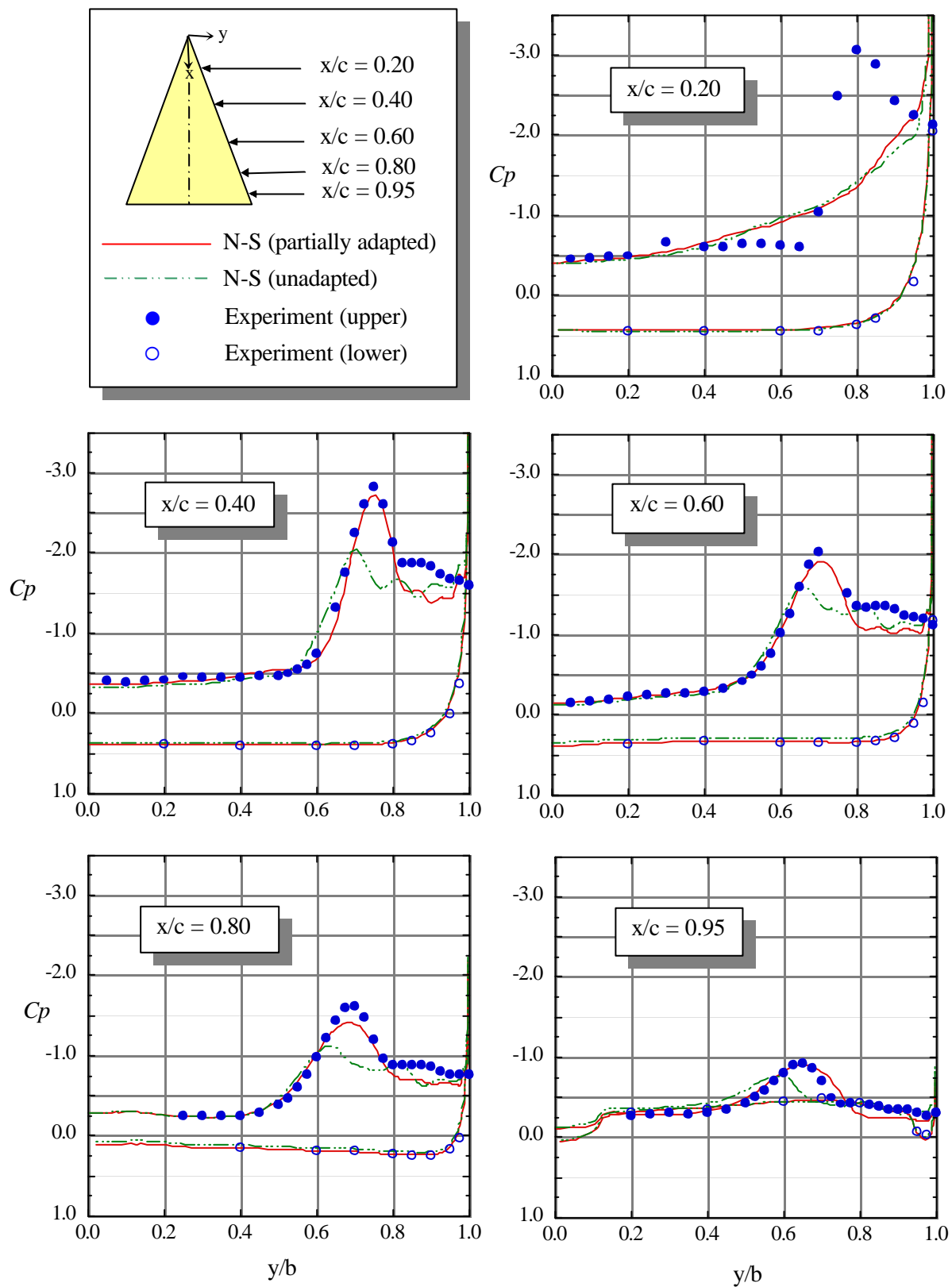


Figure 16: Comparison of spanwise surface pressure coefficients for the 65-degree delta wing with a medium radius leading edge at $M_\infty = 0.4$, $\alpha = 20.0$ degrees, and $Re_{MAC} = 6.0 \times 10^6$.

computed vortex formation is not fully understood at this time and requires further investigation. Possible causes include coarseness of the initial surface grid (unrefined by the partial adaptation) at the leading edge and the solution techniques employed in the flow solver such as the turbulence model, wall function, lack of laminar-to-turbulence transition, etc. Further study of CFD vortex prediction on blunt leading edges is planned for future work in conjunction with a full implementation of the "viscous" grid adaptation. Figure 16 shows that adaptation has considerably improved the prediction of the primary vortex at other stations. However, the partial refinement has not enhanced the solution accuracy at the secondary vortex location (near the boundary layer) where the viscous portion of the grid remains unrefined.

11.3.1.3 Large Leading-Edge (Radius = 0.30 % MAC)

The last test on the Delta wing was performed on the model geometry with a leading edge of large radius. As in the preceding blunt-edge case, an initial grid was generated with a manual refinement of the grid around the leading edge but not in the field. This grid contains 33,014 boundary nodes, 326,096 total nodes, and 1,839,186 tetrahedrons. The surface grid, along with the corresponding surface pressure distribution, is depicted in Figure 17a. After a partial adaptation, the total node and cell counts increase to 819,482 and 4,718,896, respectively, but the surface grid remains intact. Figure 17b shows the adapted surface mesh and the corresponding solution on the surface. The surface pressure distributions in Figure 17 indicate that the onset of the vortex is further delayed to about 40 percent of the root chord because of the increased leading-edge bluntness. Unlike the medium leading-edge case in which grid adaptation produced a noticeable enhancement in the solution, the present case shows no major sign of change in the surface pressures before and after adaptation.

Figure 18 portrays the cross-sections of the initial and adapted grids along with the corresponding entropy contours. As evident, the free vortex sheet makes a smaller angle with the wing surface in this case, as compared with the preceding cases, and the primary separation point has moved further inboard away from the leading edge. In addition, the primary vortex has become even smaller and moved closer to the boundary layer as compared with that in the medium leading-edge case. As shown in Figure 18b, a large number of nodes have been added by the partial adaptation around the primary vortex core (except at the lower portion) and above the secondary vortex outside the boundary layer. Because of the smaller size of the vortices and their closer proximity to the surface in this case, a larger proportion of the region influenced by the vortices falls in the unrefined viscous grid portion. This undesirable condition may explain why the partial grid adaptation has been less effective in improving the surface pressure for this case and highlights the limitation of partial grid adaptation.

Figure 19 shows 2D plots of the surface C_p distributions for the large leading-edge case. As expected, the partially adapted solution presents marginal improvement in the surface pressure distribution. However, the overall quality of the CFD solutions is reasonably good considering the present limitation of the adaptive refinement method for viscous flow computations, and the complex nature of vortex flows on blunt leading edges. Both computations agree with the experimental data regarding the absence of the vortex at the first station ($x/c=0.20$). The largest discrepancy between the CFD and experiment data appears at Station $x/c=0.40$ where the vortex peak is under-predicted computationally. A close review of Figure 17 reveals that the onset of the vortex is predicted at about 40 percent of the root chord (the second station) where the signature of the vortex on the surface is highly diffused. The peak is slightly delayed to about 45 percent of the root chord, as indicated by a low-pressure (green) spot in Figure 17b. The agreement between the CFD and experimental data is better in other stations as illustrated in Figure 19. Figure 20 compares the vortex flows predicted by the Navier-Stokes solutions on the three leading edge cases. In this figure, velocity vectors are plotted on cross-sectional planes at the wing mid-root-chord station. As indicated, the size of the primary vortex decreases as the radius of the leading edge increases. The cross-flow velocity profiles in the boundary layer, induced by the primary vortices, are also illustrated

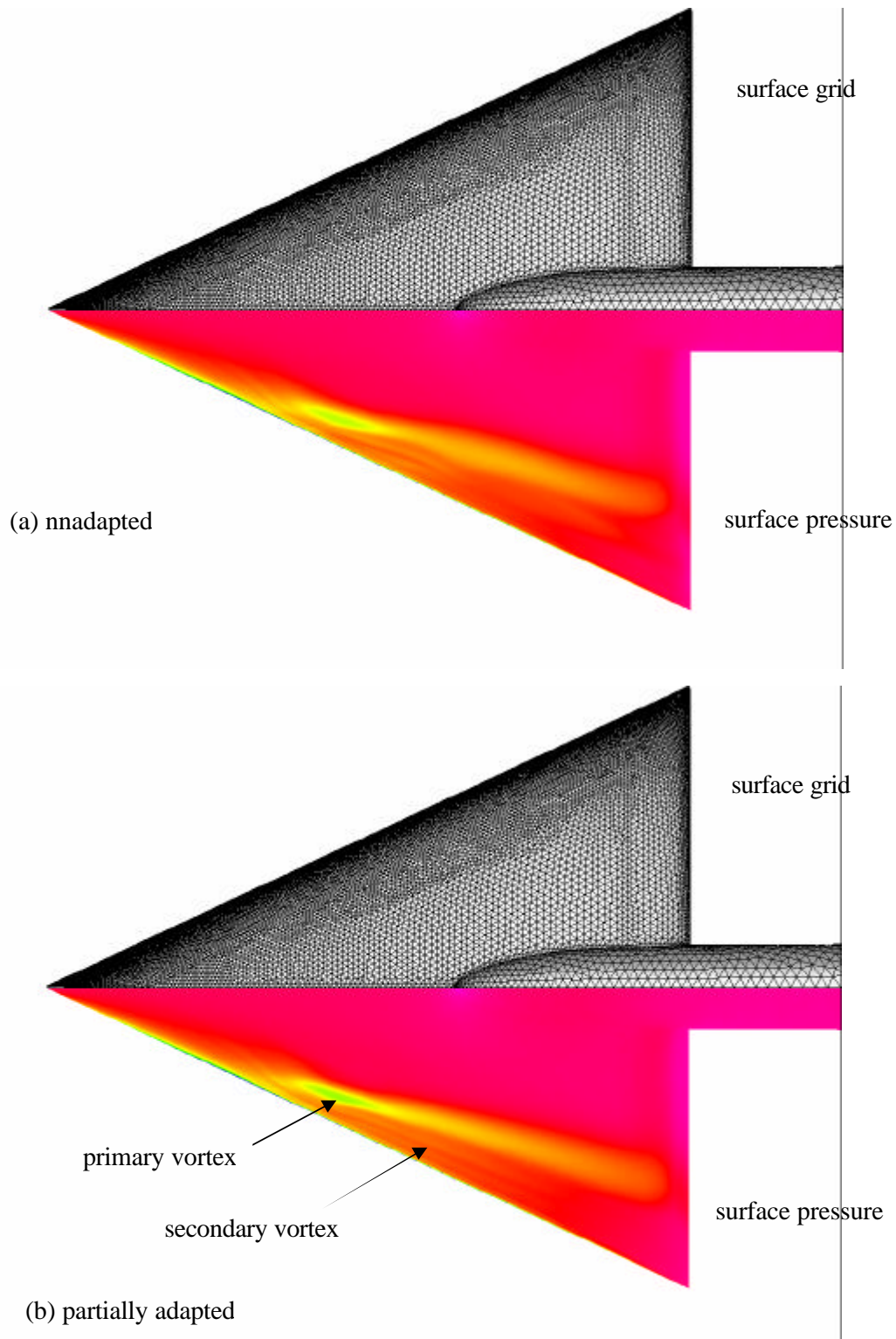


Figure 17: Comparison of Navier-Stokes flow solutions on large leading-edge Delta wing: (a) unadapted grid (1,839,186 cells) and (b) inviscid portion of grid refined adaptively (4,718,896 cells). $M_\infty = 0.4$, $\alpha = 20^\circ$, $Re_{MAC} = 6.0 \times 10^6$.

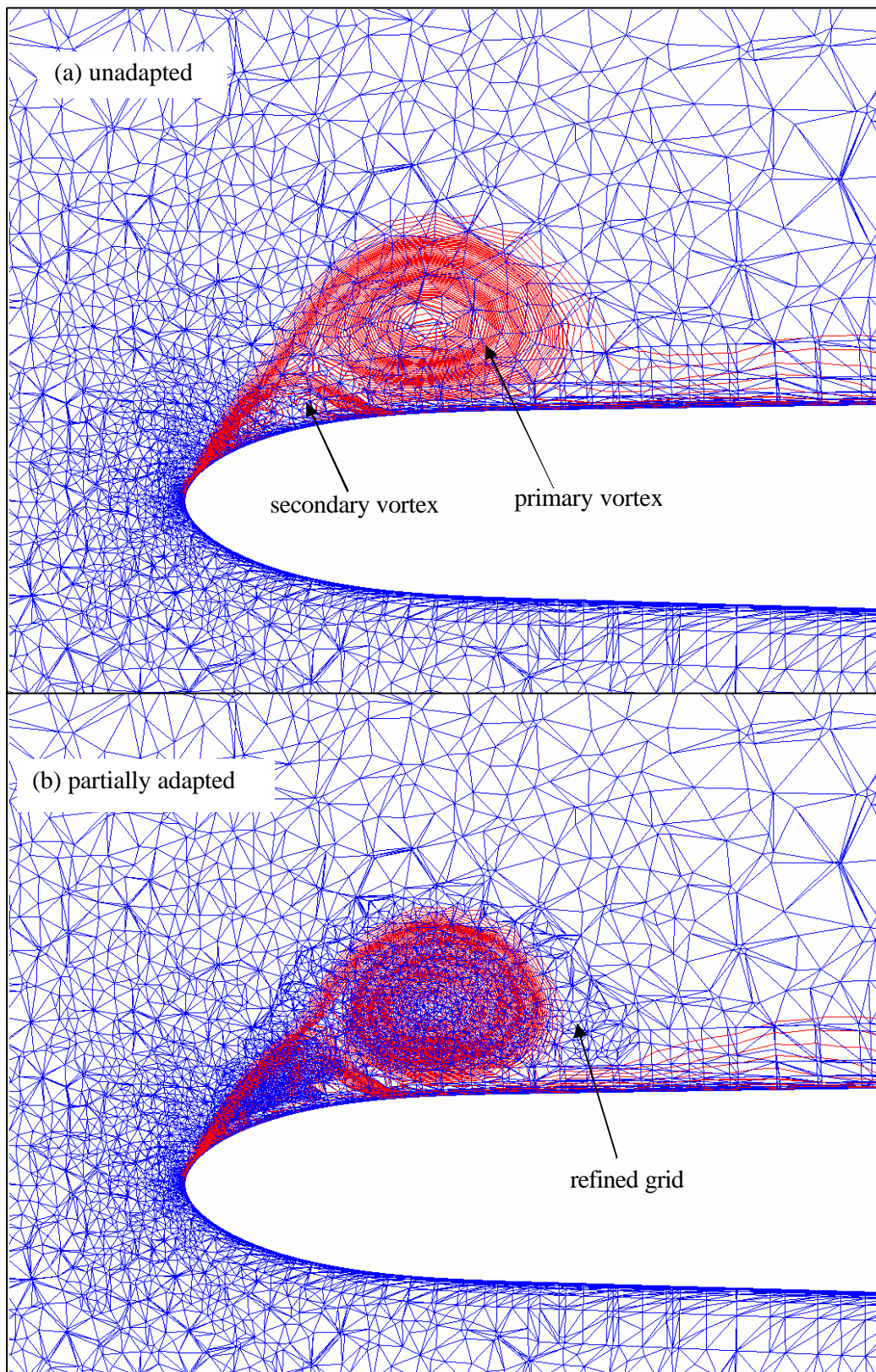


Figure 18: Comparison of Navier-Stokes flow solutions on large leading-edge Delta wing at the mid-root-chord station, (a) unadapted grid and (b) inviscid portion of grid refined adaptively. $M_\infty=0.4$, $\alpha=20^\circ$, $Re_{MAC}=6.0 \times 10^6$.

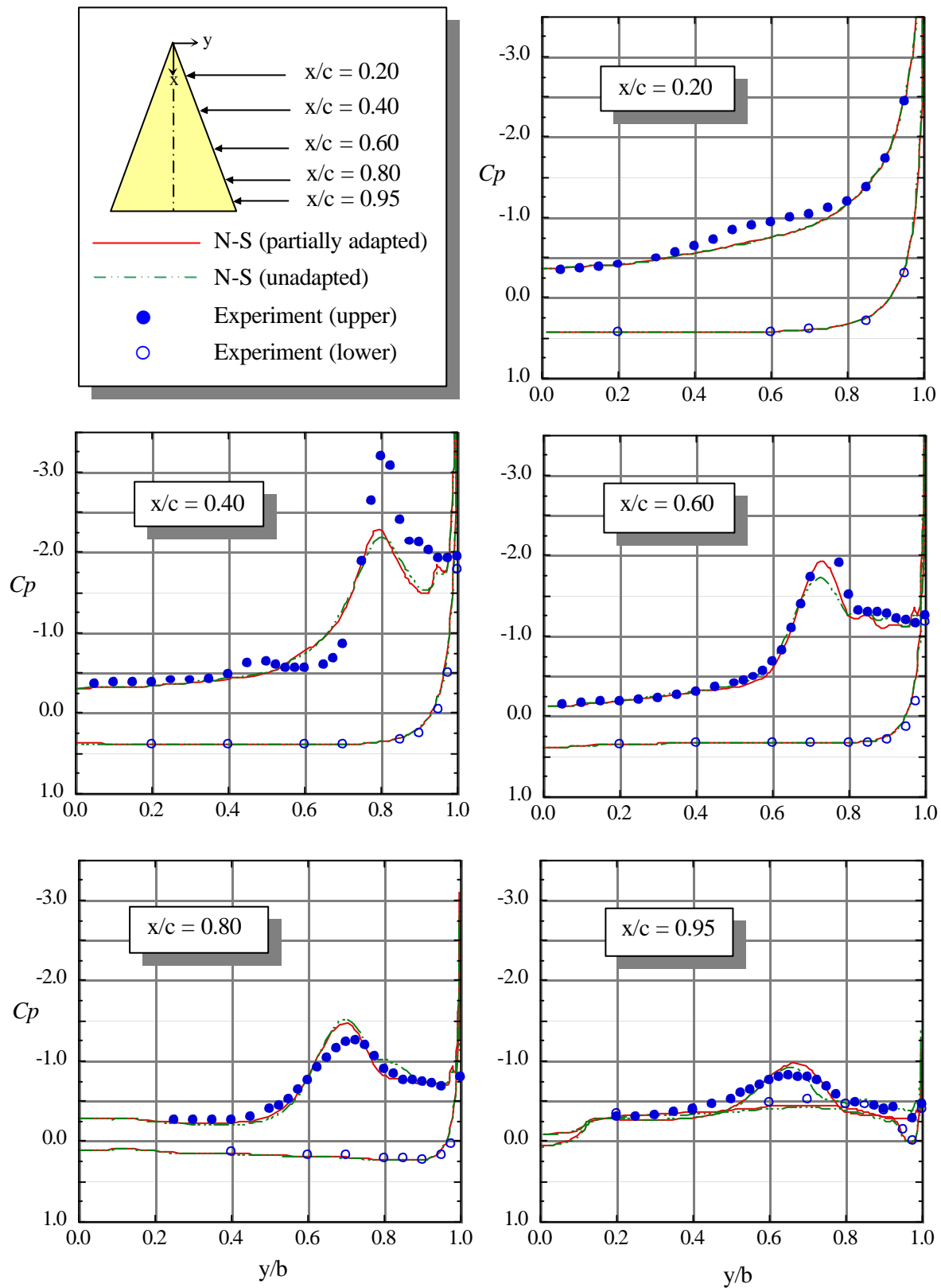


Figure 19: Comparison of spanwise surface pressure coefficients for the 65-degree Delta wing with a large radius leading edge at $M_\infty = 0.4$, $\alpha = 20.0$ degrees, and $Re_{MAC} = 6.0 \times 10^6$.

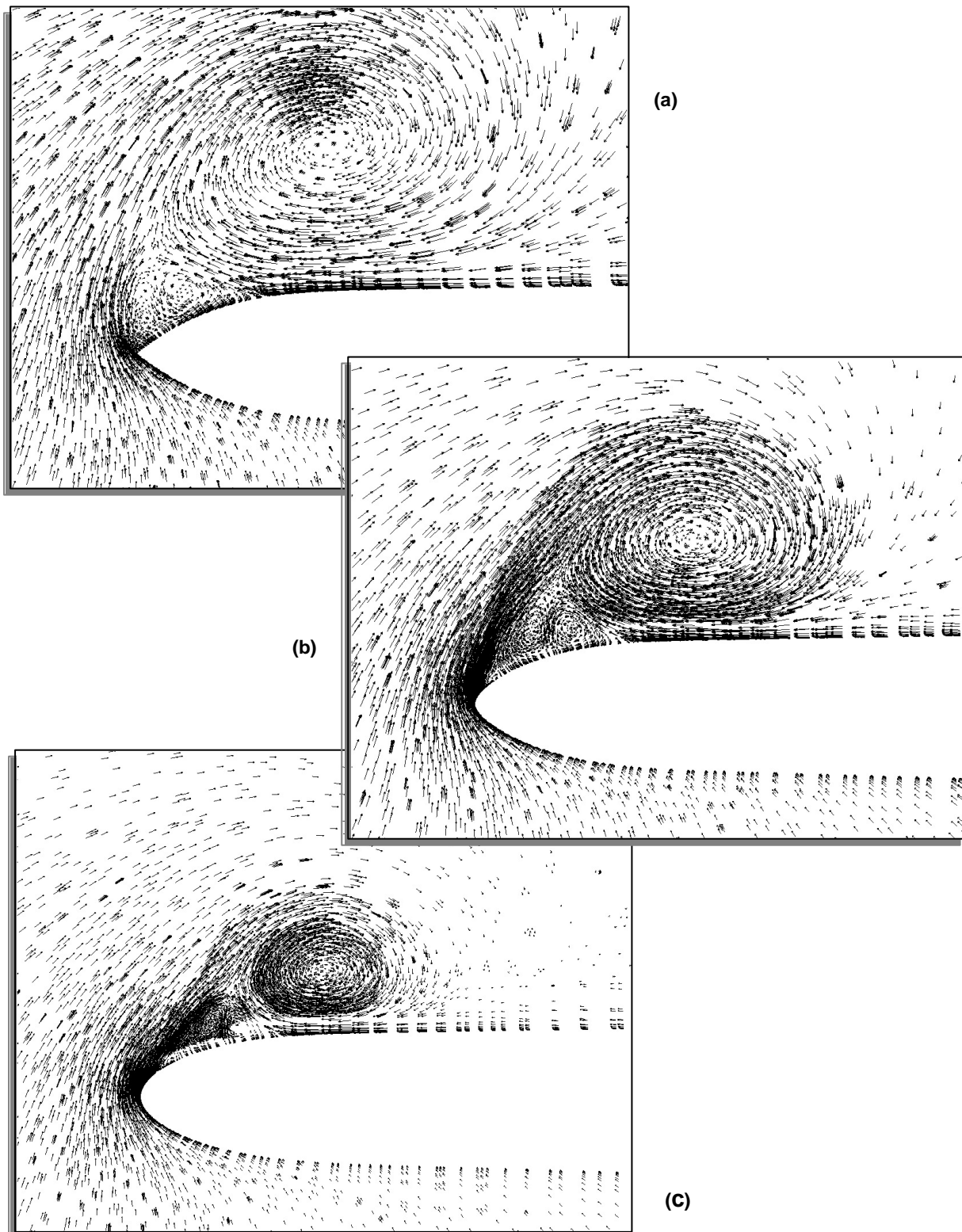


Figure 20: Delta wing velocity vectors on cross-sectional planes at the mid-root chord stations showing primary, secondary, and "tertiary" vortices: (a) sharp leading edge, (b) medium leading edge, and (c) large leading edge. Navier-Stokes solutions at $M_\infty=0.4$, $\alpha=20^\circ$, and $Re_{MAC}=6.0 \times 10^6$.

in these figures. The velocity vectors clearly show the secondary separation points followed by the boundary layer reversed flows forming the secondary vortices. Another interesting flow feature, revealed by these plots, is the presence of a third vortex rotating in the same direction sense of the primary vortex and located close to the leading edge (see, for example, Figure 20b). This additional vortex, along with the secondary vortex, has caused a "double-hump" characteristic in the computational C_p curves at the mid-root-chord station around $y/b=0.9$ (Figures 13, 16, and 19). Although a tertiary vortex is normally located between the primary and secondary vortices (see Figure 1), experiments have shown that in some cases a third vortex (also called tertiary) develops between the free vortex sheet and the secondary vortex [17]. In the absence of any off-body experimental data, it is difficult to verify the CFD prediction of a third vortex in this case. However, the experimental C_p data exhibit similar double-hump behavior at some locations, which may indicate the existence of two small vortices close to the leading edge (see, for example, the experimental C_p distribution at $x/c=0.60$ in Figure 16.)

11.3.2 Modular Transonic Vortex Interaction Configuration

The second test case concerns a generic fighter model referred to as the Modular Transonic Vortex Interaction (MTVI) shown in Figure 21. The geometry has been tested in the NASA Langley 7- by 10-foot High Speed Tunnel for a speed range of subsonic to low supersonic and at a wide range of angles of attack [18]. The geometry has also been tested in the Langley Unitary Plan Wind Tunnel for supersonic speeds up to Mach number 2.16 (unpublished at the time of preparing this paper). The experiments provide an excellent database for CFD code validation and investigating the leading-edge vortex interaction with the airframe components as well as their interference with shock waves on a realistic fighter configuration. The extensive amount of experimental data includes surface pressure measurements, force/moment data, and flow visualization both in the form of still images and movies.

The MTVI geometry consists of a chined forebody, a 60-degree cropped delta wing with a segmented leading-edge flap, and two different interchangeable vertical tails: single centerline and twin outboard. A photograph of the model with both types of vertical tails (mounted for demonstration) is shown in Figure 21a. In addition, two types of fuselage cross-sections have been tested on this configuration: baseline with a forebody chine angle of 30 degrees and a large chine with an included angle of 100 degrees (Figure 21b). The configuration features sharp edges on the chine and the wing that induce leading-edge flow separations and vortices at high angles of attack. As explained earlier, such a geometric feature makes the case suitable for inviscid flow computations. The numerical results presented here are limited to adaptive inviscid Euler solutions only. Additional flow computations on this model, planned for future work, will include adaptive Navier-Stokes results.

Two inviscid Euler computations were performed on the MTVI configuration at angles of attack of 20 and 30 degrees. These two cases were selected to demonstrate the vortex behavior and its interaction with airframe components at different conditions. As in the preceding case, a subsonic flow regime at a freestream Mach number of 0.4 was considered for this test to eliminate further flow complications due to shock/vortex interactions.

The first computation was performed at an incidence of 20 degrees. The computational model was simulated with partially deflected leading-edge flaps and twin vertical tails, and the aft portion of fuselage was extended by one body length to mimic the sting. The initial grid on half of the model contains 31,565 nodes and 163,619 tetrahedral cells that marginally resolve the main features of the flow. No attempt has been made to cluster grid points at locations where vortices are expected. After three levels of adaptation, the grid is appropriately refined at the critical locations based on an entropy indicator. The final grid contains 108,014 nodes and 564,727 cells. Figure 22a illustrates a composite image of the surface triangulation for the initial coarse grid (port) and after adaptation (starboard) side by side. The cross-sections of the initial and adapted volume grids are shown at a streamwise station ahead of the vertical tails in Figure 22b. The automatic refinement of the surface and volume grids, as adapted to the chine and

wing vortices, is clearly indicated in these figures. The corresponding initial and adapted solutions on the surface and in the field are displayed in Figure 23. The adapted solution has produced sharper footprints of the wing and chine vortices on the surface as indicated by the pressure distribution in Figure 23a. A profile of the pressure distribution in the field in front of the vertical tails, along with the surface pressure, is portrayed in Figure 23b. The figure clearly shows that the adaptation has successfully captured two well-defined vortices emanating from the sharp leading edge of the deflected flap and the wing snag (starboard side in Figure 23b). On the other hand, the unadapted solution on the port side shows a vortex system that is diffused due to the coarseness of grid around the leading edge.

The adaptive refinement of the grid has not only resolved the details of the vortex structure in this example

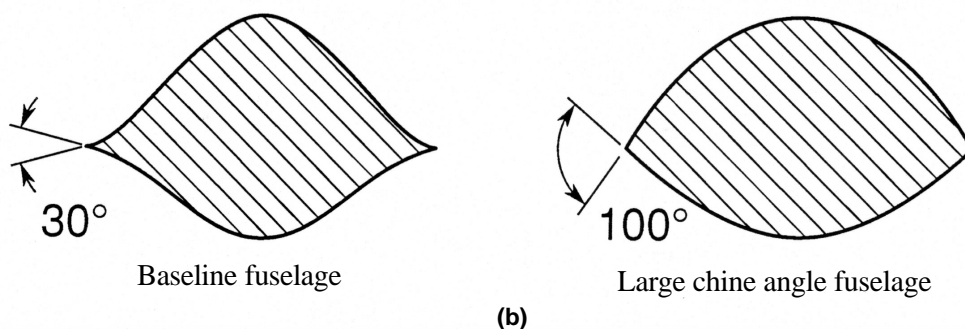
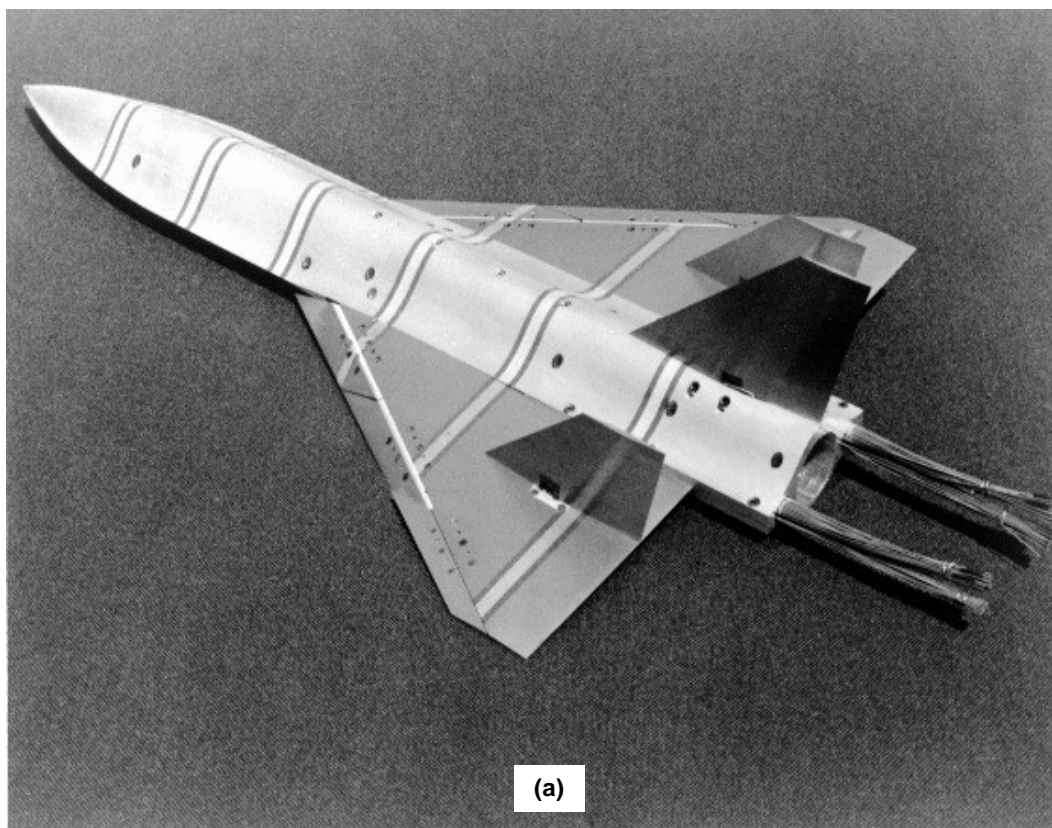


Figure 21: Modular Transonic Vortex Interaction (MTVI) configuration: (a) wind tunnel model and (b) two types of fuselage forebody cross-sections.

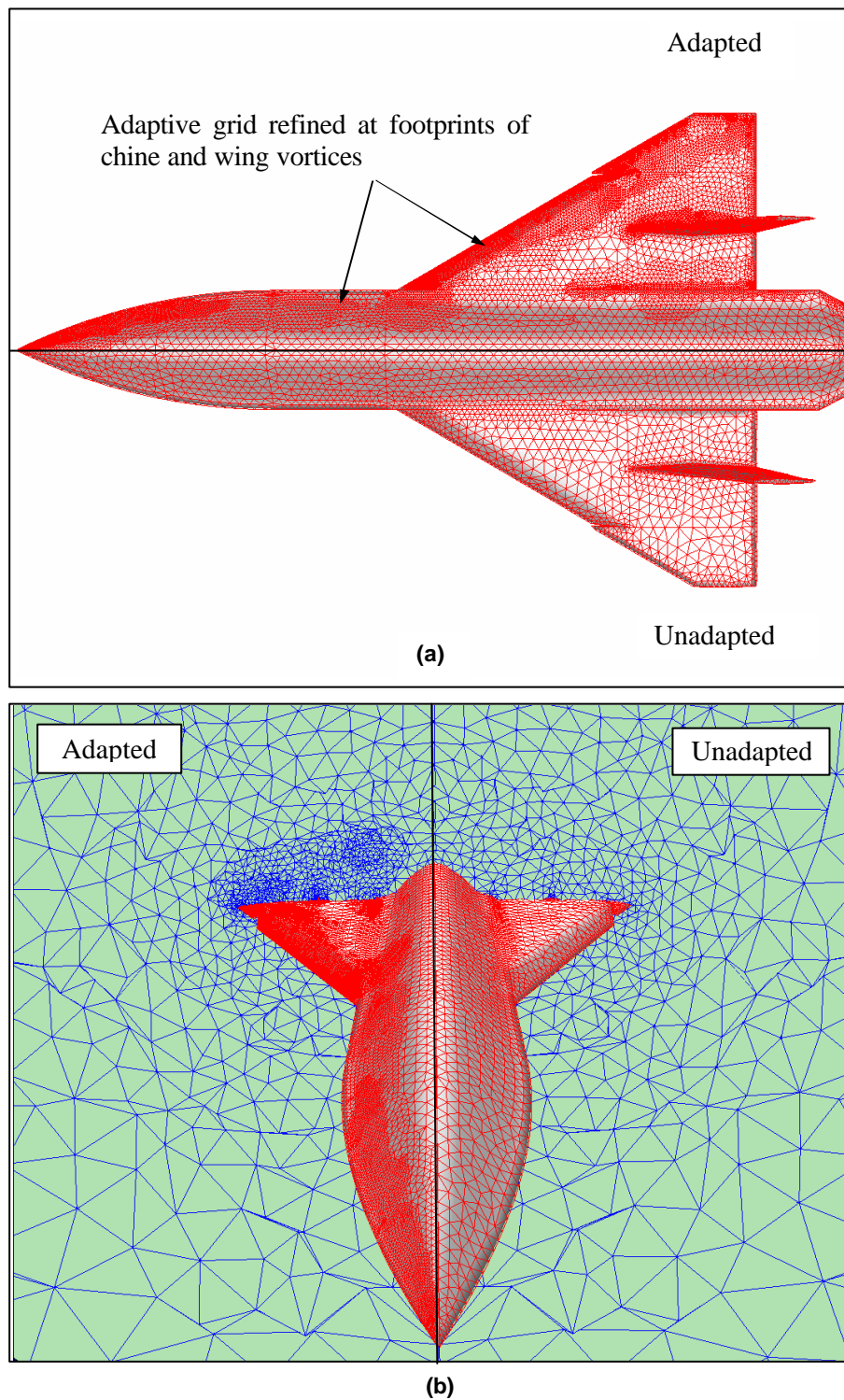
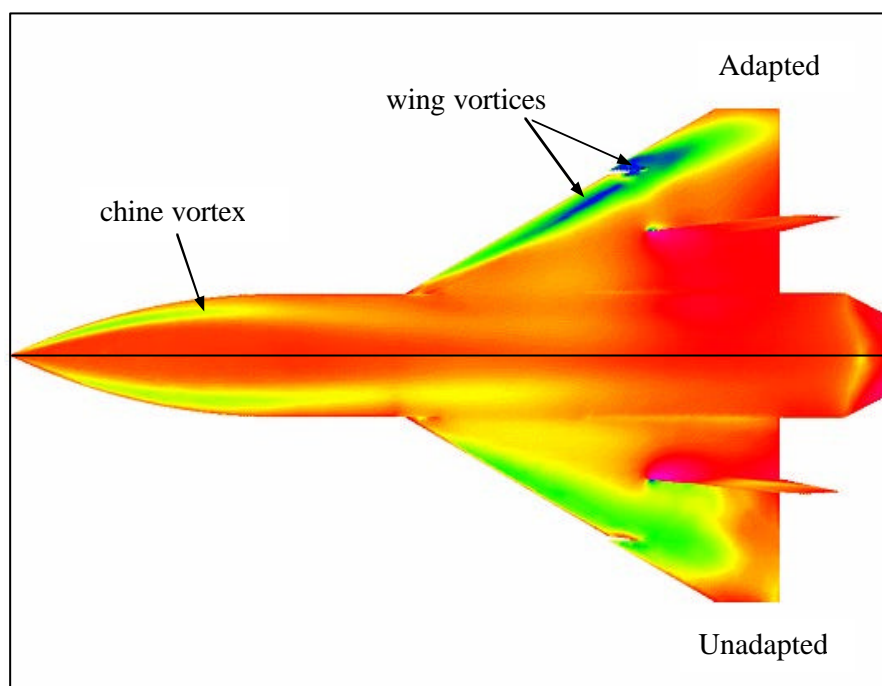
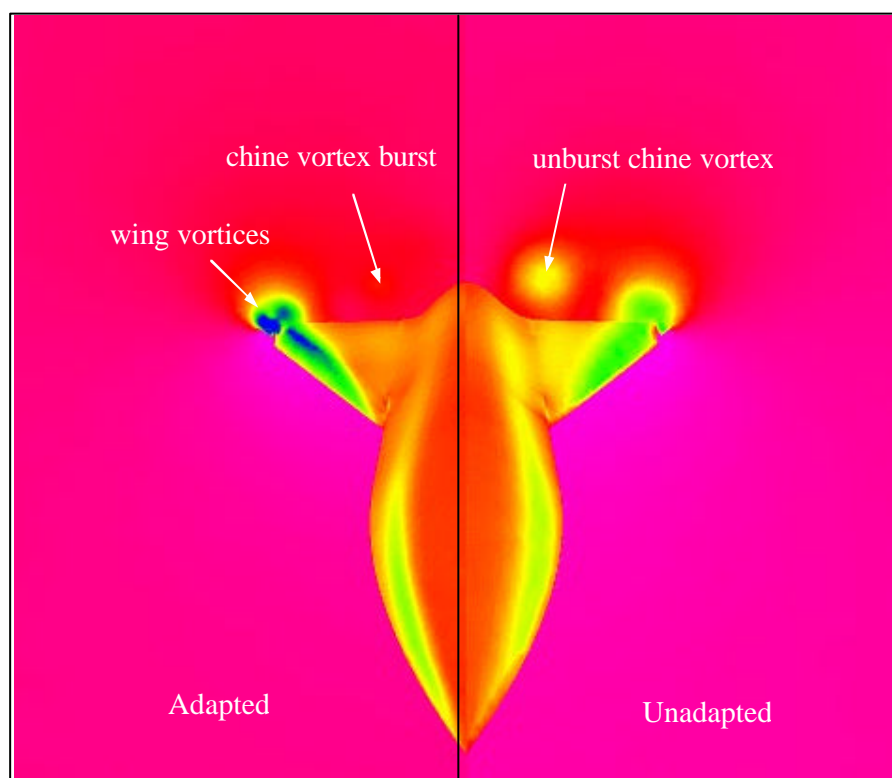


Figure 22: Initial (163,619 cells) and adapted (564,727 cells) unstructured grids on the MTVI configuration: (a) surface mesh and (b) surface/volume grid.



(a)



(b)

Figure 23: Initial and adapted static pressure distributions on the MTVI configuration: (a) surface and (b) surface/volume. $M_\infty=0.4$, $\alpha=20^\circ$.

but also correctly predicted the chine vortex breakdown in front of the vertical tails. Figure 24 shows local refinement of the volume grid (open pockets) at the vortex locations at two different stages of adaptation. A refinement of the initial grid, triggered by the first solution, indicates a chine vortex extending beyond the aircraft tail (Figure 24a). However, it is known from experimental observation on a similar case that the chine vortex bursts before reaching the vertical tail. Therefore, the initial computation has provided an inaccurate solution to the problem. After three cycles of grid adaptation, the final solution eventually verifies the breakdown of the chine vortex in front of the vertical tail. Figure 24b shows regions of high entropy in the final grid (flagged cells) at locations where the chine and wing vortices form. The sudden termination of flagged cells ahead of the vertical tail is indicative of the vortex breakdown. Similarly, the absence of a chine vortex signature on the cutting plane in Figure 23b (starboard) confirms the burst of the vortex in front of the vertical tail. In contrast, the initial solution in Figure 23b (port) shows a strong chine vortex at the same location.

As mentioned earlier, a similar formation of the chine and wing vortex system on the MTVI model has been observed in the wind tunnel as shown in Figure 25. The photograph, which is actually a clip of a movie showing the movement of the laser sheet back and forth, also confirms the breakdown of the vortex in front of the vertical tail where the laser sheet stands. The computations, in this case, have further demonstrated the significance of automatic grid adaptation for producing accurate solutions to vortical flow problems.

A second computation was performed on a slightly modified MTVI configuration at an incidence of 30 degrees and a Mach number of 0.4. The rearward extension of the fuselage, acting as a sting in the preceding computation, was removed since further study showed that the effect of the sting on the vortical flow was negligible in this case. In addition, the wing leading-edge flap was modelled undeflected for the new grid to match the configuration tested in the wind tunnel. The final adapted grid contains 189,761 nodes and 1,049,716 cells. Figure 26 illustrates tetrahedral cells in the grid experiencing high entropy production in the flow due to generation of vortices from the chine and the wing leading edges. As evident, both vortices are clearly captured in this case by grid adaptation. Unlike the preceding case in which the chine vortex bursts before reaching the vertical tail, the present condition promotes further extension of the vortex downstream. The chine vortex continues until it impinges on the vertical tail where it eventually breaks. For comparison, a photograph of the MTVI tested in the wind tunnel at the same conditions is presented in Figure 27. The vortex flow structure in this photograph resembles the computational simulation illustrated in Figure 26. Both images show that the chine vortex breakdown is delayed until it hits the vertical tail and that the wing vortex bursts above the tail.

Unlike the Euler computation in the Delta wing case that did not match the experimental data with regard to the prediction of vortex breakdown, the present inviscid approximations on the MTVI have indeed produced remarkably good solutions. Further Navier-Stokes computations on the MTVI are planned for future work.

The feature indicator employed in both MTVI cases was based on an entropy measure similar to that used for the Delta wing tests. Grid elements experiencing entropy levels of higher than a threshold (a small fraction of the maximum entropy produced in the field) were flagged for removal at each adaptation cycle. In the present cases, typical cut-off values ranging from 0.01 to 0.08 have been prescribed to locate vortices and their breakdowns.

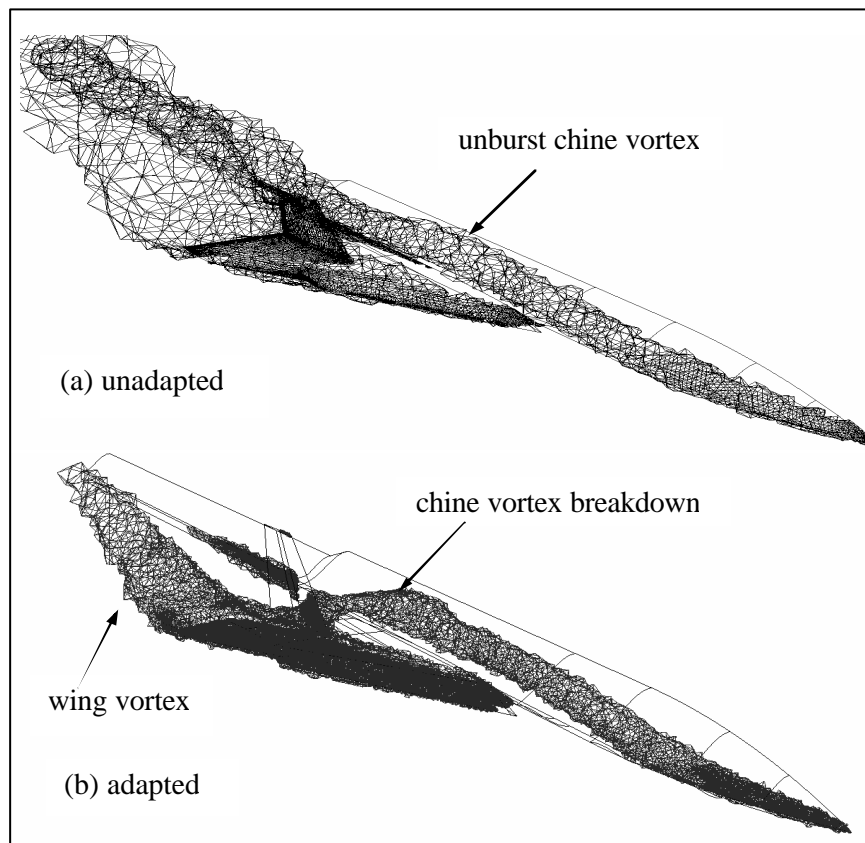


Figure 24: Local grid refinement at high entropy regions on the MTVI volume grid: (a) initial grid and (b) final adapted grid indicating the chine vortex burst.

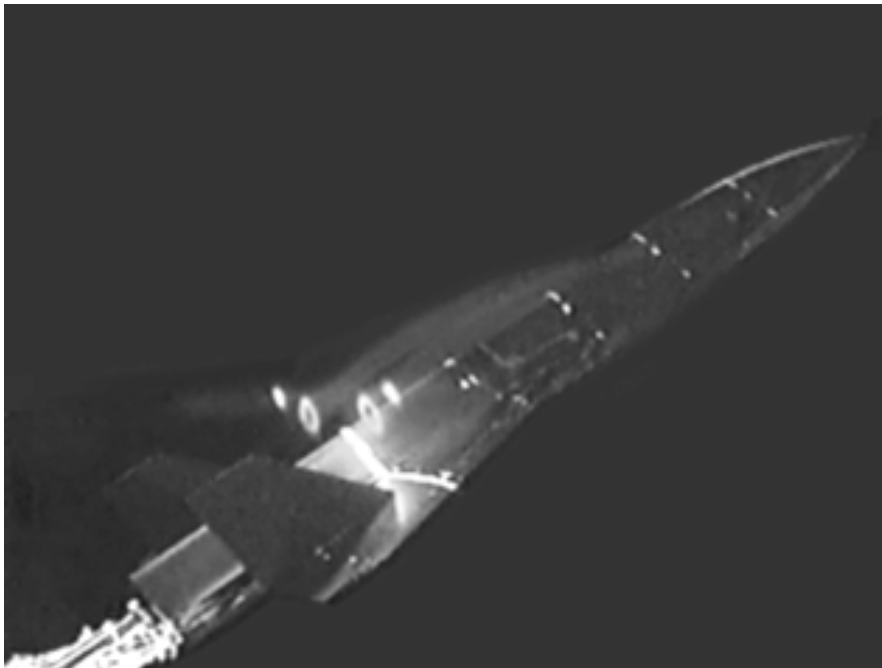


Figure 25: Wind tunnel visualization of flow around the MTVI configuration showing chine vortex burst at $M_\infty=0.4$.

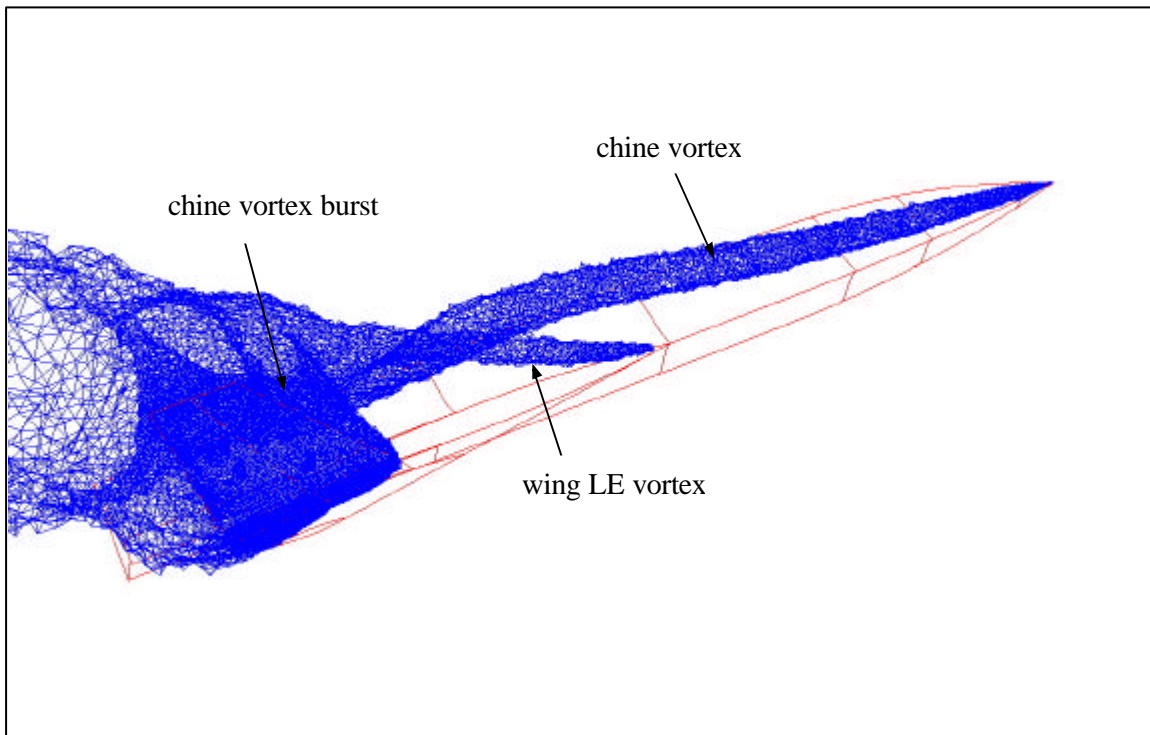


Figure 26: Adapted grid (1,049,716 cells) showing computed chine and wing vortices and their breakdowns on the MTVI configuration, $M_\infty=0.40$, $\alpha=30^\circ$.

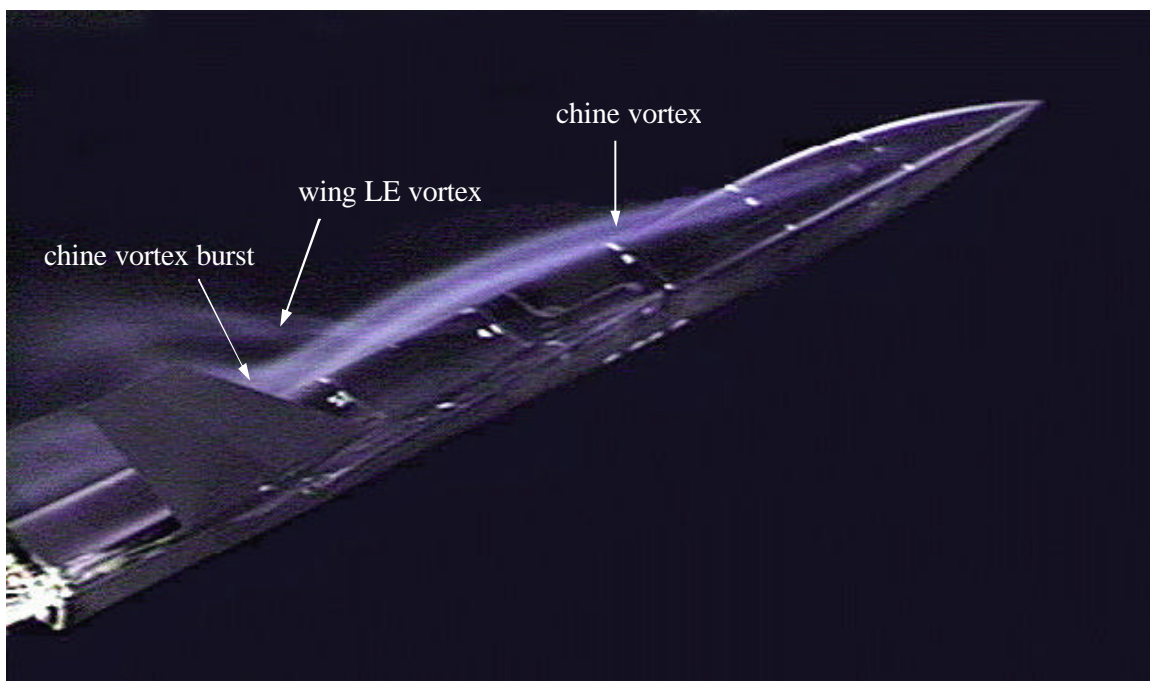


Figure 27: Experimental visualization of vortical flow around the MTVI configuration, $M_\infty=0.40$, $\alpha=30^\circ$.

11.4 CONCLUDING REMARKS

An unstructured-grid CFD methodology has been applied to two vortical flow test cases. The methodology is based on proven existing computational techniques, which has recently been extended for solution adaptive grid refinement. The "pilot" technology has demonstrated excellent potential for solving vortical flow problems in an efficient and practical manner. The objective of the present computations was to investigate on the vortex capturing capability of the method in the absence of additional flow complexities such as shock waves. Therefore, both computations were performed at subsonic flow regime. The results indicate that the present adaptive grid refinement significantly improves the accuracy of vortical flow solutions as well as automation of the computations. Although the efficiency aspect of grid adaptation has not been addressed in this paper, earlier studies have demonstrated substantial enhancement in the computational economy achieved by reducing the grid size (number of grid elements) while increasing the local grid resolution. Additional conclusions drawn from the present study are summarized below.

- CFD has matured to a level where it can play a significant role in investigating complex vortical flows.
- The present computations demonstrate that the Euler assessment of vortical flows can provide accurate prediction of vortex location and breakdown in certain cases (e.g., MTVI). However, one should be cautious in applying the inviscid methodology to general problems as it may exhibit misleading vortex flow characteristics as demonstrated with the Delta wing even with a sharp leading edge.
- Vortex flows at high angles of attack often involve additional viscous dominated features, such as large regions of flow separation, which can influence the vortex behavior. Accurate solution of such flows requires advanced CFD methods based on the Navier-Stokes equations.
- The accuracy of vortex flow computations, especially those featuring vortex breakdowns, is highly susceptible to the local grid resolution. Therefore, the implementation of an automatic adaptive refinement is essential for such problems.
- Vortex flows induced by blunt leading edges present an even greater challenge to CFD. This is due to a strong sensitivity of the leading-edge flow separation to computational factors such as turbulence models, flow transition, and other numerical elements that influence the accuracy of predicted flow separation. Application of solution adaptive grid refinement is even more critical for such cases.
- An automatic adaptive grid technique should be capable of resolving the grid not only around the vortex core but also in the boundary layer and on the surface for maximum effectiveness.
- Vortex flows and the breakdown phenomenon are inherently unsteady and should be handled with the time factor incorporated in the prediction schemes.

Additional work is required to mature the present pilot technology and extend its capabilities. Further developments, planned for future work, include extension of the method for full Navier-Stokes adaptive grid refinement and implementation of better error/feature indicators for grid adaptation in problems involving multiple dominant flow features such as vortices and shock waves. The present work on the Delta wing represents one of few attempts to compute vortex flows on blunt leading-edge wings. The majority of computational research in the literature concern delta wings with sharp leading edges. Further work is obviously required to validate CFD capabilities for predicting complex vortical flows on realistic configurations with rounded edges.

11.5 ACKNOWLEDGEMENTS

The author would like to thank Dr. John E. Lamar, Mr. Gary E. Erickson, Dr. James M. Luckring, and Dr. Neal T. Frink, NASA LaRC, for their helpful comments and many instructive technical discussions on various aspects of the present study. The support of Mr. Larry D. Leavitt, Head of the Configuration Aerodynamics Branch, NASA LaRC, is gratefully acknowledged.

11.6 REFERENCES

- [1] Erickson, G.E., "Wind Tunnel Investigation of the Interaction and Breakdown Characteristics of Slender-Wing Vortices at Subsonic, Transonic, and Supersonic Speeds," NASA Technical Paper 3114, November 1991.
- [2] Hoeijmakers, H.W.M., "Modeling and Numerical Simulation of Vortex Flow in Aerodynamics," AGARD-CP-494, Vortex Flow Aerodynamics, pp. 1.1-1.46, July 1991.
- [3] Rom, J., "High Angle of Attack Aerodynamics: Subsonic, Transonic, and Supersonic Flows," Springer-Verlag, 1992.
- [4] Frink, N.T., Pirzadeh, S.Z., Parikh, P.C., and Pandya, M.J., "The NASA Tetrahedral Unstructured Software Sysytem (TetrUSS)," *The Aeronautical Journal*, Vol. 104, No. 1040, October 2000, pp. 491-499.
- [5] Lohner, R. and Parikh, P., "Three-Dimensional Grid Generation by the Advancing-Front Method," *International Journal of Numerical Methods in Fluids*, 8, pp 1135-1149, 1988.
- [6] Pirzadeh, S., "Three-Dimensional Unstructured Viscous Grids by the Advancing-Layers Method," *AIAA Journal*, Vol. 34, No. 1, pp 43-49, 1996.
- [7] Pirzadeh, S., "Structured Background Grids for Generation of Unstructured Grids by Advancing Front Method," *AIAA Journal*, Vol. 31, No. 2, pp 257-265, 1993.
- [8] Samareh, J., "GridTool: A Surface Modeling and Grid Generation Tool," Proceedings of the Workshop on Surface Modeling, Grid Generation, and Related Issues in CFD Solutions, NASA CP-3291, 9-11 May 1995.
- [9] Pirzadeh, S., "Recent Progress in Unstructured Grid Generation," AIAA Paper 92-0445, January 1992.
- [10] Pirzadeh, S.Z., "An Adaptive Unstructured Grid Method by Grid Subdivision, Local Remeshing, and Grid Movement," AIAA Paper 99-3255, June 1999.
- [11] Pirzadeh, S., "Progress Toward a User-Oriented Unstructured Viscous Grid Generation," AIAA Paper 96-30031, January 1996.
- [12] Frink, NT, "Tetrahedral Unstructured Navier-Stokes Method for Turbulent Flows," *AIAA Journal*, Vol. 36, No. 11, pp. 1975-1982, 1998.
- [13] Pandya, M., "Low-Speed Preconditioning for an Unstructured Grid Navier-Stokes Solver, AIAA Paper 99-3134, June 1999.
- [14] Pirzadeh, S.Z., "A Solution-Adaptive Unstructured Grid Method by Grid Subdivision and Local

Remeshing," *Journal of Aircraft*, Vol. 37, No. 5, pp. 818-824, 2000.

- [15] Chu, J. and Luckring, J.M., "Experimental Surface Pressure Data Obtained on 65° Delta Wing Across Reynolds Number and Mach Number Ranges," NASA TM 4645, February 1996.
- [16] Payne, F.M., Ng, T.T., and Nelson, R.C., "Visualization and Flow Surveys of the Leading Edge Vortex Structure on Delta Wing Planforms," AIAA Paper 86-0330, January 1986.
- [17] Erickson, G.E., private communications, NASA Langley Research Center, April 2001.
- [18] Hall, R.M., "Impact of Fuselage Cross Section on the Stability of a Generic Fighter", AIAA Paper 98-2725, 1998.

Chapter 12 – ORIGIN OF STATIONARY SHEAR-LAYER SUB-STRUCTURES ABOVE DELTA WINGS

Miguel R. Visbal and Raymond E. Gordnier

Computational Sciences Branch

Air Vehicles Directorate

Air Force Research Laboratory, WPAFB, OH 45433

miguel.visbal@wpafb.af.mil

ABSTRACT

A computational study of the substructures found in the shear layer above delta wings is presented. In contrast to previous numerical efforts, the present investigation utilizes a very high-order (6th-order) spatial discretization capable of capturing finer scales of the flow field on a given mesh resolution. Computations are performed for a 75° semi-infinite swept leading edge at an angle of attack of 25°, and for several Reynolds numbers. This configuration is selected in order to isolate the shear layer dynamics from disturbances associated with vortex breakdown or trailing-edge separation, which can be present in a finite wing. Beyond a critical value of Reynolds number, unsteady substructures appear in the shear layer above the wing, and their origin moves closer to the apex. The onset of this unsteady phenomena is associated with unsteady separation of the wing upper surface boundary layer. The unsteady substructures, which are initially very coherent, exhibit secondary instabilities along their axes further downstream. This process results in the formation of concentrations of vorticity which are stretched and convected in helical paths around the leading edge vortex. A time-averaged representation of the highly unsteady computed flow field is characterized by the existence of helical substructures which co-rotate with the primary vortex similar to those observed in high Reynolds number mean experimental data. This finding suggests that the so-called stationary helical pattern, seen in the time-averaged experimental measurements, is created by the secondary instability of the unsteady substructures as they breakup and convect in the helical velocity field of the primary vortex. It is therefore postulated that, in unsteady delta wing flows, the so-called unsteady and stationary substructures are not two different physical phenomena but rather different representations of the same complex shear layer transition process.

12.1 INTRODUCTION

One of the key elements of the flowfield over a delta wing at angle of attack [1,2] is the feeding sheet from which the main leading-edge vortex arises. This spiraling 3-D shear layer has been found experimentally to support several forms of coherent substructures which are superimposed on the primary vortex and which presumably arise due to shear-layer instabilities. The first observations of substructures embedded in the vortex system above a delta wing are perhaps due to Squires *et al.* [3]. Subsequently, in flow visualizations of delta wings (with sweep angles $\Lambda = 45^\circ$ and 60°) at low Reynolds number, Gad-el-Hak and Blackwelder [4] found that the vortex sheet emanating from the leading edge rolled up periodically into discrete vortical substructures which underwent a pairing process similar to that encountered in plane mixing layers. They attributed this phenomenon to a Kelvin-Helmholtz (K-H) type instability of the shear layer and investigated their control [5] by alternating blowing/suction along the wing leading edge. Payne *et al.* [6] describe the formation of stationary substructures along the periphery of the primary vortex in their smoke flow visualizations. Lowson [7] postulates, based on flow visualizations, the existence of two distinct types of vortex sheet instability coexisting in the leading edge vortex. He suggests that the first, unsteady type, is that found by Gad-el-Hak and Blackwelder whereas the second, stationary type,

corresponds to the observations of Payne *et al.* Reynolds and Abtahi [8] also report the existence of both forms of shear-layer substructures in low-Reynolds-number water tunnel experiments.

In addition to the previous studies, which were based only on flow visualization techniques, quantitative experimental investigations have been conducted. Detailed velocity measurements (LDV) for a very slender delta wing ($\Lambda = 85^\circ$) were presented by Lowson *et al.* [9] and Riley and Lowson [10]. In their study, the existence of *steady laminar* substructures was confirmed at low values of Reynolds number. It should be noted that the stationary nature of the substructures had to be inferred from accompanying flow visualizations since a mean velocity measurement technique (LDV) was employed. The stationary substructures emerged as the local Reynolds number (Re_x) exceeded a critical value. The substructures became more distinct around the periphery of the primary vortex as Re_x increased, but eventually dissipated further downstream. They noted that with further increases in Reynolds number, vortical substructures re-emerged in the *mean* velocity field within the turbulent shear layer. In Ref. 10, no distinction was made between these time-averaged substructures and the truly steady ones observed in the laminar regime. In fact, the mean turbulent substructures are described as a continuation of the process observed in the laminar regime. Riley and Lowson attribute the formation of substructures to a form of crossflow instability of the skewed shear layer.

Verhaagen [11], Washburn and Visser [12], and more recently Mitchell *et al.* [13], documented the presence of “stationary” substructures in *mean* flow measurements of leading-edge vortices above delta wings with sweep angles $\Lambda = 70^\circ$, 76° and 80° , and for Reynolds numbers over the range $0.5 \times 10^6 < Re_c < 1.6 \times 10^6$. These vortical substructures were described as originating at the leading edge, and followed helical trajectories around the primary vortex. Washburn and Visser [12] suggested crossflow instability as a possible formation mechanism. Although these experiments [12,13] were conducted at higher Reynolds number, the lower-surface boundary layer may still remain laminar since it is subjected to a favorable pressure gradient. It then undergoes a process of transition above the wing after separating from the leading edge.

The first computational study aimed at characterizing shear layer substructures on delta wings was performed by Gordnier and Visbal [14,15]. These computations, for a 75° sweep wing at a Reynolds number $Re_c = 5.0 \times 10^4$, displayed periodic vortical substructures in the shear layer, even though no artificial forcing was applied. The computed frequency varied nearly linearly with streamwise distance and was found to be commensurate with experimental [4,7] values and with a simple two-dimensional linear stability analysis.

Recent Detached-Eddy Simulations (DES) [16] corresponding to the high-resolution experimental data of Ref. 13 have displayed both steady and unsteady vortical substructures depending upon the level of grid refinement employed. This sensitivity to grid resolution is an inherent feature of DES, as well as other hybrid turbulence simulation approaches. In addition, unlike the experiments, which contain well-defined regions of laminar and transitional boundary layer flow on the wing surface, the DES study imposes a fully turbulent boundary layer over the entire wing. In Ref. 16, the unsteady type of substructures, appearing on the finest mesh, are said to be triggered by the unsteady separation region at the blunt trailing edge.

It has been suggested [7,8,12] that the periodic type of shear-layer instability seen in experiments is caused by flow disturbances inherent to the experimental setup. In fact, the results of Ref. 7 were subjected to wind-tunnel background excitation, and surface waves were present in the water channel experiments of Ref. 8. Given the sensitivity of shear layers to natural disturbances, this could be a reasonable explanation in the experimental situation. However, it raises the question as to the origin of the unsteadiness observed in the computations where no deliberate forcing of the shear layer is applied. If one assumes the spatially-developing, three-dimensional shear layer above the delta wing to be convectively unstable, a continuous

forcing would be required for the shear layer instabilities to persist.

An additional aspect of the flow which may trigger this phenomenon, and which has received less attention is the interaction of the leading-edge primary vortex with the boundary layer on the wing upper surface. The importance of this effect was examined computationally in Refs. 17 and 18. These calculations demonstrated that the shear-layer instability is closely coupled to the unsteady boundary-layer separation process. Since the vortex/surface interaction characteristics depend on the vortex strength and its proximity to the wall, increasing Reynolds number and angle of attack, as well as reducing leading-edge sweep all promote unsteady boundary-layer separation and shear-layer unsteadiness. For the very slender wings ($\Lambda = 85^\circ$) considered in Refs. 6 and 10, unsteady boundary-layer separation on the wing is expected to be significantly delayed due to the reduced circulation of the primary vortex.

Based on the available experimental and computational evidence, a general viewpoint has emerged that two separate types of substructures - temporal and spatially-stationary - can exist in the shear layer above delta wings. However, careful distinction must be made between the various substructures being reported. According to the previously cited literature, at least three different forms or representations of the shear-layer instability process have been reported:

- (i) *steady* laminar substructures measured by Riley and Lowson [10] for very high sweep angle and low Reynolds number,
- (ii) *unsteady* shear-layer vortices in the instantaneous representation of the flow field found in experimental [4,7,19] and computational [14,15,17,18] studies, and
- (iii) *mean* substructures observed in time-averaged measurements [11-13] of transitional/turbulent shear layers for a wide range of sweep angles.

From the previous discussion, it is clear that additional computational and experimental work is required in order to fully characterize the dynamics and structure of the 3-D shear layer above a delta wing. Further insight distilled from new investigations may be valuable when considering flow control methods which involve manipulation of the feeding sheet. In addition, the relationship between the seemingly distinct forms of substructures must be established.

From the numerical standpoint, the small temporal and spatial scales associated with the shear-layer vortical substructures impose stringent computational requirements in the simulation of delta wing flows. Previous computational studies [14-16] have employed standard second-order algorithms to compute these flows. The primary objective of the present paper is to investigate the feeding sheet structure at transitional Reynolds numbers utilizing a recently developed 6th-order flow solver [20]. For this purpose, the flow field above a 75° semi-infinite swept leading edge (see Fig. 1) at an angle of attack $\alpha = 25^\circ$ is considered at several Reynolds numbers. This configuration and angle of attack permit the study of the shear layer substructures in the absence of additional complicating factors such as vortex breakdown and unsteady trailing-edge separation. The flow fields considered in this investigation are intended to represent a small region near the apex of an actual delta wing at higher Reynolds numbers.

12.2 COMPUTATIONAL APPROACH

12.2.1 Governing Equations

The full unsteady three-dimensional compressible Navier-Stokes equations are selected and are cast in strong conservative form after introducing a time-dependent curvilinear coordinate transformation $(x, y, z, t) \rightarrow (\xi, \eta, \zeta, \tau)$ [21,22]. In vector notation, and employing non-dimensional variables, these equations can

be written as:

$$\partial(\bar{U}/J)/\partial\tau + \partial\hat{F}/\partial\xi + \partial\hat{G}/\partial\eta + \partial\hat{H}/\partial\zeta = (1/\text{Re})[\partial\hat{F}_v/\partial\xi + \partial\hat{G}_v/\partial\eta + \partial\hat{H}_v/\partial\zeta] \quad (1)$$

where F, G, H, F_v, G_v, H_v are the fluxes and J is the coordinate transformation Jacobian. The specific form the fluxes appearing in Eq. (1) can be found for instance in Ref. 23.

12.2.2 Spatial Discretization

The high-order finite-difference approach of Refs. 20 and 24 is employed to discretize the governing equations. For any scalar quantity, ϕ , such as a metric, flux component or flow variable, the spatial derivative ϕ' is obtained along a coordinate line in the transformed plane by solving the tridiagonal system:

$$\alpha\phi'_{i-1} + \phi'_i + \alpha\phi'_{i+1} = b\frac{\phi_{i+2} - \phi_{i-2}}{4} + a\frac{\phi_{i+1} - \phi_{i-1}}{2} \quad (2)$$

where $\alpha=1/3$, $a=14/9$ and $b=1/9$. This choice of coefficients yields at interior points the compact five-point, sixth-order (C6) scheme of Lele [25]. Equation (2) also incorporates the standard explicit second-order method (E2), with $\alpha=0$, $a=1$, and $b=0$. At boundary points 1, 2, $IL-1$ and IL , fourth- and fifth-order one-sided formulas are employed which retain the tridiagonal form of the algorithm [20,26].

The derivatives of the inviscid fluxes are obtained by forming the fluxes at the nodes and differentiating each component with the above formulas. Viscous terms are obtained by first computing derivatives of the primitive variables. Subsequently, the components of the viscous flux are constructed at each node and differentiated by a second application of the same scheme. This approach is significantly cheaper to implement in curvilinear coordinates than that in which a Pade-type scheme is employed directly for the second-derivative. As previously demonstrated in Ref. 20, successive differentiation yields an accurate and stable method in conjunction with the added low-pass filter procedure described below.

12.2.3 Low-Pass Spatial Filtering Scheme

Compact-difference discretizations, like other centered schemes, are non-dissipative and therefore susceptible to numerical instabilities due to the unrestricted growth of high-frequency modes. These difficulties originate from several sources including mesh non-uniformity, approximate boundary conditions and nonlinear flow features. In order to provide long-term numerical stability while retaining the improved accuracy of the compact discretization approach, a high-order low-pass spatial filtering technique [20,27] is incorporated. This low-pass filter provides selective dissipation only at the high wavenumbers where the underlying spatial discretization already exhibits significant dispersion errors. If a typical component of the solution vector is denoted by ϕ , filtered values at interior points $\bar{\phi}$ in transformed space satisfy,

$$\alpha_f \bar{\phi}_{i-1} + \bar{\phi}_i + \alpha_f \bar{\phi}_{i+1} = \sum_{n=0}^N \frac{a_n}{2} (\phi_{i+n} + \phi_{i-n}) \quad (3)$$

Equation (3) is based on templates proposed in Refs. 25 and 28 and with proper choice of coefficients, provides a $2N$ th-order formula on a $2N+1$ point stencil. The $N+1$ coefficients, a_0, a_1, \dots, a_N , are derived in terms of α_f with Taylor- and Fourier-series analyses and are given in Refs. 26 and 29 along with several examples of their corresponding spectral response. On uniform meshes, these symmetric filters are non-dissipative, do not amplify any waves, preserve constant functions, and completely eliminate odd-even

modes. In this work, the filter operator is applied to the conserved variables along each transformed coordinate direction and after each time step. For the present delta wing computations, an eighth-order filter with $\alpha_f = 0.3$ is specified at interior points. For the near-boundary points, the filtering strategies described in Refs. 20 and 29 are employed. The impact of filtering on the accuracy and stability of the high-order approach has been investigated in Refs. 20, 29 and 30 for several applications including non-uniform grids, approximate boundary treatments and nonlinear governing equations.

12.2.4 Evaluation of Coordinate Transformation Metrics

The extension of high-order schemes to curvilinear meshes requires a careful evaluation of the spatial metric expressions arising from the coordinate transformation. Failure to enforce metric cancellation and freestream preservation in the finite-difference discretization of the strong-conservation form of the governing equations can catastrophically degrade the fidelity of higher-order approaches [20,29,30].

In deriving the strong-conservation flow equations, the following metric identities have been implicitly invoked,

$$\begin{aligned} I_1 &= (\xi_x/J)_\xi + (\eta_x/J)_\eta + (\zeta_x/J)_\zeta = 0 \\ I_2 &= (\xi_y/J)_\xi + (\eta_y/J)_\eta + (\zeta_y/J)_\zeta = 0 \\ I_3 &= (\xi_z/J)_\xi + (\eta_z/J)_\eta + (\zeta_z/J)_\zeta = 0 \end{aligned} \tag{4}$$

where subscripts denote partial derivatives. These identities constitute a differential statement of surface conservation for a closed cell. In a finite-difference discretization, they must be satisfied numerically in order to ensure freestream preservation.

To numerically enforce identities in Eq. (4), the transformation metrics are evaluated in the manner described in Refs. 24 and 30. This approach adopts the formulation developed in the context of lower-order methods [31], in which the metric relation, for example,

$$\xi_x/J = y_\eta z_\zeta - y_\zeta z_\eta \tag{5}$$

is evaluated by considering its analytically equivalent “conservative” form:

$$\xi_x/J = (y_\eta z)_\zeta - (y_\zeta z)_\eta \tag{6}$$

Similar expressions are employed for the remaining metric terms. As demonstrated in Refs. 24 and 30, freestream preservation and improved accuracy is achieved on general 3-D meshes when the transformation metrics are cast in the form of Eq. (6), and the derivatives are evaluated with the same high-order formulas employed for the fluxes.

12.2.5 Time Integration

For the highly stretched meshes typically employed in the simulation of wall-bounded flows, the stability constraint of explicit time-marching methods is too restrictive and the use of an implicit approach becomes necessary. For this purpose, an implicit approximately-factored scheme [32] is incorporated and augmented through the use of Newton-like sub-iterations. In delta form, and for second order temporal accuracy, the scheme may be written as

$$\begin{aligned}
 & \left[J^{-1^{p+1}} + \phi^i \Delta \tau \delta_{\xi}^{(2)} \left(\frac{\partial \hat{F}^p}{\partial U} - \frac{1}{Re} \frac{\partial \hat{F}^p}{\partial U} \right) \right] J^{p+1} \times \\
 & \left[J^{-1^{p+1}} + \phi^i \Delta \tau \delta_{\eta}^{(2)} \left(\frac{\partial \hat{G}^p}{\partial U} - \frac{1}{Re} \frac{\partial \hat{G}^p}{\partial U} \right) \right] J^{p+1} \times \\
 & \left[J^{-1^{p+1}} + \phi^i \Delta \tau \delta_{\zeta}^{(2)} \left(\frac{\partial \hat{H}^p}{\partial U} - \frac{1}{Re} \frac{\partial \hat{H}^p}{\partial U} \right) \right] \Delta U \\
 & = -\phi^i \Delta \tau \left[J^{-1^{p+1}} \frac{(1+\phi)U^p - (1+2\phi)U^n + \phi U^{n-1}}{\Delta \tau} \right. \\
 & \quad \left. + U^p (1/J) \tau^p + \delta_{\xi} \left(\hat{F}^p - \frac{1}{Re} \hat{F}_v^p \right) + \right. \\
 & \quad \left. \delta_{\eta} \left(\hat{G}^p - \frac{1}{Re} \hat{G}_v^p \right) + \delta_{\zeta} \left(\hat{H}^p - \frac{1}{Re} \hat{H}_v^p \right) \right]
 \end{aligned} \tag{7}$$

where $\partial F/\partial U$ etc are flux Jacobians, δ represents the spatial difference operator and $\Delta U = U^{p+1} - U^p$. The method combines the approximate factorization procedure of Ref. 32 with the diagonalized simplification of Ref. 33. Note that while the derivatives of the flux Jacobians have been obtained to second-order accuracy (denoted with the superscript (2)), those on the right hand side are evaluated with the compact-difference high-order method. Nonlinear artificial dissipation terms [34,35], not explicitly shown in Eq. (7), are also appended to the implicit operator to enhance stability. In order to reduce errors associated with these simplifications, a sub-iteration strategy is employed. Thus, for the first sub-iteration, $p = 1$, $U^p = U^n$ and as $p \rightarrow \infty$, $U^p \rightarrow U^{n+1}$. Typically, three sub-iterations are applied per time step. As demonstrated in Refs. 24, 36 and 37, second-order temporal accuracy is found to be adequate in several applications. The present time-implicit, compact differencing/filtering methodology has been examined extensively for a number of unsteady flows [20,38-41] including delta wings.

12.3 RESULTS

12.3.1 Flow Configuration and Boundary Conditions

The configuration considered (Fig. 1) consists of a semi-infinite 75° swept leading edge representing the front portion of a delta wing at high Reynolds number. This configuration is selected in order to isolate the shear-layer dynamics from either vortex breakdown or unsteady trailing-edge separation resulting from the adverse streamwise pressure gradient at the termination of the wing. A similar semi-infinite approach has been commonly used in the simulation of vortical flows above bodies of revolution (*e.g.*, Ref. 42 and references therein). In the discussion that follows, we refer to the swept leading edge as a delta wing for the purpose of convenience. The angle of attack and freestream Mach number are $\alpha = 25^\circ$ and $M = 0.1$ respectively. A Reynolds number, $Re_L = \rho U L / \mu$, defined in terms of the streamwise extent of the region of interest L is introduced (see Fig. 1).

The computational domain around the flat-plate delta wing is discretized employing an H-H grid topology with various levels of resolution as summarized in Table 1. Outside the domain of interest, the mesh is rapidly stretched in all coordinate directions (see Fig. 1). This treatment of the farfield boundaries is based on the approach proposed and evaluated previously in Refs. 30 and 39. This method exploits the properties of the high-order low-pass filter in conjunction with a rapidly stretched mesh. As grid spacing increases away from the region of interest, energy not supported by the stretched mesh is reflected in the form of high-frequency modes which are annihilated by the discriminating spatial low-pass filter operator. An effective “buffer” zone is therefore created using a few grid points in each coordinate direction without the need for the incorporation of more complicated boundary conditions. Since the flow disturbances generated by the wing are effectively damped prior to reaching the domain boundaries, simple boundary conditions can be applied there. On the inflow boundaries, uniform flow is specified, whereas at the outflow and side boundaries, all variables are extrapolated from the interior using first-order extrapolation. The remaining physical boundary conditions are: symmetry on the wing centerline plane, and isothermal no-slip conditions on the wing surface. Unless otherwise noted, computations are performed using the 6th-

order compact algorithm combined with an 8th-order low-pass spatial filter operator.

Grid	Size	$\Delta x / L$	$\Delta y / L$	$\Delta z / L$
1	209 x 116 x 198	0.008	0.0062	0.003
2	247 x 112 x 186	0.005	0.0052	0.003
3	247 x 143 x 186	0.005	0.004	0.003

Table. 1. Grid designation for delta wing computations. $\Delta x/L$, $\Delta y/L$, $\Delta z/L$ denote grid spacing in the vortex core at $x/L = 1.0$.

12.3.2 Preliminary Considerations

A limited assessment of the effects of spatial and temporal resolution, as well as order of accuracy of the numerical scheme was performed. The effects of spatial resolution on the computed flow field for $Re_L = 2.5 \times 10^4$ were examined. As the grid spacing is refined in the axial direction, the formation of finer unsteady features were observed in the shear layer surrounding the vortex core. The onset of these substructures also moved closer to the apex with increased spatial resolution. However, for all levels of resolution employed, the unsteady features emerge at this Reynolds number and the process remained qualitatively unchanged. A comparison of the mean axial vorticity profile in the center of the vortex (Fig. 2) indicates that the maximum sensitivity of the time-averaged solution to grid resolution takes place within the vortex core where higher values of $\langle \omega_x \rangle$ are obtained as the mesh is refined.

Computations for $Re_L = 5.0 \times 10^4$ using the standard second-order (E2) and 6th-order compact algorithms on Grid 3 are compared in Figs. 3 and 4. It can be seen that the higher-fidelity scheme displays finer scales in the instantaneous shear-layer vorticity contours, as compared to the lower-order method. However, in both cases the same qualitative unsteady shear-layer dynamics was observed. A comparison of the mean axial velocity and vorticity distributions through the vortex core (Fig. 4) indicates that employing the 6th-order compact scheme results in a sharper vortex inner core with much higher values of vorticity. With both numerical schemes the maximum mean axial velocity in the core reaches a very large value nearly four times the freestream velocity. This is considerably higher than typical values obtained in previous computations [15,43]. This increase is attributable to the much finer axial spacing employed in the current study.

The present delta wing computations are extremely demanding not only in terms of spatial but also temporal resolution due to the very high frequencies which characterize the unsteady shear layer process. To provide adequate temporal resolution a very small non-dimensional time step ($\Delta t U/L = 1.25 \times 10^{-4}$) has been used in this investigation. At $Re_L = 5.0 \times 10^4$, this value of Δt provides approximately 125 times steps per cycle for the highest frequency observed near the wing apex.

12.3.3 Reynolds Number Effects

The effect of Reynolds number on the shear-layer structure was investigated by considering values of Re_L ranging from 6.0×10^3 to 5.0×10^4 . The evolution of the instantaneous flow field structure with increasing Reynolds numbers is shown in Figs. 5 and 6 in terms of contours of vorticity magnitude on a vertical plane through the vortex core, as well as an iso-surface of axial vorticity. For the lowest value of Re_L , a steady laminar vortex system is present above the wing, with a feeding sheet devoid of any substructures. As the Reynolds number increases, the flow becomes unsteady near the end of the computational region of interest, and vortical substructures emerge in the shear-layer surrounding the vortex core. The substructures are apparent prior to their stretching and entrainment into the primary vortex. The character

and orientation of these unsteady substructures is similar to the experimental and computational results of Refs. 4 and 15. However, due to the finer computational mesh and improved high-fidelity numerical algorithm, the present substructures appear much more distinct than those found in the previous computations.

Over a relatively small range of Reynolds numbers, the increase in complexity of the vortex system is quite dramatic. As Reynolds number increases, the shear-layer transition occurs progressively closer to the wing apex, and for the highest Re_L studied it appears to cover almost the entire wing. The approximate streamwise location of the onset of unsteadiness is shown for all computed cases in Table 2 in terms of a local Reynolds number $Re_{x\ critical} = \rho U x_{inst} / \mu$, where x_{inst} denotes the location of the onset of unsteadiness (Fig. 6). For the two highest Reynolds numbers considered, $Re_{x\ critical}$ is almost the same indicating that the chordwise position where unsteady flow features emerge is approximately inversely proportional to Reynolds number. This fairly strong correlation of the flow field development with local Reynolds number (for fixed α and A) is in accordance with the experiments of Riley and Lowson [10].

Re_L	x_{inst} / L	$Re_{x\ critical}$
1.8×10^4	0.61	9.1×10^3
2.5×10^4	0.31	7.8×10^3
5.0×10^4	0.15	7.5×10^3

Table 2. Onset of instability as a function of local Reynolds number. x_{inst} denotes the location where shear layer substructures are first observed (Fig. 6).

The flow field characteristics near the streamwise location where the instabilities emerge are examined in more detail in Fig. 7 for $Re_L = 2.5 \times 10^4$. At $x/L = 0.2$, upstream of the onset of the unsteady features, the vortex system is comprised of the usual primary and secondary vortices, which are observed to be fairly steady in animations of the computed flow field. At $x/L = 0.4$, immediately downstream of the onset of unsteadiness, the vortex system is characterized by the breakup of the feeding sheet into discrete substructures, as well as by the upward ejection of opposite-sign vorticity from the secondary vortex. These observations suggest that the origin of unsteady shear-layer substructures is closely linked to the process of unsteady boundary-layer separation on the wing surface. The relationship between shear-layer unsteadiness and unsteady separation was pointed out in our previous studies [14,15,17,18] and this basic characteristic remains qualitatively unchanged despite the much finer grids and higher-fidelity numerical scheme employed in the present investigation.

Unlike the experiments, the computed shear-layer transition phenomenon takes place in the absence of any imposed freestream disturbances. The process arises naturally due to the strengthening of the interaction between the primary vortex and the upper-surface laminar boundary-layer flow. This interaction tends to promote the eruption of wall vorticity, a common occurrence in unsteady boundary-layer separation [44]. In fact, as it was demonstrated previously in Refs. 17 and 18, diminishing this interaction through an increase in sweep angle or a reduction in angle of attack resulted in a delay of unsteadiness. In addition, suction applied to the boundary layer in the region of secondary separation [17] completely eliminated unsteadiness at low Reynolds number.

Finally, unsteady trailing-edge separation and vortex breakdown can be ruled out as causative mechanisms for the formation of the unsteady vortical substructures since both of these factors have been eliminated in the present study through the introduction of a semi-infinite wing configuration.

12.3.4 Instantaneous Shear-Layer Structure

The complex instantaneous structure of the unsteady shear layer at the two largest Reynolds numbers was examined in detail. Figures 7-10 correspond to $Re_L = 2.5 \times 10^4$ whereas results for $Re_L = 5.0 \times 10^4$ are given in Figs. 11-15.

The limiting streamline pattern on the wing upper surface was examined at many instants during the computation and was found to retain the structure shown in the upper portions of Figs. 8 and 11. For both Reynolds numbers, this portrait is characterized by the presence of both secondary (SS) and tertiary (TS) separation lines of convergence. The convergence line denoted as SS corresponds to the laminar separation of the upper surface boundary layer displayed more clearly in the crossflow planes of Figs. 7 and 12.

Despite the drastic transformation and breakdown of the shear layer above the wing (e.g., Figs. 7 and 12), a fairly stable laminar secondary separation is always displayed by the surface pattern. The instantaneous secondary separation line remains well-defined at all times, and the intense unsteadiness of the flow above the wing results only in the formation of small streamwise undulations which are more apparent at the higher Re_L (Fig. 11). This points out that when describing transition to turbulence above a delta wing, one must distinguish between two distinct processes, namely the transition of the shear layer, and the transition of the upper surface boundary layer. The latter is typically discussed in the context of experimental oil-flow visualizations and occurs at higher values of local Reynolds number [45]. To the authors' knowledge, the relationship between these two transition processes has not been carefully studied.

The instantaneous flow field structure on a plane passing through the vortex axis is displayed in Figs. 9 and 13 in terms of contours of vorticity magnitude. The shear-layer, which is initially straight near the apex, is observed to breakdown into discrete concentrations of vorticity. In this sectional view, the vorticity concentrations give the appearance of a typical shear layer (K-H) instability. However, it must be kept in mind that, unlike a shear layer, the present flow is highly three-dimensional. The origin of the shear layer sub-vortices moves closer to the wing apex as the Reynolds number increases. The first few substructures appear well-defined, however, with increasing distance downstream, they become more chaotic and fine-scale features emerge. Despite the complex shear-layer transformation, the leading-edge vortex core is well-defined but displays the existence of axial disturbances. Examination of computer animations of the unsteady flow showed that the vortex core remains distinct at all times but exhibits significant unsteadiness in the form of lateral vortex wandering, as well as undulations which propagate downstream along its axis. This latter characteristic would be in agreement with the wave-guide nature of a supercritical vortex [46].

The streamwise evolution of the instantaneous flow field is examined on several transverse planes using contours of axial vorticity (Figs. 7 and 12). The breakup of the shear layer into discrete concentrations of vorticity is clearly seen. These substructures are more coherent near the leading edge but become severely distorted as they wrap around the primary vortex since they are subjected to significant straining both in the axial and transverse directions. The vorticity from the feeding sheet is entrained into the primary vortex which exhibits at some instances the formation of spiral arms ($x/L = 0.7$, Fig. 12). As discussed earlier and in previous computational studies [15,17], the shear-layer transition is also accompanied by the ejection of concentrations of vorticity of the opposite sign, emanating from the secondary separation region of the wing upper surface boundary layer. Once ejected, this vorticity is also entrained into the primary vortex.

In order to gain more insight into the complex three-dimensional nature of the flow, the instantaneous shear layer structure is visualized using an isosurface of constant axial vorticity. In Fig. 10, one can distinguish three separate regions in the streamwise evolution of the feeding sheet. In the first region, closer to the wing apex and denoted as Region I, the shear layer is smooth and without any substructures.

In this region of the flow, the shear layer is found to be essentially steady. The corresponding crossflow plane (Fig. 7, $x/L = 0.2$) exhibits the typical structure associated with a leading edge vortex, comprised of steady primary and secondary vortices. Further downstream (denoted as Region II in Fig. 10), after unsteady boundary-layer separation and secondary vorticity ejection have developed ($x/L > 0.4$, Fig. 7), the feeding sheet is characterized by discrete and fairly organized substructures. Close to the wing surface, these substructures are nearly parallel to the leading edge, but become inclined toward the apex as they wrap around the vortex. This is due to the fact that the substructures can wrap more quickly around the vortex the closer they are to the apex (*i.e.*, as the primary vortex reduces in size). This is also reflected in the frequency content of the unsteady flow, discussed later in this section. In computer animations of the flow field, the substructures are clearly observed to rotate around the leading-edge vortex. The front portion of the substructures become less coherent as they wrap around and underneath the vortex, and their coherence is eventually lost due to the severe straining they are subjected to during their entrainment into the primary vortex system. The wavelength of the shear-layer substructures in Region II is of the order of $0.07 L$. In the last portion of the wing (denoted as Region III in Fig. 10), the shear layer structure becomes progressively more complex as the substructures shed from the leading edge become susceptible to further instabilities along their axes, a process which is more clearly seen in the discussion of the higher Re_L results presented next.

At the higher Reynolds number (Fig. 14), the spatial evolution of the instantaneous feeding sheet structure is found to be qualitatively similar. However, the onset of the unsteady substructures moves closer to the wing apex, and the spatial wavelength associated with the discrete vortices in Region II also diminishes. Once again, the initiation of the coherent substructures was found to correlate with the onset of unsteady boundary layer separation and vorticity ejection (Fig. 12). In the enlarged plot of Fig. 15, one can observe more clearly the instability of the unsteady substructures as they move around the primary vortex. The fairly coherent discrete vortices are found to become susceptible to instability along their axes. As the substructures move away from the leading edge, they themselves breakdown into discrete concentrations of vorticity which are then elongated and convected along helical paths around the primary vortex system. The wavelength of this instability is of the order of $2.5\delta - 3.5\delta$, where δ denotes the approximate size of the core of the substructure. In the context of a simple shear layer, this process would be referred to as a secondary spanwise instability of the Kelvin-Helmholtz rollers. As discussed later in Section 3.6, this secondary instability has a significant impact on the time-averaged structure of the flow.

In order to characterize the time scales associated with the shear-layer unsteadiness, histories of the velocity within the substructure formation region near the leading edge were recorded at several stations along the wing. A plot of three of these time histories is shown in Fig. 16 for the spanwise component of velocity (v) corresponding to $Re_L = 2.5 \times 10^4$. Only a limited time interval is shown for the purpose of clarity. The first signal, corresponding to a station upstream of the origin of shear layer unsteadiness, is essentially constant. For a location shortly downstream of the origin of the shear layer substructures, the spanwise velocity exhibits very coherent fluctuations at a very high non-dimensional frequency ($St = fL/U \sim 42.5$). Further downstream, the signal becomes less regular and the dominant frequency of the velocity fluctuations diminishes. The intense unsteadiness associated with the formation of the shear-layer substructures results in very large amplitudes of the spanwise velocity fluctuations, with peak-to-peak values greater than twice the freestream velocity (Fig. 16).

Figure 17 displays the frequency spectra of the spanwise velocity fluctuations for $Re_L = 5.0 \times 10^4$ at locations $x/L = 0.2$ and 1.0 . These spectra are plotted using both linear and logarithmic scales. At the first station, corresponding to the region where the substructures are very regular (*i.e.*, Region II in Fig. 14), a very large dominant frequency ($St \sim 64$) is clearly observed. In this region of the flow, all the fluctuation energy is centered in a relatively narrow band about this dominant frequency. At the downstream station, a much broader spectra with a peak at approximately $St = 11.5$ is seen. In the logarithmic plot, this spectra resembles a more turbulent-like distribution. Although, the flow field has not reached a fully turbulent state, the change in character of the spectra is consistent with the evolution of the shear layer from a steady

laminar to a transitional state. The axial variation of the dominant frequency is shown in Fig. 18 for both Reynolds numbers. With the exception of the very first station for the highest Re_L , a fairly linear distribution is observed. This trend is consistent with the early results of Refs. 15 and 18.

12.3.5 Time-Averaged Shear-Layer Structure

An alternative description of the delta wing flow field can be provided in terms of the time-averaged or mean representation, which is more closely related to available mean experimental measurements [11-13].

Figures 19 and 20 show a representation of the 3-D *mean* shear layer structure for both Reynolds numbers based on an isosurface of (time-averaged) axial vorticity. Interestingly enough, the shear layer structure is now characterized by “stationary” helical substructures which co-rotate with the sense of the primary vortex system. These features are similar in character to those previously described in the context of the time-averaged experimental data [11-13].

Further description of the computed time-averaged flow field for the highest Reynolds number case is provided in Figs. 21-24. Contours of mean vorticity magnitude on a horizontal plane above the wing surface are shown in Fig. 21. Discrete concentrations of vorticity can be observed in the shear layer along the leading edge. The wavelength of these substructures is of order of $0.07 L$ towards the aft-end of the wing. The vortex core also exhibits disturbances along the streamwise direction. Contours of mean axial vorticity component are shown in Fig. 22 for several stations downstream of the location where the helical time-averaged substructures appear. Only the contours corresponding to positive (*i.e.*, clockwise) values of vorticity are included for clarity. A well-defined vortex core is seen at all stations. Along the feeding sheet, several discrete substructures can be noticed. However these substructures are not as well defined as those in the experiments of Ref. 13. This could be due to either lack of spatial resolution or the much larger Reynolds number of the experimental data.

The root-mean-square streamwise velocity fluctuations are shown in Fig. 23. High velocity fluctuations are present in the shear layer. The region of high values of $\langle u'^2 \rangle$ is observed initially near the leading edge, and progressively penetrates around the periphery of the primary vortex with increasing distance downstream. In addition, at the last two stations, discrete pockets of high fluctuations are seen which appear to correlate with the helical substructures. Therefore, the time-averaged substructures are also regions of concentrated unsteady fluctuations, as it would be expected if they represent the path of the vorticity concentrations in the unsteady flow. Similar characteristics are observed in the experiments of Mitchell *et al.* [13].

Contours of RMS pressure fluctuations are given in Fig. 24. The highest pressure fluctuations take place in the vortex core where high axial values of velocity exist, as previously discussed in reference to Fig. 4. High values of $\langle p'^2 \rangle$ are also present in the shear layer near the leading edge. In addition, discrete regions of local maxima are observed along the shear layer.

12.3.6 Relation of Unsteady and Time-Averaged Vortical Substructures

In this section, a possible explanation for the origin of the “stationary” substructures observed in time-averaged measurements is offered based on the analysis of the present unsteady computations. In relation to the instantaneous flow fields, the computed time-averaged helical substructures appear only in the aft portion of the wing (Figs. 19 and 20). This corresponds to Region III in Figs. 10 and 14. By contrast, in Regions I and II, a smooth shear-layer is present in the mean flow portrait. The very coherent nature and alignment of the unsteady substructures in Region II do not result, as one would expect, in discrete substructures in the time-averaged field. The appearance in Region III of the helical substructures for the time-averaged representation is the result of the onset of secondary instability in the unsteady vortical substructures (Fig. 15). As these sub-vortices break along their axes, the discrete concentrations of

vorticity resulting from this process are stretched and convected in helical paths by the prevailing primary vortex flow. If the process of secondary instability is regular enough in terms of its wavelength and location, one would expect its imprint to persist in the time-averaged flow field along the path followed by the secondary concentrations of vorticity. If indeed this is the case, then the unsteady and so-called “stationary” (mean) shear layer substructures are not two different physical phenomena but rather different representations of the same complex unsteady shear layer evolution around the primary vortex. The origin of the mean substructures observed in time-averaged experimental data can therefore be traced to the secondary instability or break-up of the unsteady substructures in the transitional shear layer. Experimental verification of this proposed relation between the unsteady and time-averaged vortical substructures will require detailed high-resolution experimental data for both the instantaneous and mean flow above a delta wing.

12.4 CONCLUDING REMARKS

The origin of the substructures formed in the shear layer above delta wings has been studied numerically. The shear layer formed by a 75° swept leading edge at 25° angle of attack has been computed using a validated high-fidelity implicit Navier-Stokes code. The solver is based on a 6th-order compact scheme for the spatial derivatives coupled with an 8th-order low-pass spatial Pade-type filter which provides selective dissipation only at the high wavenumbers represented by the mesh.

The evolution of the flow field with increasing Reynolds number has been considered. At very low Re , a steady shear layer without any substructures is present above the wing. As Reynolds number increases, unsteady substructures are shed from the leading edge. The location along the wing where these unsteady substructures begin moves closer to the apex with increasing Re . Near their onset, the shear-layer substructures are very coherent, and appear much more defined than those observed in previous low-order numerical simulations. The periodic formation of the unsteady substructures is caused by the onset of unsteady boundary-layer separation and vorticity ejection on the wing upper surface. This unsteadiness arises naturally and it is not induced by freestream perturbations, vortex breakdown or trailing edge separation since all of these complicating factors are absent in the present calculations.

Further downstream, the vortical substructures are observed to undergo a process of secondary instability along their axes. The substructures breakup into discrete concentrations of vorticity which are stretched and convected in helical paths around the primary vortex system. Downstream of the region where this secondary instability process occurs, the time-averaged shear-layer representation is characterized by the existence of mean helical substructures which co-rotate with the leading edge vortex.

It is postulated in this work that the *time-averaged helical substructures*, observed in high-Reynolds number mean experimental data, are the imprint left by the regular breakup of the *unsteady substructures* along their axes, as their vorticity concentrations are stretched and convected in helical paths by the prevailing helical vortex flow. This suggests that the so-called *unsteady* and *stationary* substructures are not two separate phenomena but rather different representations of the same shear-layer complex transition process. This postulated origin of the mean helical substructures should be verified by experiments capable of providing both instantaneous and time-averaged high-resolution data.

Finally, the *steady laminar helical substructures* found in experiments for very slender delta wings have not been reproduced in the present study and further computations and experiments exploring the effect of wing sweep are required.

12.5 ACKNOWLEDGMENTS

The authors are grateful for AFOSR sponsorship under tasks monitored by Maj. W. Hilbun and Dr. T. Beutner. This work was also supported in part by a grant of HPC time from the DoD HPC Shared

Resource Centers at ASC, ERDC and NAVO.

12.6 REFERENCES

1. D. Rockwell, Three-Dimensional Flow Structure on Delta Wings at High Angle of Attack: Experimental Concepts and Issues, AIAA Paper 93-0550, 1993.
2. M. R. Visbal, Computational and Physical Aspects of Vortex Breakdown on Delta Wings, AIAA Paper 95-0585, 1995.
3. H.B. Squire, J.G. Jones, and A. Stanbrook, Investigation of the Characteristics of Some Plane and Cambered 65 Deg Delta Wings at Mach Numbers from 0.7 to 2.0, ARC, R.M. No. 3305, 1961.
4. M. Gad-el-Hak and R.F. Blackwelder, The Discrete Vortices from a Delta Wing, *AIAA J.*, 23(6): 961-962, 1985.
5. M. Gad-el Hak and R.F. Blackwelder, Control of the Discrete Vortices from a Delta Wing, *AIAA J.*, 25(8): 1042-1049, 1987.
6. F.M. Payne, T.T. Ng, R.C. Nelson, and L.B. Schiff, Visualization and Wake Surveys of Vortical Flow over a Delta Wing, *AIAA J.*, 26(2):137-143, 1988.
7. M.V. Lowson, The Three Dimensional Vortex Sheet Structure on Delta Wings. In Fluid Dynamics of Three-Dimensional Turbulent Shear Flows and Transition, October 1988. AGARD-CP-438.
8. G.A. Reynolds and A.A. Abtahi, Three-Dimensional Vortex Development, Breakdown, and Control, AIAA Paper 89-0998, 1989.
9. M.V. Lowson, A.J. Riley, and C. Swales, Flow Structure over Delta Wings, AIAA Paper 95-0586, 1995.
10. A.J. Riley and M.V. Lowson, Development of a Three-Dimensional Free Shear Layer, *JFM*, 369: 49-89, 1998.
11. N.G. Verhaagen, J.P. Meeder, and J.M. Verhelst, Boundary Layer Effects on the Flow of a Leading Edge Vortex, AIAA Paper 93-3463-CP, 1993.
12. A.E. Washburn and K.D. Visser, Evolution of Vortical Structures in the Shear Layer of Delta Wings, AIAA Paper 94-2317, 1994.
13. A. Mitchell, P. Molton, D. Barberis, and J. Delery, Vortical Substructures in the Shear Layers Forming Leading-Edge Vortices, AIAA Paper 2001-2424, 2001.
14. R.E. Gordnier and M.R. Visbal, Numerical Simulation of the Unsteady Vortex Structure over a Delta Wing, AIAA Paper 91-1811, 1991.
15. R.E. Gordnier and M.R. Visbal, Unsteady Vortex Structure over a Delta Wing, *Journal of Aircraft*, 31(1): 243-248, 1994.
16. A. Mitchell, S. Morton, and J. Forsythe, Analysis of Delta Wing Vortical Substructures Using

- Detached-Eddy Simulation, AIAA Paper 2002-2968, 2002.
17. M.R. Visbal and R.E. Gordnier, Origin of Computed Unsteadiness in the Shear Layer of Delta Wings, *Journal of Aircraft*, 32(5): 1146-1148, 1995.
 18. R.E. Gordnier and M.R. Visbal, Instabilities in the Shear Layer of Delta Wings, AIAA Paper 1995-2281, 1995.
 19. K.M. Cipolla and D. Rockwell, Small-Scale Vortical Structures in Crossflow Plane of a Rolling Delta Wing, *AIAA J.*, 36(12): 2276-2278, 1998.
 20. M.R. Visbal and D.V. Gaitonde, High-Order Accurate Methods for Complex Unsteady Subsonic Flows, *AIAA J.*, 37(10): 1231-1239, 1999.
 21. M. Vinokur, Conservation Equations of Gasdynamics in Curvilinear Coordinate Systems, *Journal of Computational Physics*, 14: 105-125, 1974.
 22. J.L. Steger, Implicit Finite-Difference Simulation of Flow about Arbitrary Two-Dimensional Geometries, *AIAA J.*, 16(7): 679-686, 1978.
 23. D.A. Anderson, J.C. Tannehill, and R.H. Pletcher, Computational Fluid Mechanics and Heat Transfer, McGraw-Hill Book Company, 1984.
 24. M.R. Visbal and D.V. Gaitonde, On the Use of High-Order Finite-Difference Schemes on Curvilinear and Deforming Meshes, *Journal of Computational Physics*, 181: 155-185, 2002.
 25. S.K. Lele, Compact Finite Difference Schemess with Spectral-like Resolution, *Journal of Computational Physics*, 103: 16-42, 1992.
 26. D.V. Gaitonde and M.R. Visbal, High-Order Schemess for Navier-Stokes Equations: Algorithm and Implementation into FDL3DI. Technical Report AFRL-VA-WP-TR-1998-3060, Air Force Research Laboratory, Wright-Patterson AFB, 1998.
 27. D.V. Gaitonde, J.S. Shang, and J.L. Young, Practical Aspects of Higher-Order Numerical Schemes for Wave Propagation Phenomena, *Int. J. for Num. Methods in Eng.*, 45: 1849-1869, 1999.
 28. P. Alpert, Implicit Filtering in Conjunction with Explicit Filtering, *J. Comp. Phys.*, 44: 212-219, 1981.
 29. D.V. Gaitonde and M.R. Visbal, Further Development of a Navier-Stokes Solution Procedure Based on Higher-Order Formulas, AIAA Paper 99-0557, 1999.
 30. M. Visbal and D. Gaitonde, Very High-Order Spatially Implicit Schemes for Computational Acoustics on Curvilinear Meshes, *J. Comp. Acoustics*, 9(4): 1259-1286, 2001.
 31. P.D. Thomas and C.K. Lombard, Geometric Conservation Law and its Application to Flow Computations on Moving Grids, *AIAA J.*, 17(10): 1030-1037, 1979.
 32. R. Beam and R. Warming. An Implicit Factored Scheme for the Compressible Navier-Stokes Equations. *AIAA J.*, 16(4): 393-402, 1978.
 33. T.H. Pulliam and D.S. Chaussee, A Diagonal Form of an Implicit Approximate-Factorization

- Algorithm, *Journal of Computational Physics*, 39(2): 347-363, 1981.
34. A. Jameson, W. Schmidt, and E. Turkel, Numerical Solutions of the Euler Equations by a Finite Volume Method Using Runge-Kutta Time Stepping Schemes, AIAA Paper 81-1259, 1981.
35. T. Pulliam, Artificial Dissipation Models for the Euler Equations, *AIAA J.*, 24(12): 1931-1940, 1986.
36. M.R. Visbal and R.E. Gordnier, A High-Order Flow Solver for Deforming and Moving Meshes, AIAA Paper 2000-2619, 2000.
37. M.R. Visbal, Advances in High-Resolution Schemes for Computational Acoustics on General Geometries. Proceedings of the Symposium on Developments in Computational Aero- and Hydro-Acoustics, Oct. 2001.
38. M.R. Visbal, D.V. Gaitonde, and S.P. Gogineni, Direct Numerical Simulation of a Forced Transitional Plane Wall Jet, AIAA Paper 98-2643, 1998.
39. M.R. Visbal and R.E. Gordnier, Direct Numerical Simulation of the Interaction of a Boundary Layer with a Flexible Panel, AIAA Paper 2001-2721, 2001.
40. D.P. Rizzetta, M.R. Visbal, and G.A. Blaisdell, Application of a High-Order Compact Difference Schemes to Large-Eddy and Direct Numerical Simulation, AIAA Paper 99-3714, 1999.
41. R.E. Gordnier and M.R. Visbal, High-Order Compact Difference Schemes Applied to the Simulation of a Low Sweep Delta Wing Flow, AIAA Paper 2003-0620, 2003.
42. M.J. Stanek and M.R. Visbal, Investigation of Vortex Development on a Pitching Slender Body of Revolution, *Journal of Aircraft*, 30(5): 711-718, 1993.
43. M.R. Visbal, Computed Unsteady Structure of Spiral Vortex Breakdown on Delta Wings, AIAA Paper 96-2074, 1996.
44. T.L. Doligalski, C.R. Smith, and J.D.A. Walker, Vortex Interactions with Walls, *Annual Review of Fluid Mechanics*, 26: 573-616, 1994.
45. K. Visser and A.E. Washburn, Transition Behaviour on Flat Plate Delta Wings, AIAA Paper 94-1850-CP, 1994.
46. S. Leibovich, Vortex Stability and Breakdown: Survey and Extension, *AIAA J.*, 22(9): 1192-1206, 1984.

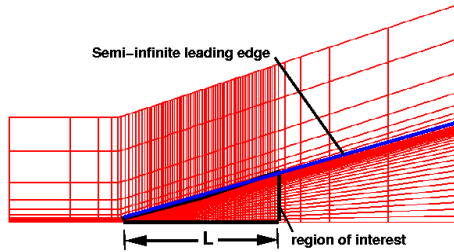


Figure 1. Flow configuration and grid structure for swept leading edge.

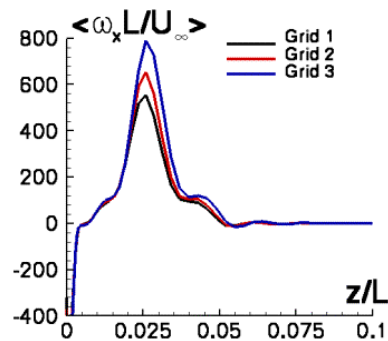


Figure 2. Effect of grid resolution on mean axial vorticity distribution in the vortex core, $Re_L = 2.5 \times 10^4$, $x/L = 0.2$.

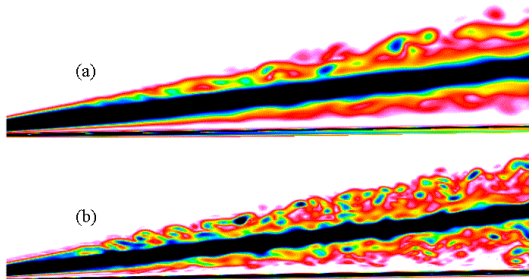


Figure 3. Effect of spatial discretization scheme on instantaneous vorticity magnitude on vertical plane through the vortex core for $Re_L = 5.0 \times 10^4$: (a) Second-order scheme (E2), (b) Sixth-order scheme (C6).

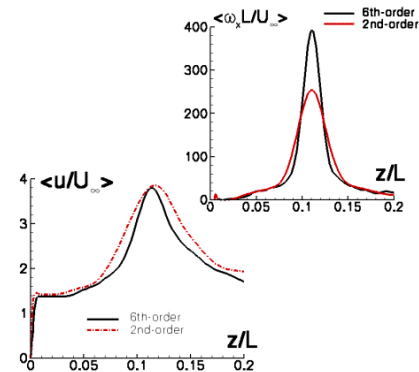


Figure 4. Effect of spatial discretization scheme on mean streamwise velocity and axial vorticity distributions in the vortex core, $Re_L = 5.0 \times 10^4$, $x/L = 1.0$.

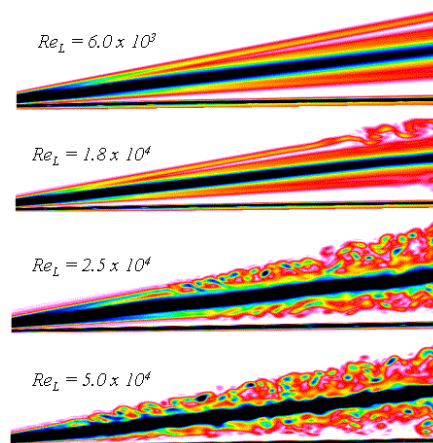


Figure 5. Evolution of vortex structure with increasing Reynolds number. Contours of instantaneous vorticity magnitude on vertical plane through vortex core.

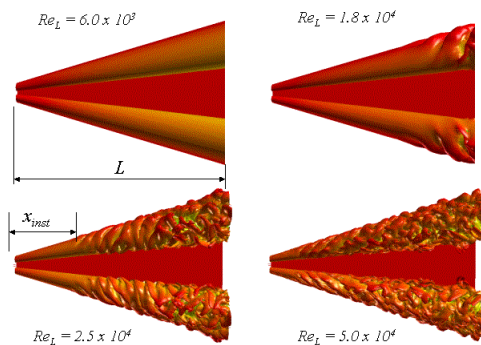


Figure 6. Evolution of shear layer structure with increasing Reynolds number depicted using an isosurface of axial vorticity.

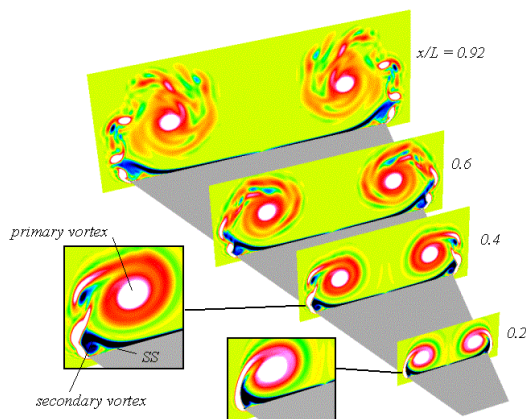


Figure 7. Contours of instantaneous axial vorticity at several crossflow planes along the wing, $Re_L = 2.5 \times 10^4$.

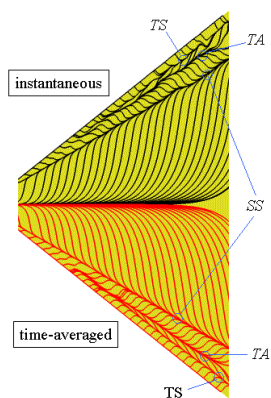


Figure 8. Instantaneous (upper half) and time-averaged (lower half) limiting streamline pattern on wing upper surface, $Re_L = 2.5 \times 10^4$, (Note: spanwise scale enlarged for the purpose of clarity).

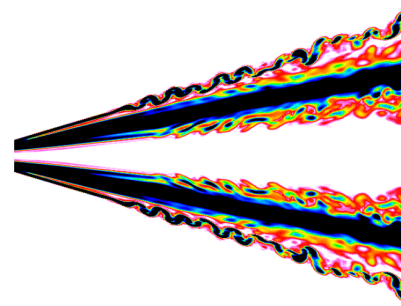


Figure 9. Contours of instantaneous vorticity magnitude on longitudinal plane through the vortex core, $Re_L = 2.5 \times 10^4$.

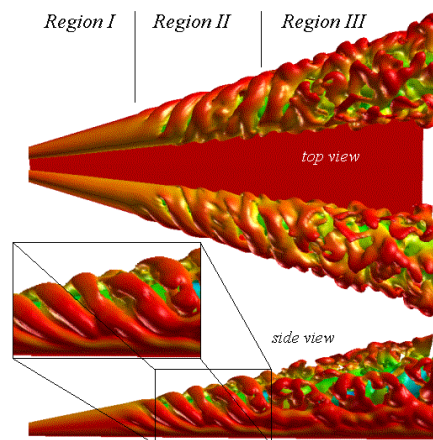


Figure 10. Instantaneous shear-layer structure depicted using an isosurface of axial vorticity, $Re_L = 2.5 \times 10^4$.

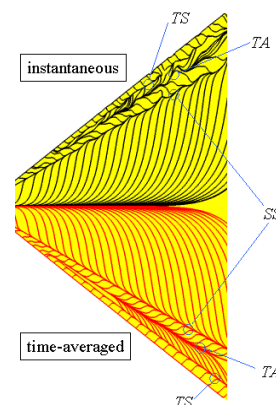


Figure 11. Instantaneous (upper half) and time-averaged (lower half) limiting streamline pattern on wing upper surface, $Re_L = 5.0 \times 10^4$, (Note: spanwise scale enlarged for the purpose of clarity).

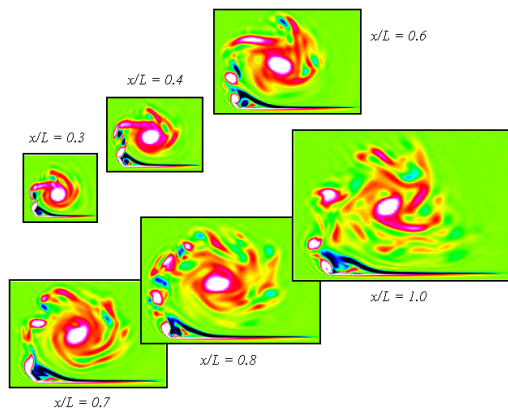


Figure 12. Contours of instantaneous axial vorticity at several crossflow planes along the wing, $Re_L = 5.0 \times 10^4$.

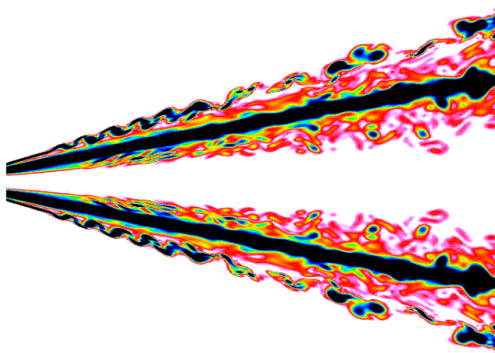


Figure 13. Contours of instantaneous vorticity magnitude on longitudinal plane through the vortex core, $Re_L = 5.0 \times 10^4$.

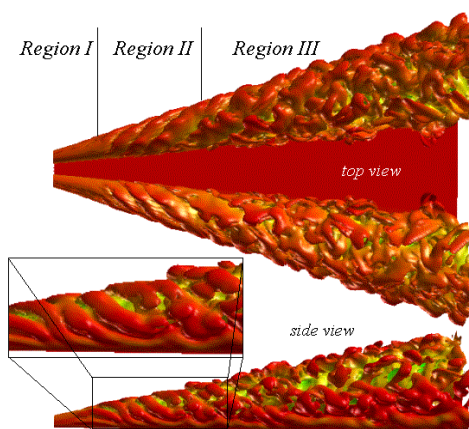


Figure 14. Instantaneous shear-layer structure depicted using an isosurface of axial vorticity, $Re_L = 5.0 \times 10^4$.

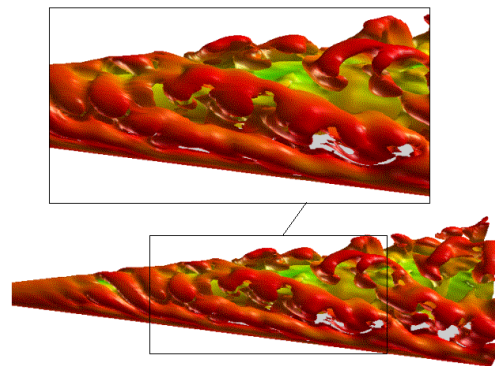


Figure 15. Isosurface of instantaneous axial vorticity showing break-up of vortical substructures along their axes, $Re_L = 5.0 \times 10^4$.

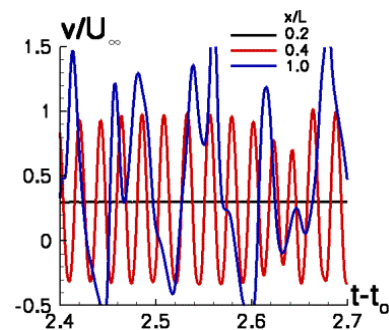


Figure 16. Time histories of spanwise velocity within the unsteady shear layer at several streamwise locations, $Re_L = 2.5 \times 10^4$.

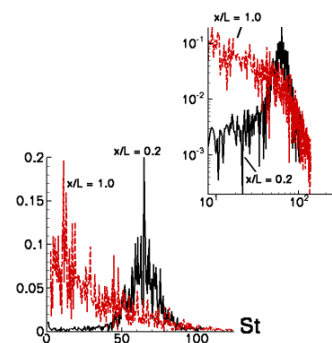


Figure 17. Spectra of spanwise velocity fluctuations within the shear layer at two streamwise locations, $Re_L = 5.0 \times 10^4$.

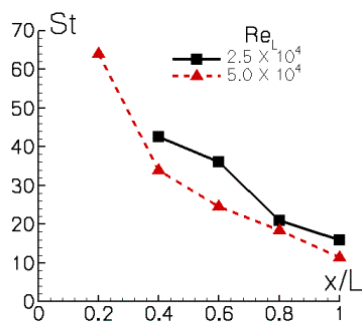


Figure 18. Streamwise variation of dominant non-dimensional frequency of shear layer fluctuations.

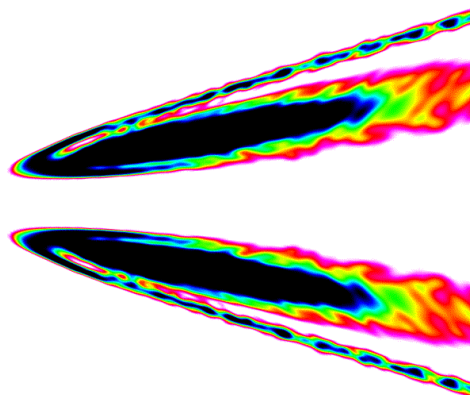


Figure 21. Contours of mean axial vorticity on horizontal plane cutting the shear layer and vortex core, $Re_L = 5.0 \times 10^4$.

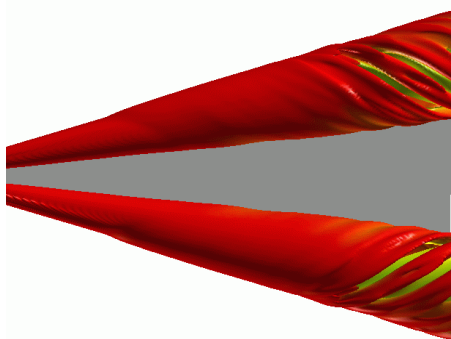


Figure 19. Time-averaged shear layer structure depicted using an isosurface of mean axial vorticity, $Re_L = 2.5 \times 10^4$.

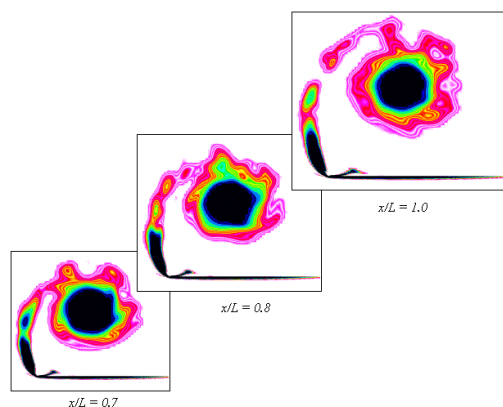


Figure 22. Contours of time-averaged axial vorticity on several crossflow planes along the wing, $Re_L = 5.0 \times 10^4$.

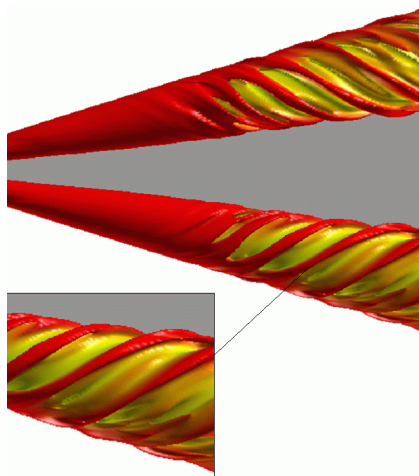


Figure 20. Time-averaged shear layer structure depicted using an isosurface of mean axial vorticity, $Re_L = 5.0 \times 10^4$.

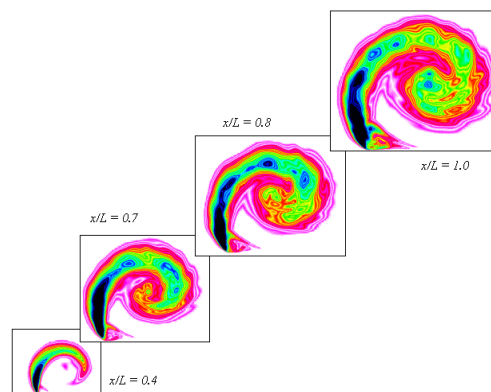


Figure 23. Contours of RMS streamwise velocity fluctuations on several crossflow planes along the wing, $Re_L = 5.0 \times 10^4$.

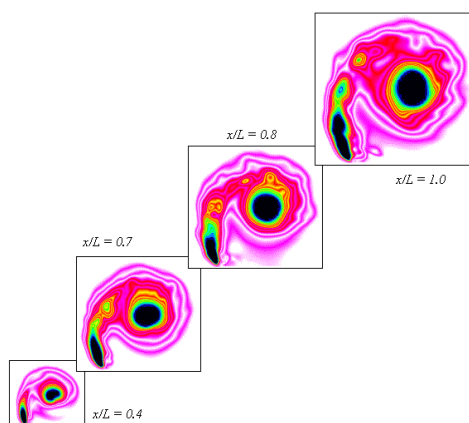


Figure 24. Contours of RMS pressure fluctuations on several crossflow planes along the wing, $Re_L = 5.0 \times 10^4$.

Chapter 13 – UNSTEADY EULER AND DETACHED-EDDY SIMULATIONS OF FULL-SPAN ONERA 70° DELTA WING

Stefan Görtz

Royal Institute of Technology (KTH), Department of Aeronautical and Vehicle Engineering
100 44 Stockholm, Sweden

goertz@kth.se

ABSTRACT

The inherently unsteady flow field over a stationary, full-span delta wing at high incidence is simulated time-accurately using the structured Navier-Stokes Multi Block (NSMB) code. Inviscid calculations are performed on an Euler-type grid using explicit global Runge-Kutta time stepping. Detached-Eddy Simulations (DES) are done on a Navier-Stokes grid using implicit dual time stepping. A time step study is conducted to verify the properties of the discretization of the time derivative operator. The full-span model Euler simulations capture vortex interactions - the numerical solutions exhibit asymmetry as well as streamwise fluctuations in the port and starboard vortex breakdown locations, despite symmetric boundary conditions and a symmetric computational grid. Flow visualization reveals that spiral-type breakdown is predicted over both sides of the wing for the predominant part of the simulations. The rotation of the port and starboard post-breakdown helical structures is shown to be out of phase at certain times. Intermittent bubble-type breakdown is also observed to occur periodically over one side or the other of the wing and related to the occurrence of asymmetry in the vortex breakdown location. For DES, a time step study and a grid sensitivity study are conducted on semi-span grids to verify time accuracy and grid resolution. The full-span DES results are compared to detailed LDV and pressure measurements for the same geometry. The breakdown location is shown to be grid sensitive. Agreement between the measured and computed breakdown locations is shown to be good on the refined grid. The surface pressure distribution is underestimated, even on the refined grid, maybe due to excessive wind-tunnel blockage effects. Finally, visualization of the computer unsteady results in a virtual-reality environment is discussed.

SYMBOLS

b	semi-span	St	Strouhal number, $St=f \cdot c/U_{\infty}$
c	root chord length	t	time
C_N, C_l	normal-force, rolling-moment coeff.	t^*	non-dimensional time, $t^*=t \cdot U_{\infty}/c$
C_p	pressure coefficient, $C_p=(p-p_{\infty})/q_{\infty}$	Δt^*	non-dimensional time step, $\Delta t^*=\Delta t \cdot U_{\infty}/c$
F	Frequency	U_{∞}	freestream velocity
M_{∞}	freestream Mach number	u, v, w	x-, y-, z-component of velocity
p_{∞}	freestream pressure	x, y, z	Cartesian coordinates, origin at wing apex
q_{∞}	dynamic pressure, $q_{\infty}=\frac{1}{2}\rho_{\infty}U_{\infty}^2$	α	angle of attack
Re_c	Reynolds number per meter	ρ_{∞}	freestream density

13.1 INTRODUCTION

Modern high-performance fighter aircraft like Saab's JAS39 "Gripen" make use of highly swept, slender wings. The subsonic high-angle-of-attack aerodynamics of such advanced aircraft configurations is dominated by separation induced vortical flows. The two counter-rotating wing vortices, which are responsible for between 30% and 60% of the total lift [1], can undergo a sudden radial expansion at high angles of attack known as vortex breakdown. Breakdown results in a loss of lift on a wing and a change in pitching moment. The flow upstream of breakdown is steady. Downstream of the breakdown point is a region of organized unsteady flow [2,3] that can cause tail buffeting and structural fatigue, especially on twin-tailed aircraft [4,5].

Vortex flows are among the most difficult to analyze because of their inherently unsteadiness and non-linear interactions. In order to reach a better understanding one therefore tries to study a model problem that contains only one generic aspect of such flows in a simple setting, free of other complications [6]. The present CFD investigation considers the flow at a freestream Mach number of 0.2 and root chord Reynolds number of 1.56×10^6 past a *full-span*, sharp-edge 70° delta wing at angles of attack of 27°, 30°, and 35°. This rather simple geometry corresponds to a wind tunnel test model [7].

In the past, numerical studies of vortex breakdown over delta wings have been limited to steady-state CFD simulations [8,9,10,11,12,13,14,15], because unsteady CFD requires far more analysis and CPU time than a corresponding steady-state analysis. Recent advances in numerical algorithms and computer power, however, make it now possible to perform time-accurate CFD simulations of vortex breakdown. Some more recent studies have looked at the feasibility of time-accurate CFD studies of semi-span delta wings [16,17,18,19,20,21]. CFD has, however, remained limited as a reliable tool for prediction of inherently unsteady vortex flows because current engineering approaches to predicting unsteady flows are based on the Reynolds-Averaged Navier-Stokes equations, which, arguably, are not suitable for this class of flow. A new and promising approach to this problem is Detached-Eddy Simulation (DES), which has been successfully applied to time-accurate simulation of vortex breakdown over semi-span delta wings by Morton *et al* [22,23,24].

So far, both steady-state and time-accurate simulations of vortex breakdown over stationary delta wings have been limited to semi-span wings. This requires a symmetry condition to be applied in the plane of symmetry, which leads to an artificial symmetry of the flow field. This symmetry conditions does not exist in reality – unless a half-span model and a so-called "splitter plate" are used – and suppresses the mutual interaction of the left and right vortices across the plane of symmetry. Among the few papers published to date on time-accurate CFD simulations of vortex breakdown over stationary full-span wings are those by Gordiner [25] and Estorf and Hummel [26], the former one dealing with first-order time-accurate laminar computations at low Reynolds numbers. Some research has also been done on computations of forced and free rolling full-span delta wings, where motion-induced vortex breakdown occurs over the wing, e.g. by Gordnier [27] and Chaderjian and Schiff [28].

13.2 PRESENT WORK

The first part of the present paper deals with time-accurate Euler simulations of three-dimensional vortex breakdown above *full-span* stationary delta wings using the Navier-Stokes Multi Block (NSMB) code. The ongoing study aims to predict streamwise oscillations of the vortex breakdown location about some mean position, which have been experimentally observed by many researchers, the rotation of the spiral structure downstream of breakdown, which is assumed to be responsible for oscillations in the aerodynamic coefficients, as well as asymmetry in the breakdown location due to the interaction between the left and right vortices. Analysis of this complex problem remains challenging and computationally

expensive, mainly because of very small time steps and large number of grid points required to resolve the physical time and length scales of the inherent flow unsteadiness time accurately. The unsteady Euler model fails, however, to correctly predict viscous effects, such as the influence of the secondary vortex on the location and strength of the primary vortex, making a comparison with experimental data difficult. The purpose of the second part of the paper is to perform a more realistic unsteady CFD simulation by including viscosity and to compare the results with experimental data. The DES approach taken here is relatively new and calls for basic and fundamental verification on how well it works.

The current research is a continuation of an earlier study [29,30,31], which was concerned with steady numerical simulations of vortex breakdown over 70° delta wings and a delta-wing/body configuration. The steady-state calculations predicted harmonic oscillations of the lift coefficient around a mean value. This, and the convergence problems of the steady-state simulation, were interpreted as a hint that the flow is unsteady and prompted the author to perform the time-accurate simulations reported in the present paper.

The paper begins with a review of the unsteady aspects of vortex breakdown over delta wings, followed by a description of the numerical approach, the wing geometry and the numerical grids. The main part deals with the discussion and analysis of the results. The paper ends with some conclusions and an outlook on ongoing and future work.

13.3 ASPECTS OF UNSTEADY VORTEX BREAKDOWN

The flow around a highly swept delta wing features most of the interesting flow phenomena of high-angle-of-attack aerodynamics, including vortex breakdown. Vortex breakdown was first observed over delta wings in water tunnel experiments in the 1950s [32,33,34,35]. The vortex breakdown mechanism is rather involved and is one of the unresolved problems in fluid mechanics [36]. The flow parameters that affect these two types of vortex breakdown, and the physical process of the breakdown mechanism, are still among the most challenging fundamental research problems in fluid dynamics [36]. The wing parameters having an influence on vortex breakdown include sweep angle, leading-edge geometry, wing thickness, as well as freestream conditions and angle of attack [37]. The breakdown location itself has been observed to dynamically oscillate in the streamwise direction [38,39,40,41,42,43,44]. The magnitude of the oscillations decreases with increasing freestream velocity [45]. Additionally, at high α or on delta wings with high sweep angles, an asymmetry in the port and starboard side breakdown location at zero roll and side-slip angle and static incidence angle has been experimentally observed [39,46,7]. With increasing leading-edge sweep angle the breakdown locations become increasingly asymmetric and unsteady [38]. The leading-edge vortices can interact in such a way that the breakdown locations on each side of the wing oscillate out of phase [45].

One can distinguish spiral and bubble type breakdown modes [35,38]. Both types occur simultaneously over the delta wing in Fig. 1. In the case of spiral-type breakdown, the vortex core filament abruptly kinks and starts to spiral around the axis of the structure, forming a corkscrew-like distortion of the vortex core. The sense of the spiral winding is opposite to the direction of rotation of the upstream vortex, however, the rotation of the winding is in the same direction as the rotation of the upstream vortex. This is illustrated in Fig. 2. The bubble-type mode is characterized by a stagnation point on the vortex axis followed by an oval-shaped recirculation zone, with the core flow spreading out symmetrically at the stagnation point and passing smoothly around the recirculation zone.

13.4 COMPUTATIONAL METHOD

All results were computed with the Navier-Stokes Multi Block (NSMB) code [47,48,49,50,51,52,53]. It is being developed in a joint European research project between universities and industry, among them KTH,

EPFL, CERACS, Saab Aerospace and EADS/Airbus. NSMB solves the governing equations, the unsteady, three-dimensional, compressible Euler or Reynolds-Averaged Navier-Stokes (RANS) equations, on block-structured grids by means of a cell-centered finite volume method. The equations are solved in time using either an explicit Runge-Kutta scheme or dual time stepping. Convergence to steady state can be accelerated using a matrix or scalar version of the implicit LU-SGS scheme, preconditioning, and multigrid.

Two of the key enabling technologies required for viscous unsteady simulations of the separated flow over delta wings, dual time stepping and Detached-Eddy Simulation (DES), are described in more detail in the following.

13.4.1 Dual Time Stepping

If the problem to solve varies in time, then the unsteady equations must be solved in a time-accurate manner and convergence-accelerating techniques like local time stepping, multigrid and preconditioning cannot be used. Usually, explicit time stepping becomes impractical because, due to stability restrictions, the explicit time step is significantly smaller than the physical time scales involved. Consequently, an unnecessary large number of time steps has to be computed to simulate a given time span. Even implicit schemes are not well-suited because they are only first-order accurate in time due to the linearization that is needed in the solution procedure. Dual time stepping is one way around this dilemma in that it offers higher-order time accuracy while allowing use of efficient convergence procedures, but at the cost of an additional iteration loop.

Dual time stepping, which was perfected by Jameson [54], introduces an outer time-stepping loop for a real time-accurate time step using a fully-implicit second-order backward scheme, and an inner loop with a fictitious or pseudo time step to reach a "steady state" at each real time step. At the convergence of the inner loop, the pseudo-temporal terms vanish and the solution is truly time-accurate (this is not quite true since, for practical reasons, the residual is never driven to zero). Existing acceleration techniques like local time stepping, multigrid or implicit schemes can then be used in the inner loop to iterate the solution to a "steady state." This does not affect the time accuracy of the method.

13.4.2 Detached-Eddy Simulation

RANS methods have demonstrated an ability to predict attached flows very well at a relatively low computational cost. Large-Eddy Simulation (LES) methods, on the other hand, have proved to accurately compute separated flow fields. Although the computing cost of LES of turbulent flows is significantly less than that of direct numerical simulation (DNS), it is still too expensive for engineering applications involving thin boundary layers near surfaces, since the resolution requirements currently are prohibitive for most computers in terms of CPU time.

Spalart *et al* [55] proposed a hybrid LES/RANS turbulence model based on the one-equation Spalart-Allmaras eddy viscosity model [56] as an alternative. This hybrid approach, also called Detached-Eddy Simulation (DES), employs traditional RANS turbulence models to overcome the near-wall resolution problem. This robust approach is aimed at high-Reynolds-number separated flows, where it smoothly switches from RANS turbulence modeling in the boundary layer to LES in the separated region, improving results noticeably over RANS modeling. This is critical to obtaining accurate estimates of aerodynamic loads for massively separated flows, like the flow over delta wings, e.g.

DES has now been applied to a range of challenging test cases [57,58,22,59,60,23,61,24], typically yielding more accurate predictions than can be obtained with RANS.

More details on the DES model implemented in NSMB can be found in the thesis of Caruelle [57]. Note

that in the original Spalart-Allmaras model, which has been used here, the production term is based on the simple vorticity. For vortical flows, Spalart and Shur [62] recommended a production term based on a comparison between vorticity and classical production (used by k - ε models, e.g.). This improved model has been implemented into the code, but has not yet been used here.

13.5 WING GEOMETRY AND COMPUTATIONAL GRIDS

The full-span delta wing model used here has a sweep angle of 70°. It has a root chord of 950 mm, a wingspan of 691.5 mm at its trailing edge, is 20 mm thick and is beveled on the windward side at an angle of 15° to form a sharp leading edge, compare Fig. 3. The sharp leading edge fixes the primary separation line of the primary vortex and makes the location of separation Reynolds number independent. Extensive wind-tunnel testing with LDV and pressure measurements has been performed on this geometry at ONERA by Mitchell [7].

13.5.1 Navier-Stokes Grid

A structured Navier-Stokes (N-S) grid was generated for the original model geometry with the cut-off trailing edge. The full-span grid was generated by mirroring a half-span grid at the plane of symmetry. A mirrored grid is preferable in order to remove any numerical asymmetry in the solution. The half-span grid was generated using the commercial software ICEM CFD Hexa. The grid is of HCH-type, H-type in chord and span-view and C-type in planform view, to ensure maximum consistency with model geometry. A C-type grid was chosen in the plane parallel to the wing planform to ensure continuity of the mesh lines at the leading edge. Three blocks were placed above the wing in an effort to avoid a singular line at the wing's apex. The same blocking was generated over the flat part of the lower surface of the wing. This grid topology was developed and tested by the author in a previous study [31]. The far-field boundaries extend 4 wing root chord lengths c upstream and $6c$ downstream from the apex of the geometry, $4c$ above and below the wing, and $4c$ in both the port and starboard spanwise directions. The boundary conditions are imposed using ghost cells as follows. Non-reflecting characteristic boundary conditions are applied at all far-field boundaries. On the delta-wing surface an adiabatic wall condition is specified. At block interfaces it is assumed that the coordinates are continuous across the interface, which means that the values of the state vector in the ghost cells at these boundaries are directly taken from the neighboring block.

The N-S grid was generated using a hyperbolic meshing law near solid boundaries. It consists of 4,231,936 finite-volume (FV) cells and 32 blocks. The first cell size in the direction normal to all wing surfaces is $\Delta z = 1.0 \times 10^{-5}c$, except for the blunt trailing edge where the wall normal spacing is $\Delta z = 1.0 \times 10^{-4}c$. The grid has 98×148 points on the upper wing surface in the chordwise and spanwise directions, respectively. The leading-edge bevels and the blunt trailing edge are discretized with 41 points. The grid is refined towards the leading edges, the trailing edge and the apex, which has a major influence on the development of the primary vortex and on the onset of vortex breakdown. The grid is also designed to be fine on the leeward side of the wing to increase the resolution in the region of the vortices, and to be coarser on the windward side.

The final grid has good mesh quality metrics. The finite-volume cells around the apex feature the smallest grid angle of 20°, which is determined by the wing's high sweep angle. The minimum cell determinant is 0.7. For a steady-state computations performed with the turbulence model of Spalart and Allmaras the maximum y^+ value (thickness of the viscous sublayer) was between 0.323 and 1.683, apart from the blunt trailing edge, where the maximum y^+ value was 6.041. Figure 5 presents the full-span N-S grid in planform view. Figure 6 shows a three-dimensional view of a section of the grid.

13.5.2 Euler Grid

A second full-span grid for Euler computations was generated. To avoid numerical problems at the blunt trailing edge, the original model was sharpened with a bevel at the trailing edge. The modified geometry is shown in Fig. 4. The grid was generated following the rules for the N-S grid above, yet with a slightly different topology to account for the trailing-edge bevel. The grid also differs from the previously described N-S grid in the first cell height, which was set to $\Delta z = 0.0042c$ at the apex and to $\Delta z = 0.0084c$ over the rest of the upper surface of the wing. The corresponding value for the lower surface is $\Delta z = 0.01c$. The grid was generated using the geometric meshing law in ICEM CFD Hexa. There are 82×148 grid points on the upper surface of the wing in the chordwise and spanwise directions, respectively. The point spacing above the wing was controlled by creating a dual layer parallel to the wing planform some distance over the wing. Up to this distance the cell height was held to a constant $\Delta z = 0.02c$, and above the grid was stretched in the usual way. The resulting grid has 1,674,752 FV cells and consists of 56 blocks that were merged down to 25 blocks.

13.6 DISCUSSION AND ANALYSIS OF RESULTS

This section is divided according to the type of computations performed. First are the results for time-accurate Euler simulations of the unsteady flow over the full-span delta wing model with a sharp trailing edge at 27° , 30° , and 35° angles of attack. Runge-Kutta time-stepping is used here, because it does not introduce any additional numerical parameters like the time step size, the number of inner iteration, etc., that need to be selected when using dual time stepping. This makes the simulation straightforward and some experience with unsteady simulations can be gained. Next, DES results of the full-span model with a blunt, or cut-off, trailing edge are presented for $\alpha = 27^\circ$. An important input to these viscous simulations are the results of a time-accuracy study performed on a semi-span delta-wing model. Dual time stepping is used for the DES simulations.

13.6.1 Time-Accurate Euler Simulations

Euler calculations have been carried out on the Euler-type grid with 1,674,752 FV cells. Solutions were obtained for a freestream Mach number of 0.2, and angles of attack of 27° , 30° , and 35° . Vortex breakdown is observed over the wing at these angles of attack in the experiment [7]. The angles of incidence and the freestream pressure and density match the experimental conditions, whereas the Mach number was increased from 0.07 to 0.2 to avoid numerical stability and convergence problems with the compressible flow solver.

The computations were carried out on two Processing Elements (PE) of a Fujitsu VX/3 vector computer with a total of three PEs. Each PE has a peak performance of 2.2 GFlop/s and 2 GByte of memory. When NSMB was run in unsteady mode, the working data set was 912 MByte in total size and resided entirely in the main memory.

During the course of the unsteady simulations, the flow-field solution was written to files in `plot3d` format at 5.0×10^{-4} s intervals, resulting in about 60 GByte of data for $\alpha = 27^\circ$, and about 36 GByte for each of the other two angles of attack. The solution files were then processed and animated using the commercial post-processor Ensight.

13.6.1.1 CFL Number and Time-Step Size

The unsteady calculations were started from a steady-state solution, which was generated by means of local time stepping. Explicit global time stepping was then done with a five-stage Runge-Kutta (R-K) scheme with two evaluations of the dissipative terms (5/2 scheme with Van der Houwen/Van Leer coefficients). This scheme is second-order accurate in time and has good stability and damping properties

[63,64,65]. It was chosen here because the extra stages extend the stability region and thus allow for a larger CFL number, which in turn maximizes the real time step. Three and four-stage R-K schemes, which are usually preferred for steady-state calculations because they are less expensive per time step and require less memory, are more restrictive in terms of stability. A Courant-Friedrichs-Lewy (CFL) number of 4.0 was specified, which is the maximum hyperbolic stability limit for this five-stage R-K scheme, compare Fig. 7(a) in Swanson and Turkel *et al* [63] and van der Houwen [66]. Increasing CFL beyond 4.0 resulted in divergence. The resulting dimensional and non-dimensional time steps, Δt and Δt^* , are summarized for all three angles of attack in Table 1 together with the number of computed time steps, the CPU wall-clock time and the total amount of data written to disk in GByte.

α	$\Delta t \cdot 10^6$ [s]	$\Delta t^* \cdot 10^4$	# Δt	CPU [h]	Data [Gb]
27°	3.370	2.41	250,000	650	60
30°	3.382	2.42	150,000	390	36
35°	3.406	2.44	150,000	390	36

Table 1: Dimensional and non-dimensional time-step size, number of computed time steps, CPU time and total file size (Euler)

The time-step is quite a bit smaller than the one that would be required to ensure time accuracy. This is because explicit time-accurate methods must advance all cells in the computational domain with the same time step to maintain consistency. The global time step is therefore limited by the most restrictive of all allowable time steps in the domain, which in turn is a function of the smallest cell size. In the present case, however, the frequency of the physical phenomena to be resolved is not too many orders of magnitude different from the characteristic frequencies of acoustic disturbances. This, and the fact that explicit schemes are inexpensive per time step, make this a reasonable and cost effective approach to the solution of the unsteady problem.

13.6.1.2 Flow Field Visualization

Streaklines¹ are an effective visualization technique for depicting vortex breakdown in unsteady flows [67]. Figure 7 shows computed streaklines at different instants in time for $\alpha=30^\circ$. Note that time increases from top to bottom, column by column. The streaklines were generated by injecting small massless particles into the flow from several seed locations along the vortex core axis upstream of breakdown at multiple time intervals. The particles were then traced both spatially and temporally, resulting in pathlines², which were animated.

The three-dimensional structure of spiral-type breakdown is clearly observed. It shows good qualitative agreement with the experimental flow visualization in Fig. 1. Upstream of breakdown, the particles follow the vortex axis, forming a straight streakline. They abruptly change direction at the point of vortex burst and start to spiral around a region of reversed flow (not visualized here), forming streaklines with a helical shape. The sense of this helix or spiral is opposite to the direction of rotation of the upstream vortex. The time sequence of images reveals that the spiral turns around with respect to time in the sense of the primary vortex, compare also Fig. 2. About one period of rotation is completed during the shown sequence of 0.008 s, corresponding to a spiralling frequency of $f=125$ Hz or a Strouhal number of $St=1.75$. This estimate will later be compared with the results of the spectral analysis of the aerodynamic coefficients. Gursul [68] has shown in experiments that the Strouhal number of the helical mode instability ranges from 1.65 to 1.75 for a 70° delta wing at $\alpha=30^\circ$. These Strouhal numbers were derived from measurements of the surface pressure at different streamwise locations underneath the breakdown.

¹ A *streakline* is a curve formed by all particles that were previously injected from a fixed location.

² A *pathline* is the trajectory of a particular fluid particle. It is different for different fluid particles.

Another interesting feature of the flow in the post-breakdown region that can be seen for $\alpha=27^\circ$ in Fig. 8 is the influence of the helical structure on the upper surface distribution. Regions of low pressure are generated where the helix comes in proximity to the delta wing surface. As time progresses these regions of low surface pressure are seen to form upstream near the initial breakdown location and move downstream with the progression of the rotating helical structure. This unsteady behavior leads to fluctuations in the normal-force and roll-moment coefficients (see discussion below).

The time sequence of images in Fig. 9 shows the evolution from spiral to intermittent bubble-type breakdown at $\alpha=30^\circ$. The left side of the figure shows streaklines of instantaneous particles. The right side shows iso-surfaces of entropy. Time advances from top to bottom. At the first instant in time, following breakdown, the port and starboard iso-surfaces are seen to wind in the direction opposite to that of the rotational sense of the upstream flow, forming a corkscrew-like distortion, very much like the streaklines of particles. The spiral structures on both sides of the wing are symmetric and in phase. In the two following instances in time, the port side spiral structure is seen to undergo a transformation to a nearly axisymmetric bubble. The downstream half of the bubble is open and irregular, which is in qualitative agreement with observations of bubble-type breakdown over a delta wing by Payne *et al* [39]. In the last set of images, bubble-type breakdown is established over the portside of the wing with spiral-type breakdown occurring simultaneously over the starboard side. This is in good qualitative agreement with the water-tunnel visualization of spiral- and bubble-type vortex breakdown occurring simultaneously over the delta wing in Fig. 1.

This transformation always occurred in a transient sense for short periods of time and was associated with a significant upstream movement of the breakdown location. The bubble transformed back into a spiral after some time to reappear as a bubble again at a later time on the opposite side of the wing (not shown here).

Such intermittent bubble-type breakdown was also predicted in time-accurate CFD simulations of the flow around a 65° stationary delta wing at $\alpha=30^\circ$ by Gordnier [25]. It was also observed in experiments by Lowson [69] and Payne *et al* [70]. Greenwell [71] postulated that this intermittent open-ended bubble burst is in fact an artefact of the tracer flow visualization technique, as transient disturbances temporarily reduce the pitch of the fundamental helical burst structure. This postulate seems to be somewhat supported by the last set of images in Fig. 9, where the streaklines on the left side of the figure are seen to form a somewhat distorted spiral instead of a bubble. The number of particles forming the streakline however is too small to draw any conclusions. More numerical and experimental work will need to be done to confirm or disprove this postulate.

13.6.1.3 Time History of Aerodynamic Coefficients

Figure 10 presents the variation of the normal-force coefficient with time for all three angles of attack. It is observed that the normal-force coefficient is not constant but fluctuates. Such fluctuations were first observed in an experimental study of vortex breakdown over delta wings by Earnshaw and Lawford [72]. They reported that the magnitude of fluctuations associated with angles of attack where vortex breakdown occurs, is between ten and twenty times that at low incidence, where no breakdown is present.

At $\alpha=27^\circ$, some initial transients have decayed after about 0.2 s. Then, the normal-force coefficient oscillates harmonically. However, a low-frequency modulation of the amplitude is observed. This "beat" is seen more clearly in Fig. 11, which shows an interval of time after the transients have decayed. Such a beat is typically caused by a superposition of harmonic oscillations. This is discussed below. Flow-field visualization reveals that, during the transients, the spiral-type vortex breakdown structure on the port and starboard sides of the wing rotate out of phase. After about 0.2 s, they rotate in phase and continue to do so until the simulation is stopped. The breakdown locations are symmetric and do not move in the

streamwise direction.

At $\alpha=30^\circ$, the fluctuations increase in intensity and are more irregular. A harmonic oscillation of the normal-force coefficient is not observed. The irregular fluctuations may be due to vortex interaction, which occurs at $\alpha=30^\circ$ but not at $\alpha=27^\circ$ because at $\alpha=30^\circ$ the vortex breakdown locations are more upstream and thus closer to each other.

A further increase in the magnitude of fluctuations is observed at $\alpha=35^\circ$. Also, a low-frequency oscillation is superimposed on the high-frequency oscillations. The latter may be due to streamwise oscillations of the vortex breakdown location. It is, however, difficult to draw such a conclusion based only on the temporal evolution of C_N , because the time history of C_N is of little use in this form.

Figure 12 shows the rolling-moment coefficient C_l as a function of time. At $\alpha=27^\circ$, a non-zero rolling moment is observed during the transients. This corresponds to the out-of-phase spiraling observed with flow-field visualization. The rolling moment decreases after the transients have decayed but remains non-zero, indeed, confirming a small flow-field asymmetry. The asymmetry is so small, however, that it is impossible to detect with flow-field visualization.

By plotting the rolling-moment coefficient C_l as a function of time for $\alpha=30^\circ$, one can see that there must be an antisymmetric oscillations of the port and starboard vortex breakdown location, causing a non-zero rolling moment. The asymmetry is due to vortex interactions, which are captured because a full-span model is simulated. The interactions are known to be more intense at higher incidences, because the vortices/breakdown locations get closer to each other. This explains the increased magnitude of the fluctuations of C_l at $\alpha=30^\circ$ compared to $\alpha=27^\circ$.

Compared to the C_l time history for $\alpha=27^\circ$ and 30° , the magnitude of fluctuations has further increased at $\alpha=35^\circ$, corresponding to larger flow-field asymmetry due to increased vortex interaction, which in turn is due to the mean breakdown location having moved further towards the apex of the wing.

13.6.1.4 Power Spectral Density of C_N

To further understand the oscillating phenomena and to determine the make-up of these frequencies, the C_N versus time data was converted from the time to the frequency domain using spectral analysis. Spectral analysis produces the Power Spectral Density (PSD) of the signal, which provides a measure of how signal power is distributed over the frequency range. Here, the PSD was obtained by taking the modulus-squared of the Discrete Fourier Transform (DFT) of the signal, which in turns was calculated using Fast Fourier Transformation (FFT) in Matlab. The PSD was then normalized by the number of samples. The PSD of the normal-force coefficient C_N at the three angles of attack is shown as a function of frequency f in Fig. 13³.

At $\alpha=27^\circ$, the PSD plot is very clean – individual peaks are clearly discernible. A distinct peak is apparent at a frequency of $f=140$ Hz, corresponding to a Strouhal number $St=f \cdot c/U_\infty$ of 1.96. Flow-field visualization reveals that this frequency corresponds to the frequency of rotation of the spiral structure in the post-breakdown region. Smaller peaks are seen at frequencies of $f=47$ Hz, 93 Hz, etc. Thus, the C_N signal is actually a superposition of harmonic oscillations with a whole-numbered frequency ratio. The harmonic frequency is $f=47$ Hz and the distinct peak at $f=140$ Hz is the third harmonic. This superposition of harmonic oscillations causes the amplitude modulation of the normal-force coefficient observed in Fig. 11. It is possible that the origin of the modulation is a small difference in the frequency of the port and starboard spiral rotation, which in turns may be due to a small difference in the port and starboard

³ PSD plots of the time history of the lift, drag and pitching moment coefficients are not included here, because they show the same dominant frequencies as the PSD of the normal-force coefficient.

locations of vortex breakdown. Such an asymmetry would cause a small non-zero rolling moment, as was discovered in the C_l vs. time plot in Fig. 12.

Compared to $\alpha=27^\circ$, the spectrum of frequencies at $\alpha=30^\circ$ is fuller. Also, there are several distinct peaks apparent. However, the main peak is now at a frequency of $f=1.97$ Hz ($St=0.028$). Other peaks are apparent at frequencies of $f=24$ Hz, 118 Hz, and 166 Hz, corresponding to Strouhal numbers of $St=0.34$, 1.65, and 2.32. The lowest frequencies seem to be in the expected range of frequencies for the fluctuations of the vortex breakdown locations (see discussion below). Mitchell [7], e.g., measured Strouhal numbers of $St=0.015$ and 0.035 for the vortex breakdown fluctuations over the port and starboard side of the same wing geometry at $\alpha=30^\circ$, respectively⁴. The higher frequencies are consistent with those of spiral rotation. In fact, the frequency of the spiral rotation identified earlier in Fig. 7 corresponds to the peak at $f=118$ Hz.

At $\alpha=35^\circ$, the normal-force coefficient has even more frequency content, especially in the frequency range of 100 to 130 Hz. This is readily seen from the PSD plot in Fig. 13. The lowest dominant frequency is at $f=3.91$ Hz, with a second peak at $f=17$ Hz ($St=0.055$ and 0.24). Then there are four distinct peaks between $f=99$ Hz and 132 Hz ($St=1.38$ to 1.85). The fuller spectrum with increasing incidence may be due to the breakdown location being closer to the apex, causing contributions to the frequency spectrum from different parts of the spiral vortex. Also, if there is an instantaneous difference in the starboard and port breakdown locations, there will be different dominant frequencies of the spiral structure over the wing. Existence of higher dominant frequencies may be due to these two factors [73].

Figure 14 shows a double-logarithmic PSD plot of C_N for $\alpha=27^\circ$, 30° and 35° . The logarithmic scale depicts the full range of frequencies. It is observed that the frequency content increases with increasing angle of attack. Also, the spectrum of dominant frequencies in the range between 100 Hz and 150 Hz is seen to shift towards lower frequencies with increasing angle of attack. For $\alpha=27^\circ$, the logarithmic scale also reveals a peak that falls into the frequency range of fluctuations of the vortex breakdown location. This peak was not discernible with the linear scale in Fig. 13.

Figure 15 is a bar graph representing the range of the computed dominant PSD frequencies, in terms of the Strouhal number $St=f \cdot c/U_\infty$. They have been superimposed over the experimental results by Menke *et al* [42,44]. The current results in Fig. 15, obtained at a higher Mach number than those of Menke *et al*, fall into the range of values that they identified as oscillations of the breakdown location, vortex shedding and the "helical mode instability". Using smoke flow visualization, Menke *et al* related this helical mode instability to spiral-type breakdown occurring over the wing. There is a slight disagreement for the breakdown location fluctuations – the current results are somewhat shifted towards lower Strouhal numbers. This may be due to the different Mach numbers or due to the rather short sample of computed data which does not adequately represent the low frequency oscillations.

The PSD plot in Fig. 13 suggest that the dominant frequency of rotation of the spiral structure decreases with increasing angle of attack. This is in qualitative agreement with the experimental findings for 70° delta wings by Gursul [68,41].

Figure 16 shows the variation of the lowest dominant PSD frequencies in the 100-150 Hz range, in terms of the Strouhal number $St=f \cdot c/U_\infty$, as a function of angle of attack. They are compared with wind-tunnel results for a 70° delta wing by Gursul [68]. Gursul extracted the dimensionless frequency $f \cdot x/U_\infty$ from pressure fluctuations measurements.

⁴ However, in another test of the same model in a different wind tunnel, Mitchell measured Strouhal numbers between $St=0.044$ and 0.048 .

There is good agreement with the experimental data, but only because at 30° and 35° the other (higher) computed PSD frequencies in the 100-150 Hz range were not included. Note, however, that Gursul's measurements are single-point measurements of pressure fluctuations on the wing. And since the dominant frequency of the helical mode instability decreases in the streamwise direction⁵, the measured frequency depends on the streamwise location [68]. Here, however, I computed the PSD of the normal-force coefficient, which represents the integrated effect (over the entire wing surface). One would naturally expect to observe more frequencies at higher incidences when the breakdown location is closer to the apex, because there will be contribution from different parts of the spiral vortex [73]. The shown comparison is therefore valid.

13.6.1.5 Fluctuations of Breakdown Locations

Figures 17 and 18 show the port and starboard vortex breakdown location as a function of time for $\alpha=27^\circ$, 30° and 35° . The vortex breakdown locations were extracted from the ca. 3,500 solution files by determining the point along the vortex axis where the chordwise component of velocity equals zero. This point corresponds to the maximum upstream penetration of the reversed axial flow (i.e., reversed u velocity). The breakdown locations were not determined for the time steps that were computed in between two solution files, giving a somewhat coarser resolution compared to the time history of the aerodynamic coefficients.

At $\alpha=27^\circ$, the starboard breakdown location is seen to oscillate harmonically between $x/c=0.8$ and 0.9 , with a mean value of around $x_b/c=0.85$. A low-frequency oscillation of the mean value is also observed. The breakdown location of the portside vortex, on the other hand, is predominantly stationary, with downstream movement occurring periodically (at $t=0.03$ s, 0.24 s and 0.46). Its mean portside breakdown location is at $x_b/c=0.82$.

The vortex breakdown location fluctuations are more irregular at $\alpha=30^\circ$. Compared to $\alpha=27^\circ$, the portside breakdown location is now seen to be fluctuating at shorter intervals in both the upstream and downstream direction, with stationary locations in between. The mean portside breakdown location is again more upstream at about $x_b/c=0.62$, compared to $x_b/c=0.65$ for the starboard side of the wing. A small arrow at $t=0.234$ s depicts the instant in time corresponding to the occurrence of bubble-type vortex breakdown shown in the last image of Fig. 9. We observe that the transformation from spiral- to bubble-type breakdown over the port side of the delta wing is associated with a significant upstream movement of the portside breakdown location and the occurrence of asymmetry in the port and starboard vortex-breakdown locations.

At $\alpha=35^\circ$, it is observed that both breakdown locations are unsteady and irregular, with breakdown locations ranging from $x/c=0.3$ to 0.6 for the portside wing and $x/c=0.35$ to 0.6 for the starboard wing. This type of unsteady, irregular motion of the breakdown location has been observed in a variety of experiments on vortex breakdown over delta wing [38,39,40,14,7,41,42,43,44]. The rather rapid large-scale fluctuations of the computed breakdown location are probably caused by the location of reversed axial flow shifting rapidly, because the axial grid resolution for the upstream location of breakdown fails to adequately capture this region of the flow. Gordnier [25] computed fluctuations of similar magnitude for the breakdown locations over a banked 65° delta wing at $\alpha=30^\circ$, $M_\infty=0.2$ and $Re=3.2\times 10^4$. He demonstrated that with improved grid resolution, these large, rapid fluctuations were no longer observed and that the mean vortex breakdown location moved downstream. Another cause of the rapid large-scale fluctuations might be that the breakdown location is extracted at rather large intervals, instead of at every computed time step. For $\alpha=35^\circ$, we also observe a clear asymmetry in the computed breakdown locations.

⁵ Disturbances rotating in the vortex core, whose radius grows linearly with x , are helical waves, implying that the wavelength $1/St$ increases with x [68].

At a given instance in time, one of the breakdown locations is upstream of the one on the other side. At another instant in time, however, the more upstream breakdown location may have changed sides. This asymmetry in the port and starboard side breakdown location at high α has also been experimentally observed [39,46,7].

It should be stressed here that the flow-field asymmetry was computed on a symmetric grid at zero sideslip, i.e. with symmetric boundary conditions applied. The asymmetry did not have to be set off in any way, but rather appeared naturally in the solution. This is in strong contrast to the CFD simulations of forebody-vortex asymmetry by e.g. Petterson [74]. Also using the flow solver NSMB, Petterson had to trigger the forebody-vortex asymmetry by either introducing a small perturbation at the nose or by using the directionally biased LU-SGS scheme, or both. In the present study, however, Runge-Kutta time stepping was used, which is not directionally biased but symmetric. The asymmetry in the present case is different in nature, however, as is the strength of the vortices.

Comparing the temporal fluctuations of the breakdown location for all three angles of attack, we see that the amplitude of the oscillations increases with increasing angles of attack. This is confirmed by experimental measurements by Menke *et al* [44] for a 70° delta wing. Mitchell, however, reported that the magnitude of the oscillations over his 70° delta wing decreased with increasing incidence angle [45]. This is contradictory to Menke's data and the present findings.

13.6.2 Detached-Eddy Simulations

In a next step, a time-accurate turbulent calculation of the unsteady flow field was aimed at. The use of the RANS equations in an unsteady flow is valid, provided that the time-scale of the unsteadiness is sufficiently far from the turbulence scales [75]. If the unsteadiness is provoked by an external source, e.g. by pitching the wing, the turbulence model does not necessarily interact with the frequency and amplitude of the unsteadiness. However, in unsteady flows, all properties of a turbulence model are put under severe scrutiny, with the result that the predictive capabilities of a model is generally significantly reduced in comparison with the equivalent steady-state conditions [75]. Here, the dilemma is that the flow unsteadiness caused by vortex breakdown over the stationary delta wing is *self-induced* and the unsteady separated flow is characterized by geometry-dependent and three-dimensional turbulent eddies, making the use of RANS turbulence models questionable. At present, there are no RANS turbulence models available that model this kind of flow correctly [75].

To overcome the deficiencies of RANS models for predicting the unsteady separated flow encountered here, the previously described DES method was used. The primary advantage of DES is that it can be applied at high Reynolds numbers, as can RANS models, but also resolves geometry-dependent, unsteady three-dimensional turbulent motion as in LES. A second-order implicit backward scheme is used for the outer time stepping, and a very efficient matrix version of the semi-implicit LU-SGS scheme [76] is employed for the inner loop. Multigrid is used to accelerate the convergence to "steady state" in the inner loop. A fourth-order skewsymmetric central scheme with second and fourth-order artificial dissipation is used for the spatial discretization. Preconditioning is used to improve the accuracy of the results and to minimize the effects of artificial dissipation on the solution.

13.6.2.1 Time-Step Study

The order of the time-stepping scheme and the choice of the time-step size influence the size of the amplitude and phase error, the two components of the temporal discretization error [75]. Generally, the influence of the time-step size on the amplitude and phase error can be reduced by employing higher-order time-stepping schemes [77].

The choice of the outer time step depends on the time-scales of the flow being analyzed. If the time step is

chosen too large, the simulation might fail to capture important flow features and mimic unphysical steady behavior [75]. It is therefore good practice to start with a relatively small time step, even though this is not required for numerical stability. In the case of explicit R-K time integration, which was employed in the Euler simulation presented above, the time step depends on the stability limits (CFL number) and the grid size and is typically smaller than the time scales of practical interest. In the case of viscous simulations, the explicit time-step restrictions are even less tolerable, since the ratio of the maximum to the minimum size of the cells in a viscous grid can span several orders of magnitude, ruling out R-K methods for this class of flow problems. In the case of the unconditionally stable implicit schemes, however, the time step is typically orders of magnitude larger and its selection depends on the time scales of the flow being analyzed, and these might not be known *a priori*.

The implicit dual time-stepping scheme used here introduces, however, the complication of deciding how many multigrid cycles are needed in the sub-iteration loop of each time step. It is reasonable to expect a trade-off – larger outer time steps advance the computation faster in simulation time, but require more iterations each time step, whereas small outer time steps advance the simulation slower, but at a reduced cost per time step. Here, the number of inner iterations per outer time step was specified implicitly by means of a convergence criterion. Convergence of the inner time-stepping loop was assumed when the residual had decreased by two orders of magnitude.

In NSMB, it is usually sufficient to converge the residual by two or three orders of magnitude [53]. Using a very similar structured multi-block, cell-centered finite-volume code, Wang *et al* [78] even found that a one order-of-magnitude residual reduction was sufficient for a time-accurate computation of the periodic self-excited turbulent flow around a thick airfoil at transonic speeds. Here, specifying a decrease by only one order of magnitude typically resulted in divergence of the inner time stepping loop after a couple of outer time steps.

A time-step study has been conducted to verify the properties of the implicit discretization operator. In order to save CPU time, the time-step study was performed using a 70° *semi-span* delta-wing model of slightly different geometry (root chord length 762 mm, thickness 12.7 mm, bevel angle 25°, bevel at the trailing edge). This model and the corresponding N-S grid (1,632,960 FV cells) was readily available at the beginning of this time-accurate study and the findings are anticipated to be transferable to the full-span model described earlier.

The unsteady calculations were started from a steady-state solution, which was generated with freestream values as initial conditions by means of local time stepping. The steady-state solution was computed for $\alpha=27^\circ$ and $M_\infty=0.2$ using the one-equation turbulence model of Spalart and Allmaras (DES cannot be used for steady-state simulations). The evolution of the lift coefficient and the decay in the density residual, the L_2 -norm of the change in density from one multigrid cycle to the next, are shown in Fig. 19.

For this angle of attack, the solution cannot be converged to steady state – after a drop of three orders of magnitude the residual remains almost constant, i.e. the solution is not diverging. Instead, the lift coefficient shows harmonic oscillations after about 700 multigrid cycles, see insert in Fig. 19. It oscillates harmonically with an amplitude of about 1% of its mean value of 0.96. This, and the behavior of the residual, indicates that the solution is globally stationary but locally unsteady, i.e. quasi-steady. Note, however, that because a local time step is used here, true time accuracy is not obtained. This sets the stage for the time-step study.

As a first guess, an outer time step Δt of 5.0×10^{-4} s, corresponding to a non-dimensional time step $\Delta t^* = \Delta t \cdot U_\infty / c$ of 0.0446, was used. This time step size resulted into divergence of the inner time-stepping loop after 47 outer time steps. The time step size was subsequently reduced to 2.5×10^{-4} s, 1.25×10^{-4} s, and 0.625×10^{-4} s. The corresponding non-dimensional time step sizes Δt^* are summarized in Table 2.

$\Delta t \cdot 10^4$ [s]	$\Delta t^* \cdot 10^2$	# Δt /period	St
5.0	4.46	9	1.95
2.5	2.23	17	2.59
1.25	1.12	32	2.73
0.625	0.56	63	2.72

Table 2: DES time-step study: dimensional and non-dimensional time-step size, number of time steps per period of oscillation, Strouhal number

Figure 20 shows the corresponding time history of C_N for three different time step sizes. The time history of C_N for $\Delta t = 5.0 \times 10^{-4}$ s is not included for reasons of clarity. Each symbol corresponds to one computed time step. All three solutions show basically similar behavior. Initially, C_N increases from 1.09, the value of the steady-state solution, until, after about 0.02 s, the transients have almost decayed and C_N oscillates harmonically around a mean value of about 1.11. Note, however, that a time step size of $\Delta t = 2.5 \times 10^{-4}$ s lowers both frequency and amplitude of the oscillations somewhat. The results for $\Delta t = 1.25 \times 10^{-4}$ s and $\Delta t = 0.625 \times 10^{-4}$ s are in very good agreement (except for a slight difference in phase and amplitude). In Table 2 we see that the Strouhal frequency differs by less than 0.5% for the last two cases. It was therefore estimated that a time step of $\Delta t = 0.625 \times 10^{-4}$ s ($\Delta t^* = 0.0056$) provides sufficient temporal accuracy to adequately resolve the unsteady behavior of vortex breakdown. With this in mind, the simulation in the following section uses this time step size.

The present time-step size is consistent with the guidelines given for DES by Spalart [79]. Assuming a local CFL number of one and a maximum velocity U_{\max} in the LES (or focus) region equal to twice the freestream velocity, the guidelines suggest a time step of $\Delta t = \Delta_0 / U_{\max} = 1.1 \times 10^{-4}$ s, where the average cell size Δ_0 in the focus region was estimated to equal 0.015 m for the grid used here.

Gordnier [25] concluded from a time-step study that a non-dimensional time step of $\Delta t^* = 0.0005$ is required for the time-accurate laminar computations of vortex breakdown over a stationary 65° delta wing at $\alpha = 27^\circ$, $M_\infty = 0.2$ and $Re = 3.2 \times 10^4$. His computations were, however, only first-order accurate in time and for a rather low Reynolds number.

It can be concluded here that a very small time step is needed to get a time-accurate solution. Note that the temporal resolution that is needed, about 60 outer time steps per period of oscillation (compare Table 2), is higher than what the smooth behavior of the C_L vs. time plot in Fig. 20 might suggest. Even if the interest here lies in a slowly-varying integrated quantity such as C_L , this suggests that it seems important to accurately capture the time history of the flow on a faster time scale. This differs from experience with unsteady Euler and RANS calculations of vortex breakdown over *forced* pitching delta wings at $M_\infty = 0.2$ conducted in a parallel study by Le Moigne [80], where accurate temporal resolution was obtained with rather large time steps (two orders of magnitude larger). The corresponding number of outer time steps per pitching cycle, however, was also 60.

The time-step study was carried out on 16 IBM SMP PPC604e nodes, each containing four processors running at 332 MHz, resulting in a theoretical peak performance of 42.5 GFlop/s. Each node has 1 GByte of memory, which is shared by the four processors. When NSMB was run in unsteady mode, the working data set was about 4 GByte in size and resided entirely in the main memory.

The results of the time-step study set the stage for the time-accurate DES study of the full-span delta wing model.

13.6.2.2 Results Full-Span Model

DES has been carried out on the full-span N-S grid with 4,231,936 FV cells. Solutions were obtained for a

freestream Mach number of 0.2, an angle of attack of 27° , and a freestream pressure and density resulting in a Reynolds number of 1.56×10^6 . Angle of attack and Reynolds number were chosen to match the experimental conditions, whereas the Mach number was increased from 0.07 to 0.2 to avoid numerical stability and convergence problems with the compressible flow solver.

A second-order implicit backward scheme is used for the outer time stepping, and a very efficient matrix version of the semi-implicit LU-SGS scheme [76] is employed for the inner loop. Multigrid is used to accelerate the convergence to "steady state" in the inner loop. A fourth-order skewsymmetric central scheme with second and fourth-order artificial dissipation is used for the spatial discretization. Preconditioning is used to improve the accuracy of the results and to minimize the effects of artificial dissipation on the solution.

The full-span DES computations were carried out on four IBM Power3 "Nighthawk" SMP nodes, each containing eight processors running at 222 MHz, resulting in a theoretical peak performance of 28.4 GFlop/s. Each node has 4 GByte of memory, which is shared by the eight processors. When NSMB was run in unsteady mode, the working data set was just over 9 GByte in size and resided entirely in the main memory. The flow-field solution was written to files in `plot3d` format at 5.0×10^{-4} s intervals (every eight outer time steps), resulting in about 750 MByte of data. The solution files were then animated using the commercial post-processor Ensight to show the temporal variation of the flow field. The solution files were also averaged to get a time-averaged solution, which is used to compare with the time-averaged experimental results by Mitchell [7]. The computation was stopped after 89 outer time steps, corresponding to $t=0.0055$ s or $t^*=0.4$. It is assumed here that the transients have not yet decayed after this time. As a consequence, the results presented below have to be interpreted with caution.

Figure 21 depicts the temporal variation of the normal-force coefficient C_N . The normal-force coefficient is observed to oscillate harmonically with changing amplitude. About 3.5 periods of oscillations are completed during the shown time interval. Spectral analysis reveals that the signal contains two dominant frequencies, $f=182$ Hz and 727 Hz, corresponding to Strouhal numbers of $St=2.5$ and 10.2. The corresponding PSD plot is shown in Fig. 22.

The lower Strouhal number, $St=2.5$, falls into the range of values that Menke *et al* [42,44] identified as the helical mode instability, i.e. rotation of the spiral structure, compare Fig. 15. It is only slightly larger than the Strouhal number predicted earlier with the unsteady Euler equations ($St=1.96$). It is, however, in very good agreement with the DES prediction for the half-span model ($St=2.72$). In their time-accurate Euler simulations of vortex breakdown over a 65° delta wing Müller and Hummel [20], on the other hand, found higher dominating frequencies compared to unsteady Navier-Stokes results. Flow-field visualization reveals that this PSD frequency is indeed associated with the rotational frequency of the vortex core in the post-breakdown region.

The higher Strouhal number predicted here, $St=10.2$, was predicted by neither the time-accurate Euler simulations nor the semi-span DES. It falls into the range of values that Menke *et al* identified as Kelvin-Helmholtz instability, compare again Fig. 15. Morton *et al* [22], who investigated a semi-span model of the same delta wing using DES, also found a dominant PSD frequency corresponding to a Strouhal number of about 10.0 in the time history of the normal-force coefficient. At the time of this writing, it is not understood what this higher dominant frequency is caused by. It is anyhow too early to draw any conclusion from the rather short time history of C_N .

As before, the vortex breakdown locations were extracted from the eight available solution files in `plot3d` format by determining the point along the vortex axis where the chordwise component of velocity equals zero. The computed minimum and maximum port and starboard breakdown locations at $\alpha=27^\circ$ are compared to experimentally measured values by Mitchell [7] in Fig. 23. The abscissa indicates angle of attack. The ordinate indicates the non-dimensional chord location x_b/c at which breakdown

occurs, where zero represents the apex of the wing. The circles in the plot are the mean measured breakdown locations, the dashed line is a quadratic curve fit to these, and the solid line with crosses gives the minimum and maximum breakdown locations measured at $\alpha=27^\circ$. The star and diamond symbols represent the minimum and maximum computed starboard and port breakdown location, respectively. The triangles denote the breakdown locations computed on a refined grid (see discussion below). The computed vortex breakdown locations range is $0.789 < x_b/c < 0.813$ for the port side and $0.769 < x_b/c < 0.797$ for the starboard side. Note that the port and starboard breakdown locations are asymmetric, indicating that the full-span DES captures the mutual interactions between the port and starboard vortices. The range of experimental values is $0.61 < x_b/c < 0.71$, with a mean value of 0.68. Note that Mitchell's data is for $M_{\infty, \text{exp}}=0.07$, whereas the present results are for $M_{\infty, \text{CFD}}=0.2$. This difference in the freestream Mach number might explain the small discrepancy between the experimental and computed breakdown locations. Another reason might be inadequate axial grid spacing. Also, when the computation was stopped, the breakdown locations on both sides of the wing were still transient, moving upstream from their most downstream position, which occurred when the simulation was started from the steady-state solution. This will be verified by doing a grid refinement study (see discussion below) and a longer simulation at the correct experimental Mach number.

Figure 24 consists of four surface pressure plots at $x/c=0.53, 0.63, 0.74$, and 0.84 , respectively. The x-axis indicates the non-dimensional wingspan location y/b , where zero represents the root chord. The y-axis represents the pressure coefficient C_p . The solid lines in the plots are the upper and lower surface computed results. The filled circles represent the experimental data by Mitchell [7]. Qualitative agreement between computed and experimental C_p is good in terms of the location of the primary suction peaks, which are located underneath the primary vortices. A secondary suction peak is seen in the computations, but not in the experiments. The experimental measurements do not resolve the secondary peak because a rather low number of pressure tabs was used. From a quantitative point of view, the numerical simulation significantly underestimates the magnitude of the suction point. Generally speaking, better agreement is obtained in the attached flow region close to the root chord. Several possible reasons for this disagreements come to mind: *i*) the grid resolution in the vortical flow region is insufficient, causing a weaker primary vortex; *ii*) wind-tunnel blockage effects are excessive due to the high angle of attack and cause a higher effective angle of attack. The influence of the grid resolution will be investigated in a further study by using a patched grid block over the wing. The second argument is somewhat supported by the fact that the computed vortex breakdown location is downstream of the experimentally measured point, which would correspond to a higher effective angle of attack in the experiments. It would be interesting to see if the surface pressures are in better agreement when a simulation is performed at a (higher) angle of attack such that the computed breakdown location matches the experimental one. Neither the experimental nor the computed surface pressure data in Fig. 24 denote the influence of vortex breakdown on the surface. This demonstrates the inability of surface pressure measurements to identify the vortex breakdown location over delta wings.

Figure 25 shows a surface contour plot of the time-averaged pressure coefficient C_p for full-span DES (left) and experiment (right). Note that the scale and color map are consistent with the experiment. The upper-surface pressure predicted by DES has an elongated ridge-like pattern, the typical footprint of a vortex. The isobars remain smooth and intact and follow the leading edge until about 80% of the chord, where the contours are constricted, indicating vortex breakdown. Also note the footprint of the secondary vortex close to the leading edges, which the experiment fails to capture. The computed C_p contours are in good qualitative agreement with the experiment, although the numerical simulation underestimates the suction underneath the primary vortex.

Another way to analyze the influence of the off-surface vortical flow field on the delta wing's surface is to visualize the surface oil flow or skin friction lines. Computed skin friction lines are presented in Fig. 26. It is observed that the skin friction pattern is almost perfectly symmetric. The primary reattachment and secondary separation lines are clearly visible. The primary separation line is the sharp leading edge.

Outboard of the primary reattachment line, the streamlines are swept outward beneath the primary vortex core towards the leading edge. The secondary separation line is located just inboard of the leading edge. A tertiary separation line is seen in between the secondary reattachment line and the secondary separation line. The tertiary reattachment line is not discernible. A region of attached flow is seen on the center part of the wing close to the trailing edge. The surface-flow pattern does not denote any clear trace of the vortex breakdown occurring over both sides of the wing. However, over the starboard side of the wing, the secondary separation line is seen to first turn outward towards the leading edge at about $x/c=0.75$, corresponding to the position of vortex breakdown. It turns inward again at about $x/c=0.85$ and forms a "whorl" pattern over the outboard tip of the wing. A similar pattern is observed to occur on the port side of the wing. This type of surface-flow pattern has been experimentally observed by Earnshaw and Lawford [72]. The computed skin-friction lines show good qualitative agreement with the surface oil flow photograph by Mitchell [45,7] in Fig. 26. In his wind-tunnel experiments of the same geometry, Mitchell observed a transition zone along the secondary separation line, from laminar to turbulent at about $x/c=0.3$, indicated by the secondary separation line turning outward towards the leading edge. This could not be observed in the present results, because the flow field is assumed to be fully turbulent.

Next, Figs. 27 to 29 depict cross-planes of longitudinal, transverse and normal velocity for time-averaged DES (left) and the experiment (right) at four distances along the root chord. Only the port half of the wing is shown here. Note that the experiment was not able to gather data very close to the surface, due to experimental limitations. At each crossplane station, the scale and color maps are consistent with the experiment. The geometry of the vortex is in good agreement with the experiment. Also the overall velocity field is well predicted by DES. However, the numerical simulation underestimates the maximum and minimum velocities in the core of the vortex. A finer grid is needed to better resolve this critical region of the flow.

13.6.2.3 Grid-Sensitivity Study

Finally, an assessment of grid refinement on the time-averaged DES results was made. The full-span grid described above was refined in the vortical flow region by increasing the number of grid points of the blocks above the wing by a factor of two in the i , j and k directions, respectively. These refined blocks were connected to the other unrefined blocks using a patched grid boundary condition. The grid was not mirrored for this preliminary grid sensitivity study. The resulting half-span patched grid has 188×140 points on the upper wing surface in the chordwise and spanwise directions, respectively, i.e. twice as many as the original grid. Figure 30 compares the surface pressure distribution at $x/c=0.32$ computed on the patched semi-span grid with that computed on the original, unrefined grid. The suction peak predicted on the refined grid is insignificantly higher than the one on the original grid. The comparison with the experimental data has not significantly improved. The longitudinal component of velocity u/U_∞ shown in Fig. 31 for the refined grid, on the other hand, compares better to the measured values in Fig. 27 than the results computed on the original grid. Especially the vortex core is better resolved on the refined grid. This may explain why the vortex breakdown locations computed on the refined grid are in significantly better agreement with the experimental data by Mitchell [7], falling within the range of uncertainty, compare triangle symbols in Fig. 23. Note that strongly reversed flow is predicted at $x/c=0.74$ on the refined grid, whereas stagnant flow is computed on the original grid, compare again Figs. 27 and 31. The reason for this is that vortex breakdown occurs upstream of that chordwise station on the refined grid, but just downstream on the original grid.

Mitchell *et al* [24], who studied a semi-span model of the same geometry using DES and adaptive mesh refinement, observed spatially stationary, co-rotating vortical substructures in the separated shear layer feeding the primary vortex in their solution. Such substructures were also observed experimentally [7]. No such substructures were observed in the present study, neither on the original nor the refined grid. This may be due to the fact that even the refined grid used here was less fine in the vortical flow region and was

not adapted to the solution.

13.6.2.4 Computational Efficiency

Typically, a considerable number of inner iterations have to be performed to reach the specified level of convergence. DES of the full-span model typically required around 55 inner iterations per outer time step. Clearly, dual time stepping is very expensive for this high Reynolds number, fully turbulent, three-dimensional flow problem.

Advances in more efficient algorithms for time-dependent analysis are thus urgently needed [81]. The implicit-explicit hybrid scheme developed by Hsu and Jameson [82] has shown great potential for substantially reducing the cost of unsteady flow simulations. Using a single alternating direction implicit (ADI)-backward difference formula (BDF) step followed by a small number of iterations (of the order of four or five) driving the solution towards the fully nonlinear BDF, they showed that second order accuracy can be obtained without the need to iterate to convergence at each real time step.

Another candidate for improving the commonly used dual time stepping is the Recursive Projection Method (RPM). RPM was initially developed by Schroff and Keller [83] for bifurcation analysis. RPM is a black-box method, which can be applied to any stationary iteration process. The method can be viewed as a compromise between Newton's Method and a fixed-point iteration scheme. It seeks to identify a small subspace responsible for the slowest convergence rate and applies a Newton-type method with a full matrix inversion on the projection of the problem on the small subspace. A fixed-point scheme is used on the complement of this subspace. Like this, RPM eliminates the influence of the dominant eigenvalues of the problem on the convergence by splitting the solution algorithm into two parts. The idea is to apply RPM to the inner loop of dual time stepping, where explicit or implicit time marching is used to solve a residual equation, much like a steady flow calculation, by iteration in every physical (outer) time step. RPM functions on top of the native flow solver inner iteration loop; all existing acceleration devices can be used without change.

Möller [84] has implemented RPM into NSMB for steady-state simulations, accelerating the convergence by a factor of up to four. More recently, RPM has been used with an unstructured CFD code, accelerating the convergence of the inner loop of dual time stepping by a factor of two for laminar time-dependent simulations of the flow around a circular cylinder at a Reynolds number of 100 [85] and by a factor of 2.5 for the turbulent time-dependent simulations of the transonic buffet flow around a biconvex airfoil [86].

13.7 VISUALIZATION USING FULLY-IMMERSIVE VIRTUAL REALITY

The computed unsteady flow field has also been visualized interactively in the Virtual-Reality (VR) environment of a six-sides CAVE, or Cube, demonstrating that the sheer sensual impact of the immersive display has a powerful effect on the physical intuition. The VR system and its setup are described in detail in [87]. Figure 32 shows an interactive visualization session inside the VR Cube. For this photograph, animation, head tracking and stereo viewing were switched off, making the display appear non-immersive (otherwise the photograph would be blurred due to the long exposure time). The delta wing and an instant in time of the corresponding unsteady flow field are projected mainly on the rear wall, together with color bars for the pressure coefficient and velocity magnitude. The flow field is visualized using a cutting plane colored by pressure coefficient, pathlines colored by velocity magnitude and pressure coefficient iso-lines on the wing's surface. Both the cutting plane and the pathlines are controlled interactively. In Fig. 33, the flow field is visualized using particles animated along pathlines. Both the pathlines and the particles are colored by velocity magnitude, where blue and red correspond to low and high velocity, respectively. Since the flow is pre-computed, it can be investigated at any length scale, and with control over time, for detailed analysis of long- and short-duration phenomena. Compared to cheaper "flat screen" visualization

methods, the benefit of visualizing the flow field inside the VR Cube is that one can "walk round" the delta wing and explore the surrounding flow. When wearing stereo glasses, the delta wing seems to "float" in the middle of the room. The sheer sensual impact of the immersive display has a powerful effect on the physical intuition.

13.8 CONCLUSIONS AND OUTLOOK

Time-accurate Euler and Detached-Eddy (DES) simulations of vortex breakdown over 70° *full-span* delta wings at 27°, 30° and 35° angle of attack and a Mach number of 0.2 have been performed. The unsteady, three-dimensional Euler and Navier-Stokes equations have been solved using second-order accurate Runge-Kutta and dual time stepping, respectively.

The unsteady Euler simulations capture the mutual interaction between the port and starboard vortices. This interaction is more intense at higher incidences. Spiral-type vortex breakdown has been observed to occur predominantly. The spiral breakdown structure shows good qualitative agreement with the spiral-type breakdown over delta wings observed in experiments. Spectral analysis of the temporal variation of the aerodynamic coefficients shows that high-frequency oscillations are due to the interaction of the spiral windings with the upper surface of the wing. Periodically, a transformation from spiral- to bubble-type breakdown occurs. It alternates between the port and starboard side. Its appearance is associated with a significant upstream movement of the breakdown location, resulting in asymmetry between the port and starboard breakdown locations. The breakdown location fluctuations and the asymmetry are responsible for low frequency oscillations of the aerodynamic coefficients.

A time-step study has been conducted for DES. It has demonstrated the demanding nature of vortex breakdown with a time-step size of the order 10^{-4} s required for time accuracy. Furthermore, a grid sensitivity study has been carried out. Patched grid refinement over the wing by a factor of two in all directions had little influence on the surface pressure distribution. However, the vortex core was better resolved on the refined grid, leading to a significantly better agreement between the computed and experimental breakdown location. These first results show that DES is capable of predicating the fluctuating vortex breakdown location quite accurately (with reservation for grid influences, which may be greater than viscosity effect). The surface pressure distribution, however, is underestimated (with reservation for blockage effects in the experiment).

In a next step, the solutions will be more thoroughly compared with experimental data, e.g. the variation of the port and starboard breakdown locations as a function of time. The transient data will be visualized in a "virtual-reality" environment to enhance the understanding of the spatial and temporal evolution of three-dimensional structures in the flow field, such as spiral and bubble-type breakdown, asymmetry, etc. For DES, I will use an improved Spalart-Allmaras turbulence model with production based on a comparison between vorticity and classical production instead of the standard model, which has been shown in several studies to add too much turbulent eddy viscosity to the vortex core. The simulation will be performed at the lower experimental Mach number of 0.07 to see if unsteady effects are magnified and if the breakdown location oscillations and asymmetry observed in the experiment at 27° angle of attack can be predicted. This will require the use of preconditioning. This work on DES is only beginning, and more needs to be done to draw firm conclusions, more grid refinement, e.g., by patched grid on a full-span model.

13.9 REFERENCES

- [1] Wentz, W. H. and Kohlman, D. L., "Vortex Breakdown on Slender Sharp-Edged Wings," *Journal of Aircraft*, Vol. 8, 1971, pp. 156–161.
- [2] Détery, J. M., "Aspects of Vortex Breakdown," *Prog. in Aerospace Sciences*, Vol. 30, 1994.
- [3] O'Neil, P., Roos, F., Kegelman, J., Barnett, R., and Hawk, J., "Investigation of Flow Characteristics of a Developed Vortex," Tech. Rep. NADC-89114-60, McDonell Aircraft Company, May 1989.
- [4] Wentz, W. H., "Vortex-Fin Interaction on a Fighter Aircraft," *AIAA Paper 87-2474*, 1987.
- [5] Dhah, G. H., Grafton, S. B., Guynn, M. D., Branson, J. M., Dansberry, B. E., and Patel, S. R., "Effect of Vortex Flow Characteristics on Tail Buffet and High Angle-of-Attack Aerodynamics of a Twin-Tail Fighter Configuration," *Proceedings of the High-Angle-of-Attack Technology Conference*, NASA LARC, Hampton, VA, November 1990.
- [6] Rizzi, A. and Purcell, C. J., "On the computation of transonic leading-edge vortices using the Euler equations," *Journal of Fluid Mechanics*, Vol. 181, 1987, pp. 163–195.
- [7] Mitchell, A. M., *Caractérisation et contrôle de l'éclatement tourbillonnaire sur une aile delta aux hautes incidences*, Ph.D. thesis, Université Paris VI, Paris, France, July 2000.
- [8] Eriksson, L.-E. and Rizzi, A., "Computations of Vortex Flow around Wings using the Euler Equations," *Notes on Numerical Fluid Mechanics*, Vol. 5, 1982, pp. 87–105.
- [9] Rizzi, A. and Mü, B., "Comparison of Euler and Navier-Stokes solutions for vortex flow over a delta wing," *The Aeronautical Journal of the Royal Aeronautical Society*, April 1988.
- [10] Fujii, K. and Schiff, L. B., "Numerical Simulations of Vortical Flows over a Strake-Delta Wing," *AIAA Journal*, Vol. 27, No. 9, 1989, pp. 1153–1162.
- [11] Ekaterinaris, J. A. and Schiff, L. B., "Numerical Simulation of the Effects of Variation of Angle of Attack and Sweep Angle on Vortex Breakdown over Delta Wings," *AIAA Paper 90-3000CP*, 1990.
- [12] Ekaterinaris, J. A. and Schiff, L. B., "Vortical Flows over Delta Wings and Numerical Prediction of Vortex Breakdown," *AIAA Paper 90-0102*, 1990.
- [13] Sirbaugh, J. R., "Euler Analysis of the AFWAL 65° Delta Wing," *AIAA Paper 87-2272*, 1987.
- [14] Agrawal, S., Robinson, B. A., and Barnett, R. M., *Prediction of Vortex Breakdown on a Delta Wing*, 5th Symp. on Numerical and Physical Aspects of Aerodynamic Flows, Calif. State University, 1993.
- [15] Strohmeier, D., Orłowski, M., Longo, J. M. A., Hummel, D., and Bergmann, A., "An Analysis of Vortex Breakdown Predicted by the Euler Equations," *ICAS Paper 1996-1.6.3*, 1996.
- [16] Gordnier, R. E. and Visbal, M. R., "Unsteady Vortex Structure over a Delta Wing," *Journal of Aircraft*, Vol. 31, No. 1, Jan.-Feb. 1994.
- [17] Visbal, M. R., "Numerical Simulation of Spiral Vortex Breakdown Above a Delta Wing," *AIAA Paper 95-2309*, 1995.

- [18] Visbal, M. R., "Computed Unsteady Structure of Spiral Vortex Breakdown on Delta Wings," *AIAA Paper 96-2074*, 1996.
- [19] Müller, J. and Hummel, D., *An analysis of vortex breakdown predicted by a time-accurate Euler code*, Notes on Numerical Fluid Mechanics, Vieweg Verlag, Braunschweig, 1999, pp. 331–338.
- [20] Müller, J. and Hummel, D., "Numerical Analysis of the Unsteady Flow above a Slender Delta Wing at Large Angles of Attack," *ICAS Paper 2000-252*, 2000.
- [21] Müller, J. and Hummel, D., "Time-accurate CFD analysis of the unsteady flow on a fixed delta wing," *AIAA Paper 2000-0138*, 2000.
- [22] Morton, S. A., Forsythe, J. R., Mitchell, A., and Hajek, D., "DES and RANS Simulations of Delta Wing Vortical Flows," *AIAA Paper 2002-0587*, 2002.
- [23] Morton, S. A., Forsythe, J. R., Squires, K. D., and Wurtzler, K. E., "Assessment of Unstructured Grids for Detached-Eddy Simulation of High Reynolds Number Separated Flows," *Proceedings of the 8th International Conference on Grid Generation in Computational Field Simulations*, June 2002.
- [24] Mitchell, A., Morton, S. A., and Forsythe, J. R., "Analysis of Delta Wing Vortical Substructures using Detached-Eddy Simulation," *AIAA Paper 2002-2968*, 2002.
- [25] Gordnier, R. E., "Numerical Simulation of a 65-Degree Delta Wing Flowfield," *Journal of Aircraft*, Vol. 34, No. 4, 1997, pp. 492–499.
- [26] Estorf, M. and Hummel, D., "Euler and Navier-Stokes Simulations for Vortex Breakdown on a Delta Wing," *unpublished report, Technische Universität Braunschweig, Germany*, 2002.
- [27] Gordnier, R. E., "Computations of Delta-Wing Roll Maneuvers," *AIAA Paper 93-2975*, 1993.
- [28] Chaderjian, N. M. and Schiff, L. B., "Navier-Stokes Predictions of Delta Wing in Roll with Vortex Breakdown," *AIAA Paper 93-3495*, 1993.
- [29] Görtz, S., *Computational Study of Vortex Breakdown over 70° Swept Delta Wings*, Master's thesis, Royal Inst. of Techn. (KTH), Dept. of Aeronautics, Stockholm, Sweden, Oct. 1998, Skrift 98-27.
- [30] Görtz, S., Rizzi, A., and Munukka, K., "Computational Study of Vortex Breakdown over Swept Delta Wings," *AIAA Paper 99-3118*, 1999.
- [31] Görtz, S. and Rizzi, A., "Computing the High-Alpha Aerodynamics Delta Wings - Evaluation and Analysis," *AIAA Paper 01-0115*, 2001.
- [32] Werlé, H., "Quelques résultats expérimentaux sur les ailes en flèches, aux faibles vitesses, obtenus en tunnel hydrodynamique," *La Recherche Aéronautique* 41, 1954.
- [33] Peckham, D. H. and Atkinson, S. A., "Preliminary Results of Low Speed Wind Tunnel Tests on a Gothic Wing of Aspect Ratio 1.0," Report CP-508, Aeronautical Research Council, 1957.
- [34] Elle, B. J., "An investigation at low speed of the flow near the apex of thin delta wings with sharp leading edges," Reports and Memoranda 3176, Aeronautical Research Council, January 1958.
- [35] Lambourne, N. C. and Bryer, D. W., "The Bursting of Leading-Edge Vortices - Some Observations

- and Discussions of the Phenomenon,” R&M 3282, Aeronautical Research Council, 1962.
- [36] Rom, J., *High Angle of Attack Aerodynamics*, Springer Verlag, New York, 1992.
- [37] Werlé, H., “Sur l’écatement des tourbillons,” ONERA Note Technique No. 175, 1971.
- [38] Payne, F. M., Ng, T. T., and Nelson, R. C., “Visualizaition and Flow Surveys of the Leading Edge Vortex Structure on Delta Wing Planforms,” *AIAA Paper 86-0303*, 1986.
- [39] Payne, F. M., Ng, T. T., and Nelson, R. C., “Experimental Study of the Velocity Field on a Delta Wing,” *AIAA Paper 87-1231*, June 1987.
- [40] Nelson, R. C., “Unsteady Aerodynamics of Slender Wings,” AGARD R-776, Aircraft Dynamics at High Angles of Attack: Experiments and Modeling, 1991.
- [41] Gursul, I. and Yang, H., “On fluctuations of vortex breakdown location,” *Physics of Fluids*, Vol. 7, No. 1, January 1995, pp. 229–231.
- [42] Menke, M., Yang, H., and Gursul, I., “Further Experiments on Fluctuations of Vortex Breakdown Location,” *AIAA Paper 96-0205*, 1996.
- [43] Menke, M. and Gursul, I., “Self-Excited Oscillations of Vortex Breakdown Location over Delta Wings,” *AIAA Paper 97-0744*, 1997.
- [44] Menke, M., Yang, H., and Gursul, I., “Experiments on the unsteady nature of vortex breakdown,” *Experiments in Fluids*, Vol. 27, 1999, pp. 262–272.
- [45] Mitchell, A. M., Barberis, D., and Détery, J., “Oscillation of Vortex Breakdown Location and Its control by Tangential Blowing,” *AIAA Paper 98-2914*, 1998.
- [46] Jun, Y.-W. and Nelson, R. C., “Leading-Edge Vortex Dynamics on a Slender Oscillating Wing,” *Journal of Aircraft*, Vol. 25, No. 9, September 1988, pp. 815–819.
- [47] Vos, J. B., Rizzi, A., Corjon, A., Chaput, E., and Soinne, E., “Recent Advances in Aerodynamics inside the NSMB (Navier-Stokes Multi Block) Consortium,” *AIAA Paper 98-0225*, 1998.
- [48] Gacherieu, C., Weber, C., and Coriolis, G., “Assessment of Algebraic and One-Equation Turbulence Models for the Transonic Turbulent Flow around a Full Aircraft Configuration,” *AIAA Paper 98-2737*, 1998.
- [49] Weber, C. et al., “Recent Applications in Aerodynamics with NSMB Structured MultiBlock Solver,” in *Frontiers of Computational Fluid Dynamics*, World Scientific Publishing 1998.
- [50] Darracq, D., Champagneux, S., and Corjon, A., “Computation of Unsteady Turbulent Airfoil Flows with an Aeroelastic AUSM+ Implicit Solver,” *AIAA Paper 98-2411*, 1998.
- [51] Bohbot, J., Bertin, D., and Darraq, D., “A Conservative Patched Grid Algorithm for Turbulent Flow Computations of 3D Complex Aircraft Configurations,” *European Congress on Computational Methods in Applied Sciences and Engineering, ECCOMAS 2000*, 2000.
- [52] Vos, J. B., Leyland, P., van Kemenade, V., Gacherieu, C., Duquesne, N., Lötstedt, P., Weber, C., Ytterström, A., and Saint Requier, C., *NSMB Handbook 4.5*, March 2000.

- [53] Vos, J. B., Bohbot, J., Champagneux, S., and others, *NSMB 5.5 User Guide*, June 2002.
- [54] Jameson, A., "Time dependent calculations using multigrid, with application to unsteady flows past airfoils and wings," *AIAA Paper 91-1596*, 1991.
- [55] Spalart, P. R., Jou, W.-H., Strelets, M., and Allmaras, S. R., "Comments on the Feasibility of LES for Wings, and on a Hybrid RANS/LES Approach," *Advances in DNS/LES, 1st AFOSR Int. Conf. on DNS/LES*, August 1997.
- [56] Spalart, P. R. and Allmaras, S. R., "A One-Equation Turbulence Model for Aerodynamic Flows," *AIAA Paper 92-0439*, 1992.
- [57] Caruelle, B., *Simulation d'Ecoulement Instationnaires Turbulent en Aérodynamique: Application à la Prédiction du Phénomène de Tremblement*, Ph.D. thesis, Institut National Polytechnique de Toulouse, Toulouse, France, October 2000.
- [58] Strelets, M., "Detached Eddy Simulation of Massively Separated Flows," *AIAA Paper 2001-0879*, 2001.
- [59] Forsythe, J. R., Squires, K. D., Wurtler, K. E., and Spallart, P. R., "Detached-Eddy Simulation of Fighter Aircraft at High Alpha," *AIAA Paper 2002-0591*, 2002.
- [60] Squire, K. D., Forsythe, J. R., Morton, S. A., Strang, W. Z., Wurtzler, K. E., Tomaro, R. F., Grismer, M. J., and Spalart, P. R., "Progress on Detached-Eddy Simulation of Massively Separated Flows," *AIAA Paper 2002-1021*, 2002.
- [61] Squires, K. D., Forsythe, J. R., Morton, S. A., Blake, D. C., Serrano, M., Wurtzler, K. E., Strand, W. Z., Tomaro, R. F., and Spalart, P. R., "Analysis of Full Aircraft with Massive Separation using Detached-Eddy Simulation," *High Performance Computing Users Group Conference*, 2002.
- [62] Spalart, P. R. and Shur, M. L., "On the Sensitization of Turbulence Models to Rotation and Curvature," *Aerospace Science and Technology*, 1997.
- [63] Swanson, R. C. and Turkel, E., "Multistage Schemes With Multigrid for Euler and Navier-Stokes Equations," *NASA Technical Paper 3631*, 1997.
- [64] Rizzi, A., Eliasson, P., and others, "The Engineering of Multiblock/Multigrid Software for Navier-Stokes Flows on Structured Meshes," *Computers and Fluids*, Vol. 22, No. 2/3, 1993, pp. 341–367.
- [65] Jameson, A., *Transonic Flow Calculations for Aircraft*, in *Lectures Notes in Mathematics*; 1127, Springer Verlag, 1985, pp. 156–242.
- [66] van der Houwen, P. J. and Jacobus, P., *Construction of Integrations Formulas for Initial Value Problems*, North-Holland Publ. Co., 1977.
- [67] Lane, D. A., "Visualizing Time-Varying Phenomena in Numerical Simulations of Unsteady Flows," *AIAA Paper 96-0048*, 1996.
- [68] Gursul, I., "Unsteady Flow Phenomena over Delta Wings at High Angle of Attack," *AIAA Journal*, Vol. 32, No. 2, February 1994, pp. 225–231.
- [69] Lowson, M. V., "Some Experiments with Vortex Breakdown," *Journal of the Royal Aeronautical*

Society, Vol. 68, May 1964, pp. 343–346.

- [70] Payne, F. M., Ng, T. T., Nelson, R. C., and Schiff, L. B., “Visualization and Wake Surveys of Vortical Flow over a Delta Wing,” *AIAA Journal*, Vol. 26, No. 2, 1988, pp. 137–143.
- [71] Greenwell, D. I., “Pitfalls in the Interpretation of Delta Wing Flow Visualization,” *NATO RTO Symposium on Advanced Flow Management*, May 7-11 2001, Loen, Norway.
- [72] Earnshaw, P. B. and Lawford, J. A., “Low Speed Wind Tunnel Experiments on a Series of Sharp-edged Delta Wings,” R & M 3424, Aeronautical Research Council, August 1964.
- [73] Gursul, I., University of Bath, private communications, October 2002.
- [74] Petterson, K., *The Aerodynamics of Slender Aircraft Forebodies at High Angle of Attack*, Ph.D. thesis, Cranfield University, College of Aeronautics, April 2001.
- [75] Casey, M. and Wintergerste, T., “Best Practice Guidelines,” ERCOFTAC Special Interest Group on “Quality and Trust in Industrial CFD”, January 2000.
- [76] Weber, C., *Développement de méthode implicite pour les équations de Navier-Stokes moyennées et la simulation des grandes échelles: Application à l’aérodynamique externe*, Ph.D. thesis, CERFACS, Toulouse, France, 1998.
- [77] Martinelli, L., Princeton University, private communications, September 2002.
- [78] Wang, D., Wallin, S., Berggren, M. and Eliasson, P., “A Computational Study of Unsteady Turbulent Buffet Aerodynamics,” *AIAA Paper 2000-2657*, 2000.
- [79] Spalart, P. R., “Young-Person’s Guide to Detached-Eddy Simulation Grids,” CR 2001-211032, NASA, 2001.
- [80] Le Moigne, Y., *CFD Simulations of a Delta Wing Pitching to High Alpha*, Licentiate thesis, Royal Inst. of Techn. (KTH), Dept. of Aeronautics, Stockholm, Sweden, Report 2002-7, February 2002.
- [81] Raj, P., “Aircraft Design in the 21st Century: Implications for Design Methods,” *AIAA Paper 98-2895*, 1998.
- [82] Hsu, J. M. and Jameson, A., “An Implicit-Explicit Hybrid Scheme for Calculating Complex Unsteady Flows,” *AIAA Paper 2002-0714*, 2002.
- [83] Schroff, G. and Keller, B., “Stabilization of Unstable Procedures: The Recursive Projection Method,” *SIAM J. Numer. Anal.*, Vol. 30, No. 4, pp. 1099-1120, August 1993.
- [84] Möller, J., *Studies of Recursive Projection Methods for Convergence Acceleration of Ateady State Calculations*, Licentiate Thesis, Royal Institute of Technology (KTH), Dept. of Numerical Analysis, Stockholm, Sweden, TRITA-NA-0119, 2001.
- [85] Görtz, S. and Möller, J., “Recursive Projection Method for Efficient Unsteady CFD Simulations,” in *Proceedings of the European Congress on Computational Methods in Applied Sciences and Engineering* (ECCOMAS 2004), 2004.
- [86] Görtz, S. and Möller, J., “Evaluations of the Recursive Projection Method for Efficient Turbulent Unsteady CFD Simulations,” in *Proceedings of the International Council of the Aeronautical*

Sciences, ICAS Paper 2004-2.1.1, 2004.

- [87] Görtz, S., and Sundström, E., "Virtual-Reality Environment for Visualization of Unsteady Three-Dimensional CFD Data," in *Proceedings of the European Congress on Computational Methods in Applied Sciences and Engineering* (ECCOMAS 2004), July, 2004.

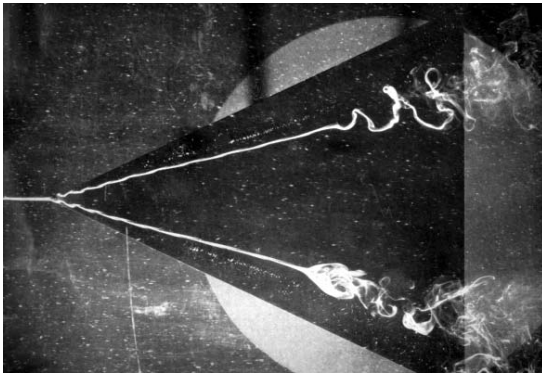


Figure 1: Water-tunnel visualization of spiral (top) and bubble-type (bottom) vortex breakdown [35]

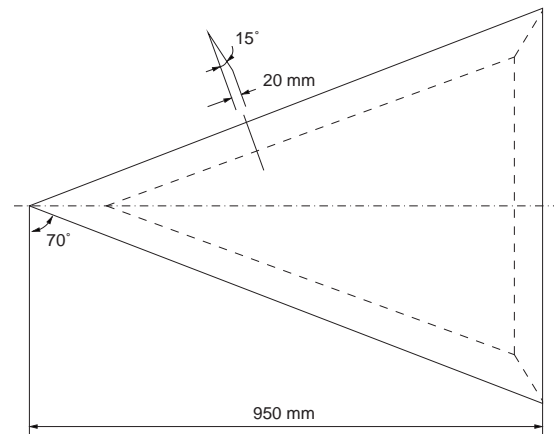


Figure 4: Geometry of full-span delta wing model with sharp trailing edge

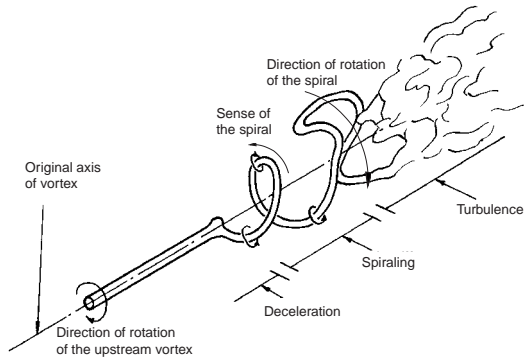


Figure 2: Spiral breakdown: stages in behavior of axial filament and sense of the spiral [35]

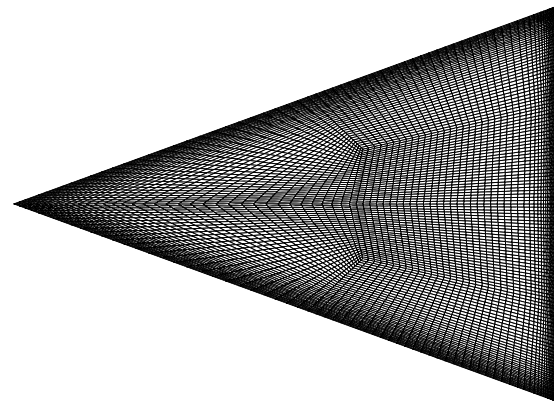


Figure 5: Full-span HCH grid: planform view

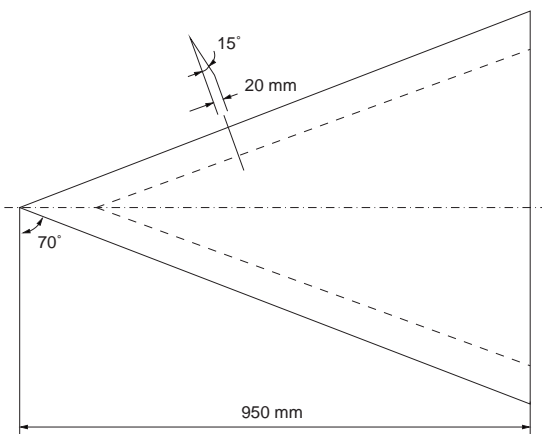


Figure 3: Geometry of full-span delta wing model [7] with cut-off trailing edge

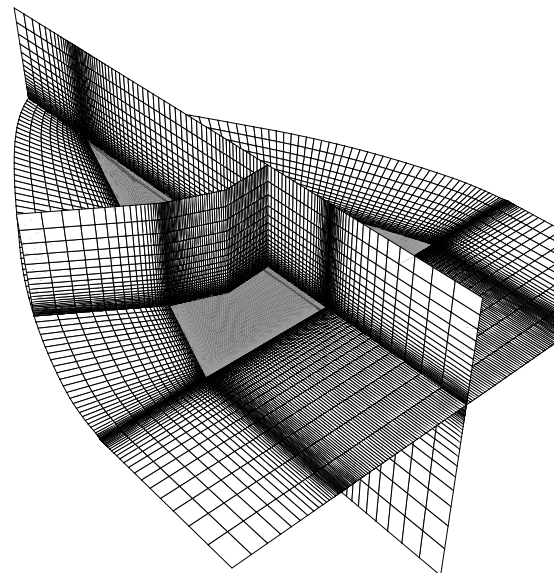


Figure 6: Full-span HCH grid: sectional 3D-view

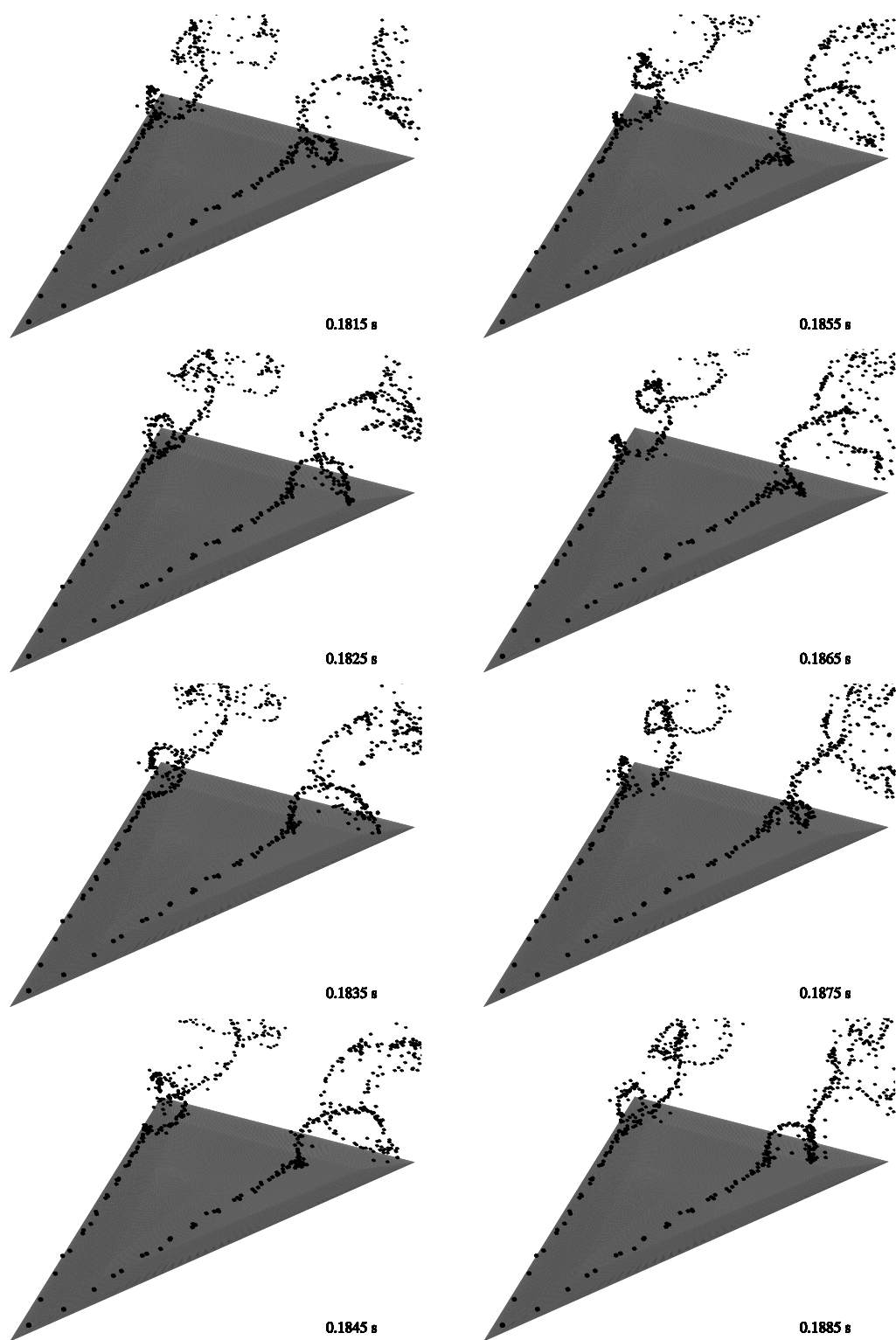


Figure 7: Time-dependent particles at different instances in time ($M_\infty=0.2$, $\alpha=30^\circ$, Euler)

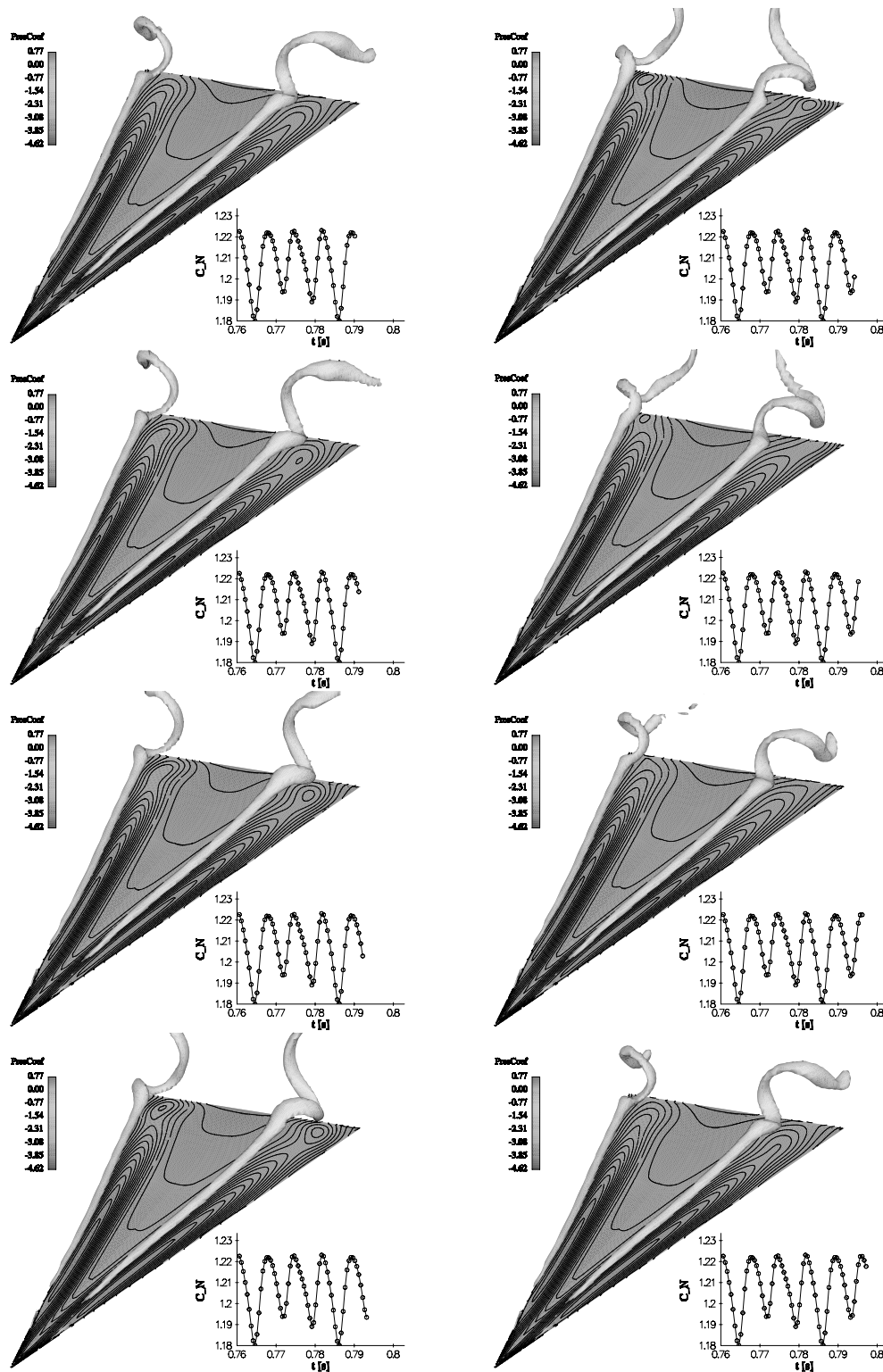


Figure 8: Contours of surface pressure coefficient and entropy iso-surface showing spiral-type vortex breakdown/surface interaction ($M_\infty=0.2$, $\alpha=27^\circ$, Euler)

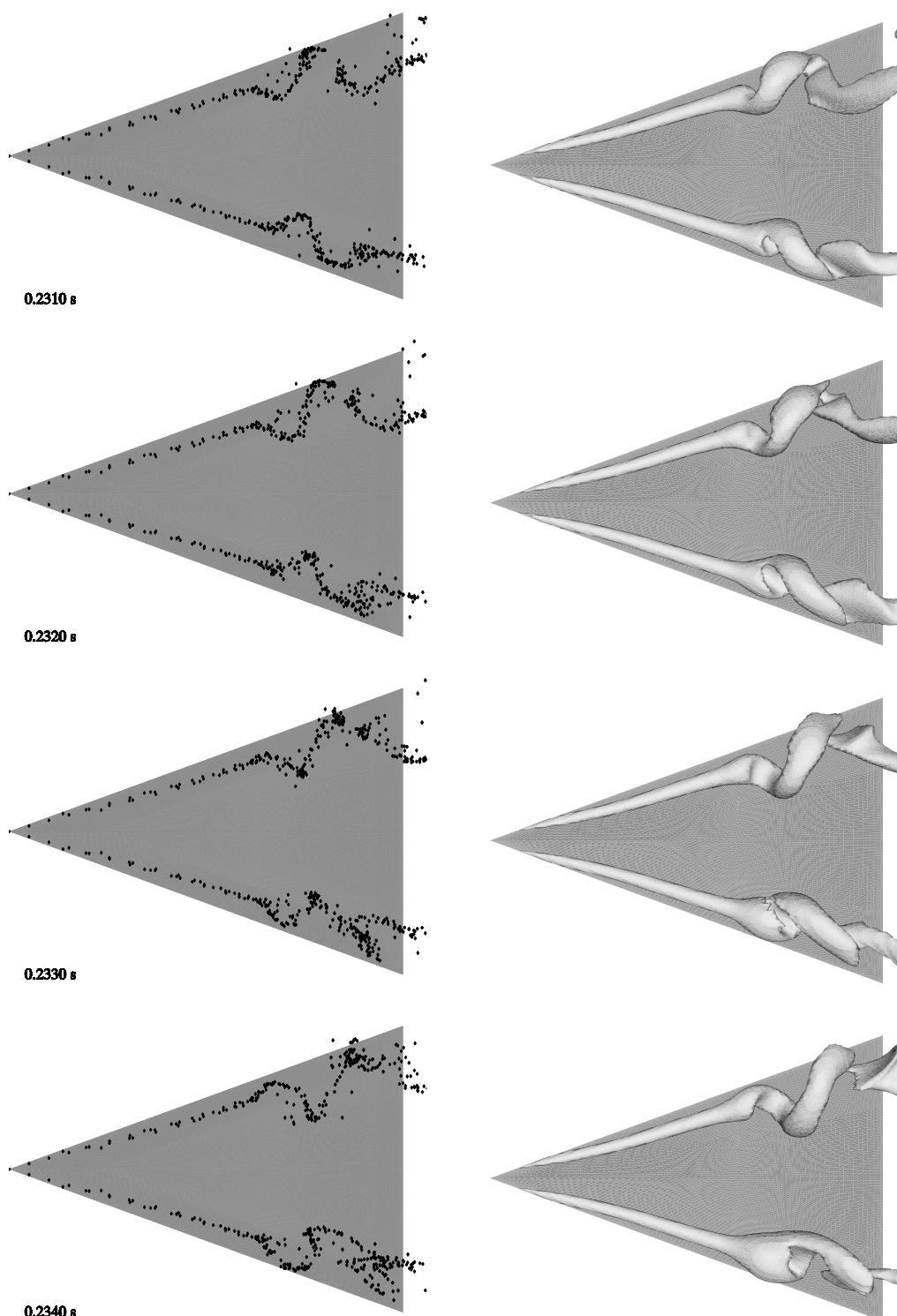


Figure 9: Time sequence of images showing the evolution from spiral to intermittent bubble-type breakdown: instantaneous particles (left) and iso-surface of entropy (right) ($M_\infty=0.2$, $\alpha=30^\circ$, Euler)

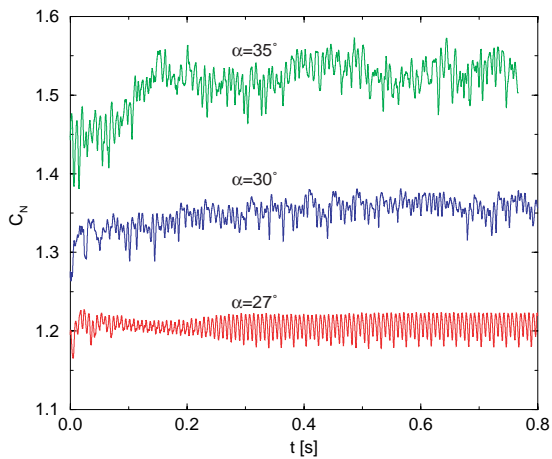


Figure 10: Normal-force coefficient time history ($M_\infty=0.2$, Euler)

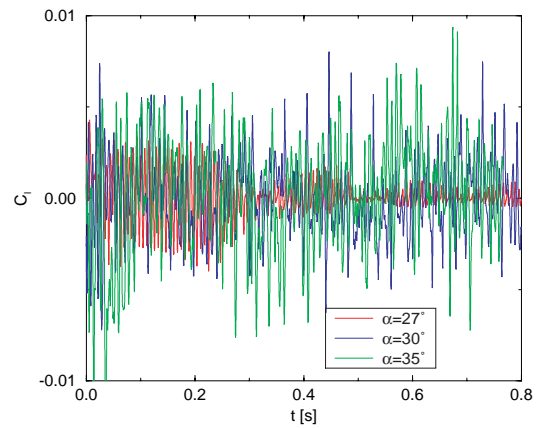


Figure 12: Rolling-moment coefficient time history ($M_\infty=0.2$, Euler)

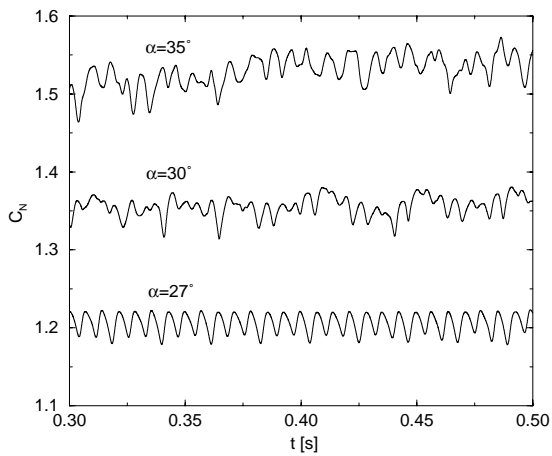


Figure 11: Detailed view of normal-force coefficient time history ($M_\infty=0.2$, Euler)

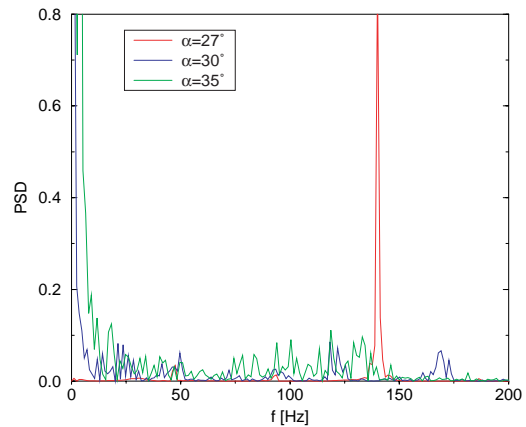


Figure 13: Power Spectral Density of C_N as a function of frequency ($M_\infty=0.2$, Euler)

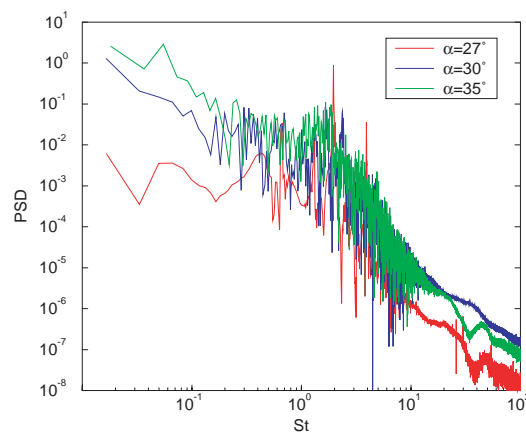


Figure 14: Power Spectral Density of C_N as a function of the Strouhal number ($M_\infty=0.2$, Euler)

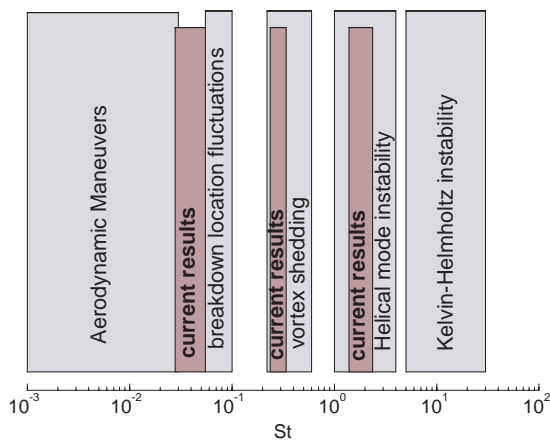


Figure 15: Strouhal numbers of current data (Euler) superimposed on experimental data [42,44]

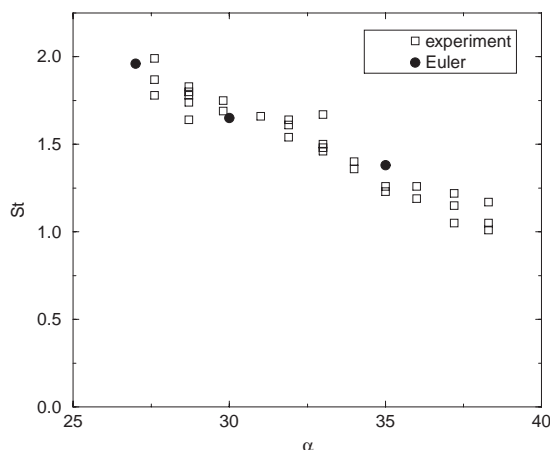


Figure 16: Comparison between computed and experiential [68] Strouhal number as function of α

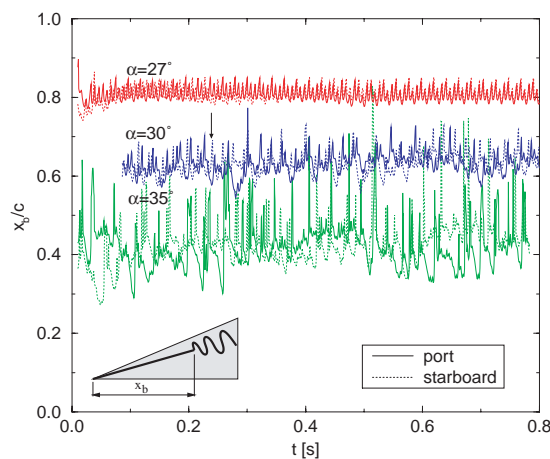


Figure 17: Time history of computed vortex breakdown locations ($M_\infty=0.2$, Euler)

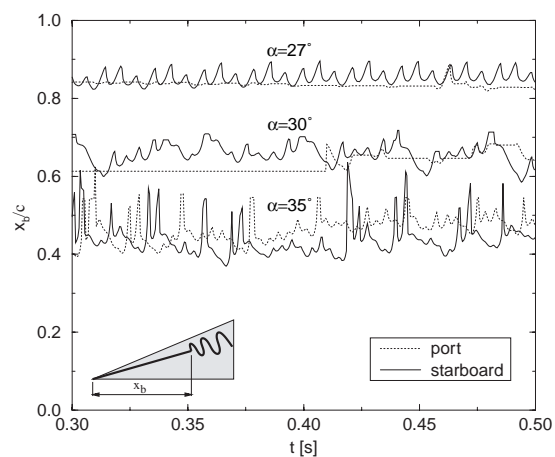


Figure 18: Time history of computed vortex breakdown locations ($M_\infty=0.2$, Euler)

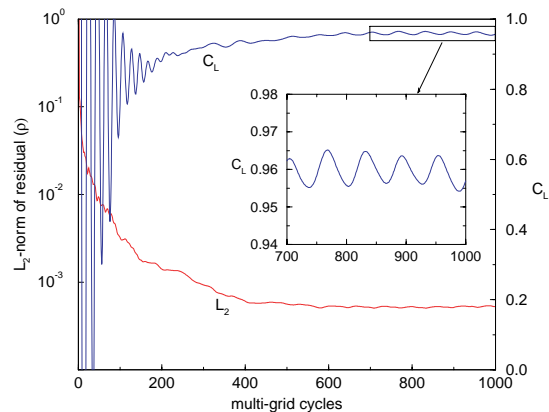


Figure 19: Conv. history of residual and lift coeff. ($M_\infty=0.2$, $Re=1.56 \times 10^6$, $\alpha=27^\circ$, S-A turbulence model, steady-state calculation, semi-span model)

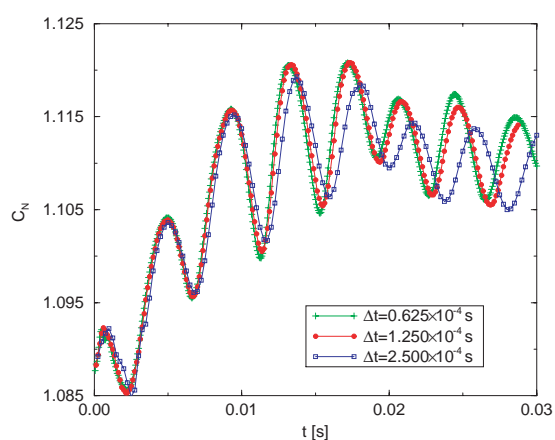


Figure 20: C_N time history, diff. time steps ($M_\infty=0.2$, $Re=1.56 \times 10^6$, $\alpha=27^\circ$, DES, semi-span model)

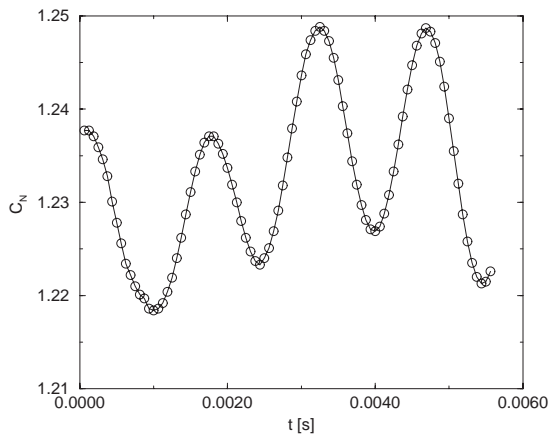


Figure 21: Normal-force coefficient time history
($M_\infty=0.2$, $Re=1.56 \times 10^6$, $\alpha=27^\circ$, DES)

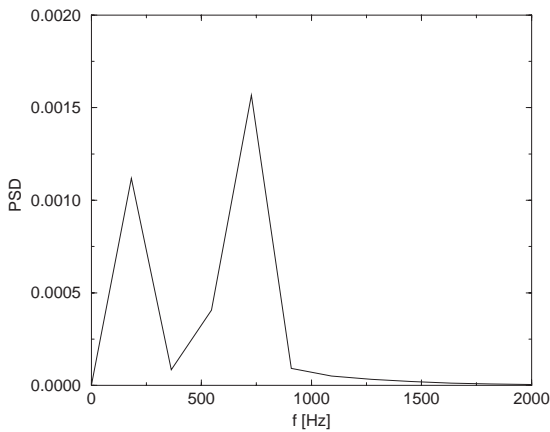


Figure 22: Power Spectral Density of C_N as function of f ($M_\infty=0.2$, $Re=1.56 \times 10^6$, $\alpha=27^\circ$, DES)

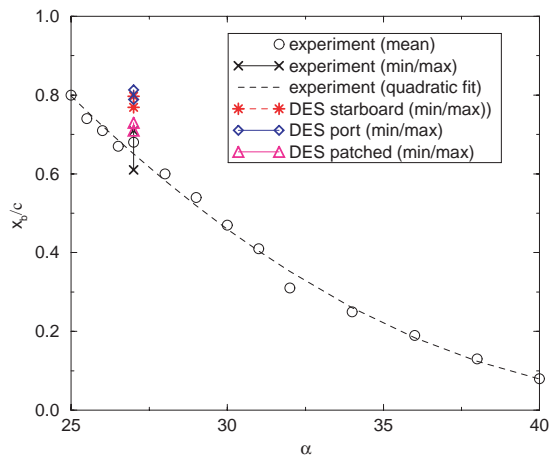


Figure 23: Computed vortex breakdown locations compared to experimental data [7]
($M_{\infty,exp}=0.07$, $M_{\infty,CFD}=0.2$, $Re=1.56 \times 10^6$)

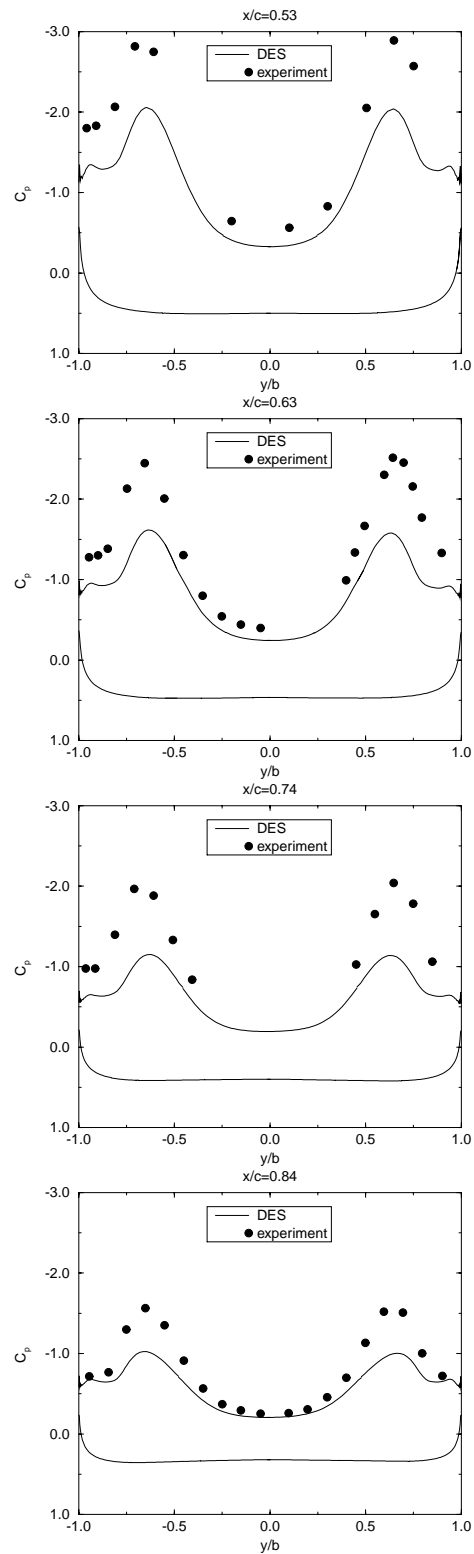


Figure 24: Computed C_p compared to exp. data [7]
($M_\infty=0.2$, $Re=1.56 \times 10^6$, $\alpha=27^\circ$, DES)

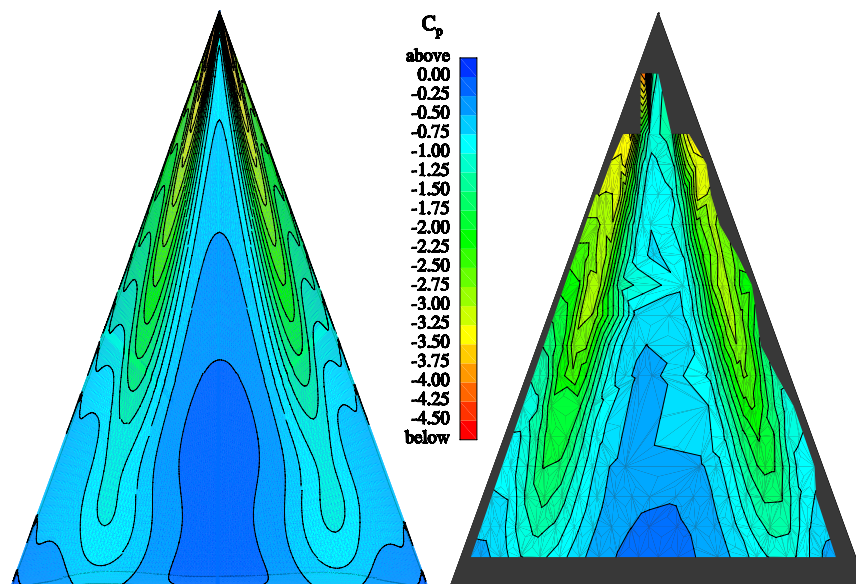


Figure 25: Computed (left) and measured [7] (right) upper-surface pressure distribution compared ($M_{\infty,CFD}=0.2$, $M_{\infty,exp}=0.07$, $Re=1.56 \times 10^6$, $\alpha=27^\circ$)

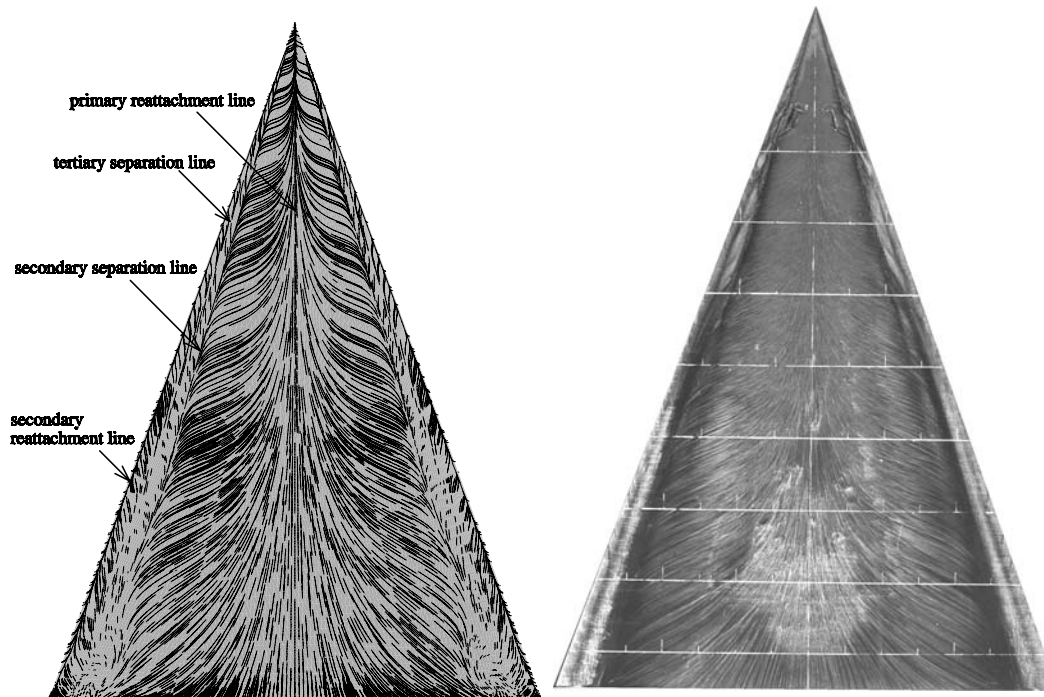


Figure 26: Computed skin-friction lines (left) and surface oil flow photograph (right) [7] ($M_{\infty,CFD}=0.2$, $M_{\infty,exp}=0.07$, $Re=1.56 \times 10^6$, $\alpha=27^\circ$)

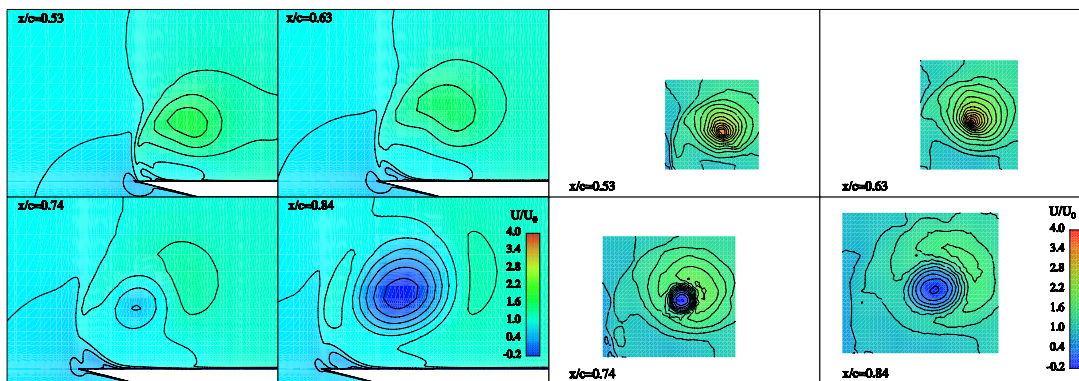


Figure 27: Computed (left) and measured (right) longitudinal component of velocity in various crossplanes ($M_{\infty,CFD}=0.2$, $M_{\infty,exp}=0.07$, $Re=1.56 \times 10^6$, $\alpha=27^\circ$)

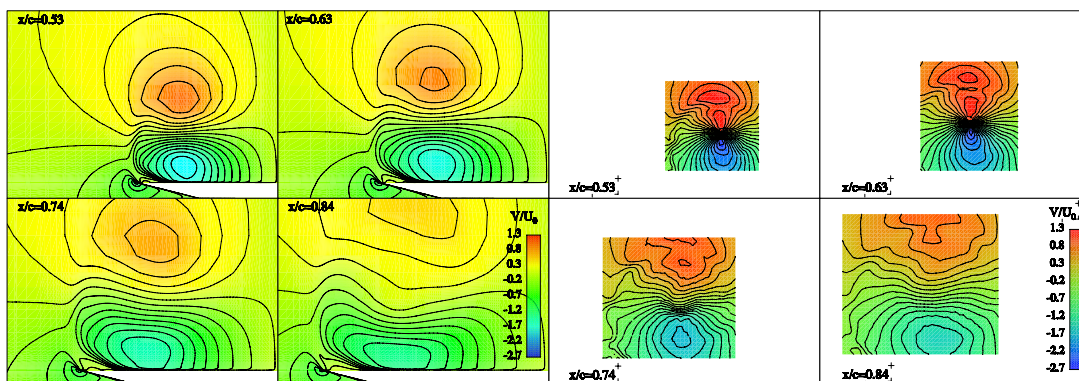


Figure 28: Computed (left) and measured (right) transverse component of velocity in various crossplanes ($M_{\infty,CFD}=0.2$, $M_{\infty,exp}=0.07$, $Re=1.56 \times 10^6$, $\alpha=27^\circ$)

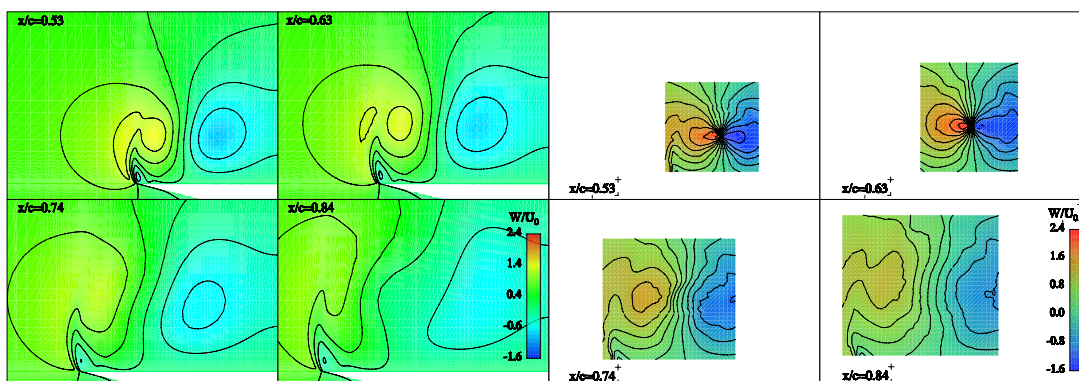


Figure 29: Computed (left) and measured (right) normal component of velocity in various crossplanes ($M_{\infty,CFD}=0.2$, $M_{\infty,exp}=0.07$, $Re=1.56 \times 10^6$, $\alpha=27^\circ$)

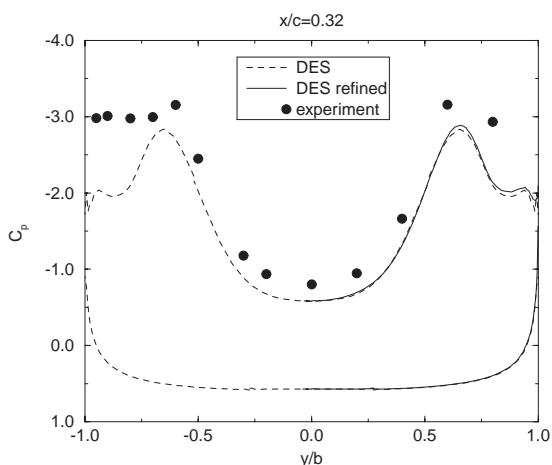


Figure 30: Influence of grid refinement on surface pressure distr. ($M_\infty=0.2$, $Re=1.56 \times 10^6$, $\alpha=27^\circ$, DES)

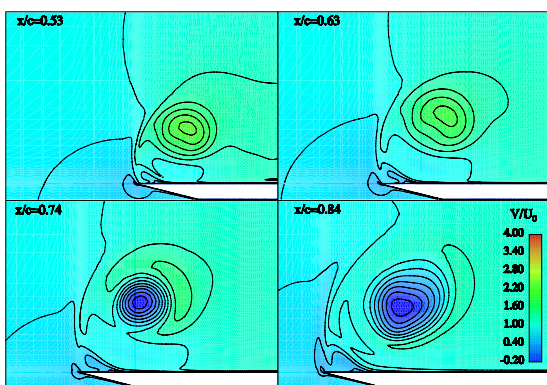


Figure 31: Influence of grid refinement on longitudinal velocity component ($M_\infty=0.2$, $Re=1.56 \times 10^6$, $\alpha=27^\circ$, DES)



Figure 32: Time-dependant flow over delta wing visualized in virtual-reality environment (animation, head tracking and stereo viewing switched off)



Figure 33: Time-dependant flow visualized in virtual-reality environment (animation, head tracking and stereo viewing switched off)

Appendix – Video Files

*There were four video files prepared for this Chapter –
Click on the links below to view the videos*

VR-Cube Video

DES Video

HHC Video

Time Accurate Euler Video

Chapter 14 – GRID STUDY FOR EULER SIMULATIONS OF A 70° DELTA WING WITH THE UNSTRUCTURED FLOW SOLVER EDGE

Yann Le Moigne¹ and Arthur Rizzi

Royal Institute of Technology (KTH) Aeronautical and Vehicle Engineering
100 44 Stockholm, Sweden

lemoigne@kth.se

ABSTRACT

Inviscid steady-state CFD simulations of a 70°-swept delta wing with sharp edges at high angle of attack where vortex breakdown is present above the wing are presented. Emphasis is put on the generation of unstructured numerical grids and in particular, the effect that the mesh has on the results. A mesh refinement study is made as well as an assessment of the effect of refining the vortical wake. Finally, an analysis of the wind tunnel walls interference is described by comparing results for the wing in free air, the wing in the wind tunnel and the wing in corrected free air conditions. To get the corrected free air conditions an analytical correction method for upflow around delta wings in wind tunnel is used. All the comparisons are made with experimental data by looking at the pressure distribution on the leeward surface of the wing and the longitudinal position of vortex breakdown. These comparisons reveal that a fine mesh is required to get satisfactory results and that the wake should be refined close to the trailing edge of the wing in order to improve the results. The presence of the wind tunnel walls in the simulation also greatly improves the quality of the results while simply correcting the results for the wind tunnel influence by a modified angle of attack does not prove sufficient.

NOMENCLATURE

C wind tunnel cross sectional area

c_R wing root chord

H wind tunnel height

ICP Interference Correction Parameter: $\left(\frac{S}{C}\right)\left(\frac{H}{2W}\right)$

S wing planform area

U_∞ free stream velocity

W half-width of wind tunnel

w_{TOT} total average upwash induced over the wing by the image system

x_{VB} vortex breakdown streamwise location

α angle of attack

$\Delta\alpha$ average upwash correction due to tunnel walls

ε wing apex half angle

μ defined in equation (2) as $\frac{c_R \tan \varepsilon}{2W}$

¹ Corresponding author

14.1 INTRODUCTION

This study is related to the one presented in an earlier chapter by S. Görtz, “Unsteady CFD Simulations of Full-Span ONERA 70° Delta Wing”. For information on the background and the work previously done in this field, both experimentally and numerically, the reader is referred to that chapter.

The present study is part of an attempt to simulate the flow around a 70°-swept delta wing in order to assess the current state of the art of CFD to reproduce or predict results obtained in wind tunnels for this kind of vortical flow. The main focus of this study is on mesh quality and mesh refinement in the vortex region for steady-state inviscid simulations on unstructured grids.

After the presentation of the CFD solver used and the general layout of the grids generated, a first general mesh refinement study is presented. It is followed by the analysis of the influence of the refinement of the wake and finally, the effect of the wind tunnel walls is assessed by comparison with results of the free air configuration.

14.2 COMPUTATIONAL METHOD

The unstructured flow solver used in this part is called EDGE [1]. It has been developed at the Swedish Defence Research Agency, FOI (formerly named FFA). EDGE solves the Reynolds Average Navier-Stokes compressible flow equations on unstructured grids of arbitrary shaped elements. The solver is based on an edge-based formulation and uses a node-centred finite volume technique to solve the governing equations. The equations are integrated explicitly towards steady state with Runge-Kutta time integration. Several convergence acceleration techniques are available like agglomeration multigrid, implicit residual smoothing and low speed preconditioning. Several turbulence models like the $k-\omega$ model and the EARSM model of Wallin and Johansson [2] are implemented in EDGE.

All the results presented here were obtained with the parallel version of EDGE implemented with the MPI library. The code was run on 4 IBM SP PPC 604e nodes containing each four processors running at 332 MHz that share 1Gbyte of memory. The peak performance of such four nodes is 10.6 GFlop/s. Typical wall clock computing time for the calculations presented below is six hours to get a residual decreased by five orders of magnitude.

All the grids generated and presented below were made using the Tetra module of the mesh generator ICEM CFD. ICEM was run on an SGI Octane with one R10000 processor and 640Mb of main memory. The rather old processor and limited amount of memory made the mesh generation and smoothing very long processes often reaching the limit of the memory leading to swapping with the disk.

All the computations presented in this chapter are inviscid simulations obtained with the unstructured flow solver EDGE. The wing is simulated with an angle of attack of 27° in order to match Mitchell’s data [3] for the wind tunnel tests without blowing. However, Mitchell’s wind tunnel free stream velocity of 24m/s is not matched: it would imply simulations at a Mach number of 0.07, which could lead to convergence problems with the compressible flow solver run without preconditioning; in order to avoid the possible influence of preconditioning on the results, the free stream Mach number is arbitrary increased to 0.2. All the results presented below were obtained after convergence of 5.5 orders of the residual for the density. This level of convergence is typically reached after 2000 multigrid iterations on the finest grid level (4 multigrid levels in a W-cycle were used with a full multigrid capability (the solution is first converged on the coarser grid level for 500 multigrid iterations before starting the cycle on the next finer level)).

14.3 GENERAL GRID DESCRIPTION

The wing geometry chosen for this unstructured mesh study is a half-span flat delta wing with a sweep angle of 70° (see Figure 1). The overall dimensions correspond to the wind tunnel model used by Mitchell [3] (root chord of 950mm, semi-span of 346mm at the trailing edge and thickness of 20mm). The main difference with the wind tunnel model is the 15° bevel on the lower surface that is extended to the trailing edge. It is thought that the cut-off trailing edge of the experimental model can lead to numerical problems and inaccurate results for inviscid calculations. The sharp trailing edge is believed not to affect the general vortical flow above the wing although the local flow on the rear part of the wing might be affected.

All the grids created but one are for a free air wing with far field non reflecting characteristic boundary conditions imposed on a rectangular box that extends, from the apex of the wing, 4 root chords upstream, above, below and in the spanwise direction and 6 root chords downstream. A symmetric boundary condition is imposed on the middle plane of the wing. The dimensions of the grid representing the wing in the wind tunnel as well as the boundary conditions used in this case are different, see section 14.6.1.

The grids were generated with ICEM CFD Tetra and contain only tetrahedral volume elements and triangles surface elements. The strategy adopted in creating the grid is to: define the small size of the elements on the wing surface; add a “density” region of small cells in the vortical flow above the wing; define a large cell size on the far field surfaces. Starting from that Tetra is able to create a first mesh with increasing cell size going from the wing to the far field. The mesh on the wing itself is refined at the leading and trailing edges by setting a smaller cell size on the curves defining these edges. The apex of the wing, which is a critical region to capture well the vortex, needs also refinement and this is achieved by dividing the wing surface in two parts the upstream part having a much smaller surface cell size (see Figure 4). Finally all the meshes created by Tetra are smoothed in order to improve the aspect ratio of the cells and get a higher mesh quality that should decrease the numerical errors.

14.4 MESH REFINEMENT STUDY

The first part of this unstructured mesh study around a half span delta wing is an ordinary mesh refinement study performed in order to get a good idea of how small the cells have to be around the wing and in the vortical region to correctly capture the vortex.

14.4.1 Grid Description

Figure 2 shows a global view of the mesh in the symmetry plane for the first mesh generated and considered as a medium mesh. The wing lies in the centre and the refined region above and behind the wing is clearly seen (more is said about this refinement in section 14.5). Figure 3 shows a close-up of the wing seen from downstream with the mesh in the symmetry plane, the refinement in the vortical region is even clearer. The original reference size of the cells on the wing is around $1/100^{\text{th}}$ of the root chord length and as small as $1/200^{\text{th}}$ for the front part (see Figure 4(a)). The size of the cells in the region above the wing is equal to $1/50^{\text{th}}$ of the root chord and increases to $1/25^{\text{th}}$ in the refined region at the far field. This results in a mesh with around 2 million finite volume cells for 340 000 nodes (as EDGE is a node-centred finite volume flow solver, it makes more sense to consider the number of nodes in the mesh rather than the number of cells or elements).

The refinement process was simply achieved by decreasing the reference cell size in Tetra and choosing $\frac{3}{4}$ of the previous one. This gives a cell size of around $1/133^{\text{rd}}$ of the root chord length for the wing surface for example (see Figure 4(b)). By doing this, the whole mesh is refined in all directions but the relative sizes of the cells in the different parts of the mesh are preserved. The number of cells increases dramatically to 4.4 million which corresponds to 755 000 nodes. This large number of nodes caused some

problems due to the limited computer hardware available.

14.4.2 Results and Discussion

Figure 5 compares the surface pressure distributions obtained with the medium and fine mesh to the experimental data [3]. General remarks can be made between experimental and numerical results. The most visible difference is the trace of vortex breakdown that is absent of the experimental results although breakdown is present and recorded to oscillate between 61% and 71% of the chord length. The numerical results on the contrary show a circular region of low pressure downstream of the main footprint of the vortex core. This second low-pressure footprint is typical of a recirculation region downstream of vortex breakdown. The predicted locations of vortex breakdown are 66.3% and 61.4% for the medium and fine mesh respectively, which is in the range measured experimentally. The second main difference is the lower suction peak predicted below the vortex. This is true for most of the results presented in this study although adding the wind tunnel walls in the simulation slightly improves the results (see section 14.6). Finally, one can also notice the absence of the footprint of the secondary vortex (visible on the left side of the experimental results) in the simulation results, which is expected since the formation of the secondary vortex is a viscous phenomenon.

When comparing the surface pressure distribution for the medium and fine mesh in Figure 5(b) and (c) respectively, one can notice the higher suction peak reached with the finer mesh. This is a general trend observed in this study: finer meshes resolve a stronger vortex with vortex breakdown whereas coarse meshes do not necessarily capture the breakdown (not shown here). The footprint of the recirculation region is found more upstream with the fine mesh matching the findings for the breakdown position.

The C_p plots in Figure 6 confirm what is seen in the overall pressure distribution picture: the finer mesh predicts a slightly higher suction peak but the maximum value is still lower than the experimental data except at the 32% chord location (Figure 6(a)). One would expect inviscid solutions to predict a higher suction peak than the experiment does but that is not the case here. The large differences in suction peak between the two meshes in Figure 6(b) and Figure 6(c) at the 53% and 63%-chord locations are due to the different positions of vortex breakdown. It is interesting to notice that the C_p distribution in the inner part of the wing (where y/b is close to zero) is also affected in these two plots. The characteristic more outboard position of the suction peak for Euler simulations (which do not capture the effect of the secondary vortex) is visible in the plots too. The irregular C_p distribution at the leading edge (close to y/b equal to -1) is thought to be due to the discontinuity at the sharp leading edge and/or mesh discretization effect spanning some cells on the wing but is by no means the trace of a secondary vortex (this effect is also seen in Figure 5(b) and (c)).

The conclusion of this mesh refinement study is that the finer mesh is more suited to the calculation of the flow around the delta wing. In particular, the pressure distribution is in better agreement with the experimental data. The reference size used for the meshes presented in the rest of this report is thus chosen to be the same as the one used in the fine mesh. However, the refinement of the vortical region in the wake of the wing costs a lot in terms of cell number. That is why the influence of this refinement is studied in the next section.

14.5 WAKE REFINEMENT STUDY

As mentioned above and shown in Figure 2, the first meshes generated had a refined region following the vortex development as far as the downstream far field boundary. It was thought that this refined region would be necessary to accurately capture the vortex behaviour and avoid the vortex dissipation due to numerical dissipation, usually seen for meshes with increasing cell size away from the wing surface. However, this refinement proved to be very expensive in terms of cell numbers especially on the refined

mesh. As the aim of the present project is to predict the flow around the wing itself and not the decay of the trailing vortex for example, a study of the mesh refinement in the vortex wake has been performed in order to assess the effect of this refinement on the wing and determine if a coarser wake region is not enough.

14.5.1 Grid Description

Two other meshes were generated: one with no wake refinement, only the part above the wing is refined and the cells start to grow after the trailing edge (see Figure 7(a)); one with a short refined wake that extends only one root chord length behind the wing (see Figure 7(b)) (Note that in all cases the region above the wing is refined in the same way leading to similar surface meshes). The refined mesh presented in the previous section is the third mesh used for comparison and will be called here mesh with full wake refinement, since the refinement extends to the limit of the domain (see Figure 7(c)). The three meshes can be considered as fine meshes since they all have the same reference cell size as the refined mesh presented previously. The refined region that surrounds the vortex is created using “density” regions in ICEM CFD Tetra. No mesh adaptation has been performed for the present study and the “densities” have been placed manually instead. A first calculation without refined wake served as a reference to determine the location of the vortex and thus, the dimension of the refined region. The fully refined wake mesh has three different “densities” to capture the vortex (as “densities” can only be boxes without curved edges, three boxes are necessary to follow the vortex bending upwards at a reasonable cost). The cell size is $1/66^{\text{th}}$ of the root chord length above the wing and in the first “density” behind the wing (extending two root chord lengths from the trailing edge in the downstream direction and approximately one half span in the spanwise direction) and $1/33^{\text{rd}}$ of the root chord length in the “density” close to the far field (extending the remaining three chord lengths in the downstream direction). The mesh with the short refined wake has the same cell size definition but the “density” downstream of the trailing edge is shorter and extends only one root chord length (instead of two). The total numbers of nodes are 116 000, 305 000 and 755 000 (668 000, 1.8 million and 4.4 million mesh cells) for the mesh with no wake refinement, a short wake refinement and the full wake refinement, respectively.

14.5.2 Results and Discussion

Figure 8(a) and (b) as well as Figure 5(c) show the surface pressure distribution on the wing with the mesh without wake refinement, with the short wake refinement and the full wake refinement, respectively. They have to be compared with Figure 5(a) that shows the experimental results. The overall remarks made in section 14.4 are still valid: the presence of a footprint from the recirculation region and in general higher pressures than the experimental ones.

In the comparison of the surface pressure results for the different meshes, the position of vortex breakdown plays again a significant role: 54.7%, 62.5% and 61.4% of the chord for the mesh without wake-, with short wake- and full wake-refinement respectively. Unfortunately no real trend can be identified, except that the mesh without refinement in the wake gives a breakdown position far upstream of the experimental values and for this, is judged inadequate. This difference in vortex breakdown position is visible on the surface pressure distribution as the position of the footprint of the recirculation region changes. In Figure 8(a), without wake refinement, the recirculation region is so upstream that it affects the pressure as far as in the symmetry plane where there is a region of lower pressure. This recirculation region also creates a widening of the vortex footprint when compared to the experimental results in Figure 5(a). Closer to the apex of the wing, the suction under the vortex is also affected by the wake refinement, the suction being lower when the wake refinement is progressively removed. This again shows that the mesh without wake refinement does not give satisfactory results.

The results for the C_p plots in Figure 9 are again rather inconclusive as no trend concerning the wake refinement presence can be identified. Far upstream of the breakdown (section $x/c=0.32$, for example),

there is no significant difference in the pressure plots and the comment is the same for sections far downstream of breakdown ($x/c=0.84$). The differences appear in the intermediate region where breakdown occurs at different locations, leading to difference in the C_p plots.

The conclusions of this study of wake refinement are mixed. On the one hand, there is no obvious effect of the refinement on the results but on the other hand, removing totally this wake refinement does not produce good enough results (“wrong” position of vortex breakdown and low suction peak below the vortex). The main conclusion is that the refinement has an effect although no trend could be identified. So, as a guideline one can say that the wake has to be refined in the proximity of the trailing edge whereas it is not so useful to refine the mesh far away from the wing and thus points can be saved there.

14.6 WIND TUNNEL WALL EFFECT

The objective of this part of the study is to see how the walls affect the vortical flow on the wing and if their effect can explain the differences observed between experimental and numerical pressure distribution. In particular, a higher suction peak is expected with the walls taken into account in the simulation (see [4]-[8] for both experimental and numerical studies of wall effect on delta wing pressure distributions).

14.6.1 Simulation of Wing in Wind Tunnel

14.6.1.1 Grid Description

A final unstructured mesh has been generated around the wing placed in the wind tunnel. The dimension of the walls and the position of the wing match exactly the experimental conditions in the 1.4x1.8 m test section of the ONERA F2 wind tunnel in Fauga-Mauzac (France) where the model has been tested [3]. The sting and the mounting system, however, have not been included.

The mesh generation was rather straightforward, once the geometry had been well defined. The upstream and downstream dimensions were kept the same (four root chords and six root chords respectively) (see Figure 10). A short wake refinement of one chord length has been used. The mesh has been divided in three parts in the length in order to have a refined region around the wing by setting the wall cell size to $1/8^{\text{th}}$ of the root chord length as opposed to $1/3^{\text{rd}}$ root chord length for the two other parts, the cell size at the inlet and outlet being approximately one root chord. Figure 10 shows the wing with the mesh on the walls and the symmetry plane and the three different parts of the mesh are visible, the middle one around the wing being removed to see the interior. Figure 11 shows the wing in the wind tunnel test section and gives a good idea of the relative size of the wing and the section. It is important to note that the walls have not been refined as much as the wing surface because the gradients of the flow quantities were not expected to be too high close to the walls. In total, the mesh is made of 1.8 million elements or 316 000 nodes.

14.6.1.2 Results

When looking at the wing surrounded by the walls in Figure 11, the large size of the model becomes clearer. The blockage at an angle of attack of 27° is estimated to 5.9%, which is rather high and is definitively expected to affect the results. Changes in streamline curvatures, in local angle of attack along the span and in dynamic pressure due to the model and its wake blockage should be seen in this experiment when compared to CFD simulations of a free air model. The walls tend to increase the suction peak on the wing below the vortex and promote vortex breakdown [4]. But maybe more important than the global blockage ratio is the large wing-span to tunnel-width ratio of 49.4% (while the wing-span to tunnel-height ratio is moderate at 38.4%). According to Allan [4], at a constant blockage ratio, the span to width ratio has the most significant effect and 49% should be considered as a high value for which the side walls

will definitely influence the flow.

The surface pressure distribution for the wing in the wind tunnel in Figure 12 shows again the footprint of the recirculation region not present in the experiment (Figure 5(a)). The vortex breakdown in this case is found at 57.6% of the chord length, which is upstream of the experimental range. The suction peak below the vortex is higher but still a bit low compared to the experiment, if one keeps in mind that Euler solutions should give higher suction peaks than the experiment. The comparison with the results obtained for the free air wing (fine mesh with short wake refinement, C_p distribution in Figure 8(b) and vortex breakdown at 62.5% chord) shows the expected trends when adding the walls: higher suction peak below the vortex and more upstream position of vortex breakdown.

The C_p plots in Figure 13 show the effect of the walls on the pressure distribution more clearly². The suction peak upstream of breakdown is higher with the walls and even higher than the experimental value (as it should be). After breakdown, at station $x/c=0.84$, the suction peak is still higher with the walls but slightly lower than the experiment. For the stations in between, the different positions of vortex breakdown explain the main differences in suction peak.

14.6.2 Wind Tunnel Correction Methods for Delta Wing Flow

The intention here is not to give an exhaustive review of all the known correction methods applied to delta wings but rather to give an introduction to the subject in order to try to understand and predict the differences in the results presented in the previous section.

It is well-known that the flow around a model in a wind tunnel is slightly different from the one in free air due to the presence of the wind tunnel walls and mounting system (see for example [9] for a list of all the possible wall interferences). Classical corrections based on potential flow theory [9] give a good estimate of the corrected dynamic pressure or the effective angle of attack around the model. However, according to [10], when the “model is not small and large regions of separated flow dominate the flow field”, as is the case here with the ONERA delta wing at high angle of attack, more advanced methods should be used. Such methods could be panel methods, boundary-measurement methods (like wall pressure signature method) or CFD simulations.

When looking at the specific case of delta wing in high angle of attack conditions, relatively few correction methods can be found. Frink [5] uses a Free Vortex Sheet code to extend the standard upflow correction to delta wing at high angle of attack. Lan et al.[6] & [11] apply the wall pressure signature method to CFD simulations of delta wings in wind tunnels in order to compute the corrections in angle of attack and dynamic pressure. In [6], correction charts for blockage and upwash “applicable to configurations with vortex flow” are presented. The corrections are a function of the Interference Correction Parameter (ICP) that accounts for the relative size of the model and the wind tunnel cross-section. These charts are only valid for vortex flows without breakdown.

Traub [12] has developed an analytical correction method for delta wings with vortex breakdown. The method predicts the upwash around the wing in the tunnel and assumes the effect of the floor and ceiling walls to be negligible. An analytical expression of the vortex circulation with breakdown is used to determine the effect of vortex images on the wing in the tunnel. Equation (1) gives the expression of the upwash angle around the wing:

² The results called “EDGE Free air correct.” are presented in section 14.6.3 and correspond to the wing in corrected free air conditions. In this section, only the results with and without walls (“EDGE Free air”) are compared.

$$\tan \Delta \alpha = \frac{w_{TOT}}{U_{\infty}} = \frac{2(2.212 \tan^{0.8} \varepsilon \sin \alpha)}{4\pi \cos \varepsilon} \left(\frac{x_{VB}}{c_R} \sqrt{1 - \frac{x_{VB}^2}{c_R^2}} + \arcsin \frac{x_{VB}}{c_R} \right) \times \int_0^{\frac{c_R}{2} \tan \varepsilon} \int_{-x \tan \varepsilon}^x \frac{1}{\left(2W + y - \frac{2}{3} x \tan \varepsilon \right) 2x \tan \varepsilon} dy dx \quad (1)$$

The double integral in equation (1) can be integrated with respect to y to give:

$$\frac{1}{2 \tan \varepsilon} \int_0^{\frac{c_R}{2} \tan \varepsilon} \ln \left(\frac{1 + \frac{1}{3} \mu \zeta}{1 - \frac{5}{3} \mu \zeta} \right) \frac{d\zeta}{\zeta}, \quad \text{where } \mu = \frac{c_R \tan \varepsilon}{2W} \quad (2)$$

(Note that Figure 2 in [12] comparing the results of the above method to Hsing and Lan's results [6] can be very misleading. Indeed, the ICP is not a parameter in Traub's method, which means that for a constant value of ICP, very different curves can be obtained for example by changing the sweep angle of the wing.)

14.6.3 Simulation of Wing in Corrected "Free Air" Conditions

As mentioned before the 70° delta wing model tested in the ONERA F2 wind tunnel is rather large. It has been shown that including the wind tunnel walls in the CFD simulations improves the agreement of the results with the uncorrected experimental data. However, most CFD simulations are performed around geometries in free air. The intention of this section is to see if regular free air simulations could be used even when the wall influences are known to be large. Of course the flow conditions have to be corrected, since numerical results at nominal conditions are of poor quality.

The correction method adopted here is the one presented by Traub [12]. The method has been chosen because it takes vortex breakdown into account but remains quite easy to use. In addition, no blockage correction method has been considered because the test case is Reynolds number independent and the simulation only made in inviscid mode (no change in dynamic pressure could have been noticed in the results). Traub's analytical correction method has been applied to the 70° delta wing in the 1.4x1.8m wind tunnel test section. The corrected angle of attack obtained with the method is shown in Figure 14: the results "without breakdown" are obtained with vortex breakdown not taken into account i.e. the strength of the vortex increases indefinitely with increasing angle of attack ($x_{VB}/c_r=1$ in equation (1)); the results "with breakdown" use a quadratic fit of Mitchell's experimental vortex breakdown locations [3] to plug x_{VB}/c_r in equation (1)³. The method predicts a maximum upwash angle of more than 4° at an angle of attack around 24° when vortex breakdown is appearing at the trailing edge of the wing. The ICP of the present configuration is 0.1676, which is much larger than what Hsing and Lan [6] give in their charts and confirms the high probability of wall interference. For a nominal angle of attack of 27°, the angle of attack chosen in the study, the estimated upwash angle is 3.885°, which means an effective angle of attack of 30.885°.

The surface pressure distribution for the wing in corrected free air conditions in Figure 15 shows a higher suction peak than previously computed. However, the vortex breakdown footprint has considerably moved

³ Using Mitchell's uncorrected angle of attack for the vortex breakdown location only gives an estimate of the corrected upwash. A more accurate prediction would require an iterative procedure to correct the breakdown location once the effective angle of attack is known.

upstream corresponding to a breakdown location of 43.4% of the root chord. This location is now far upstream of the experimental data. Nevertheless, if one only looks at the pressure distribution prior to breakdown (Figure 13 (a)), it is very encouraging to notice that the high suction peak obtained with the wing in the wind tunnel is also matched by the simulation of the wing in corrected free air conditions. This means that the correction is quite accurate when vortex breakdown is not present. Of course the upstream position of vortex breakdown highly influences the rest of the pressure distribution that is in poor agreement with the experimental data (see Figure 13 (b)-(e)). Once again we see how complex and sensitive the vortical flow is, which tends to prove that more advanced methods are required to correct the wind tunnel data. A simple change in angle of attack is not enough to reproduce the wind tunnel conditions when vortex breakdown occurs above the wing. The effect of the upflow might be well taken into account but other parameters like the tunnel induced pressure gradient will also affect the vortex breakdown.

14.7 CONCLUSION

This study has shown how complex and influential the mesh generation process is for the inviscid simulation of a 70° delta wing at an angle of attack of 27°. The vortex breakdown that occurs above the wing is very sensitive to the mesh and then influences the whole surface pressure distribution on the wing. Table 1 summarises the results for the vortex breakdown location and shows that differences of as much as 11% of the chord length can be observed while only modifying the mesh around the wing.

A first mesh refinement study showed that the original mesh was not fine enough and that a finer mesh was more suitable to get accurate prediction of the flow around the wing. A study of the refinement of the wake region downstream of the wing revealed that this too had an influence on vortex breakdown and concluded that a short refined wake should be included in the mesh.

Finally, the influence of the wind tunnel walls was investigated in order to explain discrepancies between experimental wind tunnel results and numerical results obtained for a free air wing. The presence of the walls in the simulation improves the quality of the results but the agreement is still not total. An analytic correction method is used to compute the effective angle of attack of the wing in the wind tunnel and results with these corrected free air conditions are compared to the simulation of the wing in the tunnel. The agreement is very good prior to vortex breakdown but this latter is predicted too much upstream, which ruins the usefulness of the correction method.

In the view of these conclusions, one more level of refinement on the mesh with a short wake refinement should be made in order to make sure the global size of the mesh cells is not too high. Simulations with a lower Mach number should also be performed to check the influence of the modified free-stream velocity.

Work on simple correction methods for delta wing in wind tunnel clearly remains to be done. A deeper understanding of vortex breakdown is probably a first necessary step though.

Lastly this study emphasizes, if necessary, how useful automatic mesh adaptation (not used here) can be. Obviously, well-located refined regions in the mesh improve the quality of the results and achieving that without any user intervention is a real advantage.

Table 1 : Comparison of longitudinal vortex breakdown locations for the different meshes studied

	Vortex breakdown location ⁴ in % of chord length
Experiment [3]	61-71
Medium full wake refinement	66.3
Fine full wake refinement	61.4
Fine short wake refinement	62.5
Fine no wake refinement	54.7
Fine short wake refinement + wind tunnel walls	57.6
Fine short wake refinement (corrected free air)	43.4

14.8 ACKNOWLEDGEMENTS

This work has been carried out through financing from the Parallel and Scientific Computing Institute under project number 625935, “PSCI- CFD National Code”.

14.9 REFERENCES

- [1] Eliasson, P., “EDGE, a Navier-Stokes solver for unstructured grids”, Proc. to Finite Volumes for Complex Applications III, ISBN 1 9039 9634 1, pp. 527-534, 2002.
- [2] Wallin, S. and Johansson, A., “A complete Explicit Algebraic Reynolds Stress Model for incompressible and compressible turbulent flows”, Journal of Fluid Mechanics, vol. 403, pp 89-132, 2000.
- [3] Mitchell, A.M., “Caractérisation et contrôle de l’éclatement tourbillonnaire sur une aile delta aux hautes incidences”, Ph.D. thesis, Université Paris VI, Paris, France, July 2000.
- [4] Allan, M., “A CFD investigation of wind tunnel interference on delta wing aerodynamics”, PhD thesis, Department of Aerospace Engineering, University of Glasgow, October 2002.
- [5] Frink, N.T., “Computational study of wind-tunnel wall effects on flow field around delta wings”, AIAA Paper 87-2420, 1987.
- [6] Hsing, C.C.A. and Lan, C.E., “Low-speed wall interference assessment/correction with vortex flow effect”, Journal of Aircraft, vol. 34, No. 2, pp 220-227, March-April 1997.

⁴ The vortex breakdown location is determined as the most upstream point on an isosurface of zero chordwise velocity, representing the recirculation region

- [7] Verhaagen, N.G., “Tunnel wall effect on the flow around a 76/40-deg double-delta wing”, AIAA Paper 98-0312, 1998.
- [8] de Try, F., “Computational study of vortex behaviour over 70°-swept delta wings in wind tunnels”, Master thesis, Department of Aeronautics, Royal Institute of Technology, Stockholm, skrift 99-34, 1999.
- [9] Pope, A., “Wind-tunnel testing”, Second Edition, John Wiley & Sons, New York, Chapman & Hall, London, 1954.
- [10] Ewald, B.F.R., “Wind tunnel wall correction”, AGARDograph 336, 1998.
- [11] Thomas, J.P. and Lan, C.E., “The simulation and correction of wind tunnel wall interference on delta wing lift using Navier-Stokes and Euler solutions”, AIAA Paper 91-3300, 1991.
- [12] Traub, L.W., “Prediction of tunnel wall upwash for delta wings including vortex breakdown effects”, The Aeronautical Journal, vol. 103, No. 1021, pp 139-142, March 1990.

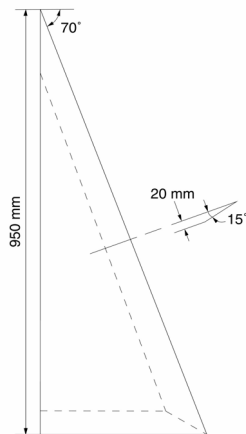


Figure 1: Wing geometry

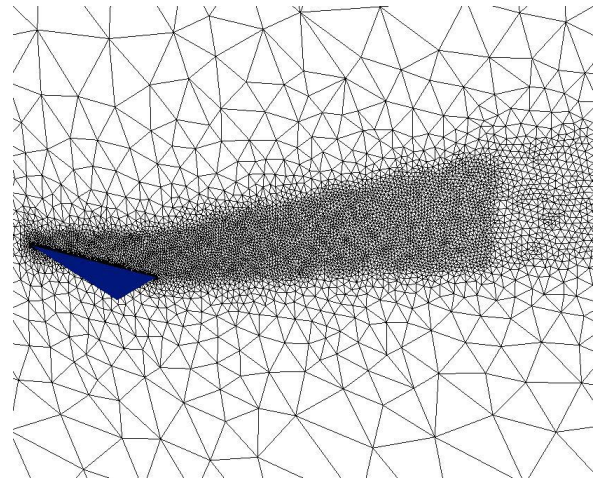


Figure 3: Close-up on the wing and the symmetry plane of the medium grid

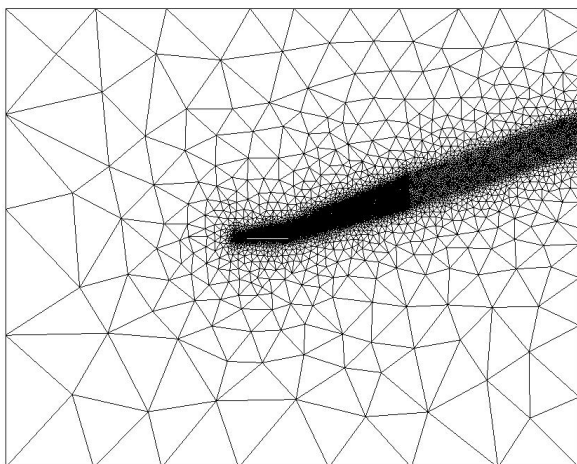
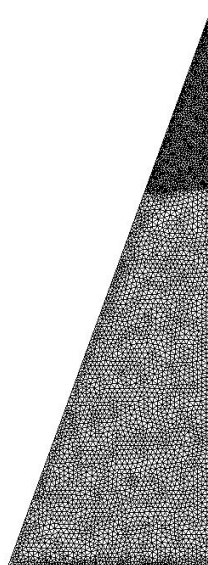
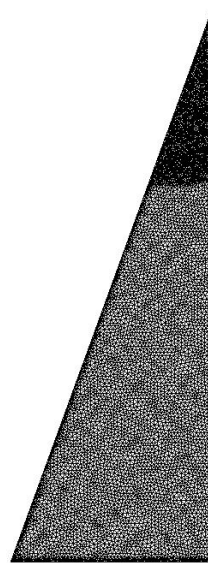


Figure 2: View of the symmetry plane of the medium mesh

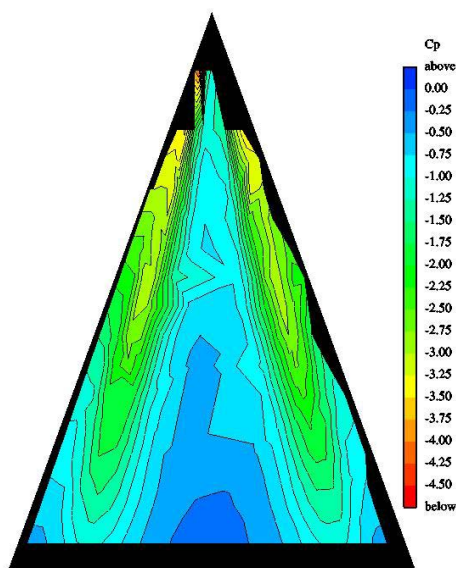


(a) Medium mesh

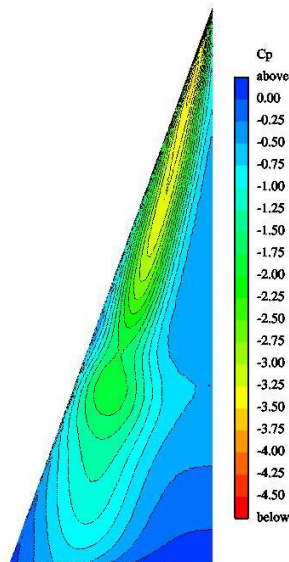


(b) Fine mesh

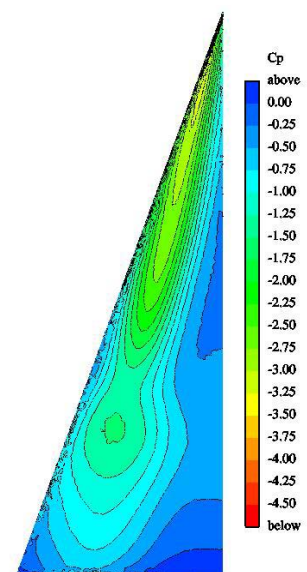
Figure 4: Comparison of wing surface mesh for the medium and fine meshes



(a) Experimental results



(c) Fine grid



(b) Medium grid

Figure 5: Comparison of surface pressure distribution: experiment, medium and fine grids

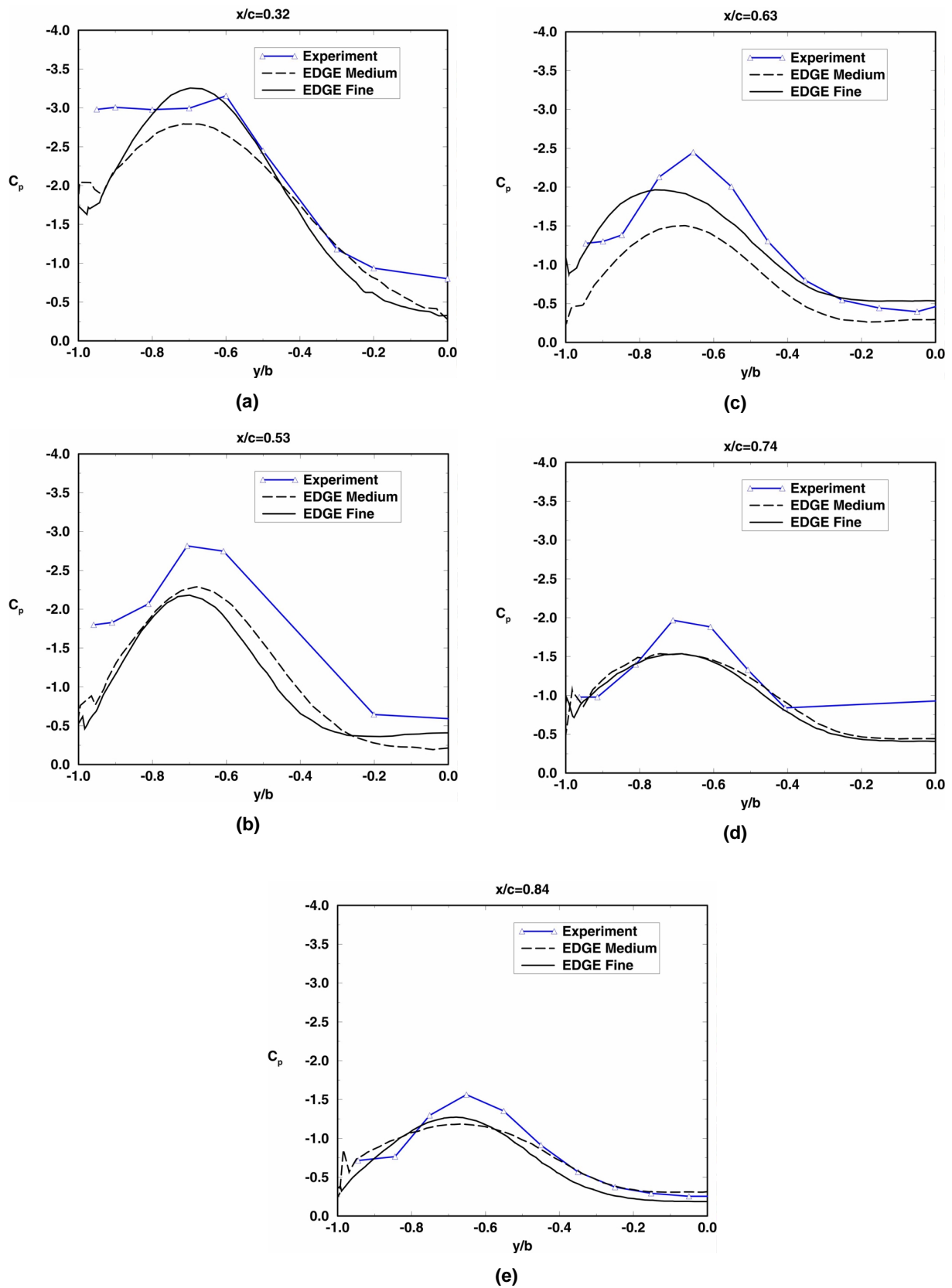
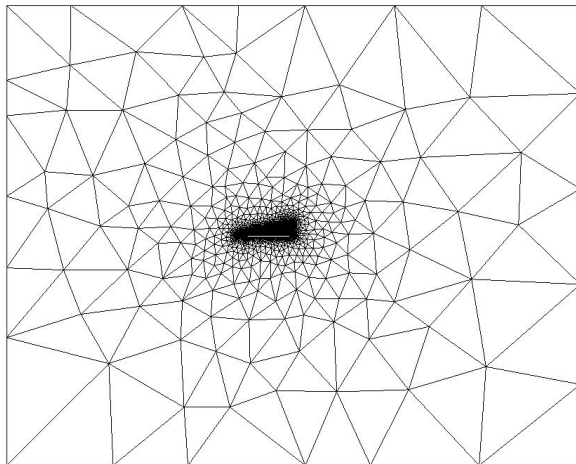
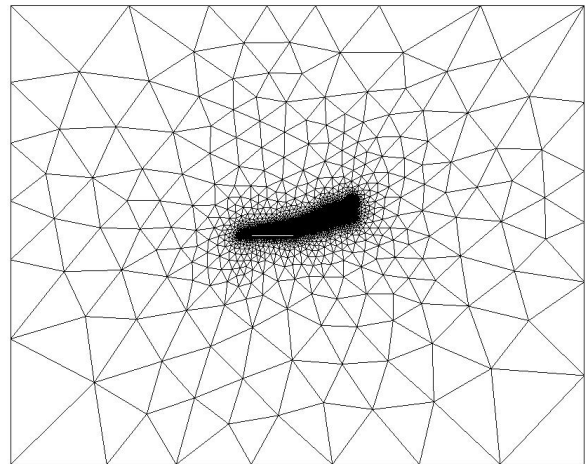


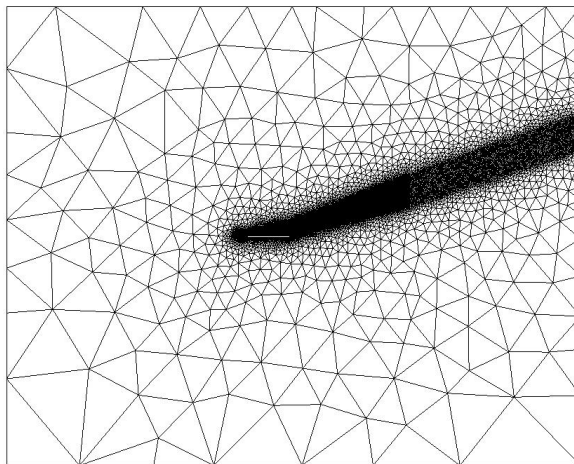
Figure 6: Comparison of C_p distribution: experiment, medium and fine grid



(a) No wake refinement

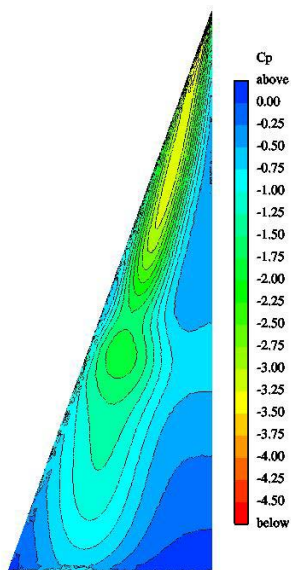


(b) Short wake refinement

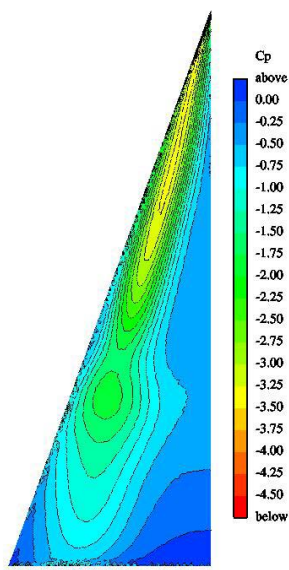


(c) Full wake refinement

Figure 7: Comparison of the mesh in the symmetry plane: no wake refinement, short wake refinement and full wake refinement



(a) No wake refinement



(b) Short wake refinement

Figure 8: Comparison of surface pressure distribution: no wake refinement and short wake refinement

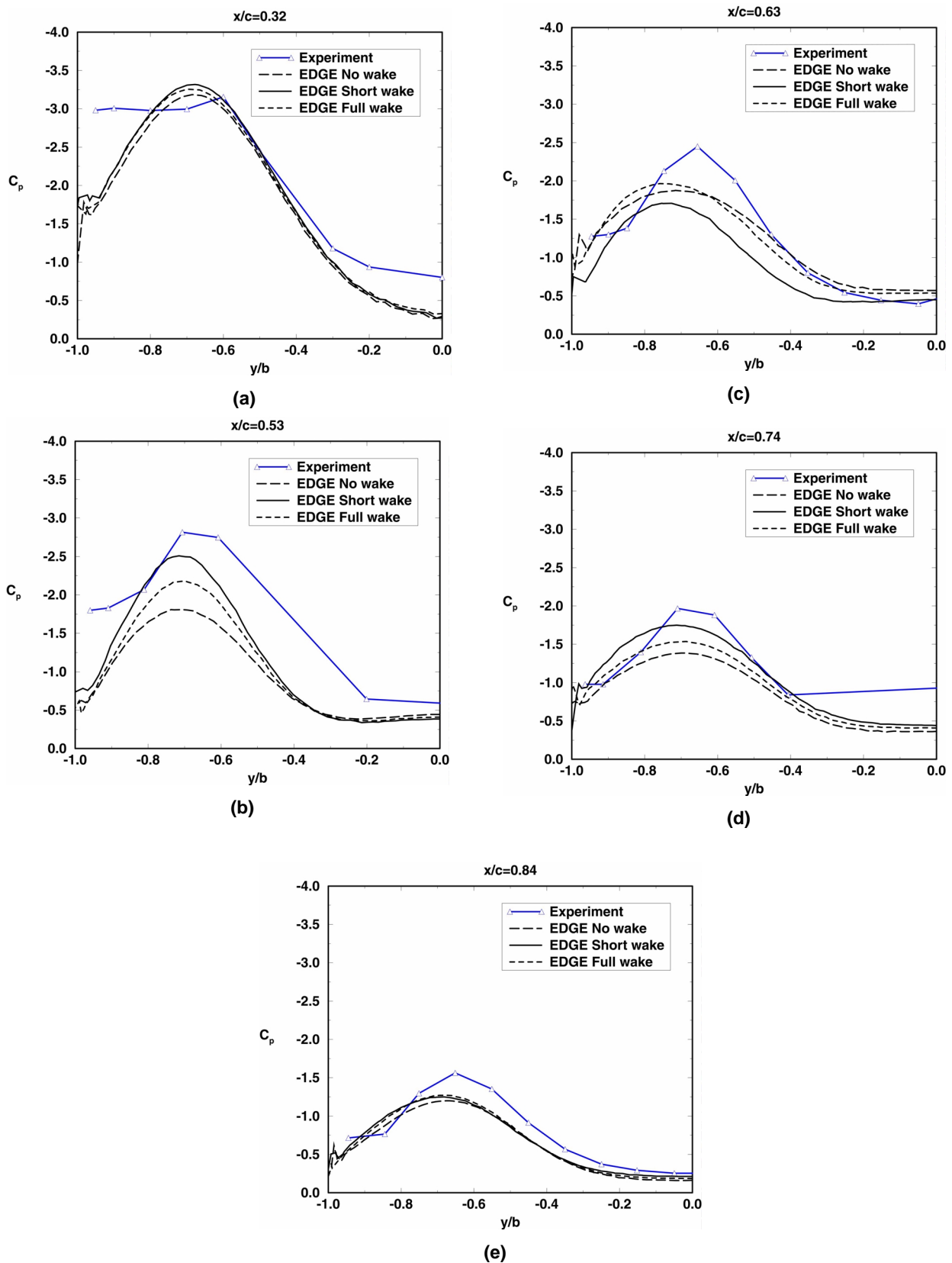


Figure 9: Comparison of C_p distribution: experimental, no wake refinement, short wake and full wake

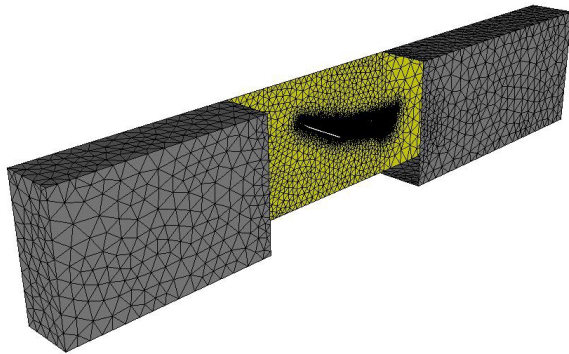


Figure 10 : Global view of the mesh with the wing in the wind tunnel

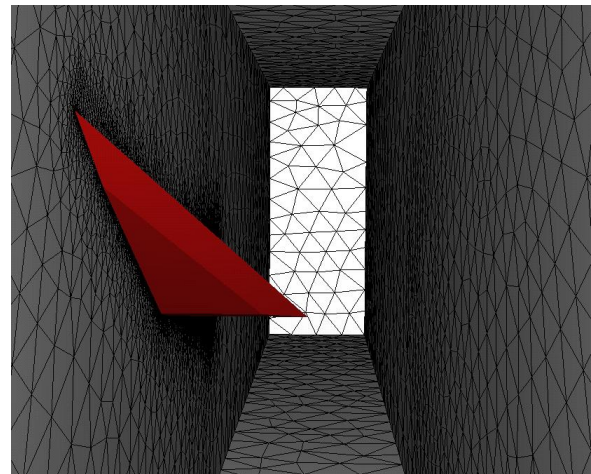


Figure 11 : View of the wing surrounded by the wind tunnel walls

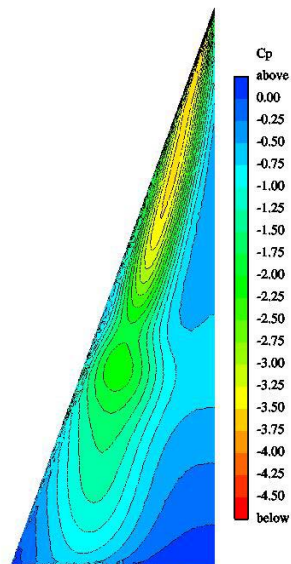


Figure 12 : Surface pressure distribution on the wing in the wind tunnel

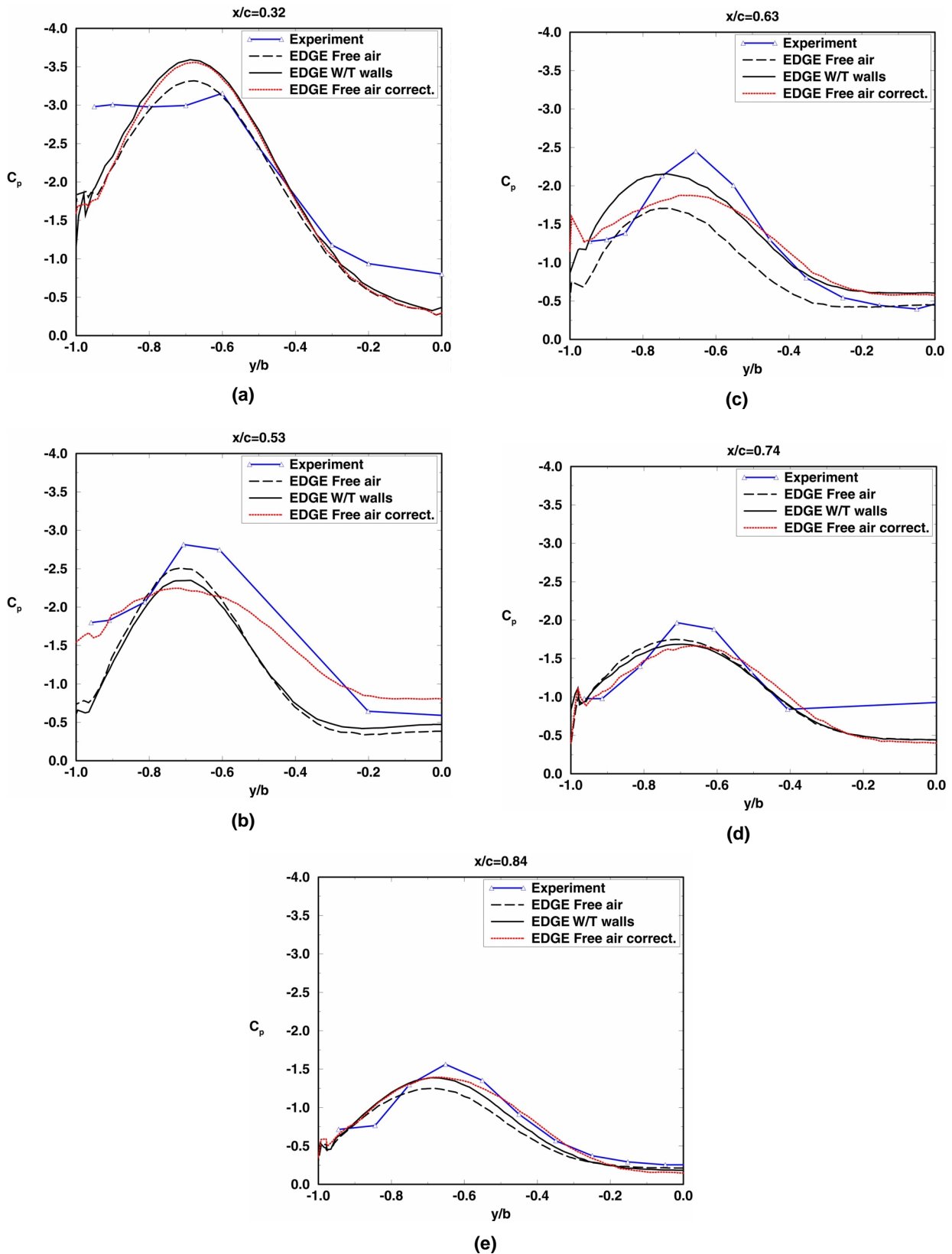


Figure 13 : Comparison of C_p distribution: experiment, free air wing, wing in wind-tunnel and wing in corrected free air conditions

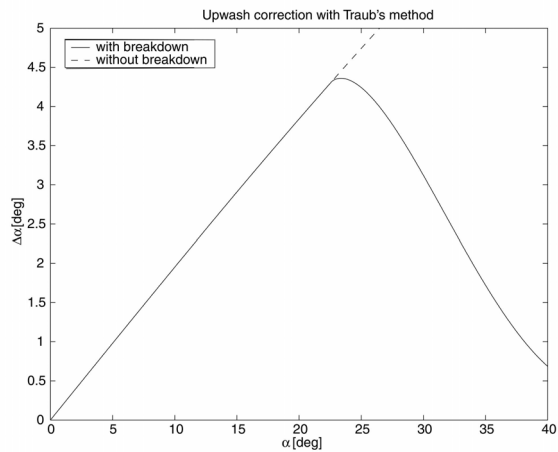


Figure 14 : Corrected angle of attack obtained with Traub's method [12] applied to the 70° delta wing in ONERA wind tunnel

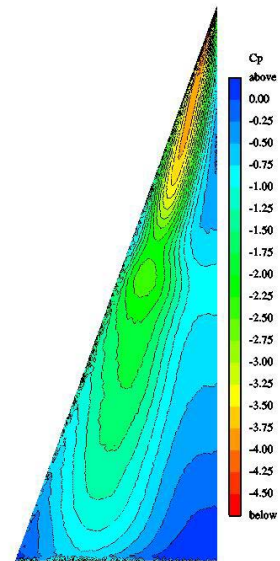


Figure 15 : Surface pressure distribution on the wing in corrected free air conditions

Chapter 15 – HIGH REYNOLDS NUMBER DETACHED-EDDY SIMULATIONS OF VORTEX BREAKDOWN OVER A 70 DEGREE DELTA WING

Scott A. Morton

2410 Faculty Dr., Suite 108
USAF Academy, Colorado 80840-6400
scott.morton@usafa.af.mil

ABSTRACT

An understanding of the vortical structures which comprise the vortical flowfield around slender bodies is essential for the development of highly maneuverable and high angle of attack flight. This is primarily due to the physical limits these phenomena impose on aircraft and missiles at extreme flight conditions. Demands for more maneuverable air vehicles have pushed the limits of current CFD methods in the high Reynolds number regime. Simulation methods must be able to accurately describe the unsteady, vortical flowfields associated with fighter aircraft at Reynolds numbers more representative of full scale vehicles. One of the goals of this paper is to demonstrate the ability of Detached-Eddy Simulation, a hybrid RANS-LES method, to accurately predict the vortical flowfield over a slender delta wing at Reynolds numbers above 1 million. Although Detached-Eddy Simulation successfully predicted the location of the vortex breakdown phenomenon in previous work, the goal of the current effort is to further validate the method with additional experimental data of ONERA, such as surface pressures and turbulent kinetic energy in the vortex core. The effect of grid density and an adaptive mesh refinement technique is also assessed through comparisons with experiment. Detailed wind tunnel geometry, such as tunnel walls and the sting mount system, are simulated and found to make a measurable difference. Finally, modeling the laminar to turbulent transition is demonstrated to have a significant effect on the vortical flowfield.

15.1 INTRODUCTION

Many of today's military vehicles exhibit vortex dominated flowfields. At a recent NATO Air Vehicle Technology conference, D. A. Lovell presented a review of "Military Vortices," [1] where he discussed the declining research budget in this area and the importance of understanding the phenomena. He classified vortex flows into three categories, "those designed into a vehicle to improve performance, those which cannot be avoided and whose adverse affects must be minimized, and those that were not expected to occur." [1] He gives examples of many of these vortex dominated flowfields: tip vortices on wings having low sweep, leading edge extension vortices from the F-18 and F-16 aircraft, fore planes on the Rafale, and flow over the MK-82 bomb, to name just a few. He also discusses the fact that governments are relying ever increasingly on the aerospace industry to perform research. Since the aerospace industry concentrates on cruise conditions for optimization of commercial aircraft, these vortical flowfields common in military aircraft are losing their place in research budgets. This is occurring at a time when the three largest US fighter development programs (F/A-18E/F, F-22, and F-35) incorporate twin tail configurations and high angle-of-attack maneuvering. The aerodynamic phenomena causing concern on these twin-tail aircraft is vortex breakdown and can be modeled with the very simple flat plate delta wing geometry.

The delta wing vortex breakdown phenomena has been studied extensively since Henri Werlé first photographed it in 1954, during water tunnel tests of a slender delta wing model at Onera [2]. This work was quickly confirmed by Peckham and Atkinson [3], Elle [4], and Lambourne and Bryer [5], and spawned a large number of experimental, computational and theoretical studies which continue today. These investigations led to the development of several theories governing vortex breakdown, although none have been universally accepted [6-10]. Despite this lack of a unified theoretical interpretation, several forms of vortex breakdown have been identified [8-11] (i.e. bubble, helical, etc.), and the global characteristics of the phenomena are understood. During the breakdown process, the mean axial velocity component rapidly decreases until it reaches a stagnation point and/or becomes negative on the vortex axis. This stagnation point, called the breakdown location, is unsteady and typically oscillates about some mean position along the axis of the vortex core [12,13]. As the angle of attack increases, the mean vortex breakdown location moves upstream over the delta wing (from the trailing edge toward the apex).

The primary vortex over a slender delta wing at angle of attack has been postulated to be principally inviscid. Unfortunately, the location of the vortex is strongly affected by a secondary vortex formed by the inter-relationship between the surface boundary layer and the primary vortex. In addition, the vortex breakdown phenomenon creates turbulent kinetic energy that must be modeled properly or resolved. Many turbulence models create orders of magnitude too high a level of turbulent eddy

viscosity in the primary vortex core which significantly alters the flowfield and in some cases eliminates breakdown observed experimentally at high Reynolds numbers. For these reasons, an accurate prediction of the flowfield over a slender delta wing at high angles of attack and high Reynolds numbers (as well as military aircraft exhibiting vortex breakdown) must model the boundary layer, primary and secondary vortex, and turbulent kinetic energy correctly.

While advances have taken place in areas such as grid generation and fast algorithms for solutions of systems of equations, CFD has remained limited as a reliable tool for prediction of inherently unsteady flows at flight Reynolds numbers. Current engineering approaches to prediction of unsteady flows are based on solution of the Reynolds-averaged Navier-Stokes (RANS) equations. The turbulence models employed in RANS methods necessarily model the entire spectrum of turbulent motions. While often adequate in steady flows with no regions of reversed flow, or possibly exhibiting shallow separation, it appears inevitable that RANS turbulence models are unable to accurately predict flows characterized by massive separation. Unsteady, massively separated flows are characterized by geometry-dependent and three dimensional turbulent eddies. These eddies, arguably, are what defeat RANS turbulence models, of any complexity.

To overcome the deficiencies of RANS models for predicting massively separated flows, Spalart et.al. [14] proposed Detached-Eddy Simulation (DES) with the objective of developing a numerically feasible and accurate approach combining the most favorable elements of RANS models and Large Eddy Simulation (LES). The primary advantage of DES is that it can be applied at high Reynolds numbers as can Reynolds-averaged techniques, but also resolves geometry-dependent, unsteady three-dimensional turbulent motions as in LES. The unstructured finite-volume solver *Cobalt* [15] has been used in conjunction with DES successfully on a number of complex problems, including a supersonic base flow [16], delta wing vortex breakdown [17], a square with rounded corners [18], the F-15E at high angle of attack [19], and the F/A-18E with unsteady shock buffet [20].

A NATO working group from the Research and Technology Organization (AVT-080) has been tasked with assessing the ability of computational fluid dynamics (CFD) to accurately predict vortex breakdown, and to document the experimental database available for verification and validation of CFD for delta wing vortex breakdown. The specific aim of this work is to document the ability of the hybrid RANS-LES method, DES, to accurately predict vortex breakdown position as well as the overall time evolution of this unsteady flowfield. In particular, grid refinement, wind tunnel wall and sting effects, and laminar to turbulent transition will be analyzed for a 70° delta wing at $\alpha = 27^\circ$, $M_\infty = 0.069$, and $Re_c = 1.56 \times 10^6$. Comparison of the computed results with the experiments of Mitchell et. al. [13] will also be presented.

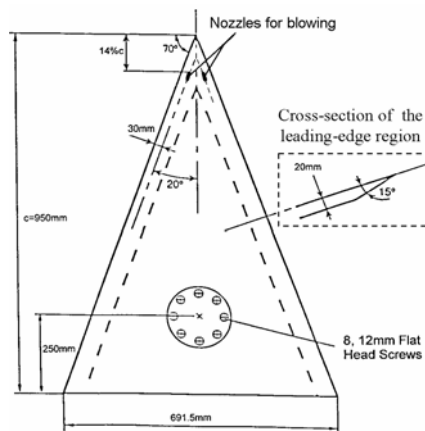


Fig. 1: Sketch of the delta wing model with nozzles for along-the-core blowing near the apex.

15.2 EXPERIMENTAL METHOD AND FACILITIES

The experimental data used for comparison was obtained by Mitchell et. al. [13] from ONERA's F2 wind tunnel. ONERA's F2 wind tunnel has a rectangular test section with a width of 1.4m, a height of 1.8m, and a length of 5m. It is powered by a 680kW DC motor that drives a fan with blades spanning 3.15m and provides a maximum free-stream velocity in the test section of 105m/s. A cooling facility maintains a constant free-stream temperature in the test section. The relative free-stream velocity, $\Delta U_0/U_0$, is estimated to have an accuracy of 1% while the mean intensity of turbulence has an accuracy of 0.1% [13].

In F2, the delta wing model depicted in Fig. 1 was mounted on a sting with a horizontal support and flexible joint for adjusting the angle of attack, with an accuracy of $\pm 0.05^\circ$. The horizontal support was manipulated in height along a vertical column so as to maintain the model close to the center axis of the test section. The model was mounted in the test section with no yaw angle with respect to the free-stream flow (estimated accuracy of $\pm 0.1^\circ$). The experimental dataset consists of steady pressure data at many locations on the top side of the delta wing and LDV data in planes parallel to the top surface, perpendicular to the top surface spanwise, and perpendicular to the top surface along the vortex core.

Name	Description	# Cells	Xmin to Xmax	Ymin to Ymax	Zmin to Zmax
G1	Half Span	1.2×10^6	$-10\text{m} < X < 10\text{m}$	$0 < Y < 5\text{m}$	$-5\text{m} < Z < 5\text{m}$
G2	Half Span	2.7×10^6	$-10\text{m} < X < 10\text{m}$	$0 < Y < 5\text{m}$	$-5\text{m} < Z < 5\text{m}$
G3	Half Span	6.7×10^6	$-10\text{m} < X < 10\text{m}$	$0 < Y < 5\text{m}$	$-5\text{m} < Z < 5\text{m}$
G4	Half Span	10.7×10^6	$-10\text{m} < X < 10\text{m}$	$0 < Y < 5\text{m}$	$-5\text{m} < Z < 5\text{m}$
G5	Half Span, Walls	2.6×10^6	$-10\text{m} < X < 10\text{m}$	$0 < Y < 2.5\text{m}$	$-1.75\text{m} < Z < 1.75\text{m}$
G6	Full Span, Walls, Based on G5	5.2×10^6	$-10\text{m} < X < 10\text{m}$	$-2.5\text{m} < Y < 2.5\text{m}$	$-1.75\text{m} < Z < 1.75\text{m}$
G7A1	Half Span, Walls, Sting	4.1×10^6	$-10\text{m} < X < 10\text{m}$	$0 < Y < 2.25\text{m}$	$-1.75\text{m} < Z < 1.75\text{m}$
G8	Full Span, Walls, Sting, Based on G7	8.2×10^6	$-10\text{m} < X < 10\text{m}$	$-2.25\text{m} < Y < 2.25\text{m}$	$-1.75\text{m} < Z < 1.75\text{m}$
G9	Half Span, No Sting	1.2×10^6	$-10\text{m} < X < 10\text{m}$	$0 < Y < 5\text{m}$	$-5\text{m} < Z < 5\text{m}$
G9A4	AMR of G9	2.4×10^6	$-10\text{m} < X < 10\text{m}$	$0 < Y < 5\text{m}$	$-5\text{m} < Z < 5\text{m}$
G9A5	AMR of G9	2.5×10^6	$-10\text{m} < X < 10\text{m}$	$0 < Y < 5\text{m}$	$-5\text{m} < Z < 5\text{m}$

Table 1: Unstructured grids developed for the ONERA 70° delta wing during the NATO Research and Technology Organization task group AVT-080.

test section. The relative free-stream velocity, $\Delta U_0/U_0$, is estimated to have an accuracy of 1% while the mean intensity of turbulence has an accuracy of 0.1% [13].

In F2, the delta wing model depicted in Fig. 1 was mounted on a sting with a horizontal support and flexible joint for adjusting the angle of attack, with an accuracy of $\pm 0.05^\circ$. The horizontal support was manipulated in height along a vertical column so as to maintain the model close to the center axis of the test section. The model was mounted in the test section with no yaw angle with respect to the free-stream flow (estimated accuracy of $\pm 0.1^\circ$). The experimental dataset consists of steady pressure data at many locations on the top side of the delta wing and LDV data in planes parallel to the top surface, perpendicular to the top surface spanwise, and perpendicular to the top surface along the vortex core.

15.3 NUMERICAL METHOD

In this section a brief description of the numerical method is provided with full details of the computational scheme and the solution method presented in Ref. [15]. Solutions were obtained for a freestream velocity of 24 m/s, an angle of attack of 27 deg, and a freestream pressure and temperature resulting in a Reynolds number of 1.56×10^6 and a freestream Mach number of 0.069. The numerical simulation matched the angle of attack, Reynolds number, and Mach number of the wind tunnel experiments [13,21] previously described. Solutions are computed using the commercially-available solver *Cobalt*. *Cobalt* is an unstructured finite-volume method developed for solution of the compressible Navier-Stokes equations with details of the approach described in Ref. [15]. The method is cell-centered and applicable to arbitrary cell topologies including hexahedrals, prisms, and tetrahedra. The spatial operator uses an exact Riemann solver, least-squares gradient calculations using QR factorization to provide second-order accuracy in space, and TVD flux limiters to limit extrema at cell faces. A point implicit method using analytic first-order inviscid and viscous Jacobians is used for advancement of the discretized system. A Newton sub-iteration scheme is employed to improve time accuracy.

15.3.1 Turbulence Models

Cobalt has several choices of turbulence models including Spalart Allmaras (SA) [22] RANS, as well as DES based on SA [14] (called SADES in this work). The SADES hybrid model was found to be a suitable method for the current study by Morton et. al. [17] due to the methods ability to eliminate spurious eddy-viscosity in the core of vortices and resolve the turbulent scales germane to the delta wing vortex breakdown problem. The following subsections describe the turbulence model used in the current work, and also provide references for more detailed descriptions.

15.3.1.1 Spalart-Allmaras Turbulence Model

The Spalart-Allmaras [22] one equation turbulence model solves a single partial differential equation for a working variable related to the turbulent viscosity. The differential equation is derived by using empiricism, arguments of dimensional analysis, Galilean invariance, and selected dependence on the molecular viscosity [22]. The model includes a wall destruction term that reduces the turbulent viscosity in the laminar sublayer and the log layer. Details of the model implementation and all coefficients are given in Ref. [17].

15.3.1.2 Detached-Eddy Simulation

The DES model was originally based on the Spalart-Allmaras one equation RANS turbulence model (discussed above, with a more detailed presentation in Ref. [17]). The wall destruction term is proportional to the square of the modified eddy-viscosity divided by the distance to the nearest wall $(\tilde{\nu} / d)^2$. When this term is balanced with the production term \hat{S} , the eddy viscosity becomes proportional to $\hat{S}d^2$. The Smagorinski LES model varies its sub-grid-scale (SGS) turbulent viscosity with the local strain rate, and the grid spacing described by $\nu_{SGS} \propto \hat{S}\Delta^2$, where $\Delta = \max(\Delta x, \Delta y, \Delta z)$. If d is replaced with Δ in the wall destruction term, the SA model will act as a Smagorinski LES model. To exhibit both RANS and LES behavior, d in the SA model is replaced by

$$\tilde{d} = \min(d, C_{DES}\Delta), \quad C_{DES} = 0.65$$

When $d \ll \Delta$, the model acts in a RANS mode and when $d \gg \Delta$ the model acts in a Smagorinski LES mode. Therefore, the model switches into LES mode when the grid is locally refined. DES was implemented in an unstructured grid solver by Forsythe et. al. [16]. They determined the C_{DES} constant could be 0.65, consistent with the structured grid implementation of Shur et. al. [24], when the grid spacing Δ was taken to be the longest distance between the cell center and all of the neighboring cell centers. All simulations in this study use the SADES hybrid RANS-LES turbulence model.

15.3.2 Grid Generation

Grids were developed using the software programs Gridtool [25], to develop the surface point distributions and background sources, and VGRIDns [26] to grow the volume grid. Grids were typically created with concentration of points near the surface in the viscous region and concentration of points in the LES focus region of the vortex core by the use of Gridtool's line sources.

After growing the tetrahedral grid with Vgrid, a *Cobalt* utility code called Blacksmith was used to "weld" the majority of tetrahedra in the viscous region into prisms. Using prisms in the viscous region produces a more orthogonal grid by improving the aspect ratio of the cells and a side benefit is a reduction in the overall number of cells. All of the grids in this study consist of an inner region of over 20 layers with an initial spacing normal to the wall in viscous wall units less than 1, and a geometric stretching factor of 1.2, and an outer region of nearly isotropic tetrahedra. The inner region consists of at least 13 layers of prisms with the remaining layers tetrahedra. The prism dimensions on the surface were a factor of approximately 200 times larger than the wall normal dimension for all grids.

Grids were also obtained by feature based adaptive mesh refinement (AMR). This grid technology is particularly well suited for DES because separated flow regions can easily be grid refined. Pirzadeh [27] presented a method

based on a tetrahedral unstructured grid technology developed at NASA Langley Research Center with application to two configurations with vortex dominated flowfields. The large improvement of the adapted solutions in capturing vortex flow structures over the conventional unadapted results was demonstrated by comparisons with wind tunnel data. Pirzadeh showed the numerical prediction of these vortical flows was highly sensitive to the local grid resolution and he also stated that grid adaptation is essential to the application of CFD to these complicated flowfields.

AMR grids were developed with the following procedure: a steady-state flow solution was computed for a particular grid, next the flowfield solution was used to create an AMR grid by eliminating all cells within an iso-surface of vorticity magnitude at a particular level, finally the more refined grid was then grown inside of the iso-surface by applying a scale factor to the baseline grid density (i.e. 0.5). This procedure was typically performed twice to create a vortex core and shear layer with $1/4^{\text{th}}$ the cell sizes (in all coordinate directions) of the original grid. The new grid was then used to compute unsteady detached-eddy simulations of the flowfield.

There were many grids developed for the current study including grids with and without wind tunnel walls, with and without a wind tunnel sting, full span and half span, and with and without AMR. Table 1 describes the details of the grids developed for this study. All of the grids were produced with Gridtool and VGRIDns to allow adaptive mesh refinement if desired.

15.4 COMPUTATIONAL RESULTS

All simulations of the current study were performed for flowfield conditions of $\alpha = 27^\circ$, $M=0.069$, and $Re_c = 1.56 \times 10^6$. The baseline turbulence treatment is to assume the flow is fully turbulent everywhere and to apply the SADES hybrid model. A study of turbulence treatments for this flowfield was performed and presented in Ref. [17]. The study included comparisons of vortex breakdown solutions computed with the Spalart-Allmaras and Shear Stress Transport RANS methods with DES versions of these turbulence models. In addition, the effect of rotation correction for the Spalart-Allmaras model was also described. The study concluded that RANS methods are too dissipative and can eliminate the physically observed vortex breakdown phenomenon, whereas, DES is able to capture vortex breakdown accurately.

A systematic time-step and Newton sub-iteration study was presented in Ref. [17] for grid G2 (2.7M cells). The study demonstrated that three Newton sub-iterations and a time step, non-dimensionalized by the freestream velocity and root chord, of 0.0025 was sufficient.

In addition to the time step study, a consistent grid sensitivity study was performed and presented in Ref. [28]. Fig. 2 demonstrates the ability of SADES to capture the fine scales of the vortex breakdown phenomena at this high Reynolds number. Instantaneous iso-surfaces of vorticity magnitude colored by the span-wise vorticity component are shown for grids G1 (1.2M cells), G2, 2.7M cells), G3 (6.7M cells), and G4 (10.7M cells).

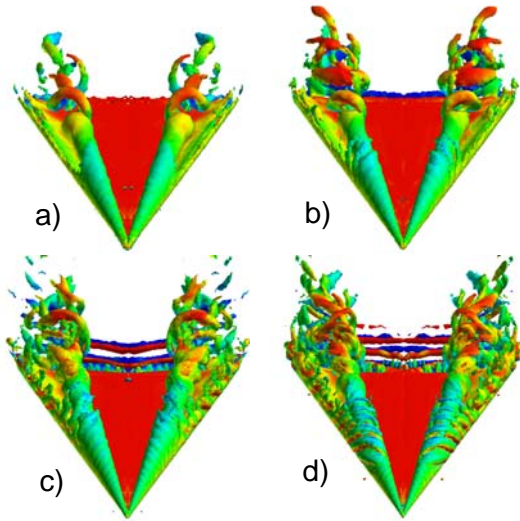


Fig. 2: Instantaneous iso-surfaces of vorticity magnitude colored by the span-wise component of vorticity for four grids: a) G1 (1.2M cells), b) G2 (2.7M cells), c) G3 (6.7M cells), and G4 (10.7M cells). The flowfield conditions are $\alpha = 27^\circ$, $M=0.069$, and $Re_c = 1.56 \times 10^6$.

Typical simulations were run for 10,000 iterations, starting from freestream conditions, and time averages were computed starting after the 2,000th iteration to eliminate transients. It is apparent in Figs. 2 a)-d) that consistent grid refinement provides a significant increase in the number of flowfield structures resolved. In the pre-breakdown region of the vortex core, substructures winding around the core are observed as the grid is refined. Also, there is a significant increase in the number of structures observed in the region of the core, post-breakdown, as the grid is refined. Trailing-edge spanwise vortical structures begin to be resolved as the grid is refined, and for grid G4, 3-D structures emanating from the blunt trailing edge that transition to these spanwise coherent vortices are also captured. An instability at the leading-edge that is time varying was also captured and resolved with increasing grid density.

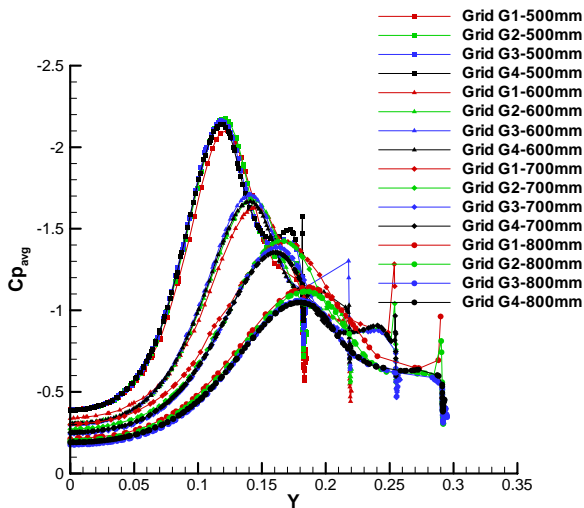


Fig. 3: Average surface pressure coefficients at four chord-wise stations (500mm, 600mm, 700mm, and 800mm) for grids G1, G2, G3, and G4.

The sensitivity of the surface pressure coefficient to grid refinement is depicted in Fig. 3 for four chord-wise stations (500mm, 600mm, 700mm, and 800mm). Although the surface pressure coefficient does vary with grid refinement, grids G3 and G4 are almost indistinguishable from each other. The differences in the surface pressure coefficient are more pronounced aft of breakdown which occurs at 0.65 (+0.05) in the experiments.

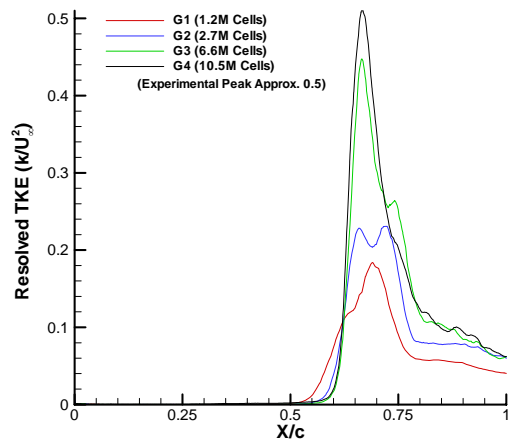


Fig. 4: Resolved turbulent kinetic energy nondimensionalized by the square of the freestream velocity along the core for four grids.

One of the more difficult quantities to predict is the resolved turbulent kinetic energy (TKE) in the core of the vortex. This quantity is sensitive to the grid density since it is a measure of the production of eddies in the core of the vortex. Fig. 4 shows the ability of SADES to capture the resolved TKE and the sensitivity to grid density. The onset of vortex breakdown is signaled by the rapid rise in TKE and the peak for grid G4 is close to the experimental value of 0.5 (when nondimensionalized by the square of the freestream velocity).

Grid	Mean	Variation
G1	0.50	+/-0.05
G2	0.58	+/-0.05
G3	0.62	+/-0.05
G4	0.62	+/-0.05
G5	0.67	+/-0.06
G6-Left	0.7	+/-0.05
G6-Right	0.71	+/-0.05
G7A1	0.605	+/-0.035
G9A5	0.61	+/-0.05
G7A1-SS	0.50	+/-0.02
G9A5-SS	0.63	+/-0.20
Experiment	0.65	+/-0.05

Table 2: Vortex breakdown positions for the experiments and various grids.

The vortex breakdown position is computed for many of the grids in Table 1 and presented in Table 2. The definition of vortex breakdown position for the purposes of this study is the chord-wise position measured from the apex where the streamwise velocity goes to zero. The DES solutions are all within the uncertainty band of the experiments, whereas the steady-state solution for the G7A1 grid is fairly far forward.

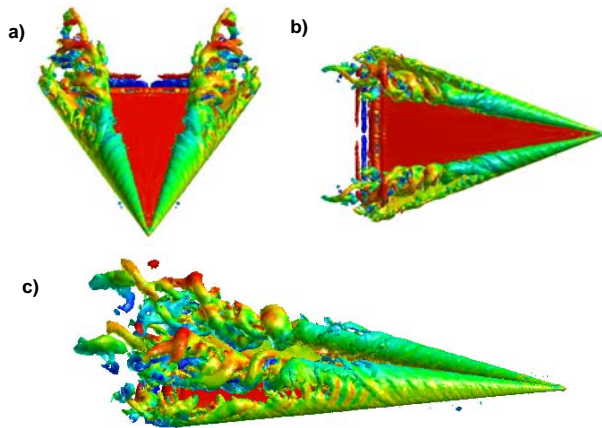


Fig. 5: Instantaneous iso-surfaces of vorticity magnitude colored by the span-wise component of vorticity for three views of the 70° delta wing G9A4 grid in a freestream (i.e., no wind tunnel walls and no sting). The flowfield conditions are $\alpha = 27^\circ$, $M=0.069$, and $Re_c = 1.56 \times 10^6$.

Although the finest grid, G4, was capable of producing relevant solutions for vortex breakdown, the grid cost was high when considering the aero surface that produces these vortices on aircraft such as the F-18 are only a small portion of the vehicle. Alleviation of this high cost was attempted with AMR. An AMR grid was produced with 2.4M cells and a concentration of these cells in the vortex core and leading-edge shear layer. Fig. 5 depicts three views of the instantaneous solution after 10,000 time steps. This grid is comparable to the G3 grid without AMR comprised of 6.7M cells.

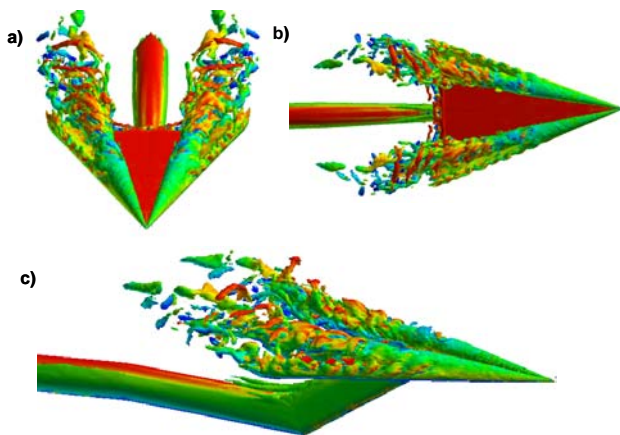


Fig. 6: Instantaneous iso-surfaces of vorticity magnitude colored by the span-wise component of vorticity for three views of the 70° delta wing G7A1 grid with wind tunnel walls and a truncated sting modeled. The flowfield conditions are $\alpha = 27^\circ$, $M=0.069$, and $Re_c = 1.56 \times 10^6$.

Another AMR grid was produced that incorporated a truncated sting and wind tunnel walls (Fig. 6). The additional complexity of the sting required a total number of 4.1M cells. Again, evidence of the leading edge shear layer instability, trailing-edge vortices, and post-breakdown structures were seen but in addition, fore body vortices off of

the sting are seen as well as interactions of the base shed vortices and the sting. Grid G7A1 was intended to simulate the ONERA F-2 wind tunnel walls but the outer boundaries of the grid did not correspond to the test section.

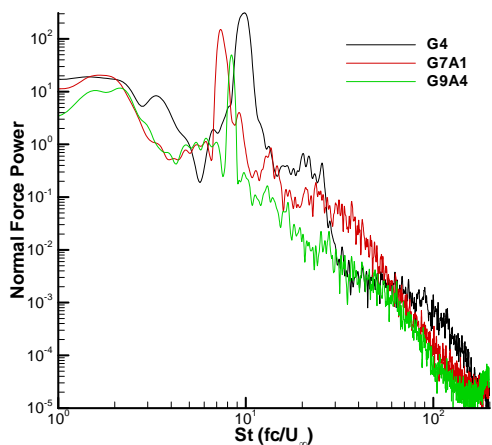


Fig. 7: Power spectral density (PSD) analysis of the delta wing normal force for three grids. PSD was computed from the last 8,000 time steps of a 10,000 time step simulation and the power is presented with respect to the nondimensional Strouhal frequency. The flowfield conditions are $\alpha = 27^\circ$, $M=0.069$, and $Re_c = 1.56 \times 10^6$.

A power spectral density (PSD) analysis was performed for these two grids and compared to the finest grid, G4, (Fig. 7) to determine the ability of these grids to capture turbulent structures and also to determine the effect of the sting and wind tunnel walls on frequency content. The grid G9A4 is lacking in the higher frequency range and is unable to accurately depict the base shedding due to a lack of resolution at the trailing edge. The G7A1 grid, on the other hand, has improved trailing-edge characteristics and also demonstrates some higher frequency content not observed with G4. This additional content is most likely due to sting interactions with the delta wing structures and/or shedding off of the sting itself. It is interesting to note the sting fore-body vortices that are visible in the “elbow” (see Fig. 6c).

Fig. 8 below depicts the surface pressure coefficient versus span at four chord-wise positions for the G7A1 and G9A4 grids, as well as the experiments of Mitchell et. al. [13]. Minor differences are seen between the G7A1 and G9A4 grids primarily in the post-breakdown locations 700mm and 800mm. This figure does however point out the major discrepancy with the experiments is observed for all grids for C_p on the surface. For example, the experimental peak C_p at $X=500\text{mm}$ is -2.9 whereas the G7A1 and G9A4 grids give a value of -2.2 (a difference of 24%). This difference is typical of all of the surface C_p data for all of the grids computed. In addition it should be noted that all of the other researchers participating in this international CFD – experimental comparison obtained similar results. Goertz [29] computed solutions of the same configuration and flowfield conditions using a structured Navier-Stokes Multi-Block code (NSMB) with a detached-eddy simulation turbulence treatment. His comparison of the peak difference at 500 mm was 23.8%. Soewarmoto et. al. [30] computed solutions using a structured Navier-Stokes solver with a RANS turbulence treatment and their peak difference at 500 mm was 22.4%. LeRoy et. al. [31] used the Navier-Stokes solver Fluent and a RANS turbulence treatment and his peak difference at 500 mm was also 23.8%. So several researchers using several computational codes obtained essentially the same surface C_p results for this flowfield.

In an effort to determine if the experimental and computational results were scaled differently, the current results were scaled until the 500 mm chord-wise station matched and then the other stations were examined to determine the quality of the comparison. Fig. 9 depicts the solution of the G9A4 grid for chord-wise stations 500 mm, 600 mm, 700 mm, and 800 mm scaled by the square root of 2. As one can see, the comparison of all stations is impressive. The author can only speculate that a possible source of the difference between all of the computational

simulations and the experimental results for surface C_p could be due to a difference in the reference dynamic pressure scaling. It should be noted that an exhaustive grid sensitivity, time-step sensitivity, wind tunnel wall sensitivity, angle of attack sensitivity, and laminar to turbulent transition sensitivity on surface C_p was accomplished with only a few percent variation.

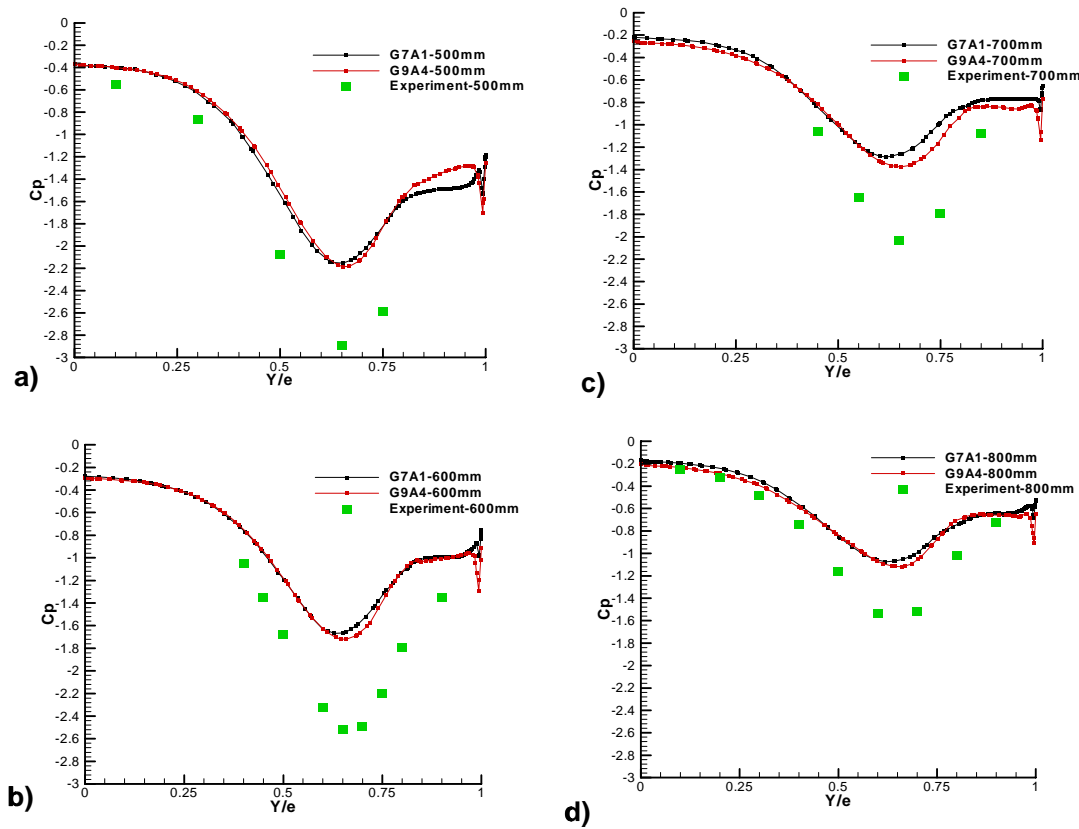


Fig. 8: Average surface pressure coefficients along the span for the G7A1 and G9A4 grid SADES solutions and the experiment at four chord-wise stations: a) 500mm, b) 600mm, c) 700mm, and d) 800mm. The flowfield conditions are $\alpha = 27^\circ$, $M=0.069$, and $Re_c = 1.56 \times 10^6$.

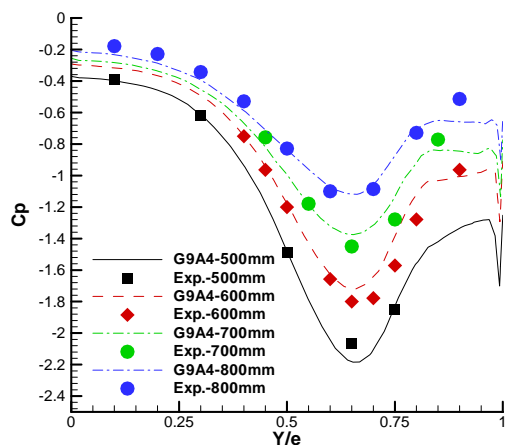


Fig. 9: Average surface pressure coefficients along the span scaled by the square root of 2 for the G9A4 grid SADES solutions and the experiment at four chord-wise stations.

The turbulent kinetic energy in a plane parallel to the delta wing surface through the vortex core was also analyzed (Fig. 10). All three of the grids G4, G7A1, and G9A4 produce TKE of the same magnitude as the experiment in the correct region of the flow post breakdown. It is interesting to note that none of the grids reproduce the TKE generated in the core of the vortex pre-breakdown.

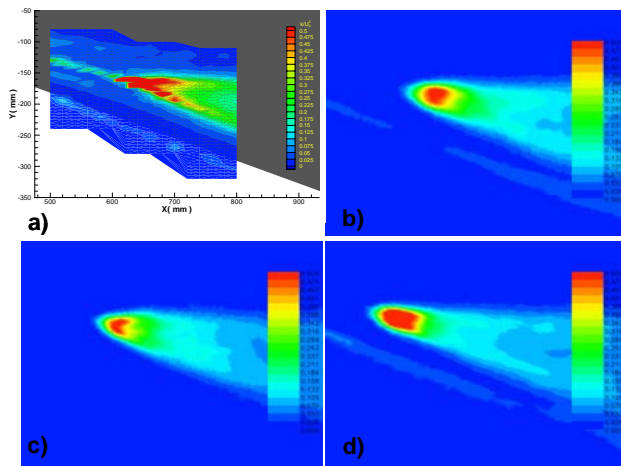


Fig. 10: Experimentally and numerically obtained resolved turbulent kinetic energy nondimensionalized by the freestream velocity squared in a horizontal plane passing through the vortex core. a) ONERA experiments of Mitchell et. al., b) G4 SADES solution, c) G9A4 SADES solution, d) G7A1 SADES solution. The flowfield conditions are $\alpha = 27^\circ$, $M=0.069$, and $Re_c = 1.56 \times 10^6$.

Fig. 11 depicts the comparison of the streamwise component of local velocity (nondimensionalized by the freestream velocity) with the experiments in a plane horizontal to the delta wing surface through the core of the vortex. Both AMR grids, G7A1 and G9A4, are similar to the experimental data but the core streamwise component of velocity is slightly lower for the unadapted G4 grid.

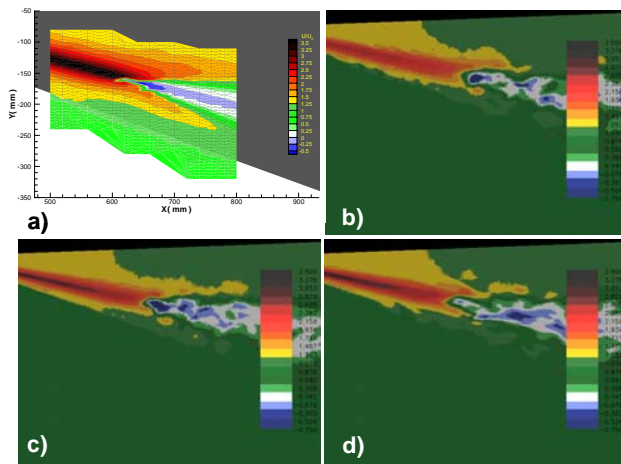


Fig. 11: Experimentally and numerically obtained streamwise velocity component nondimensionalized by the freestream velocity in a horizontal plane passing through the vortex core. a) ONERA experiments of Mitchell et. al., b) G4 SADES solution, c) G9A4 SADES solution, d) G7A1 SADES solution. The flowfield conditions are $\alpha = 27^\circ$, $M=0.069$, and $Re_c = 1.56 \times 10^6$.

15.4.1 Laminar-Turbulent Transition

All of the previous solutions have been for fully turbulent flow on the leeward and windward sides of the delta wing. Mitchell et. al. [13] have suggested that there is a transition from laminar to turbulent flow on the leeward

side of the delta wing at approximately 40% of the root chord based on oil flow visualization (see Fig. 12a). In an effort to determine the effect of laminar to turbulent flow transition, simulations were conducted for an assumed fully turbulent

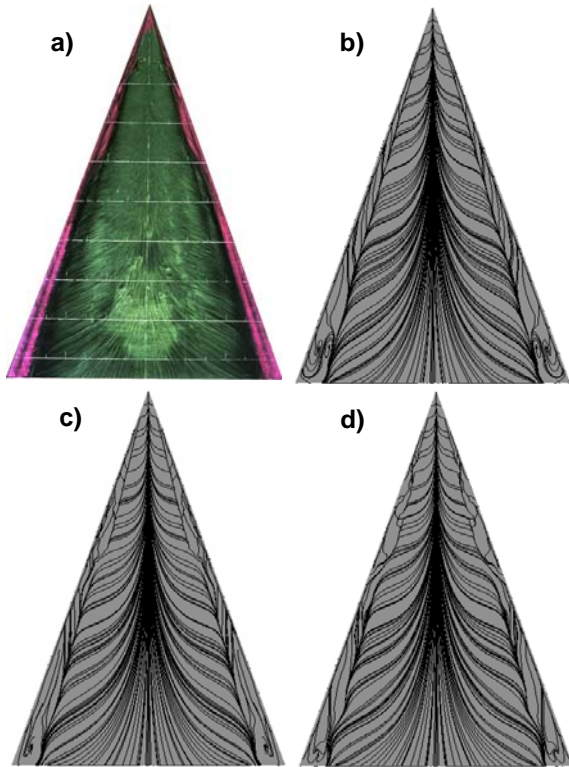


Fig. 12: Surface oil flow patterns for a) experiments of Mitchell et. al., b) grid G9A4 fully turbulent, c) grid G9A4 laminar to turbulent transition at 30% root chord, and d) grid G9A4 laminar to turbulent transition at 40% root chord. The flowfield conditions are $\alpha = 27^\circ$, $M=0.069$, and $Re_c = 1.56 \times 10^6$.

solution, an assumed laminar to turbulent transition at 30% root chord, and an assumed transition at 40% root chord. In both cases where transition was simulated, the windward side was assumed to be laminar. This was implemented by zeroing the production of eddy viscosity in a specified region of the flow (i.e. forward of 40% above the wing and all of the lower wing). Fig. 12a depicts the experimental oil flow visualization where a “pinching” of the secondary separation line occurs at the 40% root chord station. The fully turbulent SADES solution shown in Fig. 12b gives a straight secondary separation line from the apex to the trailing edge. The laminar to turbulent transition SADES solutions, on the other hand, do manifest the “pinching” of the secondary separation line and the 40% solution compares very favorably to the experiment.

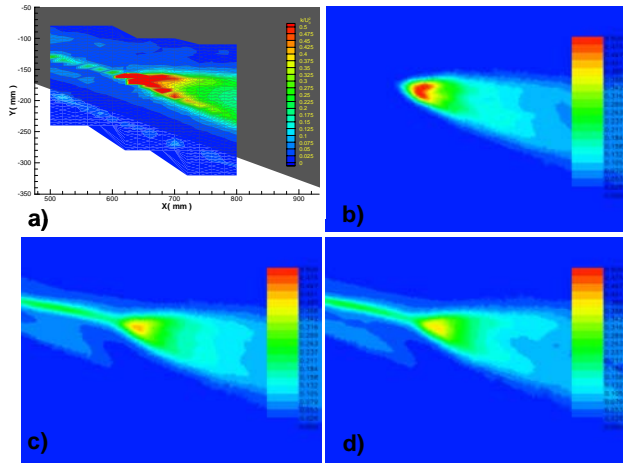


Fig. 13: Experimentally and numerically obtained resolved turbulent kinetic energy nondimensionalized by the freestream velocity squared in a horizontal plane passing through the vortex core. a) ONERA experiments of Mitchell et. al., b) grid G9A4 fully turbulent, c) grid G9A4 laminar to turbulent transition at 30% root chord, and d) grid G9A4 laminar to turbulent transition at 40% root chord. All solutions were computed using SADES and for flowfield conditions of $\alpha = 27^\circ$, $M=0.069$, and $Re_c = 1.56 \times 10^6$.

The resolved TKE in a plane parallel to the delta wing surface through the vortex core shows the effect of the laminar flow upstream of breakdown (Fig. 13). The fully turbulent solution of Fig. 13b exhibits no TKE in the core upstream of breakdown whereas the 30% and 40% transition solutions of Fig. 13 c and d, respectively, compare very well to the experiment. The peak magnitude of the TKE is lower but the grid sensitivity study discussed previously shows the sensitivity of the peak TKE to grid density, indicating the possible need for more points in the core.

Fig. 14 depicts the TKE along the core of the vortex for fully turbulent flow and transitions at 30% and 40% root chord. The fully turbulent solution generates turbulent kinetic energy in the vortex core starting at breakdown. The transitional solutions both generate turbulent kinetic energy well upstream of the forced transition in the boundary layer of 30% or 40%. The peaks and valleys of the transitional solutions upstream of breakdown are due to the fact that the core is no longer straight and the line plot of TKE is moving in and out of the center of the core (see Fig. 15).

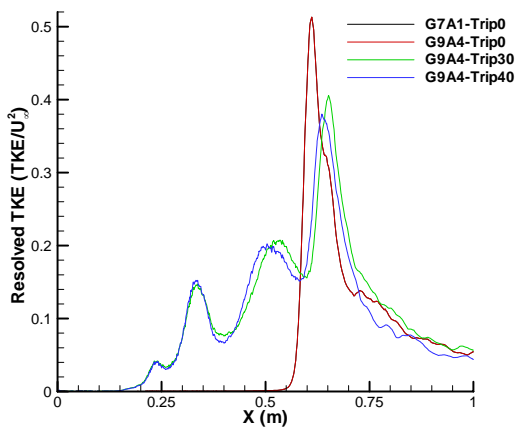


Fig. 14: Resolved turbulent kinetic energy (TKE) nondimensionalized by the freestream velocity squared along the core of the vortex for the G9A4 grid with a fully turbulent assumption, and an assumed laminar to turbulent transition at 30% root chord, and laminar to turbulent transition at 40% root chord. The flowfield conditions are $\alpha = 27^\circ$, $M=0.069$, and $Re_c = 1.56 \times 10^6$.

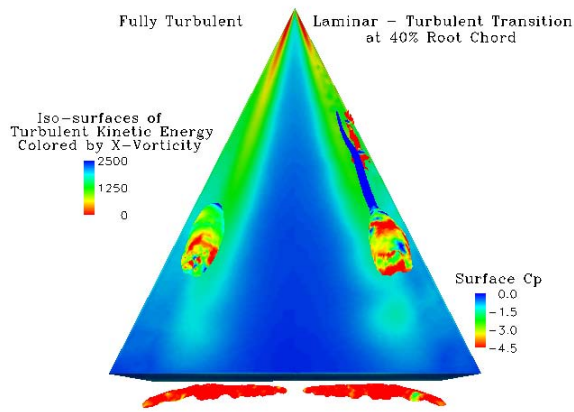


Fig. 15: Iso-surfaces of turbulent kinetic energy for the 70° delta wing. Left half depicts the SADES fully turbulent solution and the right half depicts the SADES solution with a laminar to turbulent transition at 40% root chord. The delta wing surface is colored by the surface pressure coefficient. The flowfield conditions are $\alpha = 27^\circ$, $M=0.069$, and $Re_c = 1.56 \times 10^6$.

Fig. 15 depicts the contrast between the fully turbulent solution (left side) and the 40% transition solution (right side). The core of the primary vortex and the secondary vortex both generate turbulent kinetic energy upstream of breakdown, whereas the fully turbulent solution does not. Also, the curved nature of the vortex core is evident.

15.5 CONCLUDING REMARKS

Spalart-Allmaras Detached Eddy Simulations of a delta wing experiencing vortex breakdown were successfully computed and compared to very detailed experiments. These solutions were shown to be sensitive to grid density and were greatly improved with adaptive mesh refinement. In fact, two grids were shown to give essentially the same solution even though the AMR grid has half of the standard grid points.

The effect of more detailed geometry of the test, such as a truncated sting mount and the wind tunnel walls, was also assessed. The effect of the sting is to add frequency content in the higher frequency range and also to interact with the delta wing trailing vortices. The effect of wind tunnel walls was not successfully assessed because the actual ONERA F2 tunnel geometry was not accurately modeled with the grids. The G7A1 grid is much larger in the test section than the ONERA F2 tunnel. Assessment of the actual wind tunnel wall geometry is suggested as a future area of research.

One of the most striking findings of this effort is the importance of modeling the laminar to turbulent transition. This is routinely assumed to have little effect or is determined to be too difficult to implement due to a lack of good transition models. Unfortunately for this flowfield it has a measurable effect on turbulent kinetic energy and the surface oil flows.

15.6 ACKNOWLEDGEMENTS

The author would like to express appreciation to Dr Shahyar Pirzadeh for his help producing adaptively refined meshes, as well as his enlightening discussions during this work, and Prof Russ Cummings for his help in preparing the manuscript. The author would also like to thank AFOSR for funding this project under the direction of Dr John Schmisser, and the ASC and Maui High Performance Computing Centers for their generous support of computational hours.

15.7 REFERENCES

- [1] Lovell, D A, ``Military Vortices'', Research & Technology Organization Applied Vehicle Technology Panel Meeting, Norway, 7-11 May 2001.
- [2] Werlé, H., "Quelques résultats expérimentaux sur les ailes en flèche, aux faibles vitesses, obtenus en tunnel hydrodynamique" *La Recherche Aéronautique*, No. 41, Sep.-Oct. 1954, pp. 15-21.
- [3] Peckham, D.H., Atkinson, S.A., "Preliminary Results of Low Speed Wind Tunnel Tests on a Gothic Wing of Aspect Ratio 1.0", Aeronautical Research Council Technical Report, C.P. No 508, T.N. Aero 2504, Apr. 1957.
- [4] Elle, B.J., "An Investigation at Low Speed of the Flow near the Apex of Thin Delta Wings with Sharp Leading Edges", Aeronautical Research Council R&M, No. 3176, 1961.
- [5] Lambourne, N.C., Bryer, D.W., "The Bursting of Leading-Edge Vortices-Some Observations and Discussion of the Phenomenon", Aeronautical Research Council R&M No. 3282, 1962.
- [6] Hall, M.G., "Vortex Breakdown", *Annual Review of Fluid Mechanics*, Vol. 4, 1972, pp. 195-218.
- [7] Leibovich, S., "The Structure of Vortex Breakdown," *Annual Review of Fluid Mechanics*, Vol. 10, 1978, pp. 221-46.
- [8] Sarpkaya, T. "On Stationary and Traveling Vortex Breakdowns," *Journal of Fluid Mechanics*, Vol. 45, Part 3, 1971, pp. 545-559.
- [9] Nelson, R.C., "Unsteady Aerodynamics of Slender Wings," *Aircraft Dynamics at High Angles of Attack: Experiments and Modeling*, AGARD-R-776, 1991, pp.1-1 to 1-26.
- [10] Détery, J., "Aspects of Vortex Breakdown," *Progress in Aerospace Sciences*, Vol. 30, 1994, pp. 1-59.
- [11] Faller, J.H., Leibovich, S., "Disrupted states of vortex flow and vortex breakdown", *Physics of Fluids*, Vol. 20, No. 9, 1977, pp.1385-1400.
- [12] Menke, M., Yang, H., Gursul, I., "Further Experiments on Fluctuations of Vortex Breakdown Location," AIAA-96-0205, 34th AIAA Aerospace Sciences Meeting and Exhibit, Jan 1996, Reno, NV.
- [13] Mitchell, A.M., Molton, P., Barberis, D., Détery, J., "Oscillation of Vortex Breakdown Location and Control of the Time-Averaged Location by Blowing," *AIAA Journal*, Vl. 38, No. 5, May 2000, pp.793-803.
- [14] Spalart, P. R. , Jou W-H. , Strelets M. , and Allmaras, S. R., "Comments on the Feasibility of LES for Wings, and on a Hybrid RANS/LES Approach," *Advances in DNS/LES, 1st AFOSR Int. Conf. on DNS/LES*, Aug 4-8, 1997, Greyden Press, Columbus Oh.
- [15] Strang, W.Z., Tomaro, R.F., Grismer, M.J., "The Defining Methods of *Cobalt*: A Parallel, Implicit, Unstructured Euler/Navier-Stokes Flow Solver," AIAA 99-0786, January 1999.

- [16] Forsythe, J.R., Hoffmann, K.A., Cummings, R.M., Squires, K.D., "Detached-Eddy Simulation with Compressibility Corrections Applied to a Supersonic Axisymmetric Base," *Journal of Fluids Engineering*, Vol. 124, No. 4, 2002, pp. 911-923.
- [17] Morton, S.A., Forsythe, J.R., Mitchell, A.M., and Hajek, D., "Detached-Eddy Simulations and Reynolds-Averaged Navier-Stokes Simulations of Delta Wing Vortical Flowfields," *Journal of Fluids Engineering*, Vol. 124, No. 4, 2002, pp. 924-932.
- [18] Squires, K.D., Forsythe, J.R., and Spalart, P.R., "Detached-Eddy Simulation of the Separated Flow Around a Fore body Cross-Section," Direct and Large Eddy Simulation IV, ERCOFTAC Series – Volume 8, B.J. Geurts, R. Friedrich and O. Metais, editors, Kluwer Academic Press, pp. 481-500, 2001.
- [19] Forsythe, J.R., Squires, K.D., Wurtzler, K.E. and Spalart, P.R., "Detached-Eddy Simulation of Fighter Aircraft at High Alpha", AIAA 2002-0591, January 2002.
- [20] Forsythe, J.R., Woodson, S.H., "Unsteady CFD Calculations of Abrupt Wing Stall Using Detached-Eddy Simulation", AIAA 2003-0594, Jan 2003.
- [21] Mitchell, A.M. and Molton, P., "Vortical Substructures in the Shear Layers Forming Leading-Edge Vortices," AIAA Paper 2001-2424, June 2001.
- [22] Spalart, P. R., and Allmaras, S.R., "A One Equation Turbulence Model for Aerodynamic Flows," *La Recherche Aerospatiale*, 1994, 1, p.5.
- [23] Forsythe, J.R., Hoffmann, K.A., Dieteker, F.F., "Detached-Eddy Simulation of a Supersonic Axisymmetric Base Flow with an Unstructured Flow Solver," AIAA 00-2410, June 2000.
- [24] Shur, M., Spalart, P.R., Strelets, M., and Travin, A., 1999, "Detached Eddy Simulation of an Airfoil at High Angle of Attack," 4th International Symposium of Engineering Turbulence Modelling and Measurements, Corsica, May 24-26, 1999.
- [25] Samareh, J., "Gridtool: A Surface Modeling and Grid Generation Tool," Proceedings of the Workshop on Surface Modeling, Grid Generation, and Related Issues in CFD Solution, NASA CP-3291, May 9-11, 1995.
- [26] Pirzadeh, S., "Progress Toward A User-Oriented Unstructured Viscous Grid Generator," AIAA Paper 96-0031, January 1996.
- [27] Pirzadeh, S., "Vortical Flow Prediction Using an Adaptive Unstructured Grid Method", Research & Technology Organization Applied Vehicle Technology Panel Meeting, Norway, 7-11 May 2001.
- [28] Morton, S.A., Forsythe, J.R., Squires, K.D., and Wurtzler, K.E., "Assessment of Unstructured Grids for Detached-Eddy Simulation of High Reynolds Number Separated Flows," 8th ISGG Conference, Honolulu, June 2002.
- [29] Goertz, S., "Detached-Eddy Simulations of a Full-Span Delta Wing at High Incidence," AIAA Paper 2003-4216, 21st AIAA Applied Aerodynamics Conference, Orlando, Florida, June 23-26, 2003.
- [30] Soewarmoto, B.I. and Boelens, O.J., "Simulation of Vortical Flow Over a Slender Delta Wing Experiencing Vortex Breakdown," AIAA Paper 2003-3942, 21st AIAA Applied Aerodynamics

Conference, Orlando, Florida, June 23-26, 2003.

- [31] LeRoy, J.F., Mary, I., and Rodriguez, O., "CFD Solutions of 70-deg Delta Wing Flows," AIAA Paper 2003-4219, 21st AIAA Applied Aerodynamics Conference, Orlando, Florida, June 23-26, 2003.



Chapter 16 – RANS SOLUTIONS OF 70° DELTA WING IN STEADY FLOW

J.-F. Le Roy and O. Rodriguez

ONERA – centre de Lille

5, Bd Paul Painlevé

59045 LILLE CEDEX

FRANCE

leroy@imf-lille.fr/rodriguez@imf-lille.fr

ABSTRACT

This paper presents the contribution of ONERA concerning steady Navier-Stokes computations over a 70° delta wing. All calculations have been carried out with the elsA software. The configuration is a half span delta wing at high angle of attack and moderate Reynolds number. The nature of the flow around this kind of wing has imposed the use of adapted turbulence models such as SARC and SST model. A detailed analysis has been made to extract the main features of the flow and the results have been compared with experimental data. The data presented in this frame exhibits that the main characteristics of the flow, high streamwise vorticity and vortex breakdown location, are in respect to the physics.

KEY WORDS

CFD, DELTA WING, VORTEX BREAKDOWN, SUBSONIC , STEADY

NOMENCLATURE

c	chord length, m
Kp	pressure coefficient , $= (p - p_{\infty}) / q_{\infty}$
k	turbulent kinetic energy
M	Mach number
p	static pressure, Pa
q	dynamic pressure, Pa
S	half wing area, m ²
U	freestream velocity, m/s
u	x velocity component, m/s
v	y velocity component, m/s
w	z velocity component, m/s
Re	Reynolds number based on the chord length
x, y, z	wing axes system, origin in wing apex, m
y+	law of the wall coordinate
α	angle of attack, deg
ρ	density, kg/ m ³
Ω_x	x vorticity component, $= (dw/dy - dv/dz)$
Ω_z	z vorticity component, $= (dv/dx - du/dy)$

subscript

∞ freestream

16.1 INTRODUCTION

Modern fighters need a strong capability of manoeuvring in flight domain characterised by highly separated and vortical flows. On delta wings, leading edge vortices contribute to a large part of the lift. The flow separates at leading edge if it is bevelled, or beyond a value of angle of attack for a rounded leading edge. Separation generates a mixing layer leading to two primary vortices on the upper side of the wing. According to the value of angle of attack and wing shape, a secondary vortex or even a tertiary one can be observed. At high angle of attack the primary vortex breakdown and strongly alters the flow. The lift, drag and roll coefficients then undergoes large variations because the vortices become unstable and are inclined to undergo asymmetric oscillations [1-5]. This phenomenon is characterised by a sudden expansion of the vortical core and a rapid drop of the axial velocity. The lift coefficient is then highly correlated to the longitudinal location of the vortex breakdown point. The breakdown negative effects appear not only through the average performances, but also because the essential unsteady nature of the flow generate buffeting and loss of control. Accurate CFD simulations of these type of flow will help the designer and will also allow to evaluate efficient control means of large scale vortical structures.

In the following sections the present capabilities of elsA software are given before developing the work carried out for this application : mesh and computations. The results are compared with experimental data and the paper concludes with a discussion about future tasks.

16.2 NUMERICAL METHOD

All the simulations have been done with elsA (standing for "Ensemble Logiciel pour la Simulation en Aérodynamique"). It is a software package based on object-oriented (OO) solutions for fluid dynamics numerical simulation, created by combining the C++ language, for translating object concepts, with the Fortran language for implementing time-costly scientific computation methods. Python, a public domain interpreted object-oriented language is used for the interface.

The elsA software solves the compressible, three-dimensional Reynolds average Navier-Stokes equations in a cell centered finite-volume formulation from low subsonic to high supersonic velocities. Plane or axisymmetrical two- dimensional configurations can also be computed [6].

During this work three turbulence models have been used. These models are described briefly in the next chapter.

16.2.1 COMPUTATION GRID

The recommended domain places the outer boundary at 4 Root Chord (RC) upstream from wing apex, 6 RC downstream from wing apex, 5 RC up from wing apex, 5 RC down from wing apex and 4 RC spanwise from wing centerline.

The geometry of the model is the ONERA 70 degrees delta wing with a sharp leading edge.

A structured grid has been built with ICEM Hexa. This grid is a H-H mesh to fit between the model at zero incidence and the far field. It consists of 5 blocks after merging and the total number of point is 2520369. The size of the blocks are :

- 69 x 29 x 121 (lower wing block)
- 105 x 149 x 41 (downstream block)
- 69 x 97 x 121 (upper wing block)
- 37 x 149 x 29 (upstream block)

- 37 x 149 x 121 (lateral block)

The dimensions of the mesh are expressed in mm. The reference length is the root chord of the wing (950 mm). 121 points in chordwise direction and 69 in spanwise direction on the wing's upper and lower surface (fig. 1). Normal to the upper surface 97 points are distributed, while 29 exist normal to the lower surface. In front of the wing 37 points are distributed, while 41 points in x-direction formed the wake region. The lateral region is described by 37 points in spanwise direction. 17 points along the height of the trailing edge.

The refinements are concentrated around the model. The height of the first cell is 0.01 mm for the upper wall in order to reach a y^+ of approximately 1. For the other face the height of the first cell is 2 mm. The chordwise size moves around 10 mm (10 mm at wing apex and 7 mm at trailing edge). A refinement is installed at x/c equal to 0.65 (2 mm) to better capture the vortex breakdown. The size of the cells in spanwise direction decrease from 10 mm (wing centerline) to 2 mm (leading edge) along the trailing edge.

16.2.2 COMPUTATION METHOD

The set of ordinary differential equations in time is solved by means of the backward Euler scheme. An implicit phase is used for the convective terms. The viscous terms are treated with a LU factorization. The resolution of the turbulence equations are not coupled at the others, and the Harten's parameter is fixed at a small value (0.1) to achieve precision.

A upwind scheme (Roe) associated with a Van Leer's limiter is used to compute the fluxes. The combination of this last with the backward Euler resolution is very robust and run with a smaller memory than a 4-stage Runge Kutta scheme.

Due to the fact that only the steady state is of interest the different equations are solved by a local time stepping approach based on the maximum allowable time step for each cell (CFL number varies from 1.0 to 5.0 following turbulence model)

Since the convergence speed-up is an important issue, a multi-grid technique have been used to improve the convergence rates : (2 levels) with V cycle and two or three sub-iterations on the coarse grid.

Different turbulence models have been used for these simulations. In a first stage the two-equations model (Smith kl) has been used to determine the main problems of the CFD for this application. The results of these simulation are not presented since this model is not adapted for separated flows. In a second stage, two turbulence models specifically developed for vortical flows have been used : Spalart-Allmaras-rotation Correction model and Menter's Shear Stress Transport model.

The Spalart-Allmaras-rotation Correction (SARC) is the one equation model presented by Spalart and Shur to improve the basic SA model in presence of vortical flow. The production of turbulent viscosity is reduced in regions of high vorticity. This purpose is achieved by including a new destruction term in the modified vorticity of the SA model.

Menter's Shear Stress Transport model (SST) is a hybrid $k-\epsilon$ and $k-\omega$ turbulence model. The treatment in the near wall region is done with the $k-\omega$ and switch to $k-\epsilon$ in the wake region. The SST model becomes insensitive to the freestream value. Furthermore, the turbulent viscosity is limited with respect to the vorticity.

16.2.2.1 Hardware

ElsA is installed on several machines, but for this application all runs were performed on the NEC SX5 and the Compaq HPC320. 16 CPU at 8 Gflops are installed on the NEC SX5. The Compaq is composed of 24 CPU at 833 MHz (4 CPU by node). A single processor has been used for all calculations. The memory size varies from 2115 Mo to 2326 Mo following the turbulence model. The time per iteration varies from 8 s to 5 mn respectively for the NEC and the Compaq.

16.2.2.2 Initial and Boundary Conditions

In spite of the low preconditionning method, the present calculations have been made without this option due to the use of an upwinding scheme. Consequently the upstream conditions are the following : Mach number equal to 0.2, angle of attack equal to 27.0 degrees and Reynolds number based on the chord length is equal to 1.5 million. Since the Mach number has been changed the chord of the model has been shortened to 0.34 m to keep the correct Reynolds number. The total pressure is 101325 Pa and the total temperature is 300 K. For these conditions, the characteristics of the flow are : $U = 69.16$ m/s, $p_{\infty} = 98514$ Pa and $q_{\infty} = 2758$ Pa.

Initial conditions are those of the uniform flow

For this simulation, three kinds of boundary conditions have been considered : symmetry for the plane of symmetry, no slip and adiabatic boundary conditions for the wall and freestream conditions for the far field.

The calculations have been stopped at 4000 iterations and 5000 iterations respectively for SARC and SST models when the residus stop decreasing (fig. 2) and vortex breakdown location does not move.

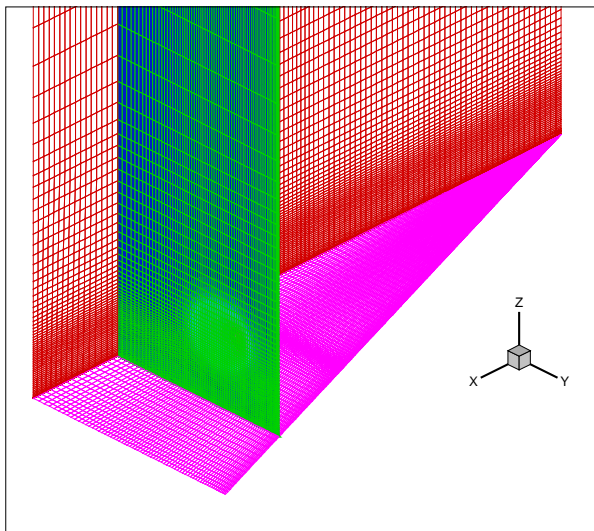


Fig. 1 : H-H mesh – upper block

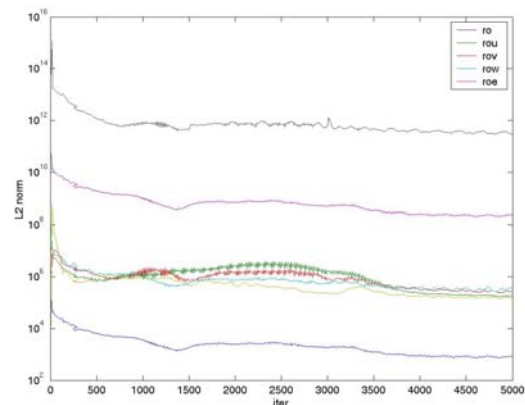


Fig. 2 : Residuals of conservative variables – SST

16.3 RESULTS

The numerical results are compared to the experiments reported and analysed by Mitchell [7].

In the computation, the vortex breakdown location is stable at 76 % of the wing chord with the SST model against 93 % of the wing chord with the SARC model.

Figures 3 to 12 present only the SST model results. The surface-pressure distribution on the delta wing is shown in figure 3. The footprints of the primary and the secondary vortex are clearly visible on the two figures.

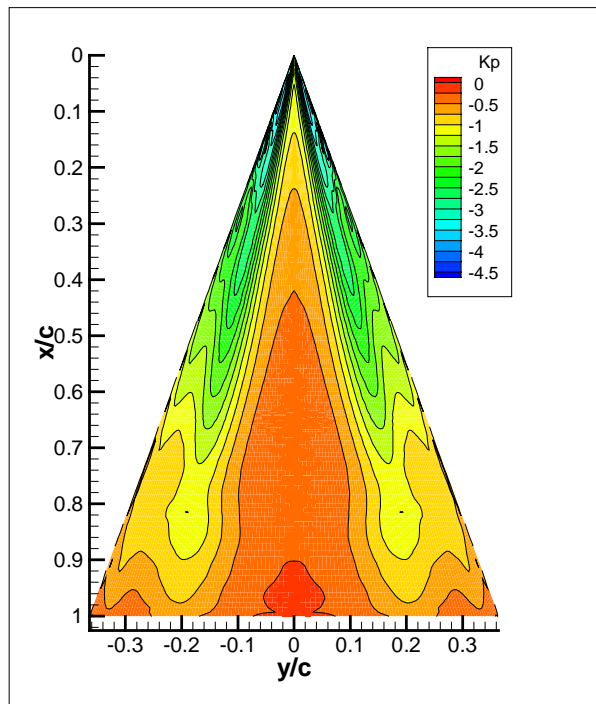


Fig.3 : Wing upper-surface pressure distribution

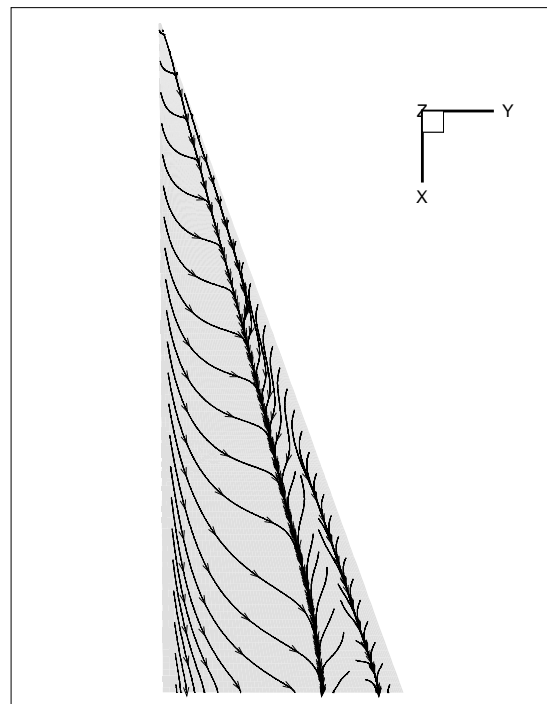
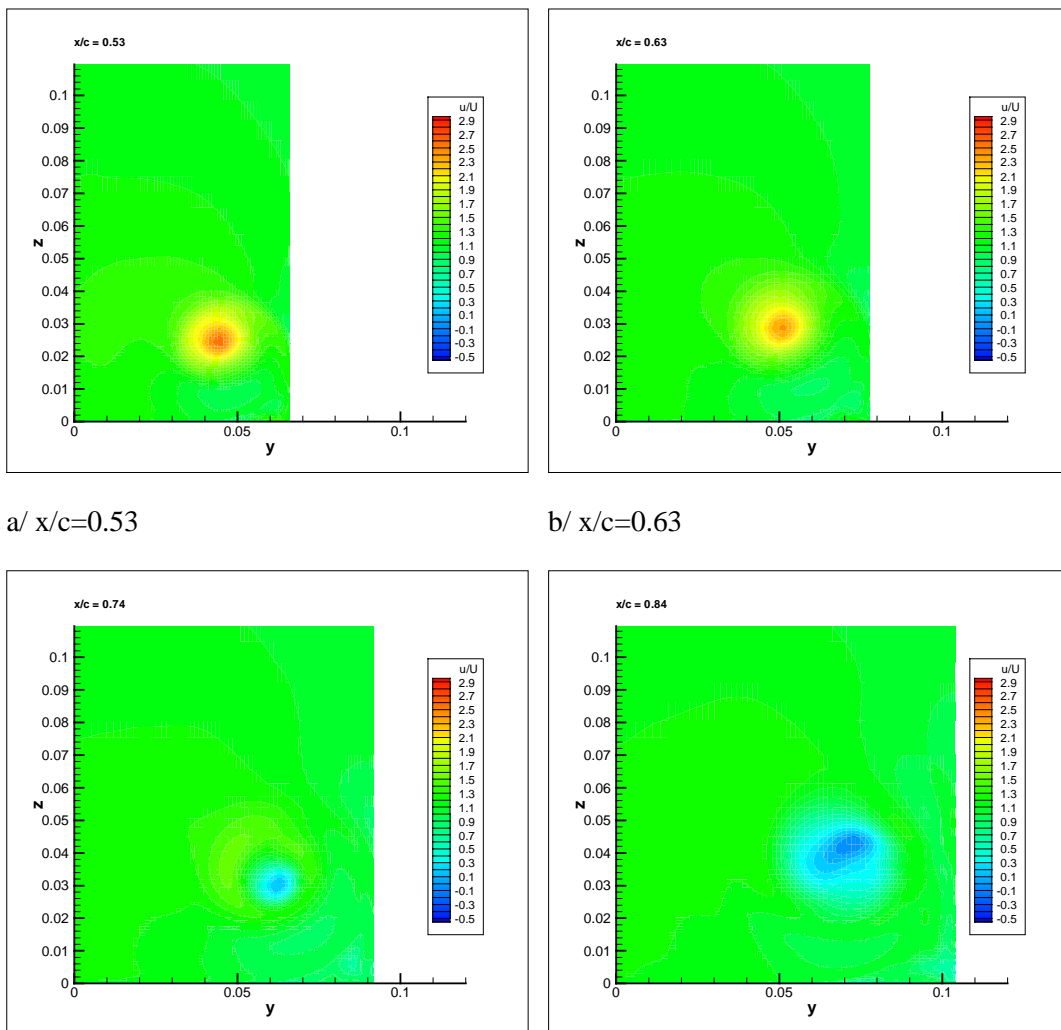


Fig.4 : Wing upper-surface streamline pattern

Figure 4 shows the surface skin-friction lines. The reattachment line of the primary vortices are in good agreement with the experimental data. The overall effect of the circulation around the primary vortex is evident in the downwash shown in the central area.

Next figures (fig.5 through 7) present a detailed velocity distribution of the leading edge vortex field in the vicinity of the vortex breakdown. For this reason, four planes normal to the wing upper-surface located at $x/c = 0.53, 0.63, 0.74$ and 0.84 have been plotted in term of nondimensionalized parallels and normal velocity component.

RANS SOLUTIONS OF 70° DELTA WING IN STEADY FLOW



a/ $x/c = 0.53$

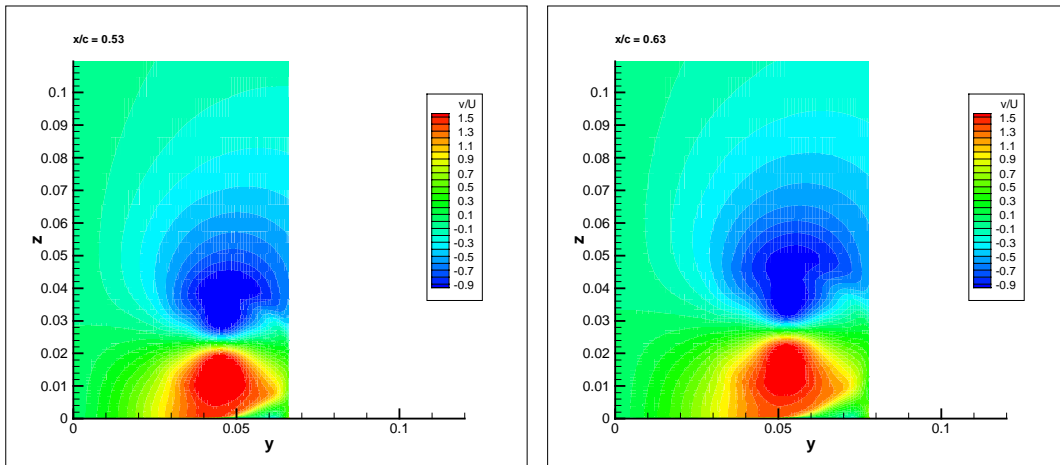
b/ $x/c = 0.63$

c/ $x/c = 0.74$

d/ $x/c = 0.84$

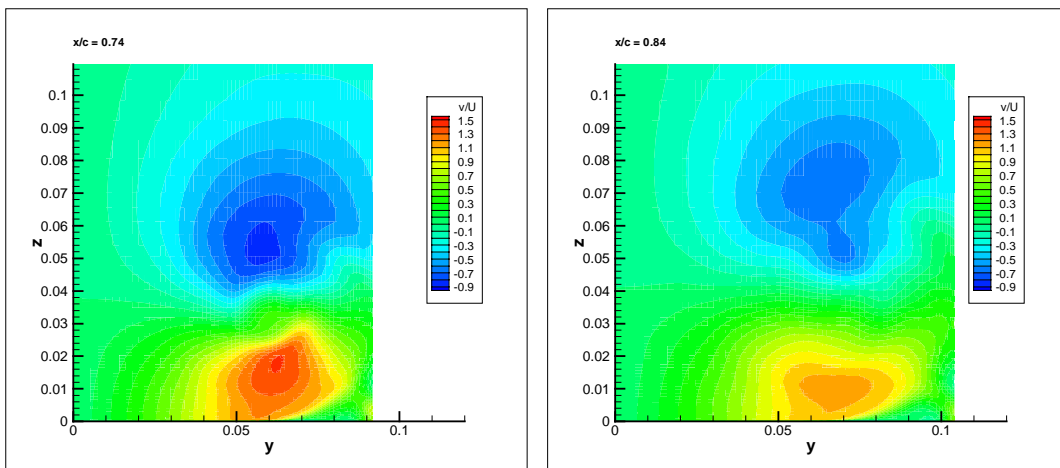
Fig.5 : Distribution of the mean u/U velocity component.

Upstream of the breakdown ($x/c = 0.53$) the longitudinal velocity component in the vortex is similar to a jet flow. The velocity peak occurs at the center of the vortex and is approximately 2.7 times freestream velocity. The indication that vortex breakdown is close to $x/c = 0.74$ is the sudden deceleration and the emergence of negative velocity at $x/c = 0.84$. Finally, a velocity defect coupled with a broadening of this region is observed at $x/c = 0.84$.



a/ $x/c=0.53$

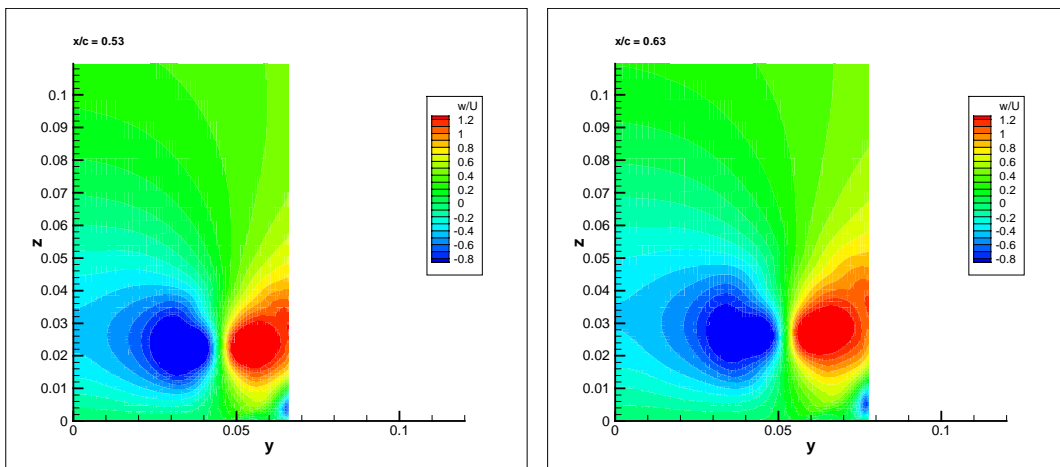
b/ $x/c=0.63$



c/ $x/c=0.74$

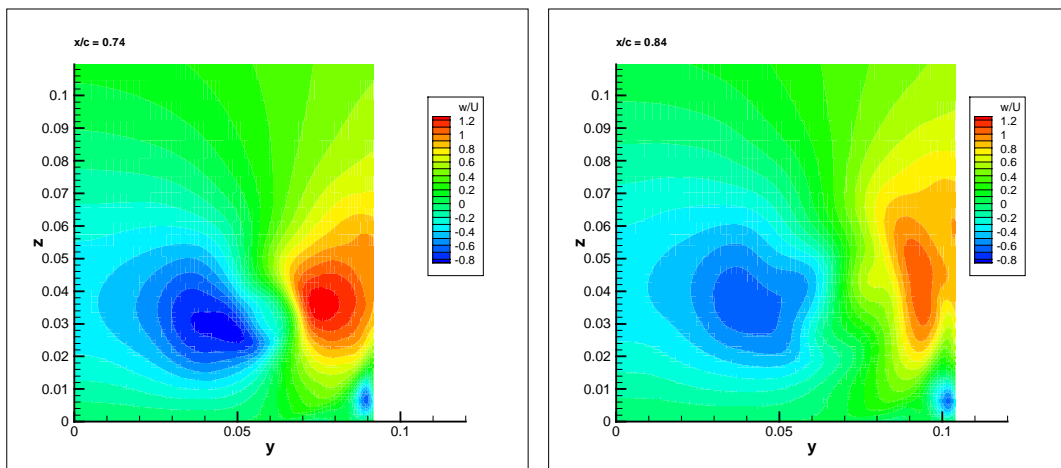
d/ $x/c=0.84$

Fig.6 : Distribution of the mean v/U velocity component



a/ $x/c=0.53$

b/ $x/c=0.63$

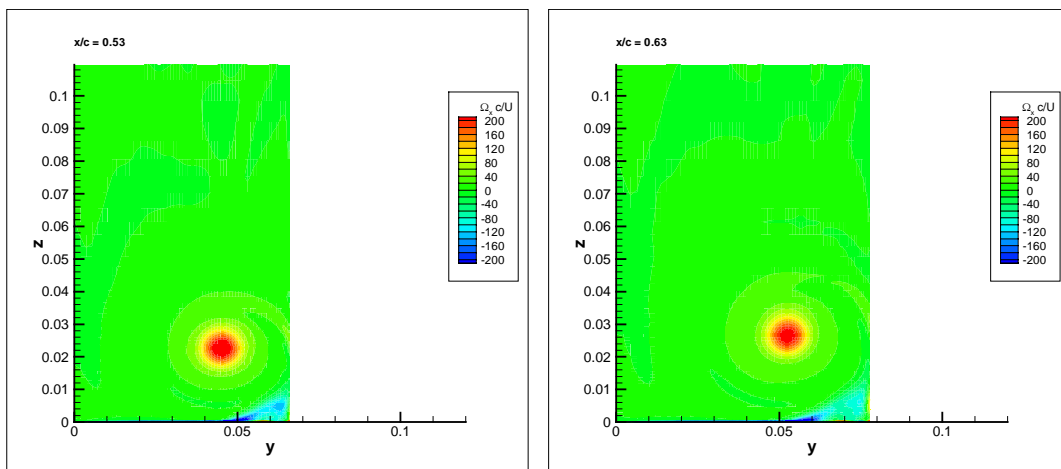


c/ $x/c=0.74$

d/ $x/c=0.84$

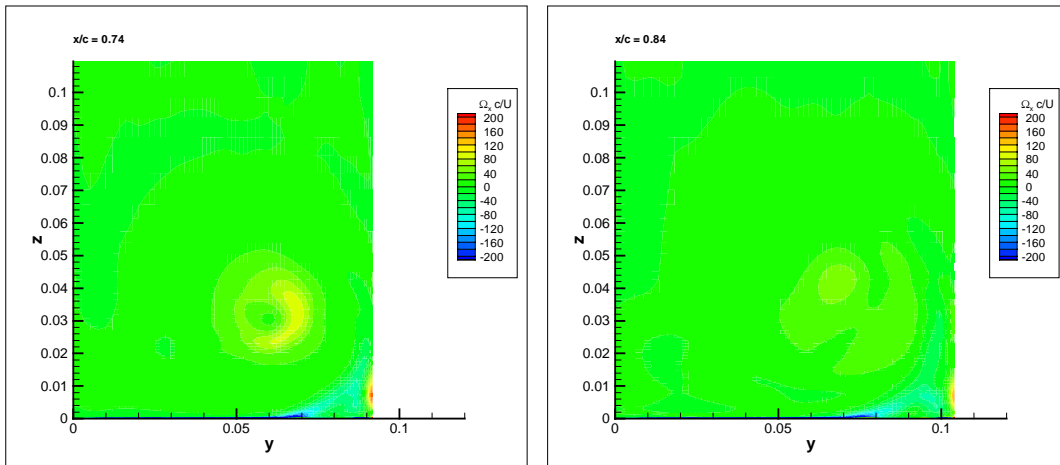
Fig.7 : Distribution of the mean w/U velocity component

The two other components show that the vortex is tightly rolled in a spiral motion upstream the vortex breakdown (large gradient). After the breakdown there is a reduction in the spanwise and normal components and a diffusion of the core.



a/ $x/c=0.53$

b/ $x/c=0.63$

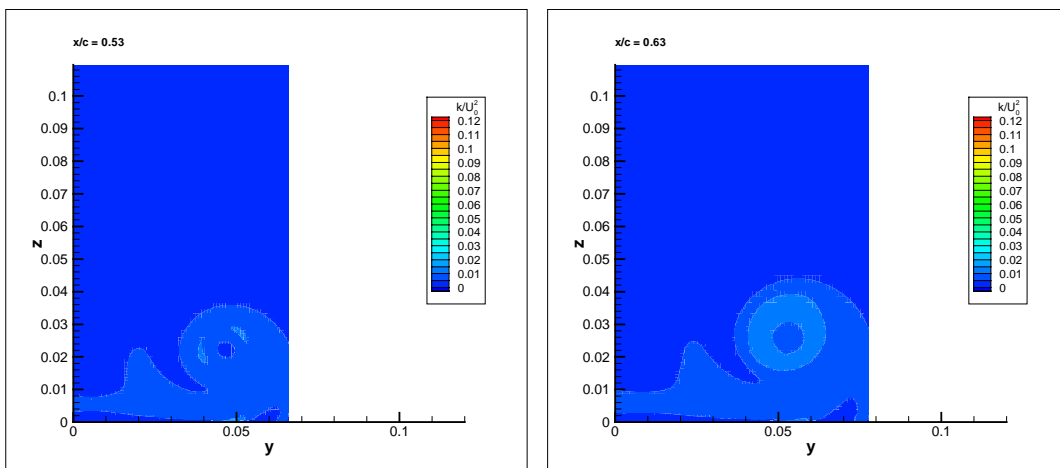


c/ $x/c=0.74$

d/ $x/c=0.84$

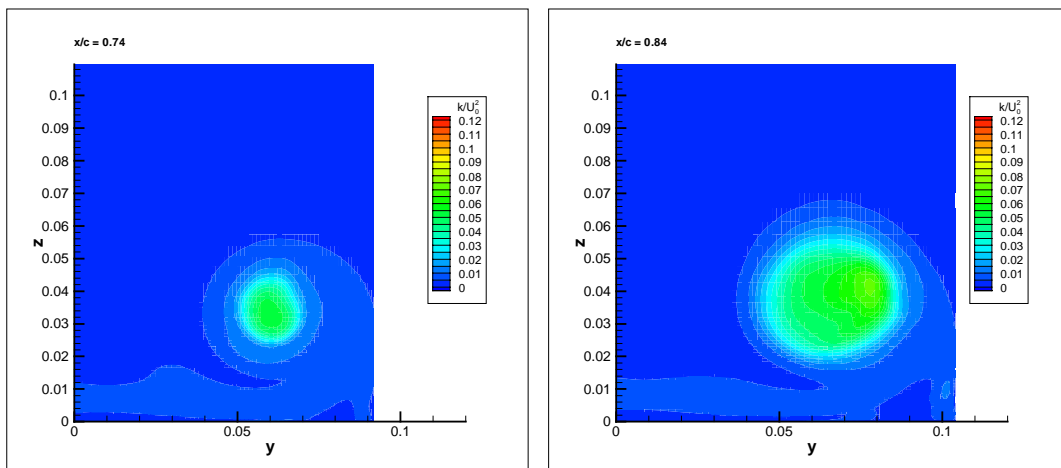
Fig.8 : Distribution of the axial-vorticity component

Figure 8 shows the x component of the vorticity and confirms the physics of the primary vortex with a high vorticity before the vortex breakdown and a significant decay downstream of this point.



a/ $x/c=0.53$

b/ $x/c=0.63$



c/ $x/c=0.74$

d/ $x/c=0.84$

Fig.9 : Distribution of the nondimensionalized turbulent kinetic energy

The comparison of turbulent kinetic energy with experimental data, not presented here, shows a huge difference (rate of about 5). Contrary to experimental behaviour that show rather intense turbulent kinetic energy peak at vortex breakdown location and decrease downstream, the computation shows a maximum of turbulent kinetic energy downstream vortex breakdown location. It appears that the behaviour of the turbulent kinetic energy along the vortex line seems to be difficult to reproduce by the computations.

The next investigations are done in a plane across the primary vortex.

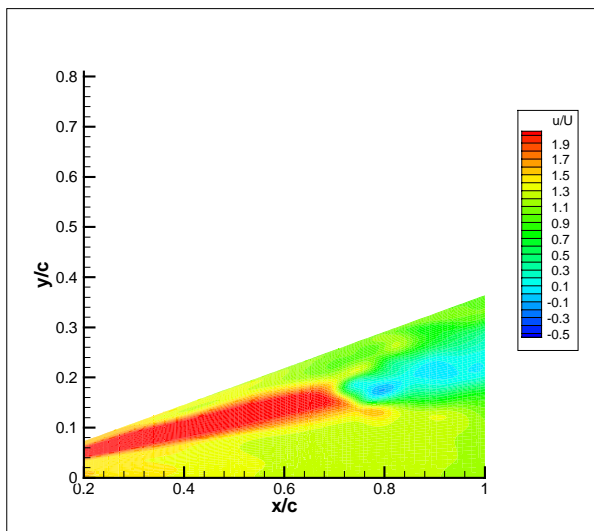


Fig.10 : Distribution of the mean u/U velocity component in the vortex plan

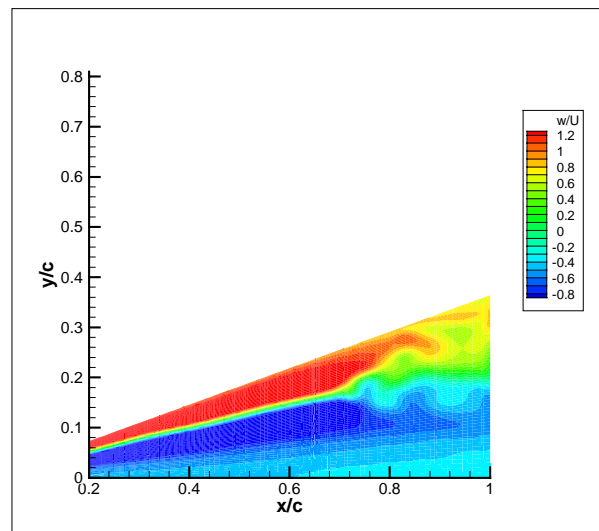


Fig.11 : Distribution of the mean w/U velocity component in the vortex plan

These two figures allow us to visualize the vortex breakdown effects. Along the vortex line the variations of the u/U velocity component are quite important. This component changes from a value greater than 2.7 to a negative value. The point where the longitudinal velocity is zero is located at 76 % of the wing chord. The other velocity component w/U shows a large expansion of the core delimited by a chaotic border.

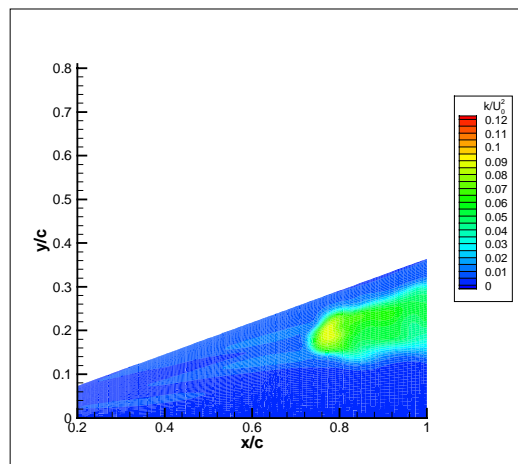


Fig. 12 : Distribution of the turbulent kinetic energy in the vortex plan.

Figure12 gives an other point of view of the production of turbulent kinetic energy downstream the vortex breakdown.

Four line plots at chordwise station $x/c = 0.53, 0.63, 0.74$ and 0.84 are presented in figure 13. The calculated pressure are compared with experimental data for the two models tested.

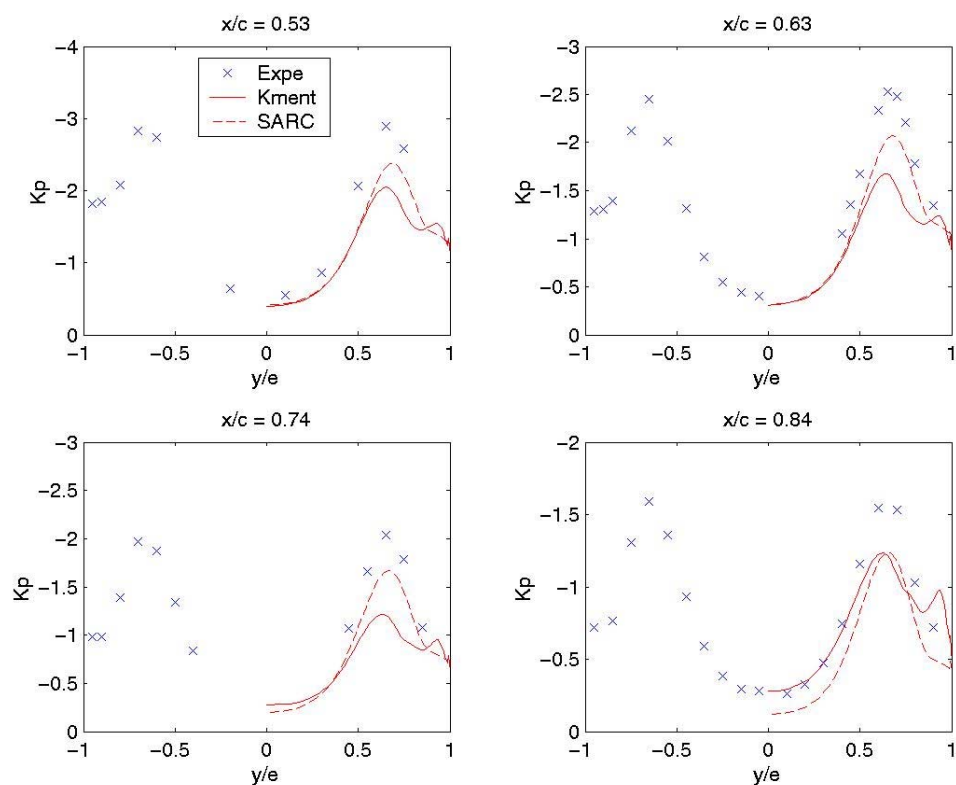


Fig.13 : Comparison of pressure distribution along four stations

Pressure levels are underestimated under the vortex for all stations. This set of figures shows that the leading edge vortex axis location is in accordance with the experimental data for the two models. The SST model produces a strong secondary vortex which has two effects on the primary vortex : it reduces its intensity and induces an inboard displacement in the rear part. The effect of the secondary vortex is too strong and the primary vortex is too weak with the SST model. The SARC model gives a better pressure distribution than the two-equations model.

16.4 CONCLUSION

The flow over a delta wing at high angle of attack is exceedingly complex, including separated flow, high streamwise vorticity and large pressure gradient. Viscosity promote a secondary vortex and influence the location of the vortex breakdown which is difficult to calculate.

The general structure of the flow with the primary and the secondary vortices and the primary vortex breakdown, is in relatively good agreement with experimental data. However, the pressure distribution on the wing and for the turbulent kinetic energy are not well predicted.

As a result, many efforts remain to do to get an accurate simulation. Several ways should be explored to determine a compromise between cost and numerical accuracy needs. In steady flow, it seems interesting to test an effect of mesh density and introduce a new capability to compute a laminar flow areas. Grid refinements can be done in high gradient area like the mixing layer and the vortex core. This will be useful to evaluate the required discretization of the domain and allow a better resolution of the scheme used in present time. The modelisation can also be improved by a combination of the SARC or SST model and laminar zone before the boundary layer transition. This could improve the location of the vortex breakdown (the transition is observed at 40 % in the experiments). Finally, the flow being unsteady, it would be interesting to try also different unsteady computational approaches (URANS, LES , DES).

16.5 REFERENCES

- [1] Anglin E.L. and Satran D.
Effects of spanwise blowing on two fighter airplane configurations.
Journal of Aircraft, Vol 17, n° 12, Dec 1980, pp. 883-889.
- [2] Miyagi K., Fujii K. and Karashima
Enhancement of the leading edge separation vortices by the trailing edge lateral blowing.
AIAA paper 94-0181, 1994.
- [3] Gu W., Robinson O. and Rockwell D.
Control of vortices on a delta wing by leading edge injection.
AIAA journal, Vol 31, n° 7, Jul. 1993, pp. 1177-1186.
- [4] Rediniotis O.K., Stapountzis H. and Telionis D.P.
Periodic vortex shedding over delta wing.
AIAA journal, Vol 31, n° 9, Sep. 1993, pp. 1555-1561.
- [5] Menke M., Yang H. and Karashami
Experiments on the unsteady nature of vortex breakdown over delta wings.
Exp. Fluids, pp. 262-272, 1999.
- [6] Cambier L. and Gazeix M.
elsA : An efficient Object-Oriented Solution to CFD complexity.
40th AIAA Aerospace Science Meeting and Exhibit. Reno (USA), January 14-17, 2002.
- [7] Mitchell A.
Caractérisation et contrôle de l'éclatement tourbillonnaire sur une aile delta aux hautes incidences.
ONERA NT 2000-6.

Chapter 17 – STEADY RANS SIMULATIONS OF A 70° DELTA WING – WITH TUNNEL EFFECTS

M. R. Allan, K. J. Badcock, G. N. Barakos, and B. E. Richards

*Computational Fluid Dynamics Laboratory,
Department of Aerospace Engineering,
University of Glasgow,
G12 8QQ, United Kingdom.*

May 14, 2003

Abstract

This paper considers steady RANS simulations of the ONERA 70° delta wing. RANS simulations of the wing inside the ONERA F2 tunnel have been validated against experimental data. The tunnel simulations and simulations with farfield conditions have shown variations in the position of vortex breakdown and vortex strength. When a delta wing is placed in wind tunnels breakdown is observed to move upstream. The secondary separation line was also observed to move outboards. Support interference effects were also considered. It was observed that with a fairly large support downstream of the wing, vortex breakdown can be delayed due to blockage effects, if the vortices do not impinge on the support. This was observed to be the case for smaller supports also.

Nomenclature

S/W	Wing span (S) to tunnel width (W)	S/H	Wing span (S) to tunnel height (H)
c_r, c	Root chord	C_P	Pressure coefficient
M_∞	Freestream Mach number	U_∞, U_o	Freestream velocity
x	Chordwise distance	η	Spanwise distance / local span
ϕ	Helix angle	Γ	Circulation

17.1 Introduction

Wind tunnels are used to test the aerodynamic characteristics of aircraft in the research and development stages. However, the influence of the tunnel walls must be taken into account when considering test results. Historically, wind tunnel corrections have been based on Linear Potential Flow Theory [1]. To obtain good quality and reliable test data, factors relating to wall interference, flow angularity, local variations in velocity, and support interference, must be taken into account. Karou [2] found that for delta wings with aspect ratio equal to one and spanning up to half the tunnel width, classical wall correction techniques can be used to correct flow field and force results up to 30° angle of attack (it should be noted that vortex breakdown was unlikely to be present over the wing). Also, for swept wings with a blockage ratio (ratio of model planform area to tunnel cross-sectional area) of less than 0.08, tunnel interference effects can usually be considered negligible [3].

Clearly, the flow conditions within a wind tunnel will be different to those a wing would experience in free air. The interactions between the wing and wall flow fields induce longitudinal and lateral variations (streamline curvature and aerodynamic twist respectively) to the freestream, in addition to those attributed to the wing alone. These differences may result in a reduction in the average downwash experienced by the model, a change in the streamline curvature about the model, an alteration to the local angle of attack along the span of the model, a change in dynamic

pressure about the model due to solid and wake blockage, and in the buoyancy effect due to the axial pressure gradient along the tunnel test section. The magnitude of these effects increases with model size (increasing solid blockage).

Weinberg [4] conducted an experimental investigation into wall effects. He tested two sets of three wings (one set with 60° sweep, and one set with 70° sweep), each wing with a different span size. The experiment was performed in a square water tunnel (low Re) at a constant flow velocity of 11m/s. The tunnel size was 45cm x 45cm. He found that for the three wings with 70° sweep, as the wing size was increased (kept at a constant angle of attack), vortex breakdown moved downstream. For the three wings with 60° sweep, he found that as the wing span-to-tunnel width ratio increased from 0.175 to 0.35, the wall effects followed the computed trends (i.e. vortex breakdown was shifted downstream with increasing wing size). However, when the wing span-to-tunnel width ratio was increased from 0.35 to 0.7, no significant change was observed. This suggested that effective camber was not the only influence. For both the 60° and the 70° wings, the difference in breakdown location observed from the smallest model to the largest model, was of the order $25\%c_r$.

Thompson and Nelson [5] investigated experimentally the influence of tunnel walls on a 70° delta wing by testing full, two thirds, and half scale models in a square tunnel (the largest model gave the ratios $S/H = S/W = 0.364$). Due to a steady hysteresis effect the wing was tested for a quasi-steady upward and downward stroke. It was found that for the smallest model tested ($S/H = S/W = 0.124$) the breakdown location shifted downstream by as much as $15\%c_r$ on both the quasi-steady upstroke and downstroke. For the half scale model and the full scale model, there appeared to be little difference in the breakdown locations. As stated by Thompson and Nelson, this shift downstream as model size is decreased is in contrast to the results of Weinberg [4]. It was noted that Weinberg used a Reynolds number an order of magnitude lower, and a constant velocity, as opposed to keeping the Reynolds number constant (as in the experiments of Thompson and Nelson). It was observed that the vortex suction on the model surface increased with model size.

More recently Pelletier and Nelson [6] studied the effect of tunnel interference on 70° delta wings. Experiments were conducted in a water tunnel with three different sized wings. These low Reynolds number tests agreed with the previous findings of Thompson and Nelson [5] who tested at higher Reynolds number, in that breakdown moved towards the apex with increasing wing size. Pelletier and Nelson used the method of images to explain this effect, concluding that the tunnel walls increased the mean incidence of the wing, thus promoting breakdown.

Verhaagen et al. [7] performed Euler calculations of the flow over a 76° delta wing inside wind tunnels of increasing size. The wing span-to-tunnel width ratios considered were 0.292, 0.389, and 0.584 and the test section was octagonal. To model the effect of a secondary separation, a small "fence" was placed where secondary separation would occur. It was found that decreasing the tunnel size (increasing the wing span-to-tunnel width ratio) increased the suction in the vortices and increased the velocities in the vortex core, due to an increase in circulation with decreasing tunnel size.

Allan et al. [8][9] performed Euler simulations of tunnel interference effects on a 65° delta wing in various tunnels for static and pitching cases. It was observed that tunnel side walls were the most influential factor on breakdown location, with roof and floor having little effect. It was also noted that in pitching simulations, the tunnel interference effects were strongest on the downstroke, during the vortex reformation.

When considering support interference effects Hummel [10] observed that the presence of an obstacle one chord length downstream of the trailing edge of a delta wing caused vortex breakdown to shift towards the apex by up to $40\%c_r$. The obstacle considered was unrealistically large (wider than the span of the delta wing), however, this early observation highlighted the possible effects that support structures can have. Recently Taylor et al. [11] varied the position of various obstacles behind the wing's trailing edge to find the effect support proximity had on vortex breakdown. It was concluded that when an obstacle was placed in the vortex core, breakdown was promoted due to the adverse pressure gradient which formed in front of the obstacle. As the obstacle was moved away from the vortex core, breakdown was observed to move downstream. It can be expected that the degree of support interference will be dependent on support size, vortex strength and trajectory. Although possibly not considered as support interference, fuselages on delta wing models

can effect the breakdown location. Some sting mounted tunnel models have upper surface fuselages to connect the model to the sting. The effect of such fuselages has been considered in a number of investigations, each of which have shown significant variations in breakdown location for a given sweep angle and incidence. See for example [12][13][14]. A possible reason for the variation in the breakdown locations was given by Ericsson [13] in which the effect of the fuselage was described as an induced camber effect. The induced camber effect alters the location of vortex breakdown, either delaying or promoting breakdown depending on the fuselage.

Three dimensional Navier-Stokes computations are necessary to correctly predict the complex leeward side flow characteristics of delta wings. The work of Allan et al. [8] presented the effect of wind tunnel wall interference on delta wing aerodynamics, where Euler simulations were used to predict the wall effects. The work of the current paper discusses RANS simulations of tunnel wall interference and downstream support structure effects on a 70° delta wing, and can be considered an extension of the previous Euler simulations.

17.2 Computational Method

All simulations described in this paper were performed using the University of Glasgow PMB3D (Parallel Multi-Block 3D) RANS solver. A full discussion of the code and turbulence models implemented is given in [15]. PMB3D uses a cell centered finite volume technique to solve the Euler and Reynolds Averaged Navier-Stokes (RANS) equations. The diffusive terms are discretised using a central differencing scheme and the convective terms use Roe's scheme with MUSCL interpolation offering third order accuracy. Steady flow calculations proceed in two parts, initially running an explicit scheme to smooth out the flow solution, then switching to an implicit scheme to obtain faster convergence. The pre-conditioning is based on Block Incomplete Lower-Upper (BILU) factorisation and is also decoupled between blocks to help reduce the computational time. The linear system arising at each implicit step is solved using a Generalised Conjugate Gradient (GCG) method. For time-accurate simulations, Jameson's pseudo-time (dual-time stepping) formulation is applied, with the steady state solver used to calculate the flow steady states on each physical time step (discussed fully in [15]).

Since the RANS equations are solved the 2 equation $k-\omega$ model is used for closure. It is well known that most linear 2-equation turbulence models over-predict the eddy viscosity within vortex cores, thus causing too much diffusion of vorticity [16]. This weakens the strength of the vortices and can eliminate secondary vortices, especially at low angles of attack where the vortices are already weak. The following modification suggested by Brandsma et al. [17] was therefore applied to the standard $k-\omega$ model of Wilcox [18] to reduce the eddy-viscosity in vortex cores.

$$P_k = \min\{P_k^u, (2.0 + 2.0\min\{0, r - 1\})\rho\beta^*k\omega\} \quad (1)$$

Here P_k^u is the unlimited production of k , P_ω^u is the unlimited production of ω , and r is the ratio of the magnitude of the rate-of-strain and vorticity tensors. When k is over predicted in the vortex core, it will be limited to a value relative to the dissipation in that region. This modification was found to improve predictions compared with the standard $k-\omega$ turbulence model [9].

The Computational Fluid Dynamics Laboratory at the University of Glasgow owns a cluster of PC's. The cluster is known collectively as Jupiter and is fully described by Badcock et al. [15]. There are 32 nodes of 750MHz AMD Athlon Thunderbird uni-processor machines, each with 768Mb of 100MHz DRAM. MPI (Message Passing Interface) is used to link up multiple nodes to create a virtual machine, which is used to execute computationally demanding problems. PMB3D balances the node loadings (number of cells per node) by spreading the blocks over all the nodes of the virtual machine. Halo cell values are passed between adjacent blocks using MPI.

17.3 Test Case: ONERA 70° Wing

The subsonic case of a 70° delta wing is considered at 27° angle of attack. At this incidence vortex breakdown is occurring over the wing. The wing has a root chord length of 950mm, a trailing edge length of 691.5mm, flat upper and lower surfaces, and a leading edge bevel of 15° . The wind tunnel model had a blunt trailing edge 20mm thick which has been beveled (15° bevel) in

Tunnel	S/W	S/H	M_∞	Re
Farfield	-	-	0.2	1.56×10^6
ONERA F2	0.49	0.38	0.2	1.56×10^6
S/W = 0.63	0.63	0.38	0.2	1.56×10^6

Table 1: ONERA 70° wing test cases

the computational model to simplify grid generation. Experimental data was obtained by Mitchell [19]. The wing was tested in the ONERA F2 tunnel (situated at Le Fauga-Mauzac Center, near Toulouse, France) which has a working section of height 1.8m, width 1.4m, and length 5m. It is a subsonic, continuous, closed-return tunnel. The wing was also tested in the ONERA S2Ch tunnel situated at the Chalais-Meudon Centre (ONERA) which is of quasi-circular cross-section with a diameter of 3m and a test section length of 4.93m. The model/tunnel ratios are S/W=0.49 and S/H=0.38 for the ONERA F2 tunnel, and S/W=0.23 and S/H=0.55 (taking into account off tunnel centreline location of wing) for the ONERA S2Ch tunnel. Despite the flow conditions being similar in both tunnels, the mean breakdown locations were closer to the apex in the ONERA F2 tunnel (the smaller of the two), when compared with those measured in the ONERA S2Ch tunnel. This suggests some test facility interference, which could be due to either the support structure or tunnel wall interference.

The flow conditions for which extensive experimental data from the ONERA F2 tunnel are available are an incidence of 27°, Reynolds number of 1.56×10^6 , and a freestream velocity of 24m/s ($M_\infty = 0.069$). For these flow conditions, flow visualisation of velocity components, vorticity components, turbulent kinetic energy components and local static pressure are available in various planes. Vortex breakdown locations were also obtained based on where the axial component of velocity becomes negative. In the simulations the Reynolds number has been matched, however the Mach number is 0.2, compared with the lower Mach number of 0.069 in the experiment. Since the current work is based on a high speed flow solver, a freestream Mach number of 0.2 was used to avoid any possible convergence issues. Transition was observed to occur at around 40% c_r in experiment, however the CFD simulations assume a fully turbulent flow.

Three boundaries have been chosen. The first has the wing in free air (farfield), the second represents the ONERA F2 tunnel, and the third the ONERA F2 tunnel side walls brought closer to the wing (increasing the S/W ratio). Full details of these configurations as well as flow parameters can be found in Table 1.

To try and assess the effects of support structures a vertical generic support was placed in the centre of the ONERA F2 tunnel downstream of the wing. Since supports in dynamic testing tend to be fairly large (driving mechanisms must also be housed) a thick support cross-sectional area was chosen. The generic support considered is a cylinder with a straight taper in the downstream direction. Figure 1 shows the support structure and dimensions. To avoid grid generation complications, the support attaching the wing to the vertical support is omitted. It may be expected that there is some interference from this mounting. The downstream support gives a frontal area blockage of around 12%.

The support was placed at two locations in the ONERA F2 tunnel case, at 0.5 c_r and 1 c_r from the trailing edge of the wing. The grids over the wing used for the support interference simulations are identical to those for the ONERA F2 tunnel without supports. Therefore there is no change in grid resolution in the vortical region above the wing. The ONERA F2 tunnel mesh was altered downstream of the wing to allow the presence of the support. In all cases the tunnel walls have been modelled with an inviscid wall boundary condition, and in the support structure simulations the supports have also been modelled with an inviscid wall boundary condition. Neglecting wall and support structure boundary layers reduces the mesh sizes significantly.

17.4 Computational Grids

The ONERA 70° wing inside the ONERA F2 tunnel is considered. A depiction of the grid around the ONERA 70° wing is given in figure 2. The mesh is of H-H topology with only half the

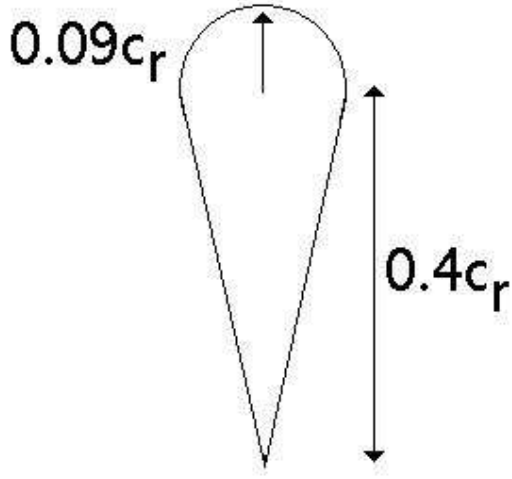


Figure 1: *Support geometry and dimensions.*

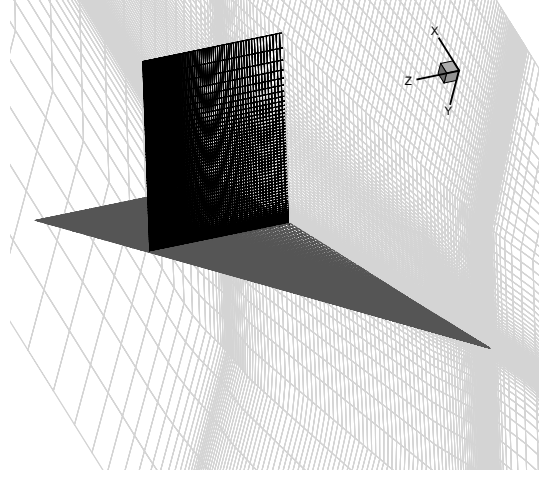


Figure 2: *ONERA 70° wing, View of ONERA F2 tunnel mesh.*

wing modelled, and the wing has been meshed at 27° . The tunnel grids have been extracted from the “farfield” grid by removing outer blocks so that the mesh resolution over the wing is identical in each case. The first cell height normal to the wing surface is $10^{-6}c_r$. This yields an average y^+ value of less than 1.0. The mesh sizes are given in Table 2. All grids had 99 points streamwise and 79 points spanwise over the wing.

Test case	Normal to upper surface	Total
Farfield	117	3,969,810
ONERA F2	103	2,904,660
S/W=0.63	103	2,664,090

Table 2: Viscous grid dimensions.

17.5 Verification and Validation

In order to validate and assess the predictions of the modified $k-\omega$ model, the ONERA 70° wing inside the ONERA F2 tunnel is considered. In order to attempt to verify the accuracy of the solutions, a limited grid dependency study has been conducted. Due to the high computational cost of solving the flow with the fine grid, only a comparison with the coarse grid solution is presented. The “coarse” grid is created by extracting a level in each direction from the standard grid. The upper surface pressure distributions are given in figure 3. The breakdown locations from the coarse and standard grids are $59.6\%c_r$ and $64.7\%c_r$ respectively. Clearly as we go from the coarse to standard grids the suction peaks increase in strength and vortex breakdown moves downstream.

Flow visualisation of the solutions indicates that a grid refinement increases the core properties (higher suction, higher axial velocities, higher vorticity) and increases turbulence levels within the vortex. Clearly as breakdown is delayed going from the coarse to the standard grid, the increase in the core properties is dominant over the dissipation of kinetic energy in the vortex, allowing the core flow to negotiate the adverse pressure gradient a little further. It should be noted that Visbal and Gordnier [20] observed for simulations on a 75° delta wing at 25° angle of attack, with Reynolds number equal to 2×10^6 , and freestream Mach number of 0.2, that on a coarse grid (H-H topology) vortex breakdown was located upstream to that computed on a finer grid. Since the grids used for the tunnel calculations have been extracted from a common farfield grid, the grid dependency of each solution will be similar. As such, despite the fact that further refinement of the vortices is required (which is not currently feasible due to computing limitations), the grid dependency is

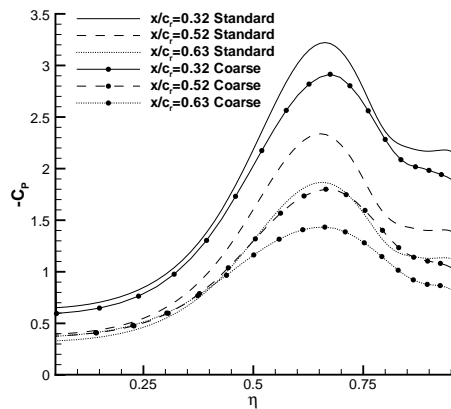


Figure 3: *Dependency of upper surface pressure distribution with grid refinement.*

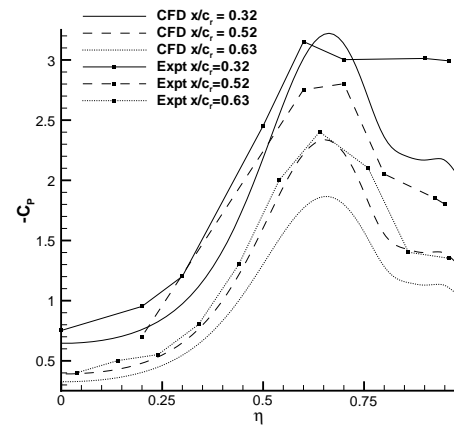
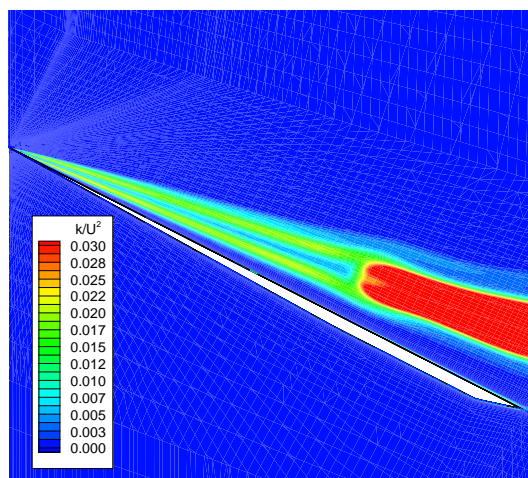
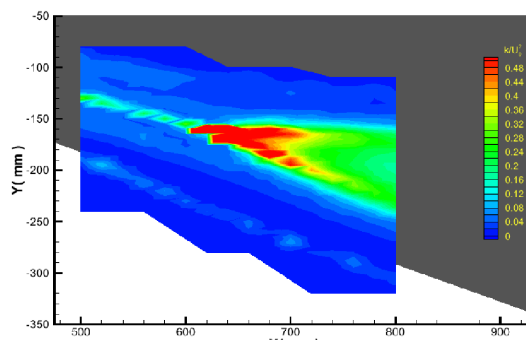


Figure 4: *Comparison of upper surface pressure distribution with experiment.*



(a) CFD



(b) Experiment

Figure 5: *Distribution of turbulent kinetic energy through the vortex core.*

equal for all cases, and therefore solution to solution comparisons for tunnel effects is still valid.

In all solutions the mean flow residual converged at least four orders of magnitude. If we look at the upper surface pressure distributions at the chordwise stations of $x/c_r = 0.32$, 0.52 , and 0.63 (figure 4), we see reasonable agreement of the experimental and predicted flow structures, with the presence of a primary and secondary vortex. It is also clear that the strength of the vortex footprint in the chordwise direction reduces faster in the CFD solutions in comparison to experiment. This may be due to the vertical position of the vortex being poorly predicted (possibly due to the laminar / turbulent transition in experiment varying the position of the vortex core), or that the grid resolution is insufficient. It should be noticed that the H-H mesh topology expands the cell sizes in the chordwise direction along a delta wing. However, in general the upper surface pressure distributions are predicted well especially close to the apex. The suction levels near the apex (where the flow is highly resolved) compare well with experiment, despite the strength of the secondary vortex possibly being under-predicted. It should be recalled, however, that in the experiment the flow is laminar until around $40\%c_r$, which may explain the weaker secondary vortex near the apex (due to turbulence effects). Further downstream, the structure of the vortex is visible despite the vortex footprint weakening faster in comparison to experiment.

The distribution of turbulent kinetic energy along a vertical slice through the vortex core is given in figure 5. It should be noted that the turbulent kinetic energy from the CFD solution is the modelled turbulent kinetic energy and is therefore expected to be lower than in experiment. Also shown is the experimental turbulent kinetic energy distribution which is “zoomed in” near the breakdown region. The effect of the production of k limiter can be seen in the vortex core region

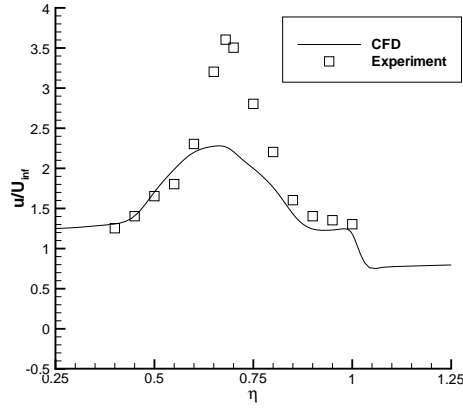


Figure 6: Comparison of axial velocity distribution through vortex core ($x/c_r=0.53$).

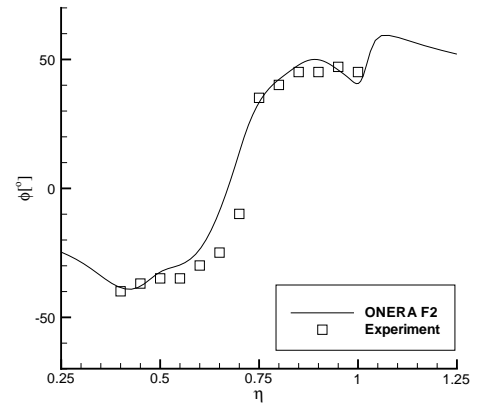


Figure 7: Comparison of helix angle distribution through vortex core ($x/c_r=0.53$).

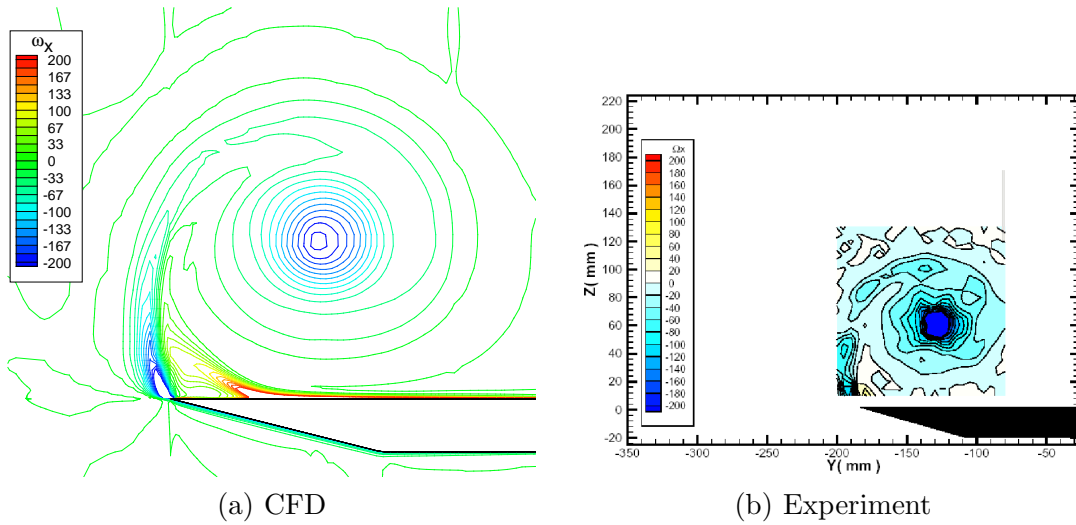


Figure 8: Distribution of axial vorticity through the vortex core.

where the turbulence levels are reduced. It is also clear there is a large generation of turbulence near the apex, which is laminar in experiment. This may account for the lower secondary suction peak in the CFD solution in figure 4 at the $x/c_r=0.32$, when compared with experiment.

The distribution of axial velocity through the vortex core at the chordwise station of $x/c_r=0.53$ is given in figure 6. It is evident that the velocity peak in the core region is poorly predicted, being around 35% lower than in experiment. This is likely to be due to an insufficient resolution of the vortex core region, which is also indicated by the gradient at which the core velocity rises towards the peak.

The helix angle, defined as

$$\phi = \tan^{-1} \left[\frac{w}{u} \right] \quad (2)$$

found in experiment and predicted by CFD are shown at the chordwise station of $x/c_r=0.53$ in figure 7. Comparing the results we see that near the edge region of the vortex the CFD solution compares well with experiment. However, as the core is approached the predictions become poorer. This is likely to be due to the poor prediction of the core properties as seen in figure 6.

The distributions of the ω_x component of vorticity from the CFD solutions and experiment, at the chordwise location of $x/c_r=0.52$, are shown in figure 8. As can be seen the core vorticity levels are predicted well indicating that the vortex strengths are predicted reasonably.

The previous discussion indicates that a better resolution of the vortex core region is required to improve the accuracy of the core predictions. However generally the structure of the vortex is well predicted and as such the effects of tunnel interference can be addressed using the current method.

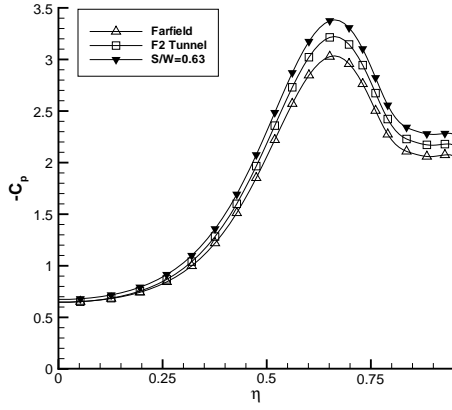


Figure 9: Comparison of upper surface pressure distributions, $x/c_r = 0.32$.

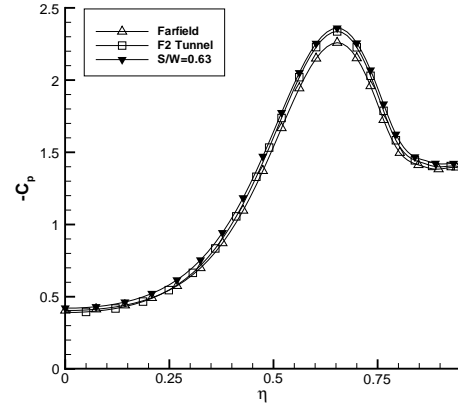


Figure 10: Comparison of upper surface pressure distributions, $x/c_r = 0.52$.

As discussed in the test cases section, a constant discretisation of the domain is used therefore any grid dependence effects will be common to all solutions, and as such differences will be due to boundary conditions (tunnel walls and wall locations).

17.6 Tunnel Effects – No Support

In order to obtain the breakdown locations above the ONERA 70° wing, the location at which the axial component of velocity becomes zero was used. This is consistent with the method used in experiment. To achieve this, a vertical slice through the vortex core was taken and the point where the axial velocity becomes zero was measured. The breakdown locations for the three test cases are given in Table 3.

TUNNEL	S/W	S/H	Breakdown Location
Farfield	-	-	68.8% c_r
ONERA F2	0.49	0.38	64.7% c_r
S/W=0.63	0.63	0.38	60.3% c_r
Experiment			
ONERA F2	0.49	0.38	65±5% c_r
Experiment			
ONERA S2Ch	0.23	0.55	≈72% c_r

Table 3: Summary of steady breakdown locations for ONERA 70° wing at 27° angle of attack.

The promotion of vortex breakdown is comparable in magnitude (though a little lower) to the promotion of vortex breakdown seen experimentally when going from the larger ONERA S2Ch tunnel to the smaller ONERA F2 tunnel. It should be kept that support effects have been omitted in the CFD solutions. As in the Euler simulations of Allan et al. [8], increasing the S/W ratio has the effect of promoting vortex breakdown. Allan et al. found that for a 65° sweep delta wing in various wind tunnels, side wall proximity promoted vortex breakdown and roof and floor proximity had little or no effect. This was confirmed with subsequent RANS simulations [9].

Figures 9 to 11 show the spanwise surface pressure distributions at the chordwise locations of $x/c_r = 0.32$, $x/c_r = 0.52$, and $x/c_r = 0.63$ respectively. Examination of the secondary separation location (taken to be where the spanwise shear stress component changes sign) indicates that the presence of wind tunnel walls causes the secondary separation line to move outboard, with the displacement increasing in extent in the chordwise direction. The reason for this is discussed later. When the flow is confined by the ONERA F2 tunnel, the primary suction peak increases, and increases further as the side wall is brought closer (the S/W=0.63 tunnel). It can also be seen that

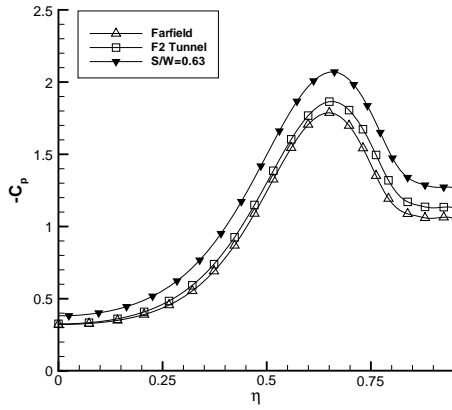


Figure 11: Comparison of upper surface pressure distributions, $x/c_r = 0.63$.

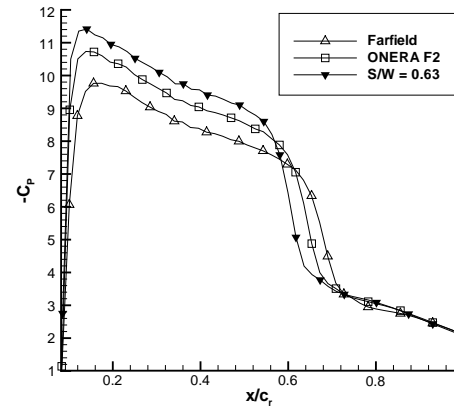


Figure 12: ONERA 70° wing, Pressure distributions along vortex cores.

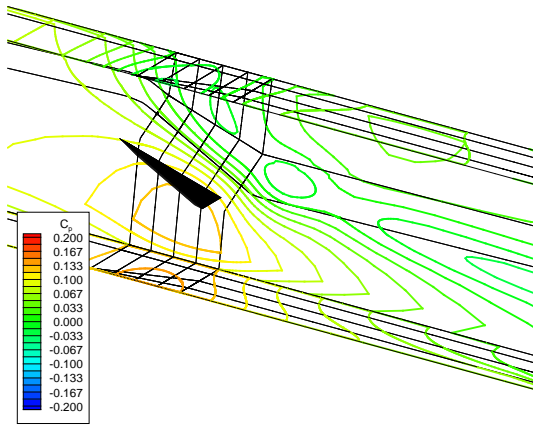
the secondary vortex increases in strength (almost equally in comparison to the primary suction peak) with increasing S/W .

In order to assess the adverse pressure gradient experienced by the vortex core, the pressure distribution along the vortex core in each tunnel is shown in figure 12. Visbal [21] found that vortex breakdown was heavily dependent on the pressure gradient along the vortex core. As the wing is placed in a wind tunnel, the suction in the vortex core prior to breakdown increases. This implies that when the vortices are placed within wind tunnels, they become stronger than those in farfield conditions. With this additional suction the adverse pressure gradient experienced by the core flow increases, thus vortex breakdown is expected to be promoted [22]. This agrees qualitatively with the results of Visbal.

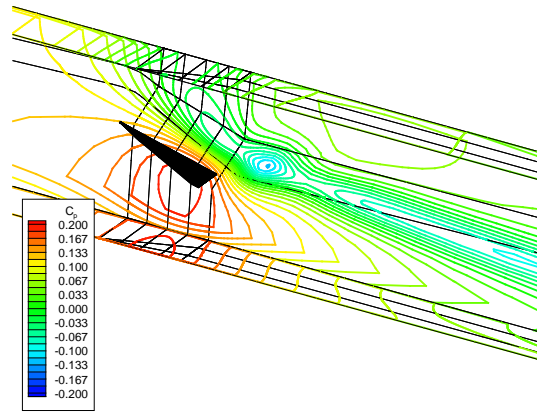
The tunnel wall pressure distributions on the ONERA F2 and the $S/W = 0.63$ tunnels are shown in figure 13. It is clear that there is a strong vortical flow pattern on the side walls which extends down the tunnel despite vortex breakdown having occurred (the persistence of vortical flow despite breakdown occurring was also observed during experiments). The flow patterns appear similar for the ONERA F2 tunnel and the $S/W=0.63$ tunnel, however the strength of the pressure distribution increases with increasing S/W ratio. Clearly there is a significant amount of interference induced by the side walls.

The flow angle (the angle at which the freestream is turned up due to the presence of the wing and side walls) variation in the streamwise direction can be seen in figure 14. Both tunnels increase the flow angle ahead of the wing in comparison to the farfield solution, and also increase the rate at which the flow angle increases along the wing. There are two possible effects present, an increase in the mean effective incidence and induced camber. Both these effects increase with increasing S/W . Since breakdown has moved towards the apex it is expected that the increase in the mean effective incidence is the dominant effect.

Figures 15 shows the distribution of the helix angle through the midline of the vortex core at the chordwise location of $x/c_r = 0.52$. At this chordwise location the vortex is unburst in all solutions. The experimental helix angle obtained in the ONERA F2 tunnel [19] is also given for comparison. As the tunnel walls are brought closer to the wing it can be seen that the helix angle increases (the turns of the vortex tighten) which can cause a promotion of vortex breakdown [23]. This is due to the side wall induced vertical velocity components which also increase in the mean effective incidence of the wing. The tightening of the vortex increases the crossflow momentum. Given that the adverse pressure gradient experienced by the wing boundary layer as it passes from beneath the primary vortex core to the secondary separation region, is unchanged (the secondary suction also increases with the primary suction), the likely cause of the delay in secondary separation in the tunnels is an increase in crossflow momentum due to the tighter winding of the vortex. It can also be seen that the location at which the helix angle changes sign (as we pass through the vortex core) does not appear to move significantly with increasing S/W ratio, indicating the vortex core does not move spanwise significantly at this chordwise station.



(a) ONERA F2 tunnel



(b) $S/W = 0.63$ Tunnel

Figure 13: Steady flow tunnel wall pressure distributions.

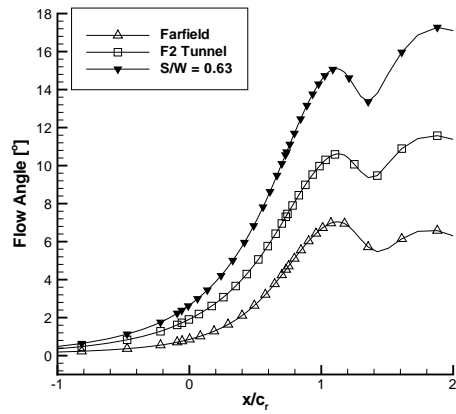


Figure 14: ONERA 70° wing, Flow angles at 1.5 wing span lengths from wing.

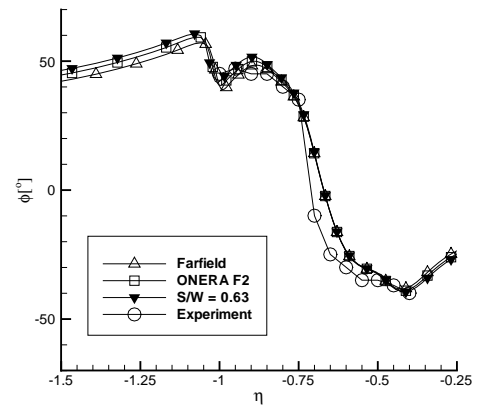


Figure 15: ONERA 70° wing, Comparison of helix angles through vortex cores at $x/c_r = 0.52$.

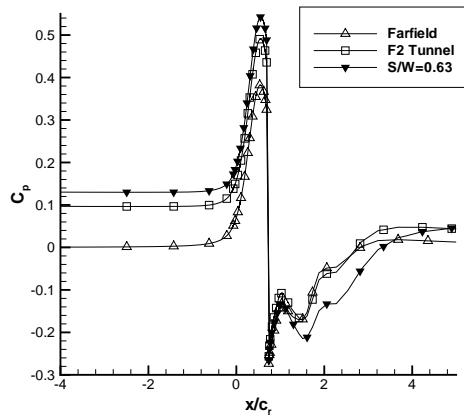


Figure 16: ONERA 70° wing, Tunnel centreline pressure distributions.

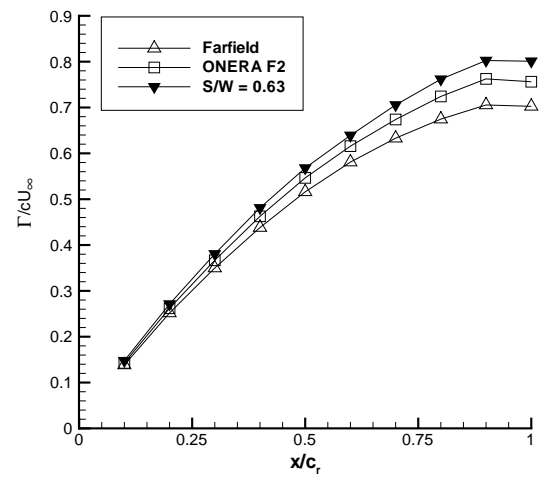


Figure 17: ONERA 70° wing, Comparison of circulation distributions.

Incidence	Support location	Breakdown location
27	$0.5c_r$	$81.0\%c_r$
27	$1c_r$	$65.9\%c_r$
27	NONE	$64.7\%c_r$

Table 4: Vortex breakdown locations with and without supports.

The static pressure distribution along the centreline of the tunnels and the farfield solution can be seen in figure 16. As the centreline passes through the wing the switch from the pressure side to the suction side can be seen as a jump in the curve at approximately $x/c_r=0.75$. It is evident that as the tunnel size decreases the static pressure beneath the wing increases (as expected due to increasing frontal area blockage). The suction over the wing upper surface also increases with decreasing tunnel size. The effect of the lifting of the broken down vortex system into the centre of the tunnel can also be seen. Behind the wing the tunnel pressure distributions are slightly above that of the farfield. However, it should be recalled that there are two effects, the blockage increasing the static pressure within the tunnel, and the vortex lifting which decreases the pressure in this region. Thus it is the difference between the pressure increment ahead of the wing and behind the wing that shows the extent of the vortex lifting. The displacement of the vortices has been confirmed with flow visualisations.

The chordwise variation in circulation along the vortex is given in figure 17. The circulation was obtained by integrating the ω_x component of the vorticity vector over ten chordwise slices. The oppositely signed secondary separation region was omitted (which would have the effect of lowering the circulation). From the apex to around the midchord position it can be seen there is a relatively linear growth in circulation in the chordwise direction, after which the rate of growth in circulation decreases [24]. Despite vortex breakdown occurring the circulation continues to increase in the chordwise direction [25], eventually becoming near constant as the trailing edge is reached. The integrations were performed over an entire extracted plane, thus it would appear rather than there being a loss in the ω_x component of vorticity, it is dispersed throughout the vortex away from the core region. If the integration region is not large enough to encompass this dispersion, it may appear that there is a loss in circulation. The circulation curves further indicate that as the wing is placed in wind tunnels the vortices become stronger, strengthening with increasing S/W ratio. This agrees with the 65° wing results of Allan et al. [9] which showed that side wall proximity increased the circulation of the vortices, with roof and floor proximity having little effect.

17.7 Tunnel Effects – With Support

The breakdown locations observed in the calculations are given in table 4. The breakdown locations have been taken where the axial velocity equals zero.

It can be seen that when the support is $1c_r$ from the trailing edge there appears to be a small influence on breakdown, with breakdown being delayed slightly in comparison to the case without support structures. Since the vertical support used in the experiments of Mitchell [19] was placed around $2c_r$ from the trailing edge of the wing, it can be safely concluded that its interference effect on the experimental breakdown location is minimal. As the support is brought closer to the trailing edge of the wing (at $0.5c_r$ from the trailing edge) it can be seen that breakdown shifts back towards the trailing edge by around $16.3\%c_r$. This is in contrast to what may be considered as the common understanding that downstream supports induce vortex breakdown due to pressure disturbances propagating upstream.

To find the reason for the tendency of this support to delay vortex breakdown, the structure of the vortices prior to breakdown was examined (for a full discussion see [9]). The flow angles (the angle at which the freestream is deflected due to the presence of the wing) were examined and it was observed that there is little change when supports are placed in the tunnel. This is due to the flow angles only being altered by the proximity of the vortices to the side wall (which induce vertical velocity components increasing the mean incidence of the wing). Indeed provided the vortices do

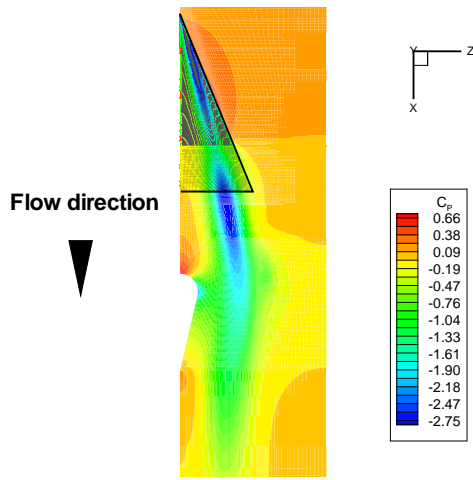


Figure 18: *Pressure distribution along a horizontal plane, support $0.5c_r$ from wing trailing edge*

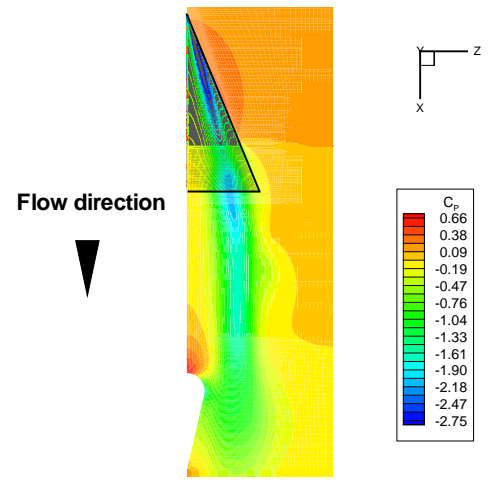


Figure 19: *Pressure distribution along a horizontal plane, support $1.0c_r$ from wing trailing edge*

not increase in strength due to the supports, the flow angles should remain the same. The surface pressure distributions above the wing at $x/c_r = 0.32, 0.52$, and 0.63 were also examined and again there was little difference, both in core location and strength. The axial vorticity distributions and chordwise distribution of circulation was finally examined and it was concluded that prior to breakdown, the support structures had no influence on the vortex structure.

Figures 18 and 19 shows the pressure distribution along a horizontal plane at the midpoint between the tunnel roof and floor for each incidence and support location. The flow direction is from top to bottom and the intersection of the horizontal plane with the wing is clearly seen upstream of the support. Evidently the vortical flow negotiates the support as opposed to impinging on it as in the experiments of Taylor et al. [11][26]. Since the mean effective incidence of the wing and strength of the vortices is unaltered prior to vortex breakdown, the only explanation for the delay in vortex breakdown is the change in the pressure gradients in the tunnels. It is well understood that vortex breakdown is sensitive to external pressure gradients [22].

The tunnel axial pressure gradients were examined. Figure 20 shows the axial pressure gradient near the side wall location. It should be noted that the pressure gradient along the axis of the tunnel was not taken since this would incorporate the adverse pressure gradient formed towards the stagnation point on the support. Since the vortices do not impinge on the support, they will not experience this adverse pressure gradient, therefore the pressure gradient at the side wall is more indicative of the pressure gradient experienced by the vortices. Clearly there is a favourable pressure gradient due to an acceleration of the flow as it negotiates the support, thus reducing the local static pressure around the support. This will have the effect of delaying vortex breakdown. To have an effect on vortex breakdown the favourable pressure gradient must be local with respect to the vortices, and so when the support is placed $1c_r$ from the wing, the favourable pressure gradient around the support has a smaller effect.

From the previous discussion it is clear that downstream support structures have the sole effect of altering the pressure gradients within the tunnel. There is little or no change to the vortex structure prior to vortex breakdown. Clearly the shape and size of the support considered in this study alters the pressure gradients in the tunnels due to blockage effects. The acceleration of the flow around the support causes a favourable pressure gradient to form, and if this pressure gradient is local with respect to the vortices breakdown is delayed. However there is also a stagnation region ahead of the support so it is possible that if the blockage effect was lower, the stagnation effect may become dominant and breakdown will be promoted. To assess any possibility of this a narrower support was placed at $0.5c_r$ from the trailing edge of the wing, with the wing at 27° angle of attack. The geometry is identical to that described in figure 1, however the radius of the cylindrical section was reduced from $0.09c_r$ to $0.045c_r$. This effectively halves the support frontal area blockage from approximately 12% to 6%. The breakdown was observed to shift from $64.7\%c_r$ to $73.8\%c_r$. Clearly despite the blockage being reduced the previous discussion applies to thinner supports. As long

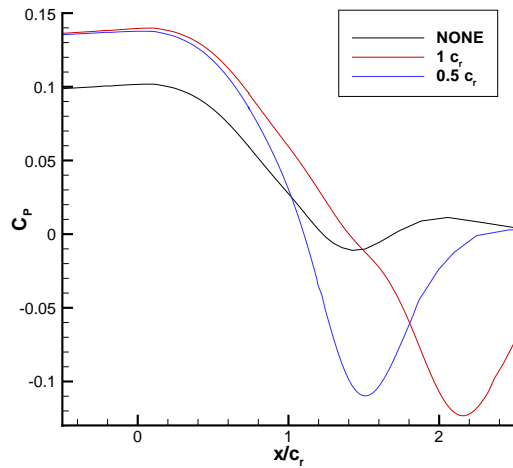


Figure 20: *Axial pressure gradient at tunnel side wall with supports.*

as the vortex cores negotiate the support breakdown can be delayed. This seems to be the case for “streamlined” tunnel-centred support structures at high Reynolds number. The effect of the favourable pressure gradient at low Reynolds number is likely to be lower.

17.8 Conclusions

A CFD investigation of wind tunnel interference effects on a 70° delta wing has been conducted. The vortical flow predictions were verified and validated, and then used to analyse the effects of wind tunnel walls. Verification of the accuracy on the grids employed has highlighted a dependency of the solutions to grid resolution. From the available literature this has been found to be common in the prediction of vortical flows. To ensure that any differences are only due to changes in boundary conditions (such as locations of tunnel walls and support structures), in all computations the vortical region of interest has been resolved with a consistent discretisation of the domain. To achieve this a farfield grid was created in such a way that by extracting outer blocks varying tunnel dimensions were obtained.

RANS simulations have confirmed previous conclusions drawn from Euler simulations [8]. It has been observed that the amount of upwash generated (and therefore the mean effective incidence) is dependent on the side wall location. As the side wall moves closer to the wing, the local effective incidence along the leading edge increases. Since the local effective incidence of the wing increases along the leading edge (tunnel interference increases toward the trailing edge as the vortices are closer to the side walls), the wing might be considered to behave as if positively cambered. A positively cambered wing is expected to delay vortex breakdown. Since breakdown is promoted it appears that the increase in mean effective incidence is the dominant factor. The helix angle of the vortices also increases due to side wall proximity. The side wall induced upwash tightens the windings of the vortex and therefore increases the vortex strength. Higher helix angles are known to induce vortex breakdown.

The influence of the tunnel side walls on the secondary vortices was also assessed. It was observed that the secondary separation location moves towards the leading edge when the wing is placed inside wind tunnels. The helix angle of the vortices increases with the presence of the tunnel side walls. This increases the strength of the primary vortices due to the increased crossflow momentum (a result of the tighter windings). However, the increased crossflow momentum also increases the strength of the secondary region, thus the adverse pressure gradient experienced by the crossflow after the primary vortex suction peak is essentially unaltered. With the increased crossflow momentum the adverse pressure gradient can be overcome longer, and therefore the secondary separation line moves outboard.

In order to assess support interference a support with a large frontal area blockage was used. The support was placed at two chordwise locations in order to assess the effect of support proximity

on the solutions. It was observed that the leading edge vortices were very sensitive to variations in pressure distributions aft of the trailing edge, due to the presence of supports. In addition the downstream support structures had no effect on the flow structure prior to vortex breakdown. The support shape considered caused a significant acceleration of the flow due to blockage which had the effect of delaying vortex breakdown. This trend was observed irrespective of support width (frontal area blockage). The trajectory of the vortex cores was such that the core flow never experienced the adverse pressure gradient ahead of the support structure. Thus it can be concluded that the effect of downstream support structures is heavily dependent on whether or not the core flow impinges on the structure, and is also likely to be dependent on Reynolds number.

17.9 Acknowledgements

The authors wish to thank Major A. Mitchell, United States Airforce Academy, for kindly providing the experimental data. The financial support from QinetiQ Ltd (formerly DERA Bedford) is gratefully acknowledged.

17.10 References

- [1] Garner, H. C., and Rogers, E. W. E. "Subsonic wind tunnel wall corrections". *AGARDograph 109*, 1966.
- [2] Karou, A. "Separated vortex flow over slender wings between side walls - theoretical and experimental investigation". *Report LR-300, Dept. of Aerospace Engineering, Delft University of Technology*, 1980.
- [3] Engineering Sciences Data Unit. "Blockage corrections for bluff bodies in confined flows". *Item 80024, London*, 1980.
- [4] Weinberg, Z. "Effect of tunnel walls on vortex breakdown location over delta wings". *AIAA Journal*, 30(6), June 1992.
- [5] Thompson, S. A., and Nelson, R. C. "Wind tunnel blockage effects on slender wings undergoing large amplitude motions". *AIAA-92-3926*, July 1992.
- [6] Pelletier, A., and Nelson, R. C. "Factors influencing vortex breakdown over 70° delta wings". *AIAA-95-3469-CP*, 1995.
- [7] Verhaagen, N. G., Houtman, E. M., and Verhelst, J. M. "A study of wall effect on the flow over a delta wing". *AIAA-96-2389*, 1996.
- [8] Allan, M. R., Badcock, K. J., and Richards, B. E. "A CFD Investigation of wind tunnel wall influences on pitching delta wings". *AIAA-2002-2938*, June 2002.
- [9] Allan, M. "A CFD Investigation of wind tunnel interference on delta wing aerodynamics". *Ph.D. Thesis, University of Glasgow, Glasgow, UK*, October 2002.
- [10] Hummel, D. "Untersuchungen über das Aufplatzen der Wirbel an schlanken Delta Flügeln". *Zeitschrift für Flugwissenschaften*, 13(5):158–168, 1965.
- [11] Taylor, G., Gursul, I., and Greenwell, D. "Static hysteresis of vortex breakdown due to support interference". *AIAA 2001-2452*, 2001.
- [12] Straka, W. A. "Effect of fuselage on delta wing vortex breakdown". *J. Aircraft*, 31(4):1002–1005, 1994.
- [13] Ericsson, L.E. "Effect of fuselage geometry on delta-wing vortex breakdown". *J. Aircraft*, 35(6), November-December 1998.
- [14] Ericsson, L. E. "Further analysis of fuselage effects on delta wing aerodynamics". *AIAA 2000-0891*, January 2000.

- [15] Badcock, K. J., Woodgate, M., Stevenson, K., Richards, B. E., Allan, M., Goura, G. S. L., and Menzies, R. Aerodynamics studies on a Beowulf cluster. In P. Wilders et al., editor, *Parallel Computational Fluid Dynamics Practices and Theory*, pages 39–46, May 2002.
- [16] Gordnier, R. E. “Computational study of a turbulent delta-wing flowfield using two-equation turbulence models”. *AIAA 96-2076*, 1996.
- [17] Brandsma, F. J., Kok, J. C., Dol, H. S., and Elsenaar, A. “Leading edge vortex flow computations and comparison with DNW-HST wind tunnel data”. *RTO / AVT Vortex Flow Symposium, Loen, Norway*, 2001.
- [18] Wilcox, D. C. “Turbulence modelling for CFD”. *DCW Industries, Inc., La Cañada, California*, 1993.
- [19] Mitchell, A. M. “Caractérisation et contrôle de l’éclatement tourbillonnaire sur une aile delta aux hautes incidences”. *Thèse de doctorat de l’Université Paris 6*, 2000.
- [20] Visbal, M. R., and Gordnier, R. E. “Compressibility effects on vortex breakdown onset above a 75-degree sweep delta wing”. *J. Aircraft*, 32(5):936–942, September-October 1995.
- [21] Visbal, M. R. “Onset of vortex breakdown above a pitching delta wing”. *AIAA Journal*, 32(8):1568–1575, August 1994.
- [22] Sarpkaya, T. “Effect of adverse pressure gradient on vortex breakdown”. *AIAA Journal*, 12(5):602–607, May 1974.
- [23] Sarpkaya, T. “On stationary and travelling vortex breakdowns”. *J. Fluid Mech.*, 45(3):545–559, 1971.
- [24] Visser, K. D. and Nelson, R. C. “Measurements of circulation and vorticity in the leading-edge vortex of a delta wing”. *AIAA Journal*, 31(1):104–111, January 1993.
- [25] Johari, H. and Moreira, J. “Direct measurement of delta-wing vortex circulation”. *AIAA Journal*, 36(12):2195–2203, December 1998.
- [26] Taylor, G., Gursul, I., and Greenwell, D. I. “An investigation of support interference in high angle of attack testing”. *To appear in AIAA conference proceedings, RENO NV, USA*, January 2003.



Chapter 18 – SIMULATION OF VORTICAL FLOW OVER ONERA 70-DEGREE DELTA WING EXPERIENCING VORTEX BREAKDOWN

B.I. Soemarwoto and O.J. Boelens

National Aerospace Laboratory NLR
Anthony Fokkerweg 2, 1059 CM Amsterdam
NETHERLANDS

soemarwt@nlr.nl, boelens@nlr.nl

ABSTRACT

This chapter presents an application of CFD methodology based on the unsteady Reynolds-Averaged Navier-Stokes (RANS) equations with a $k - \omega$ turbulence model for the prediction of vortical flows involving vortex breakdown. A variant of the $k - \omega$ turbulence model is applied that avoids excessively high eddy viscosity in the vortex cores. Time-accurate simulations are performed for subsonic flow around the ONERA 70 degree delta wing at an angle of attack of 27 degrees. Two non-dimensional time steps of different order of magnitude, are used. Both simulations predict vortex breakdown. The smaller time step leads to a self-sustained oscillation. Computational results are compared with the experimental data, and discussed in terms of pressure coefficient, velocity and vorticity components, and turbulence kinetic energy distributions on the crossflow planes and on the longitudinal plane along the vortex core. A Fourier analysis results in a spectrum with a distinct frequency peak of the Strouhal number approximately equal to 9.

18.1 BACKGROUND

Leading edge vortices are dominant phenomena in the flow around modern high performance fighter aircraft. While vortices are advantageous in augmenting lift by creating high suction fields above the wing, the phenomenon called vortex breakdown can lead to severe problems. Unsteady vortex breakdown raises serious aeroelastic concerns due to problems such as buffeting, especially for aircraft with twin vertical tails. Vertical fins immersed in a bursted vortex field experience buffet loads that may lead to early structural problems related to fatigue. Flow unsteadiness caused by vortex breakdown also affects the flutter speed and the characteristics of limit cycle oscillations.

From the performance point of view, leading edge vortices are instrumental for maneuvering in high angle-of-attack regimes. The onset of vortex breakdown, however, determines the maximum vortex-induced lift that can be attained during such maneuvers. Vortex breakdown initiates a process that reverses the angle-of-attack trends of the force and moment coefficients. Stability and control issues follow, as asymmetric vortex breakdown over the wing potentially initiates roll instabilities which can lead to departure from controlled flight, and drastic trend reversal in the longitudinal and lateral stability derivatives reduce the control authority. For aircraft with twin vertical tails, a bursted vortex impinging on a vertical fin deteriorates the effectiveness of the rudder.

A good understanding of the susceptibility to departure, the departure motion itself, and an accurate assessment of agility potential of modern high performance aircraft are critical to flight safety for which the risk of losing aircraft and/or pilot in combat situation must be minimized (Ref. [1]). A challenging task is to estimate departure boundaries (Refs. [2,3]) accurately by means of simulations based on Computational Fluid Dynamics (CFD). This task is particularly relevant as modern fighter aircraft design allows penetration into extreme flow conditions characterized by high angles of attack and high angular

rates. CFD methods account for strong non-linearities involved in such extreme flow conditions, and facilitate the evaluation of departure criteria in terms of stability and control derivatives covering non-linear flow regimes (Refs. [4,5]). A thorough assessment of the stability and control properties, however, can be obtained by complete simulation of the aircraft motion through coupling CFD methods and Flight Mechanics methods.

Both the advantages and the risks involved with leading edge vortices in high angle-of-attack flow regimes have motivated numerous experimental, theoretical and numerical investigations. Within the task group *RTO-AVT080 Vortex Breakdown over Slender Wings* an opportunity is provided to assess CFD capability to calculate vortical flow experiencing vortex breakdown on the basis of available experimental data (Refs. [6,7]). Accurate simulation of vortical flows experiencing vortex breakdown is important, because the captured characteristics of the breakdown determines in a global way the pressure distribution over the wing surface and, thus, the aerodynamic force and moment coefficients.

This paper presents an application of CFD methodology based on the unsteady Reynolds-Averaged Navier-Stokes (RANS) equations for the prediction of vortical flow involving vortex breakdown. Modelling based on RANS equations assumes a clear separation of the time scales of the vortex breakdown and the turbulence unsteadiness. The present choice for the RANS method has been made under constraints of the available computational resource, whilst a RANS simulation provides results that can be contrasted with those to be obtained using a higher fidelity modelling given by a hybrid RANS/LES method (Ref. [8]).

A variant of the $k - \omega$ turbulence model is applied that avoids excessively high eddy viscosity in the vortex cores. Time-accurate simulations are performed for subsonic flow around the ONERA 70 degree delta wing at an angle of attack of 27 degrees. Computational results are compared with the experimental data.

18.2 FLOW MODELLING

Subsonic flow around a half-span configuration of the ONERA 70 degree delta wing with sting (Ref. [6]) is considered. The delta wing has a flat surface on the leeward side where the leading edge vortices occur. The wing root chord is 950 mm. The unsteady Reynolds-Averaged Navier-Stokes (RANS) equations are employed in a flow domain discretized by structured grids. The flow domain around the wing/sting configuration is divided into 50 blocks of structured grids. Figure 1 gives an impression of the flow domain topology in the near-field and the structured grids on the wing surface, a crossflow plane and the symmetry plane. In total, the flow domain around the half-span configuration contains 3,694,080 grid cells, with 160 cells along the wing chord and 144 cells along the wing span over the upper surface.

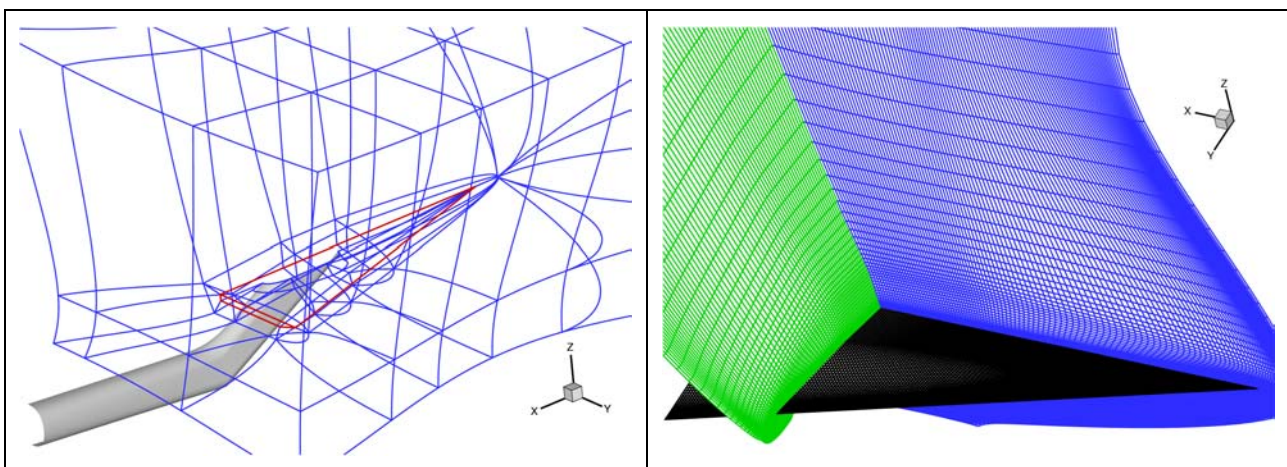


Figure 1: Impression of the Flow Domain Topology and Computational Grids.

A calorically perfect gas relation, the Stokes' hypothesis for a Newtonian fluid, and the Sutherland's law for the dynamic molecular viscosity are assumed to hold throughout the flow field. The Boussinesq assumption is used for the formulation of the Reynolds stress tensor using the concept of eddy viscosity.

No-slip and adiabatic wall boundary conditions are applied on the solid surfaces. In the experiment, a transition trip is applied at 40 % chord aft of the wing apex. However, during the simulation turbulent flow over the wing surface is enforced, allowing non-zero eddy viscosity in the vortex. The reason for this treatment is that the interfaces separating the regions of the boundary layer, the vortices, and the shear layers emanating from the leading edge, cannot be exactly identified, so that a proper zonal modelling cannot be arranged. In addition, it is considered that while the boundary layer may be laminar upstream of the transition trip, it is not clear whether the leading edge vortex and the shear layers are also laminar, as turbulence may already be generated in the shear layers and fed into the vortex.

For the determination of the turbulence kinetic energy and the eddy viscosity, a variant of the Wilcox $k - \omega$ turbulence model is applied, with the free-stream dependency and the singular behaviour near solid walls resolved (Refs. [9,10]). The turbulence-model equations and the mean flow (RANS) equations are solved simultaneously for the mean flow variables using NLR's CFD system ENFLOW (Ref. [11]). The spatial discretization employs a cell-centered finite volume scheme. For the mean flow equations, Jameson-type artificial dissipation fluxes are added consisting of blended first and third order differences with a pressure-based shock sensor. The artificial dissipation terms are implemented with matrix coefficients to enhance the accuracy. For the turbulence-model equations, artificial diffusive fluxes are also defined using blended first and third order differences, with the scaling factor given by the eigenvalue of the convective flux in the turbulence equations.

It is well known that standard RANS methods produce high levels of eddy viscosity in the vortex core giving excessive dissipation. For these methods, the details of the vortex core are lost and low suction peaks with wide vortex bases are a characteristic of the solution. As a remedy, a modification to the $k - \omega$ turbulence model is applied. A parameter r is used to detect vortex cores. This parameter is the ratio between the magnitude of strain-rate and vorticity tensor. In shear layers, the velocity gradient is dominated by the gradient in the normal direction, which gives $r \approx 1$, while in vortex cores $r \ll 1$ where the flow experiences pure rotation. Based on this parameter the production of turbulence kinetic energy is limited in vortex cores through a promoted production of the dissipation rate. This approach has proven to be effective in producing suction peak profiles in good agreement with those of experimental data (Refs. [12,13]).

For time-accurate simulations, a second-order dual-time stepping scheme is applied, using a five-stage explicit Runge-Kutta scheme for each physical time step and acceleration techniques such as local-time stepping, implicit residual averaging and multi-grid. The source terms in the turbulence equations are treated explicitly using a separate time-step for efficiency.

18.3 RESULTS AND DISCUSSION

The subsonic flow around the delta wing is defined by a Mach number $M = 0.069$, an angle of attack $\alpha = 27$ degrees, and a Reynolds number $Re = 1.56$ millions. As a low Mach number is involved, global low-Mach preconditioning was applied (Ref. [14]) to the system of equations during the simulation. The free-stream velocity U_0 is 24 m/s. As a first test, a steady simulation was performed using the free-stream velocity as an initial solution. The residuals reached a level showing a limit-cycle behaviour. The pressure contours observed on the wing surface and the occurrence of the limit-cycle behaviour of the residuals gave a clear indication of vortex breakdown occurring in the flow field.

The frequency spectrum associated with vortical flow containing vortex breakdown can be considered as consisting of three modes having different characteristic frequencies: the axial, the azimuthal and the

radial mode. Initially, constraints on the computational resources did not allow the use of a time step to enable the resolution of the complete spectrum covering all these modes. Thus, for the time-accurate simulation, a relatively large time step was selected, aimed at a low frequency mode of approximately 1 Hz. This frequency corresponds to a self-sustained oscillation of the vortex breakdown location observed in the experiment. A non-dimensional time step $\Delta t^* = 0.1$ based on the wing chord and the free-stream velocity was determined. The free-stream state was taken as the initial state for the time-accurate simulation.

Figure 2 illustrates the time history of the surface pressure distribution. Already at time step $t^* = 0.3$, a structure consisting of primary and secondary vortices can be recognized in the surface pressure contours. The suction peak region expands until the primary vortex breaks down at $t^* = 1.3$ at a location $x/c \approx 0.5$. Immediately after the onset of breakdown, this location moves rapidly upstream until $t^* = 7.2$ reaching $x/c = 0.28$, and subsequently moves slowly downstream as the flow becomes less unsteady. Finally, the flow reaches a steady-state at $t^* = 25.6$ with the vortex breakdown location converging to a location $x/c = 0.38$.

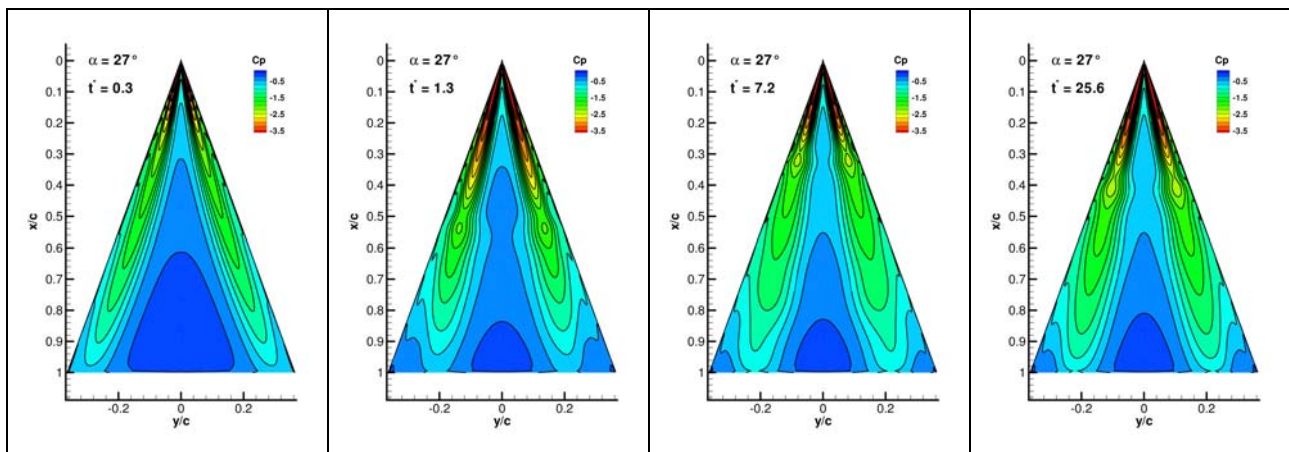


**Figure 2: Computational Time History of C_p Contours Leading to
a Steady-State Obtained with a Large Time Step ($\Delta t^* = 0.1$).**

Expecting that a smaller time step would be able to resolve unsteady phenomena, the simulation was continued (starting from the last available solution) with the non-dimensional time step equal to as small as 0.001. This continuation did not give rise to any unsteadiness. For completeness, a steady computation was performed starting with the same solution. This steady computation also did not give any indication of unsteady flow phenomena. The resulting steady-state solution is very close to the initial one, and therefore it can be interpreted as representing the asymptotic solution. It can be concluded that a large time step leads to a genuine steady-state solution of the time-dependent RANS equations. Apparently, too large a time step damps out higher frequency modes. Indeed, during the time-accurate simulation, significant unsteadiness of high frequency components was observed in regions downstream of vortex breakdown, but the magnitude of this unsteadiness was strongly decreased in time. This confirms that the high frequency modes are responsible for the self-sustained oscillating phenomena of vortex breakdown.

In the subsequent simulation, a non-dimensional time step following a baseline (Ref. [15]) $\Delta t^* = 0.0025$ is chosen, and the flow is recalculated starting from the free-stream. A self-sustained unsteady flow solution is evident after the transient appears to have decayed in $t^* = 2.25$ time steps. The simulation is performed

up to $t^* = 6.5$. It is realized that the period of the lowest frequency has not yet been covered. Nevertheless, the amplitude of the high frequency mode is sustained. The instantaneous breakdown location consistently stays in the range of 67 – 75 % chord from the apex after the onset of breakdown, in contrast to the strong shift found with the large time step of 0.1.

Figure 3 shows a power spectrum of the normal force coefficient, depicting the PSD power versus the Strouhal number resulting from the psd function of MATLAB. The figure shows a dominant peak corresponding to $St \approx 9$ ($f \approx 200$ Hz). A DES computation (Ref. [15]) for an isolated delta wing of the same geometry and flow condition captures a frequency of $St \approx 8$. Apart from the different flow modellings, the difference may also be attributed to the sting taken into account in the present computation.

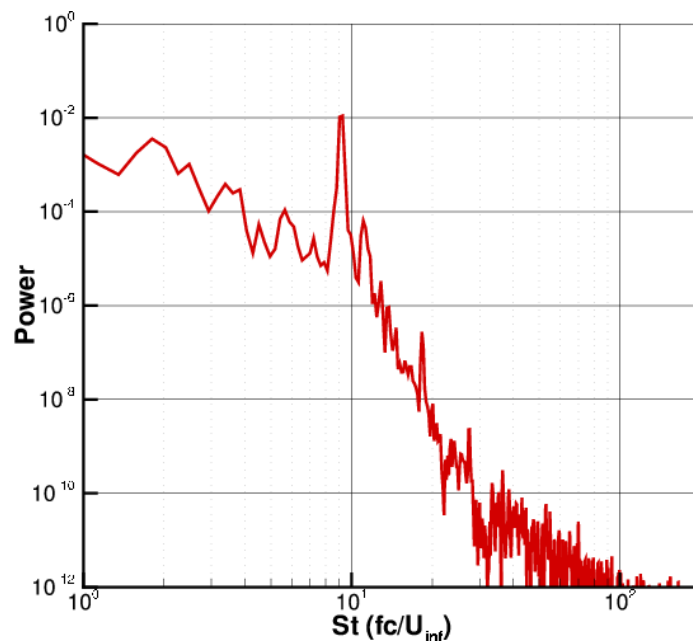


Figure 3: Computational Power Density Spectra of the Normal Force Coefficient.

The time-averaged surface C_p contours are compared with those of the experimental results in Figure 4. In general, the pressure levels and the patterns are quite similar. A closer look is given in Figure 5 depicting C_p values at the location of the pressure taps. The suction peak of the primary vortex is evident. The secondary vortices can be identified in the computational results as small suction peaks near the leading edges. Good agreement is shown up to 42 % chord. Aft of this location, the computational suction peak decreases rapidly in comparison to that of the experiment. A possible explanation is that there is no local bunching of the grid within the vortex. The crossflow-plane resolution follows the leading edge sweep giving a coarsening effect significant enough to loose the physics of the vortex core. The higher pressure in the computational results in the wing centerline area can be attributed to the turbulent boundary layer.

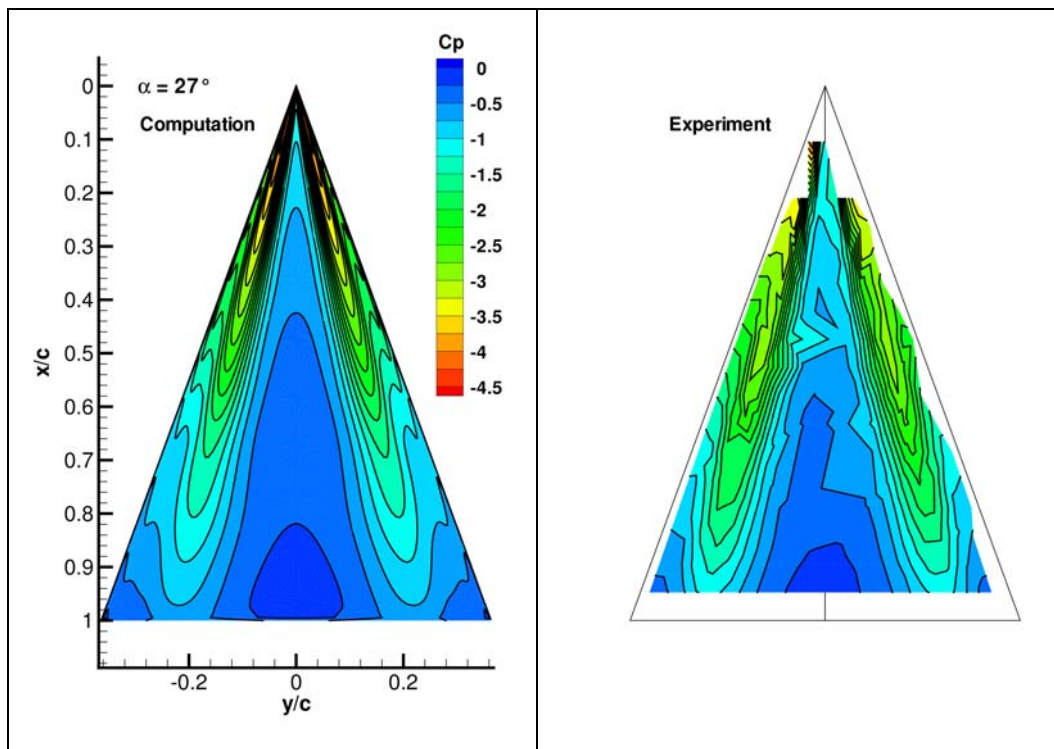


Figure 4: Computational and Experimental Time-Averaged C_p Contours.

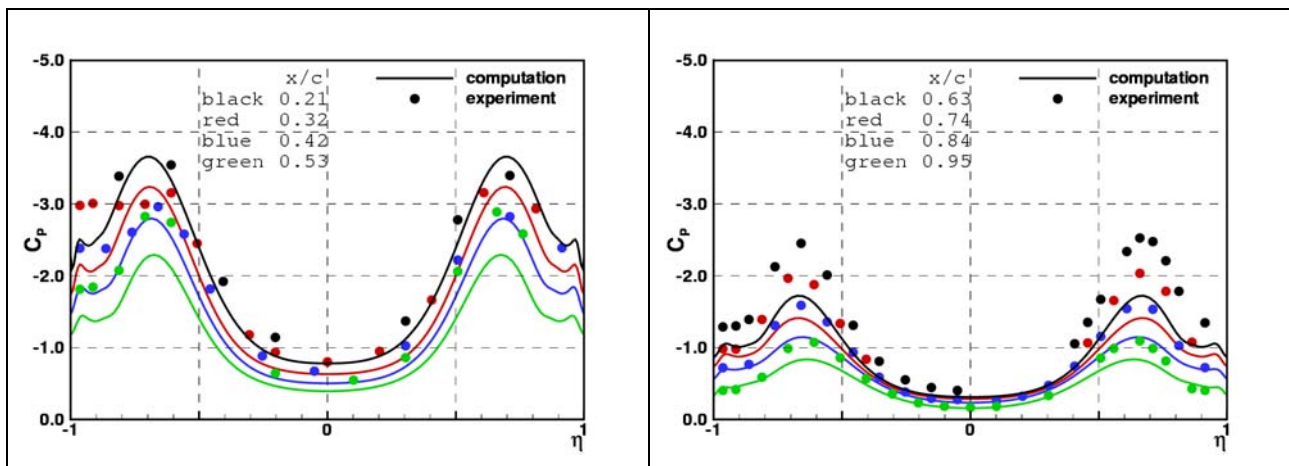
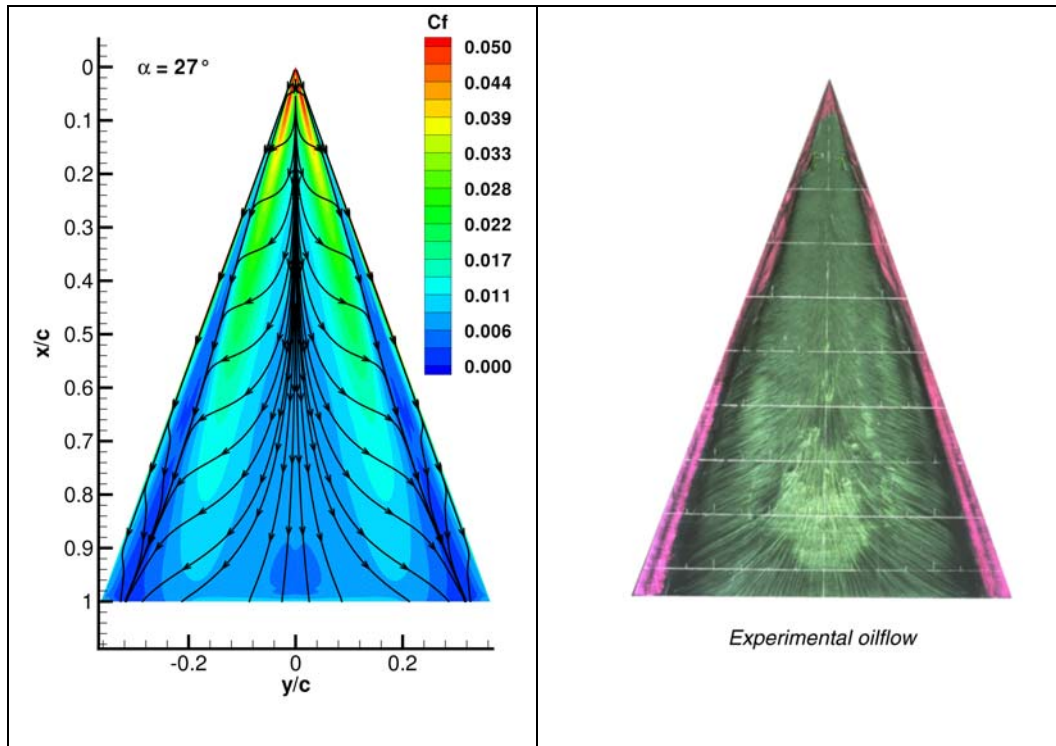


Figure 5: Computational and Experimental Spanwise C_p Distributions.

The skin friction distribution and patterns of the limiting streamlines are shown in Figure 6, which agree well with the experimental surface oil flow patterns, showing clearly a structure containing secondary vortices.



**Figure 6: Computational Surface C_f Contours and Limiting Streamlines
Compared with the Experimental Oilflow Pattern.**

Figures 7 and 8 show distributions of the axial velocity component of the time-averaged solution on the crossflow planes at $x/c = 0.53, 0.63, 0.74$ and 0.84 , and on a longitudinal plane along the vortex core. Vortex breakdown occurs at $x/c \approx 0.74$, which is determined by the criterion of zero axial velocity in the vortex core. A recirculating zone downstream of the breakdown is clearly indicated. Compared to the experimental data, the deceleration across the breakdown is mild and the magnitude of the reversed velocity in the recirculating zone is rather small. The numerical solution gives less sharp flow features. The streamwise grid resolution, in combination with the crossflow-plane resolution discussed above, can be made responsible for this “smeared” result. Higher grid densities should be used in the range of 60 – 80 % chord covering the shift of breakdown location.

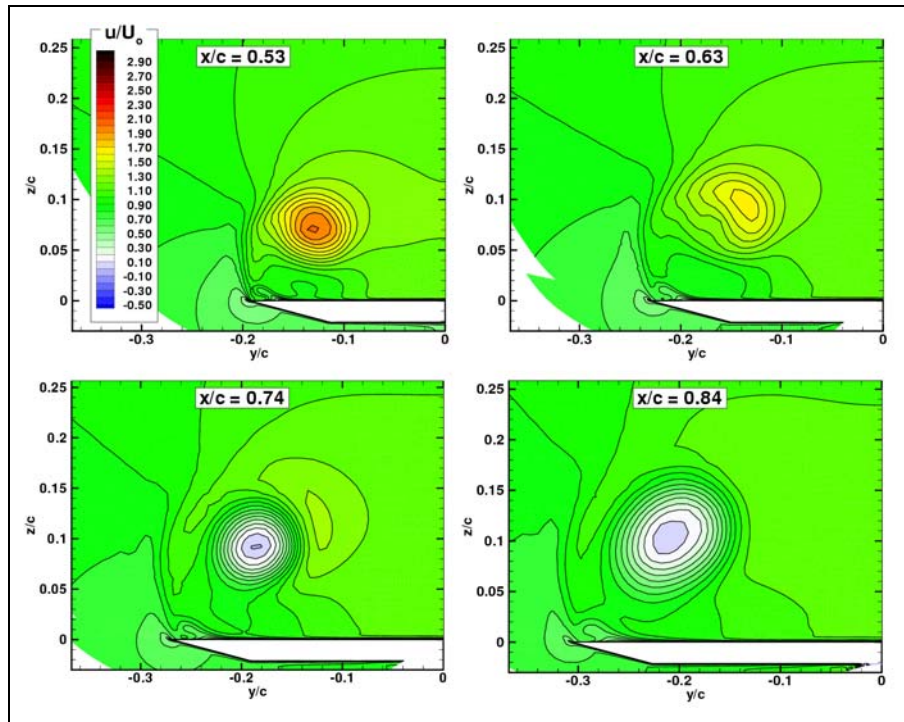
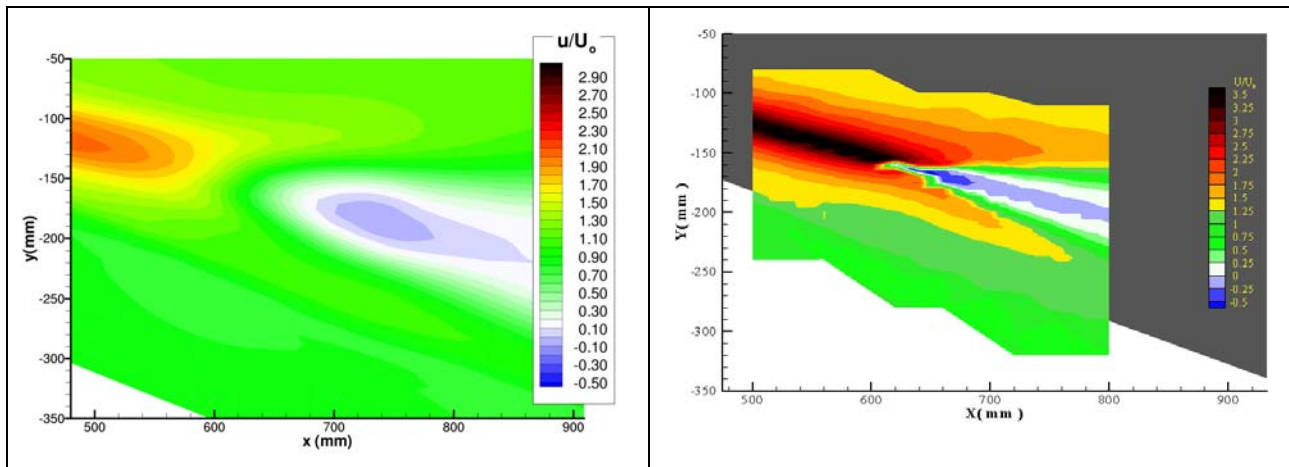


Figure 7: Computational Crossflow Distribution of the Axial Velocity.



**Figure 8: Computational (left) and Experimental (right)
Longitudinal Distribution of the Axial Velocity.**

Figure 9 presents contours of the transversal (v/U_0) and normal velocity components (w/U_0) on the crossflow planes, respectively. The contours show gradient drops around the vortex core across the onset of vortex breakdown. The general trend is similar to the experiment, noting that the simulation gives reduced velocity magnitudes and gradients and less compact vortex. The normal and transversal locations of the vortex core, defined by the positions where there are sign reversal of the velocity components, agree with those indicated in the experiment.

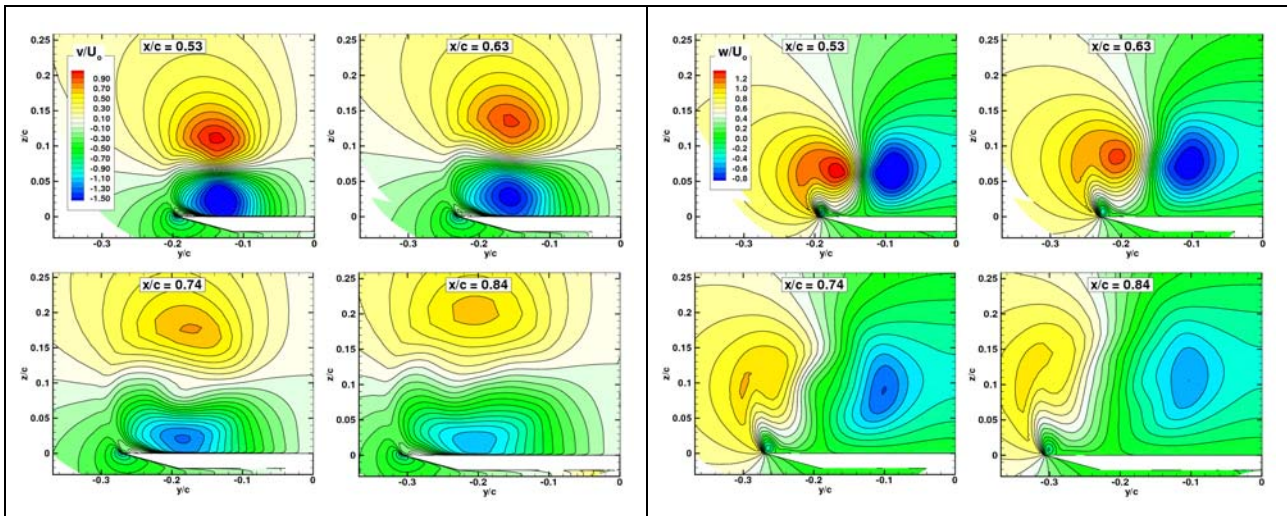


Figure 9: Computational Crossflow Distributions of the Transversal (v/U_0) and Normal (w/U_0) Velocity.

Figure 10 shows the crossflow distributions of the axial component of the vorticity. Both experimental and computational results reveal two systems having opposite signs of the vorticity. The first system contains the shear layer and the primary vortex with positive vorticity, whilst the second system contains the boundary layer and the secondary vortex with negative vorticity. The shear layer feeds vorticity into the primary vortex, while the boundary layer feeds vorticity into the secondary vortex. Across the vortex breakdown location the vorticity inside the primary vortex core is significantly dissipated. The vorticity level inside the shear layer hardly changes. Apart from the high vorticity inside the vortex (upstream of breakdown) and pockets of eddies trailing from the shear layer which are not captured by the simulation, the axial vorticity levels after breakdown are roughly the same.

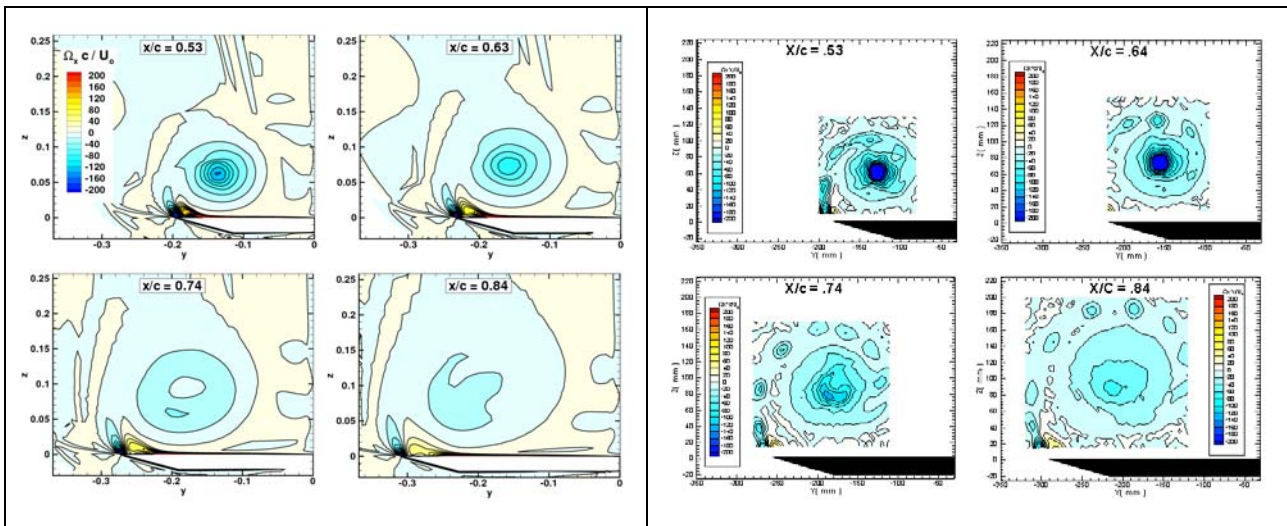


Figure 10: Computational (left) and Experimental (right) Crossflow Distributions of the Axial Vorticity Component.

The azimuthal vorticity is shown in Figure 11 on the longitudinal plane along the vortex core with the same colouring as that used for the experimental result. Similar but less compact flow features are revealed, while the computational vorticity level is significantly lower than that of the experiment.

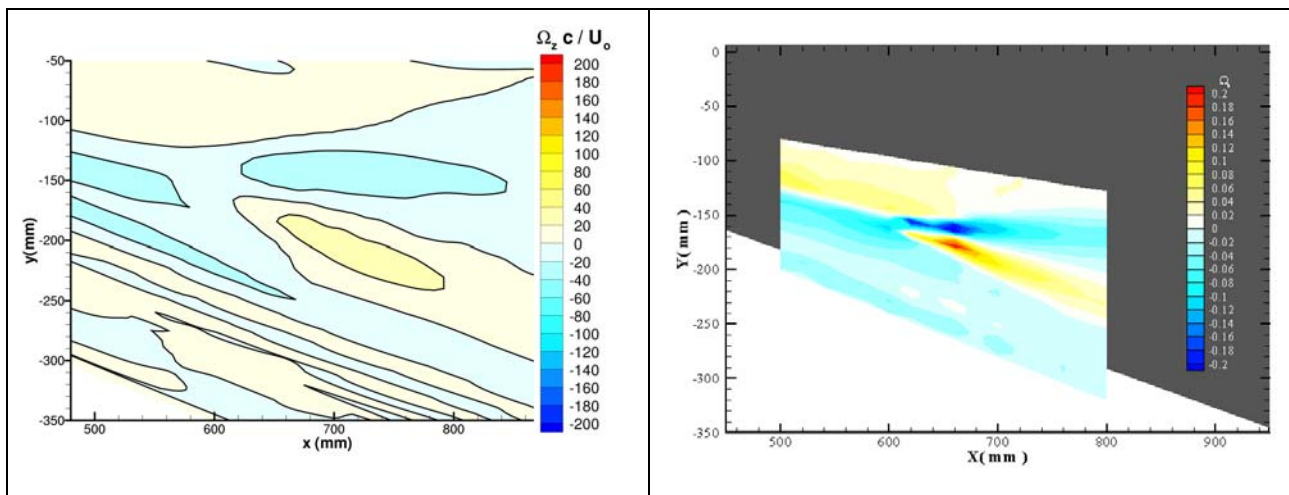


Figure 11: Computational (left) and Experimental (right) Longitudinal Distribution of the Azimuthal Vorticity Component.

Figure 12 shows the predicted turbulence kinetic energy. The turbulence intensity in the vortex is one order of magnitude less than that of the experiment. The solution features a relatively laminar vortex core, whilst there is a significant production of turbulence across the breakdown location in the vortex core. The low-turbulence vortex core is apparently a result of the modification of the turbulence model in the vortex core. This modification controls the production of the turbulence kinetic energy through promoting the production of the dissipation rate. Although the control mechanism is dynamic in the sense that the turbulence kinetic energy is not limited to a certain level, it can be considered too aggressive, as a reasonable agreement is still achieved in the traces of the shear layer where the control is not present.

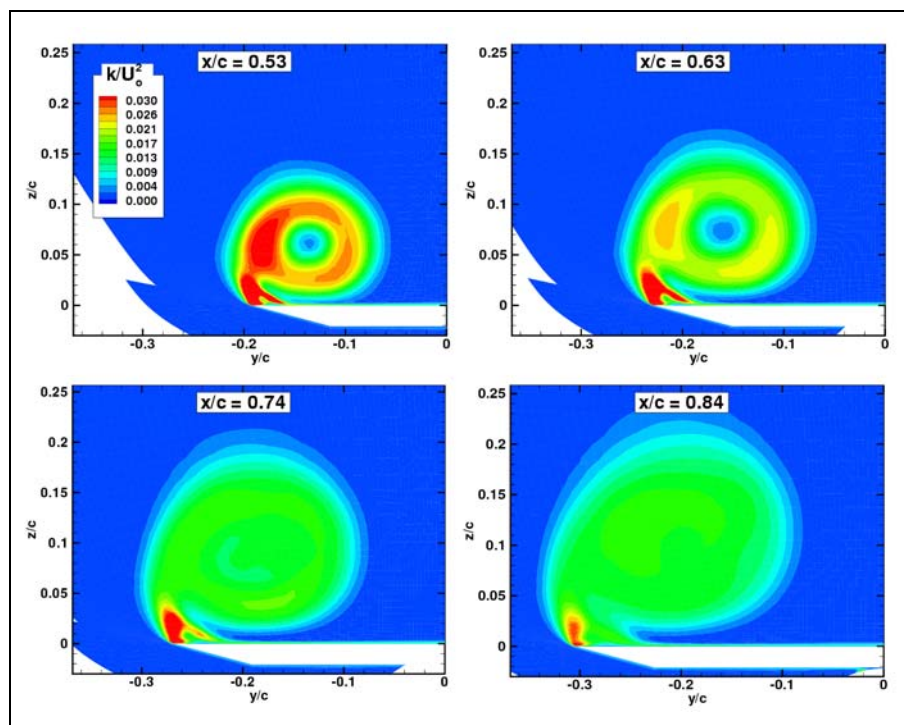


Figure 12: Computational Crossflow Distributions of the Turbulence Kinetic Energy.

Figure 13 presents an instantaneous and the time-averaged iso-surfaces of the total pressure loss. Two levels are shown, where the one with the lower value (yellow) effectively encloses that with the higher value in red. Downstream of the breakdown location, the instantaneous surface clearly indicates the spiraling characteristics stretching downstream.

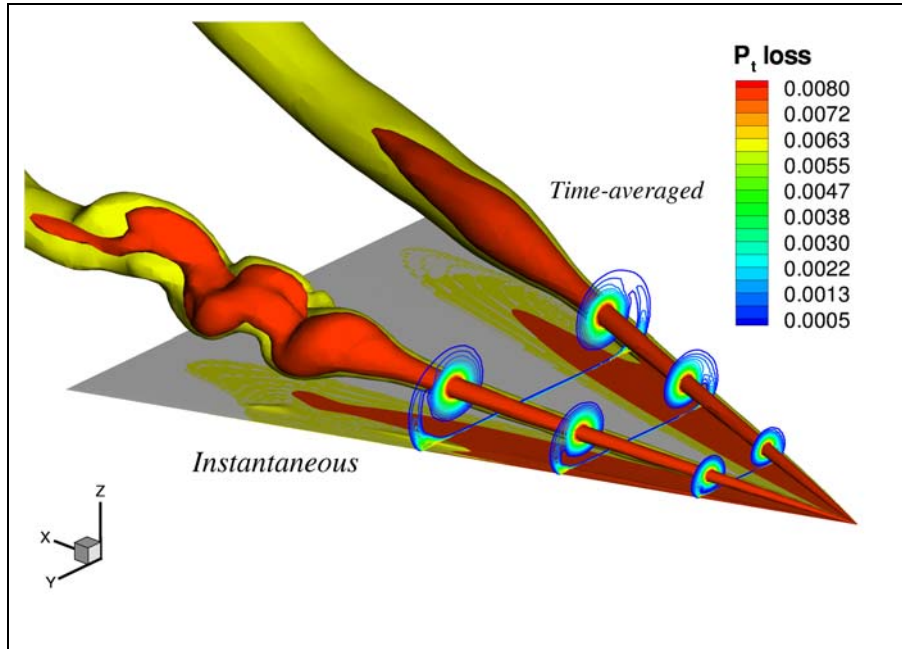


Figure 13: Computational Iso-Surfaces of the Total Pressure Loss.

18.4 CONCLUSIONS

Time-accurate simulations of a vortical flow around the ONERA 70 degree delta wing have been performed. Two non-dimensional time steps of different order of magnitude, 0.1 and 0.0025, have been used. The large time step has resulted in a steady-state solution containing vortex breakdown. In reaching the steady-state, high frequency components are observed in the flow field with the magnitudes rapidly decreasing in time. This confirms that a high frequency mode is responsible for the oscillating phenomena of vortex breakdown.

A physically meaningful solution has been obtained by the small time step, where a self-sustained oscillation is evident. The results have been compared with the experimental data. The characteristics across and downstream of vortex breakdown observed in the experimental data are qualitatively well reproduced by the simulation but to a lesser extent quantitatively. This may be inherent to physical modelling involved in the RANS equations. However, insufficient spatial grid resolutions, both in the crossflow planes and in the streamwise direction, may also be held responsible for the discrepancies, as suggested by a very good agreement in the pressure distribution up to 40 % chord where the grid density is relatively high.

An unsteady RANS (URANS) simulation assumes a clear separation between the time scale of the main unsteady feature to be captured and the turbulence time scales. The current application lacks such a separation of scales between the unsteady vortex breakdown and the turbulence. Alternatively, one could consider the current simulation as an LES with an excessively high level of eddy viscosity, with exception of the vortex core, where the level of eddy viscosity has been effectively reduced. To improve the current results, simulations will be performed with a hybrid RANS/LES model (Ref. 8).

18.5 REFERENCES

- [1] S.B. Anderson, "Handling qualities related to stall/spin accidents of supersonic fighter aircraft", J. Aircraft, Vol. 22, No. 10, 1985, pp. 875-880.
- [2] W. Bihrlé and B. Barnhart, "Departure susceptibility and uncoordinated roll-reversal boundaries for fighter configurations", J. Aircraft, Vol. 19, No. 11, 1982, pp. 897-903.
- [3] F.H. Lutze, W.C. Durham and W.H. Mason, "Development of lateral-directional departure criteria", AIAA Paper 93-3650, 1993.
- [4] M.A. Park and L.L. Green, "Steady-state computation of constant rotational rate dynamic stability derivatives", AIAA Paper 2000-4321, 2000.
- [5] E.F. Charlton, "Numerical stability and control analysis towards falling-leaf prediction capabilities of Splitflow for two generic high-performance aircraft models", NASA CR-1998-208730, 1998.
- [6] A.M. Mitchell, "Caractérisation et contrôle de l'écatement tourbillonnaire sur une aile delta aux hautes incidences", Ph.D dissertation, Université Paris 6, 2000.
- [7] A.M. Mitchell, P. Molton, D. Barberis and J. D'elery, "Characterization of vortex breakdown by flow field and surface measurements", AIAA Paper 2000-0788, 2000.
- [8] J.C. Kok, H.S. Dol, B. Oskam and H. van der Ven, "Extra-Large Eddy Simulation of Massively Separated Flows", NLR-TP-2003-200, submitted for presentation at 42nd AIAA Aerospace Sciences Meeting and Exhibit, Reno, January 2004.
- [9] J.C. Kok, "Resolving the dependence on freestream values for the $k - \omega$ turbulence model", AIAA Journal, Vol. 38, No. 3, pp. 1292-1294, 2000.
- [10] J.C. Kok and S.P. Spekrijse, "Efficient and accurate implementation of the $k - \omega$ turbulence model in the NLR multi-block Navier-Stokes system", presented at ECCOMAS 2000, Barcelona, Spain, 11-14 September, 2000, also NLR TP-2000-144.
- [11] J.W. Boerstool, A. Kassies, J.C. Kok and S.P. Spekrijse, "ENFLOW, A full-functionality system of CFD codes for industrial Euler/Navier-Stokes Flow Computations", presented at the 2nd Int. Symp. on Aeron. Science and Tech., Jakarta, 1996, also NLR TP 96286.
- [12] F.J. Brandsma, J.C. Kok, H.S. Dol and A. Elsenaar, "Leading edge vortex flow computations and comparison with DNW-HST wind tunnel data", RTO/AVT Vortex Flow Symposium, Loen, Norway, 2001.
- [13] B.I. Soemarwoto, O.J. Boelens, M. Allan, M.T. Arthur, K. Bütetisch, N. Ceresola and W. Fritz, "Towards the simulation of unsteady manoeuvre dominated by vortical flow", AIAA Paper 2003-3528, 2003.
- [14] J.C. Kok, D.R. van der Heul and H.S. Dol. "Predesign and results of extension of ENSOLF to weakly compressible and buoyant flow", NLR-TR-2003-060, 2003.
- [15] S.A. Morton, M.B. Steenman, R.M. Cummings and J.R. Forsythe, "DES grid resolution issues for vortical flows on a delta wing and an F-18C", AIAA Paper 2003-1103, 2003.

Chapter 19 – UNSYMMETRIC VORTEX BREAKDOWN FOR SYMMETRIC FREE STREAM CONDITIONS

D. Hummel and M. Estorf

Institut für Strömungsmechanik,
Technische Universität Braunschweig,
Bienroder Weg 3, 38106 Braunschweig,
GERMANY

email: d.hummel@tu-bs.de / m.estorf@tu-bs.de

Abstract

The unsteady Euler equations have been solved for the flow field around a delta wing at a large angle of attack. The calculations have been carried out without and with a symmetry condition in the centre section of the wing. Spiral-type vortex breakdown has been calculated for both sides of the wing. Using a symmetry condition the flow field turns out artificially symmetrical. Without such a symmetry condition even for symmetrical free stream conditions the flow field turned out to be unsymmetrical: Different vortex breakdown positions, frequencies and phase differences in the rotation of the spiral vortex axes and modifications of the vortex axes have been found for both sides of the wing. After a long running time of the calculations a rather irregular behaviour of the flow quantities turned out.

19.1 Introduction

On a sharp edged slender delta wing inclined against the free stream at an angle of attack α , the flow on the lower side moves outboard. Flow separations take place at the sharp leading edges and primary vortices are formed over the upper surface of the wing. Underneath these vortices suction areas are generated on the wing. The flow is directed outboard there and the steep pressure gradient towards the leading edges causes the flow again to separate and to form secondary vortices underneath the primary vortices. This vortex formation is well known since a long time, see [1].

For small and medium angles of attack the separated flow is steady. Since numerical solutions of the Euler equations cannot cover the secondary separation the lift is overpredicted, whereas Navier Stokes calculations lead to much better results [2], [3].

For large angles of attack the structure of the primary vortices changes considerably, and this phenomenon is called vortex breakdown. On a delta wing with a leading edge sweep of 65° it occurs for angles of attack $\alpha \geq 20^\circ$. An early description of vortex breakdown on a delta wing has been given by [4] and since that time a huge number of investigations on this subject has been carried out worldwide. From the two possible modes of vortex breakdown, discussed in [4], the spiral type mainly occurs in the flow field of slender delta wings. Today it is common understanding that the flow past a slender delta wing at large angles of attack becomes unsteady even for a fixed wing. This means in other words that for large angles of attack and steady boundary conditions only unsteady solutions of the Euler and the Navier Stokes equations do exist. The spiral-type vortex

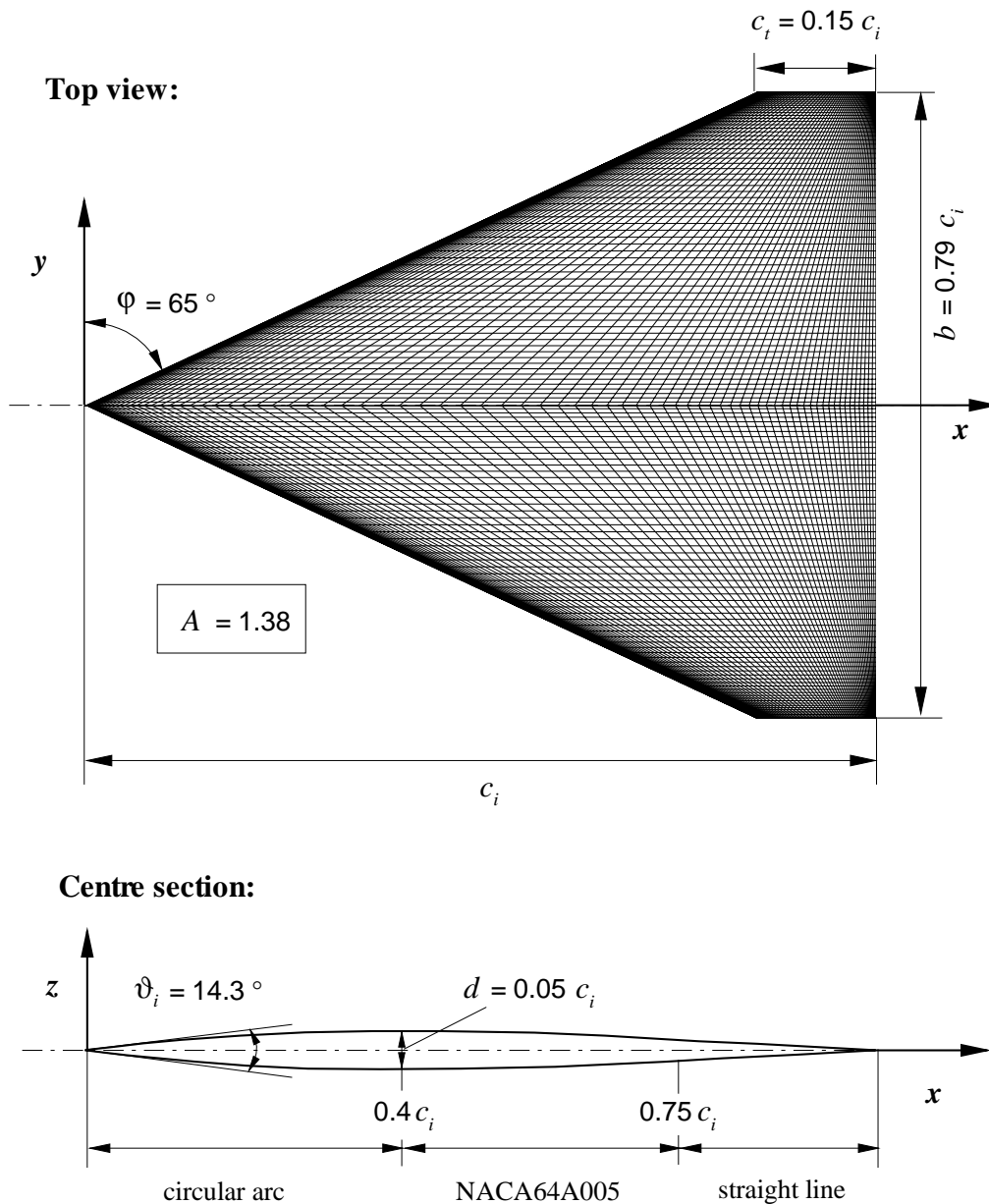


Fig. 1: Geometry and surface grid for the cropped delta wing ($A = 1.38$, $\lambda = 0.15$, $\varphi = 65^\circ$)

breakdown is well predicted by numerical solutions of the Euler and the Navier Stokes equations [5], [6], [7]: The instantaneous vortex axis spirals in space against the sense of the primary vortex and this spiral turns around with respect to time in the sense of the primary vortex, and in the centre of the spiralling motion a region of reversed flow is present. Correspondingly all quantities of the flow field, the pressure distribution on the wing as well as the overall forces and moments show oscillations. Their main frequency is that of the azimuthal mode of the spiralling motion, and this is well confirmed by experimental investigations [8], [9].

Up to now all numerical investigations on vortex breakdown on delta wings have been carried out on half wings using a symmetry condition in the centre section of the wing. This means that the pressure distribution, the position of vortex breakdown as well as the spiralling motion of the instantaneous vortex axes on both sides of the wing turned out artificially symmetrical. In real flow a symmetry condition in the centre section of the wing does not exist and a mutual interference of the two primary vortices takes place. Even in symmetrical free stream flow this could lead

to oscillations in the vortex breakdown positions and to unsymmetrical spiralling motions of the vortex axes on both sides of the wing. In order to cover such effects, in the present investigation the unsteady equations of motion have been solved for the complete flow field with two primary vortices and without using a symmetry condition in the centre section of the wing. Since spiral vortex breakdown is well predicted by solutions of the Euler and the Navier-Stokes equations [6],[7], for the sake of simplicity in the present approach the Euler equations have been solved in order to investigate the effects of the absence of a symmetry condition in the centre section of the wing.

In 1984 - 1986 the International Vortex Flow Experiment (VFE-1) [10], [11] has been carried out: On a cropped delta wing with a leading edge sweep of 65° combined with a fuselage, force and pressure measurements as well as flow field studies have been performed for a certain variety of flow conditions in various wind tunnels worldwide, and their results have been compared with numerical solutions of the Euler and the Navier Stokes equations [2], [3]. Since this configuration is well known in the scientific community, its wing has been used for the present investigation. According to Fig. 1 its data are

Aspect ratio: $A = 1.38$

Taper ratio: $\lambda = 0.15$

Leading edge sweep: $\varphi = 65^\circ$.

The sections $y = \text{const.}$ consist of the airfoil NACA 65A005, modified in the front part into a circular arc and in the rear part into a straight line.

19.2 Numerical Method

In the present approach the conservation laws for mass, momentum and energy in integral form

$$\frac{\partial}{\partial t} \int_V \mathbf{w} dV + \int_{\partial V} \mathbf{F}^c \mathbf{n} dS = 0 \quad (1)$$

are solved. Here, \mathbf{w} is the vector of conservative variables, $\mathbf{w} = [\rho, \rho \mathbf{q}, \rho E]$, which consists of the density ρ , the specific total energy E and the velocity vector $\mathbf{q} = [u, v, w]$. V denotes the control volume with boundary ∂V and with the outer normal \mathbf{n} , and \mathbf{F}^c is the convective flux-density tensor. Equ.(1) represents the Euler equations.

The presented results have been obtained using the CFD code FLOWer, which was compiled for the NEC-SX5 architecture in sequential mode. The software has been developed by the Institute of Design Aerodynamics at the DLR Braunschweig, Germany. Equ.(1) has been solved on a structured mesh. For discretization in space a second order cell-vertex scheme and central differences are used. For the damping of numerical oscillations artificial second and fourth order dissipative terms are added to the governing equations. The forth order term, which is dominant in the absence of shocks, is controlled by the user-defined damping coefficient $k^{(4)}$. Integration with respect to time utilizes a five stage Runge-Kutta scheme to converge the solution, which can be accelerated by using various techniques, e.g. a multigrid scheme [12]. For the unsteady calculations in the present approach a global time stepping procedure without implicit residual smoothing was used [13].

The calculations have been carried out on a structured grid with an O-O- topology as shown in Fig. 2. The corresponding net on the wing surface has been included in Fig. 1. For the Euler calculations a single block was used with $i \times j \times k = 81 \times 85 \times 137 = 943.245$ nodes in the case with a symmetry condition and $i \times j \times k = 81 \times 85 \times 273 = 1.879.605$ nodes in the case without a symmetry condition in the centre section of the wing. Very small time steps of $\Delta t^* = \Delta t \cdot U_\infty / c_i = 0.0012$ were necessary to cover the spiralling motion of the primary vortex axes, and for a detailed analysis of the time-dependent flow field about 75000 time steps were necessary. In the present approach the same value for the artificial damping coefficient has been used for the calculations with and without

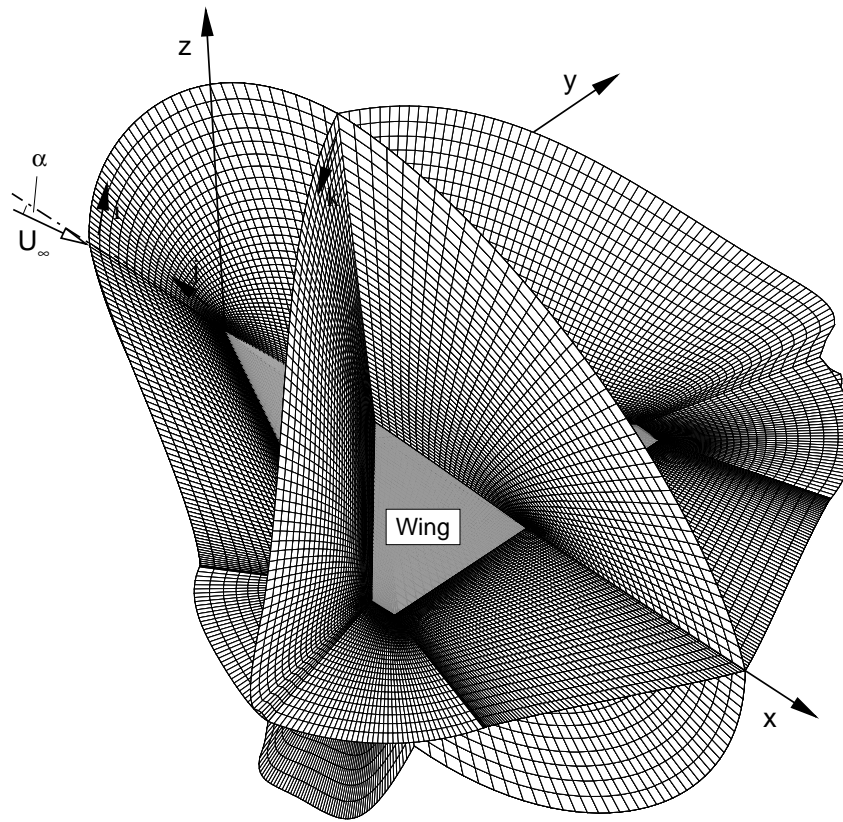


Fig. 2: Section of the mesh for Euler calculations using O-O-topology and 1 879 605 gridpoints

a symmetry condition in the centre section of the wing, and its value has been chosen as $k^{(4)} = 1/80$ according to [15] for best agreement of the vortex breakdown position with experimental data.

Since the governing equations are solved in compressible form, the numerical method encounters stability and convergence problems for very low Mach numbers. Thus, all calculations were performed for a Mach number of $M = 0.2$, where compressibility effects are still negligible.

19.3 Results

In the present investigation all studies of vortex breakdown have been carried out at Mach number $M = 0.2$ and for an angle of attack $\alpha = 25^\circ$.

19.3.1 Artificially Symmetric Solutions

19.3.1.1 Time History

Fig. 3 shows the time history of the unsteady Euler solution for the case with a symmetry condition in the centre section of the wing. Plotted are the lift coefficients of the left and the right half of the wing,

$$c_{ll} = \frac{L_{left}}{\frac{\rho}{2} U_\infty^2 S} \quad c_{lr} = \frac{L_{right}}{\frac{\rho}{2} U_\infty^2 S} \quad (2)$$

as functions of the dimensionless time $t^* = t \cdot U_\infty / c_i$. Due to the symmetry condition both values are identical in this case. Starting from a steady solution at $t^* = 1.2$, generated by means of the local time stepping mode of the code, the unsteady flow shows high frequency oscillations, which have been calculated up to $t^* = 40$.

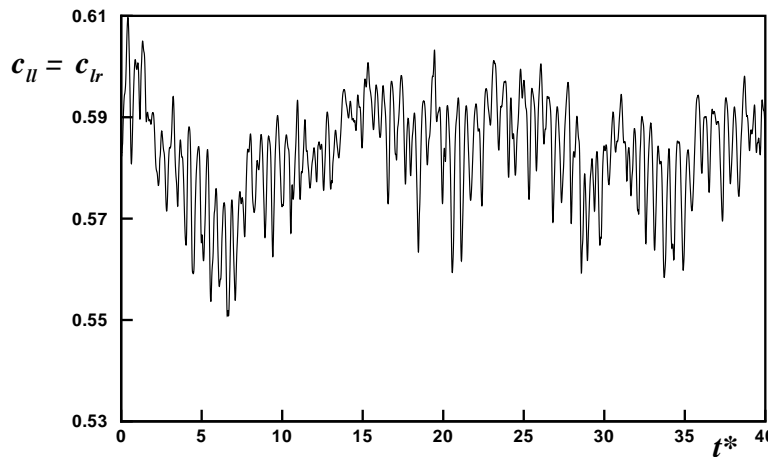


Fig. 3: Lift coefficient for left and right half-wing as function of dimensionless time. Euler solution, half wing with symmetry condition in the centre, $M = 0.2$, $\alpha = 25^\circ$

A frequency analysis has been carried out for the time interval $t_0^* = 10 \leq t^* \leq 40$. The function $c_{ll}(t^*)$ e.g. has been represented as

$$c_{ll}(t^*) = \sum_{k=0}^{N-1} \hat{c}_{llk} e^{i\omega_k^*(t^*-t_0^*)}, \quad (3)$$

with the frequencies of the various oscillations

$$\omega_k^* = \frac{2\pi}{N \cdot \Delta t_k^*} \cdot k, \quad k = 0, 1, \dots, N-1 \quad (4)$$

and the corresponding amplitudes \hat{c}_{llk} , where N denotes the number and Δt_k^* the width of the time steps. As a result of the fast Fourier transform the amplitude $\hat{c}_{ll} = \hat{c}_{lr}$ is plotted against the frequency ω_k^* in Fig. 4. The dominating frequency $\omega_k^* = 11$ is related to the azimuthal mode of the spiral vortex breakdown as described by [15]. At low frequencies $0.5 \leq \omega_k^* \leq 2.5$ large amplitudes do exist as well. The corresponding flow physics will be analyzed subsequently.

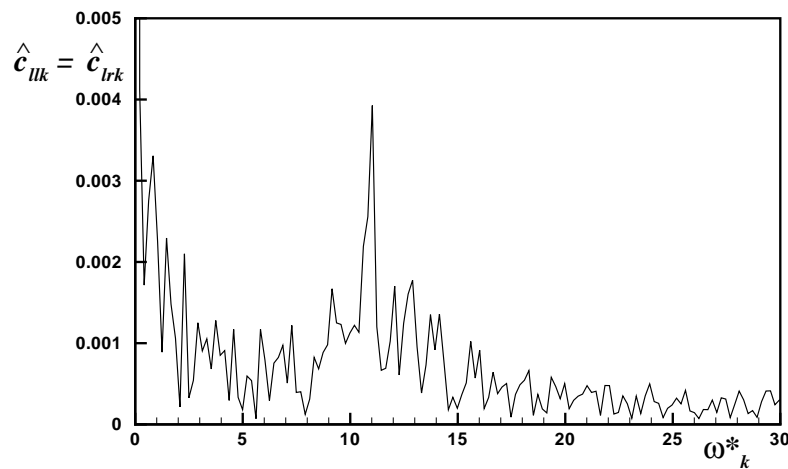


Fig. 4: Frequency spectrum for the lift coefficient . Euler solution, half wing with symmetry condition in the centre, $M = 0.2$, $\alpha = 25^\circ$

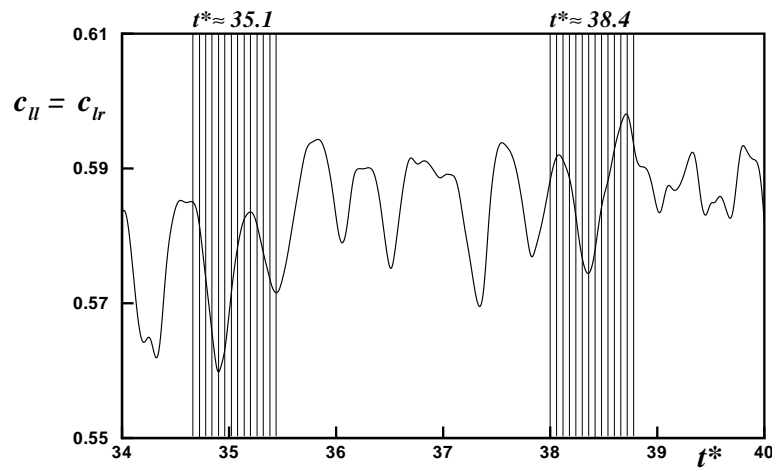


Fig. 5: Lift coefficient for left and right half-wing as function of dimensionless time with intervals for detailed analysis. Euler solution, half wing with symmetry condition in the centre, $M = 0.2$, $\alpha = 25^\circ$

19.3.1.2 Flow Analysis

A detailed analysis of the flow has been carried out in the time period $34 \leq t^* \leq 40$, see Fig. 3, which is shown enlarged in Fig. 5. The oscillations due to spiral vortex breakdown with the frequency $\omega_k^* = 11$ are easily recognized. Two time intervals have been chosen at $t^* \approx 35.1$, where the instantaneous lift coefficient is low and at $t^* \approx 38.4$, where its value is high. In both time intervals a total of 13 time steps has been considered for details. The instantaneous vortex axes have been determined as the positions of the maxima of total pressure loss, and in addition the mean values and the standard deviations of the surface pressure distribution have been evaluated for both time intervals under consideration.

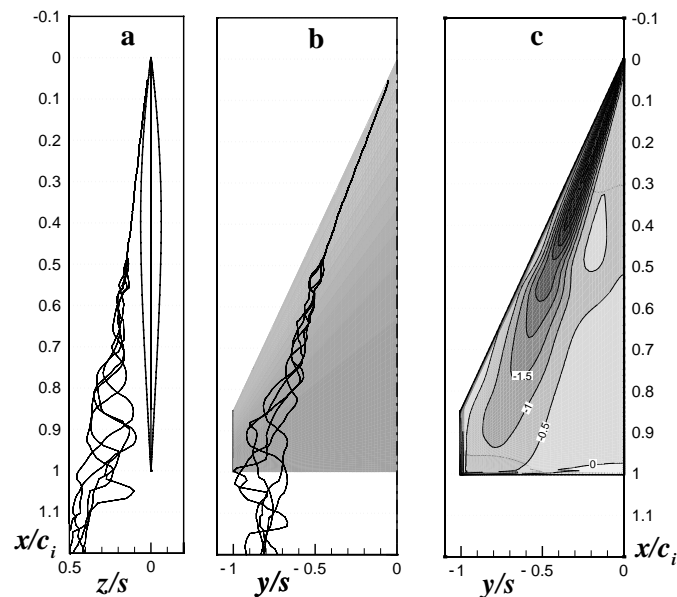


Fig. 6: Flow analysis for the time interval $t^* \approx 35.1$ according to Fig.5.

a) Vortex axes, side view

b) Vortex axes, top view

c) Mean upper surface pressure distribution, lines $\bar{c}_p = \text{const.}$

Euler solution, half wing with symmetry condition in the centre, $M = 0.2$, $\alpha = 25^\circ$

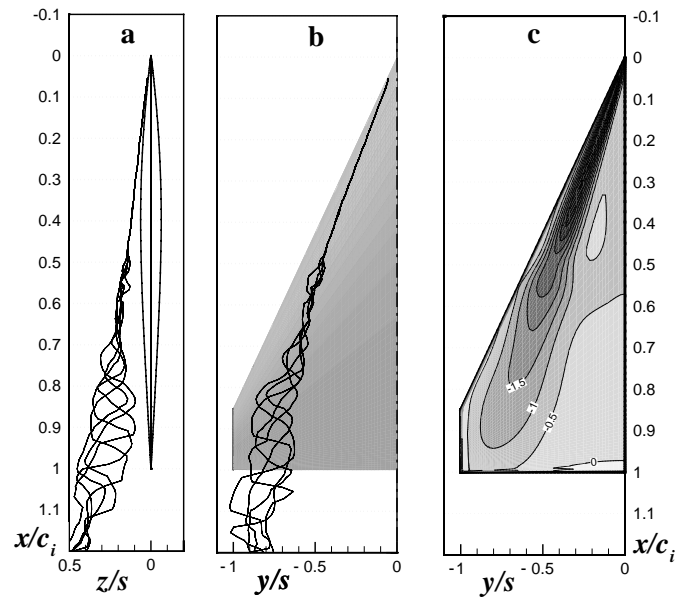


Fig. 7: Flow analysis for the time interval $t^* \approx 38.4$ according to Fig.5.

a) Vortex axes, side view

b) Vortex axes, top view

c) Mean upper surface pressure distribution, lines $\bar{c}_p = \text{const.}$

Euler solution, half wing with symmetry condition in the centre, $M = 0.2$, $\alpha = 25^\circ$

The instantaneous vortex axes are shown for five values of t^* within the time interval at $t^* \approx 35.1$ in Fig. 6a,b and at $t^* \approx 38.4$ in Fig. 7a,b. The mean upper surface pressure distributions with lines $c_p = \text{const.}$ for both time intervals are added in Fig. 6c and Fig. 7c. According to Fig. 6 at $t^* \approx 35.1$ vortex breakdown takes place at $x/c_i = 0.48$. The mean surface pressure distribution indicates a considerable loss of suction in the area underneath the vortex breakdown region, and the lift coefficient in the time interval at $t^* \approx 35.1$ is relatively low. According to Fig. 7 at $t^* \approx 38.4$ vortex breakdown occurs at $x/c_i = 0.49$. In comparison with the time interval at $t^* \approx 35.1$, see Fig. 6, the difference in the vortex breakdown position is very small. On the other hand the mean pressure distribution according to Fig. 7c indicates higher suction underneath the vortex breakdown region, and thus a larger lift coefficient is present for the time interval at $t^* \approx 38.4$.

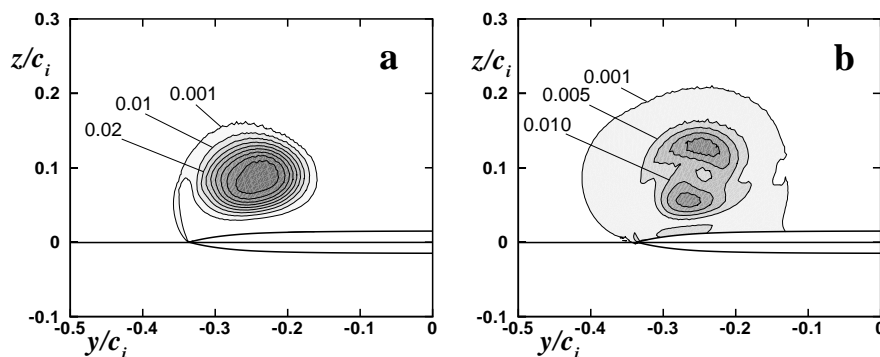


Fig. 8: Flow field in the cross section at $x/c_i = 0.72$ for the time interval at $t^* \approx 35.1$

a) Lines of constant mean values of total pressure loss, $1 - \bar{p}_t/p_{t\infty} = \text{const.}$

b) Lines of constant standard deviation of total pressure, $p'_t/p_{t\infty} = \text{const.}$

Euler solution, half wing with symmetry condition in the centre, $M = 0.2$, $\alpha = 25^\circ$

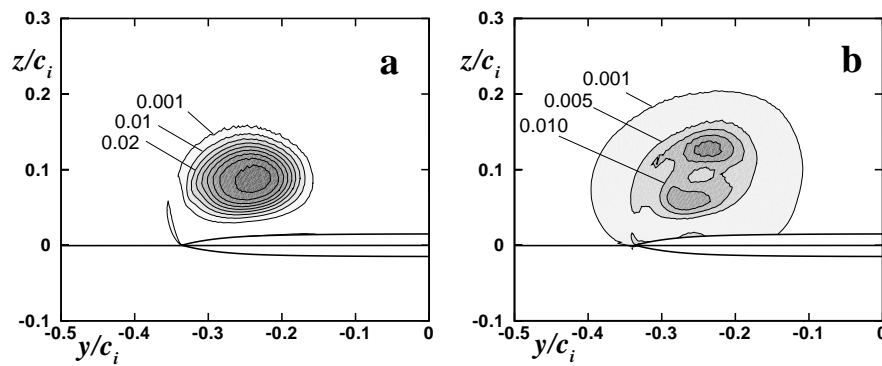


Fig. 9: Flow field in the cross section at $x/c_i = 0.72$ for the time interval at $t^* \approx 38.4$
a) Lines of constant mean values of total pressure loss, $1 - \bar{p}_t/p_{t\infty} = \text{const.}$
b) Lines of constant standard deviation of total pressure, $p'_t/p_{t\infty} = \text{const.}$
Euler solution, half wing with symmetry condition in the centre, $M = 0.2$, $\alpha = 25^\circ$

For further flow analysis the cross section at $x/c_i = 0.72$ has been chosen. For this plane lines of constant mean values of total pressure loss and lines of constant standard deviation of total pressure are shown in Fig. 8 for the time interval at $t^* \approx 35.1$ and in Fig. 9 for the time interval $t^* \approx 38.4$. According to [15] spiral vortex breakdown leads to increased total pressure losses around the mean vortex axis, and the standard deviation of total pressure reaches an annular shaped maximum at some distance from the vortex axis and shows lower values in the vortex center. This pattern is caused by the spiralling motion of the vortex axis, which leads to large fluctuations in that region of the vortex where the instantaneous vortex axis passes. The comparison of the Figs. 8 and 9 shows that the mean total pressure losses and the standard deviations of the total pressure for $t^* \approx 35.1$ (Fig. 8) are higher than those for $t^* \approx 38.4$. These details indicate again, that for $t^* \approx 35.1$ vortex breakdown occurs slightly further upstream than for $t^* \approx 38.4$ and this leads to lower suction and to a lower lift coefficient.

19.3.1.3 Discussion

The present numerical investigations based on the Euler equations have shown that in the case with a symmetry condition in the centre section of the wing for an angle of attack $\alpha = 25^\circ$ vortex breakdown takes place at about $x/c_i \approx 0.485$. With respect to time only very small oscillations of the vortex breakdown position in upstream and downstream direction take place, and this leads to corresponding oscillations of the pressure distribution and the lift coefficient with respect to time.

19.3.2 Unsymmetric Solutions

19.3.2.1 Time History

Fig. 10 shows the time history of the unsteady Euler solution for the case of the full wing without a symmetry condition in the centre section. Plotted are the lift coefficients of the left and the right half of the wing c_{l_l} and c_{l_r} as functions of the dimensionless time t^* . Starting again from a steady solution generated by means of the local time stepping mode of the code, the unsteady flow shows high frequency oscillations, but it remains symmetrical up to about $t^* = 10$. Then an unsymmetry starts suddenly. The lift coefficients of both sides are no longer equal. On each side of the wing the high frequency oscillations continue, but low frequency oscillations are superimposed, which are different on both sides of the wing.

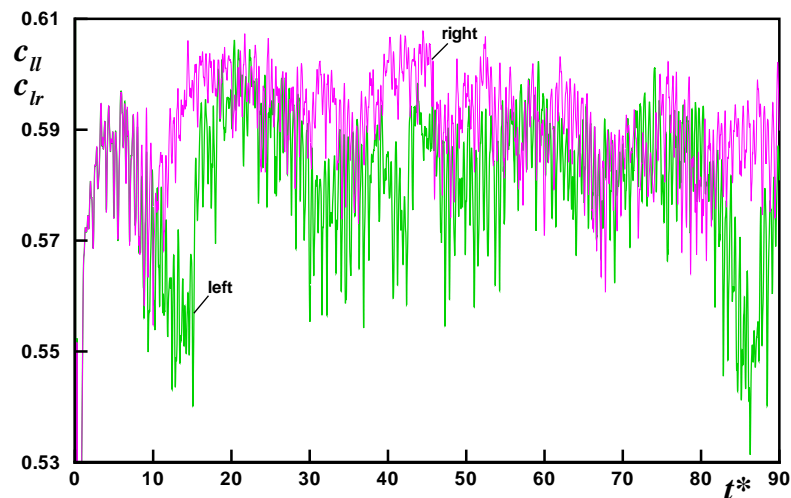


Fig. 10: Lift coefficient for left and right half-wing as function of dimensionless time. Euler solution, full wing without a symmetry condition in the centre, $M = 0.2$, $\alpha = 25^\circ$

The frequency analysis results are shown in Fig. 11 for the left and the right wing half separately. On both sides the dominating frequency, which is related to the spiral motion of vortex breakdown, lies again at $\omega_k^* \approx 11$, but the high amplitudes in its vicinity $9 \leq \omega_k^* \leq 14$ indicate that the frequency of the spiral mode of vortex breakdown might be subject to changes due to the mutual interference between the left and right side of the wing. In addition very low frequency motions take place on both sides of the wing, but these are different on both sides. The corresponding flow physics will be analyzed subsequently.

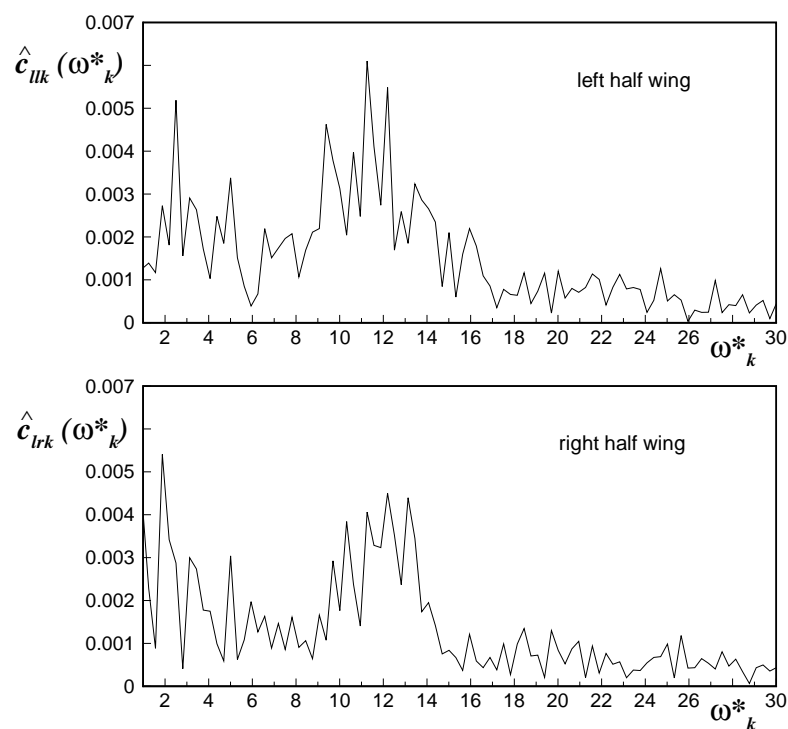


Fig. 11: Frequency spectrum for the lift coefficient of left and right half-wing. Euler solution, full wing without a symmetry condition in the centre, $M = 0.2$, $\alpha = 25^\circ$

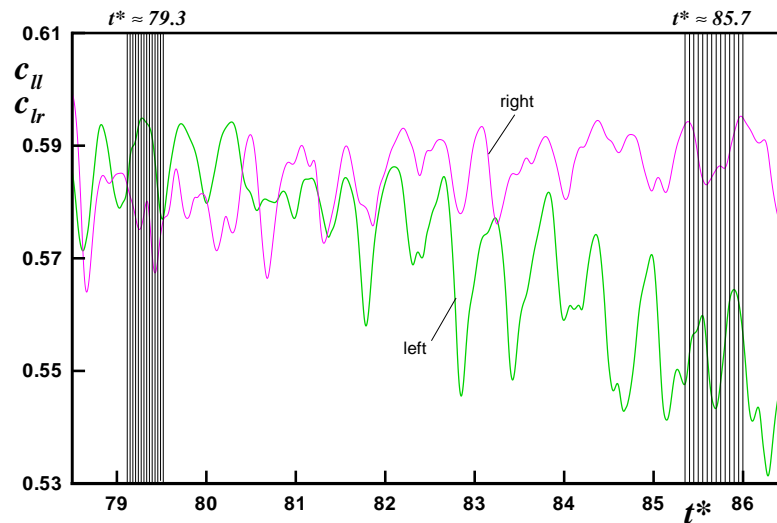


Fig. 12: Lift coefficient for left and right half-wing as function of dimensionless time with intervals for detailed analysis. Euler solution, full wing without a symmetry condition in the centre, $M = 0.2$, $\alpha = 25^\circ$

19.3.2.2 Flow Analysis

A detailed analysis of the flow has been carried out in the time period $78.5 \leq t^* \leq 86.5$, see Fig. 10, which is shown enlarged in Fig. 12. The oscillations due to the spiral mode of vortex breakdown with the frequency $\omega_k^* = 9 \div 13$ are easily recognized. Two time intervals have been chosen for further analysis: At $t^* \approx 79.3$ the instantaneous lift coefficient on the left side of the wing is slightly

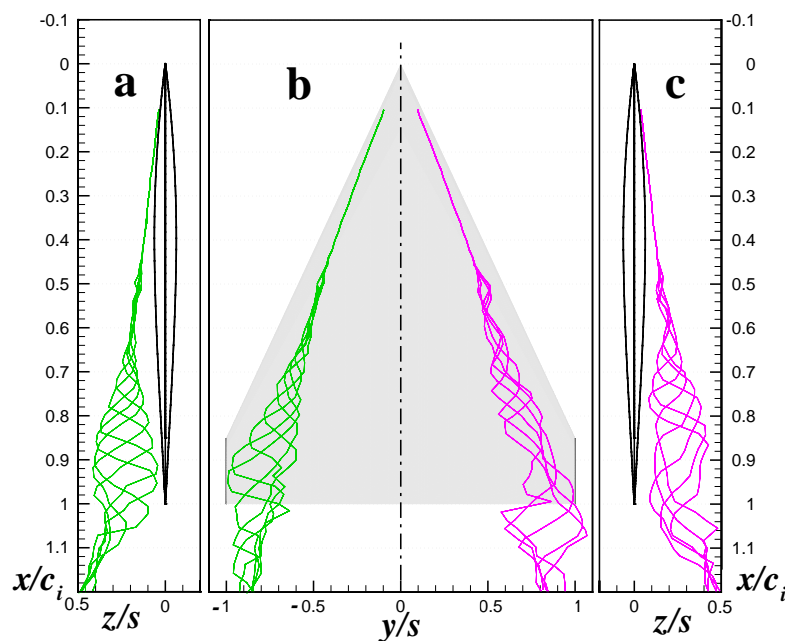


Fig. 13: Flow analysis for the time interval $t^* \approx 79.3$ according to Fig.12.

- a) Left vortex axes, side view
- b) Left and right vortex axes, top view
- c) Right vortex axes, side view

Euler solution, full wing without a symmetry condition in the centre, $M = 0.2$, $\alpha = 25^\circ$

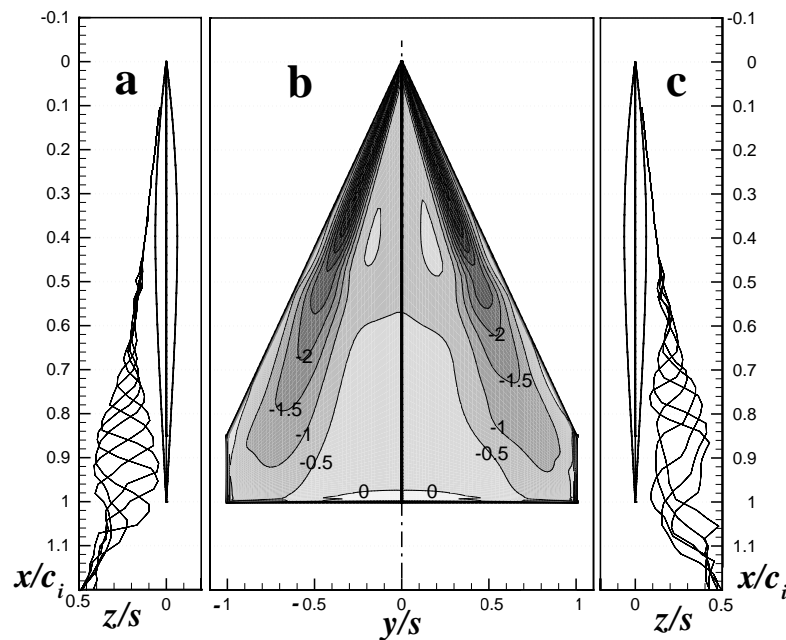


Fig. 14: Flow analysis for the time interval $t^* \approx 79.3$ according to Fig.12.

- a) Left vortex axes, side view
- b) Mean upper surface pressure distribution, lines $\bar{c}_p = \text{const.}$
- c) Right vortex axes, side view

Euler solution, full wing without a symmetry condition in the centre, $M = 0.2$, $\alpha = 25^\circ$

larger than that on the right side, $c_{ll} > c_{lr}$, and at $t^* \approx 85.7$ the situation is opposite, $c_{ll} \ll c_{lr}$. In both time intervals a total of 13 time steps has been considered for details. The instantaneous vortex axes have been determined as the positions of the maxima of total pressure loss, and in addition the mean values and the standard deviations of the surface pressure distribution have been evaluated for both time intervals under consideration.

The instantaneous vortex axes are shown for five values of t^* within the time interval at $t^* \approx 79.3$ in Fig. 13. The vortical flow field turns out to be unsymmetrical. Vortex breakdown takes place in the vortex on the left side at $x/c_i = 0.48$ and on the right side at $x/c_i = 0.46$. On both sides the spiral type of vortex breakdown occurs, but the initial spiral motion of the vortex axis is relatively weak on both sides. After a certain margin downstream in x -direction the spatial amplitude of the spiral motion of the vortex axes increases. In Fig. 14 the top view of the vortex axes of Fig. 13 is replaced by the mean upper surface pressure distribution for the time interval under consideration. This plot clearly indicates that in the vortex breakdown region in the rear part of the wing, the suction on the left half of the wing is larger than on the right half and therefore the lift coefficient of the left half of the wing is larger than that on the right half, $c_{ll} > c_{lr}$.

For the time interval at $t^* \approx 85.7$ the instantaneous vortex axes for five values of t^* are shown in Fig. 15. Again the vortical flow field is unsymmetric but in the opposite sense than in Figs. 13 and 14. Vortex breakdown takes place in the vortex on the left side at $x/c_i = 0.43$ and on the right side at $x/c_i = 0.50$. In the vortex breakdown region the initial spiral motion of the vortex axis is relatively weak on both sides, but further downstream the spiral motion of the vortex axis increases on both sides, and it is easily recognized that the vortex on the left half of the wing shows earlier and more severe vortex breakdown than that on the right side. Correspondingly the mean upper surface pressure distribution according to Fig. 16 shows more reduced suction on the left half of the wing and therefore the local lift coefficient on the left half of the wing is lower than on the right half, $c_{ll} < c_{lr}$.

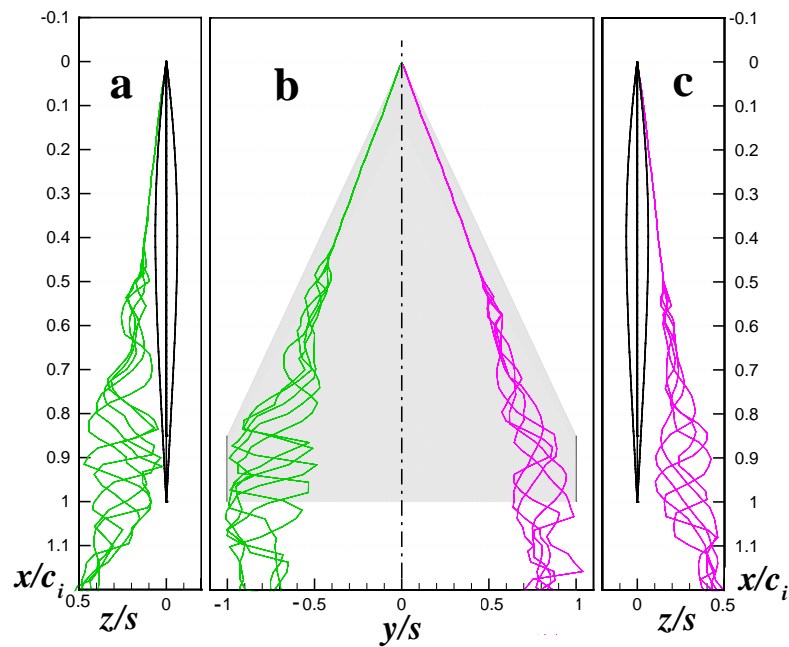


Fig. 15: Flow analysis for the time interval $t^* \approx 85.7$ according to Fig.12.

- a) Left vortex axes, side view
- b) Left and right vortex axes, top view
- c) Right vortex axes, side view

Euler solution, full wing without a symmetry condition in the centre, $M = 0.2$, $\alpha = 25^\circ$

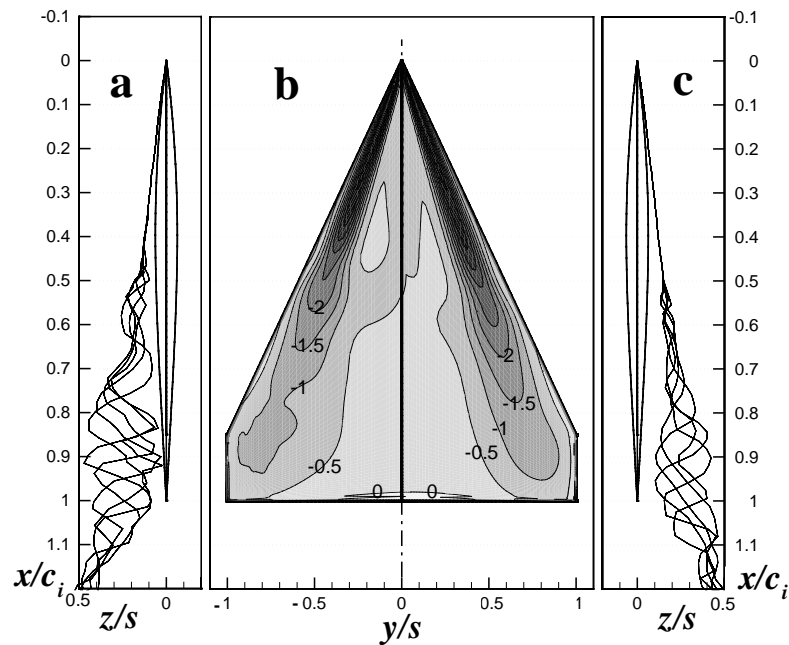


Fig. 16: Flow analysis for the time interval $t^* \approx 85.7$ according to Fig.12.

- a) Left vortex axes, side view
- b) Mean upper surface pressure distribution, lines $\bar{c}_p = \text{const.}$
- c) Right vortex axes, side view

Euler solution, full wing without a symmetry condition in the centre, $M = 0.2$, $\alpha = 25^\circ$

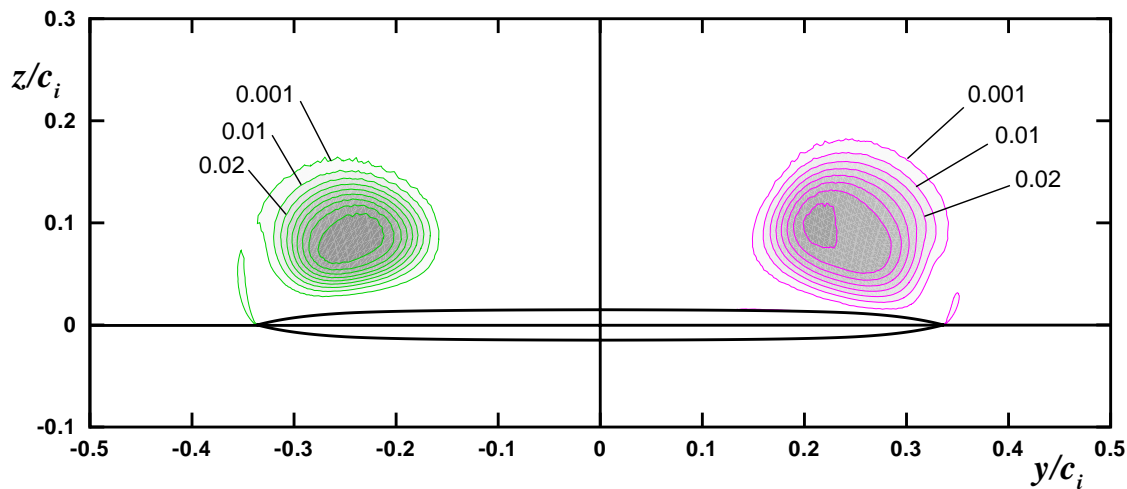


Fig. 17: Flow field in the cross section at $x/c_i = 0.72$ for the time interval at $t^* \approx 79.3$. Lines of constant mean values of total pressure loss, $1 - \bar{p}_t/p_{t\infty} = \text{const.}$ Euler solution, full wing without a symmetry condition in the centre, $M = 0.2$, $\alpha = 25^\circ$

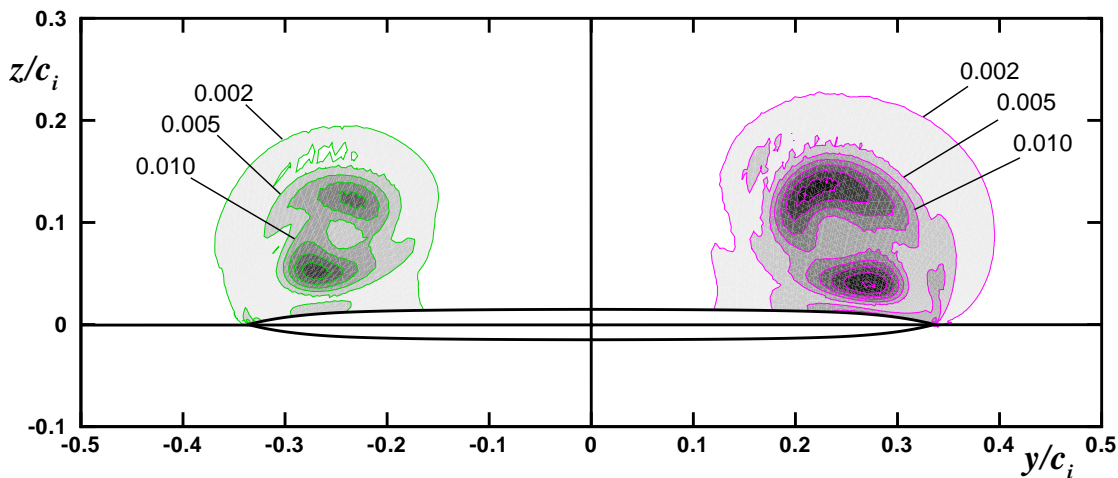


Fig. 18: Flow field in the cross section at $x/c_i = 0.72$ for the time interval at $t^* \approx 79.3$. Lines of constant standard deviation of total pressure, $p'_t/p_{t\infty} = \text{const.}$ Euler solution, full wing without a symmetry condition in the centre, $M = 0.2$, $\alpha = 25^\circ$

Further flow analysis is related to the cross section at $x/c_i = 0.72$. For this plane lines of constant mean values of total pressure loss are shown in Fig. 17 for the time interval at $t^* \approx 79.3$ and in Fig. 19 for the time interval at $t^* \approx 85.7$ and lines of constant standard deviation of total pressure are shown in Fig. 18 for the time interval at $t^* \approx 79.3$ and in Fig. 20 for the time interval at $t^* \approx 85.7$. The corresponding results for the artificially symmetric solution may be taken from Figs. 8 and 9 for comparison. The Figs. 17 and 18 show that in the cross section under consideration within the time interval at $t^* \approx 79.3$ vortex breakdown is more severe on the right wing half. The area of total pressure losses is more extensive there and the total pressure fluctuations are larger than on the opposite side. These results correspond to the flow analysis according to Figs. 13 and 14. In the cross section at $x/c_i = 0.72$ for the time interval at $t^* \approx 85.7$ the vortex on the left wing half shows more severe vortex breakdown than that on the right wing half, see Figs. 19 and 20. This corresponds to the flow analysis according to Figs. 15 and 16.

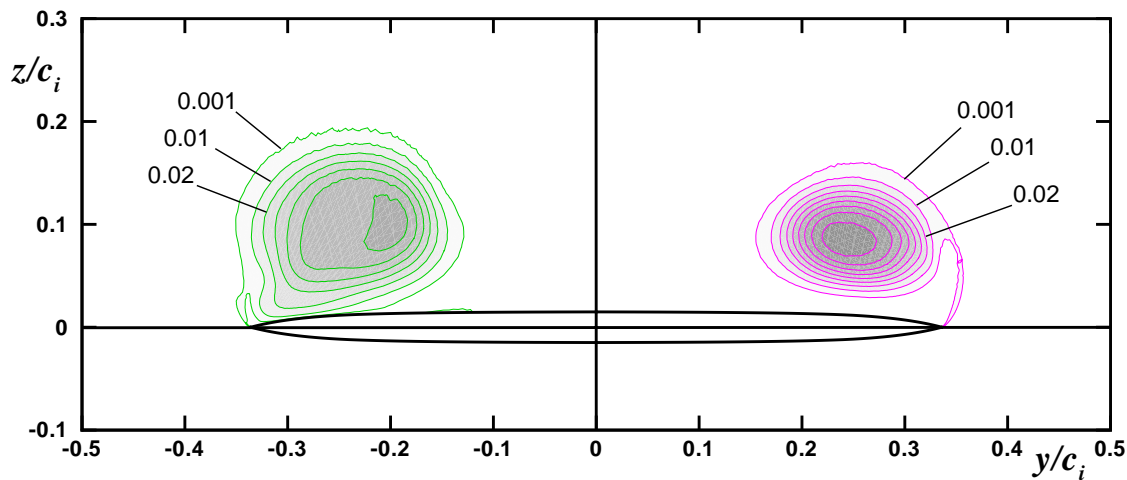


Fig. 19: Flow field in the cross section at $x/c_i = 0.72$ for the time interval at $t^* \approx 85.7$. Lines of constant mean values of total pressure loss, $1 - \bar{p}_t/p_{t\infty} = \text{const.}$ Euler solution, full wing without a symmetry condition in the centre, $M = 0.2$, $\alpha = 25^\circ$

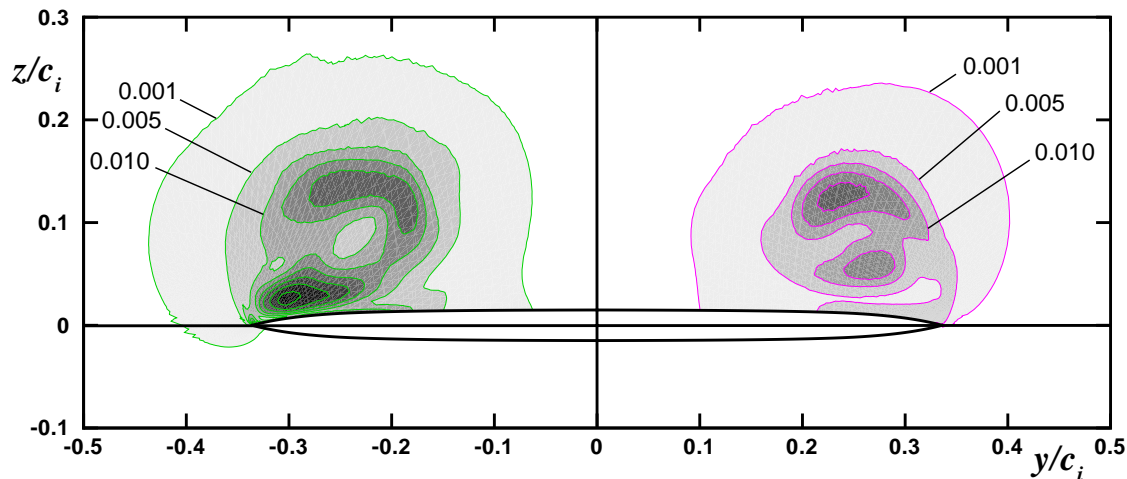


Fig. 20: Flow field in the cross section at $x/c_i = 0.72$ for the time interval at $t^* \approx 85.7$. Lines of constant standard deviation of total pressure, $p'_t/p_{t\infty} = \text{const.}$ Euler solution, full wing without a symmetry condition in the centre, $M = 0.2$, $\alpha = 25^\circ$

After this discussion of time-averaged values of the flow data in certain time intervals, the instantaneous flow field is now considered for $t^* = 85.7$. For this moment, Fig. 21 shows the total pressure loss distribution in the cross section at $x/c_i = 0.72$ and Fig. 22 presents the instantaneous vortex axes and the corresponding surface pressure distribution. As already shown for the whole time interval in Figs. 15, 16 and 19 the flow field is unsymmetric. The vortex on the left side of the wing breaks down earlier. Therefore in the cross section $x/c_i = 0.72$ the area of total pressure losses is larger on the left side of the wing and the spatial amplitude of the spiral vortex axis is also larger there. In addition to this, the instantaneous flow field results according to Figs. 21 and 22 show that the spiralling vortex axes on both sides of the wing are in different positions for the same moment in time, which is another effect of unsymmetry. Concerning the pressure distribution according to Fig. 22 the instantaneous suction is high underneath those parts of the vortex in which the vortex axis lies close to the wing surface. Due to the motion of the vortex axes with respect to time the surface pressure distribution as well as the local lift coefficients for both sides of the wing vary with time.

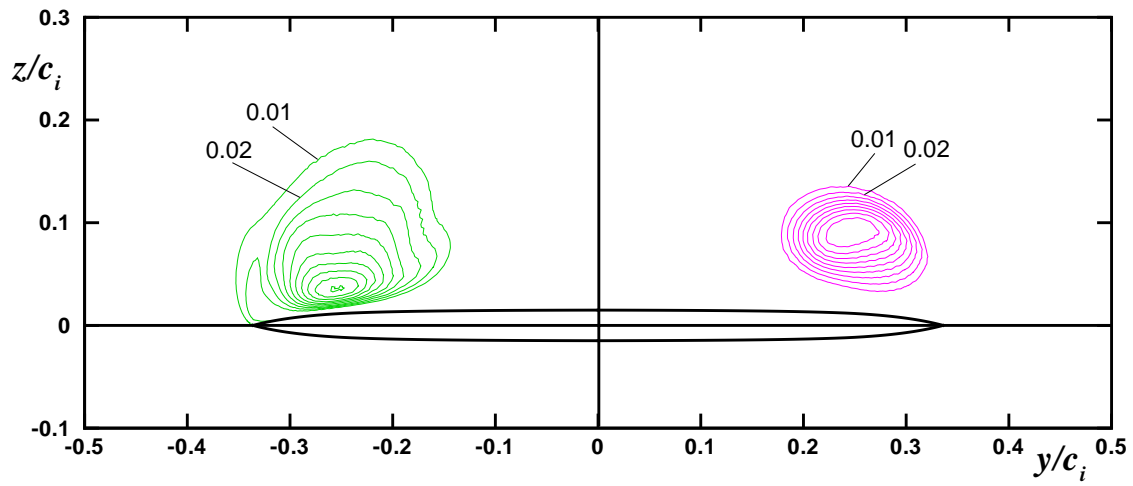


Fig. 21: Instantaneous flow field for $t^* = 85.7$: Lines of constant total pressure loss, $1 - p_t/p_{t\infty} = \text{const.}$ in the cross section at $x/c_i = 0.72$. Euler solution, full wing without a symmetry condition in the centre, $M = 0.2$, $\alpha = 25^\circ$

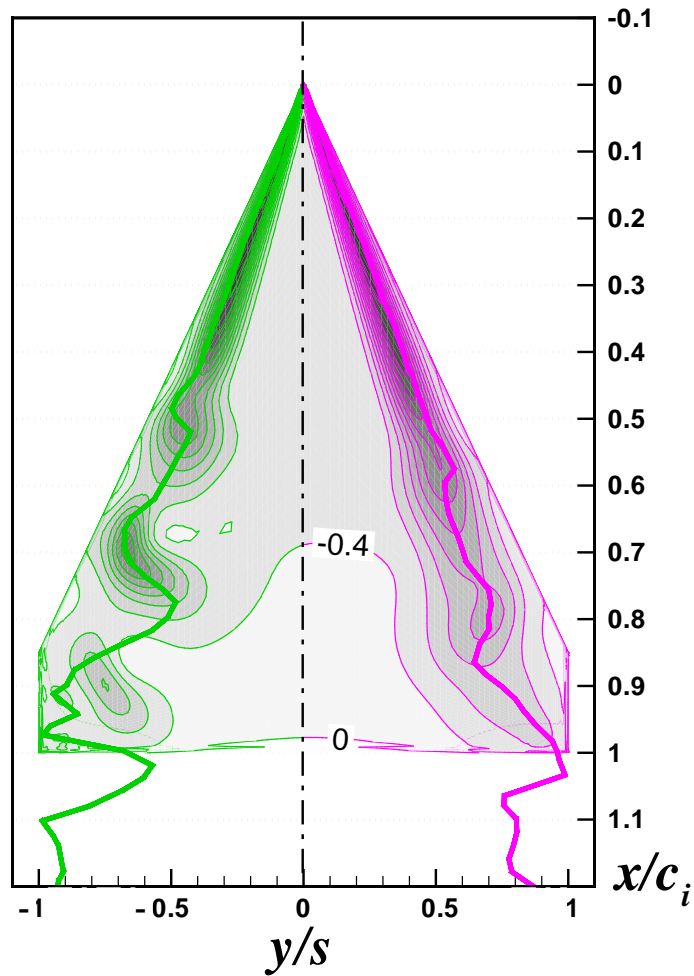


Fig. 22: Instantaneous flow field for $t^* = 85.7$: Vortex axes and upper surface pressure distribution with lines $c_p = \text{const.}$ Euler solution, full wing without a symmetry condition in the centre, $M = 0.2$, $\alpha = 25^\circ$

19.3.2.3 Discussion

The present unsteady solutions of the Euler equations have shown that in the case without a symmetry condition in the centre section of the wing even for symmetrical free stream conditions an unsymmetrical vortex formation turns out for high angles of attack where vortex breakdown takes place. The details of this unsymmetry are

- i) The position of vortex breakdown within the vortices is different on both sides of the wing. The onset of vortex breakdown moves upstream on one side and downstream on the other side and vice versa.
- ii) Concerning the rotation of the spiral vortex axes with respect to time there exists a frequency shift and a phase difference between both sides. If the motions on both sides of the wing would be symmetrical the frequency of the spiral motion should be equal on both sides and the phase difference should be 0° . The present investigations have shown that this is not the case if no symmetry condition in the centre section of the wing is applied.
- iii) The spiral shape of the vortex axis in space changes with time. In some periods of time a large amplitude spiral is present and in other periods of time a small amplitude initial part of the vortex is followed downstream by a larger amplitude second part.

An upstream movement of the vortex breakdown position according to i) leads to a reduction of the lift coefficient on the wing side under consideration, whereas the occurrence of two modes of the spiral shape of the vortex axis in space according to iii) causes an increase of the lift coefficient there. All effects together finally lead to an irregular dependence of the flow quantities with respect to time on both sides of the wing.

19.4 Performance

The results presented in the previous section were obtained running the FLOWer code in sequential mode on one of the NEC-SX5 processors. In all cases a performance of about 2 GFLOP/sec was obtained which amounts half of the possible peak performance of one processor. The vector operation ratio was always more than 99%, with vector lengths of 219 for Euler calculations. Memory requirements and run times mainly depend on the grid size and the dimensionless time t^* necessary for the analysis of the unsteady flow. In the present Euler calculations a grid with about 1.9 Mio nodes was used. For the analysis 75000 global time steps Δt^* were necessary to reach $t^* = 90$, see Fig.10, and the CPU time spent was about 65 h with about 1 GB memory requirement.

19.5 Conclusions

The NEC-SX5 platform has been used to solve the unsteady Euler equations for the flow around a delta wing at a large angle of attack for which vortex breakdown takes place in the vortices over the wing. The flow field has been calculated with and without using a symmetry condition in the centre section of the wing. In both cases spiral-type vortex breakdown has been found on both sides of the wing: The vortex axis spirals in space against the sense of the vortex motion and this spiral turns around with respect to time in the sense of the vortex motion.

In the case with a symmetry condition in the centre section of the wing the flow turns out artificially symmetrical. The flow in the vortices becomes unsteady at the breakdown position, but downstream shape and rotating motion of the spiral vortex axis is the same on both sides of the wing. Only very small oscillations of the vortex breakdown position upstream and downstream as well as in radial direction have been found as already analyzed in [15].

In the case without a symmetry condition in the centre section of the wing, even for symmetrical free stream conditions there exists a mutual interference between the vortices on both sides of the wing and this leads to an unsymmetrical vortex formation. Different vortex breakdown positions on both sides, frequency and phase differences in the rotation of the spiral vortex axes on both sides and time-dependent modifications of the spiral shape of the vortex axes on both sides have been found. In the course of the numerical calculations it took a long time until these effects were fully developed and the final irregular behaviour of the flow quantities was established.

Today it is common understanding that for large angles of attack the vortical flow over a delta wing must become unsteady even for steady boundary conditions. The first characteristics of the unsteadiness are rotating spiral vortex axes on both sides of the wing and this phenomenon is called vortex breakdown. The present investigations have shown that the mutual interference between the unsteady vortical flow fields of both sides leads to modifications of shape and rotation of the spiral vortex axes on both sides. This superimposed second order unsteadiness results in movements of the breakdown position upstream on one side and simultaneously downstream on the other side and vice versa. It can be expected that with increasing angle of attack these second order effects become more and more important. In addition to the initial frequency of the spiral motion of the vortex axes other frequencies will grow up in the unsteady flow field until finally the structure of a deadwater-type flow is established.

19.6 References

- [1] Hummel, D. and Redeker, G.: A new vortex flow experiment for computer code validation. RTO AVT Symposium on "Vortex Flow and High Angle of Attack", Loen, Norway, 7 - 11 May 2001, Paper No. 8.
- [2] Hoeijmakers, H.W.M.: Modelling and numerical simulation of vortex flow in aerodynamics. AGARD-CP 494 (1991), pp. 1-1 to 1-46.
- [3] Borsi, M.; Kordulla, W.; Hoeijmakers, H.W.M. and Williams, B.R.: Comparison of various Navier-Stokes solvers and one Euler solver for the flow about a sharp edged cropped delta wing. In: Royal Aeron. Soc.(Ed.): Proceedings of the 1993 European Forum on "Recent Developments and Applications in Aeronautical CFD", Bristol 1993, pp. 5.1 - 5.11.
- [4] Lambourne, N.C. and Bryer, D.W.: The bursting of leading edge vortices. Some observations and discussion of the phenomenon. ARC R&M 3282 (1962).
- [5] Visbal, M.R.: Computed unsteady structure of spiral vortex breakdown on delta wings. AIAA Paper 96-2074 (1996).
- [6] Müller, J. and Hummel, D.: Time-accurate CFD analysis of the unsteady flow on a fixed delta wing. AIAA Paper 2000-0138 (2000).
- [7] Müller, J. and Hummel, D.: Numerical analysis of the unsteady flow above a slender delta wing at large angles of attack. ICAS Proceedings 2000, Paper ICA 0252 (2000).
- [8] Gursul, I.: Unsteady flow phenomena over delta wings at high angle of attack. AIAA J. 32(2), 1994, 225 - 231.
- [9] Breitsamter, C.: Turbulente Strömungsstrukturen an Flugzeugkonfigurationen mit Vorderkantenwirbeln. Thesis TU München, Herbert Utz Verlag Wissenschaft (1997).
- [10] Drougge, G.: The international vortex flow experiment for computer code validation. ICAS Proceedings 1988, Vol. 1, pp. XXXV-XLI.

- [11] Elsenaar, A.; Hjelmberg, L; Bütetisch, K.A. and Bannink, W.J.: The international vortex flow experiment. AGARD-CP 437 (1988), Vol.1, pp. 9-1 to 9-23.
- [12] Radespiel, R.; Rossow, C. and Swanson, R.C.: Efficient cell vertex multigrid scheme for the three-dimensional Navier-Stokes equations. AIAA J. 28 (1990), 1464 - 1472.
- [13] Heinrich, R. and Bleeke, H.: Simulation of unsteady, three-dimensional viscous flows using a dual-time stepping method. Notes on Numerical Fluid Mechanics 60 (1997), Vieweg Verlag Braunschweig, 173 - 180.
- [14] Pahlke, K.D.: Development of a numerical method solving the unsteady Euler equations for airfoils and arbitrary motions. DLR-IB 129-92-09, DLR Braunschweig (1992).
- [15] Müller, J.: Numerische Simulation der Wirbelströmung an einem Deltaflügel. Thesis TU Braunschweig, Zentrum für Luft- und Raumfahrttechnik, ZLR-Forschungsbericht 2001-03 (2001).

Chapter 20 – COMPUTATIONAL INVESTIGATION OF THE CENTERBODY EFFECTS ON THE AERODYNAMICS OF DELTA WINGS

A. Benmeddour, Y. Mébarki and X.Z. Huang

Institute for Aerospace Research, National Research Council
Ottawa, ON, K1A 0R6, Canada

Ali.benmeddour@nrc-cnrc.gc.ca

ABSTRACT

Computational aerodynamic studies were conducted to investigate the centerbody effects on the aerodynamic characteristics of delta wings with sharp leading edges. Vortical flows around IAR 65° delta and 55° diamond wings were simulated using Computational Fluid Dynamics (CFD). Two flow solvers were employed to compute steady inviscid flows over with and without centerbody configurations of the two wings. These two solvers are an IAR in-house code, FJ3SOLV, and the CFD-FASTRAN commercial software. The computed flow solutions of the two solvers have been compared and correlated against the IAR Pressure Sensitive Paint (PSP) measurements. The major features of the primary vortex were well captured and overall reasonable accuracy was obtained. In accordance with the experimental observations for the flow conditions considered, the CFD computations revealed no major global effects of the centerbody on the surface pressure distributions of the wings. However, CFD-FASTRAN seems to predict a vortex breakdown, which is neither predicted by FJ3SOLV nor observed in the wind tunnel for the simulated flow conditions.

20.1 INTRODUCTION

Modern Unmanned Combat Air Vehicles (UCAVs) are designed using delta, double delta or diamond wing planform configurations for high manoeuvrability and agility. The delta wing planform allows the UCAVs to operate at near- and post-stall regimes (high angles of attack) taking advantage of the additional lift generated by the leading edge vortices, known as “Vortex Lift”. A disadvantage, however, is that as the angle of attack increases, the leading edge vortices experience a sudden flow disorder, known as “Vortex Breakdown”. This vortex breakdown can severely alter the flow and limit the lift gain achieved if not eliminate it altogether. This phenomenon has been identified as a source of performance loss and a cause for dangerous vibrations. In addition, since the vortex breakdown rarely occurs symmetrically on the wing, the difference in lift loss can induce a rolling moment, that could compromise the aircraft stability and control. A thorough understanding of the leading edge vortices behavior is thus mandatory in order to be able to enhance the UCAVs performance and manoeuvrability [1].

The major flow features characterizing a vortex flow over a sharp-edged delta wing are schematically presented in Figure 1. Despite significant research (mainly experimental) during the past decade [2]-[11], many aspects of the vortical flows and the complex interactions of vortices are still unknown to the aerodynamicists. Consequently, there is a continuing need for further studies (experimental, analytical and numerical) of vortical flows characteristics, especially the flow physics associated with the vortex breakdown phenomenon [1]. Moreover, experimental investigations have shown that large scatter exists in the vortex breakdown location. Geometric variation of the wing [10], wind tunnel wall and support interference effects, model deformation, Reynolds number and measurement techniques are all possible sources of the large scatter. These factors significantly affect the experimental data for any aerodynamic

analysis and design. CFD simulations can be very useful in understanding the role of these factors and quantifying their respective effects.

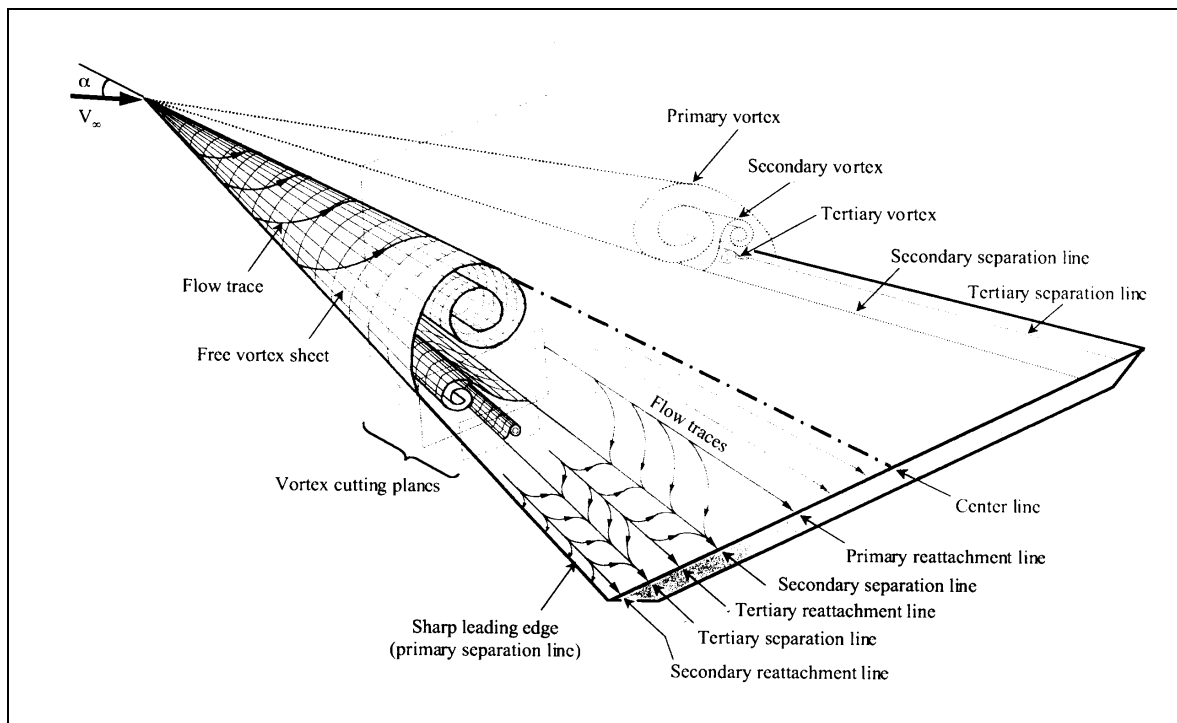


Figure 1: Vortex flow structures on a sharp-edged delta wing at high angle of attack [11]

During the last several years, vortex dynamics of more than 50 configurations were investigated in two wind tunnels and in a water tunnel at the Institute for Aerospace Research (IAR) of the National Research Council of Canada (NRC) [6]. These configurations included diamond and delta wings with sweep back angles from 55° to 75° and different leading edge shapes and center body settings. The experimental investigations included measurements of both steady and unsteady aerodynamic loads and surface pressure for angles of attack ranging from where the leading edge vortex was fully developed up to where the leading edge vortex was totally broken down. The PSP technique was also used in the measurements of the surface pressure.

This paper presents the results of inviscid vortex flow simulations for the IAR sharp-edged wings; a 65° delta wing and a 55° diamond wing. This study was carried out to assess the effects of the centerbody on the aerodynamic characteristics of the wings, and the CFD solutions were validated using the IAR PSP measurements of the surface pressure distributions.

20.2 IAR DELTA AND DIAMOND WING MODELS

To assess the effects of the centerbody on the aerodynamic characteristics of the IAR sharp-edged 65° (model G2) delta and 55° diamond (model G1) wings, flows over no-centerbody (G2-3A and G1-1A) and with centerbody (G2-3E and G1-1C) configurations of the two wings are computed. The computed configurations and their corresponding wind tunnel tested models are shown in Figure 2. For both wings, CFD and wind tunnel configurations with centerbody are identical (Figure 2a: configuration G2-3E-CFD/PSP and Figure 2b: configuration G1-1C-CFD/PSP). The only difference however, is the absence of

the sting support in the computations.

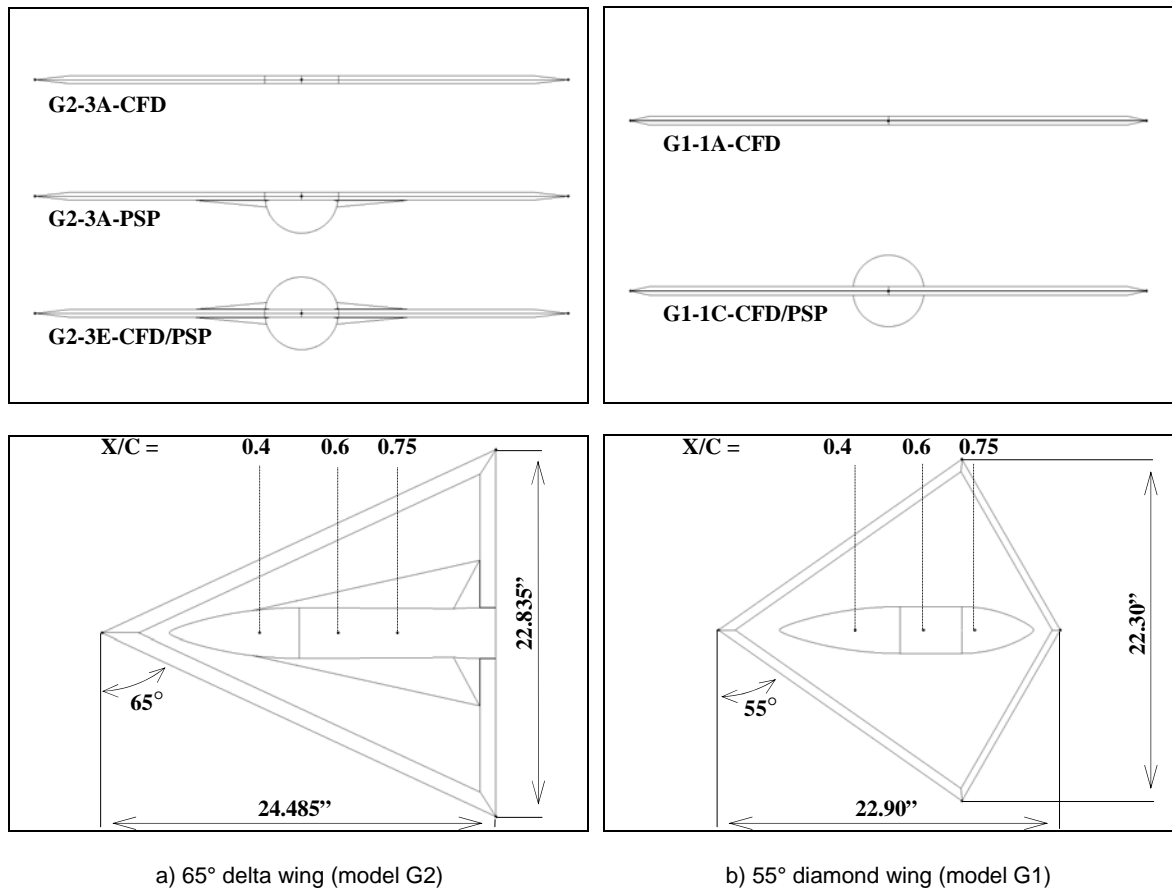


Figure 2: Wind tunnel and CFD model configurations

No PSP measurements were performed for the 55° diamond wing without a centerbody (Figure 2b: configuration G1-1C-CFD), and only CFD results will be presented for this configuration. To test the no-centerbody configuration of the 65° delta wing, a sting is required to support the model in the wind tunnel and to hold the internal balance to measure the loads. The lower half of the centerbody had to be included (Figure 2a: configuration G2-3A-PSP) to accommodate the sting and to house the balance during testing of this configuration. Without such a constraint in the CFD simulations, a true no-centerbody configuration of the wing is modeled, where the centerbody is completely removed in the computations (Figure 2a: configuration G2-3A-CFD). The sting support is also not included in the calculations.

Plan forms of the two wings are also depicted in Figure 2, along with some geometrical dimensions of the models and the chordwise locations of the stations where spanwise surface pressure coefficient comparisons are performed. The IAR wing models, considered in the current investigation, are characterized by sharp leading edges with a sweep angle of 65° for the delta wing and 55° for the diamond wing. The respective root chords, wing spans and thicknesses of the two wings are 24.485", 22.835" and 0.341" for the 65° delta wing and 22.9", 22.3" and 0.375" for the 55° diamond wing.

Configurations G2-3A, G2-3E, G1-1A and G1-1C of the two wings are among the many configurations of the IAR delta and diamond wings tested in the IAR 2m x 3m low speed wind tunnel [6]. These configurations have been tested at free stream velocities ranging from 15m/s to 90m/s and at angles of

attack between 0° and 34° . Detailed quantitative experimental measurements have been obtained; including surface pressure distributions generated using the PSP technique. The results presented in this paper are those obtained for the following free stream flow conditions; $M_\infty=0.17$ and $\alpha=21^\circ$ for the 65° delta wing, and $M_\infty=0.18$ and $\alpha=15^\circ$ for the 55° diamond wing. The corresponding wind tunnel PSP measurements are used to validate the CFD predictions.

20.3 FLOW SOLUTIONS

The inviscid vortical flows over the 65° and the 55° wings were computed using unstructured tetrahedral grids. Two flow solvers were tried out; an in-house Euler solver, FJ3SOLV, and the CFD-FASTRAN commercial CFD code. Only sharp-edged models of the wings were considered and the effects of the centerbody were investigated for one flow condition for each wing.

20.3.1 Computational Grids

Since the wind tunnel models were tested under no sideslip ($\beta = 0^\circ$) conditions, the flow was assumed symmetrical and only half of the wings were modeled in the computations to facilitate quicker CFD analyses. The unstructured tetrahedral meshes were generated using the Octree based Tetra module of ICEM CFD. The respective mesh sizes used for the different configurations of the two wings are summarized in Table 1 below, and surface grids of the with-centerbody configurations are shown in Figure 3. To eliminate the grid effects, same grids of the 65° wing models were used by both FJ3SOLV and CFD-FASTRAN.

Wing	Model	Mesh Size	
		Grid Cells	Grid Points
65° Delta	G2-3A	450,000	87,000
	G2-3E	500,000	100,000
55° Diamond	G1-1A	344,000	66,000
	G1-1C	376,000	74,000

Table1: Mesh sizes of the computed configurations

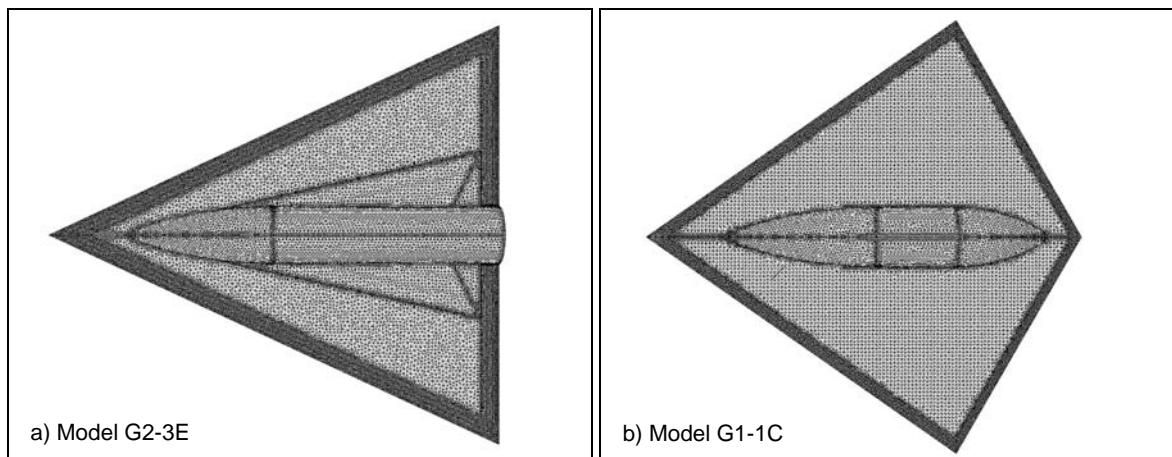


Figure 3: Computational surface grids of the with-centerbody wing models

20.3.2 Flow Solvers

20.3.2.1 FJ3SOLV

FJ3SOLV is a 3D unstructured grid Euler solver, developed at IAR [12]. It is a cell-centered code based on the finite volume formulation. The convective fluxes are discretized using Jameson's central difference scheme [13] where second and fourth order dissipation terms are added explicitly for stability. Time integration to steady state is achieved by means of an explicit 4-stage multi-step scheme and convergence is accelerated using a combination of local time stepping, implicit residual smoothing and enthalpy damping techniques.

Boundary conditions are imposed using fictitious cells outside the boundaries. Appropriate flow properties are set in these cells to satisfy the slip conditions on the solid boundaries, where the normal velocity is set to zero. At the far-field boundaries, a characteristic approach, based on Riemann invariants subject to one-dimensional analysis, is used.

20.3.2.2 CFD-FASTRAN

This is a finite volume commercial Reynolds-Averaged-Navier-Stokes (RANS) solver developed by the CFD Research Corporation [14]. CFD-FASTRAN offers two upwind differencing schemes with a variety of higher order limiters to calculate the convective terms in the transport equations. Both explicit and fully implicit time integration schemes are available for steady and unsteady flow simulations. A number of turbulence models are also implemented in CFD-FASTRAN.

In the current study, this solver is used in Euler mode to compute the vortical flows of interest. The convective fluxes are discretized by the widely used Roe's approximate Riemann solver, where the higher order scheme is utilized. This provides up to third order spatial accuracy. To respect monotonicity of the higher order scheme, the Venkatakrishnan flux limiter is employed.

Steady state solutions are achieved by means of implicit integration in time. The resulting system of linear equations is solved with the ILU-SGS method and the CFL number is ramped from 0.1 to 5 within the first 100 iteration cycles.

20.4 RESULTS AND DISCUSSIONS

The emphasis of the present study is to assess the effects of the centerbody on the aerodynamic characteristics of two IAR delta wings with sharp leading edges. Of particular interest is the vortex behavior in the presence of the centerbody. Computational solutions were obtained for both with and without centerbody configurations using Euler flow solvers. The 65° delta wing was computed using both FJ3SOLV and CFD-FASTRAN, while only FJ3SOLV was used to compute the 55° diamond wing. The purpose of running two solvers for the 65° wing is to assess the performance of the in-house solver (FJ3SOLV) and the commercial software (CFD-FASTRAN) for the prediction of vertical flows over sharp-edged delta wings.

The centerbody effects are evaluated through comparisons of surface pressure distributions. CFD predictions are also compared to the wind tunnel PSP measurements to validate the computational results and to assess the performance of the two solvers. Spanwise surface pressure coefficients are also quantitatively compared at three chordwise locations. These are $X/C=0.4$, 0.6 and 0.75 for both wings.

Results of the 65° delta wing, including convergence histories of the two solvers, are presented and analysed first, followed by those of the 55° diamond wing.

20.4.1 65° Delta Wing (Model G2)

The numerical and PSP results of this wing model are shown in Figures 4-6. The free stream flow conditions considered for this test case are $M_\infty=0.17$ and $\alpha=21^\circ$.

20.4.1.1 Convergence History

To achieve steady state solutions, 3000 iterations were performed using both solvers. FJ3SOLV was run with a CFL of 5, while CFD-FASTRAN was started with a CFL of 0.1, which was ramped to a value of 5 during the first 100 iterations. Figure 4 shows the convergence history of the lift (CL) and the pitching moment (CM) coefficients for both configurations G2-3A and G2-3E. No significant variations in the values of CL and CM are observed beyond about 600 iterations for FJ3SOLV, while it takes more than 2000 iterations for the CFD-FASTRAN predicted values to approximately reach the same level of convergence as those obtained by FJ3SOLV. It should be mentioned however, that the two solvers practically converge to similar CL and CM values.

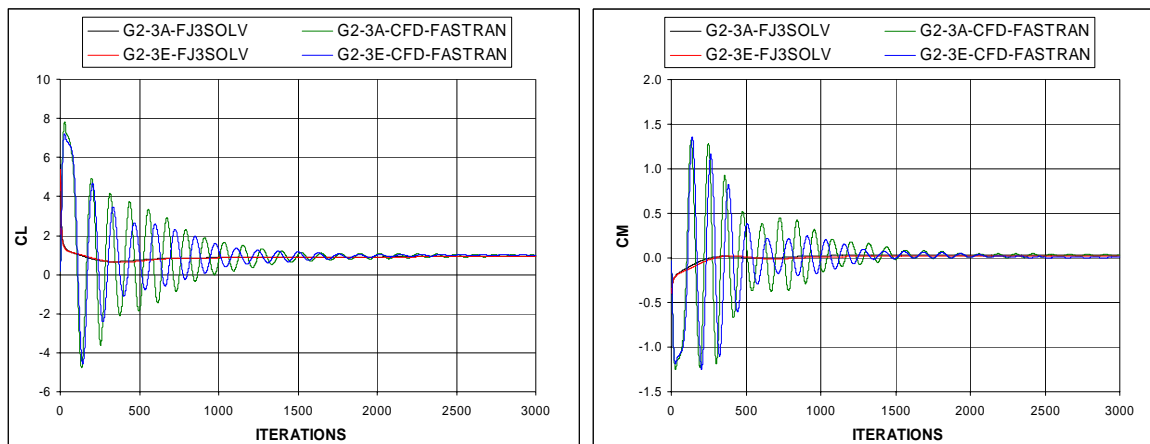


Figure 4: 65° delta wing, convergence histories of lift and pitching moment coefficients

20.4.1.2 Surface Pressure Distributions

The computed C_p distributions for the two configurations (G2-3A and G2-3E) of the IAR 65° delta wing with a sharp leading edge are compared in Figures 5 and 6. Also included in these figures are the PSP measured values to validate the CFD predictions. Figure 5 compares the global C_p distributions on the upper surfaces of the two configurations. In general, there are no significant differences in these comparisons and the CFD predicted pressure distributions resemble those of the PSP data. Most of the flow features are reasonably well captured by both FJ3SOLV and CFD-FASTRAN. It should be noted however, that CFD-FASTRAN seems to predict a vortex breakdown around $X/C=0.75$. This vortex breakdown is not revealed by the PSP and was not predicted by FJ3SOLV.

The spanwise surface pressure coefficient distributions along the chordwise stations located at $X/C=0.4$, 0.6 and 0.75 are depicted and compared in Figure 6. Both FJ3SOLV and CFD-FASTRAN predictions compare reasonably well with the PSP measurements. FJ3SOLV under predicts the suction peak at all three stations, while CFD-FASTRAN over predicts it at $X/C=0.4$. CFD-FASTRAN seems also to predict more centerbody effects than FJ3SOLV and PSP.

For both configurations, the two CFD solvers predict the vortex core slightly outboard of its PSP measured location. Both solvers also predict that the vortex core location at $X/C=0.4$ is a little outboard

with the centerbody than that without the centerbody. Moreover, it appears that the wing without the centerbody has slightly more suction in the forward portion of the wing and less suction in the aft portion. These observations are corroborated by the PSP data, where similar phenomena are observed.

Local flow accelerations are predicted for the wing with the centerbody. These are observed at $Y/b \approx 0.3$ for $X/C=0.4$ and at $Y/b=0.22$ for $X/C=0.6$ (Figure 6b). These local flow accelerations manifest themselves as little bumps in the C_p curves. The PSP data revealed similar behaviours at these two chordwise stations. The above coordinates are those where the centerbody edge is located. The local flow accelerations on the centerbody shoulder may cause these local suction bumps. Nevertheless, the comparisons show that no major global effects are caused by the presence of the centerbody at the current flow conditions.

20.4.2 55° Diamond Wing (Model G1)

Figures 7 and 8 present the results of the G1 wing model for the free stream flow conditions of $M_\infty=0.18$ and $\alpha=15^\circ$. The no-centerbody configuration (G1-1A) of this model was not PSP tested and only CFD predictions are shown here.

Figure 7 illustrates the comparison of the global surface pressure distributions between with (G1-1C) and without (G1-1A) centerbody configurations. Similar to what was observed for the 65° delta wing, in general, there are no significant differences in these comparisons. Moreover, the CFD predictions for the G1-1C configuration compare reasonably well with the PSP measurements, where most of the major qualitative flow features are captured by the FJ3SOLV.

The surface pressure coefficient, C_p , distributions along $X/C=0.4$, 0.6 and 0.75 are depicted in Figure 8. As for the 65° delta wing, the vortex core is predicted a little outboard of its respective PSP observed locations. For $X/C=0.4$ and 0.75 , the numerical results also show that the centerbody seems to slightly shift the primary core vortex location towards the outboard edge of the wing. Furthermore, the C_p comparison at $X/C=0.75$ reveals that the suction peak is numerically over predicted. A small suction peak, located near the centerbody, is observed in the PSP pressure distributions of all the three chordwise stations. This is believed to be due to the fact that the geometry of the centerbody for the G1-1C model was poorly represented, which affected the accuracy of the reduced PSP data in those regions of the wing.

Overall, and for the flow condition considered here, the CFD predicted surface pressure distributions for models G1-1A (no-centerbody) and G1-1C (with centerbody) show no major effects of the centerbody on the flow over the 55° diamond wing.

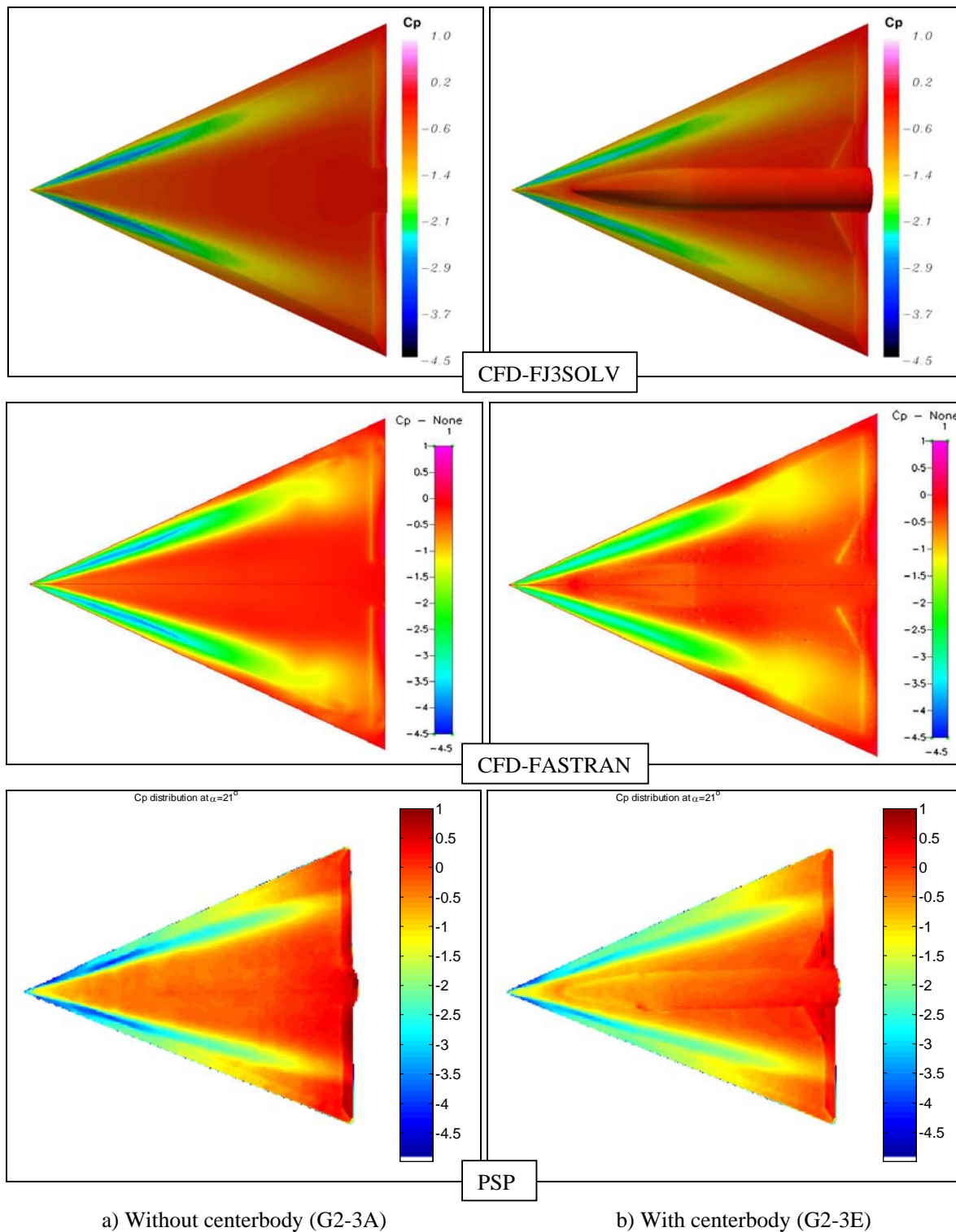


Figure 5: 65° delta wing, comparison of overall surface pressure distributions and correlation with PSP data, $M_\infty=0.17$ and $\alpha=21^\circ$

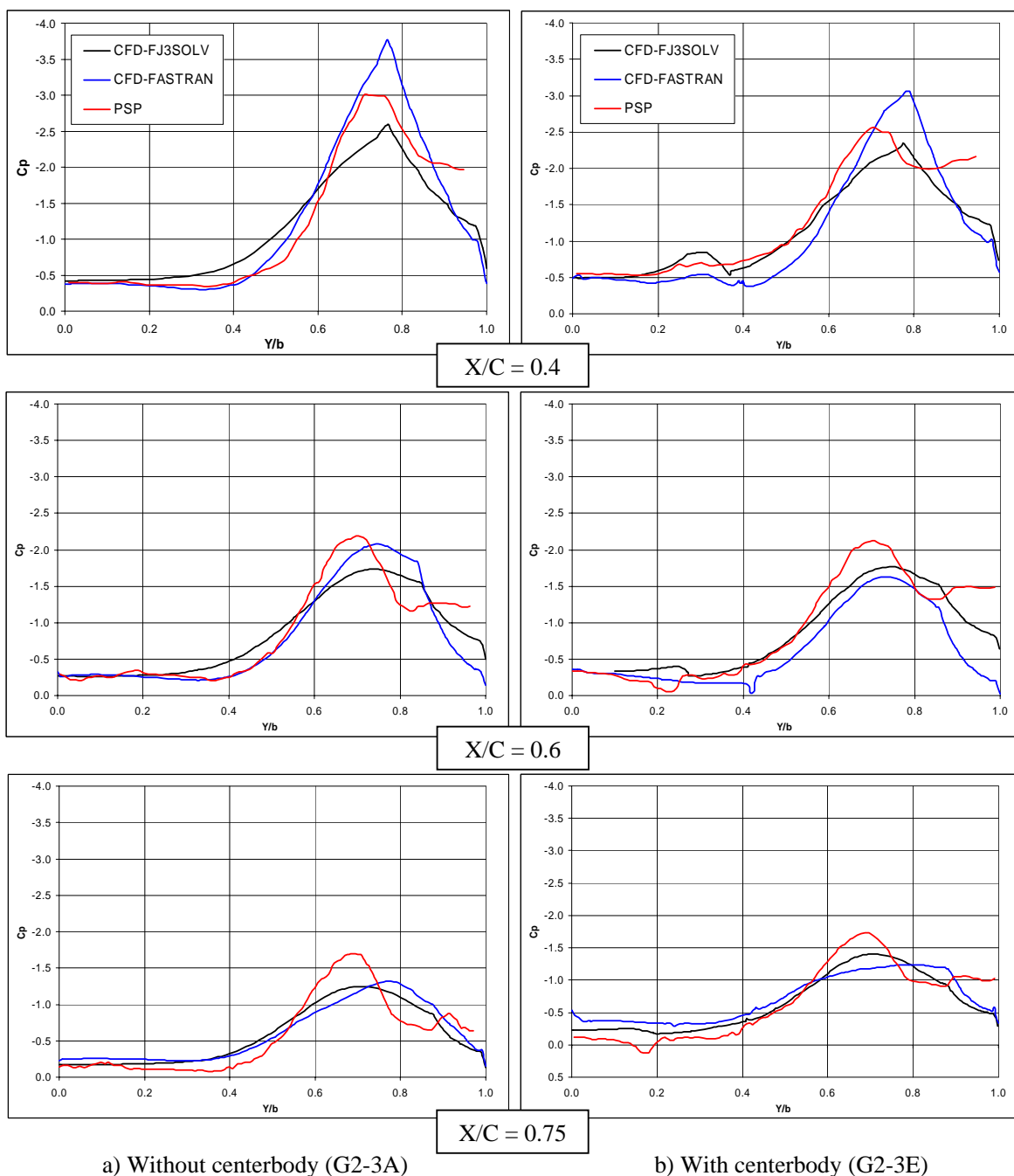


Figure 6: 65° delta wing, comparison of surface C_p distributions at different chordwise locations, $M_\infty=0.17$ and $\alpha=21^\circ$

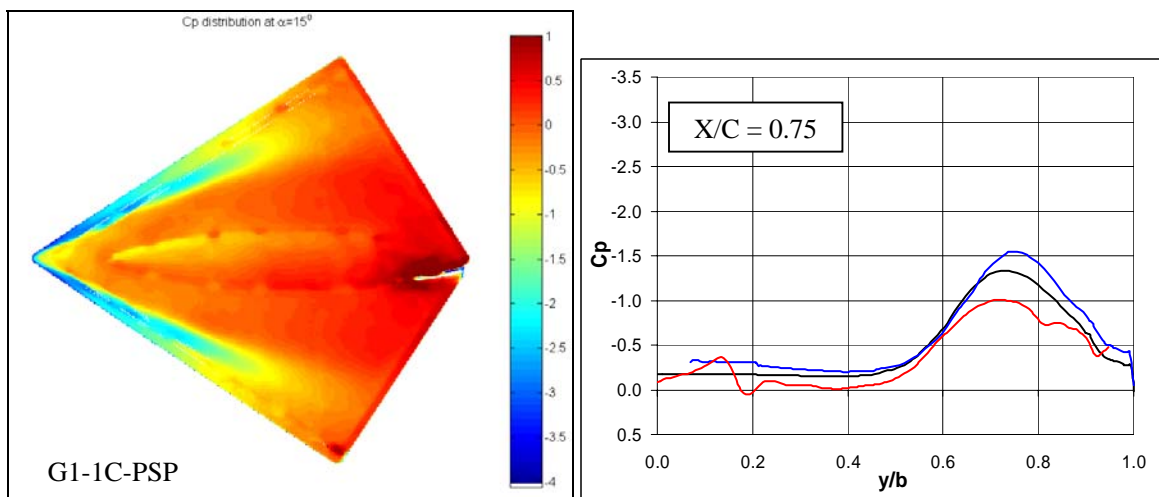
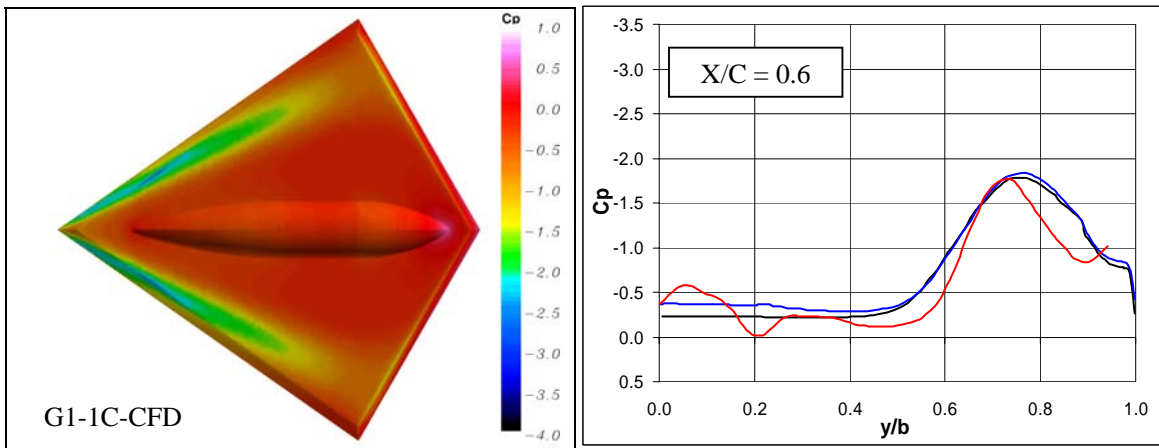
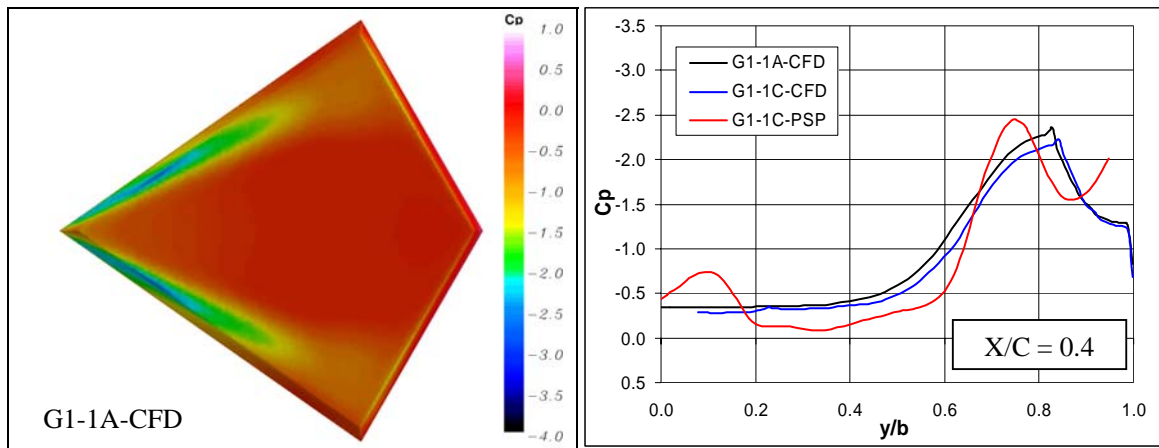


Figure 7: 55° delta wing, comparison of overall surface pressure distributions and correlation with PSP data, $M_\infty=0.18$ and $\alpha=15^\circ$

Figure 8: 55° delta wing, comparison of surface C_p distributions at different chordwise locations, $M_\infty=0.18$ and $\alpha=15^\circ$

20.5 CONCLUDING REMARKS

Computational Fluid Dynamics (CFD) was found to be a useful tool to assess the centerbody effects on the aerodynamics characteristics of two IAR sharp-edged wings. For the flow conditions considered in the current investigation, both the in-house solver, FJ3SOLV, and the commercial software, CFD-FASTRAN, were able to capture the main features the inviscid vertical flow over the 65° delta wing. Similar predictions were obtained for the 55° diamond wing using FJ3SOLV. CFD results agreed reasonably well with the PSP measurements for both with and without centerbody configurations of the two wing models. However, CFD-FASTRAN seems to predict a vortex breakdown, which was neither predicted by FJ3SOLV nor revealed by the PSP data. Overall, the computational results showed that the centerbody has negligible global effects on the aerodynamic characteristics of the two IAR wings. The CFD findings were corroborated by the PSP observations.

20.6 REFERENCES

- [1] X.Z. Huang and N.G. Varhaagen, Highlights of NATO RTO Task Group AVT-080: Vortex Breakdown over Slender Wings, AIAA Paper 2003-3939.
- [2] A.M. Mitchell, P. Molton, D. Barberis and J. Délery, Characterization of Vortex Breakdown by Flow Field and Surface Measurements, AIAA Paper 2000-0788.
- [3] L.E. Ericsson, M. View and M.E. Beyers, Requirements for Subscale Simulation of Delta-Wing Vortex Characteristics, Congress of the International Council of the Aeronautical Sciences, Toronto, Ontario, Canada, September, 2003.
- [4] M.D. Brodetsky, E. Krause, S.B. Nikiforov, A.A. Pavlov, A.M. Kharitonov and A.M. Shevchenko, Evolution of Vortex Structures on the Leeward Side of a Delta Wing, Journal of Applied Mechanics and Technical Physics, Vol. 42, No. 2, pp. 243-254, 2001.
- [5] A.M. Mitchell and J. Délery, Research into Vortex Breakdown Control, Progress in Aerospace Sciences, Vol. 37, pp. 285-418, 2001.
- [6] X.Z. Huang, Comprehensive Experimental Studies on Vortex Dynamics over Military Wing Configurations in IAR, AIAA Paper 2003-3940.
- [7] I. Mary, Large Eddy Simulation of Vortex Breakdown Behind a Delta Wing, International Journal of Heat and Fluid Flow, Vol. 24, pp. 596-605, 2003.
- [8] B.I. Soemarwoto and O.J. Boelens, Simulation of Vortical Flow over a Slender Delta Wing Experiencing Vortex Breakdown, AIAA Paper 2003-4215.
- [9] B.I. Soemarwoto, O.J. Boelens, M. Allan, M.T. Arthur, K. Bütefisch, N. Ceresola and W. Fritz, Towards the Simulation of Unsteady Manoeuvre Dominated by Vortical Flow, AIAA Paper 2003-3528.
- [10] X.Z. Huang, Y. Mébarki, A. Benmeddour and T. Brown, Experimental and Numerical Studies of Geometry Effects on UCAV's Aerodynamics, AIAA Paper 2004-0403.
- [11] S.Z. Pirzadeh, Vortical Flow Prediction Using an Adaptive Unstructured Grid Method, Symposium on Advanced Flow Management, Part I – Vortex Flow and High Angle of Attack, NATO RTO/AVT Panel Meeting, Norway, May 7-11, 2001.

- [12] F. Fortin, A. Benmeddour and D.J. Jones, Application of the Canadian Code to the F/A-18C JDAM Separation, AIAA Paper 99-0127, 1999.
- [13] A. Jameson, W. Schmidt and E. Turkel, Numerical Solution of the Euler Equations by Finite Volume Methods using Runge-Kutta Stepping Schemes, AIAA Paper 81-1259, 1981.
- [14] ESI Group, www.esi-group.com.

Chapter 21 – ‘ENGINEERING’ MODELS OF DELTA WING VORTEX BREAKDOWN AND ITS EFFECT ON AERODYNAMIC CHARACTERISTICS

D I Greenwell

Department of Aerospace Engineering, University of Bristol
Bristol BS8 1TR, UK

doug.greenwell@bristol.ac.uk

ABSTRACT

The breakdown of a delta wing leading-edge vortex is modelled as a transition from a straight unburst to a helical burst vortex structure. Applying continuity and rotational velocity constraints to the self-induced motion of a semi-infinite helical vortex results in a symmetry-breaking subcritical bifurcation from a straight to a helical vortex, at a critical swirl ratio similar to that given by conventional vortex stability analyses. The post-breakdown helix is of opposite hand to the circulation of the vortex, with a pitch directly proportional to the vortex strength, and has a stagnation point on the centreline. The model predictions are consistent with experimental data for helix pitch, inclination, radius, convection velocity, induced velocity and frequency content. A simple physical model of the impact of breakdown on wing aerodynamic characteristics is then developed which gives predictions of both the magnitude and the rate of onset of burst-induced lift-loss that also match experimental data surprisingly well. This model suggests that the fundamental mechanism driving the lift-loss phenomenon is a time-averaged reduction in the strength of the leading-edge separation shear layer as the vortex helix rotates. The implications of the model for the impact of vortex breakdown on surface flow and pressure distribution, on time-dependency of burst-induced lift loss, on the upstream influence of breakdown, and on means for alleviation of lift-loss are discussed.

21.1 NOMENCLATURE

a_0	helix radius (also r_s)
c	wing root chord
C_{MS}	binormal induced velocity coefficient
C_{VT}	tangential induced velocity coefficient
C_N	normal force coefficient
C_{NV}	vortex lift component of normal force
C_{NVNB}	vortex lift, no breakdown
C_{NVBD}	vortex lift ahead of burst
f	helix passing frequency
k	reduced helix pitch ($= p/2\pi$), vortex lift-loss factor, $= fn(x_{VB})$
k_{mean}	average vortex lift-loss factor
k_{V2}	factor on V_U^2
k_Γ	factor on circulation growth rate $d\Gamma/dx$
K	Sychev similarity parameter, $= \tan\alpha/\tan\varepsilon$
K_P	potential lift factor
K_V	vortex lift factor
p	helix pitch

r_s	radius of burst vortex helix (also a_0)
r_0	vortex core radius (also σ)
s	local wing semi-span ($= x \tan \epsilon$), distance along helix
U_∞	freestream velocity
U_C	vortex element convection velocity
U_{CL}	axial velocity on helix axis
U_{rot}	vortex element swirl velocity
V_B	binormal component of self-induced velocity
V_L	lower-surface cross-flow velocity
V_U	upper-surface cross-flow velocity
W_B	tangential component of self-induced velocity
w_{CL}	induced axial velocity on helix axis
x	chordwise location
\bar{x}	non-dimensional chordwise location, x/c
x_{VB}, \bar{x}_{VB}	vortex burst location
y_l	spanwise centroid of leading-edge suction distribution
a	angle of attack, angular parameter defining position on helix
α_{BD}	vortex burst onset incidence
β	helix inclination angle
δ	core structure factor
$\hat{\delta}$	core structure factor relative to a forced vortex
ψ, ϵ	wing semi-apex angle ($= 90^\circ - \Lambda$)
ϕ_0	swirl ratio at edge of outer vortex core
Γ	vortex strength, $= \oint n(x)$
γ	vortex sheet strength
Λ	leading-edge sweep
κ	helix curvature
ρ	fluid density
σ	vortex outer core radius (also r_0)
$\hat{\tau}$	non-dimensional helix pitch, $= k/a_0$
Ω	swirl ratio parameter
\mathbf{r}	position vector
$\mathbf{t}, \mathbf{b}, \mathbf{n}$	tangential, binormal and normal unit vectors
\mathbf{v}	induced velocity vector

21.2 INTRODUCTION

The leading-edge vortex flow structures generated by combat aircraft at high angles of attack continue to be the subject of much theoretical and experimental research. One aspect of these flow structures of particular concern is the onset of large-scale instabilities in the vortex (referred to as 'burst' or 'breakdown'), since this impacts directly (and adversely) on aircraft performance, stability and controllability. As a consequence, the leading-edge vortex breakdown phenomena has been extensively studied, with the literature running to several hundreds of papers [see 1,2,3 for recent reviews]. A wide range of theoretical mechanisms for this breakdown have been proposed, all fundamentally based on

stability analyses of an axisymmetric vortex. In general the essential factor governing the onset of breakdown vortex is identified as the swirl ratio within the vortex core. Although these analyses all give reasonably similar values for critical swirl ratio, they fail to give any significant information about the *structure* of the vortex downstream of breakdown; unfortunately, it is just this aspect of the vortex breakdown phenomenon that governs its effect on aircraft aerodynamic characteristics. In turn, the fundamental reason(s) why vortex breakdown has such a dramatic impact on aerodynamic characteristics remain unclear. Burst-induced lift-loss is usually presented as a self-evident (but unexplained) consequence of the 'collapse' or 'disintegration' of the leading-edge vortex into a 'wake-like' turbulent flow, followed by an entirely empirical modelling process.

Recent advances in computational fluid dynamics are now resulting in solutions for delta wing flows that can reproduce helical vortex breakdown structures [4]. The appropriate flow physics are presumably now being represented within the computer simulations; however, the questions posed above still remain largely unanswered. This paper therefore presents an alternative 'engineering' analysis based on a simple flow model, which addresses both the structure of 'post-burst' leading-edge vortex flow, and the mechanism by which it affects aerodynamic characteristics. The analysis is preliminary, but provides a promising conceptual framework for further work.

21.2.1 Vortex Breakdown Modelling

References 5 and 6 summarise the various possible mechanisms for breakdown so far proposed as follows:

- a hydrodynamic instability to spiral disturbances
- a standing wave phenomenon
- a finite transition (supercritical to subcritical) between conjugate flow states
- a failure of the usual quasi-cylindrical approximation to the flow (analogous to boundary layer separation)
- a result of a critical retardation of the flow
- a finite amplitude wave

A common feature of all these approaches is the emergence of the swirl ratio as the primary factor governing the onset of vortex breakdown, defined as the ratio between the swirl and the axial velocity components. Further, the critical values obtained for the swirl ratio are remarkably similar [1], being of the order of 1. Experimental studies give broadly similar critical swirl ratios [7,8], although care must be taken when comparing these that consistent definitions of the swirl ratio are used. The structure of the vortex flow downstream of breakdown becomes complex and unsteady. In flow visualisation studies in vortex tubes at least six separate topologies have been reported [1], although for leading-edge vortices only two forms – 'bubble' and 'spiral' breakdown – are seen (Figure 1 [9]).

However, although giving a reasonable agreement with experiment, a major shortcoming of these analyses is that they tell us relatively little about the post-breakdown structure of the vortex. Two major questions that need to be answered include:

- a) Why does a burst delta wing vortex generally display a rotating spiral form, with the spiral of opposite hand to the circulation [9]?
- b) What governs the wavelength and rotation frequency of the spiral vortex [10]?

21.2.2 Vortex Lift-Loss Modelling

For vortex-lift configurations, the onset of vortex breakdown has major (and generally adverse) impacts on aerodynamic characteristics. These include a loss of lift, unstable pitching and rolling moment behaviour,

heavy buffeting and long time lags in responses to aircraft motion. Relevant experimental studies have largely focussed on three aspects of vortex breakdown: firstly, the way in which the position and movement of the 'burst point' depends on angle of attack and sideslip, wing geometry, test conditions etc, secondly, the internal flow physics of the burst vortex itself, and thirdly, the impact of breakdown on wing and fin buffet.

A much smaller proportion of the literature deals with the impact of vortex breakdown on aerodynamic characteristics, and then almost invariably from a descriptive, empirical viewpoint. Many authors comment on the adverse effect of vortex breakdown on lift, pitching moment and rolling moment, a handful develop empirical models for these effects, but none address the issue of *how* and *why* they occur. Looking at the literature Three crucial unanswered questions are:

- a) Why does vortex breakdown have such a large impact on aerodynamic characteristics [11] ?
- b) Why are the effects so dependent on wing sweep angle [12] ?
- c) Why is the characteristic response time of burst-induced lift-loss an order of magnitude longer than the response time of the burst itself [13] ?

Without an understanding of these phenomena, the modelling and prediction of vortex burst induced effects on combat aircraft aerodynamic characteristics cannot progress past the empirical stage.

21.3 VORTEX BREAKDOWN MODELLING

21.3.1 Modelling Approach

21.3.1.1 Assumptions

The analysis builds on three basic experimental observations:

- a) the structure of a burst delta wing vortex is fundamentally helical (Figure 1 [9]).
- b) the burst process is essentially inviscid [14], therefore the vortex core is bounded by a material surface and the continuity equation can be applied within it.
- c) during the transition from straight unburst vortex to helical burst vortex, individual elements of the vortex core are initially deflected directly away from the vortex centreline and acquire no rotational velocity (Figure 2 [9,15]).

The burst process is then modelled in four stages, as illustrated in Figure 3. Upstream of burst there is a semi-infinite straight vortex, followed by a deceleration stage ahead of the burst onset proper. In the region of the burst onset there is a highly three-dimensional transition stage, leading into a semi-infinite helical vortex downstream of the burst region. A further initial simplifying assumption made is that by the end of the deceleration stage the mean axial core velocity increment over the freestream is small. The analysis presented below then shows that if the continuity and rotational velocity constraints from b) and c) above are applied either side of the transition region a critical swirl ratio is found above which a helical vortex solution can exist. The orientation, radius, pitch and convection velocity of this helix are then shown to be consistent with a wide range of experimental data.

In some respects this is a similar approach to that adopted in Reference 16; the critical difference being that in Reference 16 the helical vortex geometry (ie orientation, pitch and radius) is pre-determined solely on the basis of experimental data. The critical vortex strength for breakdown to occur is then assumed to be that which gives a stagnation point on the vortex centreline. The structure of the helix is therefore not 'predicted', while Reference 17 demonstrates that scaling parameters based on the concept of a critical vortex strength do not perform well when used to correlate burst progression on delta wings.

21.3.1.2 Helical Vortices

Flow visualisation (eg Figure 1) appears to show two possible structures for delta wing vortex breakdown - a 'spiral' and a 'bubble' burst. However, a restriction to the spiral case may be defended on two grounds. Firstly, that of the two structures the spiral form is by far the most common, with the bubble form only appearing intermittently. Secondly, Reference 16 notes that in the case of a bubble burst closer examination using high-speed photography reveals an underlying spiral structure. This latter observation is supported by the analysis reported in Reference 18, which suggests a possibility that the bubble form may in fact be an artefact of the flow visualisation process itself.

The velocities induced by helical vortices are discussed at length in Appendix A. Figure A1 shows a right-handed helical vortex filament of strength Γ , with helix radius a_0 and pitch p ($= 2\pi k$). The non-dimensional reduced helix pitch is $\hat{\tau}$ ($=k/a_0$), β is the local helix inclination to the centreline (positive for a right-handed helix), and the local curvature of the filament is κ . For a helical vortex with a finite rotational core radius σ the resulting binormal and tangential self-induced velocities are

$$V_B = \frac{\Gamma \kappa}{4\pi} \left(C_{MS} - \ln(\kappa [\hat{\delta} \sigma]) \right) \quad (1)$$

and

$$W_B = \frac{\Gamma \kappa}{4\pi} C_{VT} \quad (2)$$

where $[\hat{\delta} \sigma]$ is the effective viscous core radius σ_{eff} as given by equation (A-11). The self-induced normal (radial) velocity component is zero.

The coefficients C_{MS} and C_{VT} are non-linear functions of the non-dimensional helix pitch $\hat{\tau}$ and are given by equations (A-5) and (A-6). The core radius factor $\hat{\delta}$ depends on the core swirl velocity profile: for the 'forced vortex' core usually assumed in theoretical studies of helical vortex motion $\hat{\delta}$ is 1.0, whereas for a 'flat' swirl velocity profile $\hat{\delta}$ is ≈ 0.78 . Delta wing vortices typically display both forms of swirl velocity variation, with the swirl profile naturally dividing into three distinct regions [19]: a small 'inner' core where viscous effects predominate and the swirl velocity increases linearly with radius, an 'outer' core where viscous effects are small and the swirl velocity is almost constant [73], and finally a surrounding potential vortex flow with swirl velocity varying inversely with radius. The corresponding axial velocity variations give maximum swirl ratio at the edge of the *outer* core; as far as vortex stability is concerned it appears then that it is the outer core region that is critical. The inner core radius is typically 10-20% of that of the outer core, but it contains perhaps 20-30% of the total vorticity contained within a leading-edge vortex.

21.3.1.3 Continuity Constraint

Consider an initially straight vortex filament with core radius σ parallel to (and convecting with) the freestream velocity U_∞ . The core mass flux relative to a fixed point is then

$$\dot{m}_{core} = \rho \pi \sigma^2 U_\infty \quad (3)$$

If this straight vortex then 'breaks down' into a spiral form with helix angle β with the vortex elements convecting downstream with velocity U_C (Figure 4), then the core mass flux becomes

$$\dot{m}_{core} = \frac{\rho \pi \sigma^2 U_C}{\cos \beta} \quad (4)$$

Assuming steady-state conditions, the mass flux upstream and downstream of the onset of vortex breakdown must be equal. Making the further assumption that the core radius does not change significantly in the initial stages of breakdown, the convection velocity U_C is then

$$U_C = U_\infty \cos \beta \quad (5)$$

The convection velocity in a helical vortex formed from a straight vortex is therefore positive, but less than the freestream velocity. From Figure 4 the convection velocity for a helical vortex in terms of the self-induced binormal and tangential velocities is

$$U_C = U_\infty + (W_B \cos \beta + V_B \sin \beta) \quad (6)$$

Combining equations (5) and (6) gives

$$U_\infty (\cos \beta - 1) = (W_B \cos \beta + V_B \sin \beta) \quad (7)$$

21.3.1.4 Rotational Velocity Constraint

Both experimental observations [9] and CFD studies [15] suggest that in the initial stages of vortex breakdown the vortex core elements acquire little or no lateral/rotational velocity. As a consequence, the vortex helix motion is essentially translational, not rotational (Figure 2). However, when visualised, this does result in an *apparent* rotation of the spiral vortex as whole in the opposite direction to the helix, as observed experimentally for delta wing flows [9].

From Figure 4 this constraint can be written as

$$U_{rot} = (W_B \sin \beta - V_B \cos \beta) = 0 \quad (8a)$$

and hence

$$V_B = W_B \tan \beta \quad (8b)$$

At first sight this appears to be a simple case of conservation of angular momentum; however, if we take into account the internal angular momentum in the vortex core this is clearly not so. A correct application of an angular momentum conservation constraint would require a knowledge of the internal dynamics of the rotational core, which is beyond the scope of this modelling approach. The application of equation (8) to the early stages of vortex breakdown can however be justified heuristically on the basis that transfer of angular momentum from the vortex core to the outer flow is a viscous diffusion process with a timescale much greater than that for downstream convection [14].

21.3.1.5 Helix Orientation

Substituting equation (8b) into equation (7) gives

$$U_\infty (\cos \beta - 1) = W_B (\cos \beta + \tan \beta \sin \beta) = \frac{W_B}{\cos \beta} \quad (9)$$

Substituting for W_B from equations (2) and (A-6) then gives

$$U_\infty (1 - \cos \beta) = \left[\frac{1}{2} \right] \frac{-\Gamma \kappa}{4\pi} \frac{2(1 - \cos \beta)}{\cos \beta \sin \beta}$$

where the factor $[1/2]$ is introduced to account for the effect of a semi-infinite rather than infinite vortex (Figure 3). This is followed by substitution for the helix curvature κ from equation (A-2) to give

$$U_{\infty} = \left[\frac{1}{2} \right] \frac{-\Gamma}{2\pi a_0} \tan \beta \quad (10)$$

Note that the trigonometrical relation for C_{VT} introduced in equation (A-6) permits a considerable simplification.

One immediate consequence of equation (10) is that for a right-handed helix (ie positive β) the corresponding vortex strength Γ must be negative; in other words with the 'zero rotational velocity' constraint applied the helix itself is always of opposite hand to the swirl direction. This is consistent with experimental observations for delta wing vortices [16].

21.3.1.6 Centreline Stagnation

Comparing equation (10) with equation (A-8) for the axial velocity component induced by a helical vortex on the helix centreline, it can be seen that an immediate (and rather surprising) effect of the 'zero rotational velocity' constraint is that the resultant axial velocity component on the helix centreline falls to zero.

$$U_{CL} = U_{\infty} + w_{CL} = 0 \quad (11)$$

This is consistent with experimental observations [19]; indeed, zero axial velocity on the centreline is often used as an indicator of burst onset in CFD studies.

21.3.1.7 Swirl Ratio

The swirl parameter Ω is defined as the ratio between the tangential and axial velocity components at the edge of the vortex core, ie

$$\Omega = \frac{-\Gamma/2\pi\sigma}{U_{\infty}} \quad (12)$$

The minus sign is introduced here so that Ω is positive for a vortex where the swirl direction is of opposite sign to that of the helix. Substituting in equation (10) gives a straightforward relation between the helix pitch and radius, and the swirl ratio

$$\frac{1}{\Omega} = \left[\frac{1}{2} \right] \left(\frac{\sigma}{a_0} \right) \tan \beta \quad (13)$$

21.3.1.8 Helix Pitch and Frequency Content

Equation (13) can now be used to relate the helix pitch directly to the vortex strength. From equation (A-1) the helix pitch p can be written in terms of the helix radius a_0 and the filament inclination angle β as

$$p = 2\pi k = 2\pi \frac{a_0}{\tan \beta}$$

Introducing the core radius σ and substituting from equation (13) gives

$$p = \frac{2\pi\sigma}{\tan \beta(\sigma/a_0)} = \left[\frac{1}{2} \right] 2\pi\sigma \Omega$$

Now substituting for swirl ratio Ω from equation (10) gives

$$p = \left[\frac{1}{2} \right] \frac{\Gamma}{U_{\infty}} \quad (14a)$$

Introducing the chordwise location x , the non-dimensional pitch becomes

$$\frac{p}{x} = \left[\frac{1}{2} \right] \frac{\Gamma}{U_{\infty} x} \quad (14b)$$

demonstrating that the helix pitch is directly proportional to the vortex strength. Note that for conical flow, vortex pitch and strength non-dimensionalised in this manner would be constant. The corresponding ‘passing frequency’ of the helix turns is

$$f = \frac{U_c}{p}$$

where U_c is the convection velocity given by equation (5), so that from equation (14a)

$$f = \frac{U_{\infty} \cos \beta}{\Gamma / [2] U_{\infty}} \quad (15a)$$

Rearranging this equation gives

$$\frac{f \Gamma}{U_{\infty}^2} = [2] \cos \beta \quad (15b)$$

where the left-hand side corresponds to the non-dimensional vortex frequency parameter first introduced in Reference 10 on the basis of simple dimensional analysis. Equation (15) illustrates an important difference between helical breakdown of a leading-edge vortex flow and that of a confined vortex tube flow, with which the majority of theoretical and experimental study [2] has been concerned. For the former, equation (15b) demonstrates that the fundamental frequency reduces as the circulation of the vortex increases, while for the latter the frequency increases with circulation [2,20].

21.3.1.9 Helix Inclination and the Swirl Ratio

Returning to the ‘zero rotational velocity’ constraint, substituting in equation (8b) for V_B and W_B from equations (1) and (2) gives

$$\left[\frac{1}{2} \right] \frac{\Gamma \kappa}{4\pi} (C_{MS} - \ln(\kappa [\hat{\delta} \sigma])) = \left[\frac{1}{2} \right] \frac{\Gamma \kappa}{4\pi} C_{VT} \tan \beta$$

and hence

$$\ln(\kappa [\hat{\delta} \sigma]) = C_{MS} - C_{VT} \tan \beta \quad (16)$$

Next, substituting for helix curvature κ from equation (A-2) gives

$$\left(\frac{\sigma}{a_0} \right) = \frac{e^{(C_{MS} - C_{VT} \tan \beta)}}{\hat{\delta} \sin^2 \beta} \quad (17)$$

and hence from equation (13)

$$\Omega = [2] \frac{\hat{\delta} \sin \beta \cos \beta}{e^{(C_{MS} - C_{VT} \tan \beta)}} \quad (18)$$

Since from equations (A-5) and (A-6) both C_{MS} and C_{VT} are functions of the helix pitch $\hat{\tau}$, the resulting swirl ratio Ω is also a function of $\hat{\tau}$ (or equivalently the helix inclination β) only, and vice versa.

21.3.2 Burst Onset

Evaluating equation (18) numerically for a simplified delta wing 'outer' core (ie $\hat{\delta} = 0.78$) gives the results shown in Figure 5a, where the relations are inverted to give helix inclination angle β and pitch $\hat{\tau}$ as a function of swirl ratio Ω . Figure 5b shows the corresponding relative helix radius a_0/σ as given by equation (17).

Below a swirl ratio of around 1.0 there is only the trivial straight vortex solution (ie $\beta = 0^\circ$). Above $\Omega \sim 1$ two helical solutions appear, with a curve that strongly resembles a sub-critical bifurcation. Above a swirl ratio of ~ 1.1 there are only a straight and a helical vortex solution; on topological grounds alone (recalling that radius a_0 can only have positive values) one would expect one solution to be stable and one to be unstable. Previous stability analyses of columnar vortices predict instability (or breakdown) of one form or another for swirl ratios of greater than 0.8-1.2, depending on the velocity distribution and analysis approach taken [1]. Experimental measurements give critical swirl ratios for burst onset of ~ 1 [7,8]. It therefore appears reasonable to assume that above $\Omega \sim 1.1$ the helical vortex solution is stable and the straight vortex solution is unstable.

Application of the simple helical vortex model described above therefore leads naturally to a picture of the vortex breakdown process as a symmetry-breaking bifurcation from a straight vortex to a helical vortex of opposite hand to the overall swirl direction. The sub-critical nature of the pitch-fork bifurcation seen in Figure 5 gives the potential for static hysteresis in burst onset, again as observed experimentally [21]. At burst onset the helix swirl angle is $\sim 50^\circ$, increasing gradually to a maximum of $\sim 70^\circ$ as swirl ratio is increased. The initial ratio of the helix radius a_0 to the core radius σ is of the order of 0.7, increasing rapidly with swirl ratio after burst onset.

21.3.3 Comparisons with Experimental Data

21.3.3.1 'Inner' and 'Outer' Core Dynamics

In order to apply the simple model of equations (17) and (18) to experimental data for delta wings it is necessary to treat the dynamics of the 'inner' and 'outer' core regions separately. Most of the vorticity is contained in the *outer* core and critical swirl ratios are reached there first; however, it is the behaviour of the *inner* core region that conventional flow visualisation techniques tend to mark.

The hypothesis is that vortex breakdown occurs when the swirl ratio in the *outer* core reaches the critical value shown in Figure 5a. The swirl ratio in the *inner* core is initially subcritical, due to the high local axial velocity; however, as a consequence of equation (A-8) the developing 'outer' core helix induces a large reverse flow velocity component on the centreline at the burst point, which causes the 'inner' core swirl ratio to increase rapidly past the critical value as the axial velocity reduces. This increased swirl ratio will give an 'inner' core helix inclination angle β and relative radius a_0/σ greater than that of the 'outer' core (Figures 5a and 5b). The relative radius in particular will be much larger. Further, from equations (14b) and (15b) the lower relative vortex strength of the 'inner' core will result in a shorter helix pitch p and a higher passing frequency f than that of the outer core vortex. Flow visualisation (eg Figure 1) suggests that the 'inner' core helix breaks down into general turbulence relatively quickly, so that one would expect any effects of the 'inner' core dynamics to be limited to a region immediately downstream of burst onset.

21.3.3.2 Helix Convection Velocity

The inclination angle β at the critical swirl ratio of 1.08 is 52° (for increasing Ω). Numerical experimentation indicates that this value is relatively insensitive to either the velocity profile factor $\hat{\delta}$ or the finite-vortex factor [2] assumed. A direct comparison with experimental flow visualisation data for the helix inclination is obscured by the limited resolution of the available data, and the possibility that the 'inner' vortex core dynamics (as visualised) differ from the 'outer' core. An alternative parameter, which can be compared more readily with quantitative experiment, is the relative helix convection velocity U_c/U_∞ , given by equation (5). A helix inclination of 52° therefore corresponds to a convection velocity of 0.62 of the freestream velocity.

Reference 9 presents direct measurements of convection velocity for a 65° delta wing in a water tunnel using dye flow visualisation which give values between 0.55 and 0.83 depending on Reynolds Number (and hence the magnitude of the inner core jet flow). CFD predictions for a 75° wing [15] give values between 0.4 and 0.6 in the immediate vicinity of the breakdown. However, a more reliable dataset is provided by Reference 10, which derives effective convection velocities (for 70° and 75° delta wings) from the frequency and wavelength of the unsteady surface pressures under a burst vortex. These pressure are likely to be dominated by the 'outer' core flow. The dominant frequency was determined from a standard FFT analysis of the signal from a single pressure transducer, while the wavelength was derived from the phase lag between two transducers along a conical generator. Figure 6 replots these velocities as a function of incidence, compared with the prediction of equation (5). The values tend to reduce slightly with incidence (perhaps due to an increase in helix inclination?), but cluster around 0.6.

21.3.3.3 Helix Inclination

Visualised helix inclination angles are significantly larger than those derived from convection velocities above, of the order of 65° - 75° [9,22] as opposed to $\sim 50^\circ$. Noting that it is the 'inner' core that conventional flow visualisation techniques tends to mark, this increased helix inclination could indicate an 'inner' core swirl ratio well above critical (Figure 5a). This in turn should correspond to relative helix radii of $\gg 1$. As an example, smoke flow visualisation from Reference 23 for a burst vortex over a 75° delta wing at 30° incidence shows a helix inclination of $\sim 70^\circ$ and a helix radius relative to the local semispan a_0/s of ~ 0.2 . From equations (15) and (16) a 70° inclination corresponds to a theoretical relative helix radius of ~ 3.6 and a swirl ratio of ~ 2.6 . From Reference 24, the outer core of an unburst vortex for a 75° delta at 30° incidence has a radius σ_o/s of ~ 0.3 , with the inner core roughly a fifth of that at $\sigma_i/s \sim 0.06$. The latter value gives a relative helix radius for the inner core of $a_0/\sigma_i = 0.2/0.06 = 3.3$, close to that predicted for a helix inclination of 70° . These results are therefore reasonably consistent with the hypothesis advanced above, namely that the inner and outer vortex core dynamics need to be treated separately.

The theoretical value for swirl ratio of 2.6 at an inclination of 70° would imply a mean 'axial' velocity in the inner core of the order of $0.4U_\infty$, which is not unreasonable. However, the actual magnitude of local swirl ratios within the inner core of a helical vortex breakdown still remains to be settled experimentally. Modern PIV techniques should be capable of providing the required data [25], but the author has yet to see any published data which includes the 'axial' (tangential) velocity component in the spiralling inner core of a burst vortex.

21.3.3.4 Helix Pitch

Reference 10 provides data for the wavelength of the unsteady surface pressures under a spiral burst vortex (\equiv helix pitch) as a function of incidence (re-plotted in Figure 7a). The corresponding vortex strength is estimated using Hemsch & Luckring's widely accepted correlation from Reference 26 (as modified in Reference 24)

$$\frac{\Gamma}{sU_{\infty} \sin \alpha} = 4.63 \left(\frac{\tan \alpha}{\tan \varepsilon} \right)^{0.2} \quad (19)$$

The resulting variation in pitch with vortex strength is plotted in Figure 7b, compared with the prediction of equation (14b). The variation is roughly linear, although with a slope closer to 0.4 than the predicted 0.5. Given the scatter in the data and the implicit assumption of conical flow the agreement is reasonable, although suggesting that the induced velocity reduction due to a finite vortex is underestimated.

However, non-dimensional helix pitch/wavelengths derived from the pressure data of Reference 16 are relatively long, of the order of half the wing root chord (Figure 7a); helix pitches taken from comparable dye flow visualisation data [9,22] are typically much shorter, at around 0.15-0.2c. Again, these differences are consistent with the hypothesis advanced above, namely that the 'inner' and 'outer' vortex core dynamics need to be treated separately. From equation (14b) this difference in pitch would correspond to a factor of ~ 3-4 between the inner and outer vortex strength, whereas velocity measurements [6,24] show a factor of ~ 4-5, depending on how the core 'edges' are determined.

21.3.3.5 Vortex Passing Frequency

The non-dimensional passing frequency f of the burst helix is given by equation (15b) as 1.23 for a helix inclination of 52° . This can be compared with data from Reference 10, which provides unsteady surface pressure frequency data for delta wings from 60° to 75° sweep. The basic dataset is shown in Figure 8a, re-plotted in 'conical flow' non-dimensional form fx/U_{∞} as a function of incidence. Again estimating vortex strength using equation (19), Figure 8b shows the corresponding non-dimensional frequency parameter of equation (15b) compared with the model prediction. For further comparison, Figure 9 shows a widely accepted empirical buffet frequency correlation parameter due to Mabey [27,28]

$$\frac{fs}{U_{\infty}} \sin \alpha \approx 0.25 \quad (20)$$

This relation was originally derived from the same dataset(!), but has been applied with reasonable success to many other delta wing configurations [29]. The scatter in the two correlations is similar, although equation (15b) perhaps gives a marginally more linear characteristic for the lower sweep angles. The critical difference between the two correlations is that equation (20) is entirely empirical, whereas equation (15b) is based on a physical model of the vortex flow.

The residual variations in the non-dimensional frequency with incidence may be a result of two separate effects. Firstly, at high incidence, as the burst moves well ahead of the (fixed) measurement location, the reduction in self-induced velocity due to the finite vortex will decrease, so reducing the factor of $[2]$ in equation (15) and hence the characteristic helix frequency. Secondly, at low incidence the measurement location is very close to the burst point, so that the higher 'inner' core vortex frequency dominates. From equation (15b) the increased helix angle of the 'inner' core as discussed above would reduce the passing frequency by a factor of ~ 2. However, this needs to be set against a greater reduction in the strength of the 'inner' core relative to the 'outer', possibly by a factor of ~ 4-5 [24], giving an overall increase in frequency of a factor of ~ 2-3.

For comparison, Reference 30 derives helix frequencies close to the burst point from flow visualisation, which when non-dimensionalised using the vortex strength Γ give values of ~ 3-4 over an incidence range of 30° to 50° , compared with 1-1.5 from Figure 8b. This is numerically consistent with a 5:1 ratio in 'outer' to 'inner' core strengths coupled with an increase in helix inclination from $\sim 50^\circ$ to $\sim 70^\circ$. Reference 31 reports similar high non-dimensional frequencies in the upper surface pressures close to the burst point. Reference 30 also notes that hot-wire measurements in the vortex flow well downstream of the burst give much lower characteristic frequencies, consistent with the surface pressure data of Figure 8b. Reference

32 presents frequency spectra derived from PIV measurements in the burst region for a 75° delta wing, and notes that these show strong peaks at a frequency corresponding closely to that of the helical rotation/translation as determined from dye flow visualisation. However, the same spectra also almost invariably show at least one peak at a lower frequency, of the order of a quarter of the 'helix' frequency, although the small scale of the figure makes it difficult to determine the relative values with any accuracy.

21.4 VORTEX-INDUCED LIFT-LOSS

21.4.1 Current ‘Lift-Loss’ Modelling Techniques

21.4.1.1 The Modelling Process

Conventional prediction techniques for burst-induced aerodynamic effects proceed in three stages:

- a) the vortex lift is calculated assuming no breakdown over the wing.
- b) the position of the burst point for the given wing geometry and incidence is determined (Figure 11).
- c) the vortex lift *aft of the burst point* is reduced to represent the effect of breakdown (Figure 10).

Difficulties in the modelling process begin with the second stage, because burst position is generally determined on the basis of a semi-empirical curve fit to experimental data. Unfortunately, the available data on burst position as a function of sweep angle and incidence is distinguished by the remarkably high degree of scatter between datasets (Figure 11). For flat-plate delta wings with nominally sharp leading-edges, the angle of attack for burst onset for a given sweep angle can vary by as much as $\pm 5^\circ$ [17]. It should be noted that Reference 33 suggests that much of this variation is due to apparently minor detail differences in leading-edge profile. A number of attempts have been made to correlate vortex burst position as a function of sweep and incidence, ranging from simple curve fits to the available data [34] to more sophisticated models based on the concept of a ‘critical’ vortex strength [17,35,36]. Nevertheless, the scatter remains large.

It is the third stage of the modelling process where the major difficulties occur: firstly, because there is generally no fundamental physical basis to the ‘lift-loss’ factors applied, and secondly, because published correlations between burst position and lift-loss are largely based on a single(!) dataset – namely Wentz & Kohlman’s study as reported in Reference 12. The vortex burst motion with increasing incidence reported in this study differs significantly from later work, with the burst moving much more rapidly forward over the aft half of the wing. Reference 37 attributes this difference to aeroelastic deformation of the very thin model wings tested.

It appears that there are remarkably few experimental studies which report both vortex burst position and aerodynamic characteristics at *consistent* experimental conditions. Development and validation of lift-loss modelling methods has therefore had to rely on correlating force and moment data from experimental datasets, with vortex burst locations derived from rather inaccurate curve-fits.

21.4.1.2 Empirical ‘Lift-Loss Factor’ Models

With two exceptions, published lift-loss models account for vortex breakdown by reducing in some way the vortex lift component aft of the burst position. The simplest and crudest model is that used by Hanff & Huang in Reference 38, which assumes constant pressure distributions over the surface of a 65° wing oscillating in roll. Ahead of the burst, the surface pressure is made up of a constant ‘potential flow’ contribution C_{pp0} ($= -1.1$) and a ‘vortex flow’ contribution C_{pv0} ($= -0.7$). Aft of the burst, the vortex flow

contribution is set to zero (Figure 12). The effect of body axis roll angle is incorporated by (a) using the effective sweep angle of each leading-edge to determine asymmetric burst positions, (b) factoring the two pressure contributions to account for variations in effective angle of attack, and (c) displacing the wing centreline by the equivalent sideslip angle. A variation on this approach is used by Myatt & Arena [39], where the surface pressures forward of breakdown are determined using a Brown & Michael conical vortex model [40], while the pressure under the burst vortices is assumed to be constant at $C_{p0} = -0.7$. Both Reference 38 and 39 report reasonable predictions for dynamic wing, but fail to capture the details of the static rolling moment characteristics.

Huang & Hanff later improved their model [41] by incorporating an exponential decay into the 'vortex flow' surface pressure contribution aft of the burst position. Now, rather than a complete loss of vortex lift after breakdown, there is a gradual decay given by the relation

$$\Delta C_{PV} = \frac{C_{PV}}{3} \left(1 + 2\sqrt{\bar{x}_{VB}}\right) e^{-\tan\psi(\bar{x} - \bar{x}_{VB})} \quad (21)$$

where C_{PV} is the equivalent vortical pressure coefficient upstream of breakdown, \bar{x} the longitudinal position non-dimensionalised by the chord c and ψ the wing semi-apex angle. Curiously, this gives a more rapid decay in vortex lift for lower sweep angles – whereas experimental data would seem to indicate the opposite trend [12]. The term in brackets brings in an initial drop in 'vortical pressure coefficient' which becomes more marked as the burst approaches the wing apex. The reasoning behind these model appears to be a largely qualitative examination of pressure distribution trends for delta wings at high incidence. Integrating equation (1), and using Polhamus' Leading-Edge-Suction (LESA) model for vortex lift [42] to determine C_{PV} gives

$$C_N = K_p \sin\alpha \cos\alpha + K_v \sin^2\alpha \bar{x}_{VB}^2 + \frac{2(1 + 2\sqrt{\bar{x}_{VB}})}{3 \tan^2\psi} K_v \sin^2\alpha \left[(\bar{x}_{VB} \tan\psi + 1) - (\tan\psi + 1)e^{-(1 - \bar{x}_{VB})\tan\psi} \right] \quad (22)$$

Huang & Hanff then add further terms to represent the residual vortex lift found after the burst point has reached the wing apex, and to compensate for a bevelled leading-edge on their wing. This model shows some improvement over that of Reference 38.

Huang & Hanff's early method [38] and its development [41] correspond to the simplest and most complex of the 'lift-loss factor' models. An intermediate class of model simply reduces the vortex lift component downstream of the burst by a factor k , so that the lift (or in this case normal force) becomes

$$C_{N_V} = C_{N_{VBD}} + k(C_{N_{VNB}} - C_{N_{VBD}}) \quad (23)$$

where $C_{N_{VNB}}$ is the vortex lift for the whole wing assuming no breakdown, and $C_{N_{VBD}}$ is the vortex lift for the 'unburst' section ahead of the burst point. Traub [35] notes that once the burst comes onto the wing at an incidence α_{BD} , it takes on average 30° to progress to the wing apex. Assuming then that the factor k on vortex lift aft of the burst reduces linearly gives

$$k = 1 - \frac{(\alpha - \alpha_{BD})}{30^\circ} \quad (24)$$

where α_{BD} is a function of sweep angle. This linear reduction avoids sudden changes in lift at burst onset, but the assumption of a 30° interval between burst onset and burst reaching the apex leads to significant errors for lower sweep angles.

Boffadossi [43] notes that (in the basis of data in [44]) the circulation Γ_{BD} downstream of burst is reduced

by about 60% of the value for an unburst vortex Γ , which would correspond to a lift-loss factor k of 0.4 (assuming the cross-flow velocity component at the vortex position to remain constant [42]). However, Boffadossi also introduces a short transition region extending $0.2c$ downstream of the burst where

$$\frac{\Gamma_{BD}(x)}{\Gamma(x)} = 1 - 0.6 \sqrt{1 - \left(\frac{\bar{x} - \bar{x}_{BD} - 0.2}{0.2} \right)^2} \quad (25)$$

This transition region smoothes out the onset of burst-induced lift-loss.

Shephselovich [45] uses a similar approach, factoring the vortex lift component empirically. McCormick [46] factors both vortex and potential lift components, but does not specify by how much.

The most widely used form of this model is that due to Lan & Hsu [34]. In this model, the factor k does not vary with incidence or burst location, but is a function solely of the wing planform. Reference 34 derives k from the ‘standard’ Wentz & Kohlman dataset [12] by fitting a LESA-based prediction of potential and vortex lift to the measured lift at an incidence 5° above burst onset – corresponding roughly to a burst point at 50% chord. In order to extend the model to non-delta planforms, the factor k was correlated against y_l , the spanwise distance to the centroid of the leading-edge suction distribution. Figure 13 shows this correlation, and indicates the corresponding values for y_l for simple delta wings. The factor k is relatively constant at around 0.6-0.7 for higher sweep angles, then falls off rapidly as sweep is reduced below 70° .

All of these lift-loss modelling methods share three shortcomings:

- a) they are all entirely empirical,
- b) they are all based on a very limited experimental dataset, and
- c) they all ignore any effect of breakdown upstream of the burst point.

That the last may be significant is illustrated by Figure 14 [9], which shows a reduction in vortex-induced suction peak beginning well upstream of burst onset. Empirical lift-loss predictions may perhaps safely ignore this effect; but this is clearly not the case if these models are then applied to prediction of pitching and rolling moment characteristics (eg [34,35,38,41]).

21.4.1.3 Semi-Empirical ‘Lift Reduction’ Models

A much smaller class of model applies a *semi*-empirical approach to lift-loss modelling. Ashenberg’s burst model [47] is applied to a Brown & Michael [40] cross-flow vortex model. Downstream of the burst point Reference 47 adds a distribution of two-dimensional sources along the vortex centreline, generating what is effectively a semi-infinite slender body (Figure 15). This body (or bubble) acts to reduce the vorticity shed into the leading-edge vortex, and hence reduces the vortex lift. With a suitable (but entirely empirical) choice of source strength and distribution the effect of burst onset and progression on lift can be modelled reasonably well. Although the conical nature of delta wing vortex flows implies that radial velocities should in general have an ‘inflow’ direction (ie flow is entrained into the vortex), recent PIV measurements (eg [48]) of cross-flow topologies have shown a source-type flow at the centre of a burst vortex, bounded by a limit cycle. Ashenberg’s model may therefore be a more accurate representation of the true flow than it at first appears, although the required source distribution remains an empirical input to the model.

Dixon’s HASC95 lift loss model has developed from a simple assumption of separated (or ‘stalled’ flow outboard and behind of the burst point [49] to an approach in which the upstream effects of breakdown are modelled by a reduction in sectional angle of attack ahead of the burst [50]. However, the degree of

reduction is given by an empirical correlation with vortex core radius and position, based (it appears) on a single experimental dataset. The description of the model as given in References 49 and 50 is rather obscure (to say the least), but the results were good enough for it to be incorporated in the USAF conceptual design aerodynamic prediction code HASC95 [51].

21.4.2 A New Approach

21.4.2.1 Current 'Explanations'

Burst-induced lift-loss is usually presented as a self-evident consequence of the 'collapse' or 'disintegration' of the vortex into a 'wake-like' turbulent flow [eg 52]. However, this qualitative assertion really does not say very much. Despite its chaotic, disordered appearance when visualised, recent PIV studies show that a burst vortex retains a well-organised vortical structure, albeit distorted into an unsteady rotating/translating helical form [eg 53]. A particularly odd feature is that oil flow visualisation generally shows almost no discernible effect of burst onset on the surface flow topology, other than perhaps a modest outboard displacement of the secondary separation line [9,54,55].

On the other hand, static pressure measurements do show a subsidence (although rather gradual – Figure 14) and widening of the vortex-induced suction peak as the burst passes [56,57]. Clearly, this can only result from a corresponding reduction in the local vortex strength, although the limited experimental evidence is equivocal on the question of whether there is a loss of circulation as such, or simply a reduction in the rate of increase with angle of attack/chordwise location as the vortex bursts. Circulation trends derived from integration of point velocity or vorticity measurements [eg 58] tend to show a *loss* in magnitude of circulation with burst onset, while global measurement techniques (eg acoustic 'time-of-flight' [59]) tend to show a *reduction in the rate of increase* with incidence.

Either way, the vortex aft of the burst is weaker than it would be if unburst – which leads us to ask why? Loss of vorticity to increased turbulent diffusion is one possibility [60], but seems unlikely. If anything, time-averaged velocity gradients are lower in a burst vortex core than in an unburst core, whilst the burst process itself is widely acknowledged to be essentially an inviscid phenomenon. Further, the magnitude of the lift loss does not appear to be sensitive to Reynolds Number [57]. Reference 59 suggests that an interaction between feeding shear layers ('vortex crowding') is responsible for delta wing stall, but this is a high incidence mechanism which cannot explain lift-loss at burst onset. Reference 50 suggests that turbulence associated with the burst affects the Kutta condition at the trailing-edge, but this again appears unlikely; delta wing flows are relatively insensitive to trailing-edge conditions [37], whilst, as is implicit in several of the empirical models described above, the relative degree of lift loss increases as the burst nears the apex.

However, delta wing flows *are* sensitive to leading-edge shape, and it is primarily the leading-edge Kutta condition that governs the rate of vorticity shedding into the vortex system. Ashenberg's model [47] effectively incorporates such an interaction, with the source flow superimposed on the burst leading-edge vortex changing the upper and lower surface cross-flow velocities at the leading-edge. Downstream of the burst point the vortex grows in strength less quickly, and therefore vortex lift is reduced.

21.4.2.2 Burst Interaction with the Leading-Edge Flow

Although suggesting that the burst/leading-edge interaction is the means by which breakdown affects vortex, Ashenberg's model does not provide a physical mechanism, or a reason for the observed magnitude of the burst-induced lift-loss. The hypothesis presented here is that it is the unsteady rotating/translating helical structure typical of burst delta wing vortices (Figures 1 and 2) that is responsible for the adverse interaction. In order to demonstrate that this is a possible mechanism, it is first necessary to establish the relationship between the leading-edge vortex strength and position, and the

vorticity shedding process at the leading-edge.

Figure 16 shows a simplified representation of the leading-edge vortex shedding process in the cross-flow plane. The strength of the shear layer emanating from the leading-edge is given by the velocity jump across it,

$$\gamma = V_L - V_U = \frac{\partial \Gamma_{le}}{\partial y} \quad (26)$$

with the vorticity convection rate determined by the mean velocity in the shear layer, so that

$$\begin{aligned} \frac{\partial \Gamma_{le}}{\partial t} &= \frac{\partial \Gamma_{le}}{\partial y} \frac{\partial y}{\partial t} \\ &= (V_L - V_U) \frac{(V_L + V_U)}{2} = \frac{V_L^2 - V_U^2}{2} \end{aligned} \quad (27)$$

For a ‘steady-state’ vortex system to exist the rate at which circulation is shed from the leading-edge must be equal to the rate at which it is convected downstream in the leading-edge vortex [61], so that

$$\frac{\partial \Gamma}{\partial x} U_\infty \cos \alpha = \frac{\partial \Gamma_{le}}{\partial t} \quad (28)$$

where $U_\infty \cos \alpha$ is the component of the freestream velocity parallel to the wing surface. The streamwise growth in the leading-edge vortex strength is then

$$\frac{\partial \Gamma}{\partial x} = \frac{V_L^2 - V_U^2}{2U_\infty \cos \alpha} \quad (29)$$

Equation (29) illustrates the critical point that the vortex growth rate is determined largely by the difference in the squares of the upper and lower surface spanwise velocities at the leading-edge. In a steady flow this would not be important; however, in an unsteady flow the effects of vortex motion on *time-averaged* velocity and velocity² are significantly different.

21.4.3 Effect of Helical Burst on Shedding Process

21.4.3.1 Estimation of Velocities at the Leading-Edge

Flow visualisation and PIV studies have demonstrated that the fundamental structure of a burst vortex is helical; downstream of the breakdown the vortex core is deflected into a rotating/translating spiral. Section 3 suggests that the overall spiral motion is translational rather than rotational, but in terms of the flow topology in the cross-flow plane the effect is the same. The effect of this rotating/translating spiral structure is modelled in the cross-flow plane by a point vortex orbiting about the nominal vortex centreline. This approach has been shown to be effective in modelling both time-averaged [62] and unsteady [63] velocity and pressure variations in delta wing flows.

Neglecting the contribution from the vortex on the opposite wing half, the cross-flow velocity V_U induced by the vortex at the leading-edge separation point is approximated by that given by a point vortex over an infinite plane (Figure 17)

$$V_U \approx 2 \frac{\Gamma}{2\pi s} \frac{\bar{z}_0}{(1 - \bar{y}_0)^2 + \bar{z}_0^2} \quad (30)$$

where the vortex core height z_0 and spanwise location y_0 are non-dimensionalised by the local semispan s .

If an orbital motion of radius r_s is imposed on the vortex core, it is found that for representative vortex positions and radii the *time-averaged* induced velocity V_U is identical to that given by a static vortex of the same strength at (y_0, z_0) . As a first approximation, then, an orbital motion representing a spiral burst can be imposed on the vortex without significantly affecting the steady lower surface flow. This result also provides an explanation for the almost negligible effect of vortex breakdown on surface flow topology as visualised using oil flow.

However, equation (29) shows that the vorticity shedding rate is a function of V^2 , not V . Once again imposing an orbital motion on the vortex core, it is found that the *time-averaged* value of V_U^2 for a rotating vortex is significantly increased over that given by a static vortex. This is illustrated by Figure 18, which shows the ratio (k_{V2}) of the 'rotating' to 'static' values of $\overline{V_U^2}$, as given by equation (30). The ratio k_{V2} is plotted as a function of non-dimensional core height z_0/s for a range of spiral radii r_s/s at a typical spanwise location $y_0/s = 0.7$. Also indicated on Figure 18 are representative core height and spiral burst radii for a range of sweep angles.

Core height is given by a correlation described in Appendix B (Figure B-2), based on the work of Reference 14

$$\frac{z_0}{s} = \frac{0.78K}{2.52 + K} + 0.016K \quad (31)$$

where K is the Sychev similarity parameter $\tan\alpha/\tan\varepsilon$ [26]. For spiral radius r_s , the simple engineering model of vortex breakdown described in Section 3 and Reference 64 suggests that the radius of a spiral vortex burst should scale with the vortex core radius, which in turn is a function of the vortex strength Γ and swirl ratio ϕ_0 . Applying Hemsch & Luckring's correlation for vortex strength [26] and typical values for K and ϕ_0 at burst onset then gives

$$\frac{a_0}{s} = \frac{r_s}{s} \approx 0.37 K^{0.2} \frac{\sin\alpha}{\phi_0} \approx 0.5 \sin\alpha \quad (32)$$

Figure B-3 indicates that equation (32) gives a reasonable fit to the limited experimental data available for helix core radius, and asymptotes to a sensible limit of half the local semispan.

Figure 18 demonstrates that a spiral vortex burst represented in the cross-flow plane by a orbiting point vortex can have a very substantial effect on the vorticity shedding process at the leading-edge, and that because of the appearance of K in equation (31) the impact is strongly sweep dependent. Increases in the time-averaged value $\overline{V_U^2}$ relative to the static vortex case range from 20-60% as the burst crosses the trailing-edge to 25-90% as the burst reaches the wing apex. Referring to equation (29), an increase in V_U^2 will reduce the rate at which circulation is fed into the vortex, hence the effect shown in Figure 18 leads directly to a reduction in overall vortex lift. Overall, the lower the sweep angle, the greater the effect of breakdown on the upper surface cross-flow at the leading-edge.

Figure 18 gives a value for $\overline{V_U^2}$; however, without an estimate for the corresponding lower surface velocity contribution V_L^2 extending into the burst region, the impact on vortex strength implied by equation (29) cannot be quantified. In the absence of direct experimental data for this velocity, a rough estimate was made using equations (29) and (30) and the extensive experimental database for *unburst* vortex core strength and position above the wing, as described in Appendix C.

The variation of the resulting estimate of lower-surface cross-flow velocity (Figure C-1) was found to be

reasonably well represented by the semi-empirical relation

$$V_L = k_a U_\infty \sin \alpha + k_{le} \tan \varepsilon U_\infty \cos \alpha \quad (33)$$

where k_a lies between 3 and 3.5, and k_{le} between 0.5 and 0.8, depending on wing geometry and test conditions. Physically, equation (33) can be interpreted as consisting of a term proportional to the cross-flow component of the freestream velocity $U_\infty \sin \alpha$, and a *sweep-dependent* term proportional to the cross-flow component of the velocity parallel to the wing leading-edge $U_\infty \tan \varepsilon \cos \alpha$ (Figure C-3). The latter term would go to zero for a symmetric leading-edge (or a thin flat-plate wing), but is positive for the lower-surface bevelled leading-edge typical of the delta wing literature. The more slender the wing, the smaller this term will be.

21.4.3.2 Magnitude of Lift Loss

Denoting the ratio of the time-averaged to static values of V_U^2 described previously as k_{v2} , the corresponding reduction in the rate of growth of the vortex circulation k_Γ is given by equation (30), hence

$$\begin{aligned} k_\Gamma &= \frac{(\partial \Gamma / \partial x)_{VB}}{(\partial \Gamma / \partial x)_0} = \frac{V_L^2 - k_{v2} V_U^2}{V_L^2 - V_U^2} \\ &= 1 - (k_{v2} - 1) \frac{V_U^2}{V_L^2 - V_U^2} \end{aligned} \quad (34)$$

The effects of incidence and sweep angle on the upper velocity factor $(k_{v2} - 1)$ are effectively shown in Figure 18. An estimate of the vorticity shedding parameter $V_U^2 / (V_L^2 - V_U^2)$ is shown in Figure 19, with datapoints derived from experimental data using equation (30) for the upper velocity V_U and equation (33) for the lower velocity V_L . The trends were extrapolated to the higher angles of attack using equations (33), (31) and (32). Also indicated on Figure 19 are angles of attack for burst onset and for burst at the wing apex.

Comparing Figure 18 and Figure 19, two contrasting trends with sweep angle are seen: the upper velocity factor $(k_{v2} - 1)$ reduces rapidly as the sweep angle is increased, whereas the vorticity shedding parameter $V_U^2 / (V_L^2 - V_U^2)$ increases with sweep angle.

In order to convert the circulation growth factor k_Γ into an equivalent lift-loss factor k a further approximation needs to be made. In the absence of sufficient experimental data, the basic assumption is made that if at a given chordwise location the vortex strength is reduced due to an upstream burst, then in order to maintain the Kutta condition at the leading-edge the mean core position (y_0, z_0) moves so as to keep the time-averaged upper-surface induced velocity \bar{V}_U constant. This is consistent with visualisation data in Reference 6, which shows burst cores tending to move outboard and downward, closer to the leading-edge. As a result, the vorticity shedding parameter $V_U^2 / (V_L^2 - V_U^2)$ will remain constant downstream of the burst point. The corresponding velocity factor $(k_{v2} - 1)$ should tend to increase, but in the absence of reliable data on core location and spiral radius a constant value will be assumed.

This assumption leads to a constant value of the vortex circulation growth factor k_Γ downstream of the burst point. Examination of Wentz & Kohlman's experimental dataset [12] suggested that this was a reasonable result. For a conical lift distribution, assuming loss in vortex lift to be proportional to loss in circulation [42], the corresponding lift loss factor k for equation (23) is

$$k = k_\Gamma + \frac{2(1 - k_\Gamma)(\bar{x}_{VB} - \bar{x}_{VB}^2)}{(1 - \bar{x}_{VB}^2)} \quad (35)$$

Applying equations (34) and (35) to the extrapolated trends presented in Figures 18 and 19 gives a predicted lift loss factor k shown in Figure 20 as a function of burst point location and wing sweep.

For comparison, Figure 21 shows vortex lift factor k derived from Wentz & Kohlman's data [12] (Figure 10), using a curve fit to the LESA vortex lift model coupled with equation (23). It can be seen that this analysis gives a remarkably good prediction of the vortex lift factor, capturing the magnitude, the shape of the curves, and the effect of sweep angle. These initial results do not predict the increased lift loss seen experimentally for the 60° delta wing; however, the simple correlations do tend to underpredict both helix radius (and hence the upper velocity factor k_{V2}), and the vorticity shedding parameter $V_U^2/(V_L^2 - V_U^2)$ at lower sweep angles. A small increase in helix radius for the 60° wing would give an increase in k_{V2} sufficient to match the lift loss seen in Figure 21, but given the uncertainty in both the experimental data and the vortex core position correlations, further ad hoc adjustments were not thought to be appropriate at this stage of the model development.

21.4.4 Other Implications

21.4.4.1 Surface Pressure Distribution

Reference 56 suggests that one indication of vortex breakdown is a change in the shape of the wing upper-surface spanwise pressure distribution, as characterised by the half-width of the vortex-induced suction peak. Given that time-averaged tangential velocity distributions outside the immediate vicinity of the vortex core remain close to that of a potential vortex even in the presence of breakdown [eg 6], the reason for this shape change was not clear. However, for the unsteady flow induced by a burst vortex the surface pressure will be given by the unsteady Bernoulli equation [84]

$$\frac{p_\infty - p}{\rho} = \frac{V^2}{2} + \frac{\partial \Phi}{\partial t} \quad (36)$$

Despite the apparently small changes in time-averaged velocities seen, the combination of the increase in time-averaged velocity squared discussed above and the time-varying potential function in equation (36) could lead to a significant variation in the *shape* of the surface pressure distribution underneath a rotating vortex.

21.4.4.2 Time Lag in Lift-Loss Response to Wing Motion

The interaction between vortex core location and the leading-edge vorticity shedding rate could also introduce an additional time-dependency into the response of wing lift to vortex breakdown. Reference 13 notes that flow visualisation studies show a characteristic response time of the order of 1.5 (when non-dimensionalised by root chord and freestream velocity). This is broadly consistent with the review reported in Reference 85, which showed that the dynamic vortex burst response to wing motion resembled that of a heavily damped second order system, with non-dimensional natural frequency 2 and damping ratio 1.7. This natural frequency is roughly consistent with theoretical studies of the dynamic response of helical vortices [eg 69], but no explanation has been advanced for the very high level of damping. One possibility which deserves further study is that there is a cross-flow viscous drag force acting on the vortex core as it lags behind the wing motion.

However, in contrast to the relatively short time constant of the vortex burst itself (~1.5), the corresponding aerodynamic forces on the wing show lag times an order of magnitude greater (eg ~15) [13,86]. Curiously, this discrepancy does not appear to have been widely noted, or any explanation put forward. Given that the lift-loss mechanism proposed above is a time-dependent interaction between the leading-edge vorticity shedding rate and the vortex core location, it also appears to be an obvious candidate for the change in lag time between burst point motion and burst-induced lift loss. Clearly, there must be a convective lag between any change in the leading-edge conditions and the corresponding change

in vortex strength, although the combination of the motion of the vortex core in the cross-flow plane and the longitudinal motion of the burst point itself make the analysis far from straightforward.

21.4.4.3 Alleviation of Vortex Lift Loss

If the lift loss mechanism proposed here can be confirmed, then it would provide a basis for an improved lift-loss model for preliminary aircraft design codes. Additionally, it would also give a clear indication of how to alleviate burst-induced lift loss on future combat aircraft. Previous vortex control techniques have focussed on suppressing the burst itself, and have broadly been either 'steady-state' techniques applied over a significant area (eg leading-edge vortex flaps) or 'unsteady' techniques applied at a point (eg pulsed core blowing). The helical vortex model suggests that in order to alleviate lift-loss a flow control system would need to be situated at the leading-edge, and would have to vary both with time (ie at the helix rotation rate) and with chordwise position (ie at the helix pitch). This would appear to be an ideal application for MEMS devices (eg direct, localised control of the leading-edge separation) or smart structures (eg time-varying wave-like leading-edge deflections). Reducing lift-loss aft of the burst could also help delay the vortex breakdown progression, due to a reduction in the adverse longitudinal pressure gradient along the core.

21.5 CONCLUSIONS

Development of improved models of vortex breakdown and its impact on aerodynamic characteristics rests on three main factors:

1. the position of vortex breakdown as a function of wing geometry (in particular leading-edge cross-section and sweep angle) and of flight/tunnel conditions (angle of attack and sideslip, pitch, yaw and roll rate, Reynolds Number, turbulence, fin interference, tunnel constraint etc)
2. the structure and behaviour of the vortex in its burst state
3. the mechanism by which the burst vortex affects wing aerodynamics (lift-loss, buffet etc)

The first is partially addressed by existing theoretical analyses of vortex stability (primarily by providing the swirl ratio as a critical parameter), but nevertheless in practice is largely based on relatively crude correlations of experimental data. The second is now receiving more attention, driven by recent improvements in both computational methods and non-intrusive flow measurement techniques, but remains controversial. Astonishingly, the third rather fundamental element appears not to have been addressed seriously, with lift-loss usually presented as a self-evident consequence of the 'collapse' or 'disintegration' of the vortex into a 'wake-like' turbulent flow, before passing on to other matters.

The 'engineering' models presented in this chapter address the second and third elements, providing at least the basis of an overall model of the impact of vortex breakdown that captures the essentials of the flow physics.

The breakdown process of a delta wing vortex is modelled as a symmetry-breaking subcritical bifurcation from an axisymmetric unburst vortex to a helically symmetric translating spiral burst form. Applying continuity and rotational velocity constraints to the motion of a semi-infinite helix results in a critical swirl ratio similar to that given by conventional vortex stability analyses. The post-burst helix is of opposite hand to the circulation of the vortex, with a pitch directly proportional to the vortex strength, and convects downstream at a rate less than freestream by a factor dependent on the helix inclination. The resultant velocity on the helix centreline is zero, giving the stagnation point that is a characteristic feature of vortex breakdown. Comparison with published experimental data for delta wing vortices is made rather difficult by the complex internal structure of a leading-edge vortex core, but is possible on the assumption that the inner and outer core dynamics can be addressed separately. On that basis the model predictions agree

reasonably well with measured helix pitch, inclination, radius, convection velocity, induced velocity and fundamental frequency. Given the major simplifications made in the initial derivation of the model, this agreement is very encouraging.

Burst-induced lift-loss is modelled by considering a rotating/translating helical burst vortex as an orbiting point vortex in the cross-flow plane. It is suggested that the interaction between the rotating vortex and the leading-edge flow reduces the rate at which vorticity is shed into the flow, and hence the rate at which the leading-edge vortex grows downstream. Some initial estimates of burst-induced lift-loss based on a simple cross-flow model of the vortex/leading-edge interaction and experimental data on vortex strength, core height and burst helix radius have been made. These show that this mechanism leads to predictions of the magnitude and the rate of onset of burst-induced lift-loss, and the effect of sweep, that are very similar to those seen experimentally. The model used is rather crude; nevertheless the agreement is again encouraging.

Five questions were posed at the beginning of this chapter:

- a) Why does a burst delta wing vortex generally display a rotating spiral form, with the spiral of opposite hand to the circulation?
- b) What governs the wavelength and rotation frequency of the spiral vortex?
- c) Why does vortex breakdown have such a large impact on aerodynamic characteristics?
- d) Why are the effects so dependent on wing sweep angle?
- e) Why is the characteristic response time of burst-induced lift-loss an order of magnitude longer than the response time of the burst itself?

The helical breakdown model presented in Section 3 has gone a long way to answering the first two, namely why does a burst vortex display a spiral form of opposite hand to the circulation, and what governs the wavelength and rotation frequency of the spiral. The model itself requires more work, particularly on the effect of the axial velocity excess in the vortex core and on the initial evolution of the helical structure, but it does indicate potentially fruitful areas in which to focus future experimental studies of time-dependent flow structures in leading-edge vortex breakdown. For example, are there in fact separate inner and outer core dynamics? Post-breakdown, is there an axial velocity excess or defect within the inner core? What are the limitations of the assumptions made on continuity and rotational velocity?

The basic lift-loss mechanism proposed in Section 4 has provided an answer for the third and fourth questions. The rotating helical nature of vortex breakdown has a significant impact on the vorticity shedding process at the leading-edge, while the effect of sweep comes from a combination of the proximity of the vortex to the leading-edge (greater for low sweep), the relative contribution of the upper-surface cross-flow velocity V_U to the rate of vorticity shedding (greater for high sweep) and the relative magnitude of the vortex lift (greater for high sweep).

Although the last question has not been addressed directly in this paper, the proposed lift-loss mechanism does indicate a route to a possible solution. Changes in the rate of vorticity shedding at the leading-edge cannot be reflected instantaneously in changes in vortex strength, but will be delayed by the time it takes for changes in vortex sheet strength to be convected along the spiral feeding shear layer from the leading-edge into the vortex core. It seems entirely likely then that a significant additional time lag could be introduced into the response of delta wing aerodynamic characteristics to wing motion. The differing effect of helical vortex rotation on *time-averaged* upper-surface velocity V_U (unchanged) and velocity squared V_U^2 (reduced) may also provide an explanation for the negligible impact of breakdown on surface oil flow visualisation compared with the significant impact on surface pressure distributions.

The models presented here are admittedly crude; preliminary results are very encouraging, but

considerable further work is required. The three-dimensional (non-conical) nature of delta wing vortex flows with breakdown will be critical, giving a burst helix interaction with the leading-edge which will vary with both chordwise location and time. The upstream influence of the burst needs to be clarified, since this will impact significantly on predictions of pitching and rolling moments. Again, the proposed lift-loss mechanism provides a means for this effect to be modelled.

A problem with further development of any vortex lift-loss model is the glaring lack of any single consistent experimental dataset of sufficient comprehensiveness, a situation which is less than satisfactory given the notorious sensitivity of delta wing flows to test conditions and detail wing geometry. Nevertheless, the results are (a) sufficiently encouraging, and (b) of such potential significance, that it seems that an experimental study directed specifically at determining the critical model parameters would be worthwhile. It would be necessary to measure cross-flow velocities near the leading-edge, vortex strength, vortex core positions (before & after burst), helix radii, and normal force simultaneously, but modern non-intrusive flow measurement techniques should make this a relatively straight-forward task.

21.6 REFERENCES

- [1] Delery, J.M., "Aspects of Vortex Breakdown", Progress in Aerospace Sciences, Vol 30, 1994, pp1-59
- [2] Lucca-Negro, O. and O'Doherty, T., "Vortex Breakdown: a Review", Progress in Energy and Combustion Science, Vol 27, 2001, pp431-481
- [3] Nelson, R.C. and Pelletier, A., "The Unsteady Aerodynamics of Slender Wings and Aircraft Undergoing Large Amplitude Manoeuvres", Progress in Aerospace Sciences, Vol 39, 2003, pp185-248
- [4] Pirzadeh, S.Z., "Vortical Flow Prediction Using an Adaptive Unstructured Grid Method", paper A-13 in Proceedings of NATO RTO-AVT Symposium on 'Advanced Flow Management', Norway, May 2001
- [5] Ng, T.T., "On Leading-Edge Vortex and its Control", AIAA Paper 89-3346, 1989
- [6] Payne, F.M., "The Structure of Leading-Edge Vortex Flows Including Vortex Breakdown", PhD thesis, University of Notre Dame, 1987
- [7] Spall, R.E., Gatski, T.B. and Grosch, C.E., "A Criterion for Vortex Breakdown", Physics of Fluids, Vol. 30, No. 11, November 1987, pp.3434-3440
- [8] Cornelius, K.C., "Analysis of Vortex Bursting Utilising Three-Dimensional Laser Measurements", Journal of Aircraft, Vol. 32, No. 2, March-April 1995, pp.297-306
- [9] Lambourne, N.C. and Bryer, D.W., "The Bursting of Leading-Edge Vortices – Some Observations and Discussion of the Phenomenon", ARC R&M 3282, April 1961
- [10] Gursul, I., "Unsteady Flow Phenomena over Delta Wings at High Angle of Attack", AIAA Journal, Vol. 32, No. 2, February 1994, pp.225-231
- [11] Kegelman, J. and Roos, F., "Effects of Leading-Edge Shape and Vortex Burst on the Flowfield of a 70 Degree Sweep Delta Wing", AIAA-89-0086, January 1989
- [12] Wentz, W.H. and Kohlman, D.L., "Wind Tunnel Investigations of Vortex Breakdown on Slender

- Sharp-Edged Wings”, NASA CR-98737, November 1968
- [13] Goman, M., and Khrabrov, A., “State-Space Representation of Aerodynamic Characteristics of an Aircraft at High Angles of Attack”, *Journal of Aircraft*, Vol 31 No 5, September-October 1994, pp1109-1115
 - [14] Erickson, G.E., “Vortex Flow Correlation”, AFWAL-TR-80-3143, January 1981
 - [15] Visbal, M.R., “Computed Unsteady Structure of Spiral Vortex Breakdown on Delta Wings”, AIAA-96-2074, 1996
 - [16] Jumper, E.J., Nelson, R.C. and Cheung, K., “A Simple Criterion for Vortex Breakdown”, AIAA Paper 93-0866, 1993
 - [17] Gursul, I., “Criteria for Location of Vortex Breakdown over Delta Wings”, *The Aeronautical Journal*, May 1995, pp.194-196
 - [18] Greenwell, D.I., “Pitfalls in the Interpretation of Delta Wing Vortex Flow Visualisation”, paper A-5 in Proceedings of NATO RTO-AVT Symposium on ‘Advanced Flow Management’, Norway, May 2001
 - [19] Pagan, D. and Solignac, J.L., “Etude Experimentale de l’Eclatement d’un Tourbillon Engendré par une Aile Delta”, *La Recherche Aérospatiale*, May-June 1986, pp.197-219
 - [20] Chanaud, R.C., “Observations of Oscillatory Motion in Certain Swirling Flows”, *Journal of Fluid Mechanics*, Vol. 21, 1965, pp.111-127
 - [21] Cunningham, A.M., “Vortex Flow Hysteresis”, paper 11 in NASA CP-2416, 1986, pp.231-248
 - [22] Shih, C. and Ding, Z., “Unsteady Structure of Leading-Edge Vortex Flow over a Delta Wing”, AIAA Paper 96-0664, January 1996
 - [23] Werle, H., “Flow Visualisation Techniques for the Study of High Incidence Aerodynamics”, paper 3 in AGARD LS-121, ‘High Angle-of-Attack Aerodynamics’, March 1982
 - [24] Visser, K.D., “An Experimental Analysis of Critical Factors Involved in the Breakdown Process of Leading-Edge Vortex Flows”, PhD thesis, University of Notre Dame, 1991
 - [25] Lin, J.-C. and Rockwell, D., “Transient Structure of Vortex Breakdown on a Delta Wing”, *AIAA Journal*, Vol. 33, No. 5, January 1995, pp.6-12
 - [26] Hemsch, M.J. & Luckring, J.M., “Connection between Leading-Edge Sweep, Vortex Lift and Vortex Strength for Delta Wings”, *Journal of Aircraft*, Vol. 27, No. 5, May 1990, pp.473-475
 - [27] Mabey, D.G., “A Review of the Vortex Shedding Frequencies of Aerofoils, Flat Plates and Delta Wings”, Defence Research Agency report DRA/AS/HWA/TR94064/1, March 1995
 - [28] Mabey, D.G., “Similitude Relations for Buffet and Wing Rock on Delta Wings”, *Progress in Aerospace Sciences*, Vol 33 No 7/8, 1997, pp481-511
 - [29] Jupp, M.L., Coton, F.N. and Green, R.B., “A Statistical Analysis of the Surface Pressure Distribution on a Delta Wing”, *The Aeronautical Journal*, July 1999, pp.349-357

- [30] Traub, L.W., Rediniotis, O.K., Klute, S.M., Moore, C.T. and Telionis, D.P., "Instabilities of Vortex Breakdown: Their Structure and Growth", AIAA Paper 95-2308, June 1995
- [31] Molton, P., Mitchell, A., Barberis, D., Afchain, D., Rodriguez, O. and Pruvost, J., "Experimental Investigation of Vortex Breakdown over a Delta Wing with Consideration of Control by Fluid Injection", paper A-19 in Proceedings of NATO RTO-AVT Symposium on 'Advanced Flow Management', Norway, May 2001
- [32] Sahin, B., Akilli, H., Lin, C.-H. and Rockwell, D., "Vortex Breakdown-Edge Interaction: Consequence of Edge Oscillations", AIAA Journal, Vol. 39, No. 5, May 2001, pp.865-876
- [33] Lowson, M.V. and Riley, A.J., "Vortex Breakdown Control by Delta Wing Geometry", Journal of Aircraft, Vol 32 No 4, July-August 1995, pp832-838
- [34] Lan, C.E. and Hsu, H.-C., "Effects of Vortex Breakdown on Longitudinal and Lateral-Directional Aerodynamics of Slender Wings by the Suction Analogy", AIAA-82-1385, 1982
- [35] Traub, L.W., 'Prediction of Vortex Breakdown and Longitudinal Characteristics of Swept Slender Wing Planforms', Journal of Aircraft, Vol 34 No 3, May-June 1997, pp353-359
- [36] Huang, X.Z., Sun, Y.Z. and Hanff, E.S., "Circulation Criterion to Predict Leading-Edge Vortex Breakdown over Delta Wings", AIAA-97-2265, 1997
- [37] Huang, X.Z., Sun, Y.Z. and Hanff, E.S., "Further Investigations of Leading-Edge Vortex Breakdown over Delta Wings", AIAA-97-2263, 1997
- [38] Hanff, E.S. and Huang, X.Z., "Effect of Vortex Behaviour on Loads Acting on a 65 Degree Delta Wing Oscillating in Roll at High Incidence", Israel Annual Conference on Aeronautics and Astronautics, February 1992
- [39] Myatt, J.H. and Arena, A.S., "A Theoretical/Empirical Model for Rolling Delta Wings with Vortex Breakdown", AIAA-98-2527, 1998
- [40] Brown, C.E. and Michael, W.H., "Effect of Leading-Edge Separation on the Lift of a Delta Wing", Journal of the Aeronautical Sciences, Vol 21, 1954, pp690-694
- [41] Huang, X.Z. and Hanff, E.S., "Prediction of Normal Force on a Delta Wing Rolling at Incidence", AIAA-93-3686, August 1993
- [42] Polhamus, E.C., "A Concept of the Vortex Lift of Sharp-Edge Delta Wings Based on a Leading-Edge Suction Analogy", NASA TN D-3767, October 1966
- [43] Boffadossi, M., "Calculation of Vortex Breakdown over Delta Wing by a Vortex-Lattice Method", ICAS-96-1.6.4, 1996
- [44] Nelson, R.C. and Visser, K.D., "Breaking Down the Delta Wing Vortex: the Role of Vorticity in the Breakdown Process", paper 21 in AGARD CP-494 'Vortex Flow Aerodynamics', 1990
- [45] Shephselovich, M., "Vortex Lift Predictions for Cambered Wings", Israel Journal of Technology, Vol 14, May 1976, pp18-22
- [46] McCormick, B.W., "A Vortex Lattice Model for Delta Wings with Bursting", SAE TP-910991,

April 1991

- [47] Ashenberg, J., "A Model for Vortex Breakdown on Slender Wings", AIAA Journal, Vol 25 No 12, December 1987, pp1622-1624
- [48] Cipolla, K.M. and Rockwell, D., "Instantaneous Crossflow Topology on a Delta Wing in Presence of Vortex Breakdown", Journal of Aircraft, Vol 35 No 2, March-April 1998, pp218-223
- [49] Dixon, C.J. and Driskill, G.T., "A Unique Applied Computational Method for Vortex Lift Aerodynamics and Vortex Burst for Arbitrary Aircraft", AIAA-85-4057, 1985
- [50] Dixon, C.J., "Semi-Empirical Analysis of Vortex Breakdown with Aerodynamics and Buffet Effects", AIAA-94-3483, 1994
- [51] Albright, A.E., Dixon, C.J. and Hegedus, .C., "Modification and Validation of Conceptual Design Aerodynamic Prediction Method HASC95 with VTXCHN", NASA CR-4712, March 1996
- [52] Nelson, R.C., "Unsteady Aerodynamics of Slender Wings", paper 1 in AGARD AR-776 'Aircraft Dynamics at High Angle of Attack: Experiments and Modelling', April 1991
- [53] Rockwell, D., "Three-Dimensional Flow Structure on Delta Wings at High Angle of Attack: Experimental Concepts and Issues", AIAA-93-0550, January 1993
- [54] Huang, X.Z., Hanff, E.S. and Jobe, C.E., "Surface Flow Topology on a Delta Wing at High Incidence for a Range of Roll Angles", AIAA-96-2398, 1996
- [55] Addington, G.A., and Nelson, R.C., "The Predictability of Skin-Friction Line Topology on a Rolled Delta", AIAA-98-4352, 1998
- [56] Greenwell, D.I. and Wood, N.J., "Determination of Vortex Burst Location on Delta Wings from Surface Pressure Measurements", AIAA Journal, Vol 30 No 12, November 1992, pp2736-2739
- [57] Roos, F.W. and Kegelman, J.T., "An Experimental Investigation of Sweep-Angle Influence on Delta Wing Flows", AIAA-90-0383, January 1990
- [58] Visser, K.D., "An Experimental Analysis of Critical Factors Involved in the Breakdown Process of Leading-Edge Vortex Flows", PhD thesis, University of Notre Dame, 1991
- [59] Johari, H. and Moreira, J., "Direct Measurement of Delta-Wing Vortex Circulation", AIAA Journal, Vol 36 No 12, December 1998, pp2195-2203
- [60] Ng, T.T., "On Leading Edge Vortex and its Control", AIAA-89-3346, 1989
- [61] Fidler, J.E., "Approximate Method for Estimating Wake Vortex Strength", AIAA Journal, Vol 12 No 5, May 1974, pp633-635
- [62] Backstein, S. and Staufenbiel, R., "Some Experimental Results on Spiral Vortex Breakdown", Z. Flugwiss. Weltraumforsch., Vol 19, 1995, pp359-365
- [63] Gursul, I. and Xie, W., "Physics of Buffeting Flows over Delta Wings", AIAA-98-0688, January 1998
- [64] Greenwell, D.I., "A Simple Engineering Model for Delta-Wing Vortex Breakdown", Journal of

Aircraft Vol 40 No 3, May-June 2003

- [65] Mezić, I., Leonard, A. and Wiggins, S., "Regular and Chaotic Particle Motion Near a Helical Vortex Filament", *Physica D*, Vol. 111, 1998, pp.179-201
- [66] Saffman, P.G., *Vortex Dynamics*, Cambridge University Press, 1995, pp.208-229
- [67] Moore, D.W. and Saffman, P.G., "The Motion of a Vortex Filament with Axial Flow", *Philosophical Transactions of the Royal Society of London, Series A*, Vol. 272, July 1972, pp.403-429
- [68] Kuibin, P.A. and Okulov, V.L., "Self-Induced Motion and Asymptotic Expansion of the Velocity Field in the Vicinity of a Helical Vortex Filament", *Physics of Fluids*, Vol. 10, No. 3, March 1998, pp.607-614
- [69] Lundgren, T.S. and Ashurst, W.T., "Area-Varying Waves on Curved Vortex Tubes with Application to Vortex Breakdown", *Journal of Fluid Mechanics*, Vol. 200, 1989, pp.283-307
- [70] Watts, T, private communication, July 2001
- [71] Ricca, R.L., "The Effect of Torsion on the Motion of a Helical Vortex Filament", *Journal of Fluid Mechanics*, Vol 273, 1994, pp.241-259
- [72] Sarasua, L.G., Sicardi Schifino, A.C. and Gonzalez, R., "The Stability of Steady, Helical Vortex Filaments in a Tube", *Physics of Fluids*, Vol. 11, No. 5, May 1999, pp.1096-1103
- [73] Hall, M.G., "A Theory for the Core of a Leading-Edge Vortex", *Journal of Fluid Mechanics*, Vol. 11, 1961, pp.209-228
- [74] Greenwell, D.I., "Comment on: Assessment of the Accuracy of representing a Helical Vortex by Straight Segments", *AIAA Journal*, Vol 41 No 2, February 2003, p332
- [75] Elle, B.J., "An Investigation at Low Speed of the Flow near the Apex of Thin Delta Wings with Sharp Leading-Edges", *ARC R&M 3176*, January 1958
- [76] Fink, P.T., "Some Early Experiments on Vortex Separation", *ARC R&M 3489*, September 1966
- [77] Carcaillet, R., Manie, F., Pagan, D. and Solignac, J.L., "Leading Edge Vortex Flow over a 75° Swept Delta Wing – Experimental and Computational Results", *ICAS-86-1.5.1*, 1986
- [78] Erickson, G.E., "Water-Tunnel Studies of Leading-Edge Vortices", *Journal of Aircraft*, Vol 19 No 6, June 1982, pp442-448
- [79] Ol, M.V., "An Experimental Investigation of Leading-Edge Vortices and Passage to Stall of Non-Slender Delta Wings", paper 2 presented at the NATO RTO/AVT Symposium on 'Advanced Flow Management: Vortex Flows and High Angle of Attack', Loen, May 2001
- [80] Skow, A.M. and Erickson, G.E., "Modern Fighter Aircraft Design for High Angle of Attack Manoeuvring", paper 4 in *AGARD LS-121, 'High Angle of Attack Aerodynamics'*, March 1982
- [81] Wedemeyer, E., "Vortex Breakdown", paper 9 in *AGARD LS-121, 'High Angle of Attack Aerodynamics'*, March 1982
- [82] Lowson, M.V., "Visualisation Measurements of Vortex Flows", *Journal of Aircraft*, Vol 28 No 5,

May 1991, pp320-327

- [83] Pelletier, A. and Nelson, R.C., "Factors Influencing Vortex Breakdown over 70° Delta Wing", AIAA-95-3469, 1995
- [84] Katz, J., and Plotkin, A., *Low-Speed Aerodynamics: From Wing Theory to Panel Methods*, McGraw-Hill Inc., 1991
- [85] Greenwell, D.I. and Wood, N.J., "Some Observations on the Dynamic Response to Wing Motion of the Vortex Burst Phenomenon", *The Aeronautical Journal*, Vol 98 No 972, February 1994, pp49-59
- [86] Greenwell, D.I., "Frequency Effects on Dynamic Stability Derivatives Obtained from Small-Amplitude Oscillatory Testing", *Journal of Aircraft*, Vol 35 No 5, September-October 1998

21.7 ACKNOWLEDGEMENTS

The work reported here was carried out as part of a CRP Fellowship project, funded by the UK Ministry of Defence under Technology Group 3 of the Corporate Research Programme.

FIGURES

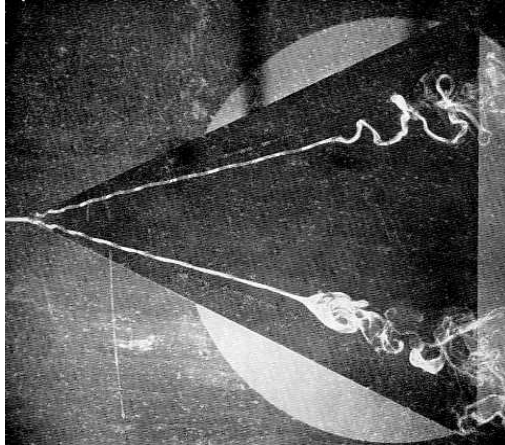


Figure 1: Spiral and bubble vortex breakdown [9]

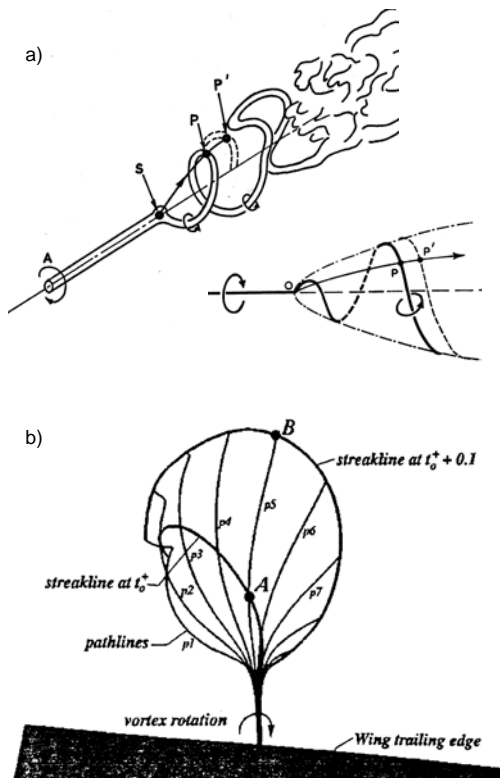


Figure 2: Particle paths in a spiral burst: (a) experimental [9], and (b) computational [15]

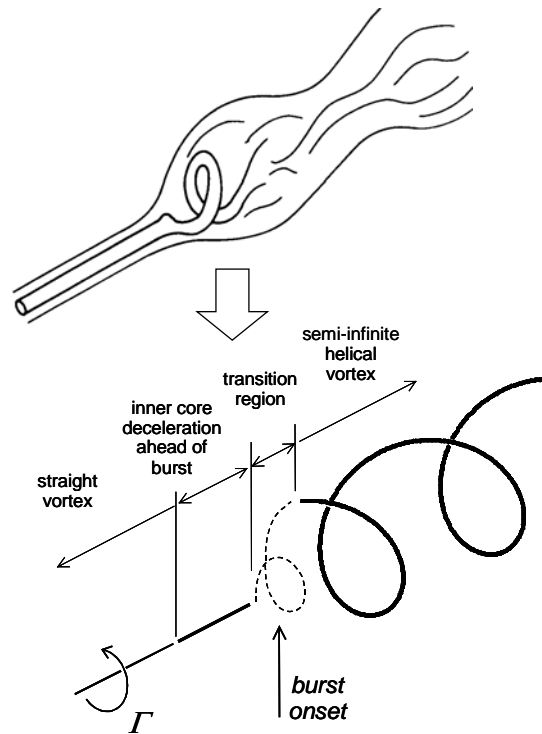


Figure 3: Schematic of basic helical vortex breakdown model

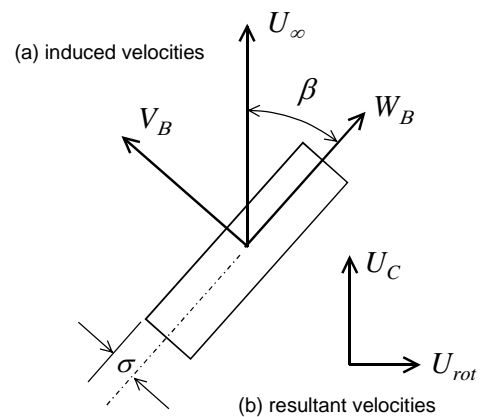


Figure 4: Velocities induced on a vortex element

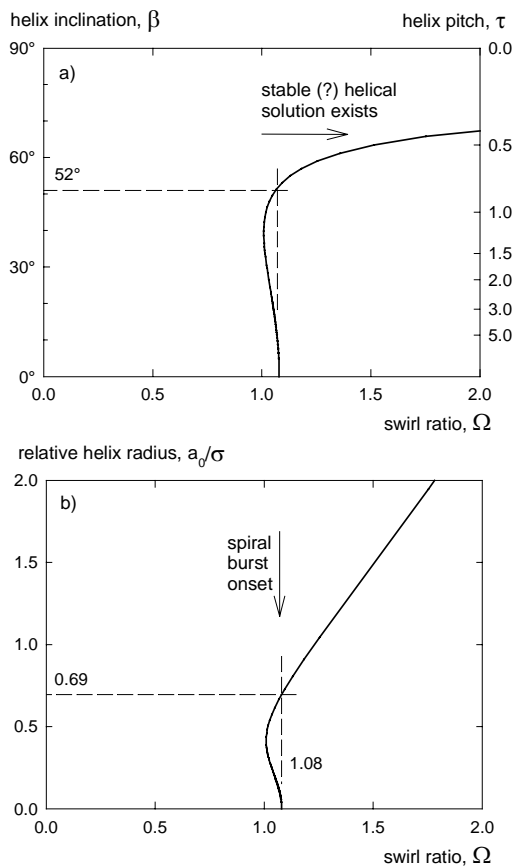


Figure 5: Helix inclination and radius as a function of swirl ratio ($\delta = 0.78$)

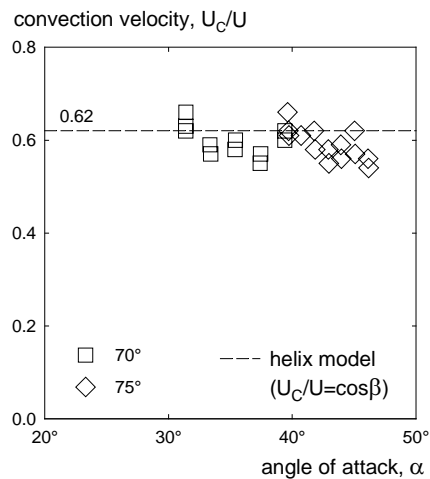


Figure 6: Effective disturbance convection velocity (replotted from Reference 10)

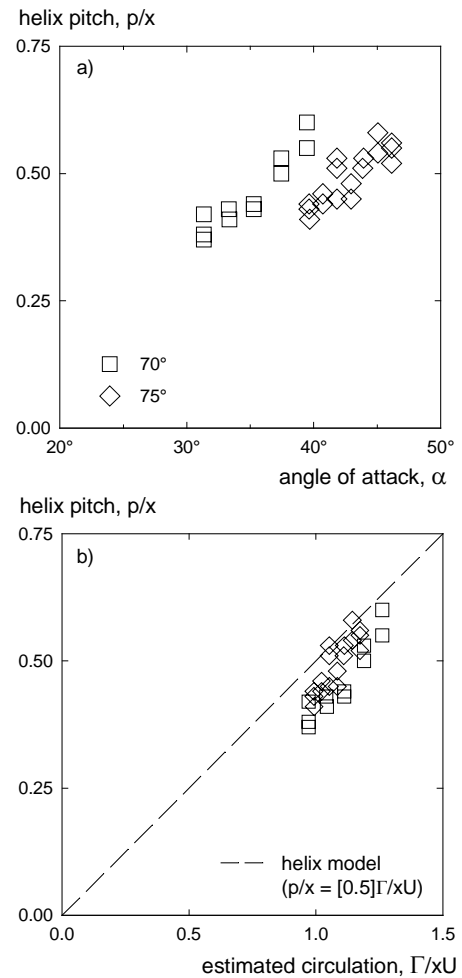


Figure 7: Effective disturbance wavelength: (a) replotted from Reference 10, (b) variation with estimated vortex strength

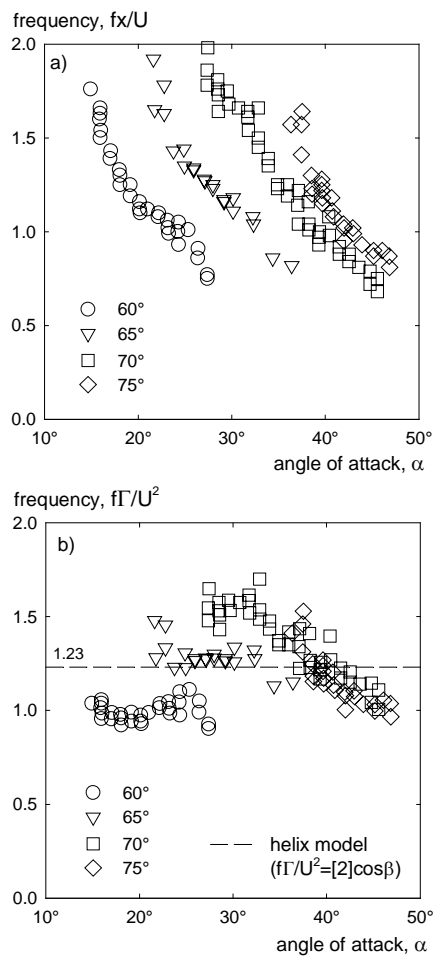


Figure 8: Disturbance frequency: (a) from Reference 10, (b) non-dimensionalised using estimated vortex strength

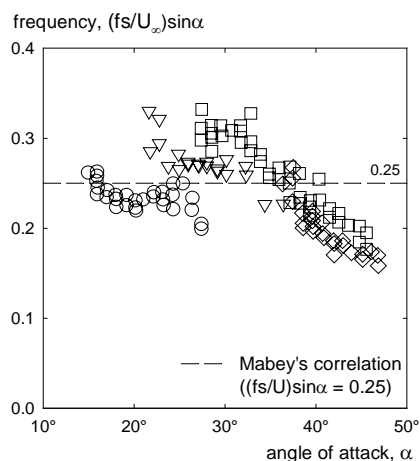


Figure 9: Mabey's vortex shedding frequency correlation [27,28] (key as Figure 8)

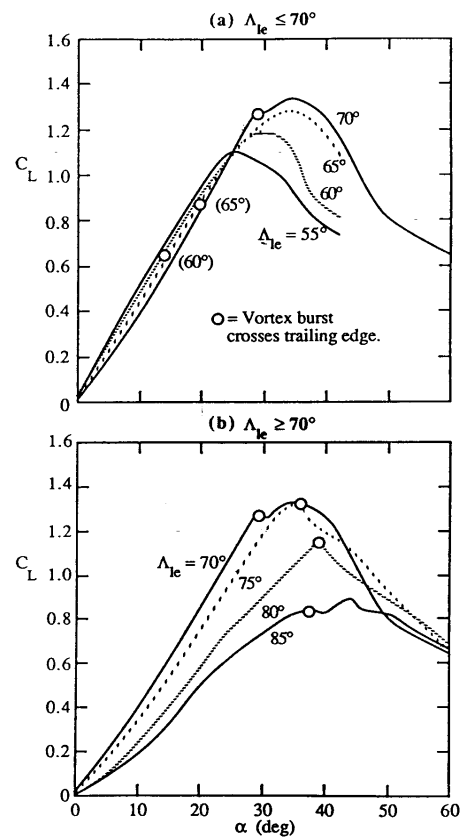


Figure 10: Effect of burst onset and sweep angle on lift curve slope [12, as replotted in 11]

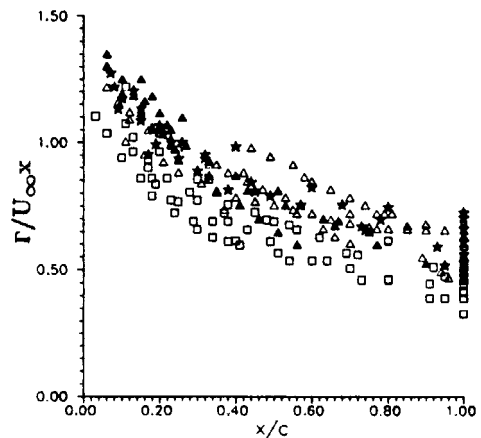


Figure 11: Example of scatter in vortex burst position correlations [17]

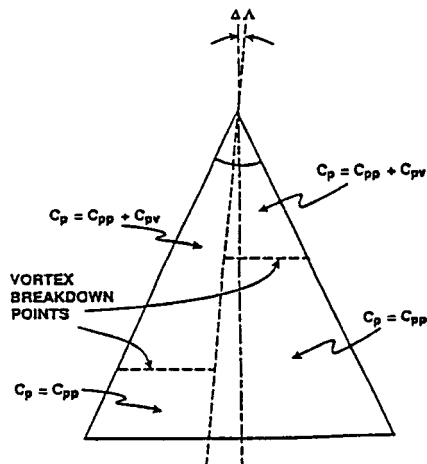


Figure 12: Model for vortex breakdown in roll from Reference 38

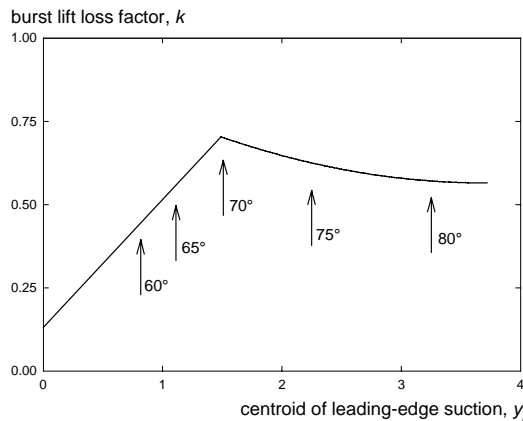


Figure 13: Lan & Hsu's lift-loss factor, replotted from [34]

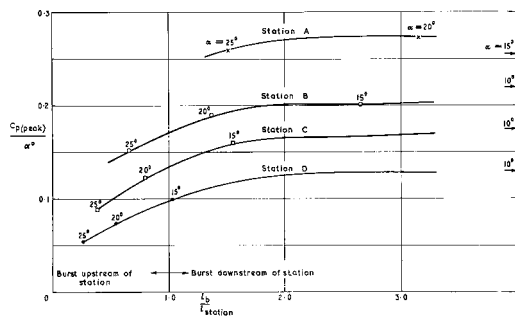


Figure 14: Suction peak reduction ahead of vortex breakdown [9]

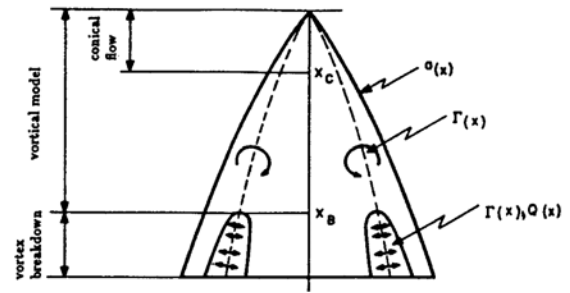


Figure 15: A 'bubble' model for the effects of vortex breakdown [47]

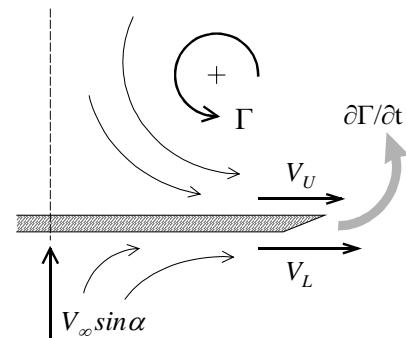


Figure 16: Cross-flow velocities induced by a leading-edge vortex

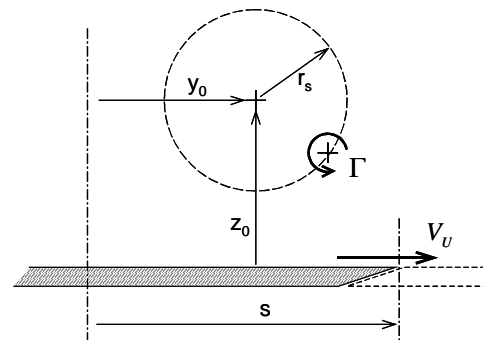


Figure 17: Helical vortex in the cross-flow plane

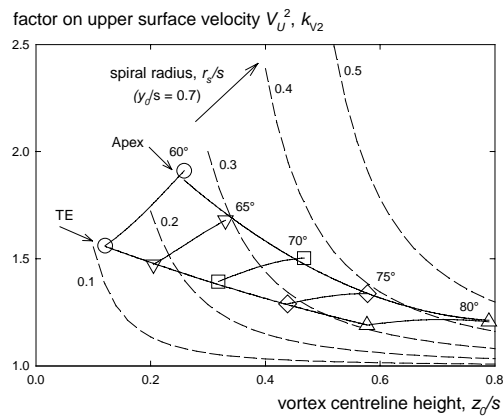


Figure 18: Effect of burst spiral radius on upper surface cross-flow velocity at the leading-edge

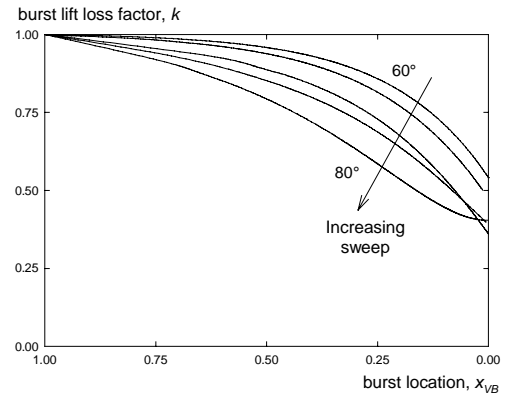


Figure 20: Predicted vortex lift factor \$k\$

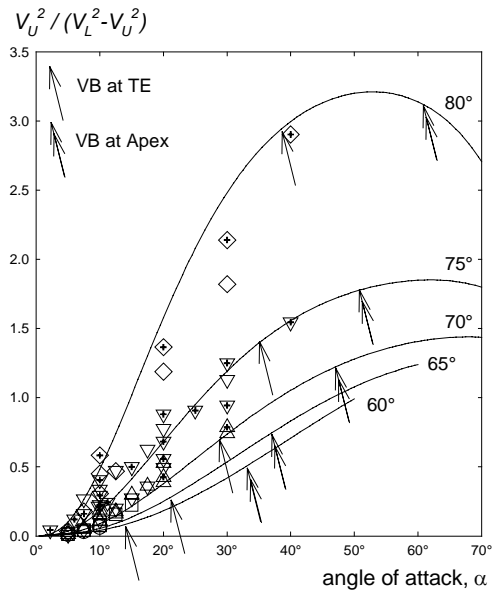


Figure 19: Effect of incidence and sweep on vorticity shedding parameter

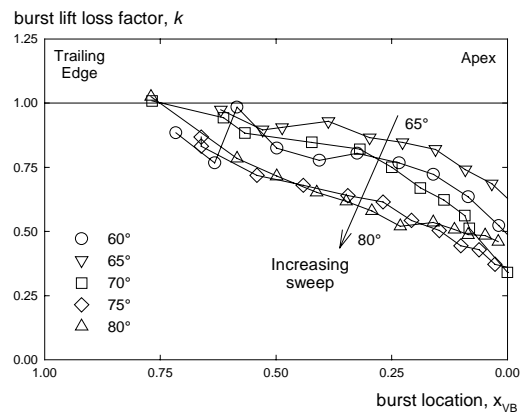


Figure 21: Vortex lift factor \$k\$ derived from experimental force data in Reference 9

APPENDIX A – VELOCITIES INDUCED BY A HELICAL VORTEX

A.1 Helix Geometry

Figure A1 shows a right-handed helical vortex filament of strength Γ , with helix radius a_0 and pitch p ($= 2\pi k$). The non-dimensional reduced pitch $\hat{\tau}$ [65,66] is defined as

$$\hat{\tau} = \frac{k}{a_0} = \frac{1}{\tan \beta} \quad (\text{A-1})$$

where β is the local helix inclination to the centreline (positive for a right-handed helix). The local curvature κ is

$$\kappa = \frac{a_0}{a_0^2 + k^2} = \frac{\sin^2 \beta}{a_0} \quad (\text{A-2})$$

Figure A1 also shows a consistent local orthogonal coordinate system consisting of the normal, tangential and binormal unit vectors \mathbf{n} , \mathbf{t} and \mathbf{b} .

A.2 Self-Induced Velocities

The velocity induced by a general line vortex is given by the Biot-Savart integral [66]

$$\mathbf{v}(\mathbf{x}) = \frac{\Gamma}{4\pi} \int_{-\infty}^{+\infty} \mathbf{s} \times \frac{\mathbf{x} - \mathbf{r}(s)}{|\mathbf{x} - \mathbf{r}(s)|^3} ds$$

However, this integral diverges as the field point approaches the vortex filament, which for a curved vortex results in the 'self-induced' velocity becoming infinite [66,67]. The integral can be desingularised by subtracting an osculating vortex ring with a finite rotational core of radius σ . This approach gives an equation for the self-induced velocity V_B on the vortex filament in the binormal direction \mathbf{b} of the form [65,66]

$$V_B = \frac{\Gamma \kappa}{4\pi} (C_{MS} - \ln(\kappa \sigma)) \quad (\text{A-3})$$

where the coefficient C_{MS} is a non-linear function of the non-dimensional helix pitch $\hat{\tau}$. The self-induced velocity W_B in the tangential direction \mathbf{t} (along the filament) is independent of vortex core size, and is given by

$$W_B = \frac{\Gamma \kappa}{4\pi} C_{VT} \quad (\text{A-4})$$

where the coefficient C_{VT} is also a non-linear function of $\hat{\tau}$. The self-induced velocity component in the normal (radial) direction \mathbf{n} is zero.

A.3 Binormal Velocity Component V_B

The majority of previous work on helical vortices has used Kelvin's 'large pitch' approximation [66] to the binormal velocity component. However, spiralling burst vortices tend to have relatively small pitches for which this approximation is rather inaccurate. Reference 68 gives a semi-empirical curve-fit to numerical results for intermediate values of the helix pitch, where for positive pitch

$$C_{MS} \approx \ln\left(\frac{\hat{\tau}}{1+\hat{\tau}^2}\right) - \frac{1}{4} + \frac{1+1.455\hat{\tau}+1.723\hat{\tau}^2+0.711\hat{\tau}^3+0.616\hat{\tau}^4}{\hat{\tau}+0.486\hat{\tau}^2+1.176\hat{\tau}^3+\hat{\tau}^4} \quad (\text{A-5})$$

A.4 Tangential Velocity Component W_B

The tangential velocity component is generally neglected in theoretical analyses of helical vortex motion [69], so has not received the consideration given to the binormal component. However, it can be shown [70,74] that there is a straightforward expression for this component. For the tangential velocity component W_B the Biot-Savart integral reduces [71] to

$$W_B = \frac{\Gamma}{4\pi} \frac{a_0^2 k}{\sqrt{a_0^2 + k^2}} \int_{-\infty}^{+\infty} \frac{2(1 - \cos \alpha) - \alpha \sin \alpha}{(2a_0^2(1 - \cos \alpha) + k^2 \alpha^2)^{3/2}} d\alpha$$

where α is an angular parameter defining position along the vortex filament. Note that there is no singularity in this expression, so the result is independent of core size. The integrand is even, so the velocity W_B is twice the value of the same integral with limits 0 and $+\infty$. Making the substitutions

$$\gamma = \frac{\alpha}{2}, \quad x = \frac{\sin \gamma}{\gamma}$$

gives the elementary integral

$$\begin{aligned} W_B &= \frac{2\Gamma}{4\pi} \frac{a_0^2 k}{\sqrt{a_0^2 + k^2}} \int_0^1 \frac{x}{(a_0^2 x^2 + k^2)^{3/2}} dx \\ &= \frac{2\Gamma}{4\pi} \left(\frac{1}{\sqrt{a_0^2 + k^2}} - \frac{k}{a_0^2 + k^2} \right) \end{aligned}$$

Substituting from equations (A-1) and (A-2) for β and κ then gives

$$W_B = \frac{\Gamma}{4\pi a_0} 2 \sin \beta (1 - \cos \beta)$$

and hence from equation (A-4)

$$C_{VT} = \frac{2(1 - \cos \beta)}{\sin \beta} \quad (\text{A-6})$$

A.5 Axial Velocity Induced on the Centreline

The *axial* velocity component induced by a helical vortex at a point (r, ϕ) is given [72] by

$$w_{axial} = \frac{\Gamma}{4\pi} \int_{-\infty}^{+\infty} \frac{-(a_0 r \sin \phi \cos \alpha + a_0 r \cos \phi \sin \alpha - a_0^2)}{((r \cos \phi - a_0 \sin \alpha)^2 + (r \sin \phi - a_0 \cos \alpha)^2 + k^2 \alpha^2)^{3/2}} d\alpha$$

where again α is an angular parameter defining position along the vortex filament. On the centreline of the helix $r = 0$, and hence

$$w_{CL} = \frac{\Gamma}{4\pi} \int_{-\infty}^{+\infty} \frac{a_0^2}{(a_0^2 + k^2 \alpha^2)^{3/2}} d\alpha = \frac{\Gamma}{4\pi a_0} \int_{-\infty}^{+\infty} \frac{1}{(1 + \hat{\tau}^2 \alpha^2)^{3/2}} d\alpha \quad (\text{A-7})$$

The integral is elementary, evaluating to

$$w_{CL} = \frac{\Gamma}{4\pi a_0} \frac{2}{\hat{r}} = \frac{\Gamma}{2\pi a_0} \tan \beta \quad (\text{A-8})$$

For a swirl velocity of opposite hand to the burst helix (eg negative Γ and positive β , or vice versa) the induced axial velocity on centreline is therefore negative (ie directed upstream).

A.6 Numerical Solution

The flowfield induced by a helical vortex filament on itself can be determined numerically using the Biot-Savart integral law combined with a 'local induction approximation' to avoid infinite velocities on the filament centreline [66]. A section of the filament about the control point is excluded from the integral, so that the Biot-Savart integral becomes

$$\mathbf{v}(s) = \frac{\Gamma}{4\pi} \int_{[\delta]} \mathbf{s}' \times \frac{\mathbf{r}(s) - \mathbf{r}(s')}{|\mathbf{r}(s) - \mathbf{r}(s')|^3} ds' \quad (\text{A-9})$$

where $[\delta]$ denotes that the portion $-\sigma\delta < (s' - s) < +\sigma\delta$ is omitted. The factor δ depends on the distribution of swirl and axial velocities within the core, with Reference 66 giving the relation valid to leading order as

$$\log 2\delta = \frac{1}{2} - \frac{2\pi^2 \sigma^2 \overline{v_\theta^2}}{\Gamma^2} + \frac{4\pi^2 \sigma^2 \overline{w_0^2}}{\Gamma^2} \quad (\text{A-10})$$

A 'forced vortex' velocity profile (ie with the swirl velocity v_θ increasing linearly with radius) gives a value for δ of $0.5e^{0.25}$ (≈ 0.642). This is the profile invariably used in published work on helical vortex dynamics and stability. For a 'flat' velocity profile with constant swirl velocity (more representative of the outer cores of delta wing vortices [6]) δ is 0.5. These values assume a zero axial velocity excess w_0 . Application of equation (A-3) to the general case therefore requires the use of an effective core radius based on the ratio of the factor δ to that of a forced vortex, ie

$$\sigma_{eff} = \left(\frac{\delta}{0.642} \right) \sigma = \hat{\delta} \sigma \quad (\text{A-11})$$

Figure A2 compares numerical values for C_{MS} and C_{VT} for a 'forced vortex' core (ie $\delta = 0.642$) with the theoretical and empirical expressions given above, and with some common approximations [66,68]. It can be seen that for pitches typical of burst vortices (ie $\hat{r} \sim 1$) both large- and small-pitch approximations give significant errors. Caution must therefore be exercised in the application of published stability analyses for large-pitch helical vortices [eg 67,69,71] to the small-pitch burst leading-edge vortex case. Numerical experimentation also established that adding linear longitudinal variations in vortex strength $\Gamma(z)$ and in helix radius $a_0(z)$ has no significant effect on the induced velocities given by equations (A-3) and (A-4), if the local vortex and helix parameters are used. To a first approximation then, the analysis presented here should apply equally well to a conical helix.

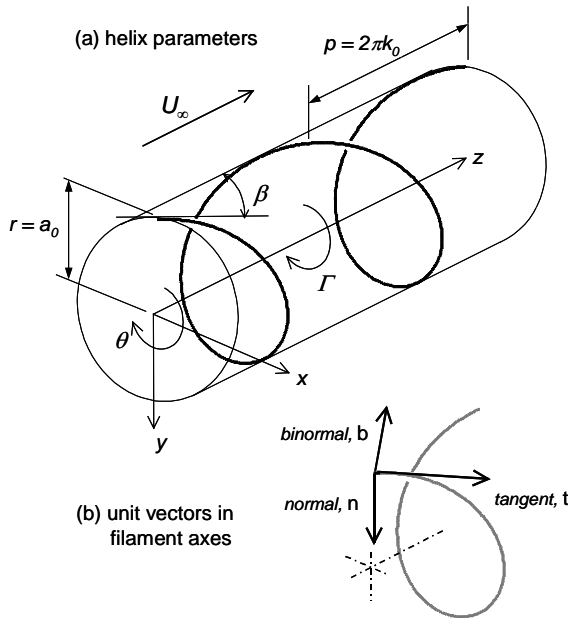


Figure A-1: Helical vortex geometry, showing positive sense for all parameters

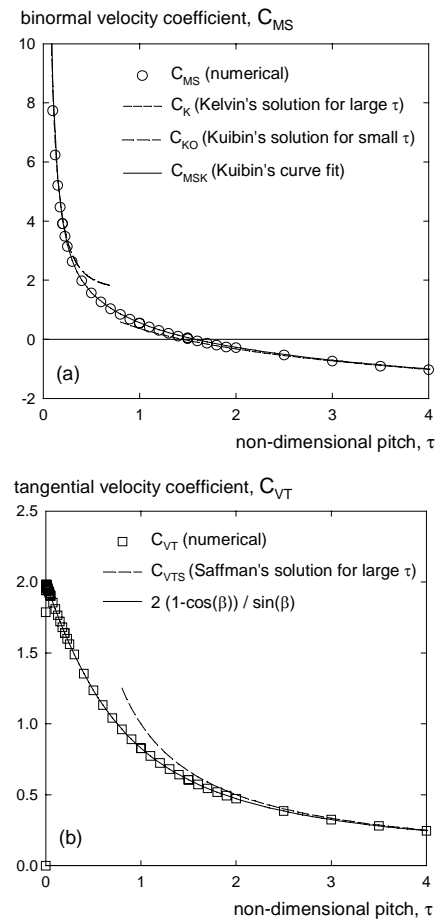


Figure A-2: Effect of helix pitch on binormal and tangential induced velocity coefficients

APPENDIX B – DELTA WING VORTEX CORRELATIONS

B.1 Vortex Core Location

In order to quantify the effect of a translating/rotating helix on the leading-edge vorticity shedding, the vortex core position and the radius of the helix are needed. For unburst vortices the spanwise core location is essentially constant for higher angles of attack, at $y_0/s \approx 0.65$ to 0.70 (depending on experimental conditions – Figure B-1a [14]). The core height z_0/s increases with incidence, as shown in Figure B-2 [6,14,57,75..78]. This figure correlates core height with the Sychev similarity parameter K [25] where

$$K = \frac{\tan \alpha}{\tan \varepsilon} \quad (\text{B-1})$$

At low angles of attack

$$\bar{z}_0 = \frac{z_0}{s} \approx 0.25K \quad (\text{B-2})$$

corresponding to an inclination of the vortex core to the surface of 0.25α (as also seen in Figure B-1b [14]). At higher incidences a reasonable (but wholly empirical) fit to the data is given by

$$\bar{z}_0 = \frac{z_0}{s} = \frac{0.78K}{2.52 + K} + 0.016K \quad (\text{B-3})$$

B.2 Vortex Strength

The vortex strength can be estimated from the angle of attack and sweep angle using the well-known semi-empirical correlation due to Hemsch & Luckring [26,24]

$$\bar{\Gamma} = \frac{\Gamma}{sU_\infty \sin \alpha} = 4.63 \left(\frac{\tan \alpha}{\tan \varepsilon} \right)^{0.2} = 4.63 K^{0.2} \quad (\text{B-4})$$

The more conventional non-dimensionalisation in terms of chordwise location x is

$$\frac{\Gamma}{xU_\infty} = 4.63 \tan \varepsilon \sin \alpha \left(\frac{\tan \alpha}{\tan \varepsilon} \right)^{0.2} \quad (\text{B-5})$$

B.3 Vortex Core Radius

For the radius of the burst helix the first question to be addressed is what is an appropriate correlating parameter. The vortex burst modelling developed in Section 3 (eg equation (17)) indicates that the helix radius should scale with the outer vortex core radius r_0 , with $r_s \geq 0.5r_0$ (or $a_0 \geq 0.5\sigma$ - see Figure 5b). The outer core radius is in turn directly related to the vortex strength Γ and swirl ratio ϕ_0

$$r_0 = \frac{\Gamma}{2\pi U_\infty \phi_0} \quad (\text{B-6})$$

Substituting into equation (B-4) gives

$$\begin{aligned}\bar{r}_s = \frac{r_s}{s} &\approx 0.5 \frac{r_0}{s} \\ &\approx 0.37 K^{0.2} \frac{\sin \alpha}{\phi_0}\end{aligned}\tag{B-7}$$

Theoretical and experimental studies of vortex breakdown give critical swirl ratios of the order of 0.8 to 1.0 [7], while for representative burst onset conditions $K^{0.2}$ does not vary greatly (≈ 0.85 to 1.35), giving

$$\bar{r}_s \approx 0.5 \sin \alpha \tag{B-8}$$

One desirable feature of this equation is the (physically essential) limitation of the helix radius to half the local semispan.

The limited experimental data for burst helix radii [9,16,22,23,30,79..83] is plotted against angle of attack in Figure B-3, showing that the theoretically derived equation (B-8) does give a reasonable fit to the trend with incidence. There is a high degree of scatter, particularly for lower sweep angles where the proximity of the surface gives a non-axisymmetric helix, and clearly there is significant room for improvement, but for the purposes of the analysis reported here this correlation was felt to be adequate.

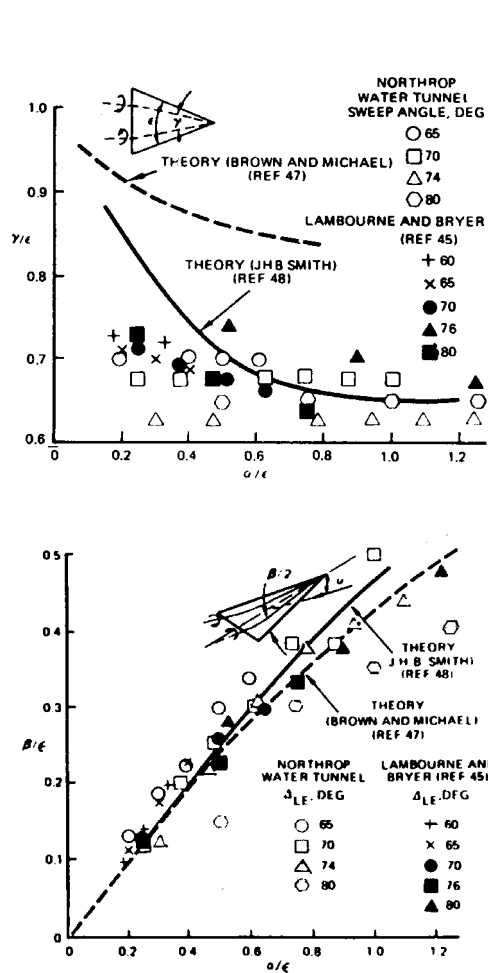


Figure B-1: Low incidence variation in core position with angle of attack [14]

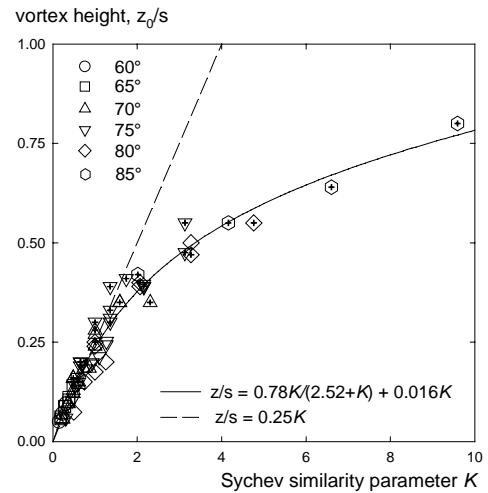


Figure B-2: Variation in core height with angle of attack [6,14,57,75..78]

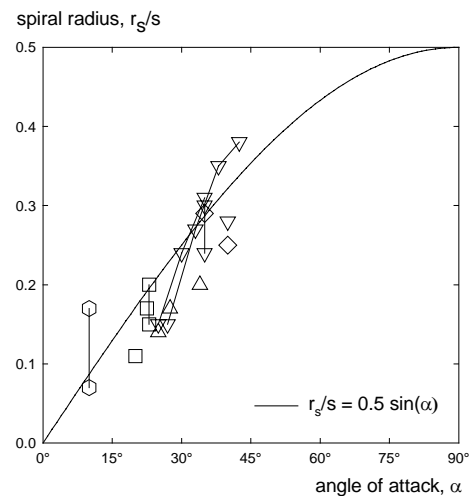


Figure B-3: Correlation of spiral burst radius with incidence [9,16,22,23,30,79..83]

APPENDIX C – ESTIMATION OF INDUCED CROSS-FLOW VELOCITY

C.1 Approximation to Upper Surface Velocity

In the absence of direct experimental data for the lower surface cross-flow velocity at the leading-edge a rough estimate can be obtained from the vortex growth equation (Section 4)

$$\frac{\partial \Gamma}{\partial x} = \frac{V_L^2 - V_U^2}{2U_\infty \cos \alpha} \quad (29)$$

and the upper surface velocity estimate

$$V_U \approx 2 \frac{\Gamma}{2\pi s} \frac{\bar{z}_0}{(1 - \bar{y}_0)^2 + \bar{z}_0^2} \quad (30)$$

if the vortex strength and position are known. The core position is readily extracted from flow visualisation data, while the non-dimensional vortex strength is given by the correlation of equation (B-4). For conical (unburst) flow, integrating equation (29) gives

$$\frac{\Gamma}{x} = \frac{V_L^2 - V_U^2}{2U_\infty \cos \alpha} \quad (C-1)$$

which can be rewritten (using equation (B-4) and recalling that $\tan \varepsilon = s/x$) as

$$\frac{\Gamma}{sU_\infty \sin \alpha} \frac{\tan \varepsilon}{\tan \alpha} = \frac{V_L^2 - V_U^2}{2U_\infty^2 \sin^2 \alpha} \quad (C-2)$$

Equation (30) can then be rearranged to give the upper surface velocity V_U in non-dimensional terms as

$$\bar{V}_U = \frac{V_U}{U_\infty \sin \alpha} \approx \frac{\Gamma}{sU_\infty \sin \alpha} \frac{1}{\pi} \frac{\bar{z}_0}{(1 - \bar{y}_0)^2 + \bar{z}_0^2} \quad (C-3)$$

C.2 Correlation for Lower Surface Velocity

Substituting in equation (C-2), in conjunction with equation (B-4), gives the lower surface velocity V_L as a function of angle of attack α , wing semi-apex angle ε and vortex core position (y_0, z_0)

$$\begin{aligned} \bar{V}_L^2 &= \left(\frac{V_L}{U_\infty \sin \alpha} \right)^2 \\ &\approx 2\bar{\Gamma} \left(\frac{\tan \varepsilon}{\tan \alpha} \right) + \left(\bar{\Gamma} \frac{1}{\pi} \frac{\bar{z}_0}{(1 - \bar{y}_0)^2 + \bar{z}_0^2} \right)^2 \end{aligned} \quad (C-4)$$

Application of equation (C-4) to a wide range of experimental measurements of vortex core position as a function of angle of attack and sweep angle [6,14,57,75..78] gives remarkably consistent results (eg Figures C-1 & C-2) which can be fitted using the simple semi-empirical relation

$$\bar{V}_L = k_a + k_{le} \frac{\tan \varepsilon}{\tan \alpha} \quad (C-5)$$

In dimensional terms this becomes

$$V_L = k_a U_\infty \sin \alpha + k_{le} \tan \varepsilon U_\infty \cos \alpha \quad (C-6)$$

where k_a lies between 3 and 3.5 and k_{le} between 0.5 and 0.8 depending on the dataset.

C.3 Physical Interpretation of Correlation Function

Physically, equation (C-6) can be interpreted as consisting of a component proportional to the cross-flow velocity $U_\infty \sin \alpha$ and a sweep-dependent component proportional to the velocity parallel to the wing surface $U_\infty \cos \alpha$. The magnitude of the 'cross-flow' contribution k_a (>3) shows the result of flow acceleration around the leading-edge into the separating shear layer, and tends to reduce gradually as sweep is increased (Figure C-1), presumably due to the corresponding reduction in local semi-span. A small increase in k_a is also seen with Reynolds Number (Figure C-2), which may be due to the reducing displacement thickness of the lower surface boundary layer increasing the effective flow curvature at the leading-edge.

One possible explanation for the presence of the second term in equation (C-6) is sketched in Figure C-3, which shows that the velocity *along* the wing leading-edge 'attachment line' is $U_\infty \cos \alpha / \cos \varepsilon$. This in turn generates an additional contribution to the cross-flow velocity of $U_\infty \cos \alpha \tan \varepsilon$ outwards in the immediate vicinity of the leading-edge. For an uncambered (symmetric section) wing in attached flow the cross-flow increment is the same on both the upper and lower surfaces and has no effect on the overall lift. However, the delta wings tested were all flat-plate wings with sharp-leading-edges bevelled on the lower surface only, giving a degree of negative camber. When coupled with the additional asymmetry introduced by the leading-edge separation, the net result is an increase in the velocity differential across the shear layer of up to $+U_\infty \cos \alpha \tan \varepsilon$, depending on the leading-edge geometry. This is consistent with observed trends in k_{le} , which is relatively unaffected by Reynolds Number but tends to increase gradually with leading-edge bevel angle, wing thickness/chord ratio and sweep angle (all of which increase the local leading-edge 'bluntness').

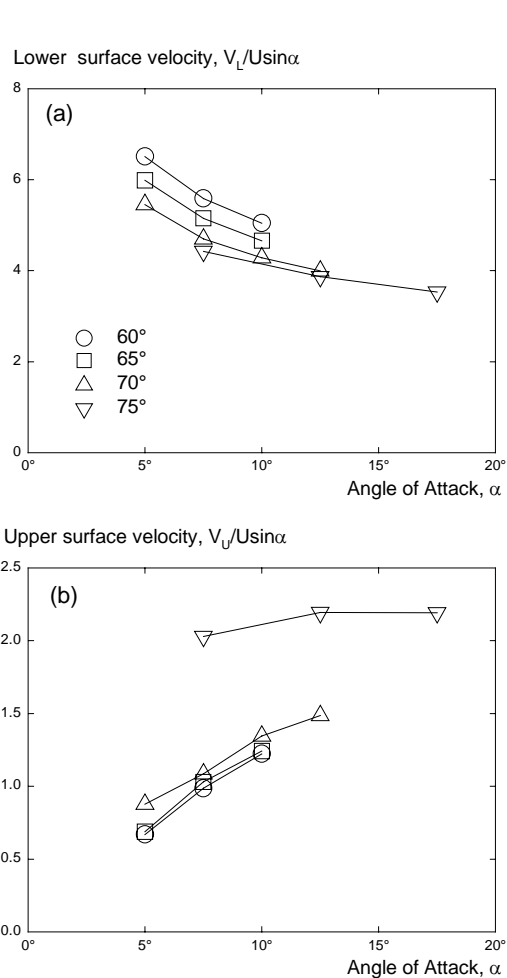


Figure C-1: Effect of sweep angle on estimated lower and upper leading-edge velocities V_L and V_U [75]

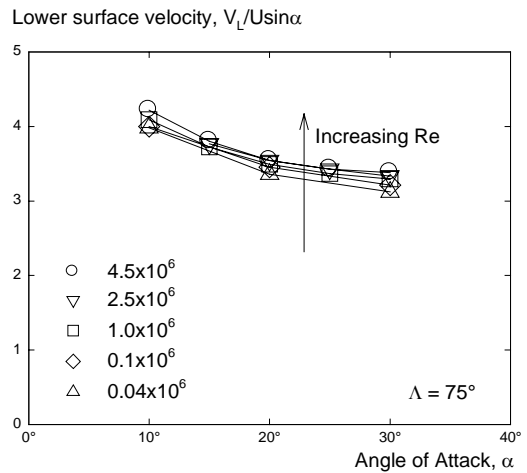


Figure C-2: Effect of Reynolds Number on estimated lower surface leading-edge velocity [77]

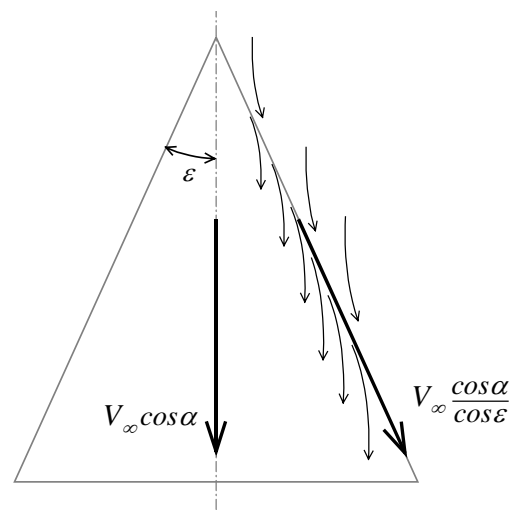


Figure C-3: Contribution from component of freestream velocity parallel to the wing surface

Chapter 22 – NON-LINEAR INDICIAL RESPONSE AND INTERNAL STATE-SPACE (NIRISS) REPRESENTATION AND ITS APPLICATIONS ON DELTA WING CONFIGURATIONS

Xing Z. Huang

AL/IAR/NRC

1200 Montreal Rd., Ottawa Ont. Canada K1A 0R6

xingzhong.huang@nrc.ca

ABSTRACT

A modified nonlinear indicial response method (NIR), in conjunction with internal state-space representation (ISS) has been proposed (NIRISS). It has been found that for a delta wing, its leading-edge vortex behavior has a dominant effect on its aerodynamics and therefore the time-average vortex breakdown location is chosen as an internal variable to approximately describe the state of vortex flow over the delta wing. The response of this internal variable to arbitrary motion is estimated by a modified nonlinear indicial response functional method. By means of a vortex filament method, this variable of vortex breakdown location offers the additional information required at a given instantaneous status for calculating the surface pressure and related aerodynamic loads. Moreover, the method has been further applied to solve trajectories and the instantaneous pressure and air loads for a 65° delta wing in a free-to-roll condition.. The good comparisons between measured and predicted results such as instantaneous pressures, airloads and free-to-roll motion history, show that within the framework of the proposed mathematical model, it is possible to apply this NIRISS method into nonlinear flight regime.

22.1 INTRODUCTION

With the emphasis on fighters with high maneuverability and agility, there are growing requirements for adequate aerodynamic modeling in the near and post-stall regime. These models will be used in control system design, flight simulation, stability and agility analysis as well as flight safety. Traditional linear methods such as Bryan's formulation¹ and the linear indicial response method² are not valid under these conditions.

Unlike linear indicial responses where the responses are independent of the motion variables leading up to the step onset, the nonlinear indicial response method (NIR) initiated by Tobak and his colleagues^{3,4} provides an approach to treat nonlinear flight dynamics. This approach represents aerodynamic responses, such as force, moment, etc., due to an arbitrary motion input as a summation of nonlinear responses to a series of "step" motions leading up to step onset. Three new important concepts were introduced in this approach: (1) a nonlinear indicial response functional, (2) a generalized superposition integral and (3) under conditions where Fréchet differentiability is lost, i.e. at a critical state, a splitting of the integral plus a transient term is proposed.

Although this approach has a sound mathematical basis and can represent a wide range of important aerodynamic nonlinearities encountered in the maneuvering flight regime, difficulties in solving the integral functional equation and, especially, in searching for critical states and related transient behavior, etc. render this method impractical in real applications. As there may exist different critical states such as modality,

inaccessibility, sudden jumps, divergence and hysteresis, etc., recognizing the presence and type of the critical states is difficult for the proper description of a physical system. In spite of the fact that some critical states might be defined where discontinuity occurs in static test, a very extensive set of tests must be conducted in all independent spaces in order to identify all critical states and to establish the time constants associated with their transient response. Further difficulties are encountered in cases where critical states may be hidden by unavoidable inaccuracy of experimental and numerical results.

Thus, in order to find an alternative way, it is important to have a view on flow physics in addition to the principle of mathematics. It is known that a critical state is caused by the replacement of an unstable equilibrium flow by a new stable one at a particular value of the motion variables³. If there is a readily recognizable flow state and a variable in that flow state which has a dominant effect on the airloads, that variable might be chosen as an internal state-space variable. Those consideration leads to the NIRISS method, namely: 1) to recognize the internal state-space and related variable which has dominant effect on the airloads, and 2) to establish the relations between that variable in the internal state-space and the airloads.

It should be emphasized that although Fréchet differentiability remains invariant across this state-space transformation, the advantage of the NIRISS methodology is that by knowing the flow physics, a number of critical states which may associated with minor changes or second order, known in advance from flow physics, could be omitted. Moreover, if no flow state-space change involved there will be no discontinuity encountered in corresponding region. An analytical or non-linear relation can be obtained with much fewer difficulties.

Taking the flow over delta wing at high incidence as an example, there may exist primary, secondary and tertiary vortices over the wing. The presence of leading-edge vortices and particularly their breakdown is the main cause of airloads' non-linearities and time dependence. Generally, the effect of secondary and tertiary vortices on airloads is second order to that of the primary ones on the airloads. Although the status of second and tertiary vortices will affect the behaviour primary vortex, but their effects can be included from the status of primary vortex. Therefore, as a first order approximation the presences of the secondary and tertiary vortices can be ignored. On this basis four flow states can be defined namely, (1) fully intact leading-edge vortex, (2) vortex breakdown over the wing area, (3) spiral flow (breakdown at apex) and (4) large-scale turbulence. Transitions between these states could be associated with critical states. As a consequence, provided breakdown remains over the wing, its location can be chosen as an internal state-space variable in predicting airloads as no critical states are encountered, in which case the NIRISS method can be used rather readily to do so in terms of the motion variables. Some preliminary results have been obtained by this NIRISS method^{5,6,7}.

It is noteworthy that in the present model the vortex breakdown location corresponds to a mean value as all fluctuations due to flow unsteadiness are ignored. Since there is no time delay between the vortex response and surface pressure, no additional constrains need to be introduced in this average process compare with other direct NIR models^{8,9}.

The above methodology is not constrained to the primary vortex breakdown location. Any state variable, which has a dominant effect on the airloads, can be equally used. Possible examples are flow separation or transition location on airfoil, vortex asymmetry on slender bodies, etc.

22.2 DOMINANT EFFECT OF VORTEX BREAKDOWN ON AIRLOADS

A comprehensive experimental study had been conducted at IAR in order to understand the flow physics and to establish mathematical model in the non-linear region. The effect of leading-edge vortex breakdown on aerodynamic loads under both static and dynamic conditions is well recognized.

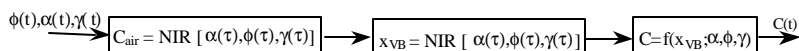
As examples, illustrations of this effect on the rolling moment coefficient of a 65° delta wing (Fig.1) at a body axis inclination $\sigma=30^\circ$ under static and dynamic conditions are shown in Fig. 2 and Fig. 3 respectively^{5,6}. Fig. 3 shows the results for roll oscillation cases with the same amplitude and varying frequency. The experimentally observed rolling moment is compared with a hypothetical one which assumes an intact vortex on the leeward wing half and breakdown at the apex on the windward wing half. Solid symbols indicate that this condition is satisfied, whereas clear ones indicate that breakdown is present over at least one wing half. Important discrepancies between the curves exist in the presence of breakdown over the wing.

Similar phenomena are observed in the pitching case¹⁰. As examples, Fig. 4 shows the normal force of a 55° diamond wing and a 65° delta wing in static situation at the angle of attack up to 34° and 56° respectively. The angles when the vortex breakdown is across the trailing edge or at the apex are also marked in these figures. It is clear that the discontinuity appears at these two angles.

The above observations cover four flow states depending on the motion variables and motion history: intact vortex flow, vortex breakdown flow, spiral flow and large-scale turbulent flow. Important critical states are associated with changes between these flow states, namely when breakdown reaches the apex or crosses the trailing edge. Thus, although the exact locations of the critical states in terms of motion variables (ϕ , α , γ , etc.) are unknown at this moment, we certainly have a good sense where they may exist and the types of these critical states. Given the importance of breakdown on the loads, it is necessary to determine its location as an internal state-space variable in predicting airloads.

22.3 MATHEMATICAL MODELING

The suggested mathematical model can be briefly shown as:



It mainly includes the following steps:

- Instead of using the motion variables (α , β , γ , etc.) explicitly to determine the airloads in the NIR formulation, identify an internal flow state variable that has a clearly dominant effect on the airloads.
- Apply NIR method to obtain the internal variable in terms of the motion variables.
- Apply a suitable method to predict airloads based on the value of the internal variable.

As mentioned above, the leading-edge vortex breakdown location, x_{VB} , can be expressed as a functional of $\sigma(\xi)$, $\phi(\xi)$ and $\Omega(\xi)$ in an arbitrary motion over the interval $-\infty < \xi < t$:

$$x_{VB}(t) = x_{VB}[\sigma(\xi), \phi(\xi), \Omega(\xi)] \quad (1)$$

or explicitly in the form of an indicial response functional:

$$x_{VB}(t) = x_{VB}[\sigma(\xi), \phi(\xi), \Omega(\xi); t, \tau] \quad (2)$$

implying that $x_{VB}(t)$ is both a functional of $\sigma(\xi), \phi(\xi), \Omega(\xi)$ and a function of t and τ . If the discussion is limited to the movement of the vortex breakdown location over the wing area, then the functional can be assumed as Frechét differentiable over $(\sigma(\xi), \phi(\xi), \Omega(\xi))$ for the motion at hand, in which the following expression applies:

$$f'(\sigma, \phi, \Omega) = f_{\sigma}(\sigma, \phi, \Omega)\Delta\sigma + f_{\phi}(\sigma, \phi, \Omega)\Delta\phi + f_{\Omega}(\sigma, \phi, \Omega)\Delta\Omega \quad (3)$$

where f stands for x_{VB} in this case and $\Delta\sigma, \Delta\phi, \Delta\Omega$ are infinitesimal step changes in σ, ϕ, Ω , respectively.

For the case of rolling motion about the body axis the rolling moment can be represented as a functional of the roll angle history:

$$C_{\ell}(t) = F[\phi(\xi)] \quad (4)$$

where ξ is a running time variable from the motion onset to time t and the functional F assigns a value to $C_{\ell}(t)$ for an arbitrary roll angle history $\phi(\xi)$.

Introducing the internal state-space variable x_{VB} :

$$C_{\ell}(t) = f(x_{VB}[\phi(\xi)]) \quad (5)$$

The vortex breakdown location can be determined by the balance of the vorticity feeding rate generated from the the boundary layer separation at the leading edge and its downstream convection rate. At the location where the vorticity convection rate is less than the vorticity feeding rate, the vortex core is forced to tilt to maintain the total angular momentum in the vortex resulting in negative azimuthal vorticity. This negative azimuthal vorticity further introduces a negative axial velocity and adverse pressure gradient resulting in a positive feedback and eventually breaks down the vortex. Both vortex feeding and convection rates depend on the model surface geometry, especially around the leading edge and the motion variables. In a dynamic situation, each step of the previous motion up to the observation time will have an effect on the balance. The response of the vorticity balance and thus of the breakdown location to the motion depends on the history of the motion up to the observation time, t . Applying the NIR method to the state of the balance, or x_{VB} , we have:

$$x_{VB} = F[\phi(\xi); t, \tau] = x_{VB}(0) + \int_0^t x_{VB_{\phi}}[\phi(\xi); t, \tau] \frac{d\phi(\tau)}{d\tau} d\tau \quad (6)$$

or approximately as:

$$x_{VB}(t) = X_s(\phi(t)) + X_q(\dot{\phi}(t)) \cdot X_s(\phi(t)) + \int_{t-T}^t X_U((t-\tau)\dot{\phi}(\tau))d\tau \quad (7)$$

where the first term represents the static value at the time t , and the second and third terms reflect the quasi-steady and unsteady effects.

The methods obtaining those three terms have been reported ^{5,6,11} and are briefly reiterated here.

The first term is taken from an assumption that the circulation distribution has a parabolic form:

$$\bar{\Gamma}(\alpha, \Lambda, x) = C_0 + Bx - Ax^2 \quad (8)$$

where L is the effective leading-edge sweep back angle of the corresponding wing half and A and B are given by:

$$A = 1.1 \cdot \sin \alpha \cdot \sin \Lambda$$

$$B = 4A$$

and C_0 is the circulation at the apex which is given by:

$$C_0 = \bar{\Gamma}_{x=1}(\alpha, \Lambda) - B + A$$

The breakdown location can be obtained by solving the following equation:

$$C_0 + Bx_{VB} - Ax_{VB}^2 = \Gamma^*(\alpha, \Lambda) \quad (9)$$

where $\Gamma^*(\alpha, \Lambda)$ is based on the critical value of the Rossby number S^* modified to account for the velocity component along the vortex axis and the interaction between the vortices on both wing halves, leading to:

$$\Gamma^*(\alpha, \Lambda) = 0.78 \cdot \cos(4(\Lambda - \Lambda_0))$$

where Λ_0 is an empirically obtained value (19.5°) that leads to the best fit to the experimental results of delta wings with sweep back angle ranging from 55° to 75° .

Extensive flow visualization experiments show that the motion of vortex breakdown location over the trailing edge can be approximately assumed as continuous process. Therefore the value of $X_S(\phi)$ for $x_{VB} > 1$ is assumed to be given by a linear extrapolation of the function at $x_{VB} = 1$. Likewise, for the purposes of modeling, breakdown is allowed to move upstream of the apex (again using a linear interpolation) in order to reflect the deficiency in circulation.

The second term in Eqn. (7) represents the motion induced quasi-steady effect. It is the effect of motion variable at the instantaneous observation time, t on the vortex breakdown. It can be obtained through static experiments with a wing deformed to reflect the motion induced quasi-steady camber. In the case of rolling motion, the quasi-steady surface coordinates are obtained by simulating the roll-rate-induced chordwise angle and section angle normal to the leading-edge. For zero instantaneous roll angle the surface coordinates are given by the following equation ¹²:

$$z(t) = \frac{\dot{\phi}(t)y}{\cos \sigma(t)} \left[(-\cos 2\Lambda(t) + \frac{1}{\sin 2\Lambda(t)(1 \pm \tan \sigma(t) \sin \phi(t) \tan \Lambda(t))}) |y| - x \right] \quad (10)$$

Through static experiments with a wing deformed to reflect the motion induced quasi-steady camber effect, the second term in rolling motion can be approximately represented by:

$$X_q(\dot{\phi}(t), \alpha) = k_q \dot{\phi}(t) = \frac{0.91}{\tan \alpha(t)} \dot{\phi}(t) \quad (11)$$

The third term in Eqn. (8) represent the unsteady effect accumulated over the release time period, T . From experimental results, a simplified response function is assumed:

$$X_u(\phi; t, \tau,) = \frac{1.65}{\tan \alpha(t)} \sin \frac{\pi \tau}{T^*} \quad (12)$$

The instantaneous vortex breakdown location can be calculated by means of Eqn. (7), (8) and from Eqn. (11) to Eqn.(12). After obtaining the instantaneous vortex breakdown, a concentrated vortex filament model is used for predicting the surface pressure and aerodynamic loads. It should be noted that the model, in general, does allow the inclusion of secondary and tertiary vortices, although they have been neglected in the present study.

The vortex induced velocity components can be approximately estimated by integrating the contribution from each segment of the vortex filament on the surface with the appropriate boundary conditions. Using vector notation the local velocity due to one vortex is given by

$$\vec{U} = \begin{pmatrix} u \\ v \\ w \end{pmatrix} = \frac{\bar{\Gamma}}{4\pi} \frac{\vec{r}_1 \times \vec{r}_2}{|\vec{r}_1 \times \vec{r}_2|^2} \vec{r}_0 \cdot \left(\frac{\vec{r}_1}{r_1} - \frac{\vec{r}_2}{r_2} \right) \quad (13)$$

where $\bar{\Gamma}$ is the average strength of the intact vortex between two ends of \vec{r}_1 and \vec{r}_2 . When vortex breakdown appears a decay function in circulation after the breakdown location is introduced, which is similar to that in Ref. 6. The normal and spanwise positions of the vortex core are functions of roll angle and angle of attack. In the case of the 65° delta wing these values were obtained from matching flow visualization results leading to the following expressions:

$$z_{\text{vortexcore}} = 0.25 * \frac{6\sigma}{\pi}$$

$$y_{\text{vortexcore}} = [0.6 + \sin(0.436 - \Lambda)](1.2 - 0.382\sigma)$$

Therefore, the total induced velocity due to the left and right vortices at a given point (P) on the wing surface becomes:

$$\vec{U}_{\text{total}} = \begin{pmatrix} u \\ v \\ w \end{pmatrix}_{\text{total}}^{(p)} = \sum_{i=1}^n \vec{U}_i^{(p)} + \sum_{j=1}^m \vec{U}_j^{(p)} \quad (14)$$

where n is the number of vortex segments on the left side and m is that on the right one.

Once the velocities over the surface are known, the surface pressure coefficient C_p can be estimated approximately by:

$$C_{p,Z=0} = -2 \frac{u}{U_{\infty}} - \frac{v^2}{U_{\infty}^2} + C_{pp} \quad (15)$$

The rolling moment can be obtained from the integral over whole wing area:

$$C_{\ell}(t) = \int_s C_p(t) \cdot ds \cdot dy \quad (16)$$

22.4 VALIDATION AND VERIFICATIONS WITH EXPERIMENTAL RESULTS

Validation of the above mathematical model has been performed step by step, starting from static cases with different roll and pitch angles, followed by harmonic rolling oscillations which were compared with experimental results previously published^{5,6,7}. Typical results are briefly restated here (Fig. 5 to Fig. 9) for completeness in describing the NIRISS method. Comparisons with CFD results from time-dependent Reynolds Average Navier-Stokes solutions^{13,14} are also included.

The challenge, however, is to apply the model to arbitrary motions and specifically to situations in which the aerodynamic results are fed back into the equation of motion such as in free-to-roll simulations. In these cases errors tend to accumulate rapidly. These difficulties have been observed by other investigators. For example, time-dependent Reynolds Average Navier-Stokes solutions^{14,15} have shown good numerical results in static cases and with harmonic motions, but poorer results for the prediction of a free-to-roll motion of a 65° delta wing at $\sigma=30^\circ$ released from $\phi=40^\circ$.

The present model was used to simulate the free-to-roll experiments conducted at the IAR 2m x 3m and WL/SARL 7 ft x 10 ft wind tunnels. A 65° delta wing model (Fig. 1) was released from an initial roll angle with zero initial angular velocity and allowed to roll freely about its axis. The system bearings introduced an approximately constant friction torque of about 4 lb-in regardless of the angular velocity and load, while the moment of inertia of the moving system was 0.27 lb-in-s.

At a freestream velocity of 300 ft/s the 65° delta wing configuration was found to have multiple stable trim points in roll (depending on σ). As examples free-to-roll motion histories with four different release roll angles are depicted in Fig. 10. The phase plane representation of these motion histories are shown by the trajectories in Fig. 11 (A, B, C and D). It was found that the trajectories intersect at several points where the roll angle and roll rate are the same for different trajectories, which highlights the very non-linear behavior of the system. Furthermore, the trajectory “A” finds the stable equilibrium point at 0°, while the trajectories “B” and “C” trim at 21°. Far more interesting is the trajectories that are nearly at 0° but don’t trimmed there. The trajectory when released from $\phi \approx 60^\circ$ (Fig. 12 which similar to the case of “C” in Fig. 11), is chosen as test case for validation and verification. Several points were marked as A to F in the figure for later comparisons.

The free-to-roll system equation of motion is assumed to be:

$$I\ddot{\phi}(t) + k \cdot \text{sign}(\dot{\phi}(t)) + C_{\ell}(\phi(t)) \cdot q_s B = 0 \quad (17)$$

where I is the moment of inertia of the moving part (model, shaft and balance system), $k \cdot \text{sign}(\dot{\phi})$ represents the bearing friction and the third term is the experimentally obtained instantaneous rolling moment.

Two methods have been used for comparison, i.e.: a direct method and an iterative method. Both of them rely on the Eqns. (16) and (17). In the first one, the rolling moment inferred from a prescribed motion (Eq. 17) is compared to that predicted using the above mentioned mathematical model, where the location of breakdown is obtained from the given motion. This is then used to calculate the pressures that lead to the rolling moment. The process is summarized in the flow diagram (Fig. 13).

In the first method, the contributions of the static, quasi-steady and unsteady components on vortex breakdown locations are shown in Fig. 14. This figure shows that when the starboard wing rolls up from $\phi=60^\circ$, the static component tends to delay vortex breakdown, reaching a maximum aft displacement at $\phi \approx 19^\circ$. However at the same time the rolling motion induces a negative camber on the starboard wing half that promotes vortex breakdown. The final location that reflects the balance of all components is shown as a solid line in Fig. 14a. The corresponding situation for the port wing is depicted in Fig. 14b.

A comparison between the experimental rolling moment (inferred from the acceleration) and that predicted using the “direct” method is shown in Fig. 15. The agreement is encouraging. There is a small discrepancy near the trim condition due to the fact that the static rolling moment in the model trims at a roll angle which is slightly larger than the experimental one.

The surface pressure contours and experimentally obtained pressures at $x=0.75$ for points **A**, **B**, **C**, **D**, **E** and **F** are shown from Fig. 16 to Fig. 21 respectively. The associated pressure measurements taken from free-to-roll experiments are superimposed. The comparisons at points **A**, **C**, **D** and **E** show nearly the same good agreement as those under static conditions shown in Fig. 9. Points **B** and **F** have noticeable discrepancies, whose cause is not clear at the present. Clearly these discrepancies affect the evolution of the calculated motion. Also, the current approach employs the vortex filament model on only the primary vortices, ignoring the secondary and tertiary ones, which will introduce some discrepancies in the pressure distribution. Further work is needed to improve this method.

The second method compares the experimentally obtained free-to-roll motion history with that predicted by the mathematical model with only the initial condition, the release roll angle, ϕ_0 . The predicted rolling motion history is obtained by the procedure shown in the diagram (Fig. 22). The instantaneous rolling moment at t is obtained from Eqn. (8) to Eqn. (12). The rolling moment is then used to calculate the angular acceleration at time t by means of Eqn. (17) and corresponding roll angle and angular rate at time $t+\Delta t$ are used in the next iteration. The results from the second (iterative) method for the same case are shown in Fig. 23. The estimated free-to-roll motion history is remarkably close to the experimental one. This is expected since the first method has already shown reasonable agreement between estimated and measured results. Additional work is underway to establish the generality of the predictive method over a range of conditions.

22.5 CONCLUSIONS

- A mathematical model (NIRISS) based on the NIR method in conjunction with internal state-space has been proposed.
- For a moving delta wing at high incidence, the movement of vortex breakdown location can be chosen as a dominant internal variable.
- The proposed mathematical model has been validated and verified with delta wing results in static, dynamic and free-to-roll experimental results.

22.6 REFERENCES

- [1]. Bryan, G.H., "Stability in Aviation," MacMillan and Co., London, 1911.
- [2]. Etkin, B., "Dynamics of Flight – Stability and Control," John Wiley and Sons, Inc., N.Y. 1959.
- [3]. Tobak, M., Chapman, G.T. and Unal, A., "Modeling Aerodynamic Discontinuities and the Onset of Chaos in Flight Dynamical Systems," NASA TM 89420, Dec. 1986.
- [4]. Tobak, M., Chapman, G.T. and Schiff, L.B., "Mathematical Modeling of the Aerodynamic Characteristics in Flight Dynamics," NASA TM 85880, Jan. 1984.
- [5]. X.Z. Huang and E.S. Hanff, "Prediction of Leading-Edge Vortex Breakdown on a Delta Wing Oscillating in Roll," AIAA paper 92-2677, June 1992.
- [6]. X.Z. Huang and E.S. Hanff, "Prediction of Normal Force on a Delta Wing Rolling at High Incidence," AIAA paper 93-3686, Aug. 1993.
- [7]. X.Z. Huang, H.Y. Lou and E.S. Hanff, "Airload Predictions for Delta Wings at High Incidence" 22nd ICAS 221, Aug. 2000.
- [8]. Jenkins, J.E., Myatt J. H. and Hanff, E.S., "Body-Axis Rolling Motion Critical States of a 65-Degree Delta Wing," J. Aircraft Vol. 33, No. 2, pages 268-278.
- [9]. Goman, M. and Khrabov, A., "State-Space Representation of Aerodynamic Characteristics of an Aircraft at High Angles of Attack," AIAA Paper 92-4651.
- [10]. Hanff, E.S. and Huang, X.Z., Rolling and Pitching Experiments on Configurations with a 65° Delta Wing at High Incidence NRC/IAR LTR-A-013.
- [11]. X.Z. Huang, Y.Z. Sun and E.S. Hanff, "Circulation Criterion for Leading-Edge Vortex Breakdown over Delta Wings," AIAA 97-2265, June 1997.
- [12]. X.Z. Huang and E.S. Hanff, "Roll-Rate Induced Camber Effect on Delta Wing Leading-Edge Vortex Breakdown," AIAA Paper 95-1793, 1995.
- [13]. N. Chaderjian and L. Schiff, "Navier-Stokes Prediction of Large-Amplitude Forced and Free-to-Roll Delta –Wing Oscillations," AIAA paper 94-1884, 1994.
- [14]. N. Chaderjian and L. Schiff, "Navier-Stokes Prediction of a Delta –Wing in Roll With Vortex Breakdown," AIAA paper 93-3495, 1993.

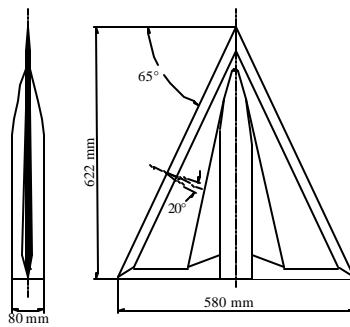


Fig. 1 65° delta wing model

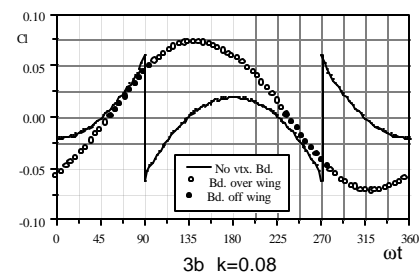
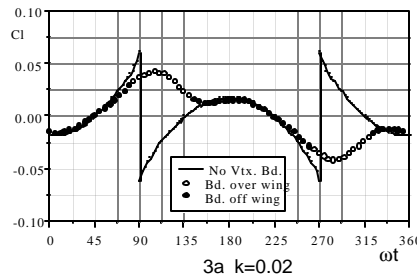


Fig. 3 Effect of vortex breakdown on rolling moment in dynamic case

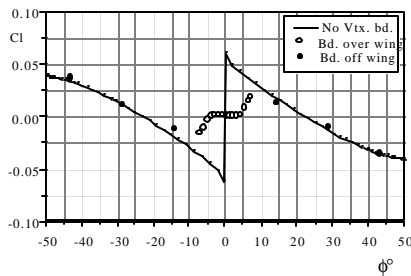
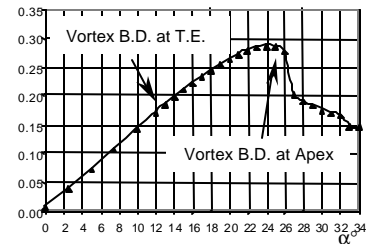
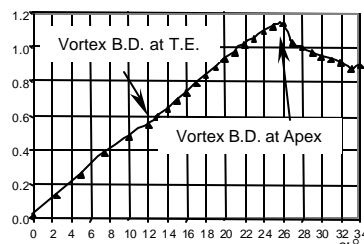


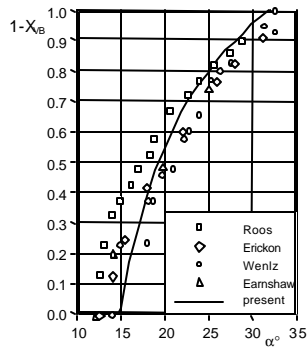
Fig. 2 Effect of vortex breakdown on rolling moment in static case



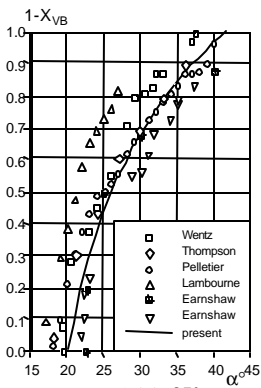
4a 55° diamond wing

4b 65° delta wing

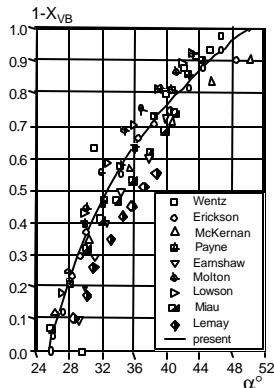
Fig. 4 Effect of vortex breakdown on normal force in static case



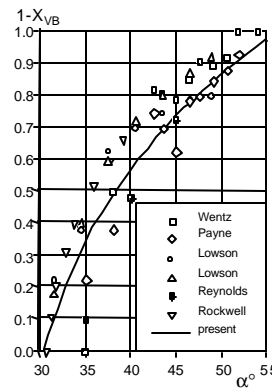
5a $\Psi = 60^\circ$



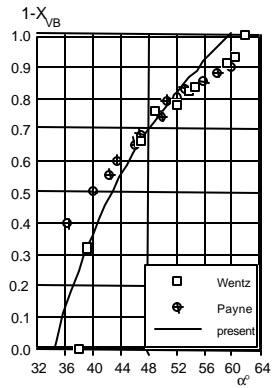
5b $\Psi = 65^\circ$



5c $\Psi = 70^\circ$



5d $\Psi = 75^\circ$



5e $\Psi = 80^\circ$

Fig. 5 Vortex breakdown locations over delta wings with different sweepback angles

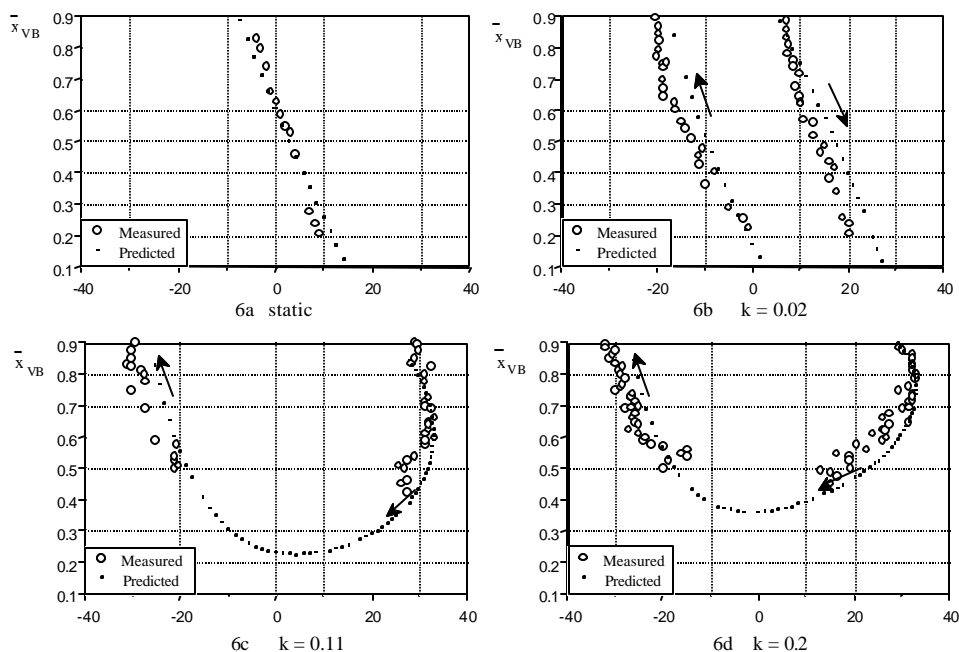


Fig. 6 Predicted and measured vortex breakdown location for rolled 65° delta wing ($\sigma=30^\circ$)

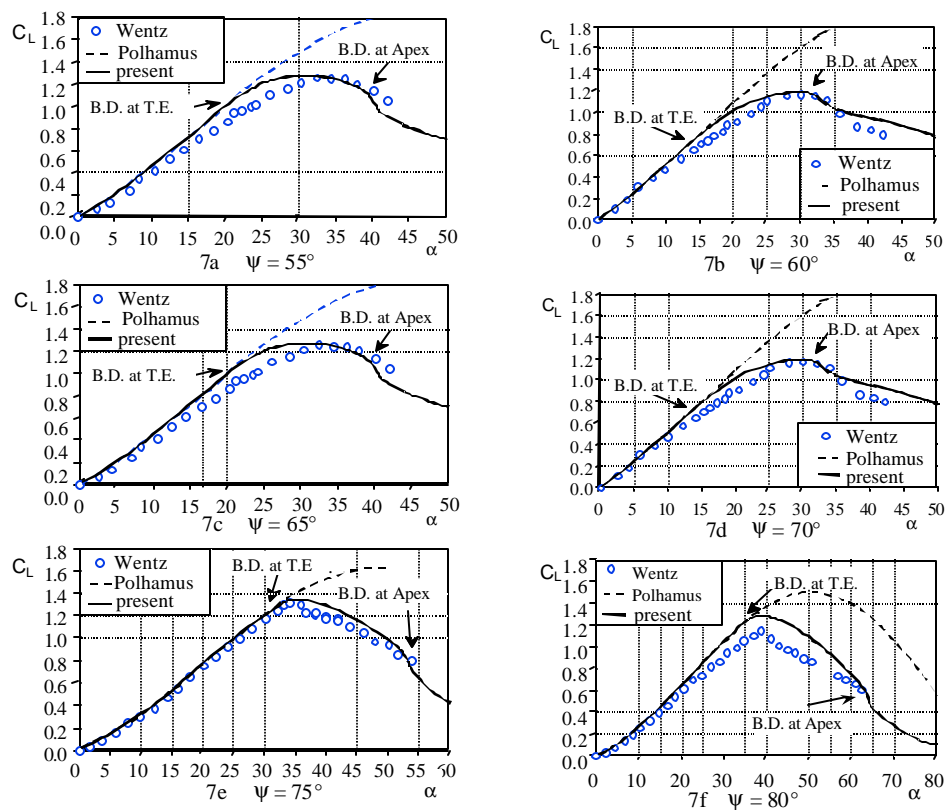


Fig. 7 Static lift coefficient for delta wings with different sweep angles

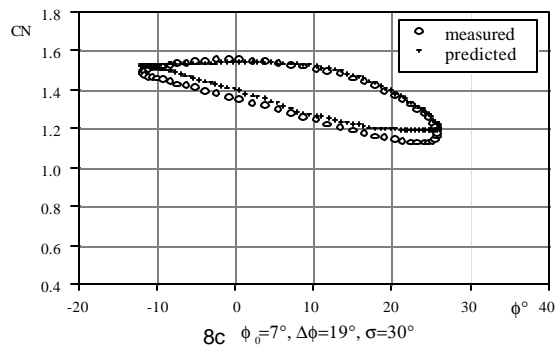
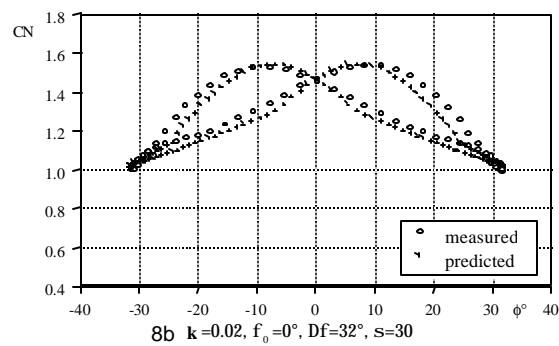
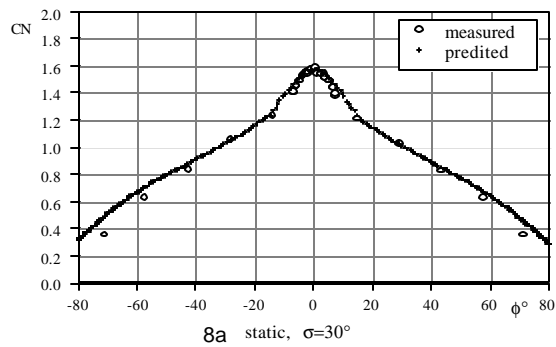


Fig. 8 Comparisons of normal force at static and rolling oscillation conditions

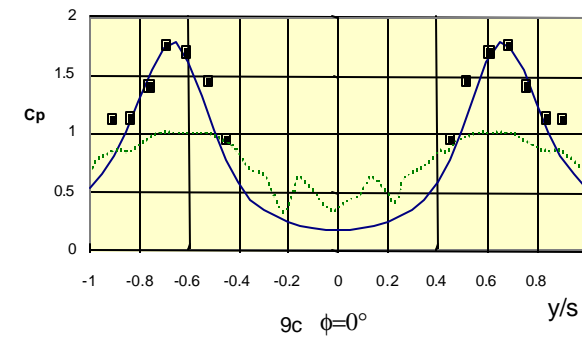
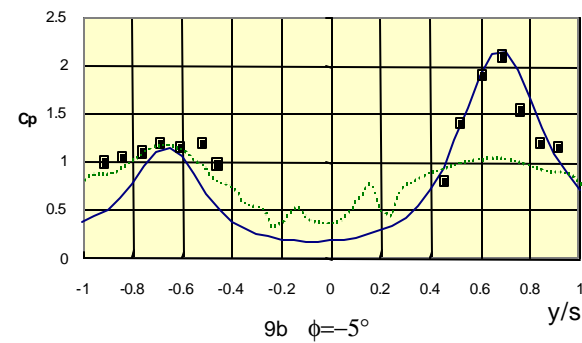
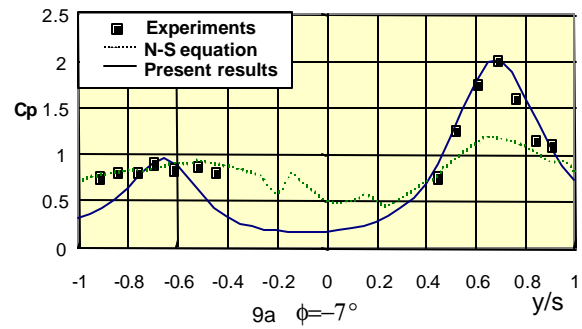


Fig. 9 Comparisons of pressure coefficient for different static conditions ($\sigma=30^\circ, x/c=0.75$)

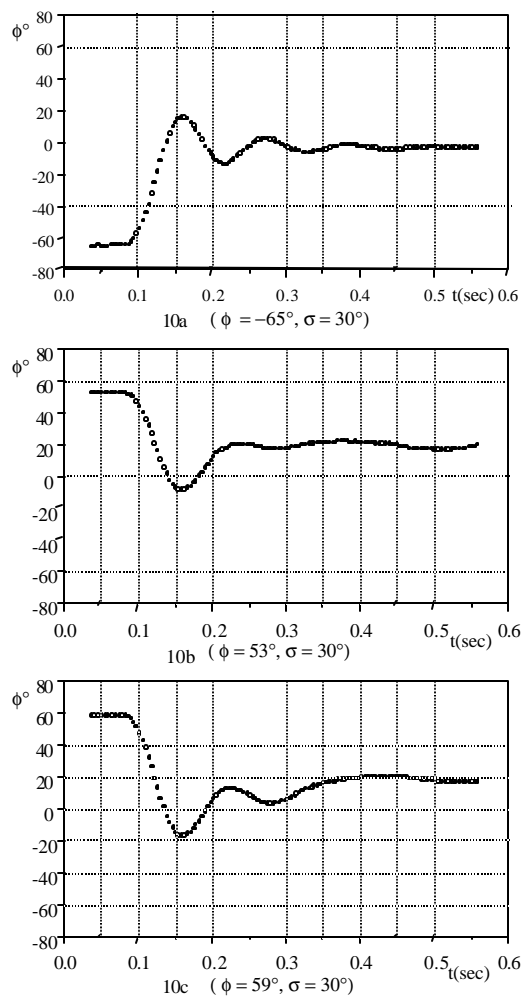


Fig. 10 Free-to-roll motion histories

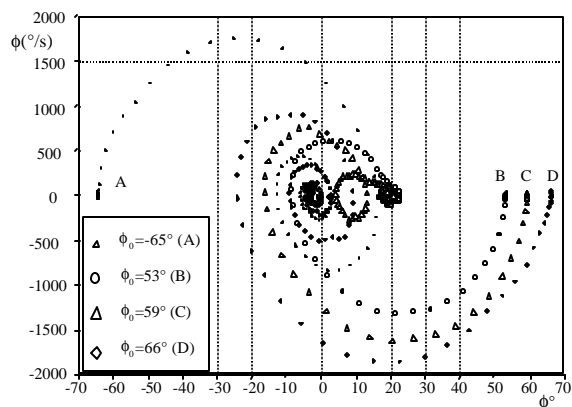


Fig. 11 Phase portrait of 65° delta wing free-to-roll motion trajectories ($\sigma = 30^\circ$)

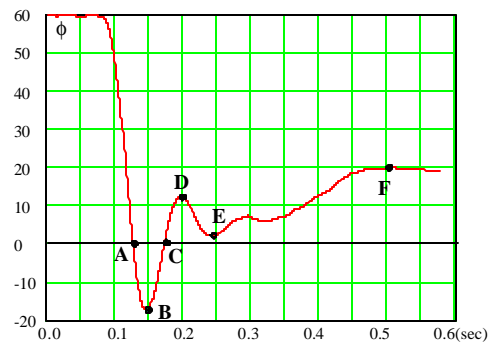


Fig. 12 Experimental case of free-to-roll motion for validation and verification

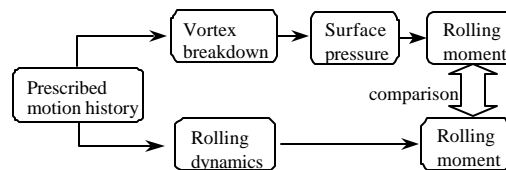
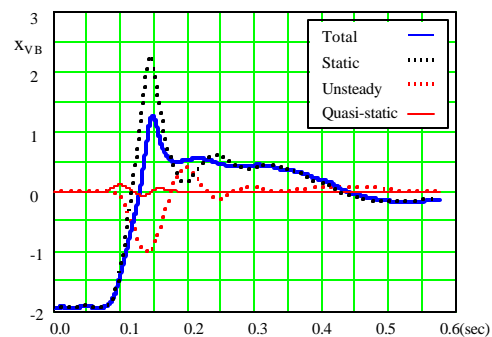
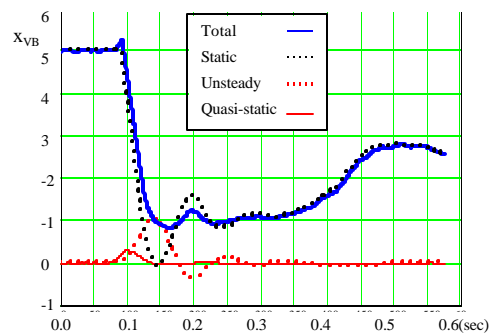


Fig. 13 Diagram of direct method for free-to-roll motion



14a contributions on starboard side



14b contributions on port side

Fig. 14 Contributions of different motion components on vortex breakdown

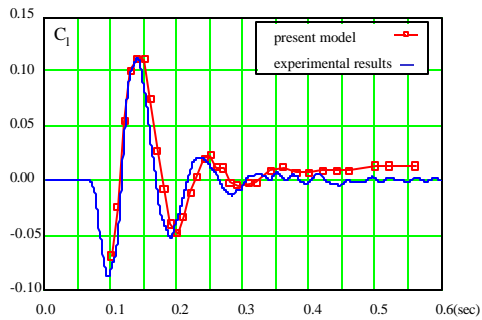
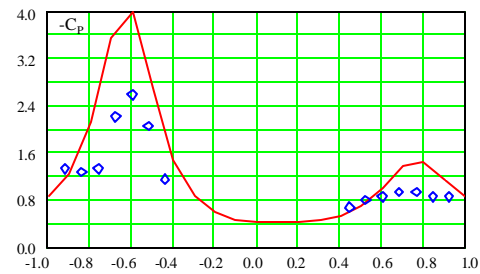
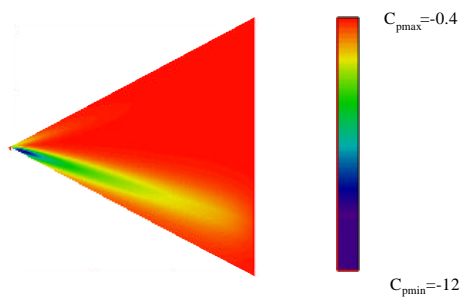


Fig. 15 Comparisons between measured and direct method during free-to-roll motion histories

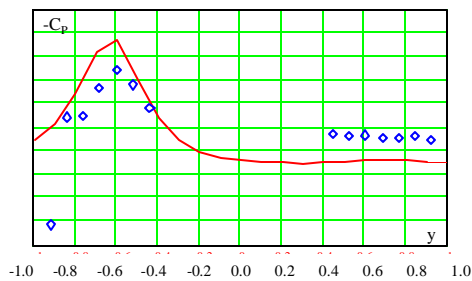


17b surface pressure at $x/c=0.75$

Fig. 17 Instantaneous surface pressure at point B ($\phi_t = -17.143^\circ$)

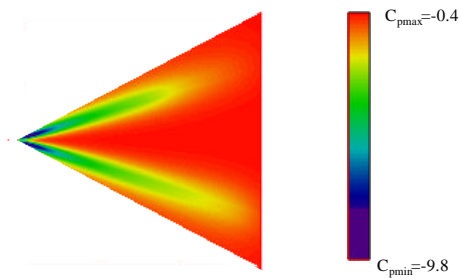


16a surface pressure contour ($\phi_t = 0^\circ$)

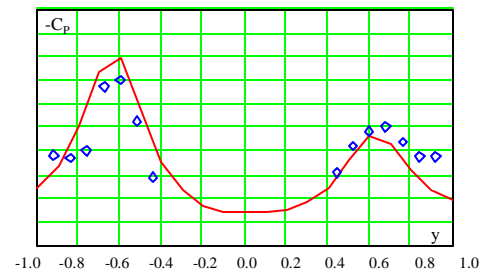


16b surface pressure at $x/c=0.75$

Fig. 16 Instantaneous surface pressure at point A ($\phi_t = 0^\circ$)

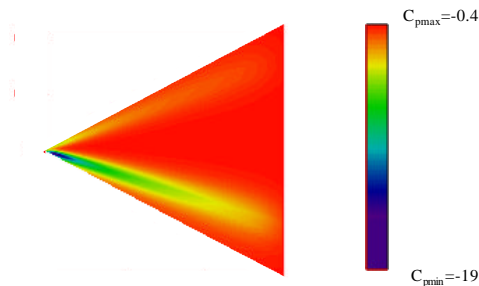


18a surface pressure contour ($\phi_t = 0.303^\circ$)

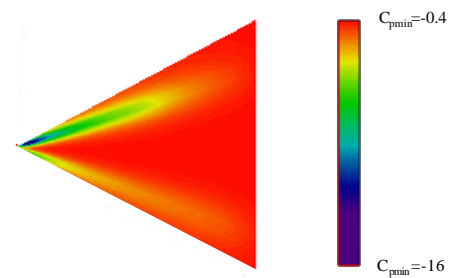


18b surface pressure at $x/c=0.75$

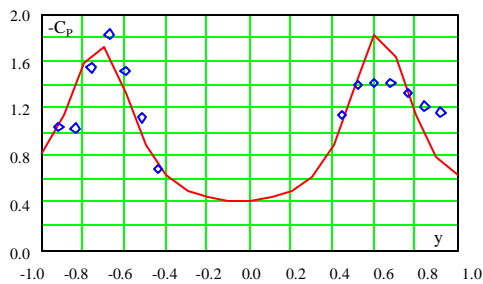
Fig. 18 Instantaneous surface pressure at point C ($\phi_t = 0.303^\circ$)



17a surface pressure contour ($\phi_t = -17.143^\circ$)

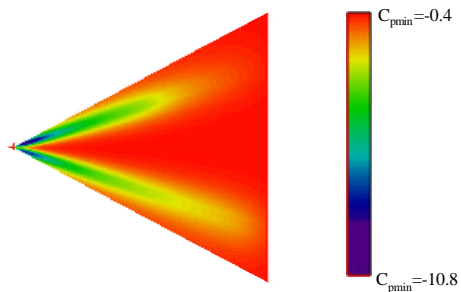


19a surface pressure contour ($\phi_t = 12.308^\circ$)

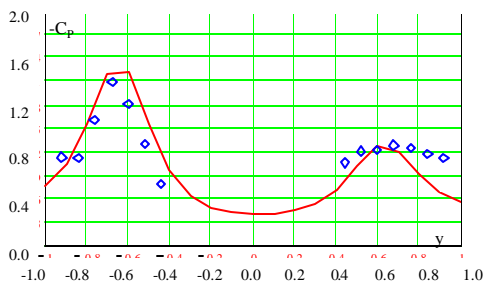


19b surface pressure at $x/c=0.75$

Fig. 19 Instantaneous surface pressure at point **D** ($\phi_t=12.308^\circ$)

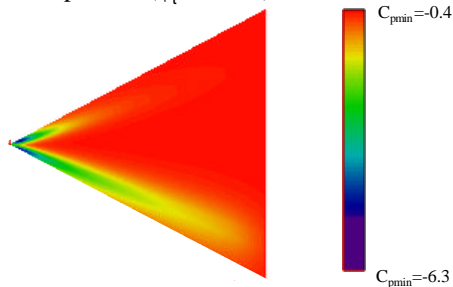


20a surface pressure contour ($\phi_t=2.183^\circ$)

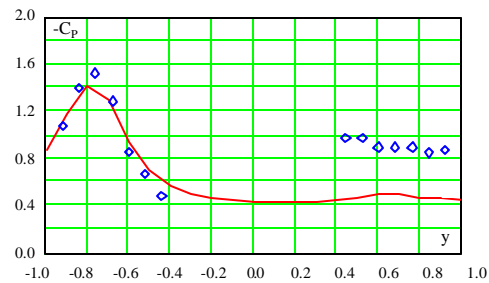


20b surface pressure at $x/c=0.75$

Fig. 20 Instantaneous surface pressure at point **E** ($\phi_t=2.183^\circ$)



21a surface pressure contour ($\phi_t=19.818^\circ$)



21b surface pressure at $x/c=0.75$

Fig. 21 Instantaneous surface pressure at point **F** ($\phi_t=19.818^\circ$)

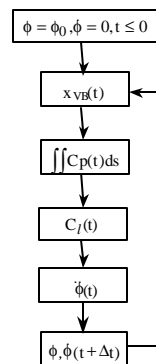


Fig. 22 Diagram of Iterative method

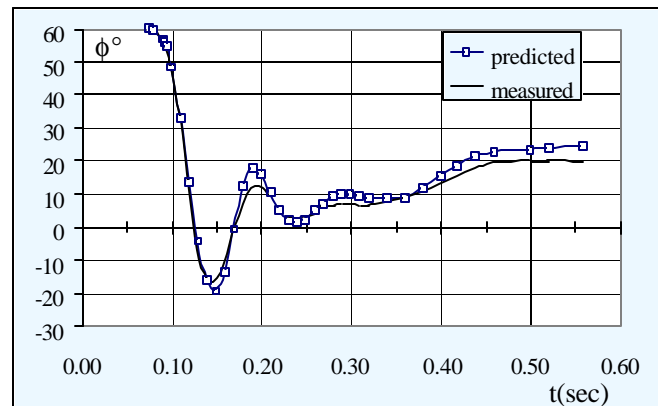


Fig. 23 Comparisons between measured free-to-roll motion histories and predicted (iterative) results



Chapter 23 – APPLYING VORTEX BREAKDOWN EMPIRICISMS TO PREDICT AERODYNAMIC CHARACTERISTICS IN SYMMETRIC & ASYMMETRIC SITUATIONS

Dr. R. K. Nangia

Nangia Aero Research Associates,
WestPoint, 78-Queens Road, BRISTOL, BS8 1QX, UK.
Tel: +44 (0)117-987 3995 Fax: +44 (0)117-987 3995
nangia@blueyonder.co.uk

ABSTRACT

On manoeuvrable aircraft manned or unmanned, it is imperative to understand the onset of wing vortex flows and their breakdown. The applications are for military and civil types featuring moderate to high sweep. An understanding of vortex flows is also required from the viewpoint of control, LE & TE devices. Quantitative information and understanding is needed on vortex flows e.g. forces, moments and loadings so as to either exploit them or avoid them. Further, symmetric and asymmetric effects are both required.

The challenge here is to predict forces and moments on a wing-body (deltas or swept trapezium wings of moderate taper, cambered, rounded LE) operating with large side-slip throughout full α range with Mach and Reynolds number effects. To address many geometric variables, a reasonably quick turn-around is required.

This paper is via the initiative of the RTO-AVT Task group AV-080. In this "condensed" version, results from an approach are presented that has attempted to model such effects for a series of 53° and 58° swept trapezium wings.

NOMENCLATURE

AR	or A, Aspect Ratio
b	= 2 s, Wing span
c	Local Wing Chord
c_{av}	= $c_{ref} = S/b$, Mean Geometric Chord
C_A	= Axial force/(q S), Axial Force Coefficient
C_{AL}	Local Axial Force Coefficient
C_D	= Drag Force/(q S), Drag Coefficient
C_{DL}	Local Drag Coefficient
CG	Centre of Gravity
C_L	= Lift Force/(q S), Lift Coefficient
C_{LL}	Local Lift Coefficient
C_l	= $l/(q S b)$, Roll Mom. Coeff, (l roll moment)
C_n	= $n/(q S b)$, Yaw Mom. Coeff, (n yaw moment)
LE, TE	Leading Edge, Trailing Edge
M	Mach Number
q	= $0.5 \rho V^2$, Dynamic Pressure, ρ Air Density
Re	Reynolds Number, based on c_{av}
s, S	semi-span, Wing Area respectively
V	Free-stream Velocity
α	AoA, Angle of Attack
β	Sideslip angle
Λ	LE Sweep Angle
η	= y/s, Non-dimensional spanwise Distance

23.1 INTRODUCTION & BACKGROUND

For highly manoeuvrable or advanced aircraft, manned / unmanned, it is imperative to understand the onset of wing vortex flows and their breakdown (Refs.1-3). The applications are to military and civil type wings featuring moderate to high sweep. **Plate.1** refers to an AoA sequence of 60° delta calculations with Euler (Mach 0.4). Although vortex breakdown can be inferred, considerable unsteadiness was evident in the calculations. An understanding of vortex flows is required from the viewpoint of control, LE / TE devices (**Fig.1**). We need qualitative and quantitative information on vortex flows e.g. forces, moments and loads so as to either exploit them or avoid them. Symmetric & asymmetric effects are required.

The challenge seen here is to predict forces and moments on a wing-body (deltas and swept trapezium wings of moderate taper, cambered, rounded LE) operating with large sideslip throughout full α range with Mach and Reynolds number effects. Further, a quick turn-around is needed to cope with many geometric and flow variables.

This Paper via the initiative of the RTO-AVT Task group AV-080. An abridge version, Ref.1 was included in a special AIAA session. We begin with a brief description of the method based on using attained LE thrust, together with simplifications and empiricisms introduced on the basis of empirical vortex effects and breakdown. TE separation model is also included. We then show predictions on a series of moderately swept trapezium wing-bodies in symmetric and asymmetric flows. Finally comparisons with experiments are made. These are promising and offer an insight into flow mechanisms. Avenues for further work are indicated.

23.2 METHODS, TECHNIQUES, MODEL

We begin with the theory that has been developed since the 1980's (Ref. 4-6). The method uses subsonic lifting surface theory with Mach & Reynolds number, attained thrust and Vortex Effects (based on NASA LaRC work, Refs.7-9). This is then adapted / coupled with the Lan et al scheme (Refs.10-12) to predict vortex breakdown. Empirical criteria have been developed, particularly for application to lower wing sweeps and a TE separation model has been inserted. Symmetric and asymmetric flows can be handled. Fuselage effects have been allowed (simply by zeroing the LE suctions locally). Confidence in the basic method has been built up over the years in analysis and design modes (Refs.13 - 17).

Fig. 2 shows the features of the approach. **Fig.3** illustrates the type of experimental data available from vortex breakdown studies on deltas and swept wings. Further detail is in Ref.4.

Fig. 4 shows a qualification of vortex breakdown onset on delta wings. This was based on Lamar's work (Ref.18-19) but has been extended to wings of moderate LE sweep using largely experimental data.

Fig. 5 summarizes the main elements of the Lan & Hsu vortex breakdown model (Ref.10). The idea is to use unattained LE suction distributions (equivalent to vortex strength by LE suction analogy), find the position where the local maximum occurs and this is then correlated with vortex breakdown onset and movement upstream through a parameter y_1 . The physical reasoning is that once suction stops growing then this "hastens" vortex breakdown.

Fig. 6 shows an analysis and extension of vortex breakdown progression upstream, using Lan et al parameters.

Fig. 7 introduces Mach number (compressibility) effects on Vortex breakdown. The α for breakdown at a given Mach number is related to α for breakdown at low (incompressible) speeds by an empirical factor F_c :

$$F_c = 0.3 - 0.213 B_c + 0.913 B_c^2, \quad B_c = \sqrt{1 - M^2}$$

A validation of the approach is via **Fig.8**. This shows the results for uncambered sharp-edged deltas (Lan and Hsu). The current method predicts identical results.

Our method has several extensions e.g. allowing for fuselage effects and finite chord wing-tip vortex flows (as per Lamar's work). A further extension has to include two types of LE / TE stall model, taking a clue from the work of Lan et al (Ref.12).

23.2.1 Boundary Layer, TE Separation

For wings with relatively low sweep, the flow breakdown pattern at high α is related more to 2-D BL (viscous) stall. Existing methods for dealing with such flows are not entirely satisfactory. Following Ref.10-12, & 20, a method based on utilizing the 2-D aerofoil section data up to stall within a lifting-line framework has been developed. The main assumption is that flow separation reduces the local incidence at each spanwise station. Further details are in the references cited.

23.2.2 Experimental Model for Evaluation of Approach

Fig. 9 gives an idea of the wing+body model geometry used for symmetric and asymmetric wind tunnel tests. The wing is pivoted, thus providing wing sweep variation. The wing-tips introduce a problem however as they are not always "streamwise". The wings were cambered and twisted. Selected Mach and Re test results were available for comparisons with theory.

Mach	Re values R1, R2 & R3 range (based on c_{av})
0.2	1.6, 2.9 & 4.3 $\times 10^6$
0.35	2.0, 3.4 & 4.8 $\times 10^6$

We can now review some theory results to give a flavour of the work.

23.3 SYMMETRIC FLOWS & VORTEX BREAKDOWN RESULTS

Fig. 10 shows the 58° model with the vortex-lattice used.

It was useful firstly to understand the flow details on an uncambered wing even though there is no equivalent experimental model.

Planar Wing

The top picture of **Fig.11** refers to the 58° wing at Mach 0.35. For $\alpha = 16^\circ$ & 20° , the top picture shows typical spanwise loadings of $C_{NL} c/c_{av}$, $C_{AL} c/c_{av}$, $C_{LL} c/c_{av}$ and $C_{DL} c/c_{av}$ at R1 & R3. Note the development of vortex breakdown effects in relation to the two basic flow states of 0% and 100% LE suction.

The lower picture in **Fig.11** shows the longitudinal force relationships ($C_L - \alpha$, $C_D - \alpha$, $C_D - C_L$, $C_A - \alpha$, $k - \alpha$, $L/D - C_L$). Here R1, R2 & R3 cases are considered and a simple TE stall model has been included. The lift induced drag factor 'k' for a wing of aspect ratio (A) follows from the conventional definition of C_D :

$$C_D = C_{D0} + C_{Di}$$

$$k = \pi A C_{Di} / C_L^2 = \pi A (C_D - C_{D0}) / C_L^2.$$

The $k - \alpha$ relationship offers a sensitive indication of the onset of flow separation effects. These graphs bear out the Re dependence at a given M. The departure from 100% LE suction conditions is delayed as M increases. To further delay the departure from the 100% LE suction conditions, LE droop will be required.

Cambered Wing

Fig.12 shows the longitudinal total forces C_L , C_D , C_A relationships. The $k - \alpha$ and $C_A - \alpha$ relationships indicate the onset of vortex breakdown near $\alpha = 14^\circ$ for 0% LE suction state. For the other Re cases, the vortex lift is smaller and breakdown is delayed to α between 14° and 16° . The TE separation occurs for α between 25° and 28° .

23.4 ASYMMETRIC FLOWS & VORTEX BREAKDOWN

As mentioned, we persist with the challenge to predict forces and moments on a wing-body (trapezium wing, moderate sweep, moderate taper, cambered) operating with large β through a full α range with M and Re effects.

Fig.13 shows aspects of side-slipping flows. The LE suction distribution on the two "halves" of the wing changes in shape and magnitude. Further the wing-tips and fuselage have sizeable effects. In particular, one tip becomes part of LE whilst the other is a part of TE. With side-slip, **Fig. 14** shows aspects of modelling the 58° configuration and the vortex-lattice used. Note the assumptions necessary for the wing-tips.

Take the uncambered wing first to look at the basics.

Planar 58° Wing, Mach 0.35, Re: R1, R2 & R3

Fig.15 shows the longitudinal total forces C_L , C_D , C_A relationships. Note the breaks in curves due to vortex breakdown and TE stall.

Cambered 58° Wing, Mach 0.35, Re: R1, R2 & R3

Fig.16 shows the longitudinal total forces C_L , C_D , C_A relationships. As anticipated, the breaks in curves due to vortex breakdown and TE stall are at different places c.f. those in **Fig.15**.

Planar 53° Wing, Mach 0.2, Re: R1, R2 & R3

Fig.17 shows the longitudinal total forces C_L , C_D , C_A relationships.

Cambered 53° Wing, Mach 0.2, Re: R1, R2 & R3

The top picture in **Fig.18** shows the longitudinal total forces C_L , C_D , C_A relationships.

The lower picture shows loadings of $C_{LL} c/c_{av}$ and $C_{DL} c/c_{av}$ (α varying) for three different flow states, 100% LE suction, 0% LE suction and at Re = R1. This emphasises the vortex breakdown effects that lead to departure from 100% LE suction curves when evaluating rolling and yawing moments.

23.5 COMPARISONS WITH EXPERIMENT

Comparisons for 53° wing, $\beta = 10^\circ$

The upper two pictures in **Fig.19** shows the theoretical $C_L - \alpha$ curves for the wing with the two different TE stall models. The lower picture shows the experimental results for the wing + body case. The cambered body leads to an intercept on C_L axis c.f. the predictions.

Fig 20 shows the lateral derivatives C_l and C_n against α for $\beta = 4^\circ$, 6° & 10° , Re = R1 & R3. These emphasize the significance of TE stall at high α .

For $\beta = 10^\circ$, **Fig 21** compares ΔC_l and ΔC_n from theory and experiment for $Re = R1$ and $R3$. To discount the fuselage effects (to first order), the $\alpha = 0^\circ$ intercepts have been removed. It is interesting that the theory predicts the character of the experimental ΔC_l curves at very high α . For ΔC_n , the fuselage effects dominate, the theory suggests some agreement in shape for α above 20° . Overall the large discontinuities in ΔC_n lie within the band of 100% LE suction and other Re predictions. We can infer that the present theory offers substantial improvement over the usual subsonic approaches that correspond to 100% LE suction results.

Predictions show promising correlation with available experiment. In the context of vortical flow breakdown we could have limited our work to α near 20° . However, the simple TE stall model enables an improved insight of the flow mechanisms.

23.6 INFERENCES, CONCLUDING REMARKS & FURTHER WORK

For highly manoeuvrable or advanced aircraft, manned or unmanned, it is imperative to understand the onset of wing vortex flows and their breakdown. The applications are for military and civil types featuring moderate to high sweep. An understanding of vortex flows is required also from the viewpoint of control, LE & TE devices.

We need qualitative and quantitative information for vortical flow e.g. forces, moments and loadings so as to either exploit them or to avoid them. Further, symmetric and asymmetric effects are required.

The continued challenge is to predict forces and moments on a wing-body (trapezium wing, moderate sweep, moderate taper, cambered, rounded LE) operating with large β throughout the full α range with Mach and Re effects.

We have described such an approach. Results have been presented for a series of 53° and 58° swept trapezium wings. Predictions show promising correlation with available tests giving an insight into flow mechanisms.

23.6.1 Possible Future Work

Several avenues for future work have arisen e.g.

- More Detailed modelling of Wing-Body effects. Wings may have moderate sweep, cranks and finite tip chords and winglets. See **Fig.22**. Operate with large β throughout the full α range with Mach and Re effects
- Vortex breakdown & LE / TE Stall effects merge.
- Include other surfaces, Canards, Tails
- CFD modelling, using unsteady codes.

Further development is still needed. The challenge is there for method developers to improve on implied empiricisms and several PhD topics exist!

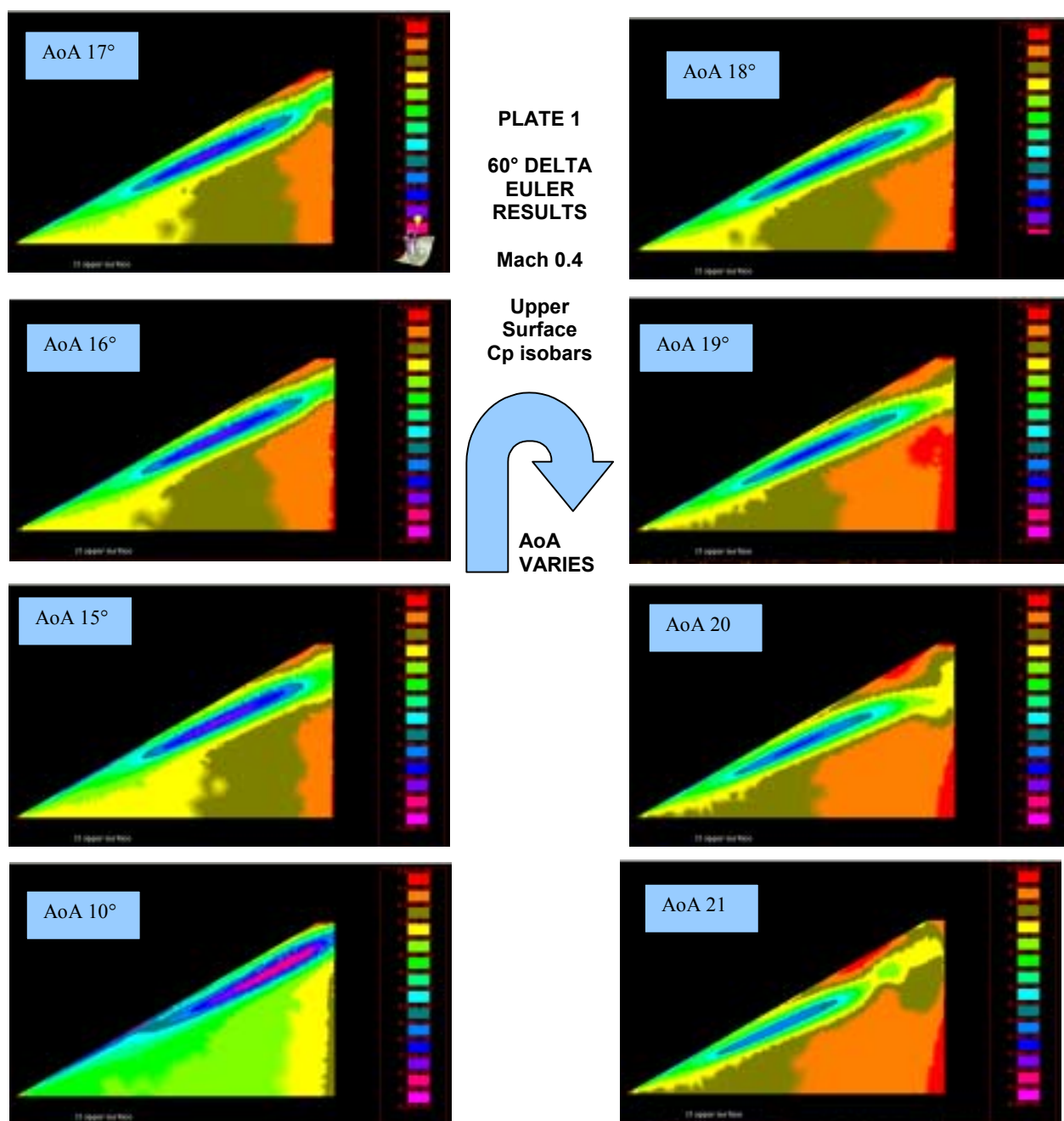
23.7 ACKNOWLEDGEMENTS

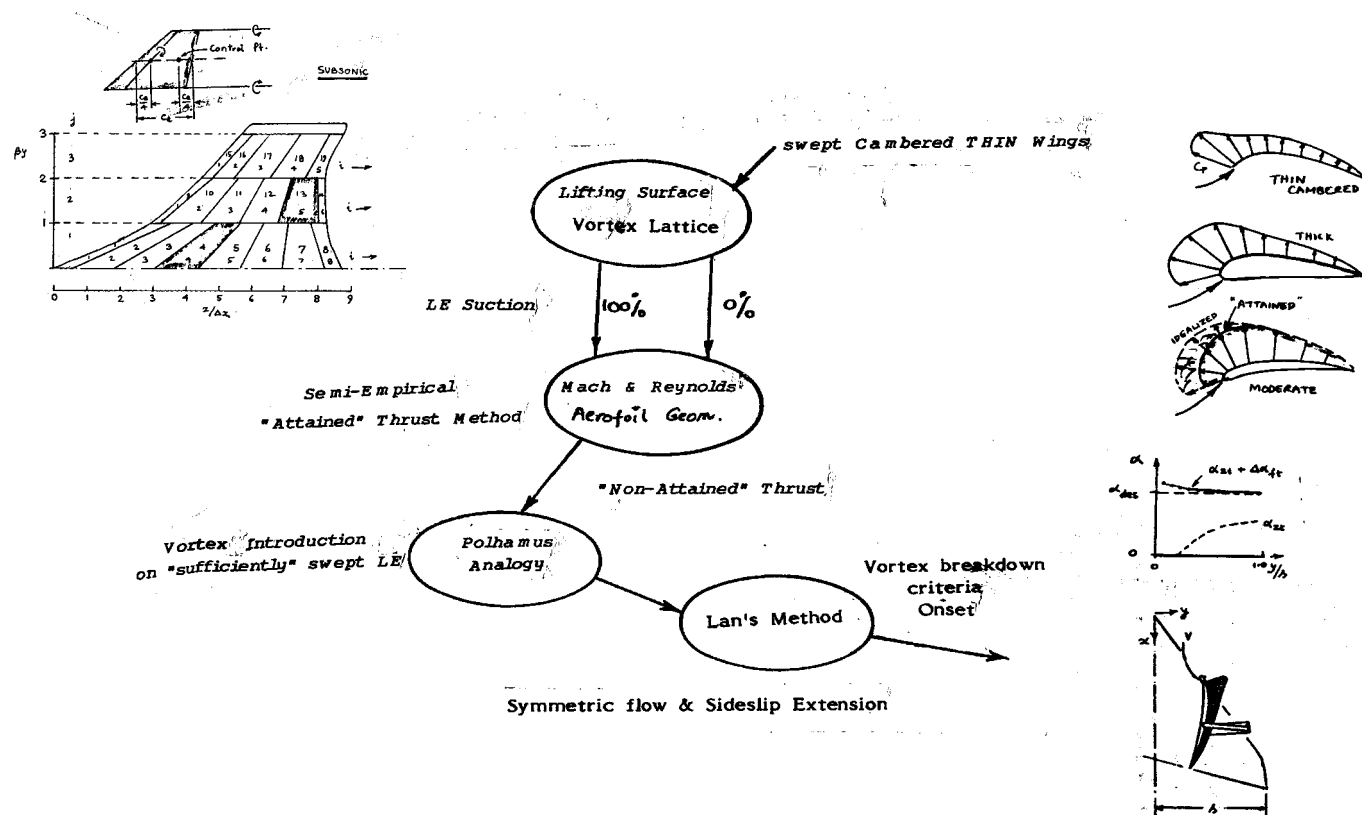
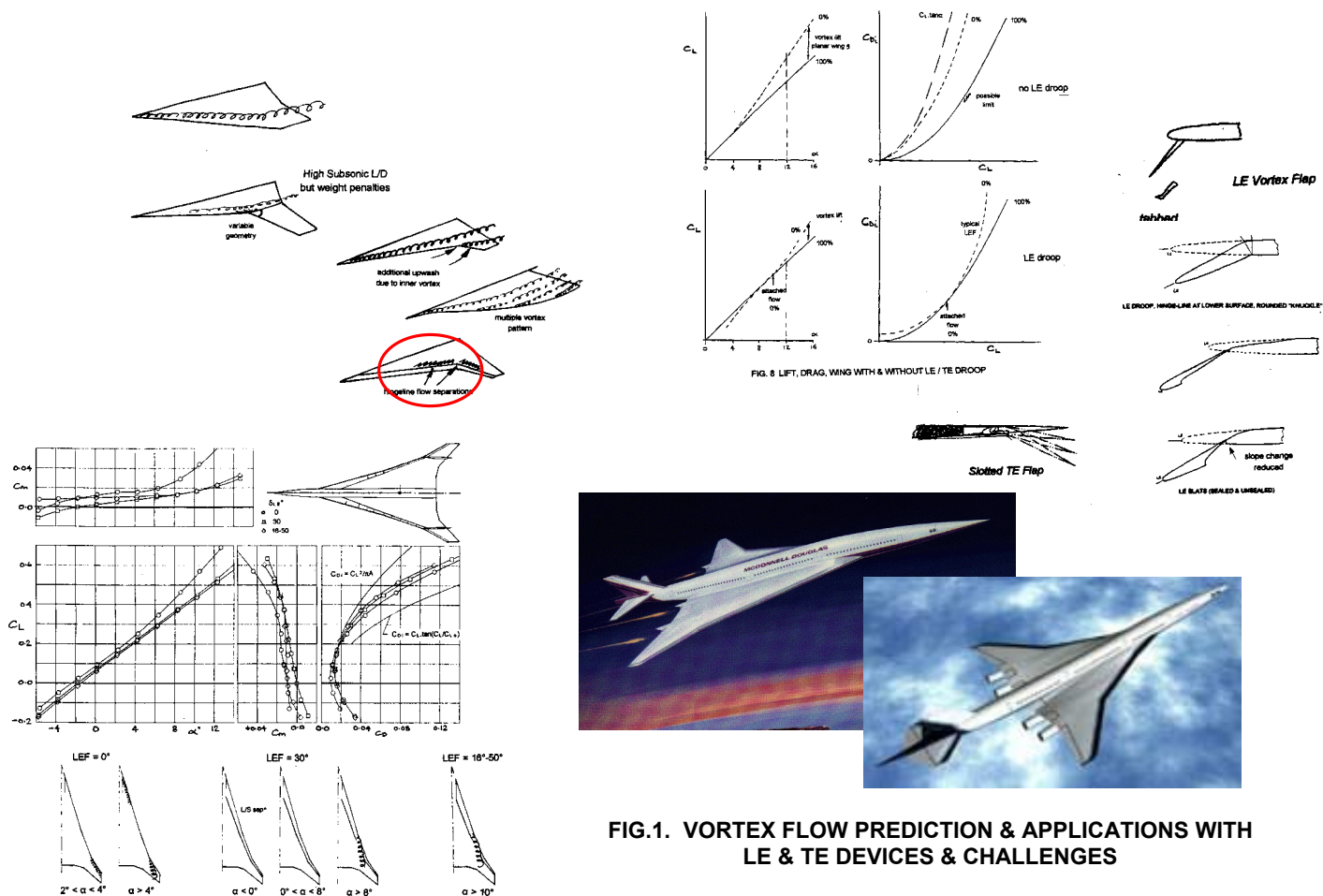
This work is part of in-house R & D activities and was also supported in part in its early stages (90's) by the RAE (UK). The author has pleasure in acknowledging helpful discussions with Mr. D. A. Lovell and Dr. D.I. Greenwell. Any opinions expressed are those of the author. Opportunities for collaboration are invited.

23.8 REFERENCES

1. NANGIA, R.K. "Applying Vortex Breakdown Empiricisms to Predict Aerodynamic Characteristics in Symmetric & Asymmetric Situations", AIAA Applied Aerodynamics Conference, AIAA-2003-3945, 2003, Orlando, FL., USA, 2003.
2. NANGIA, R.K. & MILLER, A.S. "Vortex Flow Dilemmas & Control on Wing Planforms for High Speeds", RTO AVT Symposium "Advanced Flow Management, Vortex Flows & High Angle of Attack", Loen, Norway, May 2001.
3. NANGIA, R.K., "Low Speed Performance Optimisation of Advanced Supersonic Civil Transport with Different LE & TE Devices", EAC'94, Toulouse, France, Oct.94.
4. NANGIA, R.K. "Development of an "Attained" LE Thrust Method for Use in Combat Aircraft Wing Design", Contractor Report, 1989
5. NANGIA R.K., "Calculations of the Effects of Reynolds Number on the Forces and Moments experienced by Wings of 58° and 53° Sweep Including the Effects of Sideslip & Vortex Breakdown", Contractor Report, 1993.
6. NANGIA, R.K., "The Design of Manoeuvrable" Wings using Panel Methods, Attained Thrust & Euler Codes", ICAS-92.
7. CARLSON, H. W. & MACK, R.J., "Studies of LE Thrust Phenomena", AIAA jo. Of Air., Vol. 17, No.1 2, pp. 890-7, December 1990.
8. POLHAMUS, E.C., "Predictions of Vortex-Lift Characteristics by a LE Suction Analogy", AIAA JI. of Air., Vol.8, No. 4, pp.193-9, April 1971.
9. POLHAMUS, E.C., "Charts for Predicting the subsonic Vortex-lift Characteristics of Arrow, delta, and Diamond Wings". NASA TN-D-6243, April 1971.
10. LAN, C.E. & HSU, C.H., "Effects of Vortex Breakdown on Longitudinal and Lateral aerodynamics of Slender Wings by the Suction Analogy", AIAA-82-1385, 1982.
11. LAN, C.E., "Theoretical Prediction of Wing Rocking", AGARD CP-386, 1985.

12. TSENG, J.B. & LAN, C.E., "Calculation of Aerodynamic Characteristics of Airplane Configurations at High AoA", NASA CR-4182, 1988.
13. NANGIA, R.K. & GALPIN, S.A., "Towards Design of High-Lift Krueger Flap Systems with Mach & Reynolds No. Effects for Conventional & Laminar Flow Wings", CEAS European Forum, Bath, UK, 1995.
14. NANGIA, R. K. & GALPIN, S.A., "Prediction of LE & TE Devices Aerodynamics in High-Lift Configurations with Mach & Reynolds No. Effects", ICAS-1996-2.7.6.
15. NANGIA, R.K. & GREENWELL, D.I., "Wing Design of an Oblique-Wing Combat Aircraft", ICAS-2000-1.6.1.
16. NANGIA, R.K., PALMER, M.E. & GREENWELL, D.I., "Design of Conventional & Unconventional Wings for UAV's", RTO-AVT Symposium,, Turkey, October 2000.
17. NANGIA, R.K., PALMER, M.E. & DOE, R.H., "A Study of Supersonic Aircraft with Thin Wings of Low Sweep", AIAA-2002-0709, January 2002.
18. LAMAR, J.E., "Some Recent Applications of the Suction analogy to Vortex-Lift Estimates", NASA-TM-X-72785, 1972.
19. LAMAR, J.E. & CAMPBELL, J.F., "Recent Studies at NASA Langley of Vortical Flows with Neighbouring Surfaces", AGARD-CP, 1983..
20. ANDERSON, J.D.Jr., "Fundamentals of Aerodynamics", Wiley, 1984.





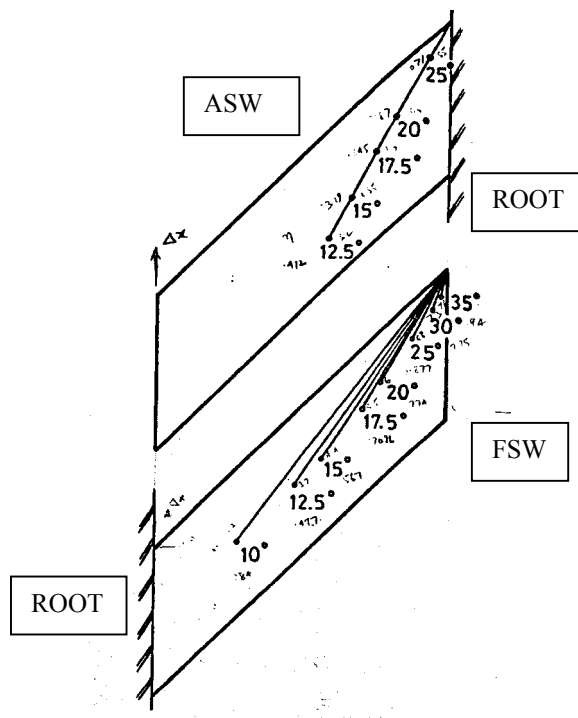
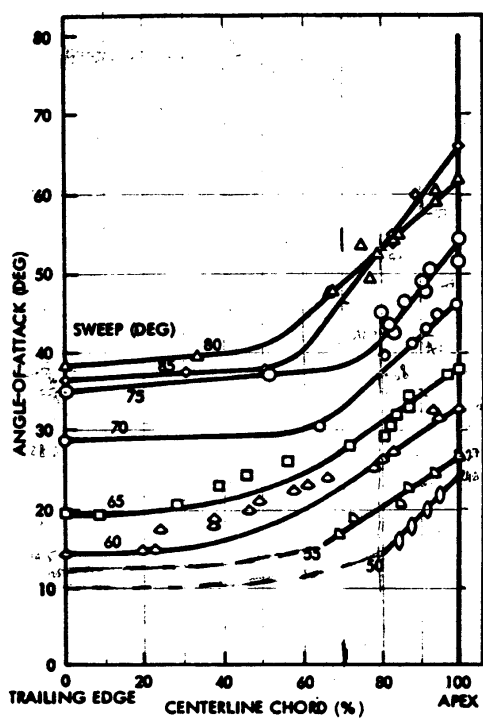
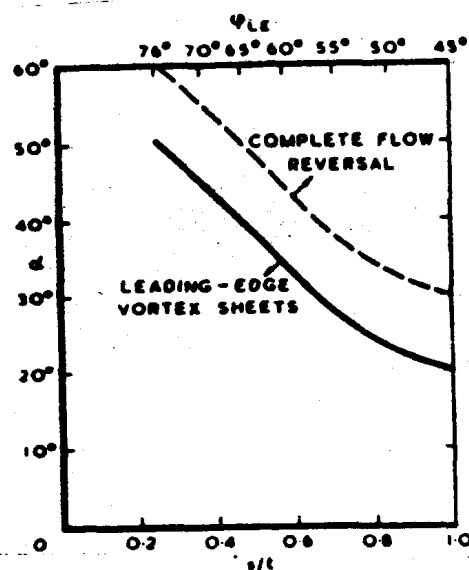
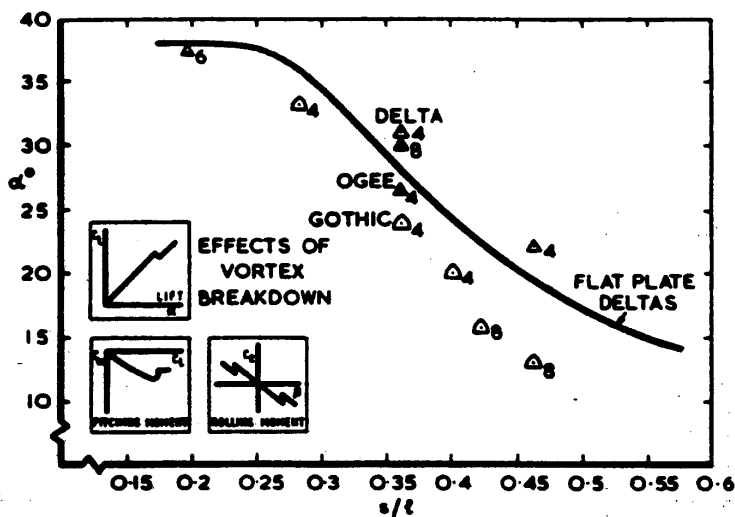
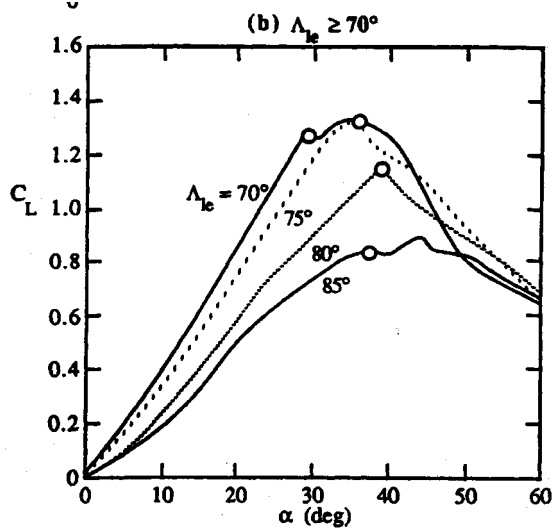
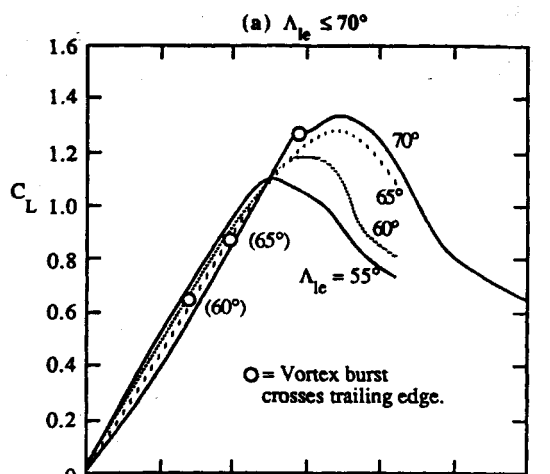


FIG. 3 PREVIOUS EXPERIMENTAL KNOWLEDGE ON VORTEX BREAKDOWN ONSET ON DELTA WINGS & SWEEP WINGS

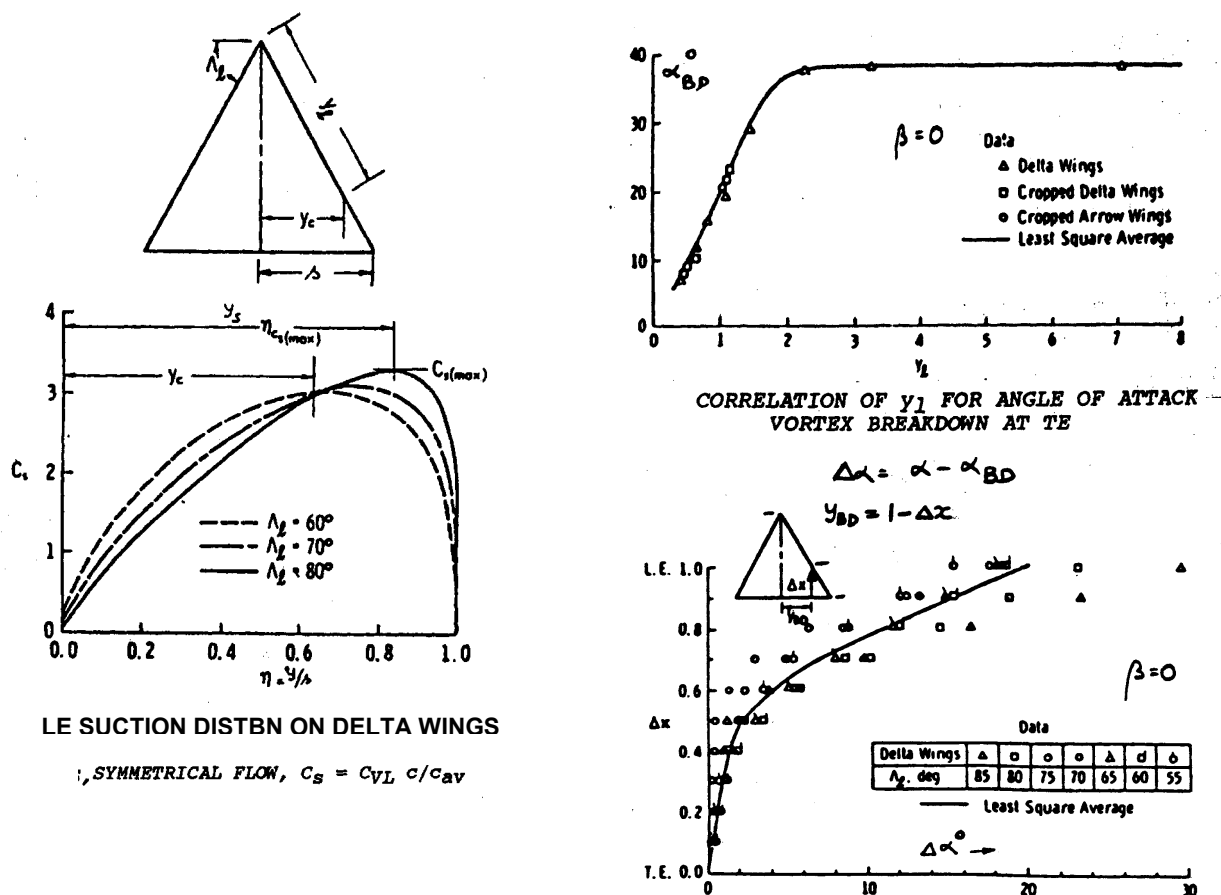
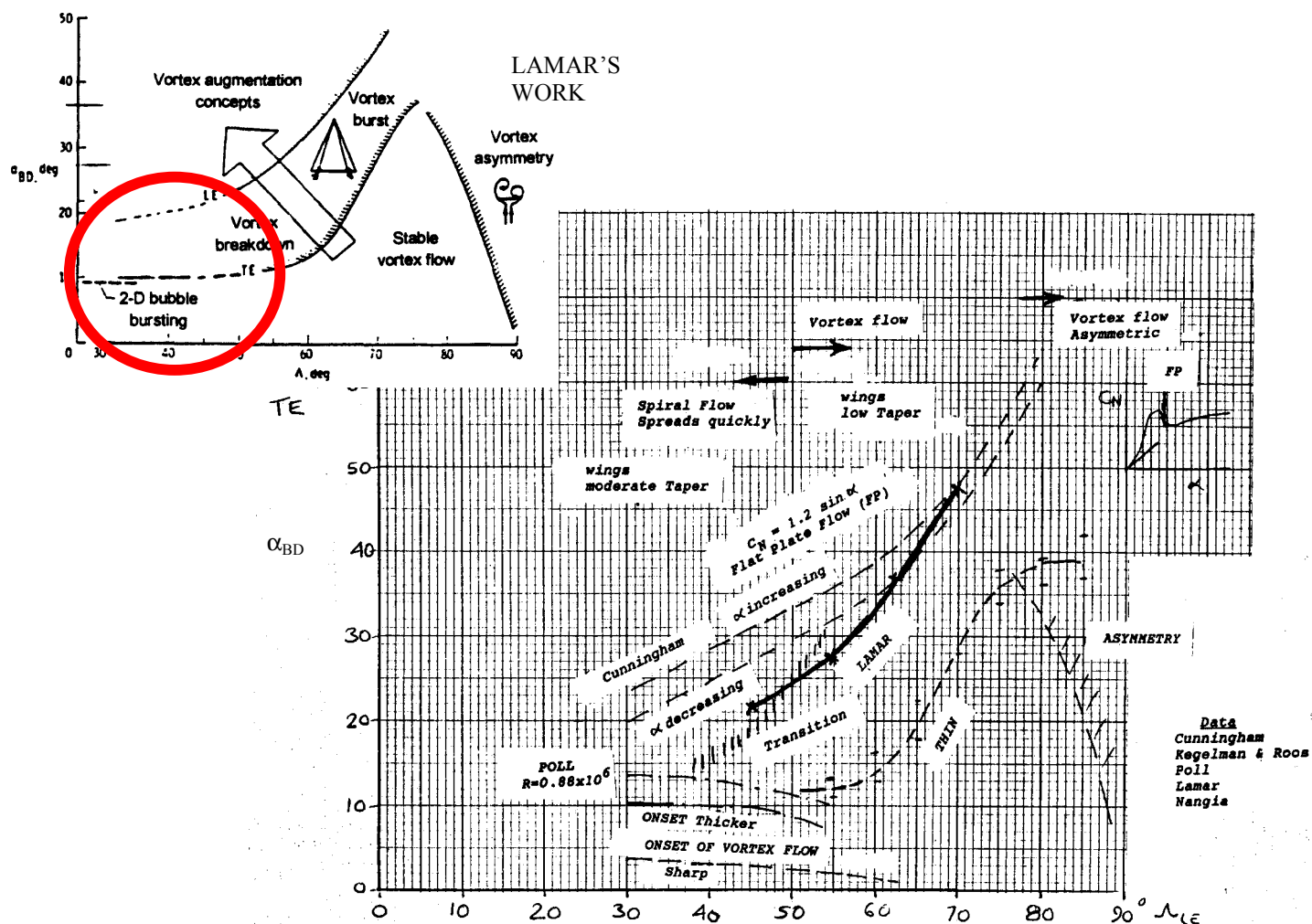
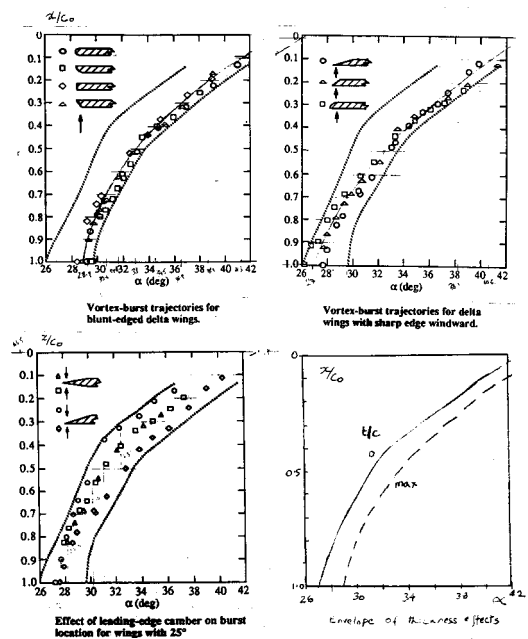
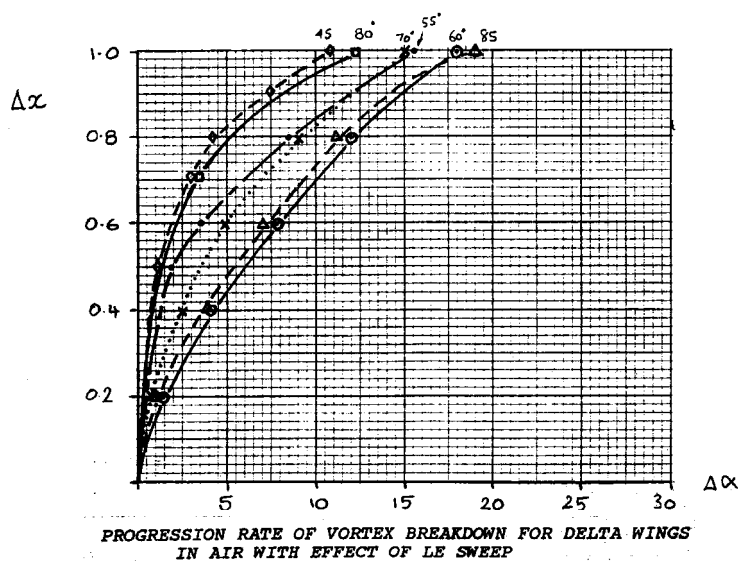
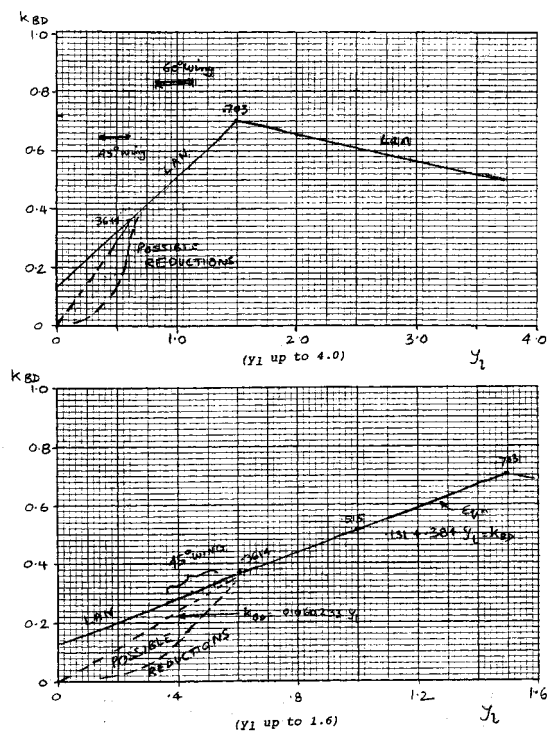


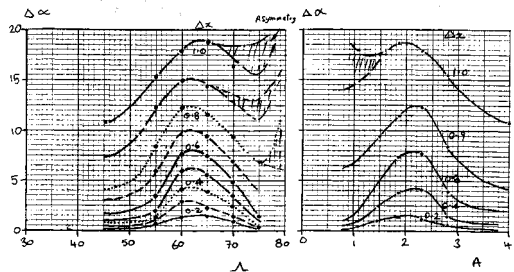
FIG. 5 LAN & HSU METHOD FOR INCORPORATING VORTEX BREAKDOWN, SYMMETRIC FLOWS ON DELTA WINGS



EFFECT OF LE SHAPE ON VORTEX BURST PROGRESSION
(KEGELMAN & ROOS)



Variation of k_{bd} with y_1



PROGRESSION RATE OF VORTEX BREAKDOWN FOR DELTA WINGS
IN AIR WITH EFFECT OF LE SWEEP & ASPECT RATIO

FIG. 6 ANALYSIS & EXTENSION OF VORTEX BREAKDOWN PROGRESSION, USING LAN & HSU PARAMETERS

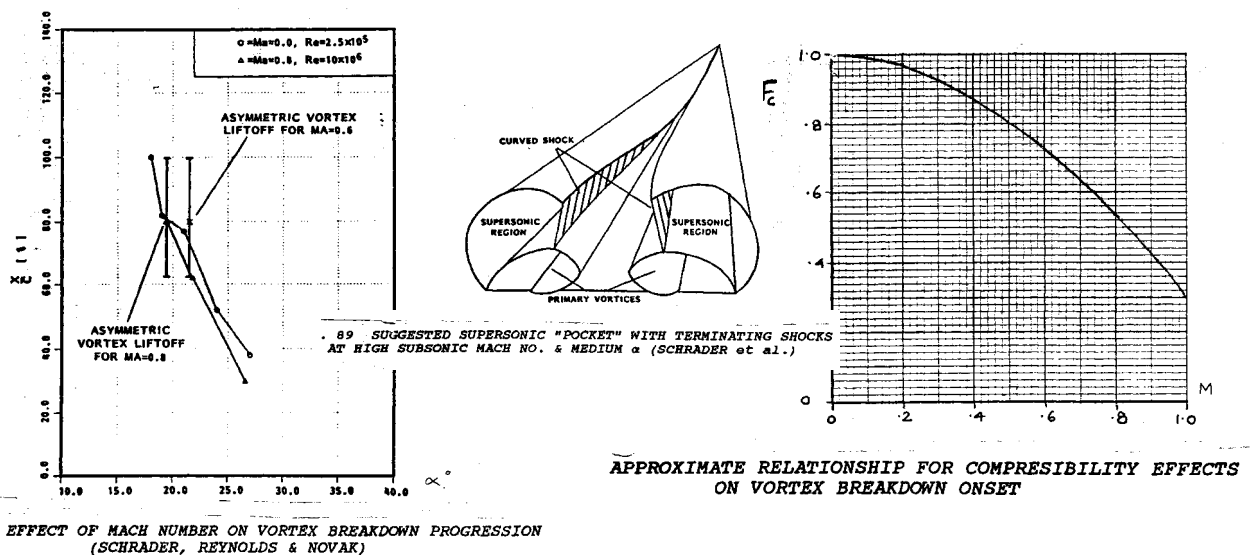


FIG. 7 INTRODUCING MACH NUMBER COMPRESSIBILITY EFFECTS ON VORTEX BREAKDOWN

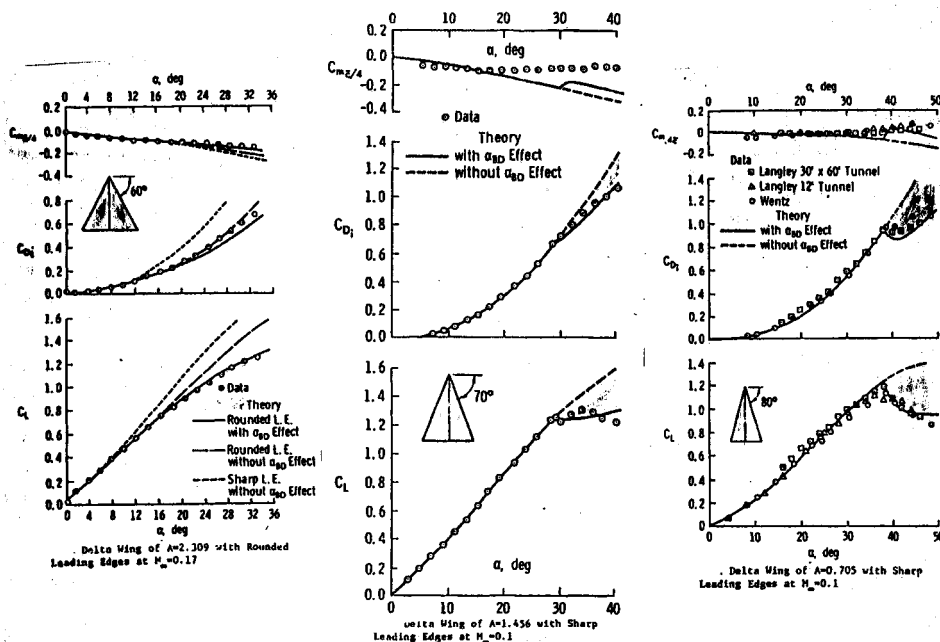


FIG. 8 RESULTS FOR PLANAR, SHARP-EDGED DELTA WINGS OF VARYING LE SWEEP (LAN & HSU)

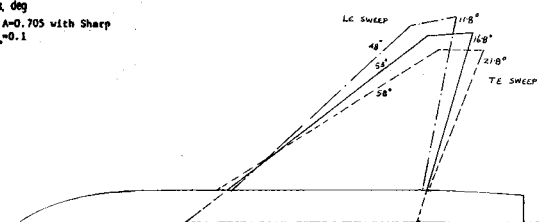
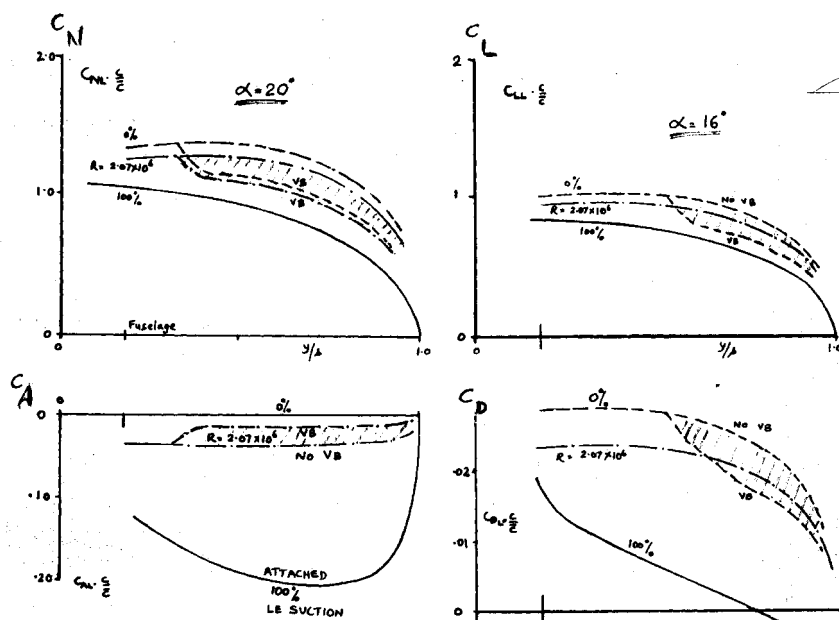


FIG. 9 EXPERIMENTAL MODEL WITH PIVOTED TWISTED & CAMBERED WINGS



(a) Symmetric Spanwise Loads

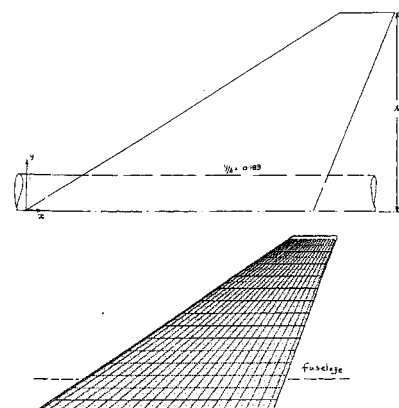
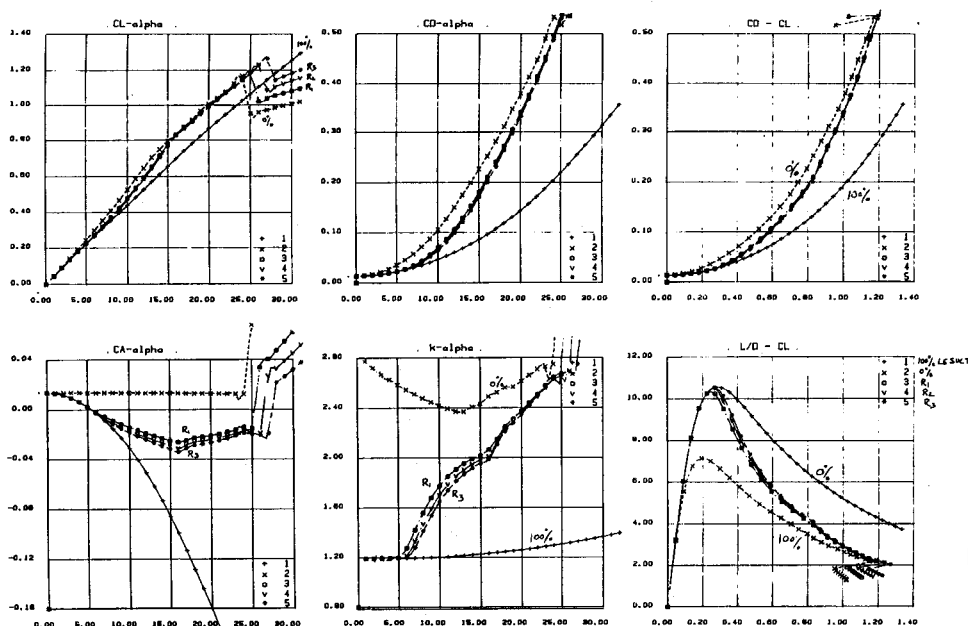


FIG. 10 TYPICAL MODELLING OF SYMMETRIC WING 58°



(b) Total Forces with Vortex Breakdown effects, R1, R2 & R3

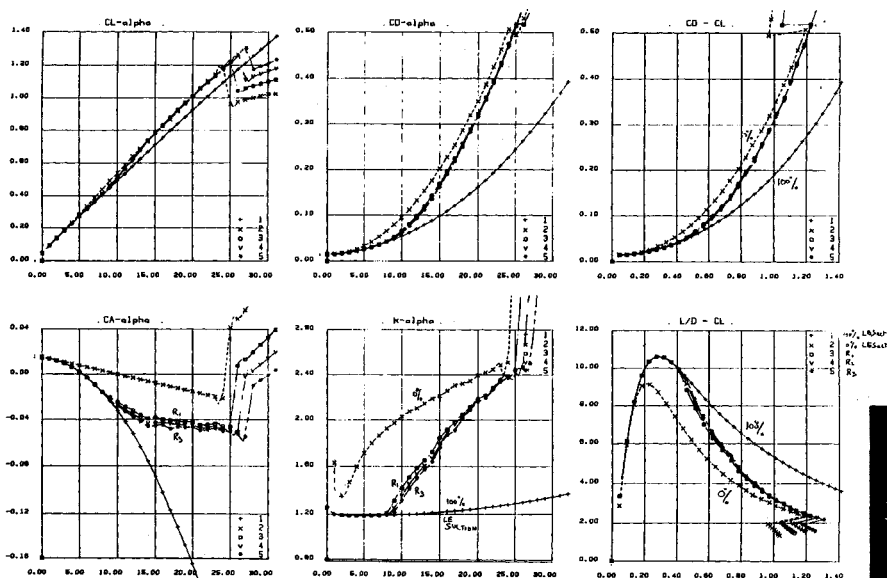


FIG. 12 TYPICAL RESULTS ON A SYMMETRIC 58° CAMBERED WING WITH VORTEX BREAKDOWN, TOTAL FORCES DEPICTED, $M=0.35$

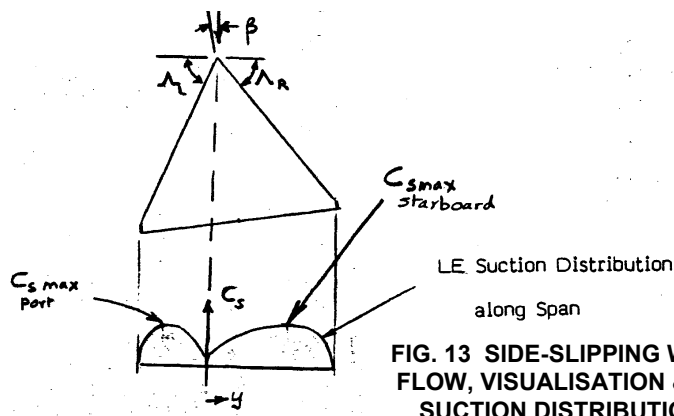


FIG. 13 SIDE-SLIPPING WING FLOW, VISUALISATION & LE SUCTION DISTRIBUTION

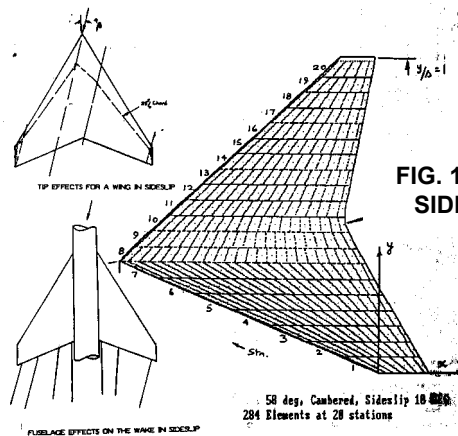


FIG. 14 MODELLING OF SIDE-SLIPPING WING

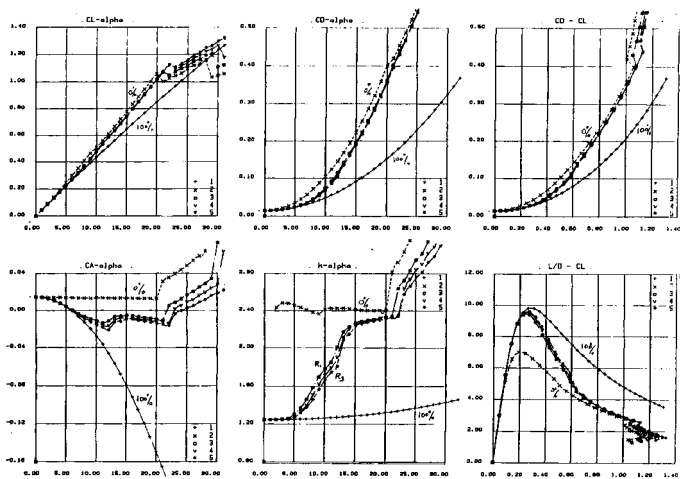
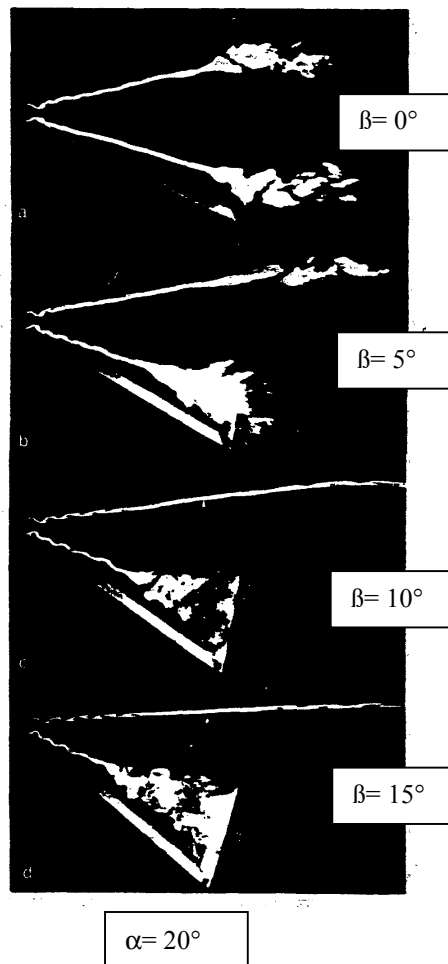


FIG. 15 TYPICAL RESULTS ON A PLANAR 58° WING, $\beta = 10^\circ$, WITH VORTEX BREAKDOWN, TOTAL FORCES

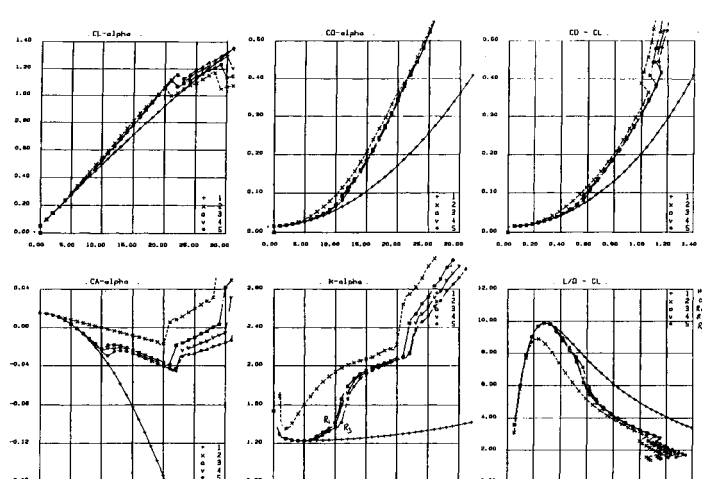


FIG. 16 TYPICAL RESULTS ON A CAMBERED 58° WING, $\beta = 10^\circ$, WITH VORTEX BREAKDOWN, TOTAL FORCES

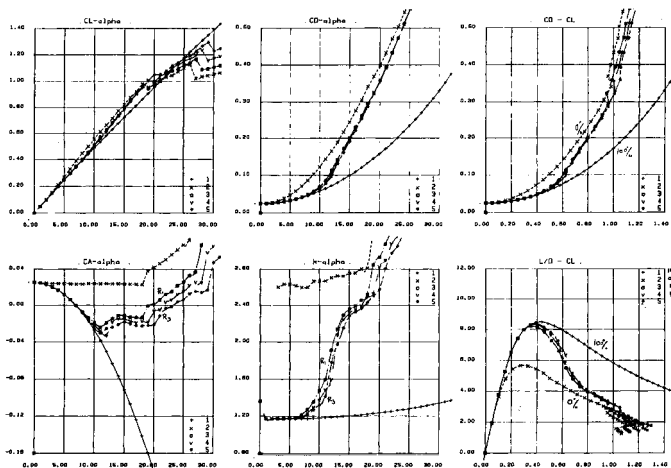


FIG. 17 TYPICAL RESULTS ON A PLANAR 53° WING, SIDESLIP 10°, WITH VORTEX BREAKDOWN, TOTAL FORCES, $M = 0.2$

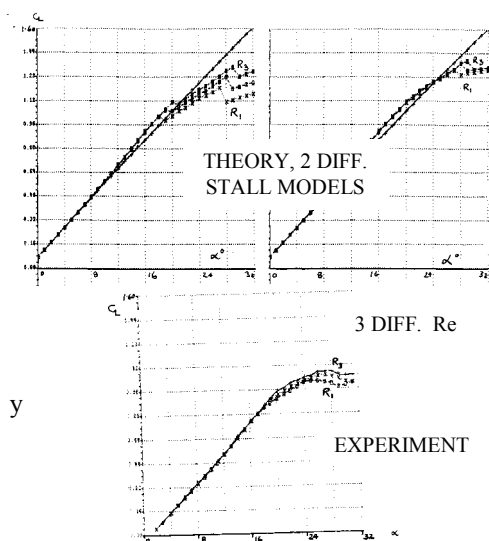


FIG. 19 $CL - \alpha$ GRAPHS ON CAMBERED 53° WING, $\beta = 10^\circ$, THEORY & EXPERIMENT, $M = 0.2$

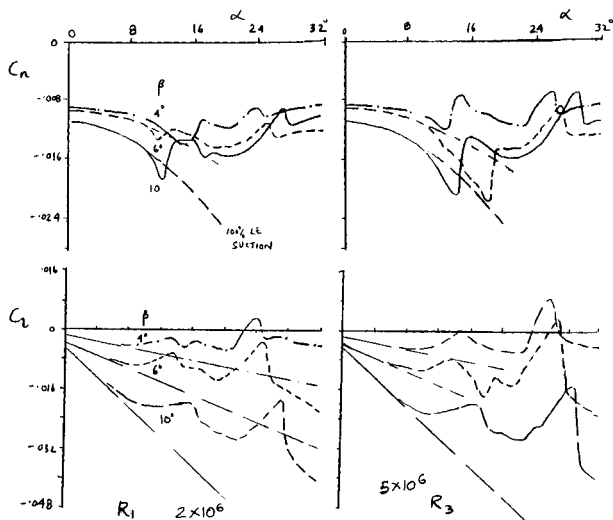


FIG. 20 53° CAMBERED WING, SIDESLIP EFFECT ON C_1 & C_n RELATIONSHIPS, THEORY WITH STALL MODEL, $M = 0, 2$, $Re: R_1$ & R_3

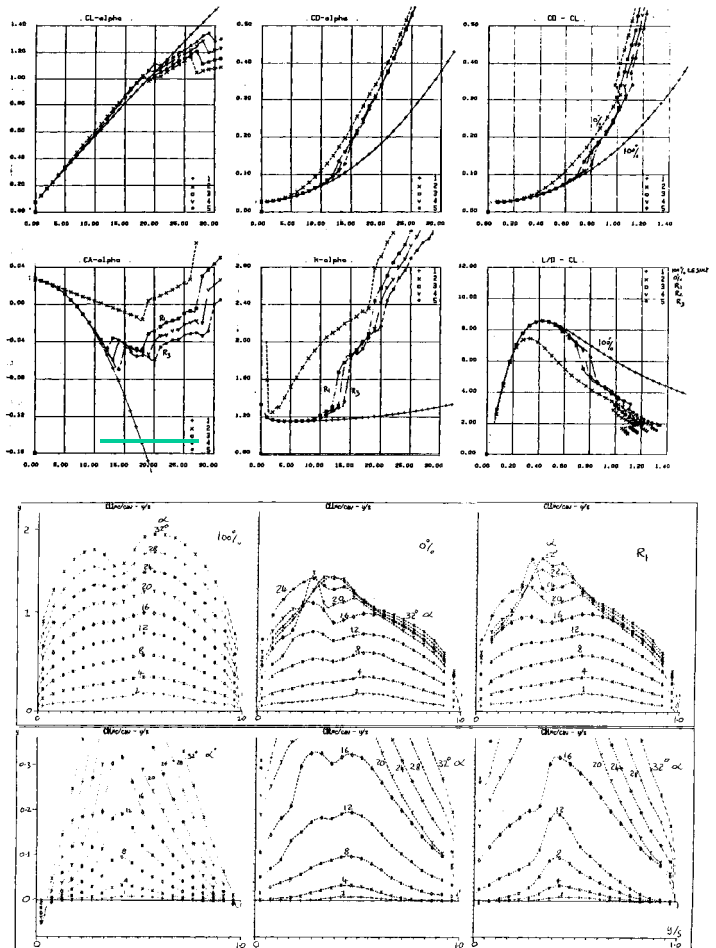


FIG. 18 TYPICAL RESULTS ON A CAMBERED 53° WING, $\beta = 10^\circ$, WITH VORTEX BREAKDOWN, TOTAL FORCES SPANWISE LOADS, $M = 0.2$

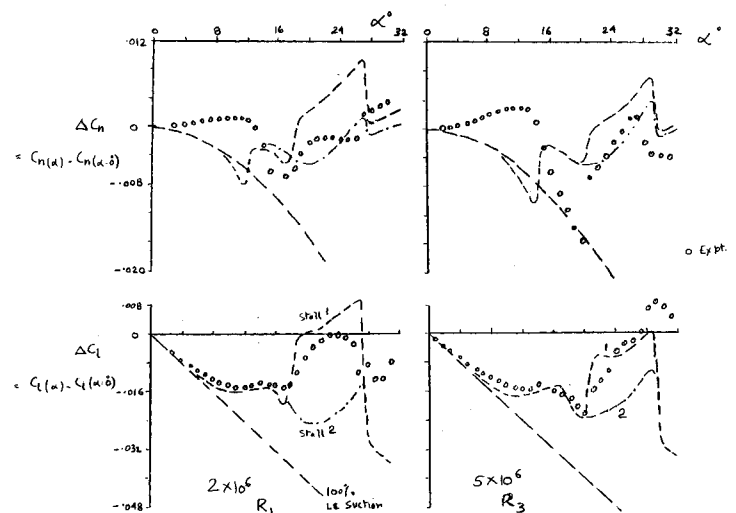
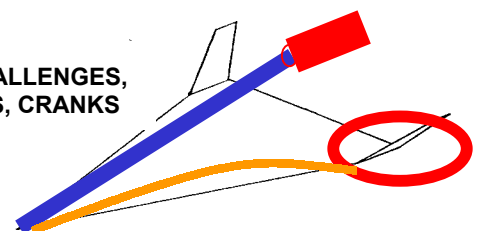


FIG. 21 53° CAMBERED WING, ΔC_1 & ΔC_n (Discount intercepts at $\alpha = 0^\circ$) RELATIONSHIPS, THEORY & EXPERIMENT, $\beta = 10^\circ$, $M = 0, 2$, $Re: R_1$ & R_3

FIG. 22 CHALLENGES, WINGLETS, CRANKS



Chapter 24 – CONCLUSIONS AND RECOMMENDATIONS

N. Verhaagen

Delft University of Technology
Department of Aerospace Engineering
P.O. Box 5058, 2600 GB, Delft, the Netherlands
n.g.verhaagen@tudelft.nl

X. Huang

Institute for Aerospace Research
National Research Council
1200 Montreal Rd.
Ottawa, Ont. Canada K1A 0R6
xingzhong.huang@nrc.ca

Extensive results and findings of the NATO Research and Technology Organization (RTO) Applied Vehicle Technology Panel (AVT) Task Group – 080 “Vortex Breakdown over Slander Wings” have been presented in three major categories.

The Experimental Sub-Group has compiled an extended experimental database consisting of eight test cases generated at various research institutes. Most experimental data has been obtained on models with leading-edge sweeps ranging from 55° to 80°. Most models have sharp leading edges, whereas some models were provided with elliptical or round leading edges. Static and/or dynamic data were generated in water and wind tunnels at Reynolds numbers up to 120×10^6 and Mach number up to 0.9. The dynamic data were obtained from tests performed on models undergoing pitch and/or roll oscillations and coning motions.

The test cases were subdivided into three categories; time-average results at static model conditions, ensemble-average results at dynamic model conditions and unsteady results at static/dynamic model conditions.

The static data provided the time-averaged model surface skin-friction-line pattern and conjectured surface flow topology, the surface pressure distribution as measured by pressure taps or Pressure Sensitive Paint (PSP), the time-averaged vortex breakdown location, three-dimensional velocity vector field measured by Laser Doppler Velocimetry (LDV) or Particle Image Velocimetry (PIV), and the forces and moments. At dynamic model conditions results are given of smoke/laser-light-sheet flow visualization, ensemble-average balance data, surface-pressure distributions (measured with unsteady pressure transducers), as well as the free and forced motion history. Unsteady results at static/dynamic model conditions include recordings of the instantaneous azimuthal vorticity, RMS swirl velocity, spectra and fluctuation of breakdown locations, pressure fluctuations on wing and tail fin, etc.

Considering the limited time, manpower and CFD capability available, it has been decided to limit the benchmark for the CFD exercise to a first category test case; a study of the time-averaged vortex behaviour at static model conditions on an ONERA 70° swept delta wing has been taken as the benchmark for the validation and verification of the CFD solutions. Although this and the other compiled test cases provide very valuable data, there still exists an imminent demand for a comprehensive experimental data set containing measurements of both the flow on and off the model surface as well as balance measurements. As vorticity flux and its unsteady behaviour in the boundary layer before its separation have a remarkable impact on the vortex and vortex breakdown, more detailed information is needed on the location of the laminar-to-turbulent transition line and – in the case of a rounded leading edge - the location of the primary separation line and separation on-set. Along with steady data, detailed unsteady

CONCLUSIONS AND RECOMMENDATIONS

surface and flowfield data also needs to be generated in order to complete the dataset on the free shear layer and vortex breakdown flow phenomenon. Moreover, as the vortex, especially its breakdown, has nonlinear response to the model motion, the spectral information, in frequency domain, and time delay or the response function, in time domain, are even challenges both in academic and real application

The CFD-subgroup has generated nine state-of-the-art solutions for the flow over the ONERA 70° swept delta wing and for some other delta wing planforms. The choice of governing equations included Euler, Reynolds-Averaged-Navier-Stokes (RANS) with and without rotation corrections, Detached Eddy Simulations (DES) and Large Eddy Simulations (LES). Both steady and unsteady solutions were computed and structured and unstructured grid solvers were used.

Euler calculations gave a relatively accurate prediction of the vortex breakdown locations, but did not capture the details of the physics of the leading-edge vortices.

Both structured and unstructured solvers demonstrate the ability to capture vortex breakdown as long as there is enough grid resolution in the vortex core and the model has sharp leading-edge. Grid-refinement studies show that a finer grid increases the core properties and turbulence levels within the vortex, whereas vortex breakdown is delayed. It is further demonstrated that adapted-grid solutions are superior in capturing the vortex flow structure over the conventional unadapted-grid solutions. High-order spatial discretization is capable of capturing finer scales of the flow field on a given mesh resolution and of resolving the origin of the so-called unsteady and stationary substructures observed in the vortex flow experiments. Time accuracy is another important parameter when computing unsteady flow phenomenon such as vortex breakdown.

Computational results demonstrate the importance of including both the sting and wind tunnel walls for validation of CFD results with the experimental data at all angles of attack. The solutions show that the local effective incidence along the leading edge increases when the sidewall moves closer to the wing. This increases the vortex helix angle and tends to promote vortex breakdown. The influence of the sidewalls on the secondary vortices was also assessed; the secondary separation line moves towards the leading edge and its helix angle increases with decreasing tunnel width.

Downstream support structures with a large frontal area were found to have no effect on the flow prior to vortex breakdown. The blockage of the support caused a significant acceleration of the flow, which had the effect of delaying vortex breakdown. The effect of the downstream support is heavily dependent on whether or not the core flow impinges on the structure. The effects are likely to be Reynolds number dependent.

The computational results show the importance of modelling a full-span delta wing in order to accurately capture the oscillations of the vortex breakdown locations and the asymmetry in the breakdown location on the port and starboard halves of the delta wing. The interactions between the leading-edge vortices are lost when semi-span grids are used, especially, at higher angles of attack.

Calculations were performed for the case of a semi-span wing with a symmetry condition in the center section of the wing and for the case of a full wing without such a symmetry condition. Without a symmetry condition, even for symmetrical free stream conditions the flow field turned out to be unsymmetrical: different vortex breakdown positions, frequencies and phase differences in the rotation of the spiral vortex axes and modifications of the vortex axes were found for both sides of the wing.

The calculations were performed using a wide variety of turbulence models. The type of turbulence model applied has a significant effect on both the characteristics of the vortical flow field and the vortex breakdown location. Dissipation of turbulent kinetic energy and vorticity drastically alter the flow field characteristics. Rotational corrections have a significant impact on the computational solutions. DES is capable of predicating the fluctuating vortex breakdown location quite accurately

Transition from laminar to turbulent flow is a key aspect in defining the characteristics of the vortical flow field. Transition occurs over the surface of the delta wing, but also within the vortex core. At this time,

there is no reliable method of computationally identifying transition. It can be artificially forced within the computations in order to more closely match the

The Analytical-subgroup has examined three analytical methods.

An engineering method predicts the structure and behavior of the vortex in its broken down state. The dynamics of the inner and outer core regions are treated separately. The breakdown process was modelled as a symmetry-breaking sub critical bifurcation from an axisymmetrical unburst vortex to a helically symmetric translating spiral burst form. Predictions agreed reasonable well with measured helix pitch, inclination, radius, induced and convection velocity, and frequency content. To predict the impact of vortex breakdown on the delta wing characteristics, a simple lift-loss model was developed. Predictions for the magnitude and the rate of onset of breakdown-induced lift loss agree with experimental data.

A modified Non-linear Indicial Response Functional model in conjunction with Internal State-Space representation method (NIRISS) uses the time-averaged vortex breakdown location as an internal variable to approximately describe the state of separated and vortex flow over the delta wing. The mathematical model was applied to estimate time-averaged vortex breakdown locations, normal force over delta wings with different sweep back angles, surface pressures and free-to-roll motion histories on a 65° delta wing. The comparisons between measured and estimated data showed that within the framework of the proposed mathematical model, it is possible to apply this method to predict quantities in the nonlinear flight regime.

An empirical method predicts the forces and moments on delta-wing/body (and other) configurations in symmetric and asymmetric flights, including Mach and Reynolds number effects. The method is based on subsonic lifting surface theory, semi-empirical “attained” thrust and vortex effects and coupled with a model to predict vortex breakdown. Predictions for the forces and moments of 53° and 58° swept trapezium wings, with and without sideslip, for various Mach and Reynolds numbers showed a promising correlation with available experimental data.

CONCLUSIONS AND RECOMMENDATIONS



REPORT DOCUMENTATION PAGE																								
1. Recipient's Reference	2. Originator's References	3. Further Reference	4. Security Classification of Document																					
	RTO-TR-AVT-080 AC/323(AVT-080)TP/253	ISBN 978-92-837-0078-4	UNCLASSIFIED/ UNLIMITED																					
5. Originator Research and Technology Organisation North Atlantic Treaty Organisation BP 25, F-92201 Neuilly-sur-Seine Cedex, France																								
6. Title Vortex Breakdown over Slender Delta Wings																								
7. Presented at/Sponsored by This Report documents the goals and achievements of NATO/RTO/AVT Task Group AVT-080.																								
8. Author(s)/Editor(s) Multiple			9. Date October 2009																					
10. Author's/Editor's Address Multiple			11. Pages 594																					
12. Distribution Statement There are no restrictions on the distribution of this document. Information about the availability of this and other RTO unclassified publications is given on the back cover.																								
13. Keywords/Descriptors																								
<table border="0"> <tbody> <tr> <td>Aerodynamic characteristics</td> <td>Delta wings</td> <td>Predictions</td> </tr> <tr> <td>Aerodynamic configurations</td> <td>Flow control</td> <td>Swept wings</td> </tr> <tr> <td>Aerodynamic stability</td> <td>Flow distribution</td> <td>Vortex dynamics</td> </tr> <tr> <td>Aerodynamics</td> <td>Flow structure</td> <td>Vortex stability and breakouts</td> </tr> <tr> <td>Boundary layer</td> <td>Leading edges</td> <td>Vortices</td> </tr> <tr> <td>Computerized simulation</td> <td>Mathematical models</td> <td>Wings</td> </tr> <tr> <td>Data acquisition</td> <td>Models</td> <td></td> </tr> </tbody> </table>				Aerodynamic characteristics	Delta wings	Predictions	Aerodynamic configurations	Flow control	Swept wings	Aerodynamic stability	Flow distribution	Vortex dynamics	Aerodynamics	Flow structure	Vortex stability and breakouts	Boundary layer	Leading edges	Vortices	Computerized simulation	Mathematical models	Wings	Data acquisition	Models	
Aerodynamic characteristics	Delta wings	Predictions																						
Aerodynamic configurations	Flow control	Swept wings																						
Aerodynamic stability	Flow distribution	Vortex dynamics																						
Aerodynamics	Flow structure	Vortex stability and breakouts																						
Boundary layer	Leading edges	Vortices																						
Computerized simulation	Mathematical models	Wings																						
Data acquisition	Models																							
14. Abstract																								
<p>The report contains a study of the phenomenon of leading-edge vortex breakdown over slender delta wings conducted by the NATO/RTO/AVT Task Group AVT-080. After an introduction and discussion of highlights, a chapter is devoted to a critical assessment of available experimental studies of the vortex breakdown phenomenon. Eight reliable experimental data sets are collected and compiled. These data sets are described in separate chapters and were obtained on more or less identical delta wing models tested in different wind tunnel test facilities. The datasets include time-average results at static model conditions, ensemble-average results at dynamic model conditions and unsteady results at static/dynamic model conditions. Based on the critical assessment, a benchmark test case is selected that provides sufficiently reliable data for validation of the numerical predictions. In separate chapters ten state-of-the-art numerical solutions from various research institutes are described that have been obtained for the benchmark test case configuration and test conditions. Studies of the effects of parameters like grid density, turbulence modeling, time scaling, etc., have been performed. In addition, for a special delta wing configuration, the effects of tunnel wall interference and of interactions between vortices have been calculated. In the final three chapters advanced analytical methods are described.</p> <p>The report is of great value to scientists involved in the development of design methods for military aircraft configurations, but also for high speed civil and/or space aircraft.</p>																								





BP 25

F-92201 NEUILLY-SUR-SEINE CEDEX • FRANCE
Télécopie 0(1)55.61.22.99 • E-mail mailbox@rta.nato.int**DIFFUSION DES PUBLICATIONS**
RTO NON CLASSIFIEES

Les publications de l'AGARD et de la RTO peuvent parfois être obtenues auprès des centres nationaux de distribution indiqués ci-dessous. Si vous souhaitez recevoir toutes les publications de la RTO, ou simplement celles qui concernent certains Panels, vous pouvez demander d'être inclus soit à titre personnel, soit au nom de votre organisation, sur la liste d'envoi.

Les publications de la RTO et de l'AGARD sont également en vente auprès des agences de vente indiquées ci-dessous.

Les demandes de documents RTO ou AGARD doivent comporter la dénomination « RTO » ou « AGARD » selon le cas, suivi du numéro de série. Des informations analogues, telles que le titre et la date de publication sont souhaitables.

Si vous souhaitez recevoir une notification électronique de la disponibilité des rapports de la RTO au fur et à mesure de leur publication, vous pouvez consulter notre site Web (www.rto.nato.int) et vous abonner à ce service.

CENTRES DE DIFFUSION NATIONAUX**ALLEMAGNE**

Streitkräfteamt / Abteilung III
Fachinformationszentrum der Bundeswehr (FIZBw)
Gorch-Fock-Straße 7, D-53229 Bonn

BELGIQUE

Royal High Institute for Defence – KHID/IRSD/RHID
Management of Scientific & Technological Research
for Defence, National RTO Coordinator
Royal Military Academy – Campus Renaissance
Renaissancelaan 30, 1000 Bruxelles

CANADA

DSIGRD2 – Bibliothécaire des ressources du savoir
R et D pour la défense Canada
Ministère de la Défense nationale
305, rue Rideau, 9^e étage
Ottawa, Ontario K1A 0K2

DANEMARK

Danish Acquisition and Logistics Organization (DALO)
Lautrupbjerg 1-5, 2750 Ballerup

ESPAGNE

SDG TECEN / DGAM
C/ Arturo Soria 289
Madrid 28033

ETATS-UNIS

NASA Center for AeroSpace Information (CASI)
7115 Standard Drive
Hanover, MD 21076-1320

FRANCE

O.N.E.R.A. (ISP)
29, Avenue de la Division Leclerc
BP 72, 92322 Châtillon Cedex

GRECE (Correspondant)

Defence Industry & Research General
Directorate, Research Directorate
Fakinos Base Camp, S.T.G. 1020
Holargos, Athens

HONGRIE

Department for Scientific Analysis
Institute of Military Technology
Ministry of Defence
P O Box 26
H-1525 Budapest

ITALIE

General Secretariat of Defence and
National Armaments Directorate
5th Department – Technological
Research
Via XX Settembre 123
00187 Roma

LUXEMBOURG

Voir Belgique

NORVEGE

Norwegian Defence Research
Establishment
Attn: Biblioteket
P.O. Box 25
NO-2007 Kjeller

PAYS-BAS

Royal Netherlands Military
Academy Library
P.O. Box 90.002
4800 PA Breda

POLOGNE

Centralny Ośrodek Naukowej
Informacji Wojskowej
Al. Jerozolimskie 97
00-909 Warszawa

PORTUGAL

Estado Maior da Força Aérea
SDFA – Centro de Documentação
Alfragide
P-2720 Amadora

REPUBLIQUE TCHEQUE

LOM PRAHA s. p.
o. z. VTÚLaPVO
Mladoboleslavská 944
PO Box 18
197 21 Praha 9

ROUMANIE

Romanian National Distribution
Centre
Armaments Department
9-11, Drumul Taberei Street
Sector 6
061353, Bucharest

ROYAUME-UNI

Dstl Knowledge and Information
Services
Building 247
Porton Down
Salisbury SP4 0JQ

SLOVAQUIE

Akadémia ozbrojených síl
M.R. Štefánika, Distribučné a
informačné stredisko RTO
Demanova 393, P.O.Box 45
031 19 Liptovský Mikuláš

SLOVENIE

Ministry of Defence
Central Registry for EU and
NATO
Vojkova 55
1000 Ljubljana

TURQUIE

Milli Savunma Bakanlığı (MSB)
ARGE ve Teknoloji Dairesi
Başkanlığı
06650 Bakanlıklar
Ankara

AGENCES DE VENTE**NASA Center for AeroSpace
Information (CASI)**

7115 Standard Drive
Hanover, MD 21076-1320
ETATS-UNIS

**The British Library Document
Supply Centre**

Boston Spa, Wetherby
West Yorkshire LS23 7BQ
ROYAUME-UNI

**Canada Institute for Scientific and
Technical Information (CISTI)**

National Research Council Acquisitions
Montreal Road, Building M-55
Ottawa K1A 0S2, CANADA

Les demandes de documents RTO ou AGARD doivent comporter la dénomination « RTO » ou « AGARD » selon le cas, suivie du numéro de série (par exemple AGARD-AG-315). Des informations analogues, telles que le titre et la date de publication sont souhaitables. Des références bibliographiques complètes ainsi que des résumés des publications RTO et AGARD figurent dans les journaux suivants :

Scientific and Technical Aerospace Reports (STAR)

STAR peut être consulté en ligne au localisateur de ressources
uniformes (URL) suivant: <http://www.sti.nasa.gov/Pubs/star/Star.html>
STAR est édité par CASI dans le cadre du programme
NASA d'information scientifique et technique (STI)
STI Program Office, MS 157A
NASA Langley Research Center
Hampton, Virginia 23681-0001
ETATS-UNIS

Government Reports Announcements & Index (GRA&I)

publié par le National Technical Information Service
Springfield
Virginia 2216
ETATS-UNIS
(accessible également en mode interactif dans la base de
données bibliographiques en ligne du NTIS, et sur CD-ROM)



BP 25

F-92201 NEUILLY-SUR-SEINE CEDEX • FRANCE
Télécopie 0(1)55.61.22.99 • E-mail mailbox@rta.nato.int



DISTRIBUTION OF UNCLASSIFIED RTO PUBLICATIONS

AGARD & RTO publications are sometimes available from the National Distribution Centres listed below. If you wish to receive all RTO reports, or just those relating to one or more specific RTO Panels, they may be willing to include you (or your Organisation) in their distribution.

RTO and AGARD reports may also be purchased from the Sales Agencies listed below.

Requests for RTO or AGARD documents should include the word 'RTO' or 'AGARD', as appropriate, followed by the serial number. Collateral information such as title and publication date is desirable.

If you wish to receive electronic notification of RTO reports as they are published, please visit our website (www.rto.nato.int) from where you can register for this service.

NATIONAL DISTRIBUTION CENTRES

BELGIUM

Royal High Institute for Defence – KHID/IRSD/RHID
Management of Scientific & Technological Research
for Defence, National RTO Coordinator
Royal Military Academy – Campus Renaissance
Renaissancelaan 30
1000 Brussels

CANADA

DRDKIM2 – Knowledge Resources Librarian
Defence R&D Canada
Department of National Defence
305 Rideau Street, 9th Floor
Ottawa, Ontario K1A 0K2

CZECH REPUBLIC

LOM PRAHA s. p.
o. z. VTÚLaPVO
Mladoboleslavská 944
PO Box 18
197 21 Praha 9

DENMARK

Danish Acquisition and Logistics Organization (DALO)
Lautrupbjerg 1-5
2750 Ballerup

FRANCE

O.N.E.R.A. (ISP)
29, Avenue de la Division Leclerc
BP 72, 92322 Châtillon Cedex

GERMANY

Streitkräfteamt / Abteilung III
Fachinformationszentrum der Bundeswehr (FIZBw)
Gorch-Fock-Straße 7
D-53229 Bonn

GREECE (Point of Contact)

Defence Industry & Research General Directorate
Research Directorate, Fakinos Base Camp
S.T.G. 1020
Holargos, Athens

HUNGARY

Department for Scientific Analysis
Institute of Military Technology
Ministry of Defence
P O Box 26
H-1525 Budapest

ITALY

General Secretariat of Defence and
National Armaments Directorate
5th Department – Technological
Research
Via XX Settembre 123
00187 Roma

LUXEMBOURG

See Belgium

NETHERLANDS

Royal Netherlands Military
Academy Library
P.O. Box 90.002
4800 PA Breda

NORWAY

Norwegian Defence Research
Establishment
Attn: Biblioteket
P.O. Box 25
NO-2007 Kjeller

POLAND

Centralny Ośrodek Naukowej
Informacji Wojskowej
Al. Jerozolimskie 97
00-909 Warszawa

PORTUGAL

Estado Maior da Força Aérea
SDFA – Centro de Documentação
Alfragide
P-2720 Amadora

ROMANIA

Romanian National Distribution
Centre
Armaments Department
9-11, Drumul Taberei Street
Sector 6, 061353, Bucharest

SLOVAKIA

Akadémia ozbrojených síl
M.R. Štefánika, Distribučné a
informačné stredisko RTO
Demanova 393, P.O.Box 45
031 19 Liptovský Mikuláš

SLOVENIA

Ministry of Defence
Central Registry for EU & NATO
Vojkova 55
1000 Ljubljana

SPAIN

SDG TECEN / DGAM
C/ Arturo Soria 289
Madrid 28033

TURKEY

Milli Savunma Bakanlığı (MSB)
ARGE ve Teknoloji Dairesi
Başkanlığı
06650 Bakanlıklar – Ankara

UNITED KINGDOM

Dstl Knowledge and Information
Services
Building 247
Porton Down
Salisbury SP4 0JQ

UNITED STATES

NASA Center for AeroSpace
Information (CASI)
7115 Standard Drive
Hanover, MD 21076-1320

SALES AGENCIES

NASA Center for AeroSpace Information (CASI)

7115 Standard Drive
Hanover, MD 21076-1320
UNITED STATES

The British Library Document Supply Centre

Boston Spa, Wetherby
West Yorkshire LS23 7BQ
UNITED KINGDOM

Canada Institute for Scientific and Technical Information (CISTI)

National Research Council Acquisitions
Montreal Road, Building M-55
Ottawa K1A 0S2, CANADA

Requests for RTO or AGARD documents should include the word 'RTO' or 'AGARD', as appropriate, followed by the serial number (for example AGARD-AG-315). Collateral information such as title and publication date is desirable. Full bibliographical references and abstracts of RTO and AGARD publications are given in the following journals:

Scientific and Technical Aerospace Reports (STAR)

STAR is available on-line at the following uniform resource
locator: <http://www.sti.nasa.gov/Pubs/star/Star.html>
STAR is published by CASI for the NASA Scientific
and Technical Information (STI) Program
STI Program Office, MS 157A
NASA Langley Research Center
Hampton, Virginia 23681-0001
UNITED STATES

Government Reports Announcements & Index (GRA&I)

published by the National Technical Information Service
Springfield
Virginia 2216
UNITED STATES
(also available online in the NTIS Bibliographic Database
or on CD-ROM)